

***Evaluation of High Temperature
Gas Cooled Reactor Performance:
Benchmark Analysis Related to
the PBMR-400, PBMM,
GT-MHR, HTR-10 and
the ASTRA Critical Facility***



IAEA

International Atomic Energy Agency

EVALUATION OF HIGH TEMPERATURE GAS COOLED REACTOR PERFORMANCE

The following States are Members of the International Atomic Energy Agency:

AFGHANISTAN	GUATEMALA	PANAMA
ALBANIA	HAITI	PAPUA NEW GUINEA
ALGERIA	HOLY SEE	PARAGUAY
ANGOLA	HONDURAS	PERU
ARGENTINA	HUNGARY	PHILIPPINES
ARMENIA	ICELAND	POLAND
AUSTRALIA	INDIA	PORTUGAL
AUSTRIA	INDONESIA	QATAR
AZERBAIJAN	IRAN, ISLAMIC REPUBLIC OF	REPUBLIC OF MOLDOVA
BAHRAIN	IRAQ	ROMANIA
BANGLADESH	IRELAND	RUSSIAN FEDERATION
BELARUS	ISRAEL	RWANDA
BELGIUM	ITALY	SAUDI ARABIA
BELIZE	JAMAICA	SENEGAL
BENIN	JAPAN	SERBIA
BOLIVIA	JORDAN	SEYCHELLES
BOSNIA AND HERZEGOVINA	KAZAKHSTAN	SIERRA LEONE
BOTSWANA	KENYA	SINGAPORE
BRAZIL	KOREA, REPUBLIC OF	SLOVAKIA
BULGARIA	KUWAIT	SLOVENIA
BURKINA FASO	KYRGYZSTAN	SOUTH AFRICA
BURUNDI	LAO PEOPLE'S DEMOCRATIC REPUBLIC	SPAIN
CAMBODIA	LATVIA	SRI LANKA
CAMEROON	LEBANON	SUDAN
CANADA	LESOTHO	SWAZILAND
CENTRAL AFRICAN REPUBLIC	LIBERIA	SWEDEN
CHAD	LIBYA	SWITZERLAND
CHILE	LIECHTENSTEIN	SYRIAN ARAB REPUBLIC
CHINA	LITHUANIA	TAJIKISTAN
COLOMBIA	LUXEMBOURG	THAILAND
CONGO	MADAGASCAR	THE FORMER YUGOSLAV REPUBLIC OF MACEDONIA
COSTA RICA	MALAWI	TOGO
CÔTE D'IVOIRE	MALAYSIA	TRINIDAD AND TOBAGO
CROATIA	MALI	TUNISIA
CUBA	MALTA	TURKEY
CYPRUS	MARSHALL ISLANDS	UGANDA
CZECH REPUBLIC	MAURITANIA	UKRAINE
DEMOCRATIC REPUBLIC OF THE CONGO	MAURITIUS	UNITED ARAB EMIRATES
DENMARK	MEXICO	UNITED KINGDOM OF GREAT BRITAIN AND NORTHERN IRELAND
DOMINICA	MONACO	UNITED REPUBLIC OF TANZANIA
DOMINICAN REPUBLIC	MONGOLIA	UNITED STATES OF AMERICA
ECUADOR	MONTENEGRO	URUGUAY
EGYPT	MOROCCO	UZBEKISTAN
EL SALVADOR	MOZAMBIQUE	VENEZUELA
ERITREA	MYANMAR	VIETNAM
ESTONIA	NAMIBIA	YEMEN
ETHIOPIA	NEPAL	ZAMBIA
FIJI	NETHERLANDS	ZIMBABWE
FINLAND	NEW ZEALAND	
FRANCE	NICARAGUA	
GABON	NIGER	
GEORGIA	NIGERIA	
GERMANY	NORWAY	
GHANA	OMAN	
GREECE	PAKISTAN	
	PALAU	

The Agency's Statute was approved on 23 October 1956 by the Conference on the Statute of the IAEA held at United Nations Headquarters, New York; it entered into force on 29 July 1957. The Headquarters of the Agency are situated in Vienna. Its principal objective is "to accelerate and enlarge the contribution of atomic energy to peace, health and prosperity throughout the world".

EVALUATION OF HIGH TEMPERATURE GAS COOLED REACTOR PERFORMANCE

BENCHMARK ANALYSIS RELATED TO
THE PBMR-400, PBMM, GT-MHR, HTR-10 AND
THE ASTRA CRITICAL FACILITY

COPYRIGHT NOTICE

All IAEA scientific and technical publications are protected by the terms of the Universal Copyright Convention as adopted in 1952 (Berne) and as revised in 1972 (Paris). The copyright has since been extended by the World Intellectual Property Organization (Geneva) to include electronic and virtual intellectual property. Permission to use whole or parts of texts contained in IAEA publications in printed or electronic form must be obtained and is usually subject to royalty agreements. Proposals for non-commercial reproductions and translations are welcomed and considered on a case-by-case basis. Enquiries should be addressed to the IAEA Publishing Section at:

Marketing and Sales Unit, Publishing Section
International Atomic Energy Agency
Vienna International Centre
PO Box 100
1400 Vienna, Austria
fax: +43 1 2600 29302
tel.: +43 1 2600 22417
email: sales.publications@iaea.org
<http://www.iaea.org/books>

For further information on this publication, please contact:

Nuclear Power Technology Development Section
International Atomic Energy Agency
Vienna International Centre
PO Box 100
1400 Vienna, Austria
email: Official.Mail@iaea.org

© IAEA, 2013

Printed by the IAEA in Austria
April 2013

IAEA Library Cataloguing in Publication Data

Evaluation of high temperature gas cooled reactor performance:
benchmark analysis related to the PBMR-400, PBMM,
GT-MHR, HTR-10 and the ASTRA critical facility. – Vienna:
International Atomic Energy Agency, 2013.
p. 30 cm. – (IAEA-TECDOC series, ISSN 1011-4289;
no. 1694)
ISBN 978-92-0-137610-7
Includes bibliographical references.

1. Gas cooled reactors. 2. Nuclear power plants –
International cooperation. 3. Nuclear reactors – Computer
programs.
I. International Atomic Energy Agency. II. Series.

IAEAL

13-01321

FOREWORD

The IAEA has facilitated an extensive programme that addresses the technical development of advanced gas cooled reactor technology. Included in this programme is the coordinated research project (CRP) on Evaluation of High Temperature Gas Cooled Reactor (HTGR) Performance, which is the focus of this TECDOC.

This CRP was established to foster the sharing of research and associated technical information among participating Member States in the ongoing development of the HTGR as a future source of nuclear energy. Within it, computer codes and models were verified through actual test results from operating reactor facilities.

The work carried out in the CRP involved both computational and experimental analysis at various facilities in IAEA Member States with a view to verifying computer codes and methods in particular, and to evaluating the performance of HTGRs in general. The IAEA is grateful to China, the Russian Federation and South Africa for providing their facilities and benchmark programmes in support of this CRP. The IAEA officers responsible for this publication were M. Methnani and B. Tyobeka of the Division of Nuclear Power.

EDITORIAL NOTE

This publication (including the figures, tables and references) has undergone only the minimum copy editing considered necessary for the reader's assistance.

The views expressed do not necessarily reflect those of the IAEA, the governments of the nominating Member States or the nominating organizations.

The use of particular designations of countries or territories does not imply any judgement by the publisher, the IAEA, as to the legal status of such countries or territories, of their authorities and institutions or of the delimitation of their boundaries.

The mention of names of specific companies or products (whether or not indicated as registered) does not imply any intention to infringe proprietary rights, nor should it be construed as an endorsement or recommendation on the part of the IAEA.

The authors are responsible for having obtained the necessary permission for the IAEA to reproduce, translate or use material from sources already protected by copyrights.

CONTENTS

1.	INTRODUCTION.....	1
2.	THE HTR-10 BENCHMARKS	2
2.1.	HTR-10 GENERAL INFORMATION.....	2
2.1.1.	Facility description	2
2.1.2.	Recommended material properties and correlations for main components.....	16
2.2.	HTR-10 STEADY STATE BENCHMARK DESCRIPTION AND RESULTS	19
2.2.1.	Steady state temperature distribution benchmark problem description.....	19
2.2.2.	HTR-10 steady state temperature distribution analysis and results.....	20
2.3.	HTR-10 LOSS OF PRIMARY FLOW WITHOUT SCRAM BENCHMARK PROBLEM	110
2.3.1.	Loss of primary flow without scram benchmark problem description.....	110
2.3.2.	Loss of flow without scram benchmark analysis and results	111
2.4.	HTR-10 CONTROL ROD (CR) WITHDRAWAL WITHOUT SCRAM BENCHMARK PROBLEM	135
2.4.1.	HTR-10 CR withdrawal without scram benchmark problem description	135
2.4.2.	HTR-10 CR withdrawal without scram benchmark analysis and results.....	136
2.5.	REFERENCES FOR CHAPTER 2.....	148
3.	ASTRA CRITICAL FACILITY	151
3.1.	ASTRA GENERAL INFORMATION	152
3.1.1.	Facility description	152
3.1.2.	Benchmark problem descriptions	160
3.2.	BENCHMARK PROBLEM ANALYSIS AND RESULTS	165
3.2.1.	ASTRA experimental results (submitted by South Africa).....	165
3.2.2.	ASTRA results, South Africa	170
3.2.3.	ASTRA results, China	176
3.2.4.	ASTRA results, Indonesia	179
3.2.5.	ASTRA results, Turkey	184
3.2.6.	ASTRA results, France.....	188
3.2.7.	ASTRA results, United Kingdom.....	194
3.3.	REFERENCES FOR CHAPTER 3.....	202
4.	PEBBLE BED MODULAR REACTOR	205
4.1.	PBMR GENERAL INFORMATION	205
4.1.1.	Facility description (Status in 2004/2005)	205
4.1.2.	PBMR core	208
4.1.3.	PBMR fuel.....	211
4.1.4.	Power conversion unit	212
4.1.5.	PBMR safety	214
4.1.6.	PBMR commercialization	218
4.1.7.	PBMR company status (2011).....	220

4.2.	PBMR-400 NEUTRONICS AND THERMAL HYDRAULICS	220
4.2.1.	Neutronics and thermohydraulics benchmark problem descriptions	220
4.2.2.	Benchmark calculational case definitions	237
4.2.3.	Analysis and results for PBMR-400 neutronics and thermohydraulics	240
4.3.	PBMR ‘PEBBLE BOX’	324
4.3.1.	PBMR ‘pebble box’ benchmark problem definition	324
4.3.2.	‘Pebble box’ analysis and results	330
4.4.	REFERENCES FOR CHAPTER 4.....	382
5.	PEBBLE BED MICROMODEL	385
5.1.	LAYOUT OF THE PBMM	385
5.1.1.	Description of the PBMM cycle.....	385
5.1.2.	Objectives of the PBMM project.....	386
5.2.	COMPONENT DATA.....	387
5.2.1.	Major components	387
5.2.2.	Compressor and turbine data	397
5.2.3.	Heat exchangers.....	415
5.2.4.	Heat source	419
5.2.5.	Aft and forward components	422
5.2.6.	Pressure boundary	423
5.2.7.	Control valves.....	424
5.3.	BENCHMARK DEFINITIONS	425
5.3.1.	Boundary conditions for steady state benchmarks	426
5.3.2.	Transient benchmark	427
5.4.	PBMM ANALYSIS AND RESULTS	428
5.4.1.	Experimental and simulation results for the PBMM benchmarks, South Africa.....	428
5.4.2.	PBMM results, United States of America	435
5.4.3.	PBMM results, Japan.....	443
5.4.4.	PBMM Results, Republic of Korea.....	451
5.4.5.	PBMM results, France	460
5.5.	REFERENCES FOR CHAPTER 5.....	483
6.	GAS TURBINE-MODULAR HELIUM REACTOR (GT-MHR).....	485
6.1.	GT-MHR GENERAL INFORMATION	485
6.1.1.	Facility description	485
6.2.	GT-MHR PLUTONIUM FUEL BENCHMARK PROBLEM DEFINITION	490
6.2.1.	The GT-MHR benchmark — Investigation of elementary cells	490
6.2.2.	The GT-MHR benchmark — Investigation of fuel assembly cell and 3-D reactor model.....	497
6.3.	GT-MHR PLUTONIUM FUEL BENCHMARK RESULTS	511
6.3.1.	GT-MHR plutonium fuel benchmark results, Russian Federation.....	511
6.3.2.	GT-MHR benchmark results, France	548
6.3.3.	GT-MHR benchmark problem results, Republic of Korea	571
6.4.	REFERENCES FOR CHAPTER 6.....	596
7.	COMPARISON OF RESULTS AND CONCLUSIONS.....	599

7.1.	HTR-10 BENCHMARK COMPARISON OF RESULTS	599
7.1.1.	Temperature distribution comparison of results	599
7.1.2.	Temperature distribution conclusions/recommendations	603
7.1.3.	HTR-10 loss of flow comparison of results	603
7.1.4.	Loss of flow conclusions/recommendations	604
7.1.5.	HTR-10 CRD withdrawal without scram comparison of results	606
7.1.6.	CRD withdrawal conclusions/recommendations	607
7.1.7.	Final comments on the HTR-10 code to measured benchmark	607
7.2.	ASTRA CRITICAL FACILITY	608
7.2.1.	Critical core height — Comparison of results	608
7.2.2.	Control rod worth — Comparison of results	609
7.2.3.	Differential rod worth vs insertion depth — Comparison of results	611
7.2.4.	Effect of critical height on critical parameters — Comparison of results	611
7.2.5.	General comments	612
7.3.	PBMR-400 COLLATION OF RESULTS	612
7.3.1.	PBMR neutronics and thermohydraulic benchmarks — Comparison of results	612
7.3.2.	‘Pebble Box’ benchmark — Comparison of results	619
7.3.3.	Comments and conclusions on the PBMR-400 and ‘Pebble Box’ benchmark test cases	624
7.4.	PBMM COLLATION OF RESULTS	625
7.4.1.	Comparison of results	625
7.4.2.	Conclusions and recommendations	630
7.5.	GT-MHR COLLATION OF RESULTS	631
7.5.1.	Analysis of simple cells benchmarking results	631
7.5.2.	Analysis of FA1 and reactor benchmarking results	634
7.6.	CONCLUSIONS AND RECOMMENDATIONS	636
APPENDIX	ADDITIONAL BENCHMARK ANALYSIS ASSOCIATED WITH IAEA-TECDOC-1382	637
CONTRIBUTORS TO DRAFTING AND REVIEW		673
RESEARCH COORDINATION MEETINGS		675
RELATED IAEA PUBLICATIONS		675

1. INTRODUCTION

International coordination in the development of the modular High temperature Gas cooled Reactor (HTGR) as a safe and efficient nuclear energy source for the production of electricity and industrial process heat applications is a primary function of the IAEA's Gas Cooled Reactor (GCR) programme.

A key aspect of this development process is the predicted capability for this advanced nuclear plant to achieve a high degree of safety through reliance on passive safety features. Because of this, the investigation and validation of the safety and operational aspects of the HTGR were the primary focus for many of the Coordinated Research Projects (CRPs) initiated by the IAEA in the 1990s and early 2000s. These included:

- The neutronic physics behaviour of the HTGR core;
- Fuel performance and fission product behaviour;
- The ability of the HTGR to dissipate decay heat by natural transport mechanisms;
- The design and evaluation of the HTGR-related heat utilization systems;
- Evaluation of the HTGR performance: Benchmark analysis related to initial testing of the High Temperature Test Reactor (HTTR) and HTR-10.

The primary tools utilized in these CRPs included scientific research and engineering development through analytical evaluation of benchmark problems, application of new and/or existing computer codes and models, and utilization of test apparatus and loops for specific component validation.

The focus of this TECDOC is the verification of system performance and safety under projected and actual HTGR operating conditions as defined within the scope of the CRP on 'Evaluation of High Temperature Gas Cooled Reactor Performance'. Specifically, it documents the results of benchmark problems associated with China's HTR-10, Russian Federation's GT-MHR and the ASTRA critical facility, and South Africa's PBMR-400 and the Pebble Bed Micro Model (PBMM). The objectives of this CRP include:

- Validation of analytical codes and performance models to actual operating conditions of HTGRs;
- Independent evaluation of benchmark problems for use in the Research and Development (R&D) and safety programmes for the HTR-10, PBMR, GT-MHR and the ASTRA facilities;
- Investigation of analytical codes and models associated with the proposed GT-MHR and PBMR-400 gas turbine plants;
- Investigation of code-to-experiment benchmarks associated with the three-shaft gas turbine micro model (PBMM).

Demonstration of the HTGR safety characteristics

Performance-based HTGR code and model verification during startup, steady state and transient operational conditions of the HTR-10 test facility is being evaluated within the scope of this CRP. The utilization of national research and testing facilities and computer models to investigate the areas of core physics, safety characteristics, and system performance of the GT-MHR and PBMR plants is also included.

Due to the broad scope of this research programme and the need for timely dissemination of benchmark problem analyses relative to the status of the HTTR and HTR-10, two individual TECDOCs were utilized to document the results of this CRP. The first publication (IAEA-TECDOC-1382) focused on the initial core physics evaluation and testing associated with the HTTR and HTR-10 and selected thermohydraulic benchmarks on the HTTR, while the second part of the work is reflected in this document.

This TECDOC documents the benchmark problem results obtained by Chief Scientific Investigators (CSIs) from China, France, Germany, Indonesia, Japan, the Netherlands, the Republic of Korea, the Russian Federation, South Africa, Turkey, the United Kingdom and the United States of America for the following areas:

- Reactor physics benchmark analysis of the ASTRA critical facility with respect to development of the PBMR-400. These benchmarks include core height for criticality, control rod worth and

related differential reactivity and interference coefficients, and investigation of critical parameters for differing heights of the pebble bed reactor.

- Code comparison benchmark problems of cell calculations (K_{inf} and isotope content vs. burnup) and reactor physics of control rod worth and isothermal reactivity coefficients for the GT-MHR fuelled with plutonium.
- Code-to-experiment benchmark analysis related to the testing programme of the HTR-10 plant including steady state temperature distribution with the reactor at full power, loss of primary coolant flow without scram, and control rod withdrawal without scram.
- Neutronics and thermohydraulic code comparison benchmarks for the PBMR-400.
- Micro model investigation of steady state and transient operating conditions for a three-shaft gas turbine power conversion system.

The presentation of this TECDOC is by facility, with Chapter 2 devoted to the operational benchmarks of the HTR-10 test reactor, Chapter 3 to the ASTRA critical facility, Chapter 4 to the PBMR-400, Chapter 5 to the three-shaft gas turbine micro model, and Chapter 6 to the GT-MHR. Chapter 7 provides general TECDOC results and conclusions as delineated by the participating Member States.

2. THE HTR-10 BENCHMARKS

The 10 MW pebble bed high temperature gas cooled reactor (HTR-10), designed, constructed and operated by the Institute of Nuclear and New Energy Technology (INET), is a major project in the energy sector of the Chinese National High Technology Programme. The first criticality of the HTR-10 was reached in December 2000. Full power operation with a core outlet temperature of 700°C was achieved in January 2003 [2-1] with the plant connected to the electrical grid and power generated via the steam turbine cycle.

Operational experiments and safety demonstration tests are currently in progress. After accomplishment of these tests, the second phase of this project, which is to include installation of a direct gas turbine power generation unit into the HTR-10 primary system, will begin. The purpose of this phase is to investigate R&D of nuclear helium turbine technology.

The objective of the HTR-10 is to verify and demonstrate the technical and safety features of the modular HTGR and to establish an experimental base for developing nuclear process heat applications. The specific aims of the HTR-10 have been defined as follows:

- Acquire the experience of the HTGR design, construction and operation;
- Carry out irradiation tests for fuel elements;
- Verify the inherent safety features of the modular HTGR;
- Demonstrate the electricity/heat cogeneration and steam/gas turbine combine cycle;
- Develop the high temperature process heat utilizations [2-2].

From 1986 to 1990, INET of Tsinghua University has been the leading institution for organizing and carrying out the key technology development, conceptual design, and the feasibility study of the HTGR. Subsequently, INET has been responsible for the design, license application, construction and operation of the HTR-10. The HTR-10 is constructed at the site of INET, which is located in the north-west suburb of Beijing [2-3].

2.1. HTR-10 GENERAL INFORMATION

2.1.1. Facility description

The primary system of the HTR-10 is shown in Fig. 2.1. The HTR-10 represents the main design features and safety characteristics of the modular HTGR concept. The reactor core and the steam generator are housed in two separate steel pressure vessels connected by a vessel comprised of concentric piping with the innermost pipe being the hot gas duct. Reactor structures next to the pebble bed core are composed of graphite reflectors and carbon bricks. The core is comprised of spherical elements with Triple Coated Isotropic (TRISO) coated fuel particles. These fuel elements go through the core in a multipass pattern. The main design parameters of the HTR-10 [2-1] are listed in Table 2.1.

2.1.1.1. Plant layout and confinement system

The HTR-10 plant includes the reactor building, a turbine/generator building, two cooling towers, and a ventilation centre and stack. These buildings are arranged and constructed on an area of $100 \times 130 \text{ m}^2$. The civil engineering on these buildings was contracted to companies associated with the China National Nuclear Corporation. Ground excavation was completed in late 1994 with the initial concrete poured for the reactor building foundation on 14 June 1995.

The HTR-10 plant does not contain a leak-tight pressure-containing system. The concrete compartments that house the reactor and the steam generator as well as other parts of the primary pressure boundary are preferably regarded as confinement (see Fig. 2.2). This confinement, together with the accident ventilation system, serves as the last barrier to the release of radioactivity into the environment. During normal operation, the confinement is ventilated to be held subatmospheric. In the event that the integrity of the primary pressure boundary is lost, the primary helium coolant is allowed to be released into the environment without filtering because of its low radioactivity content. Afterwards, the confinement is again ventilated and the gases in it are filtered before reaching the environment [2-4].

TABLE 2.1. MAIN DESIGN PARAMETERS OF THE HTR-10

Parameter	Value
Reactor thermal power, MW	10
Primary helium pressure, MPa	3.0
Average helium temperature at reactor outlet, °C	700
Average helium temperature at reactor inlet, °C	250
Helium mass flow rate at full power, kg/s	4.32
Main steam pressure at steam generator outlet, MPa	4.0
Main steam temperature at steam generator outlet, °C	440
Feed water temperature of steam generator, °C	104
Main steam flow rate, kg/s	3.47
Electricity power generated by steam turbine, MW	3.0

2.1.1.2. Description of the HTR-10 reactor structure

The reactor [2-1] consists of the Reactor Pressure Vessel (RPV), internal graphite and carbon brick components, metallic components, fuel elements, control rods and their driving mechanisms, small absorber ball shut-down system, fuel charging and discharging system components, etc. Vertical and horizontal cross-sections of the HTR-10 reactor are given in Figs 2.3 and 2.4.

Graphite reflectors enclose the active core zone. The lower part of the core is cone-shaped. In the initial core, fuel elements and graphite dummy balls together constitute the pebble bed. There is a discharging tube below the coned core to unload fuel elements. Graphite reflectors are categorized as the top reflector, the side reflector and the bottom reflector.

Radially, the side reflector structure is divided into the inner graphite zone and the outer boronated carbon brick zone. The inner graphite zone serves as neutron reflector of the active core and the outer carbon bricks play the role of thermal insulator and neutron absorber. Vertically, the entire side reflector is made up of multiple layers of graphite blocks and carbon bricks. Circumferentially, every layer of the side reflector consists of 20 graphite blocks and 20 carbon bricks.

The graphite blocks are connected and integrated by graphite pin keys, whose role includes positioning and helium leakage reduction. There are 20 channels near the active core zone in the side reflector, including 10 control rod channels, 7 absorber ball channels, and 3 reserved irradiation

channels. 20 cold helium channels are designed at the outer part of the side reflector graphite blocks. The hot helium plenum is located in the bottom reflector.

Reactor internal metallic components include the core vessel, bottom support plate, top support plate, etc. The core vessel is a cylindrical shell hung in the reactor vessel by the hold-down plate. The core vessel ensures the radial positioning of graphite structures and the structure's integrity under seismic conditions. The RPV consists of the shell body and the upper and lower closures. The annular space between the core vessel and the RPV is filled with cold helium.

A fuel element is a spherical ball with a diameter of 60 mm. The inner part with a diameter of 50 mm is the graphite matrix containing homogeneously dispersed coated fuel particles. The outer layer of the fuel element consists of a graphite shell with a thickness of 5 mm. The UO_2 kernel of the fuel particle has a diameter of 0.5 mm. Its initial enrichment is 17%. Design parameters of the fuel element and dummy balls are given in Table 2.2. The reactor structure parameters of the HTR-10 can be found in Table 2.3.

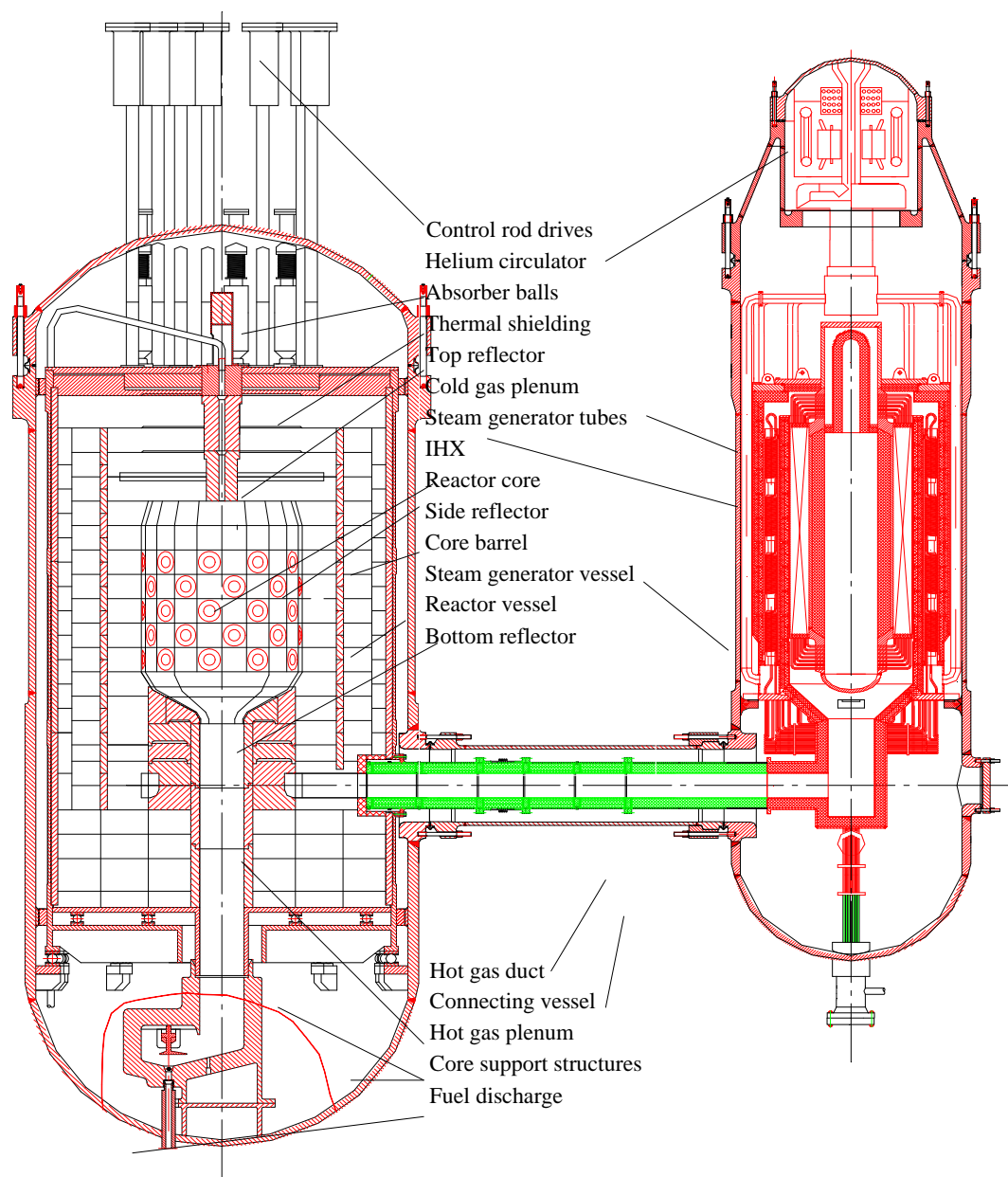


FIG. 2.1. HTR-10 primary system.

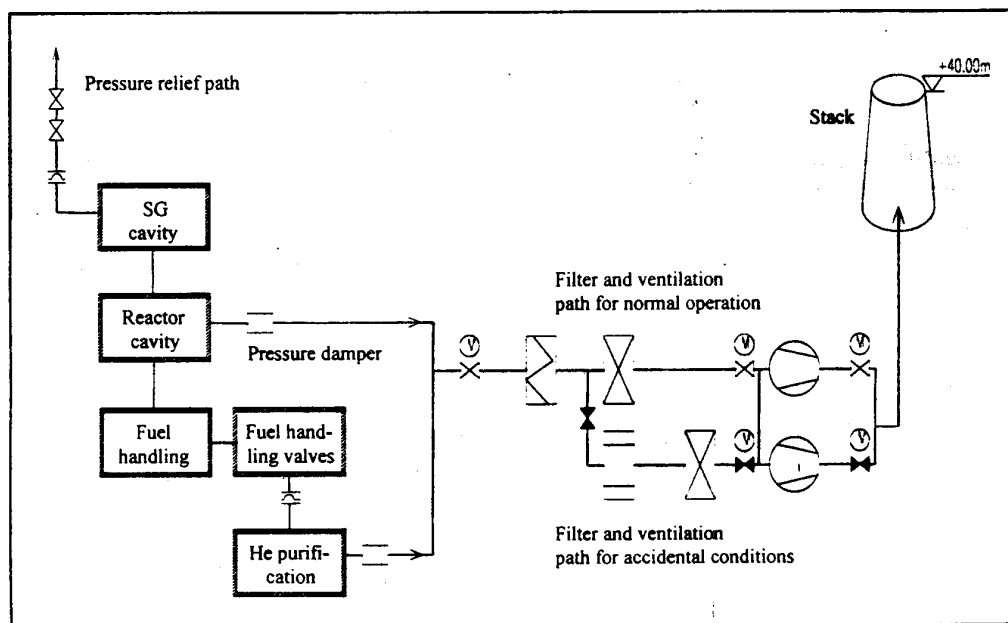


FIG. 2.2. Schematic of the HTR-10 confinement system.

TABLE 2.2. DESIGN PARAMETERS OF FUEL ELEMENTS, DUMMY BALLS AND LOADING RATIO

Fuel element	
Diameter of ball	6.0 cm
Diameter of fuel zone	5.0 cm
Density of graphite in matrix and outer shell	1.73 g/cm ³
Heavy metal (uranium) loading (weight) per ball	5.0 g
Enrichment of U-238 (weight)	17%
Volumetric filling fraction of balls in the core	0.61
Coated Particle	
Fuel Kernel	
Radius of the kernel	0.25 mm
UO ₂ density	10.4 g/cm ³
Coatings	
Coating layer materials (starting from kernel)	PyC/PyC/SiC/PyC
Coating layer thickness (mm)	0.09/0.04/0.035/0.04
Coating layer density (g/cm ³)	1.1/1.9/3.18/1.9
Dummy Balls	
Diameter of ball	6.0 cm
Density of graphite	1.73 g/cm ³
Loading ratio of fuel balls to dummy balls	57:43

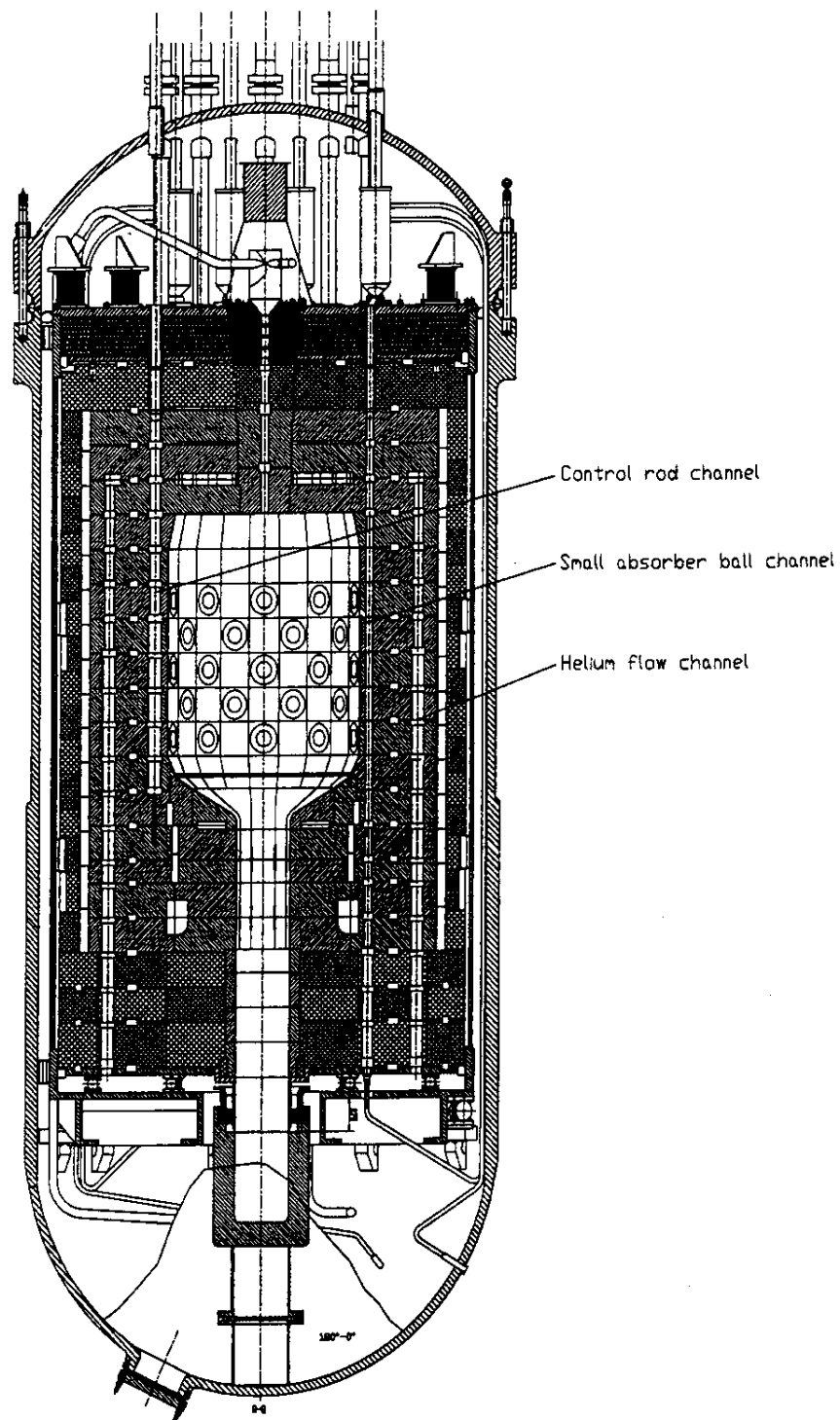


FIG. 2.3. HTR-10 reactor vertical cross-section.

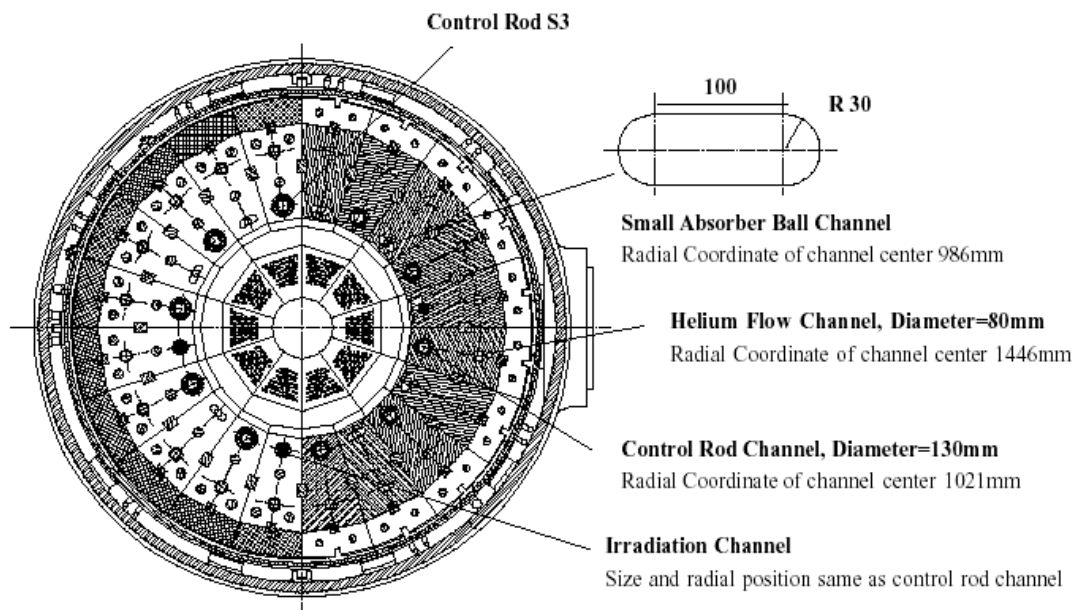


FIG. 2.4. HTR-10 reactor horizontal cross-section.

2.1.1.3. Description of HTR-10 reactor thermohydraulic calculation model

The reactor core is cooled by helium gas. The pressure of the primary system is 3 MPa and the coolant mass flow is 4.32 kg/s. Helium is pumped into the RPV by the helium circulator. After entering the RPV, helium flows downwards through the annular space between the core vessel and the RPV and changes its flow direction at the lower part of the RPV. A small part of the helium flows into the fuel discharging tube and merges into the core helium flow after cooling the fuel elements in the discharging tube. Most of the helium goes around the support structures at the reactor bottom and enters into the cold helium channels in the graphite blocks of the side reflector [2-1].

At the top of side reflector, helium is collected in the cold helium plenum located in the upper part of the top reflector. A small part of the helium then flows into the control rod channels to serve as coolant for the control rods, and at the bottom of the bottom reflector it passes through the side holes and flows into the small plenum located in the bottom reflector. Starting from the top of the core, mainstream helium goes downwards and continuously passes in succession through the reactor core and the channels in the bottom reflector, and finally flows into the hot helium plenum in the reactor bottom. The helium flows with different temperatures are sufficiently mixed in the hot helium plenum and the mixture with an average temperature of 700°C flows out of the RPV.

In the thermohydraulic calculations, the following flow rates and leakages are assumed:

- The Rated Coolant Flow Rate (RCFR) is 4.32 kg/s.
- 1% of the RCFR passes through the fuel discharging tube for cooling fuel elements in the tube.
- 2% of the RCFR flows through the control rod channels to cool the control rods.

Part of the helium coolant bypasses the main flow path (leaks) due to the occurrence of clearances among graphite blocks. Maximum bypassing leakage is taken as 10% of RCFR. Conservatively, it is assumed that this bypassing part of the helium flows directly from cold helium entry to hot helium exit, so that it is non-effective for core cooling.

87% of the RCFR flows through the pebble bed zone for effectively cooling fuel elements in the core.

For any fuel elements, the nuclear reaction heat is generated only in the zone where fuel kernels are dispersed and there is no heat source in the outer shell. Nuclear heat is transferred to the fuel element surface by conduction, so that there is an evident temperature gradient from the central zone to the outer zone within an element.

TABLE 2.3. REACTOR STRUCTURE DATA OF THE HTR-10

Parameter	Value
Reactor core	
Equivalent diameter, cm	180
Average height, cm	197
Volume, m ³	5
Volumetric filling fraction of balls in the core	0.61
Height of the empty cavity above the pebble bed, cm	41.7
Diameter of fuel discharging tube, cm	50
Top reflector area	
Thickness of the top reflector, cm	90
Thickness of top boronated carbon brick, cm	40
Outer diameter of the cold helium plenum, cm	166
Inner diameter of the cold helium plenum, cm	50
Height of the cold helium plenum, cm	10
Holes connecting the cold helium plenum to pebble bed	460 × Φ25
Side reflector	
Equivalent thickness of the side reflector graphite, cm	77.8
Equivalent thickness of the side boronated carbon brick, cm	22.2
Number of control rod channels	10
Diameter of the control rod channel, cm	13
Radial coordinate of the control rod guide channel, cm	102
Number of small absorber ball channels	7
Dimension of small absorber ball channel, cm	16 × 6
Radial coordinate of the small absorber ball channel, cm	98.6
Number of irradiation channels	3
Diameter of irradiation channel, cm	9.2
Radial coordinate of irradiation channel, cm	98.6
Number of cold helium flow channels	20
Diameter of cold helium flow channel, cm	8
Radial coordinate of the cold helium flow channel centre, cm	144.6
Bottom reflector area	
Height of the cone-shaped reflector, cm	37.5
Thickness of the bottom reflector, cm	121.2
Thickness of the bottom boronated carbon brick, cm	30
Thickness of the bottom non-boronated carbon brick, cm	70
Density of the reflector graphite, g/cm ³	1.76

TABLE 2.3. REACTOR STRUCTURE DATA OF THE HTR-10 (CONT.)

Parameter	
Density of the boronated carbon brick including B ₄ C, g/cm ³	1.59
Equivalent outer diameter of the hot helium plenum, cm	166
Equivalent inner diameter of the hot helium plenum, cm	112
Equivalent height of the hot helium plenum, cm	25
Holes connecting core to the hot helium plenum	640 × Φ16
RPV	
Inner diameter of the shell body, cm	420
Total height, cm	1115.5
Thickness of the vertical shell body, cm	8
Total weight, t	167
Material (carbon steel)	SA516-70
Core vessel	
Inner diameter, cm	382
Thickness, cm	3
Height, cm	737
Material	SA387-11

Figures 2.5 and 2.6 show the detailed thermohydraulic models, one heat conduction model, and one convection model. Tables 2.4 and 2.5 list material, solid mass fraction and void fraction in every zone. The models use an R-Z coordinate in cm. The horizontal axis is the R-direction and the vertical the Z-direction. The zero points of the Z- and R-axis correspond to the crossing point of the upper surface and the central axis of the active pebble bed core. Zones 4 and 16 in Fig. 2.6 or zones 25 and 40 in Fig. 2.5 represent the hot sink and cold sink respectively. Some components and zones outside the RPV, which are not significant for steady state temperature calculation and can be eliminated in this benchmark problem, are included in these models.

2.1.1.4. Boundary conditions

In normal operation, nuclear heat generated in the active core is mainly carried out by helium flow. The helium temperature at the core inlet is about 250°C and 700°C at the core outlet. At the same time, a small part of heat is dissipated through the Decay Heat Removal System (DHRS). At normal operation, the DHRS is in operation and plays the role of cooling the RPV supports and the reactor cavity. Therefore, heat rejected by the RPV is mainly carried out by the DHRS. The DHRS includes water cooling panels and air-coolers. Water cooling panels are installed on the inner side of the reactor cavity concrete wall. Water cooling panels consist of steel plates and cooling water tubes going through air-coolers which are installed outside the reactor cavity. The RPV transfers heat to the water cooling panels through radiation and natural convection. The water cooling panels and air-coolers form natural circulation loops, and the air-coolers reject heat to air, which is the final heat sink. The temperature of the water cooling panels is around 50°C.

In the calculation of the HTR-10 steady state temperature distribution, the boundary condition is defined as follows:

- The temperature of the water cooling panels (material identification number 39, as shown in Fig. 2.5) is taken as 50°C.

- The temperature of concrete walls (material identification number 15, as shown in Fig. 2.5) is taken as 50°C.

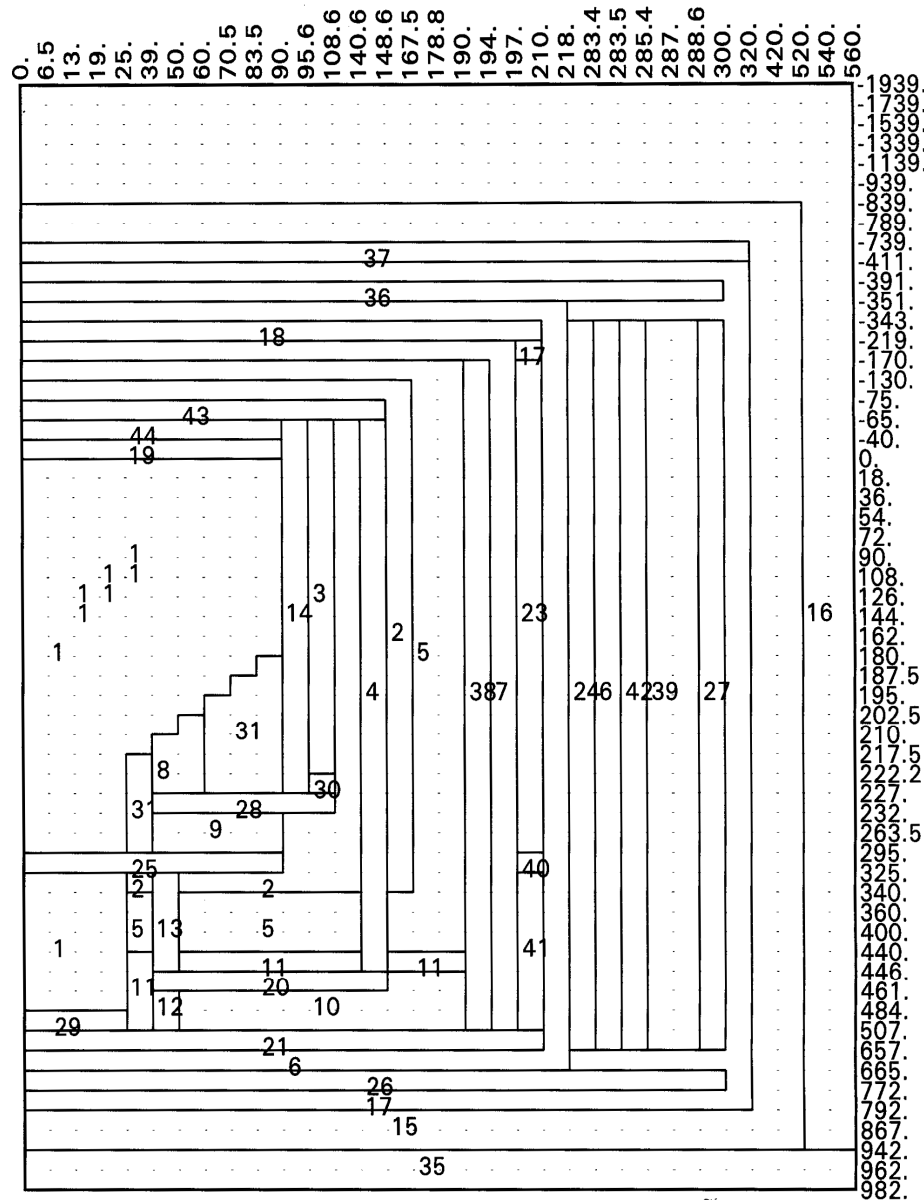


FIG. 2.5. Heat conduction calculation model for HTR-10.

Recommended material properties and correlations for main components are addressed in Section 2.1.2.

2.1.1.5. Heat generation distribution of the initial core

For the initial core loading, dummy balls (no-fuel graphite balls) were first placed into the discharging tube and the bottom cone-shaped zone of the reactor core. Then, a mixture of fuel elements and dummy balls (to the ratio of 57:43) was loaded gradually to approach first criticality. After first criticality was reached, mixed balls were further loaded to full core in order to make the reactor capable of being operated at full power. The full core (including the cone-shaped zone) is estimated to have a volume of 5 m³.

Heat generation rate distribution of the initial core is calculated. The calculation result is given in Table 2.6 using the R-Z coordinate system described above.

For the initial core, there is no heat generated in the lower part of the reactor core and the fuel discharge tube [2-5].

TABLE 2.4. HEAT CONDUCTION MODEL SPECIFICATION

No.	Zone	Material	Mass fraction
1	Pebble bed	Fuel elements	0.61
2	Side reflector without flow path	Graphite	1.0
3	Side reflector with control rod channels	Graphite	0.793
4	Side reflector with coolant flow paths	Graphite	0.862
5	Carbon brick insulator	Carbon bricks	1.0
6	RPV	Steel	1.0
7	Core vessel	Steel	1.0
8	Upper bottom reflector with flow paths	Graphite	0.769
9	Lower bottom reflector with flow paths	Graphite	0.932
10	Reactor bottom steel supporting structure 1	Steel	0.5
11	Reactor bottom steel supporting structure 2	Steel	1.0
12	Reactor bottom annular cold helium flow path	Helium	0.01
13	Leaking flow zone in steel structures	Steel	0.96
14	Side reflector without coolant flow path	Graphite	1.0
15	Concrete	Concrete	1.0
16	Side fluid boundary		1.0
17	Thermal insulation		1.0
18	Helium cavity inside RPV	Helium	1.0
19	Gas plenum at core entry	Helium	1.0
20	Reactor bottom gas rounding flow paths	Helium	1.0
21	Bottom helium cavity inside RPV	Helium	1.0
22	Null		
23	Side helium gap between core vessel and RPV	Helium	1.0
24	Air cavity outside RPV	Air	1.0
25	Hot gas plenum at core bottom exit	Helium	1.0
26	Bottom air cavity outside RPV	Air	1.0
27	Side cavity of reactor cavity	Air	1.0
28	Small plenum in bottom reflector	Helium	1.0
29	Entry throttle of cooling gas for fuel discharging tube	Graphite	0.993
30	Exit throttle of cooling gas for control rods	Graphite	0.998
31	Bottom reflector without flow paths	Graphite	1.0
32	Null		
33	Null		
34	Null		
35	Reactor bottom fluid boundary		
36	Top air cavity outside RPV	Air	1.0
37	Top air cavity of reactor cavity	Air	1.0
38	Side helium gap inside core vessel	Helium	1.0
39	Water cooling panels		
40	Helium entry flow path inside RPV	Helium	1.0
41	Annular flow path inside RPV	Helium	1.0
42	Air gap outside insulating plates of reactor cavity	Air	1.0
43	Helium plenum in top reflector	Helium	1.0
44	Helium flow zone in top reflector	Graphite	0.911

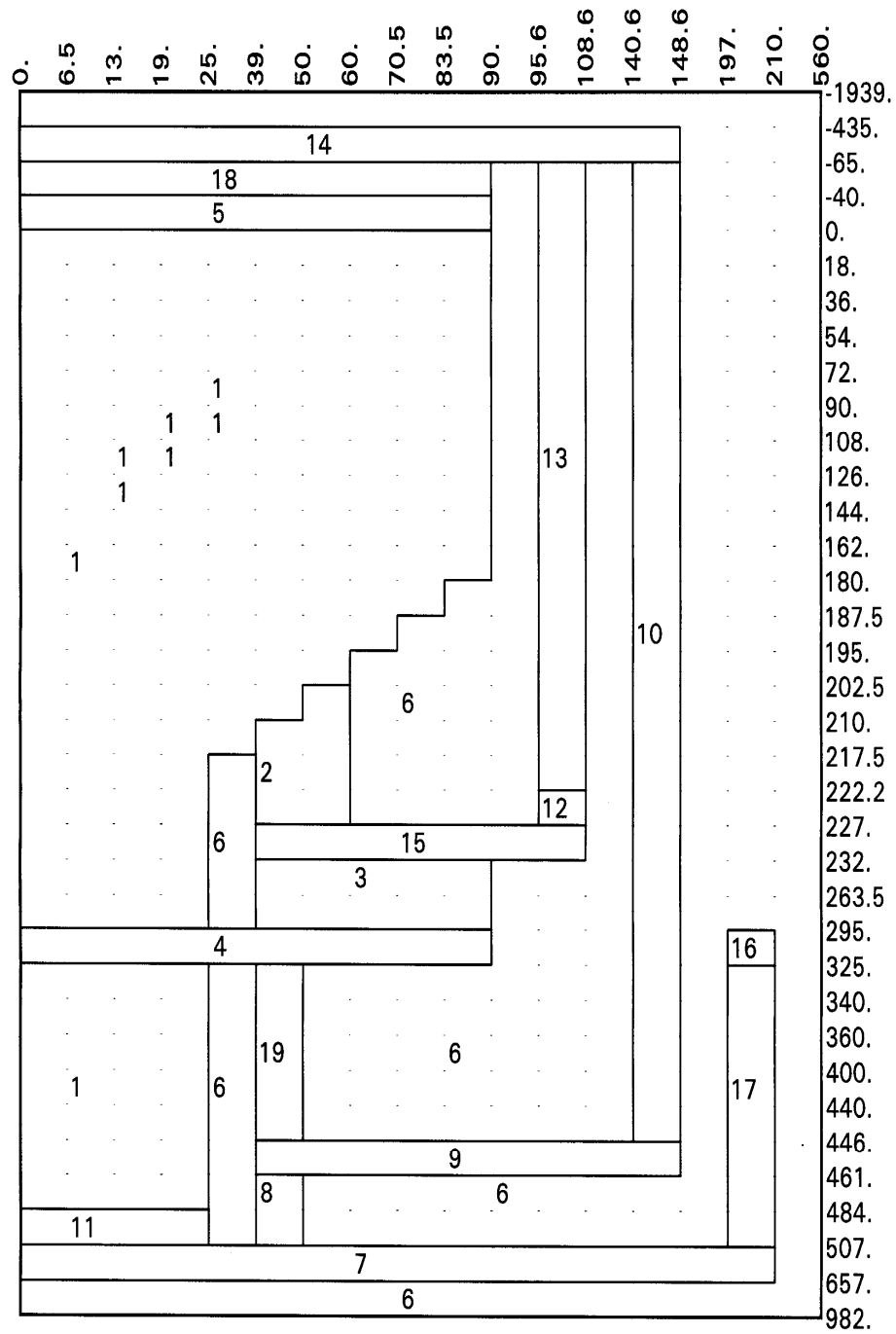


FIG. 2.6. Convection calculation model for HTR-10.

TABLE 2.5. CONVECTION MODEL SPECIFICATION

No.	Zone	Void Fraction
1	Pebble bed	0.39
2	Flow zone in the upper bottom reflector	0.23
3	Flow zone in the lower bottom reflector	0.068
4	Hot helium plenum at the core bottom exit	1.0
5	Cold helium plenum at the core entry	1.0
6	Non-flowing zone	
7	Cavity of the RPV bottom closure	1.0
8	Annular coolant flow path at reactor bottom	0.99
9	Gas rounding flow path at reactor bottom	1.0
10	Coolant flow paths in the side reflector	0.138
11	Entry throttle of cooling gas for the fuel discharging tube	0.0067
12	Exit throttle of the control rod channels	0.0024
13	Control rod channels in side reflector	0.207
14	Helium plenum in the top reflector	1.0
15	Small plenum in the bottom reflector	1.0
16	Helium entry flow cavity inside the RPV	1.0
17	Annular helium flow path inside the RPV	0.99
18	Flow path zone in the top reflector	0.089
19	Gap leaking flow zone	0.046

TABLE 2.6. POWER DISTRIBUTION OF THE INITIAL CORE (W/CM³)

Z\R(cm)	0	6.5	13	19	25	39	50	60	70.5	83.5	90
0	1.79	1.79	1.79	1.78	1.75	1.71	1.68	1.65	1.63	1.65	
18	2.12	2.11	2.10	2.08	2.06	2.01	1.95	1.89	1.86	1.89	
36	2.46	2.45	2.44	2.41	2.35	2.26	2.18	2.10	2.07	2.09	
54	2.61	2.60	2.58	2.56	2.49	2.43	2.33	2.27	2.22	2.22	
72	2.78	2.77	2.75	2.72	2.65	2.56	2.46	2.39	2.30	2.30	
90	2.84	2.84	2.82	2.79	2.71	2.55	2.45	2.33	2.26	2.26	
108	2.66	2.65	2.63	2.60	2.56	2.49	2.38	2.29	2.22	2.21	
126	2.49	2.49	2.47	2.44	2.37	2.29	2.19	2.08	2.01	2.00	
144	2.36	2.35	2.33	2.30	2.22	2.11	2.02	1.93	1.85	1.82	
162	2.33	2.32	2.29	2.25	2.16	2.02	1.93	1.83	1.73	1.66	
180	1.53	1.53	1.51	1.48	1.42	1.33	1.27	1.21	1.13	0.0	
187											

Temperature measurement

Fixed thermocouples have been arranged at corresponding positions on the side reflector, top reflector and bottom reflector, carbon brick thermal insulator, core vessel and pressure vessel. The measurement results can depict the general situation of temperature distribution within the reactor. Measured locations and their coordinates are listed in Table 2.7 for a total of 22 measurement locations.

TABLE 2.7. COORDINATES OF TEMPERATURE MEASUREMENT LOCATIONS

No.	R (cm)	Z (cm)	No.	R (cm)	Z (cm)
Side reflector			Top reflector		
1	193	80	13	60	-40
2	189	80		Hot helium plenum	
3	167	80	14	40	234
4	133	80	15	60	234
5	117			Bottom carbon bricks	
6	93	80	16	70	440
7	193	170	17	50	400
8	189	170	18	50	370
9	167	170	19	50	340
10	133	170		Fuel discharging tube	
11	117	170	20	26	340
12	93	170	21	26	300
			22	26	260

2.1.1.6. Clarification of HTR-10 benchmark problem definitions

The following items of clarification on the HTR-10 benchmark problem descriptions were provided by INET as a result of discussions at the 5th Research Coordination Meeting (RCM) in Vienna, 6–10 December 2004 [2-6].

Power distribution for steady state temperature benchmark

Power distribution of the initial core is given in Table 2.6. Only one point is revised, i.e. the cell ($Z = 180$ cm, $R = 83.5\sim 90$ cm). Its original value was 1.03 W/cm^3 and the revised value is 0.0 W/cm^3 ;

For the initial core, there is no heat generated in the lower part ($Z > 180$ cm) of the reactor core and the fuel discharging tube.

Coolant flow paths in the bottom reflector

Regarding the coolant flow paths in the bottom of core, please refer to Figs 2.1, 2.3, 2.4, 2.5 and 2.6.

Definition of maximum fuel temperature

For each fuel element, there is a centre temperature. It is the temperature in the centre of fuel sphere. For the whole reactor core, the Maximum Fuel Temperature is the maximum value in the centre temperatures of all fuel elements;

In our calculations, the fuel sphere is divided into five zones. The outer diameter of the central zone is 0.3 cm. The average temperature of this central zone is regarded as the centre temperature of each fuel element.

Reactivity coefficient definition of moderator and fuel temperature

The fuel temperature reactivity coefficient is defined as the reactivity variation caused by 1°C variation of fuel temperature within the whole core. Its unit is pcm/ $^\circ\text{C}$ or $10^{-5}\Delta k/k/^\circ\text{C}$.

In our benchmark definition, an overall average core temperature coefficient of reactivity at operational state was given. It is a sum of temperature coefficients in all core zones. Approximately, the overall average core temperature coefficient of reactivity can be subdivided into all core zones according to their power fraction.

The definition of moderator temperature reactivity coefficient is similar to the above definition of fuel temperature reactivity coefficient.

Operation history on burnup and afterheat

- Before the safety demonstration experiments, the reactor had operated for approximately 3000 MW-hour.
- At the starting points of safety demonstration experiments, xenon equilibrium state was achieved.
- Investigators can calculate the afterheat power versus time by themselves.
- In the INET's calculation, the afterheat power curve shown as Fig. 2.7 was utilized.

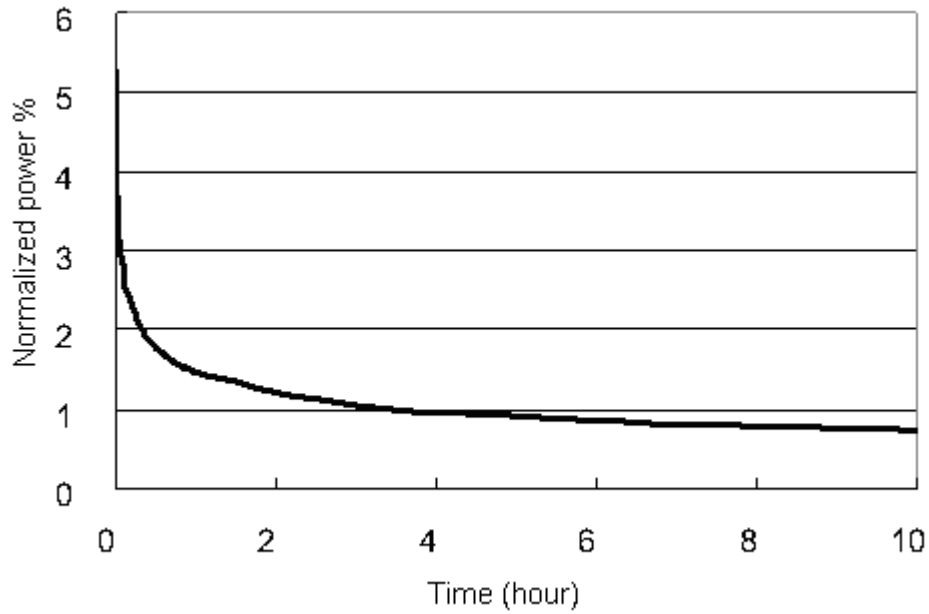


FIG. 2.7. Htr-10 afterheat power vs time calculated by inet.

2.1.2. Recommended material properties and correlations for main components

The material properties of various components (helium gas, fuel element, reflector graphite and carbon bricks) of the HTR-10 are provided and summarized in Tables 2.8–2.12. The steel components of the HTR-10 are located at the low-temperature zones of the core supports, core vessel, RPV and water cooling tube. The thermal conductivity and the specific heat capacity of steel materials are shown in Figs 2.8 and 2.9, respectively.

TABLE 2.8. THERMAL PROPERTIES OF HELIUM

Property	Correlation	Comments
Density	$\rho = 48.14 \cdot \frac{P}{T} \left(1 + 0.4446 \cdot \frac{P}{T^{1.2}} \right)^{-1} \text{ [kg/m}^3\text{]}$ <p>where P and T are pressure [Pa] and temperature [K]</p>	standard deviation is $\sigma = 0.03\sqrt{P} \%$
Specific heat capacity	<p>Cp = 5195 J/kg·K (constant pressure), Cv = 3117 J/kg·K (constant volume)</p>	$\sigma = 0.05 \cdot P^{\left(0.6 - 0.1 \frac{T}{T_0}\right)} \%$
Dynamic viscosity	$\eta = 3.674 \cdot 10^{-7} \cdot T^{0.7} \text{ [Pa}\cdot\text{s]}$ <p>where T is temperature [K].</p>	$\sigma = 0.0015 \cdot T \%$
Conductivity	$\lambda = 2.682 \cdot 10^{-5} \left(1 + 1.123 \cdot 10^{-3} \cdot P \right) \cdot T^{0.71(1 - 2 \cdot 10^{-4} \cdot P)}$ <p>[W/cm/K], where P and T are pressure [Pa] and temperature [T]</p>	$\sigma = 0.0035 \cdot T \%$. applicable range for all 1 MPa ≤ P ≤ 10 MPa 293K ≤ T ≤ 1773 K

TABLE 2.9. MATERIAL PROPERTIES OF THE GERMAN GRAPHITE FUEL PEBBLE

Property	Correlation	Comments
Density	$\rho = 1720 \text{ [kg/m}^3\text{]}$	
Specific heat capacity	$C_v = 1.75 \times (0.645 + 3.14 \times 10^{-3} \times T - 2.809 \times 10^{-6} \times T^2 + 0.959 \times 10^{-9} \times T^3)$ [J/cm ³ /K], where T is temperature [°C]. Applicability: $T \leq 1200 \text{ }^\circ\text{C}$	For all graphite German Company HRB
Conductivity of fuel element	$\lambda = ((-0.3906 \times 10^{-4} \times T + .06829) / (DOSIS + 1.931 \times 10^{-4} \times T + 0.105) + 1.228 \times 10^{-4} \times T + 0.042) \times 1.2768$ [W/cm/K], where T is temperature [°C], DOSIS is irradiation dosage of fast neutrons [10 ²¹]. Applicability: $450 \text{ }^\circ\text{C} \leq T \leq 1300 \text{ }^\circ\text{C}$	if $T \leq 450 \text{ }^\circ\text{C}$, then $T = 450 \text{ }^\circ\text{C}$, if $DOSIS > 2.5$ then $DOSIS = 2.5$
Conductivity of uniformed pebble bed	$\lambda = 1.1538 \cdot 10^{-6} \cdot T_1^{1.6622} \text{ [W/cm/K]}$ $T_1 = T + 100$ If $T < 250 \text{ }^\circ\text{C}$, then, $T = 250 \text{ }^\circ\text{C}$	German breitbach correlation

TABLE 2.10. HEAT TRANSFER AND PRESSURE DROP OF THE FUEL PEBBLE

Property	Correlation	Comments
Heat transfer on fuel element Surface	$Q = \alpha A_K (T_K - T_G), \quad \alpha = \frac{Nu \lambda}{d}, \quad Re = \frac{(m / A) d}{\eta},$ $\varepsilon = f\left(\frac{D}{d}\right)$ $Nu = 1.27 \frac{Pr^{1/3}}{\varepsilon^{1.18}} Re^{0.36} + 0.033 \frac{Pr^{1/2}}{\varepsilon^{1.07}} Re^{0.86}$ where A is the flow path area of the pebble bed (empty pebble bed); A _K is the surface area of single fuel element; ε is the vacancy fraction of the pebble bed; m is the gas flow rate in the pebble bed; Q is the heat transferred from the fuel surface to helium; α is the average heat transfer coefficient of fuel surface; T _K is the average temperature at fuel element surface	where η is the dynamic viscosity of helium; λ is the heat conductivity of helium; T _G is the temperature of helium; d is the outer diameter of fuel element; D is the diameter of the pebble bed. Applicability: $100 \leq Re \leq 10^5$; $0.36 \leq \varepsilon \leq 0.42$; $D/d \geq 20, H \geq 4d$. The deviation is ±20% and the creditability is 95%.
Frictional pressure loss in the pebble bed	$\frac{\Delta P}{\Delta H} = \Psi \frac{1-\varepsilon}{\varepsilon^3} \frac{1}{d} \frac{1}{2\rho} \left(\frac{m}{A}\right)^2, \quad \Psi = \frac{320}{\left(\frac{Re}{1-\varepsilon}\right)} + \frac{6}{\left(\frac{Re}{1-\varepsilon}\right)^{0.1}}$ where ΔP is the frictional pressure loss; H is the height of the pebble bed; Ψ is the fractional coefficient; ρ is the density of helium	Applicability: $1 < Re/(1-\varepsilon) \leq 10^5$; $0.36 \leq \varepsilon \leq 0.42$; $H > 5d$

TABLE 2.11. MATERIAL PROPERTIES OF THE GRAPHITE REFLECTOR

Property	Correlation	Comments
Conductivity of side reflector	$\lambda = 1.15 \cdot (1.5648 - 0.3162 \log(T + 100)) \cdot F$ $F = F1 / (Y - F2) + F3$ $F1 = -0.0054705 + 0.00038214 \cdot T / 1000 + 0.13487(T / 1000)^2$ $F2 = -0.013951 + 0.12064 \cdot T / 1000 - 0.32955 \cdot (T / 1000)^2$ $F3 = -0.07264 + 0.41459 \cdot T / 1000 + 0.23149 \cdot (T / 1000)^2$ $Y = D/10$ Applicability: $0 \leq T \leq 2000^\circ\text{C}$	where λ is conductivity [W/cm/K], T is temperature [$^\circ\text{C}$] and D is fast neutron irradiation dosage [10^{21}]
Conductivity of bottom and top reflector	$\lambda = 1.15 \cdot (1 - 1.084 \cdot T_1 + 0.743 \cdot T_1^2 - 0.213 \cdot T_1^3)$ $T_1 = T / 1000$ Applicability: $T \leq 1700^\circ\text{C}$	where, λ is conductivity [W/cm/K], T is temperature [$^\circ\text{C}$]

TABLE 2.12. MATERIAL PROPERTIES OF CARBON BRICK

Property	Correlation	Comments
Specific heat capacity	$C_v = 1.55 \times (.645 + 3.14 \times 10^{-3} \times T - 2.809 \times 10^{-6} \times T^2 + 0.959 \times 10^{-9} \times T^3)$; Applicability: $T \leq 1200^\circ\text{C}$.	Where: C_v is specific heat capacity [J/cm ³ /K] and T is temperature [$^\circ\text{C}$].
Heat conductivity	$\lambda = 0.05 + 0.03 \times 10^{-3} \times T$ Applicability: $T \leq 1000^\circ\text{C}$	Where: λ is conductivity [W/cm/K] and T is temperature [$^\circ\text{C}$].

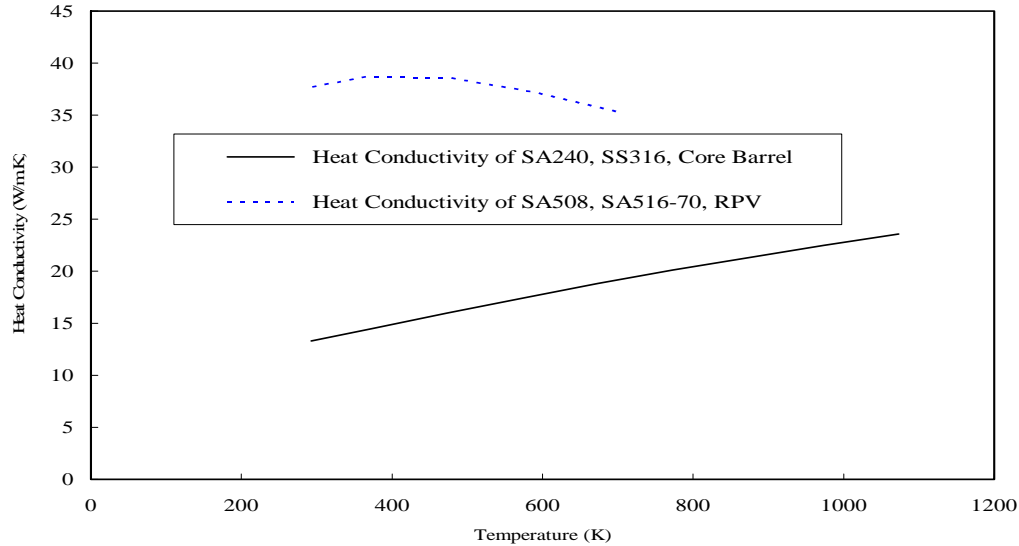


FIG. 2.8. Heat conductivity of steel components.

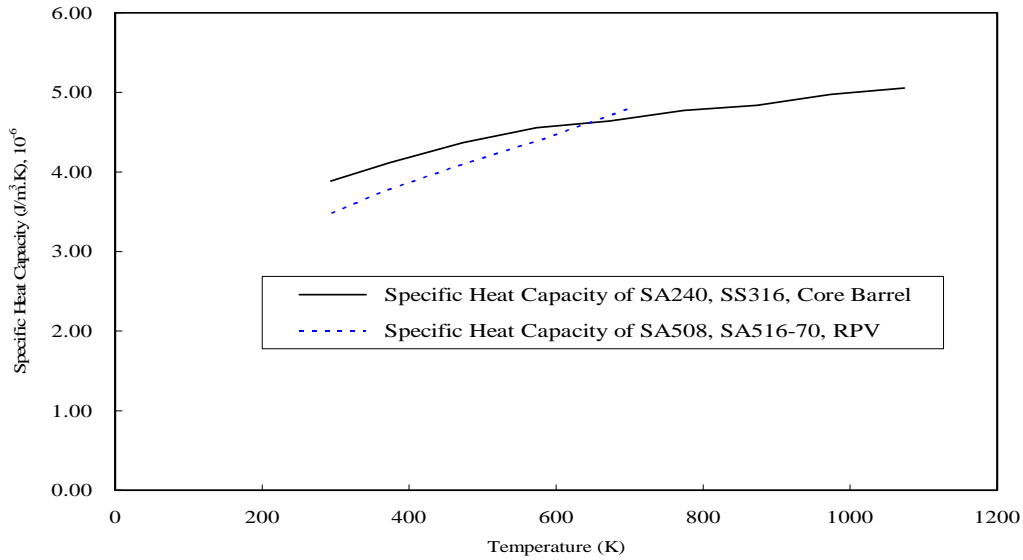


FIG. 2.9. Specific heat capacity of steel components.

Reference values of emission coefficients of cavities are given in Table 2.13.

TABLE 2.13. REFERENCE VALUES OF EMISSION COEFFICIENTS OF CAVITIES

Component	Emission Coefficient
Cold helium plenum in the top reflector	0.85
Annular flow path inside the RPV	0.79
Side helium gap inside the core vessel	0.82
Hot gas plenum at the core bottom exit	0.85
Side helium gap between the core vessel and RPV	0.85
Air cavity outside the RPV	0.85
Gas plenum at the core entry	0.85
Helium cavity inside the RPV	0.79

2.2. HTR-10 STEADY STATE BENCHMARK DESCRIPTION AND RESULTS

2.2.1. Steady state temperature distribution benchmark problem description

After reaching initial criticality, additional fuel balls and graphite balls (to the ratio of 57:43, the same as that of the already loaded pebble bed) have been loaded into the reactor core to such a level that the reactor can operate at full power. In this document, this reactor core status is defined as the Full Power Initial Core (FPIC). The steady state temperature distributions in the HTR-10 reactor for FPIC are to be calculated for benchmarking purposes. There are a number of thermocouples in the reactor structures which have recorded the temperatures at FPIC. The proposed temperature distributions to be calculated in the benchmark problem go beyond those measured temperatures. Therefore, the problems defined in this document are both for code-to-code and for code-to-experiment benchmarking. The benchmark calculations shall only cover temperatures within the reactor unit. The steam generator and hot gas duct are not included.

The temperatures to be calculated and compared within the frame of this benchmark problem cover the following aspects:

Temperature distribution within the pebble bed;

Solid material temperature values at measured places;

Calculation of the maximum temperature values of the main components, namely, fuel elements (at centre and surface), side reflector and bottom reflector.

2.2.1.1. Definition of benchmark problem

The purpose of this benchmark problem is to calculate and compare the HTR-10 steady state temperature distribution for FPIC. It includes the following three problems:

Calculation of temperature distribution within the pebble bed, including profiles of $R = 0$ cm, $R = 45$ cm, $R = 90$ cm, $Z = 0$ cm, $Z = 80$ cm and $Z = 170$ cm in the defined coordinate as shown in Fig. 2.5.

Calculation of solid material temperature values at measured places. Exact coordinates of measured places can be found in Table 2.7.

Calculation of the maximum temperature values of the main components: fuel elements (at centre* and surface), side reflector, and bottom reflector (*see Section 2.1.1.6. for definition).

2.2.1.2. Calculation model and codes

The calculation model used by INET has been described in the previous sections. It includes the fuel zone and non-fuel zone of the core, reflectors, carbon bricks, cavity, thermal shield, core vessel, RPV, cavity cooler and coolant flow paths, etc. The two dimensional rotation symmetric heat conduction model in the R-Z geometry for the HTR-10 consists of 33 radial and 57 axial mesh points, and there are 44 different calculating regions. The pebble bed, reflectors and gas cavity are treated to be homogeneous media whose heat capacities can be determined according to the void fraction in these regions. The heat transfer of conduction, radiation and natural convection is considered in this model. The gas convection model consists of 19 different flow regions and there are 18 radial and 38 axial mesh points.

The code system used in calculating the steady state temperature distribution in the reactor core is the Thermix-Konvek code system. The Thermix code, which is two dimensional, is used to calculate the solid material temperatures in the calculation model. The two codes are coupled together to calculate gas flow problems including gas temperatures, flow rates and pressure drops.

2.2.2. HTR-10 steady state temperature distribution analysis and results

2.2.2.1. Calculation results and comparison with experimental results, China

The summary provided here was submitted to the CRP as Ref. [2-7].

Calculation results of temperature distribution within the pebble bed

Figures 2.10 and 2.11 provide axial and radial calculation temperature profiles within the pebble bed respectively. Due to the existence of the cone and fuel discharging tube at the bottom of core, the height values of the pebble bed at different radii are different. At the core inlet, the temperatures are nearly equal radially. In the lower part of core, the temperature of the centre zone is evidently higher than that of the peripheral zone. At $Z = 170$ cm, the central temperature achieves nearly 900°C . In the lower part of the core ($Z = 180$ cm), the maximum temperature achieves 925°C .

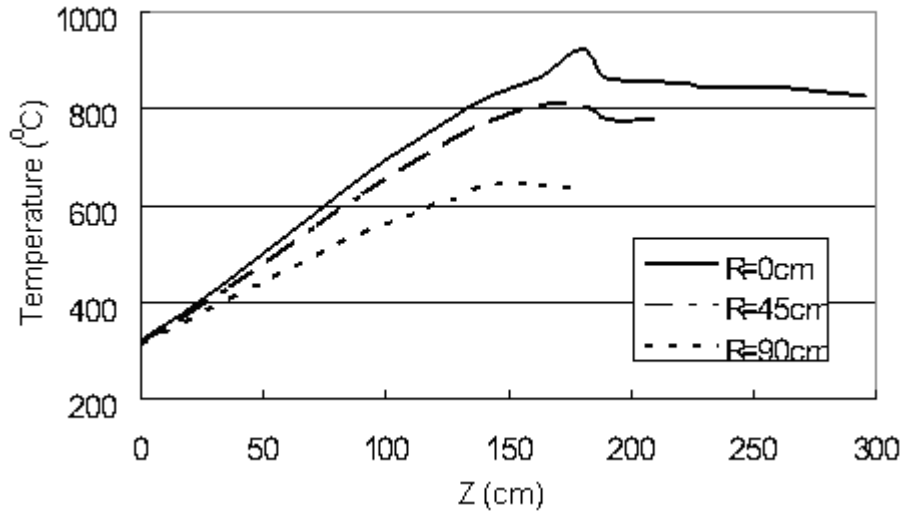


FIG. 2.10. Axial temperature profiles ($R = \text{const}$) within the pebble bed.

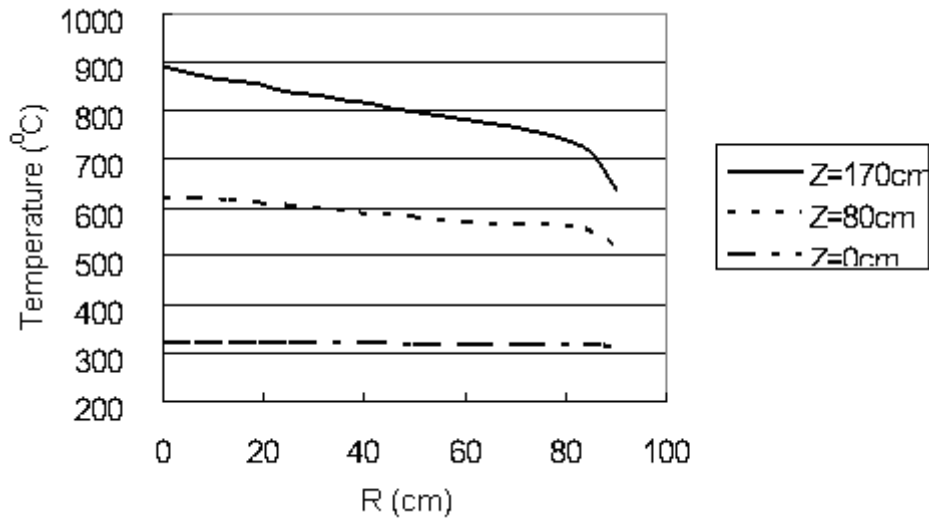


FIG. 2.11. Radial temperature profiles ($Z = \text{const}$) within the pebble bed.

Comparison of solid material temperature values

Table 2.14 provides the calculation and experimental temperatures at measured places. Figures 2.12 and 2.13 provide the comparison of temperatures of side reflector and fuel discharging tube respectively. The following points can be found from the comparison:

The calculation temperatures of the top reflector and side reflector agree basically with the experimental values. However, the maximum deviation of individual points exceeds 50 K.

The calculational and experimental temperatures of bottom carbon bricks do not agree well at $R = 50 \text{ cm}$ and $Z = 340 \text{ cm}$, and the deviation is more than 60 K. The deviations of the other three measured places are acceptable.

The calculation significantly underestimates the temperatures of the fuel discharging tube. The deviation is close to 100 K, especially in the upper part of the fuel discharging tube.

The calculational and experimental temperatures of the hot helium plenum basically agree. However, the deviation of about 50 K is comparatively large.

The large deviations occurred mainly around the hot helium plenum. The calculation underestimated the temperature values since the two dimensional calculation model could not properly simulate the complicated structure of this zone.

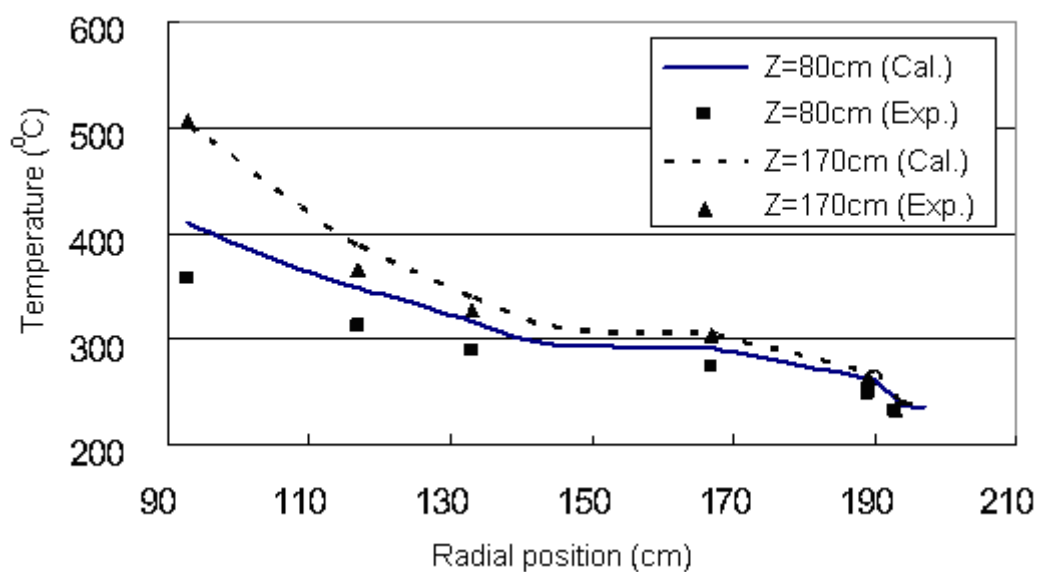


FIG. 2.12. Temperature comparison of the side reflector.

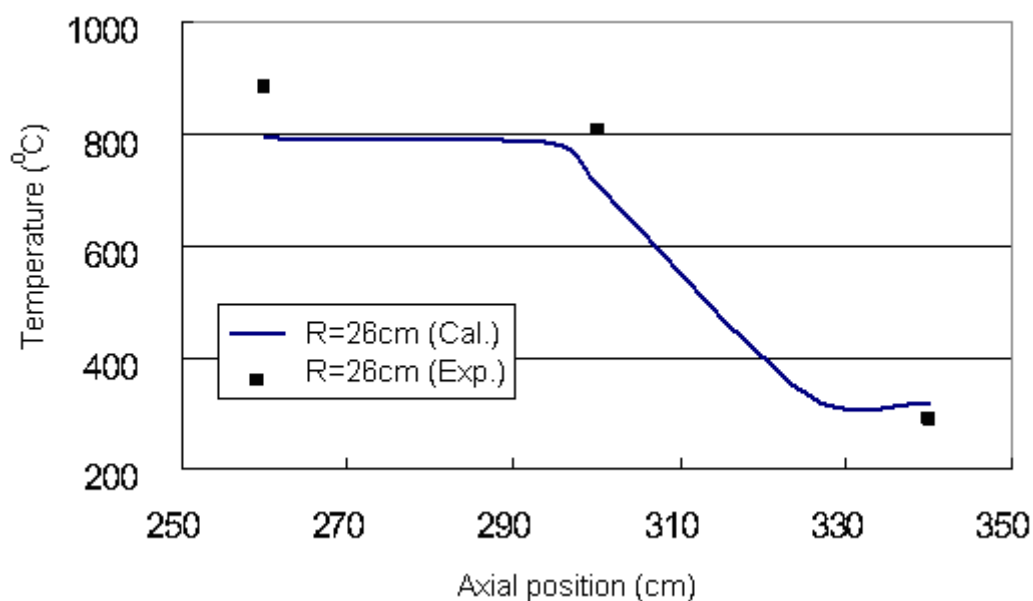


FIG. 2.13. Temperature comparison of the fuel discharging tube.

TABLE 2.14. COMPARISON BETWEEN CALCULATIONAL
AND EXPERIMENTAL TEMPERATURES

No.	R (cm)	Z (cm)	Exp. (°C)	Calc. (°C)	Deviation (°C)
Side reflector					
1	193	80	231.3	243.9	12.6
2	189	80	249.3	263.5	14.2
3	167	80	274.3	291.6	17.3
4	133	80	289.1	316.4	27.3
5	117	80	313.3	349.5	36.2
6	93	80	357.7	410.4	52.7
7	193	170	234.9	247.3	12.4
8	189	170	264.8	270.9	6.1
9	167	170	303.9	305.3	1.4
10	133	170	328.5	341.5	13.0
11	117	170	365.3	388.8	23.5
12	93	170	507.1	501.3	-5.8
Top reflector					
13	60	-40	245.7	260.8	15.1
Hot helium plenum					
14	40	234	800.2	769.9	-30.3
15	60	234	763.1	714.1	-49.0
Bottom carbon bricks					
16	70	440	224.1	239.5	15.4
17	50	400	245.7	263.7	18.0
18	50	370	296.2	295.4	-0.8
19	50	340	406.7	339.8	-66.9
Fuel discharging tube					
20	26	340	334.2	316.8	-17.4
21	26	300	806.1	707.4	-98.7
22	26	260	881.7	792.7	-89.0

Calculation results of the maximum temperature values

The calculation results of the maximum temperature values of the main components are shown in Table 2.15. In normal full power operation, the maximum fuel temperature can achieve 988°C. The maximum temperatures of the side and bottom reflector can achieve 500°C and 800°C respectively.

TABLE 2.15. MAXIMUM TEMPERATURE VALUES OF THE MAIN COMPONENTS

Component	Position	Max. Temperature (°C)
Fuel element	Centre	988.2
	Surface	924.5
Side reflector	Surface	511.8
Bottom reflector	Surface	789.3

2.2.2.2. *HTR-10 steady state temperature benchmark analysis and results, Turkey*

Introduction

This study covers the thermohydraulic calculations of the HTR-10 initial core. The temperature and flow distributions for the HTR-10 are calculated by the Fluent v6.1.22 code, a general-purpose and commercial computational fluid dynamics code, after the generation of the grid structure of the HTR-10 in the fluent code's pre-processor named Gambit v2.2.

Set-up of the analysis

Two temperature models are used for the analysis. Fuel surface temperatures are coupled with coolant and solid temperatures. The calculations are performed with respect to the two dimensional (2-D) axisymmetric model of the HTR-10 specified in the CRP-5 benchmark problem [2-8] as conduction and convection models. For the generation of the grid structure, the conduction model specified in the CRP-5 benchmark problem was taken as reference. The model was modified to establish the cone-shaped structure between the upper core region and the discharging tube and the resulting model shown in Fig. 2.14 was used.

The meshing of the whole geometry was done according to the scheme with quadrilateral (Quad) elements and 'Map'-type meshing that creates structured mesh where appropriate and 'Pave'-type meshing that creates unstructured mesh for the remaining regions. The unavoidable aspect ratios (length to width) of some structures in the model forced the meshing to be partially structured. The quasi-automatic smoothing was done for refinement of the mesh through the whole geometry. To override the mesh sensitivity during the analysis, various mesh sizes were examined. The resulting model was composed of 1 partition, 18762 cells, 41315 faces and 22488 nodes. The model was then carried to the Fluent code and further smoothing was automatically done. The Fluent code uses a domain reordering method, named Reversed Cuthill-McKee, that reduced the bandwidth by 45.72.

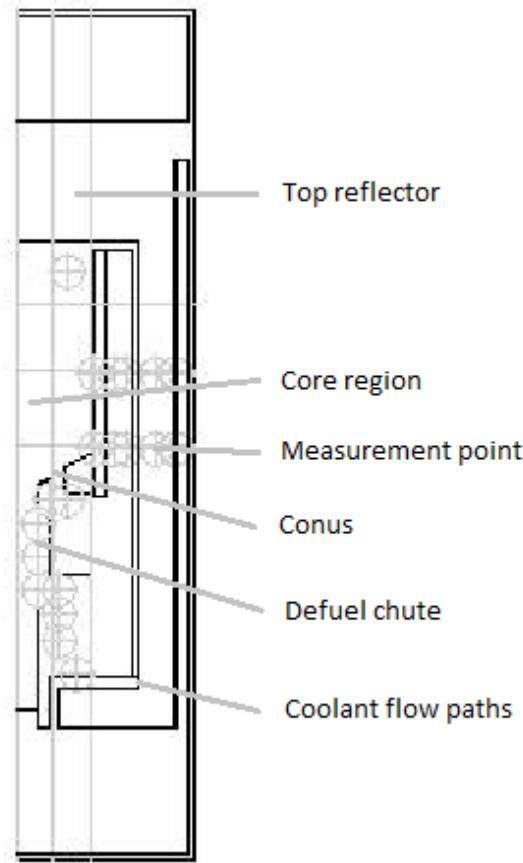


FIG. 2.14. 2-D axisymmetric model of the HTR-10.

For the analysis in the fluent code, the axisymmetric solver was set and the standard k-epsilon model was chosen for consideration of viscosity with respect to turbulence. All the solid materials were set and their properties were implemented into the analysis via benchmark specifications. The core region was left as a fluid zone and a user-defined scalar equation was assigned to it to represent the fuel surface temperatures. The viscous model in this region was changed and set as laminar. The reason for this assumption is that by its nature, the ‘Correlation for Frictional Pressure Loss in the Pebble Bed’ represents turbulence effects. The boundary conditions were implemented according to the benchmark. The boundary condition for the RPV walls was set to transfer heat via radiation to 50°C.

Equations

The conservation equations solved are as follows:

- The Mass Conservation Equation for 2-D Axisymmetric Geometry in the R-Z coordinate system;

$$\frac{\partial}{\partial z}(\rho v_z) + \frac{\partial}{\partial r}(\rho v_r) + \frac{\rho v_r}{r} = 0$$

- The Momentum Conservation Equation in 2-D Axisymmetric Geometry in the R-Z coordinate system;

$$\begin{aligned} \frac{1}{r} \frac{\partial}{\partial z}(r \rho v_z v_z) + \frac{1}{r} \frac{\partial}{\partial r}(r \rho v_r v_z) = & -\frac{\partial p}{\partial z} + \frac{1}{r} \frac{\partial}{\partial z} \left[r \mu \left(2 \frac{\partial v_z}{\partial z} - \frac{2}{3} (\nabla \cdot \vec{v}) \right) \right] \\ & + \frac{1}{r} \frac{\partial}{\partial r} \left[r \mu \left(\frac{\partial v_z}{\partial r} + \frac{\partial v_r}{\partial z} \right) \right] + F_z \end{aligned}$$

and

$$\begin{aligned} \frac{1}{r} \frac{\partial}{\partial z} (r \rho v_z v_r) + \frac{1}{r} \frac{\partial}{\partial r} (r \rho v_r v_r) = & -\frac{\partial p}{\partial r} + \frac{1}{r} \frac{\partial}{\partial z} \left[r \mu \left(\frac{\partial v_r}{\partial z} + \frac{\partial v_z}{\partial r} \right) \right] \\ & + \frac{1}{r} \frac{\partial}{\partial r} \left[r \mu \left(2 \frac{\partial v_r}{\partial r} - \frac{2}{3} (\nabla \cdot \vec{v}) \right) \right] - 2 \mu \frac{v_r}{r^2} + \frac{2}{3} \frac{\mu}{r} (\nabla \cdot \vec{v}) + \rho \frac{v_z^2}{r} Fr \end{aligned}$$

where the source terms in the core region are inserted into F as:

$$F_z = \Psi \frac{1-\varepsilon}{\varepsilon^3} \frac{1}{d} \frac{\rho}{2} v_z^2 \text{ and } F_r = \Psi \frac{1-\varepsilon}{\varepsilon^3} \frac{1}{d} \frac{\rho}{2} v_r^2$$

with:

$$\Psi = \frac{320}{\text{Re}} + \frac{6}{\left(\frac{\text{Re}}{1-\varepsilon} \right)^{0.1}}, \varepsilon \text{ void fraction and } d \text{ fuel outer diameter.}$$

The effect of near-wall porosity variations was implemented into the code according to the experimental results of Benenati and Brosilow [2-9], yet not overriding the limitations of the pressure drop correlation. The core is divided into two regions; half a diameter of a pebble from the walls is set as one region while the remainder is set as the other. The calculations of the values for the void fraction for these two regions are shown below for the near-wall porosity and core porosity respectively.

$$\begin{aligned} \varepsilon_w &= \frac{63.6}{\left(\frac{D}{d} + 15 \right)^2} + 0.43 \\ \varepsilon_c &= \frac{\varepsilon_t - \varepsilon_w}{\left(1 - \frac{d}{D} \right)^2} + \varepsilon_w \end{aligned}$$

The flow zones with void fractions that represented in the convection model of the benchmark, less than unity, are set as porous regions and the source terms for the momentum equations in these regions are introduced into F as:

$$F_z = \frac{f \rho |v| v_z}{2d_h} \text{ and } F_r = \frac{f \rho |v| v_r}{2d_h}$$

where

$$f = \frac{0.3164}{\text{Re}^{1/4}}$$

- The Energy Conservation Equation for Porous Regions;

Energy equations in the porous regions are treated as the modification of the conductive flux and the transient term. It is established by setting up an effective conductivity throughout the region and including the thermal inertia of the solid region. The modified equation is represented below.

$$\nabla \cdot (\vec{v} (\rho_f E_f + p)) = \nabla \cdot \left[k_{eff} \nabla T - \left(\sum_i h_i J_i \right) + (\vec{\tau} \cdot \vec{v}) \right] + S_f^h$$

where

E_f is the total fluid energy

E_s is the total solid energy

γ is the porosity of the medium

k_{eff} is the effective thermal conductivity

S_f^h is the fluid enthalpy source term

And the effective thermal conductivity is calculated by using the volume ratios.

$$k_{eff} = \gamma k_f (1 - \gamma) k_s$$

where

γ = porosity of the medium

k_f = fluid phase thermal conductivity

k_s = solid medium thermal conductivity

– The Energy Conservation Equation for Coolant;

$$\nabla \cdot (\vec{v}(\rho E + p)) = \nabla \cdot (k \nabla T + (\vec{\tau}_{eff} \cdot \vec{v})) + S_{he}$$

where

$$E = h - \frac{p}{\rho} + \frac{v^2}{2} \quad S_{he} = \frac{6\alpha(1-\varepsilon)}{d} (T_{fuel} - T_{he})$$

$$\alpha = \frac{Nu}{d} k \quad \text{and} \quad Nu = 1.27 \frac{Pr^{1/3}}{\varepsilon^{1.18}} Re^{0.36} + 0.033 \frac{Pr^{1/2}}{\varepsilon^{1.07}} Re^{0.86}$$

– The Energy Conservation Equation for Fuel Surface Temperatures;

$$-\nabla \cdot k \nabla T_{fuel} = S_{fuel}$$

where

$S_{fuel} = \dot{Q} - S_{he}$ and \dot{Q} is the power distribution matrix specified in the benchmark.

– The Energy Conservation Equation for the Solid Structure Temperatures;

$$-\nabla \cdot k \nabla T_{solid} = 0$$

The coupling regarding the interaction between the fuel surface temperatures and the solid structures that are in contact is done by implementing internal boundaries in the form of Fourier's law as:

$$\vec{q}'' = -k \nabla T$$

where the boundary utilizes the thermal conductivity k of the fuel region as the effective pebble bed thermal conductivity correlation since conduction and radiation heat transfer mechanisms are taken into account in the correlation. This enables modelling heat transfer between core walls and the coolant and the fuel zone together.

Results of the benchmark problem

Temperature distributions of the pebble bed and static temperatures representing the coolant and the solid structures at specified locations, namely, $R = 0$ cm, $R = 45$ cm, $R = 90$ cm, $Z = 0$ cm, $Z = 80$ cm and $Z = 170$ cm, as shown in Figs 2.15–2.27.

While maintaining effective cooling, it is seen that the coolant is responsible for the heating of the dummy balls below the active core region. The sharp fall in the temperature values below the region that the part of the main stream of the coolant leaving the exiting from the discharge tube–hot gas plenum connection can be seen in Fig. 2.17.

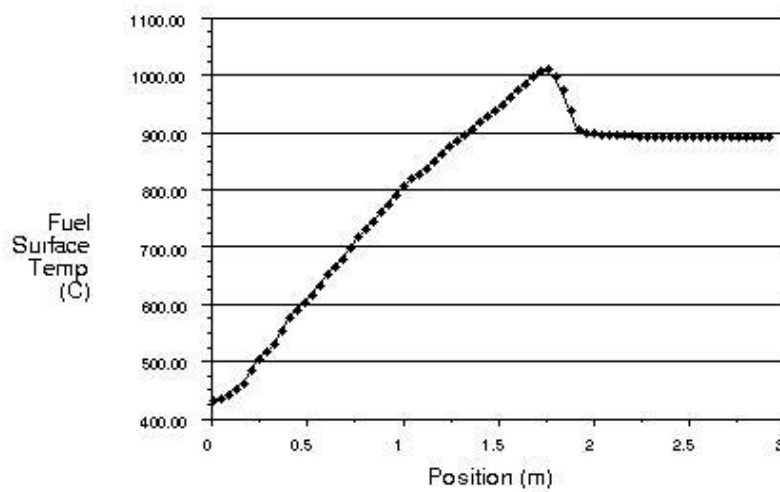


FIG. 2.15. Fuel element surface temperature at $R = 0$ m.

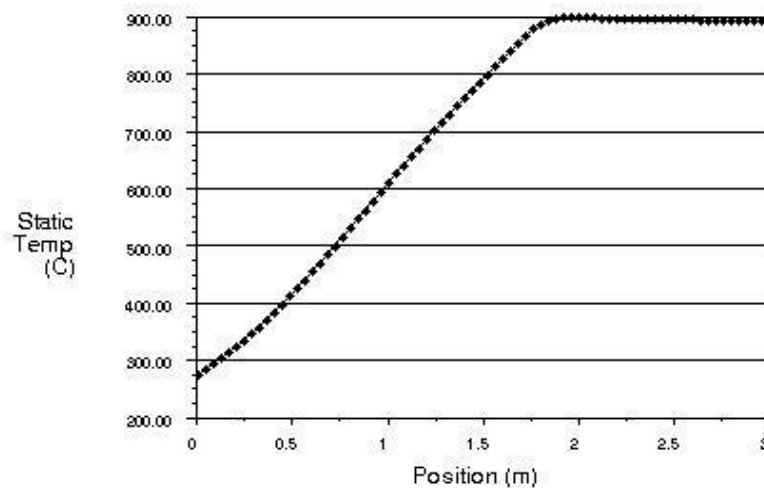


FIG. 2.16. Coolant temperature at $R = 0$ m.

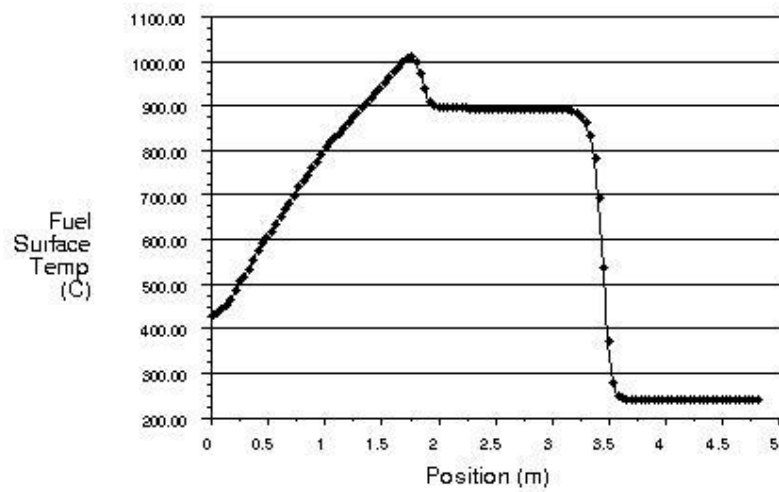


FIG. 2.17. Fuel element surface temperature at $R = 0$ m including the discharge tube.

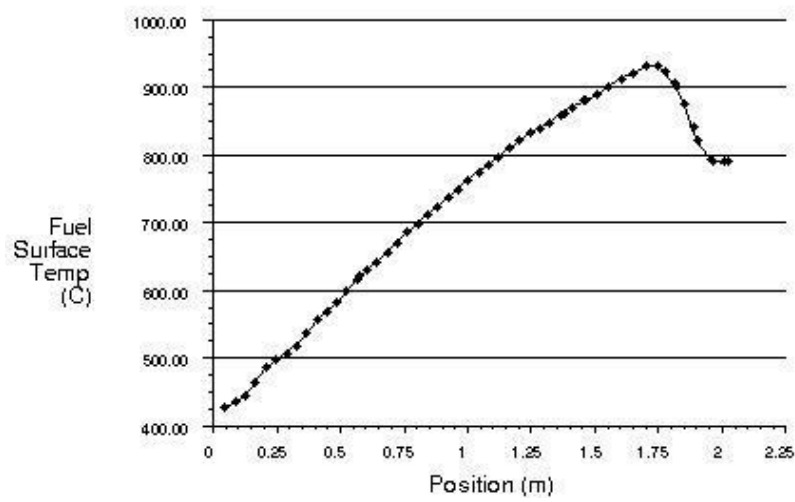


FIG. 2.18. Fuel element surface temperature at $R = 0.45$ m.

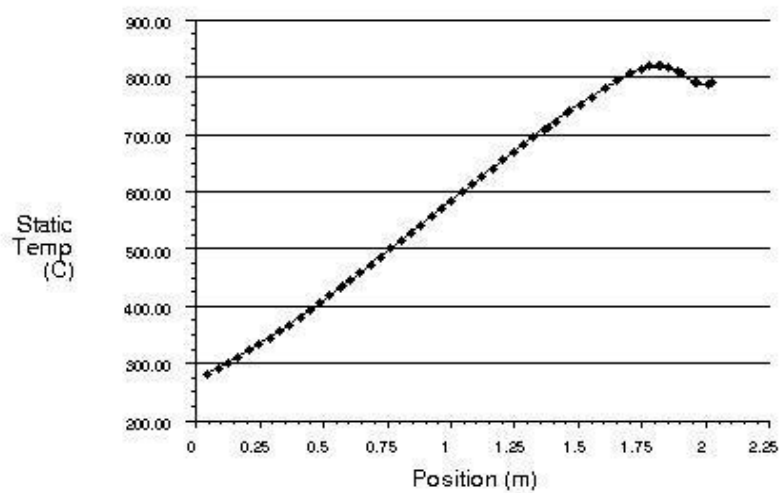


FIG. 2.19. Coolant temperature at $R = 0.45$ m.

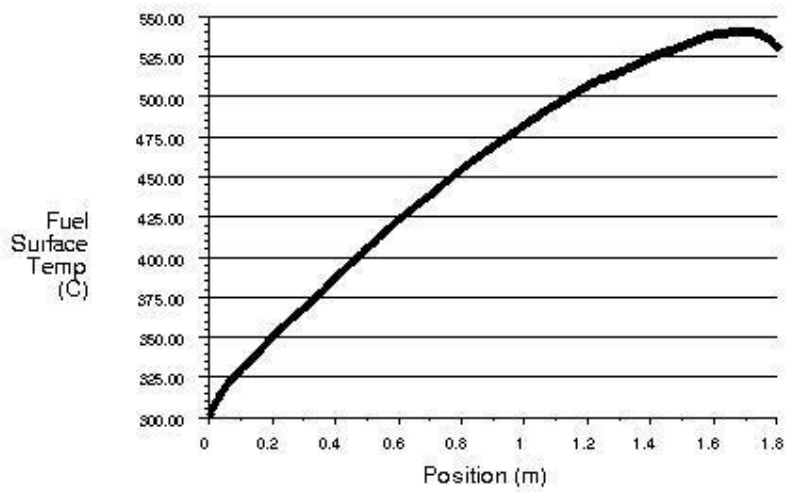


FIG. 2.20. Fuel element surface temperature at $R = 0.9$ m.

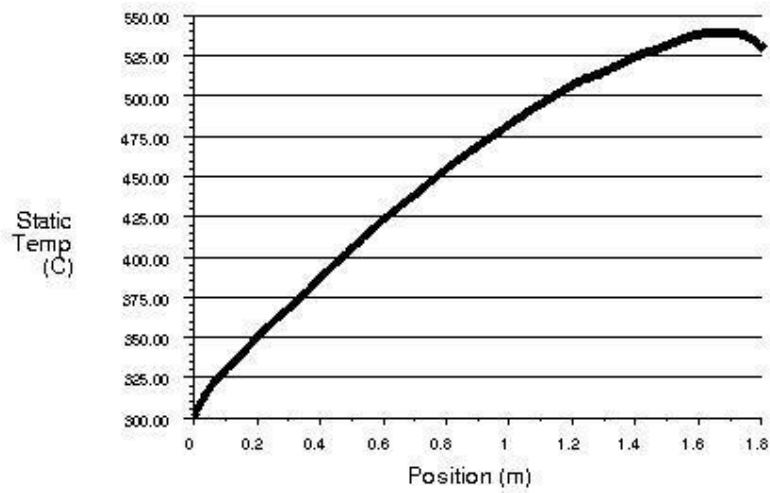


FIG. 2.21. Coolant temperature at $R = 0.9$ m.

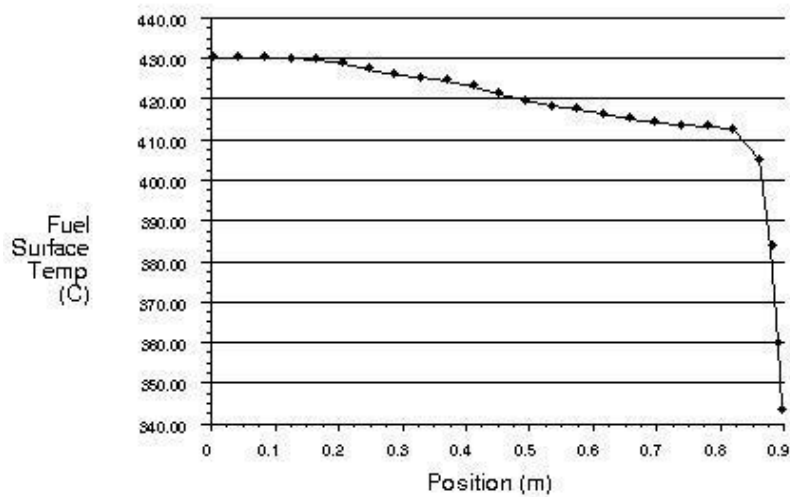


FIG. 2.22. Fuel element surface temperature at $Z = 0$ m.

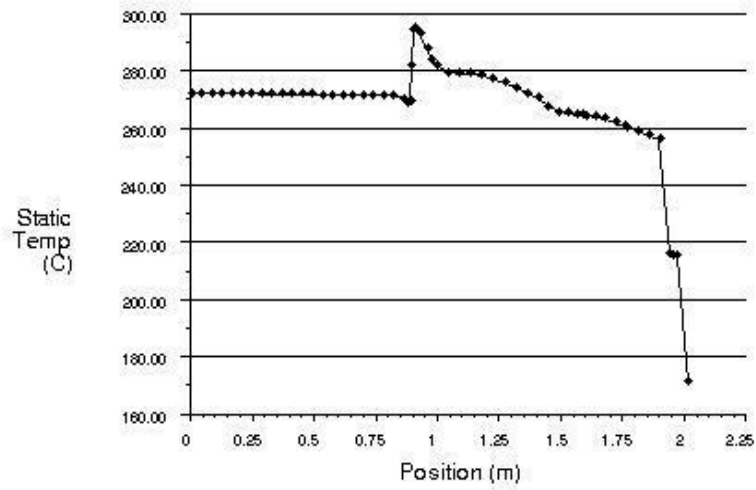


FIG. 2.23. Static temperature at $Z = 0$ m.

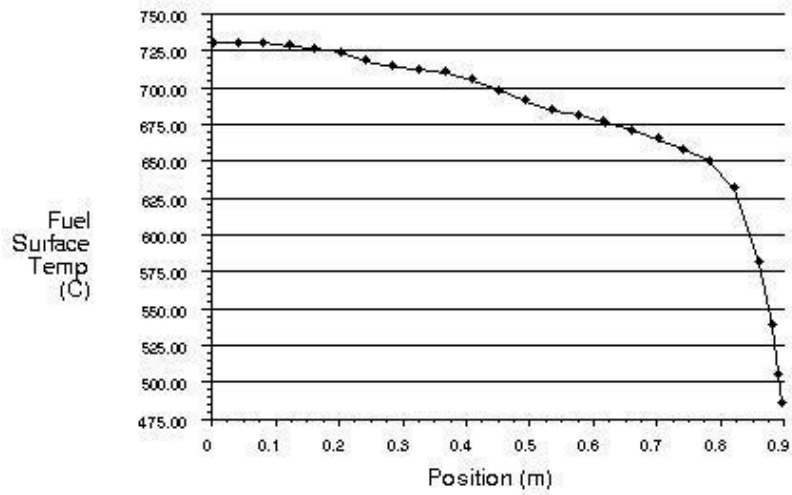


FIG. 2.24. Fuel element surface temperature at $Z = 0.8$ m.

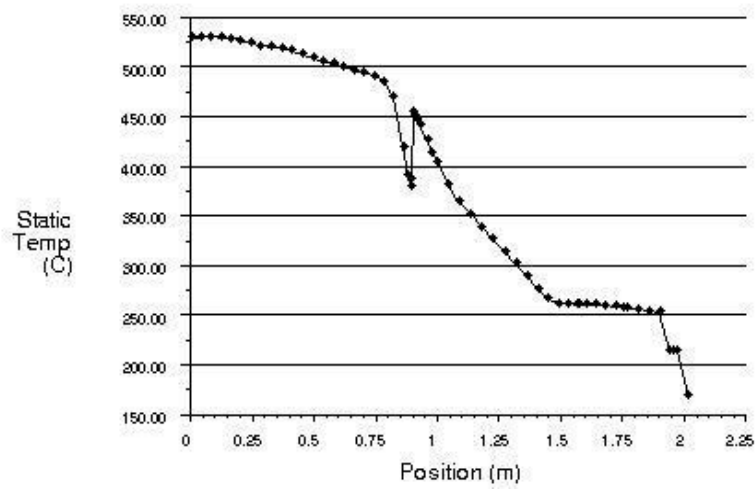


FIG. 2.25. Static temperature at $Z = 0.8$ m.

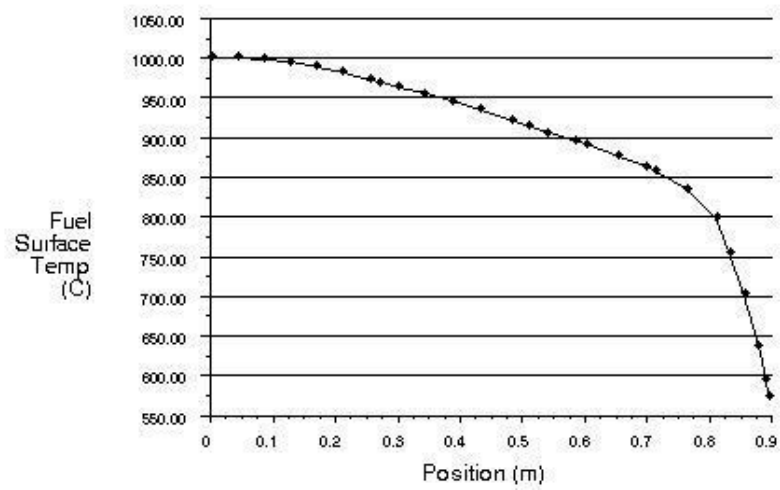


FIG 2.26. Fuel element surface temperature at $Z = 1.7$ m.

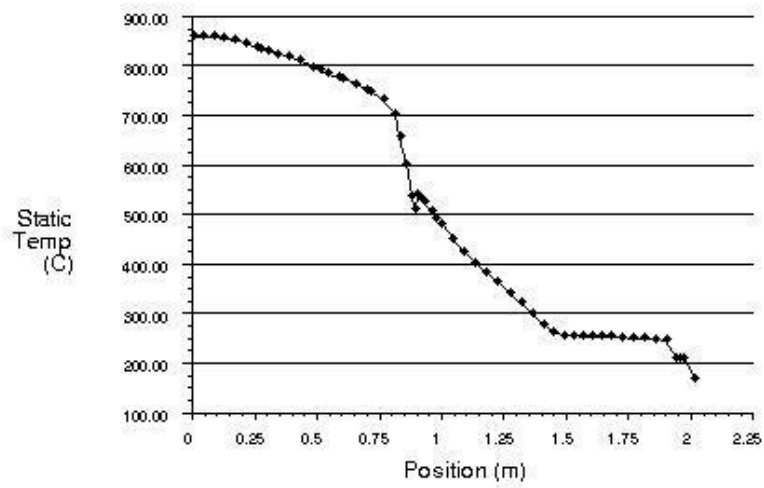


FIG. 2.27. Static temperature at $Z = 1.7$ m.

TABLE 2.16. SOLID TEMPERATURE VALUES

No.	R (cm)	Z (cm)	T (°C)	T (°C) (Experiment)
Side reflector				
1	193	80	223.7	231.3
2	189	80	253.2	249.3
3	167	80	260	274.3
4	133	80	298	289.1
5	117	80	341	313.3
6	93	80	440.8	357.7
7	193	170	219.7	234.9
8	189	170	247.2	264.8
9	167	170	253.4	303.9
10	133	170	314.8	328.5
11	117	170	386.3	365.3
12	93	170	523.6	507.1
Top reflector				
13	60	-40	267.1	245.7
Hot helium plenum				
14	40	234	820.1	800.2
15	60	234	737.8	763.1
Bottom carbon bricks				
16	70	440	246.1	224.1
17	50	400	245.1	245.7
18	50	370	251.7	269.2
19	50	340	340.1	406.7
Fuel discharging tube				
20	26	340	323.1	334.2
21	26	300	819.9	806.1
22	26	260	828.8	881.7

Table 2.16 shows the solid temperature values obtained at selected locations within the HTR-10.

The maximum temperature values for the specified locations are as follows:

Fuel element centre = 1025.6°C;

Fuel element surface = 1008.3°C;

Side reflector = 580.6°C;

Bottom reflector = 836.0°C.

It is seen that the model used seems to be suited to represent the system. The energy coupling procedure causes computational load which can be reduced by further modifications of the algorithm. The results seem to correspond well with the experimental values in most cases, with only a few outliers. The spread in results is similar to those of most of the other participants — see Section 7.1.

2.2.2.3. HTR-10 steady state temperature benchmark results, France

Introduction

The HTR-10 is a pebble bed HTGR designed, constructed and operated by INET in China. Full power operation with a core outlet temperature at 700°C was achieved in January 2003. This reactor operates with a primary helium pressure of about 3 MPa and a core inlet temperature of 250°C. The benchmark proposed within the CRP-5 framework is devoted to steady state temperature distribution inside the

reactor vessel for FPIC. It has been proposed both for code-to-code and for code-to-experiment benchmarking. Thermocouples have been installed in the reactor cavity to provide experimental results. CEA contributes to this benchmark exercise with a Computational Fluid Dynamics (CFD) code named ARCTURUS, which is a part of the CAST3M code, a fluid and structural mechanics code dedicated to gas cooled thermal hydraulics [2-10, 2-11]. This section is divided into three main parts. In the first part, the specifications of the benchmark exercise are recalled including reactor geometry, proposed material properties and correlations, and initial and boundary conditions. The CAST3M/ARCTURUS model is described in the second part, whereas the third part is dedicated to the benchmark results and comparisons. Finally, some conclusions follow.

Benchmark specifications

Short description of the HTR-10 reactor structure

The active core is cylinder-shaped and cone-shaped at the bottom to unload fuel elements. Graphite reflectors categorized as top, side and bottom reflectors surround the core. The active core and reflectors are radially enclosed in a core vessel and upper and lower core support plates axially. Stagnant helium between this core vessel and the RPV acts as insulation and most of the heat is transferred by thermal radiation. After entering the RPV, the cold helium flows downwards through the annular gap between the core vessel and the RPV. Then it changes its flow direction to flow upwards. A small part of this cold helium goes through the cone-shaped discharging tube to cool the fuel elements and afterwards merges with the hot helium. The major part of the helium goes around the core support structures and enters into the cold helium channels in the side reflector. At the top of this reflector, cold helium is collected in the so-called upper plenum and it then changes its flow direction for a second time. Part of this helium goes through the control rod channels and is collected in a small plenum above. The main stream of helium flows through the active core and is collected in the lower hot plenum (Fig. 2.28).

Geometrical characteristics

All the geometrical data is given in a detailed description provided in the benchmark specification document [2-1].

Heat transfer coefficient

Heat transfer coefficient h can be evaluated according to the following formula:

$$h = \frac{Nu \lambda_{He}}{d_{fuel}}$$

with

$$\lambda_{He} = 2.772 \cdot 10^{-3} T^{0.714}$$

the thermal conductivity in W/m/K

where the temperature T is in Kelvin;

$d_{fuel} = 0.06$ fuel diameter in m;

The Nusselt number Nu is derived from the following correlation:

$$h = 1.27 \frac{Pr^{1/3}}{\varepsilon^{1.18}} Re^{0.36} + 0.033 \frac{Pr^{1/2}}{\varepsilon^{1.07}} Re^{0.86}$$

with

$\varepsilon = 0.39$ the pebble bed porosity;

$Pr = \frac{\mu_{He} C_{p_{He}}}{\lambda_{He}}$ is the Prandtl number;

$\mu_{He} = 3.674 \cdot 10^{-7} T^{0.7}$ the helium dynamic viscosity in Pa.s;

where

the temperature T is in K ;

$C_{p_{He}} = 5195 \text{ J/kg/K}$ is the specific heat capacity;

the Reynolds number is $Re = q d_{fuel} / A \mu_{He}$ with q the gas mass flow rate in the pebble bed (kg/s);

A is the flow path area of the empty pebble bed.

For other equivalent porous media zones, classical correlations for turbulent forced convection are used, and a constant Nusselt number is used below a certain Reynolds number value assuming conduction dominant heat transfer:

$$Nu = 0.023 Re^{0.8} Pr^{0.4}$$

Frictional pressure loss in the pebble bed

Frictional pressure loss in the pebble bed can be calculated using the following specified formula:

$$\vec{\nabla}P = \frac{1}{2} \frac{\rho f}{d_H} u^2$$

and the friction coefficient f is defined by:

$$f = \left[\frac{320}{\frac{Re}{1-\varepsilon}} + \frac{6}{\frac{Re^{0.1}}{1-\varepsilon}} \right] \frac{1-\varepsilon}{\varepsilon^3}$$

For the other equivalent porous media zones, classical correlations for turbulent friction term are used:

$$f = 0.316 Re^{-0.25}$$

Material properties

Properties of the different components (helium gas, fuel element, reflector graphite, carbon bricks and cavity) are provided in the benchmark specifications and are not recalled here. One important datum is the equivalent heat conductivity of the uniformed pebble bed including conductive, convective and radiative heat transfers. This heat conductivity ($W/cm/K$) has been provided in the specification document [2-1] according to the following formula:

$$\lambda = 1.1538 \cdot 10^{-6} (T + 100)^{1.6622}$$

where T is the pebble bed temperature in $^{\circ}C$.

Boundary conditions

The boundary conditions are provided in the specification document [2-1]. The first one is the inlet temperature of the helium gas entering the reactor vessel at $250^{\circ}C$. Then, the inlet mass flow rate is set at 4.32 kg/s and this flow rate is supposed to be distributed through the different parts of the reactor vessel according to Fig. 2.28. No specifications are given for the bypass after the core region.

The delivered nuclear power is also prescribed in the benchmark specifications (Table 4 of Ref. [2-1]). This provided, grid (R,Z) has been projected on the used grid to create the nuclear power distribution. The reference point (0,0) is located in the upper centre of the pebble bed.

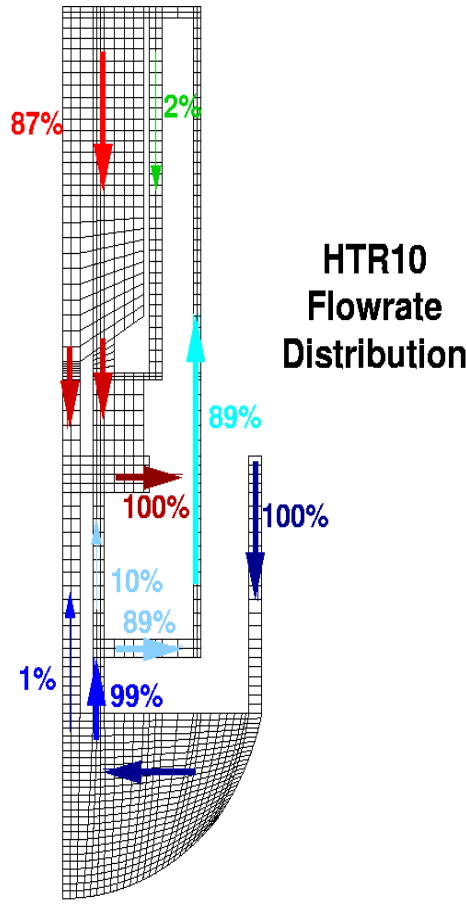


FIG. 2.28. HTR-10 — Specified mass flow rate distribution.

Description of CAST3M/ARCTURUS models

Description of ARCTURUS models

The asymptotic low Mach number flow model using equivalent porous media formulation developed for the ARCTURUS code solves the following set of equations:

Let us introduce the porous media velocity $\vec{u}_D = \beta \vec{u}$, where β represents the porosity (fluid volume versus total volume) and \vec{u} the velocity. The dynamic pressure p' ($P(x,t) = P(t) + p'(x,t)$) is recovered from the velocity divergence constrain:

$$\nabla \cdot \vec{u}_D = -\frac{1}{\rho} \left(\beta \frac{\partial \rho}{\partial t} + \vec{u}_D \cdot \nabla \rho \right)$$

The velocity field \vec{u}_D is obtained from the momentum equation [2-12]:

$$\frac{\rho}{\beta} \frac{\partial \vec{u}_D}{\partial t} + \frac{\rho}{\beta^2} \vec{u}_D \cdot \nabla \vec{u}_D = \vec{F} + \rho \vec{g} - \nabla p' + \frac{\mu + \mu_T}{\beta} \Delta \vec{u}_D$$

where

\vec{F} represents the frictional pressure loss;

\vec{g} the gravity;

μ_T the turbulent viscosity.

This equation is not straightforward and various formulations may be obtained from the literature review. The fluid temperature T_f comes from the fluid energy balance:

$$\rho C p_f \beta \frac{\partial T_f}{\partial t} + \rho C p_f \vec{u}_D \cdot \vec{\nabla} T_f = \beta \nabla \cdot (\lambda + \lambda_T) \vec{\nabla} T_f + Q_{fs}$$

where λ_T represents the turbulent heat conductivity and Q_{fs} the heat flux inside the porous media determined by correlations for the heat exchange coefficient.

The expression of the diffusive term may be discussed. The effect of this modelling has to be especially assessed on simplified test cases. Then, the solid temperature T_s is expressed from the solid energy balance:

$$(1 - \beta) \rho_s C p_s \beta \frac{\partial T_s}{\partial t} = \lambda_{eq} \Delta T_s - Q_{fs} + \Phi_{rad} + \Phi_{neutro}$$

where

λ_{eq} represents the equivalent thermal conductivity of the homogenized porous media;

Φ_{rad} the power exchanged by thermal radiation; and

Φ_{neutro} the nuclear power.

Finally, the state equation is used with constant thermodynamic pressure (steady state) to recover the fluid density ρ :

$$\rho T_f = \text{constant}$$

The spatial discretization uses finite elements (Q2P1) and the numerical method uses a semi-implicit incremental projection method [2-13]. The linear system is solved by using classical iterative methods. Thermal radiation is based on classical gray surfaces emissivity in enclosure methods available in the CAST3M code [2-14].

Description of the HTR-10 model for the ARCTURUS code

The proposed model is a 2-D axisymmetric grid of the HTR10 reactor vessel (Fig. 2.29). The reference mesh corresponds to about 20000 nodes in the fluid and solid regions (753 elementary surfaces are considered for thermal radiation).

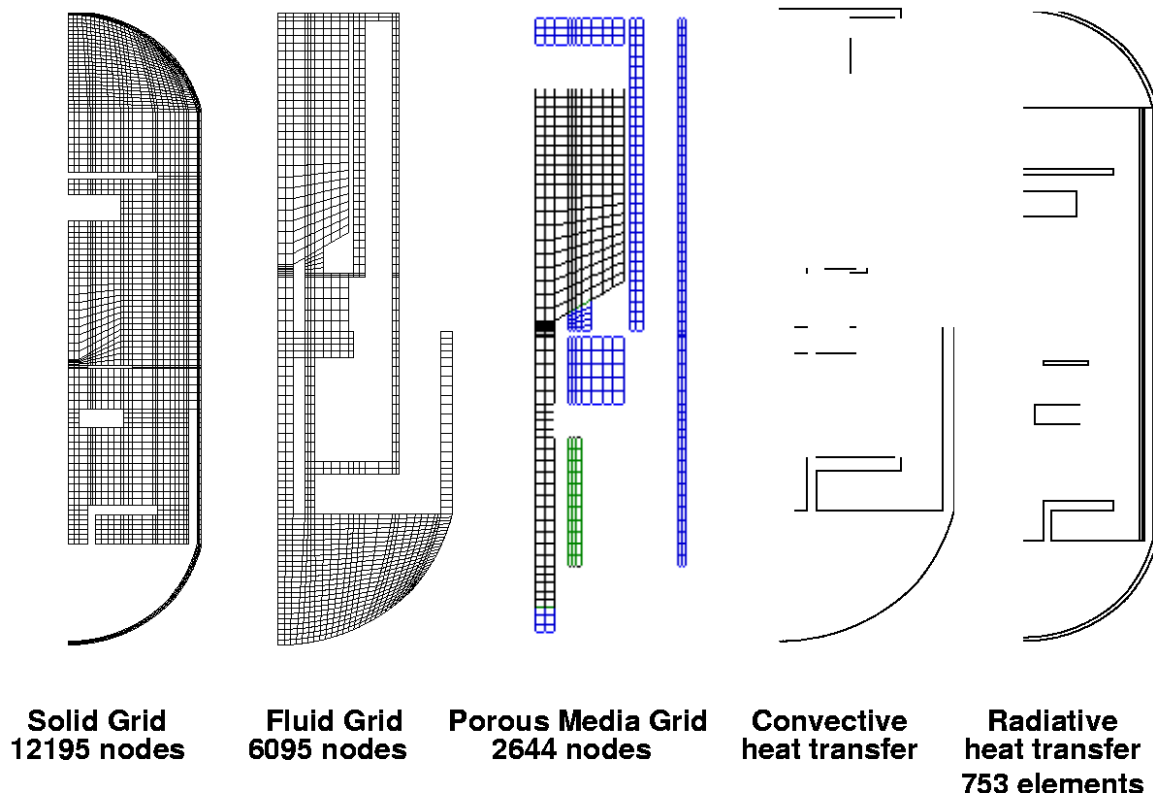


FIG. 2.29. HTR-10 — CAST3M/ARCTURUS mesh description.

The specified mass flow rate distribution between the different parts of the reactor vessel is achieved by adding specific pressure losses in the different bypasses (lower part of the fuel discharging tube, lower plenum bypass and control rods channels) in order to compute the proposed distribution (this adjustment has been performed with isothermal flow). The steady state values are reached by using a transient simulation. An indicative Central Processing Unit (CPU) time for this calculation on a 2.3 GHz Personal Computer (PC) with a 2Gig Random Access Memory (RAM) is about 50 000 s.

Benchmark results

The requested results for the benchmark exercise are the vertical temperature profiles in the pebble bed at $R = 0$ cm, $R = 45$ cm and $R = 90$ cm as shown in Fig. 2.30. These profiles clearly show that the maximum pebble bed solid temperature is located in the lower part of the bed at approximately -1.7 m from the top of the active core (due to the shape of the nuclear power distribution and the effect of the convective heat transfer). A sharp temperature profile is also computed near the hot plenum where downward hot flow meets upward cold flow in the discharging tube. The comparison with the experimental results in this region (Table 2.17) shows some deviations in the exact location of this transition (radial profile is also present in this region; see Fig. 2.31).

TABLE 2.17. FUEL DISCHARGING TUBE TEMPERATURE

No.	R (cm)	Z (cm)	Calc. Tsol (°C)	Calc. Tflu (°C)	dT/dr (°C/m)	dT/dz (°C/m)	Exp. T (°C)
20	26	340	305	282	410	847	334.2
21	26	300	761	809	-1671	69	806.1
22	26	260	796	803	-310	18	881.7

One important assumption concerns the flow distribution between the fuel discharging tube and the bypass at the end of the V-shape, i.e. no information is given for this distribution and this may act on the temperature field in the fuel discharging tube. One has to also keep in mind that the present model gives homogenized temperature values and a significant decrease of the temperature may be computed

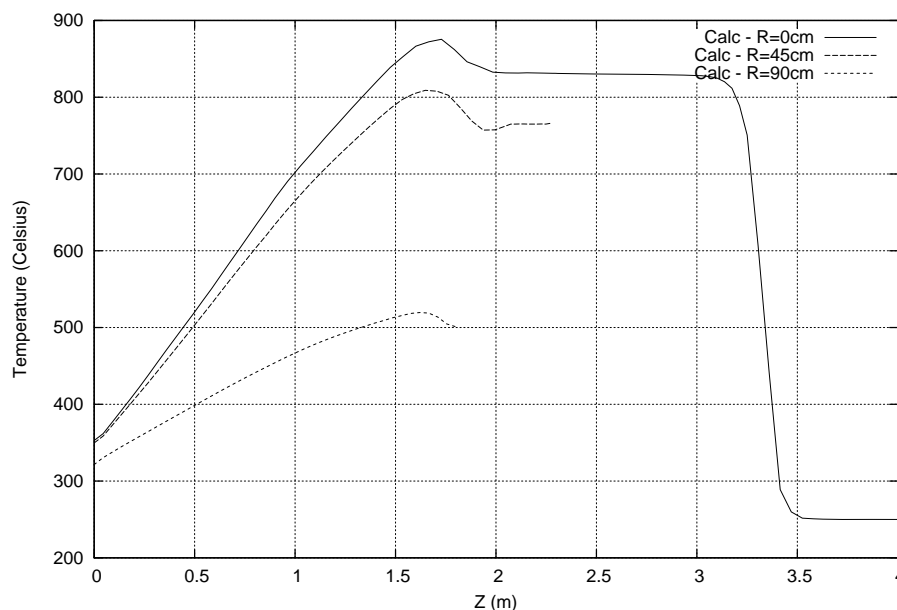


FIG. 2.30. HTR-10 — CAST3M/ARCTURUS results — Vertical temperature profiles (Solid).

(reconstruction is usually needed). Concerning this last point, steady state calculations on a block fuel assembly of a Gas Cooled Fast Reactor have shown differences of about 80°C in the maximum solid temperature using equivalent porous media or real geometry [2-10].

Three radial solid temperature profiles are then plotted at $Z = 0$ cm, $Z = 80$ cm and $Z = 170$ cm as shown in Fig. 2.31. First, the computed results do not start at 0.0 m radius because of symmetry axis translation needed by quadratic finite-element discretization. Second, the computed profile at $Z = 170$ cm is not reported in the active core due to grid deformation (Fig. 2.29).

The comparison with the experimental results shows a rather poor comparison especially in the middle core axial level (Table 2.18). Nevertheless, it seems that the slopes are rather good (right computed conduction fluxes). One important reason for that deviation could be the thermal effect of the bypass through the control rods. In this region, a bypass of 2% of the total mass flow rate creates a laminar flow through the control rods channels and in the computation, the heat extracted by this convective transfer may be perhaps too low compared to the reactor case. Some additional experimental information or code-to-code comparison is needed to point out some conclusions about this special point. In the lower part (at the active core exit), the comparison is better and the slopes get closer.

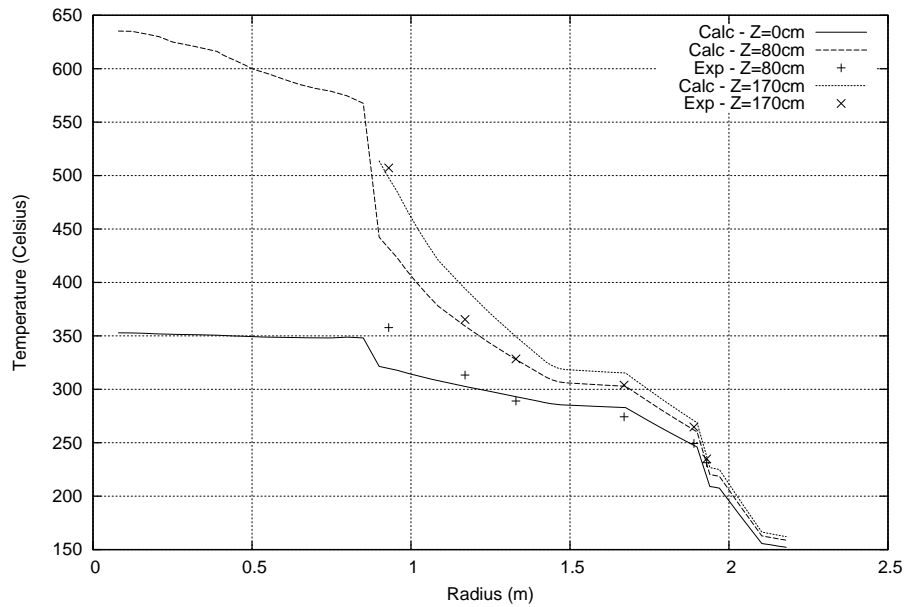


FIG. 2.31. HTR-10 — CAST3M/ARCTURUS results - Radial temperature profiles (Solid).

TABLE 2.18. SIDE REFLECTOR TEMPERATURE

No.	R (cm)	Z (cm)	Calc. Tsol (°C)	Calc. Tflu (°C)	dT/dr (°C/m)	dT/dz (°C/m)	Exp. T (°C)
1	193	80	220	271	-588	-11	231.3
2	189	80	260	271	-465	-15	249.3
3	167	80	303	271	-99	-22	274.3
4	133	80	329	274	-181	-39	289.1
5	117	80	360	279	-213	-63	313.3
6	93	80	433	288	-341	-125	357.7
7	193	170	227	265	-620	-3	234.9
8	189	170	269	265	-493	-5	264.8
9	167	170	315	265	-107	-8	303.9
10	133	170	350	267	-260	-11	328.5
11	117	170	395	302	-305	-10	365.3
12	93	170	499	323	-505	128	507.1

The solid temperature at different locations is also reported in Tables 2.18–2.21. Fluid temperature at the nearest point and temperature gradients are also reported. Locations of the different temperature gauges are reported in Fig. 2.32 and the three series correspond to the experimental location, the computed solid nodes and the computed fluid nodes close to this prescribed location. All the calculated results are compared to those released by the project [2-5]. Fluid temperature at the nearest point is also reported in the tables and the solid temperature gradient in the R - and Z -directions. This can give an estimation of the ‘uncertainty’ of the given temperature value.

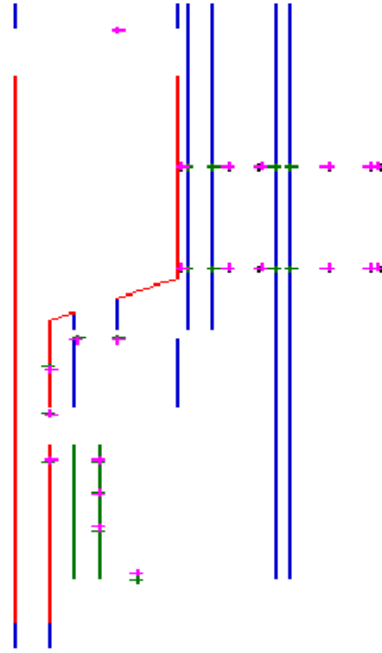


FIG. 2.32. HTR-10 thermal gauge location (pink: exp, black: calc. aolid and green: calc. fluid).

Regarding the top reflector (Table 2.19), the measured temperature is lower than the calculated one and this may perhaps be due to the thermal effect of the bypass through the control rods. In Fig. 2.33, it can be observed that the conductive heat transfer coming from the side reflector affects the top reflector.

TABLE 2.19. TOP REFLECTOR TEMPERATURE

No.	R (cm)	Z (cm)	Calc. Tsol (°C)	Calc. Tflu (°C)	dT/dr (°C/m)	dT/dz (°C/m)	Exp. T (°C)
13	60	-40	278	275	3	-24	245.7

In the hot helium plenum (Table 2.20), the calculated temperatures are lower than the measured ones (about 20°C) and the radial difference is adequate. One has to remember that the computed values correspond to homogenized values of the solid temperature and no reconstruction is proposed in the present study to recover the solid temperature.

TABLE 2.20. HOT HELIUM PLENUM TEMPERATURE

No.	R (cm)	Z (cm)	Calc. Tsol (°C)	Calc. Tflu (°C)	dT/dr (°C/m)	dT/dz (°C/m)	Exp. T (°C)
14	40	234	783	785	-159	-8	800.2
15	60	234	740	742	-220	-55	763.1

In the bypass region (Table 2.21 and Fig. 2.33), agreement between the calculated and measured results is rather poor. First, the experimental value concerning the lowest point is below the inlet temperature of the helium gas and this means that important heat losses are not taken into account in the computation. The upper part of this region is also very challenging for computation because the temperature value is the result of an energy balance between conduction (from the hot helium plenum where most of the heat from the upper surface to the lower surface is transferred by thermal radiation) and convection due to the bypass (conservatively, the 10% of the mass flow rate bypass has been taken into account). The results presented in Fig. 2.34 also show that strong temperature gradients are radially present due to the absence of convective heat transfer.

TABLE 2.21. BOTTOM CARBON BRICKS TEMPERATURE

No.	R (cm)	Z (cm)	Calc. T _{sol} (°C)	Calc. T _{flu} (°C)	dT/dr (°C/m)	dT/dz (°C/m)	Exp. T (°C)
16	70	440	250	249	2	18	224.1
17	50	400	251	250	58	8	245.7
18	50	370	257	251	251	36	296.2
19	50	340	288	255	946	355	406.7

The temperature fields (solid and fluid) and the velocity field are plotted in Figs 2.33 and 2.34.

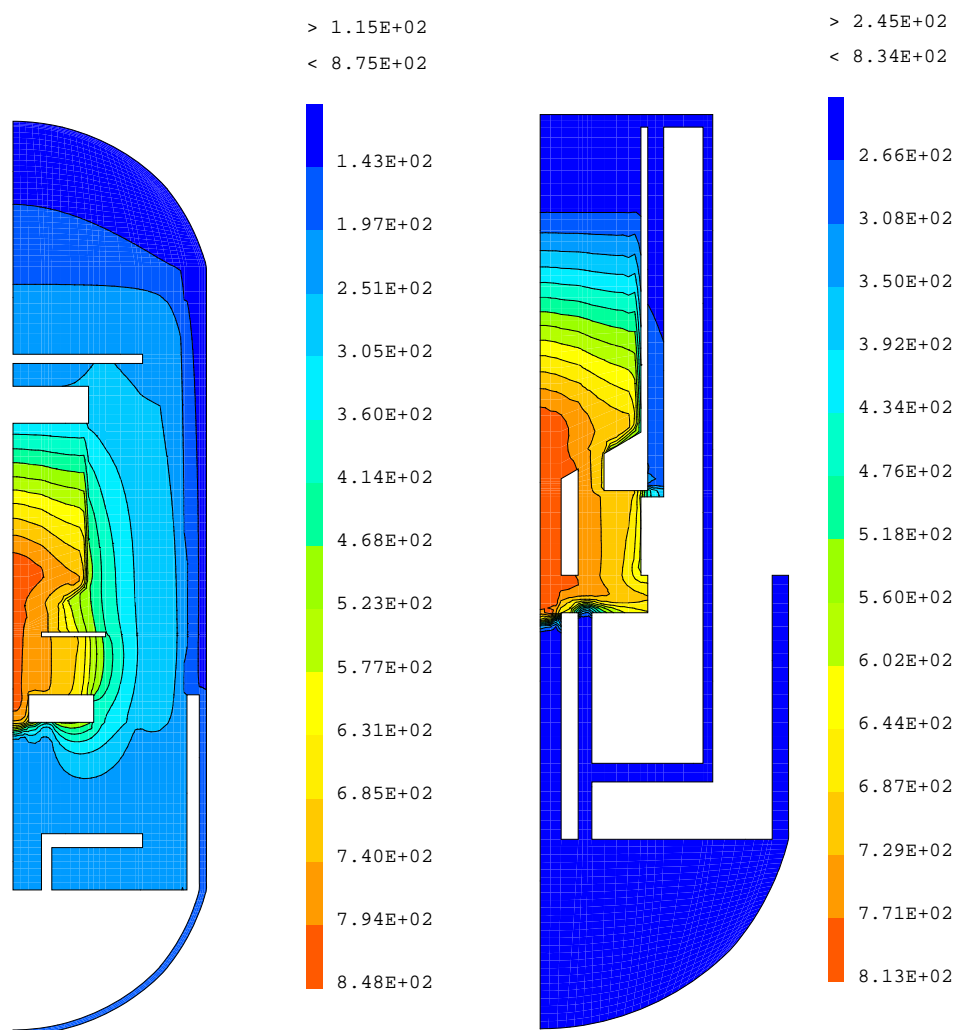


FIG. 2.33. HTR-10 — CAST3M/ARCTURUS — Solid temperature and fluid temperature.

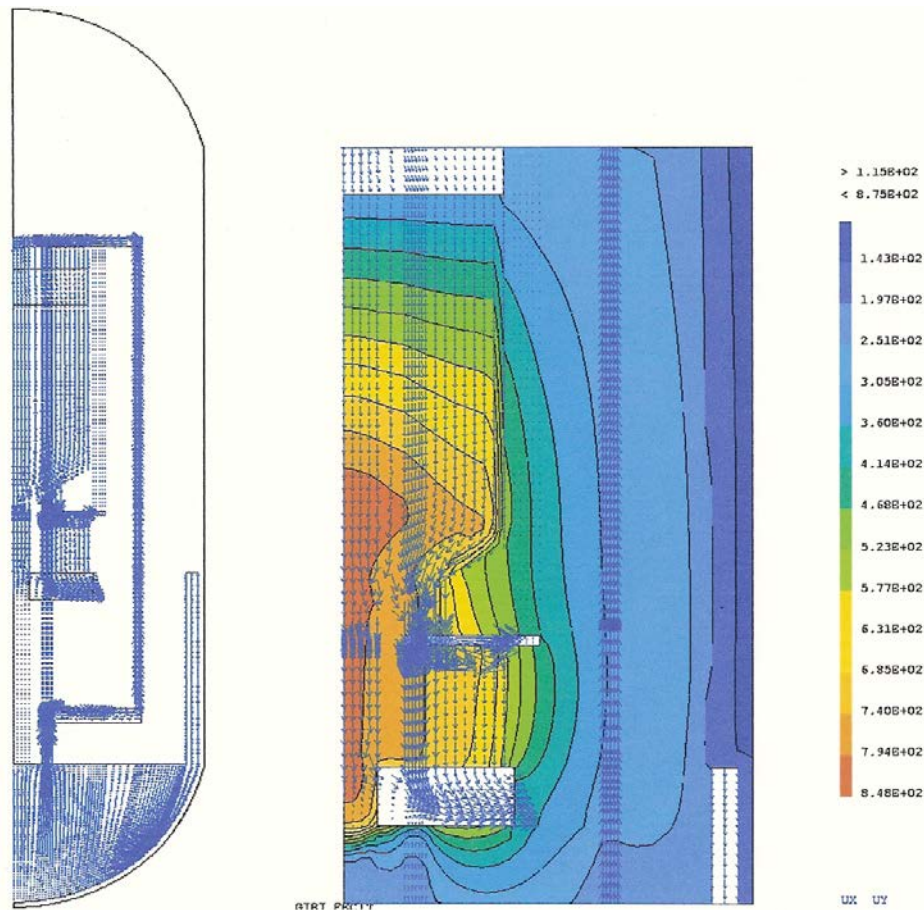


FIG. 2.34. HTR-10 — CAST3M/ARCTURUS — Velocity field and solid temperature.
Velocity field (zoom).

Final results taking benchmark clarifications into account

The core power distribution has been slightly modified [2-15] and therefore the CASTEM model calculations repeated. Discrepancies between results coming from the old and the revised benchmark are depicted in Fig. 2.35. It shows that there is no significant impact on the key-temperatures results given previously in Tables 2.17–2.21. However, these key temperatures have been recomputed and provided to China, the host country for this benchmark, for the final comparison. Only small differences are visible in the radial and axial temperature profiles, near the zone where the core power density had been changed. Radial profiles at $Z = 170$ cm and axial profiles at $R = 90$ cm depict some temperatures which are lower.

Finally, the revised benchmark [2-6] offered an opportunity to complete the results. Indeed, the maximum temperatures achieved in the reflectors and in the fuel elements have been estimated from the maximum *solid* temperature of the porous media given by the CASTEM model. As far as the maximum fuel temperature is concerned, it amounts to 875°C in a mesh located at the bottom part of the core where the average power density is 2.33 W/cm^3 . A dehomogenization model has been applied to reconstruct the temperature profile inside the pebbles and led to the final values gathered in Table 2.22.

Conclusions

This benchmark exercise has demonstrated the capabilities of the CAST3M/ARCTURUS code system to simulate steady state temperature fields including complex convective, conductive and radiative heat transfers. Some discrepancies between the calculated and measured values still exist especially where convective heat transfer is important (bypass regions). Some adjustments may be made after discussions of the present results with the experimental team and also other code simulations.

TABLE 2.22. MAXIMUM TEMPERATURES OF THE MAIN COMPONENTS

Component	Maximum temperature
Fuel element: centre	889°C
Surface	865°C
Side reflector	520°C
Bottom reflector	808°C

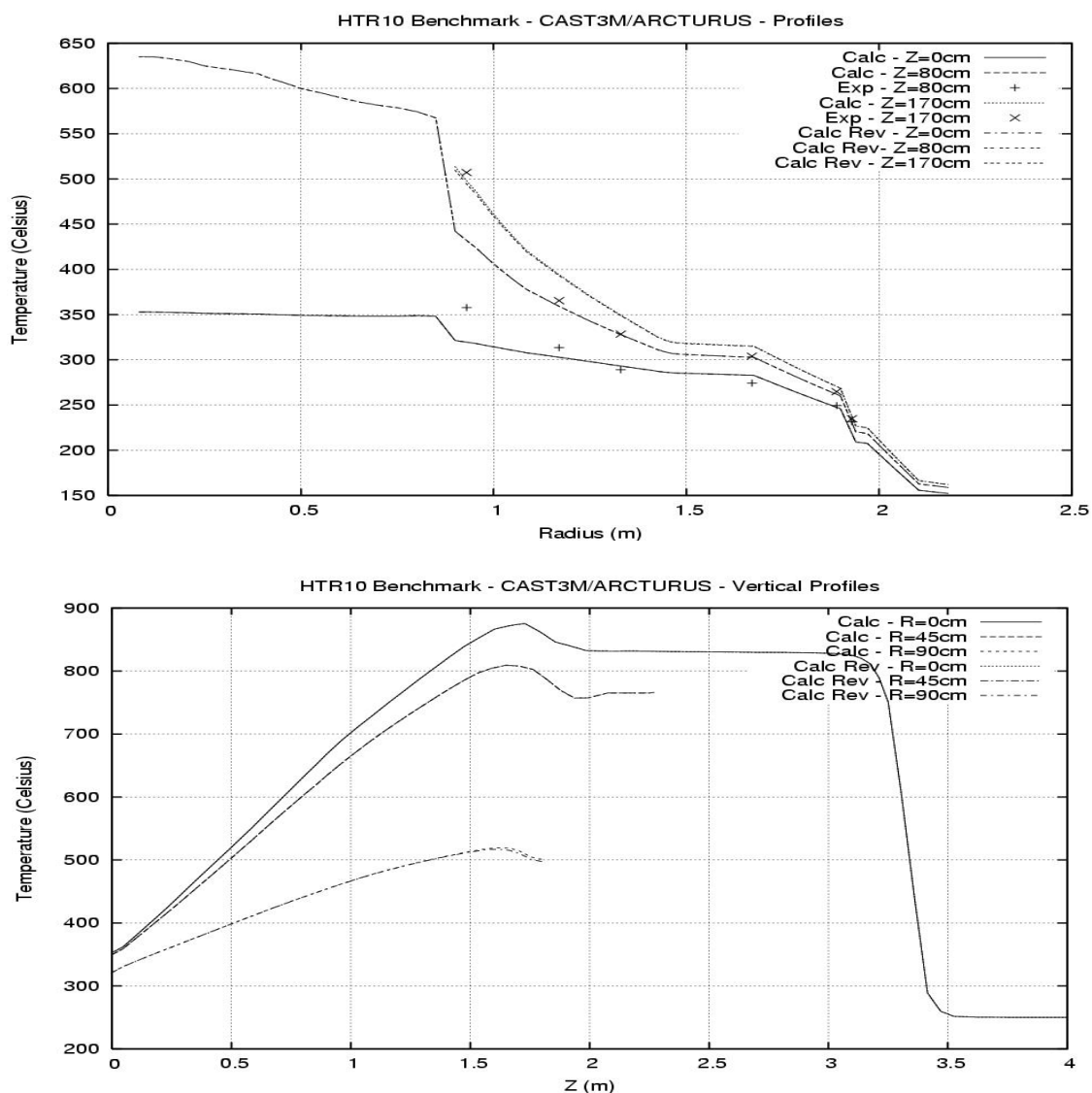


FIG. 2.35. HTR-10 — CAST3M/ARCTURUS results — Axial and vertical temperature profiles (Solid). Comparison between original and revised benchmark.

Evaluation of the present model under transient behaviour is also an important and difficult task. Additional experimental results may perhaps be delivered to assess this important point. Another interesting point is the transient behaviour under natural convection, but it is of interest for HTRs where the power density is low and the thermal inertia high.

Introduction

This document describes the KAERI benchmark calculations of the HTR-10 [2-15] steady state FPIC. The HTR-10 is a pebble-bed-type high temperature helium gas cooled reactor, which has been designed and operated by INET in China [2-16]. The steady state 10 MW_{th} FPIC operated with a reactor outlet temperature of 700°C, a reactor inlet temperature of 250°C, a flow rate of 4.32 kg/s and a primary helium pressure of about 3 MPa from January 2003. The CRP-5 benchmark problem [2-1] provided the measured temperature distribution inside the reactor vessel at these FPIC conditions for code-to-experiment benchmarking. KAERI tries to perform this benchmark exercise with the Gas Multi Component Mixture Analysis (GAMMA) code [2-17], which is a system thermal hydraulics and safety analysis code of the Very High Temperature Gas cooled Reactor (VHTR) system.

This section is divided into three main parts. The first part describes the analysis method of the GAMMA code including the models of a fluid part, a solid part and a radiation heat transfer, each component material properties and boundary conditions in the HTR-10 reactor. The calculation results of the GAMMA code are explained in the second part. The calculation results are especially compared with the measured solid material temperatures [2-1] at 22 fixed instrumentation positions in the HTR-10. Finally, some conclusions follow.

Analysis method

Description of the GAMMA code

The GAMMA code [2-17] is developed to predict the thermofluid and chemical reaction behaviour expected to occur in a VHTR. Based on the thermal fluid characteristics of the VHTR, the following code requirements are considered and implemented into the GAMMA code:

- Fluid transport and material properties;
- Multidimensional heat conduction;
- Multidimensional fluid flow;
- Chemical reactions;
- Multicomponent molecular diffusion;
- Fluid heat transfer and pressure drop;
- Heat generation and dissipation;
- Radiation heat transfer.

The fluid flow and heat transport in the GAMMA code are solved unsteadily by the thermal non-equilibrium model, consisting of two sets of equations for both the gas and the solid. The governing equations of the gas are Eqs (2-1)–(2-4) and those of the solid parts are Eqs (2-5) and (2-6) respectively. In addition, the basic equations are formulated with a porous media model to consider heat transport in solid–fluid mixed components. In the gas flow medium, the multidimensional governing equations for a chemically reacting flow consist of the spatially averaged conservation equations for continuity, momentum, energy of the gas mixture and the mass of each species. A gas mixture contains several types of species, namely, He, H₂, N₂, O₂, CO, CO₂, CH₄, H₂O and air as a single species. Together with the multidimensional analysis feature, the GAMMA code has one dimensional analysis capability for modelling a general network of pipe flow.

$$\frac{\partial \varphi \rho}{\partial t} + \frac{\partial \rho u_i}{\partial x_i} = \varphi \sum_s R_s \quad (2-1)$$

$$\frac{1}{\varphi} \frac{\partial \rho u_j}{\partial t} + \frac{u_i}{\varphi^2} \frac{\partial \rho u_j}{\partial x_i} = B_j - \frac{\partial P}{\partial x_j} + \frac{1}{\varphi} \frac{\partial}{\partial x_i} \left[\mu \left(\frac{\partial u_i}{\partial x_j} + \frac{\partial u_j}{\partial x_i} \right) \right] + \rho g_j \quad (2-2)$$

$$\frac{\partial \phi \rho H}{\partial t} + \frac{\partial \phi \rho u_i H}{\partial x_i} = \frac{\partial}{\partial x_i} \left(\phi \lambda \frac{\partial T}{\partial x_i} \right) - \frac{\partial}{\partial x_i} \left(\phi \sum_{s=1}^m H_s J_{si} \right) + \dot{q}_{ch}'' + \dot{q}_{sf}'' \quad (2-3)$$

$$\frac{\partial \phi \rho Y_s}{\partial t} + \frac{\partial \phi \rho u_i Y_s}{\partial x_i} = - \frac{\partial \phi J_{si}}{\partial x_i} + \phi R_s \quad (2-4)$$

In Eqs (2-1) and (2-4), the species generation and dissipation rate (R_s) due to chemical reaction is described by two parts, namely, the gas phase homogeneous reaction and the heterogeneous reaction on the solid surface. The surface reaction rate is described by the mass transfer relation, i.e. $R_s = k_s (Y_s^{wall} - Y_s^{bulk})$. The additional body force (B_j) in Eq. (2-2) is due to friction and geometric form loss or flow resistance in the j-direction caused by a porous medium, modelled by the Forchheimer extended Darcy's law.

Equation (2-3), which is an energy equation, includes the intermolecular energy transport term due to molecular diffusion, the heat generation and dissipation rate (\dot{q}_{ch}'') due to chemical reaction and the heat exchange term (\dot{q}_{sf}'') between the fluid and the solid part. The molecular diffusion flux (J_{si}) is modelled by the full multicomponent diffusion formulation of Hirschfelder. The cubic equation of state is adopted to obtain the thermodynamic properties (density, sensible enthalpy, etc.) analytically in a wide range of pressure for the gas mixture. Physical properties such as the viscosity and the thermal conductivity for each gas component and gas mixtures are obtained from the handbooks of gas properties.

The heat transport in the solid parts and a pebble bed is modelled by the continuous porous medium approach. Particularly, the solid region in a reactor core is divided by two zones, which are the fuelled zone by Eq. (2-5) and the unfuelled zone by Eq. (2-6). The fuelled zone heat conduction equation is solved one-dimensionally.

$$(\rho C_p)_f \frac{\partial T_f}{\partial t} = \frac{1}{\xi} \frac{\partial}{\partial r} \left(\xi \lambda_f \frac{\partial T_f}{\partial r} \right) + \dot{q}_N'' - \dot{q}_{sf}'' \quad (2-5)$$

$$\left[(1 - \phi) \phi_s (\rho C)_w \right] \frac{\partial T_w}{\partial t} = \frac{\partial}{\partial x_i} \left(\lambda_{eff} \frac{\partial T_w}{\partial x_i} \right) + \dot{q}_{het}'' - \dot{q}_{sf}'' + \dot{q}_{gf}'' \quad (2-6)$$

Equations (2-5) and (2-6), which are heat conduction equations, include the volumetric nuclear heat production (\dot{q}_N''), the heat generation and dissipation rate (\dot{q}_{het}'') due to the graphite oxidation, the heat exchange term (\dot{q}_{sf}'') between the fluid and the solid part, and the additional heat exchange term (\dot{q}_{gf}'') between the fuelled zone and the unfuelled graphite zone. The heat transport between the fluid and the solid is described by the heat transfer relation, i.e. $\dot{q}_{sf}'' = h(T_{wall} - T_{fluid})$, in which the heat transfer coefficient is determined by a generalized heat transfer package modelling the forced, free and mixed convection. In the enclosure, the radiation heat transfer is modelled by using an irradiation/radiosity method [2-18] which assumes that the fluid is non-participating and the radiation exchange between surfaces is gray and diffuse.

As a numerical approach for the fluid equations, the GAMMA code adopts the semi-implicit and first-order upwind scheme. Equations (2-1)–(2-4), which are fluid-governing equations, are discretized in the staggered mesh layout and then dependent variables are linearized by the Newton method. By inserting the velocity component expressed as a function of pressure only into the scalar equations, a huge system matrix reduces to a single pressure matrix.

Equations (2-5)–(2-6) are solved by the Crank-Nicolson method. By inserting the discretized Eq. (2-5) into Eq. (2-6), the combined heat conduction equation is solved in an implicitly coupled way. In this way, the multidimensional temperature distribution in the unfuelled zone as well as the temperature profile within the fuelled zone are obtained simultaneously.

GAMMA code models for the HTR-10 reactor system

The fluid system of the HTR-10 consists of the helium gas cooling system for cooling the reactor core and the Reactor Cavity Cooling System (RCCS) for cooling the air cavity between the RPV and the concrete wall. Figure 2.36 shows the flow pass and the R-Z coordinates in the HTR-10 for the GAMMA code model. The active core of the HTR-10 is cylinder-shaped but cone-shaped at the bottom to unload fuel elements. Graphite reflectors and carbon brick reflectors surround the core at the top, side and bottom zones. In the GAMMA code, the active core is modelled simply cylindrically with an average height of 1.97 m for convenience.

After entering the RPV, the cold helium flows downwards through the annular gap between the core vessel and the RPV. Then the flow changes direction upwardly. A small part of this cold helium is expected to go directly through the fuel discharging tube to the hot core, therefore the benchmark problem assumes that 1% of the total coolant flow passes through this zone. All the remaining helium goes around the core support structures and the major part of this flow enters into the cold helium channels in the side reflector. The benchmark problem also defines that 10% of the total flow bypasses due to the occurrence of clearances among graphite blocks, 2% of the total flow goes through the control rod channels and 87% of the total flow cools the pebble bed zone effectively.

The calculation of the helium cooling system is modelled up to the horizontal coaxial hot gas duct connecting the RPV and the steam generator. The heat generated in the reactor core is cooled by conduction and radiation heat transfer of the reactor structures as well as by convective heat transfer of the fluid system. Figure 2.37 shows the fluid part model in the primary cooling system. The number in the flow diagram is the name of each fluid part, and the number in parenthesis is the calculation grid number. The number of the arrows means the name of the junction which connects the adjacent fluid parts in the GAMMA code. A two dimensional flow calculation is performed in the zones of the top plenum, pebble bed core and reactor cavity. The other regions are simplified by one dimensional flow.

The solid conduction is calculated by setting the solid region and then providing the input data of the geometrical information related to the fluid convection heat transfer, heat generation, material properties and boundary conditions for each region.

Figure 2.38 shows the solid part model of the GAMMA code. The pebble bed core has a porosity of 0.39. The numbers in the solid diagram also mean the name of each solid part and grid number. A solid zone may contain various materials in the R-direction such as graphite, carbon and steel in the side reflector zones. Therefore, a fine grid is needed to follow up the temperature gradient in the composite material. The calculation sets up the same grid number (10×11) of the solid part with that of the fluid part in the pebble core to account for the fluid heat transfer.

Using the effective thermal conductivity of Zehner-Schluender [2-19] and the fluid-to-pebble interfacial heat transfer coefficient of the German KTA correlation [2-20], the core solid temperature, the fuel average temperature and the centreline fuel temperature are calculated. The solid part is solved by two dimensional heat conduction as shown in Fig. 2.38. The solid parts containing the partial helium zone such as a control rod channel and a riser channel are regarded as porous mediums.

In the GAMMA code, the radiation heat transfer is calculated by using an irradiation/radiosity method, which assumes that the radiation exchange between surfaces is gray and diffuse, and the fluid is a non-participating one. The emissivity of the solid surface material properties is in the range of 0.79–0.85 for the several cavities in the HTR-10 reactor. The view factors are dependent on the geometrical configuration.

Radiation in the pebble bed core is considered by the effective thermal conductivity of Zehner-Schluender [2-19]. In this calculation, the radiation heat transfer is calculated in the zones of the top plenum, the helium gap inside the RPV, and the air gap between the RPV and water cooling tube.

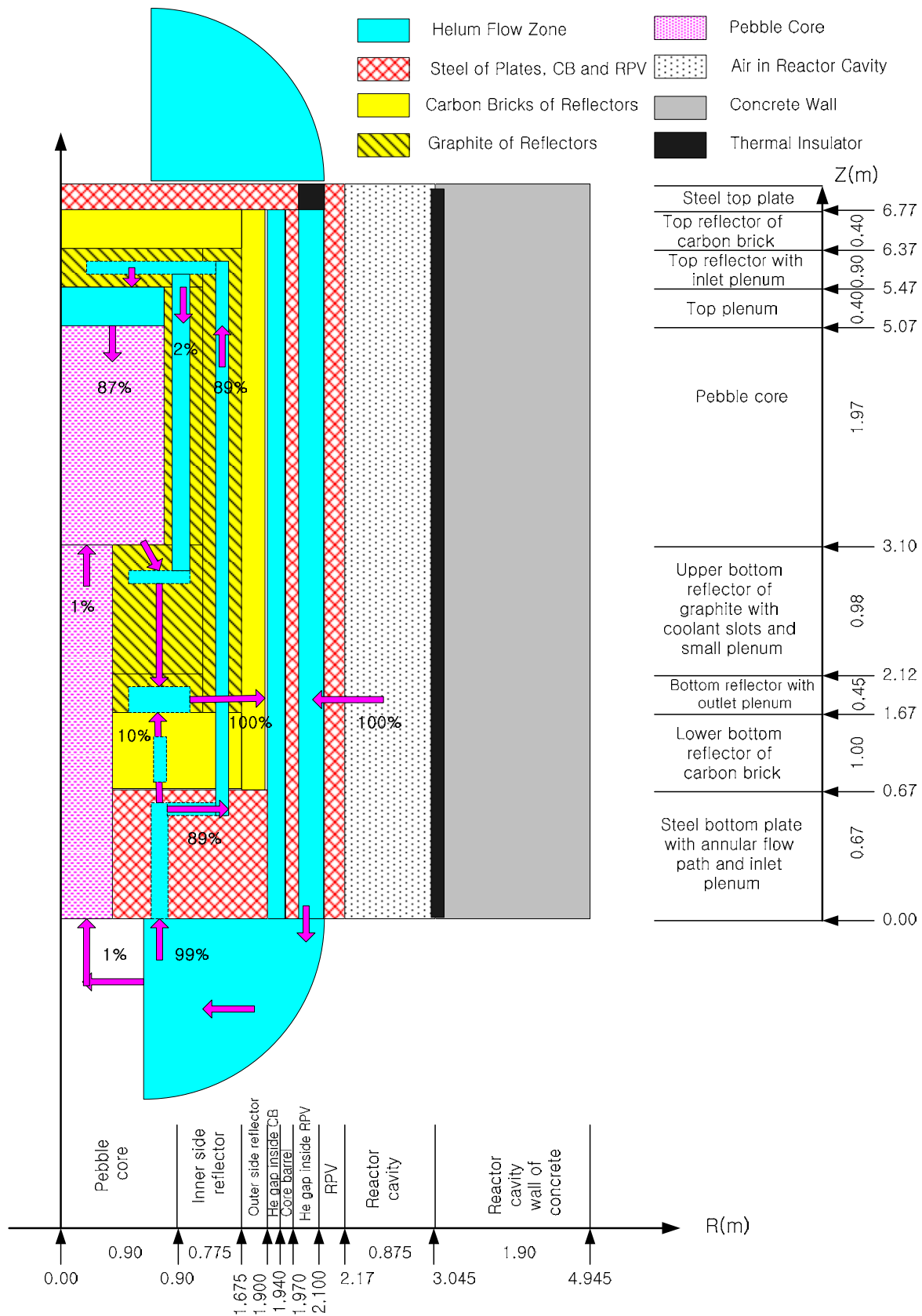


FIG. 2.36. Flow pass model in the HTR-10 for the GAMMA Code.

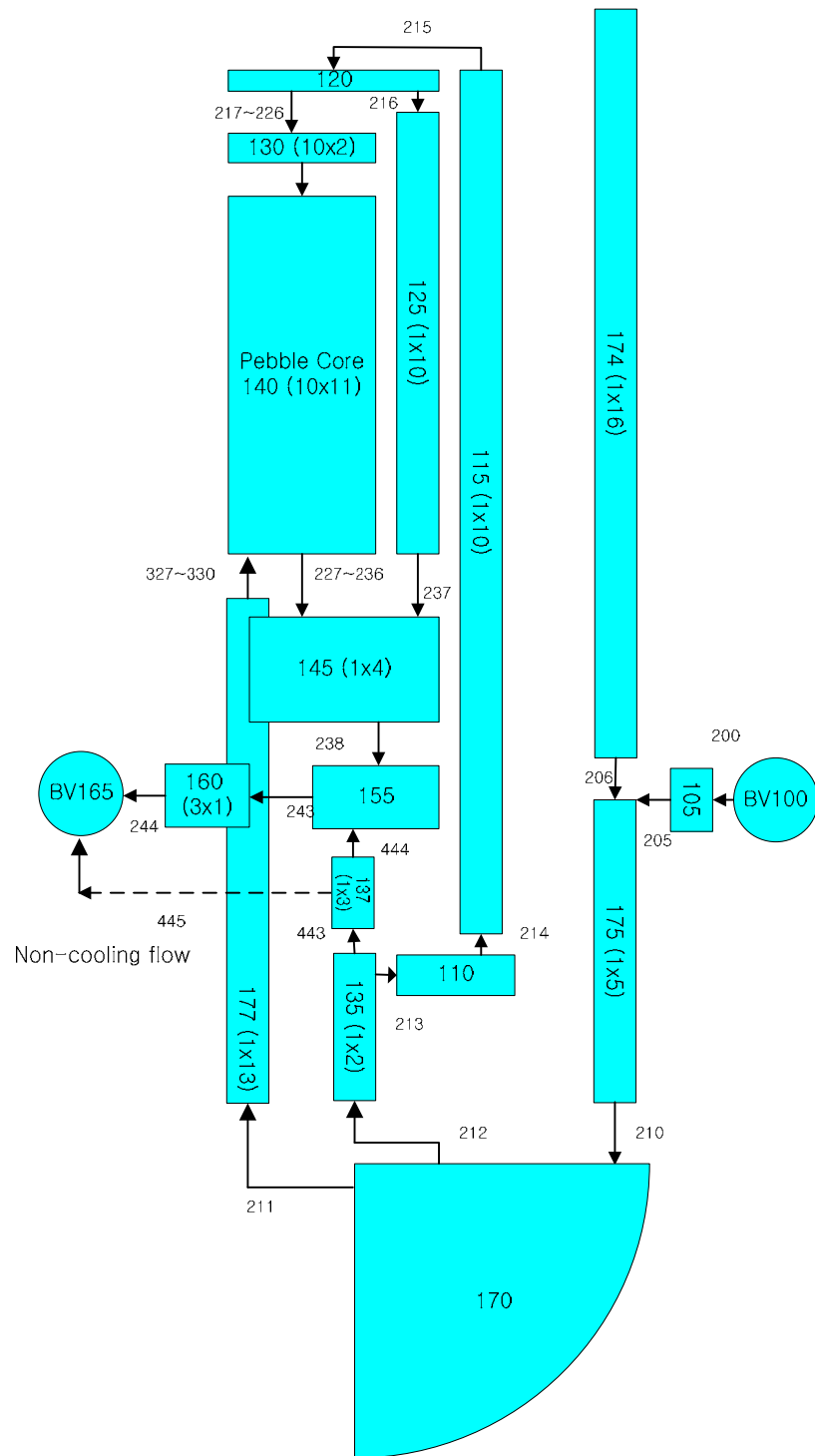


FIG. 2.37. Fluid part model of the HTR-10 for the GAMMA code.

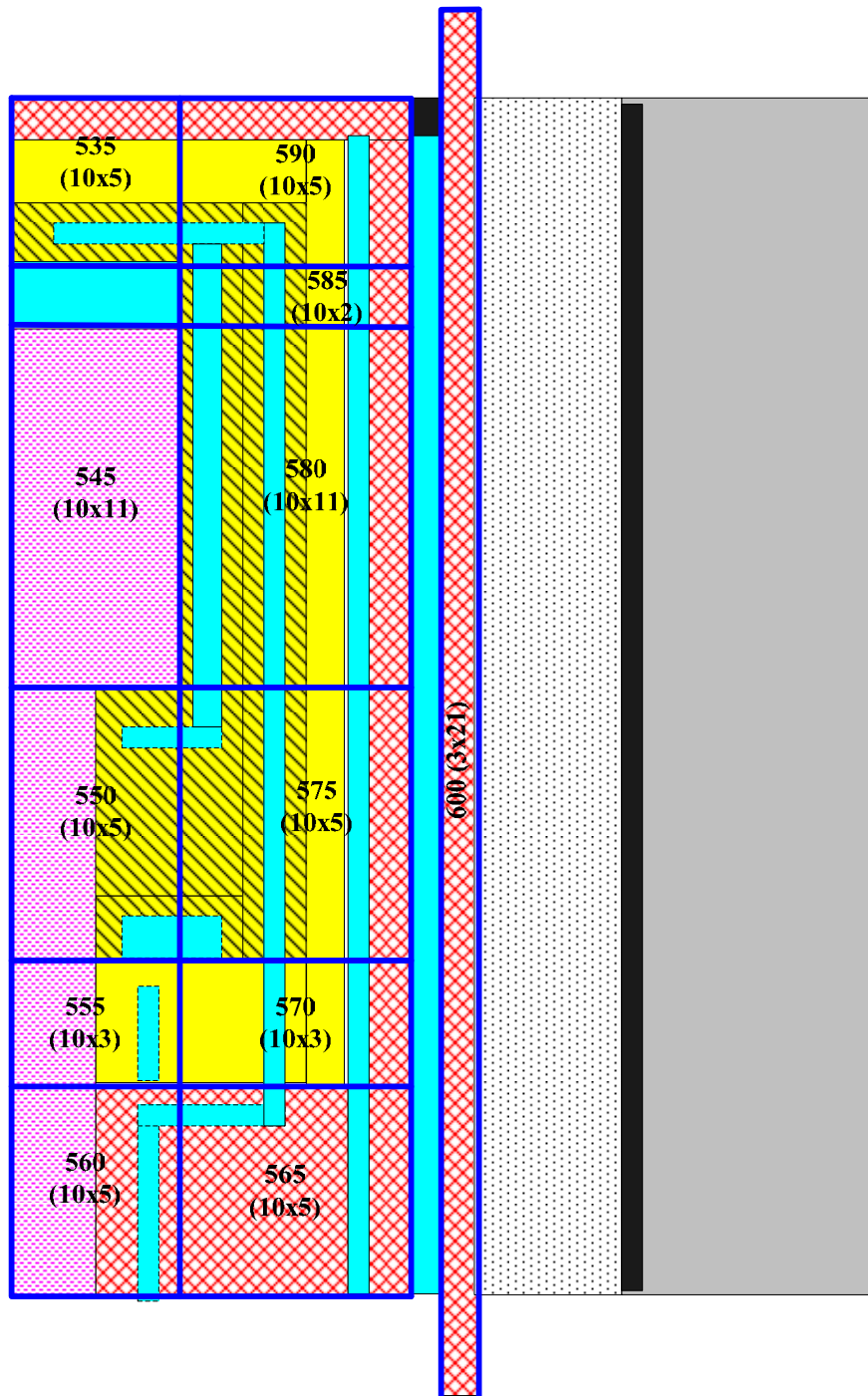


FIG. 2.38. Solid part model of the HTR-10 for the GAMMA Code.

Recommended correlations and material properties

The material properties as defined were used in most cases. In the GAMMA code, the volumetric heat capacity and the thermal conductivity are to be provided in the sub-domain of the solid part to calculate the wall temperature distribution. The irradiation effect of fast neutrons on the thermal conductivity is contained in the correlations of the fuel element and the side reflector. In this calculation, DOSIS of 2.5 and 0.0 are used to calculate the thermal conductivity of the fuel element and side graphite respectively. It is noted that instead of the equivalent heat conductivity of the uniform pebble bed in Table 2.9, the effective thermal conductivity of Zehner-Schluender is used in the GAMMA code.

Boundary conditions

It is difficult to predict the main and bypassing flow rates through the actual flow path due to the occurrence of a clearance among the graphite blocks. An accurate prediction of the flow rate needs a detailed flow resistance of the fluid part, although the leakage is not considered. This calculation uses the flow pass model of the core flow rate, bypassing flow and leakages as shown in Fig. 2.36. The total reactor inlet flow rate is 4.32 kg/s. 87% of the total flow is used for effective cooling of the pebble bed zone and 2% of the total flow goes through the control rod channels [2-1]. 1% of the total flow goes up through the fuel discharging tube to the pebble bed zone. It is assumed that 10% of the total flow bypasses due to the occurrence of clearances among graphite blocks. Among this leakage flow, 7.9% of the total flow goes into the hot outlet plenum and 2.1% of the total flow is a non-effective cooling flow into the reactor outlet boundary volume as shown in Fig. 2.35. These leakages are used to adjust the reactor outlet temperature to 700°C with boundary conditions of the inlet temperature of 250°C, inlet pressure of 3 MPa, outlet pressure of 2.992 MPa and a fixed temperature at the RCCS water cooling tube of 50°C.

Calculation results

Overall temperature distribution

The reference Z point of the benchmark problem is located in the upper part of the pebble bed, but the Z-axis of the GAMMA code starts from the bottom plate as shown in Fig. 2.36. To distinguish coordinates in this section, the meter unit and the centimeter unit are used for the R-Z coordinates of the GAMMA code and the benchmark problem respectively.

Figure 2.39 shows the overall solid temperature distribution of the HTR-10 except the reactor cavity zone. The solid temperature distribution in the pebble bed core shows that the minimum temperature of 356°C is located at the upper core and the maximum temperature is 893°C at Z = 170 cm near the bottom of the core centre. A higher temperature zone than 800°C is located at the inner region of a 0.5 m radius at the bottom of the core centre. The solid temperature decreases as one moves radially and axially away from the bottom of the core centre. The core bottom and small hot plenum zones have a higher temperature distribution than 700°C. The maximum temperature of the RPV is 222°C and the maximum values of the fuel average temperature and pebble centreline temperature are 909°C and 935°C respectively. They are much lower than the fuel temperature limitation of 1230°C.

Figure 2.40 shows the velocity field distributions of the helium gas in the pebble bed core and the air in the reactor cavity. The core flow goes downwards and meets in the region of bottom core adjacent to the bottom reflector and the fuel discharging tube. It is expected that this velocity field distribution will change partway in the region of the bottom core when the actual cone-shaped bottom core is modelled. The air velocity distribution shows the natural circulation between the RPV and the water cooling tube. The air near the RPV in the reactor cavity goes upwards with a velocity of 0.40 m/s and the air close to the water cooling tube goes downwards with a velocity of 0.32 m/s at the middle of the core.

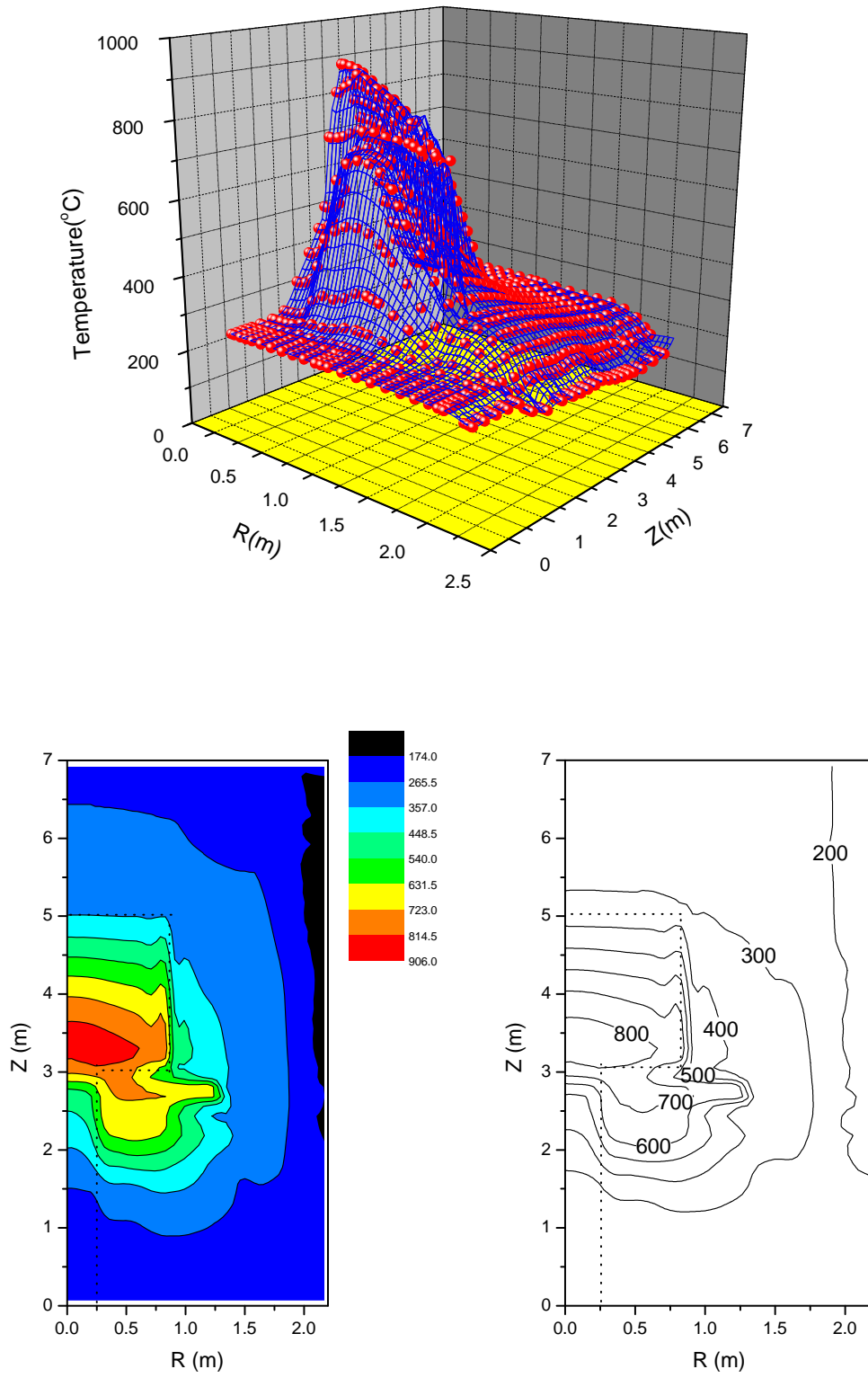


FIG. 2.39. Distribution of the overall solid temperature in the HTR-10.

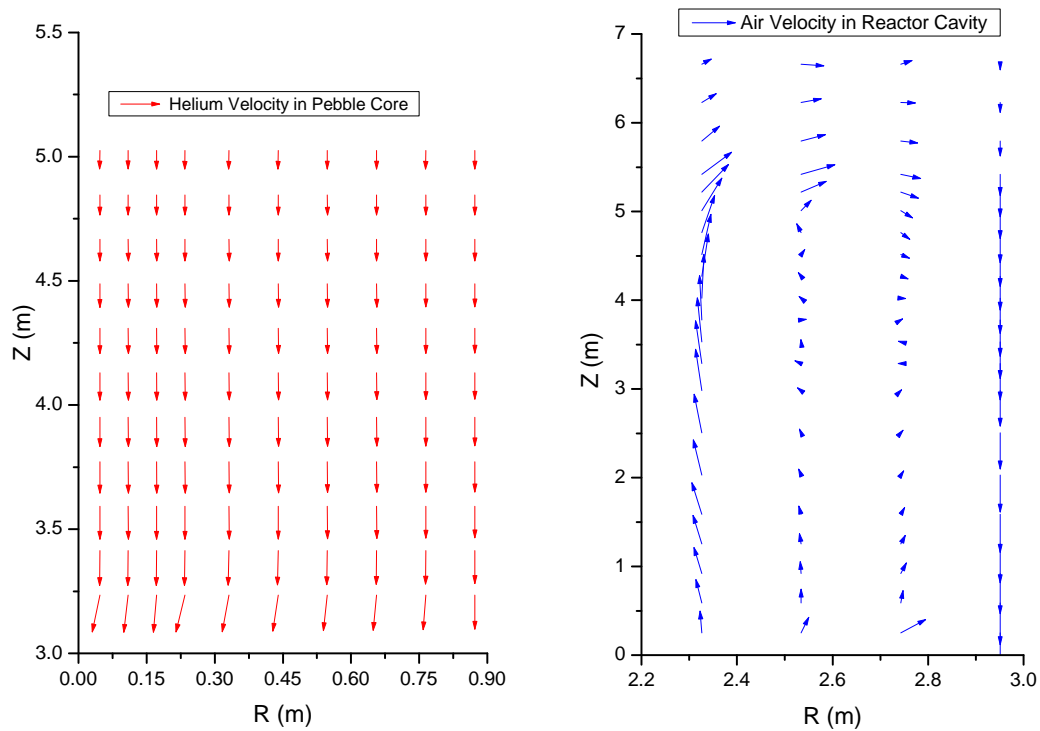


FIG. 2.40. Fluid velocity field in the pebble core and reactor cavity.

Comparison with the measured solid temperatures

Twenty-two data points of the measured solid temperatures [2-1] at the side reflector, the top reflector, the hot helium plenum, the bottom carbon bricks and the fuel discharging tube are provided by the benchmark problem. Table 2.23 shows the calculated solid temperatures at these measurement locations.

Three radial temperature profiles (at $Z = 80, 170$ and 234 cm) and a single temperature point of the top reflector (at $Z = -40$ cm) are plotted in Fig. 2.41. The comparison with the experimental data shows that the calculation results are very close to the measured values in the side reflector region (at $Z = 80$ cm and 170 cm) and the small hot helium plenum (at $Z = 234$ cm) of the bottom reflector zone with a prediction error less than $\pm 10\%$. As shown in Table 2.23, the prediction error in the hot helium plenum may seem to be small (less than 7%), but a flat temperature profile and a large underestimation of about 72°C appear. The porous medium approach of this calculation could give a homogenized temperature which was lower than the actual hot point temperature in the complicated geometry of the bottom reflector zone. The prediction of a single point of the top reflector (at $Z = -40$ cm) shows an overestimation, with a temperature deviation of 32°C . In addition, the measured temperature of 245.7°C at 40 cm away from the upper core is less than the inlet coolant temperature of 250°C . Thus, this calculation value of 277.7°C may be close to the real temperature at the top side reflector.

TABLE 2.23. THE CALCULATED TEMPERATURES AT THE MEASURED LOCATIONS

No.	Coordinates of benchmark Problem		Temperature (°C)		Temperature (°C)
	R (cm)	Z (cm)	Calc. T	Exp. T	Difference
Side reflector					
1	193	80	222.3	231.3	-9
2	189	80	239.6	249.3	-10
3	167	80	289.4	274.3	15
4	133	80	317.1	289.1	28
5	117	80	338.7	313.3	25
6	93	80	385.5	357.7	28
7	193	170	222.1	234.9	-13
8	189	170	245.1	264.8	-20
9	167	170	310.6	303.9	7
10	133	170	355.7	328.5	27
11	117	170	396.8	365.3	32
12	93	170	488.6	507.1	-18
Top reflector					
13	60	-40	277.7	245.7	32
Hot helium plenum					
14	40	234	727.9	800.2	-72
15	60	234	734.0	763.1	-29
Bottom carbon bricks					
16	70	440	253.9	224.1	30
17	50	400	266.6	245.7	21
18	50	370	310.8	296.2	15
19	50	340	412.4	406.7	6
Fuel discharging tube					
20	26	340	352.1	334.2	18
21	26	300	487.7	806.1	-318
22	26	260	585.0	881.7	-297

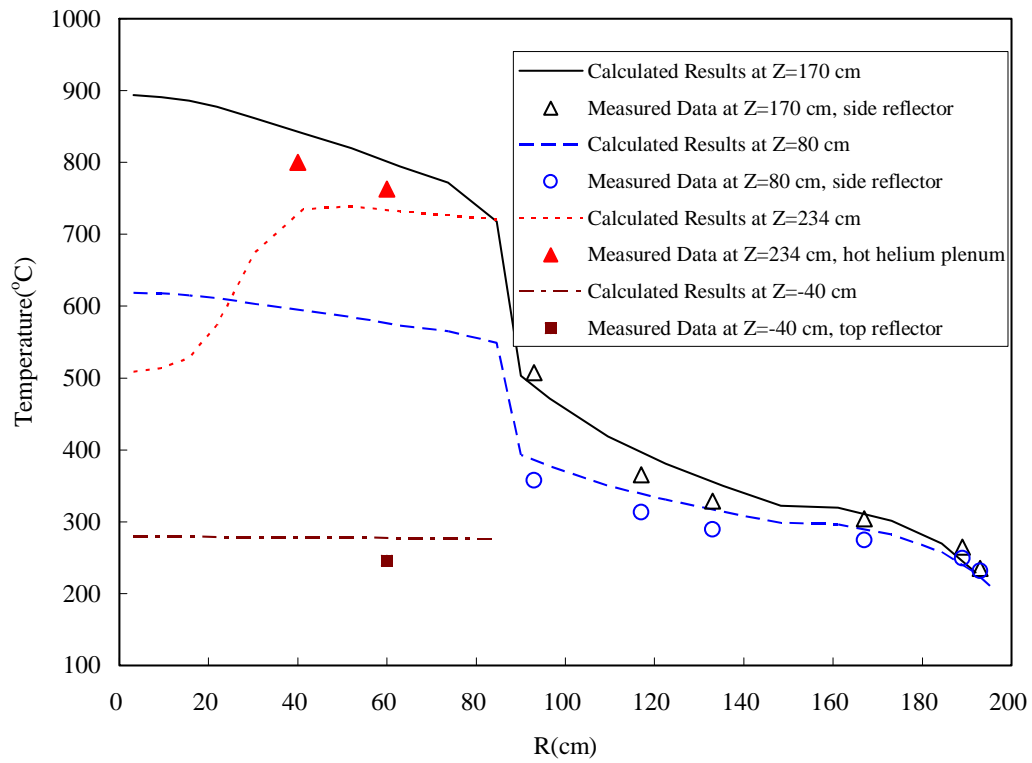


FIG. 2.41. Radial temperature results at the measured locations.

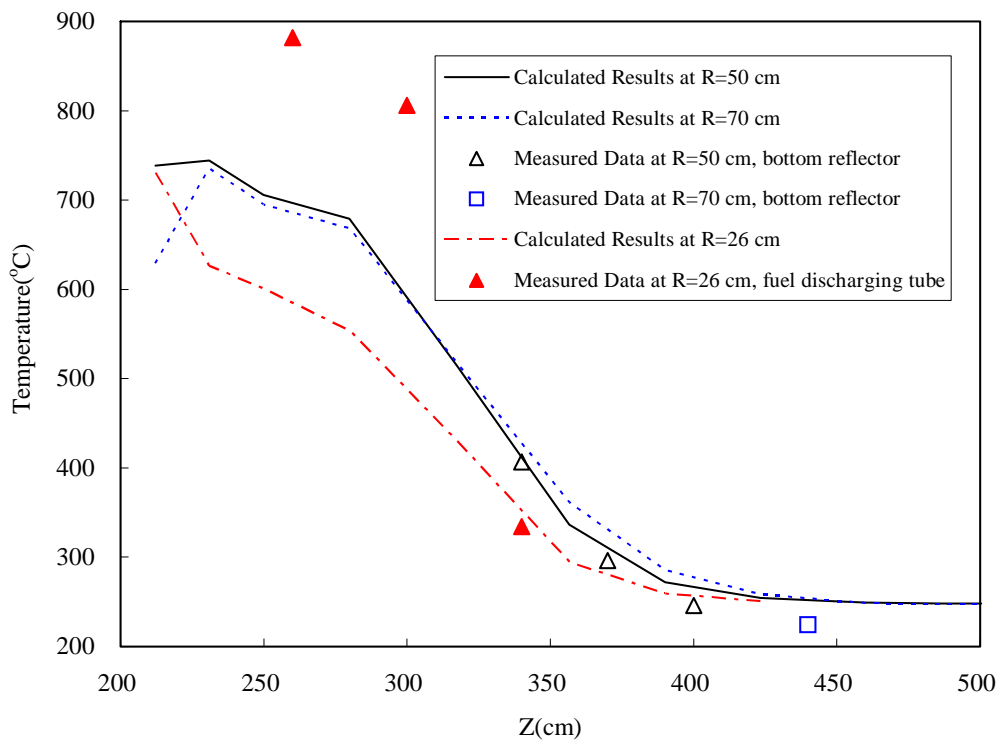


FIG. 2.42. Axial temperature results at the measured locations.

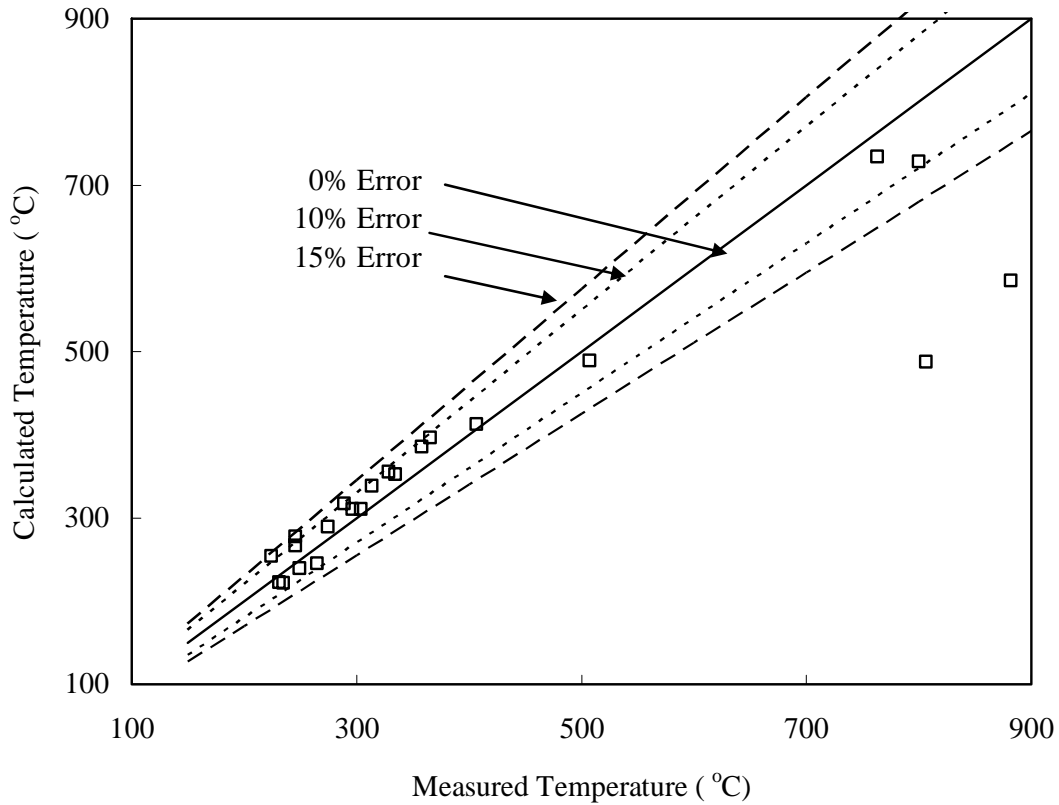


FIG. 2.43. Solid temperature prediction error.

The axial temperatures of the bottom carbon bricks (at $R = 50$ and 70 cm) and the fuel discharging tube (at $R = 26$ cm) are plotted in Fig. 2.42. The temperature value and gradient are very close to the measured data at the bottom carbon bricks and shows a little overestimation. A calculation value of the fuel discharging tube ($Z = 340$ cm) is well predicted to the measured temperature, but the other two points are significantly underestimated with differences of -318°C ($Z = 300$ cm) and -297°C ($Z = 260$ cm). The measured data is a highly steep temperature rise of 472°C from $Z = 300$ cm to $Z = 340$ cm. The temperature adjacent to the bottom core is higher than 800°C as shown in Fig. 2.39, but the temperature decreases as it moves down the fuel discharging tube.

Figure 2.43 shows the prediction error of the GAMMA code for the measured solid temperatures at twenty-two fixed instrumentation positions in the HTR-10. It shows overall good predictions with less than a $\pm 10\%$ deviation except for two data points in the fuel discharging tube zones.

Additional results

Radial (Z = 80 cm) Temperature profile within the pebble bed

TABLE 2.24. RADIAL (Z = 80 CM) TEMPERATURE PROFILE

R (cm)	Temp. (°C)	R (cm)	Temp. (°C)
3.1	618.8	41.3	594.3
9.4	617.6	52.1	584.8
15.6	615.2	62.9	572.9
21.9	611.6	73.8	564.8
30.4	603.5	84.6	548.7

Axial (R = 0 cm) Temperature profile within the pebble bed

TABLE 2.25. AXIAL (R = 0 CM) TEMPERATURE PROFILE

Z (cm)	Temp. (°C)	Z (cm)	Temp. (°C)	Z (cm)	Temp. (°C)
9.0	365.4	116.4	740.8	212.1	705.0
26.9	423.0	134.3	793.1	230.9	518.1
44.8	488.2	152.2	844.1	249.8	462.8
62.7	551.2	170.1	893.4	279.9	402.2
80.6	618.8	188.0	821.2	317.5	332.2
98.5	685.0	197.0	779.7	340.0	293.1

Maximum temperatures of main components

TABLE 2.26. MAXIMUM TEMPERATURE VALUES OF MAIN COMPONENTS

Component	Position	Max. temperature (°C)
Fuel element	Centre	935
	Surface	893
Side reflector	Surface	482
Bottom reflector	Surface	748

Note: The definition of R-Z coordinates is the same as that in the benchmark definition (i.e. the horizontal axis is the R-direction and the vertical is the Z-direction. The zero points of the Z- and R-axis correspond to the crossing point of the upper surface and the central axis of the active pebble bed core).

Conclusions

This benchmark calculation has demonstrated the capabilities of the GAMMA code to simulate the HTR-10 steady state temperature fields including complex convection, conduction and radiation heat transfers. Based on this calculation, the key results on the temperature distribution in a pebble bed, the maximum temperature values of main components and the temperatures at the measured locations were provided.

The maximum wall temperature is 893°C at Z = 170 cm near the bottom of the core centre, where the average pebble and pebble centreline temperatures are 909°C and 935°C respectively. They are much lower than the fuel temperature limitation of 1230°C. The RPV is cooled with the maximum

temperature of 222°C by the air natural circulation in the reactor cavity between the RPV and the water cooling tube. The radial temperature profiles are very close to the measured values in the side reflector and the small hot helium plenum zones with a prediction error of less than $\pm 10\%$. The axial temperature profiles also show good prediction at the bottom carbon bricks and the adjacent fuel discharging tube with a little overestimation less than 10%. A highly steep temperature rise at fuel discharging tube from $Z = 300$ cm to $Z = 340$ cm is not shown, however. The comparison with the measured temperature data shows overall good predictions with less than a $\pm 10\%$ deviation except abnormally high discrepancies in the fuel discharging tube zones.

2.2.2.5. HTR-10 steady state temperature benchmark, the Netherlands

Introduction

The first publication of this CRP, IAEA-TECDOC-1382, focused on the initial core physics evaluation and testing associated with the HTTR and HTR-10. Calculations have been performed by NRG-Petten within the framework of the HTR-10 initial core benchmark [2-21] and the models were later improved for the analysis performed and reported here. Improvements were also applied to the original HTR-10 benchmark problem, and this is reported in Appendix A.4 of this document. More details on the methodology and codes used are thus also included in Appendix A.4 and not repeated here.

Codes and methodology

The HTR-10 has been modelled in the PANTHERMIX code [2-22], a combination of the 3-D diffusion reactor code PANTHER 5.1 [2-23] coupled to the 2-D thermohydraulics code THERMIX./DIREKT [2-24] The nuclear data necessary for the PANTHER code has been generated by means of the WIMS8 [2-25] code system.

Model

A new neutronic as well as thermohydraulic model has been prepared for the PANTHERMIX model according to the more detailed 2003 benchmark definition by INET. The scheme can be seen in Fig. 2.44. Codes and methods are similar to those as described in IAEA-TECDOC-1382.

The neutronic model comprises 2647 hexagonal reactor channels of which 451 are core channels and the remaining 2196 channels form the reflector/vessels region, shaded grey in Fig. 2.45. The flat-to-flat distance of the hexagons is 8.07 cm. Each channel consists of 60 axial meshes of which there are 25 in the active core. The neutronics calculations have been performed in a 60° symmetry to reduce calculation time.

The model comprises the area of the RPV and all within, including the big helium plenums on top and beneath the graphite structure. This model has been used in a new full power steady state of the initial core and the Loss of Forced Cooling (LOFC) without Scram transient.

Full power steady state

Measured temperatures and temperatures calculated at points nearest to the experimental points are given in Table 2.27. For the steady state thermohydraulics benchmark, the HTR-10 model does not coincide exactly with the coordinates of the requested measuring points.

Therefore, in areas with steep temperature gradients, deviations between measured and calculated values can be expected. Radial and axial distributions of the solid temperatures at the requested radii ($R = 0, 45$ and 90 cm and levels $Z = 0, 80$ and 170 cm) can be seen in Figs 2.46 and 2.47. The coordinates are those of Fig. 2.44. A graph of the solid temperature can be seen in Fig. 2.48 and one for the coolant (gas) temperature in Fig. 2.49, showing the big helium areas on top and underneath the graphite structure. Compared with former calculations, the inclusion of these areas increased the heat leakage from the core. The power profile (Fig. 2.50) has been calculated by the PANTHERMIX model. It was not possible to use the power map provided by INET as input to the analysis. It should be noted that the provided power map was also based on analysis and not a measured (or reference) value.

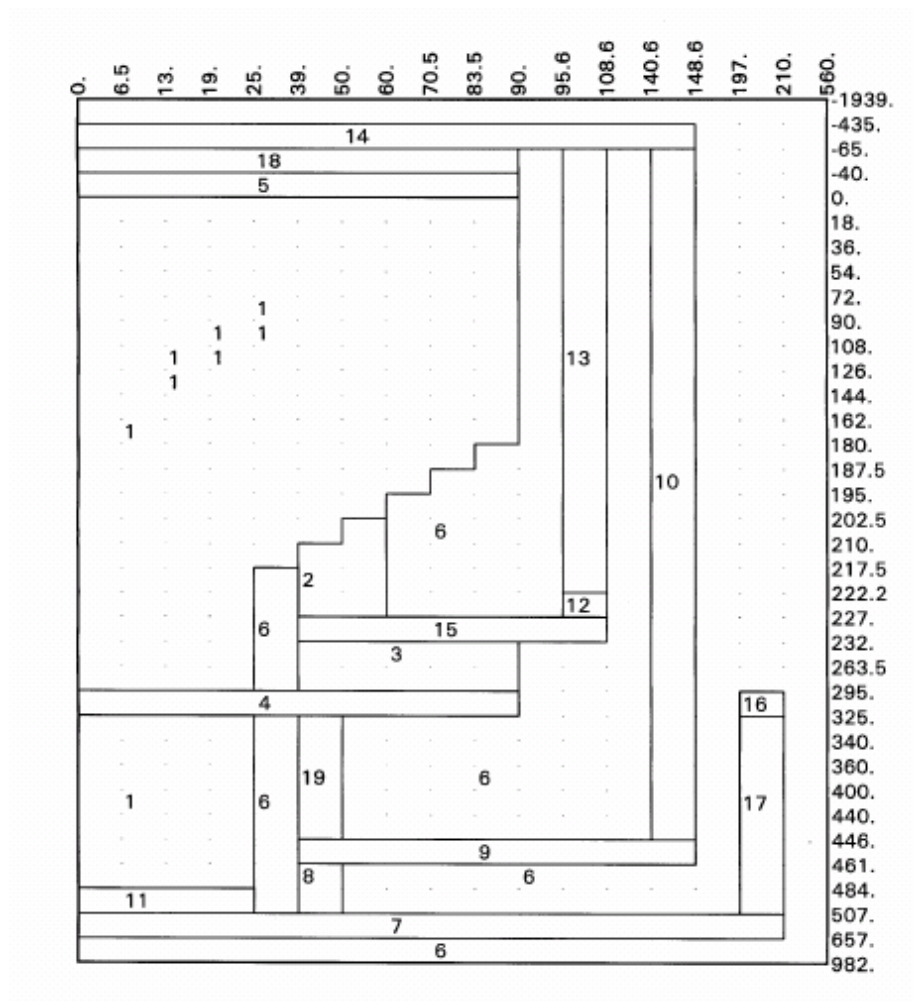


FIG. 2.44. Axial layout of the PANTHERMIX Model.

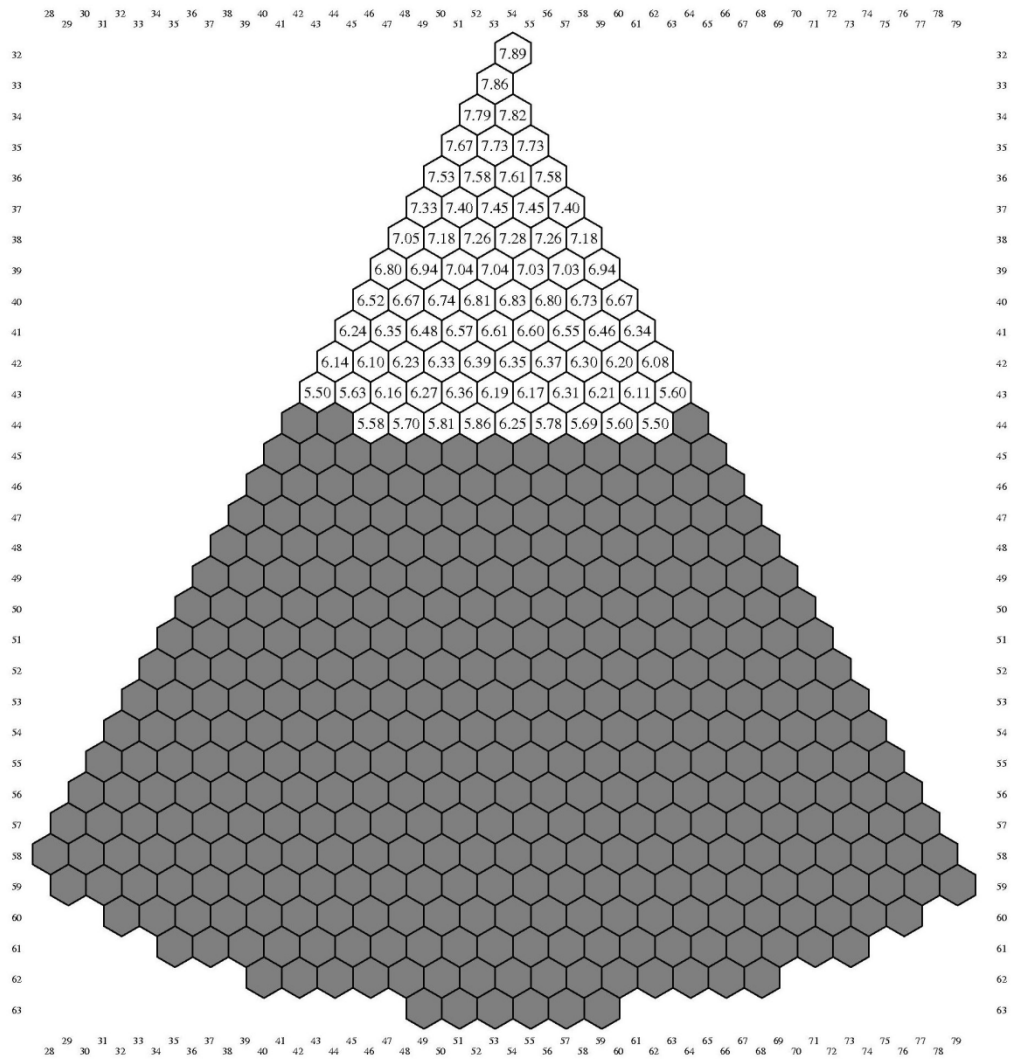


FIG. 2.45. Segment of the reactor layout with core and reflector/vessels channels (shaded grey) in the new model. The numbers in the core channels indicate the power generated in that channel for full power operation in kW.

TABLE 2.27. MEASURED AND CALCULATED TEMPERATURES
DURING FULL POWER OPERATION (INITIAL CORE)

No.	R	Z	T-meas	T-calc	ΔT	T-max	(°C)
1	193.0	80.0	231.3	203.7	-28	Fuel surface	902.5
2	189.0	80.0	249.3	224.2	-25	Fuel centre	972.9
3	167.0	80.0	274.3	290.5	16	Sid reflector	513.7
4	133.0	80.0	289.1	314.5	25	Bottom reflector	808.0
5	117.0	80.0	313.3	338.7	25		
6	93.0	80.0	357.7	379.1	21		
7	193.0	170.0	234.9	216.9	-18		
8	189.0	170.0	264.8	239.9	-25		
9	167.0	170.0	303.9	314.2	10		
10	133.0	170.0	328.5	344.3	16		
11	117.0	170.0	365.3	409.0	44		
12	93.0	170.0	507.1	501.1	-6		
13	60.0	-40.0	245.7	269.3	24		
14	40.0	234.0	800.2	795.5	-5		
15	60.0	234.0	763.1	747.7	-15		
16	70.0	440.0	224.1	249.6	26		
17	50.0	400.0	245.7	251.0	5		
18	50.0	370.0	296.2	276.2	-20		
19	50.0	340.0	406.7	367.1	-40		
20	26.0	340.0	334.2	340.0	6		
21	26.0	300.0	806.1	753.8	-52		
22	26.0	260.0	881.7	793.1	-89		

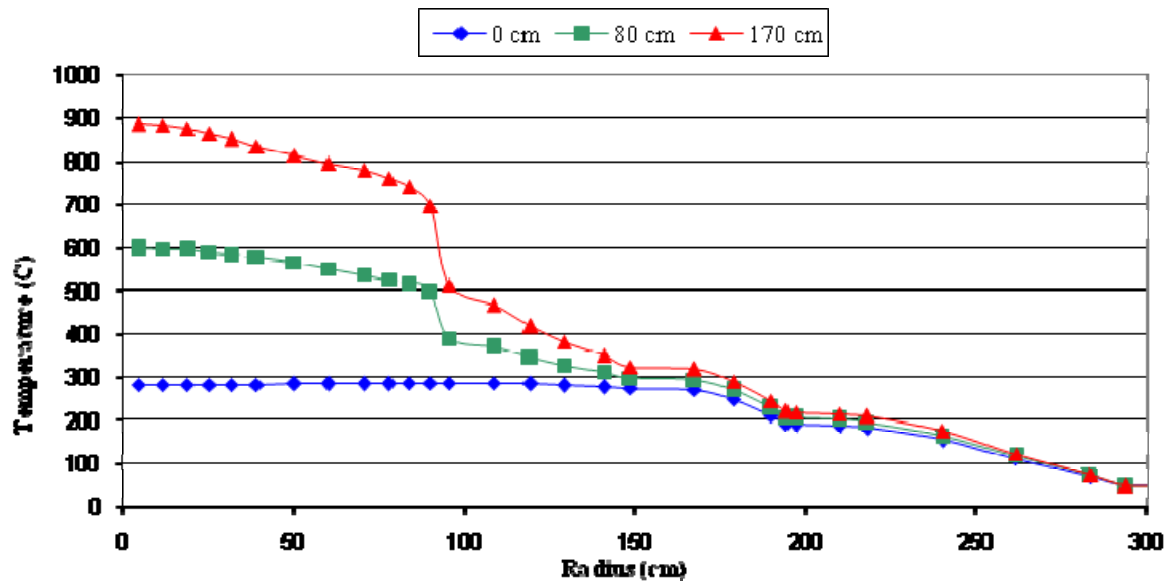


FIG. 2.46. Radial temperature distribution at different Z-levels at full power.

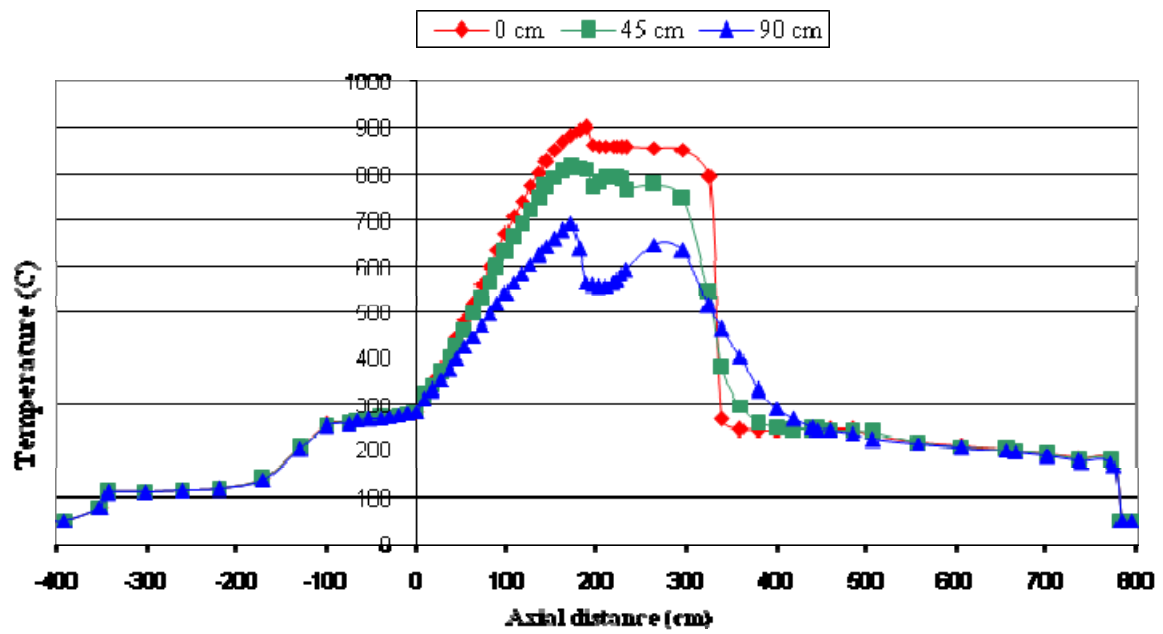
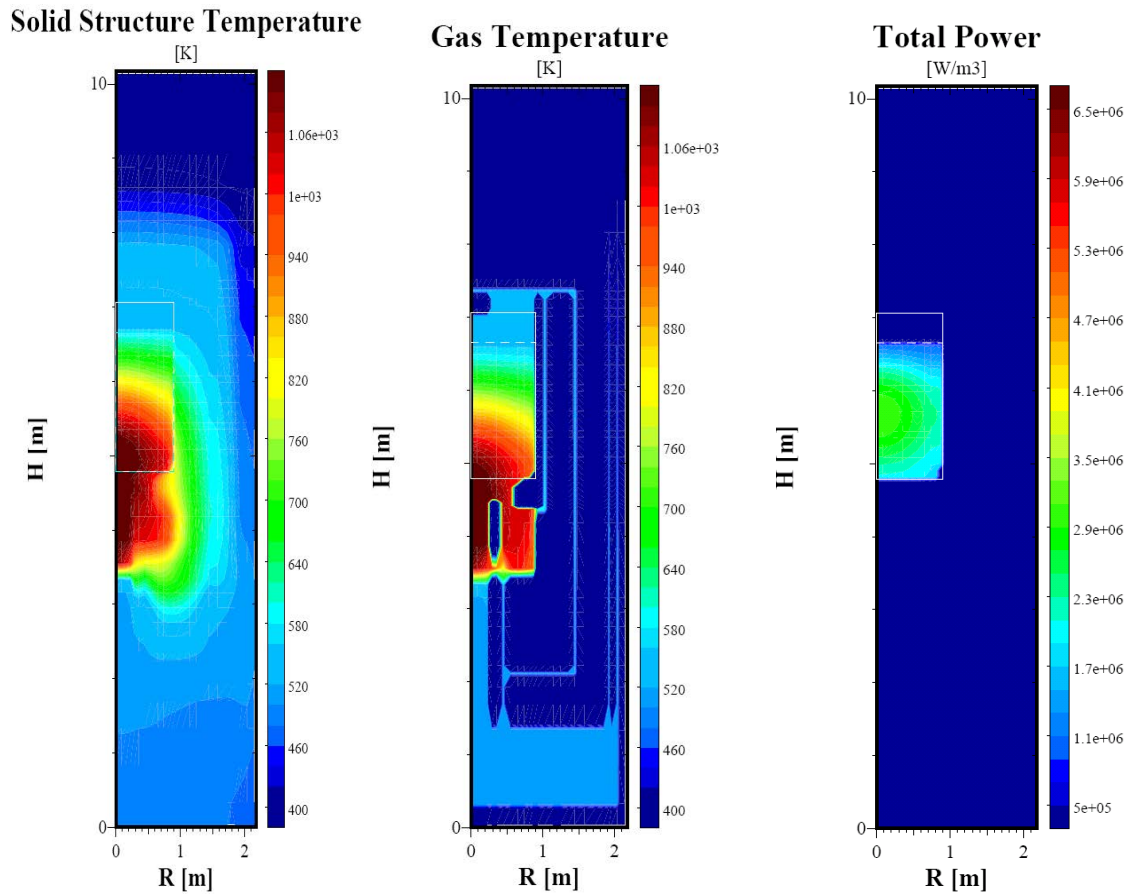


FIG. 2.47. Axial temperature distribution at different radii R at full power.



FIGS. 2.48, 2.49 and 2.50. Temperature distributions for the gaseous coolant, solid structure, and power density.

The faint white lines in the figure refer to the active core and the void space on top of the pebble bed.

2.2.2.6. HTR-10 steady state Temperature Benchmark, United Kingdom

Introduction

The steady state temperature distribution in the FPIC of the HTR-10 has been predicted using two separate computational models. The models are based on the commercially available PHOENICS CFD code and a new code named WIMSTER.

The WIMSTER and PHOENICS models of pebble bed reactors have been developed to assess the proposed PBMR reactor core. The models have been applied to the HTR-10 benchmark problem as part of the code validation process. This report describes the two thermohydraulic models and presents results for the benchmark problem.

Within the United Kingdom, this study has been performed in conjunction with and was funded by the National Nuclear Regulator (NNR) of the Republic of South Africa (RSA).

The PHOENICS code

The PHOENICS CFD code [2-26] computes numerical solutions of the differential equations describing fluid flow and heat transfer using the finite-volume method. The code allows extensive customization of the basic physical models by means of 'user-Fortran' subroutines. This allows the additional modelling required to represent a pebble bed reactor to be incorporated within a PHOENICS model.

The PHOENICS model of the HTR-10

The PHOENICS model of the HTR-10 covers the region within the inner face of the concrete containment vessel. An orthogonal R-Z mesh was used with 70 cells in the radial direction and 184 cells in the vertical direction. The curved base of the pebble bed zone was approximated by a series of steps and the domed ends of the pressure vessel were flattened. An outline diagram of the geometry is shown in Fig. 2.51.

In the PHOENICS model, the pebble bed is treated as a porous medium. User-Fortran subroutines are used to implement heat and momentum sources and sinks to represent the pebble bed. The pebble surface temperature is calculated using an additional differential equation that includes the effective diffusion of heat between the pebbles. The momentum sources, effective thermal diffusivity and heat transfer coefficient in the pebble bed region are computed from the correlations supplied in the benchmark specification.

Radiative heat transfer within the RPV and its surroundings is modelled using explicitly coded sources in selected locations. The mesh spacing in the radial direction was made sufficiently fine close to the vessel walls to resolve the natural convection boundary layers. Turbulence effects in the fluid are modelled using the PHOENICS LEVEL model, which uses an effective viscosity based on the local distance from a wall and an empirical law-of-the-wall velocity distribution.

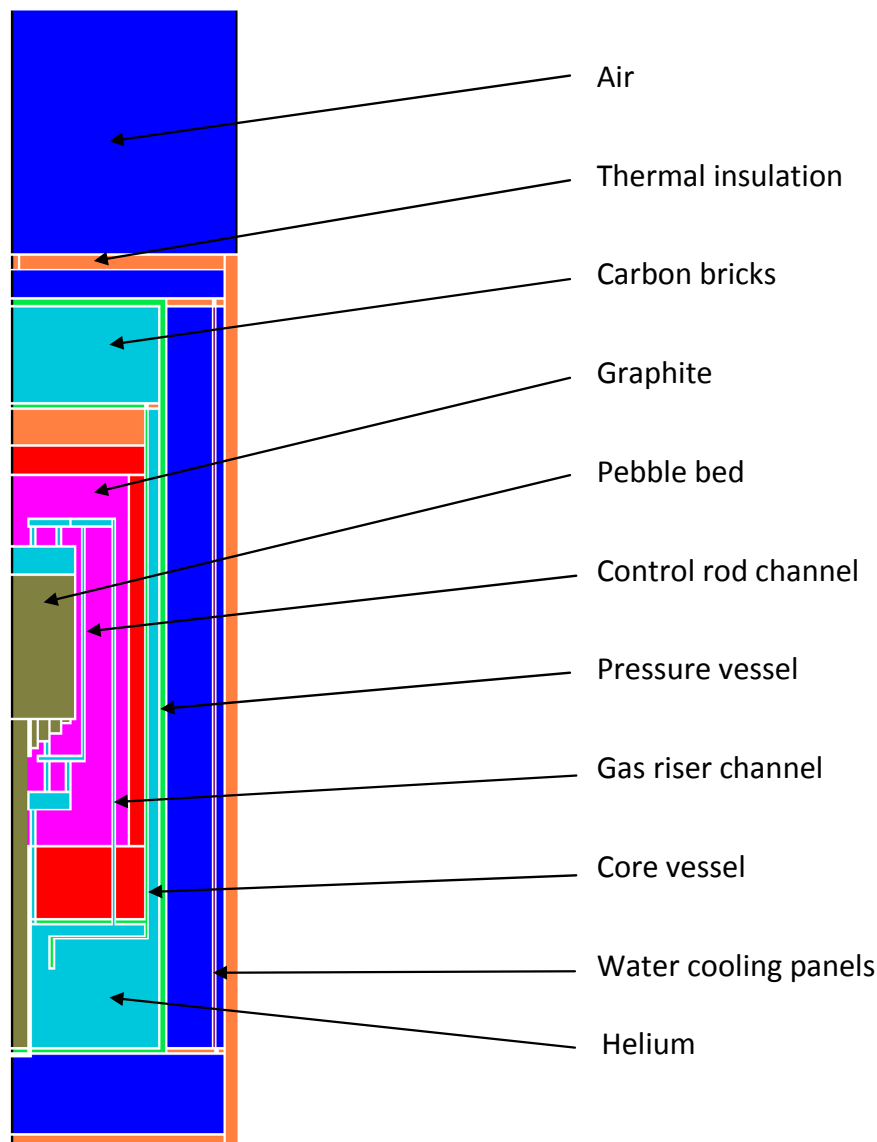


FIG. 2.51. Outline diagram of the PHOENICS model of the HTR-10 benchmark geometry.

The riser and control rod channels were resolved explicitly within the PHOENICS mesh. Two cells were used in the circumferential direction to model an 18° sector of the reactor containing a single gas riser channel. The channels were placed in one of the circumferential cells. A radial conduction through the other circumferential cell layer ensured that the channels did not split the side reflector into thermally isolated zones. In addition, hydraulic resistances were provided to adjust the flow rates in the channels and leakage paths to meet the benchmark specification. The resistances were placed in the fuel discharge tube, the control rod passage and the leakage flow path between the inlet passage and the outlet plenum.

The restricted flow regions in the top and bottom reflector, which consist of arrays of small circular flow channels, are approximated by a number of simple slots. The slots occupy only one of the two circumferential cells in the PHOENICS mesh, to ensure they do not divide the reflectors into thermally isolated regions as discussed above for the control rod and riser channels.

The boundary conditions were set as specified in the benchmark problem. The inlet for helium was placed inside the pressure vessel at the height of the hot gas duct and the outlet for helium was located in the hot gas outlet plenum. The inlet flow rate was set equivalent to a flow rate of 4.32 kg/s for the whole reactor. The temperature of the surfaces of the concrete and the water cooling panels was set to 50°C.

The WIMSTER code

The WIMSTER code is a bespoke Fortran finite-volume code that is based on standard CFD algorithms. The code has been designed to work in conjunction with the WIMS9 neutronics software [2-27] to allow fully coupled neutronic and thermohydraulic analysis of pebble bed reactors. For the HTR-10 benchmark calculation, the WIMSTER code has been used as a stand-alone thermohydraulics code.

The WIMSTER code solves the steady state mass and momentum conservation equations using the well-known Semi-Implicit Method for Pressure Linked Equations (the SIMPLE algorithm [2-28]) on a staggered cylindrical polar coordinate mesh. The temperature fields within the gas, pebble bed and the other core components are solved using standard finite-volume methods. The heat transport and fluid flow calculations are performed in a fully coupled manner. The code has been formulated to cope with two dimensional axisymmetric R-Z and three dimensional R-Z- θ geometries.

The WIMSTER thermohydraulic model has been designed to analyse the behaviour of multiple batches of pebble fuel, allowing the temperature differences between fresh and older fuel pebbles to be computed. This feature has been used to model the presence of a mixture of dummy graphite balls and power-generating fuel elements within the initial HTR-10 core.

The WIMSTER model of the HTR-10

The WIMSTER model of the HTR-10 as shown in Fig. 2.52 is restricted to the pebble bed, graphite reflectors, and the surrounding carbon insulator regions. Therefore, temperatures in the core barrel, RPV, and external concrete structures are not calculated and have not been entered into the WIMSTER code results tables. A two dimensional model has been used for the HTR-10 benchmark. An orthogonal R-Z mesh with variable cell spacing was used with 59 cells in the radial direction and 126 cells in the vertical direction. The conical base of the pebble bed zone was approximated by a simple cylinder.

In the WIMSTER model, the pebble bed is represented as a porous medium in which the pebbles occupy 61% of the total volume. The fluid drag, effective thermal diffusivity and heat transfer coefficient in the pebble bed region are computed from correlations supplied in the benchmark specification.

The flow regions in the top and bottom reflectors, which consist of arrays of small flow holes, are modelled as porous media. Heat transfer from the gas to the reflector graphite in these zones is computed using the Colburn correlation for forced convection in turbulent flow [2-29], applied to the area available for heat transfer per unit volume. This surface area is calculated using the geometry of the gas flow holes provided in the benchmark specification.

Within the WIMSTER model, the riser and control rod channels are modelled using one dimensional channel flow models. This approach permits the discrete character of the channels to be modelled without having to approximate these as annuli in the two dimensional axisymmetric representation or without requiring an excessive number of cells in three dimensions. The channel model is fully

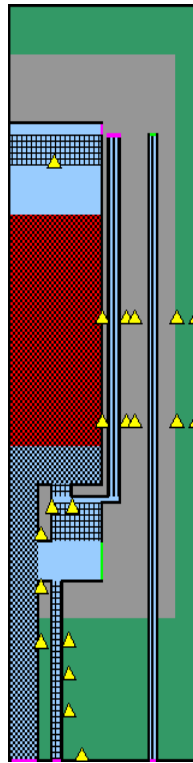


FIG. 2.52. WIMSTER model domain, restricted to pebble bed, reflectors and carbon insulator blocks, showing the location of the thermocouples.

coupled to the finite-volume equations in order to compute the heat exchanged with the side reflector graphite. The flow division between the channels is specified directly within the channel model.

It has been assumed that during normal reactor operation, the heat losses through the outer boundaries of the reflectors are small compared to the heat transferred to the coolant within the core. Therefore, simple adiabatic boundary conditions are specified on all outer solid surfaces of the WIMSTER model.

Fuel temperature models

For both the PHOENICS and WIMSTER thermohydraulic models, the average pebble surface temperature is determined within the macroscopic thermal hydraulics solution by solving a heat conduction equation within the solid fraction of the porous medium. This conduction equation features heat source and sink terms to represent heat exchange with the coolant flowing between the pebbles. The effective conductivity of the solid fraction is determined from the Breitbach correlation specified in the benchmark.

For each batch of pebbles, the surface temperature is calculated by considering the individual heat exchanges between a single pebble within the batch, the coolant and the surrounding pebble bed of ‘average’ pebbles. The temperature profile within an individual pebble is calculated using a one dimensional analytical model assuming the heat source within the fuelled part of the pebble to be spatially uniform.

PHOENICS model results

The temperature field in the vicinity of the heated region is shown in Fig. 2.53. The velocity field is shown in Fig. 2.54.

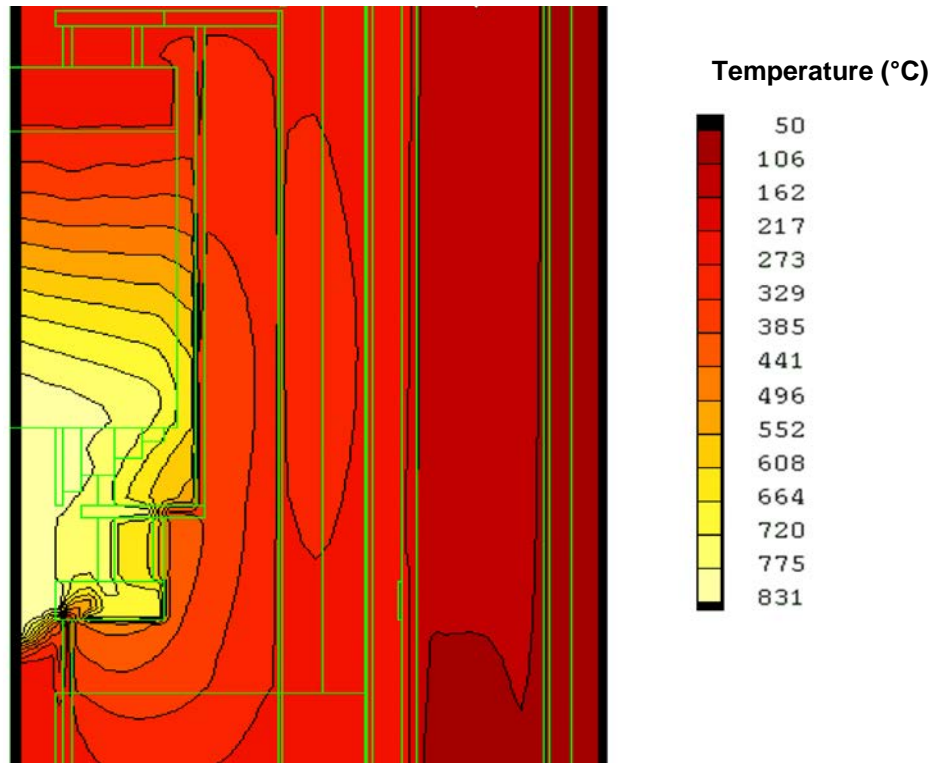


FIG. 2.53. PHOENICS model temperature contours in the core region, showing reflector and helium gas temperatures.

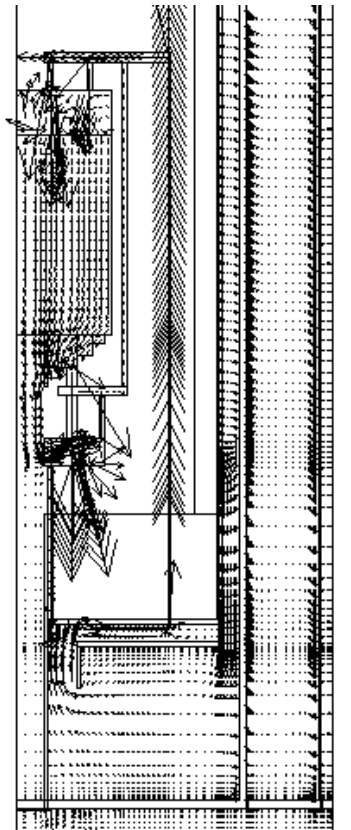
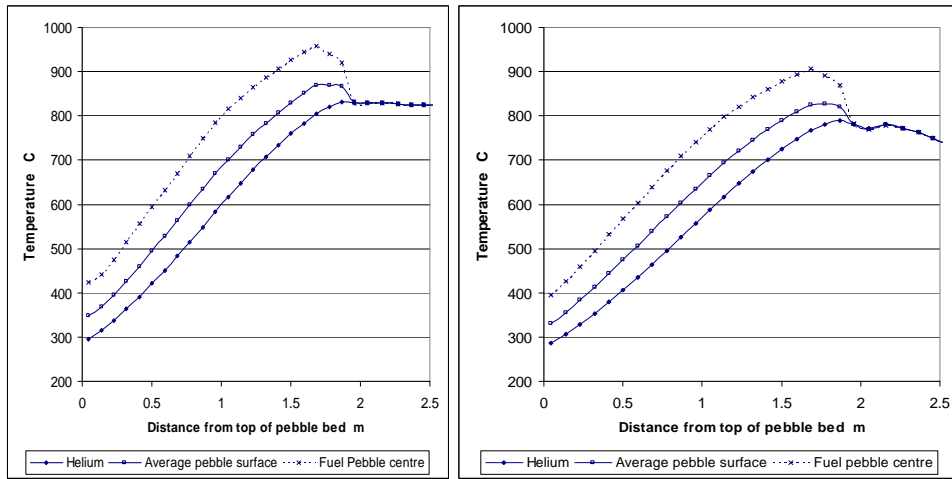


FIG. 2.54. PHOENICS model velocity vectors in the core region.

TABLE 2.28. PHOENICS MODEL AXIAL (R = 7 CM) TEMPERATURE PROFILE

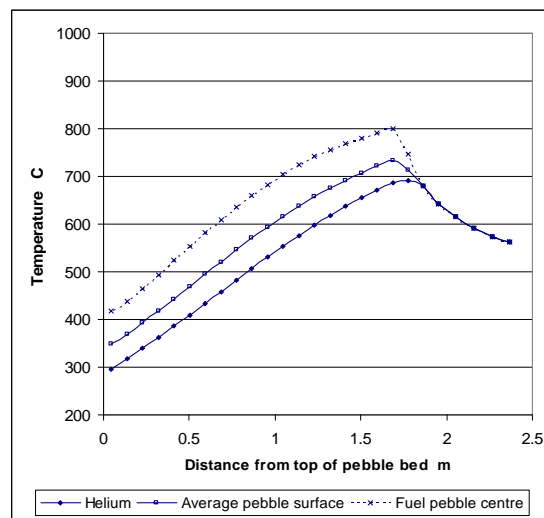
Z (cm)	Gas temperature (°C)	Average pebble surface temperature (°C)	Fuel pebble centre temperature (°C)
-5	270.1	N/A	N/A
5	294.3	349.4	423.4
14	315.3	367.4	440.6
23	338.2	395.4	475.5
32	363.5	426.6	514.3
41	391.2	460.4	555.7
50	420.6	494.3	595.2
59	451.0	527.7	632.1
68	482.6	562.4	670.6
77	515.3	598.4	710.7
87	548.7	633.8	748.6
96	582.4	669.1	785.8
105	615.5	700.9	815.7
114	647.4	730.1	841.3
123	677.9	757.7	865.0
132	706.9	783.8	887.5
141	734.3	807.9	907.7
150	759.9	830.0	925.9
159	783.6	850.7	943.7
169	805.1	868.3	958.3
178	820.8	869.7	941.1
187	831.1	866.7	921.2
195	830.5	831.3	832.0
205	829.7	829.2	828.9
216	829.5	829.0	828.6
227	828.2	827.7	827.3
237	826.0	825.5	825.1
245	825.3	824.8	824.4
253	824.8	824.3	824.0
262	824.4	823.9	823.6
270	824.0	823.6	823.3
278	823.8	823.3	823.0
286	823.6	823.2	822.9
293	823.6	823.1	822.9
298	823.5	823.1	822.8

Axial profiles of gas temperature, pebble surface temperature and pebble centre temperature are shown in Fig. 2.55 for three different radial locations. The radial locations are those of the mesh planes closest to the planes for which the results are requested in the benchmark specification. The temperature values at the centre of the core (the first cell node) are given in Table 2.28. Radial profiles of the same quantities are shown at three axial locations in Fig. 2.56. Temperature values for the radial profile at core mid-height are given in Table 2.29.



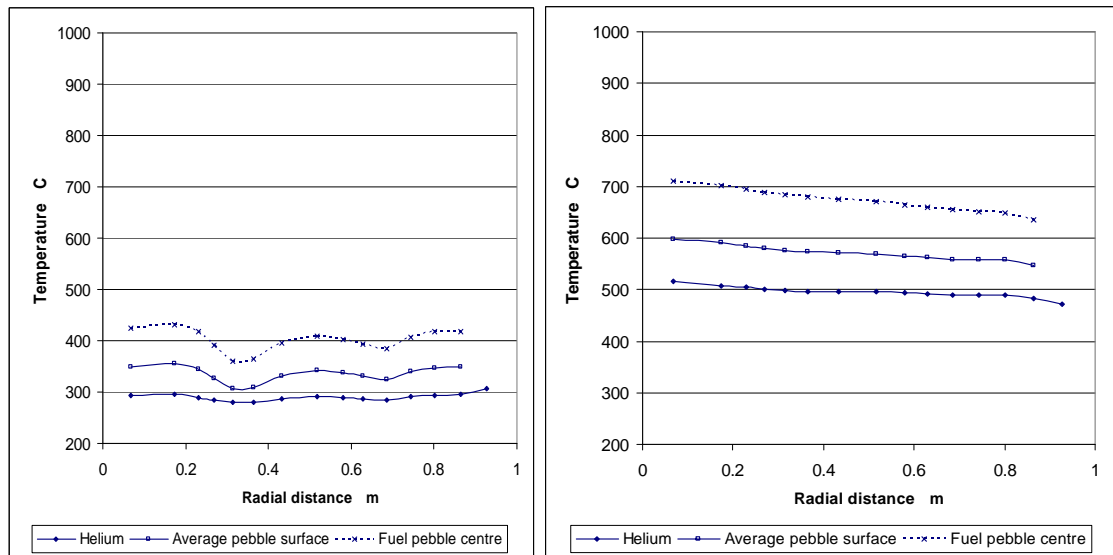
(a)

(b)



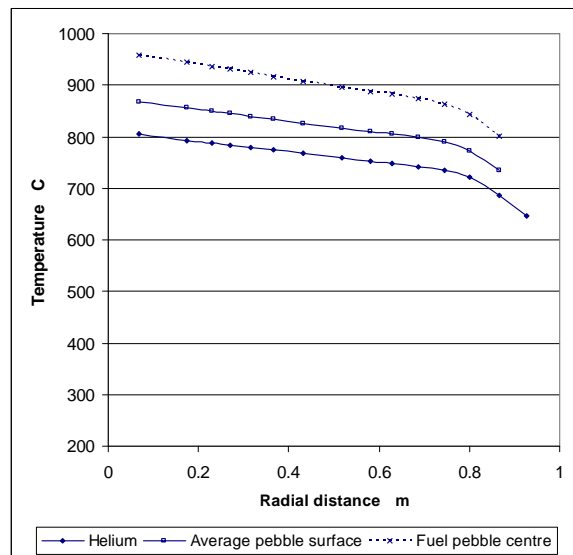
(c)

FIG. 2.55. PHOENICS axial temperature profiles in the pebble bed at radial distances (a) $R = 7$ cm, (b) $R = 43$ cm and (c) $R = 87$ cm.



(a)

(b)



(c)

FIG. 2.56. PHOENICS radial temperature profiles in the pebble bed at (a) $Z = 5$ cm, (b) $Z = 77$ cm, and (c) $Z = 169$ cm below the surface.

TABLE 2.29. PHOENICS MODEL RADIAL ($Z = 77$ CM) TEMPERATURE PROFILE

R (cm)	Gas temperature (°C)	Average pebble surface temperature (°C)	Fuel pebble centre temperature (°C)
7	515.3	598.4	626.7
17	508.1	590.1	618.1
23	504.0	584.8	612.5
27	500.8	580.7	608.1
32	497.6	576.7	603.8
37	495.7	573.8	600.5
43	495.2	571.7	597.9
52	495.0	569.3	594.8
58	492.9	565.3	590.2
63	490.7	562.3	586.8
69	488.7	559.1	583.3
74	488.9	557.9	581.7
80	489.8	557.4	580.9
87	482.4	546.2	569.8

Table 2.30 shows the maximum temperatures in the main components. The predicted temperatures at the thermocouple locations are shown in Table 2.31. The values are given for both circumferential locations. There are only small differences between the two circumferential planes except for the profile through the side reflector, where the presence of the control rod tubes and the gas riser channels (located in θ plane 1) gives rise to significant circumferential temperature gradients. These azimuthal variations are only approximately modelled here.

TABLE 2.30. PHOENICS MODEL MAXIMUM TEMPERATURE VALUES OF MAIN COMPONENTS

Component	Position	Max. temperature (°C)
Fuel element	Pebble centre	958.3
	Pebble surface	916.0
Side reflector	Surface	647.3
Bottom reflector	Surface	783.8

TABLE 2.31. PHOENICS MODEL PREDICTIONS FOR TEMPERATURES
AT THERMOCOUPLE LOCATIONS

No.	R (cm)	Z (cm)	Predicted solid temp. (°C)			Measured temp. (°C)	Difference (°C)
			θ plane 1	θ plane 2	Azimuthal Ave.		
Side reflector							
1	193	80	253.3	255.5	254.4	231.3	23
2	189	80	265.0	270.2	267.6	249.3	18
3	167	80	281.0	294.3	287.7	274.3	23
4	133	80	306.6	319.8	313.2	289.1	24
5	117	80	329.1	349.8	339.5	313.3	26
6	93	80	471.0	442.6	456.8	357.7	99
7	193	170	252.2	254.2	253.2	234.9	18
8	189	170	266.0	272.2	269.1	264.8	4
9	167	170	284.1	305.4	294.8	303.9	-9
10	133	170	325.8	347.9	336.9	328.5	8
11	117	170	364.7	401.4	383.1	365.3	18
12	93	170	646.4	584.2	615.3	507.1	108
Top reflector							
13	60	-40	270.9	271.2	542.1	245.7	296
Hot helium plenum							
14	40	234	741.2	735.1	738.2	800.2	-62
15	60	234	658.0	653.0	655.5	763.1	-108
Bottom carbon bricks							
16	70	440	249.9	249.8	259.9	224.1	36
17	50	400	265.7	265.7	265.7	245.7	20
18	50	370	293.8	293.9	293.9	296.2	-2
19	50	340	350.6	350.9	350.8	406.7	-56
Fuel discharging tube							
20	26	340	320.9	328.5	324.7	334.2	-9
21	26	300	378.6	388.6	383.6	806.1	-422
22	26	260	728.3	725.0	726.7	881.7	-155

WIMSTER model results

The WIMSTER model is shown in Fig. 2.52. The gas, reflector and pebble surface temperature fields are shown in Fig. 2.57.

Axial temperature profiles for radial positions ($R = 0, 45$ and 90 cm) are shown in Fig. 2.58. The graphs show the gas, average pebble surface temperature (averaged over both graphite spheres and fuel pebbles) and fuel pebble centre temperature. Radial profiles of the same quantities are shown at three axial locations in Fig. 2.59. The temperatures at the core centreline and at the core mid-height are tabulated in Tables 2.32 and 2.33, respectively.

The maximum temperatures of the main core components are shown in Table 2.34. The temperatures predicted for the specified thermocouple locations are given in Table 2.35.

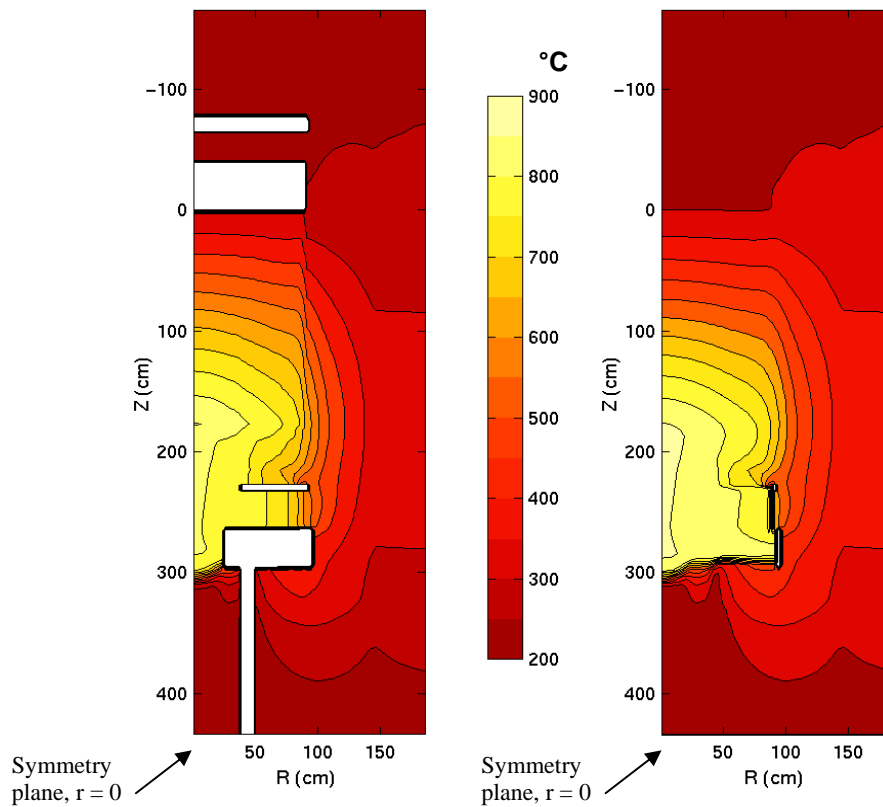
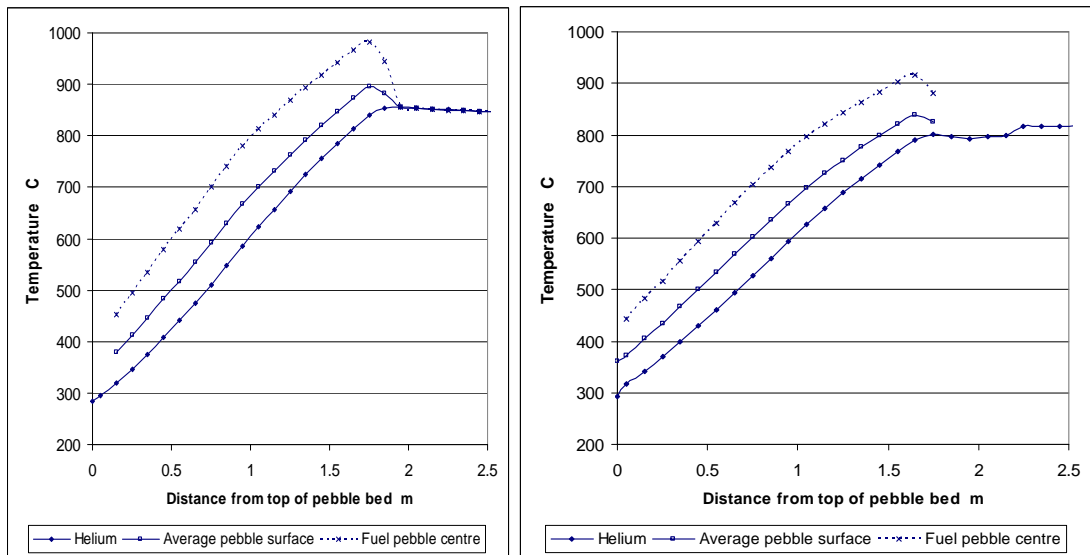
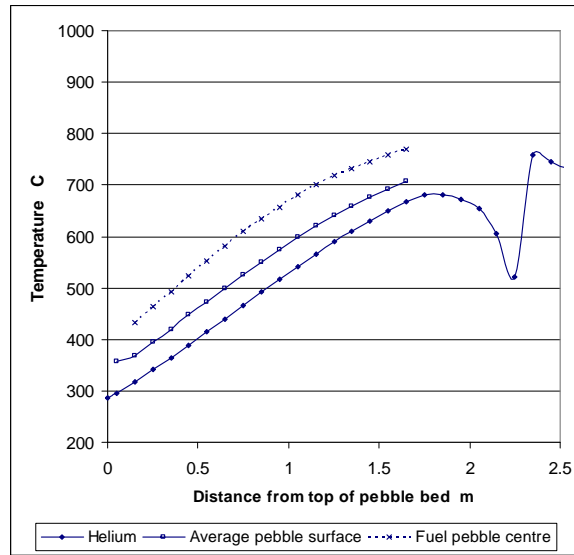


FIG. 2.57. WIMSTER model temperature results, showing the reflector and pebble surface temperature (left) and the reflector and gas temperature (right).



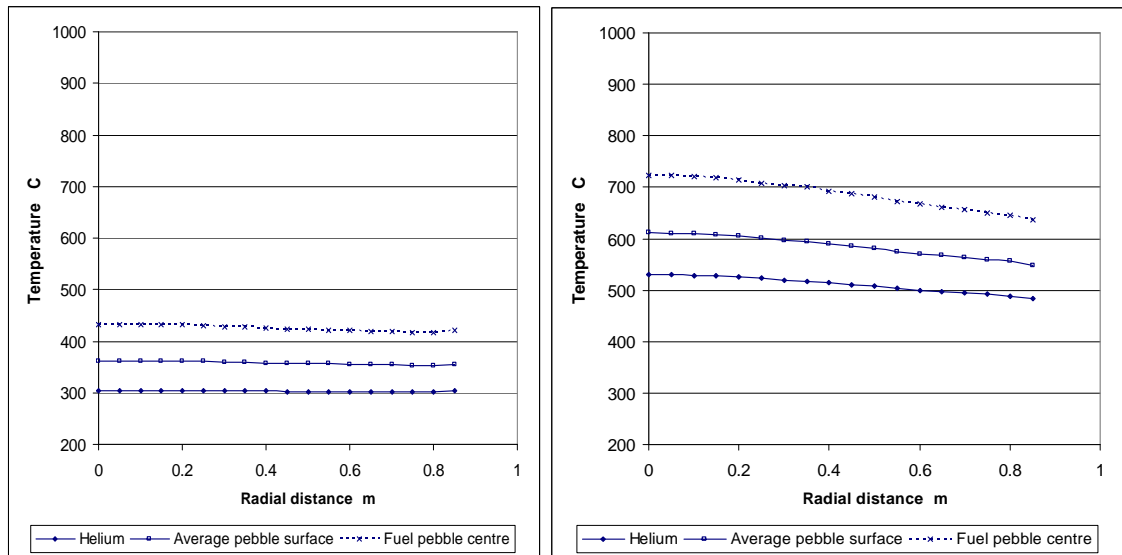
(a)

(b)



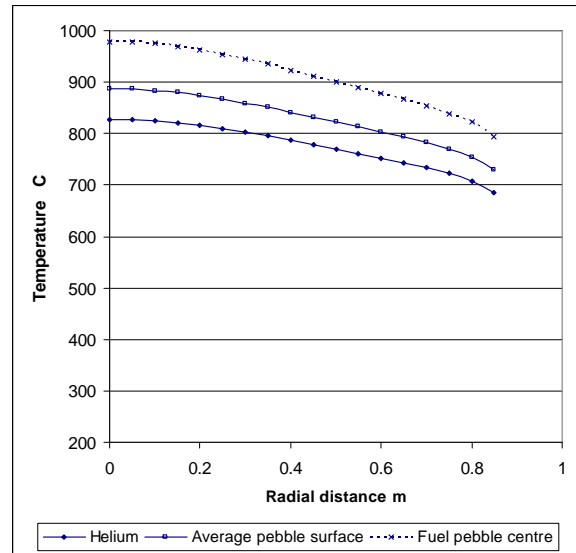
(c)

FIG. 2.58. WIMSTER model axial temperature profiles in the pebble bed at radial distances (a) $R = 0$ cm, (b) $R = 45$ cm and (c) $R = 90$ cm.



(a)

(b)



(c)

FIG. 2.59. WIMSTER Model radial temperature profiles in the pebble bed at (a) $Z = 0$ cm, (b) $Z = 80$ cm and (c) $Z = 170$ cm below the surface.

TABLE 2.32. WIMSTER MODEL AXIAL (R = 0 CM) TEMPERATURE PROFILE

Z (cm)	Gas temperature (°C)	Average pebble surface temperature (°C)	Fuel pebble centre temperature (°C)
0	284.5	370.0	372.2
5	294.6	367.0	382.2
15	319.3	378.7	451.5
25	346.5	412.7	494.8
35	375.7	445.7	534.0
45	407.8	483.0	579.6
55	441.0	518.0	618.6
65	475.4	553.5	657.2
75	511.2	592.0	701.3
85	547.9	629.3	741.0
95	585.2	667.1	781.1
105	622.2	701.9	814.5
115	657.5	732.7	840.0
125	691.7	763.8	868.2
135	724.2	792.8	893.1
145	755.6	821.0	918.0
155	785.4	848.1	942.4
165	814.0	874.6	967.2
175	839.9	895.4	982.9
185	854.5	882.2	945.0
195	855.5	856.0	N/A
205	854.0	853.6	N/A
215	852.3	851.9	N/A
225	850.8	850.4	N/A
235	849.1	848.7	N/A
245	847.5	847.2	N/A
255	846.3	846.0	N/A
265	845.4	845.2	N/A
275	845.0	844.8	N/A
285	844.5	843.7	N/A
295	828.7	815.0	N/A

TABLE 2.33. WIMSTER MODEL RADIAL (Z = 80 CM) TEMPERATURE PROFILE

R (cm)	Gas temperature (°C)	Average pebble surface temperature (°C)	Fuel pebble centre temperature (°C)
0.00	529.6	611.2	722.4
0.05	529.3	610.9	722.0
0.10	528.5	609.8	720.5
0.15	527.1	607.9	717.8
0.20	525.1	605.2	714.1
0.25	522.4	601.3	708.5
0.30	519.9	597.7	703.3
0.35	517.4	594.9	700.2
0.40	514.2	590.0	692.6
0.45	510.8	585.8	687.2
0.50	507.0	580.6	679.8
0.55	503.2	575.4	672.5
0.60	499.8	570.9	666.7
0.65	496.9	566.9	660.8
0.70	494.3	563.2	655.5
0.75	491.9	559.2	649.4
0.80	488.9	555.9	645.8
0.85	482.7	548.0	636.3
0.90	472.2	494.4	536.9

TABLE 2.34. WIMSTER MODEL MAXIMUM TEMPERATURE VALUES OF MAIN COMPONENTS

Component	Position	Max. temperature (°C)
Fuel element	Pebble centre	982.9
	Pebble surface	895.4
Side reflector	Surface	651.7
Bottom reflector	Surface	832.9

Comparison of the WIMSTER and PHOENICS model results

The gas, pebble surface and fuel centre temperatures predicted by the PHOENICS and WIMSTER models show strong quantitative agreement within the pebble bed. The agreement is exemplified by the plots showing the comparison of axial and radial temperatures profiles in Fig. 2.60. The generally good agreement between the results of the two models in the whole-core region is confirmed by the contour plots in Figs 2.53 and 2.57.

The maximum pebble temperatures in both models occur at the base of the pebble bed near the core centreline (R = 0 cm). The maximum temperature in the PHOENICS model is approximately 30°C higher than the corresponding temperature in the WIMSTER model results. This can be attributed to different approaches to modelling the bottom reflector region, which result in a different division of the coolant gas flow between the two flow paths which lead from the pebble bed to the outlet plenum.

TABLE 2.35. WIMSTER MODEL PREDICTIONS FOR TEMPERATURES
AT THERMOCOUPLE LOCATIONS

No.	R (cm)	Z (cm)	Predicted solid temp. (°C)	Measured temp. (°C)	Difference (°C)
Side reflector					
1	193	80	N/A ¹	231.3	-
2	189	80	335.1	249.3	86
3	167	80	335.4	274.3	61
4	133	80	356.9	289.1	68
5	117	80	388.6	313.3	75
6	93	80	463.3	357.7	106
7	193	170	N/A ¹	234.9	-
8	189	170	365.8	264.8	1
9	167	170	367.6	303.9	64
10	133	170	408.2	328.5	80
11	117	170	468.9	365.3	104
12	93	170	632.3	507.1	125
Top reflector					
13	60	-40	274.6	245.7	29
Hot helium plenum					
14	40	234	819.1	800.2	19
15	60	234	793.8	763.1	31
Bottom carbon bricks					
16	70	440	261.0	224.1	37
17	50	400	252.3	245.7	7
18	50	370	254.7	296.2	-42
19	50	340	263.3	406.7	-143
Fuel discharging tube					
20	26	340	253.8	334.2	-80
21	26	300	462.4	806.1	-344
22	26	260	832.3	881.7	-49

Comparison of the WIMSTER and PHOENICS model results with experimental data

Tables 2.31 and 2.35 allow the PHOENICS and WIMSTER model results to be compared with the measured temperatures supplied in the benchmark specification. No attempt has been made to revise the thermohydraulic models presented in this report to promote better agreement with the measured data.

¹ Thermocouples 1 and 7 do not lie within the domain of the WIMSTER computational model. Therefore no values are predicted by the WIMSTER model at these locations.

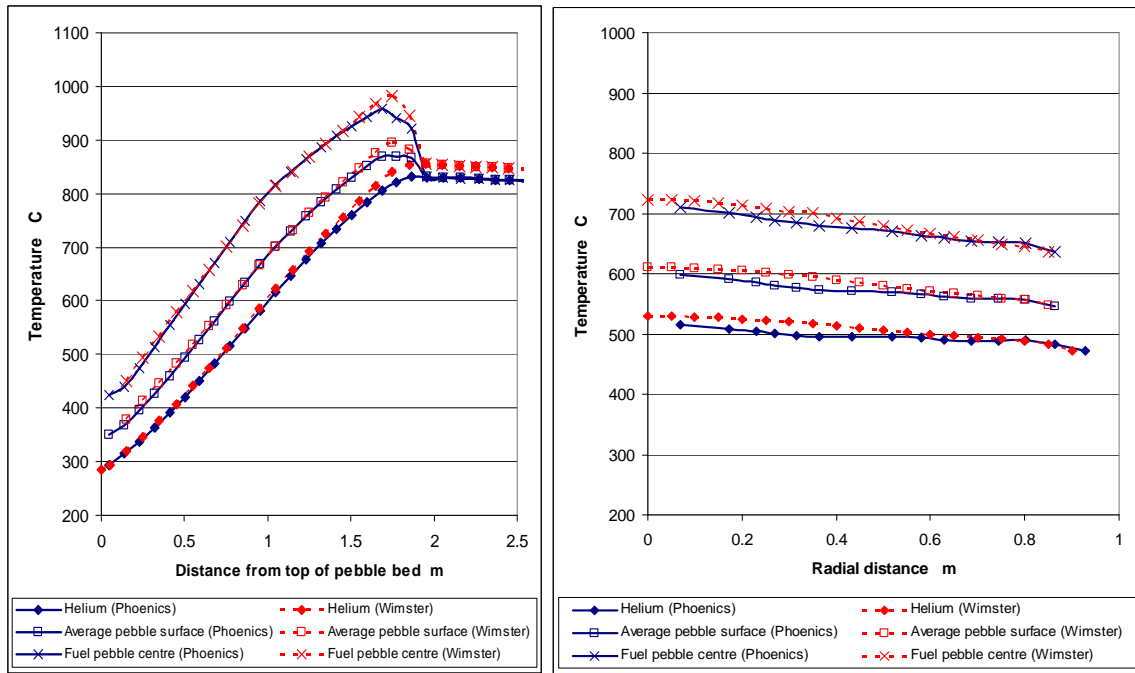


FIG. 2.60. Comparison of the axial ($R = 0$ cm, shown on the left) and radial ($Z = 80$ cm, shown on the right) temperature profiles computed by the PHOENICS and WIMSTER models.

The PHOENICS model, which includes a detailed model of the heat losses across the core barrel and RPV, shows good agreement between measured and predicted temperature values in the side reflector at $R = 117, 133, 167, 189$ and 193 cm. The reflector temperatures close to the pebble bed (at $R = 93$ cm) are overpredicted.

From Table 2.35, it is seen that the WIMSTER model over predicts the graphite temperatures throughout the side reflector, particularly so in the outer region. This is due to the simplified boundary condition used in the WIMSTER model in which heat loss from the outer surface of the side reflector is neglected. This simplification was carried over from the PBMR-400 model in which the external heat losses were considered to be not significant and, in addition, the side reflector external temperature is largely controlled by the temperature of the gas flowing through the riser channels. However, the assumption of negligible external heat loss is not true for the HTR-10, as the surface area (relative to the core volume) is large and the control of the reflector temperature by the riser channels is not strong. The reflector temperatures closer to the pebble bed between the two codes are in better agreement, with the WIMSTER model over predicting the innermost temperature by about the same amount as the PHOENICS model.

The temperature at Thermocouple 21, which is positioned in the wall of the fuel discharge tube close to the hot helium plenum, is incorrectly predicted by both the PHOENICS and WIMSTER models. This thermocouple lies close to the region in which hot gas from the pebble bed and cooler gas from the fuel discharge tube and leakage flow path meet and mix. This results in a very strong temperature gradient clearly visible in both the PHOENICS and WIMSTER models results, introducing a high degree of uncertainty into the predicted temperatures. Therefore, errors in the models' predictions at this location can be attributed to the simplified benchmark model.

Acknowledgements

The authors wish to express their gratitude to the NNR of the RSA for providing support and funding to participate in this benchmark.

Introduction

Included in this section are the results by PBMR (Pty) Ltd. for the benchmark problem depicting steady state temperature conditions on the HTR-10. This analysis includes axial and radial temperature profiles within the pebble bed as well as temperatures at selected locations within the core and maximum temperatures for core components. The analyses were performed using both the VSOP99/5 and Time Dependent Neutronics and Temperatures (TINTE) codes as appropriate and some detail on the models and assumptions used for all the HTR-10 calculations are included in this section.

VSOP [2-30] is a computer code system for the comprehensive numerical simulation of the physics of thermal reactors. It implies the set-up of the reactor and fuel element, processing of cross-sections, neutron spectrum evaluation, neutron diffusion calculation (finite-difference) in two or three dimensions, fuel burnup, fuel shuffling, reactor control, thermal hydraulics, and fuel cycle costs. This enables the user to calculate the reactor life history from loading to criticality, starting up the reactor and running it towards the equilibrium core conditions. Reprocessing and closure of the fuel cycle can be simulated under consistent control of the fuel inventory including the isotopic decay during periods of intermediate storage. The thermal hydraulics part (steady state and time dependent) is restricted to pebble bed HTRs and to two spatial dimensions. Accident phenomena can be analysed in a quasi-static approximation by repeatedly analysing the reactivity and the temperature distribution in the reactor core. The current code version, VSOP(99), represents the further-developed and much-improved version of the VSOP(94) code available at the Nuclear Energy Agency (NEA) databank and widely used for HTR analysis.

The TINTE code [2-31] was developed to investigate the nuclear and thermal transient behaviour of HTRs with full neutron, temperature and xenon feedback effects taken into account in the two dimensional R-Z geometry. The main time dependent calculational components of the code are:

- Neutron flux in two energy groups and six delayed neutron groups;
- Nuclear heat source distribution including local and non-local energy distribution fractions;
- Heat transport from the fuel kernels to the fuel sphere surface;
- Time dependent global temperature distribution;
- Coolant gas flow distribution for a specified mass flow or pressure gradient;
- Convection and its feedback on gas circulation;
- Gas mixing effects (for multiple gasses present in the system) in the model, including corrosion interactions between the gases and solid graphite structures.

Both codes were developed by KFA (Kernforschungsanlage), known today as Forschungszentrum Jülich (FZJ), over many years and obtained by PBMR (Pty) Ltd under a license agreement in 2001. A short summary of the codes and some more recent activities and plans are also provided in [2-32].

All three HTR-10 benchmark problems (steady state temperature distribution, loss of primary flow without scram, and control rod withdrawal without scram) fall within the analysis scope and capabilities of the TINTE code, while only the steady state results are presented for VSOP99/5. TINTE Release 3.0, Version 306 of June 2006 was used for the analysis of the three HTR-10 benchmark problems.

The VSOP99 and TINTE code systems are used at PBMR (Pty) Ltd. in South Africa and this work forms part of the Verification and Validation (V&V) efforts on these codes.

VSOP99 analysis and results

Calculation description and assumptions in VSOP99

The two dimensional calculation model for core physics problems is illustrated in Fig. 2.61.

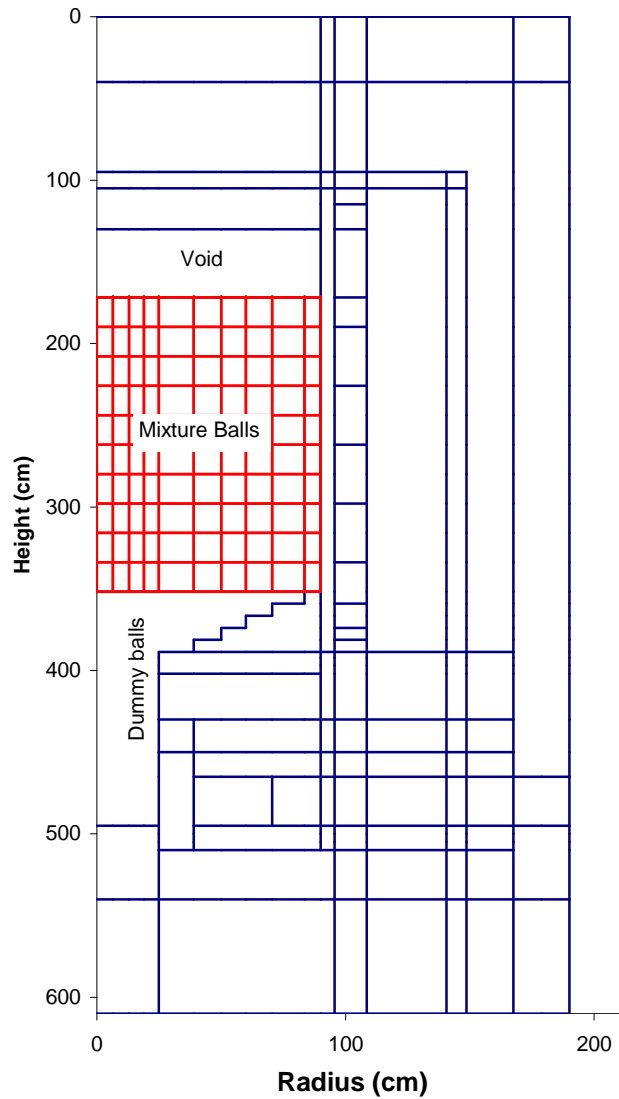


FIG. 2.61. VSOP99 2-D core physics calculation model.

The mixture balls are shown by red lines whereas the dummy balls and graphite structures are shown with blue lines. The proposed zone numbering and atomic densities in the benchmark definition are used as input to the calculations. Figure 2.61 shows the model used when the core is filled to just above the cones region with a mixture of fuel and graphite spheres or, in other words, the configuration as described in the test case. After loading, some fuel burnup was performed to the specified level. This represents ~11 days of operation.

Note that the pebble flow lines were assumed to be vertical or, in other words, no radial flow of pebbles was taken into account. The only reason this was done was to achieve a well-defined bottom boundary between the fuel/graphite mixture and the graphite-only spheres in the cone region below. A model that represents the expected pebble flow lines (for example, flowing faster in the core centre) makes the definition of such a well-defined boundary very difficult, if not impossible.

	6.5	13.0	19.0	25.0	39.0	50.0	60.0	70.5	83.5	90.0	95.6	108.6	140.6	148.6	167.5	178.8	190.0	194.0	197.0	210.0	218.0	283.4	283.5	285.4	287.0	
-740.0	66	66	66	66	66	66	66	66	66	66	66	66	66	66	66	66	66	66	66	66	66	66	66	66	36	
-411.0	34	34	34	34	34	34	34	34	34	34	34	34	34	34	34	34	34	34	34	34	34	34	34	34	36	
-391.0	65	65	65	65	65	65	65	65	65	65	65	65	65	65	65	65	65	65	65	65	65	65	65	65	36	
-351.0	33	33	33	33	33	33	33	33	33	33	33	33	33	33	33	33	33	33	33	33	33	33	33	33	36	
-343.0	63	63	63	63	63	63	63	63	63	63	63	63	63	63	63	63	63	63	63	63	63	64	67	67	36	
-219.0	17	17	17	17	17	17	17	17	17	17	17	17	17	17	17	17	17	17	17	17	17	64	23	68	39	
-170.0	62	62	62	62	62	62	62	62	62	62	62	62	62	62	62	62	62	62	62	7	16	64	23	68	39	
-130.0	57	57	57	57	57	57	57	57	57	57	58	58	58	58	58	59	59	35	7	22	64	23	68	39	36	
-75.0	56	56	56	56	56	56	56	56	56	56	55	55	55	55	55	59	59	35	7	22	64	23	68	39	36	
-65.0	40	40	40	40	40	40	40	40	40	40	40	40	40	40	55	59	59	35	7	22	64	23	68	39	36	
-55.3	41	41	41	41	41	41	41	41	41	41	14	3	52	4	54	60	60	35	7	22	64	23	68	39	36	
-40.0	41	41	41	41	41	41	41	41	41	41	14	3	52	4	54	60	60	35	7	22	64	23	68	39	36	
0.0	18	18	18	18	18	18	18	18	18	18	14	3	52	4	54	60	60	35	7	22	64	23	68	39	36	
18.0	1	1	1	1	1	1	1	1	1	1	14	3	52	4	54	60	60	35	7	22	64	23	68	39	36	
36.0	1	1	1	1	1	1	1	1	1	1	14	3	52	4	54	60	60	35	7	22	64	23	68	39	36	
54.0	1	1	1	1	1	1	1	1	1	1	14	3	52	4	54	60	60	35	7	22	64	23	68	39	36	
72.0	1	1	1	1	1	1	1	1	1	1	14	3	52	4	54	60	60	35	7	22	64	23	68	39	36	
90.0	1	1	1	1	1	1	1	1	1	1	14	3	52	4	54	60	60	35	7	22	64	23	68	39	36	
108.0	1	1	1	1	1	1	1	1	1	1	14	3	52	4	54	60	60	35	7	22	64	23	68	39	36	
126.0	1	1	1	1	1	1	1	1	1	1	14	3	52	4	54	60	60	35	7	22	64	23	68	39	36	
144.0	1	1	1	1	1	1	1	1	1	1	14	3	52	4	54	60	60	35	7	22	64	23	68	39	36	
162.0	1	1	1	1	1	1	1	1	1	1	14	3	52	4	54	60	60	35	7	22	64	23	68	39	36	
180.0	1	1	1	1	1	1	1	1	1	1	14	3	52	4	54	60	60	35	7	22	64	23	68	39	36	
187.5	1	1	1	1	1	1	1	1	1	1	14	3	52	4	54	60	60	35	7	22	64	23	68	39	36	
195.0	71	71	71	71	77	71	71	77	29	29	14	3	52	4	54	60	60	35	7	22	64	23	68	39	36	
202.5	71	71	71	71	77	71	71	77	29	29	14	3	52	4	54	60	60	35	7	22	64	23	68	39	36	
210.0	71	71	71	71	77	71	71	77	8	29	29	14	3	52	4	54	60	60	35	7	22	64	23	68	39	36
217.5	71	71	71	71	77	8	8	29	29	29	14	3	52	4	54	60	60	35	7	22	64	23	68	39	36	
222.2	71	71	71	71	72	8	8	29	29	29	14	3	52	4	54	60	60	35	7	22	64	23	68	39	36	
227.0	71	71	71	71	72	8	8	29	29	29	14	28	52	4	54	60	60	35	7	22	64	23	68	39	36	
232.0	71	71	71	71	72	26	26	26	26	26	26	50	50	51	53	61	61	35	7	22	64	23	68	39	36	
263.5	71	71	71	71	72	9	9	9	9	9	50	50	50	51	53	61	61	35	7	22	64	23	68	39	36	
295.0	71	71	71	71	72	9	9	9	9	9	50	50	50	51	53	61	61	35	7	22	64	23	68	39	36	
325.0	24	24	24	24	24	24	24	24	24	24	50	50	50	51	53	61	61	35	7	37	64	23	68	39	36	
326.0	73	73	73	73	2	13	49	49	75	49	50	50	50	51	53	61	61	35	7	38	64	23	68	39	36	
327.0	73	73	73	73	2	13	49	49	76	49	50	50	50	51	53	61	61	35	7	38	64	23	68	39	36	
340.0	73	73	73	73	2	13	49	49	49	49	50	50	50	51	53	61	61	35	7	38	64	23	68	39	36	
360.0	73	73	73	73	5	42	44	44	44	44	44	44	44	46	48	48	48	35	7	38	64	23	68	39	36	
400.0	73	73	73	73	5	42	44	44	44	44	44	44	44	46	48	48	48	35	7	38	64	23	68	39	36	
440.0	73	73	73	73	5	42	43	43	43	43	43	43	43	45	47	47	47	35	7	38	64	23	68	39	36	
446.0	74	74	74	74	11	21	30	30	30	30	30	30	30	31	32	32	32	32	7	38	64	23	68	39	36	
461.0	74	74	74	74	11	19	19	19	19	19	19	19	19	19	10	10	10	10	7	38	64	23	68	39	36	
484.0	74	74	74	74	11	12	10	10	10	10	10	10	10	10	10	10	10	10	7	38	64	23	68	39	36	
507.0	27	27	27	27	11	12	10	10	10	10	10	10	10	10	10	10	10	10	7	38	64	23	68	39	36	
657.0	20	20	20	20	20	20	20	20	20	20	20	20	20	20	20	20	20	20	20	20	64	23	68	39	36	
665.0	6	6	6	6	6	6	6	6	6	6	6	6	6	6	6	6	6	6	6	6	64	69	69	69	36	
772.0	25	25	25	25	25	25	25	25	25	25	25	25	25	25	25	25	25	25	25	25	25	25	25	25	36	
792.0	70	70	70	70	70	70	70	70	70	70	70	70	70	70	70	70	70	70	70	70	70	70	70	70	36	
793.0	15	15	15	15	15	15	15	15	15	15	15	15	15	15	15	15	15	15	15	15	15	15	15	15	36	

FIG. 2.62. Thermohydraulics calculation layout.

For thermohydraulic calculations, a different layout is used. Figure 2.62 represents the material numbering and the flow paths for THERMIX calculations. The flow path is relatively complex to model in VSOP/THERMIX and care had to be taken to get the correct coolant mass flow values.

VSOP99 model assumptions

The power and temperature profiles were obtained by the VSOP99 code performing coupled neutronic thermohydraulic calculations. The thermohydraulic module in VSOP99, THERMIX, was used as an integrated part of the code (a VSOP99 model was defined). Note that the power distribution was calculated in VSOP99 and that the power distribution provided in the benchmark (also calculated values) was therefore not used — more details are provided later. The test-case-specified correlations are used for the thermal properties of the materials where applicable. The thermal conductivity of the thermal insulation inside the concrete walls is modelled with thermal conductivity rule No. 21 which is defined as ‘Kaowool-mat (in air (Jul 992RB))’, and the thermal heat capacity of this material is modelled with ID No. 12 which is defined as ‘Thermal shield (HRB)’.

In the VSOP99/5 code, the thermal conductivity rule No. 12 which is defined as 'Pebble Bed (Breitbach/ Barthels)' has been disabled, therefore the thermal conductivity rule No. 27 which is defined as 'Lambda eff., Pebble Bed (Function of temperature and dose (Robolt+Zehner-Schlunder))' is used.

VSOP99 model clarification: pebble flow line definition

In the VSOP99 code, the downward movement of the pebbles is simulated with the flow lines. In this instance, the shape of the regions and their shuffling, if any, must fit into the flow pattern. On the other hand, the calculation of the neutron flux is performed by means of the CITATION module and this is confined to a pattern of 'CITATION-material compositions' with perpendicular boundaries in e.g. R-Z coordinates. Similarly, the THERMIX thermohydraulics module is subject to a mesh lattice of perpendicular R-Z coordinates. The transfer of relevant data of the regions to 'CITATION-material compositions' and back is provided by a volume matrix which is generated in subroutine BIRGIT.

The subroutine generates both reactor regions V(I) and CITATION-material compositions W(J). It then synthesizes a matrix of volumes VW(I,J), which is the overlapping set of the V(I) and W(J). Analogously, a transfer matrix VW(I,K) between the core regions V(I) and the corresponding fine mesh volumes W(K) of the THERMIX module is provided.

The simulation of the movement of the fuel elements can be defined by input. In this instance, a complex geometry of the core bottom of a pebble bed core and a very special flow pattern of the fuel resulting from experimental data or from theoretical research can be considered. The limiting curves of flow channels are defined by few coarse points and the curves are gained by interpolation. The radial position of the coarse points can be internally modified in order to adjust the channel volume to a predefined value. Each channel is subdivided into regions, which are numbered by the code from top to bottom starting with the first inner channel. Each region's volume in each channel is adjusted to be the same, which might cause an internal adjusting of the axial boundaries of the regions. The resulting axial and radial boundaries of the regions can be different than the CITATION-material composition boundaries, especially at the bottom part of the pebble bed core. This might result in unexpected power generation below the fuel bottom line even if the conus region is only filled with dummy (graphite) pebbles or a larger or smaller value of power generation in these regions if extra care is not taken for these regions. Figure 2.63 illustrates the overlapping of the VSOP code core regions and CITATION-material compositions.

The model used in the calculations assumed to have parallel flow of pebbles in the core and the conus region (below 187 cm from the top of the pebble bed), where there is no power generation, i.e. no fuel pebbles are present, is modelled explicitly. Therefore the core regions V(I) and CITATION-material compositions W(J) have exact axial and radial boundaries, i.e. both perpendicular (R-Z coordinates). This is clearly illustrated in Fig. 2.64.

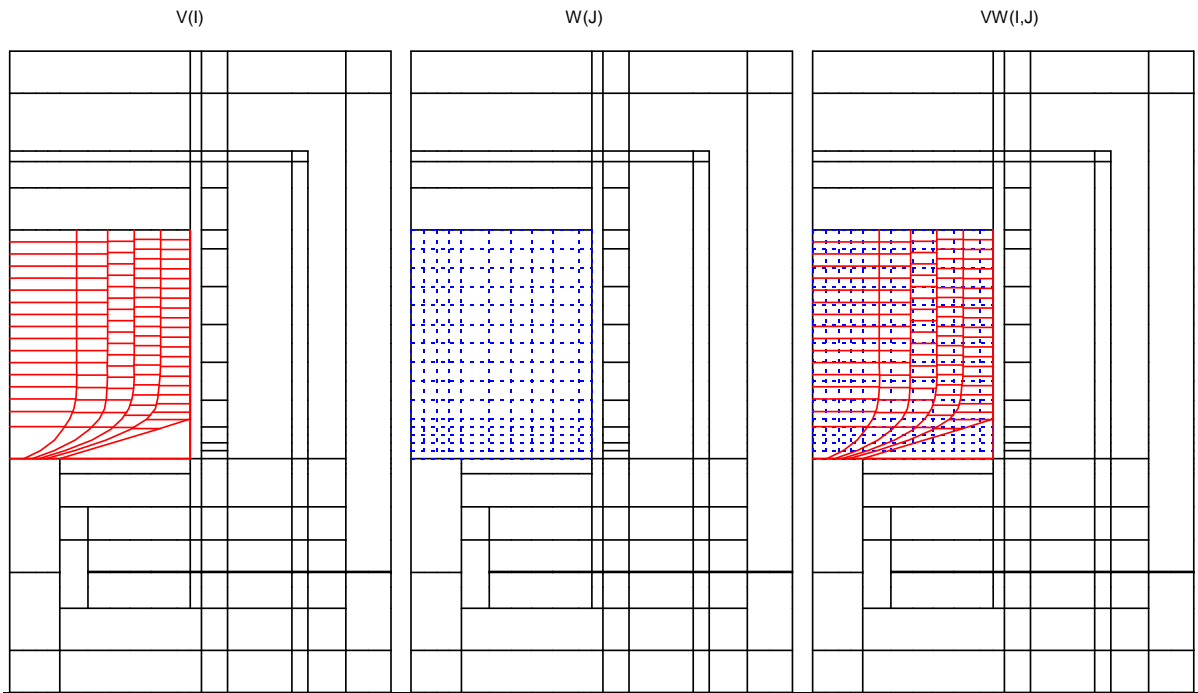


FIG. 2.63. HTR10 model with flow lines: $V(I)$ VSOP core regions, $W(J)$ CITATION-material composition and $VW(I,J)$ transfer matrix.

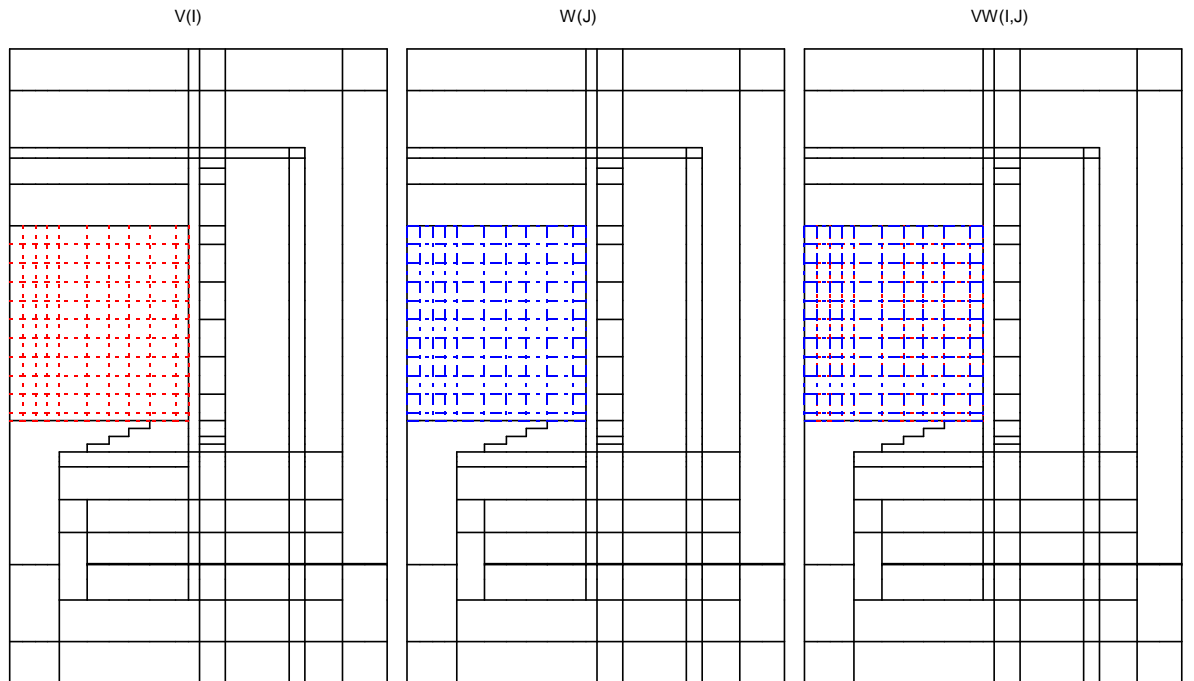


FIG. 2.64. HTR10 model without flow lines: $V(I)$ VSOP core regions, $W(J)$ CITATION-material compositions and $VW(I,J)$ transfer matrix.

VSOP99 steady state results: thermal balance and mass flows

The calculated mass flows are given in Table 2.36 whereas Table 2.37 gives the thermal balance of the model.

TABLE 2.36. CALCULATED MASS FLOWS WITH DUMMY BALLS
PRESENT IN THERMIX MODEL

Description	Value (kg/s)	
	Given	VSOP99/5
Helium inlet flow	4.32	4.32
Helium bypass flow from cold inlet to hot exit	0.43	0.05
Helium upwards flow through fuel discharge tube	0.04	0.04
Helium riser flow	3.84	4.23
Helium control rods cooling flow	0.09	0.09
Helium flow through pebble bed	3.76	4.14
Helium flow through bottom reflector	N/A	3.04
Helium downwards flow through fuel discharge tube	N/A	1.10

TABLE 2.37. THERMAL BALANCE FOR THE MODELS

	Nuclear heat (MW)	Convective heat (MW)	Heat loss (kW)	T _{in} (He) °C	T _{out} (He) °C
VSOP99/5	10.00	10.00	0.31	250.00	688.80

It was possible to construct a VSOP99 model where the mass flow rates calculated in the THERMIX module agree well with the given mass flows and also achieve thermal balance as is shown. The convective heat carried away by the coolant and the heat losses through the boundaries do add up to the nuclear heat generated. (The newest release, VSOP99/5, available at PBMR, was selected for comparison since known problems exist with some earlier versions (99/4 and 99/3) when modelling a mixture of dummy and fuel spheres. The way the pebble bed mixture is treated has been changed in VSOP99/5 in that the fuel-to-dummy ball ratio is not an input option for the thermohydraulic model anymore but is directly taken from the neutronic model.)

The following two different approaches were followed:

- (1) Reactor is critical, i.e. the control rods are inserted to compensate the positive reactivity of the full core;
- (2) Reactor is super-critical, i.e. control rods are positioned at 15.3 cm above the top cavity.

VSOP99 steady state results: power profile studies

The power distribution of the initial core (10 MW) was also supplied in the specification and is shown in Table 2.38. The calculated power distribution with and without control rods inserted is given in Tables 2.39 and 2.40 respectively. The thermohydraulic calculations are also performed with the given power distribution.

Differences in the power distribution are observed when compared with the given power distribution. The percentage differences between given and calculated power distributions are given in Tables 2.41 and 2.42, respectively, with and without the control rods inserted.

TABLE 2.38. POWER DISTRIBUTION (W/CM³) OF THE INITIAL CORE GIVEN IN SPECIFICATION

Z/R (cm)	6.5	13	19	25	39	50	60	70.5	83.5	90
18	1.79	1.79	1.79	1.78	1.75	1.71	1.68	1.65	1.63	1.65
36	2.12	2.11	2.10	2.08	2.06	2.01	1.95	1.89	1.86	1.89
54	2.46	2.45	2.44	2.41	2.35	2.26	2.18	2.10	2.07	2.09
72	2.61	2.60	2.58	2.56	2.49	2.43	2.33	2.27	2.22	2.22
90	2.78	2.77	2.79	2.72	2.65	2.56	2.46	2.39	2.30	2.30
108	2.84	2.84	2.82	2.79	2.71	2.55	2.45	2.33	2.26	2.26
126	2.66	2.65	2.63	2.60	2.56	2.49	2.38	2.29	2.22	2.21
144	2.49	2.49	2.47	2.44	2.37	2.29	2.19	2.08	2.01	2.00
162	2.36	2.35	2.33	2.30	2.22	2.11	2.02	1.93	1.85	1.82
180	2.33	2.32	2.29	2.25	2.16	2.02	1.93	1.83	1.73	1.66
187	1.53	1.53	1.51	1.48	1.42	1.33	1.27	1.21	1.13	0.00

TABLE 2.39. POWER DISTRIBUTION (W/CM³) OF THE INITIAL CORE CALCULATED BY VSOP99/5 WITH CONTROL RODS INSERTED TO 94.0 CM FROM THE TOP OF THE TOP CAVITY

Z/R (cm)	6.5	13	19	25	39	50	60	70.5	83.5	90
18	1.34	1.34	1.33	1.31	1.28	1.23	1.18	1.12	1.06	1.00
36	1.78	1.77	1.76	1.74	1.68	1.60	1.51	1.42	1.31	1.24
54	2.21	2.20	2.18	2.15	2.09	1.98	1.88	1.76	1.65	1.58
72	2.55	2.54	2.52	2.49	2.42	2.30	2.19	2.08	1.99	1.97
90	2.79	2.78	2.76	2.73	2.65	2.53	2.42	2.31	2.24	2.27
108	2.91	2.90	2.88	2.85	2.77	2.66	2.55	2.44	2.39	2.43
126	2.91	2.90	2.88	2.85	2.78	2.67	2.56	2.46	2.41	2.46
144	2.81	2.80	2.78	2.76	2.69	2.58	2.48	2.38	2.33	2.39
162	2.65	2.64	2.62	2.59	2.53	2.43	2.34	2.24	2.18	2.22
180	2.50	2.49	2.48	2.45	2.39	2.31	2.21	2.11	2.03	2.06
187.5	2.49	2.48	2.47	2.45	2.39	2.31	2.23	2.13	2.04	0.00

TABLE 2.40. POWER DISTRIBUTION (W/CM³) OF THE INITIAL CORE CALCULATED BY VSOP99/5 WHEN THE CONTROL RODS ARE SITUATED AT 15.3 CM ABOVE THE TOP CAVITY

Z/R (cm)	6.5	13	19	25	39	50	60	70.5	83.5	90
18	1.72	1.71	1.71	1.70	1.68	1.65	1.62	1.60	1.60	1.64
36	2.01	2.00	1.99	1.97	1.94	1.88	1.83	1.78	1.78	1.83
54	2.32	2.31	2.30	2.28	2.23	2.15	2.08	2.01	1.99	2.05
72	2.56	2.55	2.53	2.51	2.45	2.36	2.28	2.20	2.17	2.23
90	2.69	2.69	2.67	2.64	2.58	2.48	2.39	2.30	2.27	2.32
108	2.73	2.72	2.70	2.67	2.61	2.51	2.41	2.33	2.28	2.34
126	2.66	2.65	2.63	2.61	2.54	2.45	2.36	2.27	2.22	2.28
144	2.52	2.51	2.49	2.47	2.41	2.32	2.23	2.14	2.10	2.15
162	2.33	2.33	2.31	2.29	2.23	2.15	2.06	1.98	1.93	1.96
180	2.18	2.17	2.16	2.14	2.09	2.01	1.93	1.84	1.77	1.79
187.5	2.16	2.15	2.14	2.12	2.07	2.00	1.93	1.84	1.77	0.00

TABLE 2.41. PERCENTAGE DIFFERENCES BETWEEN THE GIVEN POWER DISTRIBUTION AND CALCULATED WITH VSOP99/5 WHEN THE CONTROL RODS ARE INSERTED TO 94.0 CM FROM THE TOP OF THE TOP CAVITY

Z/R (cm)	6.5	13	19	25	39	50	60	70.5	83.5	90
18	25.1%	25.4%	25.9%	26.2%	26.7%	27.9%	29.7%	31.8%	35.2%	39.4%
36	16.0%	16.0%	16.3%	16.5%	18.2%	20.3%	22.3%	24.8%	29.4%	34.7%
54	10.2%	10.2%	10.6%	10.7%	11.2%	12.3%	14.0%	16.0%	20.4%	24.3%
72	2.2%	2.2%	2.3%	2.7%	2.9%	5.2%	6.0%	8.5%	10.5%	11.0%
90	-0.3%	-0.3%	1.0%	-0.2%	0.0%	1.0%	1.5%	3.2%	2.5%	1.2%
108	-2.4%	-2.1%	-2.0%	-2.0%	-2.2%	-4.1%	-4.0%	-4.9%	-5.5%	-7.7%
126	-9.5%	-9.5%	-9.5%	-9.7%	-8.5%	-7.1%	-7.7%	-7.6%	-8.6%	-11.5%
144	-13.0%	-12.6%	-12.7%	-12.9%	-13.4%	-12.7%	-13.3%	-14.7%	-16.0%	-19.3%
162	-12.2%	-12.3%	-12.5%	-12.8%	-14.0%	-15.3%	-15.6%	-16.1%	-17.9%	-22.2%
180	-7.3%	-7.5%	-8.2%	-9.0%	-10.9%	-14.2%	-14.7%	-15.5%	-17.6%	-23.9%
187.5	-62.7%	-62.4%	-63.7%	-65.5%	-68.1%	-73.8%	-75.4%	-76.0%	-80.7%	

TABLE 2.42. PERCENTAGE DIFFERENCES BETWEEN THE GIVEN POWER DISTRIBUTION AND CALCULATED WITH VSOP99/5 WHEN THE CONTROL RODS ARE SITUATED AT 15.3 CM ABOVE THE TOP CAVITY

Z/R (cm)	6.5	13	19	25	39	50	60	70.5	83.5	90
18	4.1%	4.2%	4.6%	4.5%	4.0%	3.6%	3.4%	3.1%	1.9%	0.5%
36	5.3%	5.1%	5.2%	5.1%	6.1%	6.6%	6.4%	5.8%	4.5%	3.0%
54	5.6%	5.5%	5.8%	5.5%	5.3%	4.9%	4.7%	4.1%	3.6%	1.7%
72	1.9%	1.8%	1.7%	1.9%	1.6%	2.9%	2.3%	3.2%	2.4%	-0.3%
90	3.1%	3.0%	4.2%	2.9%	2.8%	3.1%	2.9%	3.6%	1.5%	-1.1%
108	4.0%	4.3%	4.3%	4.3%	3.8%	1.7%	1.5%	0.2%	-1.0%	-3.6%
126	0.0%	-0.1%	-0.2%	-0.3%	0.6%	1.7%	1.0%	0.9%	-0.2%	-3.1%
144	-1.2%	-0.9%	-1.0%	-1.2%	-1.6%	-1.1%	-1.7%	-3.0%	-4.3%	-7.3%
162	1.1%	1.0%	0.8%	0.5%	-0.6%	-1.7%	-2.0%	-2.4%	-4.1%	-7.9%
180	6.4%	6.3%	5.7%	5.0%	3.4%	0.6%	0.2%	-0.6%	-2.5%	-8.1%
187.5	-41.0%	-40.7%	-41.8%	-43.3%	-45.5%	-50.3%	-51.6%	-52.4%	-56.7%	

The calculated power distribution with control rods inserted case shows significant differences when compared with the given power distribution, whereas the power distribution calculated without the control rods inserted agrees well (within 10% except the last axial mesh) with the given power distribution. The differences in the last axial mesh could be due to the differences in the calculation models. Table 2.43 shows the power distribution with changing the last axial mesh fuel-to-dummy ball ratio from 53:47 to 35:65, whereas Table 2.44 gives the percentage differences when compared with the given power distribution.

TABLE 2.43. POWER DISTRIBUTION (W/CM³) OF THE INITIAL CORE WITH A 35:65 FUEL-TO-DUMMY BALL RATIO AT THE BOTTOM OF THE FUEL CORE (CONTROL RODS ARE SITUATED AT 15.3 CM ABOVE THE TOP CAVITY)

Z/R (cm)	6.5	13	19	25	39	50	60	70.5	83.5	90
18	1.72	1.72	1.72	1.71	1.69	1.65	1.63	1.60	1.60	1.66
36	2.04	2.04	2.03	2.01	1.97	1.91	1.86	1.81	1.80	1.87
54	2.36	2.36	2.34	2.32	2.27	2.19	2.12	2.05	2.02	2.10
72	2.60	2.59	2.58	2.55	2.49	2.40	2.31	2.24	2.19	2.27
90	2.73	2.72	2.70	2.68	2.62	2.52	2.42	2.34	2.29	2.36
108	2.76	2.75	2.73	2.70	2.64	2.54	2.44	2.36	2.30	2.37
126	2.68	2.68	2.66	2.63	2.57	2.47	2.38	2.29	2.24	2.30
144	2.53	2.53	2.51	2.49	2.43	2.33	2.24	2.16	2.10	2.17
162	2.34	2.34	2.32	2.30	2.25	2.16	2.07	1.99	1.93	1.98
180	2.19	2.19	2.17	2.15	2.10	2.03	1.94	1.86	1.78	1.80
187.5	1.40	1.40	1.39	1.38	1.35	1.30	1.26	1.20	1.15	0.00

TABLE 2.44. PERCENTAGE DIFFERENCES WHEN COMPARED WITH THE GIVEN POWER DISTRIBUTION CALCULATED WITH A 35:65 FUEL-TO-DUMMY BALL RATIO AT THE BOTTOM OF THE FUEL CORE (CONTROL RODS ARE SITUATED AT 15.3 CM ABOVE THE TOP CAVITY)

Z/R (cm)	6.5	13	19	25	39	50	60	70.5	83.5	90
18	3.7%	3.8%	4.2%	4.1%	3.6%	3.2%	3.2%	2.7%	1.7%	-0.5%
36	3.7%	3.5%	3.5%	3.4%	4.2%	4.8%	4.7%	4.0%	3.3%	1.1%
54	3.9%	3.8%	4.1%	3.7%	3.4%	3.1%	2.9%	2.2%	2.4%	-0.3%
72	0.4%	0.3%	0.2%	0.3%	-0.2%	1.2%	0.7%	1.4%	1.2%	-2.2%
90	1.8%	1.7%	2.9%	1.5%	1.2%	1.7%	1.4%	2.0%	0.5%	-2.7%
108	3.0%	3.3%	3.3%	3.1%	2.6%	0.4%	0.2%	-1.2%	-1.8%	-5.0%
126	-0.9%	-0.9%	-1.0%	-1.2%	-0.5%	0.7%	0.1%	-0.2%	-0.7%	-4.3%
144	-1.8%	-1.5%	-1.6%	-1.9%	-2.5%	-1.9%	-2.5%	-3.9%	-4.6%	-8.3%
162	0.7%	0.6%	0.4%	0.0%	-1.2%	-2.3%	-2.6%	-3.1%	-4.1%	-8.5%
180	5.9%	5.7%	5.0%	4.3%	2.6%	-0.3%	-0.7%	-1.5%	-2.8%	-8.5%
187.5	8.4%	8.6%	7.9%	6.9%	5.0%	2.0%	1.1%	0.7%	-1.5%	

The results indicate that the given power profile (also established by a calculation and not measured) could be reproduced better in the VSOP99 model only when the control rods were extracted and if the fuel-reflector mixture ratio for the last calculational mesh are adjusted. No efforts were made to adjust the ratio further to get closer to the reference.

Csteady state results: temperature profile

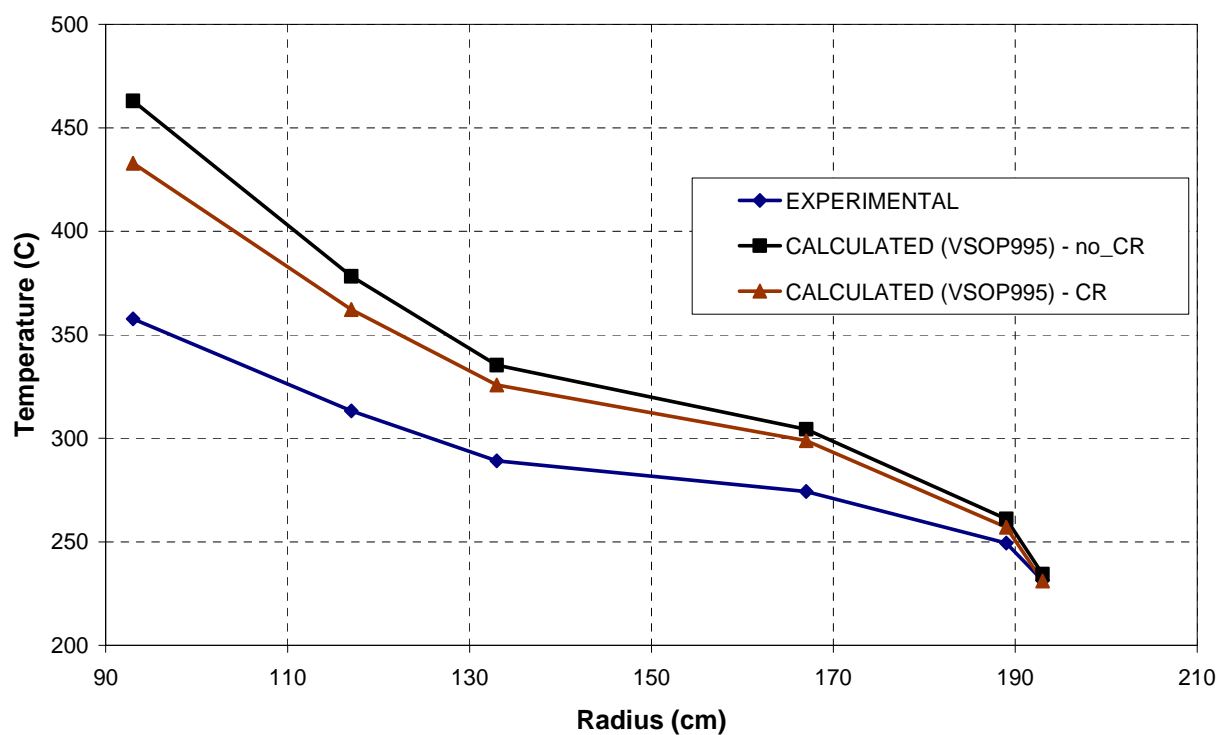
The calculated and the experimental temperatures are listed in Table 2.45 with the temperature differences compared to the experimental values also included. The calculated temperatures at the side reflector away from the core agree very well with the experimental values, whereas the temperatures close to the core are calculated much higher than the experimental value. The temperature profiles within the side reflector are illustrated in Figs 2.65 and 2.66 while the temperature profiles at the bottom carbon bricks and fuel discharge tube are illustrated in Figs 2.67 and 2.68. The requested summary of maximum temperatures in the main components is included in Table 2.46.

TABLE 2.45. CALCULATED TEMPERATURES AND % DIFFERENCES

No.	R(cm)	Z(cm)	Temperature (°C)			Temperature difference (°C)	
			Measured	VSOP995 CR	VSOP995 no CR	VSOP995 CR	VSOP995 no CR
Side reflector							
1	193	80	231.3	231.1	234.4	0	3
2	189	80	249.3	257.1	261.0	8	12
3	167	80	274.3	298.9	304.3	25	30
4	133	80	289.1	325.8	335.4	37	46
5	117	80	313.3	362.2	378.2	49	65
6	93	80	357.7	432.9	463.0	75	105
7	193	170	234.9	242.6	244.1	8	9
8	189	170	264.8	269.5	271.1	5	6
9	167	170	303.9	314.9	316.9	11	13
10	133	170	328.5	360.6	363.5	32	35
11	117	170	365.3	429.1	433.4	64	68
12	93	170	507.1	586.7	591.8	80	85
Top reflector							
13	60	-40	245.7	273.8	276.3	28	31
Hot helium plenum							
14	40	234	800.2	720.1	720.5	-80	-80
15	60	234	763.1	696.5	700.0	-67	-63
Bottom carbon bricks							
16	70	440	224.1	256.7	256.7	33	33
17	50	400	245.7	255.5	255.5	10	10
18	50	370	296.2	262.6	262.5	-34	-34
19	50	340	406.7	409.6	408.2	3	1
Fuel discharge tubes							
20	26	340	334.2	398.8	397.0	65	63
21	26	300	806.1	640.0	638.1	-166	-168
22	26	260	881.7	726.3	724.2	155	156

TABLE 2.46. MAXIMUM TEMPERATURE VALUES OF MAIN COMPONENTS WITH VSOP99

Component	Position	Max. temperature (°C)
		VSOP99/5
Fuel element	Centre	880.8
	Surface	811.7
Side reflector		561.0
Bottom reflector		723.6

FIG. 2.65. Side reflector temperatures at $Z = 80$ cm.

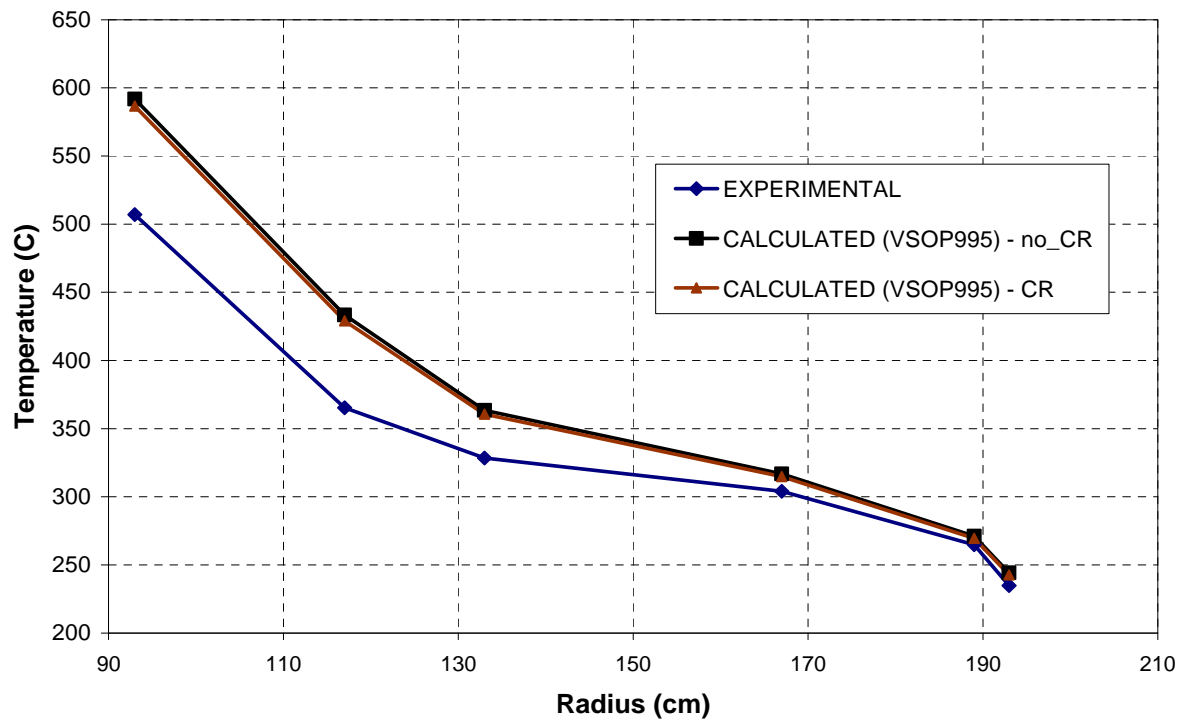


FIG. 2.66. Side reflector temperatures at $Z = 170$ cm.

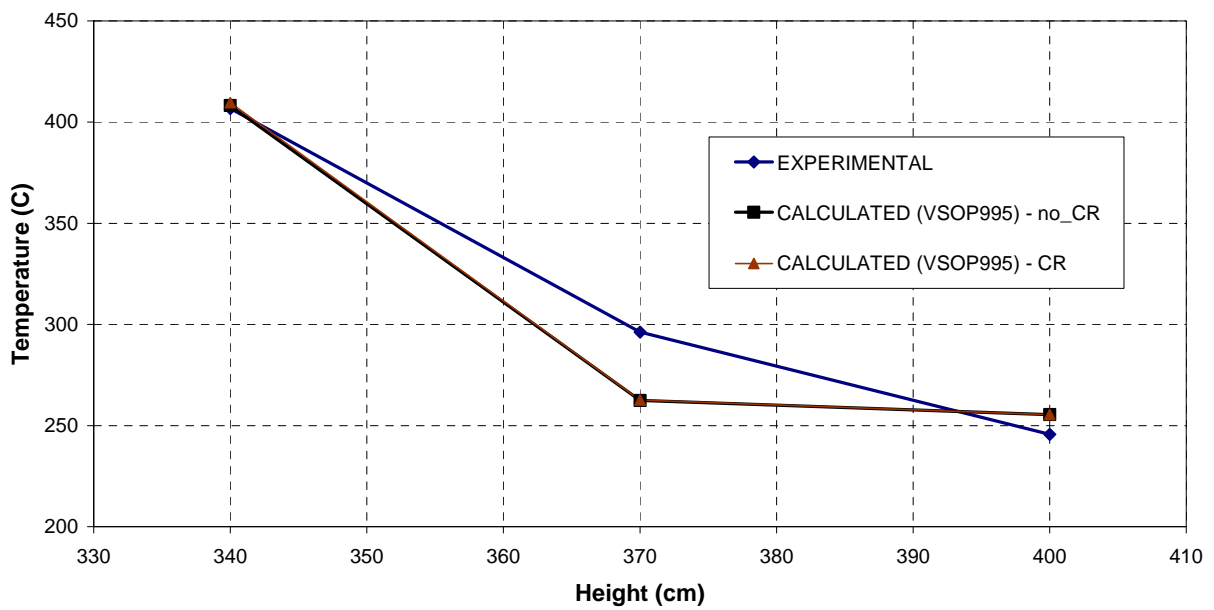


FIG. 2.67. Bottom carbon brick temperatures at $R = 50$ cm.

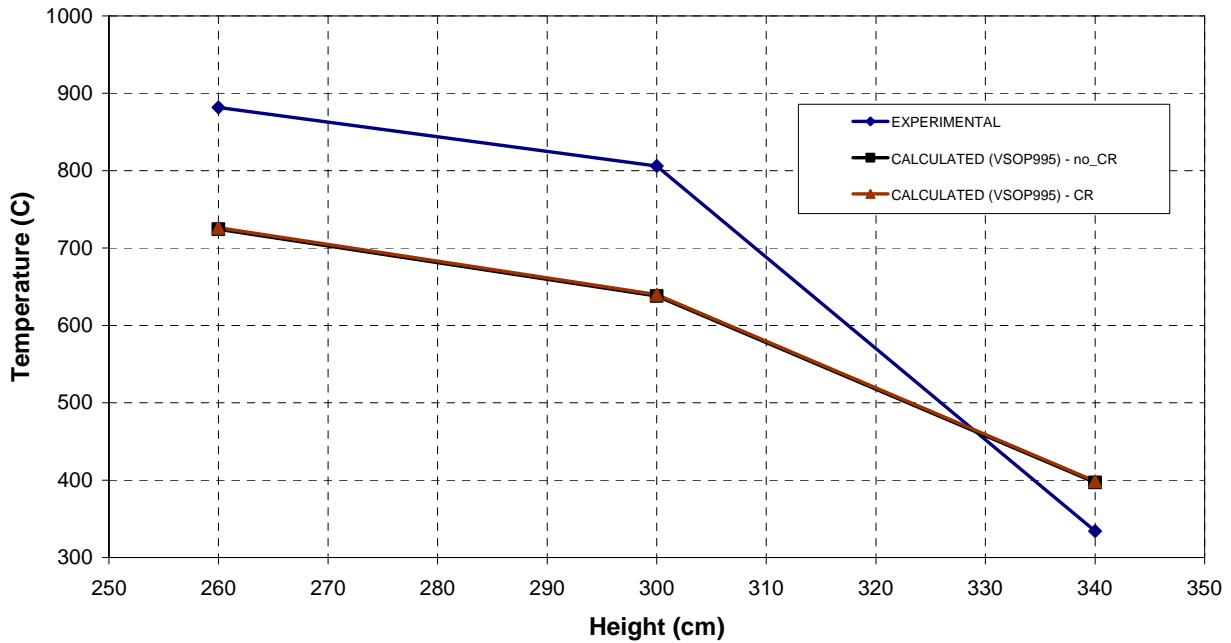


FIG. 2.68. Fuel discharge tube temperatures at $R = 26$ cm.

Summary of VSOP99 steady state results and conclusions

The thermohydraulic benchmark results show discrepancies with the experimental values. The side reflector temperatures, far from the core, are in very good agreement with the experimental values while the temperatures close to the core are higher than the experimental values.

TINTE analysis and results

TINTE HTR-10 model description and assumptions

A single geometrical model is sufficient for the analysis of the three HTR-10 benchmark problems. The material property data for the solid materials and gas flow in the model is depicted in Fig. 2.69. The initial data to prepare a cross-section library is obtained from a code such as VSOP99 and include the fuel and reflector material isotopic compositions. A pre-processing step is used to generate a cross-section library making use of a spectrum (the TISPEC spectrum/slowing down code) calculation and a basic cross-section library (MUPO library). Other aspects addressed is the diffusion coefficients for neutron streaming in cavities in the model (cavity in-between the pebble bed and top reflector), and the fuel burnup history that is given per batch number, for the fuel that is composed of a mixture of fresh and reloaded fuel in a multipass refuelling mode of reactor operation.

There are only two fuel batches for the HTR-10 benchmark problems. The first batch represents the dummy graphite spheres and the second batch the fuel spheres. Since no cycling of fuel spheres has as yet taken place, only one batch is needed to represent all the fuel spheres. Mesh-wise, the region in the TINTE model in which neutronic calculations are performed must map one to one with the CITATION mesh (from the VSOP99 model described above). For ease of transfer of data between the TINTE and VSOP99 models, the coarse mesh layouts for both codes were kept as close as possible to each other.

With regard to the HTR-10 material property definitions provided, they were matched with TINTE code materials that have the closest resemblance to the given definitions. However, for the side reflector thermal conductivity, a different and more sophisticated correlation is the only available option in TINTE. In addition, the specified Core Barrel (CB) and RPV steels are not available in TINTE and, therefore, stainless steel (SA-240) was selected for the CB, and another type of pressure vessel steel (SA-508) for the RPV in the TINTE model. The material specification for the thermal insulation (as indicated in Table 2.4) was not provided and the 'Cerafelt' (Material no. 38) was used in the TINTE HTR-10 model.

Furthermore, some uncertainty was experienced with the interpretation of some of the HTR-10 model definition data presented in Tables 2.3 and 2.8 and viewed against the detail displayed in Figs 2.5 and 2.6. Some examples are:

- The vertical flow width (radial dimensions), directly above the core, of the helium plenum in the top reflector.
- The helium gap width in-between the carbon bricks of the side reflector and the core barrel.
- The type and properties of the thermal shield that encloses the RPV radially.
- Do the emissivity coefficients apply to the gap as an entity or to the surfaces of the cavity? This is specifically important in the case where the gap is being formed by dissimilar materials.

Although the TINTE model is based on and use some core isotopic distribution and decay heat data from VSOP, it must be pointed out that the model was created independently. The focus of the TINTE code is the analysis of transient cases. Therefore, most of the uncertainties raised above are more important in the heat loss transient cases than in the steady state dominated by the coolant gas flow heat transfer phenomena.

A temperature boundary condition was applied to all three outer model boundaries of the TINTE model (Material numbers 15, 39 and 70). A value of 50°C, as specified in Section 2.1.1.4, was applied to the three TINTE model boundaries.

For any coupled neutronic-thermal run with the TINTE model, a steady state calculation is a prerequisite step in determining the starting conditions for a TINTE transient run. Additionally, for calculations utilizing the neutronics module in the TINTE model, the code allows the selection of local or non-local heat deposition of thermal energy generated by the neutron fission process. The local heat deposition option (heat energy deposited in the pebble bed only) was selected for all three benchmark problems. The non-local option (heat energy deposited in the pebble bed and adjacent graphite reflector structures) is the option that corresponds to reality. For benchmark purposes, it is reasonable to start with the local option because of the reduction in the complexity of analysing the benchmark problem. Only after satisfactory results have been obtained with the local option would one attempt the more complicated case of non-local heat deposition. It is not just a case of changing an option in the input, it also requires a more detailed model with respect to coolant flow and leak paths in structures such as the side reflector, detail not defined in this benchmark problem.

[illegible]

FIG. 2.69. TINTE geometrical model for the HTR-10 benchmark problems.

TINTE HTR-10 steady state benchmark results

A set of TINTE files was prepared for this case to account for the 10 MW power level and helium mass flow of 4.32 kg/s. In addition, the VSOP99/5 code data that was converted for use corresponds to a 10 MW neutronic power level that was achieved with the lower tip of the control rods being inserted to -55.3 cm. The helium mass flow distribution was attained in the TINTE model through the adjustment of flow resistance factors in the affected flow channels.

The TINTE model-calculated mass flows are listed in Table 2.47 and a plan view of the gas temperatures under steady state operating conditions is presented in Fig. 2.70.

TABLE 2.47. CALCULATED MASS FLOWS IN THE TINTE MODEL

Flow channels	Value (kg/s)	
	Specified	TINTE
Helium inlet flow	4.320	4.320
Helium bypass flow from cold inlet to hot exit	0.432	0.432
Helium upwards flow through fuel discharge tube	0.043	0.043
Helium riser flow	3.845	3.845
Helium control rods cooling flow	0.086	0.087
Helium flow through pebble bed	3.759	3.758
Helium flow through bottom reflector	N/A	3.351
Helium downwards flow through fuel discharge tube	N/A	0.407

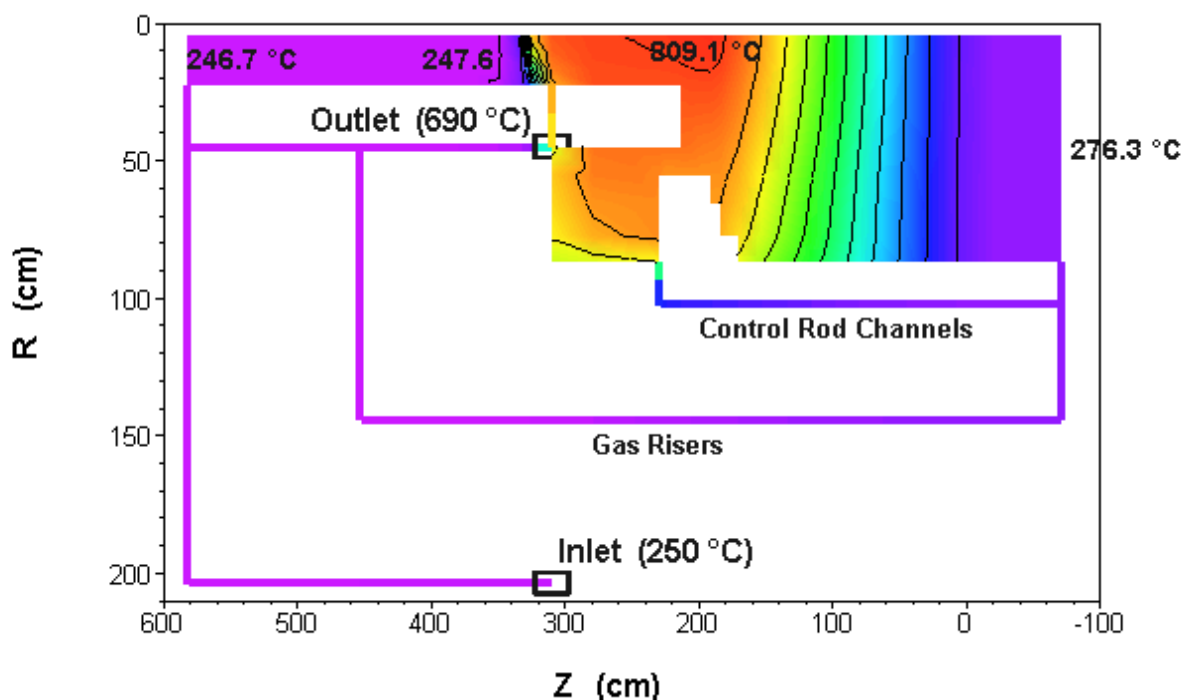


FIG. 2.70. TINTE steady state gas temperatures.

From Fig. 2.70, it is observed that the gas temperature stays close to the inlet temperature for all the flow paths outside the core, and even so in the fuel discharge tube below the level of the hot helium outlet plenum. Also, in the lower part of the reactor, below the bottom core barrel support structures, the solid material temperatures are as much as 64°C below the gas temperature which result in the

transfer of heat from the gas to the solid material. This situation is a direct consequence of the 50°C boundary condition, thermal resistance of the flow path and the amount of heat flowing through the lower boundary in the TINTE reactor model.

Power profile

The TINTE power distribution (shape) is determined by the data that was incorporated from the equivalent VSOP99/5 run for steady state conditions. If needed, the TINTE model allows the scaling of the power distribution through the specification of the power level (other than 10 MW) or by changing the shape by inserting/withdrawing the control rods to a height that differs from the height in the VSOP99/5 run. For the TINTE model steady state results as presented, no adjustments were made to the VSOP99/5 steady state data that was obtained with the control rods inserted to -55.3 cm (see Fig. 2.69).

The TINTE model calculated steady state neutronic power profile is listed in Table 2.48 and graphically displayed in Fig. 2.71. The differences in the TINTE model calculated neutronic power distribution, expressed as a percentage relative to the specified power distribution, are listed in Table 2.49, except for the last fuel row in the core, centred at a $Z = 187.5$ cm, where large percentage differences occur, in contrast to the remaining differences which are below 10% and viewed as reasonable.

TABLE 2.48. TINTE STEADY STATE POWER DISTRIBUTION (W/CM³)

Z/R (cm)	6.5	13	19	25	39	50	60	70.5	83.5	90
18	1.741	1.738	1.732	1.724	1.704	1.674	1.648	1.629	1.647	1.738
36	1.998	1.991	1.980	1.964	1.924	1.865	1.809	1.767	1.783	1.907
54	2.315	2.308	2.292	2.271	2.218	2.138	2.063	1.999	1.996	2.121
72	2.552	2.542	2.525	2.501	2.440	2.347	2.258	2.181	2.165	2.288
90	2.683	2.673	2.655	2.629	2.564	2.464	2.368	2.284	2.259	2.379
108	2.713	2.703	2.685	2.658	2.592	2.491	2.392	2.305	2.275	2.391
126	2.652	2.642	2.624	2.598	2.532	2.433	2.336	2.249	2.215	2.325
144	2.504	2.495	2.478	2.455	2.394	2.301	2.210	2.125	2.089	2.188
162	2.305	2.297	2.283	2.262	2.207	2.120	2.035	1.956	1.917	1.999
180	2.135	2.128	2.117	2.099	2.052	1.978	1.899	1.822	1.769	1.816
187.5	2.130	2.125	2.116	2.102	2.062	1.998	1.927	1.848	1.775	0.00

TABLE 2.49. PERCENTAGE DIFFERENCES FOR THE TINTE POWER DISTRIBUTION, RELATIVE TO THE SPECIFIED POWER DISTRIBUTION

Z/R (cm)	6.5	13	19	25	39	50	60	70.5	83.5	90
18	-2.74	-2.92	-3.23	-3.16	-2.65	-2.08	-1.92	-1.28	1.04	5.36
36	-5.76	-5.62	-5.72	-5.58	-6.59	-7.21	-7.22	-6.53	-4.14	0.90
54	-5.88	-5.81	-6.05	-5.76	-5.6	-5.4	-5.39	-4.81	-3.57	1.47
72	-2.23	-2.23	-2.13	-2.32	-2.02	-3.41	-3.08	-3.93	-2.49	3.04
90	-3.49	-3.49	-3.45	-3.33	-3.24	-3.75	-3.72	-4.44	-1.79	3.45
108	-4.46	-4.81	-4.8	-4.74	-4.35	-2.33	-2.36	-1.08	0.65	5.79
126	-0.32	-0.30	-0.24	-0.07	-1.08	-2.29	-1.86	-1.8	-0.24	5.21
144	0.55	0.19	0.34	0.60	1.01	0.49	0.91	2.15	3.94	9.38
162	-2.33	-2.26	-2.03	-1.67	-0.61	0.48	0.76	1.35	3.61	9.83
180	-8.37	-8.28	-7.58	-6.72	-5.02	-2.09	-1.59	-0.46	2.27	9.39
187.5	39.2	38.9	40.1	42.0	45.2	50.2	51.7	52.7	57.1	0.0

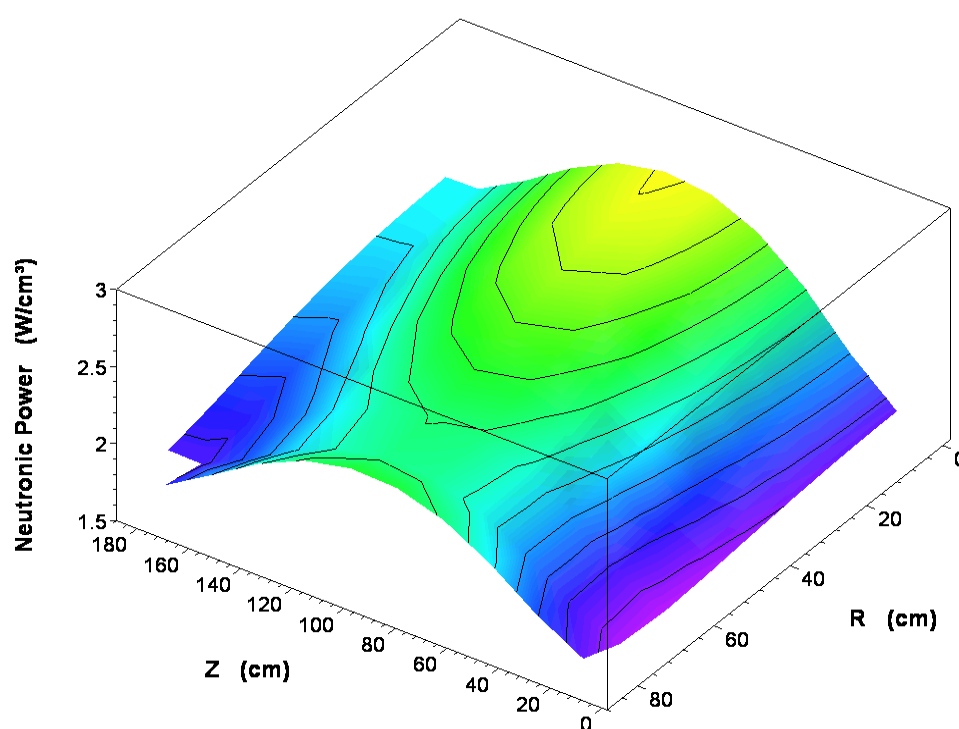


FIG. 2.71. TINTE steady state neutronic power distribution at 10 MW.

TINTE steady state solid material temperatures

This section reports on the solid material temperatures at the specified locations. Table 2.50 provides the maximum component temperatures while Table 2.51 provides a summary of the TINTE model calculated temperatures, along with in-reactor measured temperature values. The deviation in the TINTE model temperature values from the measured temperatures, expressed as a difference in °C, is also listed.

TABLE 2.50. TINTE CALCULATED MAXIMUM COMPONENT TEMPERATURES

Component	Position	Max. temperature (°C)
Fuel element	Centre	904.9
	Surface	844.9
Side reflector		600.4
Bottom reflector		780.2

TABLE 2.51. EXPERIMENTAL AND TINTE CALCULATED TEMPERATURES

No.	R(cm)	Z(cm)	Temperature (°C)		Difference (°C)
			Measured	TINTE	
Side reflector					
1	193	80	231.3	243.9	13
2	189	80	249.3	260.2	11
3	167	80	274.3	305.4	31
4	133	80	289.1	342.0	53
5	117	80	313.3	380.4	67
6	93	80	357.7	456.0	98
7	193	170	234.9	257.1	22
8	189	170	264.8	274.4	10
9	167	170	303.9	324.3	20
10	133	170	328.5	381.8	53
11	117	170	365.3	450.9	86
12	93	170	507.1	598.2	91
Top reflector					
13	60	-40	245.7	282.4	37
Hot helium plenum					
14	40	234	800.2	775.0	-25
15	60	234	763.1	752.6	-10
Bottom carbon bricks					
16	70	440	224.1	252.2	28
17	50	400	245.7	255.1	9
18	50	370	296.2	271.5	-25
19	50	340	406.7	346.7	-60
Fuel discharge tubes					
20	26	340	334.2	308.9	-25
21	26	300	806.1	715.1	-91
22	26	260	881.7	783.1	-99

From comparison of the TINTE model temperature values with the measured values, as well as the calculated values presented by the benchmark host institution (INET), it is observed that the core temperatures close to the side reflector are in good agreement with the measured values. However, the radial gradient of the TINTE curves, as reflected in Fig. 2.73, is flatter, which imply that the pebble bed thermal conductivity is too large or that a larger helium mass flow passes through the central part of the core in the TINTE model. In addition, for the calculated axial core temperature profiles (see Fig. 2.72), the observation is that the general shape of the TINTE curves agree well with the measured values, but the TINTE maximum core temperature values, which occur close to the lowest fuel row in the core ($Z \sim 183.75$ cm), are again lower than the measured values. The reasons given above for the mismatch in radial core temperatures, equally apply for the lower axial temperatures that were obtained with the TINTE model. The same pattern is repeated in the TINTE model axial bottom reflector temperatures as shown in Fig. 2.75.

In the side reflector, the opposite situation prevails, namely, that the temperatures in the side reflector adjacent to the core are substantially higher than the measured and calculated values by INET. From Fig. 2.74 and the measured values, it is noted that the TINTE model temperature drop over the core side reflector contact surface is much smaller, implying that the contact interface resistance as calculated by the TINTE model may be less than for some of the other calculational tools. In addition, on the outer surface of the carbon bricks ($R = 190$ cm), the TINTE temperature values agree fairly well with the measured and INET-calculated values. A significant feature of the radial temperature profiles in the side reflector is that it undergoes a marked decrease in its slope at the radial location of the helium riser channels, which is a clear indication that a substantial portion of the radial heat flow is transferred to the helium in the riser channels. The temperature of the helium in the riser channels increases by about 30°C from the inlet of the risers to the entry into the helium plenum in the top reflector. The increase in the helium temperature in the riser channels is also confirmed by the change in colour as depicted in Fig. 2.70.

Since no fast fluence adjustment has been made to the side reflector thermal conductivity beyond the helium riser channels, it is reasonable to assume that the thermal conductivity for this portion of the side reflector would be close, or even identical, to the INET values since the specified correlations for reflector graphite and carbon bricks have been used by the TINTE model. Therefore, the steeper slope of the TINTE model temperature profile through the side reflector indicates that in the TINTE model, more heat is being radially released as compared to the measured temperatures and the INET values. This in turn means that less heat is flowing in the axial direction in the TINTE model, requiring a smaller temperature gradient and thus the underprediction by the TINTE model for the axial temperature profiles. A further observation is that the temperature gradient from the outer side reflector surface to the inner core barrel surface as calculated by the TINTE model is also less than the measured and calculated values.

Finally, the temperature maps from the TINTE model steady state calculations are also shown as a temperature contour plot in Figs 2.76 and 2.77.

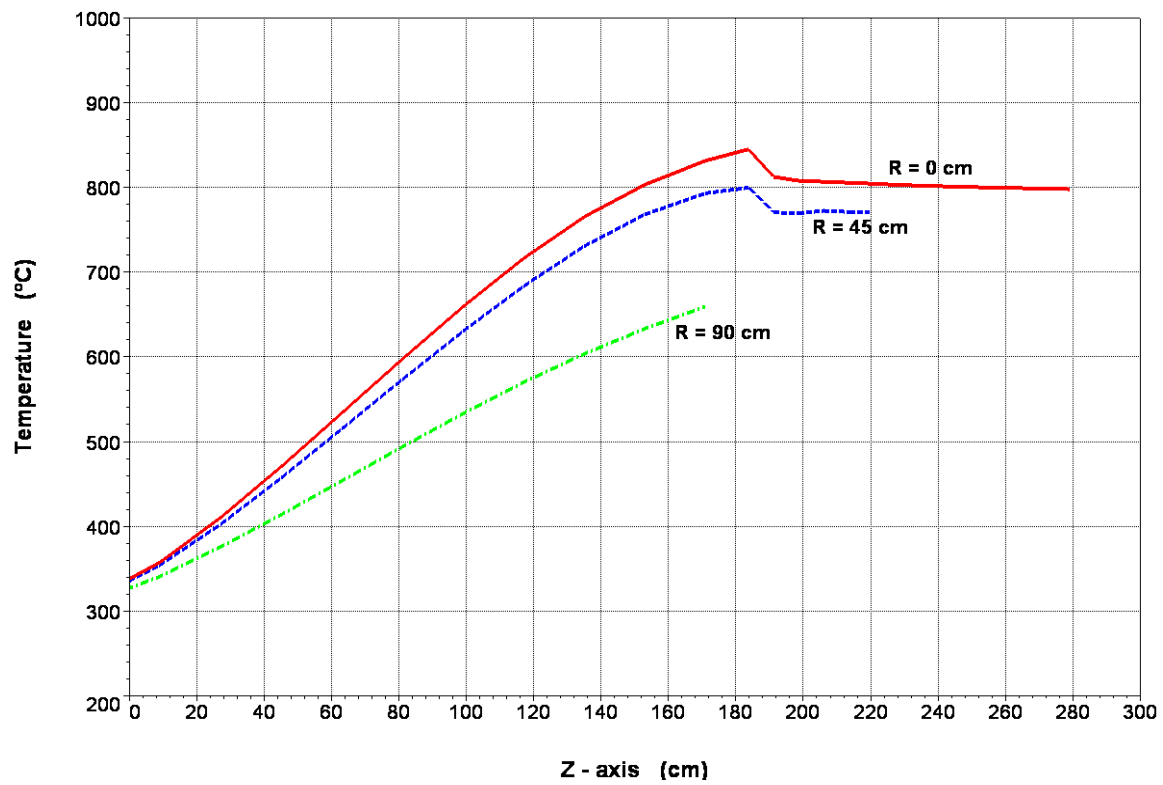


FIG. 2.72. TINTE model steady state axial core temperatures.

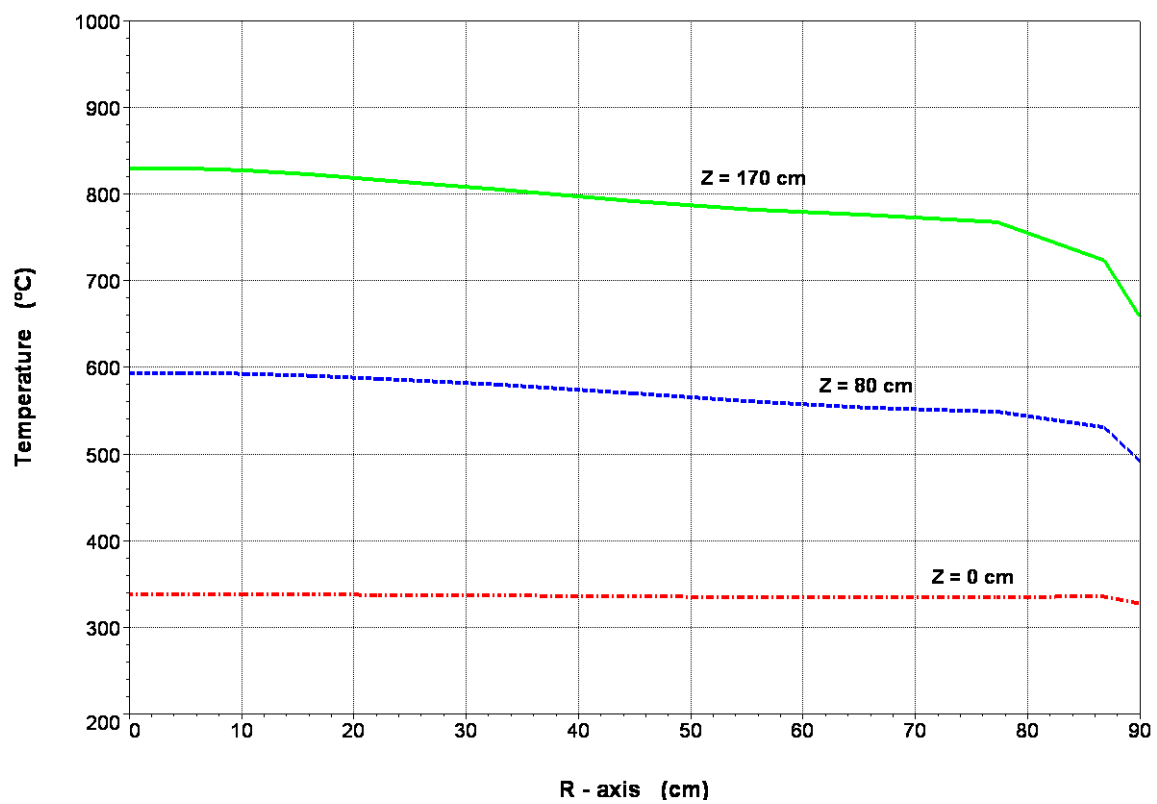


FIG. 2.73. TINTE model steady state radial core temperatures.

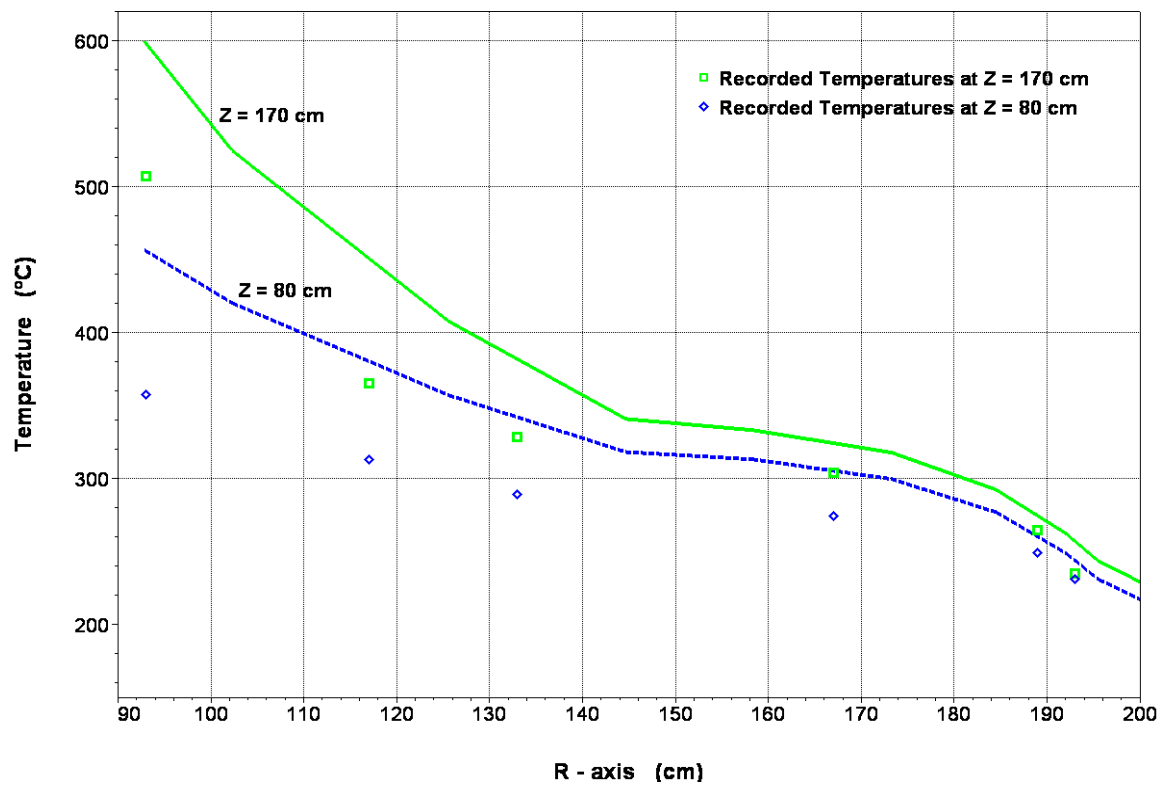


FIG. 2.74. TINTE model steady state radial side reflector temperatures.

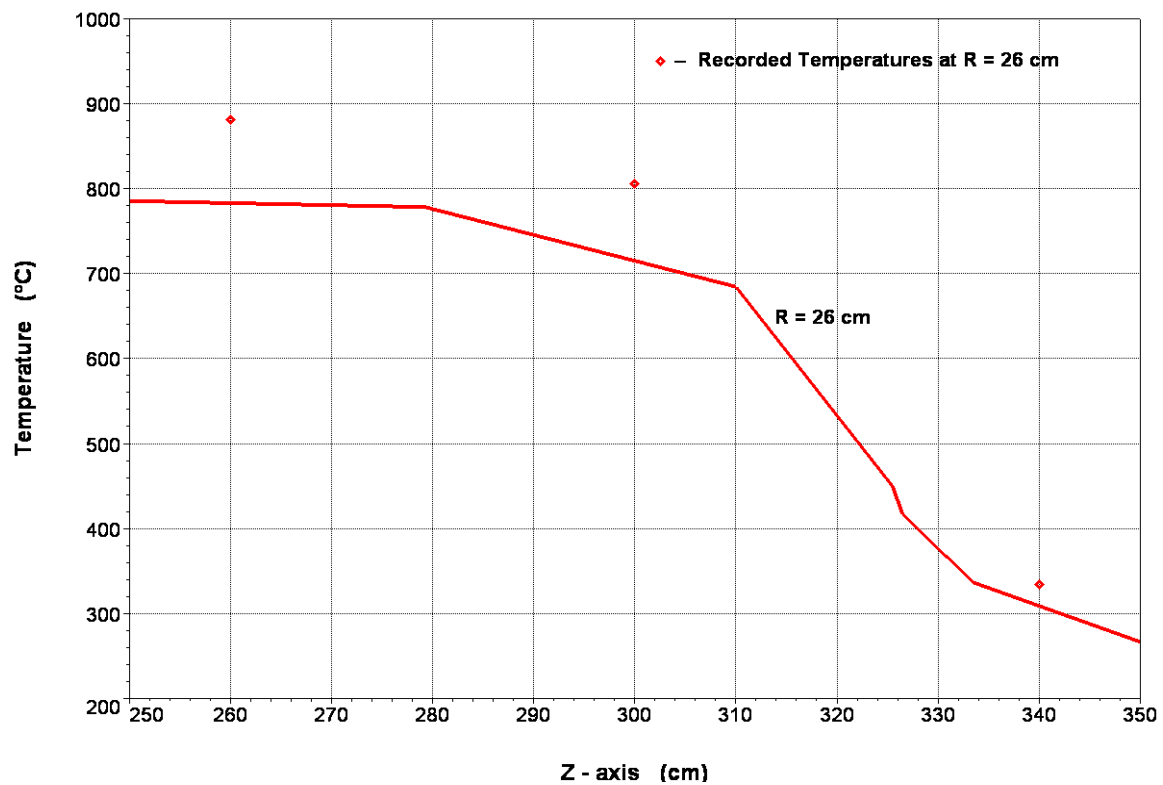


FIG. 2.75. TINTE model steady state axial fuel discharge tube temperatures.

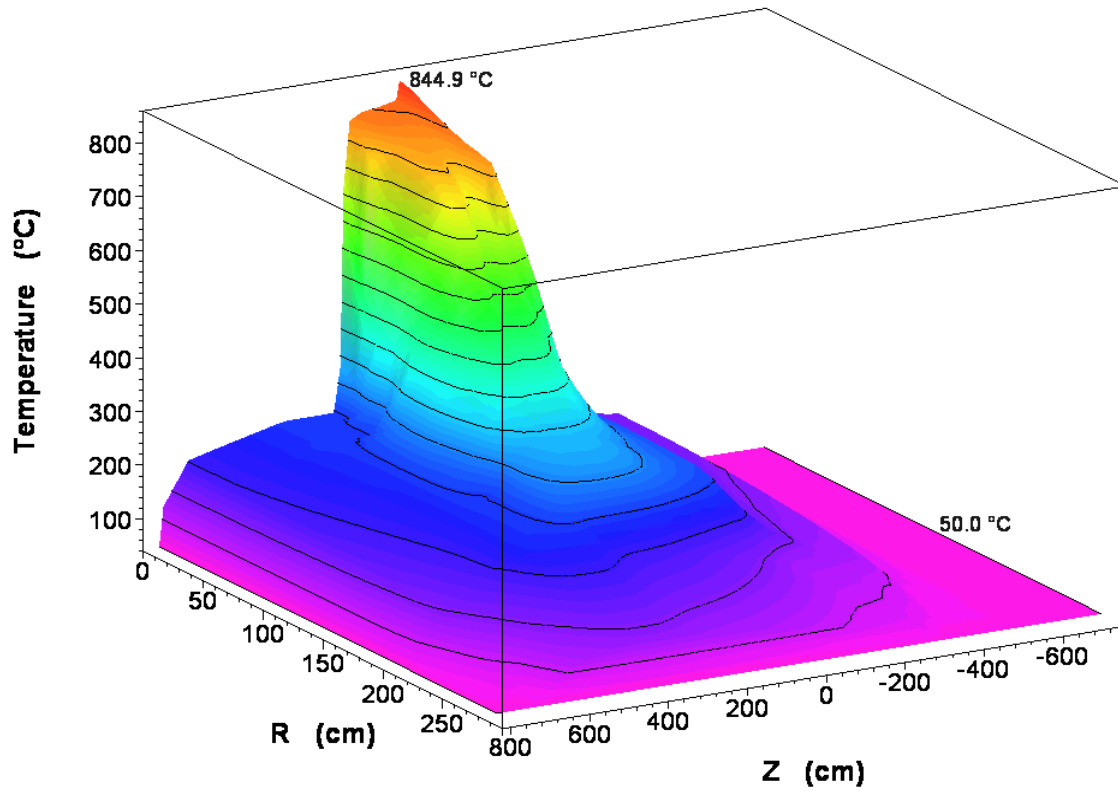


FIG. 2.76. TINTE model steady state solid material temperatures.

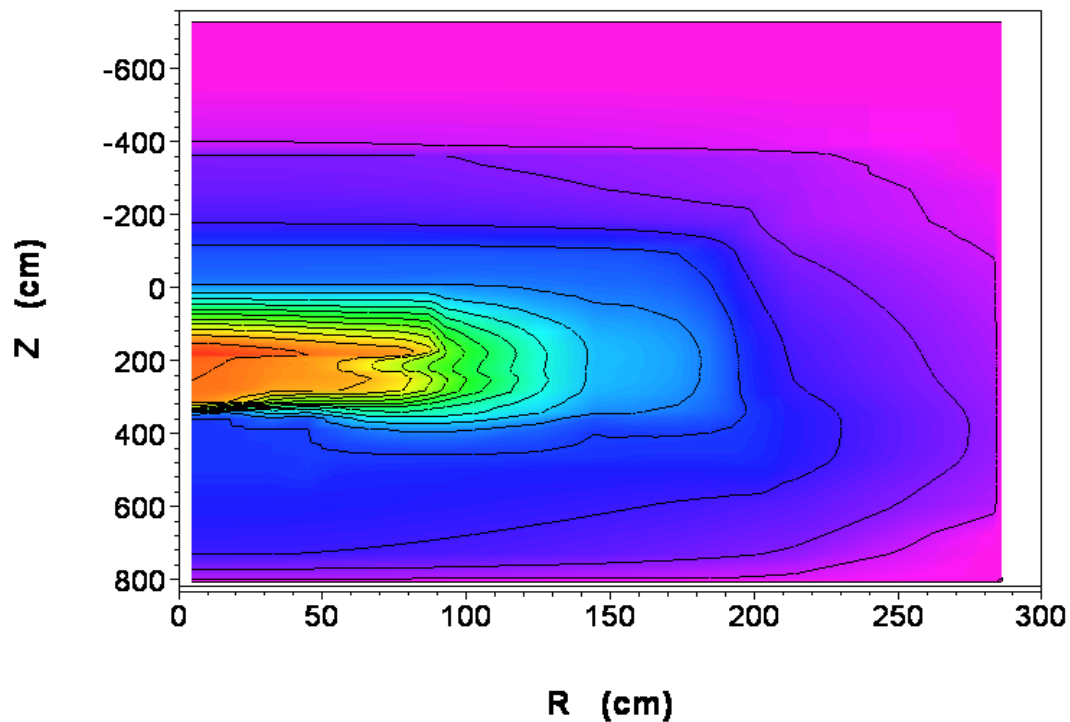


FIG. 2.77. Plan view of the TINTE model steady state solid material temperatures.

Summary of steady state results and conclusions

The reason(s) for the lower radial thermal resistances in the TINTE model need to be determined and corrected;

It is crucial to resolve the mismatch between the specified power density at the lowest fuel row in the core and that calculated by the VSOP99/5 and TINTE models. In addition to that, the width and radial positioning of the helium plenum in the top reflector needs to be clarified. By starting off, in the TINTE model, a heat source that does not match the specified heat source, as well as an incorrect flow distribution at the top of the core, will certainly produce undesirable results;

Omitted or incomplete data, such as the insulation and thermal shield material property data, needs to be supplied to ensure consistency in developing models of the HTR-10 benchmark problems by users of the various HTR analysis codes.

2.2.2.8. HTR-10 steady state temperature benchmark, Japan

Introduction

The summary provided here was submitted to the CRP as Ref. [2-33].

The HTR-10, which is a pebble-bed-type HTGR with a thermal power of 10 MW and a reactor outlet coolant temperature of 750°C, is the first HTGR in China. This report describes the calculation result of the benchmark problems related to the steady state temperature distribution for the HTR-10 rated power operation.

Calculation model

The TAC-NC code, which is a two dimensional and time dependent thermal analysis code for the safety evaluation of the HTGR, is applied to the benchmark calculation of the HTR-10.

Figure 2.78 shows the R-Z cylindrical calculation model for the HTR-10. The region of the calculation model is from the centre of the reactor core ($R = 0$ cm) to the water cooling panel outside the insulating plates of the reactor cavity ($R = 285.4$ cm) for the radial direction and from the top air cavity to the bottom air cavity outside the RPV for the axial direction. The adiabatic boundary condition is applied to the upper, lower and central boundary. As for the radial boundary condition of the water cooling panel outside the insulating plates of the reactor cavity, the constant temperature boundary of 50°C is assumed. In this radial boundary, heat transfers due to thermal conductivity of air and radiation (emissivity is 0.85) are considered and heat transfer due to natural convection is not considered. The primary coolant channels of the reactor core are modified as ten radial meshes given the coolant flow rate, heat transfer area, cross-sectional area, and so on. The effective core coolant fraction is 87% in the HTR-10 calculation. The heat transfer calculation condition is shown in Table 2.52. The heat transfer coefficient for the pebble bed reactor core is evaluated by the following:

$$\alpha = \frac{Nu\lambda}{d}$$

$$Nu = 1.27 \frac{Pr^{0.33}}{\varepsilon^{1.18}} Re^{0.36} + 0.033 \frac{Pr^{0.5}}{\varepsilon^{1.07}} Re^{0.86}$$

$$Re = \frac{(m/A)d}{\eta}$$

where

α is the heat transfer coefficient;

Nu is the Nusselt number;

λ is the thermal conductivity of helium;

d is the equivalent diameter ($d = 0.06$ m);

Pr is the Prandtl number;

Re is the Reynolds number;

ε is the vacancy fraction of the pebble bed;

($\varepsilon = 0.39$ is used in this benchmark calculation)

m is the coolant flow rate in the pebble bed;

A is the flow path area of the empty pebble bed;

($A = 2.545\text{m}^2$ for the HTR-10)

η is the dynamic viscosity of helium.

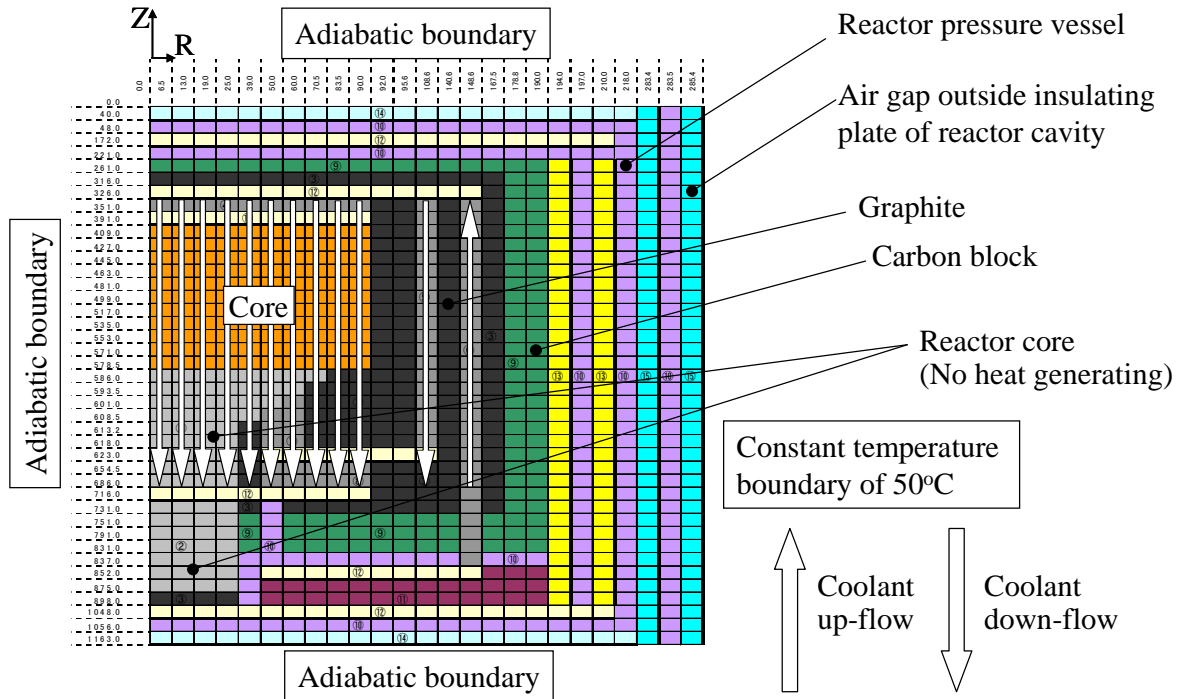


FIG. 2.78. Calculation mesh for the HTR-10 benchmark problems.

TABLE 2.52. HEAT TRANSFER CALCULATION CONDITION IN THE COOLANT CHANNEL

Mesh No. (radial direction)	Coolant flow direction	Inlet coolant temperature (°C)	Coolant flow rate (kg/s)	Heat transfer area (m ² /m)	Equivalent diameter (m)	Type of coolant channel
2	Down	250	0.02	0.8	0.06	Pebble bed
3	Down		0.06	2.4		Pebble bed
4	Down		0.09	3.7		Pebble bed
5	Down		0.12	5.1		Pebble bed
6	Down		0.42	17.2		Pebble bed
7	Down		0.45	18.8		Pebble bed
8	Down		0.51	21.1		Pebble bed
9	Down		0.64	26.3		Pebble bed
10	Down		0.93	38.4		Pebble bed
11	Down		0.52	21.6		Pebble bed
14	Down	250	0.56	4.08	0.13	Tube
16	Up		4.32	5.03	0.08	Tube

Calculation result

The calculation results of steady state temperature distribution for FPIC are shown in Figs 2.79–2.81 with comparison to the experiment results. Figures 2.79 and 2.80 show the radial temperature distribution at the axial position $Z = 80$ cm and $Z = 170$ cm respectively. As shown in these figures, the calculation results agree with the experiment results. As for the axial temperature distribution, there are big differences between calculation and experiment, especially in measurement place No. (21). Due to the fact that the region, including the measurement places No. (20) to (22), is in the fuel discharging tube, it is thought that the spent fuel in this region would be heating due to fission product decay or some nuclear fission. In addition, the comparing positions are not the same, in the calculation the temperature distribution is for $R = 32$ cm and for $R = 26$ cm in the experiment.

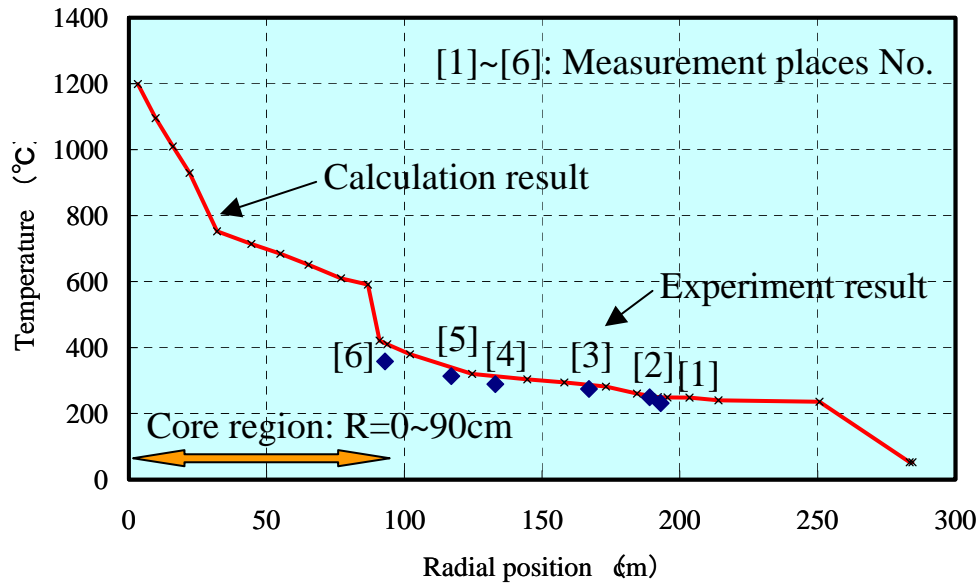


FIG. 2.79. Radial temperature distribution at axial position $Z = 80$ cm.

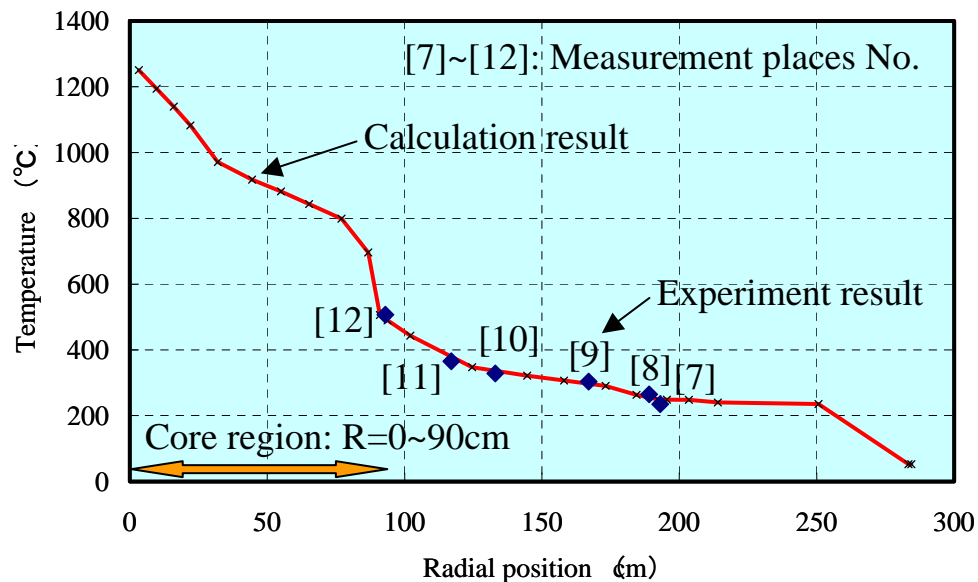


FIG. 2.80. Radial temperature distribution at axial position $Z = 170$ cm.

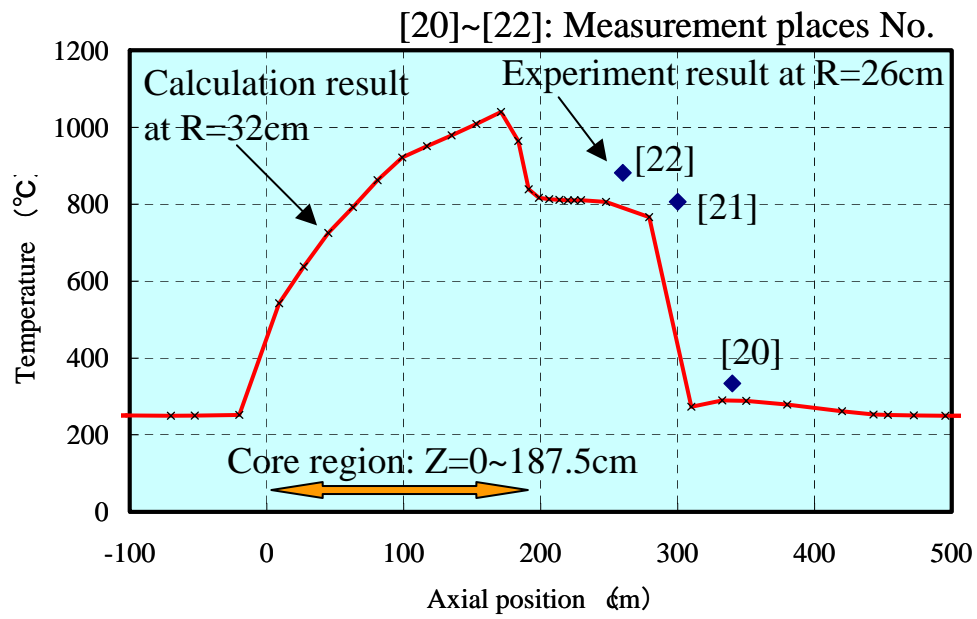


FIG. 2.81. Axial temperature distribution at radial position $R = 32$ cm.

Conclusion

Steady state calculation of the HTR-10 during the rated power operation of 10 MW was performed by using the TAC-NC code. It was found that the TAC-NC code can simulate the temperature distribution of a pebble-bed type.

2.2.2.9. HTR-10 steady state temperature benchmark, United States of America

Introduction

Steady state calculations of the HTR-10 temperature profiles were made using the ORNL GRSAC code (described in Section 4.1.10 in this TECDOC). These calculations assumed initial HTR-10 operating conditions at full power (10 MW(t)), with the pebble distribution of 57% fuelled pebbles and 43% dummy (graphite only) pebbles dispersed randomly, designated for this benchmark as FPIC. The USA calculations were performed for three of the four benchmark cases as noted below. Note that the definition of R-Z coordinates is the same as that specified in the benchmark definition (i.e. the horizontal axis is the R-direction and the vertical is the Z-direction where the zero points of the Z-axis and R-axis correspond to the crossing point of the upper surface and the central axis of the active pebble bed core). Results are presented in Tables 2.53 and 2.54 using the prescribed templates. Graphical representations are included in the summary and conclusions section for this benchmark.

Axial (R = 0 cm) Temperature profile within the pebble bed

Results are assumed to be average pebble surface temperatures in each region (block temperatures in lower reflector).

TABLE 2.53. COMPUTED AXIAL (R = 0 CM) TEMPERATURE PROFILE

Z (cm)	Temperature (°C)
10	371
30	450
50	526
70	595
90	658
110	713
130	759
150	797
170	829
190	857
254	766
295	746

Radial (Z = 80 cm) temperature profile within the pebble bed

As in Case 1, the results are assumed to be average pebble surface temperatures in each region.

TABLE 2.54. RADIAL (AT Z = 80 CM) TEMPERATURE PROFILE

R (cm)	Temperature (°C)
0	720
16	718
27	715
38	710
49	690
60	653
71	602
82	495

Maximum temperature values of main components

Temperatures shown in Table 2.55 are the maximums of all computed temperatures in the active core and reflectors.

TABLE 2.55. MAXIMUM TEMPERATURE VALUES IN THE MAIN COMPONENTS

Component	Position	Max. Temperature (°C)
Fuel element	Centre	951
	Surface	893
Side reflector	Centre	504
Bottom reflector	Centre	766

Conclusions

Computed values of the HTR-10 FPIC temperatures generally agreed well with those of other participants in this code-to-code benchmark exercise.

2.3. HTR-10 LOSS OF PRIMARY FLOW WITHOUT SCRAM BENCHMARK PROBLEM

2.3.1. Loss of primary flow without scram benchmark problem description

The summary provided here was submitted to the CRP as Ref. [2-34].

2.3.1.1. Initial benchmark conditions

The starting condition of the transient is as follows:

- The reactor has reached steady state operation at partial load of 30% of full power, i.e. 3 MW.
- The primary helium pressure at steady state partial-load operation is 2.5 MPa (this pressure remains basically unchanged during the transient).
- The helium temperatures at reactor inlet and outlet are 250°C and 650°C respectively at steady state partial-load operation (helium flow rate is defined by this temperature difference and helium pressure).
- The calculated power density distribution is as given in Table 2.56. For the initial core, there is no heat generated in the lower part of the reactor core and the fuel discharging tube.
- Before the safety demonstration experiments, the reactor had operated for approximately 3000 MW-hour. At the starting point of the safety demonstration experiments, the xenon equilibrium state was achieved. The host institution suggests that investigators calculate the afterheat power versus time independently. The curve used by INET is shown in Fig. 2.7.

The transient is started (time point zero) by shutting down the primary helium blower, stopping the primary helium flow and isolating the primary system from the water cooling systems on the secondary side of the steam generator. For calculation purposes, these actions are assumed to be finished instantly. All control units remain where they were before the transient is started.

It is recommended that the participants perform the calculation of neutron flux and other neutronics parameters independently. The following data, which is used by the benchmark host institution, is given for reference.

Reactivity coefficients are defined as follows:

- The fuel temperature reactivity coefficient is defined as the reactivity variation caused by 1°C variation of fuel temperature within the whole core. Its unit is pcm/°C or $10^{-5}\Delta k/k/^\circ\text{C}$. In this benchmark definition, an overall average core temperature coefficient of reactivity at operational state is given. It is a sum of temperature coefficients in all core zones. Approximately, the overall average core temperature coefficient of reactivity can be subdivided into all core zones according to their power fraction;
- Definitions of moderator and graphite reflector temperature reactivity coefficient are similar to the above definition of fuel temperature reactivity coefficient;
- Fraction of delayed neutrons: $\beta = 0.726\%$;
- Prompt generation time: $\Lambda = 0.00168$ s;
- Overall average core temperature coefficients of reactivity at operational state;
 - Fuel = -2.13 pcm/°C;
 - Graphite moderator = -16.2 pcm/°C;
 - Graphite reflector = 7.71 pcm/°C.

It is proposed to calculate the reactor power transient response after the initiation of the transient. The experimental results are shown in Figs 2.82 and 2.83.

TABLE 2.56. CALCULATED POWER DISTRIBUTION
AT STEADY STATE 3 MW PARTIAL-LOAD OPERATION (W/CM³)

Z/R cm	0	6.5	13	19	25	39	50	60	70.5	83.5	90
0	0.539	0.539	0.536	0.533	0.526	0.514	0.505	0.494	0.491	0.497	
18	0.635	0.634	0.631	0.625	0.619	0.605	0.586	0.568	0.560	0.568	
36	0.738	0.737	0.732	0.725	0.707	0.679	0.654	0.632	0.622	0.628	
54	0.783	0.782	0.776	0.768	0.749	0.729	0.700	0.683	0.665	0.668	
72	0.824	0.822	0.816	0.807	0.786	0.761	0.730	0.710	0.685	0.687	
90	0.852	0.850	0.844	0.835	0.812	0.764	0.733	0.699	0.678	0.677	
108	0.799	0.797	0.791	0.782	0.769	0.748	0.716	0.689	0.667	0.664	
126	0.749	0.747	0.741	0.732	0.711	0.688	0.658	0.626	0.605	0.600	
144	0.703	0.701	0.694	0.683	0.658	0.626	0.598	0.571	0.546	0.536	
162	0.699	0.696	0.689	0.676	0.649	0.606	0.578	0.549	0.516	0.492	
180	0.460	0.459	0.454	0.446	0.428	0.400	0.381	0.362	0.339	0.0	
187											

2.3.2. Loss of flow without scram benchmark analysis and results

2.3.2.1. Loss of flow benchmark results, China

Experimental results, China

The experimental results of the loss of flow without scram test on the HTR-10 are provided in Figs 2.82 and 2.83.

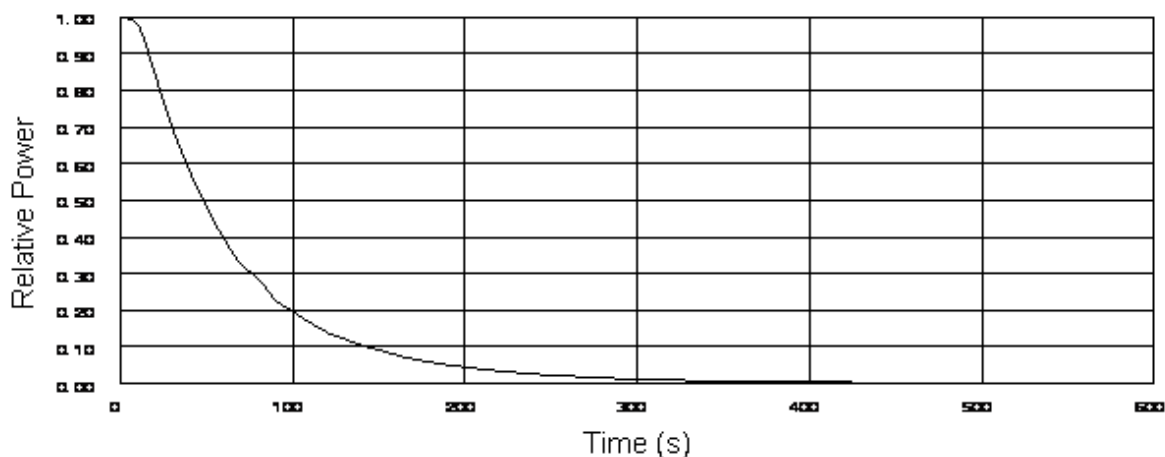


FIG. 2.82. HTR-10 power on first 600 s after loss of flow without scram transient.

As shown in Fig. 2.83, the core recriticality occurs after 4075 s and the power peak is reached at 4325 s with a relative value of 0.25. A second peak is reached 1250 s later with a relative power level of 0.1.

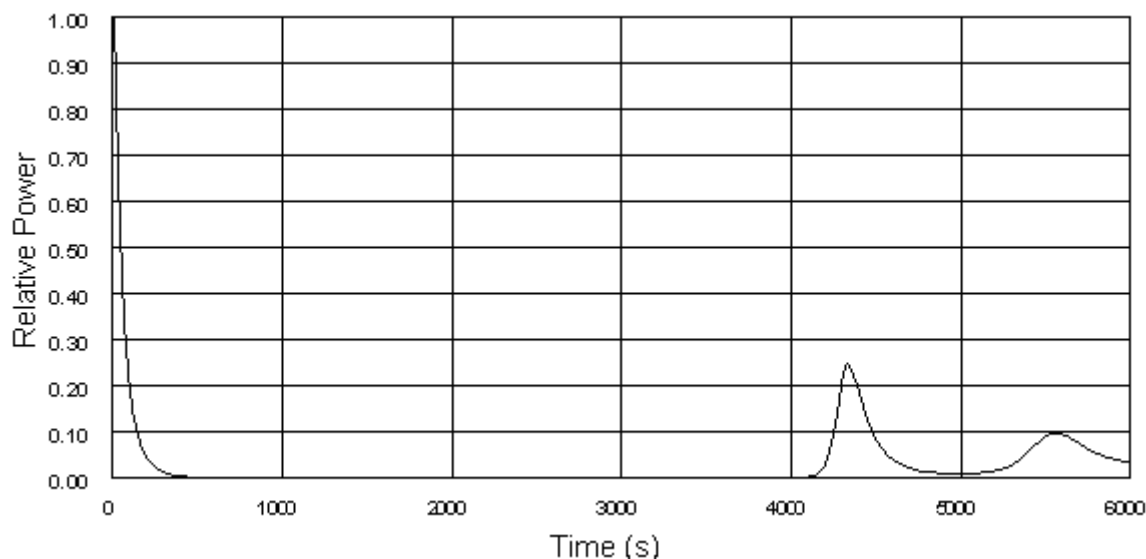


FIG. 2.83. HTR-10 power through 6000 s on loss of flow transient.

Calculated result and comparison with the experimental results, China

Calculation model and codes

The calculation codes and models include:

- THERMIX: A two dimensional time dependent heat conduction calculation program used to calculate the solid material temperatures. The two dimensional rotation symmetric heat conduction model in R-Z geometry for the HTR-10 is shown in Fig. 2.5 and Table 2.4 of Section 2.1.1 of this document. The model includes the fuel zone and non-fuel zone of the core, reflectors, carbon bricks, cavity, thermal shield, core vessel, RPV, cavity cooler and coolant flow paths, etc. The pebble bed, reflectors and gas cavity are treated to be homogeneous media whose heat capacities can be determined according to the void fraction in these regions.
- KONVEK: A two dimensional program to calculate gas flow problems, including gas temperatures, flow rates and pressure drops. The gas convection model consists of 19 different flow regions as shown in Fig. 2.6 and Table 2.5 of Section 2.1.1 of this document.
- KINEX: A point kinetic program used to calculate reactor power transients by solving the kinetic equations with six-group delayed neutrons, considering reactivity changes caused by effects of xenon transients, temperature changes and externally introduced reactivity changes.

The above three codes are coupled so that they can be used to calculate the transients as defined by this benchmark problem.

Calculational results and comparison with experimental results

The partial load operational status is initially indicated in the benchmark problem definition of this document. The defined transient is then simulated. The simulation uses the following parameters:

- Fraction of delayed neutrons: $\beta = 0.726\%$;
- Prompt generation time: $\Lambda = 0.00168$ s;
- Overall average core temperature coefficients of reactivity at operational state include:
- Fuel = -2.13 pcm/ $^{\circ}\text{C}$, graphite moderator = -16.2 pcm/ $^{\circ}\text{C}$ and graphite reflector = 7.71 pcm/ $^{\circ}\text{C}$.

The calculated reactor power transient curve is shown in Fig. 2.84 together with the experimental curve. Calculation and experiment both show that when the helium blower is stopped, the reactor fission power will decrease and the reactor will automatically shut down. After some time, the reactor will become critical again and there will be some fission power oscillations.

It can be seen from Fig. 2.84 that for the first phase of the transient (the reactor shutdown phase), the calculation and experiment results agree relatively well. For the recriticality and power oscillation phase, there exist certain differences between calculation and experiment in terms of the recriticality time, power oscillation peak and periods. These differences need to be further addressed when detailed consideration is given in the calculation to several important factors such as xenon and decay heat power.

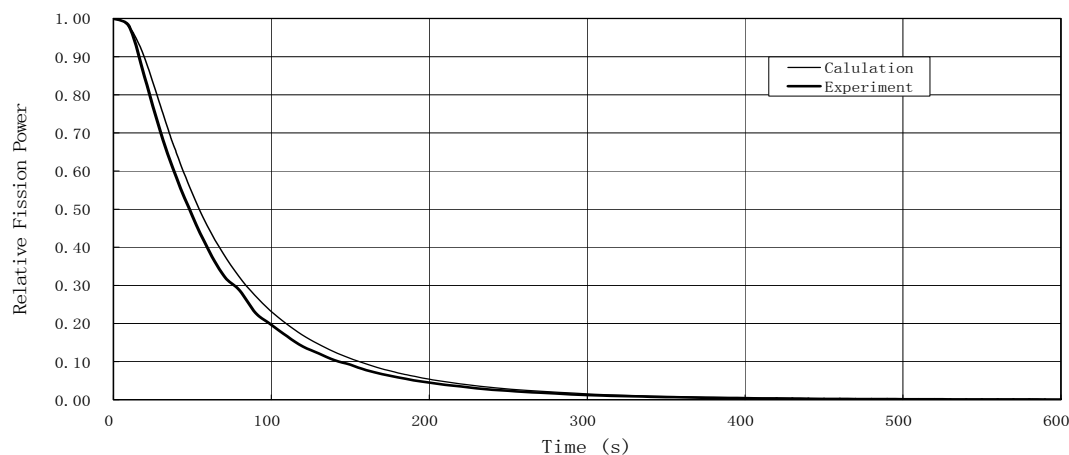


FIG. 2.84. Comparison of calculated and experimental fission power of the HTR-10 during a loss of flow transient.

2.3.2.2. HTR-10 loss of flow benchmark results, United States of America

The summary provided here was submitted to the CRP as Ref. [2-35].

Introduction

The results of Loss of Forced Cooling (LOFC) accident scenario simulation including Anticipated Transient without Scram (ATWS) are presented, along with representative sensitivity studies that indicate uncertainties involved in the accident outcome predictions. The first ATWS case involves a LOFC with no control rod (or scram) response, while a second is a LOFC accompanied by a control rod withdrawal, reported later. The Graphite Reactor Severe Accident Code (GRSAC) features are described briefly in this TECDOC's section on the PBMR T/H benchmark (Chapter 4). Some special programming changes were needed to accommodate the two HTR-10 ATWS cases. This section describes both the initial benchmarking attempts as well as subsequent simulations that involved the use of updated information about the tests and the models used. Some of the sensitivities of the predictions to subsequent changes are of interest in the overall benchmarking process, so both efforts are described.

Reference case models

The reference models and parameters used for the HTR-10 are based on material provided by INET in the benchmark description and on some 'built-in' characteristics of the GRSAC core models. Data for the initial core power peaking distribution and for the worth of the withdrawn rod versus time was incorporated via special code modifications.

HTR-10 initial conditions

The initial conditions (ICs) for the LOFC-ATWS accident simulations are generated by GRSAC in the initial condition mode, where the model is run until equilibrium values are reached. For these tests, thermal equilibrium at 30% power or 3 MW(t) was attained, also allowing sufficient time for xenon equilibrium. Calculated radial flow distributions, core coolant outlet temperature distributions and fuel temperatures for any of the ten axial regions can be displayed. Figure 2.85, for example, shows the fuel temperature distributions in the bottom (outlet) axial region for the active core. Along with the temperature map, various input parameter adjustment 'controls' may be noted.

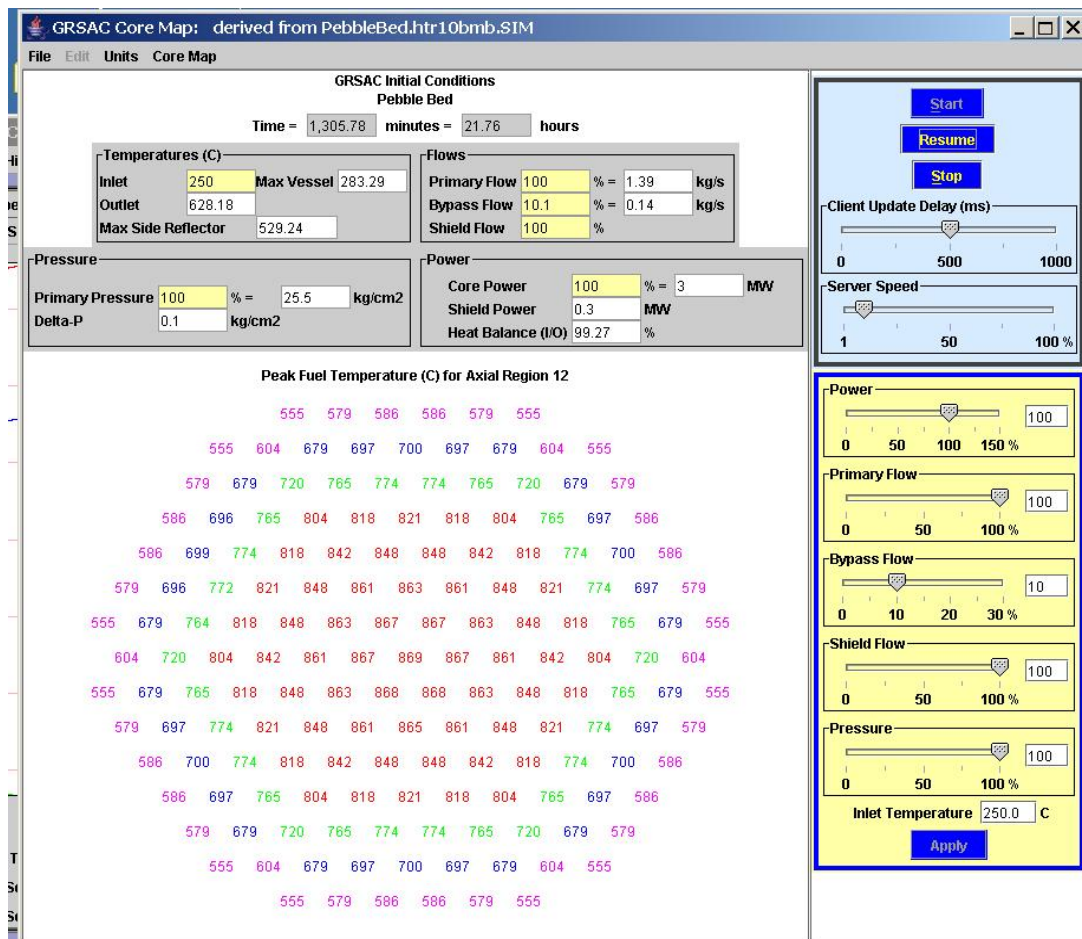


FIG. 2.85. HTR-10 peak fuel temperature distribution at 30% Power — bottom of active core.

HTR-10 LOFC ATWS accident — Initial simulations

For each of the two LOFC cases, a rapid-flow coastdown occurs at time \sim zero and block valves 'isolate' the core from the steam generator. The RCCS is assumed to function for the duration of the test. The natural circulation of the pressurized helium coolant within the core tends to make core temperatures more uniform, therefore lowering the peak temperatures. This is in contrast to the case for a depressurized core, where the buoyancy forces would not establish significant recirculation flows. In the first case, all control rod positions are fixed as defined in the experiment (no scram, as would occur normally for such an event). In the second case, reported later, a control rod withdrawal accompanies the LOFC.

While initial GRSAC runs showed inherent shutdown and recriticality fission power response behaviour similar to the test data, there was typically not good correspondence in delay times for the initial recriticality. Substantial core cooldown in the first one to two hours was needed to effect recriticality. Conduction heat transfer to the reflectors and beyond was not sufficient, so some convection cooling was postulated. Natural convection cooling, via leakage flows of the pressurized helium coolant between the core and steam generator, was assumed, and a special model option was added to GRSAC to characterize this resulting cooled flow entering the outlet (lower) plenum and creating a net upflow in the core.

However, this assumption was apparently not a valid one. The coolant flowing upward from the lower plenum is heated by the initially hot large lower reflector and support structure and was thus ineffective at lowering the core's nuclear average temperature sufficiently to cause a return to criticality. In a typical run, the average fuel temperature axial profiles would show a flattening, but little average decrease (4°C) from 50 to 100 minutes into the upflow cooling transient. This corresponds to a positive reactivity contribution of only 9¢. In the same time period, the reflector heat-

up was very small (corresponding to a 1¢ increase), while the xenon poison build-up accounted for only a 4¢ decrease. Hence the only apparent mechanism for such an assumption was for a coolant flow to enter the inlet (upper) plenum, and this was not feasible under these circumstances.

For the initial calculations, two other parameter adjustments were required to achieve recriticality delays similar to those seen in the experiments. The assumed 'leakage' flow entering the inlet plenum was $\sim 1.7\text{ kg/min}$ and the standard afterheat curve (for 3 MW initial power) was assumed to be $\sim 2/3$ of the equilibrium value, since the reactor probably had not attained its saturated (maximum) value before the test. The same point kinetics and other nuclear parameter assumptions (see description for the control rod removal case) were used for both the cases.

Initial results were consistent with the experimental data. The short term, initial power transient is shown in Fig. 2.86. Once again, the longer-term recriticality transient power characteristics (Fig. 2.87) were very similar to the observed results, but with peak powers smaller than the measured values. The computed fuel temperature transients (maximum and average) are shown for this transient in Fig. 2.88 and indicate the extent of the cooling needed to achieve recriticality.

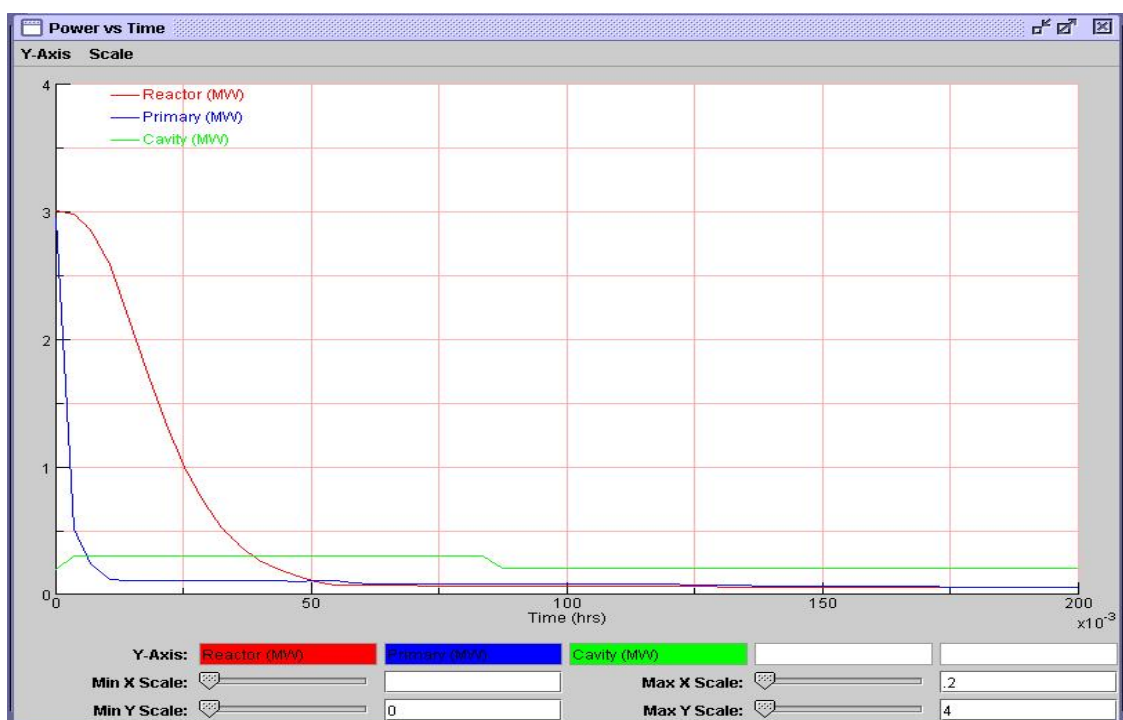


FIG. 2.86. Flow coastdown ATWS initial power transient — drops quickly on loss of flow.

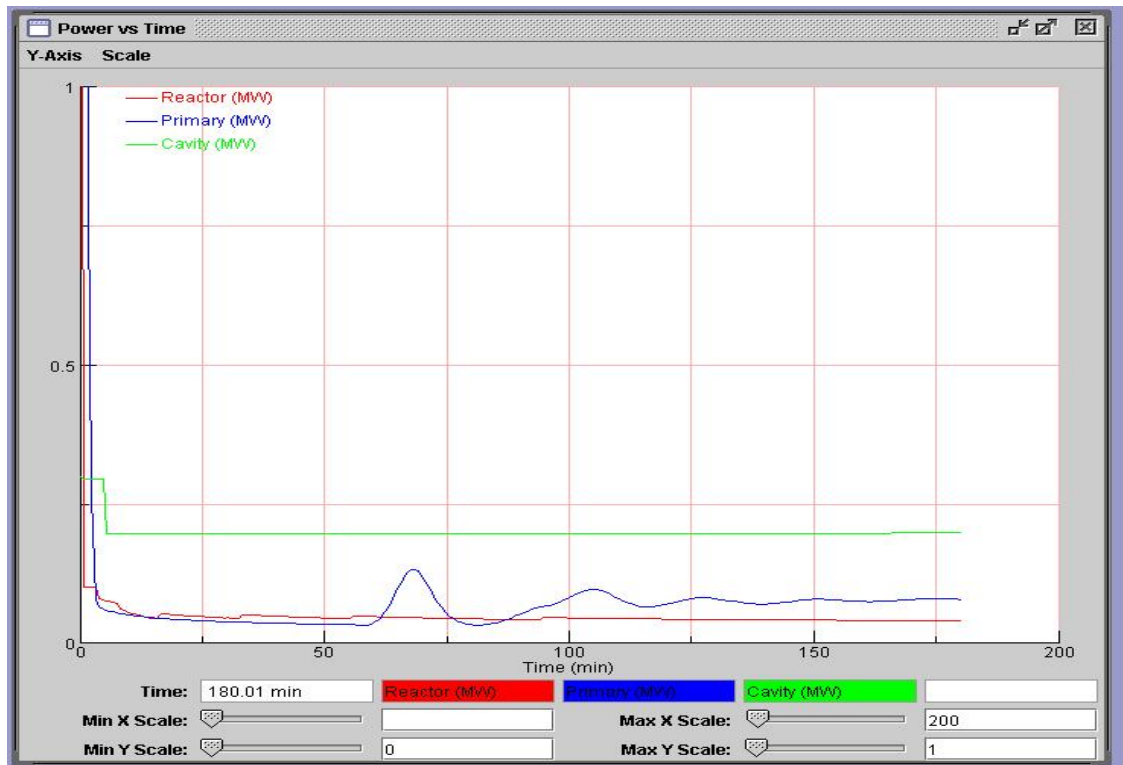


FIG. 2.87. Long term power response: flow coastdown ATWS test showing recritical power oscillations.

A number of initial sensitivity study runs were conducted for both ATWS cases. In general, they showed that parameter variations increasing the effective core heat capacity tended to make the power response (upon recriticality) more oscillatory. Some responses were complicated by the tendency for recirculating flows to occur within the core when the postulated net incoming flows were not large enough to overcome the recirculation forces. The vessel cooling system (or RCCS) capacity had very little effect on the recriticality in the one-to-three hour time frame but would of course affect very long term recriticals.

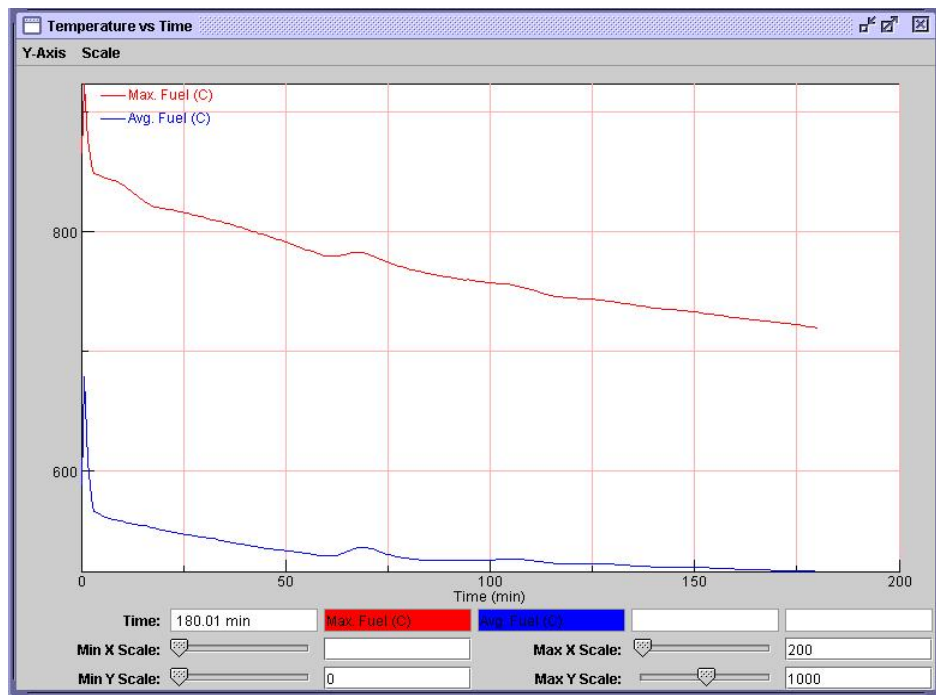


FIG. 2.88. Long term fuel temperature response: flow coastdown ATWS Test.

HTR-10 LOFC ATWS accident – subsequent simulations

In response to additional information provided by INET and PBMR personnel, several changes were made to the GRSAC model and run assumptions that made it unnecessary to assume an ‘artificial’ mechanism to effect a more rapid cooldown of the core (nuclear average) temperature (and recriticality). These changes were:

- An afterheat curve that properly accounted for the prior reactor operating history, resulting in a lower power versus time input;
- A near-immediate shutdown of the circulator to near-zero in ~10 s, with a residual leakage flow of ~0.1 kg/min;
- A modification of the core nodal temperature importance weighting (for reactivity feedback) from flux squared to proportional to flux;
- An improved model for the core specific heat (vs temperature) resulting in a lower core heat capacity;
- A compensation for no radial convection flow in the core (a GRSAC model limitation) that approximates the effect by doubling the effective radial conduction calculation.

Another observation was the likely importance of the effects of natural convection within the core following the shutdown, as evidenced by the change in axial temperature profile (and thus the nuclear average temperature calculation) in the time period of interest. This convection flow term makes a significant change in the core axial temperature profile in the first 100 minutes, as shown in Fig. 2.89 for the ATWS only (no rod withdrawal) case.

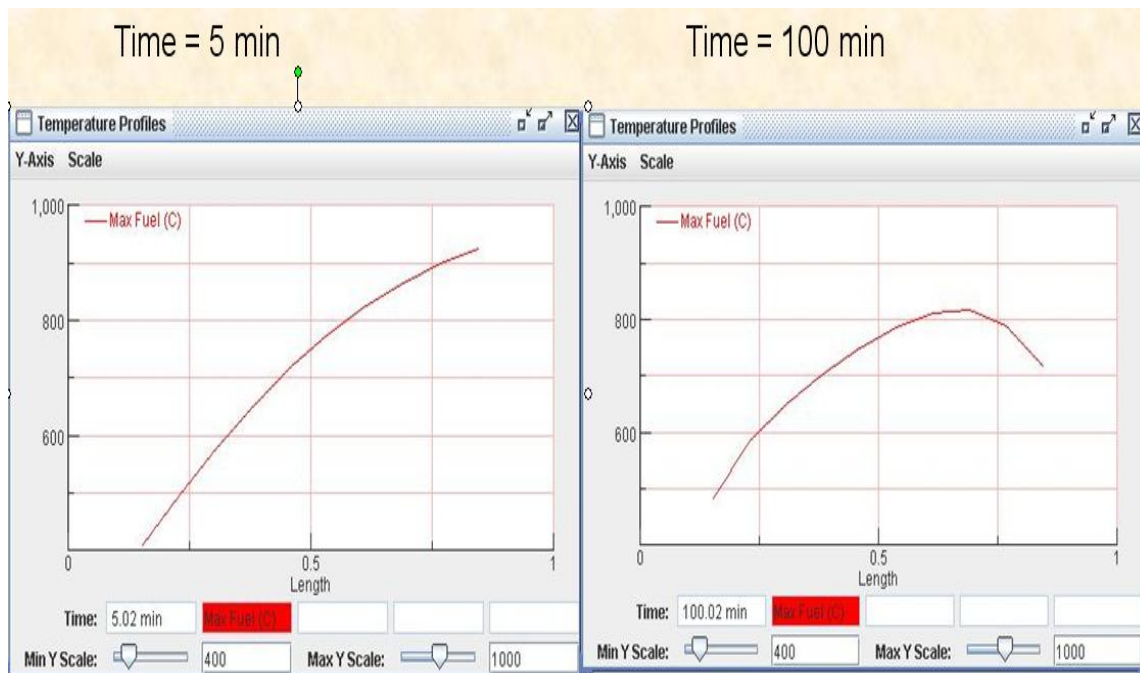


FIG. 2.89. Core axial temperature profiles showing effects of natural convection cooling in the core at times = 5 and 100 min after start of run.

Figure 2.90 shows that with the new assumptions, the reference calculation of recriticality occurs at ~80 min, compared with the observed ~70 min, however, the magnitude of the predicted observations was smaller than those observed.

Another observation of interest was that repeat ATWS tests run under essentially the same conditions had recritical times that differed significantly from the benchmark test value of ~70 min. This indicates the high sensitivity of the return-to-power time to perhaps small details of the reactor operation. Sensitivity studies with variations upon the new model assumptions included changing the effective core radial conductivity multiplier and varying the assumed afterheat multiplier. Changing the radial conductivity multiplier to 1.0 (the original function) resulted in a delay in the recriticality of 115 min (versus 80) and for a multiplier of 3.0, recriticality occurred 5 min earlier and resulted in a very oscillatory power history thereafter. A 10% reduction in afterheat resulted in a 10 min earlier recriticality.

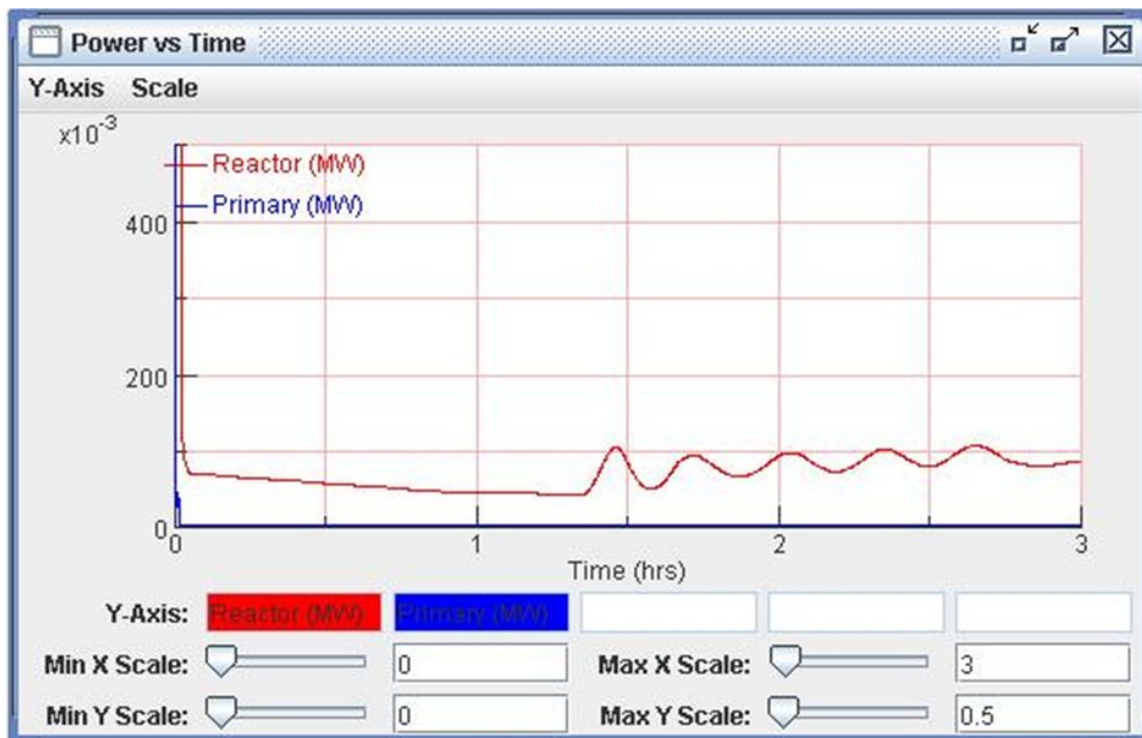


FIG. 2.90. Revised reference calculation of recriticality occurring at time = 80 min.

Conclusions

The GRSAC core thermohydraulic and neutronic models were able to capture some but not all of the essential features of the HTR-10 ATWS benchmarks. In the initial simulations, the mechanism needed for a core cooldown rate required to effect the observed recriticality delay times were artificial in that it necessitated a post-shutdown ‘leakage’ coolant flow entering the core at the upper (rather than the lower) plenum. Later improvements in the model enabled prediction of recriticality at close to the observed time, however, the predicted oscillations were smaller than those observed. Sensitivity studies showed the recriticality details to be very sensitive to model variations. In the GRSAC model, larger recritical power oscillations could only be effected by increasing the rate of change of reactivity at the point of recriticality.

2.3.2.3. HTR-10 loss of flow benchmark results, the Netherlands

Introduction

For the loss of flow transient, the initial condition is that the reactor is at 3 MW and the exit coolant temperature still at 700°C which reduces the coolant flow from 4.32 kg/s at full power to 1.18 kg/s. The coolant mass rate has then been linearly lowered to zero in 10 s. The time steps used are 1 s during the first 60 s and then 2 s until the end of calculation at 20000 s. The decay heat has been internally calculated in the PANTHERMIX code according to DIN norms for fission in U-235. The delayed neutron fraction and spectrum were also used in the usual six groups.

Results

Results for this transient can be seen in Figs 2.91–2.93.

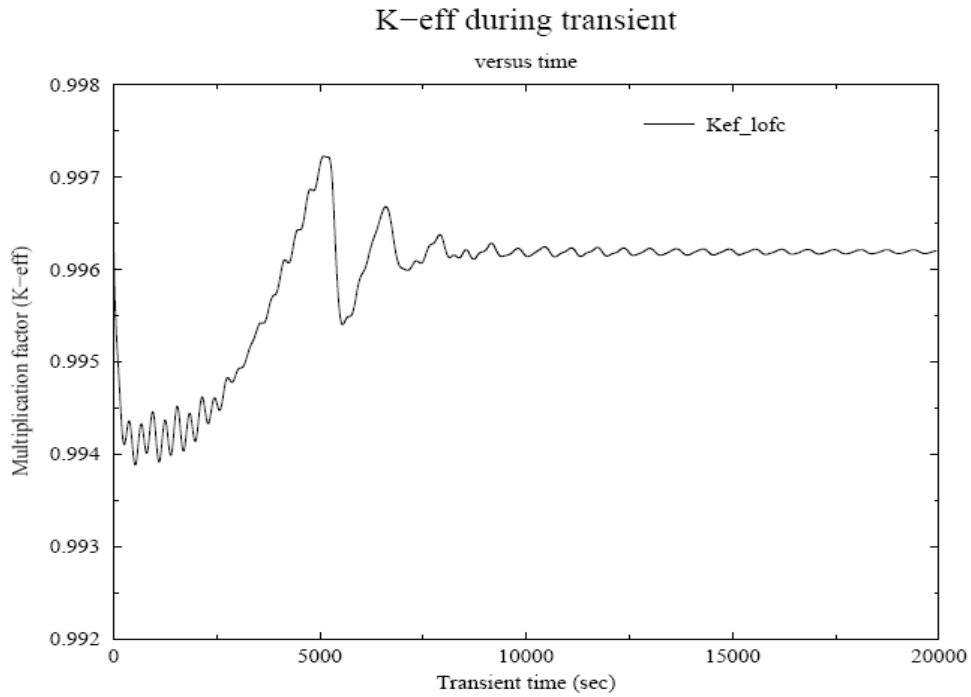


FIG. 2.91. Evolution of the core reactivity during the LOFC transient.

In Fig. 2.91, one can notice rapid oscillations ($t = 275$ s) during the first part of the transient and at the same time, unstable eddies in the helium of the void space above the pebble bed could be seen influencing the heat transfer from the core. For the second part of the transient, the small fluctuations ($t = 635$ s) occurred together with unstable mass currents in the top and bottom pleni, influencing the heat transfer from the reactor. Small dependence on the time step length indicates a possible numerical origin.

Another influence of the inclusion of the pleni is that, compared to calculations without them, the time of recriticality came down from about 9500 to 5200 s. The time between two main power oscillations is 1435 s.

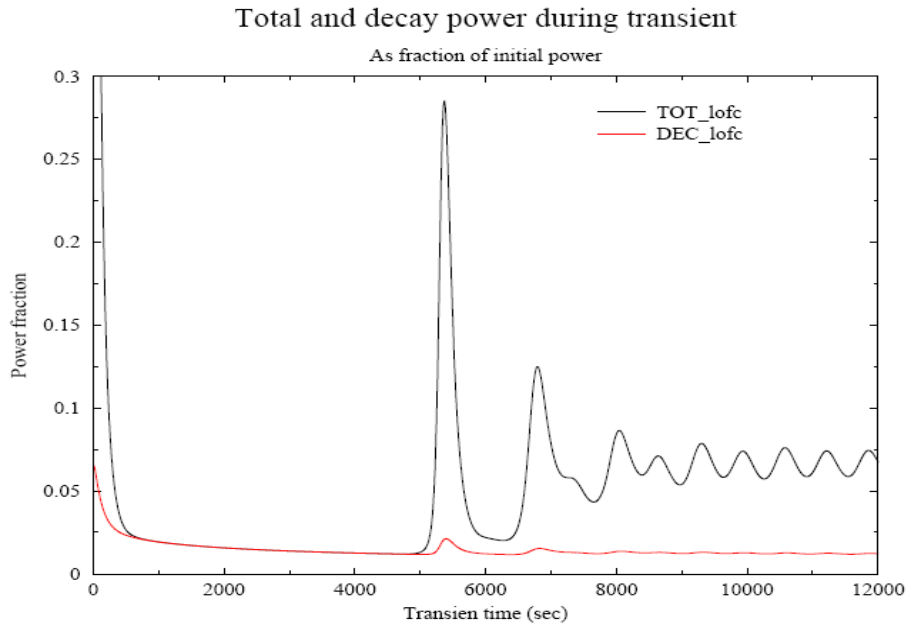


FIG. 2.92. Evolution of the total and the decay power as fraction of the initial power (3 MW).

A shorter period for recriticality (5000 vs 9500 s) as seen in the former calculations indicate the importance of the inclusion of the big helium spaces on top and beneath the graphite structure resulting in an increased heat transfer to the ambient. This makes the transient behaviour of the HTR-10 more dependent on the decay of the core temperature than on the decay of xenon as in larger HTGRs. This is demonstrated in Fig. 2.94: at the moment of first power peaks (see Fig. 2.92), the Xe135 continues to increase, even until about $t = 15000$ s, indicating that recriticality is mainly controlled by the temperature.

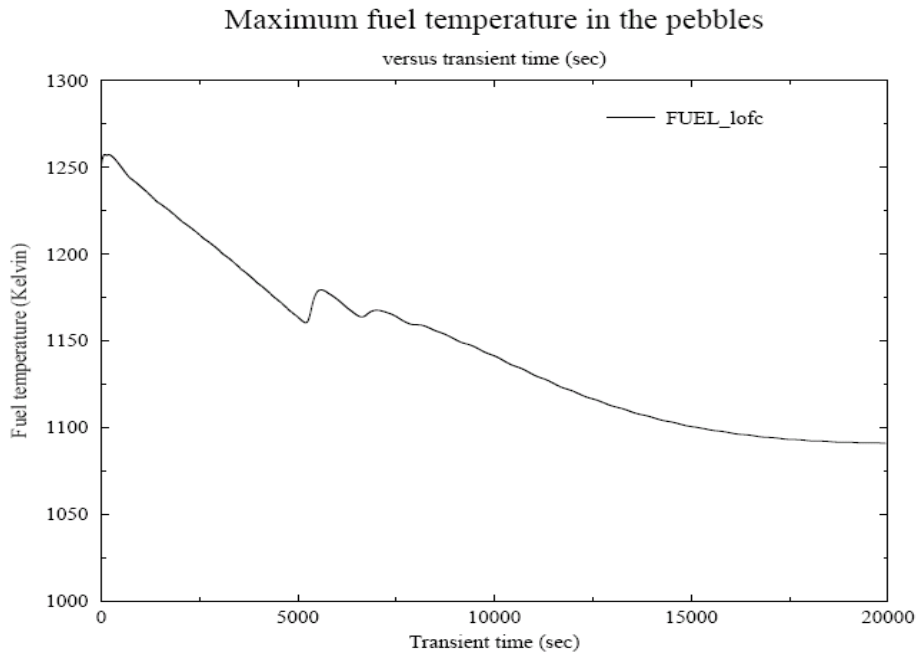


FIG. 2.93. Evolution of the maximum fuel temperature (wherever they occur) in the core.

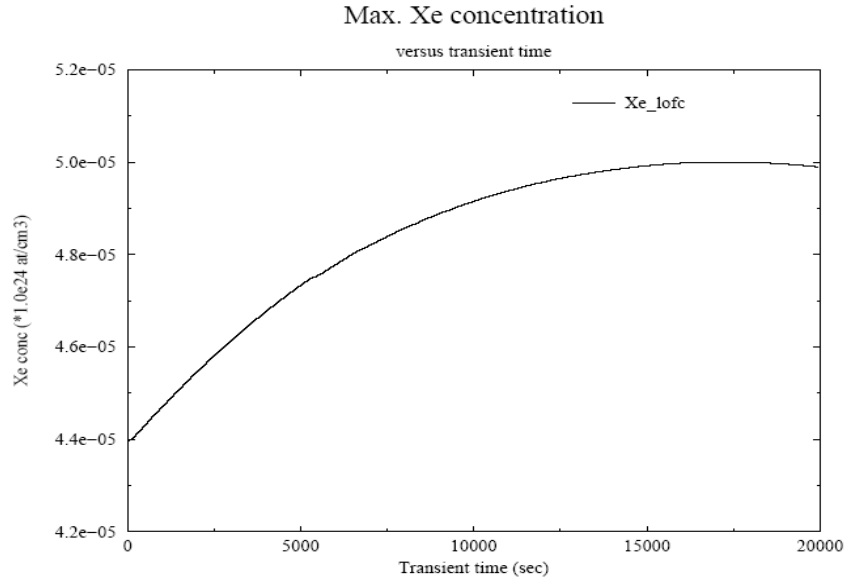


FIG. 2.94. Evolution of the peak Xe135 concentration during the LOFC transient.

2.3.2.4. HTR-10 loss of flow benchmark results, Turkey

Introduction

This study covers the thermohydraulic transient analysis of the HTR-10. The temperature and flow distributions for the HTR-10 are calculated by a general-purpose and commercial CFD code named FLUENT v6.1.22 with the grid structure of the HTR-10 generated in GAMBIT v2.2, the FLUENT code's pre-processor that was used for thermohydraulic calculations of the HTR-10 initial core.

Analysis set-up

Two temperature models are used for the analysis. Fuel surface temperatures are coupled with coolant and solid temperatures. The transient that is run on the facility and to be calculated is 'Loss of Primary Flow without Scram'. At the initiation of the transient, a helium blower trip occurs and the primary system is isolated from the water cooling system. It is run on partial load. The objective of this analysis is to calculate the reactor power transient response. The results should demonstrate the inherent safety features of the HTR-10. The module is to shut itself down due to its negative reactivity coefficient and remove the decay heat via conduction, convection and radiation. During the transient, the limitations for the maximum fuel temperatures are not to be exceeded. The mass flow rate for the coolant is not specified and was to be calculated by means of inlet and outlet temperatures. The initial conditions for the analysis were obtained by running a steady state case with the power distribution and the system pressure defined in the CRP-5 benchmark problem [2-36] and the calculated mass flow rate.

Equations

The conservation equations solved used to represent the system and solved are as follows:

The Mass Conservation Equation for 2-D Axisymmetric Geometry in R-Z Coordinate System

$$\frac{\partial \rho}{\partial t} + \frac{\partial}{\partial z}(\rho v_z) + \frac{\partial}{\partial r}(\rho v_r) + \frac{\rho v_r}{r} = 0$$

The Momentum Conservation Equation in 2-D Axisymmetric Geometry in R-Z Coordinate System

$$\begin{aligned} \frac{\partial}{\partial t}(\rho v_z) + \frac{1}{r} \frac{\partial}{\partial z}(r \rho v_z v_z) + \frac{1}{r} \frac{\partial}{\partial r}(r \rho v_r v_z) = -\frac{\partial p}{\partial z} + \frac{1}{r} \frac{\partial}{\partial z} \left[r \mu \left(2 \frac{\partial v_z}{\partial z} - \frac{2}{3} (\nabla \cdot \vec{v}) \right) \right] \\ + \frac{1}{r} \frac{\partial}{\partial r} \left[r \mu \left(\frac{\partial v_z}{\partial r} + \frac{\partial v_r}{\partial z} \right) \right] + F_z \end{aligned}$$

and

$$\begin{aligned} \frac{\partial}{\partial t}(\rho v_r) + \frac{1}{r} \frac{\partial}{\partial z}(r \rho v_z v_r) + \frac{1}{r} \frac{\partial}{\partial r}(r \rho v_r v_r) = -\frac{\partial p}{\partial r} + \frac{1}{r} \frac{\partial}{\partial z} \left[r \mu \left(\frac{\partial v_r}{\partial z} + \frac{\partial v_z}{\partial r} \right) \right] \\ + \frac{1}{r} \frac{\partial}{\partial r} \left[r \mu \left(2 \frac{\partial v_r}{\partial r} - \frac{2}{3} (\nabla \cdot \vec{v}) \right) \right] - 2 \mu \frac{v_r}{r^2} + \frac{2}{3} \frac{\mu}{r} (\nabla \cdot \vec{v}) + \rho \frac{v_z^2}{r} Fr \end{aligned}$$

where the source terms, in the core region are inserted in to F as:

$$F_z = \Psi \frac{1-\varepsilon}{\varepsilon^3} \frac{1}{d} \frac{\rho}{2} v_z^2 \quad \text{and} \quad F_r = \Psi \frac{1-\varepsilon}{\varepsilon^3} \frac{1}{d} \frac{\rho}{2} v_r^2$$

with

$$\Psi = \frac{320}{\frac{\text{Re}}{(1-\varepsilon)}} + \frac{6}{\left(\frac{\text{Re}}{(1-\varepsilon)} \right)^{0.1}},$$

where ε is the void fraction and d is fuel outer diameter.

The effect of near-wall porosity variations was implemented into the code according to the experimental results of Benenati and Brosilow [2-9], yet not overriding the limitations of the pressure drop correlation. The core is divided into two regions: half a diameter of a pebble from the walls is set as one region, while the remainder is set as the other. The calculations of the values for the void fraction for these two regions are shown below for near-wall porosity and the core porosity respectively.

$$\varepsilon_w = \frac{63.6}{\left(\frac{D}{d} + 15 \right)^2} + 0.43$$

$$\varepsilon_c = \frac{\varepsilon_t - \varepsilon_w}{\left(1 - \frac{d}{D} \right)^2} + \varepsilon_w$$

The flow zones with void fractions less than unity in the convection model of the benchmark, are set as porous regions and the source terms for the momentum equations in these regions are introduced into F as:

$$F_z = \frac{f \rho |v| v_z}{2d_h} \text{ and } F_r = \frac{f \rho |v| v_r}{2d_h}$$

where

$$f = \frac{0.3164}{\text{Re}^{1/4}}$$

The energy conservation equation for the coolant

$$\frac{\partial}{\partial t}(\rho E) + \nabla \cdot (\vec{v}(\rho E + p)) = \nabla \cdot (k \nabla T + (\vec{\tau}_{eff} \cdot \vec{v})) + S_{he}$$

with

$$E = h - \frac{p}{\rho} + \frac{v^2}{2} \quad S_{he} = \frac{6\alpha(1-\varepsilon)}{d}(T_{fuel} - T_{he})$$

$$\alpha = \frac{Nu}{d}k \text{ and } Nu = 1.27 \frac{\text{Pr}^{1/3}}{\varepsilon^{1.18}} \text{Re}^{0.36} + 0.033 \frac{\text{Pr}^{1/2}}{\varepsilon^{1.07}} \text{Re}^{0.86}$$

The energy conservation equation for fuel surface temperatures

The equation representing the fuel surface temperatures is kept at its steady form while the source term was set to handle the time dependent thermal behaviour of the fuel region. This was done according to the interaction between fuel surface temperatures and static temperatures throughout the system. The large heat inertia of graphite creates a slow response on temperature deviations. According to energy balance

$$E_{gen} = E_{st} + E_{conv} + E_{cond} + E_{rad}$$

the user-defined equation is set as:

$$-\nabla \cdot k \nabla T_{fuel} = S_{fuel}$$

where

$$\dot{E}_{str} = \rho c_p \Delta \bar{T}_{fuel} \quad S_{fuel} = \dot{Q} - S_{he} - \dot{E}_{str}$$

\bar{T}_{fuel} is the average fuel temperature and \dot{Q} is the power distribution matrix specified in the benchmark. The average fuel temperature is calculated by a dependent implicit finite-difference approximation to the time dependent temperature equation in radial coordinates, representing the time dependent temperature profile of the fuel pebble.

The Energy conservation equation for the solid structure temperatures

$$\frac{\partial}{\partial t}(\rho h) = \nabla \cdot (k \nabla T_{solid})$$

where h represents the sensible enthalpy. The coupling regarding the interaction between the fuel surface temperatures and the solid structures that are in contact is done by implementing internal boundaries in the form of Fourier's law as:

$$q'' = -k \nabla T$$

This boundary utilizes the thermal conductivity k of the fuel region in the form of the effective pebble bed thermal conductivity correlation provided in the benchmark specifications. Since conduction and radiation heat transfer mechanisms are taken into account in the correlation, this assumption is expected to simulate the physical process effectively. This enables modelling heat transfer between core walls and the coolant and the fuel zone together.

Results

After calculating the flow and temperature distributions via steady-analysis, the model was changed to simulate the blower trip effect. The inlet and outlet boundaries previously set for steady-analysis were changed to wall boundaries to keep the system pressurized without the any coolant entrance. The numerical solution of six group point kinetics equations was used to analyse the transient power response due to reactivity feedback to the model. The transient was run for 600 s. The history of power and the maximum fuel surface temperature are shown in Figs 2.95 and 2.96 respectively.

Conclusion

Results close to the experimental values show that our model was suitable for this analysis. The finite-differencing algorithm and the numerical solution of the point kinetics equations sensibly increased the computational time required for the analysis. Results showed us the inherently safety features of the HTR-10. Its negative reactivity feedback, large heat capacity and passive cooling mechanisms were capable of keeping the maximum temperature values below the design limits during the transient.

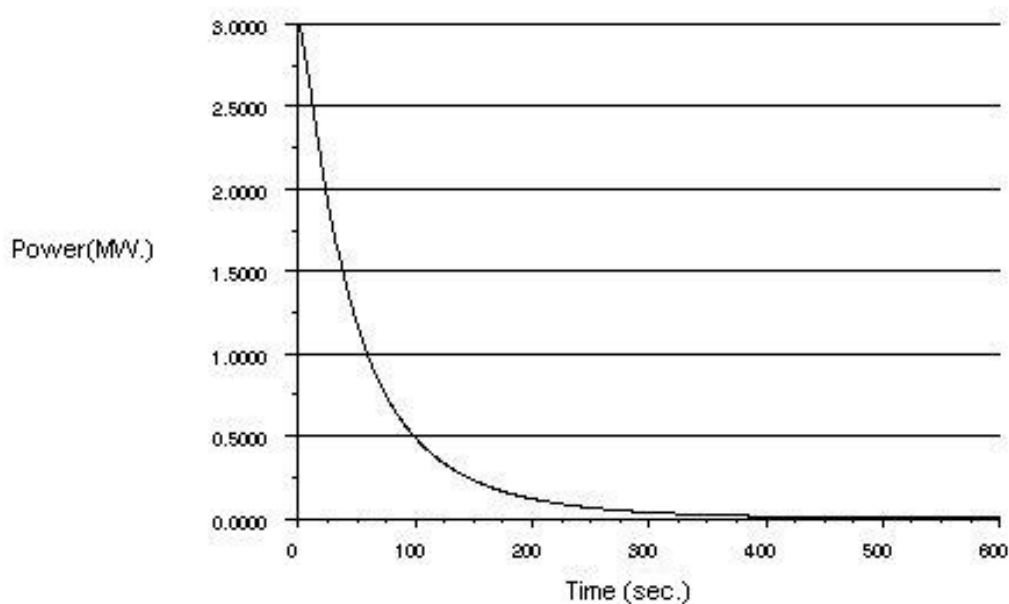


FIG. 2.95. Power vs time.

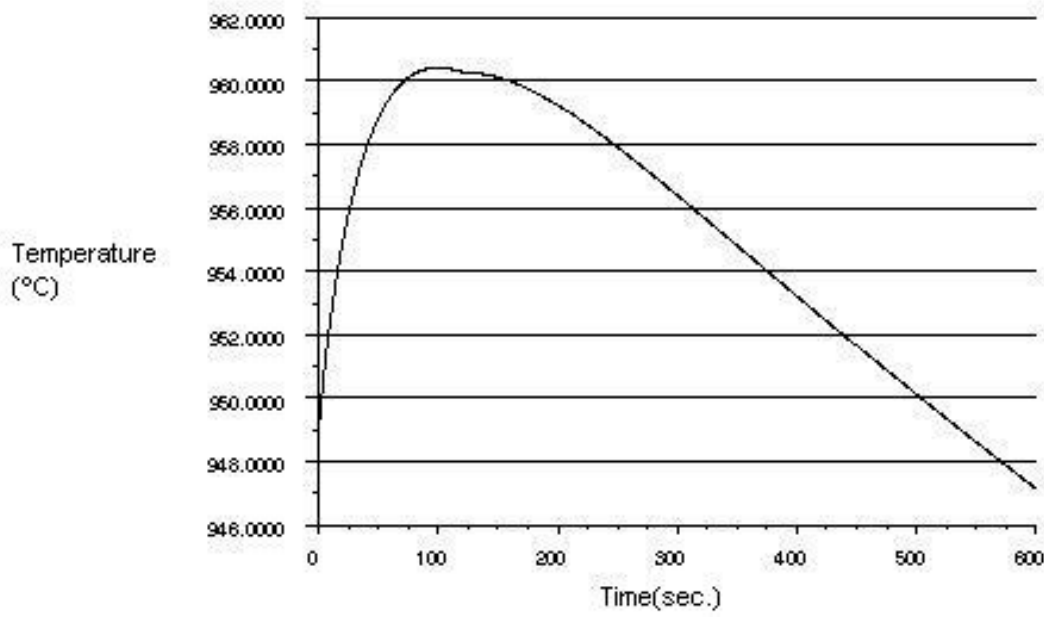


FIG. 2.96. Maximum fuel surface temperature vs time.

2.3.2.5. HTR-10 loss of flow benchmark results, Japan

The summary provided here was submitted to the CRP as Ref. [2-37].

Introduction

This report describes the calculation result by JAEA of the benchmark problems related to the reactor transient during the loss of primary flow without scram for the HTR-10 rated power operation.

Calculation model

The TAC-NC code [2-38], which is a two dimensional and time dependent thermal analysis code for the safety evaluation of the HTGR, was applied to the benchmark calculation. The code system was also used in the safety evaluation of the HTTR licensing in Japan. More information of the code and application to the HTTR can be found in [2-39].

The TAC-NC code is improved so as to consider the reactor kinetics during the loss of primary flow without scram and control rod withdrawal without scram in the HTR-10. Point kinetics, with six delayed neutron groups, is applied in the TAC-NC code. The reactor core is modified as the smeared model including pebble bed balls and coolant helium in the two dimensional TAC-NC code. Therefore, the feedback effect during the HTR-10 safety demonstration tests such as loss of primary flow without scram and control rod withdrawal without scram is considered as the following:

$$\rho_{feedback} = \Delta T_{core} \alpha_{fuel} + \Delta T_{core} \alpha_{moderator}$$

where

$\rho_{feedback}$ is the feedback reactivity;

ΔT_{core} is the average temperature of the smeared reactor core;

α_{fuel} is the fuel temperature coefficient of reactivity (-2.13pcm/°C in this benchmark);

$\alpha_{moderator}$ is the moderator temperature coefficient of reactivity (-16.2pcm/°C in this benchmark).

The improved TAC-NC code can also take into account the reactivity effect due to the density change of xenon as poison with negative reactivity effect. The reactor kinetics parameters used in the reactor transient calculation such as the loss of primary flow without scram and control rod withdrawal without scram are as follows:

Fraction of delayed neutrons: 0.726%;

Prompt lifetime: 1.68×10^{-3} s.

Calculation result

The calculation results of loss of primary flow without scram are shown in Figs 2.97 and 2.98 with comparison to the experiment results. The initial power decrease compares well with the experimental result but the recriticality time is later (~5200 s) compared to the experimental result (~4200 s). The power after recriticality compares reasonably. The importance of the decay heat and thus possible effect of uncertainties in the operating history before the event was tested by including a second case where the decay heat was not taken into account. In this case, the cooldown and recriticality are achieved much earlier (~1500 s) and thus clearly shows the sensitivity to the decay heat. This confirms that the irradiation history and thus the level of decay heat during the experiment is critical to the correct analysis of the event. The reactivity balance during the test is shown in Fig. 2.99. In this test, the reactor power decreases just after shutting down the primary helium blower due to the negative feedback effect of reactivity. The reactivity then increases due to reactor core temperature decrease because the reactor power decreases following a subcritical state. The reactor becomes recritical at the time when the total reactivity increases and becomes zero. According to calculation result, the recritical time is about 1300 s after shutting down the primary helium blower as shown in Fig. 2.99. The time obtained in the calculation when the reactor power reaches the first peak after the recritical is much later by about 1000 s than the time in the experiment.

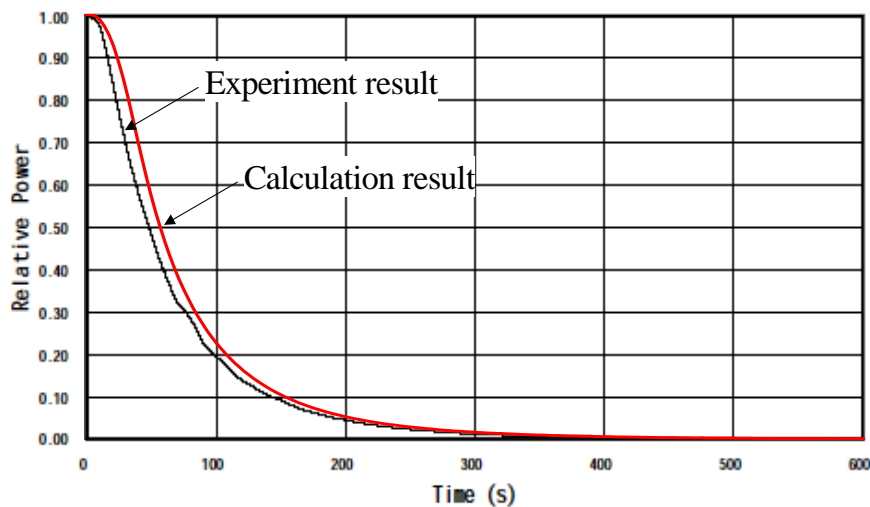


FIG. 2.97. Short term transient of reactor power during LOFC without Scram.

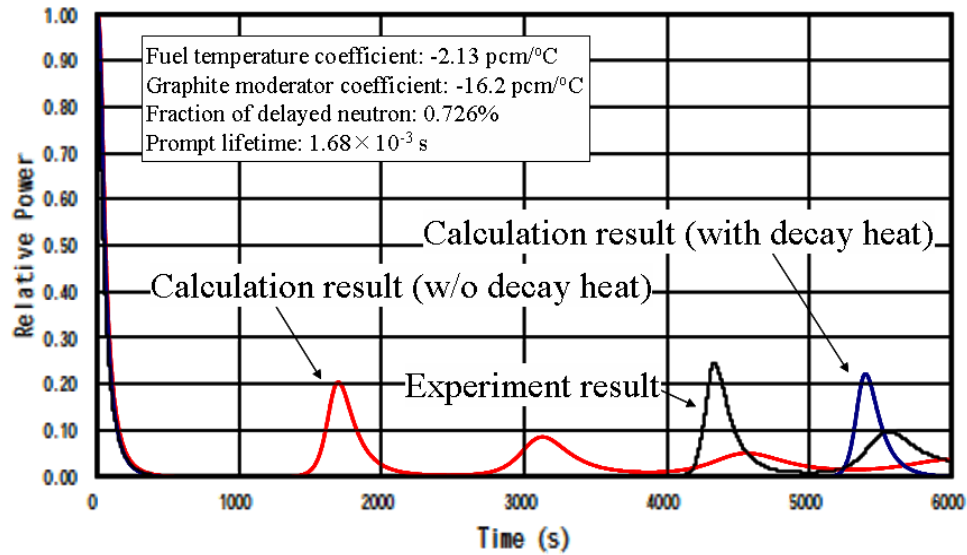


FIG. 2.98. Long term transient of reactor power during LOFT without Scram.

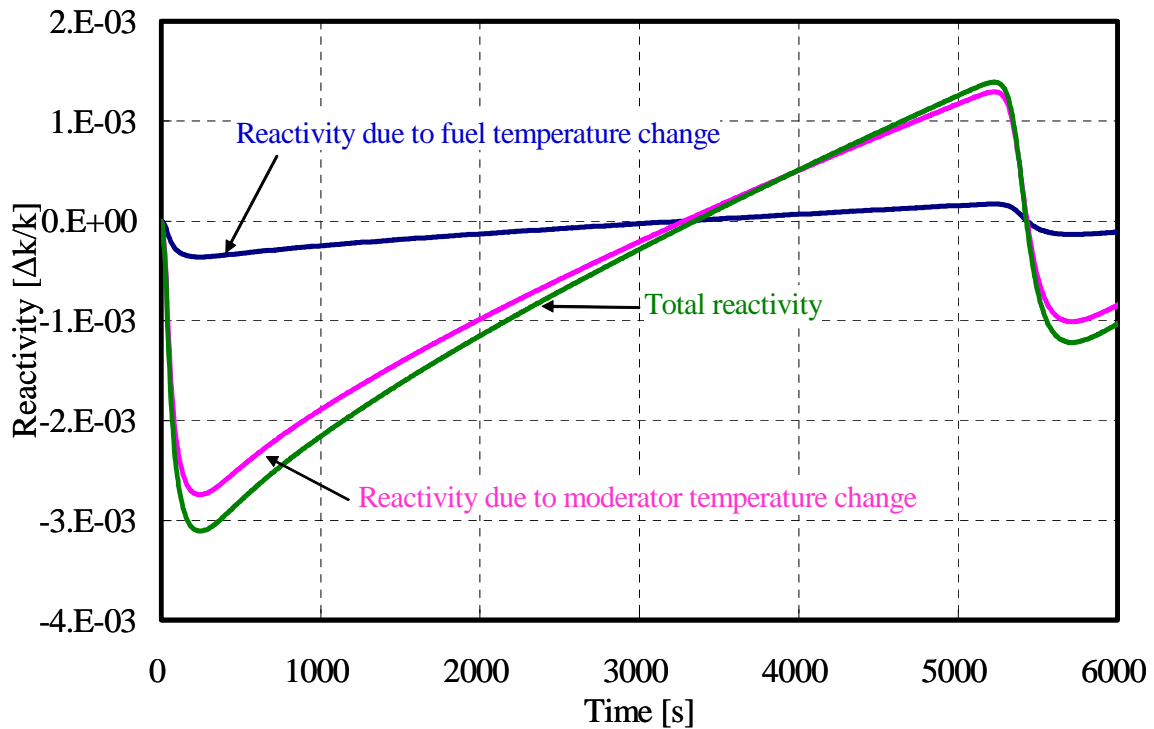


FIG. 2.99. Reactivity balance during LOFC without Scram.

Conclusion

The calculation of loss of primary flow without scram of the HTR-10 was performed by using the improved TAC-NC code. It was found that the improved TAC-NC code was able to simulate the main phenomena by using the reactor kinetics during the loss of primary flow without scram in the pebble-bed-type HTGR. The time of recriticality calculated was later than the experiment while the alternative case (with no decay heat) shows the sensitivity to the decay heat level (dependent on the irradiation history before the start of the safety illustration experiment).

2.3.2.6. HTR-10 loss of flow benchmark results, South Africa

Introduction

In order to analyse the two HTR-10 transient events, which start from a steady state power level of 3 MW, the generation of a new set of neutronic input files with the VSOP99/5 code is required. In addition, for the 3 MW power level, the lower tip of the control rods in the VSOP99/5 code run was kept at the same level (-55.3 cm) as applied in the 10 MW case. This decision was based on the almost symmetrical shape of the specified power profile at 3 MW, which signifies no control rods inserted or only a few fully inserted. Without the actual process being described in the benchmark definition, of how the reactor was brought from 10 MW to 3 MW power level, it was decided to utilize the VSOP99/5 code data as produced for 3 MW and with the control rods withdrawn to -55.3 cm level.

TINTE model at 3 MW power level

The geometrical model used for the 10 MW steady state TINTE model calculations was also used for the two HTR-10 transient benchmark problems at a power level of 3 MW. However, the power level, reactor outlet pressure, helium mass flow and the temperature-dependent material property input data were adjusted to reflect the 3 MW power level in the TINTE thermofluid input file. The required mass flow for 3 MW conditions was not specified and by using average temperature and pressure values, a mass flow of 1.44 kg/s was calculated. It was assumed that the mass flow ratios for the various flow channels remain the same as for the 10 MW power level. A basic assumption/requirement that applies to all TINTE runs is that the reactor should be critical (a k_{eff} of close to and slightly above 1 from past experience compared to VSOP99) for calculating the steady state conditions that provide the initial or starting conditions for a TINTE transient run. (This limits the need and size for the global reactivity adjustment that assures a critical starting condition.) Therefore, it was necessary to insert the control rods in the TINTE model to the 18 cm level (tip of the control rods in line with the top of the second fuel mesh along the Z-axis) to attain a steady state k_{eff} of 1.00426. Note that the final adjustment to obtain a critical core is made by the code by an internal adjustment.

Only a loss of primary flow constitutes the definition for the transient benchmark event, Loss of Primary Flow without Scram. Thus, in the TINTE transient definition file, this event is defined by specifying a steady state calculation, followed by a mass flow ramp that reduces the helium mass flow rate from 1.44 kg/s to zero over 1 s. Additionally, the user enters the time steps at which the output should be dumped to file and at which time step the TINTE calculation should stop.

TINTE steady state power profile at 3 MW

As indicated above, the control rods were inserted to 18 cm (top of the axial second fuel mesh) which produces a power profile that has a smaller power density at the top of the core and a larger power density in the bottom of the core in order to produce the specified 3 MW total power output (see Table 2.57). The reference values as provided by the host country exhibit a small tilting of the power profile in the opposite direction by having slightly larger values at the top of the core as compared to the bottom of the core. These opposing features in the two power profiles contribute to the larger percentage deviation of the TINTE model values from the reference values, evident from the values in Table 2.58. As for the 10 MW steady state case, the deviation in the values for the bottom fuel mesh is substantially larger in the rest of the core. Additionally, at the start of this transient, the TINTE decay heat curve, as shown in Fig. 2.101, is also significantly higher than the reference decay curve that is shown in Fig. 2.7 of Section 2.1.1. The TINTE steady state decay power is at a level of 6.7% of the total neutronic power, whereas the reference decay power curve indicates about 5.3% of the steady state power level. It is therefore to be expected that both these above-mentioned factors would have a prominent impact on the TINTE model calculated time for first recriticality after the start of the LOFC transient. Since the quantity of decay heat produced in the core as well as its spatial distribution (similar as the power profile in Fig. 2.100) dictate the time to recriticality, it is therefore necessary that the reasons for the TINTE model deviations from the reference case be established.

TABLE 2.57. TINTE POWER DISTRIBUTION (W/CM³)

Z/R (cm)	6.5	13	19	25	39	50	60	70.5	83.5	90
18	0.426	0.425	0.422	0.419	0.411	0.399	0.386	0.374	0.366	0.370
36	0.546	0.543	0.540	0.534	0.521	0.501	0.480	0.462	0.455	0.476
54	0.667	0.665	0.660	0.653	0.636	0.610	0.584	0.562	0.557	0.589
72	0.761	0.758	0.752	0.745	0.725	0.695	0.667	0.642	0.636	0.674
90	0.820	0.817	0.811	0.803	0.782	0.751	0.720	0.693	0.686	0.728
108	0.845	0.842	0.836	0.828	0.806	0.774	0.743	0.715	0.707	0.750
126	0.837	0.834	0.828	0.820	0.799	0.767	0.736	0.709	0.700	0.743
144	0.801	0.798	0.793	0.785	0.765	0.734	0.704	0.678	0.669	0.709
162	0.744	0.741	0.736	0.729	0.711	0.683	0.655	0.630	0.620	0.655
180	0.692	0.690	0.686	0.681	0.665	0.641	0.617	0.593	0.580	0.605
187.5	0.694	0.692	0.689	0.684	0.672	0.652	0.631	0.609	0.592	0.0

TABLE 2.58. PERCENTAGE DIFFERENCES FOR THE TINTE POWER DISTRIBUTION, RELATIVE TO THE SPECIFIED POWER DISTRIBUTION

Z/R (cm)	6.5	13	19	25	39	50	60	70.5	83.5	90
18	-21.0	-21.2	-21.2	-21.4	-21.9	-22.4	-23.5	-24.2	-25.4	-25.6
36	-14.1	-14.3	-14.5	-14.5	-15.8	-17.3	-18.0	-18.6	-18.7	-16.2
54	-9.6	-9.8	-9.9	-10.0	-10.1	-10.2	-10.6	-11.0	-10.5	-6.2
72	-2.9	-3.1	-3.0	-3.1	-3.2	-4.6	-4.8	-6.1	-4.4	0.96
90	-0.46	-0.58	-0.60	-0.51	-0.50	-1.4	-1.4	-2.42	0.09	5.9
108	-0.82	-0.95	-0.96	-0.89	-0.70	1.3	1.3	2.3	4.3	10.8
126	4.8	4.7	4.7	4.9	3.9	2.6	2.8	2.9	5.0	11.9
144	7.0	6.9	7.0	7.2	7.6	6.7	7.0	8.2	10.6	18.2
162	5.8	5.7	6.1	6.8	8.1	9.2	9.6	10.3	13.6	22.3
180	-0.97	-0.83	-0.41	0.68	2.5	5.8	6.8	8.0	12.4	22.9
187.5	50.8	50.8	51.8	53.4	56.9	62.9	65.7	68.2	74.6	0.0

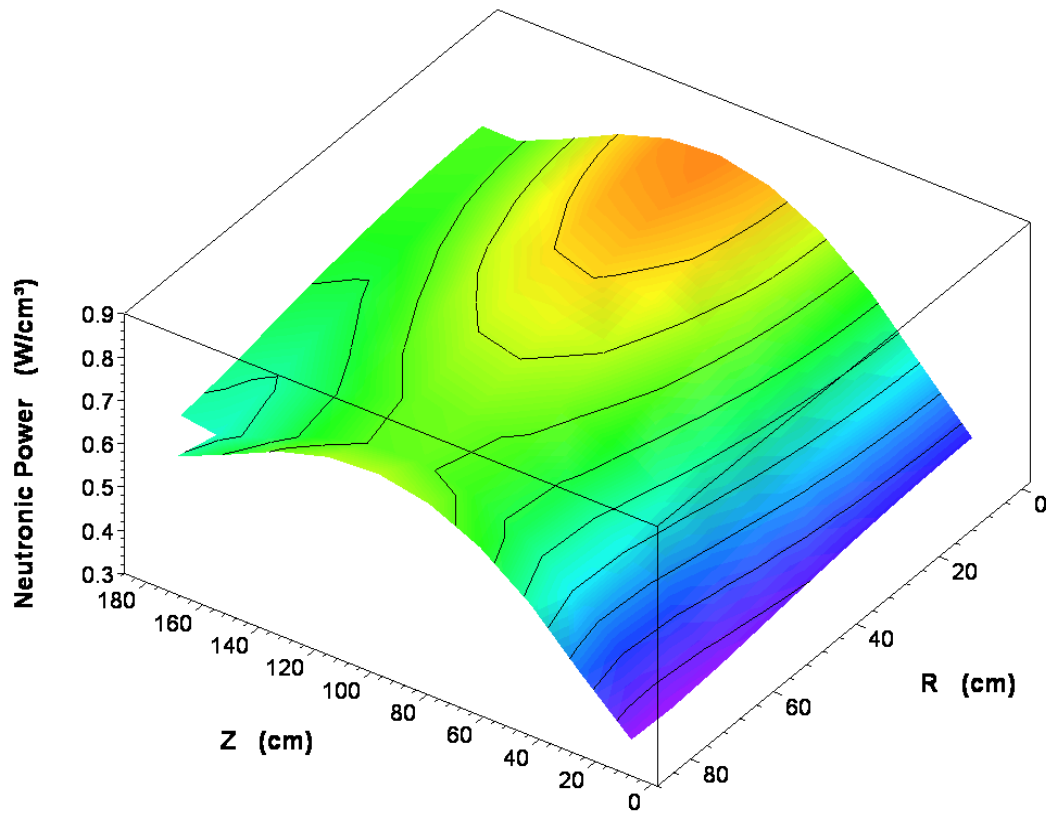


FIG. 2.100. TINTE steady state neutronic power distribution at 3 MW.

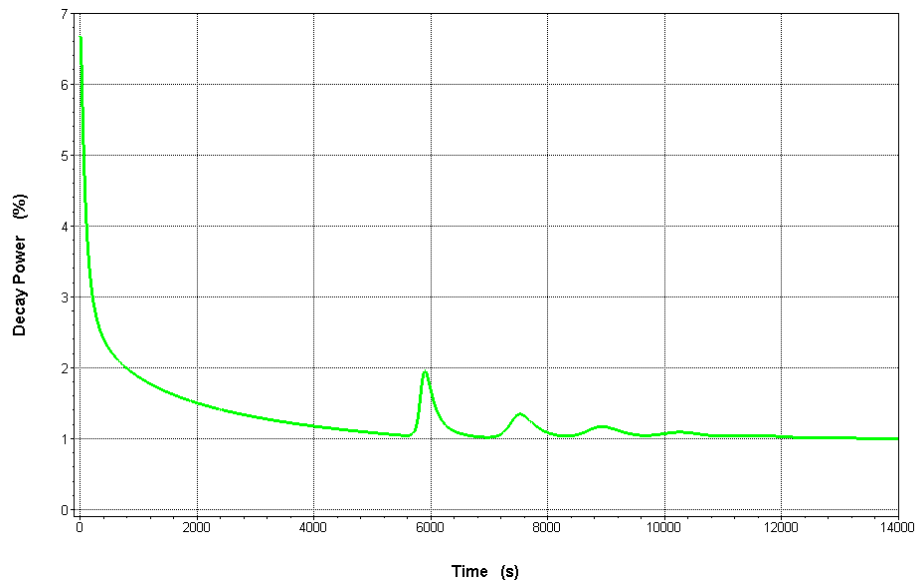


FIG. 2.101. TINTE decay power curve for the LOFC transient.

TINTE results for the LOFC transient event

The loss of forced convection at the start of the LOFC transient results in the rapid increase in the temperatures of the fuel in the core and the adjacent side reflector. The higher temperatures result in feedback that shuts down the fission process completely within the first 600 s from the start of the

LOFC transient. The TINTE model results for the first 600 s, as depicted in Fig. 2.102, show excellent agreement with the experimental results (see Section 7.1). The detailed fission power results are also included in Table 2.59.

In Fig. 2.103, the longer-time behaviour and the recriticality of the reactor analysis with TINTE are shown. The comparison with the experimental result is made in Section 7.1. As to be expected from the observed differences in the TINTE model decay power properties from the INET-calculated values, the TINTE model's prediction for first recriticality is about 1550 s later than the experimental value. The second peak is 1650 s after the first, as calculated by the TINTE model, while the experimental measurements indicate about 1300 s. With respect to the amplitudes of the first two power peaks, for which experimental data is presented, the TINTE model's value for the first peak is $\pm 26\%$ and the experimental value $\pm 25\%$ and for the second peak, the TINTE model's value is 10% which is the same as the experimental value. Thus, the spatial distribution of the decay power in the TINTE model's core and the rate at which the decay heat dissipates out of the core and the adjacent graphite structures are the main contributors in the time delay of the fission power peaks.

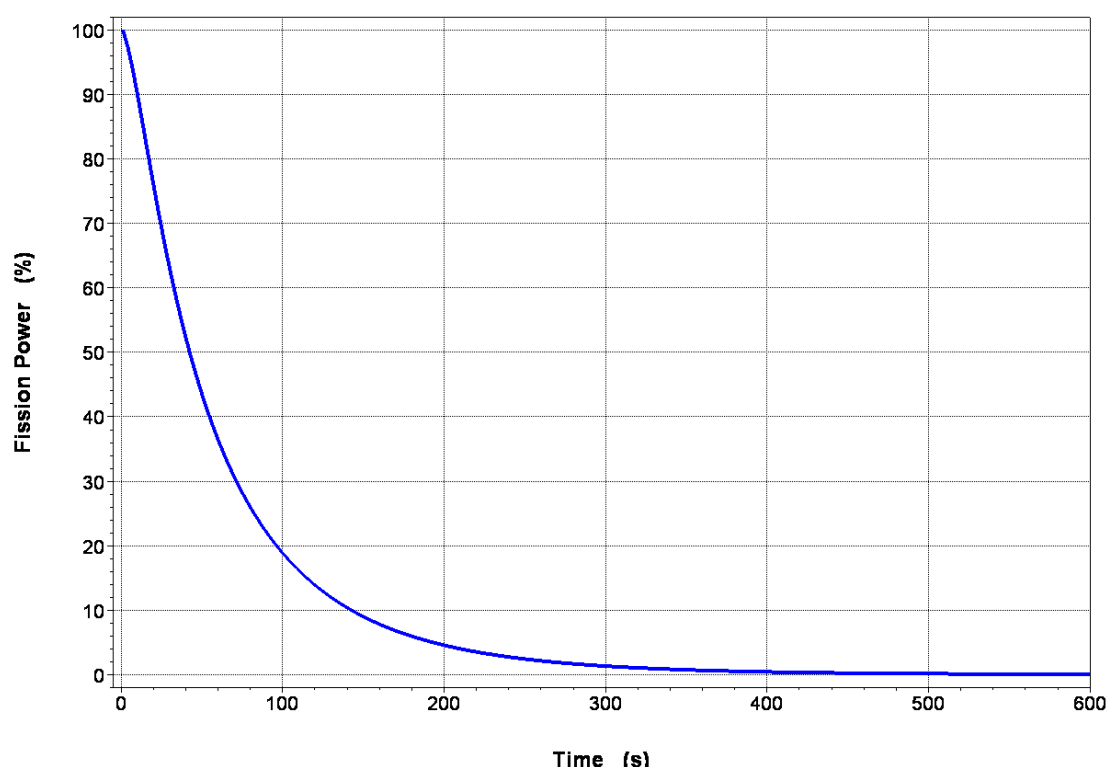


FIG. 2.102. TINTE fission power curve for LOFC (0–600 s).

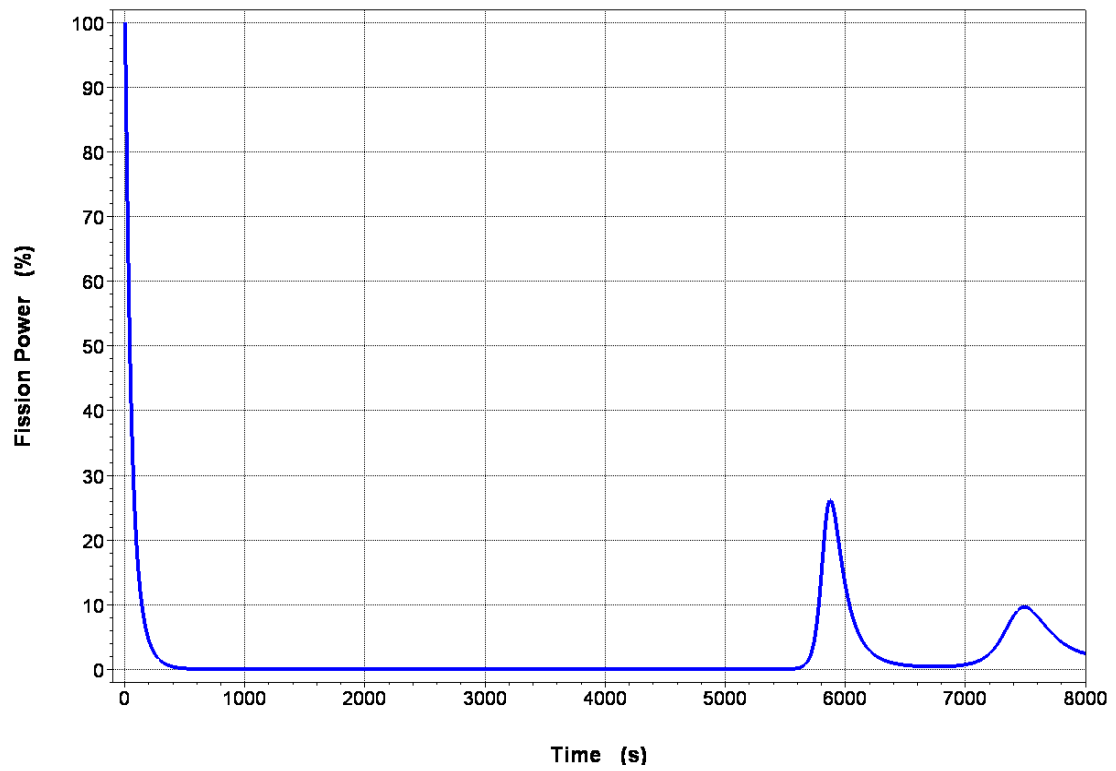


FIG. 2.103. TINTE fission power curve for LOFC (0–8000 s).

TABLE 2.59. RELATIVE FISSION POWER VS TIME

t (s)	Relative fission power	t (s)	Relative fission power	t (s)	Relative fission power
0	1.00	234.000	0.029481	6015.950	0.11497
1.200	0.99802	259.000	0.021631	6036.950	0.097415
3.100	0.98309	290.000	0.014884	6058.950	0.081968
4.600	0.96835	329.000	0.0094149	6082.950	0.068082
6.600	0.94541	380.000	0.0052494	6108.950	0.055933
8.600	0.91997	453.000	0.002315	6137.950	0.045221
11.600	0.87901	575.100	0.0005999	6171.950	0.035594
17.600	0.79392	876.700	0.00002179	6211.950	0.027247
23.000	0.71957	5512.950	0.00032637	6258.950	0.020316
27.000	0.66778	5611.950	0.0023527	6317.950	0.014508
31.000	0.61936	5653.950	0.0059491	6394.950	0.009872
35.000	0.57447	5680.950	0.011056	6502.950	0.0064217
39.000	0.53305	5700.950	0.017632	6660.950	0.0044395
43.000	0.49494	5716.950	0.025644	6863.950	0.004742
47.000	0.45993	5730.950	0.035513	7004.950	0.0075131
51.000	0.42778	5742.950	0.046738	7092.950	0.011955
55.000	0.39823	5753.950	0.059752	7154.950	0.017798
59.000	0.37108	5764.950	0.075732	7204.950	0.025252
64.000	0.34016	5774.950	0.092989	7249.950	0.034846
69.000	0.31225	5785.950	0.11488	7292.950	0.046899
74.000	0.28701	5798.950	0.14394	7346.950	0.065079
80.000	0.25982	5830.950	0.21694	7405.950	0.08419
86.000	0.23561	5839.950	0.23345	7437.950	0.091566
92.000	0.21398	5847.950	0.24528	7466.950	0.09539
99.000	0.1916	5855.950	0.25405	7495.575	0.096295
106.000	0.17187	5863.950	0.25963	7526.500	0.094353
114.000	0.15211	5871.950	0.26205	7562.125	0.089211
122.000	0.1349	5879.550	0.26163	7612.750	0.078835
131.000	0.11813	5888.550	0.2581	7740.250	0.051881
141.000	0.10219	5898.550	0.25101	7805.875	0.041498
152.000	0.087394	5909.550	0.24029	7876.200	0.033282
165.000	0.072915	5924.550	0.22256	7956.825	0.026851
179.000	0.060243	5951.550	0.18736	8000.000	0.024437
195.000	0.048669	5976.550	0.15614		
213.000	0.038498	5995.950	0.13451		

Summary of the LOFC Transient event results and conclusions

- The spatial decay power distribution and the dissipation of the decay heat from the core and adjacent graphite structures appear to be the controlling parameters for recriticality during a LOFC transient event;
- Given the importance of decay power for this event, it is therefore important that the standard used to derive the reference decay curve be stated;
- In addition, the duration and modes of operation that were followed to bring the reactor from the full power 10 MW steady state condition to a 3 MW power level need to be supplied, in order to produce the correct power distribution in the core, and also the correct fission product isotopic concentrations that are used for the decay power calculations.

2.4. HTR-10 CONTROL ROD (CR) WITHDRAWAL WITHOUT SCRAM BENCHMARK PROBLEM

2.4.1. HTR-10 CR withdrawal without scram benchmark problem description

The summary provided here was submitted to the CRP as Ref. [2-40].

Introduction

The Control Rod (CR) withdrawal without scram benchmark problem is provided to the IAEA Coordinated Research Project Evaluation of HTGR Performance by the Institute of Nuclear and New Energy Technology of Tsinghua University.

Benchmark problem description

The starting condition of the transient is as follows:

- The reactor has reached steady state operation at partial load of 30% of full power, i.e. 3 MW;
- The primary helium pressure at steady state partial-load operation is 2.5 MPa (this pressure remains basically unchanged during the transient).
- The helium temperatures at reactor inlet and outlet are 250°C and 650°C respectively at steady state partial-load operation (helium flow rate is defined by this temperature difference and helium pressure).
- The power density distribution is as given in Table 2.61. For the initial core, there is no heat generated in the lower part of the reactor core and the fuel discharging tube.
- Before the safety demonstration experiments, the reactor had operated for approximately 3000 MW-hour. At the starting points of safety demonstration experiments, xenon equilibrium state was achieved. The benchmark host institution suggests that investigators calculate the afterheat power versus time independently. The curve used by the benchmark host institution is shown in Fig. 2.7.

The transient is started (time point zero) by withdrawing one control rod at operational speed so that positive reactivity is introduced. The insertion speed is given in Table 2.60.

The Reactor Protection System (RPS) responds but the reactor is intentionally not tripped. At the ninth second into the transient, primary helium flow is stopped and the primary system is isolated from the water cooling systems on the secondary side of the steam generator. For calculation purposes, these actions are assumed to be finished instantly at the ninth second into the transient.

It is recommended that the participants perform the calculation of neutron flux and other neutronics parameters independently. The following data, which is used by the benchmark host institution, is given for reference.

Reactivity coefficients are defined as follows:

- The fuel temperature reactivity coefficient is defined as the reactivity variation caused by 1°C variation of fuel temperature within the whole core. Its unit is pcm/°C or $10^{-5}\Delta k/k/^\circ\text{C}$. In this benchmark definition, an overall average core temperature coefficient of reactivity at

operational state is given. It is a sum of temperature coefficients in all core zones. Approximately, the overall average core temperature coefficient of reactivity can be subdivided into all core zones according to their power fraction.

- Definitions of moderator and graphite reflector temperature reactivity coefficient are similar to the above definition of fuel temperature reactivity coefficient.
- Fraction of delayed neutrons: $\beta = 0.726\%$.
- Prompt generation time: $\Lambda = 0.00168$ s.
- Primary helium temperatures at reactor inlet and outlet and helium flow rate during the first 9 s of the transient are assumed to be the same as at steady state partial-load operation.
- Overall average core temperature coefficients of reactivity at operational state: Fuel = -2.13 pcm/°C, graphite moderator = -16.2 pcm/°C and the graphite reflector = 7.71 pcm/°C.

It is proposed to calculate the reactor power transient response after the initiation of the transient. The experimental results are shown in Fig. 2.104.

2.4.2. HTR-10 CR withdrawal without scram benchmark analysis and results

2.4.2.1. HTR-10 CR withdrawal without scram benchmark problem results, China

Experimental results

The experimental results of the Control Rod Drive (CRD) withdrawal without scram test on the HTR-10 are provided in Fig. 2.104.

Calculational results and comparison with the experiment, China

Calculation model and codes

The calculation codes and models include:

- THERMIX: A two dimensional time dependent heat conduction calculation program used to calculate the solid material temperatures. The two dimensional rotation symmetric heat conduction model in the R-Z geometry for the HTR-10 is shown in Fig. 2.5 and Table 2.4 of Section 2.1.1. The model includes the fuel zone and non-fuel zone of the core, reflectors, carbon bricks, cavity, thermal shield, core vessel, RPV, cavity cooler and coolant flow paths, etc. The pebble bed, reflectors and gas cavity are treated as homogeneous media whose heat capacities can be determined according to the void fraction in these regions;
- KONVEK: A two dimensional program to calculate gas flow problems including gas temperatures, flow rates and pressure drops. The gas convection model consists of 19 different flow regions as shown in Fig. 2.6 and Table 2.5 of Section 2.1.1 of this document;
- KINEX: A point kinetic program used to calculate reactor power transients by solving the kinetic equations with six-group delayed neutrons, considering reactivity changes caused by effects of xenon transients, temperature changes, and externally introduced reactivity changes.

The above three codes are coupled so that they can be used to calculate the transients as defined by this benchmark problem.

TABLE 2.60. CRD INSERTION SPEED VS INDUCED POSITIVE REACTIVITY

Time (s)	Introduced reactivity (mk)	Time (s)	Introduced reactivity (mk)	Time (s)	Introduced reactivity (mk)	Time (s)	Introduced reactivity (mk)
0	0	33	2.4986	65	3.6612	97	4.4222
1	0.0825	34	2.5385	66	3.6876	98	4.4451
2	0.1905	35	2.5806	67	3.7139	99	4.4618
3	0.2984	36	2.6226	68	3.7403	100	4.4795
4	0.4064	37	2.6646	69	3.7666	101	4.4973
5	0.5144	38	2.7066	70	3.793	102	4.515
6	0.6223	39	2.7487	71	3.8193	103	4.5327
7	0.7303	40	2.7907	72	3.8457	104	4.5505
8	0.8383	41	2.8327	73	3.8721	105	4.5682
9	0.9462	42	2.8748	74	3.8963	106	4.586
10	1.0542	43	2.9168	75	3.9192	107	4.6037
11	1.1086	44	2.9588	76	3.942	108	4.6214
12	1.172	45	3.0009	77	3.9649	109	4.6392
13	1.2353	46	3.0429	78	3.9878	110	4.6569
14	1.2987	47	3.0849	79	4.0106	111	4.6747
15	1.3621	48	3.1269	80	4.0335	112	4.6924
16	1.4254	49	3.169	81	4.0564	113	4.7101
17	1.4888	50	3.211	82	4.0792	114	4.7279
18	1.5521	51	3.253	83	4.1021	115	4.7456
19	1.6155	52	3.2951	84	4.125	116	4.7634
20	1.6788	53	3.3371	85	4.1478	117	4.7811
21	1.7422	54	3.3713	86	4.1707	118	4.7988
22	1.8052	55	3.3976	87	4.1936	119	4.8166
23	1.8682	56	3.424	88	4.2164	120	4.8343
24	1.9312	57	3.4503	89	4.2393	121	4.852
25	1.9943	58	3.4767	90	4.2622	122	4.8698
26	2.0573	59	3.5031	91	4.285	123	4.8875
27	2.1204	60	3.5294	92	4.3079	124	4.9053
28	2.1834	61	3.5558	93	4.3307	125	4.923
29	2.2464	62	3.5821	94	4.3536	126	4.9407
30	2.3095	63	3.6085	95	4.3765	127	4.9585
31	2.3725	64	3.6348	96	4.3993	128	4.9762
32	2.4356						

TABLE 2.61. POWER DISTRIBUTION
AT STEADY STATE 3 MW PARTIAL-LOAD OPERATION (W/CM³)

Z\R cm	0	6.5	13	19	25	39	50	60	70.5	83.5	90
0	0.539	0.539	0.536	0.533	0.526	0.514	0.505	0.494	0.491	0.497	
18	0.635	0.634	0.631	0.625	0.619	0.605	0.586	0.568	0.560	0.568	
36	0.738	0.737	0.732	0.725	0.707	0.679	0.654	0.632	0.622	0.628	
54	0.783	0.782	0.776	0.768	0.749	0.729	0.700	0.683	0.665	0.668	
72	0.824	0.822	0.816	0.807	0.786	0.761	0.730	0.710	0.685	0.687	
90	0.852	0.850	0.844	0.835	0.812	0.764	0.733	0.699	0.678	0.677	
108	0.799	0.797	0.791	0.782	0.769	0.748	0.716	0.689	0.667	0.664	
126	0.749	0.747	0.741	0.732	0.711	0.688	0.658	0.626	0.605	0.600	
144	0.703	0.701	0.694	0.683	0.658	0.626	0.598	0.571	0.546	0.536	
162	0.699	0.696	0.689	0.676	0.649	0.606	0.578	0.549	0.516	0.492	
180	0.460	0.459	0.454	0.446	0.428	0.400	0.381	0.362	0.339	0.335	

Calculation results and comparison with experimental results

The partial load operational status is simulated as indicated in the problem definition of this document. The defined transient is then simulated. The simulation uses the following parameters:

- Fraction of delayed neutrons: $\beta = 0.726\%$;
- Prompt generation time: $\Lambda = 0.00168$ s;
- Overall average core temperature coefficients of reactivity at operational state: Fuel = -2.13 pcm/°C, graphite moderator = -16.2 pcm/°C and the graphite reflector = 7.71 pcm/°C.

Reactivity insertion is simulated as defined in Section 2.4.1 of this document. At the ninth second into the transient, the helium blower is tripped and heat exchange between primary helium and secondary water/steam stops. The calculated reactor power transient curve is shown in Fig. 2.105 together with the experimental curve. Calculation and experiment both show a peak of reactor fission power in the first phase of the transient, followed by reactor self-shutdown. After some time, the reactor will get critical again and there will be some fission power oscillations, then the reactor fission power stabilizes at a low level.

Conclusions

It can be seen from Fig. 2.105 that for the first phase of the transient (the power peak and reactor self-shutdown), the calculation and experiment results agree relatively well. The experimental results are shown by the bold line and first recriticality occurs at ~ 3400 s while the calculational recriticality occurs earlier at ~ 2500 s. For the recriticality and power oscillation phase, there exist certain differences between calculation and experiment in terms of the recriticality time, power oscillation peak and periods. These differences need to be further addressed when detailed consideration is given in the calculation to several important factors such as xenon and decay heat power. Comparisons with other contributors are shown in Section 7.1.

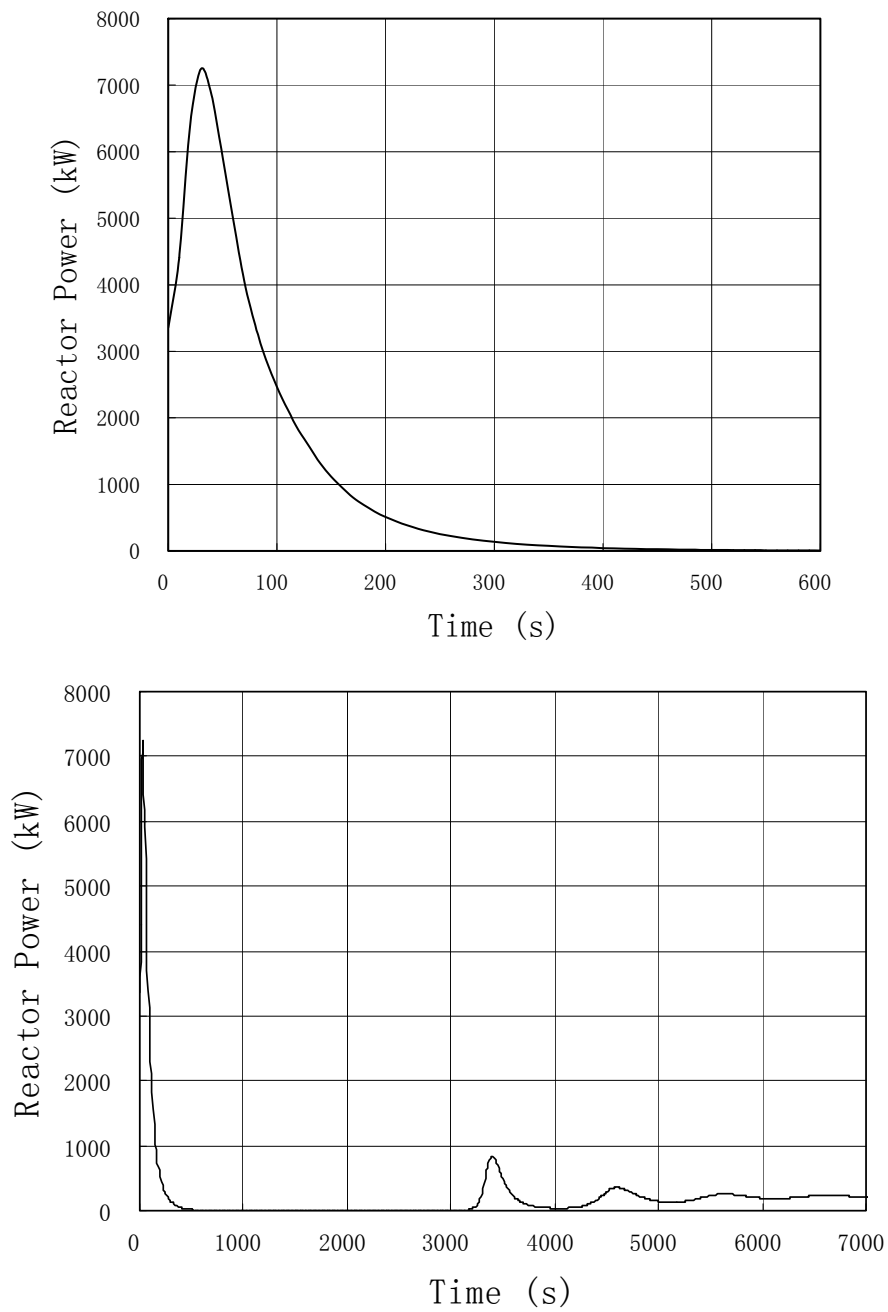


FIG. 2.104. Experimental curve of reactor fission power for CRD withdrawal without scram test.

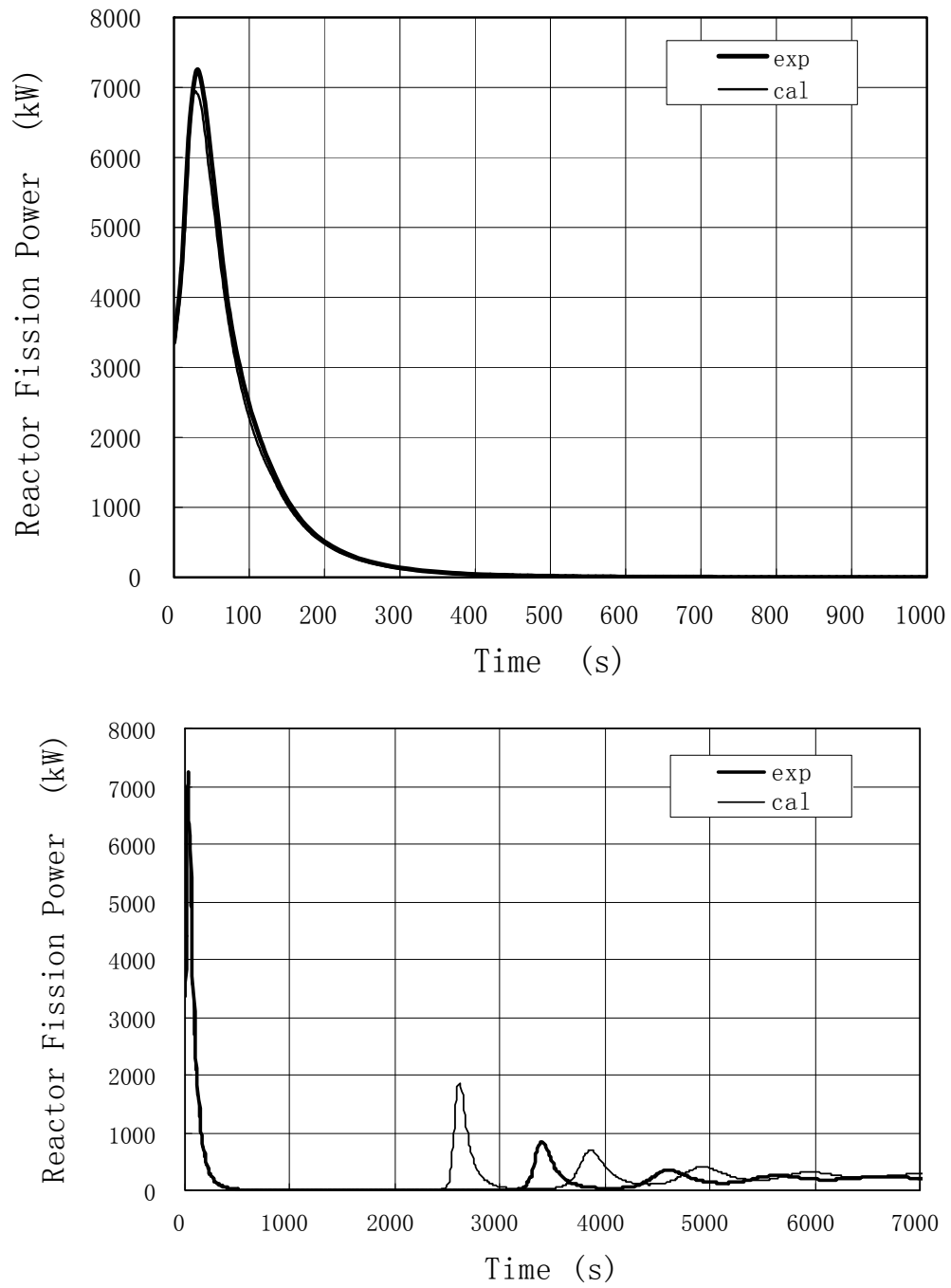


FIG. 2.105. Calculated and experimental reactor power transient curve.

2.4.2.2. HTR-10 CR withdrawal without scram benchmark problem results, Japan

The summary provided here was submitted to the CRP as Ref. [2-41].

Introduction

This section describes the calculation result of the benchmark problems related to the reactor transient during the CRD withdrawal without scram for the HTR-10 power operation of 3 MW.

Calculation model

The details of the TAC-NC code, which is a two dimensional and time dependent thermal analysis code considering reactor kinetics, are shown in Sections 2.2.2.8 and 2.3.2.5.

Calculation result

The calculation results of the CRD withdrawal without scram are shown in Figs 2.106 and 2.107 including comparison with the experiment results. The reactivity balance during the test is shown in Fig. 2.108. In this test, the CRD is withdrawn to insert the reactivity up to $5 \times 10^{-3} \Delta k/k$ in 128 s as shown in Fig. 2.106. At 9 s after starting the control rod withdrawal, the primary helium flow is stopped. As shown in Fig. 2.106, the calculated peak reactor power after control rod withdrawal is much lower than that obtained in the experiment. As for the time obtained in the calculation when the reactor power reaches the first peak after the recriticality, the reactor power shows a similar transient as the loss of primary flow without scram. In Fig. 2.107, a case where the decay heat is not taken into account is also shown. The recriticality in this case occurs much earlier and shows the sensitivity of the results to the correct representation of the decay heat.

Conclusion

The calculation of the CRD withdrawal without scram of the HTR-10 was performed using the improved TAC-NC code. It was found that the improved TAC-NC code was able to simulate the reactor kinetics phenomena (power excursion and recriticality) during the CRD withdrawal without scram in the pebble-bed-type HTGR. The large difference in the maximum power after CDR removal needs more investigation and although the first recriticality time and power level compare reasonably well, the second power excursion after recriticality is much later than the experimental value.

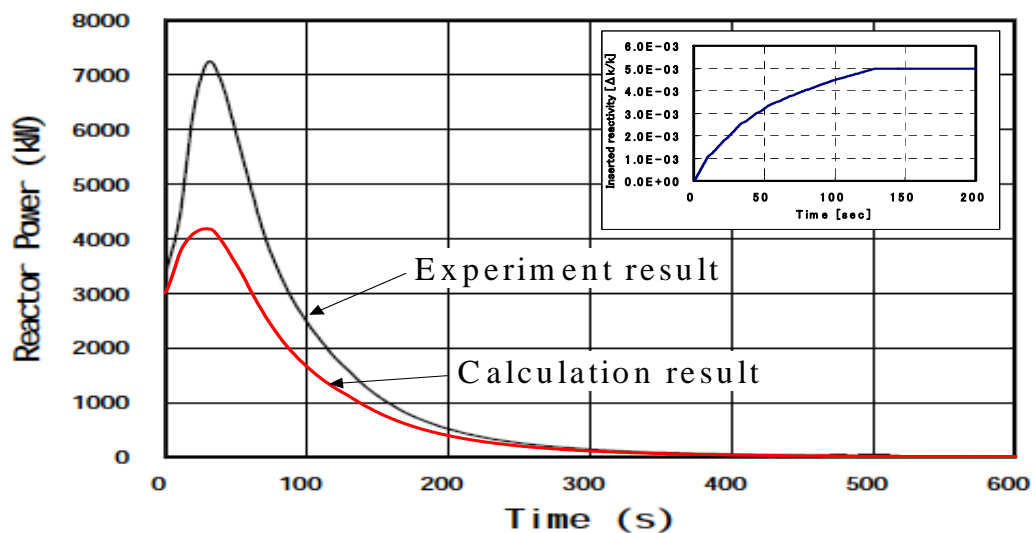


FIG. 2.106. Short term transient of reactor power during CRD withdrawal without scram.

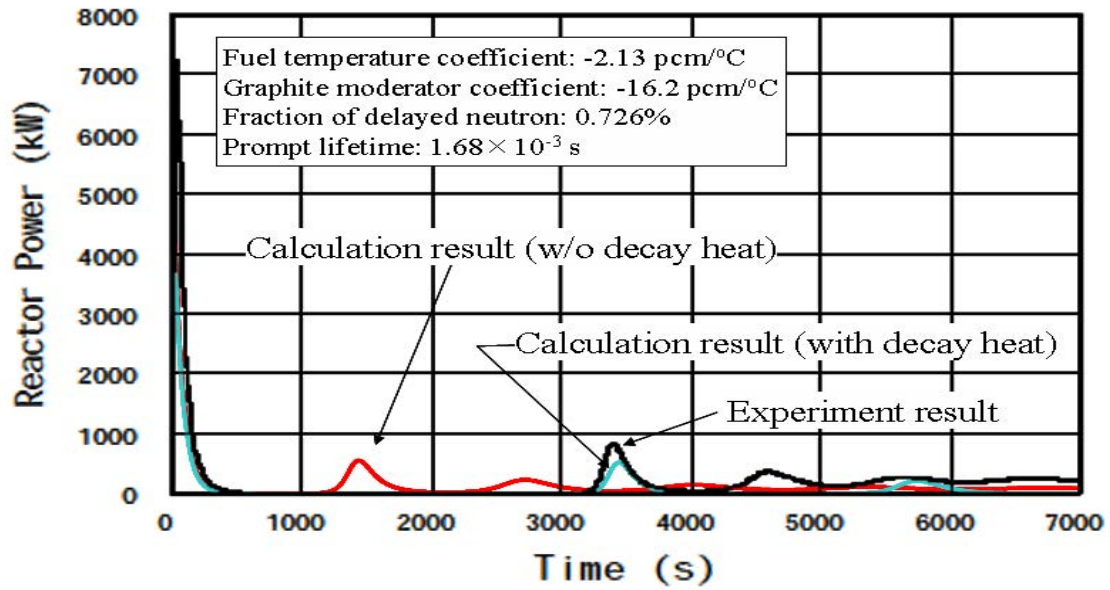


FIG. 2.107. Long term transient of reactor power during CRD withdrawal without scram.

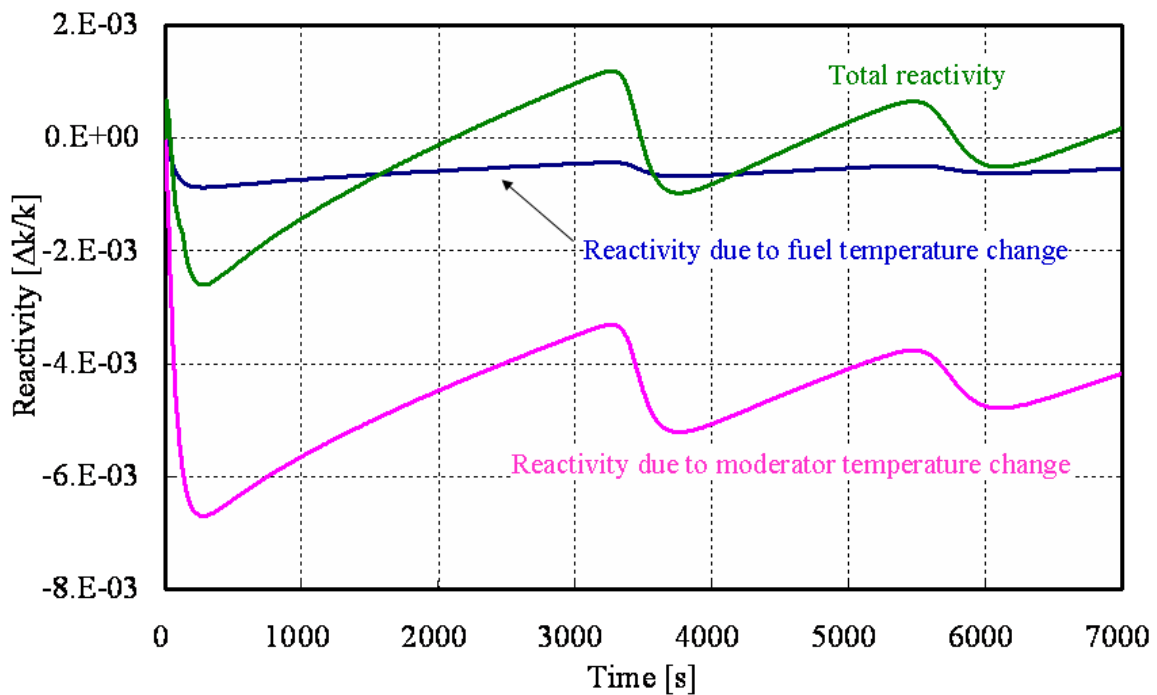


FIG. 2.108. Reactivity balance during CRD withdrawal without scram.

2.4.2.3. HTR-10 CR withdrawal without scram benchmark problem results, South Africa

Introduction

The description as provided in Section 2.3.2.6 under the subsection headings labelled ‘Introduction’, ‘TINTE model at 3 MW Power Level’ and ‘TINTE steady state power profile at 3 MW’ applies equally to this section with respect to the steady state properties of the TINTE model since the same

model was used for both HTR-10 transient benchmark problems. It is only the TINTE transient definition files that differ between the two transient event cases.

In the case of reactivity insertion in the core, the basic option available in the TINTE model is the withdrawal of control rods to a specified height and over a specified time interval or alternatively, the direct specification of a reactivity insertion in the core as a function of time. The second TINTE model's option was used, since the HTR-10 reactivity insertion data corresponds to the input format for that option. Of importance in the TINTE model is that the direct specification of a reactivity insertion provides a global adjustment of the reactivity in the whole core, whereas the movement of control rods tend to affect the reactivity change in the core more in a localized fashion, especially under normal full power operations where the insertion depth of the control rods is small in relation to the height of the core.

The TINTE model's transient definition file for this control rod withdrawal event without scram contains the instruction for a steady state calculation, which is then followed with the chronological input of the reactivity insertion as defined in Table 2.60 of Section 2.4.1. At the ninth second, the instruction to decrease the mass flow to zero over one second was added on the next data line after the reactivity input data line. Following the reactivity input data, the time steps at which output is dumped to the output files are given and finally, the time step at which the TINTE run is stopped.

TINTE results for the control rod withdrawal, without scram, transient event

From Fig. 2.109, it is seen that at just over 40 s the fission power peak attains its maximum. This is despite the fact that the addition of reactivity continues up to 128 s, thus more than 80 s after the maximum fission power peak has been attained. This illustrates the dominant effect of the temperature feedback on the neutron fission process. The termination of forced convection flow at 9 s into the transient accelerated the heat-up of the fuel spheres and pebble bed which then even more strongly suppresses the fission process, causing the power peak to be so early in the reactivity insertion transient. The increase in the fission power also leads to an increase in fission products and, consequently, an increase in the decay power. The decay power reaches its maximum about 10 s after the fission power peak due to the delay in time from the formation of the short-lived fission isotopes and their decay times. More details over the total transient calculational time are also given in Figs 2.110, 2.111 and Table 2.62. The comparison with the experimental results is included in Section 7.1.

The reason for the TINTE model's maximum power peak being about 2 MW lower than the experimental value is not known. One possible cause is the higher decay power that is calculated in the TINTE model, as compared to the INET calculations, and this will suppress the fission process at a steeper rate than the actual rate in the reactor. In addition, the spatial temperature distribution in the core and the larger quantity of thermal energy generated there result in a small delay in the time that the TINTE model's maximum power peak is attained. Later in the event, the accumulated effect of the higher decay power in the TINTE model, is more pronounced and that leads to a larger delay of ± 700 s in the time for the TINTE model to go critical again. The then-produced thermal energy raises the fuel temperature, the fission process dies out, and the reactor goes subcritical. This oscillatory process will continue, but the amplitude will become smaller over time until some equilibrium conditions are attained. The amplitudes of the TINTE model's fission power during these recriticality phases are in excellent agreement with the measured values and that confirms that the neutronic feedback effects are treated accurately in the TINTE code during this phase. The simulated withdrawal of the control rods (global reactivity insertion) makes the reactor more reactive (less absorption of neutrons) and that causes the reactor to go recritical sooner and at a higher average pebble bed temperature, as is the case for the LOFC transient event of the previous section.

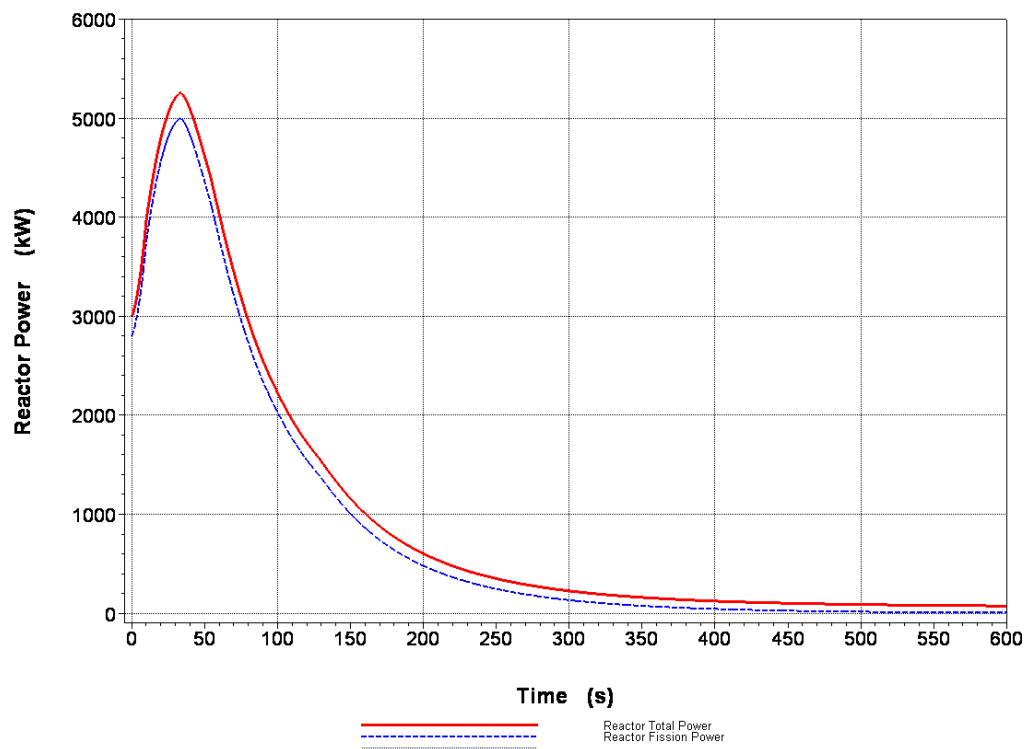


FIG. 2.109. TINTE total and fission power curves for the control rod withdrawal transient (0–600 s).

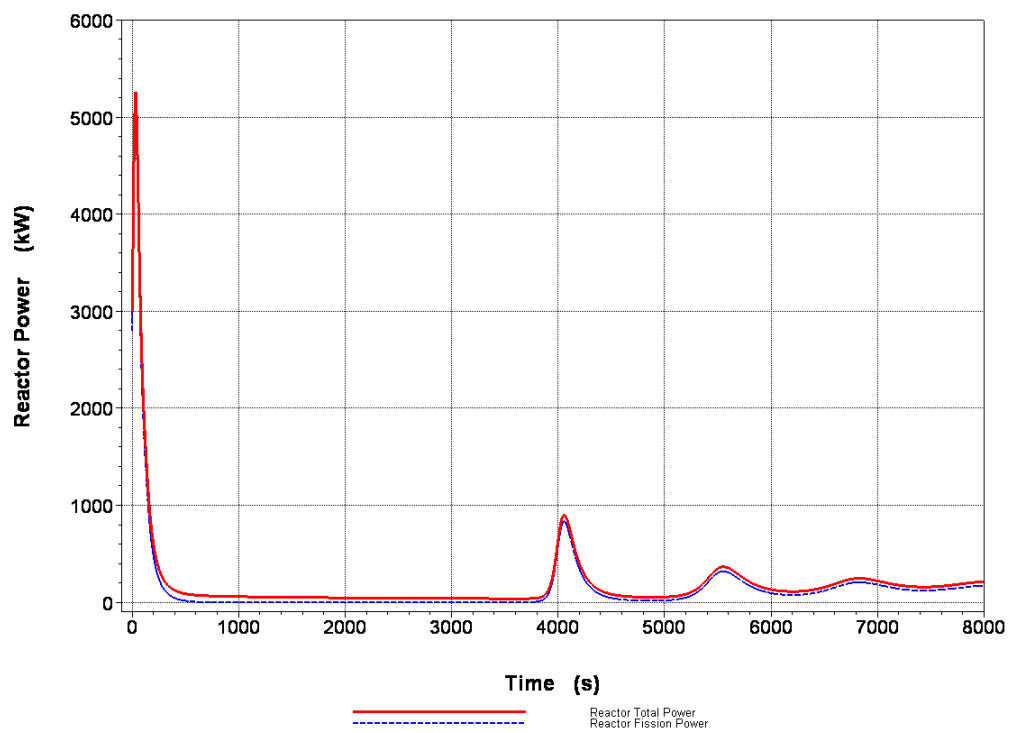


FIG. 2.110. TINTE total and fission power curves for the control rod withdrawal transient (0–8000 s).

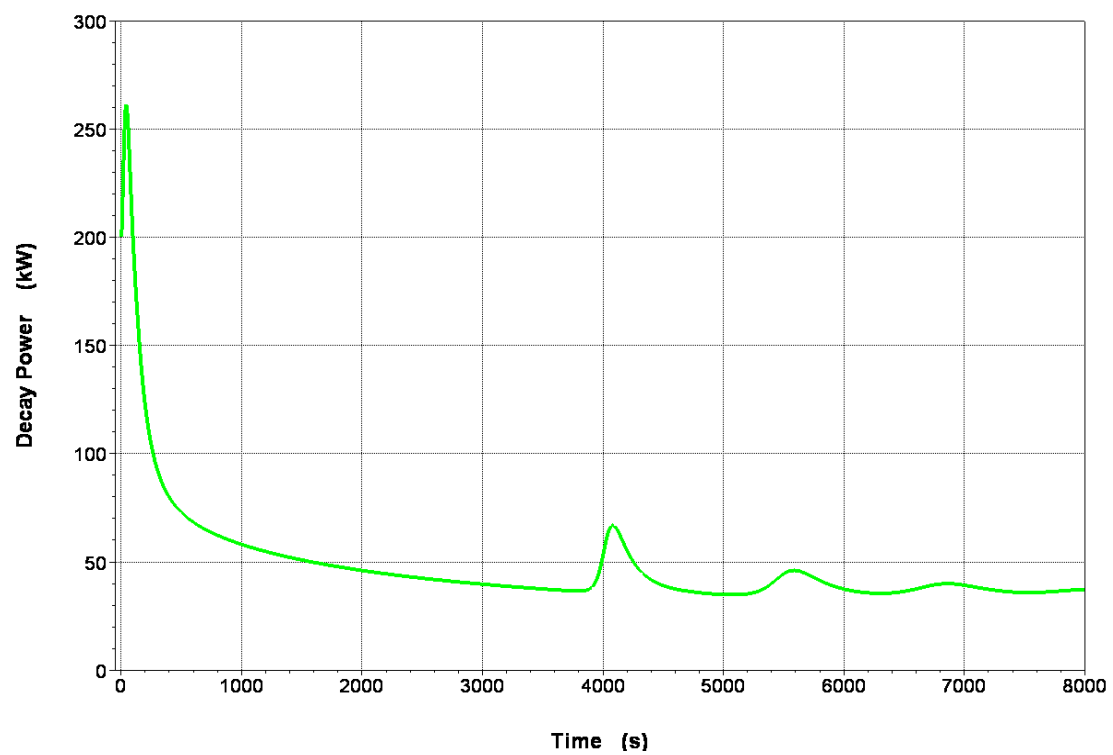


FIG. 2.111. TINTE decay power curve for the control rod withdrawal transient (0–8000 s).

TABLE 2.62. RELATIVE FISSION POWER VS TIME

t (s)	Relative fission power	t (s)	Relative fission power	t (s)	Relative fission power
0	1.00	96.000	0.76733	4064.644	0.29644
2.000	1.0303	104.000	0.68531	4077.644	0.2874
3.000	1.0545	111.000	0.62235	4094.644	0.26739
4.000	1.0827	118.000	0.56767	4121.644	0.227
5.000	1.1149	125.000	0.52021	4164.644	0.16439
6.000	1.151	136.000	0.44597	4194.000	0.12982
7.000	1.1914	146.000	0.38212	4225.000	0.10104
8.000	1.2363	155.000	0.33245	4260.000	0.07654
9.000	1.2858	165.000	0.28538	4300.000	0.056406
10.000	1.3403	176.000	0.24209	4349.000	0.039663
10.600	1.3626	188.000	0.2032	4412.000	0.026206
12.800	1.4377	201.000	0.16892	4498.000	0.015996
15.000	1.5049	216.000	0.13732	4628.000	0.0089588
17.000	1.5593	233.000	0.10936	4844.000	0.0057272
19.000	1.6076	253.000	0.084393	5084.950	0.0091062
21.000	1.65	277.000	0.062522	5205.950	0.01774
23.000	1.6864	306.000	0.044118	5283.950	0.030805
25.000	1.717	343.000	0.028794	5345.950	0.048732
27.000	1.742	392.000	0.016763	5416.950	0.077534
29.000	1.7616	461.000	0.0080802	5489.950	0.10524
32.000	1.7816	572.000	0.0026083	5531.950	0.11307
34.000	1.7834	808.400	0.00025249	5574.950	0.11299
36.000	1.7702	2470.000	0.00000007	5625.950	0.10455
38.000	1.7501	3823.733	0.0039047	5714.950	0.081086
41.000	1.7106	3871.556	0.012213	5822.950	0.055896
44.000	1.6632	3900.000	0.024592	5922.950	0.040807
49.000	1.5754	3921.000	0.041181	6039.950	0.031091
55.000	1.462	3938.000	0.061867	6185.950	0.026922
60.000	1.3515	3954.000	0.089104	6343.950	0.030176
66.000	1.2247	3969.000	0.1222	6484.950	0.040706
71.000	1.1284	3986.000	0.16723	6671.950	0.063636
76.000	1.0406	4019.000	0.25558	6783.950	0.072737
81.000	0.96008	4031.000	0.27841	6878.950	0.07258
86.000	0.88815	4042.000	0.29187	7000.000	0.064734
91.000	0.82417	4053.000	0.29778		

2.4.2.4. HTR-10 CR withdrawal without scram benchmark problem results, United States of America

Introduction

The GRSAC code system was used by the United States of America in analysing the HTR-10 ATWS benchmarks. The results of a single control rod withdrawal accompanied by a Loss of Forced Cooling (LOFC) accident scenario are simulated. The modelling details and sensitivity studies (especially adjustments to return to criticality earlier) were presented in Section 2.3.2.2.

Model adjustments and results

In the GRSAC, the core neutronic behaviour is characterized by a point kinetics model with prompt-jump and a single delay group. The reactivity feedback terms for the fuel and moderator were derived initially from flux-squared weighting of all active core node temperatures. The short term nuclear parameters were determined from the initial 5–10 minutes of the rod withdrawal ATWS test. A good fit was attained via a 10% reduction in the benchmark's prescribed fuel and moderator reactivity-temperature feedback coefficients and they were used as reference values for the balance of the calculations. The initial power transient calculated for the rod withdrawal ATWS (Fig. 2.112) shows a peak power of just over 7 MW, followed by a rapid decay. This maximum power compares well with the experiment (note that the input parameters into the point kinetics model were adjusted to achieve this as described above) but the time of the maximum (~ 48 s) is much later than the experimental maximum (at ~ 32 s). This suggests some shortcomings in the methodology used or the ability of the simplified method of using the point kinetics model with prompt-jump and a single delay group to model the relative slow and localized (control rod removed) transient.

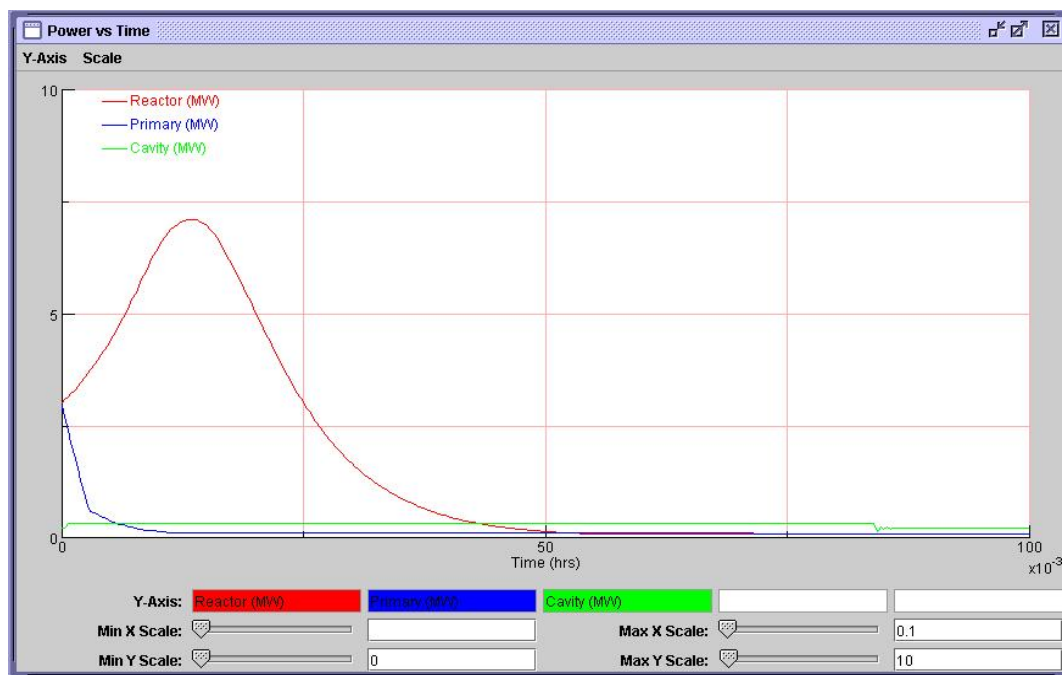


FIG. 2.112. Rod withdrawal ATWS showing initial fission power peak just above 7 MW.

The reference (long term) power response calculation for the rod withdrawal ATWS case is shown in Fig. 2.113, where the power peaking characteristics are similar in general behaviour to the experimental results, but the computed power peaks are much lower than those observed (~ 0.18 MW compared to the ~ 0.8 MW measured). The calculated first recriticality peak is at ~ 3400 s and coincides with the measured first peak time. The second recriticality peak occurs late (~ 5100 s) compared to the experimental result at ~ 4250 s.

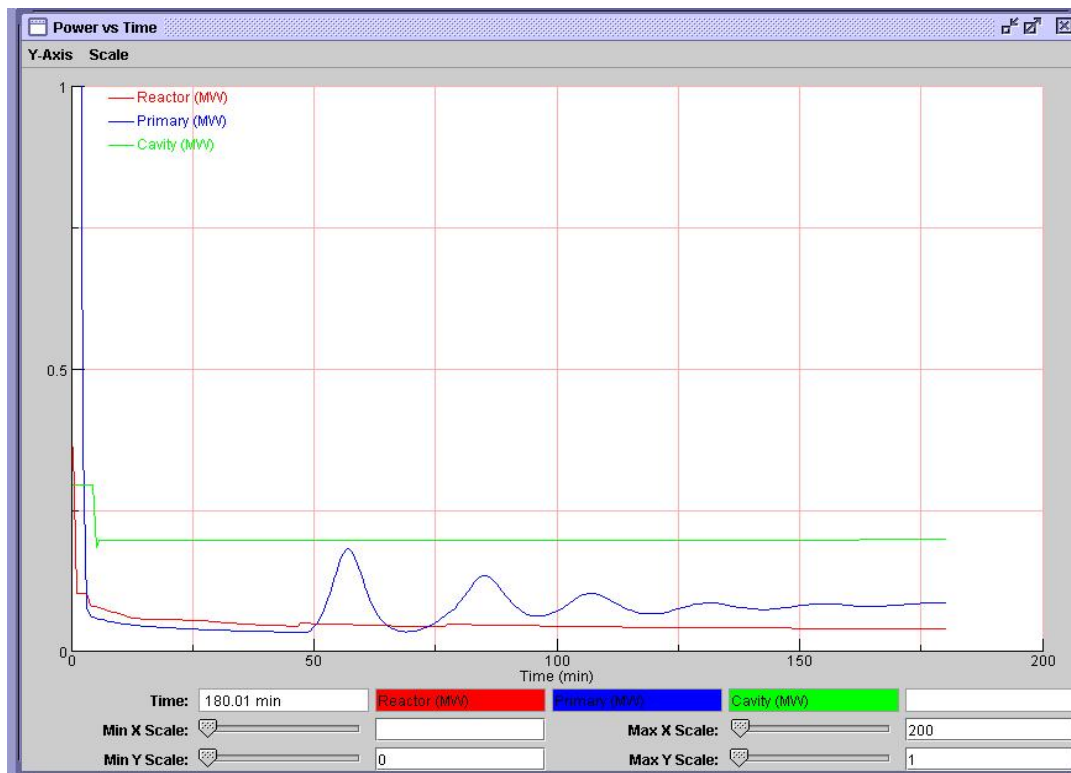


FIG. 2.113. Initial long term power response prediction for the rod withdrawal ATWS Test showing recritical oscillations.

2.5. REFERENCES FOR CHAPTER 2

- [2-1] DONG, Y., SUN, Y., 'Benchmark Problem of the HTR-10 Steady State Temperature Distribution for Full Power Initial Core, Version 2003-06, INET, Beijing, China (June 2003).
- [2-2] ZHONG, D., XU, Y., 'Progress of the HTR-10 Project', Design and Development of Gas Cooled Reactors with Closed Cycle Gas Turbines', IAEA-TECDOC-899, IAEA, Vienna (August 1996).
- [2-3] ZHONG, D., QIN, Z., 'Overview of the 10 MW High temperature Gas cooled Reactor Test Module', Proceedings of the Seminar on HTGR Application and Development, INET, Beijing, China (March 2001) 194–206.
- [2-4] SUN, Y., XU, Y., 'Relevant Safety Issues in Designing the HTR-10 Reactor', Safety Related Design and Economic Aspects of HTGRs, IAEA-TECDOC-1210, IAEA, Vienna (April 2001).
- [2-5] SUN, Y., DONG, Y., 'Additional Information to Benchmark Problem of the HTR-10 Steady State Temperature Distribution for Full Power Initial Core', Version. 2003-06, INET, Beijing, China (September 2004).
- [2-6] DONG, Y., SUN, Y., 'Clarification of HTR-10 Benchmarks definition', INET (Ver. 2005-06-28), Beijing, China (2005).
- [2-7] DONG, Y., SUN, Y., 'Calculation Benchmark Problem of the HTR-10 Steady State Temperature Distribution for Full Power Initial Core', INET, Beijing, China (September 2005).
- [2-8] DONG, Y., SUN, Y., 'Benchmark Problem of the HTR-10 Steady State Temperature Distribution for Full Power Initial Core', Version 2005-12', INET, Beijing, China (December 2005).

- [2-9] BENENATI, R.F., BROSILOW, C.B., Void Fraction Distribution in the Beds of Spheres, A.I.Ch.E.J. 8 No. 6 (1962) 223–236.
- [2-10] STUDER, E. et al., ‘Cast3m/Arcturus: A coupled heat transfer CFD code for Thermal-hydraulics analyses of Gas-cooled Reactors’, NURETH11 Conference, Avignon, France (2005).
- [2-11] LIMAIE, I., DAMIAN, F., RAEPSAET, X., STUDER, E., ‘Very high temperature reactor physics studies using a 3D neutronic/thermal-hydraulics coupling system for block type gas cooled reactors’, PHYSOR 2006 Conference, Vancouver, Canada (2006).
- [2-12] GREGOIRE, O., Établissement formel d’un modèle diphasique à 6 équations. Lien avec le modèle macroscopique à 4 équations de FLICA4, CEA internal report, France (2004).
- [2-13] STUDER, E., DABBENE, F., MAGNAUD, J.P., BLUMENFELD, L., QUILLICO, J.J., PAILLIERE, H., On the use of the MISTRA Coupled Effect Test Facility for the Validation of Containment Thermal-Hydraulics Codes, NURETH10 Conference, Seoul, Republic of Korea (2003).
- [2-14] BULIK, M., COULON, N., Modélisation du rayonnement thermique dans Castem 2000, CEA report DMT/97-142, France (1997).
- [2-15] ZONGXIN WU, DENGCAI LIN, DAXIN ZHONG, The Design Features of the HTR-10, Nuclear Engineering and Design 218 (2002) 25–32.
- [2-16] INTERNATIONAL ATOMIC ENERGY AGENCY, Current Status and Future Development of Modular High Temperature Gas Cooled Reactor Technology, IAEA-TECDOC-1198, IAEA, Vienna (2001).
- [2-17] HONG SIK LIM, HEE CHEON NO, GAMMA Multidimensional Multicomponent Mixture Analysis to Predict Air Ingress Phenomena in an HTGR, Nuclear Science and Engineering 152 (2006) 1–11.
- [2-18] HOLAMAN, J.P., Heat Transfer, McGraw-Hill (1986).
- [2-19] NIELD, D.A., BEJAN, A., Convection in Porous Media, Springer-Verlag, New York (1999).
- [2-20] German Safety Guide KTA3102.2 and KTA3102.3, German Nuclear Safety Standards Commission (1981).
- [2-21] JING, X., SUN, Y., Benchmark Problem of the HTR-10 Initial Core (Draft Version). Institute of Nuclear Energy Technology, Tsinghua University, Beijing, December 1998.
- [2-22] OPPE, J., DE HAAS, J.B.M. and KUIJPER, J.C., PANTHERMIX: a PANTHER-THERMIX interaction. Technical Report ECN –I-96-022. Netherlands Energy Research Foundation (ECN). Petten, Netherlands, May 1996.
- [2-23] HUTT, P.K., Overview Functional Specification of PANTHER: A Comprehensive Thermal Reactor Code for Use in Design, Assessment and Operation. Technical Report PANTHER/FSPEC/OVERVIEW 2.0, Nuclear Electric Plc., United Kingdom, December 1992.
- [2-24] STRUTH, S., THERMIX-DIREKT: Ein Rechenprogramm zur instationären, zweidimensionalen Simulation Thermohydraulischer Transienten. Forschungszentrum Jülich GmbH, September 1995.
- [2-25] AEA Technology: The ANSWERS Software Package WIMS. (A WIMS Modular Scheme for Neutronics Calculations). User Guide ANSWERS/WIMS. Atomic Energy Agency Technology (AEA), Winfrith, United Kingdom, 1997.
- [2-26] SPALDING, D.B., PHOENICS Overview, TR 001, CHAM (2002).
- [2-27] The ANSWERS Software Service, WIMS9 User Guide, ANSWERS /WIMS(99)9, Serco Assurance Report (2004).
- [2-28] PATANKAR, S.V., Numerical Heat Transfer and Fluid Flow, McGraw-Hill (1980).

- [2-29] COLBURN, A.P., A method of correlating forced convection heat transfer data and a comparison with fluid friction, *Trans. AIChE*, 19 (1933) 174–210.
- [2-30] RÜTTEN, H.J., HAAS, K.A., BROCKMANN, H., OHLIG, U., SCHERER, W., V.S.O.P. (99) for WINDOWS and UNIX computer code system for reactor physics and fuel cycle simulation, Jül –3820.
- [2-31] GERWIN, H., SCHERER, W., TEUCHERT, E., The TINTE Modular Code System for Computational Simulation of Transient Processes in the Primary Circuit of a Pebble-Bed High-temperature Gas-cooled Reactor, *Nuclear Science and Engineering*, 103 (1989) 302–312.
- [2-32] REITSMA, F., RÜTTEN, H.J., SCHERER, W., An overview of the FZJ-tools for HTR core design and reactor dynamics, The past, present and future, *Proceedings of the Mathematics and Computation, Supercomputing, Reactor Physics and Nuclear and Biological Applications*, Palais des Papes, Avignon, France, September 12-15, 2005, on CD-ROM, American Nuclear Society, LaGrange Park, IL (2005).
- [2-33] NAKAGAWA, S., TAKAMATSU, K., KUNITOMI, K., JAEA Calculation of HTR-10 Steady State Benchmark Problem, Japan Atomic Energy Agency, Oarai, Japan (August 2006).
- [2-34] SUN, Y., GAO, Z., Benchmark Problem of the HTR-10 Loss of Primary Flow without Scram, Version 2003-12, INET, Beijing, China (December 2005).
- [2-35] BALL, S., CRP-5 Benchmark Calculations for INET HTR-10 Loss Of Forced Cooling (LOFC) ATWS Accidents, Nuclear Science and Technology Division, Oak Ridge National Laboratory, Oak Ridge, TN, United States of America (December 13, 2006).
- [2-36] DONG, Y., SUN, Y., Benchmark Problem of the HTR-10 Loss of Primary Flow without Scram, Prepared for the IAEA Coordinated Research Program ‘Evaluation of High Temperature Gas Cooled Reactor Performance’, Institute of Nuclear Energy Technology, Beijing, China (2005).
- [2-37] NAKAGAWA, S., TAKEMATSU, K., KUNITOMI, K., JAEA Calculation of HTR-10 Loss of Primary Flow Withdrawal without Scram Benchmark Problem, Japan Atomic Energy Agency, Oarai, Japan (August 2006).
- [2-38] KUNITOMI, K. et. al., Two-dimensional Thermal Analysis Code TAC-NC for High Temperature Engineering Test Reactor and its Verification, JARI-M 89-001, Japan Atomic Energy Agency, Oarai, Japan (1989).
- [2-39] IAEA-TC-386.26. Gas Cooled Reactor Technology Safety and Siting, Section A-2 of the report of a IAEA technical committee meeting, Dimitrovgrad, USSR, 21–23 June 1989.
- [2-40] SUN, Y., GAO, Z., ‘Benchmark Problem of the HTR-10 Control Rod Withdrawal without Scram’, Version 2003-12, INET, Beijing, China (December 2005).
- [2-41] NAKAGAWA, S., TAKEMATSU, K., KUNITOMI, K., JAEA Calculation of HTR-10 CRD Withdrawal without Scram Benchmark Problem, Japan Atomic Energy Agency, Oarai, Japan (August 2006).

3. ASTRA CRITICAL FACILITY

The PBMR features a 400 MWt pebble bed reactor coupled to a power conversion system in a direct cycle configuration. An annular pebble bed reactor core design with a fixed graphite centre column has been selected for the PBMR. The advantage of an annular arrangement is that there is no power production in the centre of the reactor but a shifting of the peak power radially outward to the centre of the annulus enables a significantly higher power output while still maintaining the required fuel safety margin. There is also a higher thermal neutron flux in the graphite reflector where the control systems are active, thereby automatically increasing the effectiveness of the control and shutdown systems [3-1]. Earlier designs of the PBMR also had an annular core but with a dynamic central pebble reflector [3-2]. The loading of graphite spheres in the centre of the reactor and fuel spheres closer to the periphery resulted in a central graphite-only region surrounded by a mixing zone containing a mixture of fuel and graphite spheres and finally an outer fuel-only region. It is this configuration that was simulated in the ASTRA critical facility.

The ASTRA critical facility at the Russian Research Centre Kurchatov Institute is being used for neutron physics investigation of the PBMR reactor. The main purpose is to perform benchmark experiments simulating specific characteristic features of the earlier PBMR design with the dynamic central reflector, so that it can be used for the validation of codes to be used for that design. With this in mind, particular care was taken that the physical configuration of the ASTRA facility allowed for the possibility of carrying out experiments simulating pebble bed physics at the facility [3-3].

3.1. ASTRA GENERAL INFORMATION

3.1.1. Facility description

TABLE 3.1. OVERALL DESIGN DATA [3-4]–[3-6]

Outer diameter	cm	380
Side reflector height	cm	460
Fuelling zones		Graphite/mixed/fuel
Equivalent diameter of the core	cm	181
Core octagon definition	Corner points	(-87.5, 37.5), (-87.5, -37.5), (-37.5, 87.5), (-37.5, -87.5), (37.5, 87.5), (37.5, -87.5), (87.5, 37.5), (87.5, -37.5)
Outer diameter of the mixing zone	cm	105.5
Outer diameter of the inner reflector zone	cm	72.5
Inner diameter of the inner reflector zone	cm	10.5
Ratio of fuel spheres (FS) to absorber spheres (AS) in fuel zone		95/5
Ratio of FS to AS to graphite spherical Elements (moderator spheres – MS) in Mixing Zone		47.5/2.5/50
Pebble bed packing ratio		0.625
Pebble bed porosity		0.375
Number of control rods	#	5
Number of shutdown rods	#	8
Number of manual rods	#	1
Number of experimental channels for detectors	#	9
Number of experimental chambers channels	#	6

The most important characteristics of the ASTRA critical facility are outlined in Table 3.1. The facility represents an upright circular graphite cylinder (the side reflector) with an octagon-shaped core region inside. The core is divided into three zones, namely, a fuel zone, a mixing zone and an inner reflector zone. Figure 3.1 provides a schematic view of the critical assembly cross-section. Figure 3.2 shows the longitudinal section.

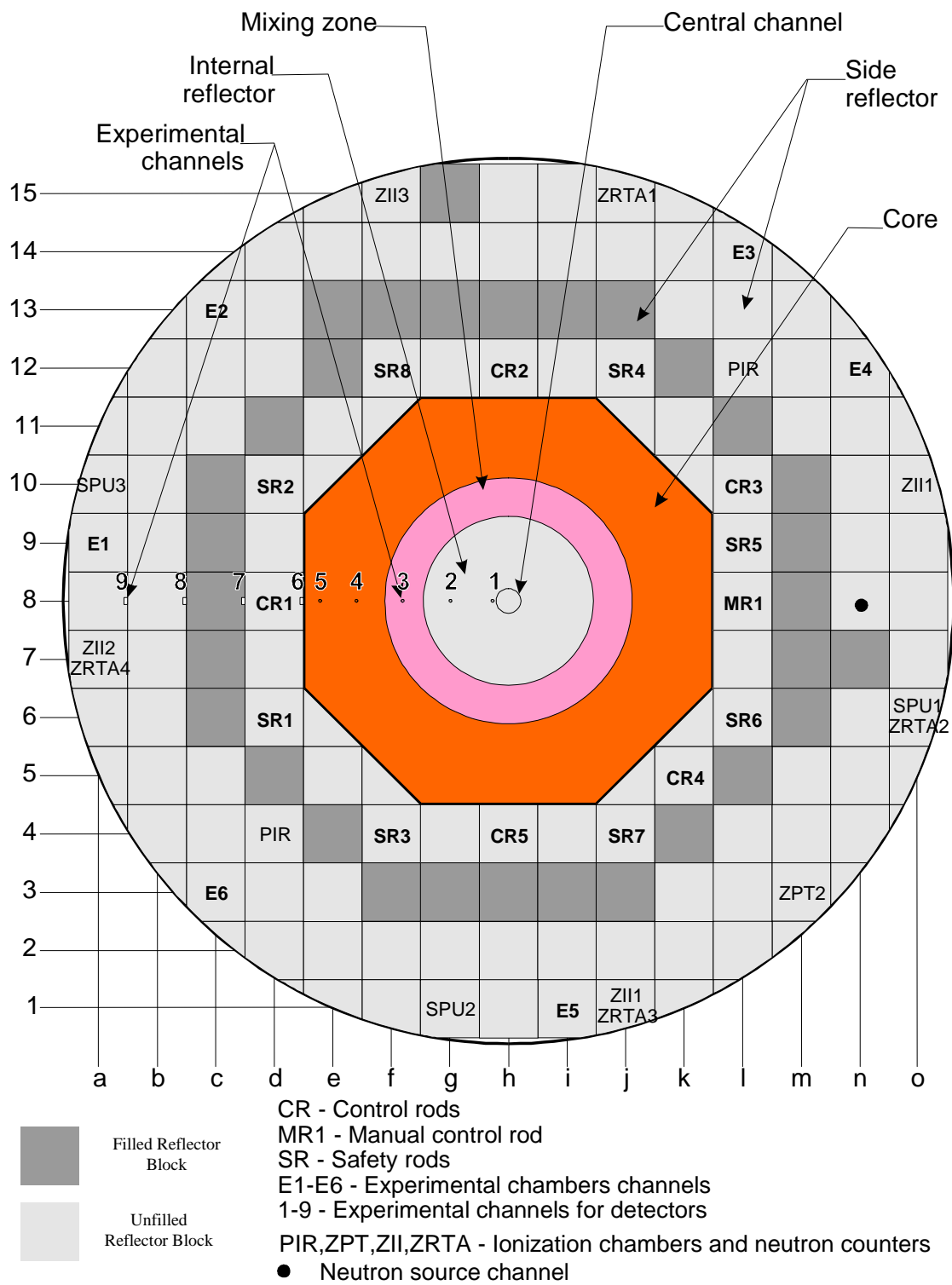


FIG. 3.1. ASTRA critical facility [3-7].

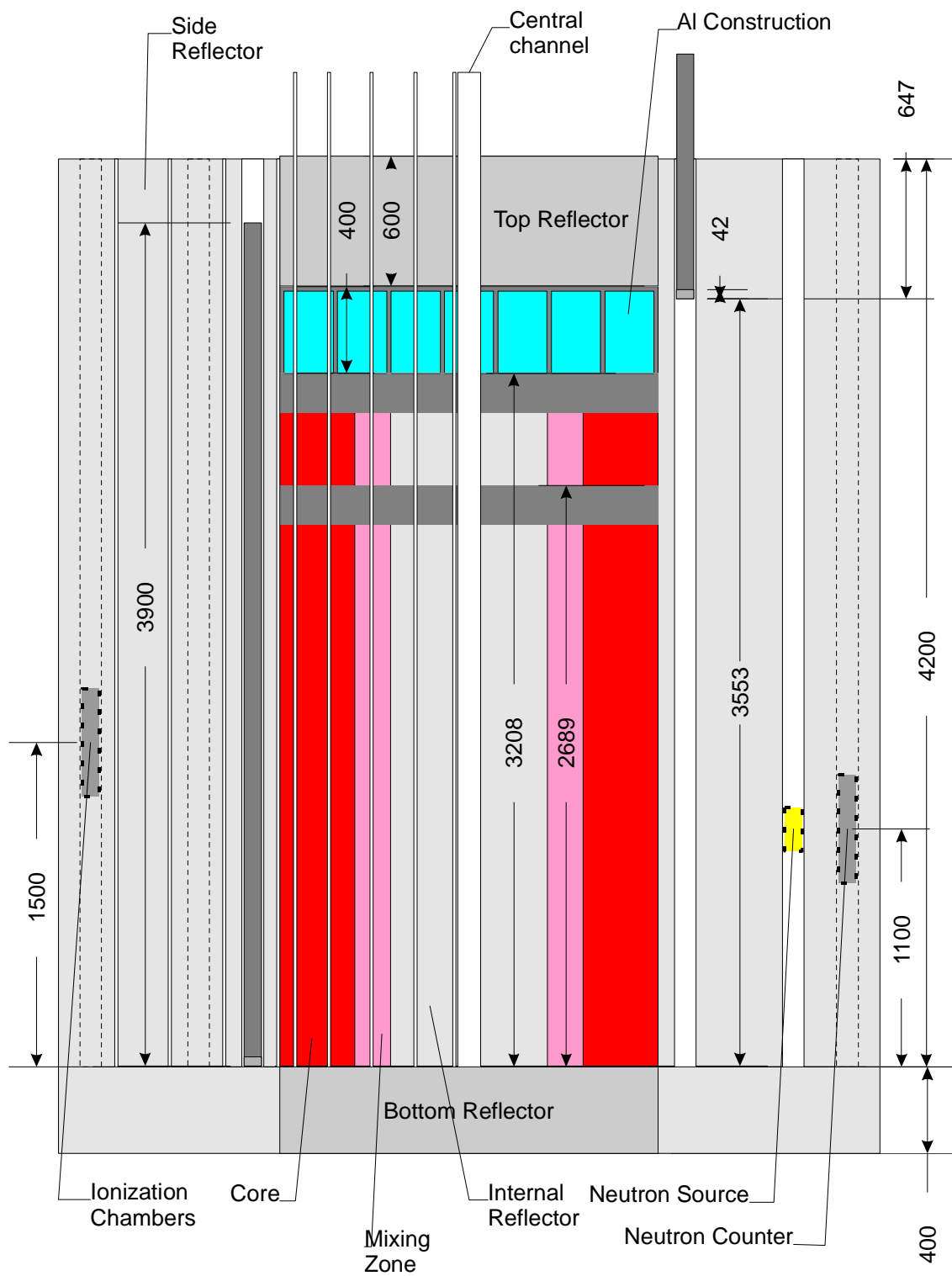


FIG. 3.2. Schematic of the critical assembly longitudinal section (dimensions given in mm) [3-7].

3.1.1.1. Description of the sphere types

Three types of spheres are employed in the ASTRA critical facility, namely, Fuel Spheres (FS), Absorber Spheres (AS) and Graphite Spheres (Moderator Spheres – MS). The fuel and absorber spheres consist of a central sphere containing the fuel/absorber material in a graphite matrix surrounded by a graphite shell. Table 3.2 provides a brief overview of the spherical elements.

TABLE 3.2. OUTLINE OF SPHERICAL ELEMENTS [3-5]

Sphere type	Diameter of matrix (cm)	Diameter of sphere (cm)	Density of graphite matrix (g/cm ³)	Density of graphite shell (g/cm ³)	Impurity [B(Nat) eq.] ppm by wt.	Loading (g/SE)
FS	5.0	6.0	1.85	1.85	1	Uranium 2.44
MS	-	6.0	-	1.68	1	-
AS	4.0	6.0	1.75	1.75	1	Boron 0.1

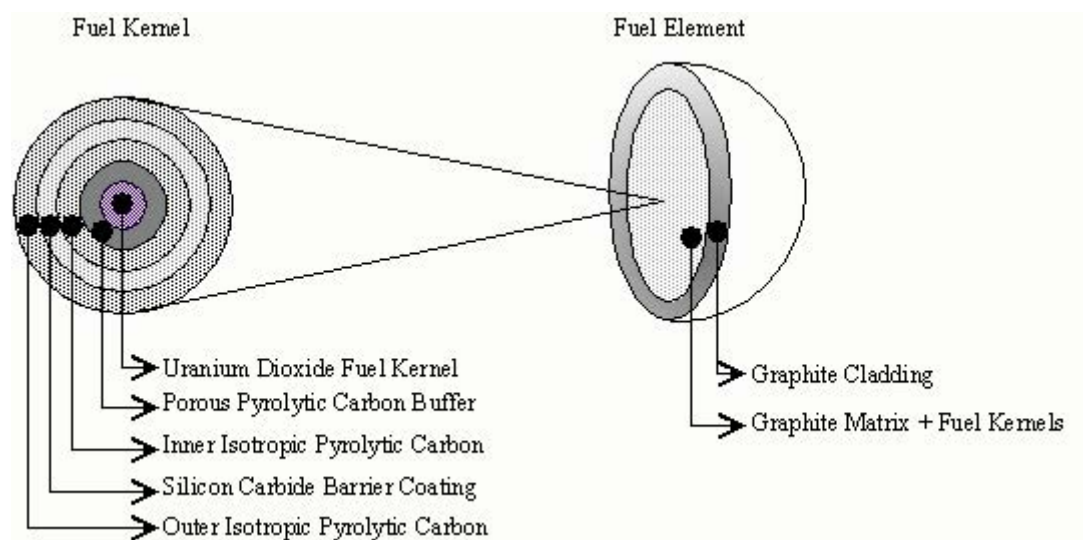


FIG. 3.3. Fuel sphere composition.

3.1.1.2. Fuel spheres

The fuel structure is shown in Fig. 3.3. Each fuel sphere contains coated UO_2 fuel kernels that are uniformly distributed in a graphite matrix, which together constitute the fuel sphere fuel zone. The fuel sphere fuel zone in turn is coated with a layer of graphite which serves as a clad and moderator. The detailed UO_2 fuel kernel (micro-sphere) specifications, the atom percentages along with the fuel sphere overall composition, are listed in Tables 3.3 and 3.4.

TABLE 3.3. UO₂ FUEL PARTICLE SPECIFICATION [3-5]

Layer	Thicknes (microns)	Outer diameter (microns)	Density (g.cm ⁻³)	Atom %	
UO ₂	-	500	10.1	Isotope atom densities in the uranium	
				U-234	0.15
				U-235	20.66
				U-236	0.09
				U-238	79.10
Buffer pyro C	90	680	1.1	C-12	100
Dense layer pyro C	70	820	1.8	C-12	100
SiC	60	940	3.2	Si-28	50
				C-12	50
Pyro C	60	1060	1.8	C-12	100

TABLE 3.4. FUEL SPHERE COMPOSITION [3-5]

Total mass of uranium per FS	2.44 g
Enrichment	approx. 21%
Number of coated particles	approx. 4190
Density of graphite in matrix	1.85 g.cm ⁻³
Mass of graphite in matrix	121.08 g
Diameter of FS	6.0 cm
Diameter of FS fuel zone	5.0 cm
Thickness of graphite cladding	0.5 cm
Equivalent boron concentration of impurities in graphite matrix	1 ppm by weight

3.1.1.3. Absorber spheres

Absorber spheres consist of a graphite matrix with neutron absorbing material (boron carbide particles) uniformly distributed over its central region. Table 3.5 lists the properties of the absorber spheres.

TABLE 3.5. ABSORBER SPHERE COMPOSITION [3-5]

Outer diameter of AS	6.0 cm
Diameter of absorbing zone	4.0 cm
Average size of boron carbide particle	60 μm
Boron carbide density	2.4 g/cm ³
Total mass of boron in the AS	0.1 g
Density of absorber sphere matrix graphite (including impurities)	1.75 g/cm ³
Equivalent boron concentration of impurities in graphite matrix	1 ppm by weight

3.1.1.4. Graphite spheres (Moderator spheres)

Graphite spheres are made up of high-purity reactor-grade graphite. The composition is given in Table 3.6.

TABLE 3.6. GRAPHITE SPHERE COMPOSITION [3-5]

Outer diameter of MS	6.0 cm
Density of graphite	1.68 g/cm ³
Equivalent natural boron concentration of impurities	1 ppm by weight

3.1.1.5. Control rods, safety rods and manual rods

The control rods, Safety Rods (SR) and manual rod (MR) in the ASTRA critical facility are situated in the side reflector inside the axial channels of the graphite blocks. The exact positions are indicated in Fig.3.1. All rods have the same configuration, consisting of 15 steel tubes arranged in a circle. See Table 3.7 for details on the configuration and Fig. 3.4 for a graphical representation.

The MR1 control rod is made as two coaxially arranged aluminium tubes. The outer tube is 9 cm in outer diameter and has a wall thickness of 0.25 cm. The inner tube is 7.6 cm in outer diameter and its wall is 0.25 cm thick. Its total height is 388.5 cm.

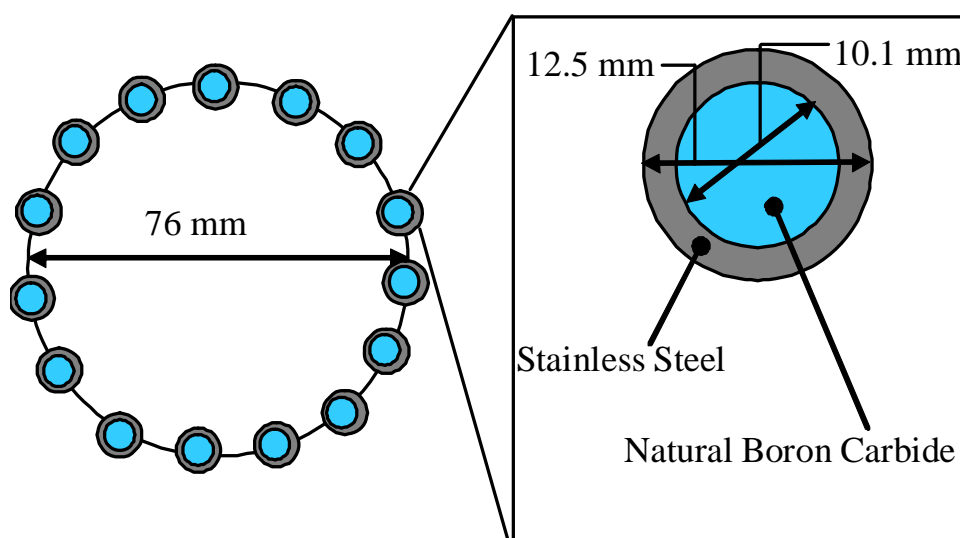


FIG 3.4. Control and manual rod configuration.

TABLE 3.7. CONTROL AND SHUTDOWN ROD CONFIGURATION [3-5]

Number of steel tubes	15	
Diameter of circle in which the tubes are arranged	7.6 cm	
Tube wall composition	Stainless Steel (12X18H10T)	
Steel density	7.9 g/cm ³	
Stainless steel composition	Element	weight %
	Fe	69.1
	C	0.12
	Si	0.08
	Mn	2.0
	Cr	18.0
	Ni	10.0
	Ti	0.7
Tube wall outer diameter	1.25 cm	
Tube wall thickness	0.12 cm	
Filling material composition	Natural Boron Carbide	
Filling material density	1.53 g/cm ³	
Height of absorbing material	~ 380 cm	
Diameter of rod channel	11.4 cm	

3.1.1.6. Reflector configuration

All reflectors at the ASTRA facility are composed of square graphite blocks that have a central channel which can be plugged with graphite if desired. Fig. 3.1 indicates which channels are plugged and which are not. Table 3.8 provides a listing of the reflector configuration. The side reflector's outer boundary is cylindrical in shape. The top reflector is optional.

The control, safety and manual rods are inserted into the central channels of the graphite blocks of the side reflector where required.

TABLE 3.8. REFLECTOR CONFIGURATION [3-4], [3-5], [3-8]

Outer diameter of side reflector	380 cm
Equivalent inner diameter of side reflector	181 cm
Height of bottom reflector	40 cm
Height of (optional) top reflector	60 cm
Composition of reflectors	High-purity reactor-grade graphite blocks
Average effective graphite density (taking gaps into account)	1.65 g/cm ³
Equivalent natural boron concentration of impurities	0.55 ppm by weight
Square cross-section of graphite blocks	25 x 25 cm
Axial channel diameter (hole in graphite block)	11.4cm

3.1.1.7. Experimental tubes and channels

Several experimental tubes and channels are included in the facility. They are both situated in the core region and in the side reflector (see Fig. 3.1 for the positions). The central experimental channel is situated in the centre of the inner reflector. Experimental samples, neutron detectors and graphite plugs can be placed in this tube. Table 3.9 shows the composition of the central experimental tube.

TABLE 3.9. CENTRAL EXPERIMENTAL TUBE COMPOSITION [3-5]

Outer diameter	10.5 cm
Wall thickness	0.25 cm
Wall composition	Aluminium (Al)

A further five aluminium tubes are situated in the core along the same axial line. These tubes extend the entire height of the pebble bed (see Table 3.10). These tubes are denoted 1 to 5 in Fig. 3.1.

TABLE 3.10. DETAILS ON ALUMINIUM TUBES [3-5]

Outer diameter	1.2 cm
Wall thickness	0.1 cm
Wall composition	Aluminium (Al)
Number of tubes	5
Locations (from centre of facility to centre of tube)	5.5 cm, 25 cm, 45 cm, 65 cm, 80 cm

Four small-sized experimental channels are located in the side reflector along the same radial line as the aluminium tubes. The square section of these channels is 1.5 cm × 3 cm and they are located (from the centre of the core) at 88.2, 113.2, 138.2 and 163.2 cm. These channels are denoted 6 to 9 in Fig. 3.1.

3.1.1.8. Material data assumed for neutronics calculations

Table 3.11 provides a listing of the material constants that are assumed.

TABLE 3.11. MATERIAL CONSTANTS [3-5], [3-9]

Material	Density (g/cm ³)	Atomic weight (g/mol)	Atom density (10 ²⁴ /cm ³)
Graphite matrix	***	12.011	***
Boron carbide B ₄ C	***	55.291	***
Stainless steel (12X18H10T)	7.9	55.84	0.08520
Boron B ^{Nat}	**	10.82	**
Aluminium (Al)	*2.6989	26.98154	*0.06024
Isotopic composition ¹⁰ B/ ¹¹ B		19.8%/80.2%	
Avogadro's constant L (10 ²⁴ /mol):		0.6022045	

* Data not available from documentation – generic value quoted [3-9];

** Data not applicable;

*** Dependent on position.

A summary of the ASTRA configuration was made available to the participants [3-10] extracted from all the references provided by the Russian Research Centre Kurchatov Institute [3-4, 3-5, 3-7, 3-8, 3-11–3-15].

3.1.2. Benchmark problem descriptions

The summary provided here was submitted to the CRP as Ref. [3-16].

Four calculational benchmark problems are to be performed for the ASTRA facility. The first and fourth tasks involve criticality, while the other tasks are related to control rods worth.

3.1.2.1. Core height for criticality

The experiment performed at the ASTRA critical facility involved increasing the height of the pebble bed core until criticality was reached. At this point, the height of the bed was recorded. Experimental measurements showed that the pebble bed porosity at this time was approximately 0.375. Criticality was achieved with no control rods or shutdown rods inserted, but the manual rod (MR1) was inserted

to 326.5 cm (this information was only obtained later in the benchmark definition history and may not be included in analysis). No top reflector was present in this experiment and no structures (loading device) above the pebble bed should be modelled.

The requirement for this task is thus to determine the height at which the ASTRA facility will achieve criticality, assuming that no control rods or shutdown rods are inserted.

An alternative case was also defined to determine the criticality (multiplication factor) for the ASTRA facility. The following should be assumed:

- 268.9 cm pebble bed height;
- 38584 spheres in total;
- Packing fraction of 0.6333 (porosity of 0.3667);
- MR1 was inserted to 326.5cm;
- No top reflector/no fuel loading device structure.

The alternative case excludes the uncertainties introduced in the packing fraction and pebble bed height measurements and uses the more reliable definition of the total number of spheres in the facility at the time of criticality.

3.1.2.2. Control rod worth

This task involves the determination of the worth of control rods depending on their position in the side reflector, as well as determining the effect of interference of a system of control rods. For the experiments performed, the pebble bed height is $H_{pb} = 268.9$ cm. The worth was measured by the rod drop method using the PIR-4 reactivity meter wherein inverse kinetics equations are synchronously solved in point approximation.

Worths of control rods depending on their position in the side reflector

This task involves determining the worth of individual control rods located in the side reflector at various distances. The rods that are to be moved are relocated in the side reflector in two directions (beams A and B as shown in Fig. 3.1). The CR2 is to be moved in direction A and the CR4 rod in direction B. Note that for this task, the graphite blocks located in the outer layer relative to the control and safety rods have graphite blocks in their channels. In Fig. 3.1, this layer is shown in a darker colour.

This task requires the determination of the control rod worth for six distances (L_N) from the core boundary to the axis of the control rod. Table 3.12 provides details on the positioning of the control rods.

TABLE 3.12. POSITIONS OF THE CONTROL RODS

Control rod type	Block coordinates	
	Block No.	L _N (cm)
CR2	h12	12.5
CR4	k5	17.7
CR2	h13	37.5
CR4	l4	53.0
CR2	h14	62.5
CR2	h15	87.5

Interference of a system of control rods

For this problem, the coefficient of interference ξ is defined as;

$$\xi = \frac{\Delta R}{\sum_{i=1}^n \rho_i}$$

where

n is the number of control rods in a given combination;

ΔR is the total worth of the entire system of control rods;

ρ_i is the worth of individual control rod i being inserted in the critical assembly (where only the MR1 manual control rod has been inserted).

Control rods worths are to be determined for single control rods as well as for combinations of two and three rods. See Table 3.13 for the single control rods that is to be investigated and Table 3.14 for the various combinations of rods. For these combinations, it is necessary to determine the worth as well as the interference coefficient.

TABLE 3.13. SINGLE CONTROL RODS TO INVESTIGATE

Control rod(s)	Block coordinates	
	Block No.	L _N (cm)
CR1	d8	13.0
CR2	h12	12.5
CR4	k5	17.7
CR5	h4	12.5

TABLE 3.14. CONTROL ROD COMBINATIONS TO INVESTIGATE

Control rod combinations
CR1 + CR5
CR2 + CR5
CR4 + CR5
CR1 + CR2 + CR5
CR1 + CR4 + CR5
CR2 + CR4 + CR5

3.1.2.3. Differential reactivity of the control rod depending on depth of insertion

This task requires the evaluation of the differential reactivity of the CR5 and MR1 control rods. See Tables 3.15 and 3.16 for the depth at which the CR5/MR1 rods should be inserted.

TABLE 3.15. VARYING POSITIONS OF THE CR5 CONTROL ROD

No.	Depth of the rod insertion in the assembly* (cm)
1	0
2	128.1
3	145.6
4	181.2
5	198.6
6	224.7
7	244.9
8	261.6
9	276.9
10	284.4
11	300.5
12	342.7

*Depth of insertion as measured from the top of the assembly.

TABLE 3.16. VARYING POSITIONS OF THE MR1 ROD

No.	Depth of the rod insertion in the assembly*, (cm)
1	0
2	76.5
3	146.6
4	180.6
5	221.3
6	247.0
7	267.7
8	291.1
9	345.9

*Depth of insertion as measured from the top of the assembly.

3.1.2.4. Investigation of critical parameters with varying height of the pebble bed

For this task, it is required to determine the change in reactivity due to an increase in the height of the ASTRA critical assembly pebble bed. The heights to be considered are shown in Table 3.17.

TABLE 3.17. VARIOUS HEIGHTS OF THE PEBBLE BED THAT ARE TO BE INVESTIGATED

Pebble bed height (cm)
268.9
274.4
281.4
285.9
291.8
297.4
303.5
309.4
315.2
320.8

The benchmark problem then calls for determining the criticality of the system for various configurations as shown in Table 3.18.

TABLE 3.18. VARIOUS CONFIGURATIONS

No	Configuration	Average height of the pebble bed (cm)	Critical position of control rods, (cm)*			
			CR1	CR2	CR5	MR1
1	Without the top reflector and supporting structure	268.9	↑	↑	↑	326.5±26
2	Without the top reflector and supporting structure	285.8	↑	↑	355±2	↑
3	Without the top reflector and supporting structure	320.8	↓	↑	325±1	↑
4	Without the top reflector and supporting structure	320.8	↑	↓	376±1	↑

*Height as measured from the bottom of the assembly. ↑ Indicates rod completely out, ↓ indicates rod completely inserted.

3.2. BENCHMARK PROBLEM ANALYSIS AND RESULTS

This section includes a review of the individual Member State analysis and results of the ASTRA critical facility benchmark problems. The Member States providing this information include China, France, Indonesia, South Africa, Turkey and the United Kingdom. An overall correlation of these results and associated conclusions is provided in Chapter 7, Section 7.2 of this TECDOC.

3.2.1. ASTRA experimental results (submitted by South Africa)

This section provides the experimental results obtained at the ASTRA critical facility (see references from Kurchatov Institute) with which the computational results of the tasks provided in the benchmark description are to be compared.

Note that any calculational results quoted in this section refer to results obtained from calculations performed by the Russian Research Centre Kurchatov Institute in support of the ASTRA critical facility as reported in the progress reports to PBMR Company in South Africa.

Task 1: Height of the pebble bed core

The physical startup of the pebble bed annular core was performed using a special loading device to ensure that the core regions have the required dimensions.

The parameters of the assembly listed in Table 3.19 were noted at criticality:

TABLE 3.19. PARAMETERS NOTED AT CRITICALITY

Parameter	Value	
Pebble bed height	≈	2 689 ± 15 mm
Diameter of the central zone	≈	725 mm
Outer diameter of the mixing zone	≈	1 055 mm
Pebble bed porosity	≈	0.375
Reactivity margin of the assembly with all control/shutdown/manual rods withdrawn	≈	0.1
Total mass of spherical elements in the assembly	≈	7 976.0 kg

Note that the pebble bed height was determined in 14 different positions (different radii and azimuthal angles) and the height varied from 267.5 cm to 290.9 cm. This is to be expected with a randomly packed pebble bed with individual pebble diameters of 6 cm and variations in packing densities. In [3-3], the number of spheres in this configuration was also given as a total of 38584 spheres, with 27477 fuel spheres, 9659 graphite spheres and 1448 absorber spheres. Note that this is the only exact specification and that the values given in Table 3.19 are only approximate values (using the number of fuel spheres, core volume and pebble bed height as input, a slightly different packing density will be obtained).

Task 2: Investigating the worth of control rods

Task 2a: The worth of control rods depending on their position in the side reflector

Figure 3.5 and Table 3.20 indicate the worth of a control rod with increasing distance from the core.

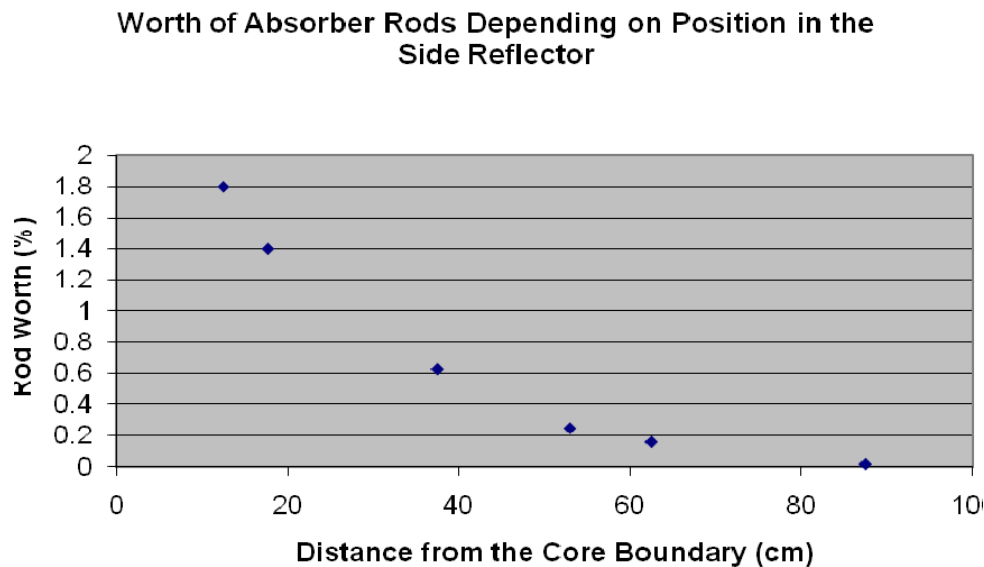


FIG. 3.5. Control rod worth as a function of the distance from the core boundary.

TABLE 3.20. CONTROL ROD WORTH AT VARYING DISTANCES FROM THE CORE

CR Type	Block coordinates		Worth of the CR
	Block No.	L_N (cm)	$\rho_{\text{meas}} (\beta_{\text{eff}})$
CR2	H12	12.5	-2.55
CR2	H13	37.5	-0.88
CR2	H14	62.5	-0.22
CR2	H15	87.5	-0.03
CR4	K5	17.7	-1.95
CR4	L4	53	-0.34
CR5	H4	12.5	-2.53

Task 2b: Interference of a system of control rods

Both individual control rods as well as combinations of two or three control rods were investigated to determine their interference. Refer to Tables 3.21–3.23 for the results.

TABLE 3.21. WORTH OF INDIVIDUAL CONTROL RODS

CR Type	Block coordinates		Worth of the CR Rod
	Block No.	L_N (cm)	$\rho_{\text{meas}} (\beta_{\text{eff}})$
CR1	d8	13	-2.46
CR2	h12	12.5	-2.55
CR4	k5	17.7	-1.95
CR5	h4	12.5	-2.53

TABLE 3.22. WORTH OF CONTROL ROD COMBINATIONS

CR combinations	Worth of the CR combinations
	$\rho_{\text{meas}} (\beta_{\text{eff}})$
CR1 + CR5	-5.16
CR2 + CR5	-5.57
CR4 + CR5	-4.31
CR1 + CR2 + CR5	-8.42
CR1 + CR4 + CR5	-7.15
CR2 + CR4 + CR5	-7.57

TABLE 3.23. INTERFERENCE PARAMETER FOR DIFFERENT CONTROL ROD COMBINATIONS

CR Combinations	Interference Coefficient ξ
	Experiment
CR1 + CR5	1.03
CR2 + CR5	1.09
CR4 + CR5	0.96
CR1 + CR2 + CR5	1.11
CR1 + CR4 + CR5	1.03
CR2 + CR4 + CR5	1.07

Task 3: Differential reactivity of the control rod depending on the depth of its insertion in the assembly

Tables 3.24 and 3.25 show the experimental results for the differential reactivity of the control rods. The same information is shown in Figs 3.6 and 3.7 respectively.

TABLE 3.24. RESULTS OF MEASURING THE CR5 ROD WORTH WITH VARYING POSITION ALONG THE ASSEMBLY HEIGHT

No.	Rod position along the assembly height H (cm)	Depth of the rod insertion in the assembly (H - H ₀) (cm)	Reactivity ρ_{meas} (H-H ₀), (β_{eff})
1	100.6	0	0
2	228.7	128.1	-0.112
3	246.5	145.6	-0.207
4	281.1	181.2	-0.533
5	299.2	198.6	-0.757
6	325.3	224.7	-1.143
7	345.5	244.9	-1.469
8	362.2	261.6	-1.737
9	377.5	276.9	-1.95
10	385	284.4	-2.067
11	401.1	300.5	-2.253
12	443.3	342.7	-2.543

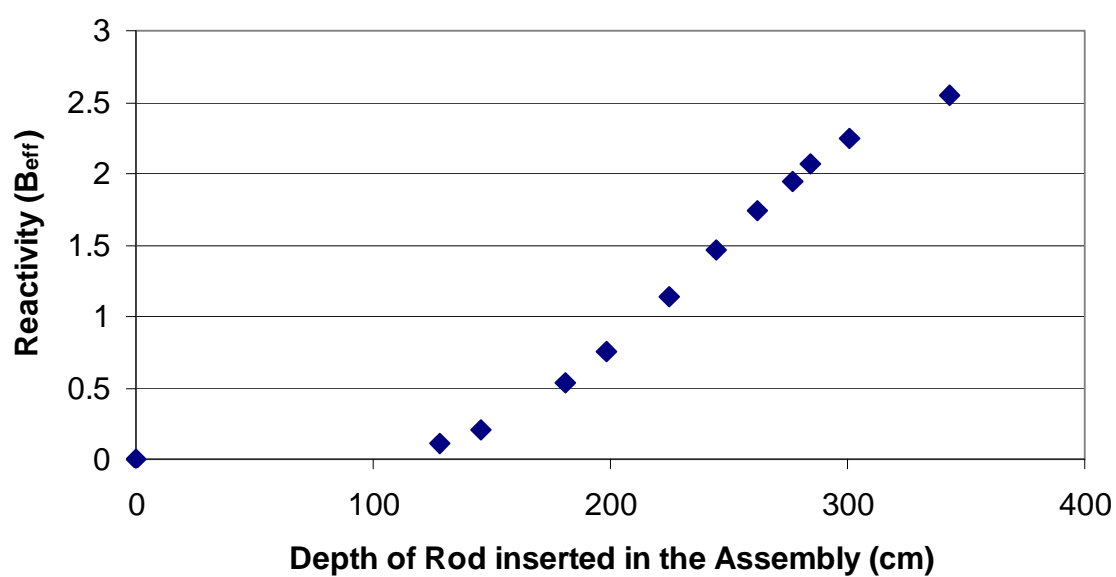


FIG. 3.6. Differential reactivity of the CR5 control rod.

TABLE 3.25. RESULT OF MEASURING THE MR1 ROD WORTH WITH VARYING POSITION ALONG THE ASSEMBLY HEIGHT

No.	Rod position along the Assembly height H (cm)	Depth of the rod insertion in the Assembly (H - H ₀) (cm)	Reactivity $\rho_{\text{meas}} (H-H_0)$, (β_{eff})
1	93.3	0	0
2	169.8	76.5	-0.001
3	239.9	146.6	-0.015
4	273.9	180.6	-0.047
5	314.6	221.3	-0.076
6	340.3	247.0	-0.1
7	361.0	267.7	-0.118
8	384.4	291.1	-0.135
9	439.2	345.9	-0.157

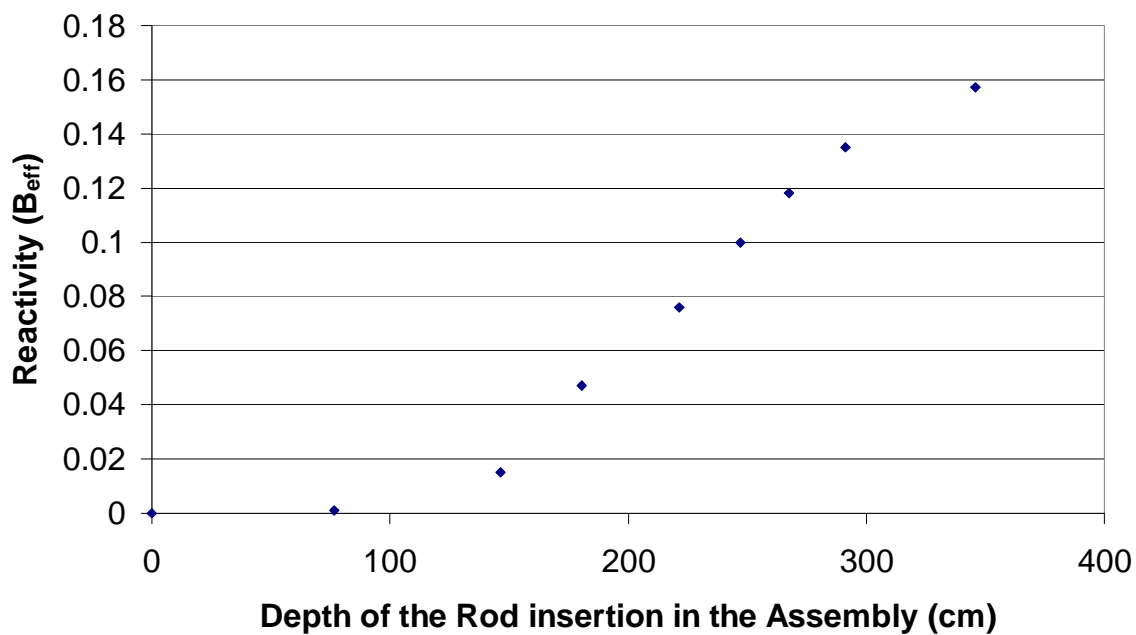


FIG. 3.7. Differential reactivity for the MR1 manual rod.

Task 4: Investigating the critical parameters with varying height of the critical assembly pebble bed

Tables 3.26 and 3.27 show the results of the investigation into the critical parameters. In Table 3.26 the reactivity is shown to increase as the different layers are added. Note that the manual rod and control rods were used to maintain the core critical and that the 'clean core' (without any control or manual rods) reactivity values shown was determined by a procedure based on the control rod worths (and interference) and the addition of small portions of spherical elements loaded in the core to build up its height [3-3].

TABLE 3.26. VARIATION IN THE PEBBLE BED HEIGHT AND ASSEMBLY REACTIVITY MARGIN WHEN LOADING NINE LAYERS OF THE PEBBLE BED

Layer No.	Number of spherical elements	Pebble bed height (cm)	Assembly reactivity margin ρ/β_{eff}	$\Delta\rho/\beta_{\text{eff}}$ for a Given layer
0	38 584	268.9	0.10 ± 0.01	-
1	39 432	274.4	0.64 ± 0.01	0.54 ± 0.01
2	40 280	281.4	1.14 ± 0.01	0.50 ± 0.02
3	41 128	285.9	1.58 ± 0.01	0.44 ± 0.02
4	41 976	291.8	2.01 ± 0.02	0.43 ± 0.02
5	42 824	297.4	2.43 ± 0.02	0.42 ± 0.02
6	43 672	303.5	2.85 ± 0.02	0.42 ± 0.02
7	44 520	309.4	3.26 ± 0.02	0.41 ± 0.02
8	45 368	315.2	3.66 ± 0.02	0.40 ± 0.02
9	46 216	320.8	4.03 ± 0.02	0.37 ± 0.02

TABLE 3.27. EXPERIMENTAL AND CALCULATIONAL RESULTS FOR THE CRITICALITY OF THE ASSEMBLY FOR VARIOUS CONFIGURATIONS

No.	Configuration	Average height of the pebble bed (cm)	Critical position of control rods (cm)				K_{eff}
			CR1	CR2	CR5	MR1	
1	Without the top reflector and supporting structure	268.9	↑	↑	↑	326.5±26	1.000
2	Without the top reflector and supporting structure	285.8	↑	↑	355 ± 2	↑	1.000
3	Without the top reflector and supporting structure	320.8	↓	↑	325 ± 1	↑	1.000
4	With the top reflector and supporting structure	320.8	↑	↓	376 ± 1	↑	1.000

3.2.2. ASTRA results, South Africa

The summary provided here was made from Refs [3-17] and [3-18].

3.2.2.1. Introduction

The deficiencies of diffusion theory to model highly absorbing regions are well known and numerous methods have been developed to calculate the so-called equivalent diffusion parameters. In the PBMR design and in the ASTRA critical facility, the positioning of these highly absorbing regions in the side reflector, where the leakage out of the core adds a directional dependence to the flux, further complicates the problem. Despite these problems, reasonable results have been reported using the Method of Equivalence Cross-sections (MECS) [3-19, 3-20].

This benchmark exercise is therefore of particular importance since the equivalent cross-sections method for pebble-bed-type reactors is evaluated by applying it to calculations of control rod experiments performed at the ASTRA critical facility at the Russian Research Centre Kurchatov Institute in Moscow.

3.2.2.2. Calculation methodology and models

The method of equivalent cross-sections [3-19]

The principle is to model the absorber and its environment in transport theory (S-N) and then extract cross-sections and diffusion parameters from the reference transport solution that will represent the absorber region accurately in subsequent three dimensional diffusion calculations. It involves equating the reaction rates of transport and diffusion theory in the absorber region and outside by relating the leakage rates in the two methods.

The main steps in the method ensure that the volumes of the control rod regions are conserved (and thus material balance) between the transport and diffusion calculations. Equivalence between the transport and the diffusion flux is then assumed at some point outside the absorber region surface. As applied in this study, making use of a one dimensional transport calculation, flux symmetry at points of equal distance from the absorber region (independent of absorber geometry) must also be assumed. Finally, the methodology applied must be consistent with the diffusion code's solution method.

The macroscopic absorption and removal cross-sections for the equivalent absorber region are determined from flux-volume weighting of the selected regions in the one dimensional transport model.

Equivalent boron concentration

A very simplified method used in the analysis, called the Equivalent Boron Concentration (EBC), consists of adding a certain amount of boron absorber homogeneously into a 'borated region' representing the control rod. The concentration of the boron is adjusted so that the control rod worth is conserved. The method assumes that the rod reactivity worth is known from experiment or other methods such as MECS. Although the reactivity of the control rod can be preserved, the flux and reaction rates in the diffusion calculation are not necessarily the correct ones.

When using equivalent boron for the control rod regions, one would normally insert a boron concentration as to equate the worth of the MECS calculation. Since the worth of a control rod at fully inserted was determined experimentally for the ASTRA facility, it is possible to use these results to determine the number density of boron to use. Further calculations, such as differential control rod worth, can then be performed using this density.

The code systems used

The VSOP calculational system [3-21] with the CITATION code as the flux solver was used for the three dimensional ASTRA core calculations. The XSDRNRSP [3-22, 3-23] transport code was used for the transport calculation while a new code (TOTNEW) was developed to calculate the MECS parameters [3-18].

The steps followed in this work can be summarized as follows:

- Perform a 1-D cylindrical unit cell transport calculation for a heterogeneous control rod model (fine group, fine spatial discretization, S-8/P-3);
- Calculate the few-group equivalent macroscopic cross-sections and equivalent diffusion constants;
- Perform the three dimensional ASTRA core calculations in the VSOP code in six groups, making use of the equivalent macroscopic parameters in the absorber region.

More details on the models and calculational approach can be found in [3-17] and [3-18].

The ASTRA core model

For the three dimensional VSOP ASTRA model, a cylindrical geometry was selected. The result of this was that the octagonal core of the facility had to be modelled as a volume-preserving cylinder, 180.6288 cm in diameter. (More detail on how this was verified in [3-17]).

A problem of the cylinderized core is the position of the control rods. Maintaining exact positions (relative to the origin at the core centre) would lead to incorrect distances between the control regions

and the core edge. As expected and confirmed by experiments, the core-to-control-rod distance plays an important part in the worth of the control rods. The rods were therefore modelled in positions corresponding to their equivalent distance from the core. Since the control rods in the ASTRA facility are positioned at various distances from the core and due to mesh restrictions imposed by MECS, the VSOP models have to be defined to either conserve the distance of one specific control rod or to represent an average distance in the case when two or more control rods need to be modelled.

Figure 3.8 shows a representation of the radial and axial model of the ASTRA facility as set up in VSOP.

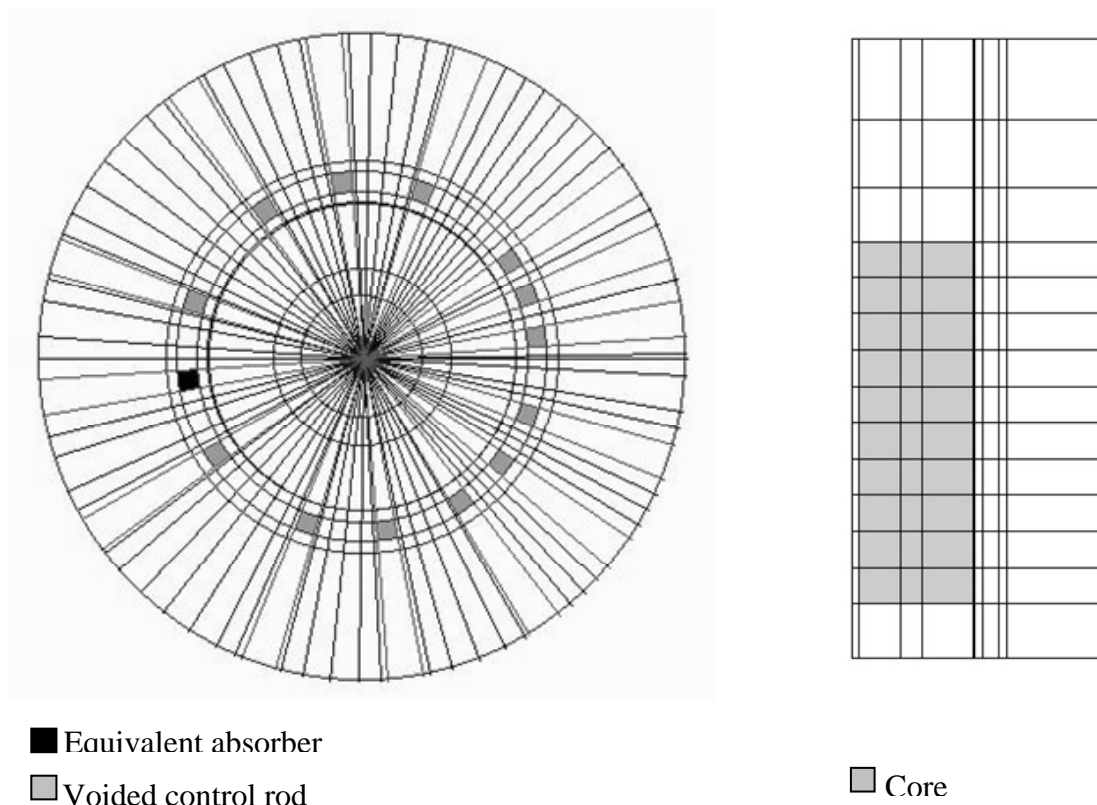


FIG. 3.8. The radial and axial ASTRA geometry representation in VSOP.

Note that the mesh shown corresponds to the material mesh specification and that the mesh was further divided to obtain the converged finite-difference calculational mesh. The radial and angular meshes are chosen so as to conserve the absorber region volume for each control rod region and neighbours, then subdividing the region in between. Axially, the model was subdivided so as to separate the top and bottom reflector. Calculations were performed in six energy groups, one thermal group and five fast groups with the group upper energy boundaries 10 MeV, 1 MeV, 4 keV, 0.4 keV, 29 eV and 1.86 eV. The convergence in the CITATION code was set to be 10^{-5} in k-effective and 10^{-4} for the flux.

3.2.2.3. Benchmark results

The summary provided here was made from Refs [3-17] and [3-18].

Task 1: Height of pebble bed core

The first experiment performed at the facility was attainment of criticality. In the VSOP calculations, a full 3-D model of the ASTRA facility was set up, and the height set to 268.9 cm, the height at which criticality was attained. The porosity factor was assumed to be 0.375.

The k calculated was $1.0053 \pm 0.6\%$, a difference of 530 pcm from the experimental result and within the given measurement uncertainty. An independent full-detail MCNP calculation resulted in a k -value of 1.00400 ± 0.00175 and is thus in very good agreement with the VSOP code's result [3-18].

Task 2: Investigating the worth of control rods

The reactivity for each control rod is given in dollars where the experimentally measured β of 0.0072 [3-11] was assumed.

Task 2a: The worth of control rods depending on their position in the side reflector

The reactivity worth as calculated with the VSOP three dimensional models using MECS parameters for the control rod regions is given in Table 3.28. Note that a separate model was constructed for each control rod position due to the cylindrical model selected and special mesh requirements of MECS.

TABLE 3.28. REACTIVITY WORTH OF INDIVIDUAL CONTROL RODS REPRESENTED BY MECS

CR and block position		Distance from core (cm)	Measured [\$]	VSOP [\$] (MECS)	% Difference
CR2	h12	12.5	-2.55	-2.39	-6.2%
CR2	h13	37.5	-0.88	-0.75	-15.2%
CR2	h14	62.5	-0.22	-0.20	-11.2%
CR2	h15	87.5	-0.03	-0.022	-26.7%
CR4	k5	17.7	-1.95	-1.92	-1.6%
CR5	h4	12.5	-2.53	-2.40	-5.2%

The calculated results compare favourably with the measured values for the control rods positioned in the closest reflector positions (first and last rows). When the results for increasing distances are considered, the differences are generally larger. At larger distances from the core, the error made by diffusion theory is expected to increase but it is evident that the reactivity effect of the control rod also decreases with an associated increase in the relative error.

Task 2b: Interference of a system of control rods

The reactivity worths of individual control rods are given in Table 3.29 for both the measured and the VSOP calculation, making use of MECS. Results compares favourably.

TABLE 3.29. WORTH OF INDIVIDUAL CONTROL RODS
CALCULATED WITH VSOP AND MECS

CR and block position		Distance from core (cm)	Measured [\$]	VSOP [\$] (MECS)	% Difference
CR1	d8	13.0	-2.46	-2.43	-1.3%
CR2	h12	12.5	-2.55	-2.39	-6.2%
CR4	k5	17.7	-1.95	-1.92	-1.6%
CR5	h4	12.5	-2.53	-2.40	-5.2%

The combined reactivity worth of several combinations of rods inserted in ASTRA was compared with the measured result in Table 3.30. In this case, the boron poison fraction (EBC) for each control rod was determined by matching the experimental result and applied in the VSOP calculations. It is therefore only the interference effect that is tested in the analyses since each individual control rod will yield the reference measured value by definition.

TABLE 3.30. REACTIVITY WORTH OF COMBINATION OF CONTROL RODS
EACH REPRESENTED BY ITS EQUIVALENT BORON CONCENTRATION

Control rod combination	Measured [\$]	VSOP [\$] Boron equivalent	Percentage difference
CR1 + CR5	-5.16	-5.12	-0.9%
CR2 + CR5	-5.57	-5.53	-0.7%
CR4 + CR5	-4.31	-4.34	0.8%
CR1 + CR2 + CR5	-8.42	-8.43	0.1%
CR1 + CR4 + CR5	-7.15	-7.31	2.2%
CR2 + CR4 + CR5	-7.57	-7.76	2.5%

The results obtained are satisfactory and it can be concluded that the EBC method can be used to represent the reactivity effects of control rods, provided that an EBC is calculated for each 'type' of control rod (in the sense of design or placement in the core). The interference is thus correctly captured. The interference coefficients are not shown since they will show the same relative differences at the reactivity worth as the experimental worths were matched for the individual control rods.

Task 3: Differential reactivity of the control rod depending on the depth of its insertion in the assembly

In the experiments, the worth of the control rod was measured at various heights of insertion of CR5. In the VSOP calculations, the EBC for the control rod at full insertion was determined by matching it with the measured value and then used for the subsequent differential worth calculations. The results obtained, as shown in Fig. 3.9, are satisfactory and it can be concluded that EBC can be used for differential control rod worth calculations provided, of course, that the total worth is known from measurement or calculated with MECS.

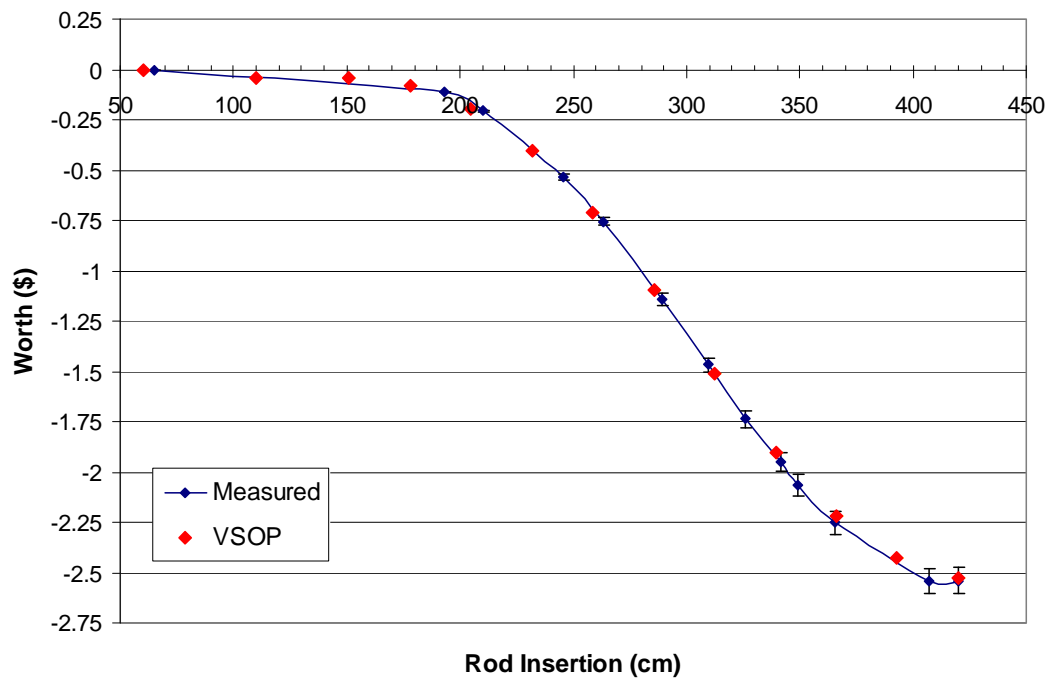


FIG. 3.9. Differential reactivity comparison of the CR5 control rod between VSOP making use of EBC and measurement.

Task 4: Investigating the critical parameters with varying height of the critical assembly pebble bed

The variation of the multiplication factor with the increased height of the pebble bed was calculated with VSOP and the results compared with the measured values in Table 3.31. Some large differences in the reactivity effect for the pebble bed height increase of a few centimetres (or layer) can be seen, but the accumulative effect is predicted with better accuracy. Larger measurement uncertainties are also expected in the measured height used in the analysis than if the number of spheres packed in the facility (not available in the task definition) could be used.

Finally, different critical configurations were calculated representing different pebble bed heights, control rod configurations, and a variation in the presence of the top reflector. The VSOP results are shown in Table 3.32 and compared to the critical configurations. The difference for the first three configurations show good agreement (less than 550 pcm), but the final configuration, with the top reflector in place, shows a larger difference in results.

TABLE 3.31. VARIATION IN THE REACTIVITY MARGIN [\$] WITH INCREASING HEIGHT

Layer No.	Height [cm]	Accumulative reactivity margin [\$]			Reactivity margin for layer [\$]		
		VSOP	Measured	%	VSOP	Measured	%
0	268.9	N/A ²	0.10 ± 0.01				
1	274.4	0.60	0.64 ± 0.01	-9.3	0.50	0.54 ± 0.01	-9.3
2	281.4	1.22	1.14 ± 0.01	7.1	0.62	0.50 ± 0.02	24.0
3	285.9	1.62	1.58 ± 0.01	2.6	0.40	0.44 ± 0.02	-9.1
4	291.8	2.09	2.01 ± 0.02	4.0	0.47	0.43 ± 0.02	9.3
5	297.4	2.54	2.43 ± 0.02	4.5	0.45	0.42 ± 0.02	7.1
6	303.5	3.01	2.85 ± 0.02	5.5	0.47	0.42 ± 0.02	11.9
7	309.4	3.43	3.26 ± 0.02	5.1	0.42	0.41 ± 0.02	2.4
8	315.2	3.80	3.66 ± 0.02	3.8	0.37	0.40 ± 0.02	-8.1
9	320.8	4.18	4.03 ± 0.02	3.7	0.38	0.37 ± 0.02	0.7

TABLE 3.32. VSOP CALCULATIONAL RESULTS FOR THE CRITICALITY OF THE ASSEMBLY FOR VARIOUS CONFIGURATIONS

No.	Configuration	Average height of the pebble bed (cm)	Critical position of control rods (cm)				K _{eff}	
			CR1	CR2	CR5	MR1	Experiment	VSOP Calculation
1	Without the top reflector and supporting structure	268.9	↑	↑	↑	326.5±26	1.000	1.0053
2	Without the top reflector and supporting structure	285.8	↑	↑	355 ± 2	↑	1.000	1.0017
3	Without the top reflector and supporting structure	320.8	↓	↑	325 ± 1	↑	1.000	1.0046
4	With the top reflector and supporting structure	320.8	↑	↓	376 ± 1	↑	1.000	0.9917 ³

3.2.3. ASTRA results, China

3.2.3.1. Facility configuration

The host organization of the ASTRA benchmark problem has provided facility description and calculation task definition in Refs [3-10] and [3-24]. The following statements represent features of the ASTRA facility which INET understands as important ones based on which the calculation has been made.

Figures 3.1 and 3.2 present cross-sectional views of the ASTRA facility. In the radial direction, the facility has the following main features:

- An experimental aluminium tube is designed in the centre of the facility. The tube has an outside diameter of 105 mm and a wall thickness of 2.5 mm.
- Surrounding the aluminium tube is a zone of graphite spheres which is called the inner reflector zone ($52.5 \text{ mm} < R < 362.5 \text{ mm}$).
- Surrounding the inner reflector zone is a zone of mixed spheres consisting of fuel spheres, absorber spheres and graphite spheres at the ratio of 47.5/2.5/50. This zone is called the mixing zone ($362.5 \text{ mm} < R < 527.5 \text{ mm}$).
- Then follows the core zone, which is loaded with fuel spheres and absorber spheres to the ratio of 95/5. The outer surface of the core takes the form of an octagon. The equivalent outer diameter of the core zone is 1810 mm.
- Surrounding the core octagon are all square graphite blocks ($250 \times 250 \text{ mm}$) with central holes (hole diameter 114 mm). These graphite blocks form the side reflector zone. The outer diameter of the side reflector zone is 3800 mm. While some of the blocks are filled with graphite columns, most are not, as is shown in Fig. 3.1.
- Control and measurement devices are arranged in some of the graphite blocks as shown in Fig. 3.1.

In the axial direction, the bottom graphite reflector is 400 mm thick. The top graphite reflector above the core is 600 mm. Between the top reflector and the pebble bed core, there is a ~400 mm high aluminium construction which is the support structure for the top reflector. The facility has an overall height of 4600 mm. The available height for core loading is 3208 mm.

3.2.3.2. *Materials and specifications*

The facility involves among others the following key components:

- Fuel spheres with coated fuel particles;
- Absorber spheres;
- Graphite spheres;
- Reflector graphite blocks.

The specifications of these material components are given in Tables 3.3, 3.4, 3.5, 3.6 and 3.8 of this document.

3.2.3.3. *Task definitions*

The host organization has defined four benchmark calculation tasks for the ASTRA criticality facility [3-16]. Only Task 1 has been performed by INET.

Core height for criticality

The experiment that was performed at the ASTRA critical facility involved increasing the height of the pebble bed core until criticality was reached. At this point, the height of the pebble bed was recorded. Experimental measurements showed that the pebble bed porosity at this time was approximately 0.375. The requirement for this task is thus to determine the height at which the ASTRA facility will achieve criticality, assuming that no control rods or shutdown rods are inserted.

3.2.3.4. *Calculation methodology and modelling*

The Monte Carlo simulation approach has been applied to perform the calculation. The code version used is MCNP-4A.

The geometries of the various zones have been simulated in the three dimensional facility model. Therefore, the model includes the central aluminium tube, the inner reflector zone, the mixing zone, the core zone and the side reflector zone. Graphite blocks are either plugged with graphite columns or remain unplugged according to Fig. 3.1. No control rods have been included into the model as stated in the task definition. The experimental aluminium tubes in the pebbles (designated 1-5 in Fig. 3.1) are considered in the model. The top reflector and aluminium support structure are not considered in the

model, as it is understood that these two components are absent for the experiment case that Task 1 corresponds to.

Theoretically, there are 4188.47 coated particles in the fuel zone of each fuel sphere. To model a fuel sphere, a hexahedron lattice with 2.50006286 mm edge dimension has been used for the fuel zone of a fuel sphere, with each hexahedron containing a coated particle.

Similarly, the absorbing zone of a absorber sphere is modelled with a hexahedron lattice of 0.41446865 mm edge dimension and there are 470655.92 boron carbide particles in the absorbing zone of each absorber sphere.

The arrangement of the spheres in the model is top-to-top in the Z-direction and hexagonal prism lattice in the X-Y plane. The compacting factor of such an arrangement is about 0.62. The core octagon has an equivalent outside diameter of 1806.2 mm.

In the MCNP calculation, continuous energy neutron cross-section data is used. The number of cycles is 140. The number of source neutrons is 10000 per cycle. The number of cycles skipped is 5 for collecting K_{eff} .

The atmosphere in the facility is understood to be air. In the calculation, 0.1013 MPa and 27°C air has been assumed. Moisture is assumed in the air. The moisture is assumed to have a density of 2.57×10^{-5} g/cm³. Total density of the moisture air is taken as 1.175×10^{-3} g/cm³. The nitrogen and oxygen compositions in the air are 75.53% and 23.14% respectively.

3.2.3.5. Calculation results of Task 1

Two core loading heights are simulated, namely, 246 and 258 cm. The calculation results are summarized in Table 3.33.

TABLE 3.33. MONTE CARLO CALCULATION RESULTS FOR ASTRA TASK ONE

Core height (cm)	K_{eff}	Standard deviation	99% Confidence intervals
246	0.99466	0.00083	0.99246-0.99686
258	1.00312	0.00085	1.00088-1.00536

The critical core loading height would be 253.57 cm by interpolation using K_{eff} values in Table 3.33.

3.2.3.6. Comparison and analysis of the calculation results

In comparison with the given critical core loading height of the experimental result of 268.9 cm, the calculation error would be $(253.57-268.9)/268.9 = -5.7\%$ in terms of core loading height. However, from other sources [3-16], the loading height of 268.9 cm corresponds to a configuration where MR1 is at the position of 326.5 cm, and this could have a small effect. Other aspects such as the pebble packing fraction may also have an effect.

3.2.4. ASTRA results, Indonesia

The summary provided here was submitted to the CRP as Ref. [3-25].

BATAN has analysed the core height for criticality of the ASTRA facility based on the calculation results utilizing the WIMS, SRAC and CITATION calculation in two dimensional R-Z reactor geometry. WIMS/D4, which is a cell calculation code, and SRAC-CELL, using a spherical model, were employed to generate group constants of the fuel zone, mixing zone and reflector.

3.2.4.1. Computational model

The core criticality calculation of ASTRA facility was performed according to the flow diagram shown in Fig. 3.10.

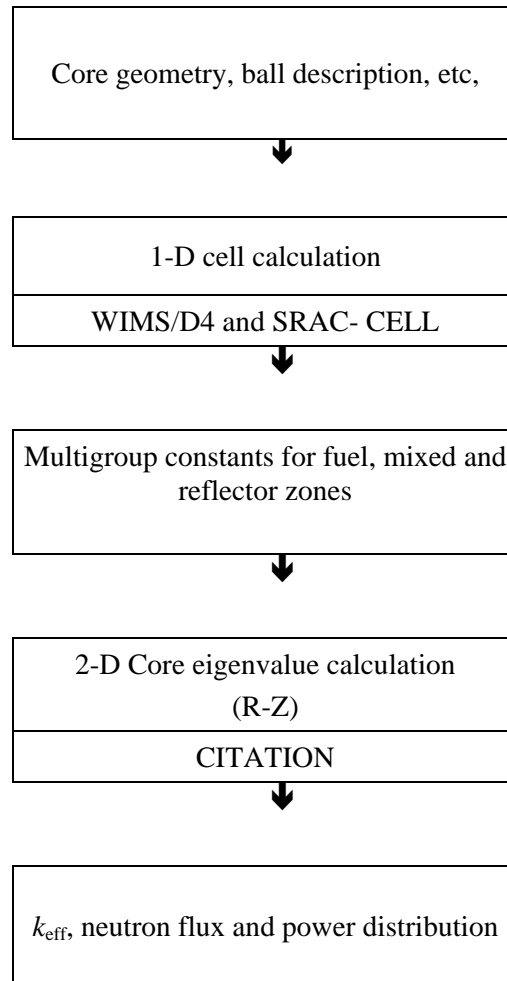


FIG. 3.10. Flow diagram of criticality calculation.

Cell model

The WIMS one dimensional code [3-26] and SRAC-CELL [3-27] were both used for generating macroscopic group constants for fuel, mixed zone and reflector zones. In the WIMSD code calculations, energy groups were condensed from 69 groups to 4 groups, namely, 10 MeV — 821 keV, 821 keV — 5.53 keV, 5530 eV — 0.625 eV and 0.625 eV — 0 eV. While in SRAC CELL code, the energy groups were condensed from 107 groups to 3 groups, namely 10 MeV — 9.1 keV, 9.1 keV — 2.38 eV and 2.38 eV — 1.0-4 eV.

The spherical model of the fuel was used for both WIMS and SRAC code calculation for homogenizing the fuel and absorber balls with the ratio of 95/5. The cell radius of the fuel zone was calculated as follows:

Volume of a cell of fuel zone centred at a fuel ball is

$$V_c = V_p (1 + m)/f,$$

where

m describes the ratio of fuel ball to moderator ball;

f is the packing ratio;

V_p is the volume of a pebble with a radius of 3 cm.

Upon using the data in Table 3.1, one can obtain the following:

$$R_1 = 2.5 \text{ cm};$$

$$R_2 = 3.0 \text{ cm};$$

$$R_3 = (100/95)^{1/3} \times R_2 \cong 3.0517 \text{ cm};$$

$$R_4 = R_3 / (0.625)^{1/3} \cong 3.5693 \text{ cm}.$$

A similar model was used to homogenize the mixed region and obtain the following:

$$R_1 = 2.5 \text{ cm};$$

$$R_2 = 3.0 \text{ cm};$$

$$R_3 = (100/95)^{1/3} \times R_2 \cong 3.0517 \text{ cm};$$

$$R_4 = (100/50)^{1/3} \times R_3 \cong 3.8449 \text{ cm};$$

$$R_5 = R_4 / (0.625)^{1/3} \cong 4.4971 \text{ cm}.$$

A similar evaluation was used to homogenize the reflector or moderator zone.

For the core cavity in the top of the core, an approach developed by Gerwin and Scherer [3-28] was used by incorporating a lower-density graphite in the helium atmosphere. The nuclide composition in this calculation is shown in Table 3.34. The cell models used in this calculation are described in Figs 3.11 and 3.12 for the fuel and mixture zone respectively.

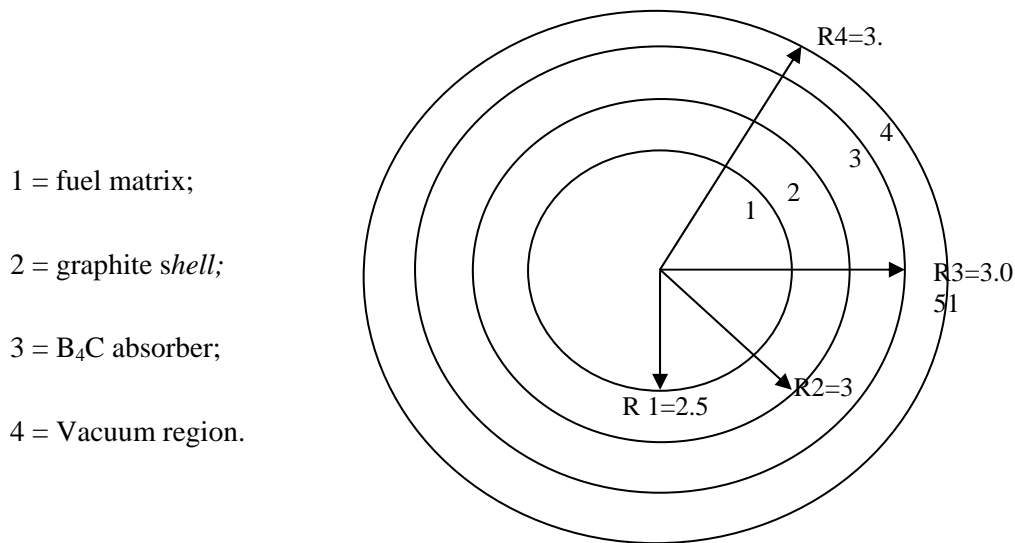


FIG. 3.11. Spherical model for fuel zone (FA/AS).

- 1 = Fuel matrix region;
- 2 = Graphite *shell*;
- 3 = B₄C absorber;
- 4 = Graphite moderator;
- 5 = Vacuum region.

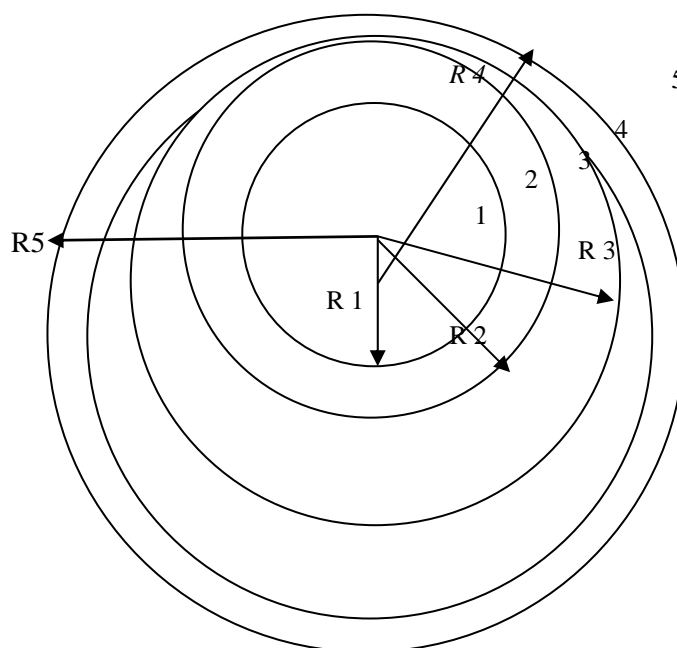


FIG. 3.12. Spherical model for mixed zone (FA/AS/MS).

TABLE 3.34. NUCLIDE COMPOSITION AT FUEL ZONE, MIXED ZONE AND REFLECTOR

Nuclide	Fuel Matrix (ϕ 5 cm)	Graphite shell (t = 0,5 cm)	Absorber B ₄ C	Graphite moderator	Graphite reflector
B-10	1,86888E-9	1,83823E-8	3,23595E-5	1,83823E-8	9,01726E-9
B-11	7,56991E-8	7,44576E-8	1,31073E-4	7,44576E-8	3,65245E-8
Karbon	2,38473E-3	9,28399E-2	6,18411E-2	9,28399E-2	8,28031E-2
Oksigen	1,88775E-4	0,0	0,0	0,0	0,0
Silikon	2,25449E-4	0,0	0,0	0,0	0,0
U-234	1,41582E-7	0,0	0,0	0,0	0,0
U-235	1,95005E-5	0,0	0,0	0,0	0,0
U-236	8,49489E-8	0,0	0,0	0,0	0,0
U-238	7,46608E-5	0,0	0,0	0,0	0,0

3.2.4.2. Criticality calculation

The effective multiplication factor (k_{eff}) was calculated as indicated in Fig. 3.10. First, the cell calculation was performed using the WIMS/D4 code. This was followed by the core calculation with the CITALDI code to solve the neutron flux eigenvalue problem by using diffusion theory approximation from the neutron transport equation through the direct iteration method.

CITALDI is a version of CITATION developed by T. Fowler and released in March 1996 [3-29]. The results of the SRAC-CELL calculation were followed with the core calculation using the CITATION [3-30] module of the SRAC.

The first criticality of the ASTRA facility was achieved after adding some fuel, moderator and absorber balls with a certain ratio to a certain height. This process started from a core height of 190 to 280 cm. The criticality calculation flow diagram with two dimensional R-Z reactor geometry is given in Fig. 3.10.

The side reflector region consisted of reflectors, with and without plugs, divided into three zones, namely, the unplugged reflector zone 1, plugged reflector zone and unplugged reflector zone 2 with their radius R1, R2, and R3 respectively. From Fig. 3.1, it can be known that the numbers of unplugged and plugged rectangular reflectors are 28 and 31 respectively. The radial dimension of the side reflector was then calculated with the formula:

$$\text{Unplugged zone : } \pi (R12 - 90.52) = 28 \times 252;$$

$$\text{Plugged zone : } \pi (R22 - R12) = 31 \times 252, \text{ and the following variables were obtained:}$$

$$R1 \approx 117.31 \text{ cm;}$$

$$R2 \approx 141.17 \text{ cm;}$$

$$R3 \approx 190.00 \text{ cm.}$$

3.2.4.3. Results

The calculation result for the first criticality of ASTRA is shown in Table 3.35. It can be observed that, according to SRAC-CELL results, the effective multiplication factor (k_{eff}) will be exactly one in the fuel loading height of near 220 cm, while the WIMS/D4 result showed that the criticality may be achieved after a loading height of 260 cm. If the WIMS/D4 calculation result was linearly interpolated, the predicted ASTRA first criticality will be achieved with a core height of 259 cm according to WIMS/D4 calculation. As for the SRAC calculation, the results showed that the loading height at criticality was 220 cm with an effective multiplication factor of 1.0016. The WIMS/D4 result is relatively close to INET's Monte Carlo result of 248 cm loading height [3-31].

TABLE 3.35. RESULTS OF CRITICALITY CALCULATION OF ASTRA

Pebble bed height (cm)	k_{eff}	
	SRAC-CELL	WIMS/D4
200	-	0,8905184
210	0.9944	0,9136195
220	1.0016	0,9352059
230	1.0087	0,9554173
240	1.0143	0,9743823
250	1.0199	0,9922202
260	-	1,0090355
270	-	1,0249256

For the HTR, the double-heterogeneity calculation between coated fuel particles in the pebble ball was employed in group constant processing, but in WIMS/D4, this calculation was not carried out. In this case, the homogenous calculation was assumed. The large differences between SPRAC and WIMS/D4 will partially be due to the non-treatment of the double heterogeneity in the resonance self-shielding WIMS/D4 calculation (which also explain why the k_{eff} is lower).

Table 3.36 shows the relative differences of 4.43 and 12.61% compared to MCNP-4A and SRAC95-CITATION calculations respectively. It also shows the comparison of BATAN's calculation results relative to INET's Monte Carlo calculation results. It was shown that the WIMS/D4 result is closer than that of SRAC.

TABLE 3.36. COMPARISON OF CALCULATION RESULTS
FOR CRITICAL HEIGHTS OF ASTRA

MCNP-4A (INET)	SRAC95-CITATION	WIMS/D4-CITALDI
248 cm	220 cm	259 cm

Although not part of the defined problem, the temperature effect on criticality was analysed to understand possible temperature effects (the experiments were done at room temperature). Table 3.37 shows the effect of temperatures on the effective multiplication factors of ASTRA as calculated by the SRAC Code system. The k -effectives at 20°C, 250°C and 500°C at the loading height of 230 cm were 1.0087, 0.9862 and 0.9596 respectively. It was obvious that as temperature increases, the effective multiplication factor decreases.

TABLE 3.37. SRAC CALCULATION RESULTS
FOR TEMPERATURE DEPENDENT ON FULL CORE REACTIVITY

Temperature	k_{eff} (air) (Loading Height = 230 cm)
20°C	1.0087
250°C	0.9862
500°C	0.9595

Axial neutron flux distribution obtained by the CITATION module of the SRAC calculation is shown in Fig. 3.13. The calculation was performed in three energy groups. It can be seen that the neutron flux was relatively flat in the fuelled region of ASTRA. The flux went down in the void region and the upper reflector region at the top of the core as well as in the bottom reflector region.

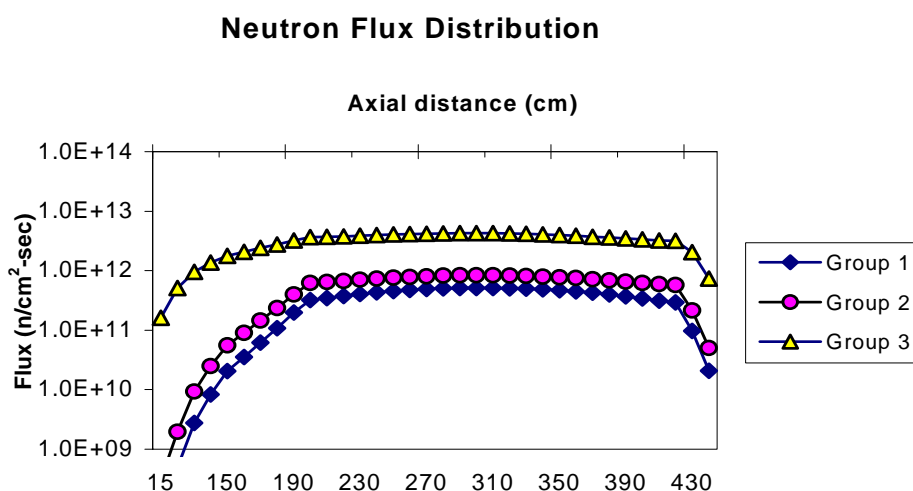


FIG. 3.13. Axial flux distribution in ASTRA.

3.2.5. ASTRA results, Turkey

The summary provided here was submitted to the CRP as Ref. [3-32].

The octagon core of the ASTRA test facility is modelled by the MCNP4B Monte Carlo transport code and the benchmark problems. Criticality calculations for the ASTRA test facility are performed with Monte Carlo particle transport simulations carried out by the MCNP-4B code system. The model of the facility is prepared in two main parts. First, the fuel region is modelled in terms of hexagonal prismatic cells as repeating structures. A layerwise assembly of fuel-graphite-absorber ball mixture with relevant fractions is considered. Therefore, computational steps in criticality analysis were performed by adding new layers with a height of 9.798 cm. Any necessary criticality value in intermediate steps is obtained by linear interpolation using neighbouring layers. Normally, the filling fraction of the assembly is given as 0.625. However, in our case, it is determined to be 0.61 due to the model utilized in this study. The model geometry is presented in Figs 3.14 and 3.15.

Two sets of results are presented here. In the first set (Case I), channels in the reflector region are unplugged. The second set of results (Case II) are obtained as the reflector channels assigned for control, manual and safety rods, experimental channels, ionization chamber and the neutron source are plugged. The gap regions are filled with air at 0.1013 MPa and 27°C with 2.57 mg/cm³ moisture. Initially, it was not clear if these reflector regions were plugged or unplugged during the experiments – the results presented here thus show the sensitivity to the reflector configuration and may assist to explain any discrepancies between the calculations and the experiments.

The following sections present the results obtained in Tables 3.38–3.43. Comparisons with the experimental results and the contributions of other Member States are given in Section 7.2.

3.2.5.1. Results

Task 1: Core height for criticality with no control rods inserted

TABLE 3.38. K-EFFECTIVE VS LOADING HEIGHT

Loading height (cm)	k _{eff} Case I	k _{eff} Case II
201.96	0.93254 ±0.00096	0.94706 ±0.00096
211.76	0.94427 ±0.00101	0.95750±0.00095
221.56	0.95631 ±0.00111	0.96990±0.00101
231.35	0.96782 ±0.00102	0.97856±0.00105
241.15	0.97612 ±0.00099	0.98773±0.00104
250.95	0.98337 ±0.00098	0.99675±0.000102
260.75	0.99336 ±0.00098	1.00449±0.00093
270.55	0.99854 ±0.00099	1.01177±0.00092
280.34	1.00484 ±0.00096	1.01821±0.00099
290.14	1.01389 ±0.00106	1.02521±0.00103
299.94	1.01971 ±0.00105	1.02928±0.00106
309.74	1.02488 ±0.00109	1.03477±0.00099
319.54	1.03053 ±0.00105	1.03942±0.00094
329.33	1.03426 ±0.00101	1.04653±0.00104

The estimated critical height is 270.5 cm for Case I and 255.06 for Case II.

Task 2: Investigation of the worth of control rods**Task 2.1: Worth of control rods depending on their position in the side reflector**

TABLE 3.39. ROD WORTH BY CONTROL ROD NUMBER

Control rod No.	Block No.	Rod Worth (%)	
		Case I	Case II
CR2	H12	1.62	1.83
CR2	H13	0.35	0.85
CR2	H14	0.15	0.28
CR2	H15	0.02	0.14
CR4	K5	1.54	1.60
CR4	I4	0.41	0.83

Task 2.2: Interference of a system of control rods

TABLE 3.40. INTERFERENCE VS CONTROL ROD CONFIGURATIONS

Control rod(s)	Block No.*	Case I		Case II	
		Rod Worth (%)	Interference	Rod worth (%)	Interference
CR1	D8	1.74	-	2.01	-
CR2	H12	1.62	-	1.83	-
CR4	K5	1.54	-	1.60	-
CR5	H4	2.21	-	2.43	-
CR1+CR5	D8+H4	4.13	1.046	4.19	0.94
CR2+CR5	H12+H4	4.39	1.146	4.13	0.97
CR4+CR5	K5+H4	3.41	0.909	3.57	0.89
CR1+CR2+CR5	D8+H12+H4	6.55	1.176	6.32	1.01
CR1+CR4+CR5	D8+K5+H4	5.89	1.073	5.76	0.95
CR2+CR4+CR5	H12+K5+H4	5.91	1.101	5.80	0.99

* Block numbers are used as described in Fig. 3.1.

**Task 3: Differential reactivity of the control rod
depending on the depth of its insertion in the assembly**

TABLE 3.41. REACTIVITY VS DEPTH OF CONTROL ROD CR5 INSERTION

Depth of insertion (cm)	Reactivity (%)
0	0.1378
128.1	-0.0210
145.6	-0.1161
181.2	-0.4884
198.6	-0.5965
224.7	-1.1020
244.9	-1.2863
261.6	-1.4477
276.9	-1.6157
284.4	-1.7553
300.5	-1.8984
342.7	-2.5000

TABLE 3.42. REACTIVITY VS DEPTH OF CONTROL ROD MR1 INSERTION

Depth of insertion (cm)	Reactivity (%)
0	0.1378
76.5	0.0360
146.6	-0.0640
180.6	-0.6259
221.3	-0.8085
247.0	-0.9418
267.7	-1.4178
291.1	-1.4765
345.9	-1.7750

**Task 4: Investigation of critical parameters
with varying height of the critical assembly pebble bed**

TABLE 3.43. PEBBLE BED HEIGHT VS CRITICAL POSITION OF CRS

Average height of the pebble bed	Critical position of control rods(cm)				
	CR1	CR2	CR5	MR1	
270.5	Out	Out	Out	326	1.00184
285.2	Out	Out	355	Out	1.00992
319.5	In	Out	325	Out	1.01042
319.5	Out	In	376	In	1.01182

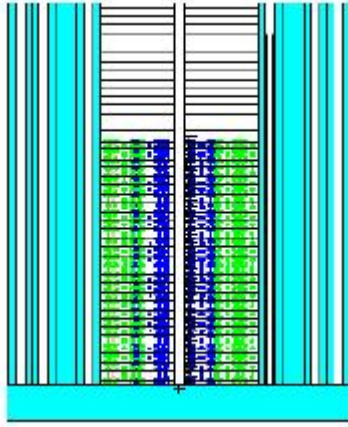


FIG. 3.14. Vertical cross-sectional view of MCNP model for ASTRA test facility.

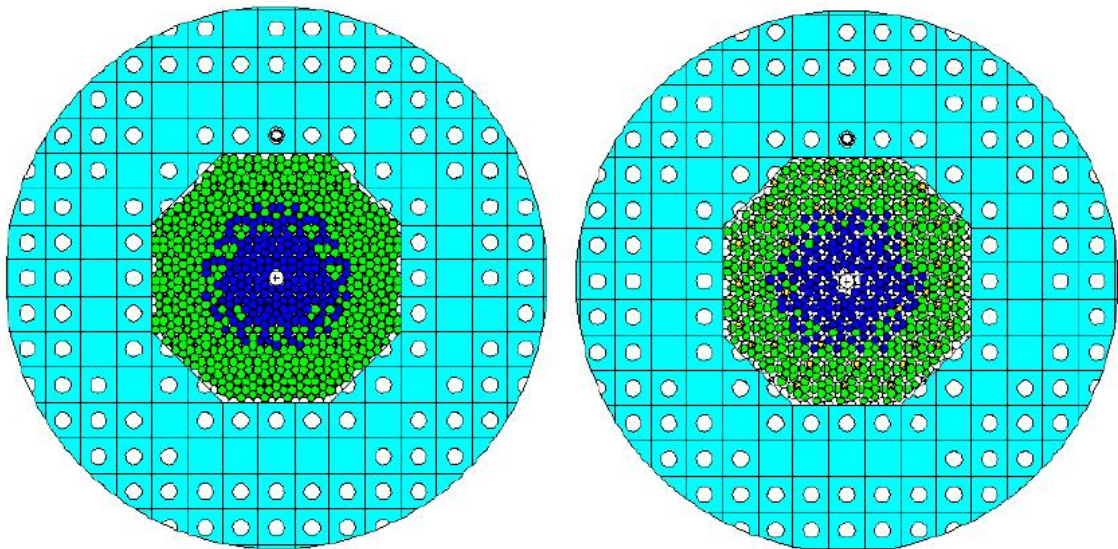


FIG. 3.15. Horizontal cross-sectional views of MCNP model for two different layers at mid- and top-elevations.

3.2.6. ASTRA results, France

3.2.6.1. Introduction

In reactor physics, a multi-concept approach is systematically adopted at CEA throughout the code development, the methods improvement, the validation steps, the nuclear data treatment, etc. The definition of a deterministic calculation scheme for a reactor conceptual study implies qualification and validation phases that always follow the same strategy. A systematic validation against the Monte Carlo code constitutes a preliminary stage performed on a different scale of the reactor model (fuel rod, fuel assembly, two dimensional core and full-scale validation). To do that, the use of NJOY and CALENDF [3-33] codes provides means to generate coherent nuclear data for both the deterministic codes and for the Monte Carlo code. This coherence allows comparing both types of codes using cross-sections of the same origin.

In an HTR, on the one hand the fuel in a form of dispersed particles, and on the other hand the treatment of the pebble bed core, impose a stochastic approach to the geometry in the Monte Carlo calculations. This may question the principle of the reference that today constitutes the Monte Carlo methods with regard to the deterministic methods. Such critical experiments as ASTRA and PROTEUS and HTR-10 are particularly well suited for the validation of Monte Carlo codes, because the composition of fresh fuel is very well known and room-temperature cross-section libraries are readily available.

3.2.6.2. Codes and previous PBR studies

In the following ASTRA calculations, the TRIPOLI-4.3 French reactor physics transport code [3-34] has been used. As indicated in Fig. 3.16, the data libraries used throughout the study are based on JEF2.2 and have been processed with the THEMIS/NJOY code.

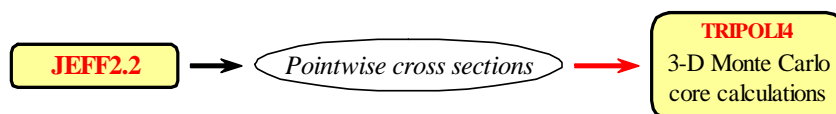


FIG. 3.16. Library and Monte Carlo code used for the calculation.

TRIPOLI4 is a three dimensional code that uses the Monte Carlo method. It can be used to simulate the transport of neutrons, photons, electrons and positrons for shielding calculations (long-distance propagation with flux attenuation) and neutronic calculations (criticality and subcriticality basis). This makes it possible to compute k_{eff} , flux, currents, reaction rate and multigroup cross-section. TRIPOLI4 allows calculations with continuous description in terms of cross-section energy and multi-group homogenized cross-sections. Surface and combinational geometrical representations are both available. The code uses cross-section libraries in ENDF/B format (such as JEF2.2, ENDF/BVI and JENDL) for point description and cross-sections in APOTRIM format (from the APOLLO2 code) specific to TRIPOLI4 for multigroup descriptions.

Previous calculations performed on the HTTR and HTR-10 were done on the basis of the same TRIPOLI4 code but with specific assumptions [3-35]:

- In the HTTR, a calculation scheme based on a Multigroup Transport/Monte Carlo method led to the Coated Fuel Particles (CFPs) being treated as a homogeneous medium with 172 gr self-shielded cross-sections coming from a previous transport calculation. Since that time, other HTGR modelling with TRIPOLI4 has been done on the PROTEUS [3-36] experiment and
- HTR-10 [3-37] and block-type reactors [3-38] and confirmed, on the basis of comparison with explicit CFP description, that this homogenous approach is validated;
- In the HTR-10, significant discrepancies occurred between the experimental result and the calculations due to the pebble bed description. A Face-Centred-Cubic pebble lattice in the core cavity with randomly removed pebbles in order to get the actual filling fraction [3-35]. After

that, a new pebble bed arrangement was set up respecting the actual filling fraction and lead to a good accordance with the experimental values [3-37]. These studies have shown that the pebble arrangement in a PBR is important for Monte Carlo methods. On the contrary, it has been shown that the system reactivity is insensitive to the type of arrangement of fuel particles in the fuel pebble.

In summary, the TRIPOLI4 results reproduced the system reactivity observed experimentally on both PBR cores (HTR-10 and PROTEUS [3-36, 3-37]) quite well. The present ASTRA simulations have been performed in order to complete these previous TRIPOLI4 simulations.

3.2.6.3. Coated fuel particles description in the fuel spheres

A fine description of the CFP has been done in TRIPOLI4 accounting for the different coatings of the uranium kernel. In the actual fuel spheres these particles are randomly distributed in a graphite matrix. In the model, two different treatments of this inner fuel zone of the fuel spheres were adopted. The CFP were uniformly placed according two regular lattices: the first one is a cubic lattice, the other one is a simple hexagonal column lattice with an edge of 0.151 cm and a height of 0.262 cm. Figures 3.17 and 3.18 depict an example of the CFP arrangement obtained in ASTRA. While preliminary core calculations showed no real differences between both CFP arrangements, the hexagonal lattice was kept in most of the core models used hereafter.

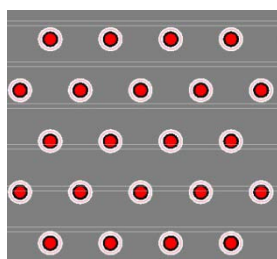


FIG. 3.17. Fuel pebble description in TRIPOLI4: Hexagonal CFP lattice.

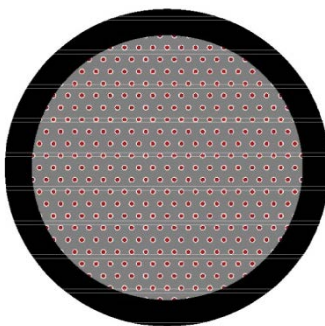


FIG. 3.18. Fuel pebble description in TRIPOLI4: Simple cubic CFP Lattice.

3.2.6.4. Fuel pebble description in the core cavity

As far as the three dimensional core model is concerned with TRIPOLI4, the reflector, the main channels in reflector and all the other important components were described in detail except the supporting structure and the top reflector (aluminium and graphite) which have been considered separately. Nevertheless, according to the stochastic features of the core cavity geometry, different assumptions have been made to describe the arrangement of the spheres in the core.

Packing fraction

First of all, a Column-Hexagonal-Point-on-Point (CHPOP) arrangement of the pebble bed has been chosen to describe the core cavity. This arrangement of balls corresponds to a hexagonal prism lattice

in the X-Y plane and is top-to-top in the Z-direction. The theoretical CHPOP filling factor of 0.6046 is very close to the one observed experimentally in cores like those of the HTR-10 and PROTEUS (~ 0.61). However, the ASTRA benchmark data pack mentioned a packing fraction of 0.625. Therefore, an adjustment of the radius for all types of pebbles (fuel, graphite and absorber) was made in order to respect this higher packing fraction. In this condition, the simulated packing fraction is exactly the actual one. The very small modification of the pebble's radius led to a slightly higher graphite shell density of the fuel and absorber spheres and a higher graphite density for the graphite spheres. The graphite mass balance per pebble was then preserved.

In order to quantify the impact of a more dense shell of the fuel pebble on the reactivity and the neutron balance, some calculations of one fuel pebble in infinite medium surrounding with helium or moist air have been performed. Only the shell thickness and its density were modified. The analysis has been carried out on $\sim 21\%$ enriched pebbles of two different sizes, namely, 3 cm (the original one) and 2.967 cm (the geometry used in ASTRA calculations). It turned out that no significant discrepancies appeared between the different cases for both the reactivity and the neutron spectrum.

Respect of the proportion between the different types of pebbles

As shown in Fig. 3.19, the coolant and all the structures of the pebbles (fuel and moderator) loaded into the core have been described explicitly. The fuel-to-moderator pebble ratio of the ASTRA core loading was taken into account with the help of a specific treatment. A basic pebble cluster (hexagonal regular lattice in X-Y plane) was defined. The number of pebbles involved in that cluster was adjusted in order to get a good proportion and distribution of the fuel, graphite and absorber pebbles. Finally, this cluster was radially duplicated to fill the core cavity.

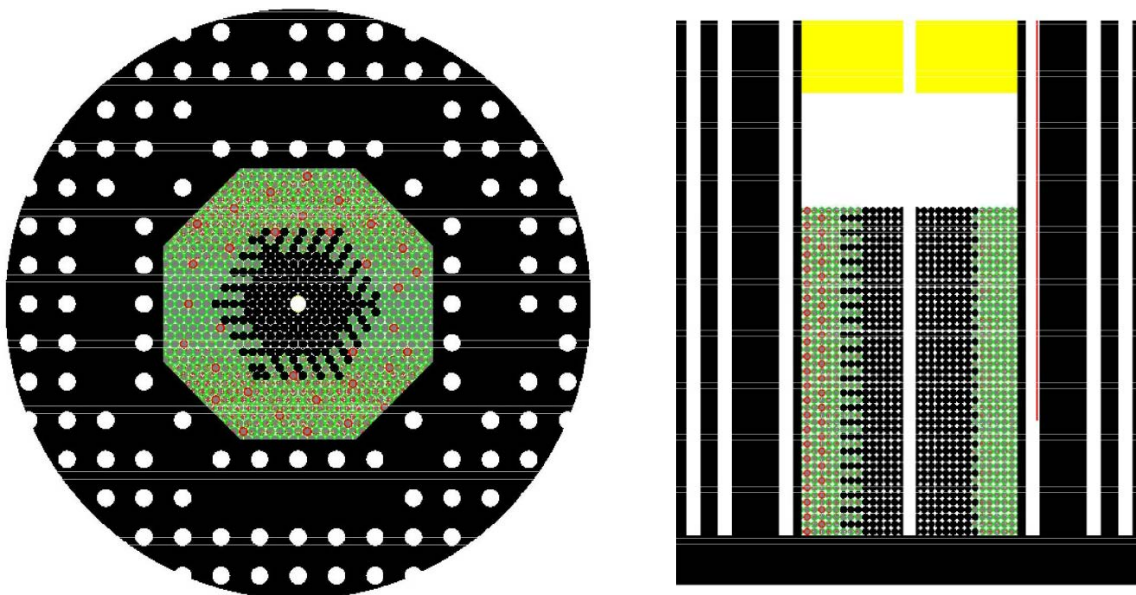


FIG. 3.19. Core modelling in Monte Carlo code TRIPOLI4.

Pebble bed modelling: absorber spheres and neutron streaming

Although each layer is superposed in the axial direction, it is worth mentioning that the absorber spheres make an artificial column in the simulation and could minimize the global boron absorption rate. In order to avoid that configuration, the basic pebble cluster previously defined was differently oriented (turned in the radial direction) as a function of the axial direction.

Finally, it is worth noting that the CHPOP arrangement leads to an ‘artificial neutron streaming’ created by the axial superposition of the inter-pebble voids. This phenomenon can be avoided when each layer is radially shifted by a half pebble distance. This shifted arrangement has been tested on the HTR-10 and compared to the original CHPOP. The small discrepancies evaluated from the HTR-10

three dimensional calculations allowed us to keep the original CHPOP arrangement in the ASTRA simulations.

Control rods modelling

One control rod has been modelled in the side reflector of ASTRA. Fifteen B₄C small rods housed in an outer sleeve of stainless steel have been assumed. In TRIPOLI4, all these stainless steel tubes containing the B₄C small rods have been explicitly modelled according to a circular arrangement as described in the benchmark data pack (Fig. 3.20). In the second step, the MR1 control rod in aluminium has been modelled.

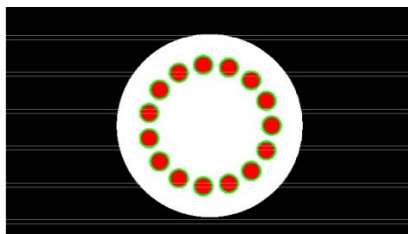


FIG. 3.20. Control rod modelling in TRIPOLI4.

3-D Core calculation results

One of the ASTRA configurations among those proposed in the benchmark has been investigated. In this case, the core height was fixed at 268.9 cm and the MR1 control rod was inserted until 326.5 cm (configuration no.°1 of the Task 4). It should be noticed that in this configuration, criticality has been achieved experimentally. Several sets of three dimensional core simulations have been performed with the TRIPOLI4 Monte Carlo code, taking into account the different CFP modelling as described previously. Nevertheless, only the CHPOP regular arrangement has been considered with respect to the core models of each case.

Calculational Task 1 and Task 4

First of all, the reactivity worth due to the presence of the supporting structure and the graphite reflector (Fig. 3.18) had been evaluated to 0.4% $\Delta k/k$ and presented at one of the coordinated meetings of the present CRP-5. After clarification, it turned out that no top reflector was present in this experiment and no structures (loading device) above the pebble bed should be modelled.

In the first phase, different three dimensional core simulations have been performed assuming that the MR1 control rod was in boron.

Table 3.44 gathers all the results for two different core heights (267.08 and 272.96 cm) corresponding to two different numbers of layers of pebbles. In this way, it becomes possible to evaluate either the critical height of pebbles (number of pebbles to get the core critical) or the k_{eff} factor for a given height of pebbles. First, these Monte Carlo calculations complete the previous results obtained on the core of the HTR-10 and PROTEUS. It had been shown that the system reactivity was insensitive to the type of arrangement of fuel particles in the fuel pebbles. This also remains true for ASTRA. Secondly, preliminary observation let believe that the results were in quite good accordance with the experiment (38584 pebbles). Indeed, in that condition, the TRIPOLI4 results slightly underestimate the core reactivity. The maximum underestimation would be 0.5% in terms of the critical height, which represents approximately about 200 pebbles in the core cavity. The discrepancies with the experiment in term of reactivity would then be less than 0.1%.

TABLE 3.44. CORE REACTIVITY AND NUMBER OF PEBBLES
AS A FUNCTION OF THE CORE HEIGHT AND THE CORE MODELS (MR1 IN BORON)

Pebble bed height in TRIPOLI4	CFPs	Core Model	Core $k_{\text{eff}} \pm \sigma$	$H_{\text{crit.}}$ [cm]	Estimated k_{eff} at 268.9 cm
H = 267.08 cm	HEX	CHPOP	0.99787 ± 0.00077	270.1	0.99916
H = 272.96 cm	HEX	CHPOP	1.00208 ± 0.00075	38111	
H = 267.08 cm	CUB	CHPOP	0.99772 ± 0.00076	270.4	0.99895
H = 272.96 cm	CUB	CHPOP	1.00173 ± 0.00077	38153	

In the second phase, the MR1 operating control rod was assumed in aluminium. The results provided in Table 3.45 indicate on the contrary an overestimation of the reactivity up to 1% corresponding to a smaller estimated critical height of pebbles (~ 10 %). Nevertheless, it is important to note that this last value is very close to the former MCNP results presented by China [3-31] within that CRP-5.

TABLE 3.45. CORE REACTIVITY AND NUMBER OF PEBBLES
AS A FUNCTION OF THE CORE HEIGHT (MR1 IN ALUMINIUM)

Pebble bed height in TRIPOLI4	CFPs	Core model	Core $k_{\text{eff}} \pm \sigma$	$H_{\text{crit.}}$ [cm]	Estimated k_{eff} at 268.9 cm
H = 267.08 cm	HEX	CHPOP	1.01101 ± 0.00068	~ 243 34287	1.01185
H = 272.96 cm	HEX	CHPOP	1.01373 ± 0.00071		

Absorber spheres distribution

Previous studies ([3-35] and [3-37]) have shown that a well-adapted regular lattice for describing the pebbles is able to provide a good representation of the actual random distribution of the spheres if some precautions are taken into account. In the ASTRA facility, three different kinds of pebbles (fuel, graphite and absorber) have to be considered in a core cavity. That yields much more difficult the description of random geometry with a regular arrangement [3-39]. Indeed, it turns out that the unknown position of the boronated spheres could have a strong impact on the system reactivity, depending on the near or far position from the graphite reflectors.

In order to quantify this effect, different distributions of the boron spheres have been simulated with TRIPOLI4 assuming three different radial positions of these spheres inside the mixing zone. Only a part of the boron spheres has been placed successively close to the inner reflector, in the middle of the mixing zone, and finally at the periphery of the mixing zone. The results are gathered in Table 3.46. It turns out that for two extreme positions of the absorber spheres in the mixing zone, the discrepancy between the simulations could achieve more than ten times the standard deviation given by the Monte Carlo code. Moving the boron pebbles towards an outer location (along the annular fuel zone) apparently corresponds to favouring the thermal neutron spectrum in the mixing zone, increasing the system reactivity. Moreover, the absorption in those pebbles might also be minimized because of the harder neutron spectrum existing in the annular core zone.

TABLE 3.46. EFFECT OF DIFFERENT ABSORBER SPHERES DISTRIBUTIONS IN THE MIXING ZONE

Absorber sphere position	Pebble bed height in TRIPOLI4	Core $k_{\text{eff}} \pm \sigma$	$H_{\text{crit.}}$ [cm]	Estimated k_{eff} at 268.9 cm	$\Delta k/k$
Inner	H = 267.08 cm	0.99713 ± 0.00042	271.1	0.99844	-0.07 %
	H = 272.96 cm	1.00137 ± 0.00042	38252		
Central	H = 267.08 cm	0.99787 ± 0.00077	270.1	0.99916	-
	H = 272.96 cm	1.00208 ± 0.00077	38111		
Outer	H = 267.08 cm	1.00152 ± 0.00042	264.8	1.00276	0.36 %
	H = 272.96 cm	1.00553 ± 0.00041	37263		

Similar calculations were carried out, this time by shifting the boron pebbles located in the annular fuel zone of the core, leading to the same amplified effect, i.e. up to 1.4% of excess of reactivity could be achieved compared to a standard situation ('Normal' in Table 3.47) where the absorber pebbles would be uniformly distributed. Among the possible explanations for this extreme case, there is on the one hand a possible shadowing effect obtained by gathering together the absorber pebbles, and on the other hand an increase of the thermal neutron spectrum in the annular zone as already observed in the mixing zone.

Finally, the three cases analysed Table 3.47 have been reproduced with the MR1 control rod in aluminium. The results presented in one of the coordinated meetings of the present CRP-5 show identical effects. As it could be observed in those tables on the whole, the simulated core configurations indicate an increase of the reactivity and cannot explain the overestimated reactivity of the previous calculations (Table 3.45). Additional analyses should be performed to see whether or not other core configurations could lead to an inverse physical effect for which this overestimated reactivity would be counterbalanced by some specific absorber spheres arrangements.

TABLE 3.47. EFFECT OF DIFFERENT ABSORBER SPHERES DISTRIBUTIONS IN THE ANNULAR FUEL ZONE

Absorber sphere position	Pebble bed height in TRIPOLI4	Core $k_{\text{eff}} \pm \sigma$	$H_{\text{crit.}}$ [cm]	Estimated k_{eff} at 268.9 cm	$\Delta k/k$
Central	H = 267.08 cm	1.00024 ± 0.00039	266.6	1.00126	0.21%
	H = 272.96 cm	1.00354 ± 0.00039	37617		
Normal	H = 267.08 cm	0.99787 ± 0.00077	270.1	0.99916	-
	H = 272.96 cm	1.00208 ± 0.00077	38111		
Outer	H = 267.08 cm	1.01246 ± 0.00039	245.6	1.01353	1.43%
	H = 272.96 cm	1.01592 ± 0.00039	34654		

3.2.6.5. Conclusion

The ASTRA core physics benchmarks have been partially treated with the TRIPOLI-4.3 Monte Carlo code. Table 3.48 summarizes the results. The fully detailed three dimensional calculations lead to an overestimation of the reactivity greater than 1% with regard to the available experimental results [3-3, 3-17]. However, the results are in good accordance with the MCNP calculations also performed in the framework of CRP-5 [3-31].

In addition, Table 3.48 shows that the packing fraction of 0.625 and the critical height of 268.9 cm given in the benchmark data pack are not consistent with the number of pebbles (38584) observed experimentally. Nevertheless, these differences are not sufficient for explaining the reactivity overestimation of 1% coming out of the Monte Carlo calculations. According to these first results, most of the work has been devoted to trying to explain the discrepancies.

TABLE 3.48. SUMMARY OF THE PRESENT STUDY

Tripoli4 - MR1 in boron	Experiment — MR1 in aluminium	Tripoli4 — MR1 in aluminium
38111 pebbles	38584 pebbles	34287 pebbles
270.1 cm - (0.625)	273.4 cm - (0.625) 268.9 cm - (0.635)	~ 243 cm - (0.625)

Finally, these Monte Carlo calculations complete the previous results obtained on the core of the HTR-10 and PROTEUS. They confirm the negligible influence of the manner used to describe the fuel particles inside each pebble. On the contrary, it turns out that it is more difficult than in HTR-10 and PROTEUS to define a regular lattice which would provide a good representation of the actual random distribution of the pebbles in the ASTRA experiment. Indeed, three different kinds of pebbles (fuel, graphite and absorber) have to be considered in a core cavity, which itself is made up of three different regions. Due to the unknown position of this small amount of absorber pebbles, the core reactivity estimation could only be given with an additional uncertainty related to the unknown geometry. The treatment of the stochastic geometry questions the principle of the Monte Carlo method as an absolute reference for that type of core. However, it should be stressed that the specific ASTRA's core configuration, with a small amount of absorber spheres distributed among the pebble bed, remains far from a standard core configuration of a power reactor.

3.2.7. ASTRA results, United Kingdom

Introduction

The ASTRA critical facility at the Russian Research Centre Kurchatov Institute has been used for neutron physics investigation of the PBMR reactor. A benchmark with regard to the prediction of the critical height of the PBMR core in ASTRA has been specified. The analysis of the benchmark presented here relates specifically to the critical height without absorbers.

Within the United Kingdom, this study has been performed in conjunction with and was funded by the NNR of the RSA.

Method of calculation

The analysis of the benchmark has been performed using the WIMS9 thermal reactor code scheme [3-40, 3-41]. WIMS9 contains a large number of modules for representation of different types of thermal reactor. A calculation route is set up using appropriate modules for the reactor type which communicate with each other via data interfaces.

WIMS9 contains a largely JEF2.2-based cross-section library in the 172 energy groups shown in Table 3.49. The calculations presented here have used the full 172 groups of this library.

The main WIMS modules used for this benchmark are:

- PIJ: A two dimensional collision probability module which is used to represent radial models of the core for the production of reflector cross-sections;
- FLURIG: A one dimensional collision probability module which is used to represent graphite pebbles which do not contain fuel;
- PROCOL: A collision probability module which represents all the levels of heterogeneity present in a PBMR pebble. That is, fuel particles with their various coatings are represented within a

graphite matrix, which in turn is surrounded by a pure graphite layer to represent the whole pebble. Homogenized fuel cross-sections are produced for the pebbles and associated coolant;

- SNAP: A mesh-centred, finite-difference and diffusion theory module which was used for this problem in R-Z geometry, to represent the whole core and reflectors.

The general method of calculation used for the ASTRA core has been to produce homogenized cross-sections for the pebble bed and reflectors using WIMS9 collision probability cell models in which geometric details are represented. The homogenized cross-sections are then fed into the diffusion theory module representing the overall geometry of the ASTRA core. A PIJ radial model was used to produce reflector cross-section data with BEHRENS streaming corrections [3-42] for the reflector blocks containing central holes. These reflector cross-sections are combined with fuel and graphite pebble cross-sections and fed into the SNAP diffusion theory module. Diffusion coefficients for the void region above the core were produced using the method of Gerwin and Scherer [3-28].

With the geometric options available within SNAP, it was not possible to precisely model the outer octagonal geometry of the ASTRA fissile zone. An R-Z geometry model was therefore set up with equivalent volumes of core and reflector regions. The model is shown in Fig. 3.21.

Neutronics model

The prediction of the k-effective using finite-difference methods has some dependence on the size of the meshes used. To remove this dependence, three separate sets of mesh sizes have been used to extrapolate to zero mesh size assuming a linear dependence of reactivity on the square of the mesh dimension. The radial meshes used are given in Table 3.50. Axial meshes of 5, 10 and 20 cm were employed.

These meshes were applied to a core with 260 cm fissile height to derive corrections to the reactivity, which can then be applied to the SNAP k-effective using the finest mesh. It was assumed that these corrections would be insensitive to fissile height and could be applied to SNAP cases at other fissile heights. Further SNAP runs were performed at fissile heights of 265 and 270 cm, using the finest radial and axial meshes, and quadratic interpolation was used to determine the critical core height. In all calculations, temperatures have been assumed to be 300 K.

Results

Corrections for mesh size

The results of the analysis of the effect of mesh size at a fissile height of 260 cm are presented in Table 3.51. Trendlines have been fitted to the variation of k-effective with square of the mesh size in Figs 3.22 and 3.23 for the radial and axial mesh refinements. These give corrections to zero mesh size of -2 pcm axially and +25 pcm radially, a net correction of +23 pcm.

Calculation of critical fissile height

Using the fine mesh model, the results of the SNAP calculations at fissile heights of 260, 265 and 270 cm are given in Table 3.52 together with k-effectives corrected to zero mesh size. The corrected k-effectives are plotted in Fig. 3.24, where a quadratic is fitted for the purpose of interpolation. The critical fissile height is estimated to be 263.4 cm.

Effect of the gerwin and Scherer diffusion coefficients

The sensitivity to the use of the Gerwin and Scherer diffusion coefficients for the void region has been assessed for the 260 cm core. A further case was run in which this region was modelled with cross-sections for air at 1 bar, which resulted in a k-effective of 399 pcm lower. This reduction in reactivity translates into an estimated critical height of 269.5 cm.

Conclusions

The best estimate of the critical height of the ASTRA core is that derived using the Gerwin and Scherer diffusion coefficients and amounts to 263.4 cm. However, there is some sensitivity of the core height to the diffusion coefficients used in the void region above the active core.

TABLE 3.49(A). ENERGY GROUP STRUCTURE OF THE WIMS9 CROSS-SECTION LIBRARY
(GROUPS 1–92)

Group	Lower energy	Upper energy	Group	Lower energy	Upper energy
	E ₁ (eV)	E ₂ (eV)		E ₁ (eV)	E ₂ (eV)
1	1.733E+07	1.964E+07	47	5.531E+03	7.466E+03
2	1.492E+07	1.733E+07	48	5.005E+03	5.531E+03
3	1.384E+07	1.492E+07	49	3.527E+03	5.005E+03
4	1.162E+07	1.384E+07	50	3.355E+03	3.527E+03
5	1.000E+07	1.162E+07	51	2.249E+03	3.355E+03
6	8.187E+06	1.000E+07	52	2.035E+03	2.249E+03
7	6.703E+06	8.187E+06	53	1.507E+03	2.035E+03
8	6.065E+06	6.703E+06	54	1.434E+03	1.507E+03
9	5.488E+06	6.065E+06	55	1.234E+03	1.434E+03
10	4.493E+06	5.488E+06	56	1.010E+03	1.234E+03
11	3.679E+06	4.493E+06	57	9.142E+02	1.010E+03
12	3.012E+06	3.679E+06	58	7.485E+02	9.142E+02
13	2.466E+06	3.012E+06	59	6.773E+02	7.485E+02
14	2.231E+06	2.466E+06	60	4.540E+02	6.773E+02
15	2.019E+06	2.231E+06	61	3.717E+02	4.540E+02
16	1.653E+06	2.019E+06	62	3.043E+02	3.717E+02
17	1.353E+06	1.653E+06	63	2.040E+02	3.043E+02
18	1.225E+06	1.353E+06	64	1.486E+02	2.040E+02
19	1.108E+06	1.225E+06	65	1.367E+02	1.486E+02
20	1.003E+06	1.108E+06	66	9.166E+01	1.367E+02
21	9.072E+05	1.003E+06	67	7.567E+01	9.166E+01
22	8.208E+05	9.072E+05	68	6.790E+01	7.567E+01
23	6.081E+05	8.208E+05	69	5.560E+01	6.790E+01
24	5.502E+05	6.081E+05	70	5.158E+01	5.560E+01
25	4.979E+05	5.502E+05	71	4.825E+01	5.158E+01
26	4.505E+05	4.979E+05	72	4.552E+01	4.825E+01
27	4.076E+05	4.505E+05	73	4.017E+01	4.552E+01
28	3.020E+05	4.076E+05	74	3.727E+01	4.017E+01
29	2.732E+05	3.020E+05	75	3.372E+01	3.727E+01
30	2.472E+05	2.732E+05	76	3.051E+01	3.372E+01
31	1.832E+05	2.472E+05	77	2.761E+01	3.051E+01
32	1.228E+05	1.832E+05	78	2.498E+01	2.761E+01
33	1.111E+05	1.228E+05	79	2.260E+01	2.498E+01
34	8.230E+04	1.111E+05	80	1.945E+01	2.260E+01
35	6.738E+04	8.230E+04	81	1.593E+01	1.945E+01
36	5.517E+04	6.738E+04	82	1.371E+01	1.593E+01
37	4.087E+04	5.517E+04	83	1.122E+01	1.371E+01
38	3.698E+04	4.087E+04	84	9.906E+00	1.122E+01
39	2.928E+04	3.698E+04	85	9.190E+00	9.906E+00
40	2.739E+04	2.928E+04	86	8.315E+00	9.190E+00
41	2.479E+04	2.739E+04	87	7.524E+00	8.315E+00
42	1.662E+04	2.479E+04	88	6.160E+00	7.524E+00
43	1.503E+04	1.662E+04	89	5.346E+00	6.160E+00
44	1.114E+04	1.503E+04	90	5.043E+00	5.346E+00
45	9.119E+03	1.114E+04	91	4.129E+00	5.043E+00
46	7.466E+03	9.119E+03	92	4.000E+00	4.129E+00

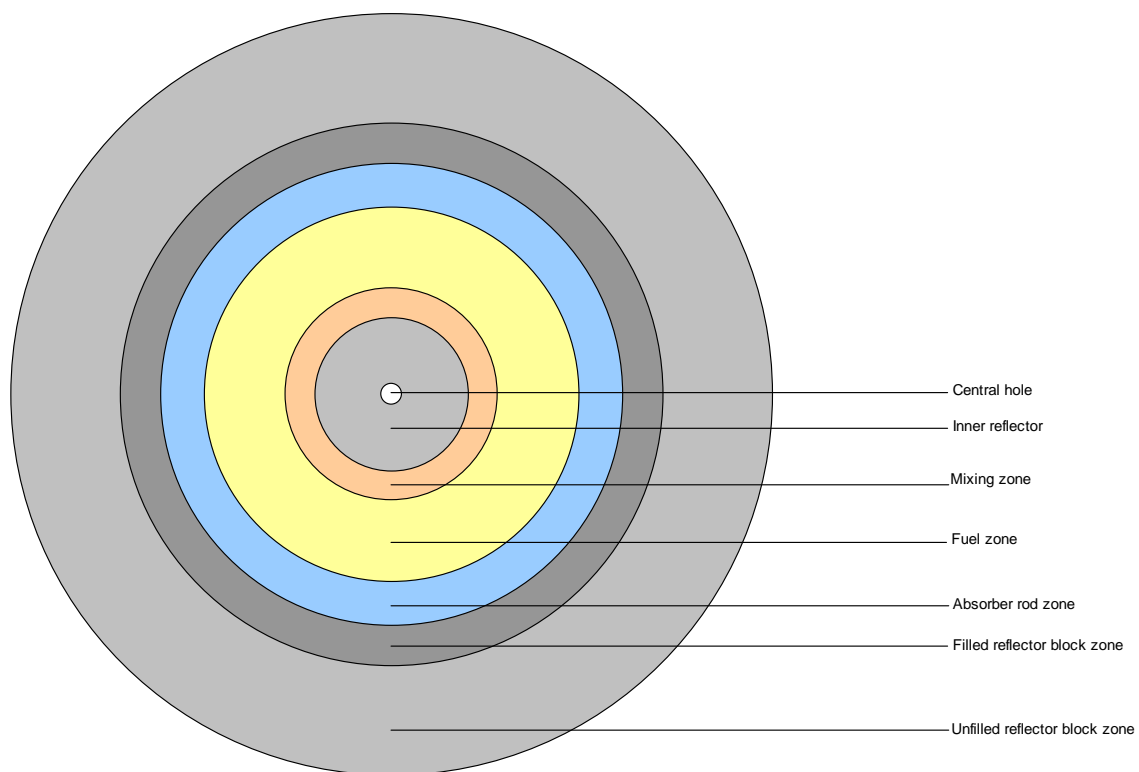
TABLE 3.49(B). ENERGY GROUP STRUCTURE OF THE WIMS9 CROSS-SECTION LIBRARY
(GROUPS 93–172)

Group	Lower energy	Upper energy	Group	Lower energy	Upper energy
	E ₁ (eV)	E ₂ (eV)		E ₁ (eV)	E ₂ (eV)
93	3.381E+00	4.000E+00	133	7.800E-01	7.900E-01
94	3.300E+00	3.381E+00	134	7.050E-01	7.800E-01
95	2.768E+00	3.300E+00	135	6.250E-01	7.050E-01
96	2.720E+00	2.768E+00	136	5.400E-01	6.250E-01
97	2.600E+00	2.720E+00	137	5.000E-01	5.400E-01
98	2.550E+00	2.600E+00	138	4.850E-01	5.000E-01
99	2.360E+00	2.550E+00	139	4.330E-01	4.850E-01
100	2.130E+00	2.360E+00	140	4.000E-01	4.330E-01
101	2.100E+00	2.130E+00	141	3.910E-01	4.000E-01
102	2.020E+00	2.100E+00	142	3.500E-01	3.910E-01
103	1.930E+00	2.020E+00	143	3.200E-01	3.500E-01
104	1.840E+00	1.930E+00	144	3.145E-01	3.200E-01
105	1.755E+00	1.840E+00	145	3.000E-01	3.145E-01
106	1.670E+00	1.755E+00	146	2.800E-01	3.000E-01
107	1.590E+00	1.670E+00	147	2.480E-01	2.800E-01
108	1.500E+00	1.590E+00	148	2.200E-01	2.480E-01
109	1.475E+00	1.500E+00	149	1.890E-01	2.200E-01
110	1.440E+00	1.475E+00	150	1.800E-01	1.890E-01
111	1.370E+00	1.440E+00	151	1.600E-01	1.800E-01
112	1.338E+00	1.370E+00	152	1.400E-01	1.600E-01
113	1.300E+00	1.338E+00	153	1.340E-01	1.400E-01
114	1.235E+00	1.300E+00	154	1.150E-01	1.340E-01
115	1.170E+00	1.235E+00	155	1.000E-01	1.150E-01
116	1.150E+00	1.170E+00	156	9.500E-02	1.000E-01
117	1.123E+00	1.150E+00	157	8.000E-02	9.500E-02
118	1.110E+00	1.123E+00	158	7.700E-02	8.000E-02
119	1.097E+00	1.110E+00	159	6.700E-02	7.700E-02
120	1.071E+00	1.097E+00	160	5.800E-02	6.700E-02
121	1.045E+00	1.071E+00	161	5.000E-02	5.800E-02
122	1.035E+00	1.045E+00	162	4.200E-02	5.000E-02
123	1.020E+00	1.035E+00	163	3.500E-02	4.200E-02
124	9.960E-01	1.020E+00	164	3.000E-02	3.500E-02
125	9.860E-01	9.960E-01	165	2.500E-02	3.000E-02
126	9.720E-01	9.860E-01	166	2.000E-02	2.500E-02
127	9.500E-01	9.720E-01	167	1.500E-02	2.000E-02
128	9.300E-01	9.500E-01	168	1.000E-02	1.500E-02
129	9.100E-01	9.300E-01	169	6.900E-03	1.000E-02
130	8.600E-01	9.100E-01	170	5.000E-03	6.900E-03
131	8.500E-01	8.600E-01	171	3.000E-03	5.000E-03
132	7.900E-01	8.500E-01	172	1.100E-04	3.000E-03

TABLE 3.50. SNAP RADIAL MESHES (CM)

Standard			Intermediate			Coarse		
Mesh number	Mesh width	Cumulative radius	Mesh number	Mesh width	Cumulative radius	Mesh number	Mesh width	Cumulative radius
1	2.625	2.625	1	5.25	5.25	1	5.25	5.25
2	2.625	5.25	2	4.43	9.68	2	5.25	10.50
3	2.63	7.88	3	4.43	14.11	3	5.15	15.65
4	2.63	10.50	4	4.43	18.54	4	5.15	20.80
5	2.58	13.08	5	4.43	22.97	5	5.15	25.95
6	2.58	15.65	6	4.43	27.40	6	5.15	31.10
7	2.58	18.23	7	4.43	31.83	7	5.15	36.25
8	2.58	20.80	8	4.42	36.25	8	5.50	41.75
9	2.58	23.38	9	5.50	41.75	9	5.50	47.25
10	2.58	25.95	10	5.50	47.25	10	5.50	52.75
11	2.58	28.53	11	5.50	52.75	11	5.40	58.15
12	2.58	31.10	12	4.70	57.45	12	5.36	63.51
13	2.58	33.68	13	4.70	62.14	13	5.36	68.87
14	2.58	36.25	14	4.70	66.84	14	5.36	74.23
15	2.75	39.00	15	4.70	71.53	15	5.36	79.59
16	2.75	41.75	16	4.70	76.23	16	5.36	84.95
17	2.75	44.50	17	4.70	80.92	17	5.36	90.31
18	2.75	47.25	18	4.70	85.62	18	5.44	95.75
19	2.75	50.00	19	4.70	90.31	19	5.44	101.19
20	2.75	52.75	20	4.50	94.81	20	5.44	106.63
21	2.70	55.45	21	4.50	99.31	21	5.44	112.07
22	2.70	58.15	22	4.50	103.81	22	5.44	117.51
23	2.68	60.83	23	4.50	108.31	23	4.56	122.07
24	2.68	63.51	24	4.50	112.81	24	4.55	126.62
25	2.68	66.19	25	4.70	117.51	25	4.55	131.17
26	2.68	68.87	26	4.50	122.01	26	4.55	135.72
27	2.68	71.55	27	4.50	126.51	27	9.00	144.72
28	2.68	74.23	28	4.50	131.01	28	9.00	153.72
29	2.68	76.91	29	4.71	135.72	29	9.00	162.72
30	2.68	79.59	30	4.50	140.22	30	9.00	171.72
31	2.68	82.27	31	4.50	144.72	31	9.00	180.72
32	2.68	84.95	32	4.50	149.22	32	9.28	190.00
33	2.68	87.63	33	4.50	153.72			
34	2.68	90.31	34	4.50	158.22			
35	2.72	93.03	35	4.50	162.72			
36	2.72	95.75	36	4.50	167.22			
37	2.72	98.47	37	4.50	171.72			
38	2.72	101.19	38	4.50	176.22			
39	2.72	103.91	39	4.50	180.72			
40	2.72	106.63	40	4.50	185.22			
41	2.72	109.35	41	4.78	190.00			
42	2.72	112.07						
43	2.72	114.79						
44	2.72	117.51						
45	2.28	119.79						
46	2.28	122.07						
47	2.28	124.35						
48	2.28	126.62						
49	2.28	128.90						
50	2.28	131.17						
51	2.28	133.45						
52	2.28	135.72						
53	4.50	140.22						
54	4.50	144.72						
55	4.50	149.22						
56	4.50	153.72						
57	4.50	158.22						
58	4.50	162.72						
59	4.50	167.22						
60	4.50	171.72						
61	4.50	176.22						
62	4.50	180.72						
63	4.64	185.36						
64	4.64	190.00						

Plan View



Side View

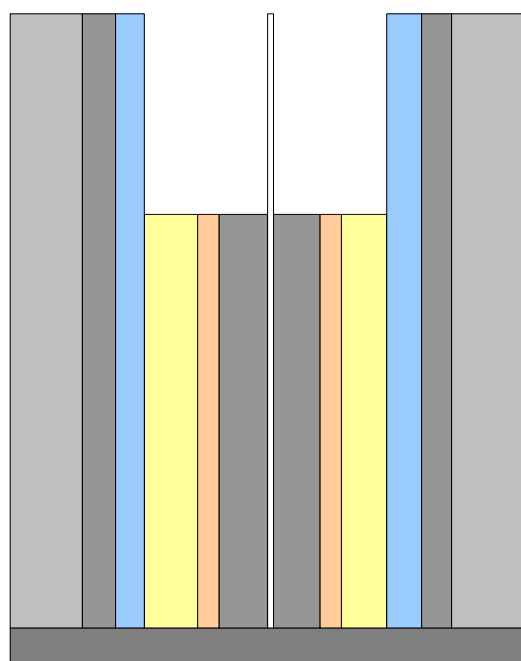


FIG. 3.21. SNAP R-Z Geometry Model of the ASTRA Core.

TABLE 3.51. VARIATION OF K-EFFECTIVE WITH MESH SIZE FOR 260 CM FISSILE HEIGHT

Radial mesh variation

Axial mesh height (cm)	Average radial mesh width (cm)	K_{eff}
10	2.97	0.99741
10	4.63	0.99709
10	5.94	0.99669

Axial mesh variation

Axial mesh height (cm)	Average radial mesh width (cm)	K_{eff}
5	2.97	0.99735
10	2.97	0.99741
20	2.97	0.99765

TABLE 3.52. K-EFFECTIVE AS A FUNCTION OF FISSILE HEIGHT

Fissile height (cm)	SNAP k-effective	K_{eff} Extrapolated to zero mesh size
260	0.99735	0.99758
265	1.00090	1.00113
270	1.00430	1.00453

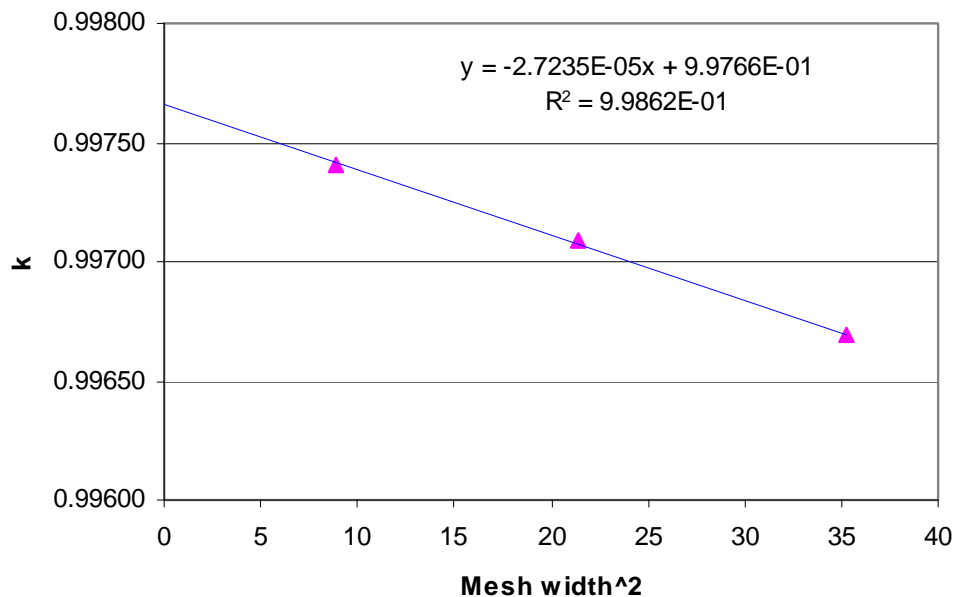


FIG. 3.22. Extrapolation to zero mesh using fissile height of 260 cm (radial mesh).

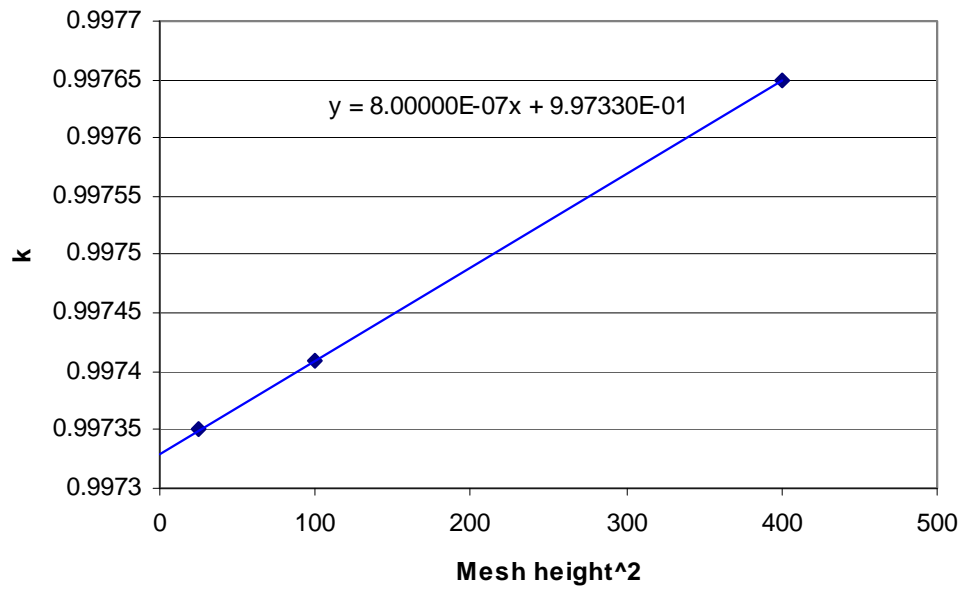


FIG. 3.23. Extrapolation to zero mesh using fissile height of 260 cm (axial mesh).

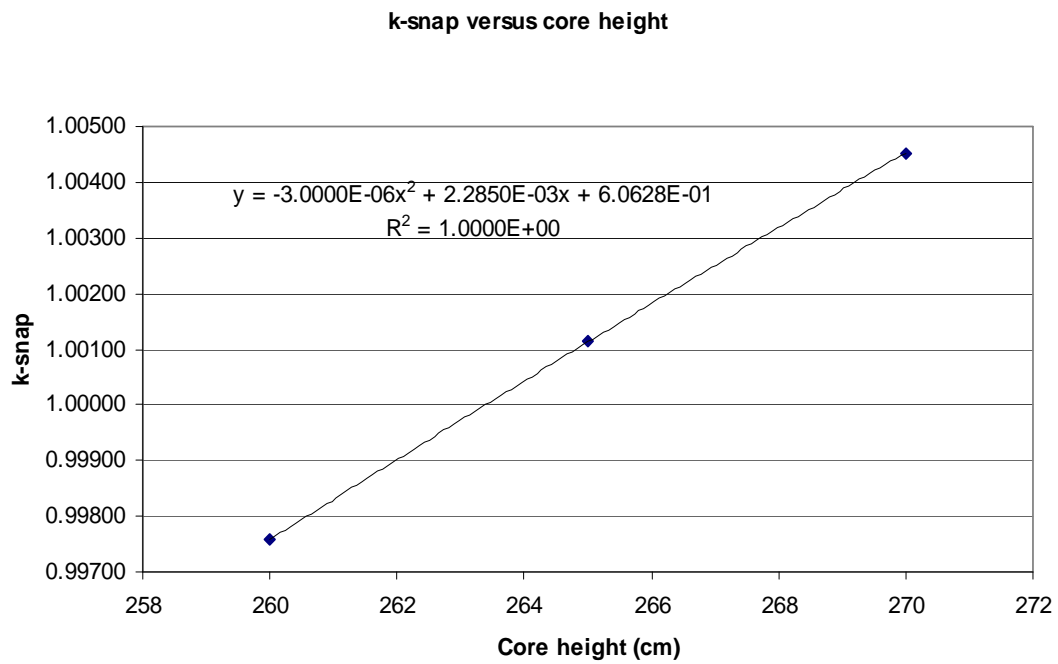


FIG. 3.24. Interpolation to critical core height.

Acknowledgements

The authors wish to express their gratitude to the NNR of the RSA for providing support and funding to participate in this benchmark.

3.3. REFERENCES FOR CHAPTER 3

- [3-1] INTERNATIONAL ATOMIC ENERGY AGENCY, Current Status and Future Development of Modular High Temperature Gas Cooled Reactor Technology, IAEA-TECDOC-1198, IAEA, Vienna (2001).
- [3-2] MATZNER, D., PBMR Project Status and the Way Ahead, Proc. of the 2nd International Topical Meeting on HTR Technology, Beijing, China (2004).
- [3-3] PONOMAREV-STEPNOI, N.N., et al., Experiments on HTR criticality parameters at the ASTRA facility of the Kurchatov Institute, Nuclear Engineering and Design 222 (2003) 215–229.
- [3-4] KURCHATOV INSTITUTE, Report ‘Execution of Physical Start-up of the Annular Core Critical Assembly Simulating the PBMR Reactor at the ASTRA Facility’ (Stage A-1.1.8), RRC KI, Moscow (1999), PBMR Internal Report.
- [3-5] KURCHATOV INSTITUTE, ‘Reporting Materials on the Subject: Services to be Performed at the ASTRA Critical Facility for the PBMR Plant, Stage A-1.1.9’, RRC KI, Moscow (1999), PBMR Internal Report.
- [3-6] Personal Communication, RRC KI, Moscow (2000).
- [3-7] NECHAEV, Y.A., ‘Stage A-1.2.4 Measurements of Reactivity Effects of Components and Materials Important for the PBMR Reactor, and of Spatial Distribution of Reaction Rates, Neutron Fluxes and Power in Axial and Radial Directions in the ASTRA Facility’, RRC KI, Moscow (28 February 2000), PBMR Internal Report.
- [3-8] GARIN, V.P., et al., ‘Stage A-1.2.3 Investigation of Critical Parameters with Varying Height of the Pebble Bed, Worth of Control Rods Depending on their Position in the side reflector, and Differential Reactivity of the Control Rod Depending on the Depth of its Insertion, With Computational Analysis of Results Obtained (Revised in accordance with Dr Venter’s comments on February 28, 2000)’, RRC KI, Moscow (2000), PBMR Internal Report.
- [3-9] PARRINGTON, J.R., KNOX, H.D., BRENNEMAN, S.L., BAUM, E.M., and FEINER, F., ‘Nuclides and Isotopes (Fifteenth Edition) Chart of the Nuclides’, Copyright © 1996 General Electric Co. and KAPL, Inc, Revised (1996).
- [3-10] PBMR, ‘ASTRA Critical Facility Configuration Report’, Document No. 003402, Revision: A, PBMR, Centurion, South Africa (Copyright 2000), PBMR Internal Report.
- [3-11] GARIN, V.P., et al., ‘Stage A-1.1.1 Technical Description of the ASTRA Facility and the Conclusion from the Evaluation of Possibility to Carry out Experiments on it’, RRC KI, Moscow, PBMR Internal Report.
- [3-12] GARIN, V.P., et al., ‘Stage A-1.1.2 Technical Requirements on the Configuration of an Annular Core that Models the PBRM Core on the ASTRA Facility’, RRC KI, Moscow (16 March), PBMR Internal Report.
- [3-13] GARIN, V.P., et al., ‘Stage A-1.1.3 Selection and Substantiation of an Annular Core Critical Assembly Configuration Simulating the PBMR Reactor Core at the ASTRA Facility’, RRC KI, Moscow (6 April 1999), PBMR Internal Report.
- [3-14] KURCHATOV INSTITUTE, ‘Report on Services to be Performed at the ASTRA Facility for the PBMR Plant Stages A-1.1.4; A-1.1.5; A-1.1.6’, RRC KI, Moscow (May 1999), PBMR Internal Report.
- [3-15] KURCHATOV INSTITUTE, Reporting Material on the Subject: ‘Services to be Performed at the ASTRA Critical Facility for the PBMR Plant, Stages A-1.1.7, A-1.1.8’, RRC KI, Moscow (1999), PBMR Internal Report.
- [3-16] NAIDOO, D., ‘ASTRA Critical Facility Computational Tasks’, Document No. 003931, Rev. A, Pebble Bed Modular Reactor, Pretoria, South Africa (May 2000), PBMR Internal Report.

- [3-17] REITSMA, F., NAIDOO, D., 'Evaluating the control rod modelling approach used in the South African PBMR: comparison of VSOP calculations with ASTRA experiments', Nuclear Engineering and Design 222 (2003) 147–159.
- [3-18] NAIDOO, D., 'VSOP Benchmark of the ASTRA Critical Facility with Special Emphasis on the Equivalent Control Rod Model' MSc dissertation, North West University, South Africa (2004).
- [3-19] FEN, V., LEBEDEV, M., SARYTCHEV, V., SCHERER, W., 'Modelling of Neutron Absorbers in High Temperature Reactors by Combined Transport-Diffusion Methods.' KFA-Jülich Report, Jül-2573 (1992).
- [3-20] SCHERER, W., NEEF, H.J., 'Determination of Equivalent Cross-sections for Representation of Control Rod Regions in Diffusion Calculations,' KFA-Jülich Report, Jül-1311 (1976).
- [3-21] TEUCHERT, E., '*VSOP (94), Computer Code System for Reactor Physics and Fuel Cycle Simulation Input Manual and Comments*', Jül-2897 (1994).
- [3-22] MÜLLER, E.Z., 'XSDRNRSP: A One-dimensional Ordinates Code with Improved Cross-section Weighting Facilities Utilizing Transport Corrections', PEL 317 (1992).
- [3-23] GREEN, N.M., PETRIE, L.M., 'XSDRNP-S: A One-dimensional Discrete-Ordinates Code for Transport Analysis', NUREG/CR-0200, Volume 2, Section F3 (1983).
- [3-24] NAIDOO, D., MULDER, E., 'ASTRA Critical Facility, Current Benchmark Status', Third Research Coordination Meeting of IAEA CRP-5 'Evaluation of High Temperature Gas-cooled Reactors', Oarai Research Establishment, JAERI, Japan (March 2001).
- [3-25] AZIZ, F., SUWOTO, Z., RAVAI, A.K., 'Core Calculation Task-1 of ASTRA Critical Facility', National Nuclear Energy Agency of Indonesia, Serpong, Indonesia (2002).
- [3-26] ASKEW, J.R., FAYERS, F.J., KEMSHELL, P.B., 'General Description of the Code WIMS', Journal of Brit. Nuc. Energy Soc. 5, United Kingdom (1966).
- [3-27] OKUMURA, K., KANEKO, K., TSUCHIHASHI, K., 'SRAC95: The Comprehensive Neutronics Calculation Code System', Dept. of Reactor Eng., JAERI, Japan.
- [3-28] GERWIN, H., SCHERER, W., 'Treatment of Upper Cavity in a Pebble-Bed High Temperature Gas-cooled Reactor by Diffusion Theory', Nucl. Sci. Eng., 97 (1987) 9–19.
- [3-29] FOWLER, T.B., 'CITALDI-PC: CITATION List Directed Input data', ORNL-RET, United States of America (March 1996).
- [3-30] FOWLER, T.B., VONDY, D.R., CUNNINGHAM, G.W., 'Nuclear Reactor Core Analysis Code; CITATION', ORNL-TM-2496, United States of America (1969).
- [3-31] JING, X., SUN, Y., 'Calculation of Task 1 at the ASTRA Critical Facility', Presented at 3rd RCM of IAEA CRP-5, Oarai, Japan (March 2001).
- [3-32] SEKER, V., COLAK, U., KADIOGLU, O.K., 'ASTRA Test Facility Criticality Benchmark Results', Hacettepe University, Ankara, Turkey (2002).
- [3-33] SUBLET, J.C., RIBON, P., 'A probability Table Based Cross-section Processing Sysytem: CALENDF - 2001', Journal of Nuclear Science and Technology (2002).
- [3-34] BOTH, J.P., PENELIAU, Y., 'The Monte Carlo code TRIPOLI4 and its first benchmark interpretations', International Conference PHYSOR 96, Mito, Ibaraki, Japan (September 1996).
- [3-35] INTERNATIONAL ATOMIC ENERGY AGENCY, Evaluation of High Temperature Gas Cooled Reactor Performance: Benchmark Analyses related to Initial Testing of the HTTR and HTR-10', IAEA-TECDOC-1382, Vienna (November 2003).
- [3-36] KOBERL, O. (CEA), SEILER, R. (PSI), 'Detailed Analysis of Pebble-Bed HTR PROTEUS Experiments with the Monte Carlo Code TRIPOLI43'. HTR-2004 Conference, Beijing (September 2004).

- [3-37] CHANG, H., RAEPSAET, X., DAMIAN, F., LEE, Y., KOBERL, O. (CEA), JING, X., YANG, Y. (INET), 'Treatment of stochastic Geometry in Pebble Bed Reactor with Monte Carlo Code Tripoli4.3'. HTR-2004 Conference, Beijing (September 2004).
- [3-38] DAMIAN, F., RAEPSAET, X., SANTANDREA, S., MAZZOLO, A., POINOT, C., KLEIN, J.C. (CEA), BRAULT, L., GARAT, C., (FRA-ANP), 'GT-MHR Core Modelling: from reference modelling definition in Monte-Carlo code to calculation scheme validation', PHYSOR 2004 Conference, Chicago (United States of America) (25–29 April, 2004).
- [3-39] TRIPOLI-4.3 modeling of pebble bed configuration of ASTRA Critical Facility of the Kurchatov Institute, M&C 2005 Conference, Avignon (France) (12–15 September, 2005).
- [3-40] ANSWERS SOFTWARE SERVICE, WIMS9 User Guide, ANSWERS/WIMS(99)9, Serco Assurance Document.
- [3-41] HUTTON, J.L., NEWTON, T.D., PERRY, R.J., POWNEY, D.J., 'Validation of WIMS9', PHYSOR 2004 — The Physics of Fuel Cycles and Advanced Nuclear Systems: Global Developments, Chicago, Illinois (April 25–29, 2004).
- [3-42] BEHRENS, D.J., 'The effect of holes in a reacting material on the passage of neutrons', Proc. Phys. Soc. 62 (1949) 607.

4. PEBBLE BED MODULAR REACTOR

4.1. PBMR GENERAL INFORMATION

In 1993, the PBMR [4-1], [4-2] was identified by ESKOM, the electric utility of South Africa, as a leading option for the installation of new generating capacity to their electric grid. This innovative nuclear power plant incorporates a closed-cycle primary coolant system utilizing helium to transport heat energy directly from the modular pebble bed reactor to a recuperative Power Conversion Unit (PCU) with a single-shaft turbine/compressor/generator. This replacement of the steam cycle that is common in present Nuclear Power Plants (NPPs) with a direct gas cycle provides the benefits of simplification and a substantial increase in overall system efficiency with the attendant lowering of capital and operational costs.

Although the historical development of this plant is interrelated to other types of HTGRs, the principal focus herein is on the PBMR pebble bed (spherical) fuel element type reactor. The long term development of this reactor type began in Germany by the KFA Nuclear Research Center (now FZJ). Two pebble bed plants were constructed in Germany, namely the Arbeitsgemeinschaft Versuchsreaktor (AVR), 46 MW(t)/15 MW(e) plant and the 750 MW(t)/296 MW(e) Thorium High Temperature Reactor (THTR-300). Basically, these steam/electric plants validated the temperature and fission product retention capabilities of the ceramic (TRISO) coated fuel particle and the safety characteristics of the HTGR. Most notable of the operational achievements was with the AVR in sustaining long term operation at an average core outlet temperature of 950°C and demonstration of safety such as extended LOFC on the core.

The next evolution of the pebble bed plant began in the early 1980s with development of the modular reactor. This small reactor added the unique characteristic of being able to cool the core entirely by passive heat transfer mechanisms following postulated accidents without exceeding the failure temperature of the coated particles which is key to the normal safety characteristics of all HTGRs. Originally, the focus of the modular HTGR was on the steam cycle and included designs by Germany, the Russian Federation and the United States of America. These designs all incorporate the TRISO ceramic coated fuel particle and utilized steel vessels to house the primary system.

The design of the present direct cycle gas turbine modular plant such as the PBMR began in the early 1990s. This plant incorporates the basic safety attributes of the modular pebble bed reactor with the direct improvement of not being tied to the complexities and low efficiencies associated with the steam cycle. What is also attendant with the modular direct cycle PBMR is a high degree of standardization for this relatively small and simplified design. This approach allows the benefits of plant modularization and shop fabrication with corresponding improvements in quality control, reduction of construction schedules, and optimization of manufacturing procedures and processes, all resulting in improvements in schedule and capital costs. The focus of this chapter is on benchmark problems associated with PBMR neutronics and thermal hydraulics.

4.1.1. Facility description (Status in 2004/2005)

Initial development of the PBMR was to include a PCU consisting of three separate rotating shafts in a vertical configuration and equipped with magnetic bearings. The decision was made in 2004 to replace the three-shaft PCU with a single rotating machine [4-2]. This major design change was initiated due to recent developments in the application of dry gas seals that allowed the use of conventional oil bearings and improvements in gear reduction capability for high-capacity applications.

The magnitude of this design change to a single-shaft PCU will necessitate a thorough review of all plant parameters within the primary coolant system and associated subsystems. However, it is anticipated that the design parameters for the reactor plant will remain consistent with those previously determined for the 400 MW(t) reactor. Table 4.1 provides major design and operating characteristics reflecting the 400 MW(t) reactor plant.

The PBMR functions under a direct Brayton cycle with primary coolant helium flowing downward through the core and exiting at 900°C. Helium then enters the turbine, relinquishing energy to drive the electric generator and compressors.

After leaving the turbine, helium then passes consecutively through the hot side of the recuperator, then the pre-cooler, the Low pressure compressor (LPC), intercooler, High pressure compressor (HPC) and then on to the low-temperature side of the recuperator before re-entering the reactor vessel at 500°C. Figures 4.1 and 4.2 provide a schematic representation of the PBMR flow path and conceptual primary system respectively.

TABLE 4.1. MAJOR DESIGN AND OPERATING CHARACTERISTICS OF THE PBMR

PBMR Characteristic	Value
Installed thermal capacity	400 MW(t)
Installed electric capacity	165 MW(e)
Load following capability	100-40-100%
Availability	≥ 95%
Plant overhauls	30 days each 72 months
Core configuration	Vertical with fixed centre graphite reflector
Fuel	TRISO ceramic coated U-235 in graphite spheres
Primary coolant	Helium
Primary coolant pressure	9 MPa
Moderator	Graphite
Core outlet temperature	900°C
Core inlet temperature	500°C
Cycle type	Direct
Number of circuits	1
Vessel material	Steel
RPV wall thickness	0.18 metres
Cycle efficiency	≥ 41%
Plant lifetime	40 years
Emergency planning zone	400 metres

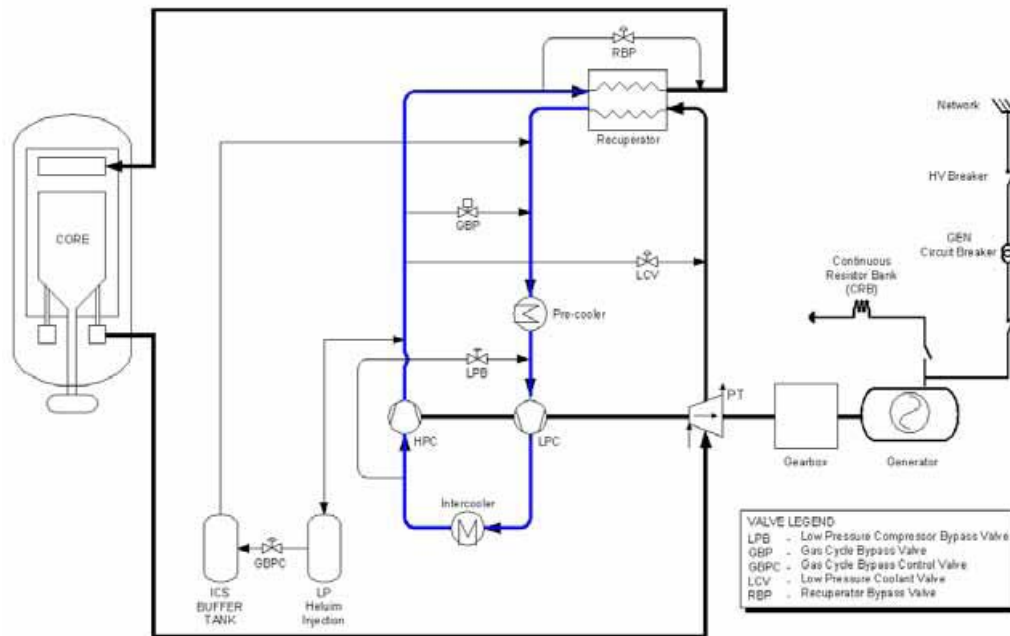


FIG. 4.1. PBMR Direct brayton cycle flow path [4-2].

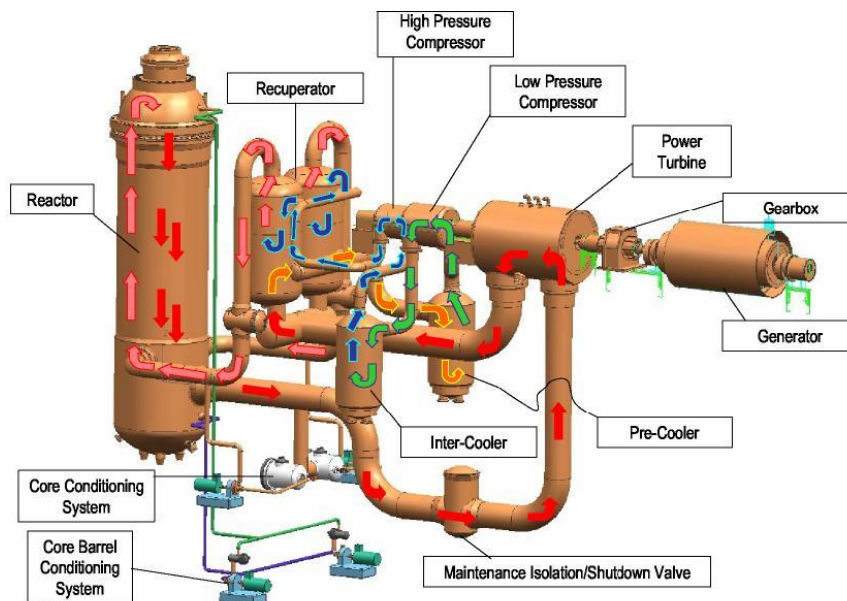


FIG. 4.2. Conceptual layout of the PBMR primary system [4-2].

Power is adjusted by regulating the mass flow rate of gas inside the primary circuit. This is achieved by a combination of compressor bypass and system pressure changes. Increasing the pressure results in an increase in mass flow rate, which results in an increase in the power removed from the core. Power reduction is achieved by removing gas from the circuit. A Helium Inventory Control System (HICS) is used to provide an increase or decrease in system pressure [4-3].

The reactor building is a single building constructed from concrete. Approximately half of the building will be constructed below ground level. The building is also designed to protect the reactor and equipment from external accidents such as external natural or man-made events, as well events caused by internal processes [4-3].

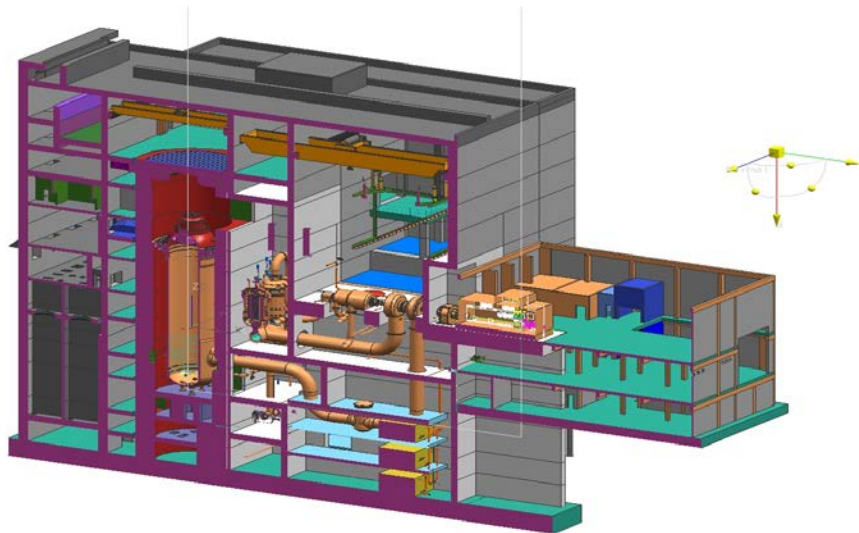


FIG. 4.3. PBMR SINGLE MODULE BUILDING [4-2].

Physical protection of each PBMR module is enhanced by the added strength of the physical building. This building is designed for a seismic acceleration of 4 g horizontal and would withstand an aircraft crash of < 2.7 ton without penetration on the outside building. A crash of a Boeing 777 aircraft has been analysed to penetrate the outside building barrier, but nuclear safety would not be compromised. Figure 4.3 provides an overview of the building surrounding a single PBMR module.

4.1.2. PBMR core

Table 4.2 delineates key core characteristics of the PBMR. The core [4-4] is comprised of ~ 452000 fuel spheres or ‘pebbles’ (Fig. 4.6). The fuel spheres have a diameter of 60 mm and each sphere contains nominally 15000 UO_2 TRISO-coated micro-spheres imbedded in a graphite matrix. The fuelling scheme employed is the continuous on-line multipass method similar to the designs used in Germany. The spent fuel system consists of a Core Unloading Device (CUD) in each of the three defuelling chutes from where the fuel is moved pneumatically to the burnup assaying equipment located at a level above the reactor unit. After burnup has been determined, the fuel is routed either to the spent fuel tanks or back to the core, depending on its burnup. The fuel spheres are reloaded into the core through three fuelling lines. The spent fuel tanks have sufficient capacity to hold all the spent fuel generated during the entire operating life of the facility [4-3].

Fresh fuel elements are added to the top of the reactor while used fuel pebbles are removed at the bottom to keep the reactor at full power. On average, each fuel pebble makes six passes through the reactor before being finally discharged to the spent fuel storage tanks [4-5]. The fuel cycle incorporates on-line refuelling with a daily fuel sphere circulation rated at ~2900 elements.

TABLE 4.2. CORE AND FUEL CHARACTERISTICS WITH REACTIVITY CONTROL DATA

Characteristic	Value
Total fuel volume	83.7156 m ³
Core outer diameter	3.7 metres
Outer diameter of the central reflector	2.0 metres
Fuel effective cylindrical height (flattened top to flattened bottom)	~11 metres
Fuel enrichment	9.6% UO ₂ for equilibrium core
Target burnup	~90000 MWd/tU
Average pebble bed packing fraction	0.61
Number of spheres in the core	~451,530
Number of reactivity control system (RCS) holes. Equally spaced around outside of core.	24
Number of reserve shutdown system (RSS) holes. Equally spaced around centre core reflector column	8
Reactivity control system material	B ₄ C
Average core power density	4.8 MW/m ³
Average daily fuel sphere circulation	~2,900
Refuelling type	On-line
Number of passes a sphere makes through the core	6 nominal
Fuel Pebble	
Fuel pebble outer radius	3.0 cm
Thickness of fuel-free zone	0.5 cm
Total heavy metal loading per fuel pebble (equilibrium fuel)	9 g
Carbon content	189 g/fuel sphere
Coated particle	
Fuel kernel diameter	500 micron
Kernel material type	UO ₂
UO ₂ density	10.4
Kernel coating material	C/C/SiC/C

The PBMR reactor core (Figs 4.4 and 4.5) is basically a long upright circular cylinder with a fuel effective height of 11 m and a diameter of 3.7 m. Twenty-four reactivity control system rod holes are equally spaced outside the core.

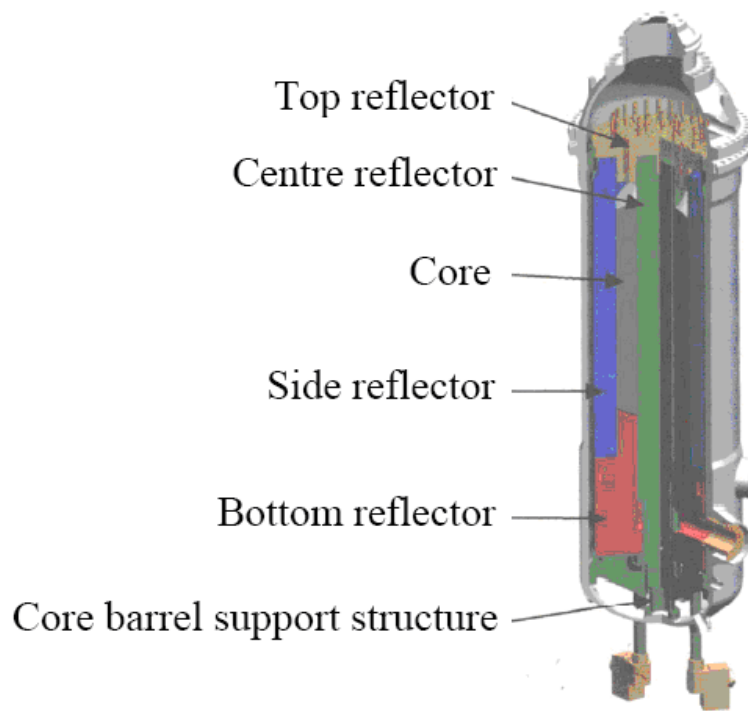


FIG. 4.4. PBMR CORE [4-1].

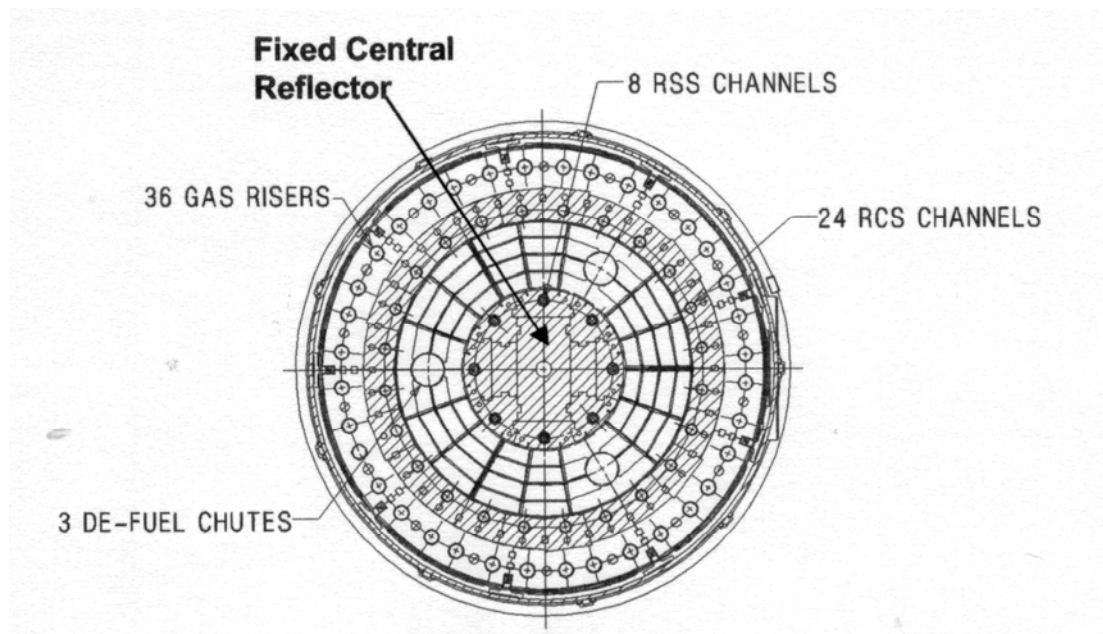


FIG. 4.5. Horizontal cross-section of PBMR Core [4-1].

For shutdown purposes and for minor reactivity adjustments, two diverse reactivity control systems are used. The one system, the Reactivity Control System (RCS), consists of 12 control rods and 12 shutdown rods. The design of both systems is identical and the positions during operation will be, within a small band, the same. The driving systems are also identical and each system has a stepper motor with a gearbox that finally drives a chain wheel that positively locates the chain on which the control rod is supported. When inserted into the reflector, the control rods move to a depth of 6.5 m

below the bottom of the top reflector and the shutdown rods move to a depth of ~10 m. The RCS rods move in borings in the side reflector.

The other system, the Reserve Shutdown System (RSS), consists of 10 mm diameter B₄C absorber spheres, which, during a shutdown operation, are dropped into the eight borings in the central reflector. The spheres are normally stored in containers at the top of the core structures and are released by opening a valve system [4-3].

The PBMR is an annular core that contains a 2 m diameter fixed graphite column with eight equally spaced holes to accept the boron carbide reserve shutdown pellets. The fixed centre column was chosen in order to reduce the amount of core bypass flow to lower the fuel temperature. The graphite column includes an interlocking design and, if required, can be replaced with remote handling equipment.

4.1.3. PBMR fuel

The PBMR utilizes the TRISO coated fuel particle. The high temperature and long term performance of this coated fuel has been demonstrated primarily by the AVR and the Ft. St. Vrain plants respectively, to allow plant radiological cleanliness that is considerably lower than previously demonstrated by NPPs throughout the past three decades. This, coupled by the high system efficiency of the PBMR and its corresponding need for less fuel to generate an equivalent amount of electricity, are distinct attributes for minimizing adverse plant environmental impact and optimizing waste management.

The reactor fuel is continually replenished with fresh and reusable fuel pebbles added at the top of the core while used fuel is removed from the bottom. Each used pebble exiting the core is measured to determine the remaining amount of fissionable material and returned to the reactor if it contains usable fissionable material. Each fuel pebble is cycled through the core ~ 6 times [4-4].

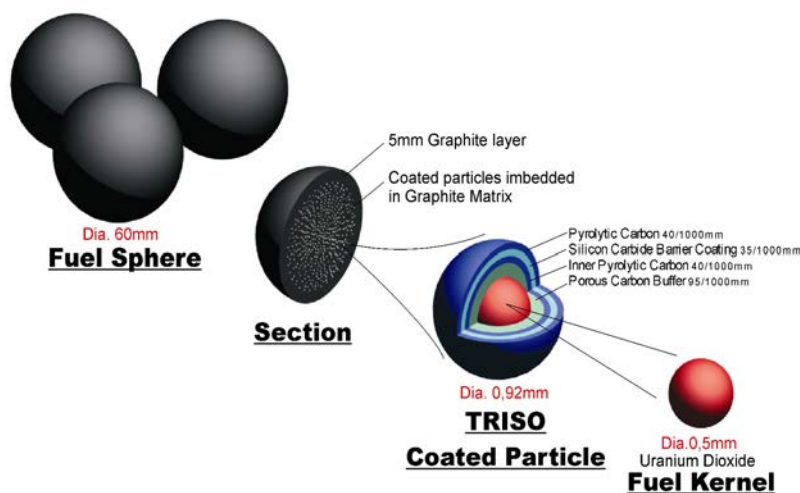


FIG. 4.6. PBMR fuel [4-2].

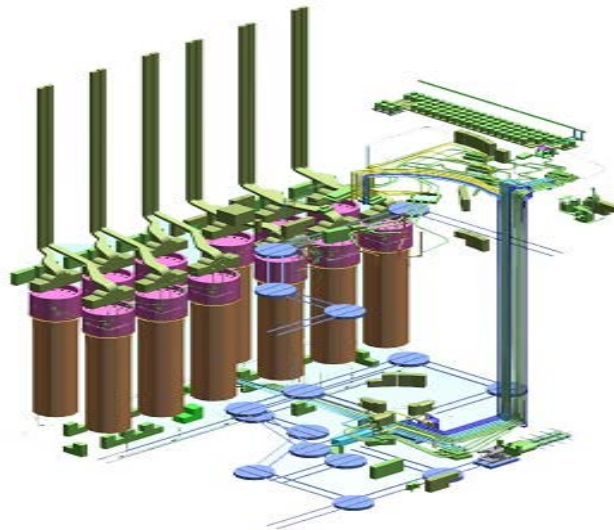


FIG. 4.7. Fuel handling and storage system [4-6].

Figure 4.7 is a representation of the Fuel Handling and Storage System (FHSS). The fuelling system has three feeding and three defuelling points. The operating pressure is up to 9 MPa (for selected parts of the system) and with a temperature of 20–260°C.

4.1.4. Power conversion unit

The single most prominent factor in projecting the low capital and Operating and Maintenance (O&M) costs for the PBMR is the plant simplification and high efficiency brought about by incorporation of the Brayton cycle. The direct conversion of the heat energy from the reactor to the PCU without an intermediate exchange of coolant medium provides for this substantial reduction in costs. In addition, incorporation of the modular reactor has added the unique characteristic of being able to cool the reactor entirely by passive heat transfer mechanisms following postulated accidents without exceeding the failure temperature of the coated particles.

The heat removal path under normal operation is the PCU with the primary energy user being the turbine and compressors. The precooler and intercooler heat exchangers are also available within this path. These coolers utilize water as the cooling medium on the secondary side.

The original design of the PBMR primary system included three separate vertically orientated rotating machines. These included the Low Pressure Turbo Compressor (LPTC), the High Pressure Turbo Compressor (HPTC) and the turbine generator. A recent major decision by the developers, PBMR (Pty) Ltd, resulted in usurping the three-shaft PCU for a single rotating machine comprised of two compressors, turbine, reduction gear and generator in a horizontal configuration with oil bearings and dry gas seals. A representation of this machine is provided in Fig. 4.8. The advantages of the single machine over the three-shaft PCU include the following:

- Approximately 1000 EMB penetrations of pressure boundary eliminated;
- Elimination of potential power turbine generator unstable operations during trip and subsequent restart;
- Less complex control system;
- Easier to balance shaft thrust forces;
- No large resistor bank required to maintain load on trip;
- Elimination of a Startup Blower System (SBS);
- Conversion from 50 to 60 Hz simplified;

- Improved maintenance very similar to combustion gas turbine systems;
- No special rotor balancing facilities required (conventional commissioning);
- Reduced cost of turbomachinery equipment;
- Significantly lower R&D required, i.e. lower development risk [4-2].

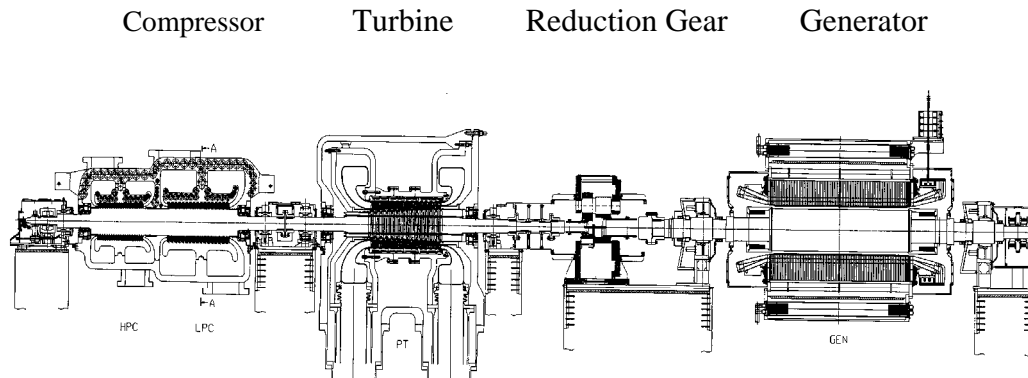


FIG. 4.8. PBMR power conversion machine (by MHI) [4-1].

The PCU system is the primary means of utilizing heat from the PBMR. Two other cooling systems are available for utilization for removal of primary system energy; the Core Conditioning System (CCS) and the RCCS. The CCS serves the functions of removal of core decay heat when the Brayton cycle is not operating and the provision of helium flow through the core for reactor heat-up purposes during startup operations [4-7].

The RCCS removes heat transferred from the reactor vessel to the cavity around the vessel. The basic functions and requirements of the RCCS are the following:

- To provide investment protection by preventing thermal radiation from impinging directly onto the concrete walls of the reactor cavity.
- To remove all heat from the reactor cavity during normal operation, thereby maintaining the concrete surfaces of the cavity below their design temperature limits being nominally 65°C under normal operating conditions.
- To remove all decay and residual heat generated in the reactor cavity during a pressurized and depressurized loss of forced core cooling event.
- In the event of the loss of active pumping capacity of the secondary cooling system, to remove heat from the reactor cavity passively and to release this heat to the atmosphere in the form of steam. This passive operation continues for a minimum period of 96 h.
- To switch from active to passive operation without any mechanical, electrical or human intervention.

It is not the primary function of the RCCS to ensure that the fuel does not exceed its maximum allowable temperature, but together with the design of the heat transfer path from the fuel to the outer surface of the RPV, the RCCS provides a heat sink for continuous removal of heat transferred from the RPV during normal operation and during a postulated LOFC event [4-3]. Figures 4.9 and 4.10 provide simplified schemes for emergency and passive heat removal paths during normal operation and accidents.

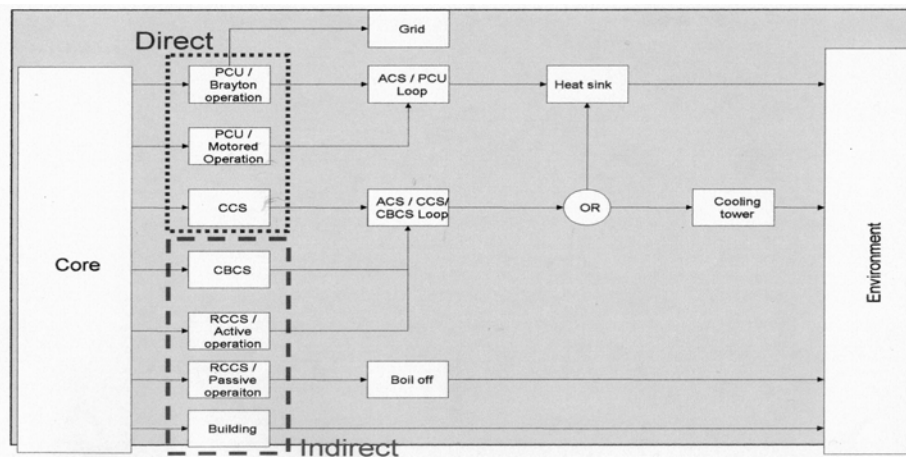


FIG. 4.9. Emergency heat removal paths [4-8].

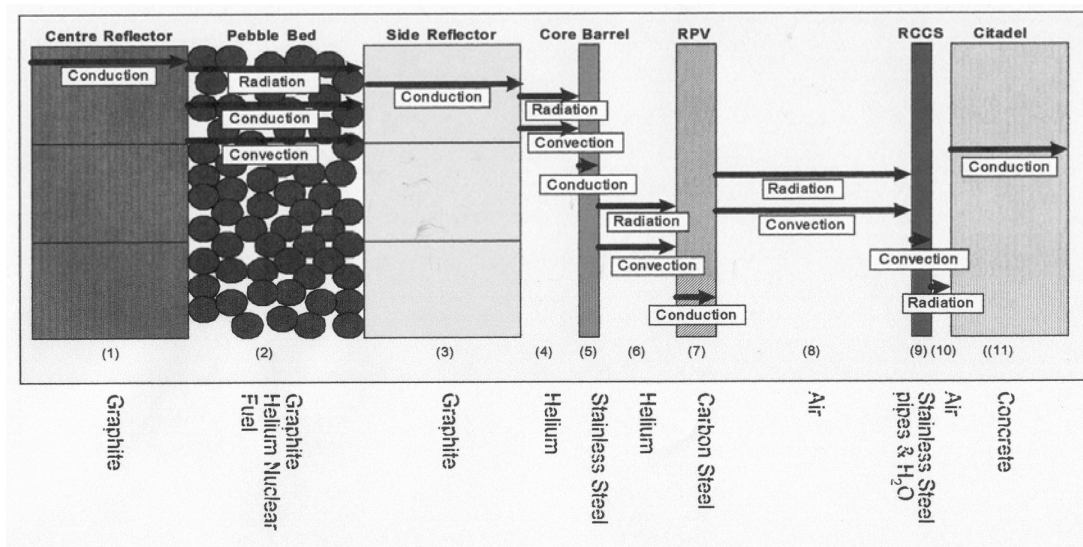


FIG. 4.10. Passive heat removal paths [4-8].

4.1.5. PBMR safety

The fundamental safety philosophy for the PBMR is based on the premise that the TRISO coated fuel will adequately retain its integrity to contain radioactive fission products under normal and accident conditions and thereby allow radiological safety to be assured. This is achieved by relying on fuel, whose performance has been demonstrated under simulated normal and accident conditions and whose integrity will therefore not be challenged even under accident conditions.

The safety design philosophy statement for the PBMR is built on the premise that the PBMR will produce nuclear power in a manner so that:

- No credible event will necessitate sheltering or evacuation of the public living at the site boundary (400 m);
- There will be no need for active engineered safety systems;
- There will be no need for early operator intervention following an accident (this includes a > 24 h design goal, although analysis has shown that ~ 96 h has been achieved);

- The plant's main safety characteristics include:
- The utilization of a small normal operational excess reactivity, made possible by continuous fuelling and defuelling;
- The radionuclide-retention capability of the fuel elements containing coated fuel particles, even at high temperatures;
- The large negative temperature coefficient of reactivity of the fuel;
- The neutron transparency of helium, used as the reactor coolant and working fluid in the gas turbine;
- The large passive heat removal capability of the reactor design due to the slender core.

The small excess reactivity at normal operation is a result of a core that is always in the equilibrium state due to continuous fuelling and defuelling. This means that no excess reactivity is needed in order to compensate for periodic excess fuel when new fuel is added in batches. Excess reactivity is therefore solely designed to allow for xenon fluctuations and load following conditions.

The high temperature radionuclide-retention capability is provided by the fuel kernel coatings consisting of multiple layers of PyC and SiC (see Fig. 4.6). These coated fuel particles have demonstrated excellent capability to contain radiologically significant gaseous and solid fission products under elevated temperature conditions.

The large negative temperature coefficient of the fuel is a result of the low enriched uranium fuel in the graphite matrix. This is caused by the temperature dependence of the resonance absorption in the fertile material U-238. This, together with the negative moderator temperature coefficient, adds up to a strong total negative reactivity coefficient for temperature which means that the reactor will quickly counteract a rise in temperature with a reduction in power.

The neutron-transparency of helium means that the void-coefficient for reactivity of the helium coolant is zero and that the loss of coolant cannot cause a reactivity accident. The chemical inertness of helium, which holds true for even very high temperatures, dictates that it will not aggravate an accident by chemically reacting with the graphite or fuel. The use of a single-phase cooling medium has additional advantages, namely, flashing and boiling of the coolant are impossible, no coolant level measurements are required, no cavitation of pumps can occur, and pressure measurements are more certain.

The long and narrow design of the reactor allows for optimal passive heat removal from the core even under conditions with no coolant flow and the reactor depressurized. Heat flow through conduction and radiation to the RPV and subsequent removal through the passive heat removal system in the reactor cavity will limit the maximum fuel temperature and the vessel temperature so that both remain in the safe region.

The primary gas envelope can also be considered a barrier against radionuclide release. However, for the short-lived fission gases, the dominant removal mechanism is radioactive decay. For the condensable fission products, the dominant removal mechanism is deposition or plate-out on the various helium-wetted surfaces in the primary circuit. The primary pressure boundary, consisting of conventional steel pressure vessels, is designed to ASME Section III Division 1. Through-wall cracks are considered unlikely. The chemically inert helium coolant minimizes corrosion and eliminates the complications associated with internal cladding and only materials for which extensive data exist are to be used in the construction of the vessels.

The reactor building is a reinforced concrete and vented confinement building. No leaktight requirement is placed on this building. In the event of a break in the primary boundary, it is only the slight gasborne activity in the primary coolant and a portion of the activity deposited on the surfaces of the primary system that may be released into the reactor building. If the vent opens, natural removal mechanisms (including radioactive decay, condensation, fallout, and plate-out) reduce the concentration of the radionuclides in the building atmosphere, reducing off-site releases [4-7, 4-9].

The protective barriers to confine and retain fission products include:

- The TRISO coated fuel particles are the primary barrier to retention of all fission products;
- The graphite encasing the fuel particles is a secondary barrier and will retain most fission products, although graphite is transparent to noble gasses;
- The helium circuit pressure boundary serves as a physical barrier for retaining short-lived fission gases until the gases decay;
- The reactor building serves as another physical barrier [4-10].

Design basis accidents and beyond design basis accidents

An extensive code/modelling programme has been in progress throughout the past decade to evaluate and assure the accuracy of the safety premise upon which the PBMR design is based. The PBMR Design Basis Accident (DBA) categories that are investigated include: plant trips (PLOFC), primary boundary leaks and ruptures (DLOFC⁵), reactivity, air ingress, seismic, internal missile, aircraft crash, loss of external heat sink, loss of all electrical power supplies, and fire, flood and water ingress. Figure 4.11 provides PBMR system representative temperatures following a LOFC accident based on 2004 code analysis.

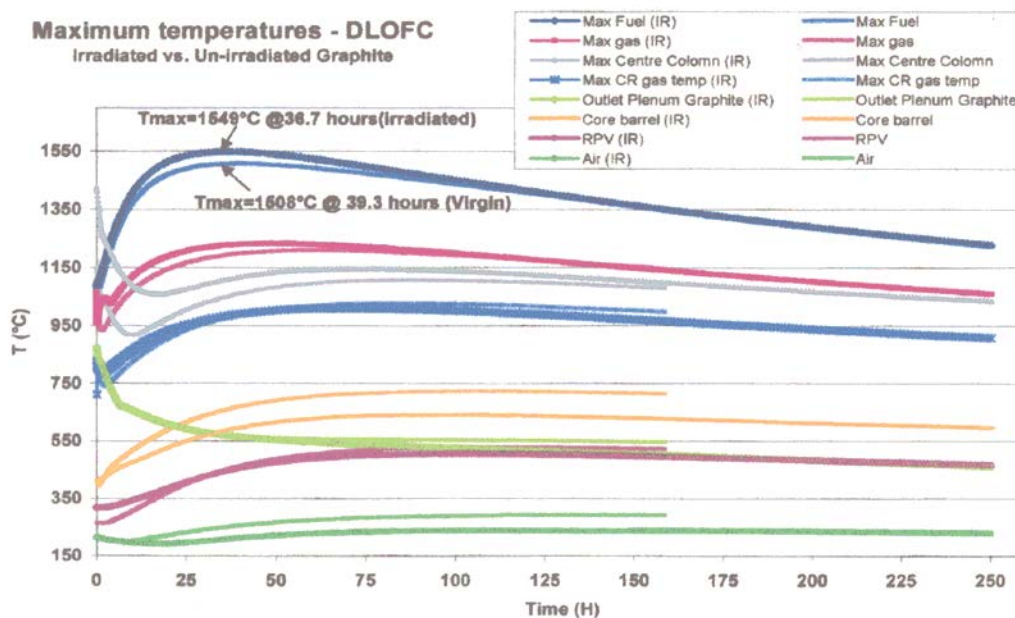


FIG. 4.11. Temperatures following a simulated DLOFC accident [4-11].

⁵ DLOFC = Depressurized Loss of Forced Cooling

Table 4.3 provides a listing of event types and associated categories for accidents under investigation.

TABLE 4.3. PBMR FREQUENCY CATEGORIES AND EVENT TYPES [4-8]

Event Type	PIE	Frequency Category	Notes
Leaks	Leaks up to 10 mm in diameter	AOO	
Breaks	Breaks between 10 and 230 mm	DBA	Including SSE (DBA) and control rod ejection (BDBA)
	Breaks between 230 and 1950 mm	BDBA	
Reactivity Transients	Group control rod withdrawal	DBA	During these events the HPB remains intact – no release of activity
	RSS removal	DBA	
	Overcooling	DBA	Due to the failure of any valves or any internal pipe work
	Drop of the top reflector on the core	BDBA	
	Inadvertent scram	DBA	
Other Reactivity Events	Xenon oscillations	AOO	
	Water/steam moderation	DBA	
	Inadvertent insertion of one RSS SAS channel	DBA	
	Inadvertent insertion of one control rod	DBA	
Transients	CCS cooling	AOO	
	PLOFC	DBA	

Note:

AOO = Anticipated Operational Occurrences.

BDBA = Beyond Design Basis Accident.

HPB = Helium Pressure Boundary.

SSE = Safe Shutdown Earthquake.

Probability of unacceptable radioactivity release beyond plant boundaries

The basic philosophy is that there shall be no identifiable accident that would result in the need to evacuate or shelter people living near the Emergency Planning Zone (EPZ) of 400 m. The design shall be that an As Low as Reasonably Achievable (ALARA) target of 10% of the regulatory limit for all Anticipated Operational Occurrences (AOO) and DBA shall be attainable for both the public and the personnel. The NNR limits for the public are:

- Normal operation and AOO - < 250 μ Sv/annum per site (freq $1-10^{-2}$);
- DBA ($10^{-2}-10^{-6}$ per event) 50 mSv;
- Beyond 10^{-6} per event, a mortality risk is applied.

PBMR expects (based on preliminary results) that there is no identifiable accident, including DBA, for which the DBA target cannot be achieved [4-8].

Proliferation resistance

Proliferation resistance is achieved within the PBMR in a multitude of ways, namely:

- A primary deterrent to the diversion of nuclear material lies with the basic design of the spherical fuel pebble. The structure of each pebble would require the disassembling of first the outer graphite coating and then the very strong individual particle coatings. Only then would the UO_2 be accessible, but only in minute quantities.
- The 9.6% new fuel enrichment is a further deterrent and is well within the guidelines for non-proliferation.
- Diversion of nuclear material that has been irradiated is further deterred by high depletion in the spent fuel (Fig. 4.12) and the need for remote handling and processing. Access to this material would require entering the PBMR structure. This represents the additional obstacles of penetration of the outside building and spent fuel cavity and, finally, the spent fuel canisters, with the attendant radiological and security considerations. In addition, the very low metal loading of each sphere (9 g) makes it necessary to obtain very large numbers of spheres ($> 10^5$) to create a significant quantity of nuclear materials.
- Finally, the design of the FHSS creates a completely enclosed system for fuel accountability assurance. Numerous monitoring points and mechanisms have been included in the design to provide remote and independent material accountability at all times.

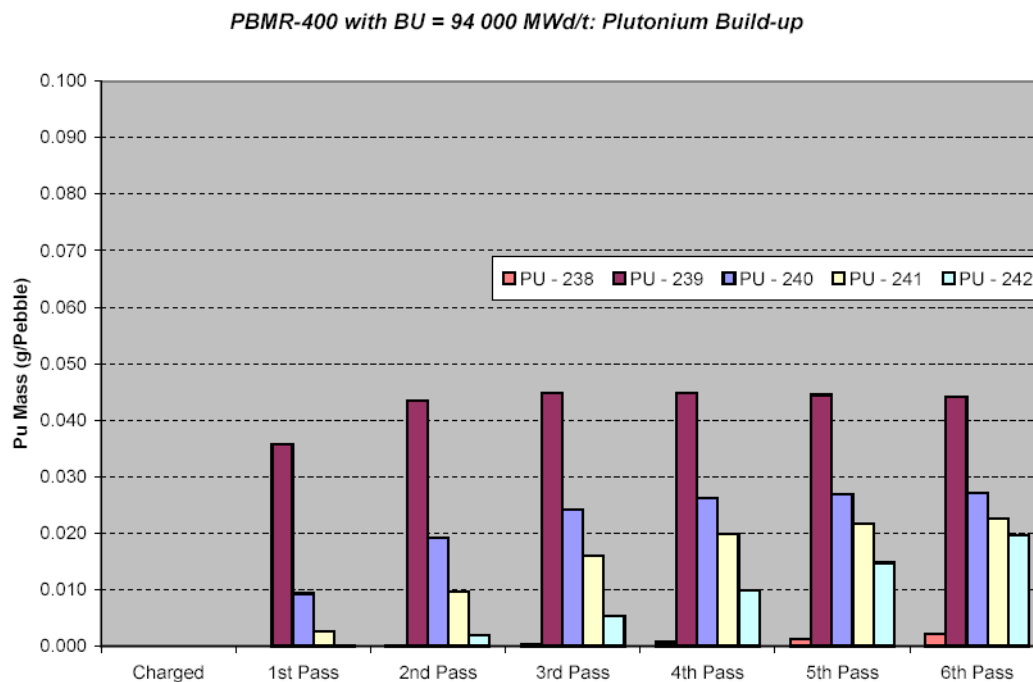


FIG. 4.12. Plutonium Build-up/Fuel Pass [4-12].

4.1.6. PBMR commercialization

The principal shareholders in the PBMR are incorporated within the South African company, PBMR (Pty) Ltd. These shareholders include (status in 2004):

- ESKOM, national South African electric utility;
- Industrial Development Corporation of South Africa, a national development financial institution;

- British Nuclear Fuel plc, a global nuclear fuel cycle company (parent of Westinghouse nuclear) solely owned by the government of the United Kingdom (note that the PBMR shareholding was transferred to Westinghouse Nuclear when Westinghouse was sold to Toshiba of Japan).

The long term marketing approach taken by the partners of PBMR (Pty) Ltd is to offer plants comprised of a multiple of modules. This has led the PBMR partners to develop early relationships with strategic suppliers for key equipment. A partial list of these strategic suppliers is shown in Table 4.4.

TABLE 4.4. PBMR STRATEGIC SUPPLIERS [4-5]

Supplier	Equipment/Service/System
GEA/Heatric (Germany/UK)	Recuperator
Nukem (Germany)	Fuel Technology
SGLCompany (Germany)	Graphite
Mitsubishi Heavy Industries (Japan)	Turbo Machinery
IST Nuclear (South Africa)	Nuclear Auxiliary Systems
ENSA (Spain)	Pressure Boundary
Sargent and Lundy (USA)	Architect/Engineering Services
Westinghouse (USA)	Instrumentation

Initial development of the PBMR is to utilize a helium-cooled pebble bed HTGR of 400 MW(t) to generate approximately 165 MW(e) of electricity with a conservative net plant efficiency of $\geq 41\%$. Construction of a In 2000, the PBMR (Pty) Ltd. Company was formed with international investment partners to build and market PBMR-based power plants. Since the technology had not previously been commercialized, the intention to build and operate a single module to serve as a demonstration plant and as a launch platform for local and international sales and an associated fuel plant was publicized. Successful completion of the demonstration phase will be followed by commercialization, with ESKOM likely to be the first customer [4-5].

Economic and plant development targets for the PBMR include:

- The overnight construction cost is expected to be less than 1,200 US\$/installed kWh (in 2003);
- Construction of the first demonstration module is projected at 30–34 months, with a 24-month construction period for additional modules;
- Combined fuel and O&M costs are projected at 9 mills/kWh.

Although the initial demonstration unit will be a single PBMR module, the commercialization strategy is to provide complete plants that incorporate eight, four or two modules. An eight-module plant would provide an electricity power block of 1320 MW(e). This multi-module business strategy relies heavily on standardization. Plant modularization and system/component standardization are key requirements of the PBMR (Pty). Ltd developers for the commercialization of the PBMR.

PBMR demonstration unit at the present Koeberg NPP site near Cape Town, South Africa, is projected to start in the first quarter of 2007 with fuel loading anticipated for mid-2010. Commercial acceptance by ESKOM is scheduled for early 2011 [4-13].

4.1.7. PBMR company status (2011)

The Pebble Bed Modular Reactor project to build a demonstration unit was abandoned in 2010 and all the employees were formally retrenched on 30 September 2010. The PBMR Company still exist as an entity and according to a government decision it will be maintained till at least 2013. Its new role is to Care and Maintain the Intellectual Property. PBMR appointed a small team of engineering specialist on contract to fulfil this role.

4.2. PBMR-400 NEUTRONICS AND THERMAL HYDRAULICS

4.2.1. Neutronics and thermohydraulics benchmark problem descriptions

The deterministic neutronics, thermohydraulics and transient analysis tools and methods available to design and analyse PBMRs may have, in many cases, lagged behind the state of the art compared to other reactor technologies. This has motivated the testing of existing methods for HTGRs to analyse the neutronics and thermohydraulic behaviour for the design and safety evaluations of the PBMR. This test-case definition addresses the benchmarking of core simulation, thermohydraulics and transient methods through a set of multidimensional computational test problems [4-14-4-16].

4.2.1.1. Simplifications introduced

The reference design for the PBMR benchmark problem is derived from the 400 MW PBMR design. In recognition of the broader audience that might be participating in the calculations, several simplifications are introduced into the design in this specification to limit the need for any further approximations as far as possible. During this process care has been taken to ensure that all the important neutronics characteristics of the reactor design are preserved. The intention is to create the possibility to apply different codes for the various areas in neutronics, thermal hydraulics, coupled neutronics/thermal hydraulics and transient analyses.

Simplifications could make the core design essentially two dimensional (R, Z). It includes flattening of the upper surface of the pebble bed and the removal of the bottom cone and defuel chutes that result in a flat-bottom reflector. Pebble flow channels within the pebble bed could be simplified to be parallel and assumed to flow at equal speed. Control rods (RCS) in the side reflector and small absorber spheres (RSS) are modelled as a cylindrical skirt (also referred to as a grey curtain) with a given B-10 concentration.

Thermohydraulic simplifications include the specification of stagnant helium between the barrel and Reactor Pressure vessel (RPV) and stagnant air between the RPV and heat sink (outer boundary). The coolant flow is restricted to upwards flow from the inlet below the core within a porous ring in the reflector and downwards flow through the pebble bed to the outlet plenum. No cooling or leakage paths were defined.

Other simplifications include the assumption that all heat sources (from fission) will be deposited locally, i.e. in the fuel and that no other heat sources exist outside the core (for example neutron absorption in boron shielding regions). Simplifications are also made in the material thermal properties in as far as constant values are employed or specific correlations are employed. These assumptions are clearly listed in the following sections.

4.2.1.2. General specification

TABLE 4.5. GENERAL SPECIFICATIONS

No.	Description	Unit	Value
1	The thermal nuclear power rating of the reactor	MW	400
2	The pebble bed packing fraction.	-	0.61
3	Temperature of the Core Barrel Conditioning System (CBCS) helium flow touching the RPV wall (if boundary condition is required)	°C	300
4	U-235 enrichment for equilibrium fuel	wt/0	9.6
5	Target burnup	MWd/t	To be calculated for equilibrium
6	Thermal/Fast energy boundary (important in comparisons of results)	eV	1.86

4.2.1.3. Reactor and core structure geometry and dimensions

The tables below provide all the reactor specifications while Fig. 4.13 provides a depiction of the PBMR-400 simplified two dimensional geometry.

TABLE 4.6. CORE GEOMETRICAL SPECIFICATIONS

No.	Description	Unit	Value
1	Equivalent core outer diameter	m	3.7
2	Outer diameter of central reflector	m	2.0
3	Effective cylindrical height of the core (flattened core surface at the top to the volume averaged flattened bottom cone)	m	11.0
4	Total fuel volume	m ³	83.7156
5	Effective height of the upper void cavity (levelled core surface to bottom of top reflector)	m	0.785
6	Outer diameter of boring/hole in centre of central reflector	m	0.2
7	Effective annular thickness of the inner reflector block	m	0.4
8	Equivalent annular thickness of the outer reflector block	m	0.5
9	Inner diameter of the core barrel	m	5.750
10	The wall thickness of the core barrel	m	0.05
11	Inner diameter of the RPV	m	6.2
12	The wall thickness of the RPV	m	0.180
13	Total height of top reflector	m	1.7
14	Total height of bottom reflector	m	5.52
15	Top steel plate thickness	m	0.3
16	Bottom steel plate thickness	m	0.1
Additional information included for completeness (not needed due to simplifications introduced)			
17	Effective volume of fuel in bottom cones (as from CAD – flattened cone surfaces)	m ³	6.7183
18	Effective volume of fuel in top fuel piles	m ³	3.8872
19	Fuel effective cylindrical height (flattened top to the top/start of cone)	m	10.117
20	Height of the upper void cavity (bottom of top reflector to top of fuel piles)	m	0.328
21	Bottom reflector cone maximum axial height from top of de-fuelling chute	m	1.483
22	Number of de-fuelling chutes		3
23	Defuelling chutes inner diameter	m	0.4
24	Defuelling chutes are equally spaced (120°) on a Pitch Centre Diameter (PCD) of:	m	2.88
25	Equi-spaced central reflector inspection holes	#	16
26	Inspection holes diameter	m	0.05
27	Inspection holes are on a PCD of:	m	1.830

TABLE 4.7. IN-CORE FLOW CHANNEL GEOMETRICAL SPECIFICATIONS

No.	Description	Unit	Value
1	Axial distance between bottom of the core and the inlet plenum cross-section	m	1.42
2	Inlet plenum inner diameter	m	4.822
3	Inlet plenum outer diameter	m	5.262
4	Inlet plenum height	m	0.6
5	Diameter of cold gas inlet pipes (2 of)	m	0.6
6	Inlet pipes centre points	° (degrees)	40 and 320
7	Number of gas risers in outer reflector	#	36
8	PCD of risers	m	5.042
9	Diameter of risers (typical)	m	0.170
10	Distance from bottom of top reflector to top of top inlet plenum	m	0.705
11	Top inlet plenum inner diameter	m	4.5
12	Top inlet plenum outer diameter	m	4.75
13	Top inlet plenum height	m	0.7
14	Centre line axial distance between bottom inlet plenum and outlet plenum	m	2.0
15	Outlet plenum inner diameter	m	1.6
16	Outlet plenum outer diameter	m	2.1
17	Outlet plenum height	m	1.2
18	Flow diameter of outlet duct to hot outlet pipe	m	1.034

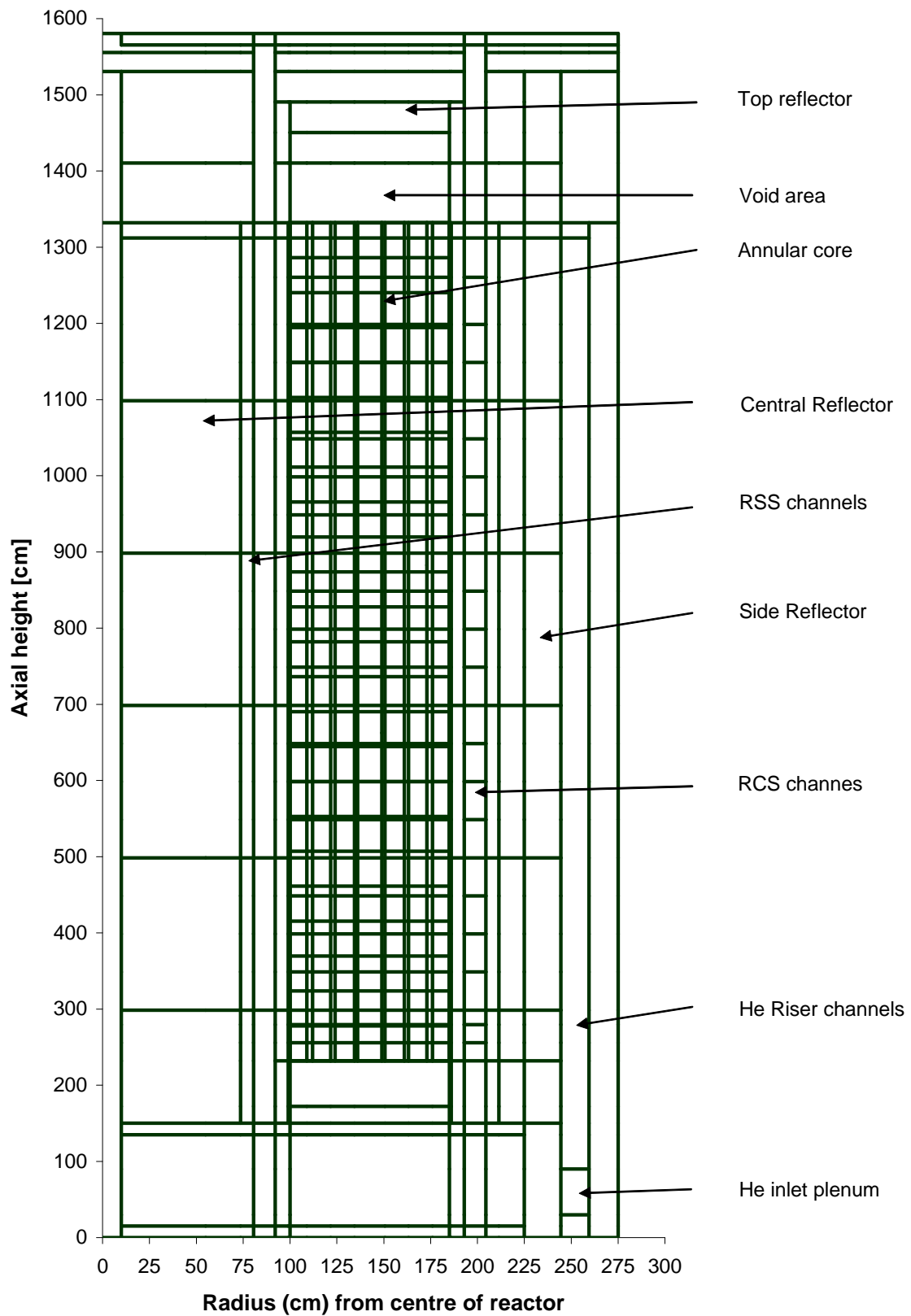


FIG. 4.13. PBMR 2-D geometry layout.

TABLE 4.8. APPROXIMATE EFFECTIVE POROSITIES IN REFLECTOR REGIONS DUE TO GAPS AND SLITS

No.	Description	Value
1	Effective void fraction of inner 60 cm block of the central reflector	0.0
2	Effective void fraction of bulk of outer block of central reflector (containing the SAS channel and inspection holes not included in this value) (60–94 cm)	0.0
3	Effective void fraction of outer region of outer block of central reflector (coolant slots only) (94–100 cm)	0.035
4	Effective void fraction of inner block of the side reflector (185–225 cm) (approximated over the mesh)	0.007
5	Effective void fraction of first part of the outer block of the side reflector (225–259.5 cm)	0.0
6	Effective void fraction of first part of the outer block of the side reflector (259.5–275 cm)	0.058
7	Effective void fraction of bottom reflector (helium outlet slots) to be used below the core.	0.193

Note: In the above values, none of the holes and penetrations was included. For example, the hole in the central reflector is not included in the central reflector inner block effective porosity.

RCSS Design

Due to the simplifications made in the definition, the Reactivity Control and Shutdown System (RCSS) can be modelled as a cylindrical grey skirt with a thickness of 115 mm positioned 69.5 mm into the side reflector. The B-10 number density in the skirt is 3.2×10^{-6} and the boron is mixed with graphite. The equilibrium insertion depth of the Reactivity Control System (RCS) is 2.285 m below the bottom of the top reflector. Details of the RCSS are included below for completeness but are not required to perform the test cases defined.

TABLE 4.9. RCSS BORINGS GEOMETRICAL SPECIFICATIONS

No.	Description	Unit	Value
1	RCS and reserve shutdown system (RSS) borings diameter	m	0.154
2	The effective diameter of the control rod holes (inside sleeve)	m	0.13
3	RCS sleeve outer diameter	m	0.15
4	The PCD of the control rod borings	m	3.974
5	The effective diameter of the RSS holes (inside sleeves).	M	0.13
6	RSS sleeve outer diameter	m	0.15
7	The PCD of the RSS borings	m	1.726
8	Number of RCS holes. The RCS holes are positioned symmetrically/equally spaced as shown in reference.	#	24
9	Number of RSS holes. The RSS holes are positioned symmetrically/equally spaced as shown in reference.	#	8

TABLE 4.10. RCSS GEOMETRICAL SPECIFICATIONS

No.	Description	Unit	Value
1	The control rod dimensions		
	Outer tube – outside diameter:	mm	105
	Wall thickness	mm	2.5
	Inner tube – outside diameter	mm	84
	Wall thickness	mm	0.5
	B4C rings – outside diameter	mm	100
	Wall thickness	mm	8
	Length of rings	mm	181
	Number of B4C rings per rod section	#	6
	Number of control rod sections	#	6
	Length of control rod sections	mm	1195
2	The minimum active control rod length	m	6.5
3	Small Absorber Sphere (SAS) packing density		0.61
4	SAS diameter	cm	1
5	The filling height of the RSS channel ends at the bottom of the top reflector	m	Top reflector

TABLE 4.11. RCSS INSERTION RULES AND INFORMATION

No.	Description	Unit	Value
1	Distance from bottom of top reflector for Group 1 and 2 totally extracted	m	0.0
2	Total travel distance of upper Group 1 (12 rods) fully inserted	m	6.9
3	Total travel distance of lower Group 2 (12 rods) fully inserted	m	9.9
4	Additional distance of lower Group 2 insertion	m	3.0
5	Volume fraction of rod suspension chain in the channel (130 mm) based on a $\phi 13$ mm chain	%	3.56%

Graphite and fuel sphere specifications

TABLE 4.12. GRAPHITE SPHERE SPECIFICATIONS

No.	Description	Unit	Value
1	Sphere outer radius	cm	3.0
2	Mass	g	195
3	Density of graphite	g.cm^{-3}	1.72
4	Equivalent boron content	mg.kg^{-1}	1.5

TABLE 4.13. FUEL SPECIFICATIONS

No.	Description	Unit	Value
Fuel pebble			
1	Fuel pebble outer radius	cm	3.0
2	Thickness of fuel-free zone	cm	0.5
3	Density of matrix graphite and graphite in fuel-free zone	g.cm-3	1.74
4	Total heavy metal loading per fuel pebble (equilibrium fuel)	g	9
5	Total heavy metal loading per fuel pebble (startup fuel)	g	9
6	Enrichment for equilibrium fuel (weight percentage)	wt/o	9.6
7	Enrichment (NU235/NU) for startup (weight percentage) ⁶	wt/o	5.76
8	Carbon content	g/fuel sphere	189
9	Equivalent boron content in graphite	mg.kg-1	1.3
Coated particle			
10	Fuel kernel diameter	μm	500
11	Particle material type		UO ₂
12	UO ₂ density	g.cm-3	10.4
13	Coating material		C/C/SiC/C
14	Buffer layer thickness	μm	95
15	Inner PyC layer thickness	μm	40
16	SiC layer thickness	μm	35
17	Outer PyC layer thickness	μm	40
18	Buffer layer density	g.cm-3	1.05
19	Inner PyC layer density	g.cm-3	1.9
20	SiC layer density	g.cm-3	3.18
21	Outer PyC layer density	g.cm-3	1.90

⁶ The enrichment used for the PBMR 400 MW startup fuel will be lower than 5% enriched (4.2–4.5%).

Other material specifications and properties

TABLE 4.14. MATERIAL SPECIFICATIONS AND DENSITIES

No.	Description	Unit	Value
1	The reflector graphite density for the inner/front block of the outer reflector (Grade A)	g.cm-3	1.80
2	The reflector graphite density for the outer/back block of the outer reflector (Grade C)	g.cm-3	1.79
3	SGL Grade A equivalent thermal (2 200 m/s) absorption cross-section (See Note below table)	mbarn	4.01
4	SGL Grade C equivalent thermal (2 200 m/s) absorption cross-section	mbarn	Same as Grade A
5	Reinforced concrete	g.cm-3	2.45
6	Density of RPV: SA 508	g.cm-3	7.83
7	Density of core barrel: Type 316 Stainless Steel (at 300°C)	g.cm-3	7.9
8	Incoloy 800H control rod sleeves	g.cm-3	8.0
	Additional information (not required for test cases)		
9	RCS B4C density	g.cm-3	2.2
10	SAS B4C loading	volume %	10
		mass %	14.4
11	SAS density	g.cm ⁻³	1.745
12	Volume of B4C per SAS	cm ³	0.0523
13	Mass of B4C per SAS	g	0.132
14	Density of B4C used in SAS manufacturing	g.cm ⁻³	2.52
15	Effective density of B4C in SAS	g.cm ⁻³	0.252

Note: Differences in the basic cross-section data of graphite, especially the thermal absorption cross-sections, can lead to noticeable differences in results. The definition of a 2 200 m/s thermal absorption cross-section of 4.01 mbarn is an attempt to eliminate this variation from the results. Some libraries include impurities and the typical ash content of graphite into the library while for others this needs to be defined separately. One way to adjust the effective thermal absorption cross-section of the reflector graphite to this value is to add small amounts of B-10 to adjust the absorption to 4.01 mbarn.

TABLE 4.15. COEFFICIENT OF EMISSION (EMISSIVITY) OF MATERIALS

No.	Description	Unit	Value
1	The emissivity of the fuel and graphite spheres.		0.85
2	The emissivity of the graphite structures.		0.8
3	The emissivity of the core barrel: Type 316 Stainless Steel		0.85
4	The emissivity of the RPV		0.91
	(The convective heat transport in the reactor cavity may be accounted for by an increase in the effective thermal conductivity.)		
5	The emissivity of the RCCS pipes		0.91
6	The emissivity of Incoloy 800H* (corrosion layer)		0.84
7	The emissivity of concrete		0.9

* Incoloy 800H is used for RCS sleeves.

TABLE 4.16. SPECIFIC HEAT CAPACITY OF MATERIALS

No.	Description	Unit	Value
1	Fuel and graphite spheres as well as reflector graphite (at 600°C)	J. kg ⁻¹ K ⁻¹	1690
2	RPV (at 316°C)	J. kg ⁻¹ K ⁻¹	566
3	Core Barrel (at 400°C)	J. kg ⁻¹ K ⁻¹	595
4	Specific heat capacity of helium	J. kg ⁻¹ K ⁻¹	5195
5	Reinforced (/ high-density) concrete (at 20°C)	J. kg ⁻¹ K ⁻¹	1150

The reflector dose to be assumed is the value after 35 full power years (FPY).

The thermal conductivity of graphite as a function of fast neutron dose and temperature is of importance for calculating the temperature distribution. This is also true for the fuel element graphite (NUKEM A3-3) as well as for the structural graphite. The A3-3 graphite data is taken from the work by Binkele [4-17] up to a fast dose of approximately $6.09 \times 10^{21} \text{ cm}^{-2}$ EDN (approximately $1.59 \times 10^{21} \text{ cm}^{-2}$ EDN is expected for the PBMR fuel) and a temperature up to 1000°C (which is the range covered by the experimental work). Above 1000°C, the data is conservatively extrapolated as a constant value (as shown in Fig. 4.14).

An effective thermal conductivity (refer to Fig. 4.15) is employed for the simulation of the heat transfer through a pebble bed. The effective thermal conductivity takes into consideration conduction and thermal radiation. Figure 4.15 depicts the limiting curves for the two models employed to describe the thermal conductivity in pebble beds. The model by Zehner–Schlünder [4-18] is employed to describe the heat transfer between pebbles at medium to low temperatures, while the model by Robold [4-19] accounts for the heat transfer by radiation at temperatures in excess of 1400°C.

The core calculations should be based on the measured properties of ATR-2E graphite being used for the reflector. In Fig. 4.16, a comparison is provided of the irradiated and un-irradiated datasets of the measured thermal conductivities for ATR-2E graphite.

TABLE 4.17. THERMAL CONDUCTIVITY OF MATERIALS

No.	Description	Unit	Value
1	Pebble bed: Zehner-Schlünder and Robold (see Table 4.18)	$\text{W m}^{-1} \text{K}^{-1}$	Correlation
2	Matrix graphite: Nukem A3-3 data irradiated at 950°C (see Fig. 4.14)	$\text{W m}^{-1} \text{K}^{-1}$	Measured data
3	Reflector graphite: Temperature-fluence dependent thermal conductivity of the inner reflector blocks and central column as provided in Fig. 4.16	$\text{W m}^{-1} \text{K}^{-1}$	Measured data
4	Core Barrel (Type 316 SS) — Assumed constant	$\text{W m}^{-1} \text{K}^{-1}$	17.0
5	RPV (SA 508) — Assumed constant	$\text{W m}^{-1} \text{K}^{-1}$	38.0
6	Helium stagnant $k = 2.682 \times 10^{-3} T^{0.71(1-2 \times 10^{-9} p)} (1 + 1.123 \times 10^{-8} p)$; where k (W/m/K), T (K), and p (Pascal).	$\text{W m}^{-1} \text{K}^{-1}$	Correlation used
7	Air stagnant $k = a \cdot b^T \cdot T^c$; where a = 9.1446E-05; b = 9.9958E-01; c = 1.0148E+00	$\text{W m}^{-1} \text{K}^{-1}$	Correlation used
8	Reinforced concrete T = 50°C	$\text{W m}^{-1} \text{K}^{-1}$	2.41

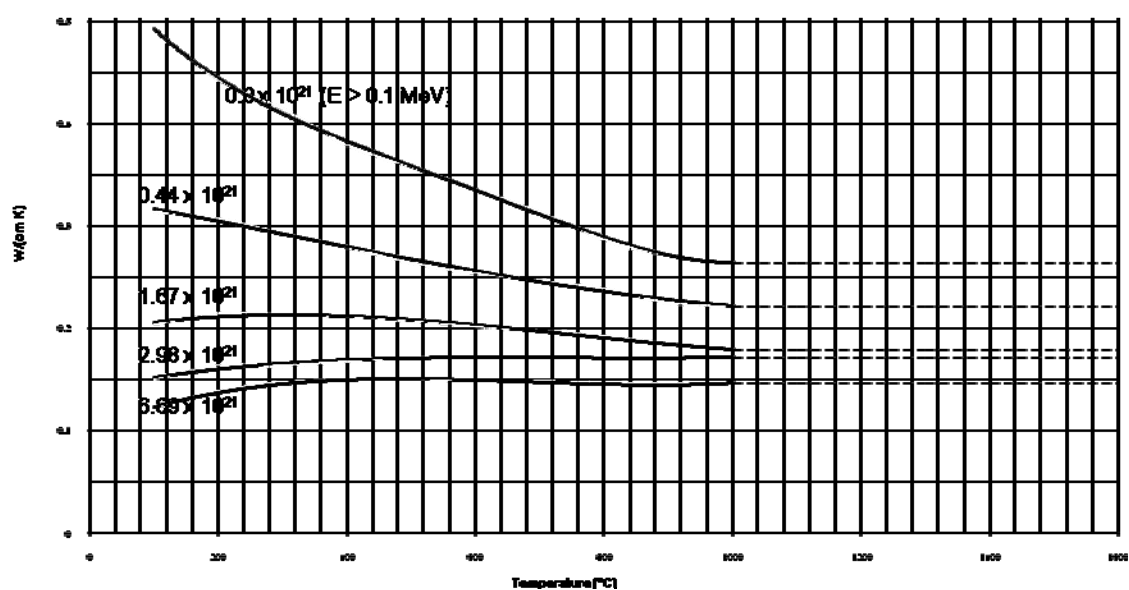


FIG. 4.14. Thermal conductivity of A3-3 matrix graphite as a function of temperature and neutron fluence irradiated at 950 C.

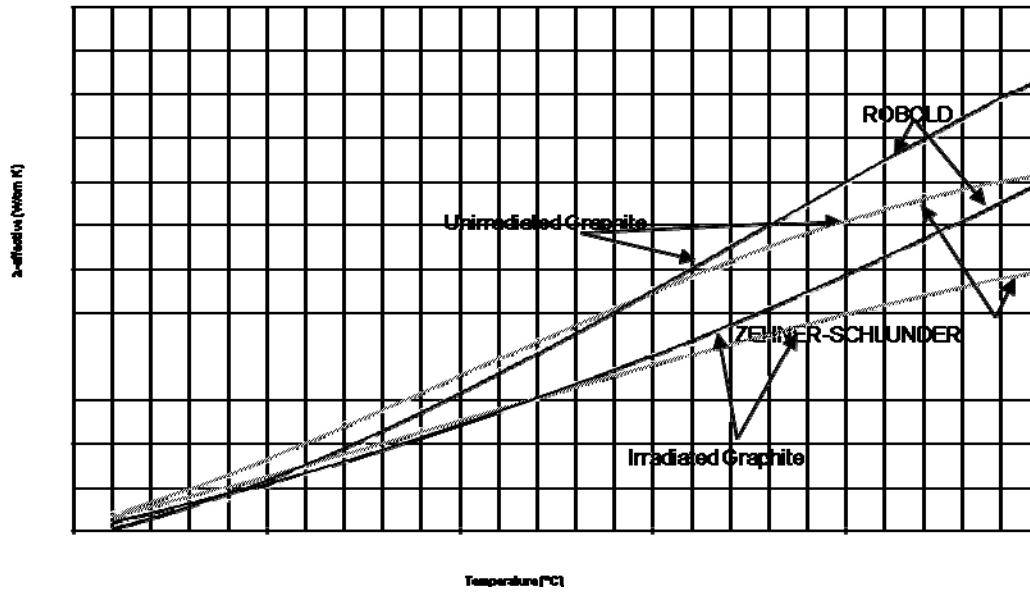


FIG. 4.15. Effective thermal conductivity in a pebble bed.

Thermal Conductivity Modeling Data for Unirradiated and Irradiated Graphite

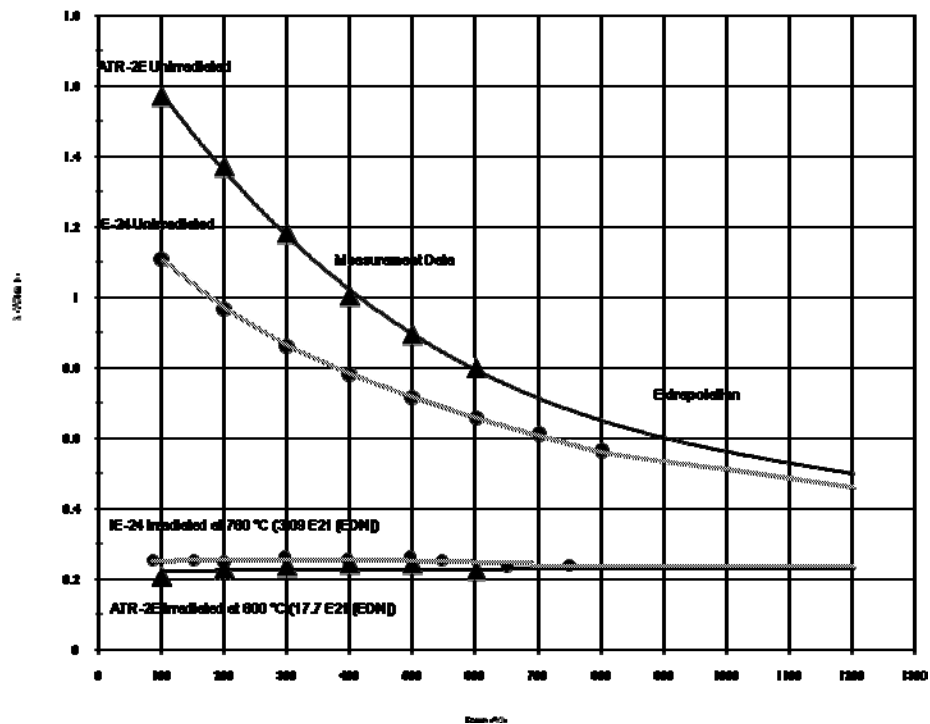


FIG. 4.16. ATR-2E graphite thermal conductivity as a function of temperature and dose.

TABLE 4.18. EXAMPLE OF ROBOLD AND ZEHNER-SCHLÜNDER CORRELATION EFFECTIVE THERMAL CONDUCTIVITY [W/CMK] AT LOW AND RELATIVELY HIGH NEUTRON DOSE

T (°C)	Robold	Zehner-schlünder	Robold	Zehner-schlünder
Fast dose (>0.1MeV)	No Dose	No Dose	6.09E21	6.09E21
100	1.12E-02	2.66E-02	1.05E-02	1.73E-02
200	1.70E-02	3.45E-02	1.57E-02	2.42E-02
300	2.56E-02	4.55E-02	2.34E-02	3.39E-02
400	3.74E-02	5.99E-02	3.33E-02	4.51E-02
500	5.24E-02	7.75E-02	4.51E-02	5.77E-02
600	6.98E-02	9.68E-02	5.76E-02	6.99E-02
700	8.86E-02	1.16E-01	7.05E-02	8.17E-02
800	1.08E-01	1.35E-01	8.14E-02	8.99E-02
900	1.30E-01	1.55E-01	9.45E-02	1.01E-01
1000	1.52E-01	1.75E-01	1.08E-01	1.12E-01
1300	2.10E-01	2.21E-01	1.49E-01	1.46E-01
1600	2.59E-01	2.54E-01	1.94E-01	1.81E-01
1900	3.00E-01	2.75E-01	2.45E-01	2.18E-01
2200	3.44E-01	2.92E-01	3.05E-01	2.53E-01
2500	4.01E-01	3.04E-01	3.78E-01	2.81E-01

If the implementation of the Robold and Zehner-Schlünder correlation is not available, a simplified linear relationship between the effective thermal conductivity and the pebble bed average temperature can be used:

$$\lambda = 1.547 \times 10^{-4} T - 8.464 \times 10^{-3}$$

with T = Temperature in °C and λ with units [W/cmK]

Reactor main coolant flow specifications

TABLE 4.19. MAIN HELIUM FLOW PARAMETERS

No.	Description	Unit	Value
1	Helium inlet temperature	°C	488.1
2	Total inlet mass flow rate	kg/s	185.31
3	Inlet pressure	kPa	8915
4	Total bypass flow (not going through the pebble bed)	%	19 ⁽¹⁾

Notes: In the test case defined, the helium coolant flow paths were simplified with no leakage or engineered bypass or reflector cooling flow paths defined. The definition of 19% bypass flow is to capture all of these flows bypassing the core in a simplified way. As such it could just be subtracted from the given inlet total flow, but this would result in a calculated outlet temperature much higher than the designed 900°C since the remixing with the colder bypass helium is then ignored. As an alternative, a simple bypass flow from the inlet to the outlet will have the desired effect.

4.2.1.4. Reactor cavity and MPS auxiliary systems specification

Reactor cavity

TABLE 4.20. REACTOR CAVITY SPECIFICATIONS

No.	Description	Unit	Value
1	Radius (from vessel centreline) of reactor cavity inner wall	m	5.1
2	Radius (from vessel centreline) of reactor cavity outer wall	m	7.6
3	Material of reactor cavity wall	-	Reinforced Concrete

Void representation

In the neutronics specification, only one void region has been specified, being the 78.5 cm between the top of the flattened pebble bed and the bottom of the top reflector. Regions where the helium coolant flows were modelled as porous regions (containing graphite and helium), but with no reduction made in the graphite density.

In the diffusion calculation, directional dependent diffusion coefficients can be used to represent the neutron streaming effects according to the method of Gerwin and Scherer [4-20]. A factor is multiplied to the radius of the void region to yield the diffusion coefficient for the R- and Z-direction, 0.1 for the R- and 0.5 for the Z-directions respectively. The values of 4.25 cm in the radial and 21.25 cm in the axial direction diffusion coefficient should thus be used.

Boundary conditions

TABLE 4.21. NEUTRONICS BOUNDARY CONDITIONS

No.	Description	Unit	Value
Neutronic model boundaries			
1	Radial	mm	2750
2	Top (beyond 100 cm of top reflector)	mm	-1250
3	Bottom (beyond 100 cm of bottom reflector)	mm	1000
4	Type of boundary conditions (on all boundaries)		BLACK/ ZERO FLUX

Test case homogeneous fuel specifications

Since many codes do not have the pebble bed multipass fuel circulation (MEDUL) or fuel depletion functionality, it was felt that other reactor compositions should also be defined. This will facilitate better and well-defined comparisons but also allow broader participation in the benchmark since calculational systems, which do not, can then also participate.

Three sets of homogenized atomic or number densities are provided as follows:

1. ND-set1: First core uranium isotopic distribution given for the material regions in the core (as a homogenized mixture);
2. ND-set2: First core uranium and graphite isotopic distribution given for the material regions in the core (as a homogenized mixture of fuel:graphite sphere ratio of 1:2);
3. ND-set3: Equilibrium core detailed isotopic distribution given for a detailed mesh (5×22) of material regions in the core (as a homogenized mixture).

For completeness, the graphite structures' graphite number density is included as well as the control rods (grey curtain) B-10 number density. These can of course be calculated directly from the given specifications.

TABLE 4.22. NUMBER DENSITIES FOR ND-SET1: FUEL AND REFLECTOR REGIONS

Isotope	Central Column	Fuel Regions	Graphite (Reflector)	Control
U-234	0.0	6.22417E-08	0.0	0.0
U-235	0.0	7.0860E-06	0.0	0.0
U-238	0.0	1.1570E-04	0.0	0.0
O-16	0.0	2.4570E-04	0.0	0.0
SI	0.0	2.77203E-04	0.0	0.0
C	8.9747E-02	5.2626E-02	9.0248E-02	7.2472E-02
B-10	0.0	0.0	0.0	3.20E-06

TABLE 4.23. NUMBER DENSITIES FOR ND-SET2: FUEL AND REFLECTOR REGIONS

Isotope	Central Column	Fuel Regions	Graphite (Reflector)	Control
U-234	0.0	2.07472E-08	0.0	0.0
U-235	0.0	2.3620E-06	0.0	0.0
U-238	0.0	3.85673E-05	0.0	0.0
O-16	0.0	8.19001E-05	0.0	0.0
SI	0.0	9.24009E-05	0.0	0.0
C	8.9747E-02	5.3203E-02	9.0248E-02	7.2472E-02
B-10	0.0	0.0	0.0	3.20E-06

Equilibrium core number density sets

To enable the simulation of the equilibrium core without the ability of performing the detailed burnup and fuel management calculations, a detailed homogenized number density distribution was provided to participants (too much detail to include in this document). The data was obtained from the equilibrium cycle analysed with the VSOP99 code.

The geometrical mesh to be used for the material specification divides the core region into 110 regions consisting of five different radial regions of 17 cm each (equal width) and 22 axial regions of 50 cm each. The regions are numbered as indicated in Fig. 4.17.

Note that by using the detailed specification of the fuel and the packing fraction, the number densities can be ‘unhomogenized’ to obtain the number densities to be used in heterogeneous fuel specifications. All the uranium, actinides and fission products can then be defined in the kernels and the graphite number densities obtained from the original specification.

Radius	100	117	134	151	168	185
Height	Size	17	17	17	17	17
0						
50	50	(1,1)	(2,1)	(3,1)	(4,1)	(5,1)
100	50	(1,2)	(2,2)	(3,2)	(4,2)	(5,2)
150	50	(1,3)	(2,3)	(3,3)	(4,3)	(5,3)
200	50	(1,4)	(2,4)	(3,4)	(4,4)	(5,4)
250	50	(1,5)	(2,5)	(3,5)	(4,5)	(5,5)
300	50	(1,6)	(2,6)	(3,6)	(4,6)	(5,6)
350	50	(1,7)	(2,7)	(3,7)	(4,7)	(5,7)
400	50	(1,8)	(2,8)	(3,8)	(4,8)	(5,8)
450	50	(1,9)	(2,9)	(3,9)	(4,9)	(5,9)
500	50	(1,10)	(2,10)	(3,10)	(4,10)	(5,10)
550	50	(1,11)	(2,11)	(3,11)	(4,11)	(5,11)
600	50	(1,12)	(2,12)	(3,12)	(4,12)	(5,12)
650	50	(1,13)	(2,13)	(3,13)	(4,13)	(5,13)
700	50	(1,14)	(2,14)	(3,14)	(4,14)	(5,14)
750	50	(1,15)	(2,15)	(3,15)	(4,15)	(5,15)
800	50	(1,16)	(2,16)	(3,16)	(4,16)	(5,16)
850	50	(1,17)	(2,17)	(3,17)	(4,17)	(5,17)
900	50	(1,18)	(2,18)	(3,18)	(4,18)	(5,18)
950	50	(1,19)	(2,19)	(3,19)	(4,19)	(5,19)
1000	50	(1,20)	(2,20)	(3,20)	(4,20)	(5,20)
1050	50	(1,21)	(2,21)	(3,21)	(4,21)	(5,21)
1100	50	(1,22)	(2,22)	(3,22)	(4,22)	(5,22)

FIG. 4.17. Number density geometrical mesh numbers.

The conversion from the homogenized fuel number densities to the number densities in the fuel kernels as modelled in a heterogeneous model is simply obtained by relating the number of atoms in the UO₂ kernel in a fuel sphere to the number of atoms in a fuel sphere in the homogenized material, thus:

$$N_{het} = N_{hom} \left(\frac{V_{pebble}}{V_{kernel} \cdot nk \cdot pf} \right)$$

where

N_{het} is the number density for the UO₂ kernel;

N_{hom} is the number density for the homogenized fuel as specified;

V_{kernel} is the volume of one kernel = $6.545 \cdot 10^{-5} \text{ cm}^3$;

V_{pebble} is the volume of one pebble = 113.10 cm^3 ;

pf is the packing fraction = 0.61;

nk is the number of kernels per pebble = 15000.

4.2.1.5. Additional thermohydraulic data

Decay heat sources

A decay heat source can be calculated by the DIN 25485 standard [4-21] for each ‘material’ mesh within the core as a function of time. Alternatively, the given decay heat source in Table 4.24, expressed as % of the operating power, can be used.

TABLE 4.24. DECAY HEAT (% OF POWER) AS A FUNCTION OF DECAY TIME

Time	% Power	Time	% Power	Time	% Power
0	6.426	22 h	0.535	62 h	0.384
10 s	4.704	24 h	0.521	64 h	0.380
60 s	3.469	26 h	0.509	66 h	0.376
10 min	2.199	28 h	0.498	68 h	0.372
30 min	1.651	30 h	0.487	70 h	0.368
1 hr	1.325	32 h	0.477	72 h	0.365
2 h	1.066	34 h	0.468	74 h	0.361
3 h	0.945	36 h	0.459	76 h	0.358
4 h	0.871	38 h	0.451	78 h	0.355
5 h	0.818	40 h	0.444	80 h	0.352
6 h	0.778	42 h	0.437	82 h	0.349
7 h	0.745	44 h	0.430	84 h	0.346
8 h	0.718	46 h	0.424	86 h	0.343
9 h	0.695	48 h	0.418	88 h	0.340
10 h	0.675	50 h	0.413	90 h	0.337
12 h	0.640	52 h	0.407	92 h	0.334
14 h	0.612	54 h	0.402	94 h	0.332
16 h	0.589	56 h	0.397	96 h	0.329
18 h	0.568	58 h	0.393	98 h	0.327
20 h	0.551	60 h	0.388	100 h	0.324

4.2.1.6. Power profile

For the thermohydraulic steady state test case (Case T-1), a simplified axially averaged power profile was constructed from the relative power distribution in five equidistant core axial channels (17 cm each). The relative power densities for the five channels are given in Table 4.25.

TABLE 4.25. RELATIVE POWER DENSITIES

1 (Fuel)	2 (Fuel)	3 (Fuel)	4 (Fuel)	5 (Fuel)
1.119	1.023	0.953	0.957	0.945

The interpretation is that the power density in the first axial flow channel is calculated as $1.119 * (400 \text{ (MW)} / 83.7156 \text{ m}^3)$, $1.023 * (400 \text{ (MW)} / 83.7156 \text{ m}^3)$ in the second, etc.

4.2.2. Benchmark calculational case definitions

4.2.2.1. Benchmark calculational cases; steady state calculations

CASE F-1: Fresh fuel and cold conditions

Make use of the neutronics model description and the following conditions:

- The core is filled with fresh first-core fuel (9 g HM and 5.768 % enriched) — use ND-set1;
- Number densities can be used for homogeneous material or volume-weighted and applied to heterogeneous fuel specifications;
- Cold conditions (300 K) are employed for all materials;
- Use of own cross-sections;
- No control rods inserted (totally extracted).

CASE F-2: First core loading with given number densities

CASE F-2 (i):

Make use of the neutronics model description and the following conditions:

- Employ a homogeneous mixture of 33.3% first-core fuel (9 g HM and 5.768 % enriched) and 66.6% graphite spheres (no fission products or higher elements) — use ND-set2;
- Number densities can be used for homogeneous material or volume-weighted and applied to heterogeneous fuel specifications;
- Constant temperature conditions (300 K) for all materials;
- Use of own cross-sections;
- No control rods inserted (totally extracted).

CASE F-2 (ii) (optional):

The same as F-2 (i) and the following conditions:

- Constant temperature conditions (600, 900 and 1200 K) for all materials;
- Use of own cross-sections.

CASE E-1: Equilibrium cycle with given number densities

CASE E-1 (i):

- Perform neutronic calculation — use ND-set3;
- Constant temperature conditions (300 and 1200 K) for all materials;
- Make use of own cross-sections;
- Control rods inserted to equilibrium position.

CASE E-1 (ii):

Make use of the thermohydraulic properties and model description and the following conditions:

- Perform neutronic calculation — use ND-set3;
- Calculate the fuel temperatures, reflector temperatures, helium temperatures, pressure drops and flow rates;
- Assume Zehner-Schlünder pebble bed effective thermal conductivities (or the simplified linear relationship supplied);
- Repeat neutronics (thermohydraulic feedback);
- Make use of own cross-sections;
- Control rods inserted to equilibrium position.

CASE E-2: Equilibrium cycle calculation

The equilibrium core is defined as the reactor operational state achieved after a considerable time of operating at a specific set of conditions. For the benchmark problem, the operating conditions are defined to be at full power and with the 24 control rods (or grey skirt) inserted 2.285 m below the bottom of the top reflector (axial position in the RCS channels in the side reflector).

Fuel is circulated six times through the core before it is discharged. After each pass, the fuel is reintroduced to the top of the core and equally distributed over any defined flow lines (or core positions). This reload process is repeated and the burnup of the discharged fuel adjusted (by changing the core residence times) until an equilibrium state is reached with a critical core (k -effective = 1.0). Once equilibrium is reached, no significant changes can be observed in the properties of the core. For example, the k -effective, power profile, temperatures and isotopic concentration distribution no longer change. In the test case, the grey cylindrical skirt is inserted as defined. The fuel specification was included as part of the benchmark as starting condition for the calculation of the equilibrium core. The full isotope depletion chains available in the tools used should be used for the equilibrium study.

Make use of the detailed fresh fuel specification, thermohydraulic properties and model description, and the following conditions:

- Implement a fuel circulation scheme with fuel passing six times through the reactor before being discharged;
- Fuel flow lines are all parallel and all fuel flow speeds are the same (no variation in core residence time), independent of the radial and azimuthal position;
- The PBMR equilibrium fuel (9.6% enrichment) is introduced and an equilibrium cycle is calculated;
- Calculate the core neutronics and thermal hydraulics (fuel temperatures, reflector temperatures, helium temperatures, pressure drops and flow rates);
- Assume Zehner-Schlünder pebble bed effective thermal conductivities (or the simplified linear relationship supplied);
- Repeat neutronics (thermohydraulic feedback);
- Make use of own cross-sections.

CASE T-1: Steady state thermal balance and fluid dynamics with given power profiles

Make use of the thermohydraulic properties and model description and the following conditions:

- Calculate the fuel temperatures, reflector temperatures, helium temperatures, pressure drops and flow rates;
- Assume Zehner-Schlünder pebble bed effective thermal conductivities (or the simplified linear relationship supplied);
- Use the given power profile/heat source profile.

4.2.2.2. Benchmark calculational cases; Quasi-steady state calculation

CASE D-1: Depressurized loss of forced cooling

Make use of the thermohydraulic properties and model description and the following conditions:

- Use the power profiles/heat sources obtained from Case E-1 (ii);
- Calculate the fuel temperatures, reflector temperatures, helium temperatures, pressure drops and flow rates at starting conditions;
- Assume Zehner-Schlünder pebble bed effective thermal conductivities (or the simplified linear relationship supplied);
- Make use of own cross-sections (if applicable);
- Assume prompt depressurization;
- Decay heat calculation from DIN 25485 or the decay heat data supplied;
- Follow the core average and maximum fuel temperatures during the transient until maximum fuel temperatures have been reached and the core starts to cool down;
- Recriticality can be prevented by inserting negative reactivity (for example by inserting the control rods) if necessary.

4.2.2.3. Output parameters

A detailed spreadsheet template with all required results is available to record all required results. All in-core two dimensional results are to be supplied according to the meshes shown in Fig. 4.17 to allow

for data comparison. A short summary of all required results is provided here, but might not be applicable to all cases.

Steady state cases

Neutronics results

- Single parameters:
 - K-effective;
 - Discharge burnup (Case E-2 only);
 - Neutron leakage from the core (thermal, epithermal and total);
 - In-core scattering (epithermal to thermal);
 - Maximum power density/power per fuel sphere;
 - (Optional — four-group micro and macro cross-sections for cases using ND-set 1 and 2, absorption, fission and scattering).
- Two dimensional profiles (in the given mesh):
 - Power densities;
 - Neutron flux distribution (thermal and epithermal with cut-off of 1.86 eV).

Thermohydraulics results

- Single parameters:
 - Inlet/outlet pressure;
 - Inlet/outlet temperatures;
 - Average fuel temperature;
 - Average moderator temperature;
 - Average helium temperature;
 - Maximum fuel temperature.
- Two dimensional profile (in the given mesh):
 - Temperatures (pebble surface, reflector);
 - Pressure differences;
 - Mass flows rates;
 - Pebble bed effective thermal conductivity (if applicable);
 - Fuel sphere surface temperatures;
 - Temperature profiles within fuel spheres (if available).

Transient Case D-1 (in addition to the steady state case results)

- Single parameters (as a function of time):
 - Total decay heat (if calculated/not if provided data is used as input);
 - Maximum fuel temperature;
 - Average fuel temperature;
 - Maximum barrel temperature;
 - Maximum RPV temperature.

- Two dimensional profile (in the given mesh):
 - Fuel temperature distribution at time of maximum fuel temperature;
 - Barrel temperature profile over core active height at time of maximum;
 - RPV temperature profile over core active height at time of maximum.

The detailed spreadsheet should be used to report the results of each case to the host CSI for consistency and easy comparisons while the results from each participating country can be presented in whichever form convenient.

4.2.3. Analysis and results for PBMR-400 neutronics and thermohydraulics

The PBMR-400 benchmarks have been set up in support of the verification and validation effort of the design and safety codes at PBMR. The opportunity to perform code-to-code comparisons with other methods and codes of other participants is valuable and interesting.

This section contains all the results submitted by the participating member countries. Comparisons are included in Section 7.3.1

4.2.3.1. South Africa analysis and results for the PBMR-400 equilibrium cycle

Methods or code systems employed

During the development of the pebble-bed-type high temperature reactor in Germany, the research centre Jülich (FZJ, formerly KFA) has established theoretical methods and computational tools with respect to core design, reactor life simulation and transient analysis. These methods thus evolved in an environment where mainly basic research was conducted. After playing an important role in the licensing talks and safety discussions of German HTR projects at that time, today these codes are used to design and license the upcoming Gen IV reactors of HTR type with their enhanced self-stabilizing safety features.

These tools have unique features that are required to model pebble bed reactors, such as the fuel management algorithms, the simultaneous treatment of nuclear, thermohydraulic and fluid-dynamic problems, and the description of fast and long term transients. Most of the codes and methods developed at FZJ were obtained by Pebble Bed Modular Reactor (Pty) Ltd under license agreements and are now used in the design and licensing of the 400 MW pebble bed modular reactor (PBMR).

This section provides an overview of the specific methods and codes. The focus of the test cases are on the reactor core neutronics and thermohydraulics behaviour, which means that the VSOP [4-22] and TINTE [4-23] code packages were used. Below a short code summary is provided with more details available in the code references and a recent summary of the FZJ codes used at PBMR provided in [4-24].

VSOP

VSOP [4-22] is a computer code system for the comprehensive numerical simulation of the physics of thermal reactors. It implies the set-up of the reactor and of the fuel element, processing of cross-sections, neutron spectrum evaluation, neutron diffusion calculation (finite-difference) in two or three dimensions, fuel burnup, fuel shuffling, reactor control, thermal hydraulics and fuel cycle costs. This enables the user to calculate the reactor life history from loading to criticality, starting up the reactor and running the reactor towards equilibrium core conditions. The thermohydraulics part (steady state and time dependent) is restricted to pebble bed HTRs and to two spatial dimensions. Accident phenomena can be analysed in a quasi-static approximation by repeatedly analysing the reactivity and the temperature distribution in the reactor core. The current code version, VSOP(99), represents the further-developed and much-improved version of the VSOP(94) code available at the NEA databank and widely used for HTR analysis. Characteristics of the life history of the fuel elements are used to calculate the decay power according to the rules of the German standard DIN 25485. The code evaluates the total decay heat power of the reactor and its spatial distribution as well as the decay power of discharged fuel for a decay time of up to 30 years.

TINTE

The TINTE (Time Dependent Neutronics and Temperatures) code [4-23] was developed to investigate the nuclear and thermal transient behaviour of high temperature reactors, with full neutron, temperature and xenon feedback effects taken into account in two dimensional r-z geometry. The flux is calculated in two energy groups with six delayed neutron groups.

The code uses a one dimensional leakage iteration method to solve the two dimensional partial differential equations resulting from neutron and heat diffusion theory. This method makes it possible to solve the differential equations in a one dimensional fine grid, where first the radial and then the axial components of the fluxes and partial currents are determined. The coupling between the radial and axial regions is obtained from the transverse leakage terms, and an iteration scheme is applied until both 1-D calculations converge for each coarse-mesh region.

The code can be used for a large variety of transient analysis with largely varying time constants. Also, due to the large heat capacity of graphite, the overall temperature changes in the PBMR are very slow and the transients may last for many days. The main time dependent calculational components are the neutron flux, the nuclear heat source distribution, the heat transport from the fuel kernels to the fuel sphere surface, the time dependent global temperature distribution, the coolant gas flow distribution for a specified mass flow or pressure gradient, convection and its feedback on circulation, and finally the gas mixing effects.

TINTE relies on a nuclear macroscopic cross-section database generated by making use of a spectrum code and basic library and using a nuclide concentration vector as produced by VSOP-99. Polynomial expansions covering wide ranges of spectrum significant nuclear features, such as fuel and moderator temperature, xenon concentration, leakage coupling and additional moderator (steam) concentrations are used to model the changes in the macroscopic cross-sections during transients of the system.

Models and methodology

VSOP99 layout

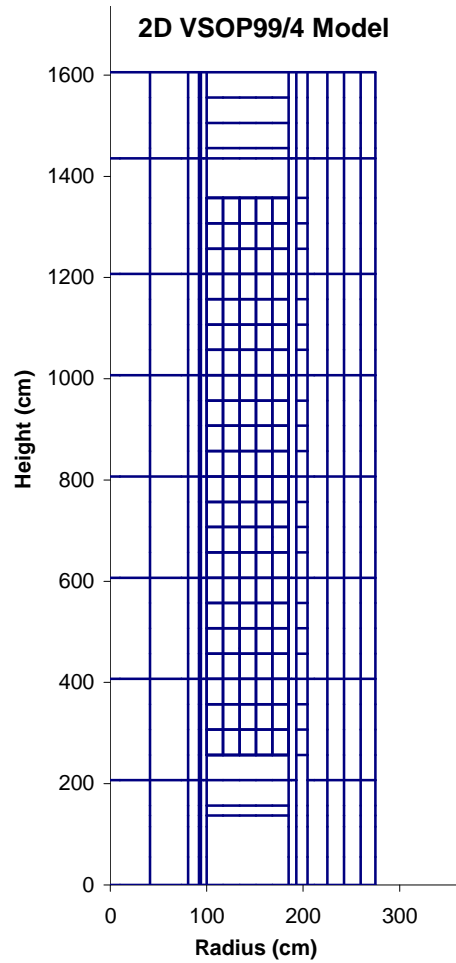


FIG. 4.18. PBMR 2-D geometry layout.

Figure 4.20 illustrates the calculational model used in the THERMIX module of VSOP99/4. The arrows show the helium flow paths. The different colours and numbers used represent different materials or regions in the model, such as central reflector, RCS hole, RPV, CB, etc.

The atom densities and the effective porosities of the compositions are calculated and listed in Table 4.26. Note that the number densities for RCS channels are directly used as given in the benchmark definition, thus the effective void fraction for RCS channels is not given. In Case E-2, the RCS channel is filled with ^{10}B with a number density of $3.20\text{E-}06.\text{barn/cm}$ up to 2.12 m from the bottom of the top reflector.

	10.00	41.00	73.60	80.55	92.05	94.00	97.00	100.00	117.00	134.00	151.00	168.00	185.00	188.00	192.95	204.45	211.40	225.00	242.50	259.50	275.00
50.00	75	75	59	59	26	107	10	10	5	5	5	5	5	18	18	34	67	67	83	91	99
100.00	75	75	59	59	26	107	10	10	4	4	4	4	4	18	18	34	67	67	83	91	99
150.00	75	75	59	59	26	107	10	10	3	3	3	3	3	18	18	34	67	67	83	91	99
170.00	75	75	59	59	26	107	10	10	2	2	2	2	2	18	18	34	67	67	83	91	99
248.50	76	76	60	60	27	108	11	11	1	1	1	1	1	19	19	35	68	68	84	92	100
298.50	76	76	60	60	27	108	11	11	0	0	0	0	0	19	19	36	68	68	84	92	100
348.50	76	76	60	60	27	108	11	11	0	0	0	0	0	19	19	37	68	68	84	92	100
398.50	76	76	60	60	27	108	11	11	0	0	0	0	0	19	19	38	68	68	84	92	100
448.50	77	77	61	61	28	109	12	12	0	0	0	0	0	20	20	39	69	69	85	93	101
498.50	77	77	61	61	28	109	12	12	0	0	0	0	0	20	20	40	69	69	85	93	101
548.50	77	77	61	61	28	109	12	12	0	0	0	0	0	20	20	41	69	69	85	93	101
598.50	77	77	61	61	28	109	12	12	0	0	0	0	0	20	20	42	69	69	85	93	101
648.50	78	78	62	62	29	110	13	13	0	0	0	0	0	21	21	43	70	70	86	94	102
698.50	78	78	62	62	29	110	13	13	0	0	0	0	0	21	21	44	70	70	86	94	102
748.50	78	78	62	62	29	110	13	13	0	0	0	0	0	21	21	45	70	70	86	94	102
798.50	78	78	62	62	29	110	13	13	0	0	0	0	0	21	21	46	70	70	86	94	102
848.50	79	79	63	63	30	111	14	14	0	0	0	0	0	22	22	47	71	71	87	95	103
898.50	79	79	63	63	30	111	14	14	0	0	0	0	0	22	22	48	71	71	87	95	103
948.50	79	79	63	63	30	111	14	14	0	0	0	0	0	22	22	49	71	71	87	95	103
998.50	79	79	63	63	30	111	14	14	0	0	0	0	0	22	22	50	71	71	87	95	103
1048.50	80	80	64	64	31	112	15	15	0	0	0	0	0	23	23	51	72	72	88	96	104
1098.50	80	80	64	64	31	112	15	15	0	0	0	0	0	23	23	52	72	72	88	96	104
1148.50	80	80	64	64	31	112	15	15	0	0	0	0	0	23	23	53	72	72	88	96	104
1198.50	80	80	64	64	31	112	15	15	0	0	0	0	0	23	23	54	72	72	88	96	104
1248.50	81	81	65	65	32	113	16	16	0	0	0	0	0	24	24	55	73	73	89	97	105
1298.50	81	81	65	65	32	113	16	16	0	0	0	0	0	24	24	56	73	73	89	97	105
1348.50	81	81	65	65	32	113	16	16	0	0	0	0	0	24	24	57	73	73	89	97	105
1398.50	81	81	65	65	32	113	16	16	6	6	6	6	6	24	24	58	73	73	89	97	105
1448.50	82	82	66	66	33	114	17	17	7	7	7	7	7	25	25	58	74	74	90	98	106
1468.50	82	82	66	66	33	114	17	17	8	8	8	8	8	25	25	58	74	74	90	98	106
1490.50	82	82	66	66	33	114	17	17	9	9	9	9	9	25	25	58	74	74	90	98	106
1550.50	82	82	66	66	33	114	17	17	9	9	9	9	9	25	25	58	74	74	90	98	106
1605.50	82	82	66	66	33	114	17	17	9	9	9	9	9	25	25	58	74	74	90	98	106

FIG. 4.19. VSOP99/4 calculational neutronics model.

	10.00	41.00	73.60	80.55	92.05	94.00	97.00	100.00	117.00	134.00	151.00	168.00	185.00	188.00	192.95	204.45	211.40	225.00	242.50	259.50	275.00	287.50	292.50	310.00	328.00	402.00	463.00	
279.50	30	30	30	30	30	30	30	30	30	30	30	30	30	30	30	30	30	30	30	30	30	30	30	30	30	30	30	
277.50	23	23	23	23	23	23	23	23	23	23	23	23	23	23	23	23	23	23	23	23	23	23	23	23	23	23	23	
248.50	31	31	31	31	14	33	8	8	4	4	4	4	4	9	9	9	9	9	12	12	12	12	21	24	25	26	27	28
198.50	31	31	31	31	14	33	8	8	4	4	4	4	4	9	9	9	9	9	12	12	12	12	21	24	25	26	27	28
148.50	31	31	31	31	14	33	8	8	3	3	3	3	3	9	9	9	9	9	12	12	12	12	21	24	25	26	27	28
98.50	31	31	31	31	14	33	8	8	3	3	3	3	3	9	9	9	9	9	12	12	12	12	21	24	25	26	27	28
78.50	31	31	31	31	14	33	8	8	2	2	2	2	2	9	9	9	9	9	12	12	12	12	21	24	25	26	27	28
0.00	31	31	31	31	14	33	8	8	1	1	1	1	1	9	9	11	9	9	12	13	12	12	21	24	25	26	27	28
50.00	31	31	31	31	14	33	8	8	1	1	1	1	1	9	9	11	9	9	12	13	12	12	21	24	25	26	27	28
100.00	31	31	31	31	14	33	8	8	1	1	1	1	1	9	9	11	9	9	12	13	12	12	21	24	25	26	27	28
150.00	31	31	31	31	14	33	8	8	1	1	1	1	1	9	9	11	9	9	12	13	12	12	21	24	25	26	27	28
200.00	31	31	31	31	14	33	8	8	1	1	1	1	1	9	9	11	9	9	12	13	12	12	21	24	25	26	27	28
250.00	31	31	31	31	14	33	8	8	1	1	1	1	1	9	9	11	9	9	12	13	12	12	21	24	25	26	27	28
300.00	31	31	31	31	14	33	8	8	1	1	1	1	1	9	9	11	9	9	12	13	12	12	21	24	25	26	27	28
350.00	31	31	31	31	14	33	8	8	1	1	1	1	1	9	9	11	9	9	12	13	12	12	21	24	25	26	27	28
400.00	31	31	31	31	14	33	8	8	1	1	1	1	1	9	9	11	9	9	12	13	12	12	21	24	25	26	27	28
450.00	31	31	31	31	14	33	8	8	1	1	1	1	1	9	9	11	9	9	12	13	12	12	21	24	25	26	27	28
500.00	31	31	31	31	14	33	8	8	1	1	1	1	1	9	9	11	9	9	12	13	12	12	21	24	25	26	27	28
550.00	31	31	31	31	14	33	8	8	1	1	1	1	1	9	9	11	9	9	12	13	12	12	21	24	25	26	27	28
600.00	31	31	31	31	14	33	8	8	1	1	1	1	1	9	9	11	9	9	12	13	12	12	21	24	25	26	27	28
650.00	31	31	31	31	14	33	8	8	1	1	1	1	1	9	9	11	9	9	12	13	12	12	21	24	25	26	27	28
700.00	31	31	31	31	14	33	8	8	1	1	1	1	1	9	9	11	9	9	12	13	12	12	21	24	25	26	27	28
750.00	31	31	31	31	14	33	8	8	1	1	1	1	1	9	9	11	9	9	12	13	12	12	21	24	25	26	27	28
800.00	31	31	31	31	14	33	8	8	1	1	1	1	1	9	9	11	9	9	12	13	12	12	21	24	25	26	27	28
850.00	31	31	31	31	14	33	8	8	1	1	1	1	1	9	9	11	9	9	12	13	12	12	21	24	25	26	27	28
900.00	31	31	31	31	14	33	8	8	1	1	1	1	1	9	9	11	9	9	12	13	12	12	21	24	25	26	27	28
950.00	31	31	31	31	14	33	8	8	1	1	1	1	1	9	9	11	9	9	12	13	12	12	21	24	25	26	27	28
1000.00	31	31	31	31	14	33	8	8	1	1	1	1	1	9	9	11	9	9	12	13	12	12	21	24	25	26	27	28
1050.00	31	31	31	31	14	33	8	8	1	1	1	1	1	9	9	11	9	9	12	13	12	12	21	24	25	26	27	28
1100.00	31	31	31	31	14	33	8	8	5	5	5	5	5	9	9	11	9	9	12	13	12	12	21	24	25	26	27	28
1150.00	31	31	31	31	14	33	8	8	5	5	5	5	5	9	9	11	9	9	12	13	12	12	21	24	25	26	27	28
1170.00	31	31	31	31	14	33	8	8	6	6	6	6	6	9	9	11	9	9	12	13	12	12	21	24	25	26	27	28
1192.00	31	31	31	31	14	33	8	8	7	7	7	7	7	9	9	11	9	9	12	13	12	12	21	24	25	26	27	28
1252.00	31	31	31	31	14	33	8	8	7	7	7	7	7	9	9	11	9	9	12	13	12	12	21	24	25	26	27	28
1307.00	31	31	31	31	14	33	8	8	7	7	7	7	7	9	9	11	9	9	12	12	12	12	21	24	25	26	27	28
1362.00	31	31	31	31	14	33	8	8	7	7	7	7	7	9	9	11	9	9	12	12	12	12	21	24	25	26	27	28
1482.00	31	31	31	31	15	15	15	15	10	10	10	10	10	16	16	16	9	9	12	12	12	12	21	24	25	26	27	28
1487.00	31	31	31	31	33	33	8	8	17	17	17	17	17	9	9	9	9	9	12	12	12	12	21	24	25	26	27	28
1492.00	31	31	31	31	33	33	8	8	17	17	17	17	17	9	9	9	9	9	12	12	12	12	21	24	25	26	27	28
1602.00	31	31	31	31	33	33	8	8	17	17	17	17	17	9	9	9	9	9	12	12	12	12	21	24	25	26	27	28
1611.00	22	22	22	22	22	22	22	22	22	22	22	22	22	22	22	22	22	22	22	22	22	22	22	22	25	26	27	28
1612.00	29	29	29	29	29	29	29	29	29	29	29	29	29	29	29	29	29	29	29	29	29	29	29	29	29	29	29	29

TABLE 4.26. NUMBER DENSITIES USED IN THE REFLECTOR REGIONS

REGION	SPECTRUM ZONE	VOID FRACTION	C (BARN/CM)
Void above core	1	0.999	5.014192E-08
Top reflector	2-5	0	9.024800E-02
Bottom reflector	6-9	0.193	7.283000E-02
Central column	10-17	0.035	8.660600E-02
Side reflector	18-25	0.007	8.961600E-02
SAS channel	26-33	0	8.974700E-02
RCS channel	34-58	N/A	7.247200E-02
Central column	59-66	0	8.974700E-02
Side reflector	67-74	0.007	8.961600E-02
Central column	75-82	0	8.974700E-02
Side reflector	83-98	0	9.024800E-02
Side reflector	99-106	0.058	8.501400E-02
Central column	107-114	0	8.974700E-02

In practice the calculations are started with the core filled with graphite balls. Fresh fuel elements (with the ND-Sets as given) are then loaded into the whole core. For Case E2, the loading scheme is then changed to shuffling the used fuel balls in different channels and taking out the spent fuel (after completely replacing the initial graphite balls with fuel balls). The calculation is carried on until the equilibrium core conditions have been reached.

The model was set up from the detailed descriptions of the core given in the benchmark definition. The radial and axial diffusion coefficients specified in the benchmark were used to represent the void region above the fuel.

TINTE layout

An interface exists between the VSOP99 and TINTE codes that facilitates the generation of identical models in the two codes. Although the model can easily be changed in TINTE, in this case the neutronic material mesh used in TINTE is identical to the VSOP99 CITATION mesh, shown in Fig. 4.19. The TINTE temperature mesh is also identical to the VSOP99 mesh (Fig. 4.20), since no additional components were modelled for the benchmark (i.e. the RCCS and CBCS flows are not present in the benchmark PBMR 400 model).

Results

Steady state cases

The results are divided into two. The summary of the results for all steady state cases that were calculated with VSOP99 are discussed in this section, while the fast and thermal flux maps, power maps, temperature and thermohydraulic property maps, where applicable, are later given separately for each case.

Global parameters

The summarized information for cases that require only neutronic analysis is given in Tables 4.27 and 4.28, whereas the results of cases that also require thermohydraulic calculations are given in Table 4.29.

Table 4.27 represents the results for Cases F1, F2 (i) and E1 (i), where an isothermal temperature of 300 K is applied to all materials. The reactor multiplication factor (k_{eff}) is the highest in Case F1 with its fresh fuel definition ($k_{\text{eff}} = 1.27178$) and decreases to $k_{\text{eff}} = 1.000395$ in Case E1 (i) since the fuel definition and thus core content is changed from fresh fuel to equilibrium core fuel.

The effect of the change in the moderation ratio is clearly seen when the results of Cases F1 and F2 (i) are compared. The two cases are similar except for the fuel-to-moderator ratio. The in-core scattering is higher in Case F2 (i) where there is more moderator present inside the core, i.e. more slowing down occurs inside the core. This also results in a softening of the spectra or decrease in the core average epithermal-to-thermal ratio as a result of more neutrons slowing down to thermal energies inside the core.

Furthermore, although the epithermal leakage from the core is not changed, the thermal leakage values are changed significantly in Case F2. The negative sign of the thermal leakage shows that a net thermal leakage occurs from the core-reflector boundary to the core. The thermal leakage to the core is also decreased as a result of the higher moderation ratio inside the core.

TABLE 4.27. NEUTRONIC CALCULATION RESULTS AT T = 300 K

	Case F1	Case F2 (i)	Case E1 (i)
Temperature (K)	300	300	300
k-eff	1.27178	1.16538	1.00395
In-core scattering epithermal -> thermal: (%)	49.44%	59.64%	48.17%
Leakage			
Epithermal (> 1.86 eV)	32.82%	33.32%	33.00%
Thermal (<1.86 eV)	-16.32%	-7.52%	-18.41%
Total	16.50%	25.79%	14.59%
Total leakage out of the system (calculational domain)	5.02%	7.46%	4.39%
Core average spectra (epithermal-to-thermal ratio over core region)	1.278	0.564	1.492
Reflector average spectra (epithermal-to-thermal ratio)	0.144	0.089	0.162

Table 4.28 gives the results for the Cases F2 (ii) (600 K, 900 K and 1200 K) and E1 (i) (1200 K), where the effect of temperature can clearly be seen. The increase in temperature introduces a negative reactivity, which can be explained by Doppler broadening and thermal spectrum shift (spectrum hardening). An increase of fuel temperature results in a shift to higher energy and deformation of Maxwellian spectrum in the fuel. The spectrum in graphite is also affected due to an increase in the graphite temperatures. The fission reaction rate in the fuel is reduced due to harder spectrum in the fuel, but the absorption reaction rate (sum of absorption in fuel and graphite) is less reduced. The ratio of the fission reaction rate and absorption reaction rate (equal to the multiplication factor) is therefore reduced.

The results for Cases E1 (ii), E2 and T1 are given in Table 4.29. Case T1 does not require neutronic calculations since the power distribution is provided. The difference between Cases E1 (ii) and E2 is the isotopic distribution in the 110 core regions. Case E1 (ii) makes use of the Nuclear Dataset (ND) NDSet3 which is given in the benchmark definition, whereas the isotopic distribution of the equilibrium core in Case E2 is calculated by VSOP99/4.

Both the neutronic and thermohydraulic results of Cases E1 (ii) and E2 do not show significant differences, since the only difference between the two cases is the isotopic distribution within the 110 fuel regions, which resulted from the different burnup values of the fuel regions.

The thermohydraulic results are significantly different in Case T1 when compared with the other two cases. Although the same materials are used in the thermohydraulic model, a given power/heat source profile is used as input for Case T1. The given power profile is axially constant over each of the five channels, which results in an axially linear temperature profile inside the core and side reflector as well as in the central column, increasing from top to bottom. Although the maximum fuel temperature is higher in Case T1, the average temperatures are lower. Due to the axially constant power profile, the

maximum fuel temperature occurs at the bottom of the core in Case T1, whereas in Case E2 the maximum fuel temperature is at the power peak, i.e. close to middle of the core. In both cases the maximum fuel temperature occurs at the core-central column boundary.

TABLE 4.28. NEUTRONIC CALCULATION RESULTS AT VARIOUS TEMPERATURES

	Case F2 (ii)	Case F2 (i)	Case F2 (ii)	Case F2 (i)	E1
Temperature (K)	600	900	1200	1200	
k-eff	1.12424	1.08875	1.06301	0.98606	
In-core scattering epithermal -> thermal: (%)	59.32%	58.94%	58.90%	45.92%	
Leakage					
Epithermal (> 1.86 eV)	33.24%	33.17%	33.11%	32.20%	
Thermal (<1.86 eV)	-6.15%	-4.91%	-3.73%	-17.30%	
Total	27.09%	28.26%	29.39%	14.90%	
Total leakage out of the system (calculational domain)	10.04%	11.90%	13.46%	6.40%	
Core average spectra (epithermal-to-thermal ratio over core region)	0.444	0.383	0.342	1.167	
Reflector average spectra (epithermal-to-thermal ratio)	0.070	0.060	0.054	0.123	

TABLE 4.29. THERMOHYDRAULIC CALCULATION RESULTS

	Case E1 (ii)	Case E2	Case T1
k-eff	0.99105	0.99998	
In-core scattering epithermal -> thermal: (%)	46.26%	45.91%	
Leakage			n/a
Epithermal (> 1.86 eV)	32.08%	32.24%	
Thermal (<1.86 eV)	-16.95%	-17.70%	
Total	15.13%	14.54%	
Total leakage out of the system (calculational domain)	5.83%	5.69%	
Core average spectra (epithermal-to-thermal ratio over core region)	1.199	1.315	
Reflector average spectra (epithermal-to-thermal ratio)	0.129	0.135	
Average fuel temperature (°C)	863.30	876.08	809.18
Average moderator temperature (°C)	851.19	857.79	797.09
Average helium temperature (in core) (°C)	772.92	766.74	727.54
Total helium mass flow rRate (kg/s)	150.00	150.00	150.00
Inlet/outlet temperature (°C)	488.1/995.7	488.1/997.3	488.1/1003.0
Inlet/outlet pressure difference (bar)	1.9125	1.8982	1.8133
Maximum fuel temperature (°C)	1080.60	1118.20	1166.5
Maximum power density	10.98	10.62	10.72
Maximum power per ball	2.04	2.73	1.99
Target burnup (MWD/ton HM)		96061	

Case results

The maps of the results are shown inside the core region only, as specified. Flux profiles are given in two energy groups; thermal flux ($E < 1.86$ eV) and epithermal flux ($E > 1.86$ eV). The power maps provided are expressed as a power density with results presented as MW/cm^3 .

Case F1

The thermal and epithermal flux profiles inside the core region are illustrated in Figs 4.21 and 4.22, respectively. Both thermal and epithermal fluxes have axial peaks at the middle of the core as expected since the core is filled with fresh fuel only (no burnup shape) and no temperature gradient is defined (all at 300 K). The power profile is shown in Fig. 4.23, and the power peak is also axially in the middle of the core but radially close to the central column.

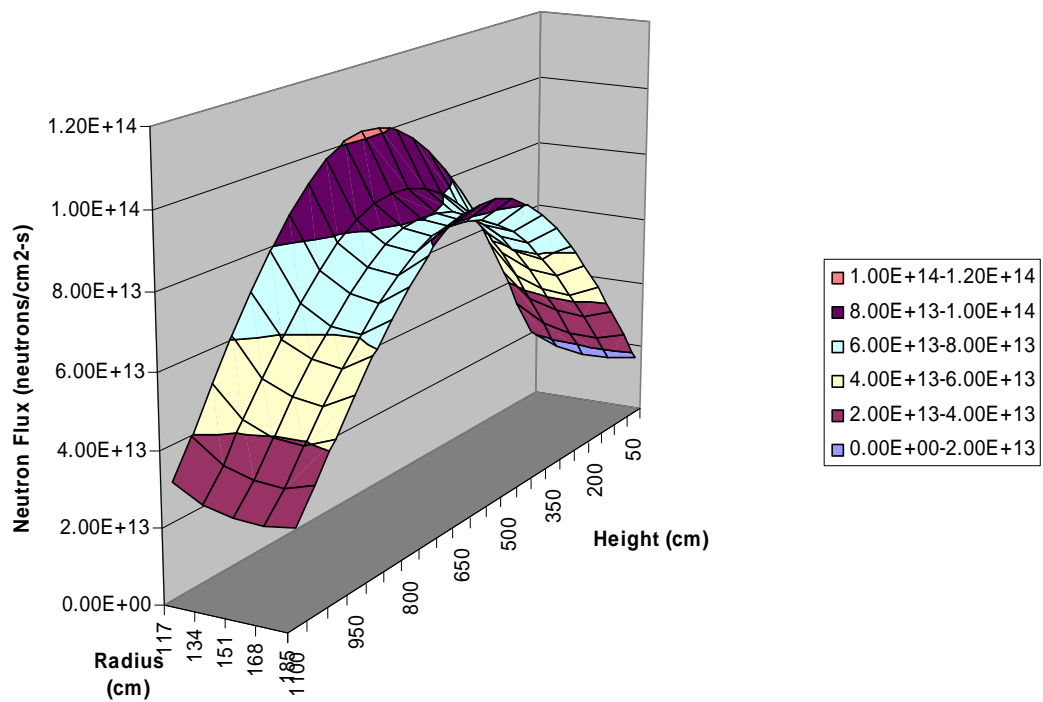


FIG. 4.21. Thermal flux profile for Case F1.

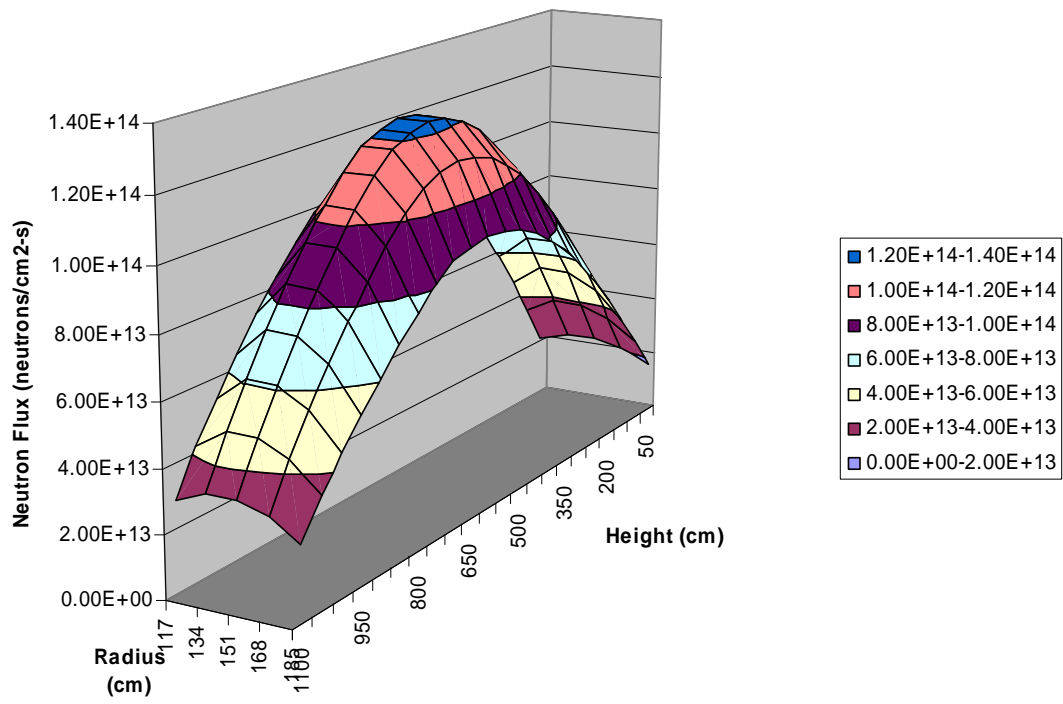


FIG. 4.22. Epithermal flux profile for case F1.

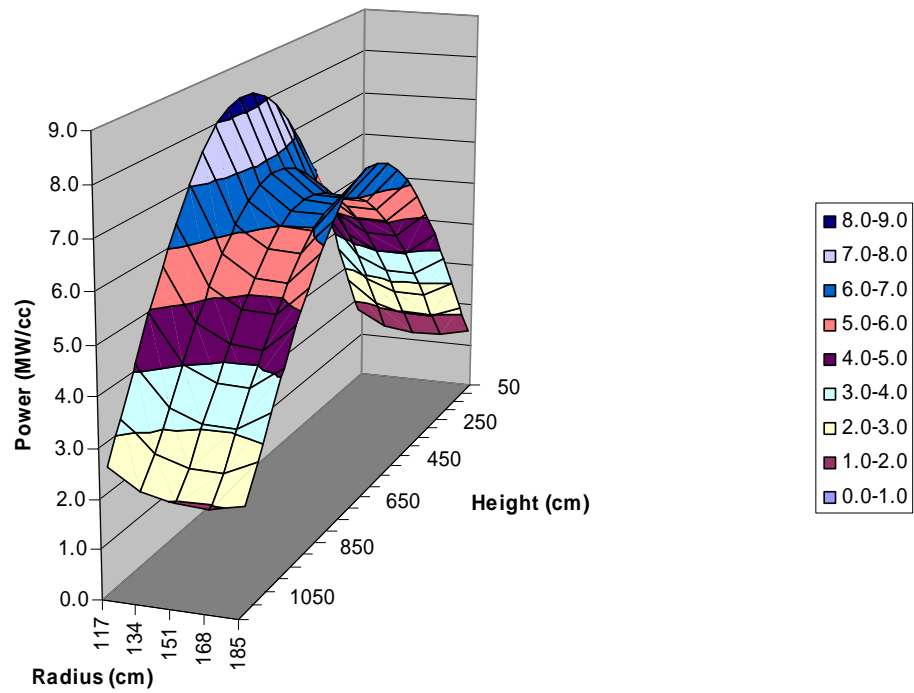


FIG. 4.23. Power profile for case F1.

Case F2

The thermal and epithermal flux profiles inside the core region are illustrated in Figs 4.24 and 4.25, respectively. Both thermal and epithermal fluxes have axial peaks at the middle of the core as expected since the core is filled with fresh fuel and graphite spheres. Due to the presence of the graphite spheres inside the core (compared to only the fresh fuel in Case F1), the thermal flux profile is radially flatter and has higher values when compared with the Case F1 thermal flux profile in Fig. 4.21. The power profile is shown in Fig. 4.26. The power peak is axially at the middle of the core close to the central column, but with radially flatter and lower values when compared with the Case F1 power profile. This can be attributed to the lower homogenized U-235 number density in Case F2.

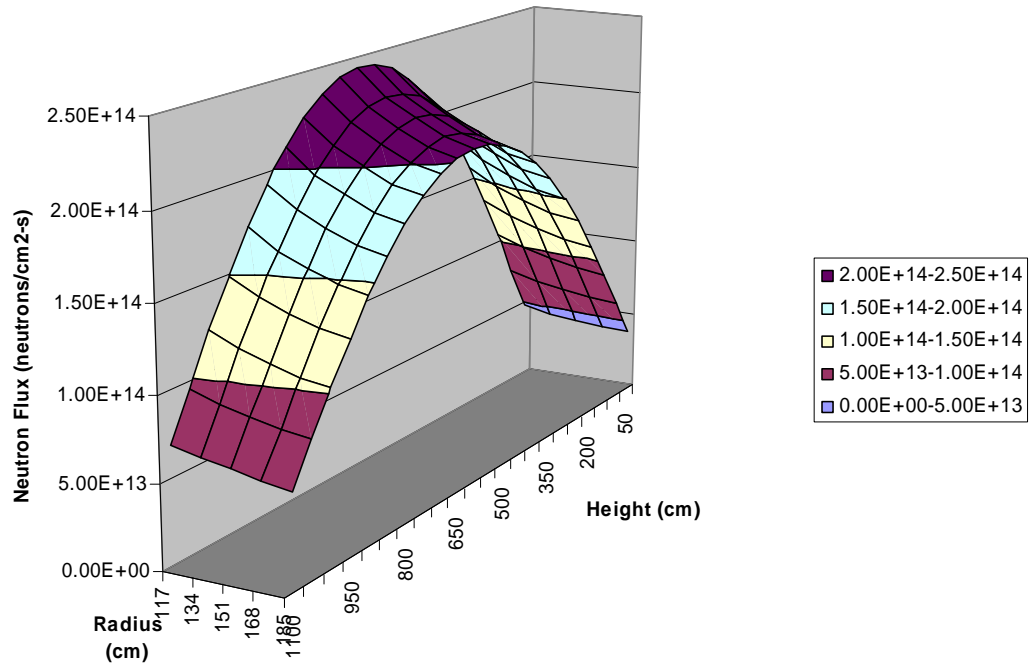


FIG. 4.24. Thermal flux profile for case F2 (i).

The flux and power shapes for Case F2 at higher temperatures (600, 900 and 1200 K) are similar to the results at 300 K although the flux levels differ. At higher temperatures, the flux levels are higher (about 1% for the epithermal flux per 100 K; and between 10% and 5% for the thermal flux per 100 K temperature increase) due to additional resonance capture in the fuel (Doppler effect) and harder spectrum. The detailed results will be included in the code-to-code comparisons section.

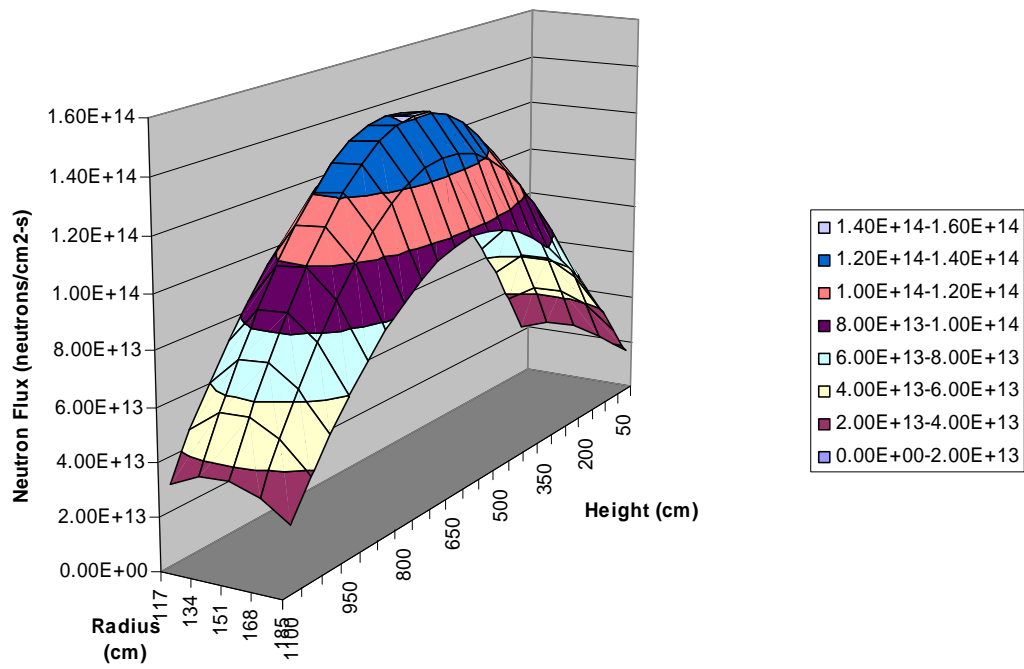


FIG. 4.25. Epithermal flux profile for case F2 (i).

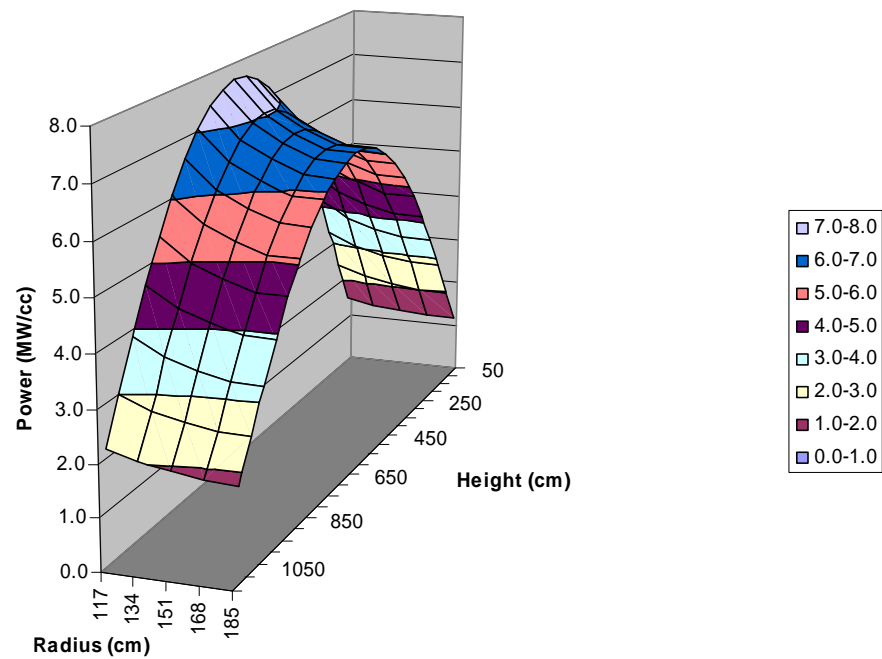


FIG. 4.26. Power profile for case F2 (i).

Case E1

Case E1 makes use of the NDSet 3 number densities (provided to the participants but not included in this document since it would take too much space) that represent an equilibrium core and thus a burnup profile from above (relatively less burned) to the bottom (burned more). For sub-case E-1 (i) at 300 K, the thermal and epithermal flux profiles inside the core region are illustrated in Figs 4.27 and 4.28, respectively. Both thermal and epithermal fluxes have axial peaks at the upper part of the core due to the introduced burnup profile. For the same reasons, the power profile shown in Fig. 4.29 has its power peak shifted upwards relative to the previous cases that had no burnup profile. Consequently, the peak values of the flux and power profiles are now larger when compared with Cases F1 and F2 (where a flatter cosine shape was noticed).

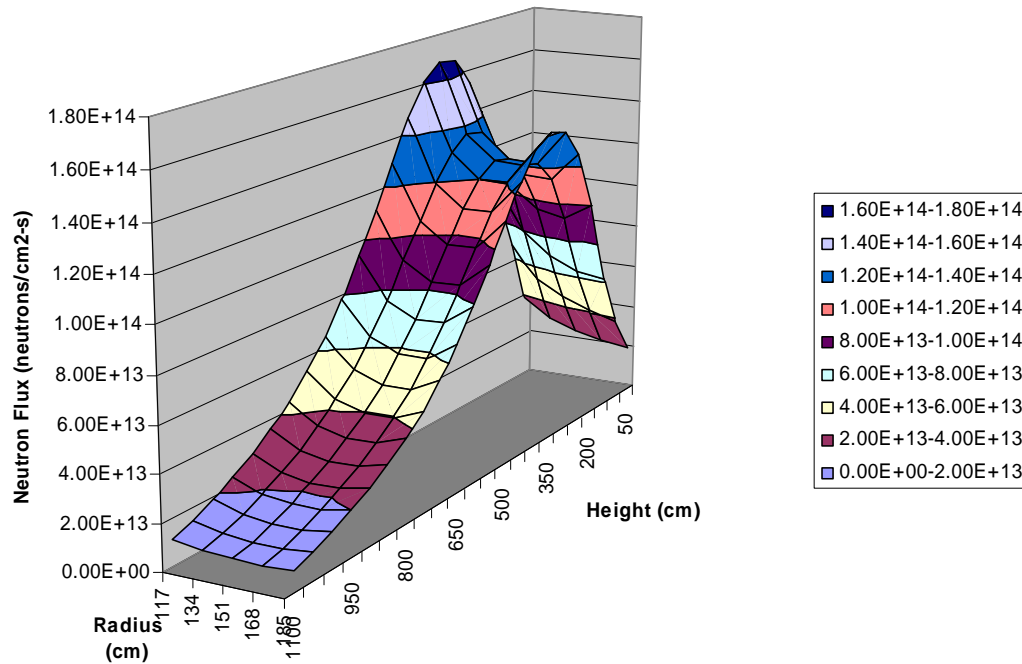


FIG. 4.27. Thermal flux profile for case E1 (i) (300 K).

Case E1 (i)

In the second case, Case E1(i) (1200 K), the temperature was increased to 1200 K. When these temperature changes were introduced for Case F2, no significant changes were seen in the flux shape. In contrast, significant flux and power shape changes are noticed for Cases E1(i) at 300 K and 1200 K. The thermal and epithermal flux profiles inside the core region are illustrated in Figs 4.30 and 4.31, respectively. The power profile is shown in Fig. 4.32, and the power peak is axially at the upper part of the core close to the central column as before. Although the shapes appear similar to Case E1(i) (300 K), closer inspection shows large differences. For example, the peak power decreases from 12 W/cm^3 at 300 K to 10 W/cm^3 for the 1200 K case. The effect is due to the changes in the spectrum and leakage and the differences these effects have for the different fuel (that for this case has a burnup shape).

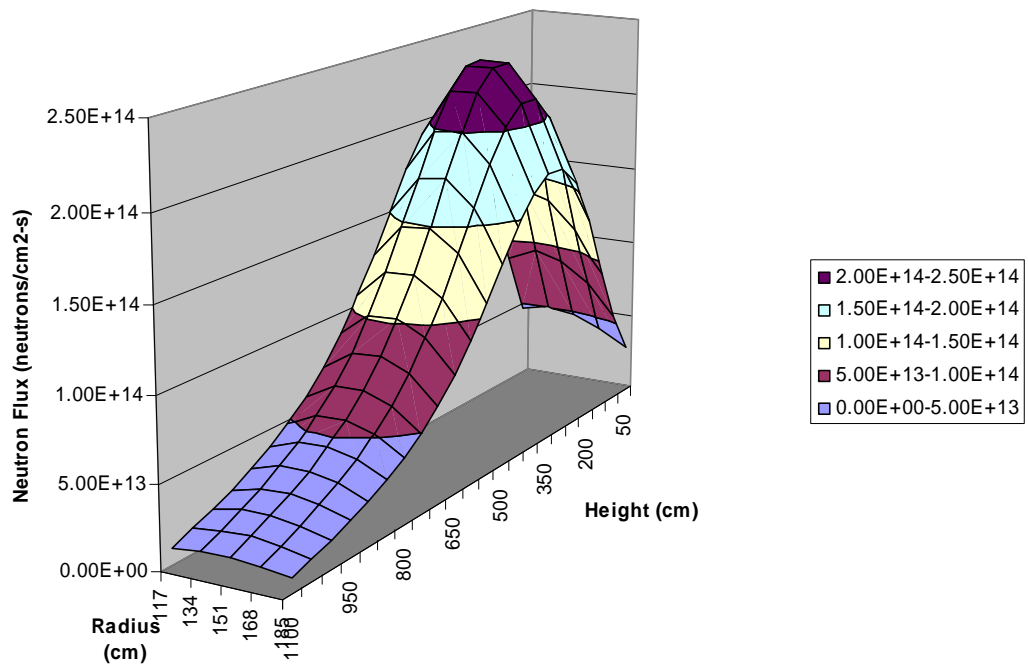


FIG. 4.28. Epithermal flux profile for case E1 (i) (300 K).

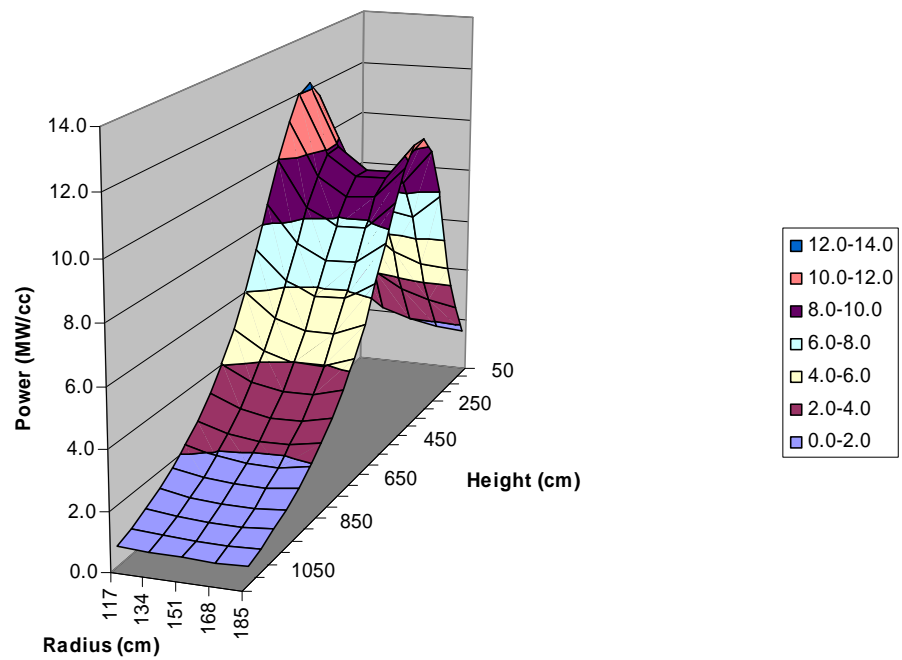


FIG. 4.29. Power profile for case E1 (i) (300 K).

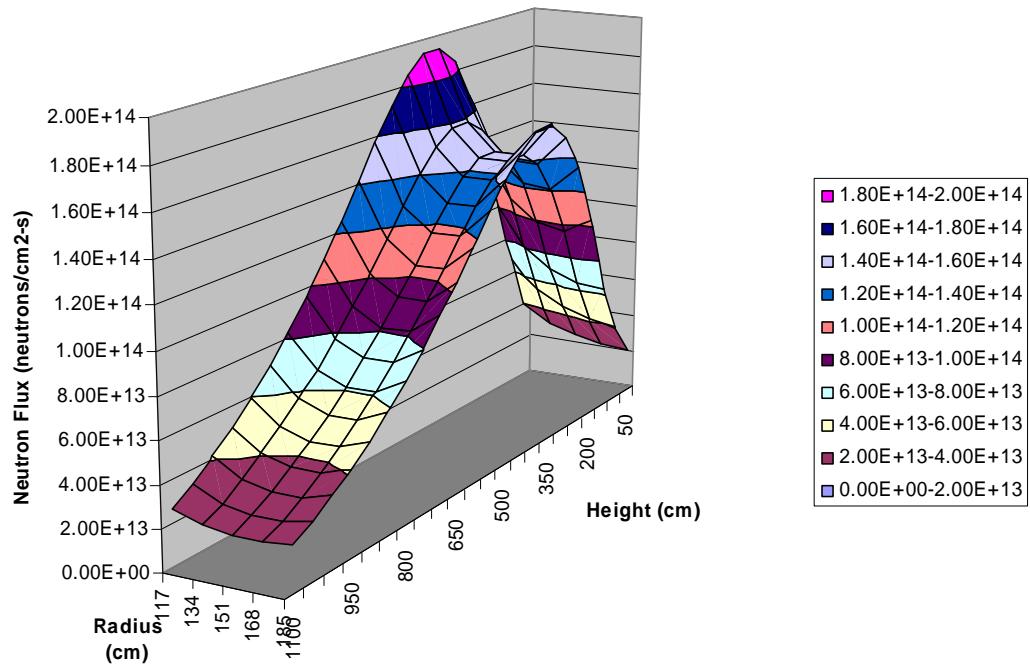


FIG. 4.30. Thermal flux profile for case E1 (i) (1200 K).

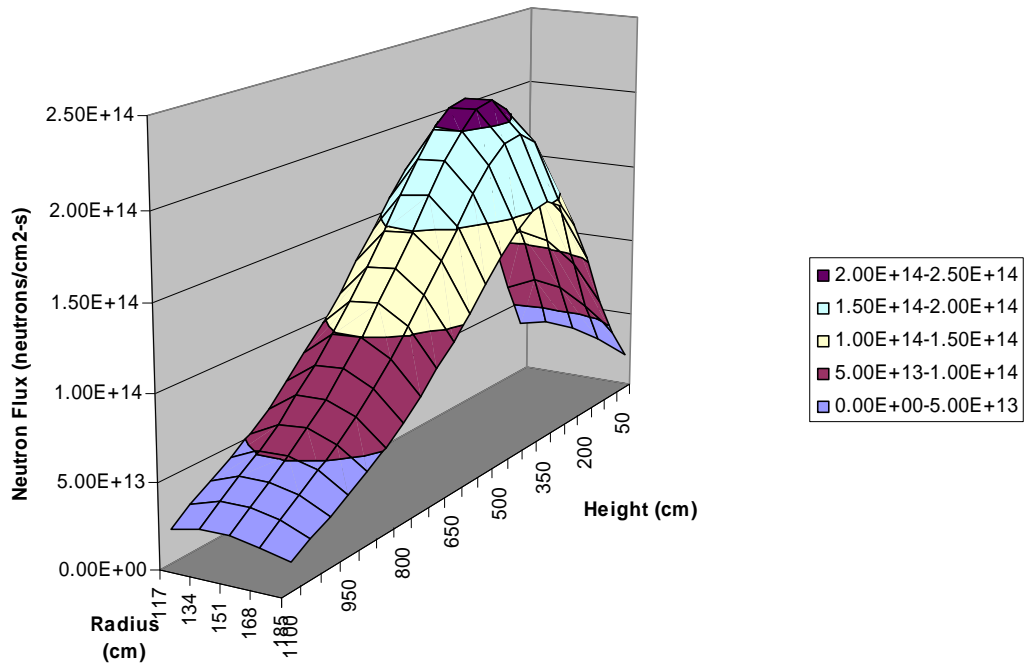


FIG. 4.31. Epithermal flux profile for case E1 (i) (1200 K).

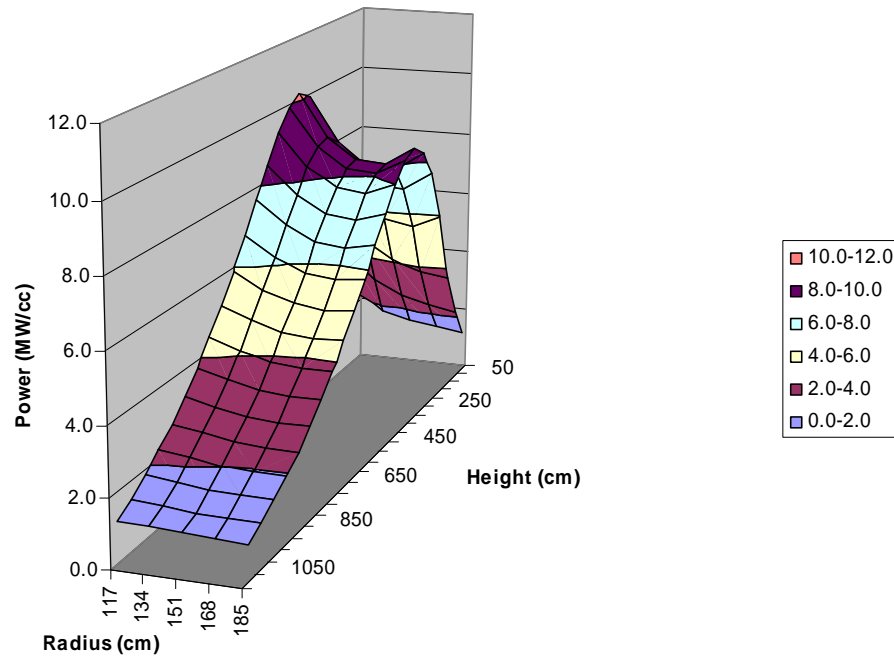


FIG. 4.32. Power profile for case E1 (i) (1200 K).

Case E1 (ii)

Case E1(ii) is the first case where the temperature profiles were calculated and thus where a constant temperature over the total model was not assumed. It thus represents the first case that realistically represents the conditions in the equilibrium core. In the test case definition, the helium coolant enters the reactor at 500 °C, flows upwards in the side reflector and then downwards through the core. The helium temperature increases as it flows through the core as illustrated in Fig. 4.33. Due to the assumed bypass flow, the helium temperature at the bottom of the core is higher than 900°C and the temperature is higher closer to the solid central reflector.

The temperature profile of the core and reflector regions is shown as the solid material temperature profile in Fig. 4.34. Although the maximum solid temperature occurs at the bottom part of the core, the maximum fuel centre line temperature actually occurs closer to the centre of the core where the helium temperatures are lower due to the higher power generation in this region. The solid temperature profile is radially constant in the central column, because of the absence of bypass cooling and power generation in this region.

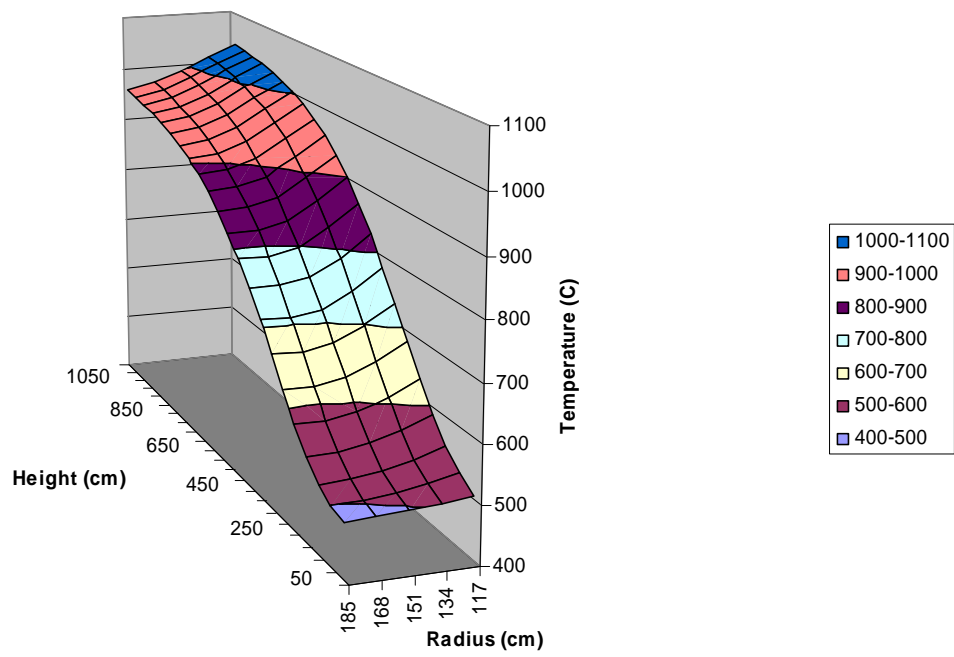


FIG. 4.33. Helium temperature for case E1 (ii).

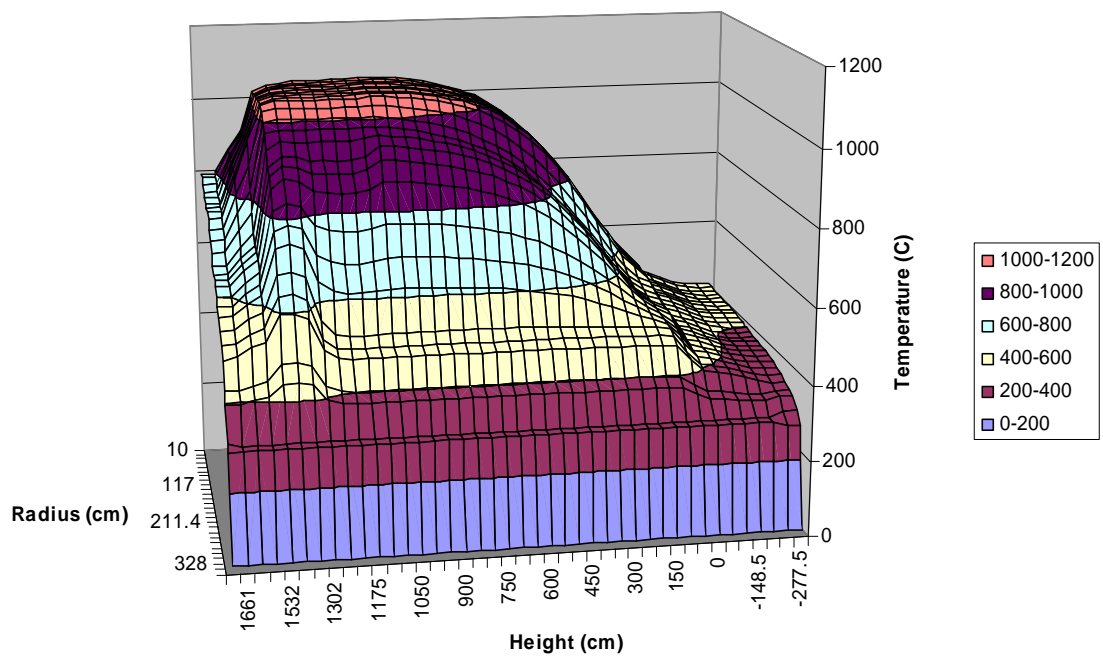


FIG. 4.34. Solid material temperature for case E1 (ii).

The pebble surface temperatures are illustrated in Fig. 4.35, whereas the pebble bed effective thermal conductivity inside the core is illustrated in Fig. 4.36. The temperature dependence of the pebble bed effective conductivity is clearly seen: as the temperature increases, the effective conductivity of the pebble bed increases.

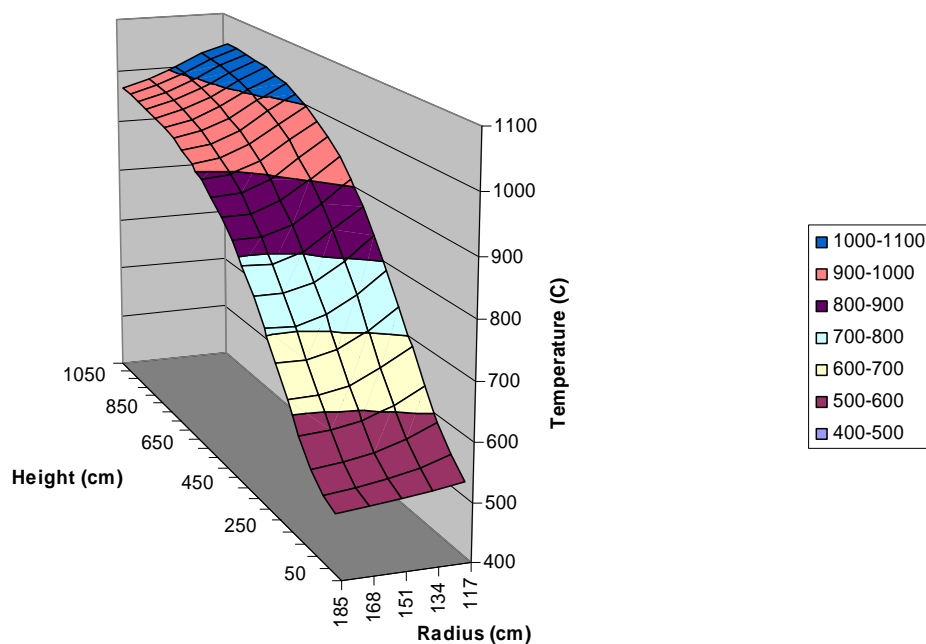


FIG. 4.35. Pebble surface temperature for Case E1 (ii).

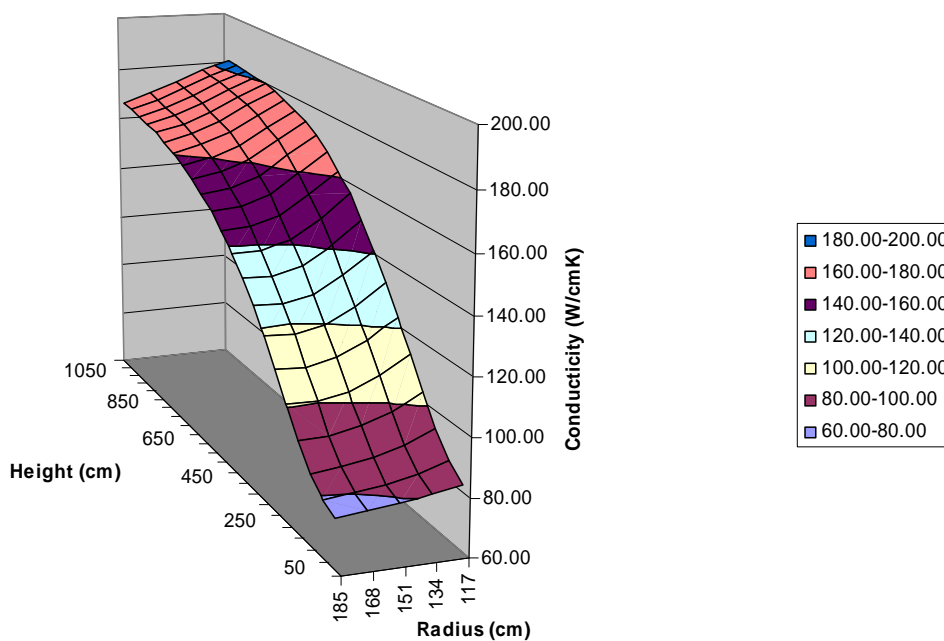


FIG. 4.36. Pebble bed effective conductivity for case E1 (ii).

The thermal and epithermal flux profiles inside the core region are illustrated in Figs 4.37 and 4.38, respectively. The power profile is shown in Fig 4.39, and the power peak is axially at the top part of the core close to the central column.

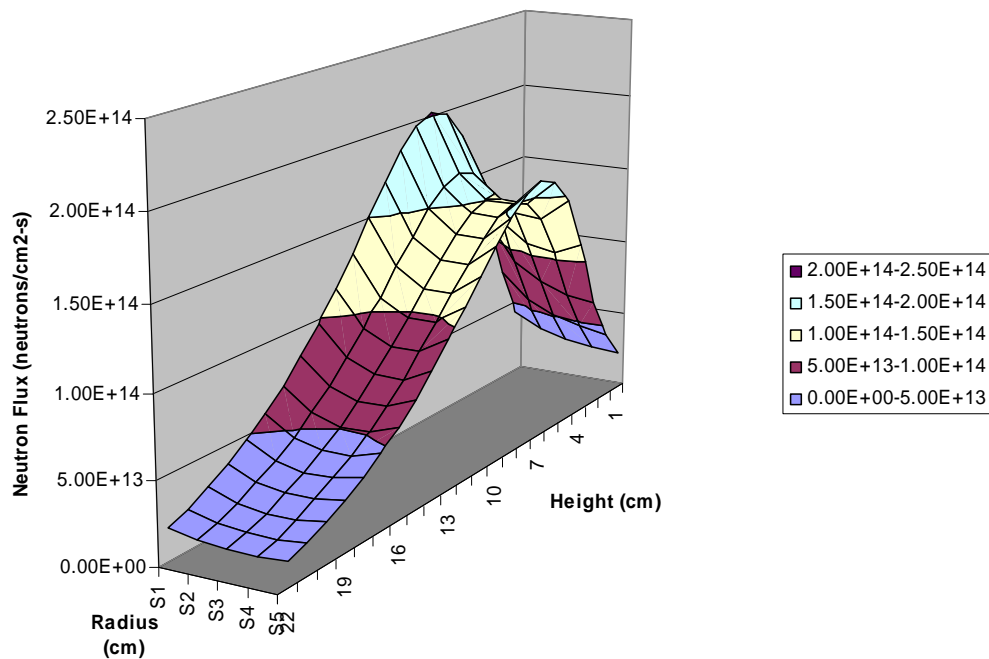


FIG. 4.37. Thermal flux profile for Case E1 (ii).

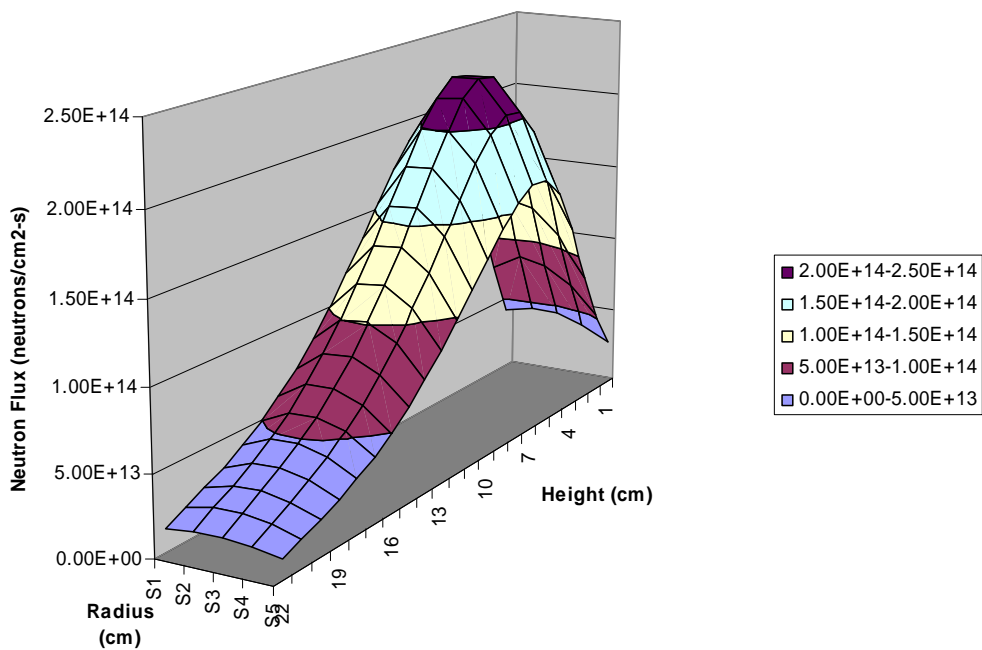


FIG. 4.38. Epithermal flux profile for Case E1 (ii).

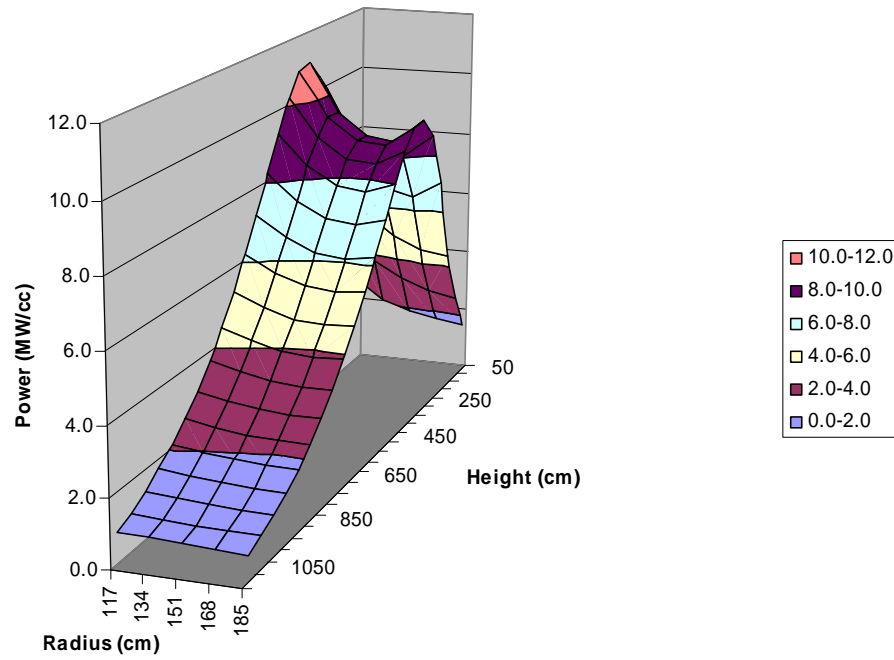


FIG. 4.39. Power profile for Case E1 (ii).

Case E2

The results of Case E2 do not show significant differences when compared with the results of Case E1 (ii); only k -effective is ~ 800 pcm higher in Case E2 due to the different isotopic distribution in the two cases, which also affects the thermohydraulic properties. The thermal and epithermal flux profiles inside the core region are illustrated in Figs. 4.40 and 4.41, respectively.

The power profile is shown in Fig. 4.42. The pebble surface temperatures are illustrated in Fig. 4.43, whereas the pebble bed effective temperature and helium temperature inside the core are illustrated in Figs 4.44 and 4.45, respectively. The solid material temperature is shown in Fig. 4.46.

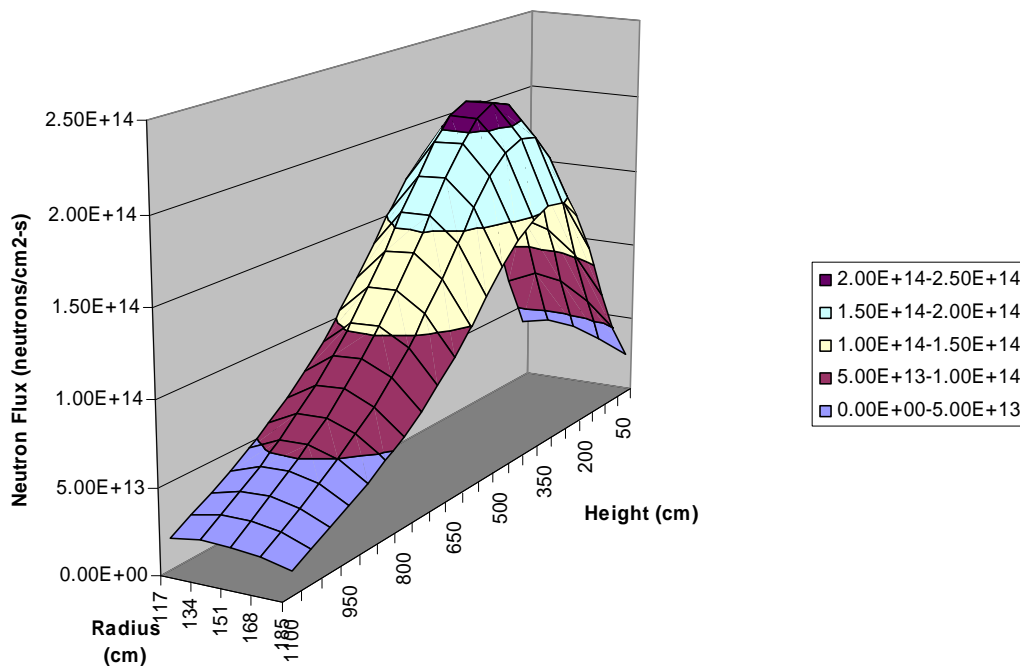


FIG. 4.40. Thermal flux profile for case E2.

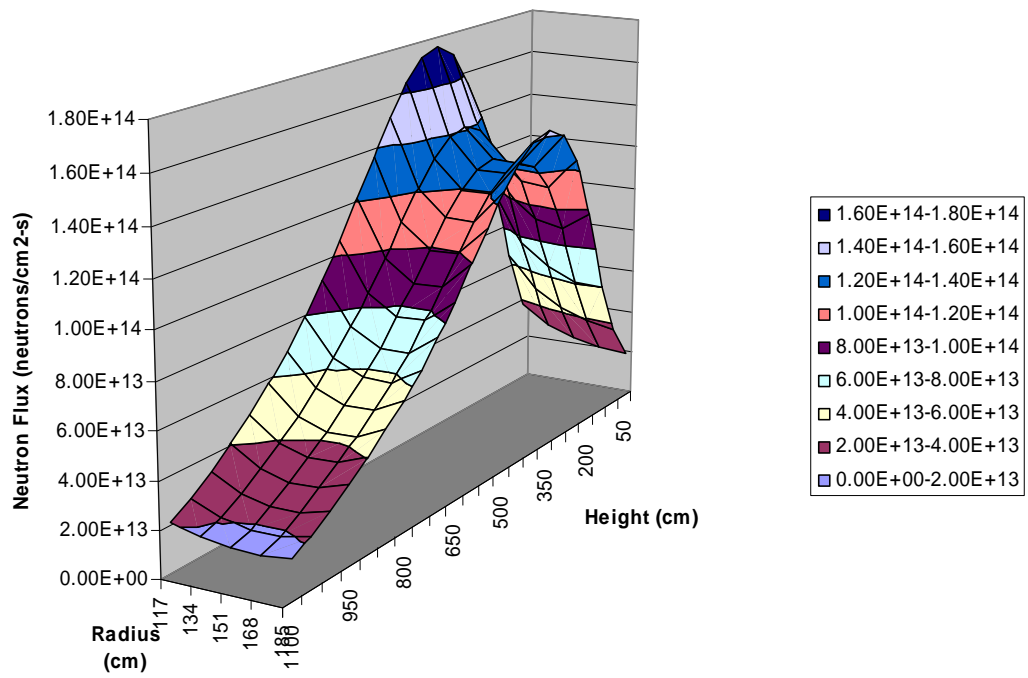


FIG. 4.41. Epithermal flux profile for case E2.

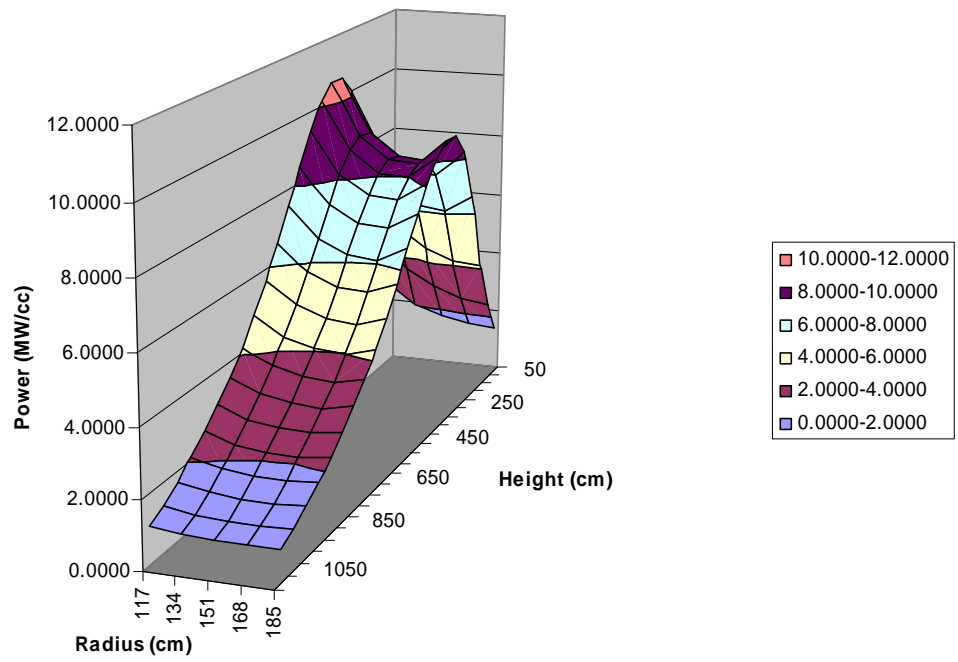


FIG. 4.42. Power profile for case E2.

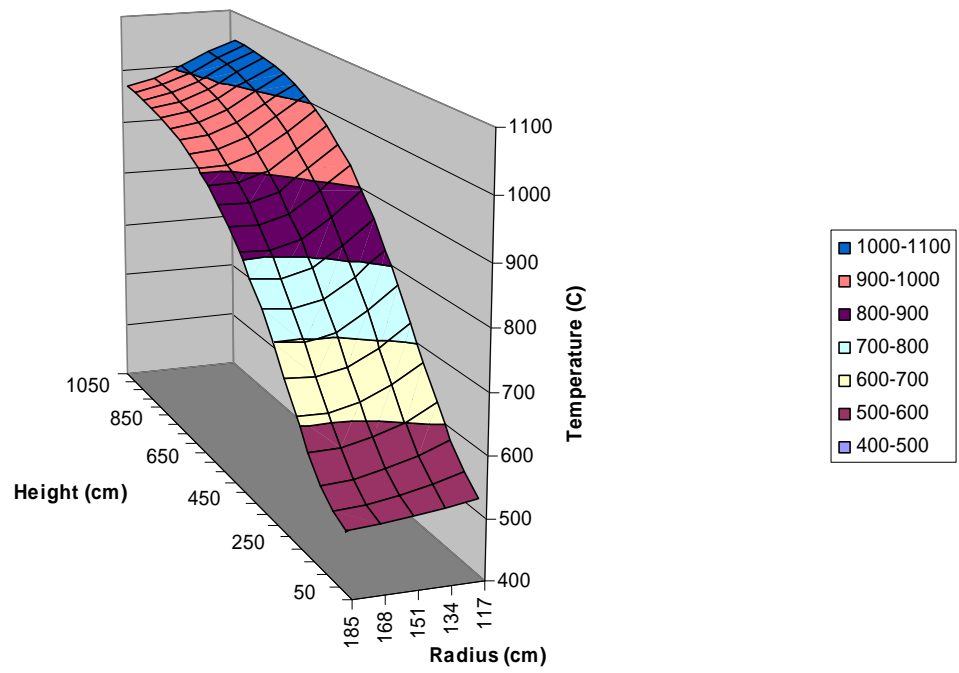


FIG. 4.43. Pebble surface temperature for case E2.

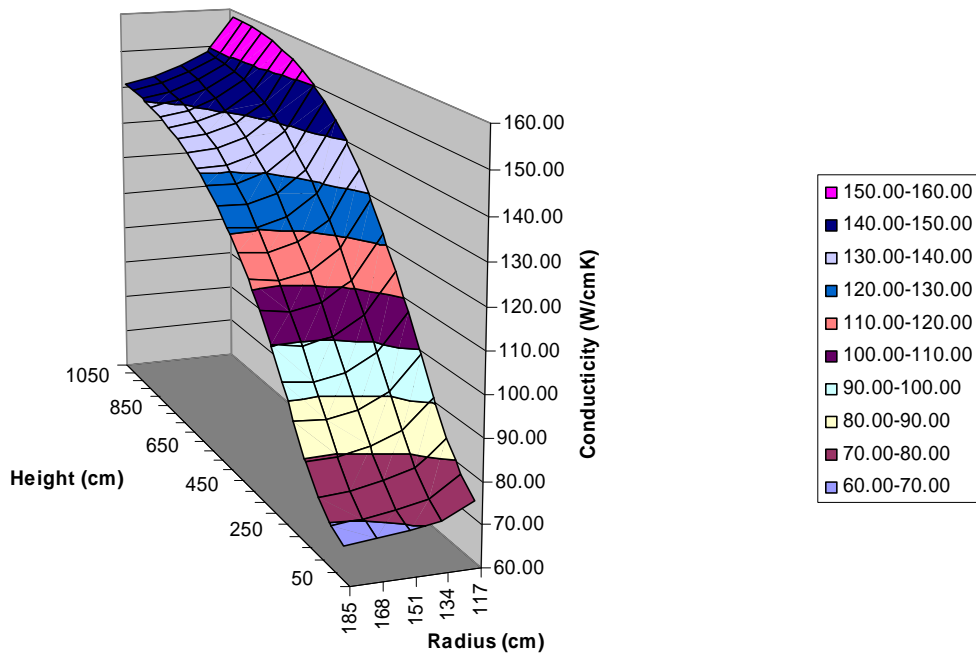


FIG. 4.44. Pebble bed effective conductivity for case E2.

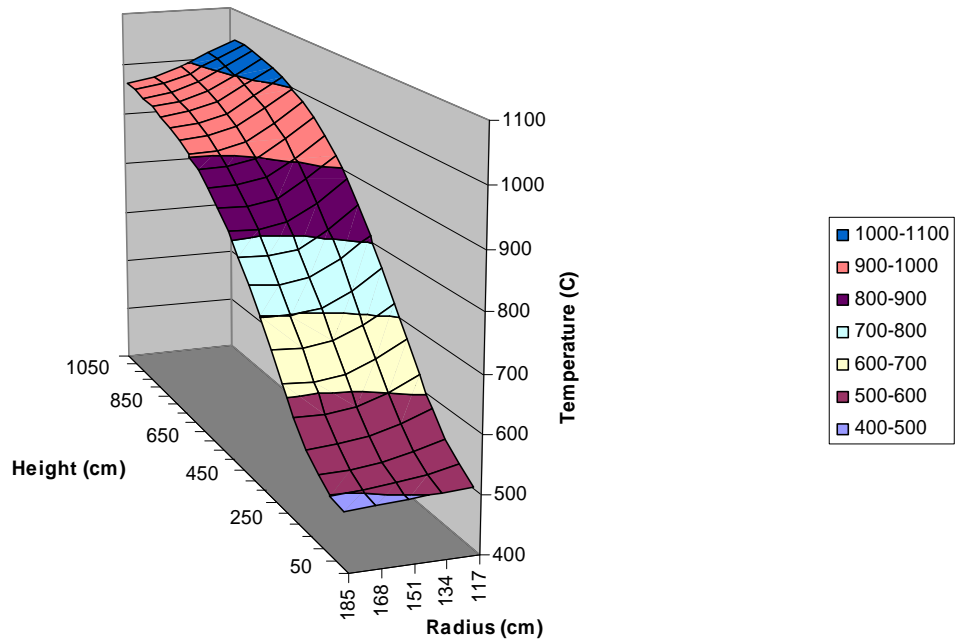


FIG. 4.45. Helium temperature for case E2.

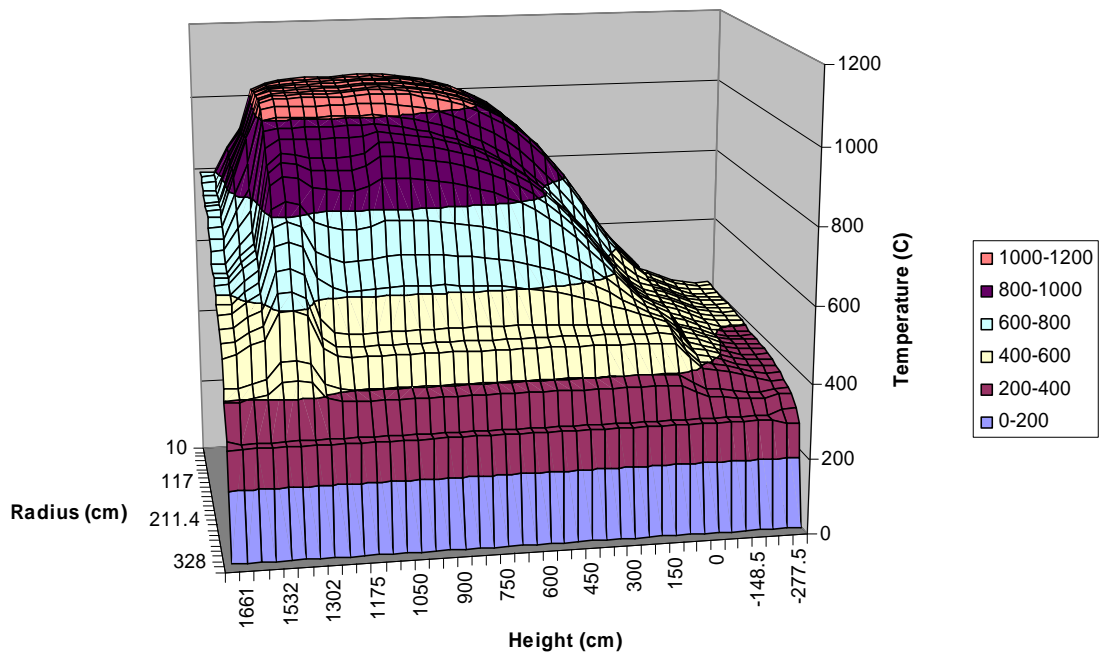


FIG. 4.46. Solid material temperature for case E2.

Case T1

The given power/heat source profile is illustrated in Fig. 4.47. The pebble surface temperatures are illustrated in Fig. 4.48, whereas the pebble bed effective temperature and helium temperature inside the core are illustrated in Figs 4.49 and 4.50, respectively.

The temperature dependence of the pebble bed effective conductivity is clearly seen from Fig. 4.49; as the temperature increases, the effective conductivity of the pebble bed increases. Due to the axially

constant power profile both helium and pebble surface temperatures show a linear profile in the axial direction. The helium temperature as it goes through the core increases, which also results in an increase in the solid material temperature as shown in Fig. 4.51, which increases linearly from the top to the bottom of the core. The maximum solid temperature and the maximum fuel centre line temperature occur at the same position due to the axially constant power generation.

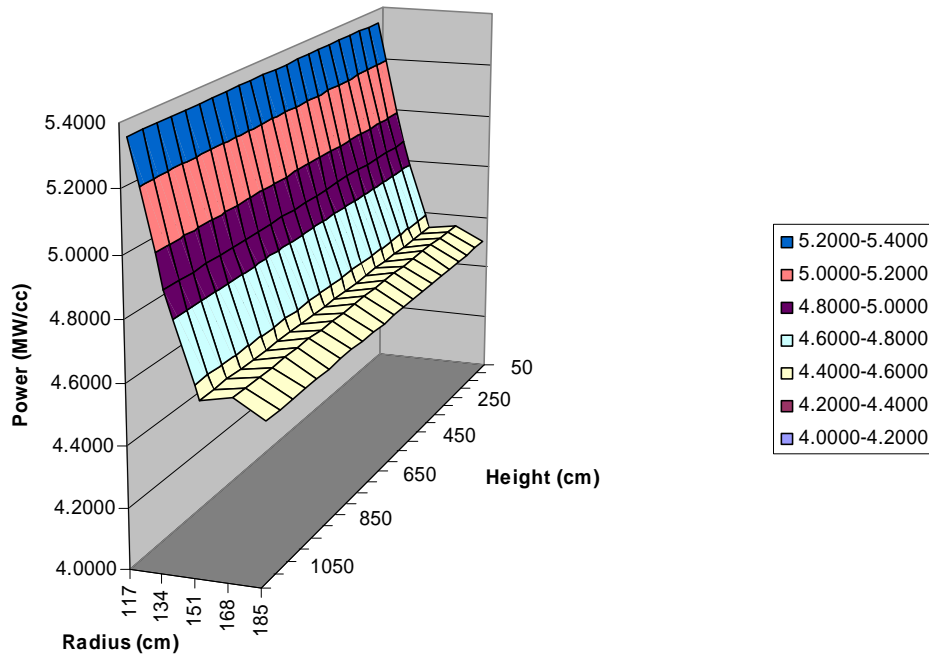


FIG. 4.47. Given power profile for case T1.

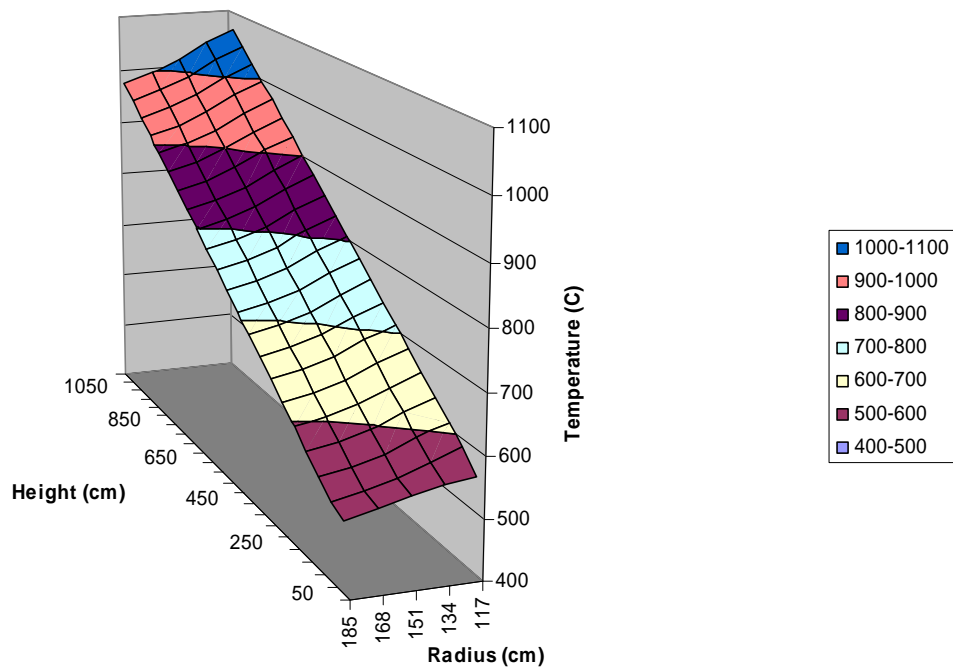


FIG. 4.48. Pebble surface temperature for case T1.

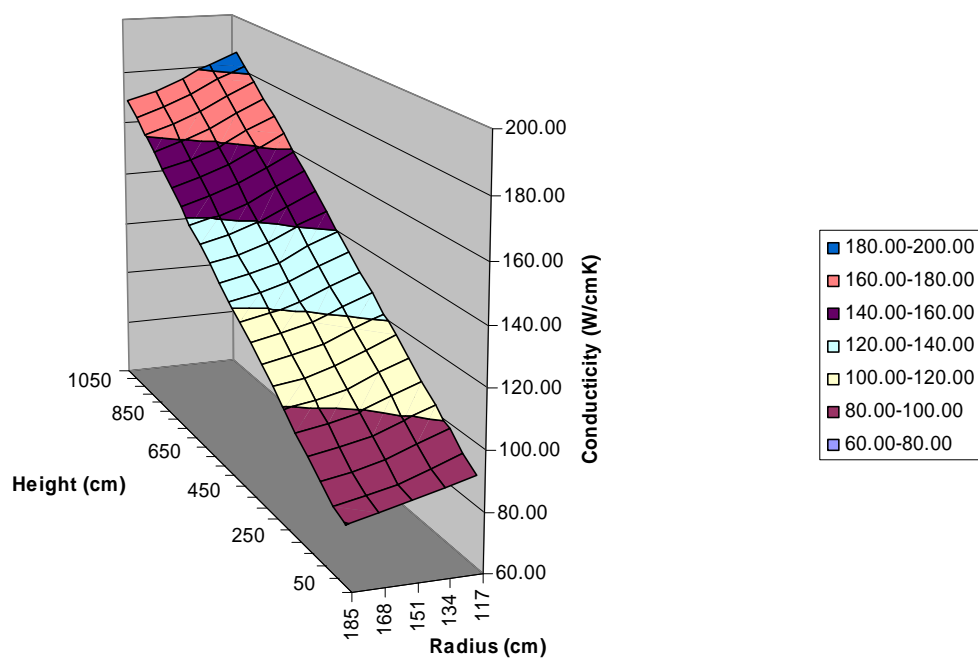


FIG. 4.49. Pebble bed effective conductivity for Case T1.

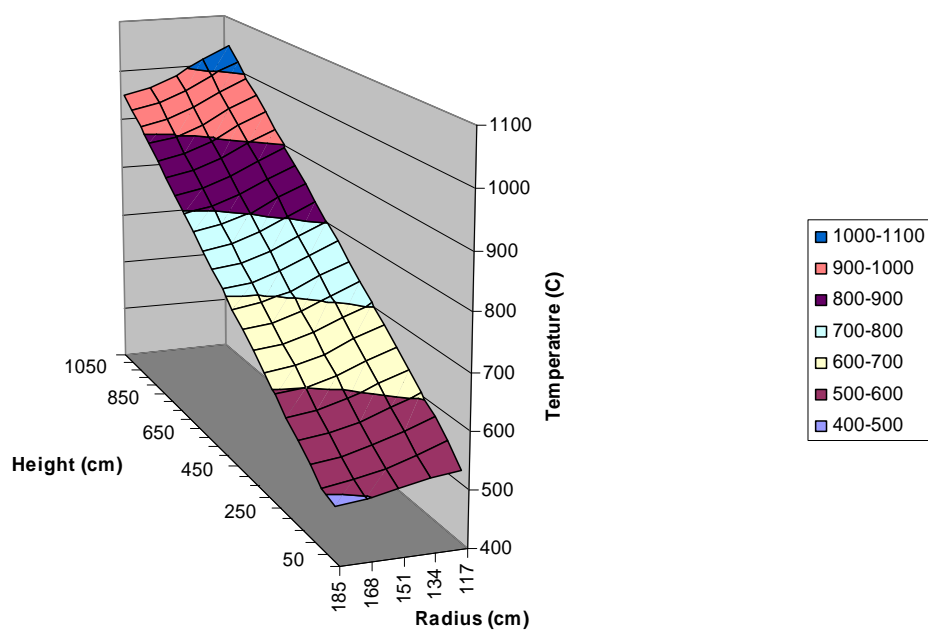


FIG. 4.50. Helium temperature for case T1.

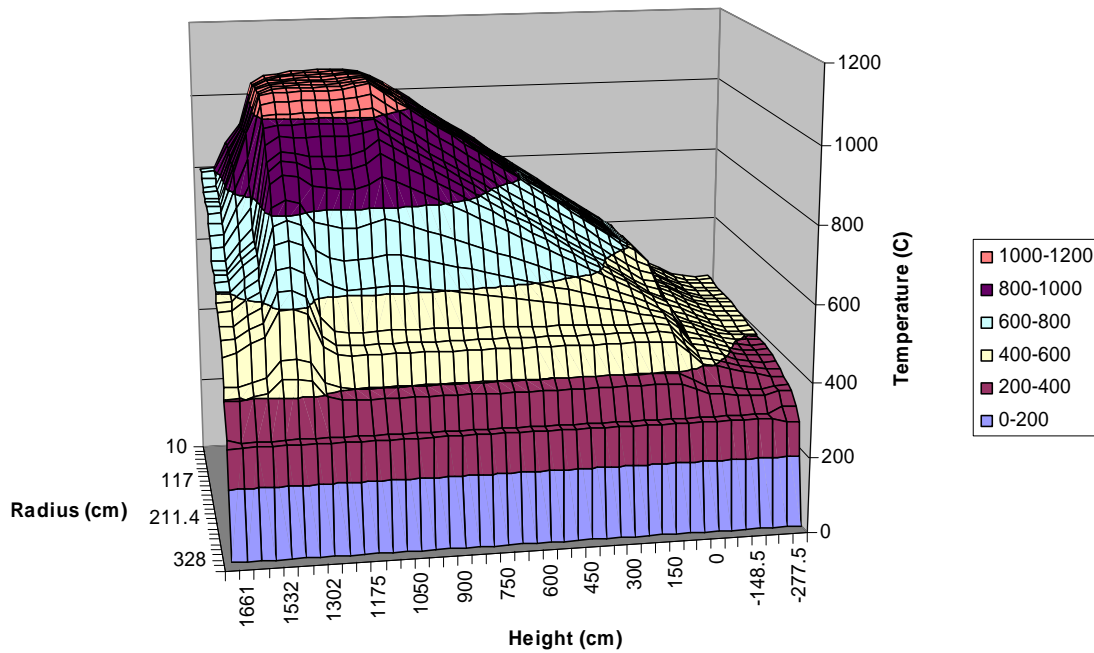


FIG. 4.51. Solid material temperature for case T1.

Transient case

Only one transient case was defined as part of the PBMR 400 MW test case. The total loss of coolant flow or Depressurized Loss of Forced Cooling (DLOFC) is often seen as the most severe event and is thus often used as the main event analysed during initial design studies. As such it is an important case to study and was included as part of the code-to-code comparisons.

Case D-1

The steady state Case E-1 (ii) modelled in VSOP99 is used to define the starting conditions for the transient Case D-1. Since the TINTE code was used to calculate Case D-1, the TINTE steady state results are also presented in this section, in addition to the transient results. Only a limited direct comparison is made in Table 4.30 between the TINTE and VSOP99 steady state results for Case E-1 (ii)/D-1 to confirm that the steady state cases are similar. Differences exist in the core thermohydraulic modelling and include the bypass flow models (total flow reduced in VSOP99 compared to the total flow modelled in TINTE). It is important to keep in mind that the TINTE model is focused on Case D-1 and that the modeller included all features believed to be important for this case (and assumptions made for the steady state case may no longer be valid).

Some additional information on the TINTE model is given below:

- The cross-sections used in the TINTE model are represented as polynomials and were generated using a spectrum code with isotopic distributions input from VSOP99.
- The decay heat calculation was based on a 24-group approximation (all groups have the same time constants of decay) of the full 24-group DIN 25485 decay heat treatment. This treatment is used since it is faster (less CPU time) but it is also known to be conservative (giving higher total decay heat values).
- Recriticality was prevented by inserting the control rods between $t = 3$ and $t = 21$ s.

Steady state results

Table 4.30 summarizes the TINTE Case D-1 steady state results. Table 4.31 presents the spatial power density at $t = 0$ h. The peak value of 11.15 W/cm^3 can be seen at $z = 300$ cm, next to the central reflector. The power distribution, peaked in the upper part of the core, is also shown in Fig. 4.52.

TABLE 4.30. CASE D-1 STEADY STATE RESULTS

Parameter	TINTE	VSOP99
k-eff	0.99458	0.99105 (-353 pcm)
Total leakage	15.7%	15.1%
Average fuel temperature (°C)	872	863
Average moderator temperature (°C)	855	851
Average helium temperature (in core) (°C)	809	773
Total helium mass Flow Rate (kg/s)	185.1	150.0*
Inlet/outlet temperature (°C)	488/902	488/996
Inlet/outlet pressure difference (bar)	2.047	1.913
Maximum fuel temperature (°C)	1051	1081
Maximum power density (W/cm ³)	11.2	11.0

* The bypass flows were simply deducted from the total flow in the simplified VSOP99 model.

TABLE 4.31. POWER DENSITY (W/CM³) AT T = 0 H

r/z (cm)	117	134	151	168	185
50	2.62	2.03	1.78	1.61	1.54
100	4.67	3.60	3.11	2.74	2.57
150	6.88	5.42	4.80	4.39	4.31
200	8.92	7.24	6.60	6.36	6.95
250	10.44	8.68	8.05	7.92	8.80
300	11.15	9.48	8.84	8.71	9.58
350	11.13	9.60	8.99	8.86	9.60
400	10.55	9.24	8.66	8.52	9.12
450	9.61	8.53	8.01	7.86	8.33
500	8.53	7.64	7.19	7.05	7.38
550	7.39	6.69	6.30	6.17	6.40
600	6.31	5.75	5.43	5.31	5.47
650	5.32	4.89	4.62	4.50	4.61
700	4.44	4.10	3.88	3.78	3.85
750	3.68	3.42	3.23	3.15	3.19
800	3.02	2.82	2.68	2.60	2.63
850	2.48	2.32	2.20	2.14	2.15
900	2.02	1.90	1.80	1.75	1.75
950	1.63	1.53	1.45	1.41	1.41
1000	1.29	1.22	1.16	1.12	1.12
1050	1.01	0.95	0.90	0.87	0.87
1100	0.79	0.77	0.74	0.71	0.68

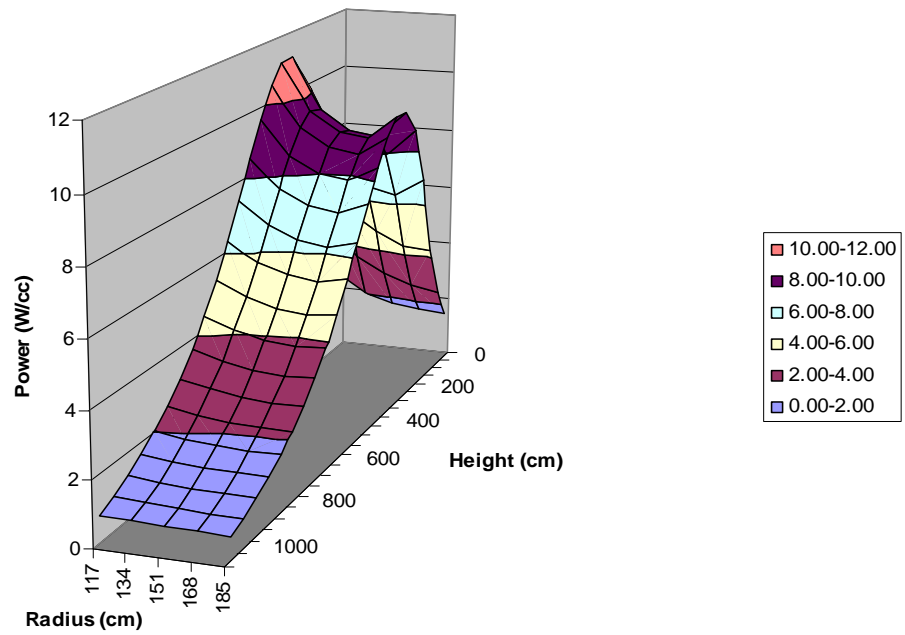


FIG. 4.52. Case D-1 power density profile at $t = 0$ h.

DLOFC transient results

The change in the solid material temperature from $t = 0$ to 38.4 hours is shown in Figs 4.53 and 4.54, respectively. The large increase in temperature in the upper part of the core, where the peak decay heat occurs, can clearly be seen.

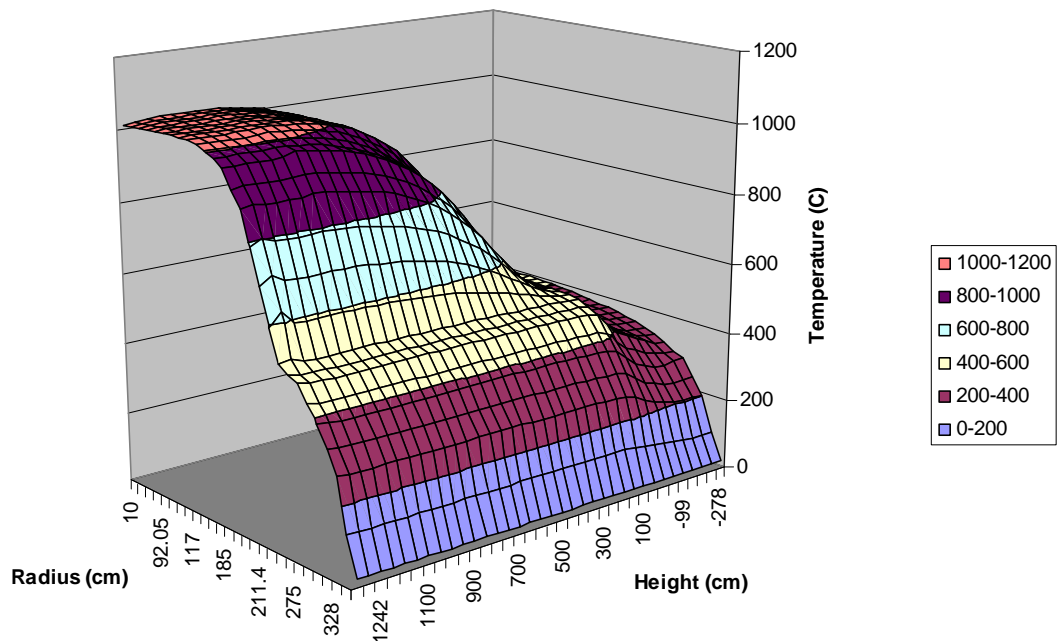


FIG. 4.53. Case D-1 Solid temperature at $t = 0$ h.

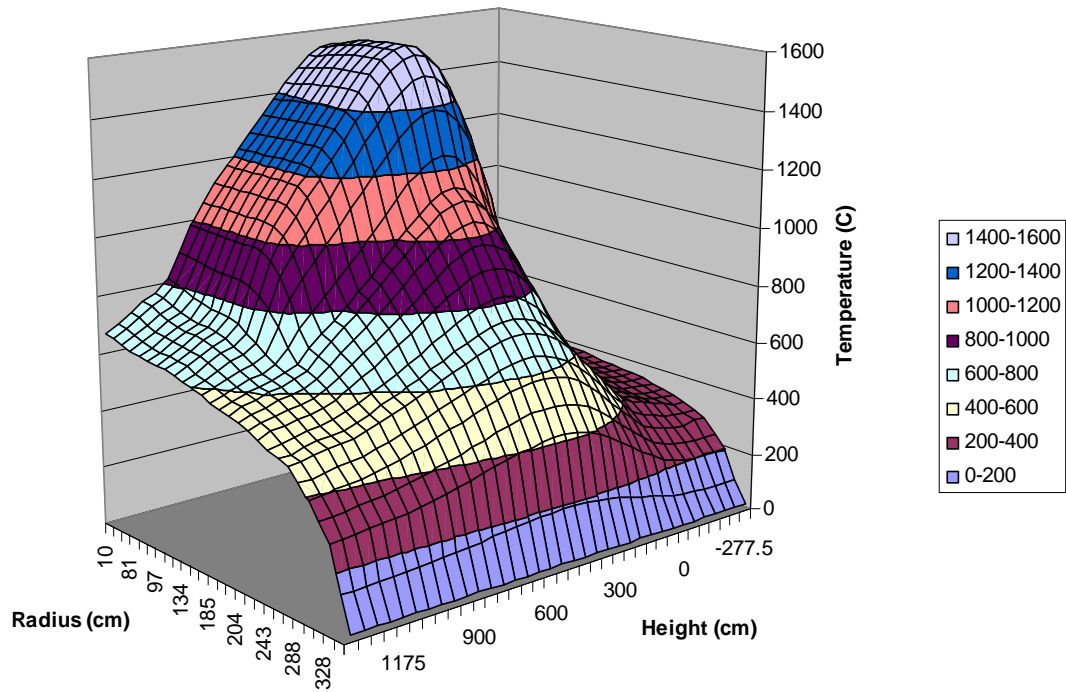


FIG. 4.54. Case D-1 solid temperature at $t = 38.4$ h.

The transfer of heat upwards in the core is also visible in the pebble surface temperature data, presented in Table 4.32 and Fig. 4.55 at 0 h and in Table 4.33 and Fig. 4.56 at 38.4 h. The tables indicate that the helium flow forces the maximum surface temperature (the underlined value in the tables) downwards in the core, while the absence of coolant flow during the DLOFC allows the core to return to a temperature profile that closely mirrors the decay heat distribution, which has a maximum location in the upper part of the core.

TABLE 4.32. PEBBLE SURFACE TEMPERATURE (IN °C) AT T = 0 H

r/z (cm)	117	134	151	168	185
50	527	519	511	504	499
100	551	536	524	515	510
150	587	567	552	542	538
200	633	608	590	580	580
250	684	656	635	625	627
300	735	705	682	671	675
350	783	752	727	716	720
400	826	796	770	759	761
450	864	835	809	797	797
500	896	869	844	831	829
550	923	898	874	860	857
600	946	923	899	885	880
650	964	944	921	907	901
700	979	961	939	925	918
750	991	975	954	940	932
800	1001	986	967	952	944
850	1008	995	977	963	954
900	1014	1001	985	971	962
950	1018	1007	992	978	969
1000	1021	1011	997	984	975
1050	1023	1014	1000	988	979
1100	<u>1024</u>	1016	1004	992	983

TABLE 4.33. PEBBLE SURFACE TEMPERATURE (IN °C) AT T = 38.4 H

r/z (cm)	117	134	151	168	185
50	690	674	647	607	551
100	889	874	835	770	676
150	1060	1042	993	915	801
200	1216	1195	1140	1050	922
250	1352	1329	1269	1173	1033
300	1459	1435	1373	1272	1126
350	1535	1509	1445	1342	1191
400	1578	1550	1485	1381	1230
450	<u>1591</u>	1563	1497	1393	1242
500	1580	1551	1486	1382	1233
550	1549	1521	1456	1354	1207
600	1506	1477	1413	1313	1169
650	1453	1424	1362	1264	1123
700	1396	1367	1306	1210	1075
750	1338	1309	1249	1156	1025
800	1280	1251	1192	1102	977
850	1224	1194	1137	1051	931
900	1168	1139	1084	1002	887
950	1112	1084	1031	953	844
1000	1050	1024	975	902	801
1050	973	950	907	843	754
1100	861	838	805	759	697

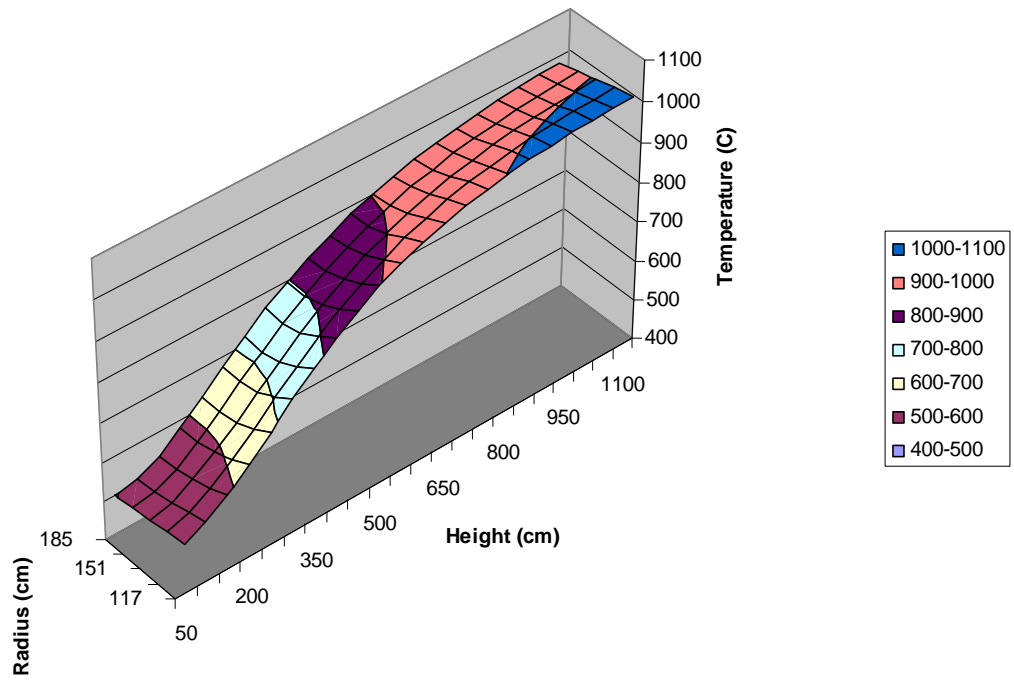


FIG. 4.55. Case D-1 Average pebble surface temperature at $t = 0$ h.

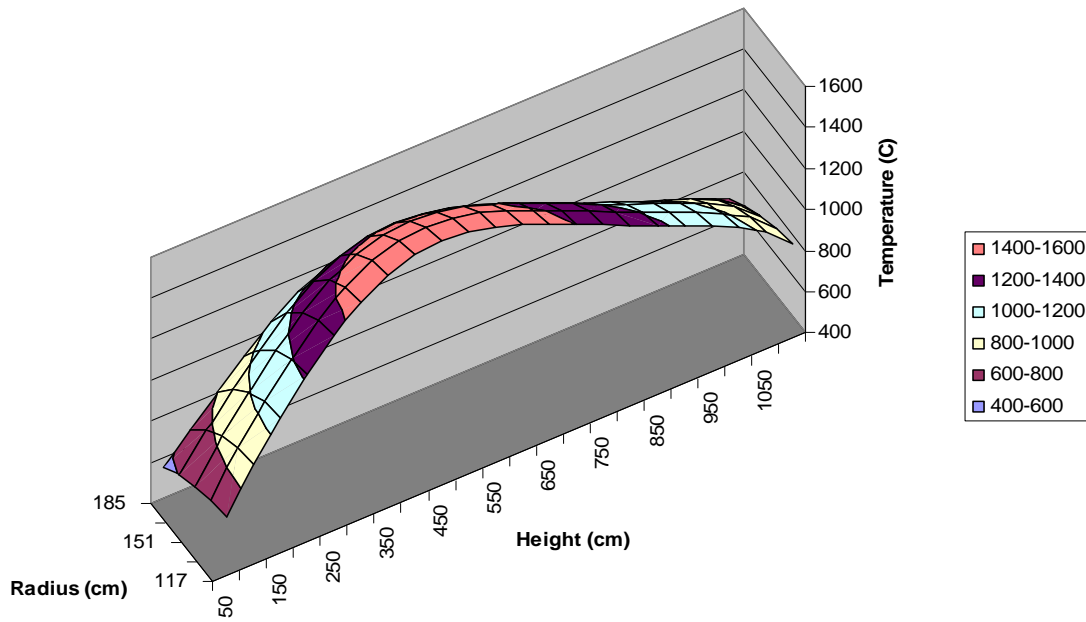


FIG. 4.56. Case D-1 Average pebble surface temperature at $t = 38.4$ h.

Tables 4.34–4.36 present the spatial values of the helium gas temperature, the pressure drop over the core, and the core effective thermal conductivity, all at $t = 0$ h. The distribution of the core thermal conductivity (as determined by the Zehner-Schlünder correlation) is shown in Fig. 4.57.

TABLE 4.34. HELIUM GAS TEMPERATURE (IN °C)

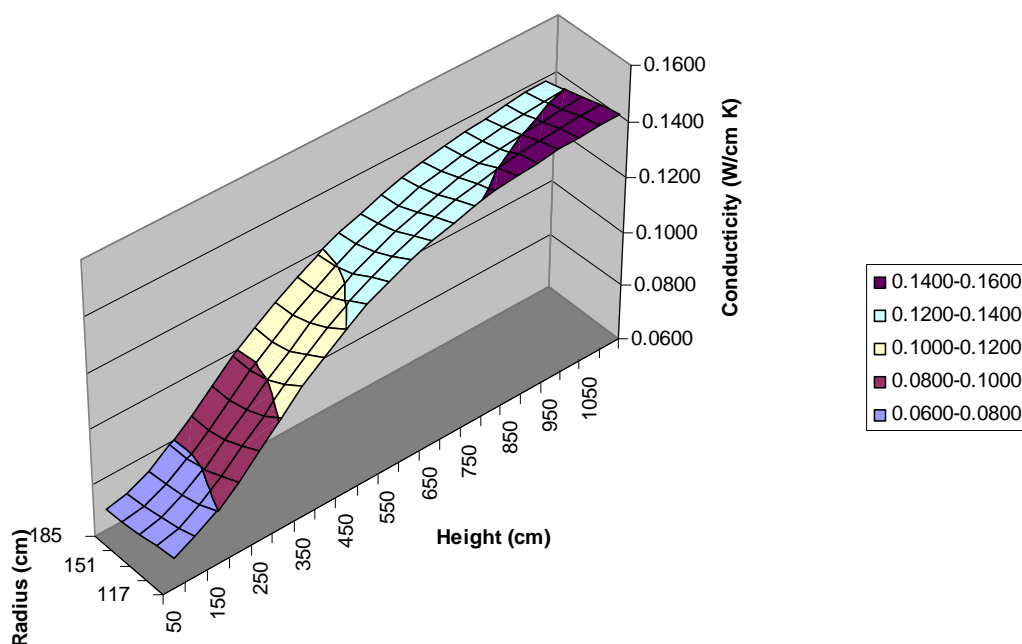
r/z (cm)	117	134	151	168	185
50	511	506	500	495	492
100	527	518	509	502	498
150	553	541	529	521	517
200	590	574	559	550	547
250	634	615	597	588	586
300	682	660	640	631	631
350	731	707	686	676	676
400	777	753	730	720	719
450	820	796	772	761	760
500	857	834	811	799	796
550	890	868	845	832	829
600	917	897	875	861	857
650	941	922	900	887	881
700	960	942	922	908	901
750	975	959	940	926	918
800	987	973	955	941	933
850	997	984	967	953	945
900	1005	993	977	964	955
950	1011	1000	985	972	964
1000	1015	1005	991	979	971
1050	1019	1009	996	985	976
1100	1021	1012	1000	989	981

TABLE 4.35. PRESSURE DIFFERENCE (IN MBAR)

r/z (cm)	117	134	151	168	185
50	1945	1947	1951	1960	1976
100	1898	1899	1900	1901	1902
150	1836	1836	1836	1836	1836
200	1770	1770	1770	1770	1770
250	1700	1700	1700	1700	1700
300	1627	1627	1627	1627	1627
350	1550	1550	1550	1550	1550
400	1469	1469	1469	1469	1469
450	1384	1384	1384	1384	1384
500	1295	1295	1295	1295	1295
550	1203	1203	1203	1203	1203
600	1108	1108	1108	1108	1108
650	1011	1011	1011	1011	1011
700	911	911	911	911	911
750	810	810	810	810	810
800	707	707	707	707	707
850	603	603	603	603	603
900	498	498	498	498	498
950	392	392	392	392	392
1000	285	285	285	285	285
1050	177	178	178	178	178
1100	70	70	70	70	70

TABLE 4.36. PEBBLE BED THERMAL CONDUCTIVITY (W/CM.K)

r/z (cm)	117	134	151	168	185
50	0.0718	0.0706	0.0696	0.0686	0.0679
100	0.0749	0.0729	0.0712	0.0700	0.0694
150	0.0798	0.0770	0.0750	0.0736	0.0730
200	0.0862	0.0828	0.0803	0.0788	0.0787
250	0.0935	0.0895	0.0866	0.0851	0.0853
300	0.1009	0.0966	0.0933	0.0917	0.0921
350	0.1080	0.1036	0.1000	0.0983	0.0986
400	0.1144	0.1100	0.1063	0.1046	0.1047
450	0.1199	0.1158	0.1121	0.1103	0.1101
500	0.1248	0.1209	0.1173	0.1153	0.1149
550	0.1289	0.1253	0.1217	0.1197	0.1191
600	0.1323	0.1290	0.1256	0.1235	0.1227
650	0.1352	0.1322	0.1289	0.1267	0.1258
700	0.1375	0.1348	0.1317	0.1295	0.1284
750	0.1394	0.1369	0.1340	0.1318	0.1306
800	0.1409	0.1387	0.1359	0.1338	0.1325
850	0.1421	0.1401	0.1375	0.1354	0.1341
900	0.1430	0.1412	0.1388	0.1368	0.1354
950	0.1437	0.1421	0.1398	0.1379	0.1365
1000	0.1442	0.1427	0.1406	0.1388	0.1374
1050	0.1445	0.1432	0.1412	0.1395	0.1382
1100	0.1448	0.1435	0.1417	0.1401	0.1388

FIG. 4.57. Case D-1 Pebble bed effective thermal conductivity at $t = 0$ h.

The variations in maximum and average fuel temperatures during the DLOFC are shown in Fig. 4.58. The maximum fuel temperature in the core (1592°C) is reached at $t = 38$ hours, with a corresponding core average fuel temperature of 1138°C . The core decay heat is presented in Fig. 4.59, where it can be seen that the initial total core heat load of 5.16 MW decreases to approximately 1.23 MW over a period of five days.

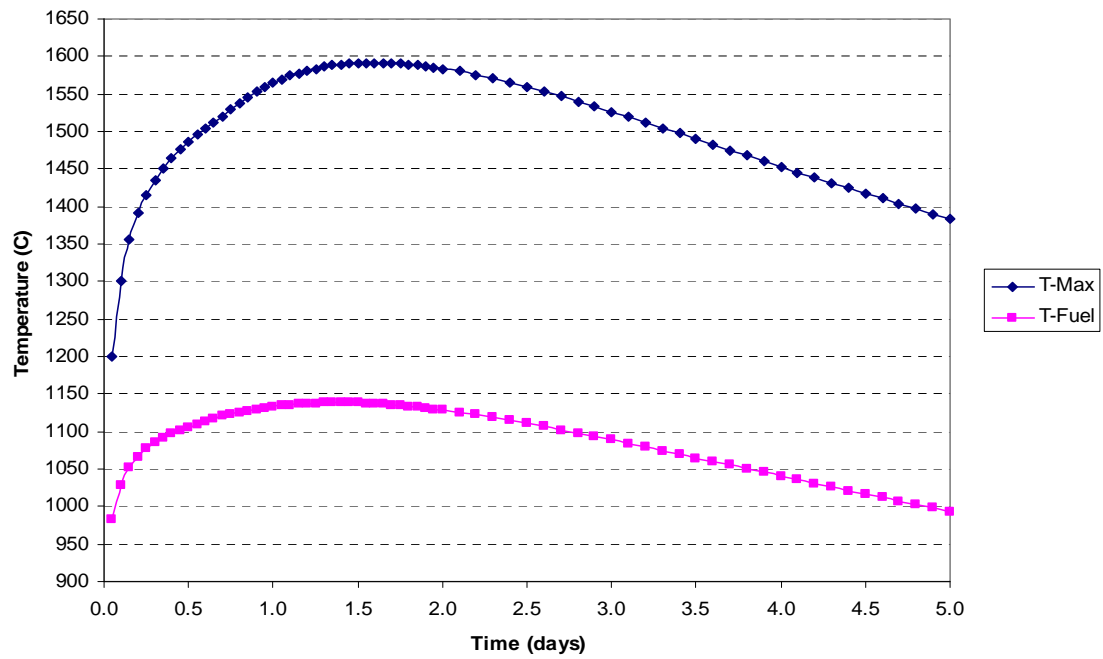


FIG. 4.58. Case D-1 maximum and average fuel temperatures over 5 d.

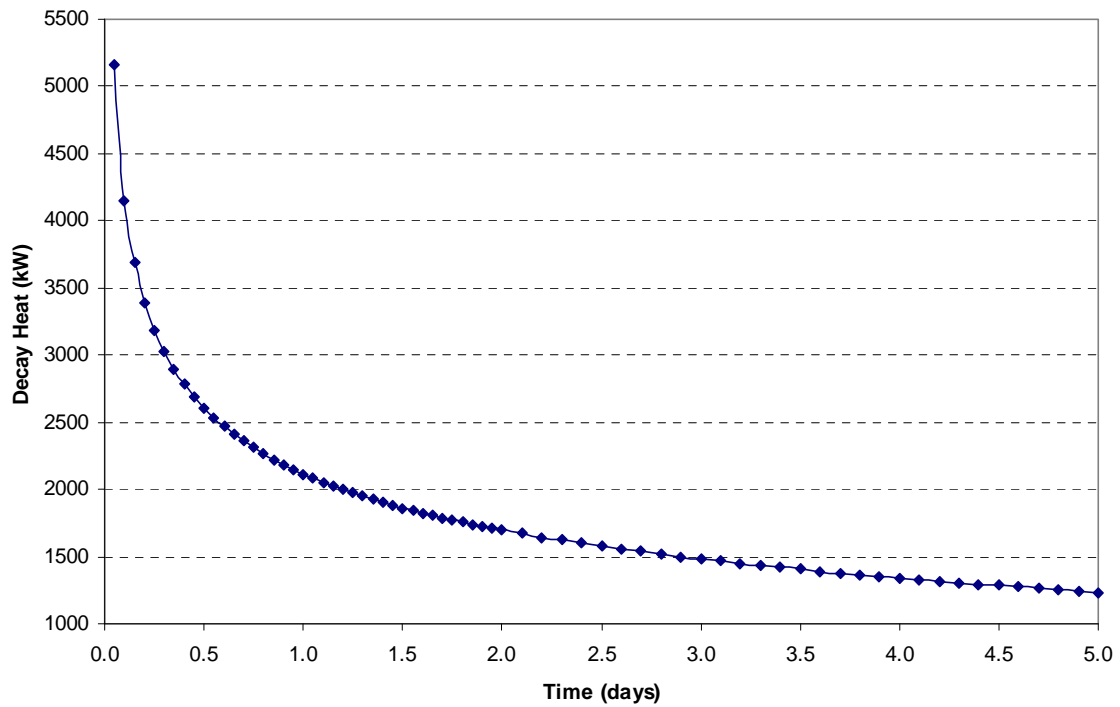


FIG. 4.59. Case D-1 decay heat over 5 d.

The core barrel and RPV axial temperature profiles are shown in Fig. 4.60, at the time point when the maximum fuel temperature during the DLOFC is reached (38.4 h). The maximum axial values of 584°C (core barrel) and 417°C (RPV) are located at approximately 450 cm.

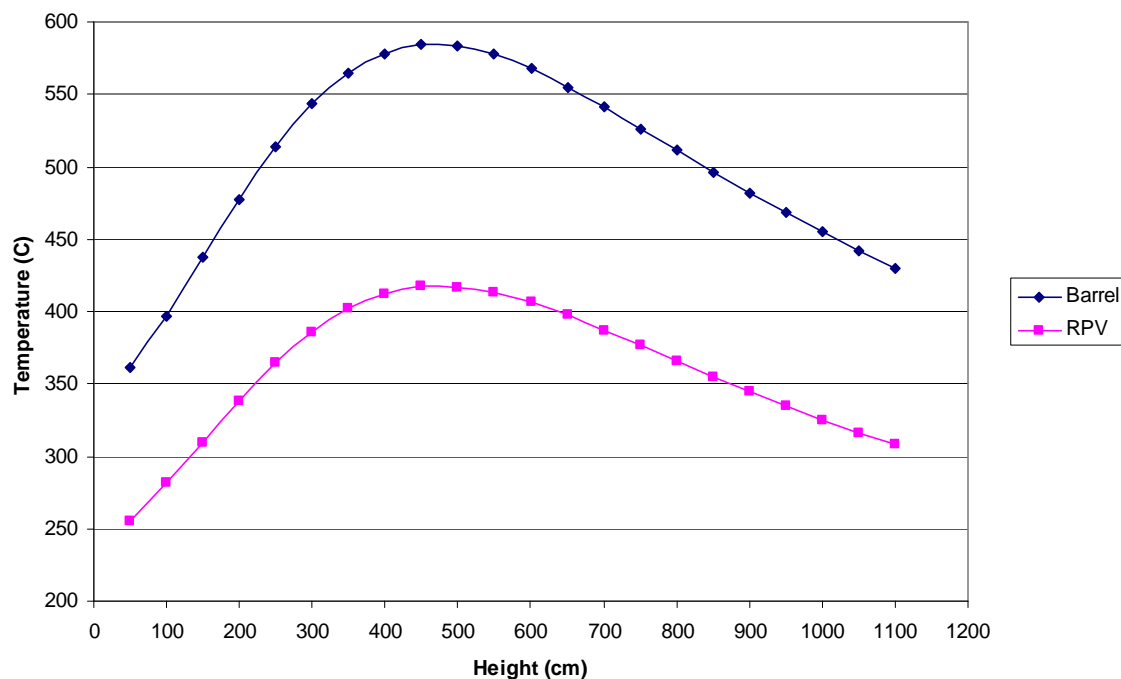


FIG. 4.60. Case D-1 core barrel and RPV axial temperature profiles at $t = 38.4$ h.

Conclusions

The CRP5 PBMR 400MW: Neutronics and thermohydraulics benchmark calculations were performed as a part of VSOP99 and TINTE codes V&V activities. Since different conditions were defined in each case, some of the phenomena related to pebble bed reactors were identified. The negative temperature reactivity coefficient of pebble-bed-type reactors, the effects of different fuel-to-moderator ratios and burnup of the fuel were discussed in the report. The results, shown in this report, show a realistic behaviour for changes in different parameters as given in theory and compared to the actual design calculations performed for the PBMR design.

The thermohydraulic properties and the temperature and burnup dependence of these parameters were discussed. The effect of the power profile was also identified.

4.2.3.2. PBMR-400 results, China

The summary provided here was submitted to the CRP as Ref. [4-25].

Fuel and sphere specification

The parameters of fresh fuel elements in Case F-1 were obtained from the first draft benchmark specification [4-15]. The atom densities used for the calculation are listed in Table 4.37 and differ only from the final specification in the definition of the poison in C (Material 150 in VSOP94) representing impurities in graphite.

The mixture of 33.3% fuel elements and 66.6% graphite spheres is used for Case F-2. The parameters of graphite spheres were from the specification so that the atom densities of mixed balls used in the calculation are similar to ND-set 2 (again with the exception of poison in C). The atom densities of mixed balls used for the calculation are listed in Table 4.37.

TABLE 4.37. NUMBER DENSITIES FOR ND-SET1 AND ND-SET2 FUEL REGION

Isotope	ND-Set1	ND-Set2
U234	0.622417E-07	0.207472E-07
U235	0.708600E-05	0.236200E-05
U-238	0.115700E-03	0.385666E-04
SI	0.275326E-03	0.917753E-04
Poison in C*	0.154194E-01	0.155885E-01
C	0.526247E-01	0.532028E-01
O-16	0.245572E-03	0.818572E-04

* Poison in C is understood as Identification Number 150 in the GAM library of VSOP.

Reactor structure

Figure 4.61 shows the PBMR-400 core physics calculation model. The reactor is divided into the following zones:

- Pebble bed and top and the bottom cone graphite area
(100cm < R < 185 cm, 0 cm < Z < 1408.5 cm in Fig. 4.61)
 - The total height of the top reflector is 170 cm;
 - The effective height of the upper void cavity is 78.5 cm;
 - The effective height of the core is 1100 cm;
 - The effective height of the bottom cone reflector is 60 cm;
 - The average pebble bed packing fraction is 0.61;
- Central reflector zone (0 cm < R < 100 cm, 0 < Z < 1408.5 cm in Fig. 4.61)
Outer diameter of hole in centre of central reflector is 20 cm.

RSS borings:

- The effective diameter of the RSS holes is 13 cm;
- The number of RSS holes is 8;
- The PCD of the RSS borings is 172.6 cm.

Inspection holes:

- The inspection holes' diameter is 5 cm;
- The number of inspection holes is 16;
- The PCD of inspection holes is 183 cm.

The effective void fraction of coolant slots (94 cm < R < 100 cm) is 0.035.

- Zone of side reflector (185 cm < R < 275 cm, 0 cm < Z < 1408.5 cm in Fig. 4.61)

RCS (reactivity control system) borings:

- The effective diameter of the RCS holes is 13 cm.
- The number of RCS holes is 24.
- The PCD of the RCS borings is 387.4 cm.

Gas risers:

- The diameter of the gas risers is 17 cm.
- The number of gas risers is 36.
- The PCD of gas risers is 504.2 cm.

The effective void fraction of inner block ($185 \text{ cm} < R < 225 \text{ cm}$) except RCS is 0.007.

The effective void fraction of outer block ($259.5 \text{ cm} < R < 275 \text{ cm}$) except gas risers is 0.058.

- Zone of bottom reflector ($0 \text{ cm} < R < 275 \text{ cm}$, $1408.5 \text{ cm} < Z < 1960.5 \text{ cm}$)
 - The total height of the bottom reflector is 552 cm.
 - The effective void fraction of the bottom reflector is 0.193.

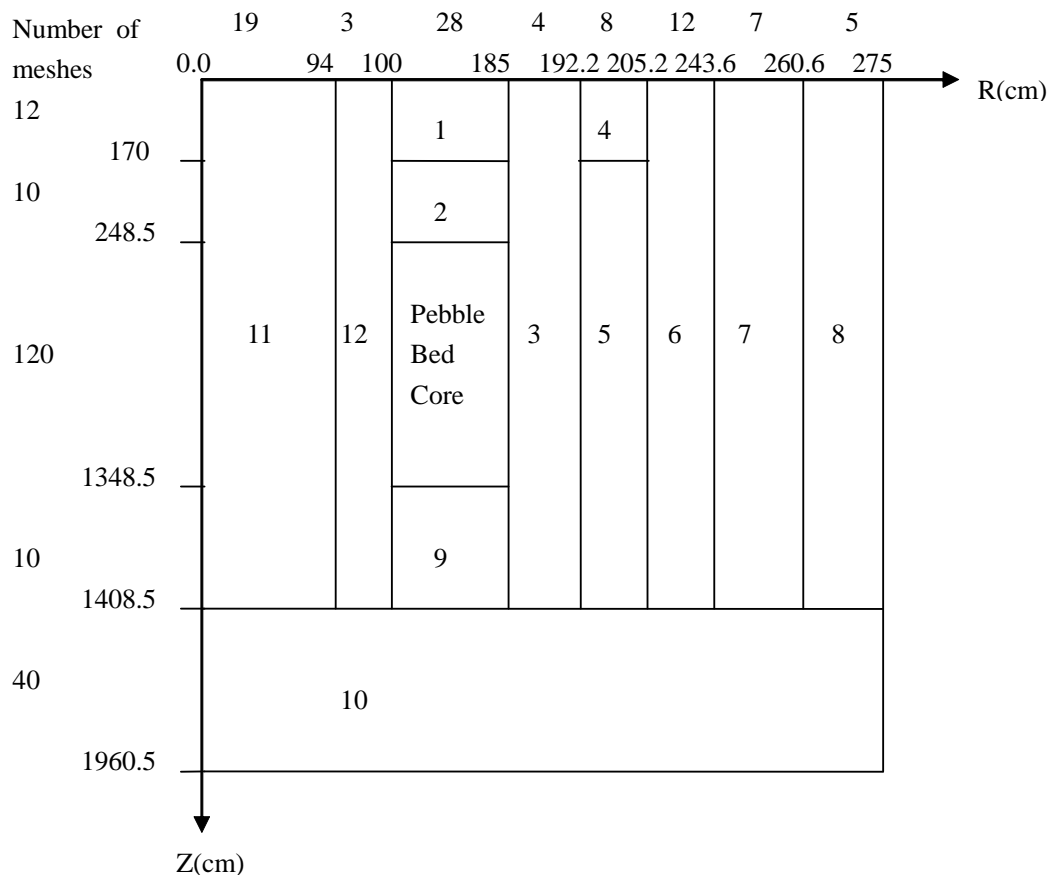


FIG. 4.61. PBMR-400 core physics calculation model.

The atom densities and effective porosities of the compositions in Fig. 4.61 are calculated and listed in Table 4.38.

TABLE 4.38. NUMBER-DENSITIES AND EFFECTIVE POROSITIES FOR REFLECTOR REGIONS

Composition ID	Porosity	Poison in C	C
1	0.0	0.28646E-01	0.90248E-01
3	7.0000002E-03	0.28445E-01	0.89616E-01
4	0.0	0.23004E-01	0.72472E-01
5	0.2032758	0.22823E-01	0.71903E-01
6	2.0131445E-02	0.28069E-01	0.88431E-01
7	0.3073225	0.19842E-01	0.62513E-01
8	5.7999998E-02	0.26985E-01	0.85014E-01
9	0.0	0.28646E-01	0.90248E-01
10	0.1930000	0.23117E-01	0.72830E-01
11	6.0887281E-02	0.26753E-01	0.84283E-01
12	3.5000000E-02	0.27490E-01	0.86606E-01

Calculation methodology and code

The VSOP code system has been used for the calculation. The code system includes GAM for the calculation of fast and epithermal spectrums and THERMOS for the calculation of thermal spectrum. The finite-mesh diffusion CITATION code in the code system calculates the eigenvalue problem in four energy groups and in two- or three dimensional reactor geometry. Cross-sections of the resolved and unresolved resonances are generated by the ZUT-DGL code. The code system takes into account the following basic features of pebble bed reactors [4-26]:

- The unique heterogeneity features of the coated particle fuel elements;
- Streaming correction of the diffusion constant in the pebble bed;
- Buckling feedback in the spectrum calculation;
- Anisotropic diffusion constants correction for the top cavity.

The identification numbers in Fig. 4.61 represent material features of the reactor. For spectrum calculations, the pebble bed core and its surrounding graphite structures are also divided into spectrum zones based on material features and eventually the temperature levels in the materials. Each spectrum zone covers an area which usually is identified by several material identification numbers.

The VSOP code system, based on diffusion approach, contains the GAM-Library and THERMOS-Library which are extracted from the basic nuclear data sets ENDF/B-V and JEF-I. The GAM-library covers the fast and epithermal spectrums from 10 MeV down to 0.414 eV in a 68 energy group structure and the THERMOS-library covers the thermal spectrum from 0.0eV up to 2.05eV in a 30 energy group structure.

For the fast and epithermal spectrum calculation with the GAM code, P1-approximation is used, based on a zero-dimensional cell of each spectrum zone. The materials in the cell were homogenized. The neutron leakage between neighbouring spectrum zones is considered by buckling, which is calculated by the diffusion of the whole reactor. The 68 fine-group cross-sections are finally merged into three broad-group cross-sections for the diffusion calculation.

The THERMOS code for the thermal spectrum calculation with a 30-group structure uses a one dimensional spherical cell model. The structure of the coated particles is taken into account. The neutron exchange between spectrum zones is considered by the albedo out of the leakage term. The THERMOS code's calculation finally provides the one-group constant for the thermal spectrum. In the

one dimensional spherical cell model of the THERMOS calculation, the mixture of fuel elements and graphite balls in the pebble bed is represented.

With the cut-off energy being 1.86 eV, four-group constants are generated for the CITATION diffusion calculation in R-Z geometry based on finite-differential methods, and the calculation gives the multiplication factor for the given reactor.

Calculation results of cases F1 and F2

Calculation of case F1

Condition: The fresh fuel is ND-set1 in Table 4.37. The cold state (300 K) is assumed for all materials. K-effective and leakage values are listed in Table 4.39.

The core is divided into five spectrum regions with equal height. K-inf values of the five spectrum regions are listed in Table 4.40.

TABLE 4.39. K-EFFECTIVE AND LEAKAGE

Case	Temperature (K)	Xenon	K _{eff}	Leakage
F-1	300	no	1.258231	1.7841E-01
F-2 (i)	300	no	1.140330	2.7592E-01
F-2 (ii)	600	no	1.100594	2.8706E-01
F-2 (ii)	900	no	1.066971	2.9798E-01
F-2 (ii)	600	Xe(400)*	1.063794	2.8155E-01
F-2 (ii)	900	Xe(400)*	1.032707	2.9210E-01

* Equilibrium xenon at 400 MW.

TABLE 4.40. K-INF FOR SPECTRUM REGION IN THE CORE

Case	Temp (K)	Xeno n	Region 1	Region 2	Region 3	Region 4	Region 5
F-1	300	no	1.4527	1.4534	1.4534	1.4534	1.4526
F-2 (i)	300	no	1.5614	1.5616	1.5616	1.5616	1.5613
F-2 (ii)	600	no	1.5311	1.5314	1.5314	1.5314	1.5311
F-2 (ii)	900	no	1.5087	1.5090	1.5090	1.5090	1.5087
F-2 (ii)	600	Xe*	1.4708	1.4675	1.4670	1.4673	1.4694
F-2 (ii)	900	Xe*	1.4503	1.4469	1.4463	1.4467	1.4489

* Equilibrium xenon at 400 MW.

Calculation of case F-2

Condition of F-2(i): ND-Set2 in Table 4.37 is used for the mixed balls. The cold state (300 K) is assumed for all materials.

Condition of F-2(ii): The same as F-2(i), but 600 K and 900 K temperatures are assumed respectively for all materials. The calculations are made for cases without xenon and equilibrium xenon of 400 MW. K-effective and leakage values are listed in Table 4.39.

The core is divided into five spectrum regions. K-inf values of five spectrum regions are listed in Table 4.40. Relative power densities for equilibrium xenon of 400 MW and 900 K are shown in Figs 4.62 and 4.63. Thermal flux ($E < 1.86$ eV) profiles for equilibrium xenon of 400 MW and 900 K are given in Figs 4.64 and 4.65.

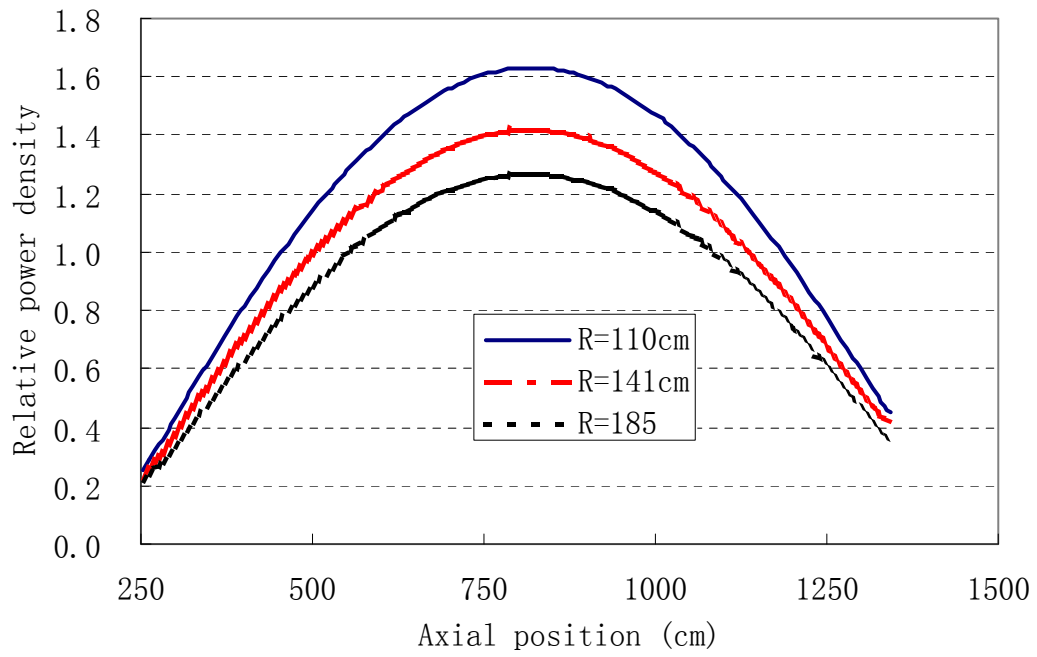


FIG. 4.62. Relative axial power density profiles with 400 MW and 900 K (equilibrium xenon).

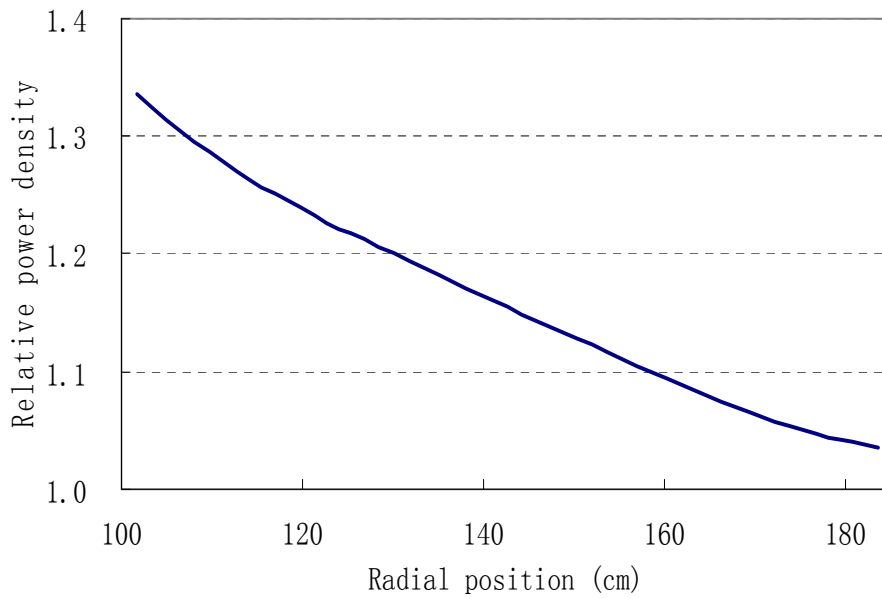


FIG. 4.63. Relative radial power density profile (326 cm from the top) with 400 MW and 900 K (equilibrium xenon).

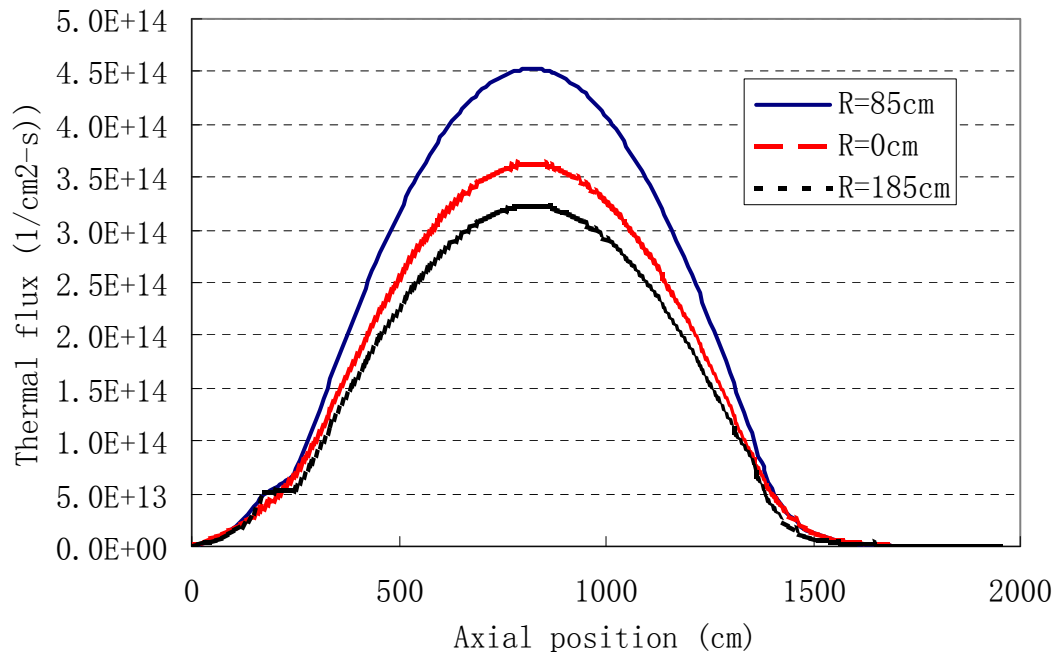


FIG. 4.64. Axial thermal flux profiles with 400 MW and 900 K in Case F-2-ii (equilibrium xenon).

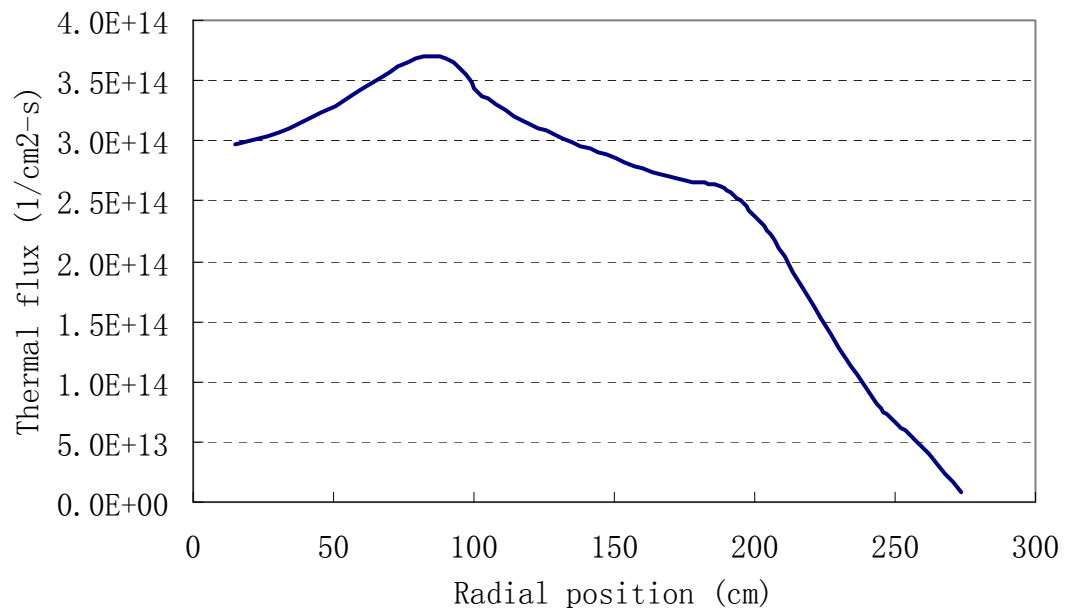


FIG. 4.65. Radial thermal flux profiles (326 cm from the top of the core) with 400 MW and 900 K in Case F-2-ii (equilibrium xenon).

4.2.3.3. PBMR-400 neutronics benchmark results, Turkey

Neutronics analysis

In this section, the results of steady state calculations without any thermohydraulics feedback for PBMR-400 are presented. Calculations are mainly covered in two parts. The first part is related to the fresh fuel core loading and the second one is for the first-core loading with a graphite and fuel balls

mixture. Criticality calculations are performed with the Monte Carlo method using the MCNP-4b computer code. Continuous-energy cross-sections are used based on ENDF-B/6 evaluations.

General descriptions

For simplicity in the calculations, it is assumed that there would be no control rod and an isotropic temperature distribution in the whole core. The MCNP-4b model of the core is illustrated in Fig. 4.66. Technical specifications for the core are given in Table 4.41 with the fuel specification exactly as defined in Table 4.12.

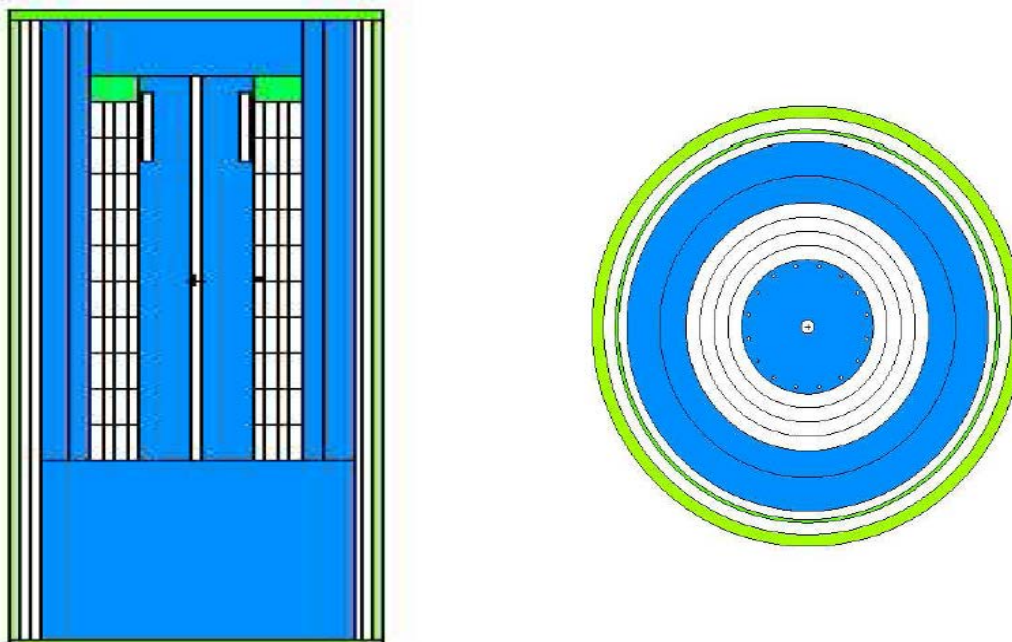


FIG. 4.66. MCNP-4b model for PBMR-400.

TABLE 4.41. TECHNICAL SPECIFICATIONS FOR THE CORE MODEL

Active fuel region core height (helium space/bottom plane)	1100 cm
Side reflector thickness	100 cm
Number of fuel region rings	4
Number of fuel region levels	10
Fuel region rings radii	121.25/142.50/163.75/185.00 cm
Fuel region levels height	110 cm

Case 1: Fresh core loading

In this phase of the benchmark, the core is filled with fresh first-core fuel (9 grams HM and 5.768 w/o enriched). Cold conditions (300 K) are employed for all materials. The fuel pebble is modelled by distributing kernels uniformly in the graphite matrix region in the pebble. The core is filled with a columnar hexagonal lattice-wise pure fuel pebble configuration. The neutron flux spectrum is acquired from each region/mesh of the core region with 238-group energy structure. Effective multiplication factors for different temperatures are given in Table 4.42 and the neutron flux spectrum calculated at 300 K is given in Fig. 4.67.

TABLE 4.42. EFFECTIVE MULTIPLICATION FACTOR
FOR THE FRESH CORE LOADING CASE

Temperature (K)	K_{eff}
300	1.27808
600	1.25577
900	1.23151

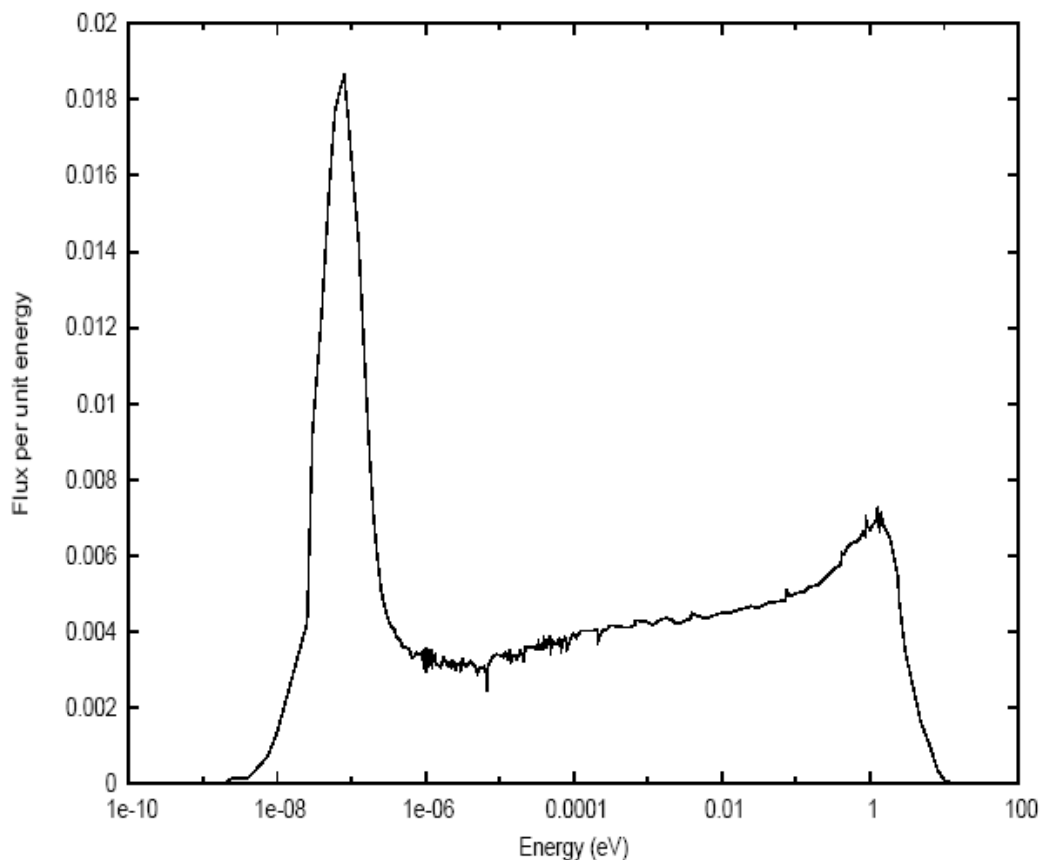


FIG. 4.67. Neutron flux at 300 K at the mid-point of fuel Region for case 1.

Case 2: First core loading

In this phase of the benchmark, the core is filled with a homogeneous mixture of 33.3 % first-core fuel (9 grams HM and 5.768 w/o enriched) and 66.6% graphite spheres (no fission products or higher elements). Constant temperature conditions (300 K) for all materials are used again. The fuel pebble is

again modelled by distributing kernels uniformly in the graphite matrix region in the pebble, but the core is filled with the columnar hexagonal lattice-wise structure in which 33.3% of the pebbles are fuel only.

Effective multiplication factors for different temperatures are given in Table 4.43 and the neutron flux spectrum calculated at 300 K is given in Fig. 4.68. For all cases, required output parameters are k-effectives of the system, macroscopic cross-sections for each mesh, leakage of the system, relative power profiles, and neutron flux distribution.

TABLE 4.43. EFFECTIVE MULTIPLICATION FACTORS
FOR THE FIRST-CORE LOADING CASE

Temperature (K)	K_{eff}
300	1.15329
600	1.11724
900	1.10873

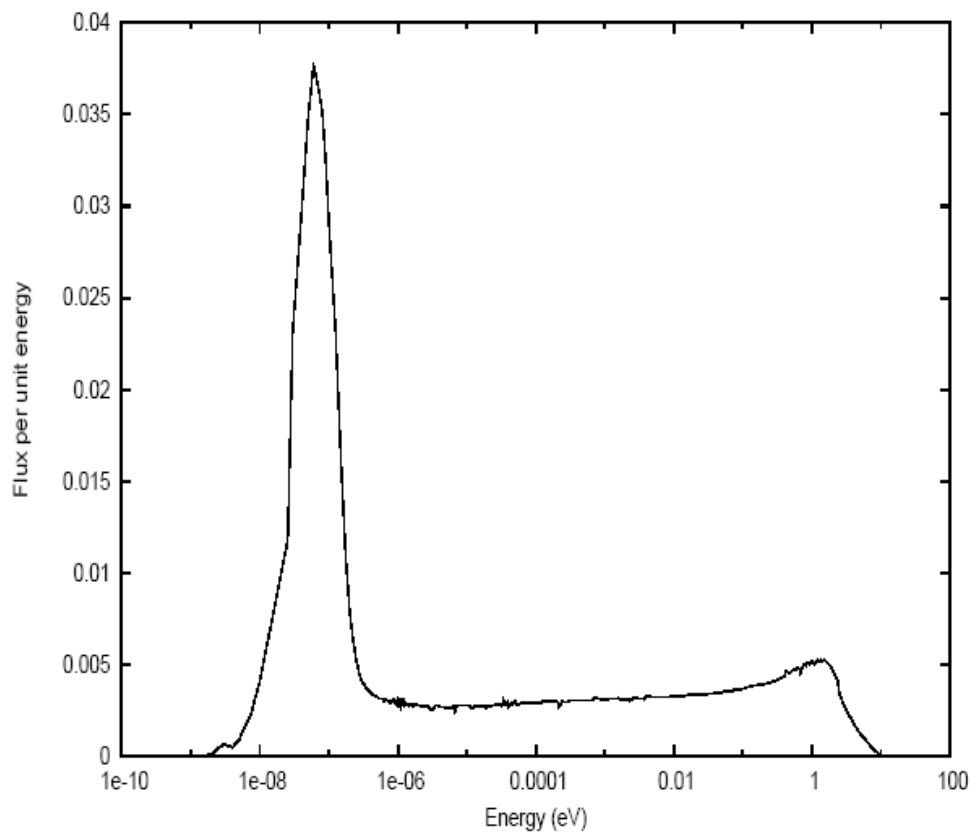


FIG. 4.68. Neutron flux at 300 K at the mid-point of fuel region for phase 2.

PBMR-400 Thermohydraulics benchmark results by the Hacettepe university

The two dimensional axisymmetric thermohydraulics analysis of PBMR is performed by FLUENT, a commercial CFD code, using the prescribed data. The FLUENT code uses a finite-volume approach for the discretization during the solution of mass, momentum and energy equations. In the FLUENT model of PBMR-400, the following methods are employed:

- A User-defined Scalar (UDS) equation is defined for fuel ball surface temperatures;
- User-defined momentum sources are used for helium flow in the pebble bed;
- Thermal sources in pebble bed, for UDS and helium are coupled by means of User-defined Functions (UDF);
- Wall boundaries between the core and reflectors are uncoupled and three boundary conditions are applied to realize the heat transfer from fuel balls to reflectors;
- The wall effect on the void distribution in the pebble bed is treated according to Benenati and Brosilow.

Simplifications introduced

In thermohydraulics analysis, the following simplifications are introduced:

- Specification of stagnant air between the RPV and heat sink (outer boundary);
- The upwards coolant flow in the reflector is restricted within a porous ring;
- Coolant inlet flow from the top inlet plenum to upper cavity and the outlet flow from core exit to outlet plenum are restricted within porous zones. Since the flow paths in these regions are not properly defined in benchmark specifications, these porous zones are used to complete the helium flow. These zones are shown in Fig. 4.69;
- No cooling or leakage paths were defined;
- The only heat source exists in the core;
- The thermohydraulics test case given in the benchmark definition is considered for core power distribution;
- The geometry is simplified to the axisymmetric two dimensional model as seen in Fig. 4.69.



FIG. 4.69. Simplified 2-D model of PBMR-400.

Methodology

The main difficulty in the thermal analysis of a pebble bed reactor system is the modelling of the core region. Although the FLUENT code has very flexible geometric modelling capabilities, the exact model of the fuel balls is not possible due to very expensive computation requirements and complicated mesh structure. To overcome these problems and to capture the physical properties of the pebble bed, the core is considered as a porous region. In addition, although the FLUENT.6 code has physical models for porous fluid zones, these are not adequate for pebble bed thermal analysis. The equations solved and the boundary conditions applied for the core zone are explained below.

Laminar flow equations are solved in the core region due to the nature of correlations used for the pressure drop in the porous pebble bed. In the core zone, in addition to conservation equations for mass, momentum and energy (see Section 2.2.2.2 for the detailed equations), a scalar equation is defined and solved. The scalar equation is used to predict ball surface temperatures. The approach to determine other properties is given below.

Thermal properties of helium

Density

$$\rho = 48.14 \frac{P}{T} \left(1 + 0.4446 \frac{P}{T^{1.2}} \right)^{-1} [kg / m^3] \quad (4.1)$$

The pressure P and temperature T are in Pa and K respectively.

Dynamic Viscosity

$$\eta = 3.674 \times 10^{-7} T^{0.7} [Pa.s] \quad (4.2)$$

where T is in K.

Conductivity

$$k_c = 2.682 \times 10^{-5} \left(1 + 1.123 \times 10^{-3} P \right) T^{0.71(1-2 \times 10^{-4} P)} [W / cm / K] \quad (4.3)$$

where pressure P and temperature T are in Pa and K respectively.

Heat conduction equation for pebble bed

The conduction equation for the pebble bed includes the following heat transfer mechanisms, namely, conduction of fuel elements, and conduction of helium and radiation among fuel element surfaces. For finding fuel element surface temperatures, an UDS equation is defined in the following form:

$$-\nabla \cdot k_p \nabla T_s = S_p \quad (4.4)$$

S_p is defined by:

$$S_p = \dot{Q} - \frac{6\alpha}{d} (1 - \varepsilon) (T_s - T_c) \quad (4.5)$$

where \dot{Q} is the local power density. The conductivity of uniform pebble bed core k_p synthesizes the effects of conduction and thermal radiation among the fuel element surfaces. The model by Zehner-Schlunder is employed to describe k_p .

Boundary conditions

Core reflector wall boundaries

Three boundary conditions are applied to wall-shadow couplings at core-wall interfaces by means of three UDFs to ensure heat transfer from fuel balls to reflector walls. These boundary conditions are applied to walls or their shadows according to their positions. The theory is defined as follows:

The diffusive flux q_f'' of a scalar Q across a boundary face f may be approximated as:

$$q_f'' = -\Gamma_f \left[\frac{(Q_0 - Q_f)}{ds} \frac{|\vec{A}|}{\vec{A} \cdot \vec{e}_s} + \nabla Q \cdot \vec{e}_s \frac{|\vec{A}|}{\vec{A} \cdot \vec{e}_s} - \nabla Q \cdot \vec{A} \frac{1}{|\vec{A}|} \right] \quad (4.6)$$

In this equation, \vec{A} is the area normal vector of boundary face f , ds is the distance between cell centroid and the face centroid and \vec{e}_s is the unit normal vector directed from centroid of cell to face centroid. See Fig. 4.70 for definitions.

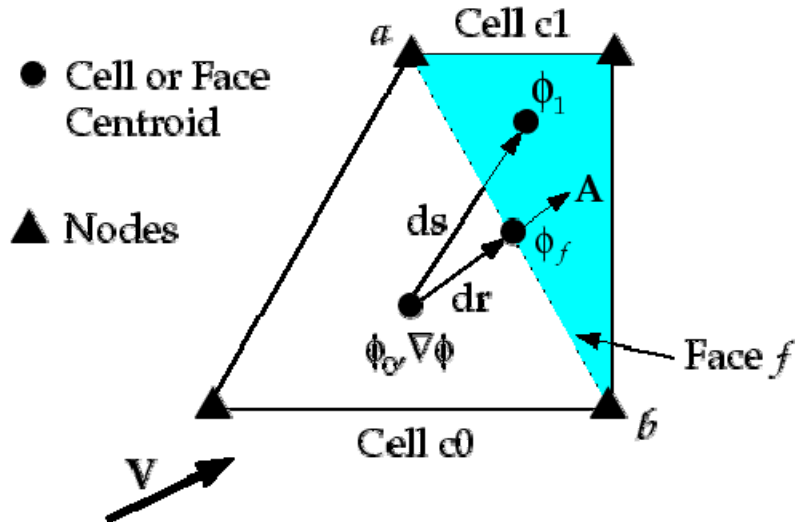


FIG. 4.70. Vector and gradient definitions.

UDS boundary condition

The UDS flux boundary condition is defined as:

$$q_{f,p}'' = -k_p \left[\frac{(T_{s,c0} - T_f)}{ds} \frac{|\vec{A}|}{\vec{A} \cdot \vec{e}_s} + \nabla T_s \cdot \vec{e}_s \frac{|\vec{A}|}{\vec{A} \cdot \vec{e}_s} - \nabla T_s \cdot \vec{A} \frac{1}{|\vec{A}|} \right] \quad (4.7)$$

Thermal boundary condition for helium on core wall

The flux boundary condition for helium on the core wall is defined as:

$$q_{f,c}'' = -k_c \left[\frac{(T_{c,c0} - T_f)}{ds} \frac{|\vec{A}|}{\vec{A} \cdot \vec{e}_s} + \nabla T_c \cdot \vec{e}_s \frac{|\vec{A}|}{\vec{A} \cdot \vec{e}_s} - \nabla T_c \cdot \vec{A} \frac{1}{|\vec{A}|} \right] \quad (4.8)$$

Thermal boundary condition for the wall on reflector side

The flux boundary condition for the reflector side wall is defined as:

$$q_{f,R}'' = k_p \left[\frac{(T_{s,c0} - T_f)}{ds} \frac{|\vec{A}|}{\vec{A} \cdot \vec{e}_s} + \nabla T_s \cdot \vec{e}_s \frac{|\vec{A}|}{\vec{A} \cdot \vec{e}_s} - \nabla T_s \cdot \vec{A} \frac{1}{|\vec{A}|} \right] + k_c \left[\frac{(T_{c,c0} - T_f)}{ds} \frac{|\vec{A}|}{\vec{A} \cdot \vec{e}_s} + \nabla T_c \cdot \vec{e}_s \frac{|\vec{A}|}{\vec{A} \cdot \vec{e}_s} - \nabla T_c \cdot \vec{A} \frac{1}{|\vec{A}|} \right] \quad (4.9)$$

Discussion and thermohydraulics results

Another way of modelling a pebble bed in the FLUENT code is the use of the Eulerian multi-phase flow model. In this model, the fuel balls are considered as the secondary solid phase. The equations solved in this model are the same as explained above. Therefore, in theory, there should be no difference in the results of the two models. However, the radiation heat transfer cannot be modelled in the Eulerian multi-phase model of FLUENT. Furthermore, the thermal radiation from the top of the bed to the cavity walls is not yet included in the model.

Global parameters

- Core Pressure Drop: 237 kPa;
- Helium Outlet Temperature: 1093 K;
- Average Fuel Surface Temperature: 1014 K;

- Average Helium Temperature in the Core: 954 K;
- Average Temperature of the Central Reflector: 1023 K;
- Average Temperature of the Outer Reflector: 754 K.

The temperature distribution is shown in Fig. 4.71. The contours in the core and cavity regions enclosed in black lines show helium temperatures and the others show solid temperatures. The same data is also represented as contour lines (with symmetry segment through the core used on the Y-axis) in Fig. 4.72. The ball surface temperatures are shown in Fig. 4.73. Contour plots for the fuel surface temperatures and the helium coolant temperatures are shown in Fig. 4.74 while the difference between these two values is included in Fig. 4.75. The effective thermal conductivity of the pebble bed is presented in Figs 4.76 and 4.78 as a contour and color plot while Fig. 4.77 again shows the fuel surface temperatures but this time as radial profiles at various axial positions.

Profiles of the fuel surface temperature and helium coolant temperature, this time in the centre of the core, is shown in Figs 4.79 and 4.80 while radial helium temperature profiles for different axial heights is included in Fig. 4.82. The central reflector (centre line) solid temperature axial profile is shown in Fig. 4.81. Finally the helium velocities through the core (represented as radial profiles at different axial heights) and the pressure drop are presented in Figs 4.83 and 4.84 respectively.

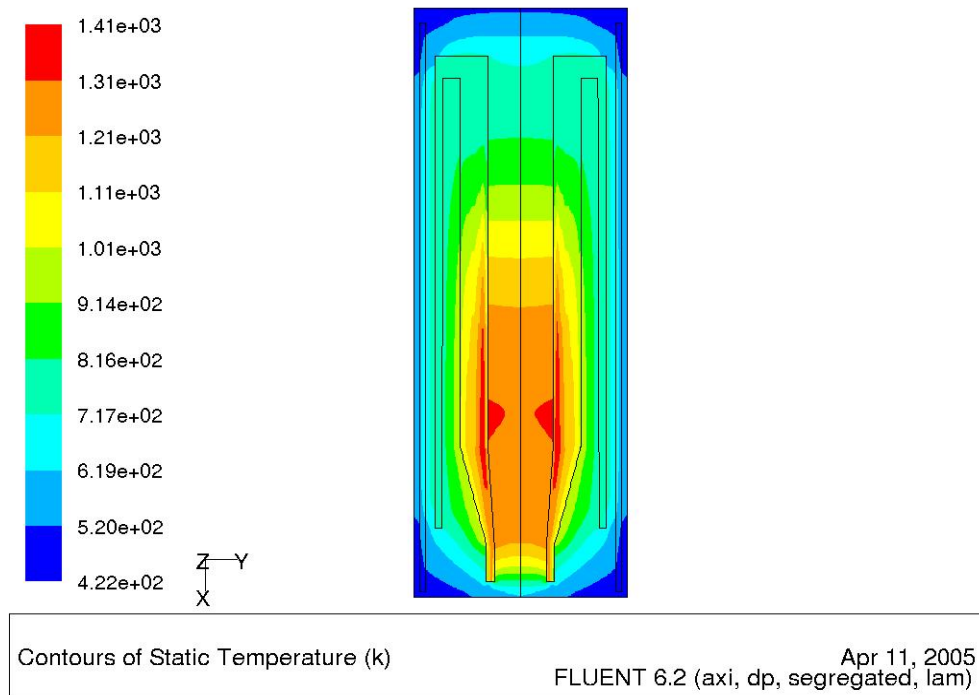


FIG. 4.71. Contours of temperature in K.

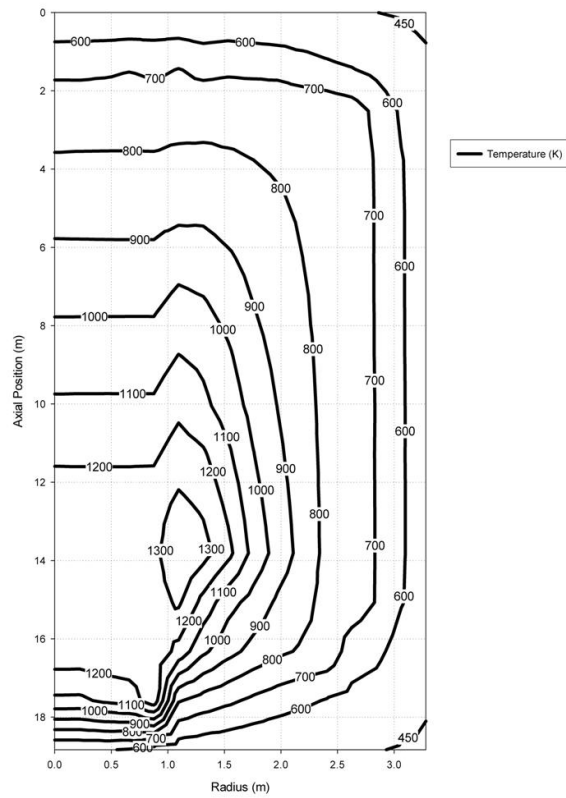
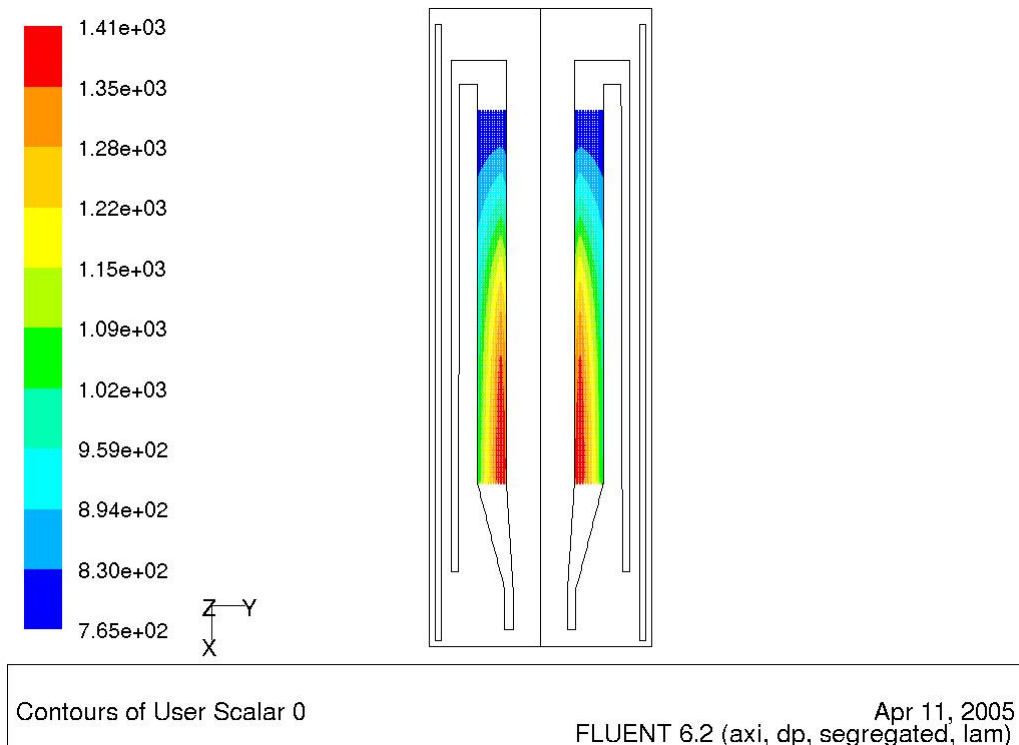


FIG. 4.72. Temperature distribution of solid materials.



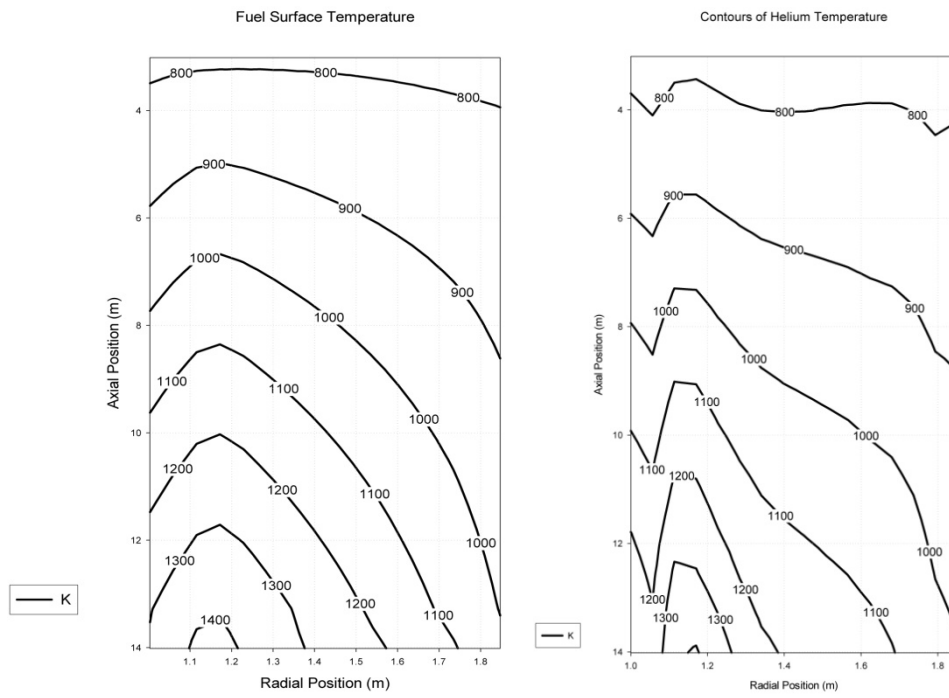


FIG. 4.74. Contours of fuel surface temperature and helium temperature.

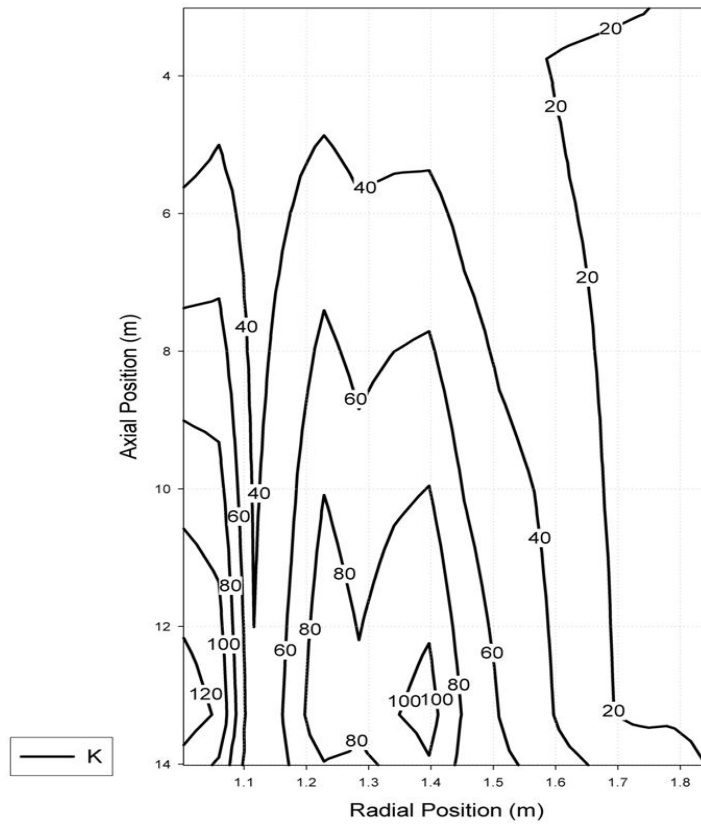


FIG. 4.75. Temperature difference between fuel surface and helium temperatures.

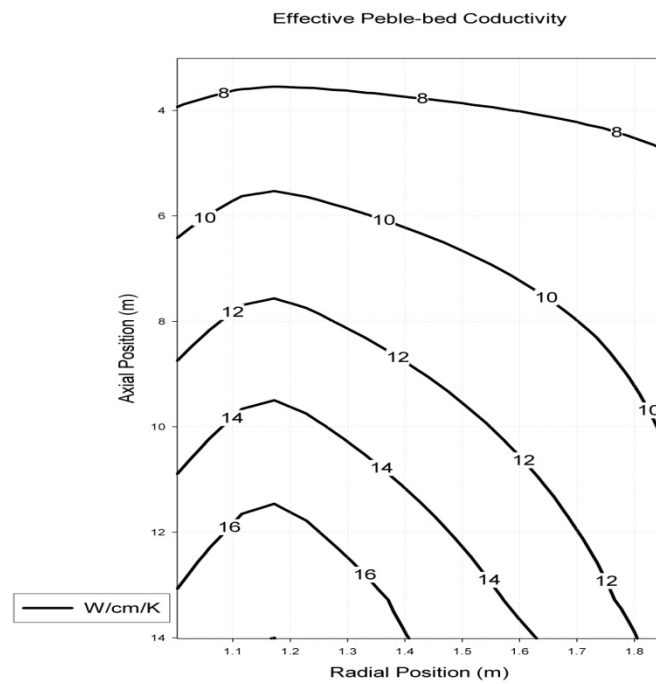


FIG. 4.76. Contours of effective pebble bed conductivity (Zehner-Schlunder).

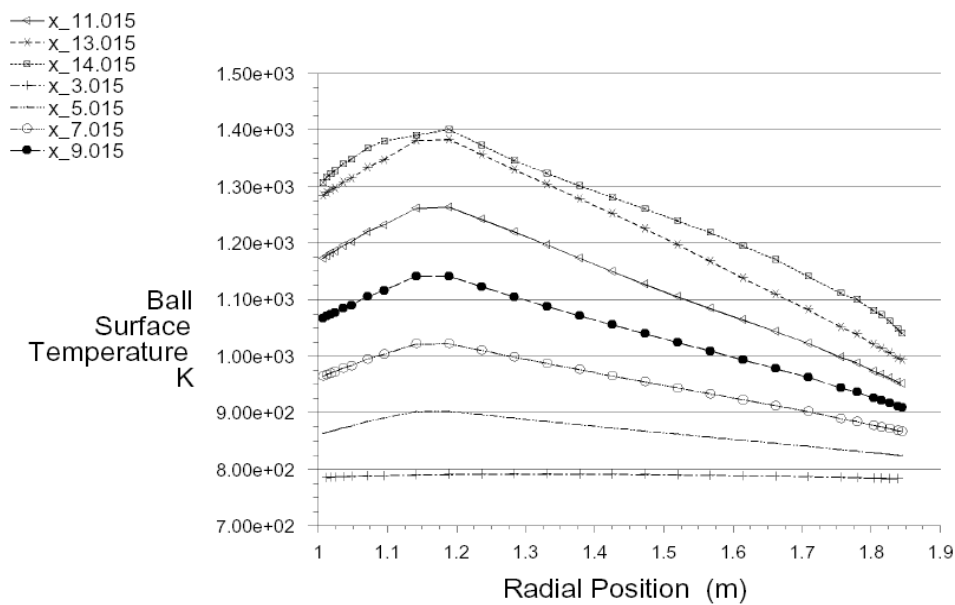


FIG. 4.77. Fuel ball surface temperatures at various axial positions.

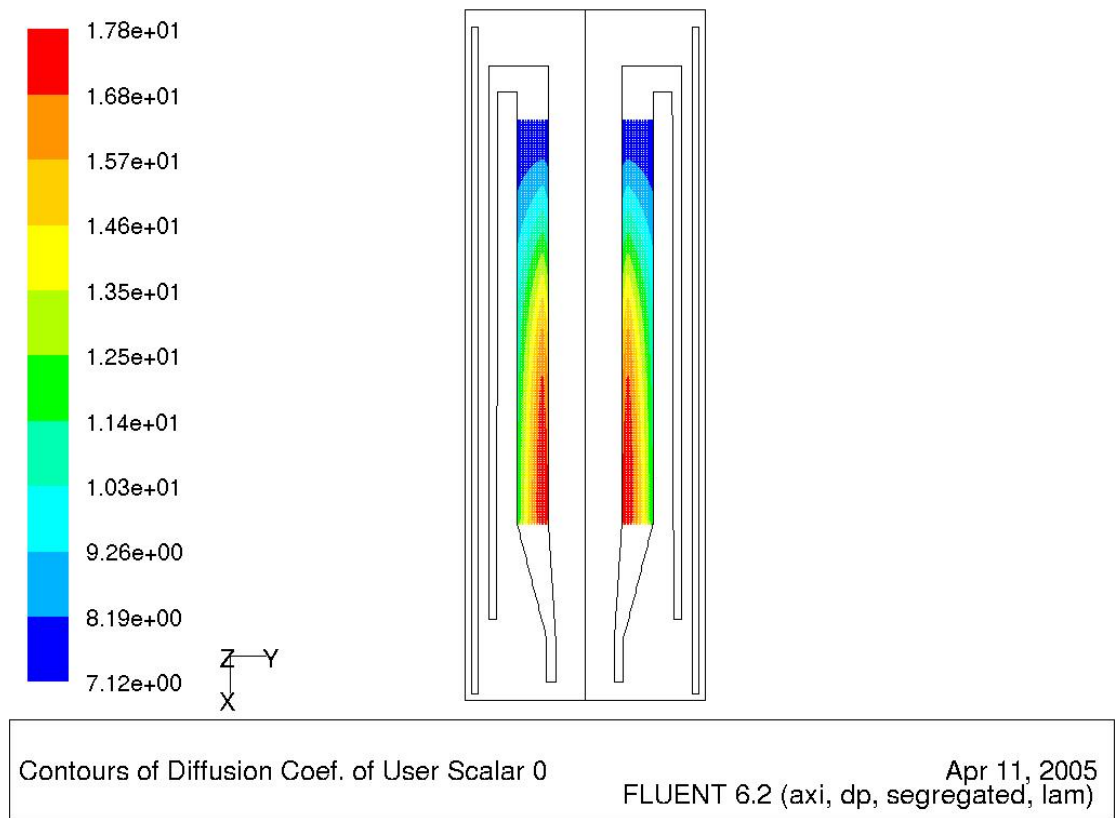


FIG. 4.78. Effective pebble bed thermal conductivity (W/m/K).

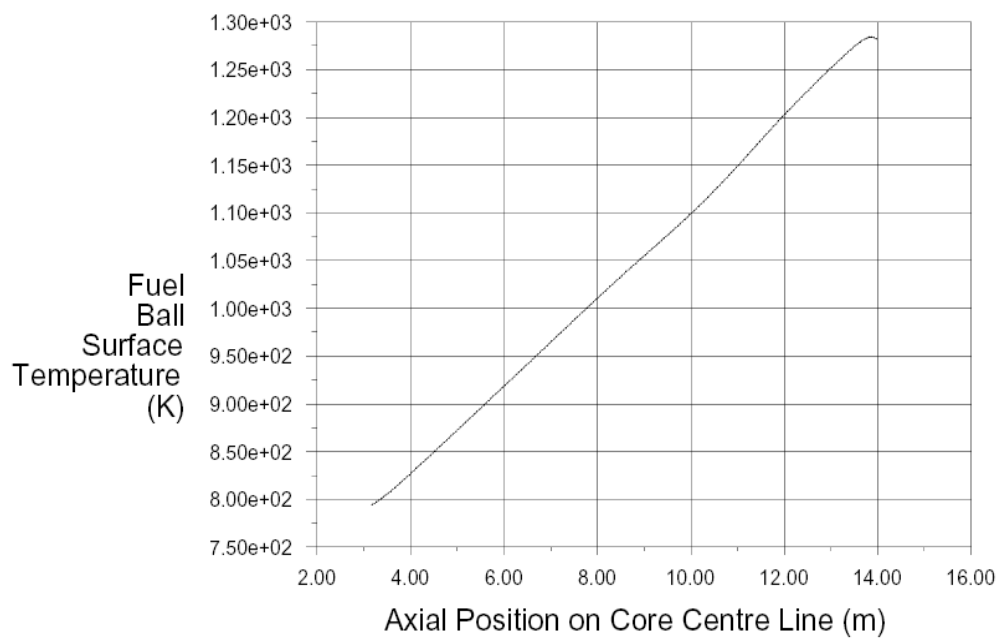


FIG. 4.79. Fuel ball surface temperatures along the centre of core.

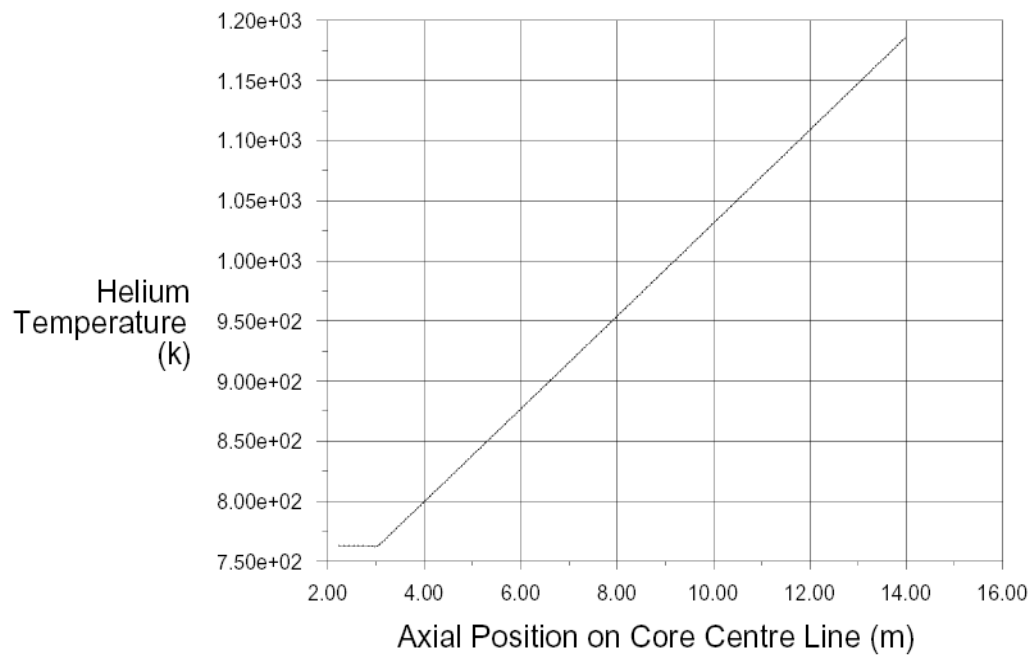


FIG. 4.80. Helium temperatures along the core centre line.

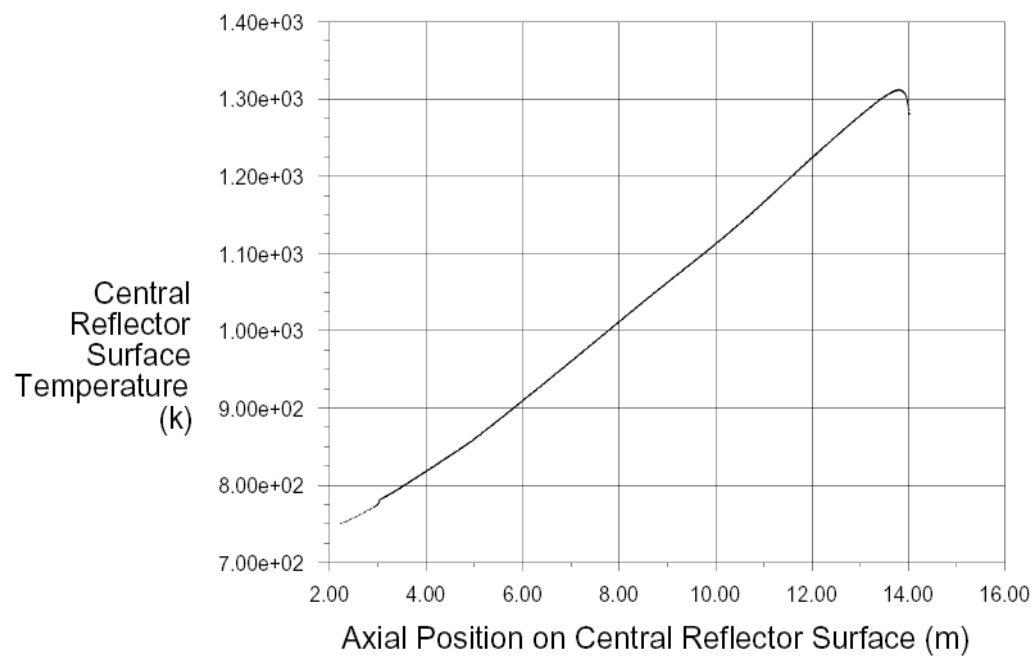


FIG. 4.81. Central reflector surface temperatures.

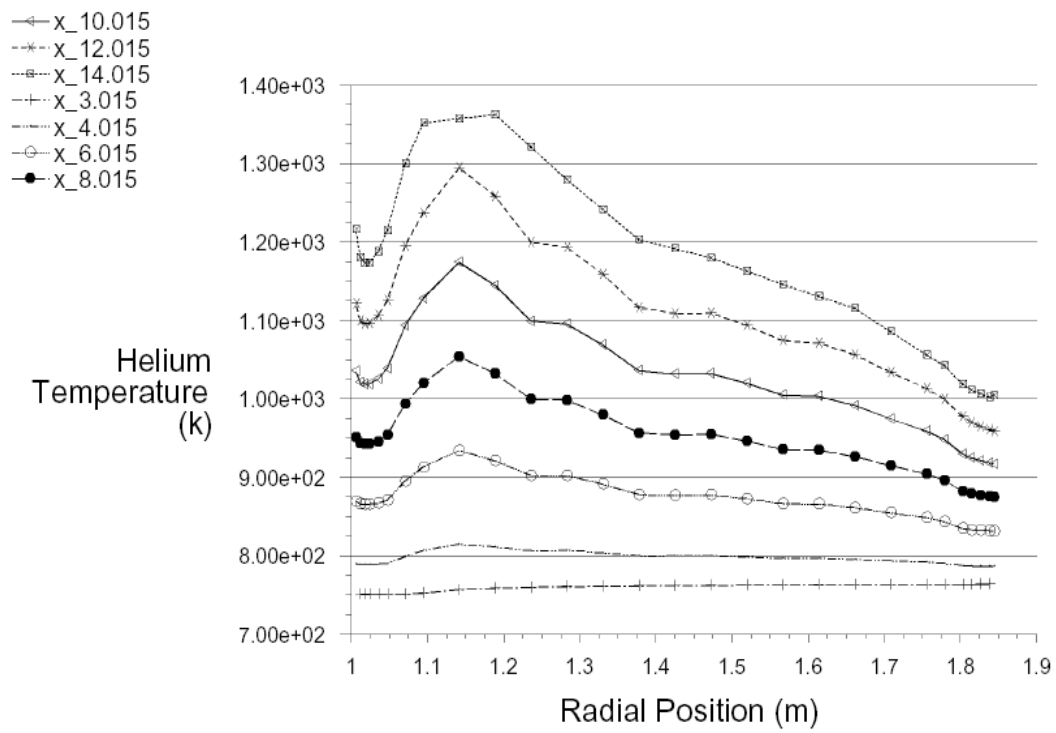


FIG. 4.82. Helium temperatures at various axial positions in the core.

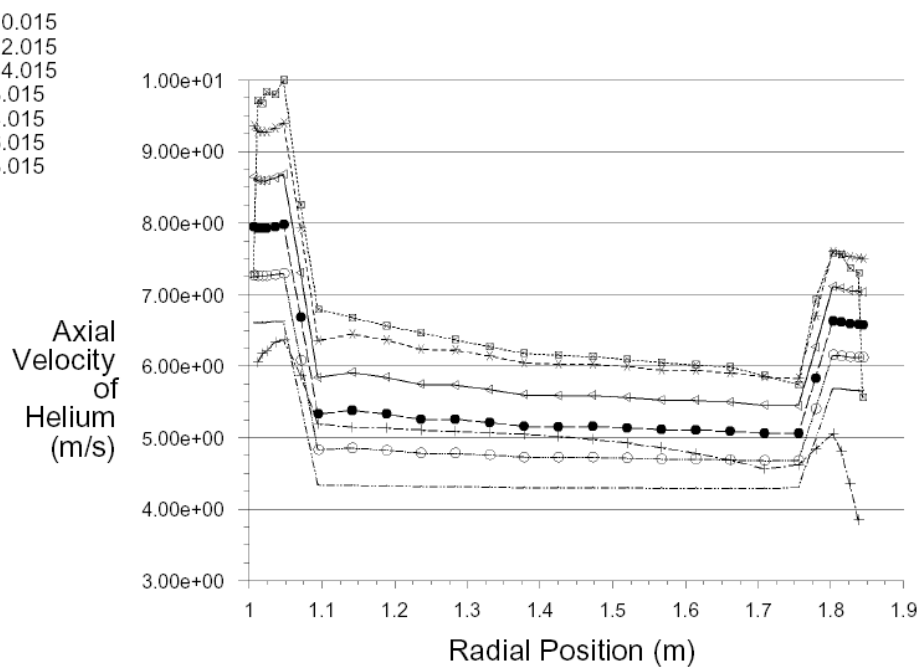


FIG. 4.83. Axial velocities of helium at various axial positions.

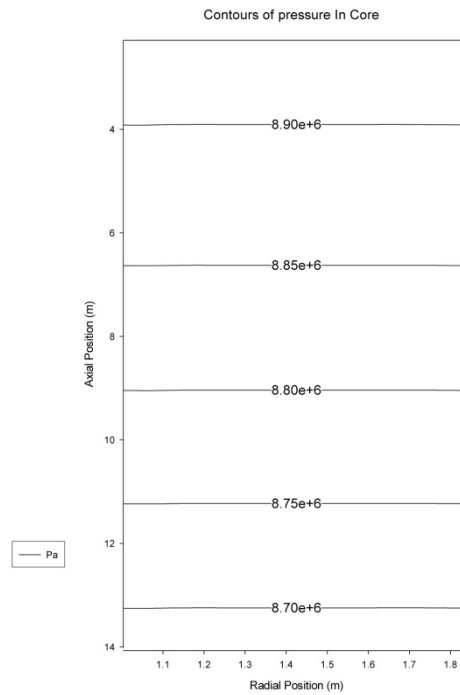


FIG. 4.84. Contours of pressure in core.

4.2.3.4. PBMR-400 results, U.S.A.

Introduction

The results of the Depressurized Loss of Forced Cooling (DLOFC) accident scenario simulations are presented, along with representative sensitivity studies that indicate some of the uncertainties involved in the accident outcome predictions.

The development, use and validation exercises of GRSAC began over 25 years ago with several predecessor codes [4-27]. Current interest in GRSAC involves the simulation of accident scenarios for various modular HTGR designs and the simulation of benchmark transients run on the HTR-10 (China) and HTTR (Japan). The GRSAC employs a detailed (~3000 nodes) three dimensional thermohydraulics model for the core, plus models for the reactor vessel, Shutdown Cooling System (SCS) and shield or RCCS. There are options to include Anticipated Transients Without Scram (ATWS) accidents and to model air ingress accidents, simulating the oxidation of graphite core materials, where air circulation is driven either via buoyancy (chimney) effects from single breaks or double breaks, or by forced circulation [4-28]. In this discussion, however, air ingress effects are not covered.

The hexagonal geometry core thermal model allows for detailed investigations of azimuthal temperature asymmetries in addition to axial and radial profiles. Variable core thermal properties are computed functions of temperature. The primary coolant flow models cover the full ranges expected in both normal operation and accidents, including pressurized and depressurized accidents (and in between), for forced and natural circulation, for upflow and downflow and for turbulent, laminar and transition flow regimes. The flows are channelized; i.e. radial coolant flows within the pebble bed are not accounted for. The primary loop pressure calculation can consider variable inventory (due to depressurization actions) and loop temperature changes, and uses a simplified model for balance of plant temperatures. The models for the RPV and the shield or the RCCS are typically different for each of the various basic reactor types.

Other GRSAC features of interest are:

- Fast running (typically ~20000 times faster than real time on a PC, for non-ATWS accidents);

- Interactive user interface with on-line and off-line plotting options;
- A 'smart front end' data input checker;
- On-line help features.

Reference case models

The reference model used for the PBMR is based on material provided in the benchmark description and on recent versions of the design. However, it does not purport to be entirely representative, since some features are still under development. Data for the initial power peaking distribution and for afterheat were not generated for this benchmark and also relied on previously obtained information.

The current South African PBMR design (Fig. 4.85) has a tall, relatively thin annular core design with fuel pebbles in an annulus surrounding a solid graphite central reflector. Major design parameters and features with nominal full power operating conditions for the reference case (which do not include mid-2004 changes in the PCU) are shown in Table 4.44. On-line refuelling allows for recirculation of the pebble fuel (six to ten times) until the desired burnups are attained. Fresh fuel is added as needed to maintain the desired excess reactivity as required for power manoeuvring.

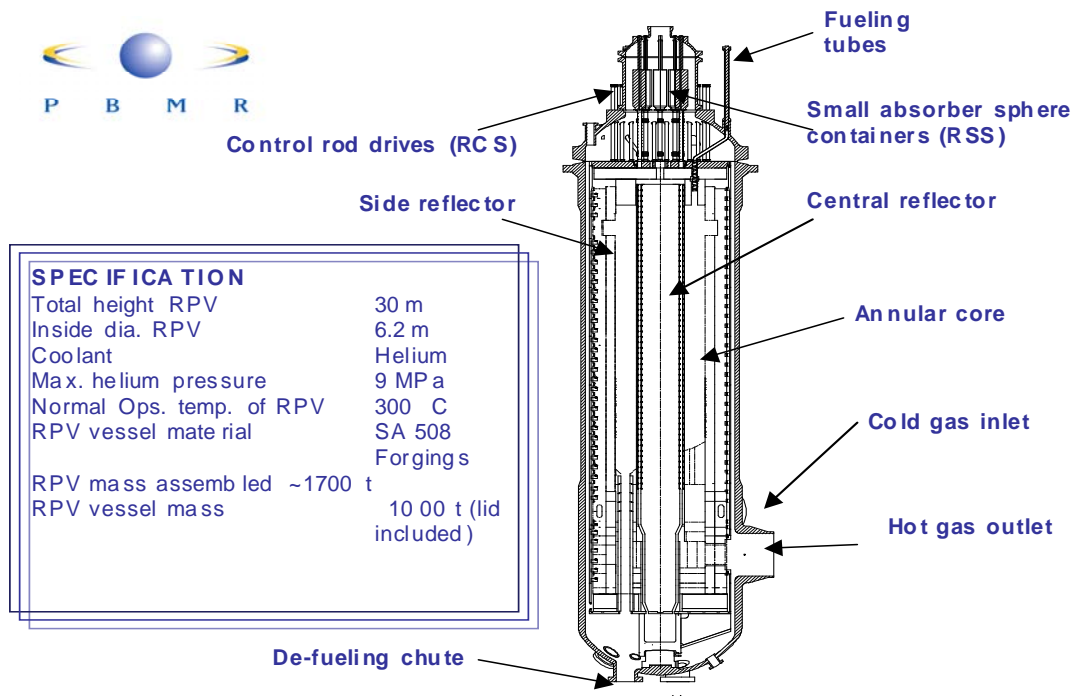


FIG. 4.85. PBMR reactor unit — vessel assembly.

TABLE 4.44. PBMR MODULE DESIGN AND FULL POWER OPERATING PARAMETERS

Reactor power, MW(t)	400
Reactor inlet/outlet temperatures, °C	500/900
Core inlet pressure, MPa	9.0
Helium mass flow rate, kg/s	193
Net electrical output, MW(e)	165
Net plant efficiency, %	41
Active core inside/outside diameters, m	2.0/3.7
Active core height, m	11
Outer reflector outside diameter, m	5.5
Other operating parameters (GRSAC simulation):	
RCCS heat removal, MW	3.1
Core inlet/outlet mean temperatures, °C	495/890
Active core coolant outlet temperature, °C	980
Maximum vessel temperature, °C	410
Maximum fuel temperature, °C	1080
Pebble bed mean void fraction	0.383
Coolant bypass fractions for side/central reflectors	0.13/0.05
Core pressure drop, MPa	0.31

PBMR initial conditions

The Initial Conditions (ICs) for the DLOFC accident simulation are generated by the GRSAC in the initial conditioning mode, where model response parameters are allowed to ‘settle out’ at equilibrium values. Flow distributions, core coolant outlet temperature distributions and fuel temperatures for any of the axial regions can be displayed. Figure 4.86, for example, shows the fuel (and centre reflector) temperature distributions in the bottom (outlet) axial region for the active core. Along with the temperature map, various input parameter adjustment ‘controls’ can be seen.

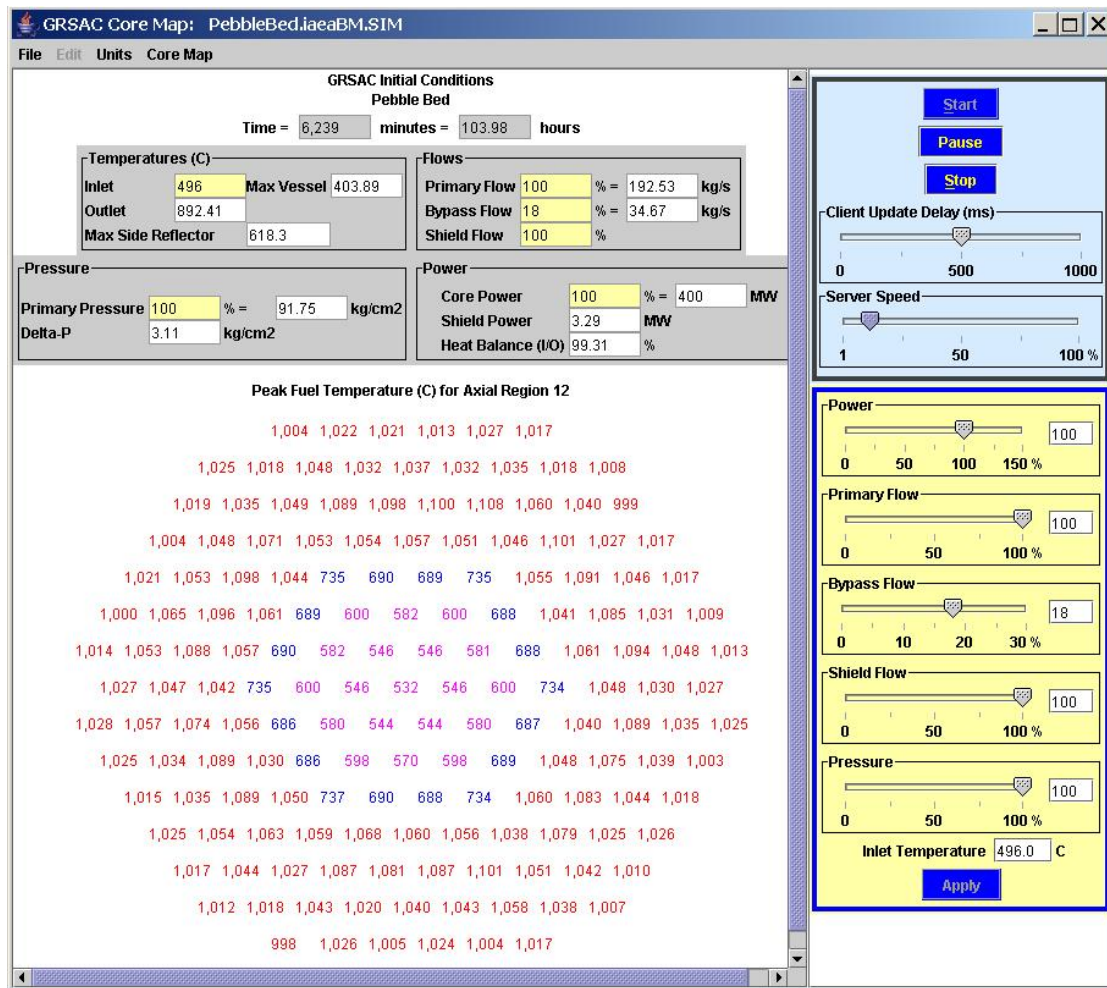


FIG. 4.86. PBMR full-power peak fuel temperature distribution — bottom of active core.

PBMR Depressurized loss of forced cooling accidents

For the PLOFC, a flow coastdown and scram at time = zero is assumed, with the passive RCCS operational for the duration. The natural circulation of the pressurized helium coolant within the core tends to make core temperatures more uniform, therefore lowering the peak temperatures, than would be the case for a depressurized core, where the buoyancy forces would not establish significant recirculation flows.

The DLOFC reference case also assumes a rapid depressurization along with a flow coastdown and scram at time ~zero. It also assumes that the depressurized coolant is helium (no air ingress). This event is known as a ‘conduction-heat-up’ (or ‘-cooldown’) accident, since the core effective conductivity is the dominant mechanism for the transfer of afterheat from the fuel to the vessel. In the reference case, the maximum fuel temperature peaks at 1587°C ~54 hr into the transient (Fig. 4.87), while the maximum vessel temperature decreases during the course of the accident. In this case, the maximum fuel temperatures at the time of the peak occur near the core beltline, or centre (Fig. 4.88),

rather than near the top as it would in the PLOFC, since the convection cooling effects for atmospheric pressure helium are nil.

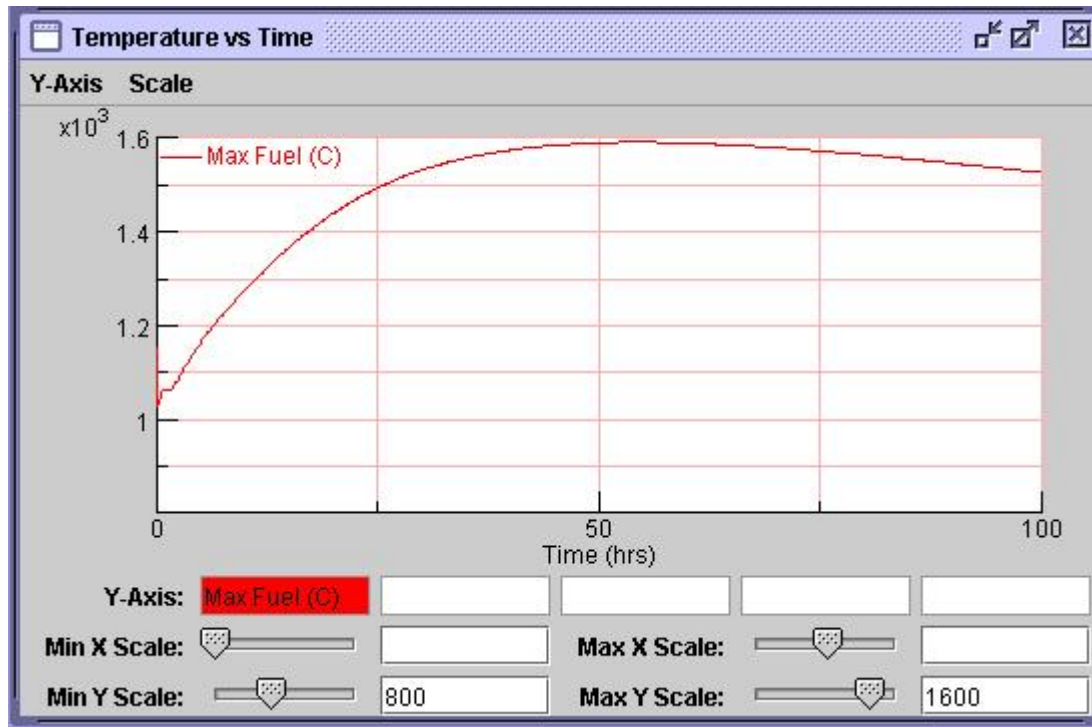


FIG. 4.87. PBMR DLOFC Accident: peak and average fuel temperatures.

There are several parameter variations of importance for this accident, which is generally considered to be the defining accident for determining the 'reference case accident peak fuel temperature, therefore sensitivity studies are important [4-29]. Due to the fact that the PBMR on-line refuelling results in a mixing of pebbles with various burnups and irradiation histories, and the effective core conductivity is usually considered to be primarily due to radiant heat transfer between pebbles, it is therefore modelled here only as a function of temperature. The reference conductivity correlation in the GRSAC is derived from a combination of the Zehner-Schlunder and Robold correlations [4-30].

Variations on this 'reference case' show the sensitivity of peak fuel temperature for parameter changes as follows:

- 25% decrease in core effective conductivity: 165°C increase in T(fuel)-maximum;
- Use of the THERMIX code default core conductivity correlation [4-31]: 64°C increase in T(fuel)-maximum;
- Use of the core conductivity correlation derived from SANA tests at KFA by H. F. Niessen (see Fig. 4.109 in [4-32]: 103°C decrease in T(fuel)-maximum;
- 15% increase in afterheat: 121°C increase in T(fuel)-maximum;
- 20% increase in maximum radial peaking factor: 17°C increase in T (fuel)-maximum.

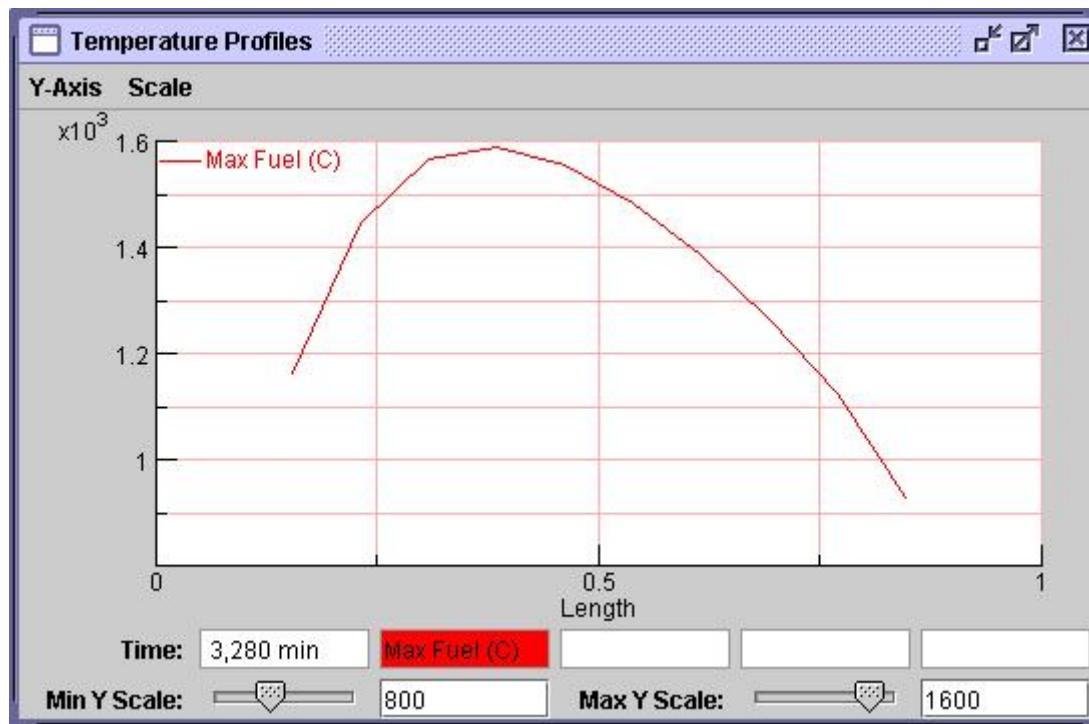


FIG. 4.88. PBMR DLOFC Accident: maximum fuel temperature axial profile.

Conclusions

Modular HTGR designs show excellent accident prevention and mitigation capabilities even for well-beyond DBA due to their inherent passive safety features. The predicted absolute values of peak temperatures for the DLOFC accident scenarios should not be taken as definitive, since finalized design features, such as vessel insulation strategies, have not been factored into the simulations. Other aspects of the predictions, such as assumed irradiated core thermal conductivities and heat-sink-related emissivities, are also dependent on many factors that should be considered in detail for specific design and operating conditions.

The value of sensitivity studies in the design and analysis phase is to provide estimates of the uncertainties in the predictions, and to guide further efforts in improving the design as well as the accuracy of the predictions. Studies have shown the importance of effective core thermal conductivity functions and afterheat in the predictions of $T(\text{fuel})\text{-max}$.

4.2.3.5. PBMR-400 results, Republic of Korea

Introduction

Though many cases are defined in the original benchmark problem, KAERI solved only one case similar to Case F-1 of the original problem. The variation from the officially defined problem is small and came about using preliminary case definitions. It could not be resolved by repeating the calculations due to time restrictions. It includes very small differences in the reflector graphite (inner and outer reflector) graphite number densities and heights of top and bottom reflectors. The effect of these differences is expected to be negligible.

Figure 4.89 shows the geometry and the dimensions of the benchmark problem that was solved. For simplicity, it was assumed that the core and reflector regions are homogeneous. The temperature was also assumed to be 300 K throughout the whole reactor. The nuclide number densities in each region of the problem are listed in Table 4.45. The reference solution was obtained from the Monte Carlo calculation by using the Monte Carlo-CARD code [4-33].

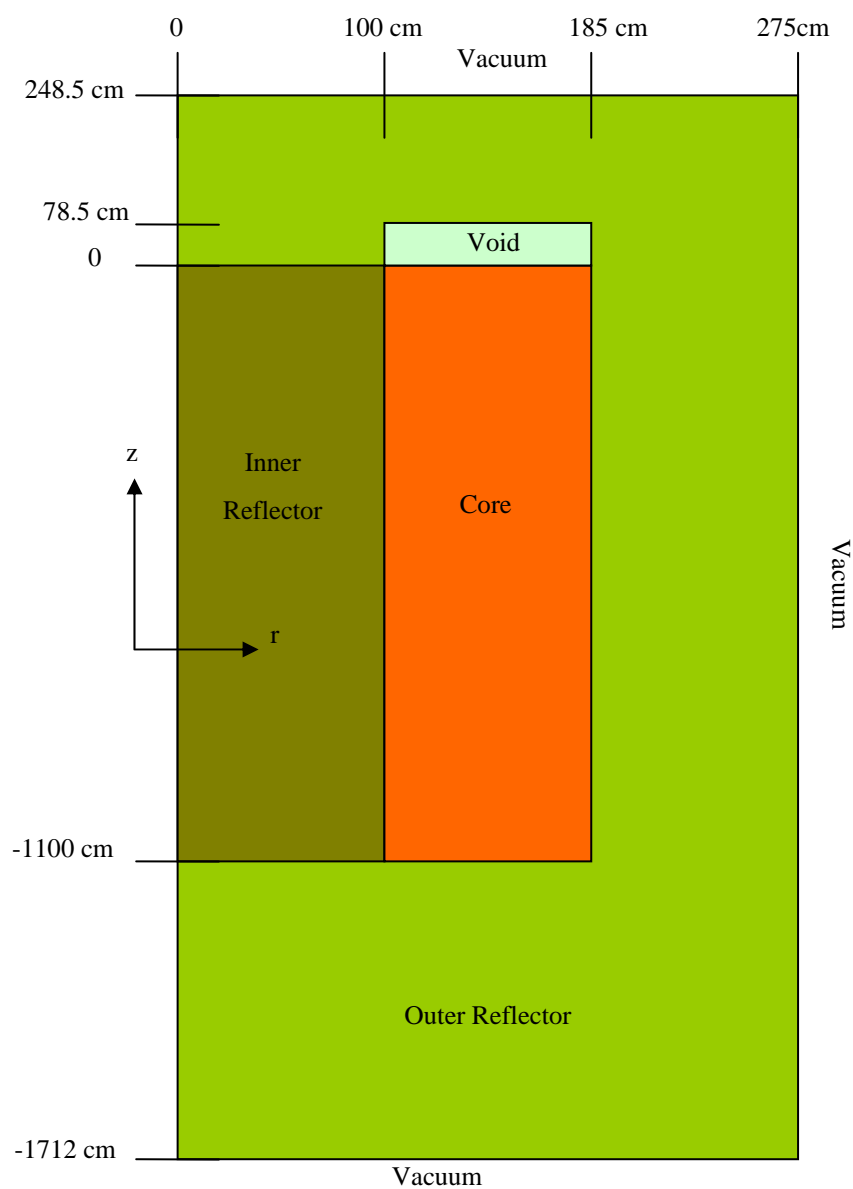


FIG. 4.89. Geometry and dimensions of the problem.

TABLE 4.45. NUCLIDE NUMBER DENSITIES IN EACH REGION

Region	Nuclide	Number density (#/barn-cm)
Core	U-234	6.22417E-08
	U-235	7.08600E-06
	U-238	1.15700E-04
	O-16	2.45700E-04
	Si	2.77203E-04
	C	5.26260E-02
Inner reflector	C	9.00000E-02
Outer reflector	C	9.00000E-02
Void	-	-

Analysis method

A two-step procedure [4-34] was adopted for the analysis of this problem. In the first step, equivalent cross-sections from a one dimensional slab spectral geometry model were generated with the help of the equivalence theory [4-35]. In the second step, KAERI performed a diffusion calculation by using the equivalent cross-sections generated in the first step. Figure 4.90 shows the one dimensional slab spectral geometry model. Although the problem is defined as a cylindrical reactor, the one dimensional spectral geometry was modelled as a slab for simplicity. KAERI preserved the distances to the core-reflector interfaces from the centre of the reactor in defining the one dimensional slab spectral geometry model.

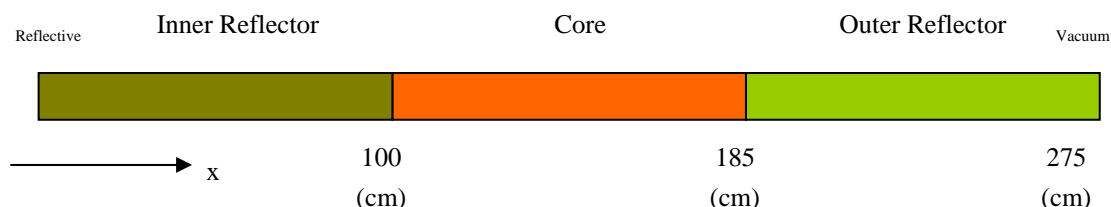


FIG. 4.90. Slab 1-D spectral geometry model.

Two approaches were tried in order to treat the spectral interaction between the core and the reflector. In the first approach, a single spectral zone in the core region was used with an eight neutron energy group structure. The group boundaries of the eight-group structure were determined so as to minimize the spatial dependency of the reaction rates [4-36]. In the second approach, four spectral zones in the core region were used with two neutron energy groups.

The HELIOS code [4-37] was used to generate the cross-sections for each spectral zone. From the cross-sections and the fluxes and the net currents at the spectral zone interfaces, the equivalent cross-sections were obtained by applying the simplified equivalence theory [4-35]. An FDM solver in the CAPP code which has been developed for the analysis of VHTR cores was used to perform the whole-core diffusion calculation in the second step of the two-step procedure. This FDM solver and other pebble-bed-specific routines in the CAPP code will become the components of the computer code which KAERI is developing for the analysis of pebble-bed-type reactors.

Results

Table 4.46, Figs 4.91 and 4.92 compare the diffusion solutions and Monte Carlo solutions calculated for the two dimensional benchmark problem shown in Fig. 4.89. The equivalent cross-sections generated from the one dimensional slab spectral geometry were used in the diffusion calculation and a large number (= 10.0) was used as the diffusion coefficients of the void region. The diffusion solutions predict the Monte Carlo solutions well and the errors are acceptable.

TABLE 4.46. COMPARISON OF K_{EFF} AND THE POWER ERROR OF THE PROBLEM

Monte Carlo-CARD M		Diffusion D	k_{eff} Error (pcm) D-M	Power error, RMS (%) D-M
1.20928	8G C ¹⁾	1.21342	+414	1.32
±3pcm	2G P ²⁾	1.21347	+419	1.30

- Eight group constant cross-sections from single core spectral zone.
- Two group position dependent cross-sections from four core spectral zones.

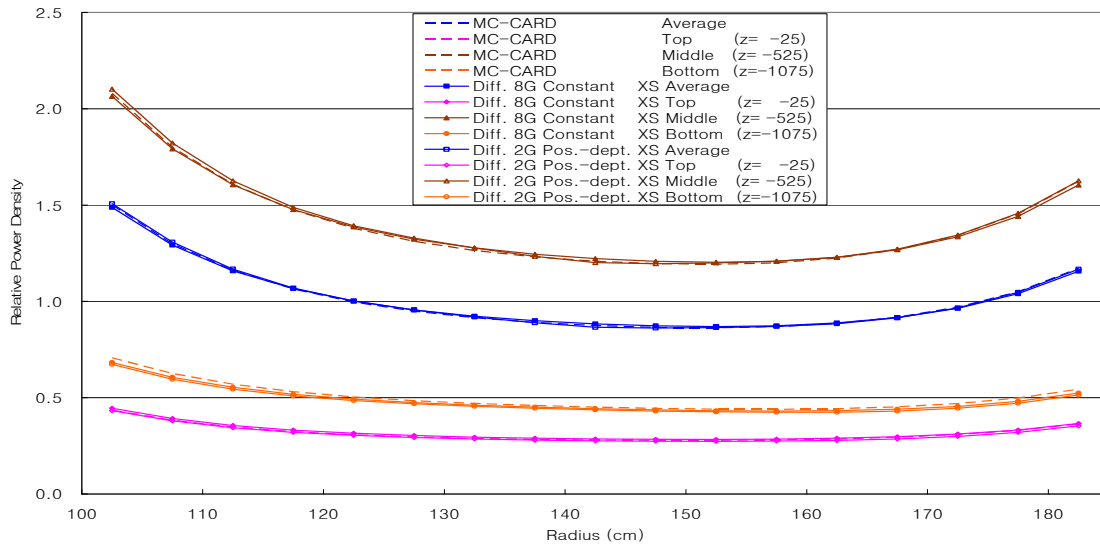


FIG. 4.91. Comparison of the radial power distributions of the problem.

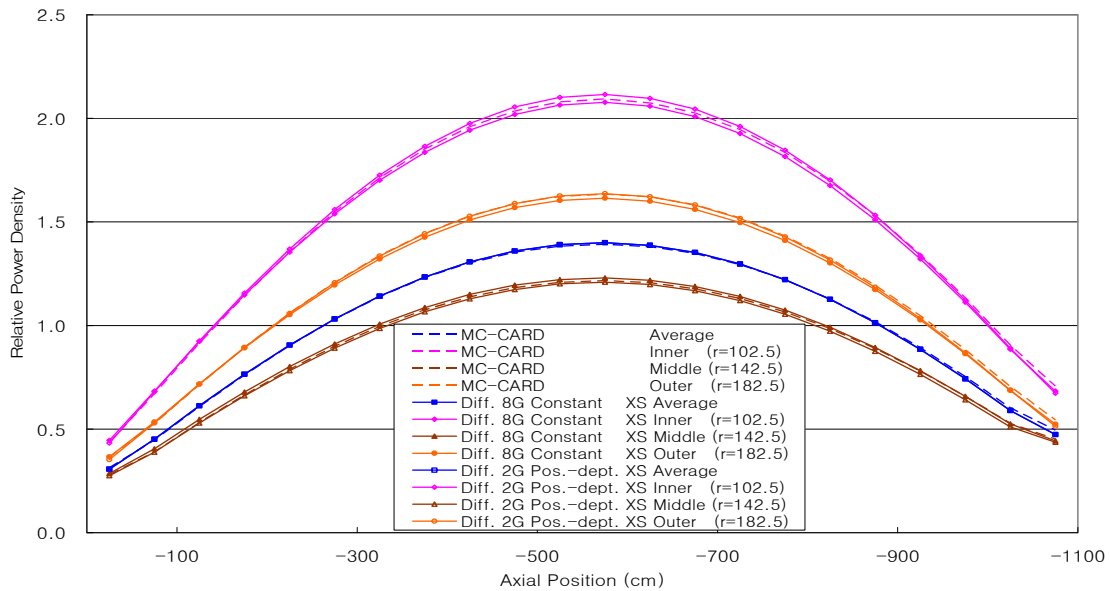


FIG. 4.92. Comparison of the axial power distributions of the problem.

4.2.3.6. PBMR-400 results, United Kingdom

Introduction

The PBMR-400 benchmarks have been set up to study the methods of reactor physics and thermohydraulics analysis when applied to a whole PBMR core. The benchmarks consist of a number of cases with increasing complexity of modelling. The solutions presented here are for Cases T-1 and E-2 only. The former is a ‘thermal hydraulics only’ test case based on a prescribed power distribution. The latter considers coupled thermal hydraulics and the full equilibrium fuel cycle of the PBMR in which the fuel irradiation distribution is calculated, rather than relying on given fuel compositions.

Within the United Kingdom, this study has been performed in conjunction with and was funded by the NNR of the RSA.

Method of calculation

Neutronics - The WIMS9 Code

The analysis of the benchmark has been performed using the WIMS9 thermal reactor code scheme [4-38, 4-39]. The WIMS9 code contains a large number of modules for representation of different types of thermal reactor. A calculation route is set up using appropriate modules for the reactor type which communicate with each other via data interfaces. The WIMS9 code does not itself contain modules which can handle the fuel pebble movements within the PBMR core or provide fuel and moderator temperatures. It has therefore been necessary to make significant developments consisting of a script to link together the various parts of the model with fuel pebble movement, and a WIMSTER thermohydraulics module, to provide full modelling of the PBMR core. The WIMSTER models the coolant flow through the core, the riser channels and absorber channels and provides fuel kernel, pebble graphite and reflector graphite temperatures throughout the model.

The general method of calculation used for the PBMR is to produce homogenized cross-sections for the pebble bed and reflectors using WIMS9 collision probability cell models in which geometric details are represented. The homogenized cross-sections are then fed into a diffusion theory module representing the overall geometry of the PBMR core.

The WIMS9code contains a largely JEF2.2-based cross-section library in the 172 energy groups shown in Tables 4.47(a) and (b). The library contains data for 231 nuclides, 90 of which are fission products (including one pseudo-fission product) allowing the representation of extensive burnup chains.

TABLE 4.47(A). ENERGY GROUP STRUCTURE OF THE WIMS9 CROSS-SECTION LIBRARY (GROUPS 1–92)

Group	Lower energy E ₁ (eV)	Upper energy E ₂ (eV)	Group	Lower energy E ₁ (eV)	Upper energy E ₂ (eV)
1	1.733E+07	1.964E+07	47	5.531E+03	7.466E+03
2	1.492E+07	1.733E+07	48	5.005E+03	5.531E+03
3	1.384E+07	1.492E+07	49	3.527E+03	5.005E+03
4	1.162E+07	1.384E+07	50	3.355E+03	3.527E+03
5	1.000E+07	1.162E+07	51	2.249E+03	3.355E+03
6	8.187E+06	1.000E+07	52	2.035E+03	2.249E+03
7	6.703E+06	8.187E+06	53	1.507E+03	2.035E+03
8	6.065E+06	6.703E+06	54	1.434E+03	1.507E+03
9	5.488E+06	6.065E+06	55	1.234E+03	1.434E+03
10	4.493E+06	5.488E+06	56	1.010E+03	1.234E+03
11	3.679E+06	4.493E+06	57	9.142E+02	1.010E+03
12	3.012E+06	3.679E+06	58	7.485E+02	9.142E+02
13	2.466E+06	3.012E+06	59	6.773E+02	7.485E+02
14	2.231E+06	2.466E+06	60	4.540E+02	6.773E+02
15	2.019E+06	2.231E+06	61	3.717E+02	4.540E+02
16	1.653E+06	2.019E+06	62	3.043E+02	3.717E+02
17	1.353E+06	1.653E+06	63	2.040E+02	3.043E+02
18	1.225E+06	1.353E+06	64	1.486E+02	2.040E+02
19	1.108E+06	1.225E+06	65	1.367E+02	1.486E+02
20	1.003E+06	1.108E+06	66	9.166E+01	1.367E+02
21	9.072E+05	1.003E+06	67	7.567E+01	9.166E+01
22	8.208E+05	9.072E+05	68	6.790E+01	7.567E+01
23	6.081E+05	8.208E+05	69	5.560E+01	6.790E+01
24	5.502E+05	6.081E+05	70	5.158E+01	5.560E+01
25	4.979E+05	5.502E+05	71	4.825E+01	5.158E+01
26	4.505E+05	4.979E+05	72	4.552E+01	4.825E+01
27	4.076E+05	4.505E+05	73	4.017E+01	4.552E+01
28	3.020E+05	4.076E+05	74	3.727E+01	4.017E+01
29	2.732E+05	3.020E+05	75	3.372E+01	3.727E+01
30	2.472E+05	2.732E+05	76	3.051E+01	3.372E+01
31	1.832E+05	2.472E+05	77	2.761E+01	3.051E+01
32	1.228E+05	1.832E+05	78	2.498E+01	2.761E+01
33	1.111E+05	1.228E+05	79	2.260E+01	2.498E+01
34	8.230E+04	1.111E+05	80	1.945E+01	2.260E+01
35	6.738E+04	8.230E+04	81	1.593E+01	1.945E+01
36	5.517E+04	6.738E+04	82	1.371E+01	1.593E+01
37	4.087E+04	5.517E+04	83	1.122E+01	1.371E+01
38	3.698E+04	4.087E+04	84	9.906E+00	1.122E+01
39	2.928E+04	3.698E+04	85	9.190E+00	9.906E+00
40	2.739E+04	2.928E+04	86	8.315E+00	9.190E+00
41	2.479E+04	2.739E+04	87	7.524E+00	8.315E+00
42	1.662E+04	2.479E+04	88	6.160E+00	7.524E+00
43	1.503E+04	1.662E+04	89	5.346E+00	6.160E+00
44	1.114E+04	1.503E+04	90	5.043E+00	5.346E+00
45	9.119E+03	1.114E+04	91	4.129E+00	5.043E+00
46	7.466E+03	9.119E+03	92	4.000E+00	4.129E+00

TABLE 4.47(B). ENERGY GROUP STRUCTURE OF WIMS9 CROSS-SECTION LIBRARY (GROUPS 93–172)

Group	Lower Energy E ₁ (eV)	Upper Energy E ₂ (eV)	Group	Lower Energy E ₁ (eV)	Upper Energy E ₂ (eV)
93	3.381E+00	4.000E+00	133	7.800E-01	7.900E-01
94	3.300E+00	3.381E+00	134	7.050E-01	7.800E-01
95	2.768E+00	3.300E+00	135	6.250E-01	7.050E-01
96	2.720E+00	2.768E+00	136	5.400E-01	6.250E-01
97	2.600E+00	2.720E+00	137	5.000E-01	5.400E-01
98	2.550E+00	2.600E+00	138	4.850E-01	5.000E-01
99	2.360E+00	2.550E+00	139	4.330E-01	4.850E-01
100	2.130E+00	2.360E+00	140	4.000E-01	4.330E-01
101	2.100E+00	2.130E+00	141	3.910E-01	4.000E-01
102	2.020E+00	2.100E+00	142	3.500E-01	3.910E-01
103	1.930E+00	2.020E+00	143	3.200E-01	3.500E-01
104	1.840E+00	1.930E+00	144	3.145E-01	3.200E-01
105	1.755E+00	1.840E+00	145	3.000E-01	3.145E-01
106	1.670E+00	1.755E+00	146	2.800E-01	3.000E-01
107	1.590E+00	1.670E+00	147	2.480E-01	2.800E-01
108	1.500E+00	1.590E+00	148	2.200E-01	2.480E-01
109	1.475E+00	1.500E+00	149	1.890E-01	2.200E-01
110	1.440E+00	1.475E+00	150	1.800E-01	1.890E-01
111	1.370E+00	1.440E+00	151	1.600E-01	1.800E-01
112	1.338E+00	1.370E+00	152	1.400E-01	1.600E-01
113	1.300E+00	1.338E+00	153	1.340E-01	1.400E-01
114	1.235E+00	1.300E+00	154	1.150E-01	1.340E-01
115	1.170E+00	1.235E+00	155	1.000E-01	1.150E-01
116	1.150E+00	1.170E+00	156	9.500E-02	1.000E-01
117	1.123E+00	1.150E+00	157	8.000E-02	9.500E-02
118	1.110E+00	1.123E+00	158	7.700E-02	8.000E-02
119	1.097E+00	1.110E+00	159	6.700E-02	7.700E-02
120	1.071E+00	1.097E+00	160	5.800E-02	6.700E-02
121	1.045E+00	1.071E+00	161	5.000E-02	5.800E-02
122	1.035E+00	1.045E+00	162	4.200E-02	5.000E-02
123	1.020E+00	1.035E+00	163	3.500E-02	4.200E-02
124	9.960E-01	1.020E+00	164	3.000E-02	3.500E-02
125	9.860E-01	9.960E-01	165	2.500E-02	3.000E-02
126	9.720E-01	9.860E-01	166	2.000E-02	2.500E-02
127	9.500E-01	9.720E-01	167	1.500E-02	2.000E-02
128	9.300E-01	9.500E-01	168	1.000E-02	1.500E-02
129	9.100E-01	9.300E-01	169	6.900E-03	1.000E-02
130	8.600E-01	9.100E-01	170	5.000E-03	6.900E-03
131	8.500E-01	8.600E-01	171	3.000E-03	5.000E-03
132	7.900E-01	8.500E-01	172	1.100E-04	3.000E-03

The main WIMS modules used for this benchmark are the following:

- PIJ: A two dimensional collision probability module which is used to represent radial models of the core for the production of reflector cross-sections.
- FLURIG: A one dimensional collision probability module which is used to represent graphite pebbles which do not contain fuel.
- PROCOL: A collision probability module which represents all the levels of heterogeneity present in a PBMR pebble. That is, fuel particles with their various coatings are represented within a graphite matrix, which in turn is surrounded by a pure graphite layer to represent the whole pebble.

- SNAP: A diffusion theory module which was used for this problem in R-Z geometry to represent the whole PBMR core.

The full calculation route contains the following features:

For non-fissile regions such as reflectors, cross-sections are produced from a radial collision probability model. Allowances for neutron streaming in coolant and control rod channels are made using the method of Behrens [4-40]. Reflector cross-sections are condensed from 172 energy groups to the reduced group structure of the whole-core model using spectra generated from the radial model. Models at a number of heights are used to represent the axial variation of reflector temperature.

Control rods are represented as a 'grey curtain' smeared together with the surrounding reflector using collision probability models. The grey curtain representation is adjusted to an MCNP benchmark in which the absorbers are represented in detail.

The fissile region of the core is split into zones in which fuel compositions and temperatures are assumed constant. For each fissile zone in the whole-core model, a collision probability cell model produces resonance self-shielded cross-sections for each batch of pebbles in the zone. The cell model uses the full 172 energy groups of the WIMS cross-section library and represents all the levels of heterogeneity within the pebble. A further level of heterogeneity is taken into account in a super-cell, allowing for interaction between the six pebble batches at different burnups.

The core is assumed to be radially divisible into a number of pebble flow streams which do not mix with one another and which can be regarded as having a uniform pebble flow rate. For each flow stream independently, burnup steps are performed sequentially in the WIMS cell models as the fuel is moved down the core, in order to produce burnt compositions for each of the fissile zones. Cross-sections are re-shielded after each burnup step. The spectrum used for the burnup is normalized using ratings derived from the whole-core model and is adjusted for leakage effects using bucklings, also derived from the whole-core model.

The macroscopic cross-sections from the different batches of pebbles are smeared together using flux and volume weighting to form the cross-sections for each zone. The cross-sections are condensed to fewer groups using the cell spectrum with neutron leakage represented by bucklings derived from the whole-core model.

The above process is repeated for each fissile zone in the reactor until a full-core model of the reactor has been developed.

At the bottom of the core, those pebbles in each exit stream which have passed through the core six times are removed. The remaining pebbles from each stream are then mixed with an appropriate proportion of fresh fuel. For each batch, an average of the compositions from the different exit streams is then formed, weighted by the volume flow rates of the streams. These average compositions for each batch are used as the core feed fuel compositions for the batches in the next iteration.

An R-Z geometry flux solution is performed for the whole core using the SNAP diffusion theory module and ratings are derived for each flux mesh within the model. Group-dependent bucklings for use in the cell models are derived for each fuel zone in the model to represent the effects of neutron leakage in the cell models.

The ratings are passed to the WIMSTER thermohydraulics code, which calculates batch-specific fuel and moderator temperatures for use by the WIMS cell model for each zone within the core model.

The fuel and moderator temperatures in each of the pebble types within each zone are passed back to the cell model (the collision probability cell model in the third step listed above), together with the bucklings and ratings, which are used to normalize the flux used for the burnup steps.

The whole process is repeated until appropriate fuel cycle conditions are reached.

Neutronics model

The model was set up from the detailed descriptions of the core given in the benchmark. The simplified number density representation, also presented in the benchmark, was not used. The radial

and axial diffusion coefficients specified in the benchmark were used to represent the void region above the fuel.

Neutron energy group structure used in the whole-core model

In the whole-core model, an 11-neutron energy group structure, shown in Table 4.48, was used.

Neutronics mesh structure used in the whole-core model

Material meshes define the zones in which the fuel materials and temperatures are represented. Within the fissile region, these meshes are 50 cm axially and 17 cm radially. These material meshes also provide the grid on which buckling feedback from the whole-core model to the cell models is defined.

Within the core, the neutron flux meshes are 10 cm axially. The radial meshes are given in Table 4.49 and fit within the radial material meshes used to define the pebble flow streams. The number of meshes adjacent to the central and radial reflector has been increased to better represent the larger flux gradients in these regions.

TABLE 4.48. REDUCED ENERGY GROUP STRUCTURE USED IN THE WHOLE-CORE MODEL

Condensed Spectrum Group	WIMS 172 Group Range	Upper Energy (eV)	Lower Energy (eV)
1	1 to 17	1.964E+07	1.353E+06
2	18 to 40	1.353E+06	2.739E+04
3	41 to 60	2.739E+04	4.540E+02
4	61 to 85	4.540E+02	9.19
5	86 to 116	9.19	1.15
6	117 to 127	1.15	0.95
7	128 to 141	0.95	0.391
8	142 to 147	0.391	0.248
9	148 to 155	0.248	0.100
10	156 to 160	0.100	0.058
11	161 to 172	0.058	1.10E-04

TABLE 4.49. THE RADIAL MESHES WITHIN THE FUEL REGION

Radial meshing within the Fuel Region					
Material mesh (cm)	17 cm	17 cm	17 cm	17 cm	17 cm
Number of flux meshes	4	3	3	3	4
Flux mesh size (cm)	5.0	5.66	5.67	5.67	4.0
	4.0	5.67	5.66	5.67	4.0
	4.0	5.67	5.67	5.66	4.0
	4.0	-	-	-	5.0

Sensitivities

To justify details of the modelling used here, some sensitivity analysis was performed with a preliminary model. The reactivity sensitivities, compared with the meshes and energy group structure used for this benchmark, are given in Table 4.50.

TABLE 4.50. SENSITIVITIES TO MODELLING ASSUMPTIONS

	Approx. Reactivity Effect (pcm)
172 neutron energy groups in the whole-core model	+240
Halved mesh size in axial and radial direction	+80
9 radial material meshes	-50

Thermal hydraulics

Thermal hydraulics models

Two models of the thermal hydraulics of the PBMR core have been developed. These are PHOENICS, a model based on the commercial CFD, and WIMSTER, a model based on a new code, which runs fully coupled with WIMS9.

The PHOENICS model consists of a 60° sector of the RPV and its contents located within the reactor cavity. At the moment, the WIMSTER model is restricted to an axisymmetric representation of the core ceramic structures to achieve fast runtimes when performing fully coupled neutronics and thermohydraulics simulations. However, the WIMSTER model has been programmed with a three dimensional capability and sufficient flexibility for the structures outside of the core ceramics to be included if necessary.

Even when using a commercial CFD code such as PHOENICS, much additional modelling has to be provided to represent the complexity of the reactor and the thermohydraulic phenomena therein. This additional modelling is included within the model in the form of the user-Fortran code. The additional models within the PHOENICS representation and the PBMR-specific models within the WIMSTER code are more or less common to both codes.

WIMSTER

WIMSTER is a bespoke Fortran finite-volume code that is based on standard CFD algorithms. The code solves the steady state mass and momentum conservation equations using the well-known Semi-Implicit Method for Pressure Linked Equations (the SIMPLE algorithm) [4-41]) on a staggered cylindrical polar coordinate mesh. The models within the core have been formulated to cope with two dimensional axisymmetric, R-Z and three dimensional R-Z- θ representations of the core. The temperature fields within the gas, pebble bed and the other core components are solved using standard finite-volume methods. The heat transport and fluid flow calculations are performed in a fully coupled manner.

The riser channels and control rod channels, which pass vertically through the side reflector, are modelled using a one dimensional channel model to compute the heat exchanged with the side reflector graphite. The channel model is fully coupled to the finite-volume equations. This approach permits the discrete character of the channels, and the effect of control rod sleeves within rod channel, to be modelled without having to approximate these as annuli in the axisymmetric representation or without requiring an excessive number of cells in three dimensions.

The thermohydraulic model analyses the behaviour of multiple batches of pebble fuel, allowing the temperature differences between fresh and older fuel pebbles to be computed.

PHOENICS

The PHOENICS code [4-42] provides numerical solutions to the differential equations that describe the fundamental physical laws governing fluid flow and heat transfer. The code uses a finite-volume approach whereby the solution domain is divided into small cells, or finite volumes, in which the physical conservation laws are applied. Built-in models exist for conjugate (fluid-solid) and radiative heat transfer. There is a provision for a user-generated code to be linked with the main solver to allow problem-dependent extensions to the basic modelling capabilities.

Rather than using a two dimensional model, as defined in the benchmark specification, the PHOENICS calculation has been performed using a three dimensional 60° sector model. This model was set up on behalf of the South African NNR for independent nuclear safety assessment of the PBMR-400 design. As such, only a few alterations to the geometry and material properties were required to comply with the benchmark specification. In its original form, this computational model calculates flow and heat transfer through the leakage paths within the core. However, for this benchmark calculation, a bypass flow value of 19% was imposed directly on this model.

The three dimensional computational mesh was built within a Cartesian coordinate system. The PHOENICS Body Fitted Coordinate (BFC) system was used to generate the mesh in the current model.

Porous region models

The complex geometry of the pebble bed and the coolant flow slots in the bottom reflector slots are treated as porous media. A scalar porosity is used to model the reduced volume available to the flow field within these zones. Empirical correlations are used to model frictional pressure losses in the gas and heat transfer between the solid core components and the coolant gas in the porous regions.

Modelling the pebble bed

Within the pebble bed, the frictional pressure losses in the coolant gas are computed according to the correlation provided in the German Nuclear Safety Standards Commission document KTA 3102.3 [4-43].

$$\mathbf{F}_{drag} = \Psi \frac{1-\varepsilon}{\varepsilon^3} \frac{1}{d} \frac{\rho}{2} |\mathbf{V}_{sup}| \mathbf{V}_{sup}$$

where

$$\Psi = \frac{320}{\left(\frac{Re}{1-\varepsilon}\right)} + \frac{6}{\left(\frac{Re}{1-\varepsilon}\right)^{0.1}}$$

and

ε is the void fraction within the pebble bed;

d is the pebble diameter;

ρ is the gas density;

\mathbf{V}_{sup} is the superficial gas velocity.

Re is the Reynolds number, evaluated using the superficial velocity:

$$Re = \rho |\mathbf{V}_{sup}| d / \mu$$

μ is the dynamic gas viscosity.

Heat transfer within the pebble bed (including heat conduction, radiative heat transfer and pebble-to-pebble conduction through the helium coolant) is modelled using the effective thermal conductivity data based on the Zehner Schlünder correlation presented in the PBMR-400 benchmark specification.

The heat transfer coefficient governing heat transfer from the fuel pebble surface to the helium coolant is calculated using the correlation provided in German Nuclear Safety Standards Commission document KTA 3102.2 [4-44].

$$h = \frac{Nu \lambda_{gas}}{d},$$

where the Nusselt number, Nu , is computed using the expression:

$$Nu = 1.27 \frac{Pr^{1/3}}{\varepsilon^{1.18}} Re^{0.36} + 0.333 \frac{Pr^{1/2}}{\varepsilon^{1.07}} Re^{0.86}$$

and

λ_{gas} is the thermal conductivity of gas;

ε is the void fraction within the pebble bed;

d is the pebble diameter;

Pr is the Prandtl number, $Pr = \mu c_p / \lambda_{gas}$;

c_p is the gas specific heat capacity at constant pressure;

Re is the Reynolds number, evaluated using the superficial velocity, $Re = \rho |\mathbf{V}_{sup}| d / \mu$;

μ is the dynamic gas viscosity;

ρ is the gas density.

An enhanced diffusion coefficient is used to model heat dispersion within the gas passing through the pebble bed, caused by the flow spreading around fuel pebbles.

Heat transfer between the pebble bed and the side reflector is assumed to occur through a combination of radiation and conduction from the pebble bed to the side reflector graphite, in addition to heat transfer directly from the helium gas.

Thermal modelling the bottom reflector

The hot helium gas flows out of the pebble bed through slots in the bottom reflector. Within the three dimensional PHOENICS model, the bottom reflector is modelled explicitly as a set of slots. Within the two dimensional WIMSTER model, the bottom reflector is assumed to be a porous medium, with a void fraction of 0.193.

The slot geometry influences heat transfer between the gas and the graphite in this region. The benchmark specification does not specify the slot geometry. Therefore, an approximate geometry has been generated, assuming a combination of radial and circumferential coolant flow slots.

In the WIMSTER model, the heat transfer coefficient between the gas and graphite is modelled using the Colburn correlation [4-45]:

$$h = \frac{Nu \lambda_{gas}}{\delta}$$

where

$$Nu = 0.023 Re^{0.8} Pr^{0.33}$$

and

λ_{gas} is the gas thermal conductivity;

Re is the Reynolds number in slot, $Re = \rho V \delta / \mu$;

V is the gas velocity in slot;

ρ is the gas density;

δ is the length parameter, equal to twice slot width, $\delta = 2d$;

Pr is the Prandtl number, $Pr = \mu c_p / \lambda_{gas}$;

μ is the dynamic gas viscosity;

c_p is the gas specific heat capacity at constant pressure;

using a slot width of $d = 2.85$ cm.

Boundary conditions and domains

The domain within the PHOENICS model extends radially from the centre-line of the reactor out to include the concrete of the reactor cavity wall. Vertically, the model extends from the floor to the ceiling of the reactor cavity. Due to the fact that the solution domain extends to the outside of the concrete walls of the reactor cavity, remote thermal boundary conditions may be applied. In normal operation, little heat escapes by conduction through the concrete and so the predicted temperatures within the reactor will not be sensitive to the ambient temperature condition imposed at the outside of the walls.

As shown in Fig. 4.93, the WIMSTER model domain is restricted to the pebble bed and reflector graphite. Therefore, temperatures in the core barrel, RPV and external concrete structures are not calculated and, thus, have not been entered into the WIMSTER code results tables. To cope with the absence of all of the structures outside of the core ceramic structures, it has been assumed that during normal reactor operation, the heat losses through the outer boundaries of the reflectors are small compared to the heat transferred to the coolant within the core. Therefore, simple adiabatic boundary conditions are specified on all outer solid surfaces of the current model.

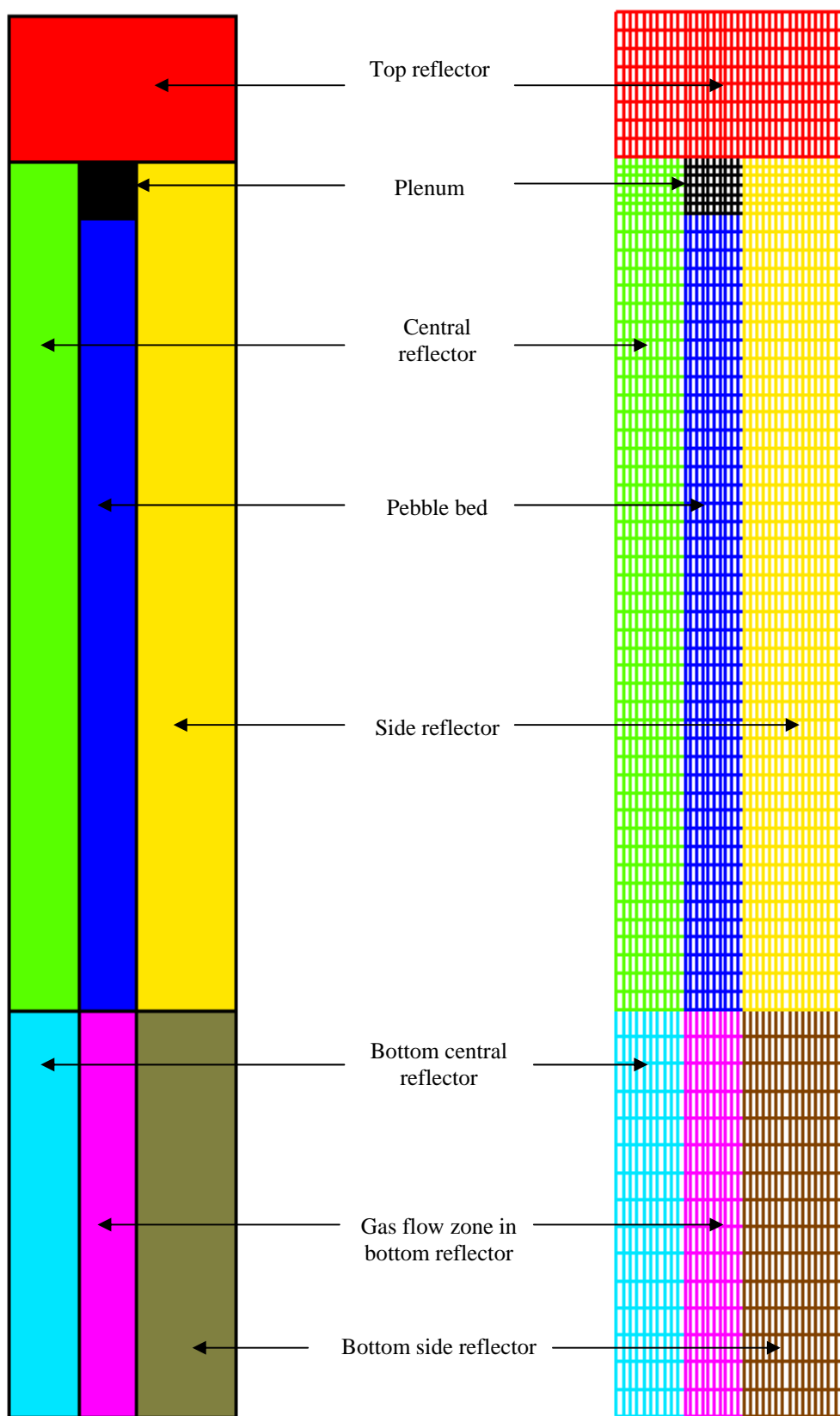


FIG. 4.93. Material layout and computational mesh for the WIMSTER thermal hydraulics model.

Fuel temperature modelling

The temperature of an individual pebble depends on its position within the core and the irradiation history of the fuel batch to which it belongs. Modelling temperature differences between fresh and old fuel are important for correctly predicting neutronic properties and fuel burnup within the PBMR core.

The surface temperature of an average pebble is determined within the ‘macroscopic’ thermohydraulics solution by solving a heat conduction equation within the solid fraction of the porous medium. This conduction equation features heat source and sink terms to represent heat exchange with the coolant flowing between the pebbles. The effective conductivity of the solid fraction is determined from the Zehner-Schlünder correlation.

For each batch of pebbles, the surface temperature is calculated by considering the individual heat exchanges between a single pebble within the batch, the coolant and the surrounding pebble bed of, assumed, average pebbles. The temperature profile within an individual pebble is calculated using a one dimensional analytical model assuming the heat source, within the fuelled part of the pebble, to be spatially uniform. The localized temperature perturbation surrounding a fuel particle and the temperature distribution within a fuel particle are modelled analytically. The particle temperatures depend on the thermal conductivity of the fuel kernel and coatings, which were not provided within the benchmark specification. The fuel and coating conductivity values assumed in the current model (taken from the 2005 OECD/NEA PBMR-400 benchmark exercise) are shown in Table 4.51.

The thermal conductivity of the graphite within the fuel pebbles decreases with exposure to fast neutrons within the core. This is modelled via the fast fluence dependence of the graphite thermal conductivity, using the correlation for A3-3 matrix graphite supplied in the benchmark specification and fast fluence values computed by the neutronics model.

TABLE 4.51. THERMAL CONDUCTIVITIES OF FUEL PARTICLE COMPONENTS

Region	Material	Thermal conductivity ($\text{W m}^{-1} \text{K}^{-1}$)
Fuel kernel	Uranium dioxide	3.7
Coating 1	Pyrolytic carbon (porous buffer layer)	0.5
Coating 2	Pyrolytic carbon	4.0
Coating 3	Silicon carbide	16.0
Coating 4	Pyrolytic carbon	4.0

Bypass flows

A simple bypass flow equal to 19% of the reactor core inlet flow has been assumed in both the PHOENICS and WIMSTER models in accordance with the benchmark specification. This has been achieved by reducing the inlet coolant mass flow rate to 81% of the reactor inlet flow rate specified in the benchmark.

No coolant flow has been modelled within the control rod channels, leakage paths in the side reflector or the boring within the central reflector.

Coupling the WIMSTER thermohydraulics model and the neutronics calculations

The coupling between the neutronics calculations and the WIMSTER model is achieved by iterating the two models, with an exchange of data at each step.

The neutronics model supplies power distributions generated by each batch of pebbles within the reactor and the distribution of the fast neutron fluence experienced by each fuel batch. The fast fluence data is used to evaluate the neutron-dose-dependent thermal conductivity of the fuel pebble graphite.

WIMSTER supplies fuel, moderator, reflector and coolant temperatures and the coolant density to the neutronics model, to enable the accurate evaluation of neutronics cross-sections. Temperature values

are supplied for the graphite shell, matrix graphite and uranium dioxide fuel kernels in each cell of the pebble bed and for each batch of fuel pebbles specifically for the pebbles.

Results

Thermohydraulics Case E-2

The whole-core thermohydraulic results for Case E-2 are shown in Table 4.52. The gas, reflector and fuel surface temperature distributions within the core are shown in Fig. 4.94. The temperature-dependent thermal conductivity of the reflector graphite and the effective conductivity of the pebble bed are shown in Fig. 4.95. The gas pressure distribution, measured relative to the pebble bed outlet pressure, is shown in Fig. 4.96. Figure 4.97 shows a detailed representation of the gas and fuel surface temperature in the pebble bed.

TABLE 4.52. WIMSTER WHOLE-CORE RESULTS DATA, CASE E-2

Parameter	Value	Unit
Pebble bed pressure drop	1.94	Pa
Inlet temperature	488	°C
Average fuel temperature	888	°C
Average moderator temperature	860	°C
Average helium temperature	805	°C
Maximum fuel temperature	1205	°C

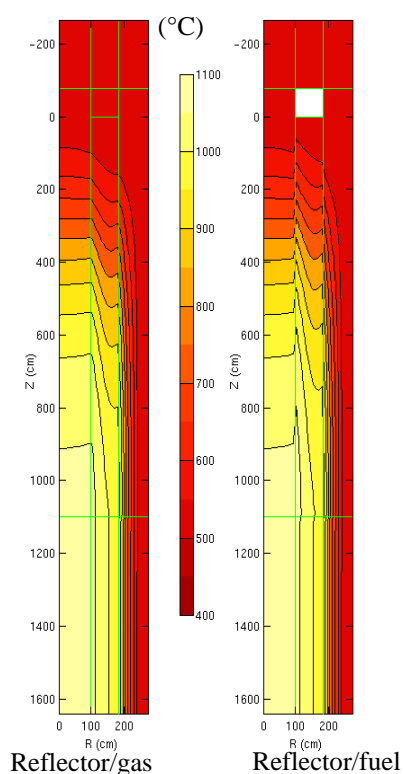


FIG. 4.94.
Temperature distributions — case E-2.

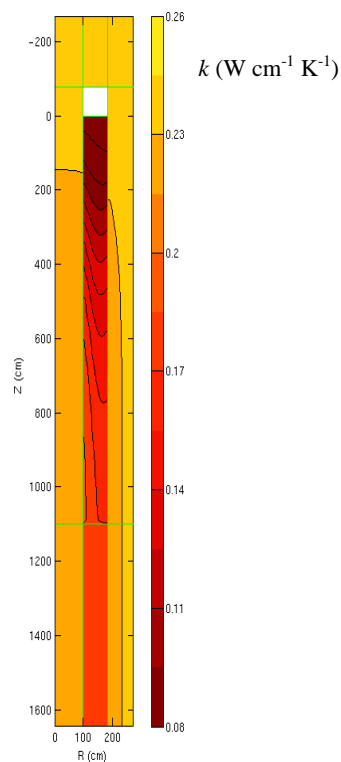


FIG. 4.95. Thermal conductivity of
the solid components and pebble bed
— case E-2.

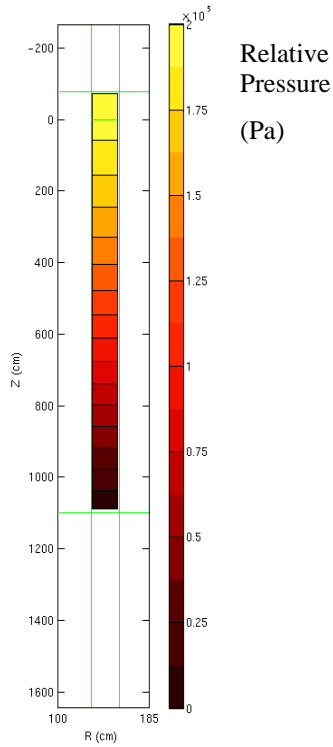


FIG. 4.96. Gas pressure within the core, relative to the outlet pressure — Case E-2.

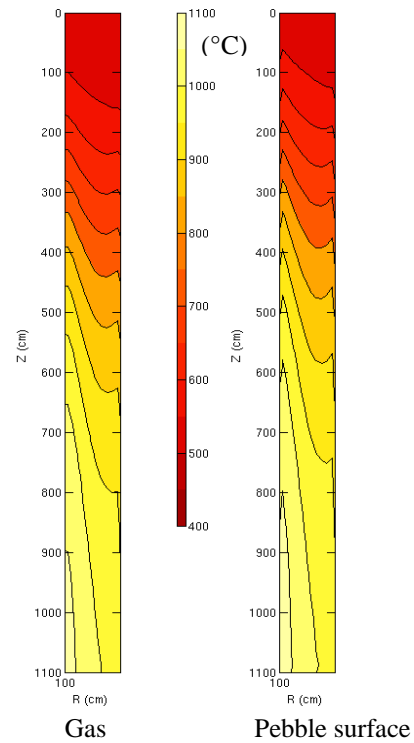


FIG. 4.97. Detailed plot of the pebble bed temperature profiles — Case E-2.

Neutronics case E-2

The flow rate of the pebbles through the core was adjusted until the k -effective at equilibrium was very close to 1.0. With a pebble flow rate down the core of 6.88 cm d^{-1} in all five flow streams, a k -effective of 0.99995 was obtained. Since this k -effective is only 5 pcm away from unity, no further adjustment was made to the pebble flow rate.

The single-parameter data calculated from this model is given in Table 4.53. The flux and rating distributions are given in Tables 4.54–4.56 and Figs 4.98 and 4.99.

TABLE 4.53. SINGLE PARAMETER RESULTS

Parameter	Result
Pebble flow rate (cm d ⁻¹)	6.88
k-effective	0.99995
Pebble mean discharge irradiation (GWd te ⁻¹)	94.4
In-core scattering: epithermal to thermal	51.5
Leakage from fissile region:	
Epithermal (>1.86 eV)	32.2%
Thermal (<1.86 eV)	-17.0%
Total	15.2%
Core average spectrum (epithermal to thermal ratio)	1.42
Reflector average spectrum (epithermal to thermal ratio)	0.153

TABLE 4.54. FISSILE REGION EPITHERMAL FLUX (>1.86 EV),
NORMALIZED TO TOTAL POWER OF 400 MW_{TH}

Neutron flux (neutrons cm ⁻² s ⁻¹)						
Outer radius		117 cm	134 cm	151 cm	168 cm	185 cm
radial mesh		17 cm	17 cm	17 cm	17 cm	17 cm
Height from top of active core	Axial mesh					
0 cm						
50 cm	50 cm	3.85E+13	4.18E+13	3.83E+13	3.16E+13	2.25E+13
100 cm	50 cm	7.51E+13	8.22E+13	7.55E+13	6.19E+13	4.36E+13
150 cm	50 cm	1.12E+14	1.25E+14	1.17E+14	9.89E+13	7.17E+13
200 cm	50 cm	1.49E+14	1.69E+14	1.64E+14	1.45E+14	1.10E+14
250 cm	50 cm	1.79E+14	2.05E+14	2.02E+14	1.81E+14	1.40E+14
300 cm	50 cm	1.94E+14	2.24E+14	2.22E+14	2.00E+14	1.55E+14
350 cm	50 cm	1.97E+14	2.28E+14	2.27E+14	2.04E+14	1.58E+14
400 cm	50 cm	1.90E+14	2.21E+14	2.19E+14	1.98E+14	1.53E+14
450 cm	50 cm	1.76E+14	2.05E+14	2.04E+14	1.84E+14	1.42E+14
500 cm	50 cm	1.59E+14	1.85E+14	1.85E+14	1.66E+14	1.28E+14
550 cm	50 cm	1.41E+14	1.64E+14	1.64E+14	1.47E+14	1.13E+14
600 cm	50 cm	1.22E+14	1.43E+14	1.43E+14	1.29E+14	9.87E+13
650 cm	50 cm	1.05E+14	1.23E+14	1.23E+14	1.11E+14	8.50E+13
700 cm	50 cm	9.00E+13	1.05E+14	1.05E+14	9.46E+13	7.25E+13
750 cm	50 cm	7.63E+13	8.95E+13	8.94E+13	8.03E+13	6.15E+13
800 cm	50 cm	6.44E+13	7.55E+13	7.55E+13	6.78E+13	5.19E+13
850 cm	50 cm	5.40E+13	6.34E+13	6.33E+13	5.68E+13	4.35E+13
900 cm	50 cm	4.49E+13	5.27E+13	5.27E+13	4.73E+13	3.61E+13
950 cm	50 cm	3.69E+13	4.34E+13	4.34E+13	3.89E+13	2.97E+13
1000 cm	50 cm	2.98E+13	3.51E+13	3.50E+13	3.14E+13	2.40E+13
1050 cm	50 cm	2.34E+13	2.76E+13	2.75E+13	2.47E+13	1.88E+13
1100 cm	50 cm	1.62E+13	1.92E+13	1.92E+13	1.72E+13	1.30E+13

TABLE 4.55. FISSILE REGION THERMAL FLUX (<1.86 eV),
NORMALIZED TO TOTAL POWER OF 400 MW_{TH}

		Neutron Flux (neutrons cm ⁻² s ⁻¹)				
Outer Radius		117 cm	134 cm	151 cm	168 cm	185 cm
Radial Mesh		17 cm	17 cm	17 cm	17 cm	17 cm
Height from Top of Active Core	Axial Mesh					
0 cm						
50 cm	50 cm	3.62E+13	2.68E+13	2.22E+13	1.88E+13	1.61E+13
100 cm	50 cm	6.47E+13	4.76E+13	3.92E+13	3.30E+13	2.81E+13
150 cm	50 cm	9.74E+13	7.29E+13	6.16E+13	5.39E+13	4.91E+13
200 cm	50 cm	1.31E+14	1.00E+14	8.75E+13	8.25E+13	8.84E+13
250 cm	50 cm	1.59E+14	1.23E+14	1.09E+14	1.06E+14	1.18E+14
300 cm	50 cm	1.76E+14	1.36E+14	1.21E+14	1.19E+14	1.34E+14
350 cm	50 cm	1.82E+14	1.41E+14	1.25E+14	1.23E+14	1.39E+14
400 cm	50 cm	1.79E+14	1.37E+14	1.22E+14	1.20E+14	1.36E+14
450 cm	50 cm	1.68E+14	1.29E+14	1.15E+14	1.13E+14	1.28E+14
500 cm	50 cm	1.54E+14	1.18E+14	1.05E+14	1.03E+14	1.17E+14
550 cm	50 cm	1.38E+14	1.05E+14	9.31E+13	9.17E+13	1.04E+14
600 cm	50 cm	1.21E+14	9.24E+13	8.17E+13	8.05E+13	9.16E+13
650 cm	50 cm	1.05E+14	8.01E+13	7.07E+13	6.97E+13	7.94E+13
700 cm	50 cm	9.02E+13	6.88E+13	6.07E+13	5.99E+13	6.82E+13
750 cm	50 cm	7.69E+13	5.86E+13	5.17E+13	5.10E+13	5.81E+13
800 cm	50 cm	6.51E+13	4.96E+13	4.37E+13	4.32E+13	4.92E+13
850 cm	50 cm	5.48E+13	4.17E+13	3.68E+13	3.63E+13	4.14E+13
900 cm	50 cm	4.57E+13	3.48E+13	3.07E+13	3.03E+13	3.45E+13
950 cm	50 cm	3.77E+13	2.87E+13	2.53E+13	2.50E+13	2.84E+13
1000 cm	50 cm	3.05E+13	2.32E+13	2.05E+13	2.02E+13	2.30E+13
1050 cm	50 cm	2.39E+13	1.83E+13	1.61E+13	1.59E+13	1.80E+13
1100 cm	50 cm	1.90E+13	1.51E+13	1.35E+13	1.31E+13	1.42E+13

TABLE 4.56. FISSILE REGION POWER DENSITY PROFILE (MW M⁻³)

Outer Radius		117 cm	134 cm	151 cm	168 cm	185 cm
Radial Mesh		17 cm	17 cm	17 cm	17 cm	17 cm
Height from Top of Active Core	Axial Mesh					
0 cm						
50 cm	50 cm	2.74E+00	2.01E+00	1.66E+00	1.40E+00	1.20E+00
100 cm	50 cm	4.78E+00	3.50E+00	2.87E+00	2.42E+00	2.07E+00
150 cm	50 cm	7.00E+00	5.26E+00	4.45E+00	3.91E+00	3.60E+00
200 cm	50 cm	9.12E+00	7.07E+00	6.24E+00	5.92E+00	6.40E+00
250 cm	50 cm	1.07E+01	8.50E+00	7.66E+00	7.47E+00	8.36E+00
300 cm	50 cm	1.15E+01	9.26E+00	8.41E+00	8.25E+00	9.21E+00
350 cm	50 cm	1.15E+01	9.39E+00	8.57E+00	8.40E+00	9.30E+00
400 cm	50 cm	1.09E+01	9.05E+00	8.28E+00	8.11E+00	8.90E+00
450 cm	50 cm	1.00E+01	8.40E+00	7.70E+00	7.53E+00	8.20E+00
500 cm	50 cm	8.96E+00	7.58E+00	6.96E+00	6.80E+00	7.35E+00
550 cm	50 cm	7.87E+00	6.70E+00	6.17E+00	6.01E+00	6.46E+00
600 cm	50 cm	6.81E+00	5.84E+00	5.38E+00	5.24E+00	5.60E+00
650 cm	50 cm	5.83E+00	5.03E+00	4.63E+00	4.51E+00	4.80E+00
700 cm	50 cm	4.96E+00	4.29E+00	3.96E+00	3.85E+00	4.08E+00
750 cm	50 cm	4.19E+00	3.64E+00	3.36E+00	3.27E+00	3.45E+00
800 cm	50 cm	3.53E+00	3.07E+00	2.84E+00	2.76E+00	2.90E+00
850 cm	50 cm	2.95E+00	2.58E+00	2.38E+00	2.31E+00	2.43E+00
900 cm	50 cm	2.45E+00	2.15E+00	1.98E+00	1.92E+00	2.01E+00
950 cm	50 cm	2.01E+00	1.77E+00	1.63E+00	1.58E+00	1.65E+00
1000 cm	50 cm	1.62E+00	1.43E+00	1.32E+00	1.28E+00	1.33E+00
1050 cm	50 cm	1.27E+00	1.12E+00	1.04E+00	1.00E+00	1.04E+00
1100 cm	50 cm	1.01E+00	9.34E-01	8.75E-01	8.31E-01	8.22E-01

Thermohydraulics case T-1

PHOENICS model

Figure 4.100 shows the structure of the computational mesh used by the PHOENICS model. The plot in Fig. 4.101 shows the temperature of the gas within the pebble bed and the temperature of the solid components in other regions of the core. Figure 4.102 shows radial temperature profiles at three points in the core height. The pressure profile within the core is shown in Fig. 4.103. The results are summarized in Table 4.57.

TABLE 4.57. PHOENICS WHOLE-CORE RESULTS DATA, CASE T-1

Parameter	Value	Unit
Pebble bed pressure drop	1.88	Pa
Inlet temperature	488	°C
Average helium temperature	756	°C
Average pebble surface temperature	779	°C
Average moderator temperature	803	°C

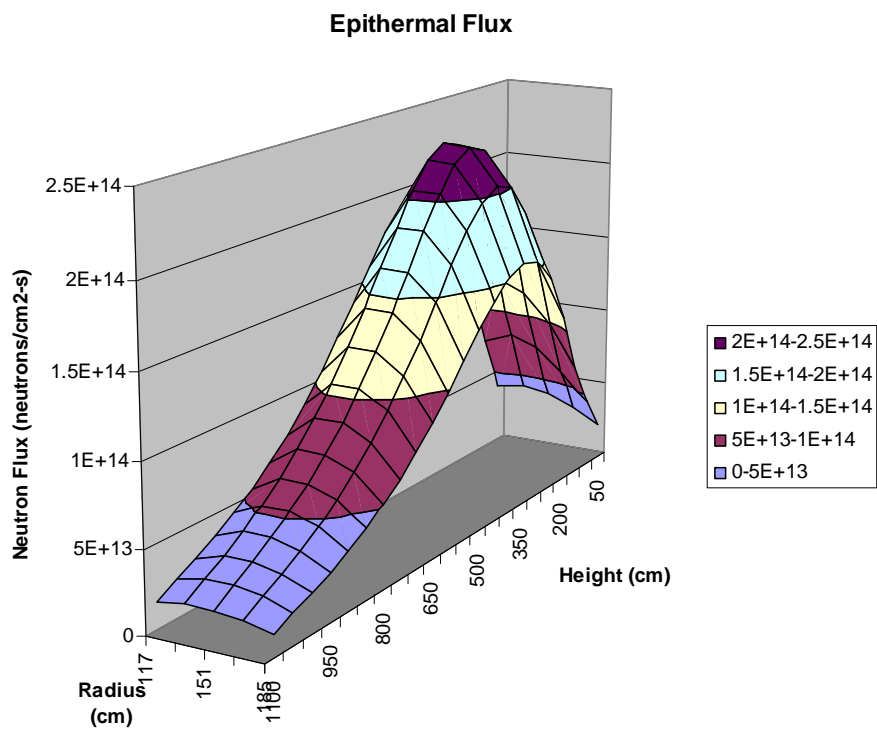
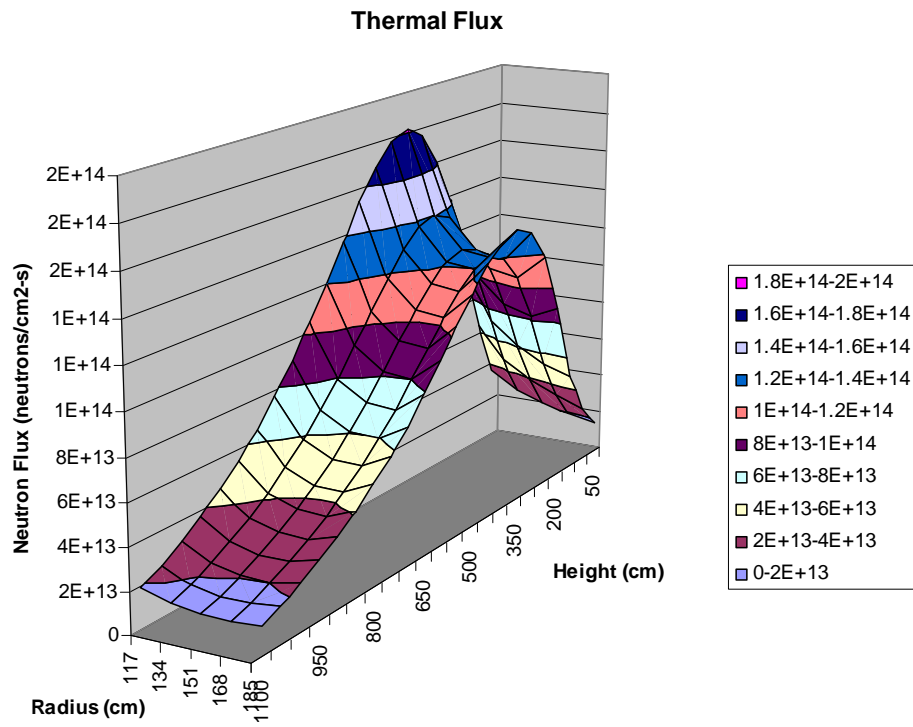


FIG. 4.98. Neutron flux distributions — case E2.

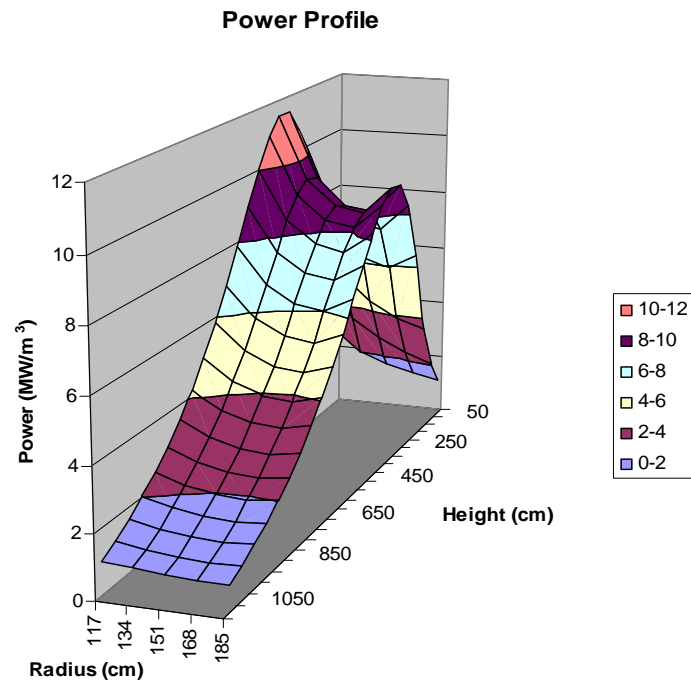


FIG. 4.99. Rating distribution — Case E-2.

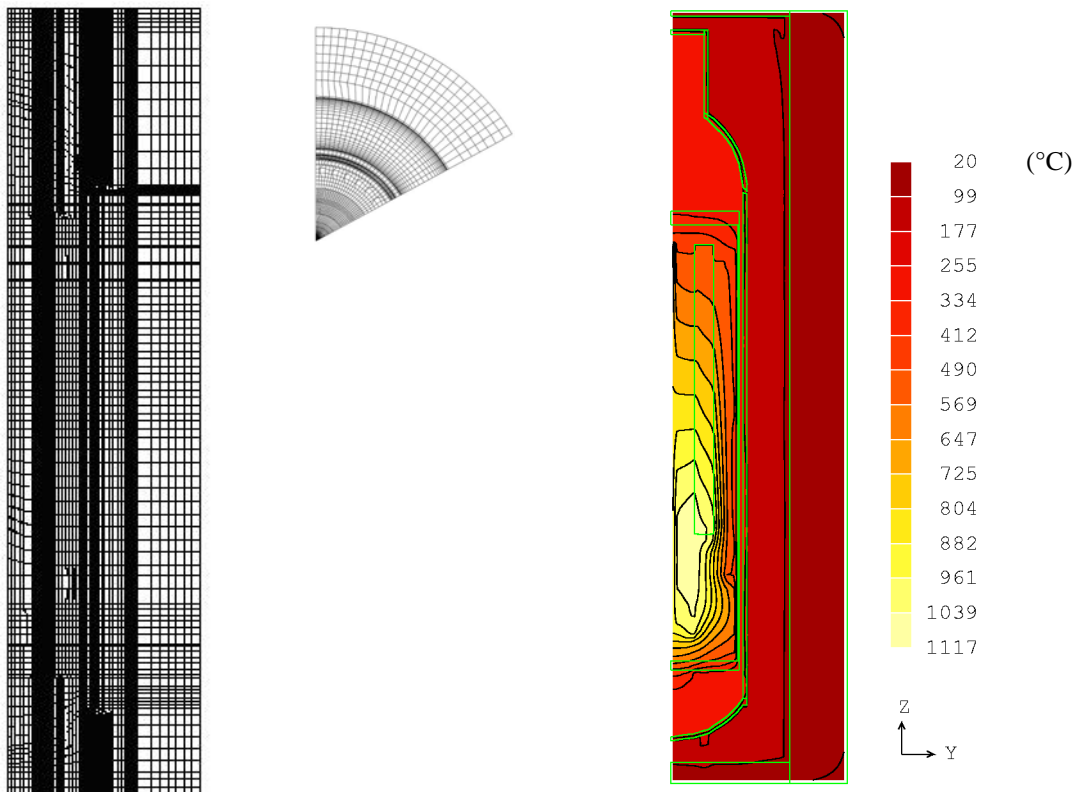


FIG. 4.100. PHOENICS mesh layout.

FIG. 4.101. Coolant temperatures (PHOENICS) — Case T-1.

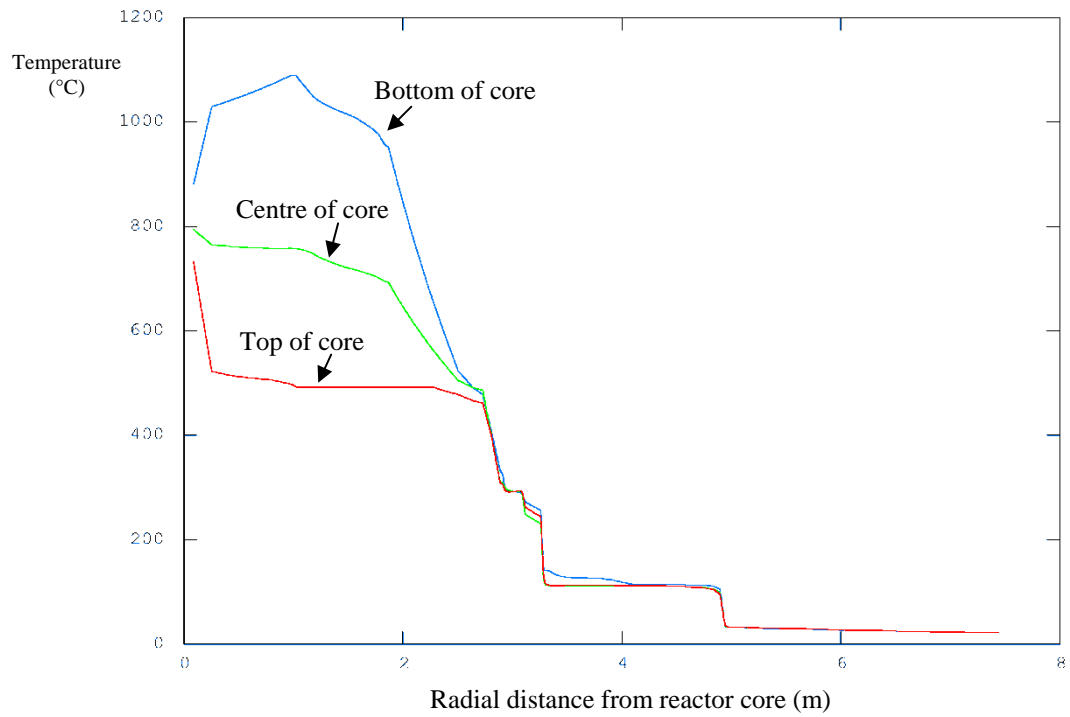


FIG. 4.102. Radial temperature profiles (PHOENICS).

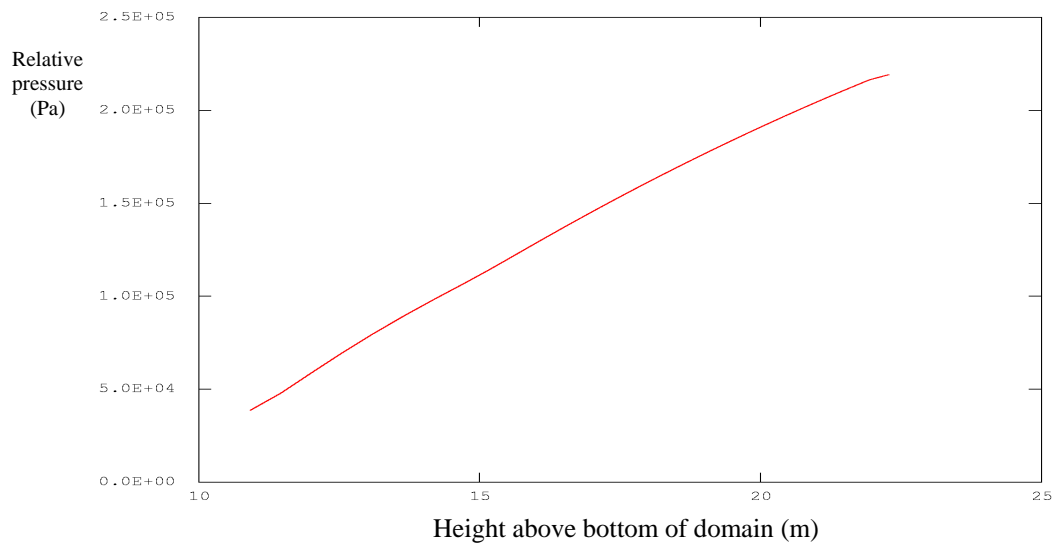


FIG. 4.103. Core pressure drop (PHOENICS).

WIMSTER

The whole-core thermohydraulic results for the WIMSTER model of Case T-1 are shown in Table 4.58. The gas, reflector and fuel surface temperature distributions within the core are shown in Fig. 4.104. The temperature-dependent thermal conductivity of the reflector graphite and the effective conductivity of the pebble bed are shown in Fig. 4.105. The gas pressure distribution, measured relative to the pebble bed outlet pressure, is shown in Fig. 4.106. Figure 4.107 shows a detailed representation of the gas and fuel surface temperature in the pebble bed.

TABLE 4.58. WIMSTER WHOLE-CORE RESULTS DATA, CASE T-1

Parameter	Value	Unit
Pebble bed pressure drop	1.83	Pa
Inlet temperature	488	°C
Average helium temperature	753	°C
Average pebble surface temperature	776	°C
Average moderator temperature	799	°C
Average fuel temperature	823	°C
Maximum fuel temperature	1157	°C

Comparison of PHOENICS and WIMSTER results for case T-1

The benchmark results for Case T-1 show good agreement between the WIMSTER and PHOENICS code results, despite the significant differences between the domains and boundary conditions used in the two models.

The average gas, pebble surface and moderator temperatures predicted by the PHOENICS and WIMSTER models are shown in Tables 4.57 and 4.58. The average temperatures in the pebble bed region of the PHOENICS model are approximately 4°C higher than the WIMSTER results, representing a difference between the models of <1% of the temperature rise across the reactor core. The predicted pressure drops over the pebble bed differ by approximately 2.7%.

The temperature distributions computed by the WIMSTER and PHOENICS models agree well within the pebble bed region and inner reflector regions. This agreement is apparent in Figs 4.101 and 4.104. This provides evidence that the simplified external boundary conditions and restricted domain used in the WIMSTER model does not affect the code's ability to predict the fuel and reflector graphite temperatures required by the coupled thermal hydraulics and neutronics modelling scheme.

Differences between the models are more significant in the bottom reflector, due to different approaches to the modelling of the hot gas outlet region of the bottom reflector. The mass flow distribution within the base of the core differs between the two models, due to the explicit three dimensional representation of the fuel discharge cones in the PHOENICS model.

The authors wish to express their gratitude to the South African NNR for providing support and funding to participate in this benchmark.

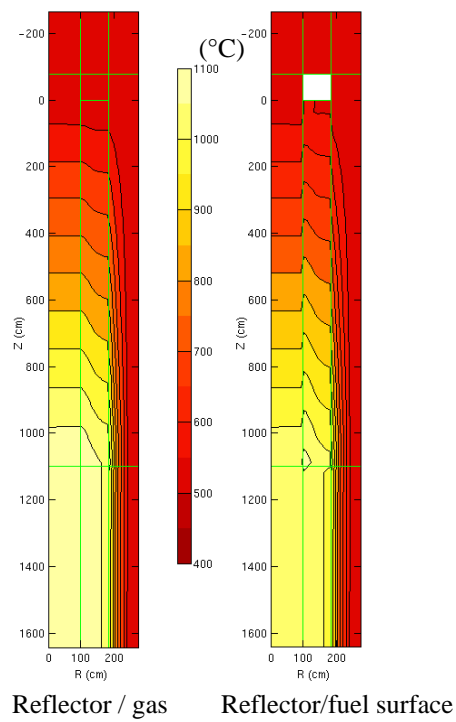


FIG. 4.104. Temperature distributions — Case T-1.

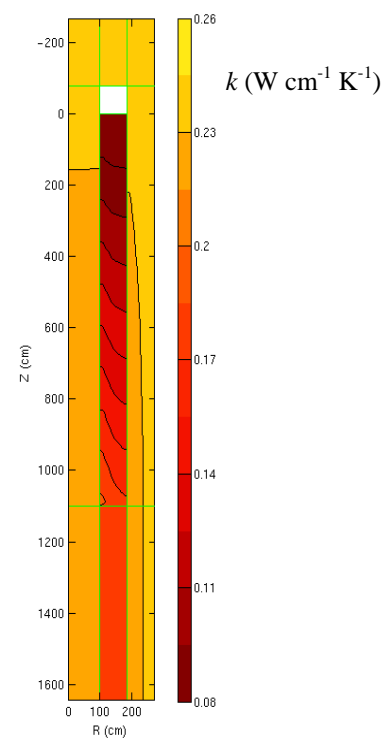


FIG. 4.105. Thermal conductivity of the solid components and pebble bed — Case T-1.

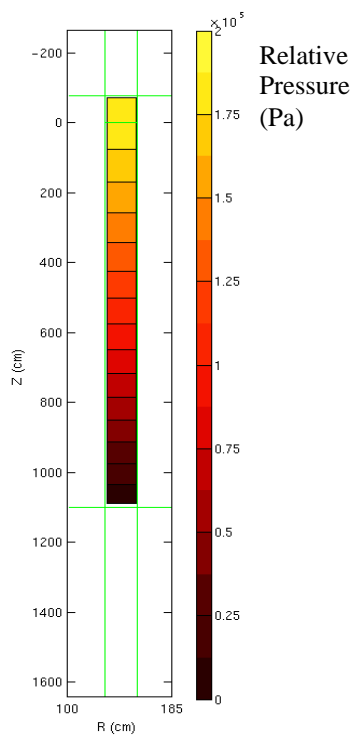


FIG. 4.106. Gas pressure within the core, Relative to the outlet pressure — Case T-1.

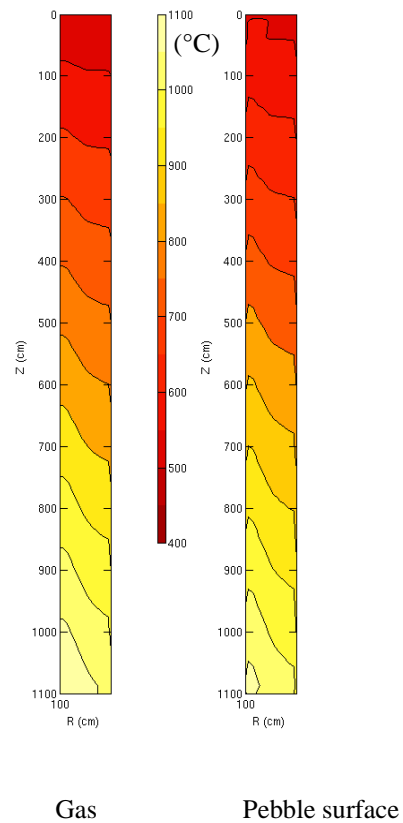


FIG. 4.107. Detailed plot of the pebble Bed temperature profiles — Case T-1.

4.3. PBMR 'PEBBLE BOX'

4.3.1. PBMR 'pebble box' benchmark problem definition

4.3.1.1. Introduction

Neutronically, small systems with relative large leakage are a challenging problem for the calculational methods typically used in the core neutronic analysis of reactors. For the pebble bed reactor designs, the traditional diffusion theory methods are still widely used. The scattering and streaming of neutrons throughout the core (between defined material regions or spectrum zones) and specifically the treatment of the thermal neutrons on the core-reflector interface are issues of particular importance in the design of nuclear reactors. In pebble bed reactors, this problem is particularly aggravated due to the graphite moderation (versus water), the double-heterogeneity (versus a single level of heterogeneity), variations in the moderation ratio (N_C/N_U), and the relatively large neutron leakage.

In full-scale reactor designs, the effects under discussion might be lessened due to a smaller surface-to-volume ratio, impurities in the matrix and reflector graphite, as well as the accompanying temperature effects in an operating HTR. It was thus decided to make use of a simplified test problem of a 1 m³ pebble box and with clearly defined material and boundary conditions to investigate these effects. The problem will be used to do code-to-code comparisons with a special focus to perform comparisons between statistical and deterministic codes.

In this study, one would like to compare k-effectives between the two codes methodologies, i.e. deterministic and Monte Carlo on the one hand, but on the other hand, one would also like to investigate the reasons for any differences in results between them.

4.3.1.2. Case Specification

The summary provided here was submitted to the CRP as Refs [4-46] and [4-47].

The test cases are defined in six steps and presented in Fig. 4.108. These are as follows:

Case 1 — Infinite homogeneous mixed cube of 1 m³ - (No heterogeneity): A non-reflected cube with side dimensions of 1 × 1 × 1 m comprised of a homogenized mixture of material. For this case, reflected boundary conditions (mirror) should be assumed. This is to simulate an infinitely homogeneous medium. Since the atom densities are identical by definition, any differences between codes should lay in the cross-section libraries or the calculational approaches;

Case 2 — Infinite array of pebbles with homogeneous fuel regions in a cube of 1 m³ - (first level of heterogeneity): A non-reflected cube with side dimensions of 1 × 1 × 1 m comprised of homogenized material inner fuel region in the fuel spheres. For this case, reflected boundary conditions (white boundary conditions) should be assumed. This is to simulate an infinitely homogeneous medium. Since the atom densities are identical by definition, any differences between codes must lay in the cross-section libraries or the calculational approaches;

Case 3 — Infinite array of pebbles in box cube of 1 m³ (second level of heterogeneity): This study involves the same layout as Cases 1 and 2, except that the structure of the fuel spheres and the coated particles with its layers are to be treated as a heterogeneous layout. This case should show whether the dual heterogeneity of the pebble bed fuel leads to additional differences in results in the different codes;

Case 4 — Reflected homogeneous cube: This has the same definition as the 1 m³ cube of Case 1, but this time with 1 m reflector around the core (3 × 3 × 3 m total size). The outer boundary condition should be defined as black (non-re-entrant boundary). In this case, the effect of the core-reflector interface is investigated;

Case 5 — Reflected 'pebble box' cube- (first level of heterogeneity): In this case, the fuel spheres are modelled with a homogenized inner core region as for Case 2 but with the 1 m reflector all around the reactor, similar to Case 4, with black boundary conditions. Besides the first level of heterogeneity

effects within the fuel spheres, the neutron streaming between the pebbles to the reflector regions need to be considered;

Case 6 — Reflected ‘pebble box’ cube - (second level of heterogeneity): In this case, the fuel spheres and coated particles are modelled explicitly as for Case 3, but with the 1 m reflector all around the reactor, similar to Cases 4 and 5, with black boundary conditions. It thus represents the physical ‘pebble box’ layout. Besides the heterogeneity effects within the fuel spheres, core fuel region and coated particles, the neutron streaming between the pebbles to the reflector regions need to be considered.

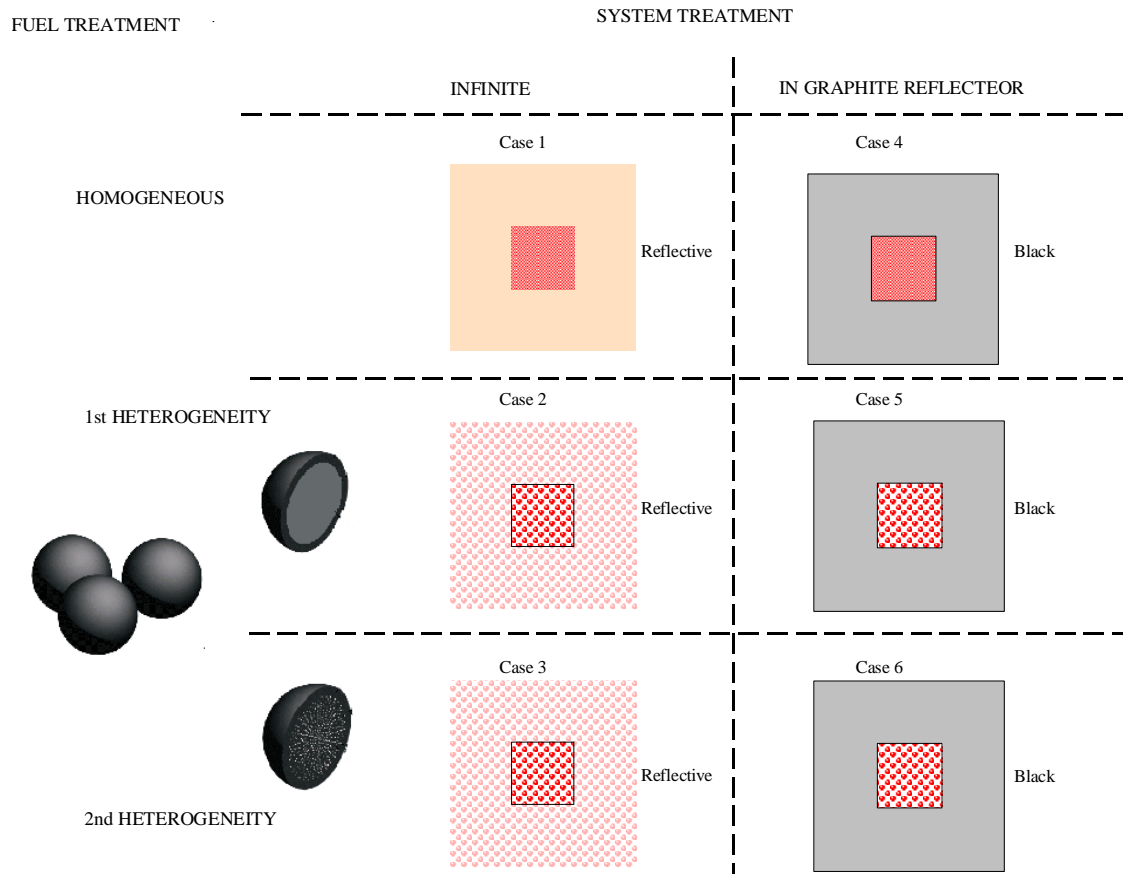


FIG. 4.108. Cases to be evaluated.

The input data for the problem is provided in Table 4.59.

TABLE 4.59. MODELLING PARAMETERS

Description	Unit	Value
Heavy metal loading	g/pebble	9
Enrichment	wt/0	9.6
UO ₂ density	g/cm ³	10.4
Diameter of pebble	mm	60
Fuel matrix density	g/cm ³	1.74
Fuel-free zone density	g/cm ³	1.74
Thickness of the fuel-free zone	mm	5
Fuel kernel diameter	μm	500
Buffer layer thickness	μm	95
Inner PyC layer thickness	μm	40
SiC layer thickness	μm	35
Outer PyC layer thickness	μm	40
Buffer layer density	g/cm ³	1.05
Inner PyC layer density	g/cm ³	1.90
SiC layer density	g/cm ³	3.18
Outer PyC layer density	g/cm ³	1.90
Packing fraction	%	61
Reflector graphite density	g/cm ³	1.80
Room temperature	K	300
Alternative temperature	K	900

This specification results in the number densities given in Table 4.60 for the different cases. Where applicable, the graphite reflector number density as defined in the first column should be used (Cases 4–6). The space between the fuel spheres in the heterogeneous cases is assumed to be vacuum.

TABLE 4.60. NUMBER DENSITIES TO BE UTILIZED FOR THE DIFFERENT CASES

Case 1/4		Case 2/5		Case 3/6	
Homogenized Material		Core Region		Particle *	
U-234	1.16809E-07	U-234	3.3090E-07	U-234	2.2057E-05
U-235	1.19358E-05	U-235	3.3812E-05	U-235	2.2539E-03
U-238	1.10859E-04	U-238	3.1437E-04	U-238	2.0956E-02
Si	2.75487E-04	Si	7.8039E-04	O-16	4.6421E-02
C	5.23349E-02	C	8.4743E-02	Coatings *	
O-16	2.45823E-04	O-16	6.9636E-04	1 C	5.2645E-02
B-Nat	1.51250E-08	B-Nat	2.4795E-08	2 C	9.5262E-02
Graphite Reflector		Shell		3 C	4.7760E-02
C	9.0248E-02	C	8.7240E-02	Si	4.7760E-02
		B-Nat	2.4795E-08	4 C	9.5262E-02
				Matrix	
				C	8.7240E-02
				B-Nat *	2.4795E-08
				Shell	
				C	8.7240E-02
				B-Nat	2.4795E-08

* For Cases 3–6, the boron impurity must be applied to the kernel and all coatings too (use the given number density)

4.3.1.3. Case variations and additional information

Differences in thermal absorption of graphite

It is known that important differences exist between the VSOP and MCNP libraries. In the VSOP library, the 2200 m/s absorption cross-section for C is 3.88 mbarn, while in the MCNP library it is 3.36 mbarn [4-48]. Similar differences may exist between the different cross-section libraries used by participants. As a variation of Case 6, an adequate amount of boron poison is added to the reflector graphite to overshadow any differences in the absorption cross-section that may exist in the different libraries. An impurity of 1 ppm B-10 should be added. This case is defined as Case 7.

Determination of temperature effects

A variation on the cases at room temperature is proposed so that temperature effects of cross-sections between different libraries and the different resonance treatment approaches can be studied. It is proposed to perform the complete set of ‘pebble box’ cases for the following combination of cases:

Set	UO ₂ Temperature	Graphite Temperature
i	300 K	300 K
ii	800 K	800 K
iii	1200 K	1200 K
iv	1200 K	800 K

The results to be reported are as for the cold cases and cases should be distinguished by the temperature set used. For Temperature Set iv, the temperature of the kernel coatings (Si and C) and boron (B-10) should also be assumed to be at 800 K.

Group structures, convergence and other practical considerations

No energy group structure or number of groups is prescribed and participants should calculate the best result with their tools available. For comparison purposes, two-group fluxes and thermal-to-fast ratios will be compared with the thermal cut-off energy taken as 1.86 eV. Convergence criteria and uncertainties must be noted by participants, but as a first guideline 1×10^{-6} could be used for k-effective and 1×10^{-5} for fluxes. Mesh convergence that must be ensured by each participant is also very important. For comparison purposes, a 2.5 cm mesh is suggested, but only to facilitate easy comparison of results and the plotting of profiles, and it is not a definition for solution mesh.

Additional data for ZUT

This section contains additional data that can be used if required for resonance treatment. Note that the use of this data is optional and it only serves the purpose of giving guidance to mainly VSOP users. The data used in the ZUT module of VSOP is given in Table 4.61.

TABLE 4.61. DATA RELEVANT TO THE CALCULATION OF THE RESONANCE INTEGRALS IN ZUT

Atomic weight of C:	12
Atomic weight of O:	16
Scattering cross-section, σ_s of C:	4.6 barn
Scattering cross-section, σ_s of O:	3.8 barn

4.3.1.4. Expected results and discussion

In total, six different geometrical cases were defined with a variation in the B-10 poisoning (of Case 6) defined as Case 7. For each case, a variation in temperatures (the four temperature sets defined) should be performed. The following results, as shown in Table 4.62, should be provided (use can be made of the spreadsheet template provided) as indicated for the different cases.

TABLE 4.62. OUTPUT REQUIRED

	Results required	
	Case 1–3	Case 4–7
Single parameters:		
k-effective	x	x
In-core scattering epithermal \rightarrow thermal ¹ : (%)	x	x
Leakage core \rightarrow reflectors ² : (%)		x
Epithermal (> 1.86 eV)		x
Thermal (<1.86 eV)		x
Total		x
Total leakage out of the system (calculational domain)		x
Core average spectra (epithermal-to-thermal ratio averaged over all the meshes in the core region)	x	x
Reflector average spectra (epithermal-to-thermal ratio averaged over all the meshes in the outer reflector region)		x
Line profiles: Results along a line from the centre of the ‘pebble box’ to the centre to the mid-plane of one of the surfaces.		
Epithermal (>1.86 eV) flux profile ³ .		x
Thermal (<1.86 eV) flux profile ³ .		x
Epithermal to thermal ratio		x
Relative Power profile in the ‘pebble box’ ⁴		x

Notes:

In-core scattering from epithermal to thermal ratio is defined as the (in-core epithermal to thermal scattering reaction rate) over the (in-core total destruction rate (absorption + leakage)).

Leakage is defined as the net leakage from the core to the reflector over the total destruction rate (absorption + leakage), in the respective energy ranges.

Fluxes are to be normalized to one neutron born in the system.

Relative power implies values normalized to an average of 1.0 over the whole core.

In the case of using deterministic codes, the studies should provide a measure of the mesh effects both in a sense of the calculational mesh and if appropriate, the material mesh (or spectral mesh). The basis for selecting an optimal mesh size should be provided. Detail of the geometrical model used, the methods applied, group structure used and source of cross-sections should be included.

In the case of Monte Carlo codes, the packing of the coated particle and the pebble packing should be explained (repeated structure used, random packing, etc). The source of the cross-sections must also be mentioned (details on which release was used).

4.3.1.5. Tabulation of results

Each participating Member State is encouraged to provide their specific results to each of the ‘pebble box’ cases in their chosen format. However, for consistency in tabulating the results and making conclusions and recommendations, it is requested that each CSI fill in the provided spreadsheet which will then be evaluated by the host CSI.

4.3.2. 'Pebble box' analysis and results

4.3.2.1. 'Pebble Box' benchmark results, South Africa

The summary provided here was submitted to the CRP and taken from Ref. [4-49].

Introduction

The benchmark problems associated with the 'pebble box' focus on neutronically small systems with relative large leakages which are a challenging problem for the calculational methods typically used in the core neutronic analysis of reactors.

A simplified test problem of a 1 m³ 'pebble box' and with clearly defined material and boundary conditions is chosen to investigate the effects of scattering and streaming of neutrons throughout the core and the treatment of thermal neutrons on the core-reflector interface. The main concern of the study is comparison of the k-effective value calculated by deterministic and statistical codes and to investigate the reasons for any differences in results between them.

Method of calculation

The methodology followed in the analysis can be described in two sections:

1. Level of heterogeneity

According to the level of heterogeneity, the fuel design (DATA-2 module of VSOP99) and resonance integral (ZUT code) calculations are performed for each case. The ZUT calculations are performed for three different specifications and the following three different fuel design inputs (cards D) are used for each case:

- Homogenous mixture (no heterogeneity);
- Homogenized fuel zone (first level of heterogeneity);
- Heterogeneous pebbles (second level of heterogeneity).

The thermal spectrum calculations in VSOP99 are performed in the THERMOS module. The effect of the grain coated particles and the neutron streaming effects through the pebbles are treated in THERMOS calculations. Therefore, for each of the cases with different levels of heterogeneity, different THERMOS inputs (cards T) are prepared with the specified level of heterogeneity.

2. System type

According to the treatment of the system, two different geometry (TRIGIT module of VSOP99) and boundary types are used in the diffusion calculations (CITATION module of VSOP99).

The 1 × 1 × 1 m cubic geometry was used for Cases 1–3 with reflective boundary conditions on all six faces. The 3 × 3 × 3 m cubic geometry with 1 × 1 × 1 m core at the centre was used for Cases 4–6 with vacuum (extrapolated) boundary conditions defined on all six faces. Due to the memory restrictions in VSOP99, one quadrant of the latter case (3 × 3 × 3 m system) is used in the geometry description.

Summary of results

The summary of the results for the seven different cases as requested in the benchmark definition is supplied in Table 4.63 for the infinite box cases (Cases 1–3) and in Table 4.64 for the reflected cube (Cases 4–7). The calculations for Case 7 are performed with 1 ppm B-10 impurity in the graphite reflector as well as 10 ppm B-10 (the definition was changed during the exercise and both are included to facilitate comparison), and the results are also supplied in Table 4.64.

The effect of the heterogeneity of the coated particles and the pebbles is clearly seen from the results (Tables 4.63 and 4.64). The k-effective values increase when the heterogeneity is taken into account due to the increase in the resonance escape probabilities. The resonance escape probability is the highest in the double-heterogeneity case due to the self-shielding of the resonance absorbers and higher slowing down in the coating particles as well as in the graphite matrix. The increase in the in-core scattering from epithermal energies to thermal energies and the decrease in the core average

spectra (epithermal-to-thermal ratio over core region) confirm the increase in the resonance escape probability and slowing-down ratio.

TABLE 4.63. SUMMARY OF THE RESULTS FOR THE INFINITE BOX

	Case 1	Case 2	Case 3
Temperature Set i (300 K)			
k-effective	1.39356	1.42921	1.51592
In-core scattering epithermal -> thermal: (%)	65.4%	67.4%	71.6%
Core average spectra (epithermal-to-thermal ratio over core region)	2.31	2.30	2.10
Temperature Set ii (800 K)			
k-effective	1.31262	1.35358	1.44312
In-core scattering epithermal -> thermal: (%)	61.9%	64.0%	68.5%
Core average spectra (epithermal-to-thermal ratio over core region)	1.98	1.89	1.77
Temperature Set iii (1200 K)			
k-effective	1.27343	1.31552	1.4046
In-core scattering epithermal -> thermal: (%)	60.1%	62.3%	66.9%
Core average spectra (epithermal-to-thermal ratio over core region)	1.77	1.68	1.58
Temperature Set iv (800 K, 1200 K)			
k-effective	1.27873	1.32098	1.41045
In-core scattering epithermal -> thermal: (%)	60.1%	2.33%	66.9%
Core average spectra (epithermal-to-thermal ratio over core region)	2.03	1.93	1.81

The effect of the temperature changes is also presented in Tables 4.63 and 4.64. Four different temperature sets are used. The effect of Doppler broadening is clearly seen when these four different temperature sets are compared.

The increase in temperature causes more neutrons captured by the resonance absorber when slowing down occurs. Therefore, a decrease in the effective reactor multiplication factor, in-core scattering from epithermal energies to thermal energies and core average spectra is seen. Temperature Set iv uses different temperatures for resonance absorber and moderator material. When the results of this case are compared with the results of Temperature Set iii, the negative temperature coefficient of the moderator is observed. Although in-core scattering from epithermal to thermal energies stays the same, the core average spectra increase, which means less neutrons are slowing down to thermal energies.

Table 4.64 represents the results of the reflected cube. The leakage from the system increases with introducing the heterogeneity of the pebbles due to the neutron streaming effects, and when the double-heterogeneity is introduced, the leakage is increased more. The leakage from the core is also increased with the heterogeneity.

The epithermal leakage to the reflector is the highest when the double-heterogeneity of the coated particles inside the graphite matrix is introduced to the system (Case 6). Due to the higher epithermal leakage to the reflector, the thermal leakage to the core is higher in the heterogeneous cases (Cases 5 and 6). Although the epithermal leakage from the core is at the same level in Case 7, where B-10 is introduced as impurity to the reflector graphite, the thermal leakage to the core is much lower than the other cases due to the absorption of the thermal neutrons in B-10 impurities. This effect is much more

pronounced when Case 7 with 10 ppm B-10 concentration case is compared with 1 ppm B-10 concentration case. Due to the absorption of the thermal neutrons in the B-10 impurities inside the reflector graphite and therefore decrease in the thermal leakage to the core, the core average spectra (epithermal-to-thermal ratio) are much higher in Case 7 when it is compared with the other cases with pure graphite reflector. The same effect is also seen in the reflector average spectra.

The mesh dimension effects for Cases 4, 5 and 6 are illustrated in Table 4.65 for each temperature set. Although the computer running time is significantly decreased with increasing mesh dimensions, the false convergence of the effective multiplication factors is observed.

The calculated thermal and fast flux values for the reflected cube cases (Cases 4–7) are shown in the following sections. The effects of the temperature changes and the level of heterogeneity are clearly seen in the flux profiles illustrated in Figs 4.109–4.128.

TABLE 4.64. SUMMARY OF THE RESULTS FOR THE REFLECTED CUBE

	Case 4	Case 5	Case 6	Case 7 (10 ppm)	Case 7 (1 ppm)
Temperature Set i (300 K)					
k_{eff}	0.98583	0.99784	1.02171	0.70138	0.93949
In-core scattering epithermal -> thermal: (%)	26.5%	26.7%	28.3%	29.2	28.5%
Leakage:					
Epithermal (> 1.86 eV)	57.8%	58.8%	59.0%	58.0%	58.8%
Thermal (<1.86 eV)	-21.0%	-21.5%	-21.1%	-3.7%	-16.7%
Total	36.9%	37.2%	37.9%	54.3%	42.1%
Total leakage out of the system (calculational domain)	0.137	0.139	0.141	0.00568	0.0284
Core average spectra (epithermal-to-thermal ratio over core region)	1.848	1.821	1.722	2.462	1.864
Reflector average spectra (epithermal-to-thermal ratio)	0.127	0.128	0.125	0.504	0.170
Temperature Set ii (800 K)					
k_{eff}	0.93817	0.94923	0.97595	0.6765	0.90733
In-core scattering epithermal -> thermal: (%)	25.4%	25.8%	27.4%	28.1%	27.5%
Leakage:					
Epithermal (> 1.86 eV)	57.3%	58.2%	58.6%	57.7%	58.4%
Thermal (<1.86 eV)	-20.1%	-20.6%	-20.2%	-3.9%	-16.5%
Total	37.2%	37.7%	38.4%	53.8%	42.0%
Total leakage out of the system (calculational domain)	0.191	0.193	0.197	0.0137	0.130
Core average spectra (epithermal-to-thermal ratio over core region)	1.497	1.461	1.394	2.036	1.503
Reflector average spectra (epithermal-to-thermal ratio)	0.104	0.104	0.102	0.368	0.130
Temperature Set iii (1200 K)					
k_{eff}	0.90228	0.91297	0.93939	0.65567	0.87725
In-core scattering epithermal -> thermal: (%)	24.9%	25.3%	26.9%	27.5%	27.0%
Leakage:					
Epithermal (> 1.86 eV)	57.0%	58.0%	58.3%	57.5%	58.2%
Thermal (<1.86 eV)	-19.0%	-19.4%	-19.0%	-3.52%	-15.6%
Total	38.0%	38.6%	39.3%	54.0%	42.5%
Total leakage out of the system (calculational domain)	0.216	0.219	0.224	0.020	0.156
Core average spectra (epithermal-to-thermal ratio over core region)	1.330	1.295	1.241	1.817	1.334
Reflector average spectra (epithermal-to-thermal ratio)	0.0945	0.0945	0.0926	0.312	0.115
Temperature Set iv (800 K, 1200 K)					
k_{eff}	0.92694	0.93861	0.96538	0.66766	0.89712
In-core scattering epithermal -> thermal: (%)	24.8%	25.2%	26.8%	27.5%	26.9%
Leakage:					
Epithermal (> 1.86 eV)	57.2%	58.1%	58.4%	57.6%	58.3%
Thermal (<1.86 eV)	-20.2%	-20.6%	-20.2%	-4.02%	-16.5%
Total	37.0%	37.5%	38.2%	53.5%	41.7%
Total leakage out of the system (calculational domain)	0.190	0.192	0.196	0.0136	0.129
Core average spectra (epithermal-to-thermal ratio over core region)	1.512	1.475	1.407	2.060	1.517
Reflector average spectra (epithermal-to-thermal ratio)	0.104	0.104	0.102	0.370	0.130

TABLE 4.65. MESH DIMENSION EFFECTS

Case No.	Temperature Set	Mesh dimension		
		2.5 cm	5.0 cm	10.0 cm
Case 4	Set i	0.98583	0.98126	0.97197
	Set ii	0.93817	0.93496	0.92754
	Set iii	0.90228	0.89939	0.89296
	Set iv	0.92694	0.92346	0.91623
Case 5	Set i	0.99796	0.99279	0.98352
	Set ii	0.94924	0.94563	0.93841
	Set iii	0.91297	0.91041	0.90358
	Set iv	0.93861	0.93622	0.92786
Case 6	Set i	1.02171	1.01655	1.00779
	Set ii	0.97595	0.97202	0.96530
	Set iii	0.93939	0.93600	0.93013
	Set iv	0.96538	0.96157	0.95480

Case 4

The calculated epithermal and thermal flux profiles for Case 4 for different temperature sets are illustrated in Figs 4.109–4.112.

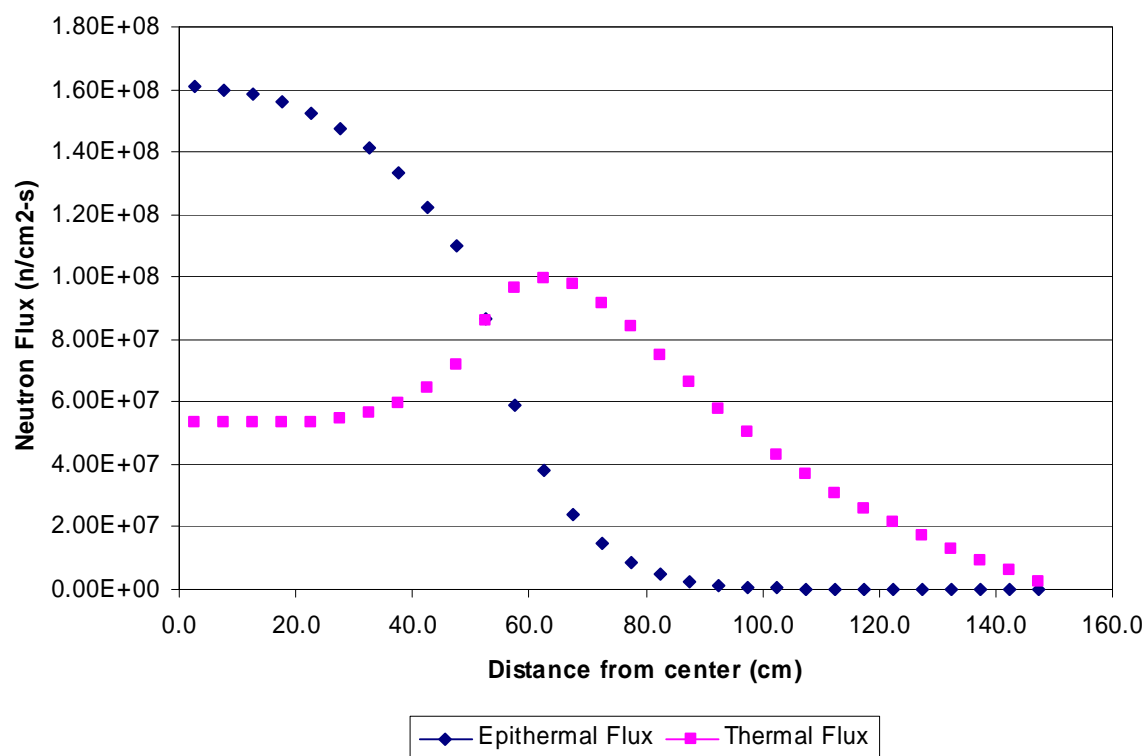


FIG. 4.109. Temperature set i (300 K).

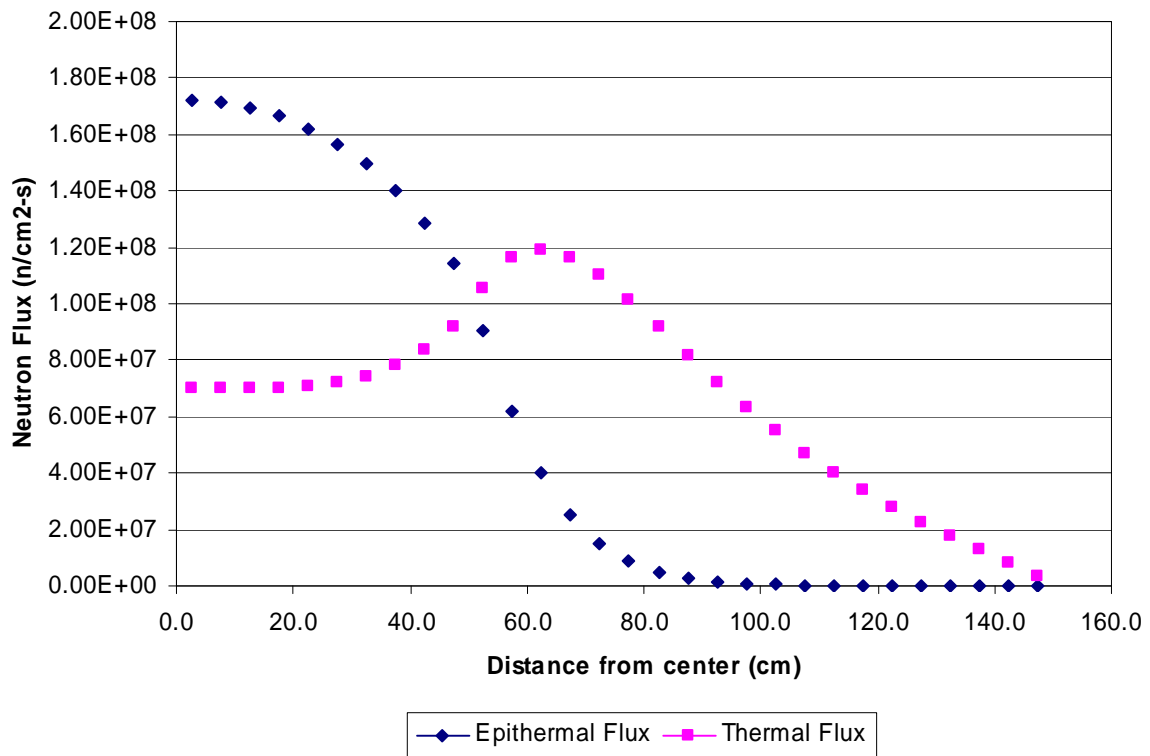


FIG. 4.110. Temperature set ii (800 K).

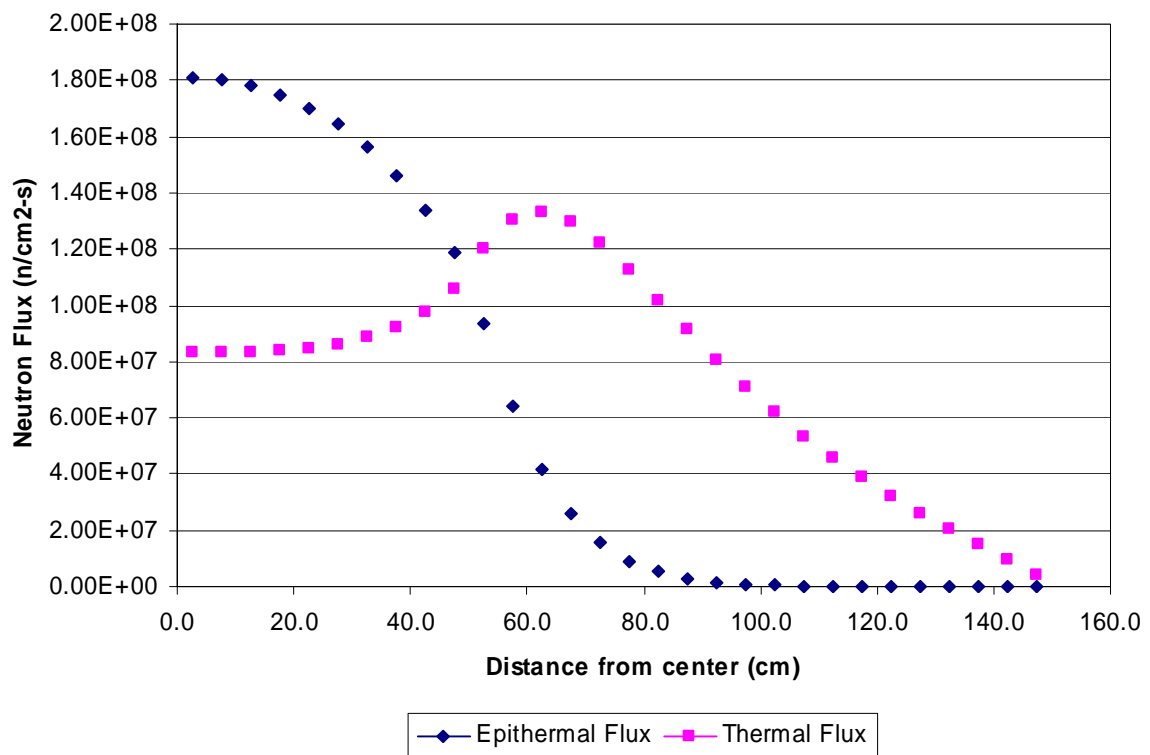


FIG. 4.111. Temperature set iii (1200 K).

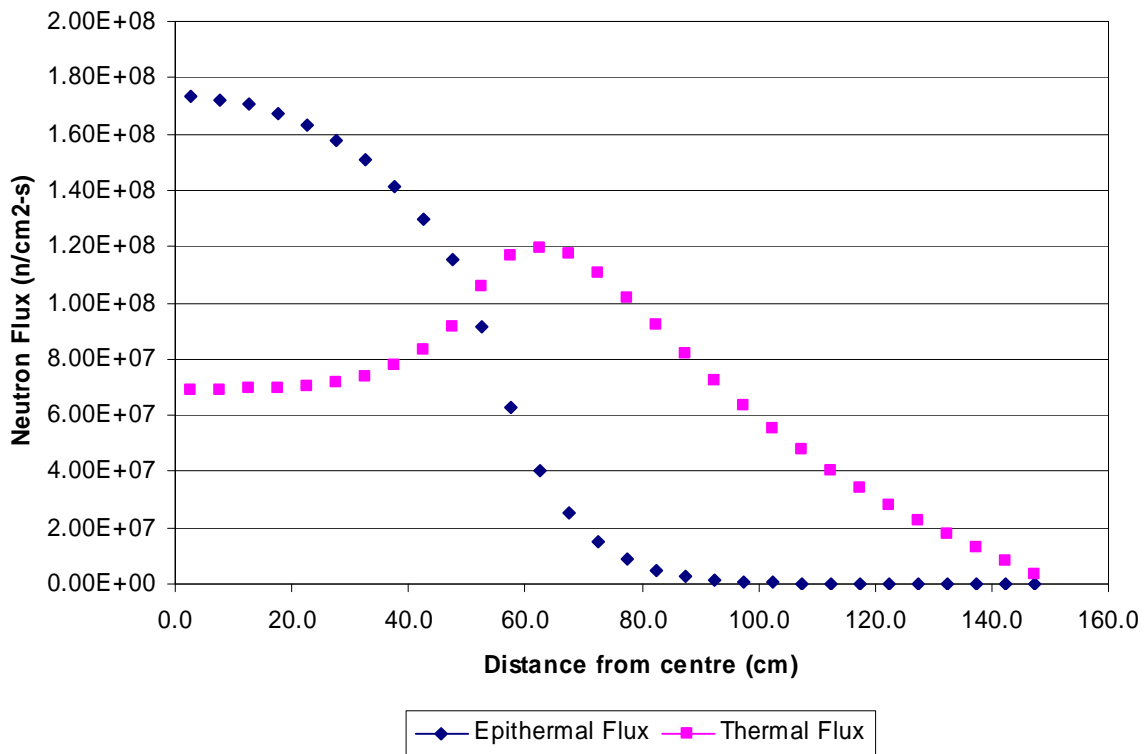


FIG. 4.112. Temperature set iv (800 K, 1200K).

Case 5

The calculated epithermal and thermal flux profiles for Case 5 for different temperature sets are illustrated in Figs 4.113–4.116.

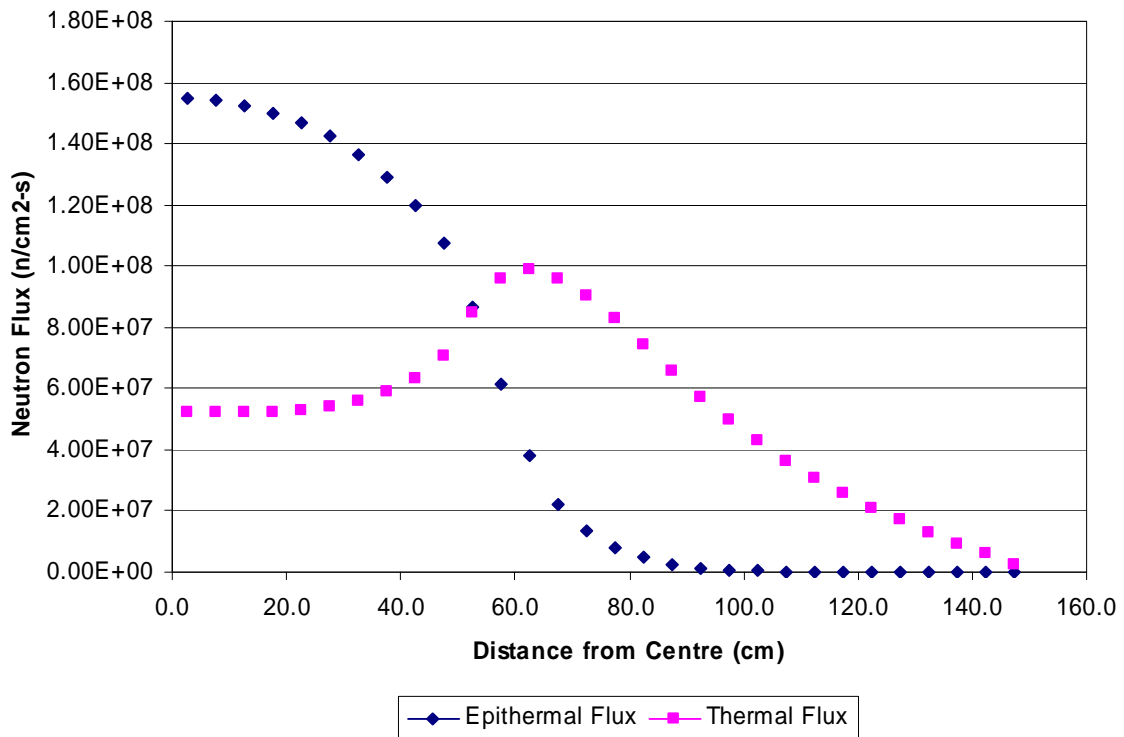


FIG. 4.113. Temperature set i (300 K).

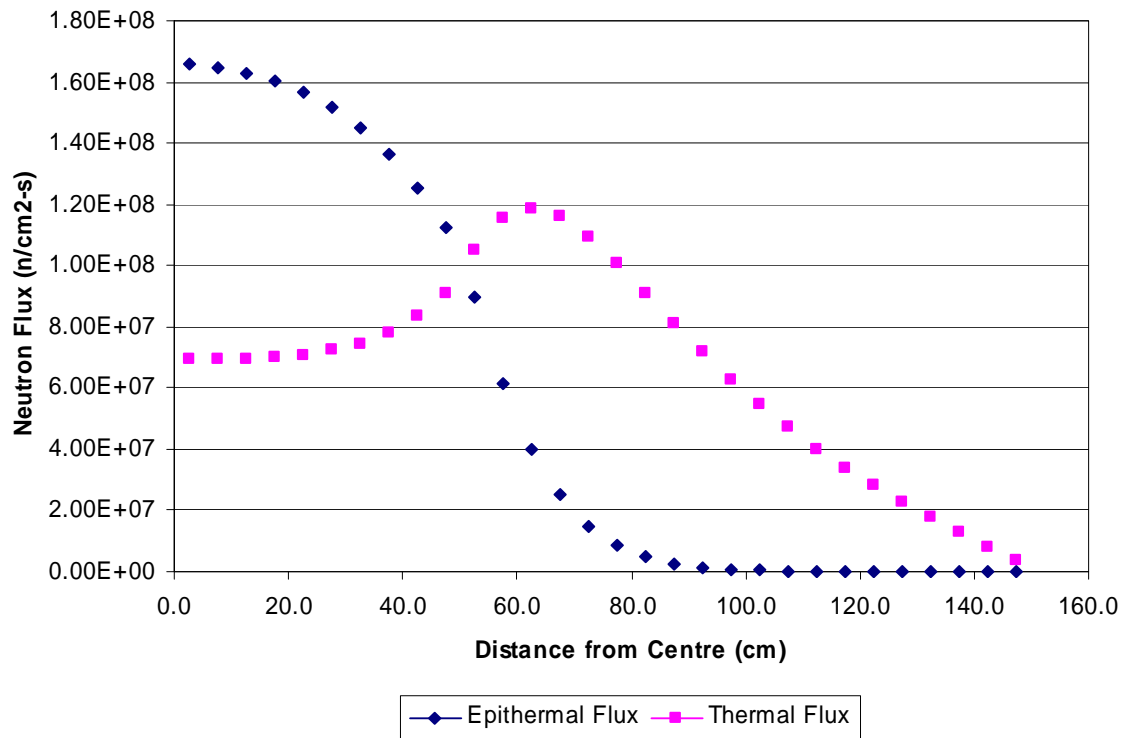


FIG. 4.114. Temperature set ii (800 K).

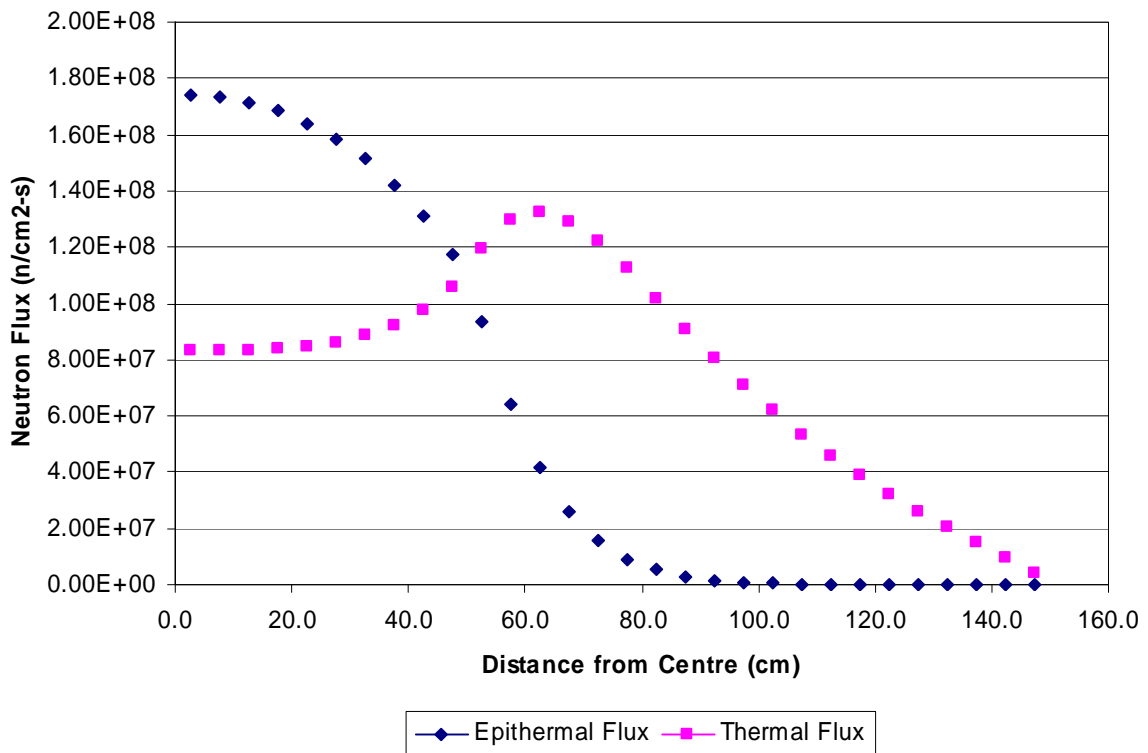


FIG. 4.115. Temperature set iii (1200 K).

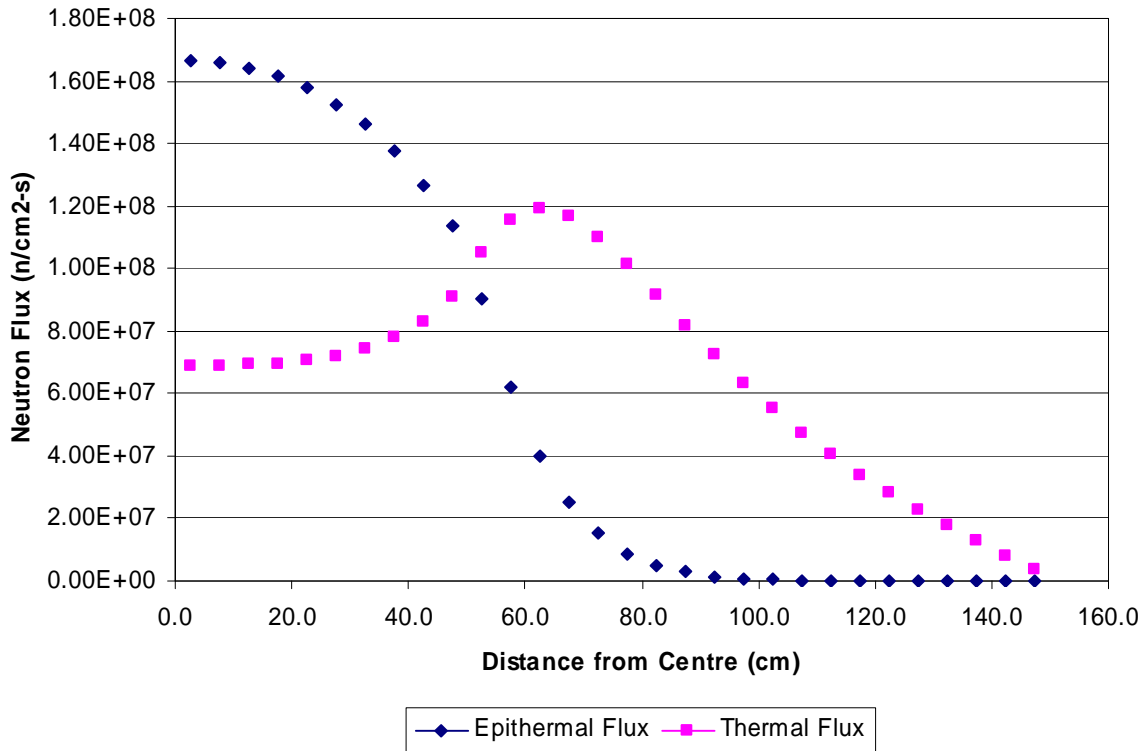


FIG. 4.116. Temperature set iv (800 and 1200 K).

Case 6

The calculated epithermal and thermal flux profiles for Case 6 for different temperature sets are illustrated in Figs 4.117–4.120.

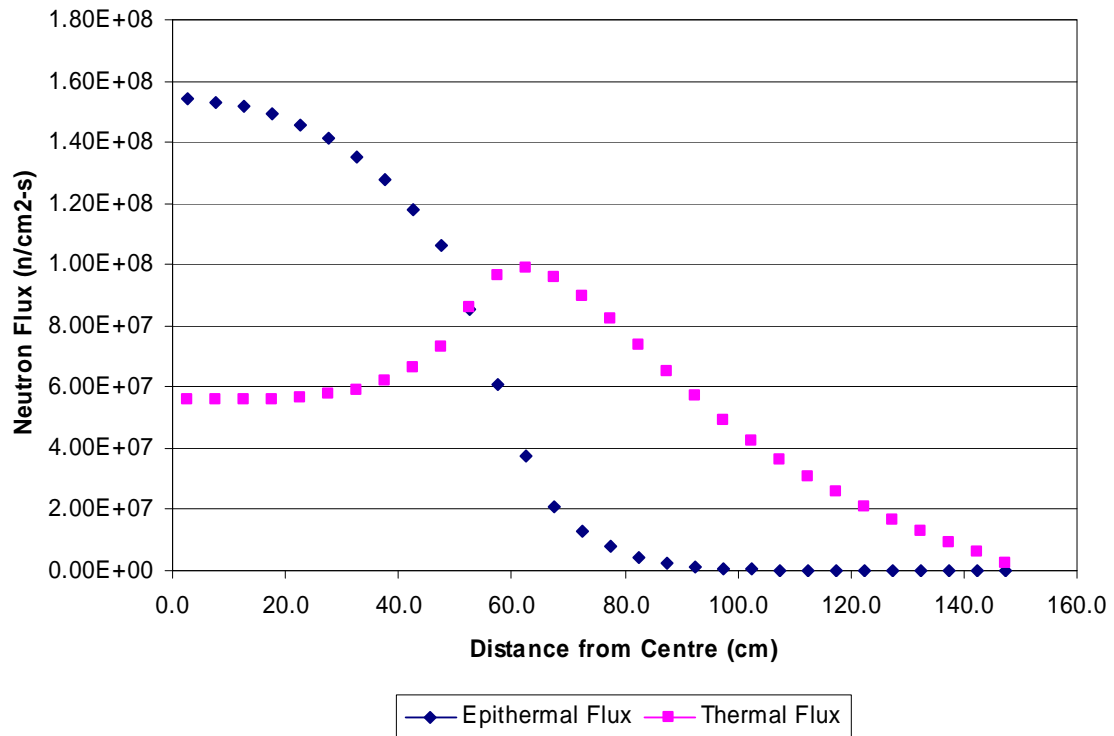


FIG. 4.117. Temperature set i (300 K).

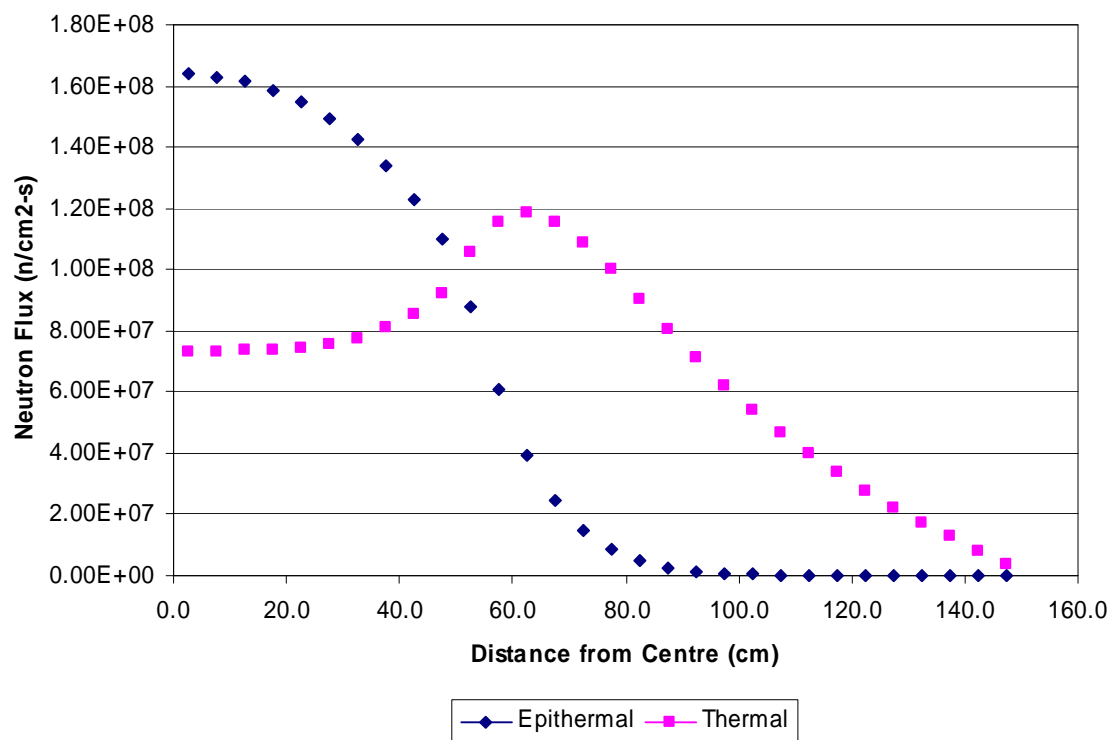


FIG. 4.118. Temperature set ii (800 K).

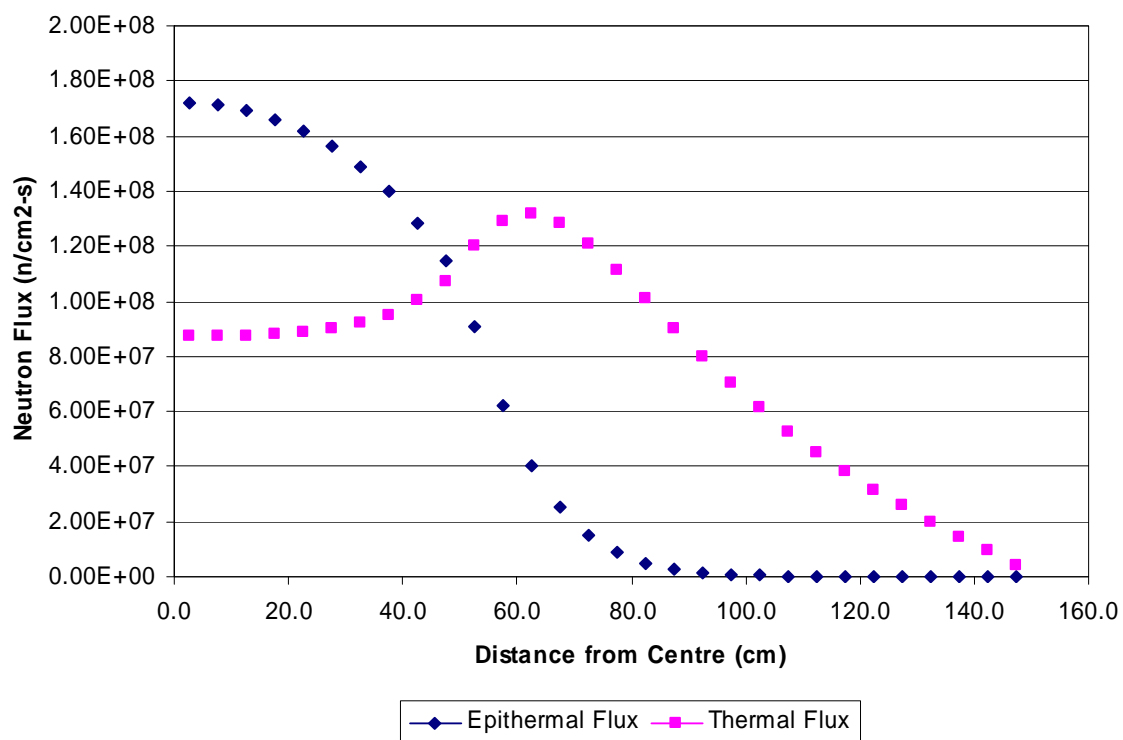


FIG. 4.119. Temperature set iii (1200 K).

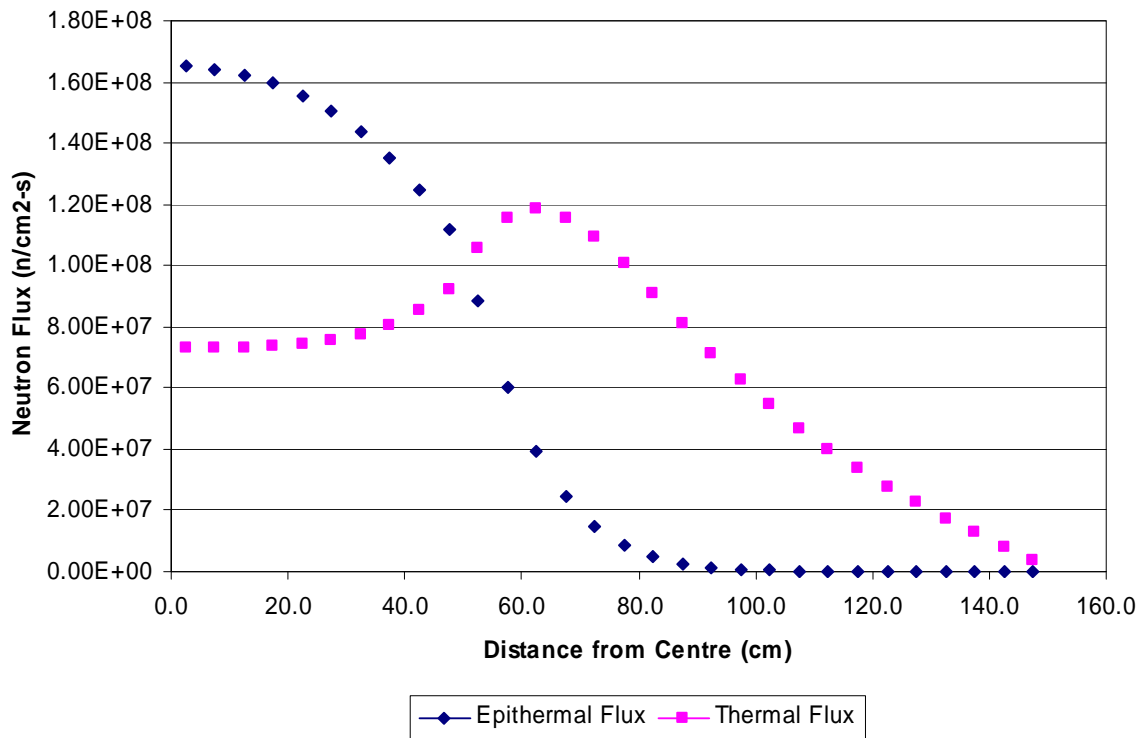


FIG. 4.120. Temperature set iv (800 and 1200 K).

Case 7: 10 ppm B-10 as Impurity

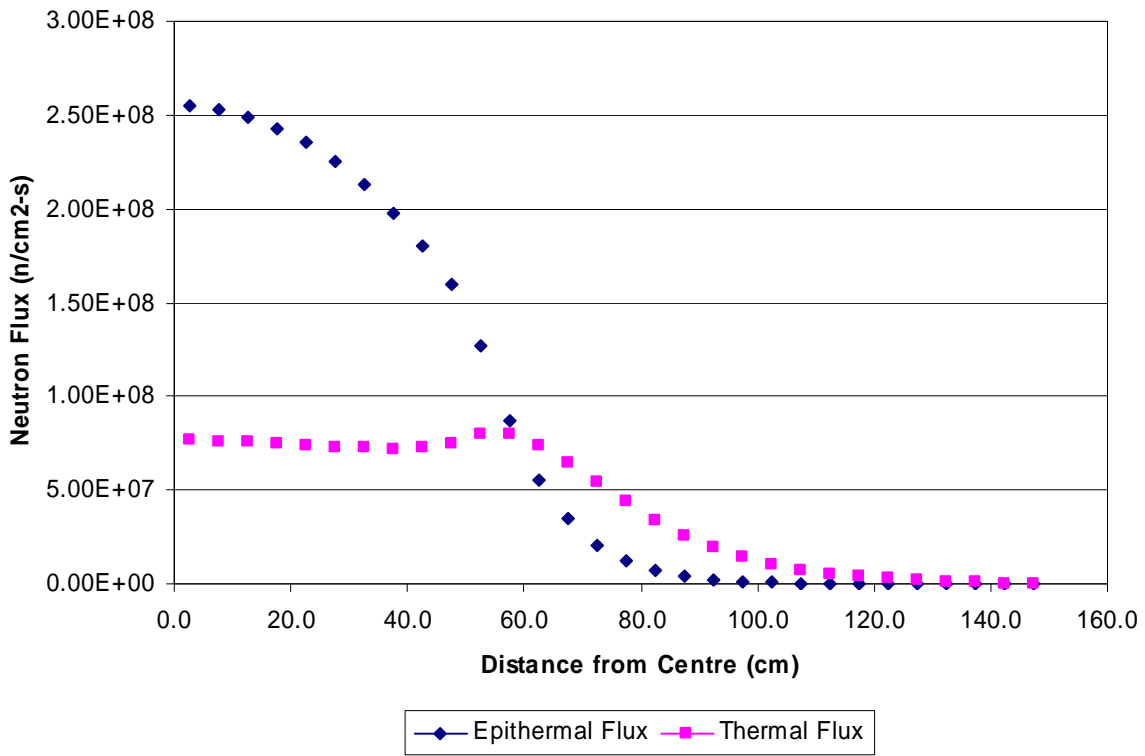


FIG. 4.121. Temperature set i (300 K).

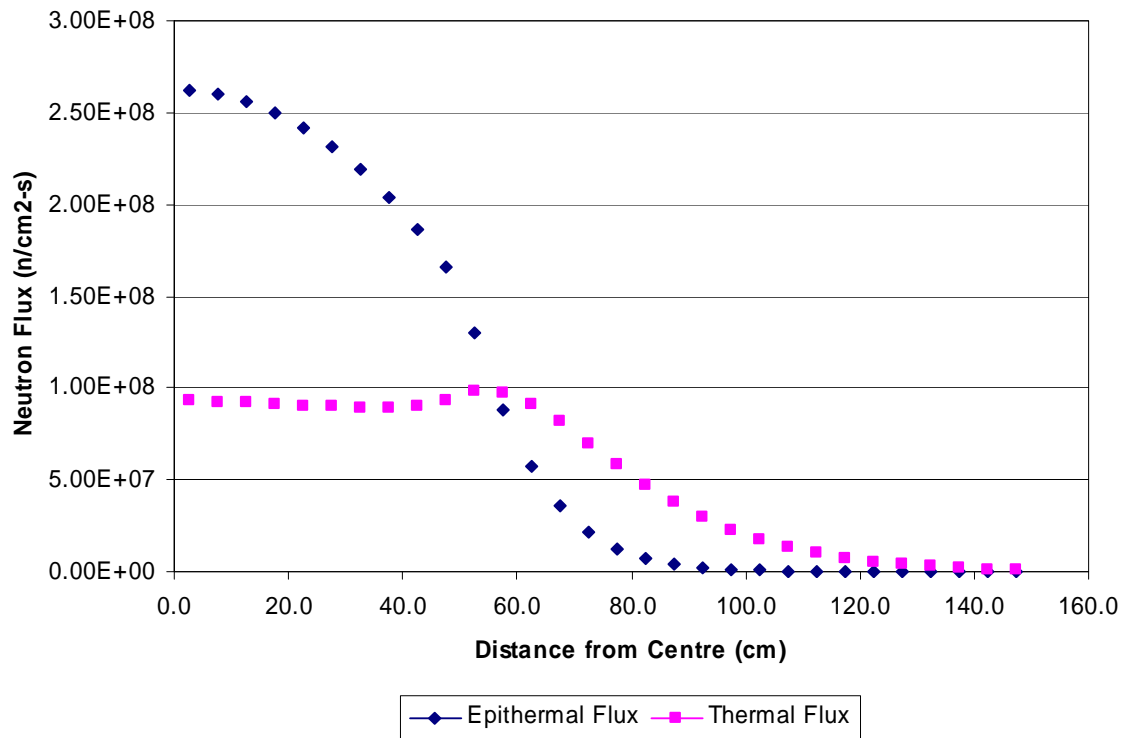


FIG. 4.122. Temperature set ii (800 K).

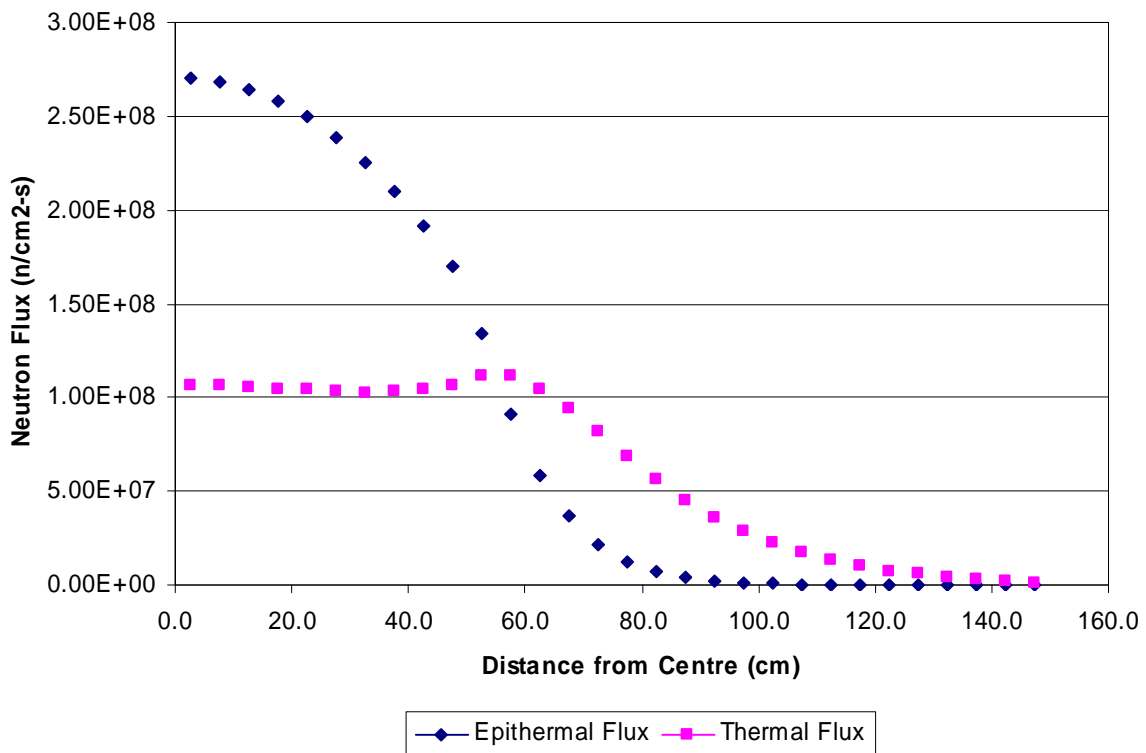


FIG. 4.123. Temperature set iii (1200 K).

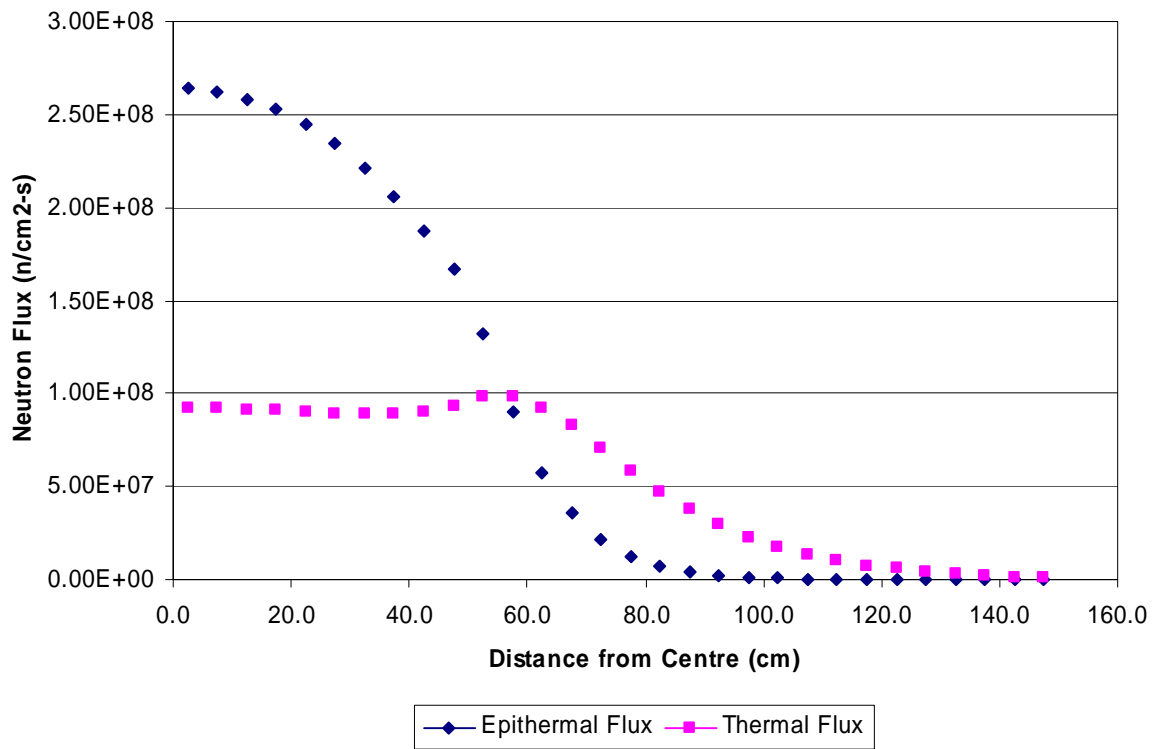


FIG. 4.124. Temperature set iv (800 and 1200 K).

Case 7: 1 ppm B-10 as Impurity

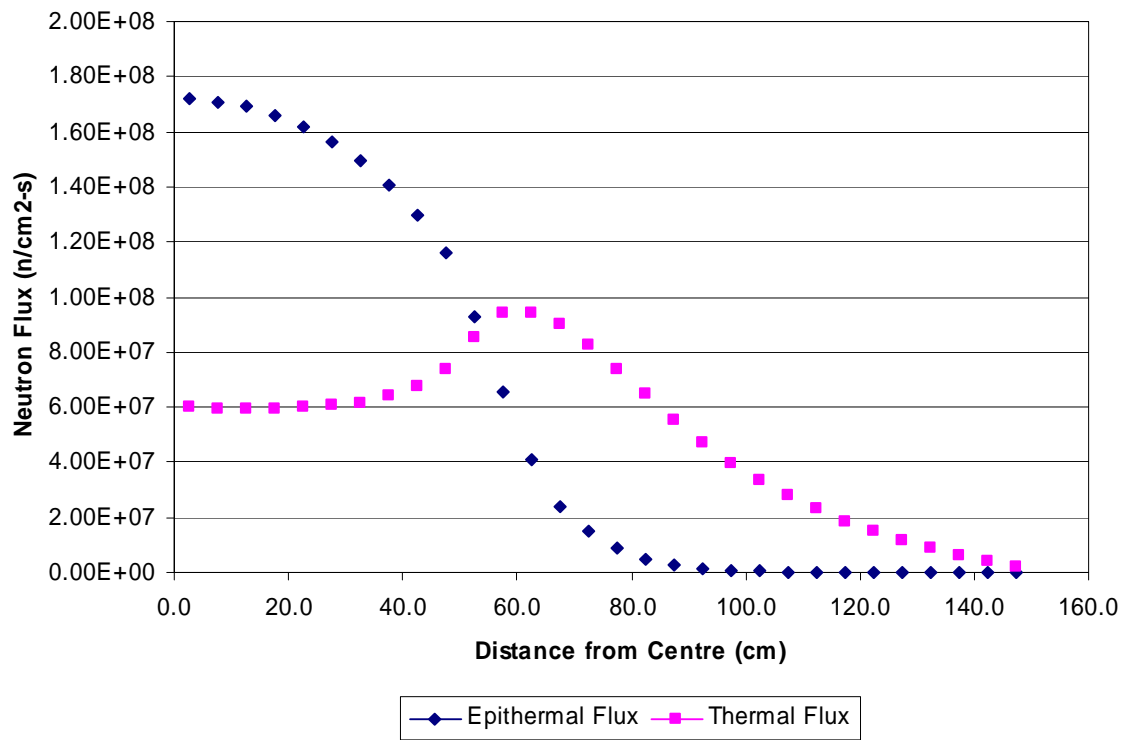


FIG. 4.125. Temperature set i (300 K).

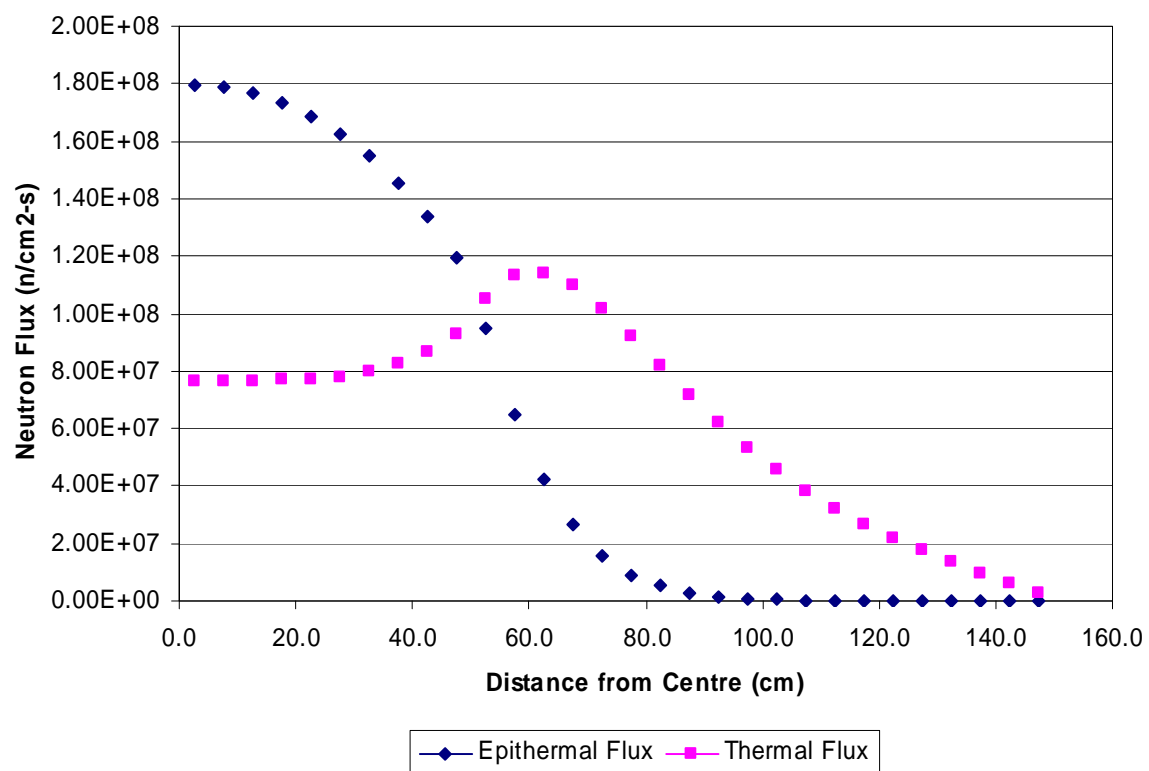


FIG. 4.126. Temperature set ii (800 K).

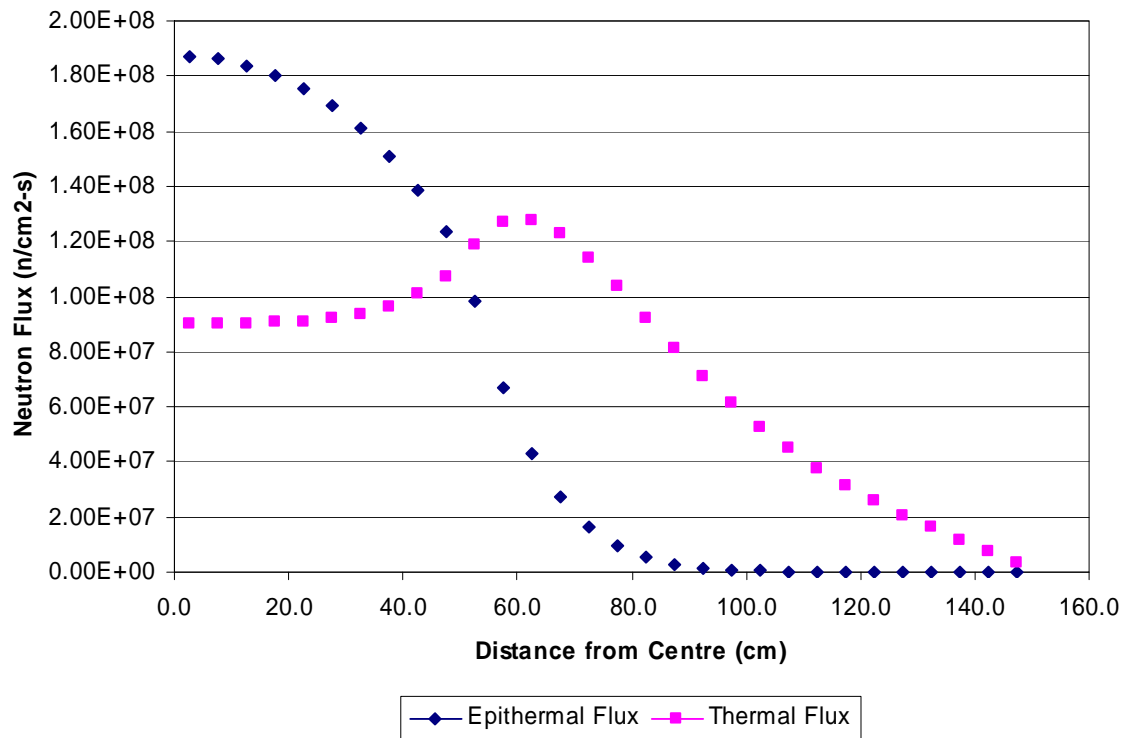


FIG. 4.127. Temperature set iii (1200 K).

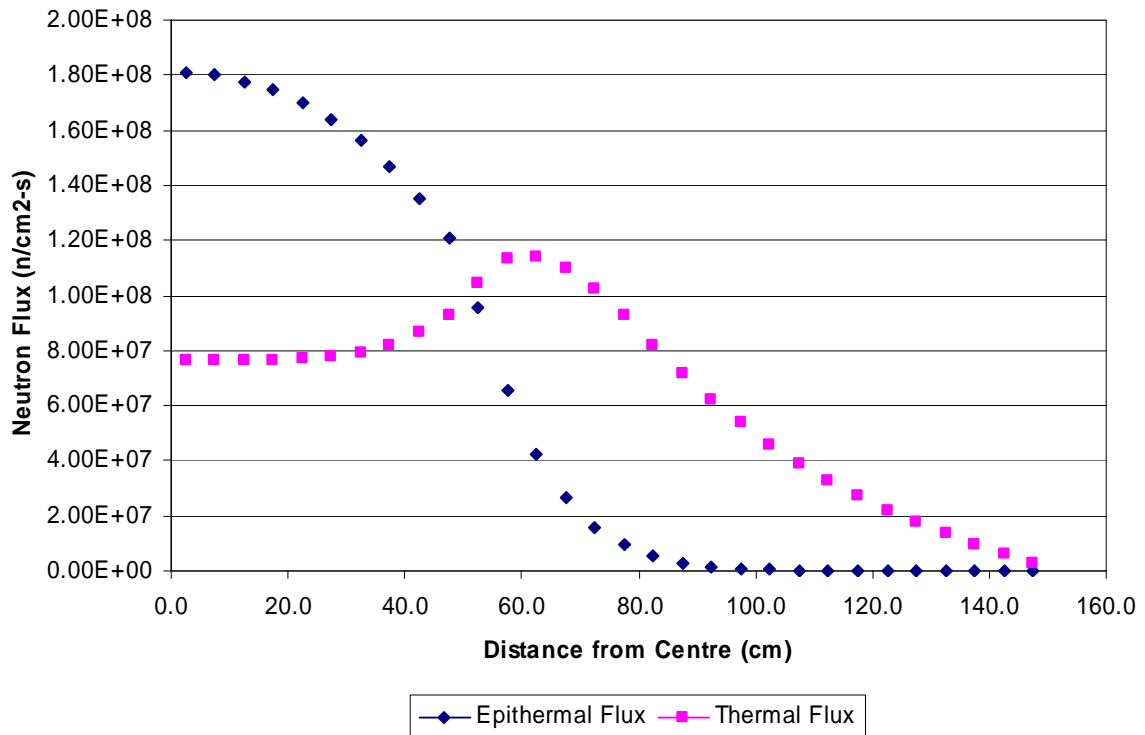


FIG. 4.128. Temperature set iv (800 and 1200 K).

Conclusions

The main purpose of the benchmark was to investigate the effects of the heterogeneity levels and the temperature changes using different calculation tools. The main effect caused by the level of heterogeneity is due to the treatment resonances and neutron streaming through the pebbles. The leakages are also investigated.

It is seen that for an infinite box, where leakage out of the system is not possible, changing from a pure homogeneous system to a double-heterogeneous system increases the effective multiplication factor by about 10000 pcm, which is purely caused by the increase in the resonance escape probabilities. When the reflected 'pebble box' system is considered, the increase in the effective multiplication factor is about 3500 pcm. Although the same resonance treatment is applied to both systems, leakages out of the system cause the decrease in the difference. The leakages from both the core and system are increased with increasing the level of heterogeneity.

The Doppler effect is clearly seen when the different temperature sets are compared. When the Temperature Sets iii and iv are compared, the multiplication factor is increased due to the decrease in the moderator temperature, which results in a negative moderator temperature coefficient. The effective multiplication factor is decreased when the Temperature Sets ii and iv are compared due to the increase in the fuel temperature.

4.3.2.2. *United Kingdom analysis and results for the 'Pebble Box' benchmark*

Introduction

The PBMR 'pebble box' benchmark has been set up to study the methods of reactor physics analysis when applied to systems with relatively large neutron leakage. Within the United Kingdom, this study has been performed in conjunction with and was funded by the NNR of the RSA. The 'pebble box' benchmark is a valuable exercise with regard to calibrating and validating the analysis methods required for the assessment of the PBMR safety case.

To recap, the benchmark consists of a 1 m³ cube containing PBMR pebbles, surrounded by either a reflective boundary condition or a 1 m thick graphite reflector with a black outer boundary. Various levels of heterogeneity are used for the pebble representation. Additionally, a final case (Case 7) considers impurities in the graphite reflector. There are seven cases overall and the calculation conditions are as specified for the benchmark, with the exception of Case 7, which considers a B-10 impurity level of 1 ppm (rather than the 10 ppm specified in the benchmark).

Method of calculation

The analysis of the benchmark has been performed using the WIMS9 thermal reactor code scheme [4-38, 4-39]. WIMS9 contains a large number of modules for representation of different types of thermal reactor. A calculation route is set up using appropriate modules which communicate with each other via data interfaces.

The general method of calculation used for this benchmark is to produce homogenized cross-sections for the pebble bed using collision probability cell models of a pebble, which are then fed into a diffusion theory module representing the overall geometry of the problem. For the PBMR 'pebble box' benchmark, the following major modules were used:

- FLURIG: A one dimensional collision probability module which is used to represent either homogeneous fuel or pebbles in which the particulate nature of the fuel is not directly modelled. This was used for Cases 1, 2, 4 and 5.
- PROCOL: A collision probability module which represents all the levels of heterogeneity present in a PBMR pebble. That is, fuel particles with their various coatings are represented within a graphite matrix, which in turn is surrounded by a pure graphite layer to represent the whole pebble. This was used for Cases 3, 6 and 7.
- SNAP: A mesh-centred diffusion theory module which was used for this problem in XYZ geometry, to represent the cube of homogenized fuel material surrounded by either reflective boundary conditions or graphite reflector.

For each case, four different sets of fuel and reflector temperatures were used as input as shown in Table 4.66. However, WIMS9 cannot assign different fuel and moderator temperatures when these are homogenized, hence Cases 1, 2, 4 and 5 cannot be performed for Temperature Set iv, in which the fuel is at 1200 K and the moderator is at 800 K.

TABLE 4.66. FUEL AND REFLECTOR TEMPERATURE SETS USED IN THE 7 CASES

Set	‘Fuel temperature’ (i.e. the material containing the heavy metal) (K)	‘Graphite temperature’ (i.e. all other materials including kernel layers where applicable) (K)
i	300	300
ii	800	800
iii	1200	1200
iv (*)	1200	800

(*) Cases 1, 2, 4 and 5 are not available for temperature set iv.

WIMS9 contains a largely JEF2.2-based cross-section library in the 172 energy groups (details of the group structure can be found in Section 4.2.3.6). This energy group structure was used throughout the calculation without any condensation.

Mesh structure in SNAP

Equal mesh dimensions were used in the X-, Y- and Z-directions. The effects of mesh sizes on k-effective were investigated for Cases 4–7 (k-effective is not dependent on mesh size for those cases with reflective boundary conditions) by using three different mesh sizes of 10, 5 and 2.5 cm. These three mesh sizes were utilized to extrapolate k-effective to zero mesh dimension using the following equation:

$$\rho_{eff}(m) = \rho_{eff}(0) + \alpha m^2$$

where $\rho_{eff} = (k_{eff} - 1)/k_{eff}$

α is a constant found by fitting a straight line to the reactivity at the three different mesh sizes;

m is the mesh dimension.

Three mesh sizes were utilized to check that the reactivity is linearly dependent on the square of the mesh size. An example of the fitting confirming the linearity is shown in Fig. 4.129 for Case 4.

SNAP Convergence

The SNAP convergence parameters are defined by:

$$\frac{R_g^n}{S_g^n} \leq 10^{-7} \quad \text{and} \quad \left(\frac{R_g^n}{S_g^n} \right) / \left(\frac{R_g^1}{S_g^1} \right) \leq 10^{-3}$$

$$\text{where } R_g^n = \sum_{ijk} |\phi_g^n - \phi_g^{n-1}| \quad \text{and} \quad S_g^n = \sum_{ijk} |\phi_g^n|$$

ϕ_g^n is the neutron flux in energy group g at iteration n , for each cell ijk in the spatial mesh.

Results

SNAP k-effective

The SNAP k-effectives for the three different mesh sizes and their extrapolation to zero mesh size are shown in Table 4.67.

Neutron spectra and leakage

The results of the calculation of neutron spectra and leakage for temperature sets i–iv are given in Tables 4.68–4.71 respectively. The boundary between the thermal and epithermal energies is taken to be 1.86 eV. It will be noted from the WIMS9 energy group structure that it does not have a boundary at exactly 1.86 eV. Interpolation between groups 103 and 104 was used to provide the results at the required energy boundary.

The k-effectives given in Tables 4.68–4.71 are those extrapolated to zero mesh size. The remaining results were obtained from the model using 5 cm meshes.

The results presented are defined as follows:

- In-core scattering from epithermal to thermal ratio is defined as the epithermal to thermal scattering reaction rate in the fissile region, divided by the total destruction rate in the fissile region (absorption + leakage) summed over thermal and epithermal energy groups and expressed as a percentage.
- Leakage from the core to the reflector is the leakage in either the epithermal or thermal group, divided by the total destruction rate in the fissile region (absorption + leakage) summed over thermal and epithermal energy groups and expressed as a percentage.
- Total leakage from the system is the leakage summed over the epithermal and thermal groups, divided by the total destruction rate in the fissile and reflector regions (absorption + leakage) summed over thermal and epithermal energy groups and expressed as a percentage.

Figures 4.130–4.133 show the flux and power profile data for Cases 4–7 respectively.

ACKNOWLEDGEMENT

The authors wish to express their gratitude to the NNR of the RSA for providing support and funding to participate in this benchmark.

TABLE 4.67. SNAP K-EFFECTIVE AS A FUNCTION OF MESH DIMENSION

Case	Mesh dimension (cm)			Extrapolated to zero mesh
	10	5	2.5	
4i	0.97448	0.98395	0.98649	0.98724
4ii	0.92280	0.92992	0.93186	0.93241
4iii	0.88823	0.89441	0.89610	0.89658
5i	0.98526	0.99463	0.99718	0.99791
5ii	0.93382	0.94092	0.94290	0.94344
5iii	0.89896	0.90514	0.90688	0.90734
6i	1.01497	1.02403	1.02631	1.02708
6ii	0.96570	0.97257	0.97456	0.97505
6iii	0.93070	0.93668	0.93850	0.93890
6iv	0.95454	0.96146	0.96343	0.96394
7i	0.92842	0.93727	0.93965	0.94035
7ii	0.89349	0.90011	0.90199	0.90248
7iii	0.86547	0.87120	0.87284	0.87326
7iv	0.88269	0.88935	0.89122	0.89172

TABLE 4.68. SUMMARY OF RESULTS FOR TEMPERATURE SET I

Case No.	1	2	3	4	5	6	7
k_{eff}	1.3894	1.4234	1.52324	0.98724	0.99791	1.02708	0.94035
In-core scattering: epithermal -> thermal: (%)	65.157	66.899	71.971	26.223	26.872	28.57	28.819
Leakage (core to reflectors):							
Epithermal (> 1.86 eV)				59.156	59.196	59.581	59.217
Thermal (<1.86 eV)				-21.584	-21.476	-21.27	-16.534
Total				37.572	37.721	38.311	42.683
Total leakage out of the system (calculational domain) (%)				15.407	15.456	15.668	8.654
Core average spectra (epithermal-to-thermal ratio over core region)	2.3899	2.3224	2.1509	1.9771	1.9464	1.8645	2.0173
Reflector average spectra (epithermal-to-thermal ratio)				0.13169	0.13077	0.12833	0.17703

TABLE 4.69. SUMMARY OF RESULTS FOR TEMPERATURE SET II

Case No.	1	2	3	4	5	6	7
k_{eff}	1.30833	1.34399	1.45167	0.93241	0.94344	0.97505	0.90248
In-core scattering: epithermal -> thermal: (%)	63.044	64.933	70.561	25.987	26.677	28.593	28.756
Leakage (core to reflectors):							
Epithermal (> 1.86 eV)				58.248	58.325	58.751	58.506
Thermal (<1.86 eV)				-19.995	-19.883	-19.618	-15.69
Total				38.253	38.442	39.133	42.816
Total leakage out of the system (calculational domain) (%)				20.875	20.968	21.318	13.820
Core average spectra (epithermal-to-thermal ratio over core region)	2.035	1.9725	1.8098	1.5327	1.5106	1.4484	1.5685
Reflector average spectra (epithermal-to-thermal ratio)				0.10588	0.10506	0.10287	0.1329

TABLE 4.70. SUMMARY OF RESULTS FOR TEMPERATURE SET III

Case No.	1	2	3	4	5	6	7
k_{eff}	1.26942	1.30493	1.4138	0.89658	0.90734	0.9389	0.87326
In-core scattering: epithermal -> thermal: (%)	63.305	65.247	71.146	26.365	27.072	29.091	29.228
Leakage (core to reflectors):							
Epithermal (> 1.86 eV)				57.864	57.954	58.391	58.185
Thermal (<1.86 eV)				-18.79	-18.671	-18.364	-14.816
Total				39.074	39.283	40.027	43.369
Total leakage out of the system (calculational domain) (%)				23.474	23.591	24.014	16.504
Core average spectra (epithermal-to-thermal ratio over core region)	1.8134	1.7572	1.6086	1.35	1.3314	1.278	1.3799
Reflector average spectra (epithermal-to-thermal ratio)				0.0967	0.09592	0.09385	0.11787

TABLE 4.71. SUMMARY OF RESULTS FOR TEMPERATURE SET IV
(NOT AVAILABLE FOR CASES 1, 2, 4 AND 5)

Case No.	1	2	3	4	5	6	7
k_{eff}			1.41778			0.96394	0.89172
In-core scattering: epithermal \rightarrow thermal: (%)			68.812			28.008	28.167
Leakage (core to reflectors):							
Epithermal (> 1.86 eV)						58.598	58.352
Thermal (< 1.86 eV)						-19.635	-15.729
Total						38.963	42.622
Total leakage out of the system (calculational domain) (%)						21.231	13.765
Core average spectra (epithermal-to-thermal ratio over core region)			1.8488			1.4616	1.5837
Reflector average spectra (epithermal-to- thermal ratio)						0.10338	0.13357

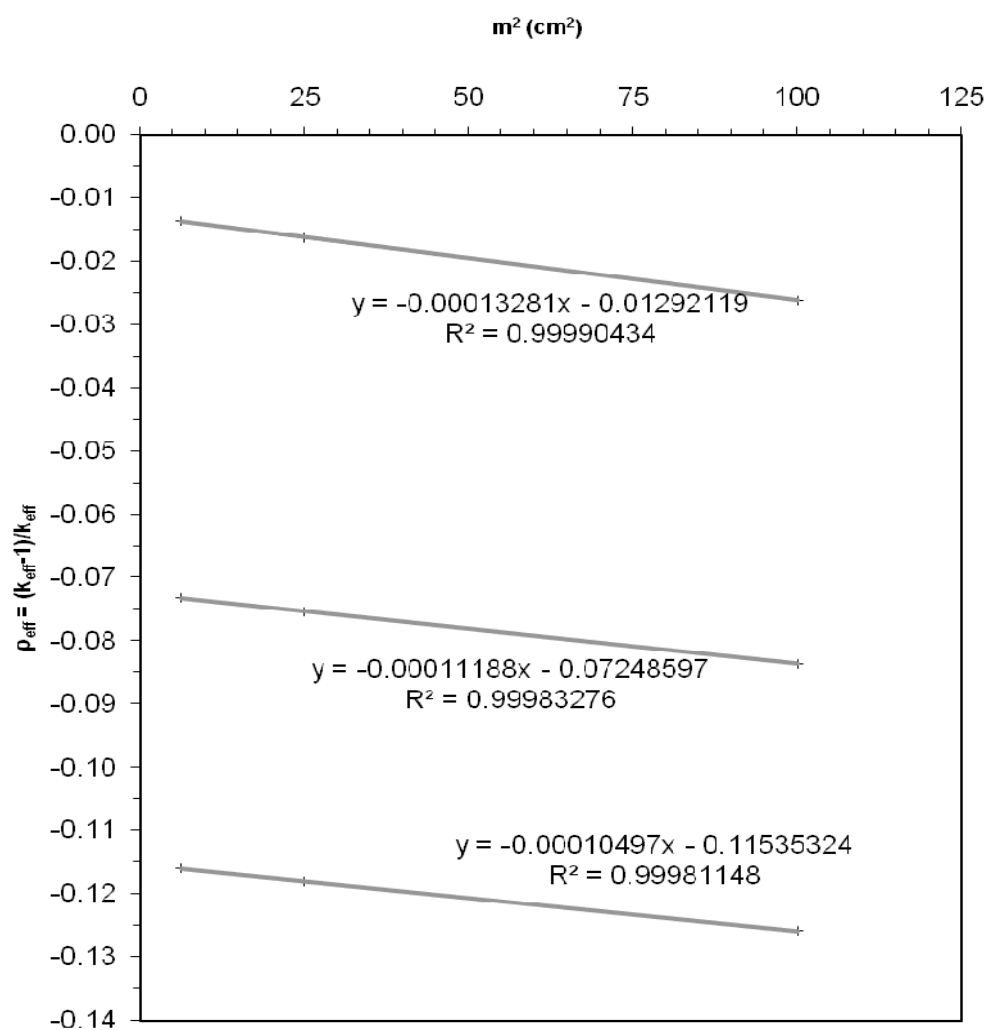


FIG. 4.129. SNAP reactivity as a function of mesh size for case 4.

Case 4 Temperature Set i

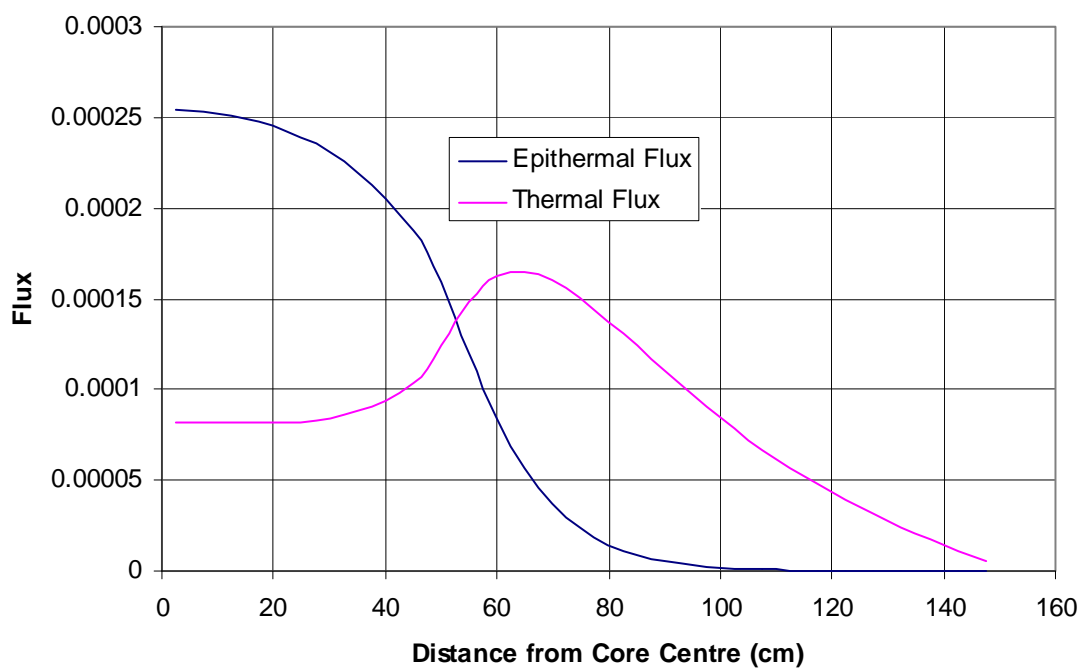


FIG. 4.130(a). Case 4 flux profiles, temperature set i.

Case 4 Temperature Set ii

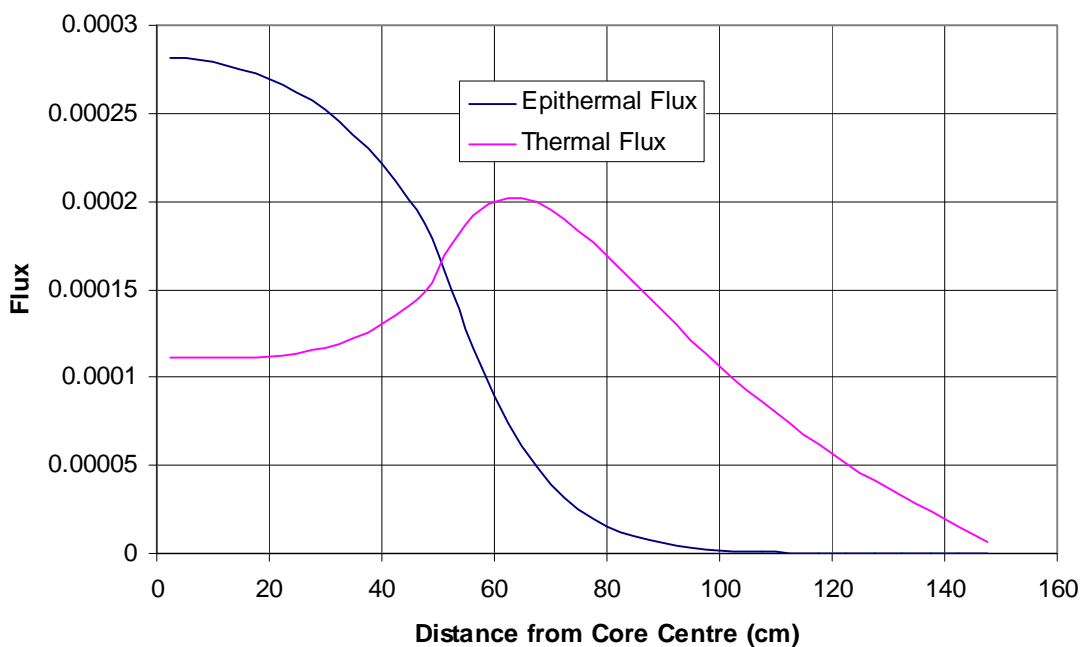


FIG. 4.130(b). Case 4 flux profiles, temperature set ii.

Case 4 Temperature Set iii

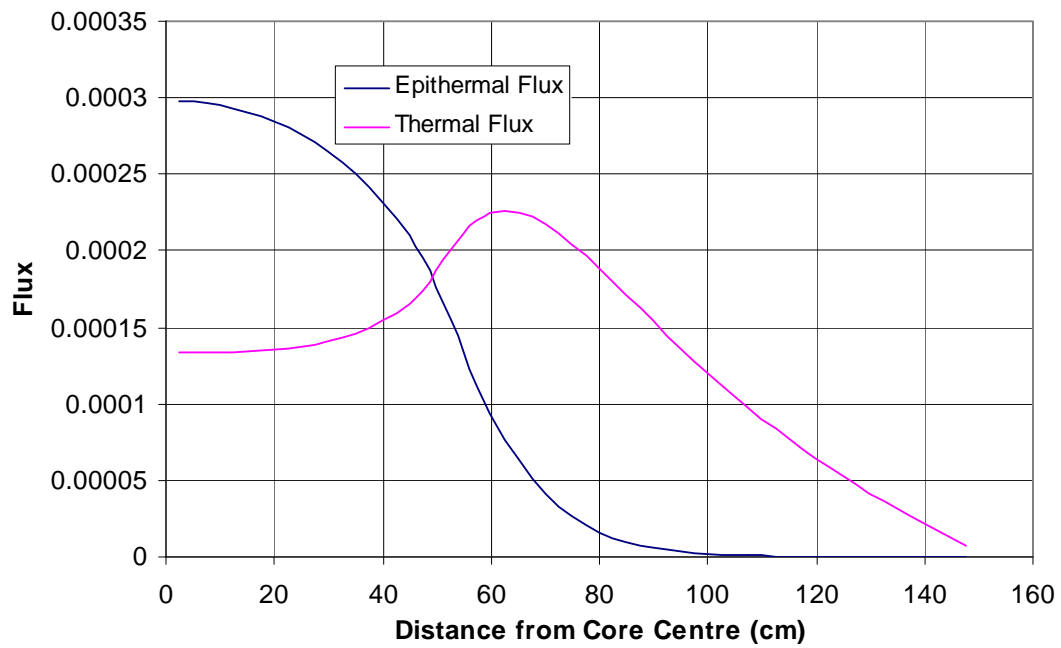


FIG. 4.130(c). Case 4 flux profiles, temperature set iii.

Case 4 Epithelial to Thermal Ratios

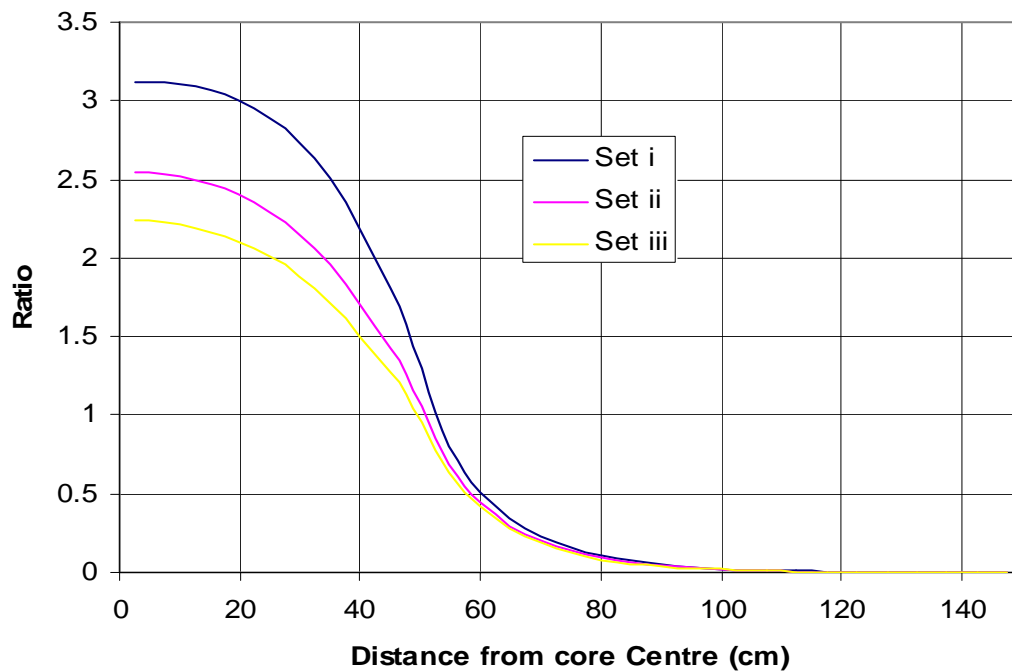


FIG. 4.130(d). Case 4 epithelial to thermal ratios.

Case 4 Power Profiles

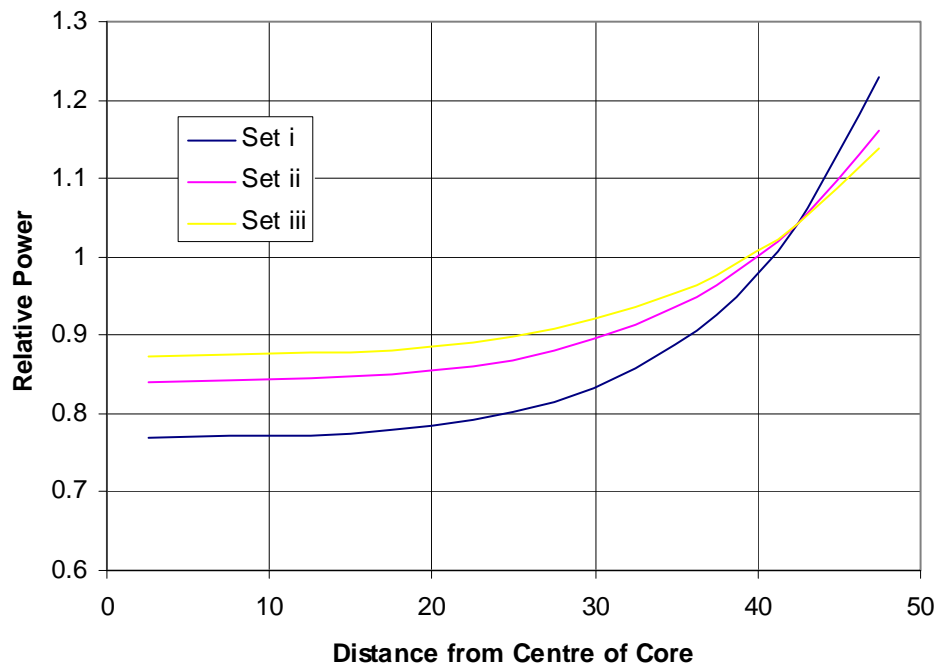


FIG. 4.130(e). Case 4 power profiles.

Case 5 Temperature Set i

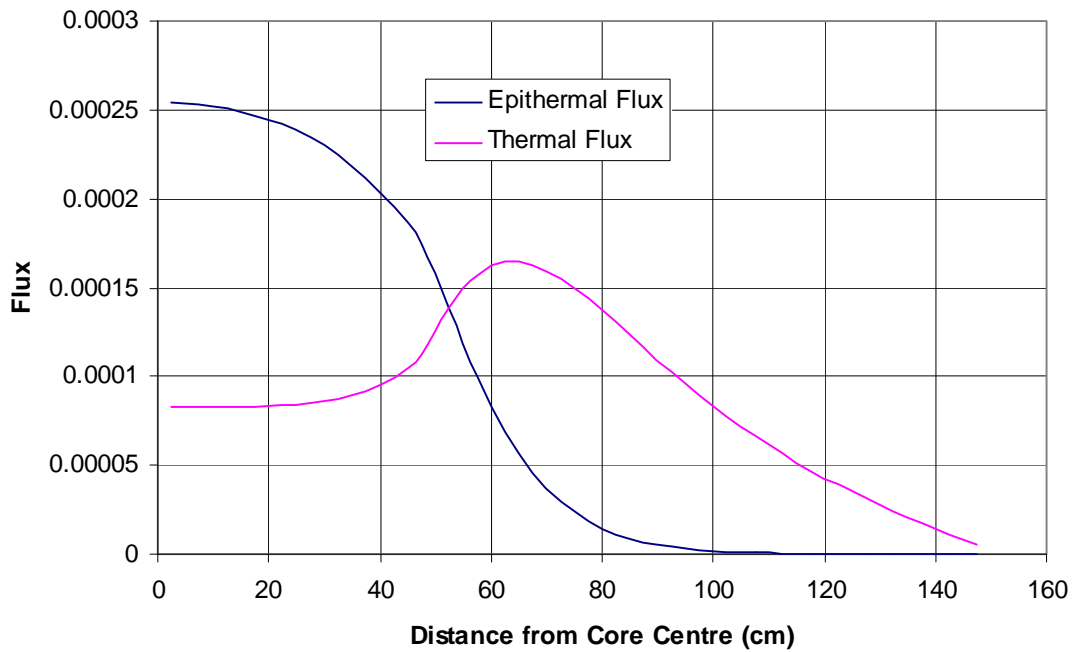


FIG. 4.131(a). Case 5 flux profiles, temperature set i.

Case 5 Temperature Set ii

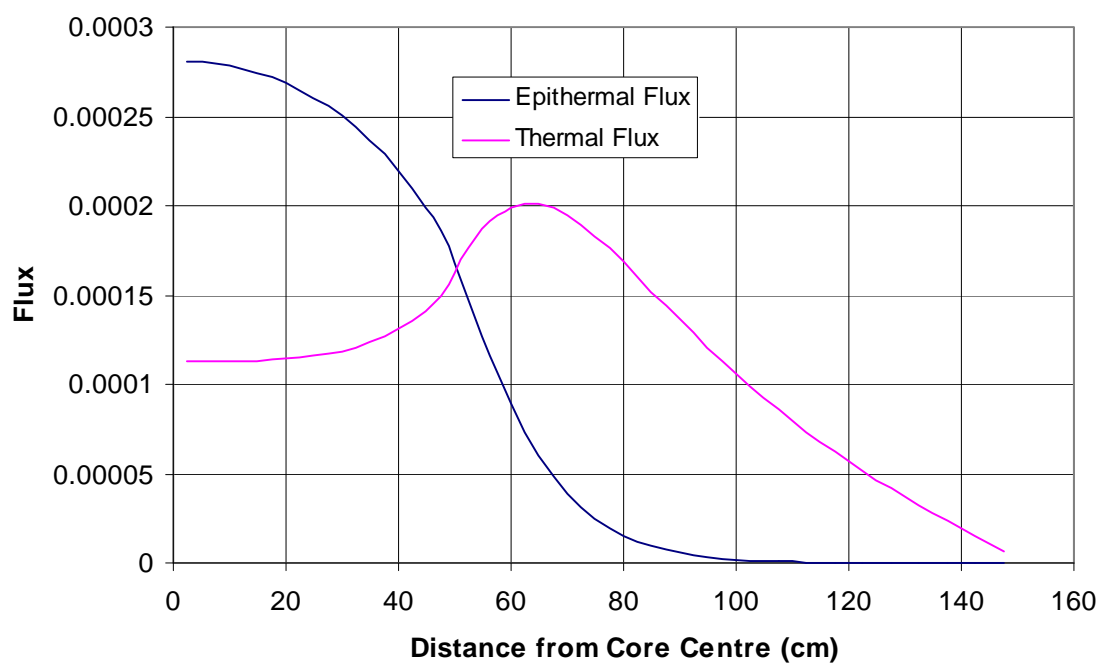


FIG. 4.131(b). Case 5 flux profiles, temperature set ii.

Case 5 Temperatures Set iii

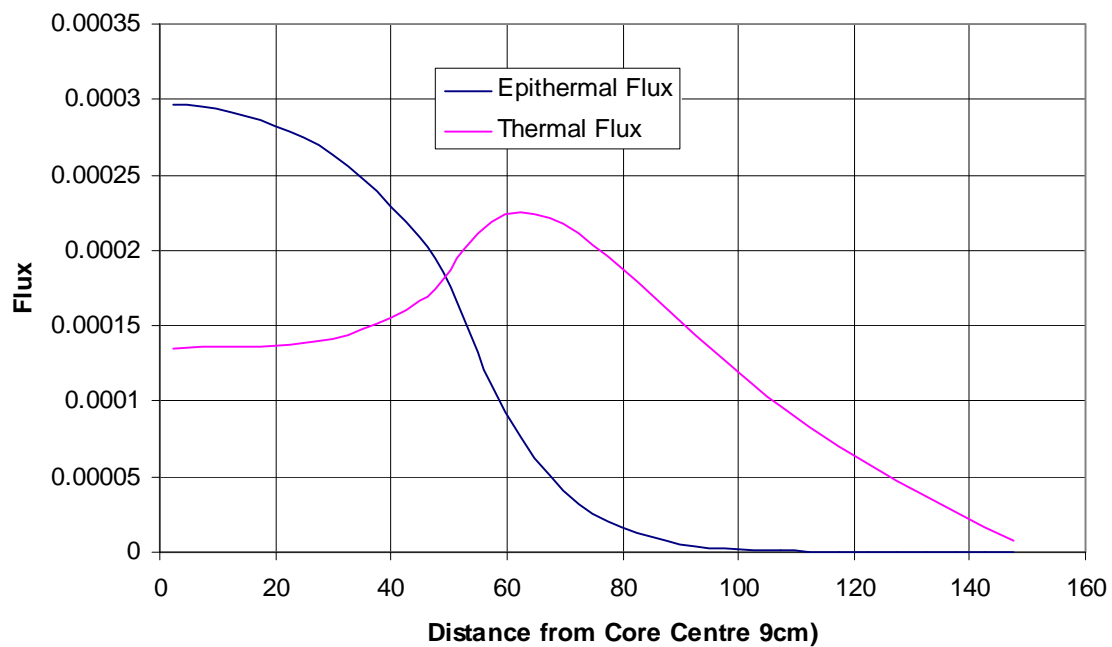


FIG. 4.131(c). Case 5 flux profiles, temperature set iii.

Case 5 Epithermal to Thermal Ratios

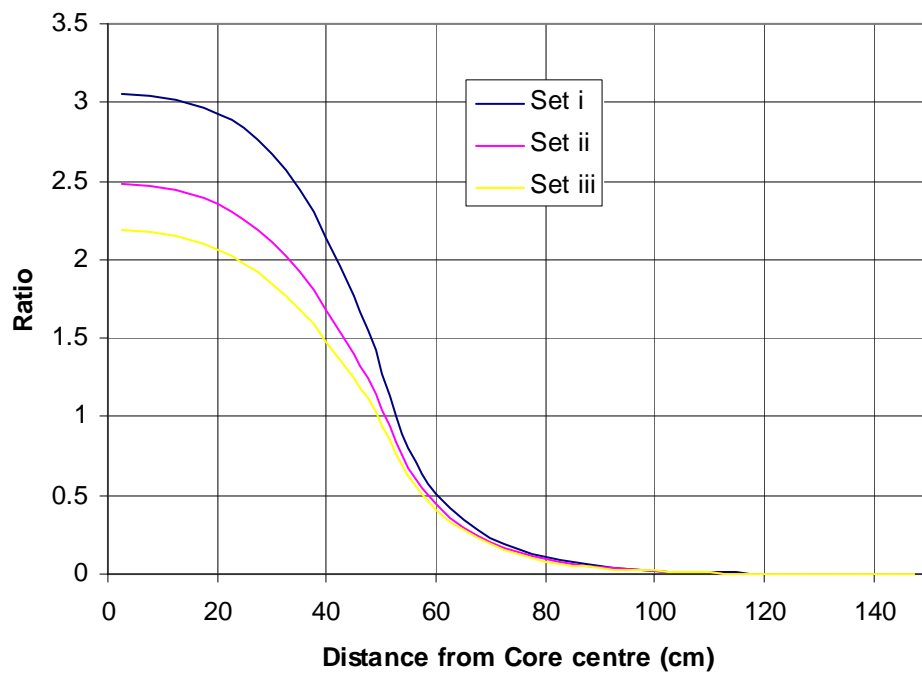


FIG. 4.131(d). Case 5 epithermal to thermal ratios.

Case 5 Power Profiles

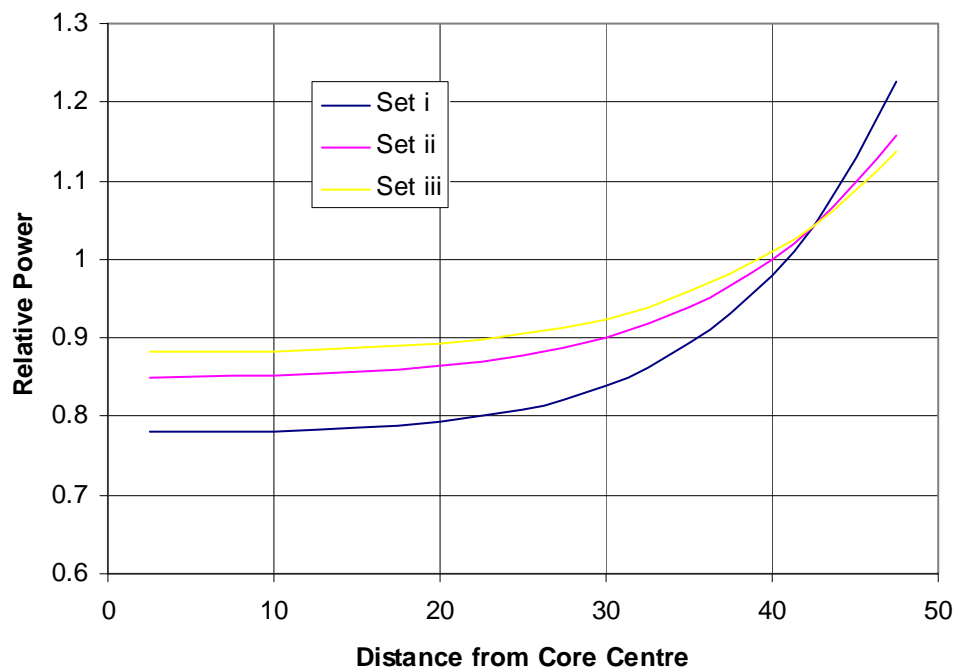


FIG. 4.131(e). Case 5 power profiles.

Case 6 Temperature Set i

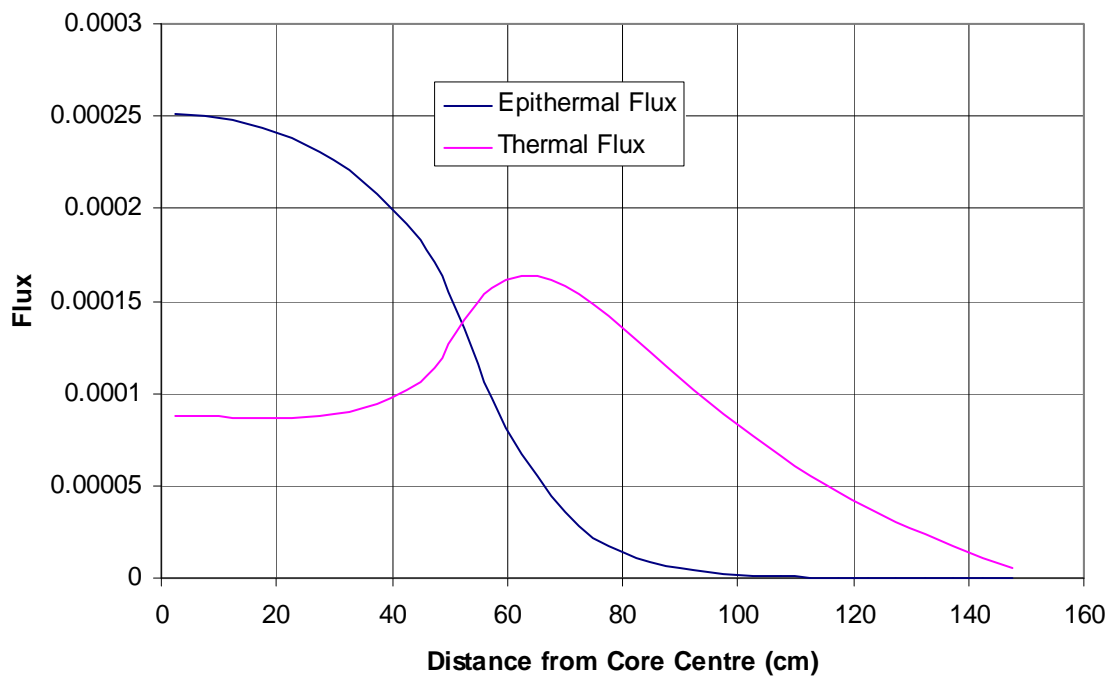


FIG. 4.132(a). Case 6 flux profiles, temperature set i.

Case 6 Temperature Set ii

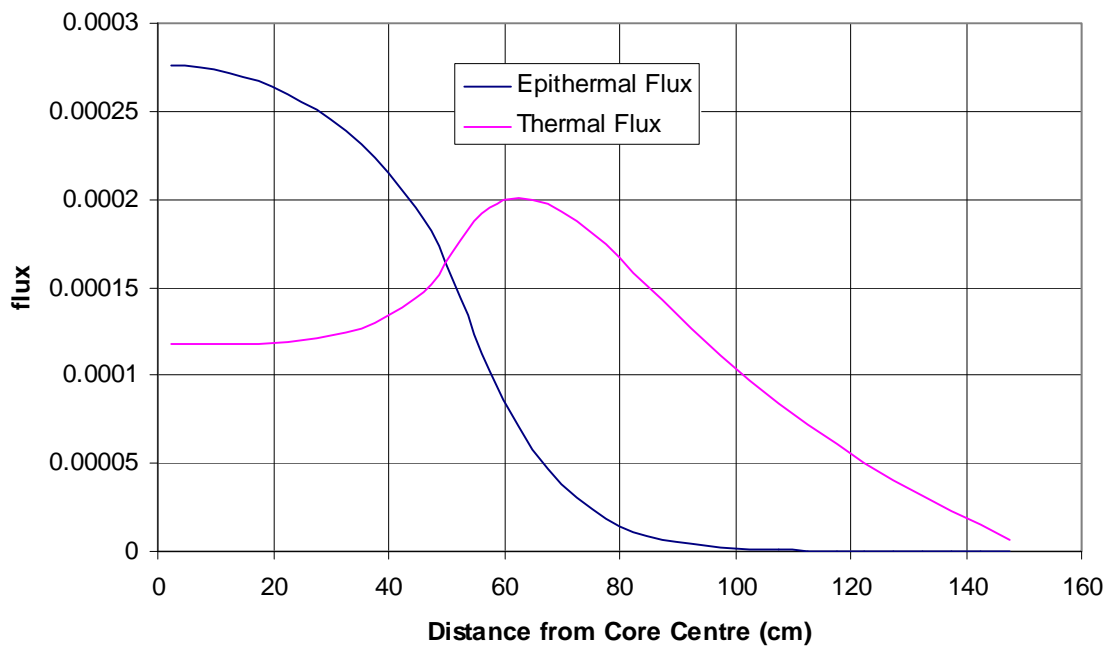


FIG. 4.132(b). Case 6 flux profiles, temperature set ii.

Case 6 Temperature Set iii

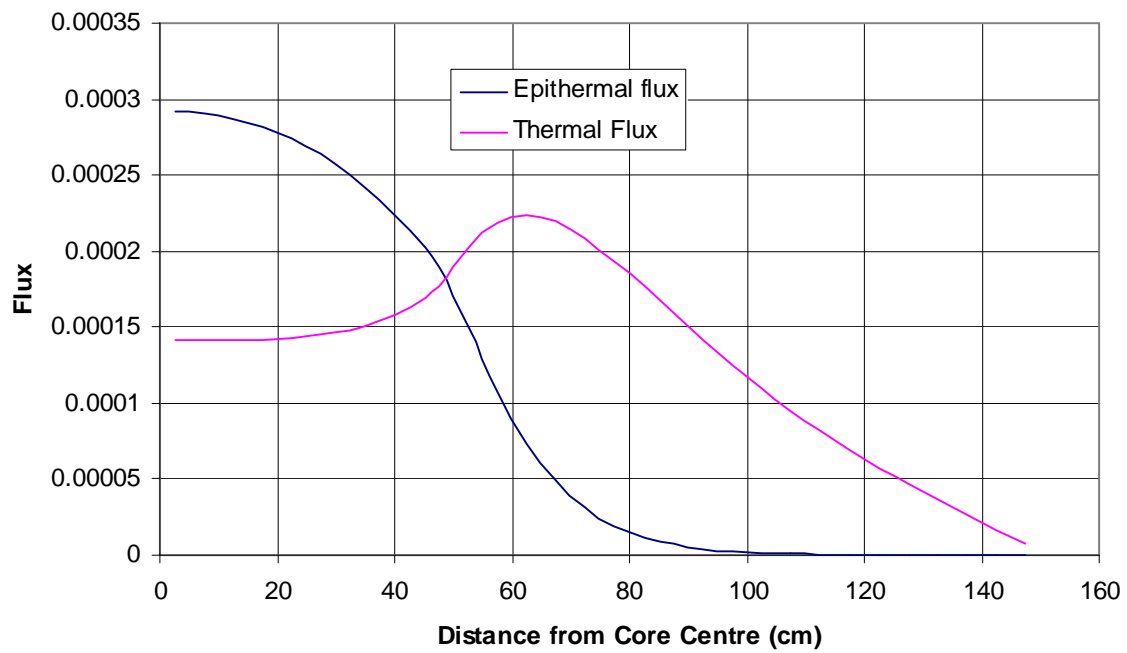


FIG. 4.132(c). Case 6 flux profiles, temperature set iii.

Case 6 Temperature Set iv

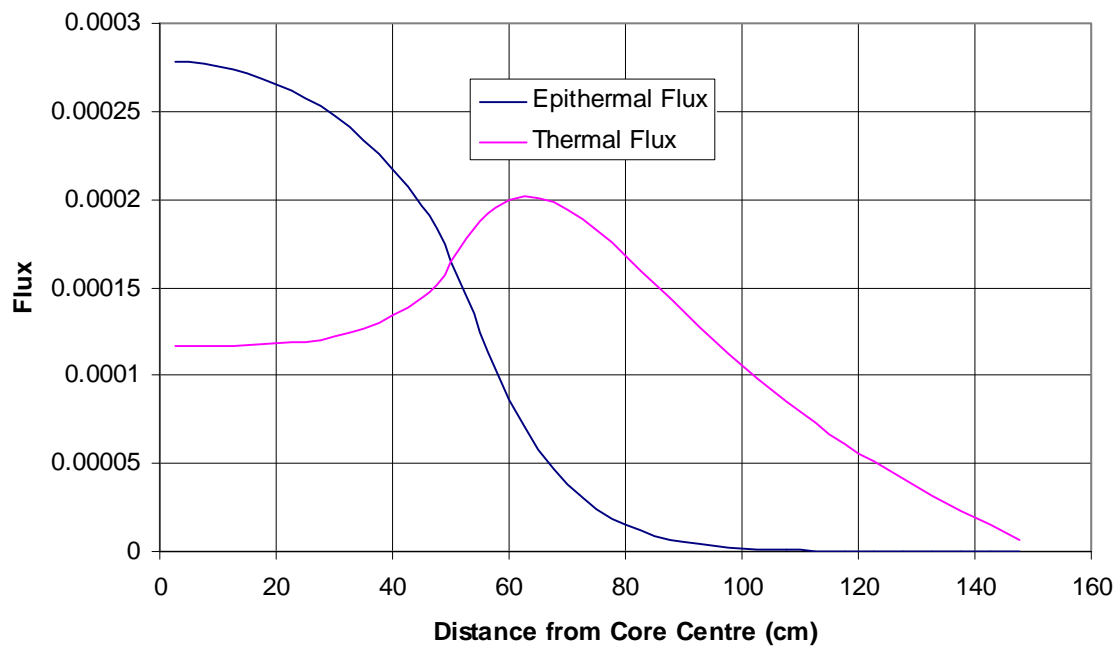


FIG. 4.132(d). Case 6 flux profiles, temperature set iv.

Case 6 Epithermal to Thermal Ratios

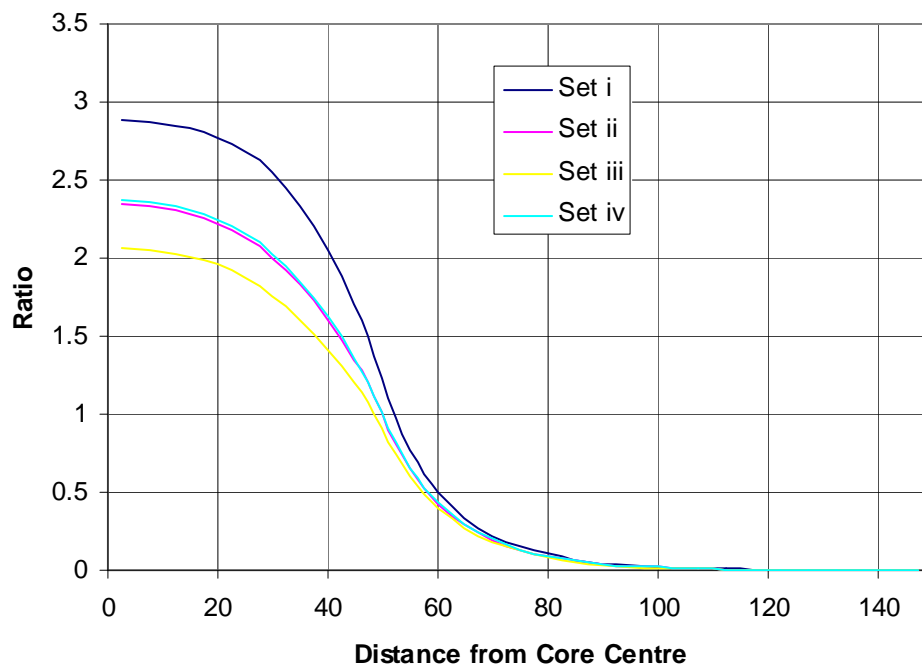


FIG. 4.132(e). Case 6 epithermal to thermal ratios.

Case 6 Power Profiles

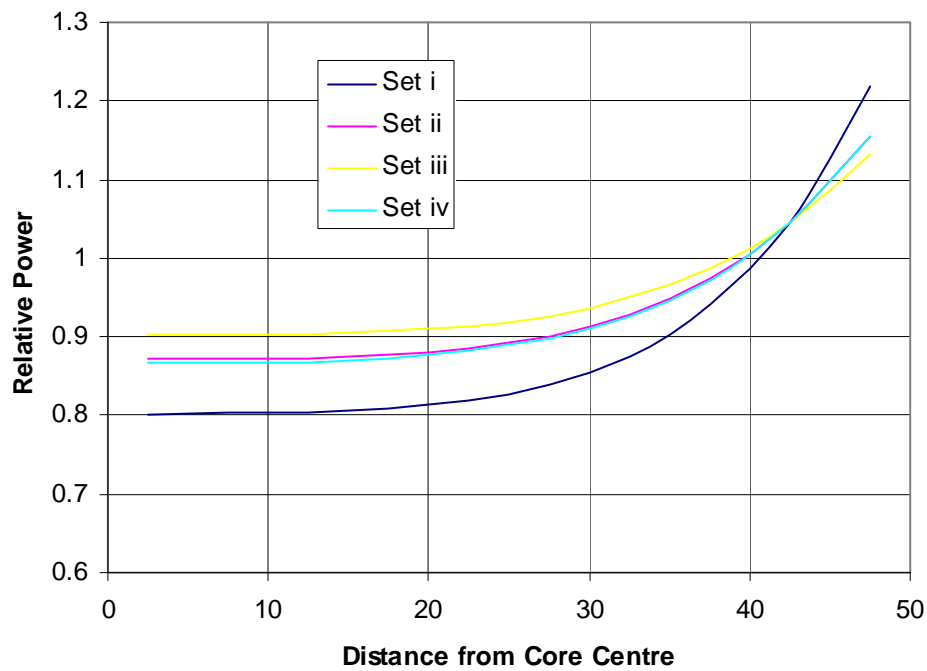


FIG. 4.132(f). Case 6 power profiles.

Case 7 Temperature Set i

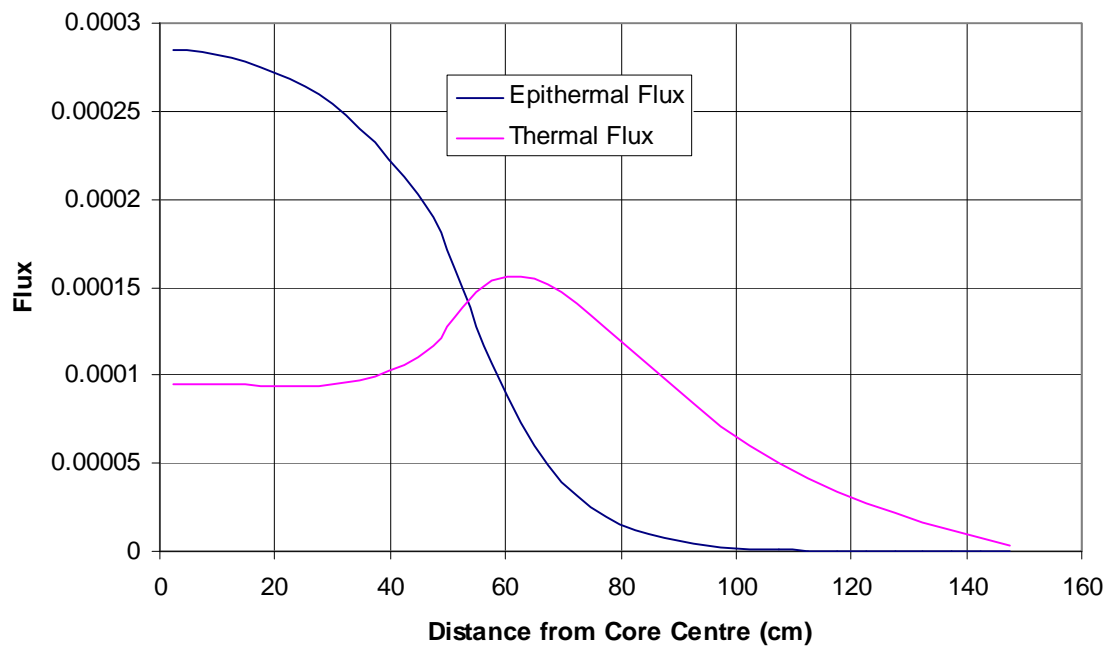


FIG. 4.133(a). Case 7 flux profiles, temperature set i.

Case 7 Temperatures Set ii

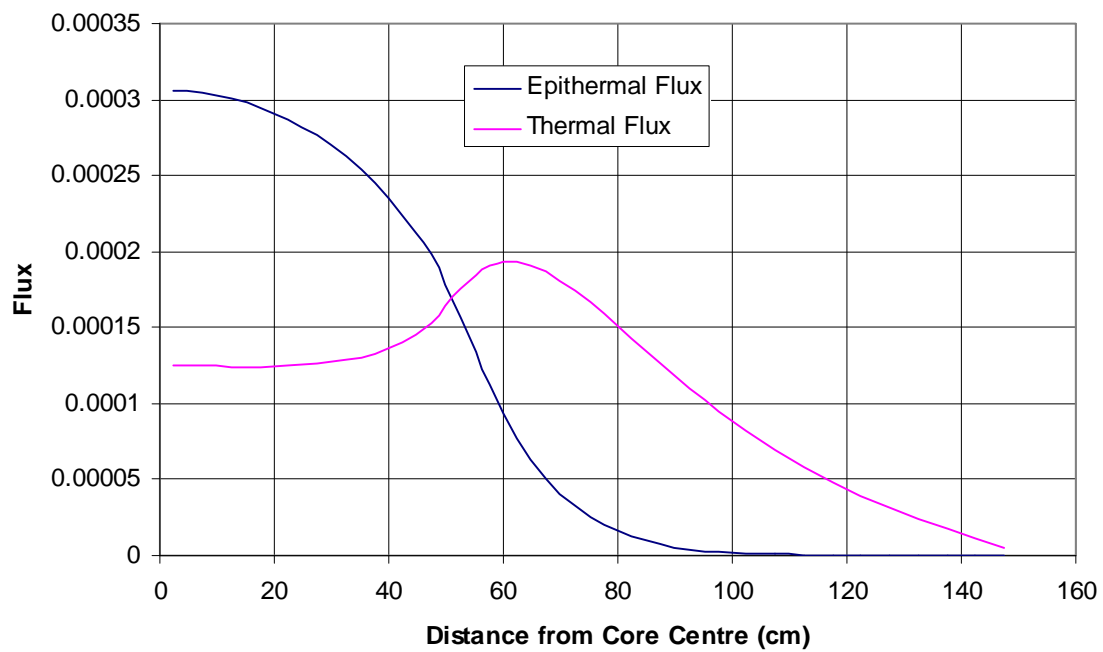


FIG. 4.133(b). Case 7 flux profiles, temperature set ii.

Case 7 Temperature Set iii

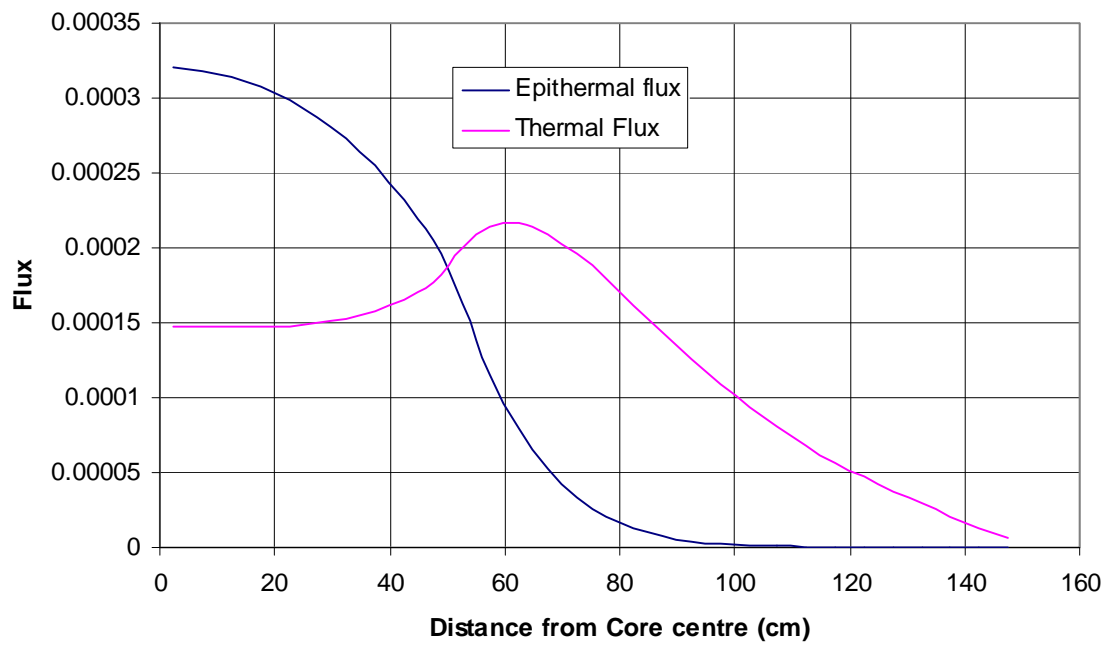


FIG. 4.133(c). Case 7 flux profiles, temperature set iii.

Case 7 Temperature Set iv

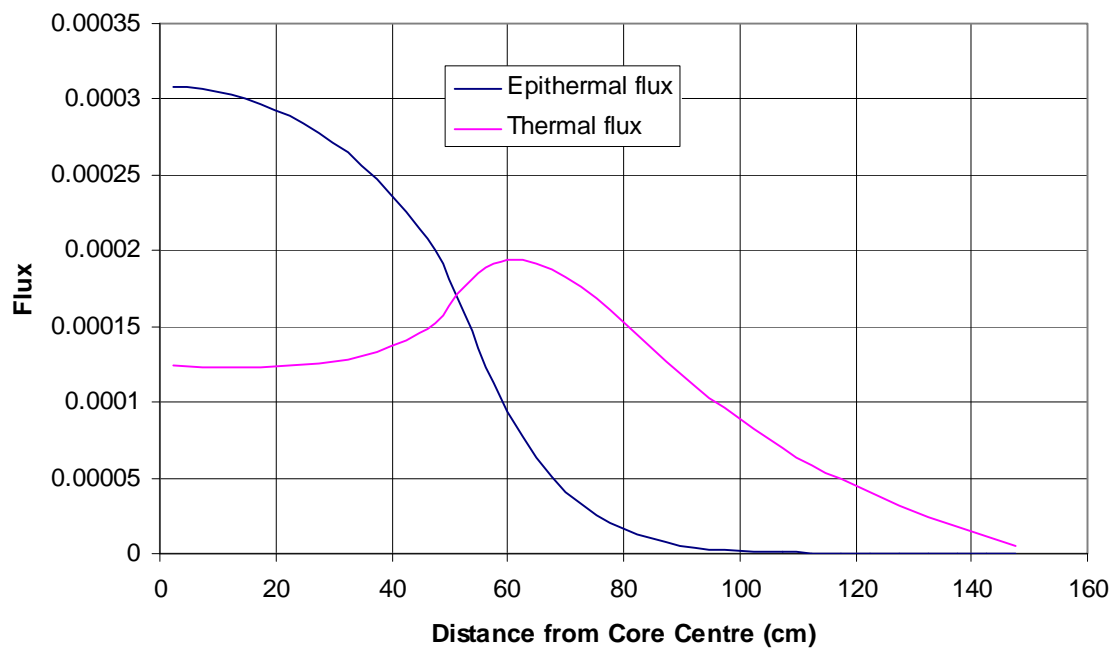


FIG. 4.133(d). Case 7 flux profiles, temperature set iv.

Case 7 Epithermal to Thermal Ratios

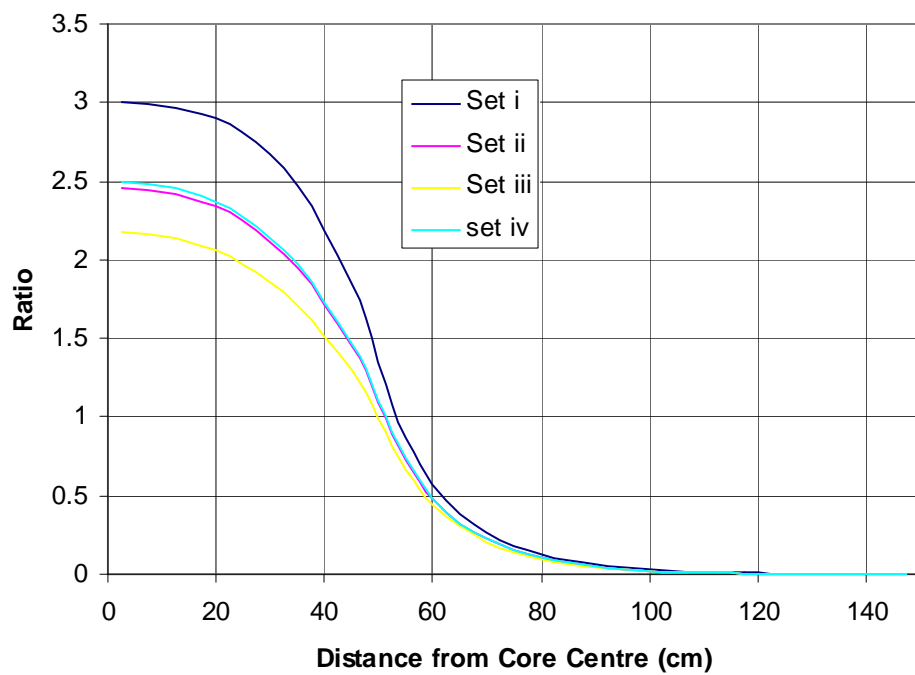


FIG. 4.133(e). Case 7 epithermal to thermal ratios.

Case 7 Power Profiles

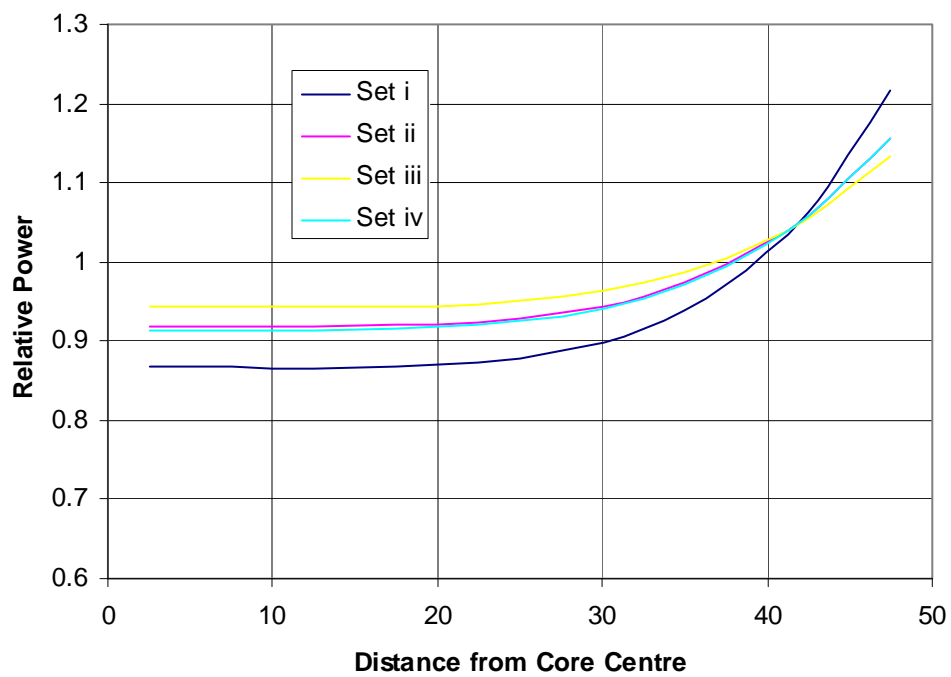


FIG. 4.133(f). Case 7 power profiles.

4.3.2.3. Pebble box results, Turkey

The summary provided here was submitted to the CRP as Ref. [4-50].

Pebble bed reactor systems introduce a number of complexities during the neutronics calculations. These complexities arise due to the geometric uncertainties as well as the double-heterogeneity associated with the system. Another shortcoming is the uncertainties associated with the codes, models employed and cross-sections utilized. Thus, it may not be adequate to check such uncertainties for the whole-core calculations. Therefore, it is useful to construct small systems representing partial structures in real cases. The ‘pebble box’ benchmark problem is such a problem representing a small unit.

The pebble box benchmark problem consists of a number of cases. The cases are constructed with a core structure, a cube with 1 m of side length. The different core configurations are taken into account. These are fully homogeneous core, pebbles with homogenized fuel section, and pebbles explicitly constructed with TRISO particles. The core region is covered with reflecting surfaces. In the second series of cases, the same core configurations are kept and the core is surrounded by a graphite reflector 1 metre thick.

Method of calculation

Calculations have been performed by the MCNP4b Monte Carlo transport code [4-51]. Cross-sections from the ENDF/B-VI dataset are used throughout the study. If the cross-sections are not provided for any specific isotope in this set, then a previous compilation has been utilized. In this analysis, it is possible to model the geometry identically with the geometry of the problem. However, certain assumptions and deviations from the exact geometry have been made due to the random nature of the problem in this case. The computational cell is shown in Fig. 4.134. These figures show the distribution of fuel spheres in the pebble box at two different layers. The overall pebble box is constructed such that partial pebbles are eliminated. This can be noticed at the surface regions. The packing fraction in the computation cell is about 60% rather than 61% percent. The total number of pebbles in the box is 5343.

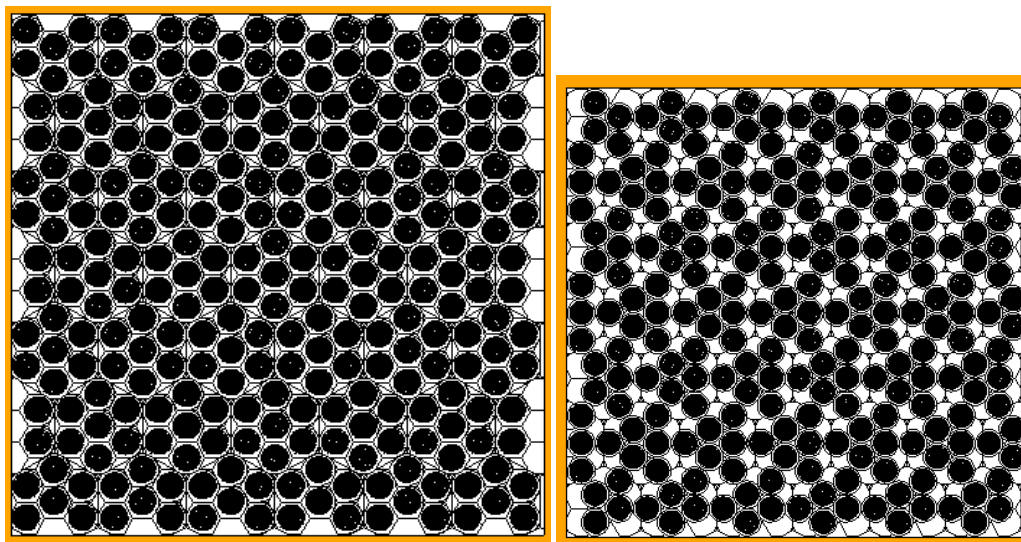


FIG. 4.134. Two layers of computational cells in the ‘Pebble Box’ benchmark problem.

Another deviation from the problem definition is the heavy metal loading per pebble. It is 9.027 g rather than 9 g. The energy boundary between the thermal and fast group is 1.86 eV. A weight cut-off of 3.1775E-02 is applied during the simulations. Neutrons with greater weights are tracked but when their weights dropping below this value are killed. The number of histories in each case of this study is taken as 1250000 in order to reduce the variance as much as possible.

Required parameters are determined using surface and detector tallies. Group scattering is evaluated using the neutron balance considering leakage and absorption. Temperatures specified for benchmark problems are applied by changing the TEMP card as well as using proper $S(\alpha, \beta)$ dataset for the graphite used in the problem.

Results

There are four different temperature sets. These are:

300 K fuel and moderator;

800 K fuel and moderator;

1200 K fuel and moderator;

800 K moderator and 1200 K fuel.

The k-effectives for each case and temperature set are shown in Table 4.72.

TABLE 4.72. K-EFFECTIVE VALUES

	Case 1	Case 2	Case 3	Case 4	Case 5	Case 6	Case 7
Temperature Set i	1.38061	1.41251	1.52632	0.9786	1.00659	1.02014	0.69156
Temperature Set ii	1.36805	1.4053	1.51681	0.9399	0.96692	0.98528	0.67808
Temperature Set iii	1.36222	1.39932	1.51124	0.91564	0.94015	0.96083	0.66763
Temperature Set iv	1.36784	1.39939	1.51716	0.94067	0.94231	0.98459	0.67592

Other parameters such as epithermal-to-thermal scattering, leakage and average spectra are also calculated and presented in Tables 4.73–4.76.

The variations of thermal flux, epithermal flux, epithermal-to-thermal flux and relative power across the core and reflector are shown in Figs 4.135–4.150.

TABLE 4.73. RESULTS FOR TEMPERATURE SET I (300 K)

Case No.	1	2	3	4	5	6	7
k_{eff}	1.38061	1.41251	1.52632	0.9786	1.00659	1.02014	0.69156
In-core scattering epithermal \rightarrow thermal: (%)	69.99	57.52	71.86	26.07	23.09	28.11	29.20
Leakage:							
Epithermal (> 1.86 eV)				58.99	58.75	60.05	58.48
Thermal (< 1.86 eV)				-21.49	-22.10	-21.44	-3.39
Total				37.50	36.65	38.61	55.09
Total leakage out of the system (calculational domain)				15.61	15.32	16.07	5.98
Core average spectra (epithermal-to-thermal ratio over core region)	2.38	2.62	2.20	2.72	2.96	2.58	3.22
Reflector average spectra (epithermal-to- thermal ratio)				0.115	0.110	0.125	0.304

TABLE 4.74. RESULTS FOR TEMPERATURE SET II (800 K)

Case No.	1	2	3	4	5	6	7
k_{eff}	1.36805	1.4053	1.51681	0.9399	0.96692	0.98528	0.67808
In-core scattering epithermal -> thermal: (%)	69.90	57.25	71.76	26.32	23.35	28.54	47.86
Leakage:							
Epithermal (> 1.86 eV)				58.39	58.16	59.39	39.68
Thermal (<1.86 eV)				-19.64	-19.99	-19.46	-1.88
Total				38.75	38.17	39.94	37.80
Total leakage out of the system (calculational domain)				21.47	21.20	22.13	1.51
Core average spectra (epithermal-to-thermal ratio over core region)	1.93	1.98	1.71	1.99	2.16	1.88	2.61
Reflector average spectra (epithermal-to-thermal ratio)				0.0831	0.0993	0.100	0.246

TABLE 4.75. RESULTS FOR TEMPERATURE SET III (1200 K)

Case No.	1	2	3	4	5	6	7
k_{eff}	1.36222	1.39932	1.51124	0.91564	0.94015	0.96083	0.66763
In-core scattering epithermal -> thermal: (%)	69.88	57.23	71.61	26.43	23.43	28.64	29.20
Leakage:							
Epithermal (> 1.86 eV)				58.26	57.94	59.20	58.28
Thermal (<1.86 eV)				-18.55	-18.62	-18.27	-2.26
Total				39.71	39.32	40.93	56.03
Total leakage out of the system (calculational domain)				24.10	23.92	24.84	21.83
Core average spectra (epithermal-to-thermal ratio over core region)	1.68	1.68	1.52	1.79	1.82	1.73	2.36
Reflector average spectra (epithermal-to-thermal ratio)				0.0786	0.0950	0.0929	0.172

TABLE 4.76. RESULTS FOR TEMPERATURE SET IV (800, 1200 K)

Case No.	1	2	3	4	5	6	7
Data required:							
k_{eff}	1.36784	1.39939	1.51716	0.94067	0.94231	0.98459	0.67592
In-core scattering epithermal -> thermal: (%)	69.89	57.04	71.75	2.628	23.20	28.43	29.30
Leakage							
Epithermal (> 1.86 eV)				58.48	58.20	59.48	58.23
Thermal (<1.86 eV)				-19.74	-18.87	-19.51	-2.60
Total				38.73	39.33	39.97	55.63
Total leakage out of the system (calculational domain)				21.48	21.83	22.16	1.50
Core average spectra (epithermal-to-thermal ratio over core region)	1.89	1.73	1.75	2.07	1.98	1.96	2.66
Reflector average spectra (epithermal-to-thermal ratio)				0.0881	0.0983	0.1074	0.238

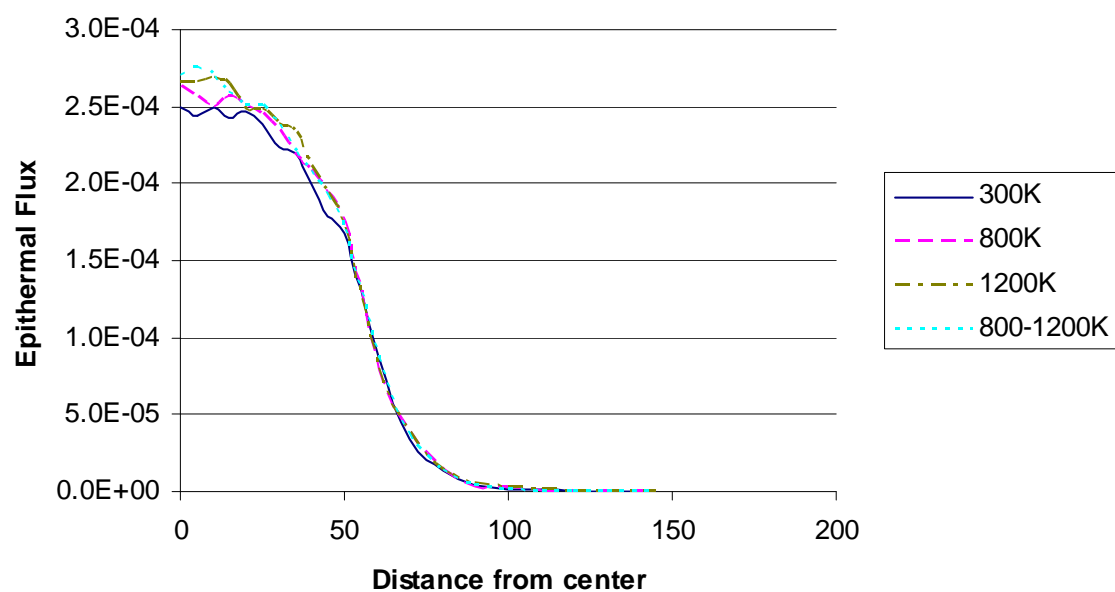


FIG. 4.135. Epithermal flux profile for case 4.

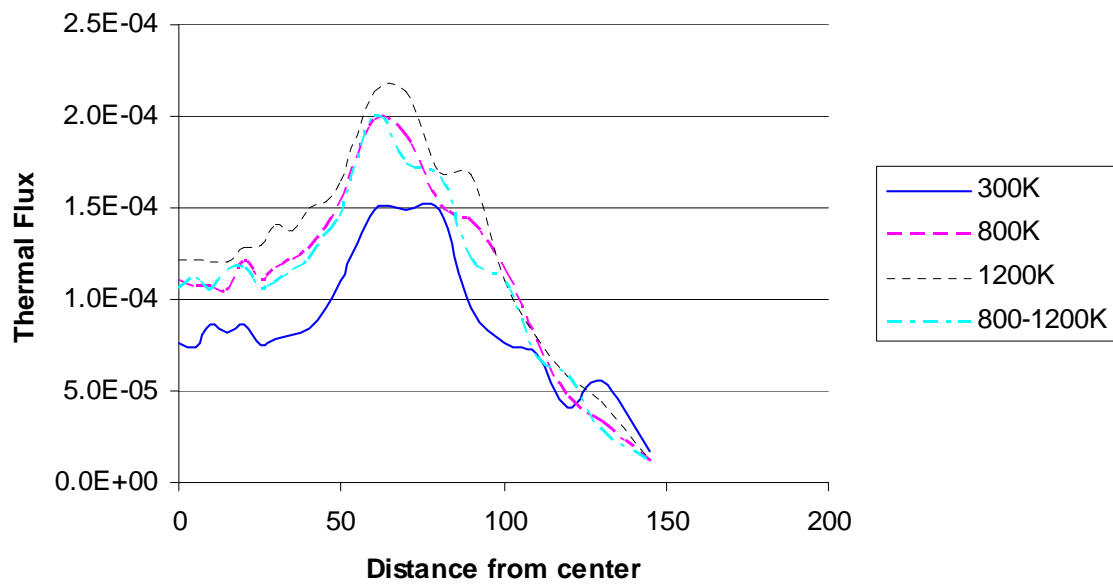


FIG. 4.136. Thermal flux profile for case 4.

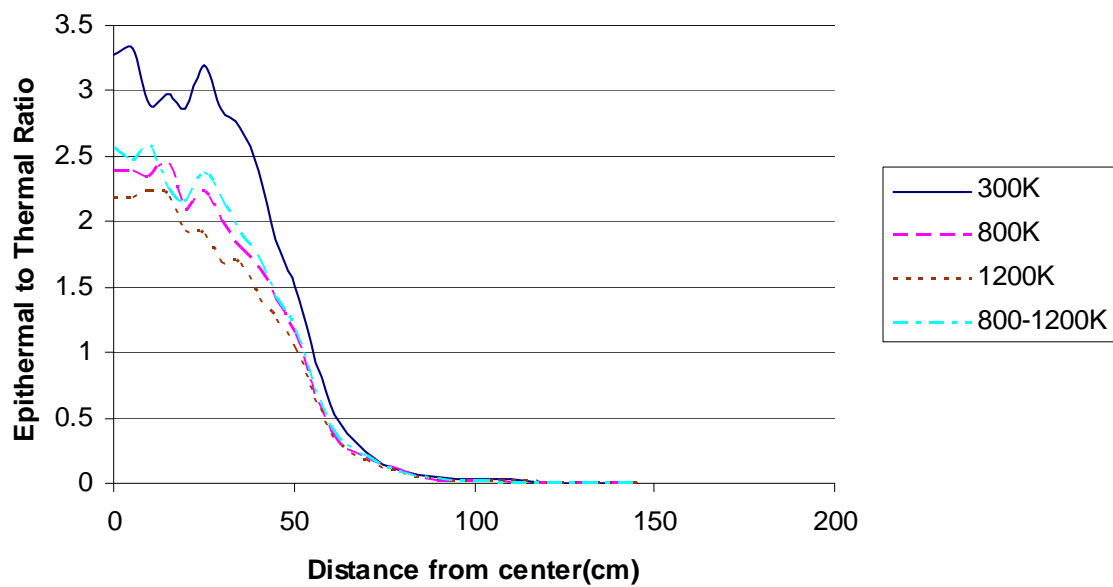


FIG. 4.137. Epithermal to thermal ratios for case 4.

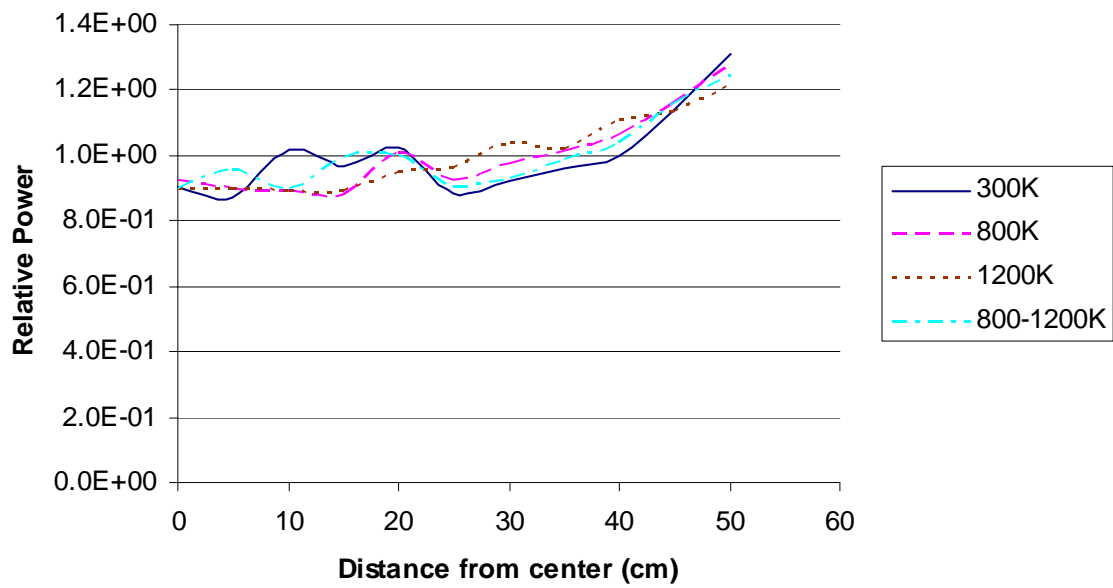


FIG. 4.138. Case 4 power profile.

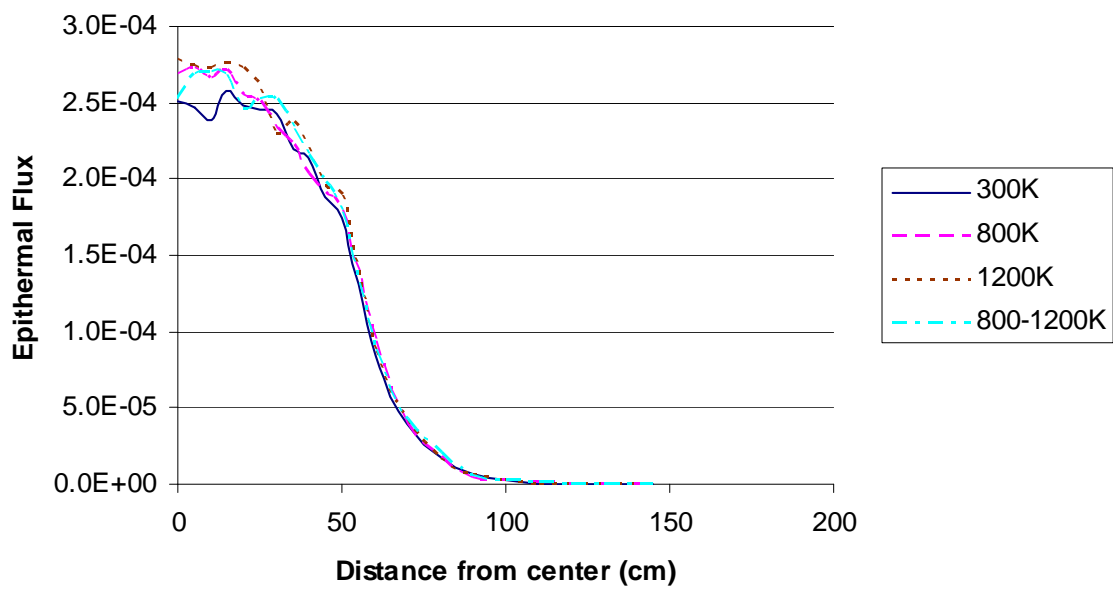


FIG. 4.139. Epithermal flux profile for case 5.

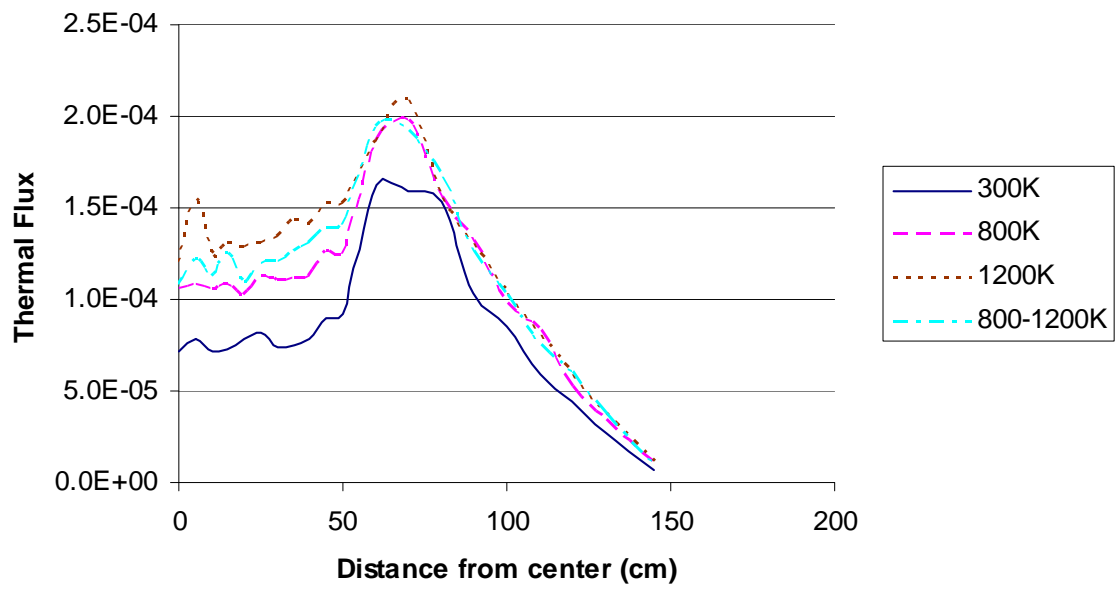


FIG. 4.140. Thermal flux profile for case 5.

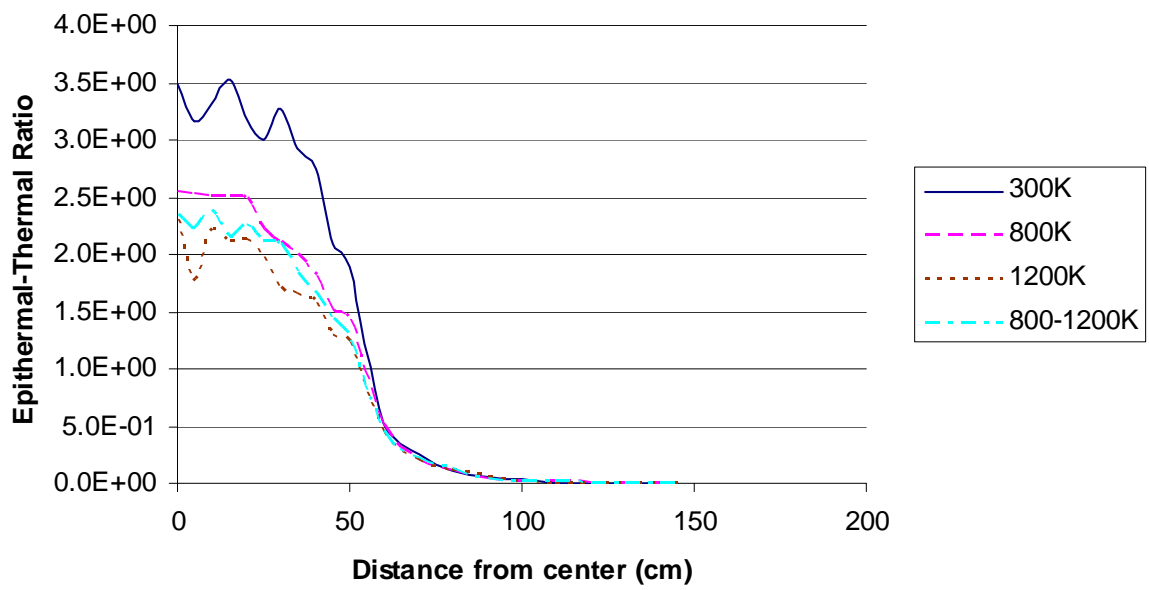


FIG. 4.141. Epithermal to thermal ratios for case 5.

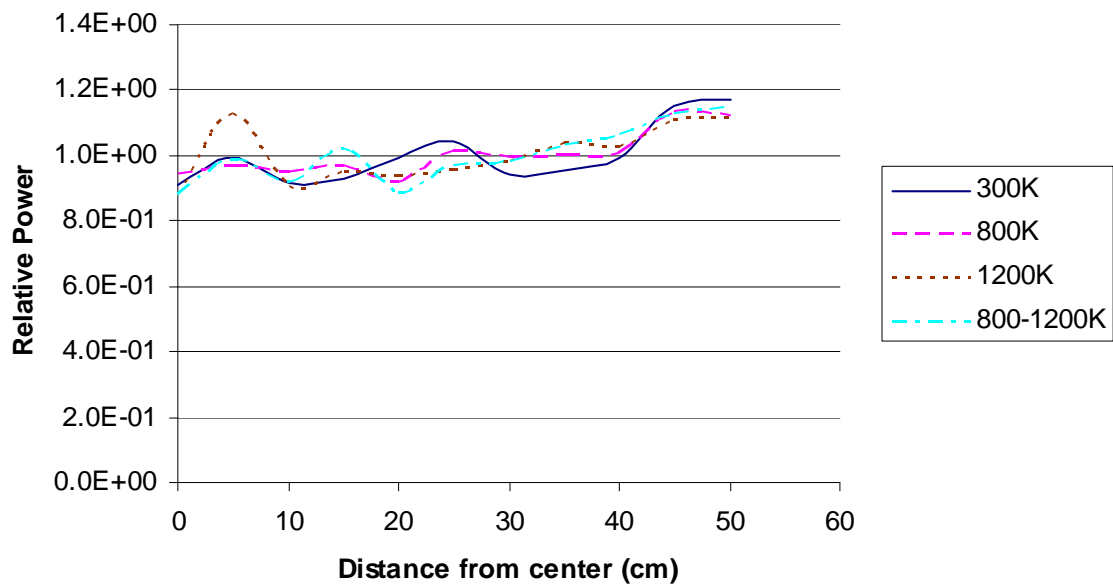


FIG. 4.142. Case 5 power profile.

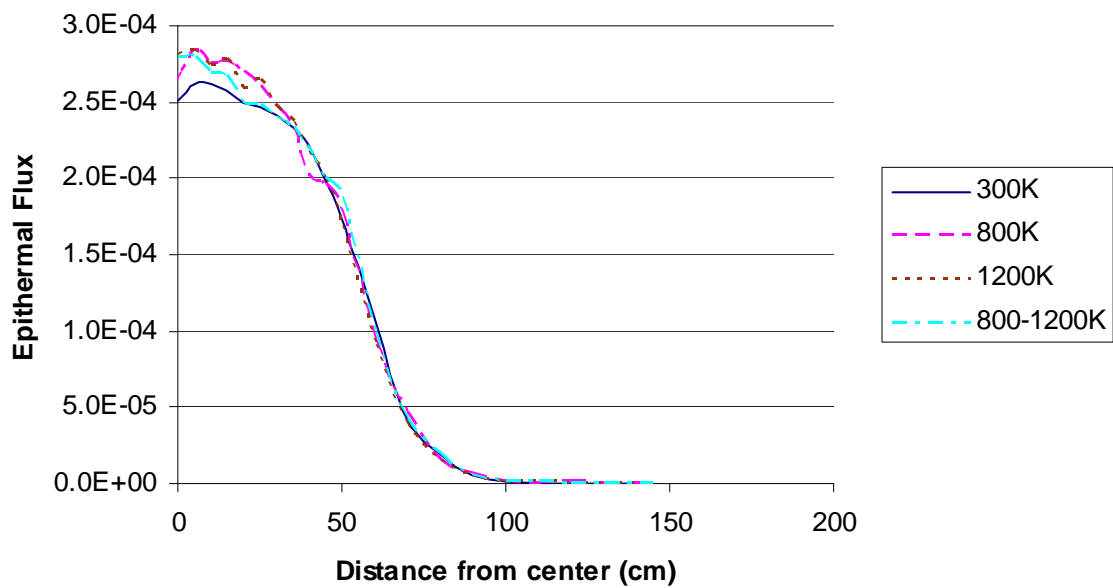


FIG. 4.143. Epithermal flux profile for case 6.

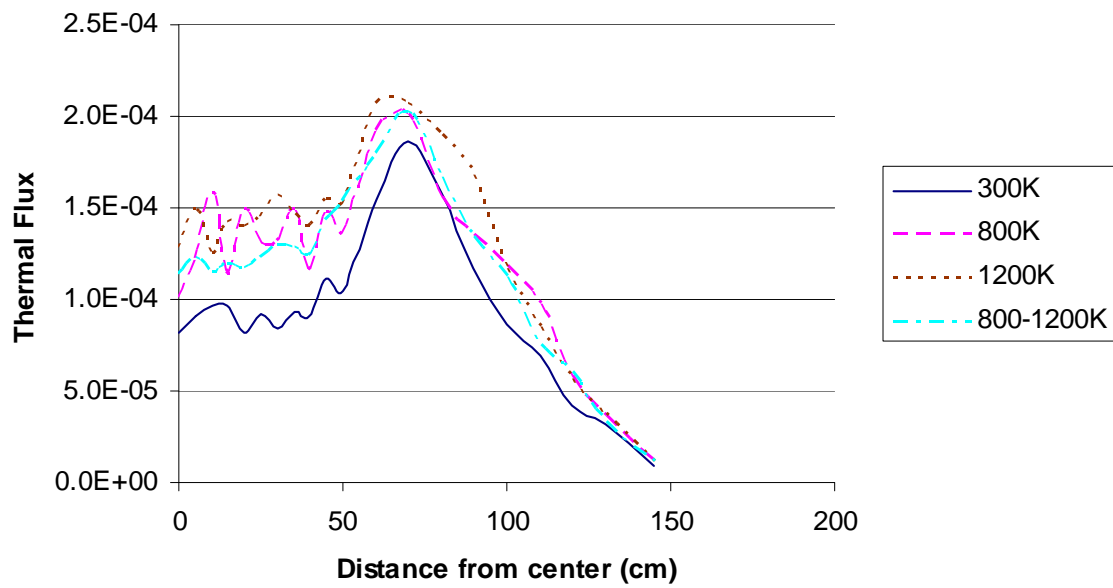


FIG. 4.144. Thermal flux profile for case 6.

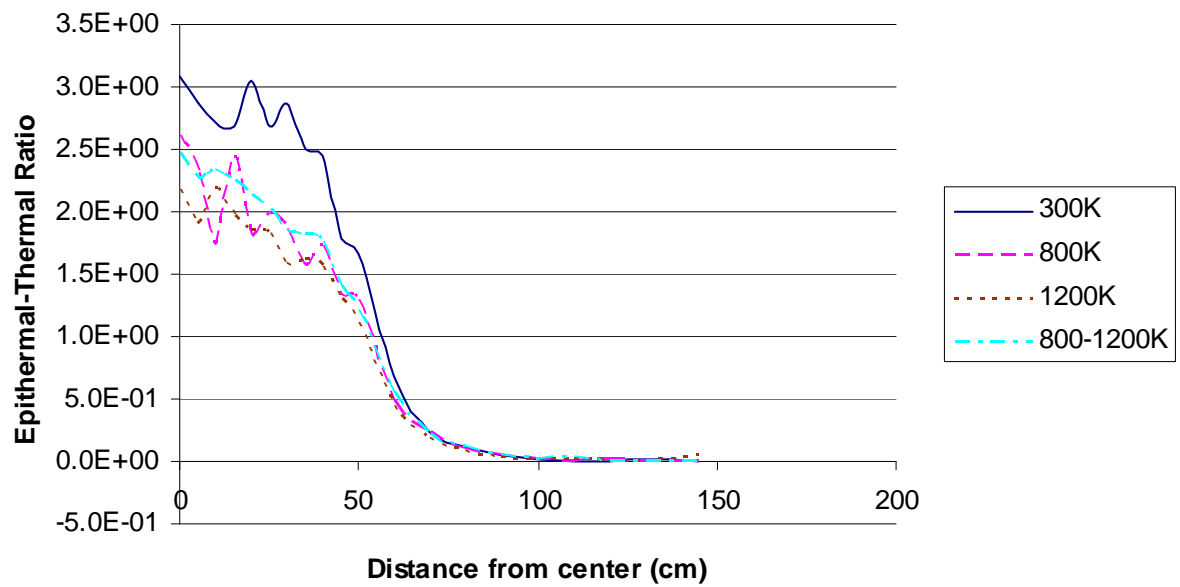


FIG. 4.145. Epithermal to thermal ratios for case 6.

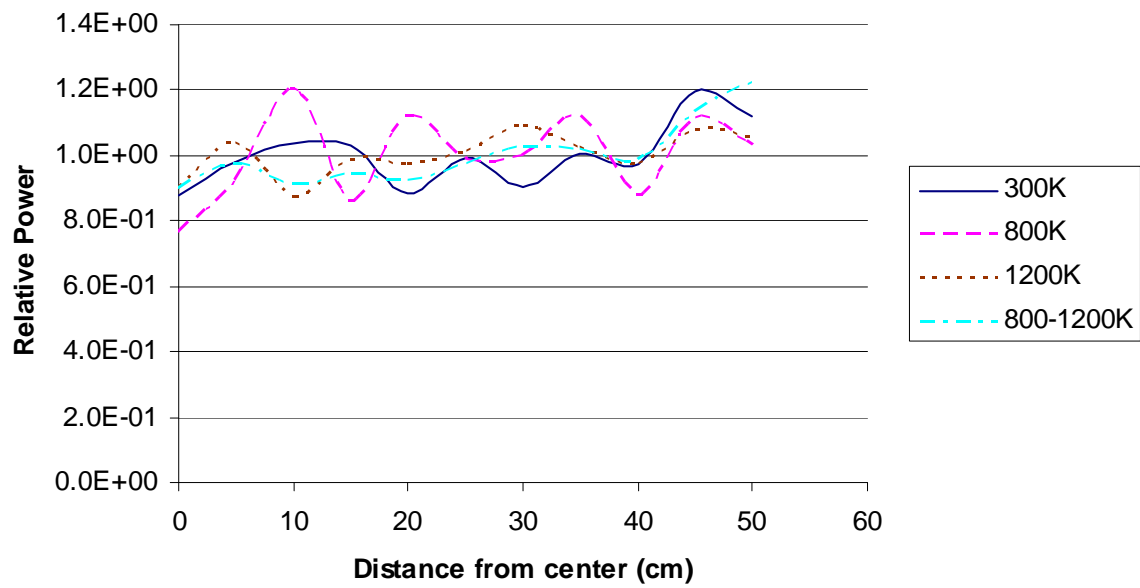


FIG. 4.146. Case 6 power profile.

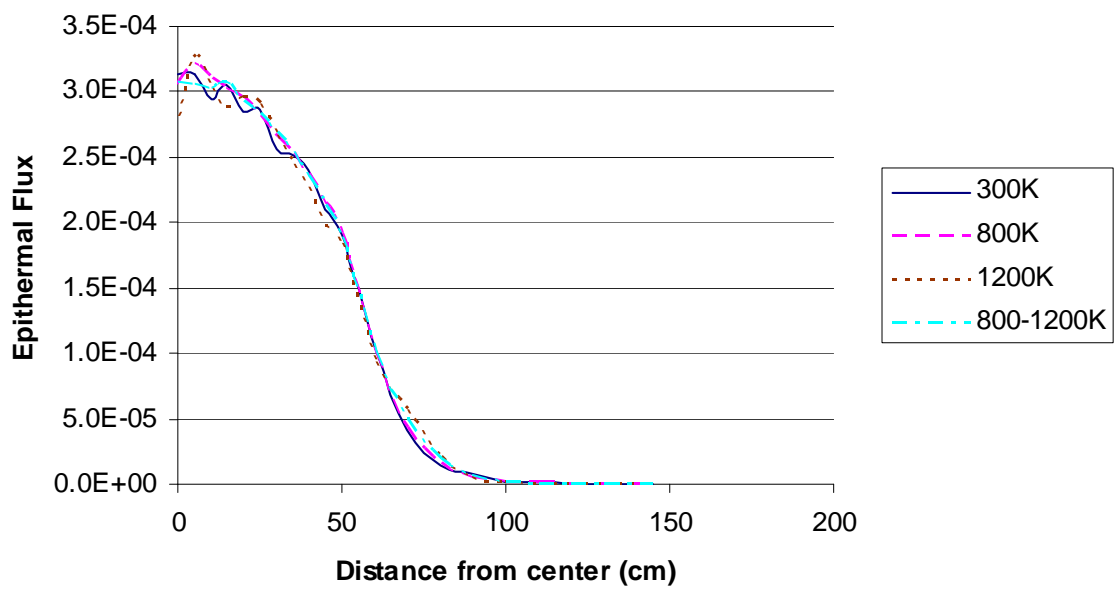


FIG. 4.147. Epithermal flux profile for case 7.

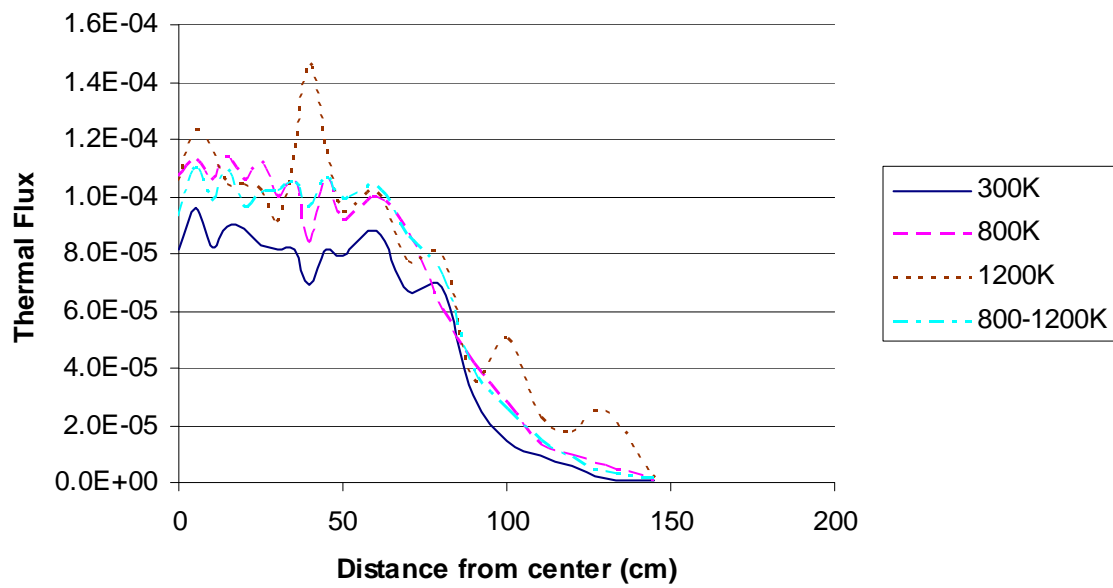


FIG. 4.148. Thermal flux profile for case 7.

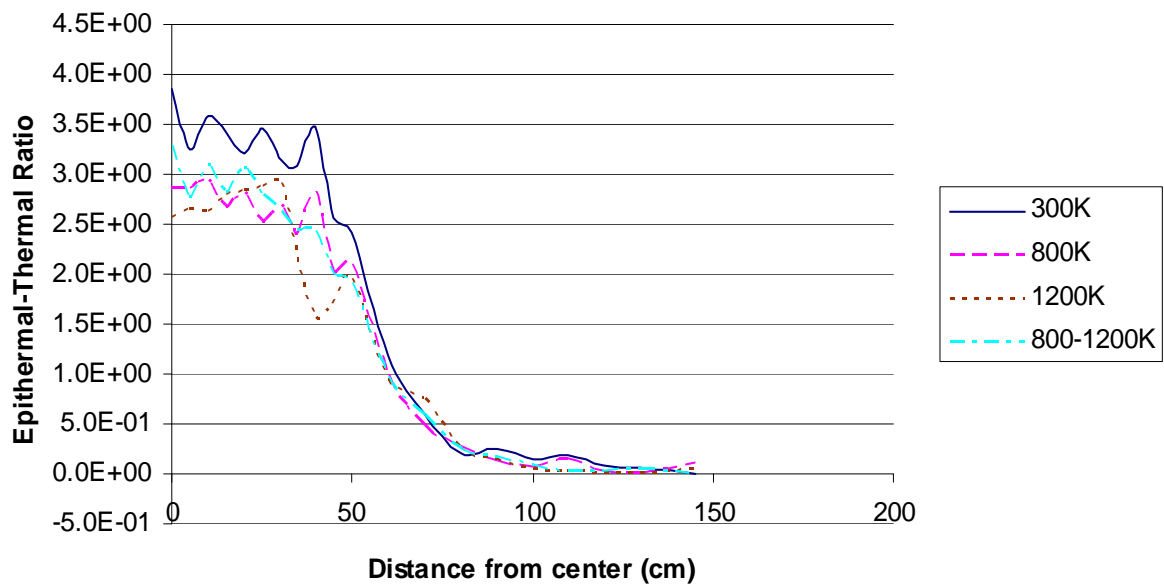


FIG. 4.149. Epithermal to thermal ratios for case 7.

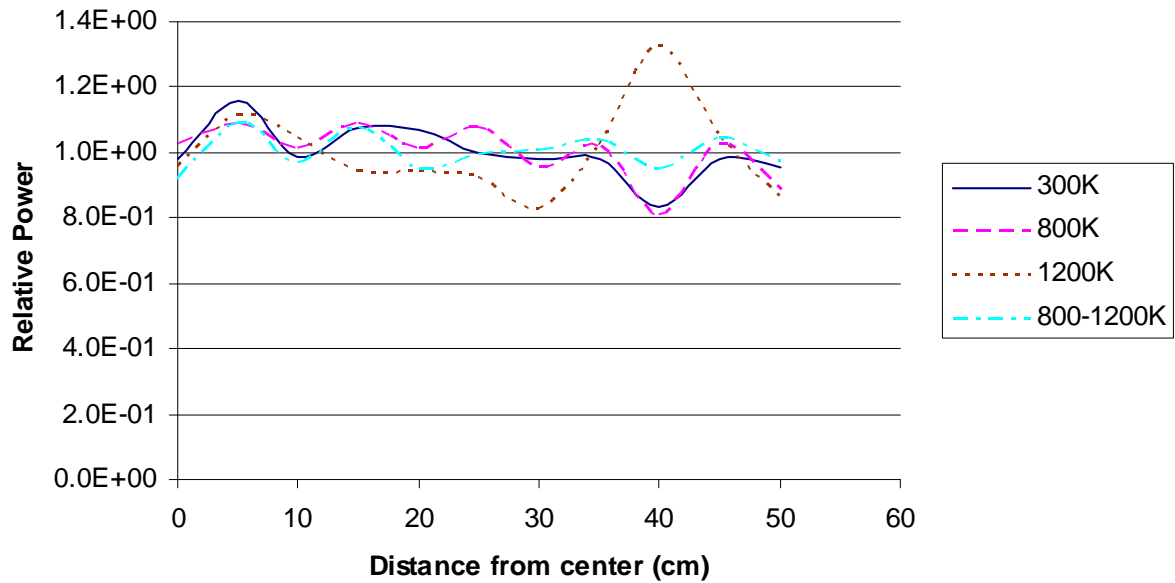


FIG. 4.150. Case 7 power profile.

Since the calculations and results presented here are based on particle transport simulations and explicit pebble modelling, the data shown in the previous graphics is not along smooth lines. Lines connecting calculated points usually vary significantly. Increasing the sampling size or the dimension of tallies (volume elements can be used) is expected to reduce the variation. Alternatively, the edits along several line segments could be averaged or several randomly packed models must be used to give an averaged smooth behaviour. There are, however, some results with unexpectedly large deviations (about 20%) from the common trend as in the case of Fig. 4.148. There is no reasonable explanation for the point with large deviation in this figure. MCNP calculations with different temperatures are presented here. However, further analyses are required to check the effect of cross-section set as well as the temperature sensitivity.

4.3.2.4. Pebble Box results, Republic of Korea

Analysis method

Monte Carlo analysis

The MCNP [4-51] code and cross-section library based on ENDF/B-VI were used for the Monte Carlo analysis. The pebbles in the cube are located in a Body Centred Cubic (BCC) lattice structure. Figure 4.151 shows the two geometry models for the problem used in this work. No broken pebbles are allowed in Model A while broken pebbles are allowed at the boundary of the 'pebble box' in Model B. In Model A, the 'pebble box' core is divided into 14 14 15 basic cells, each of which contains a pebble at its centre and several octant pebbles depending on the location in the 'pebble box'. Model A contains 5306 pebbles and the resultant packing fraction is about 60.02%.

In Model B, the 'pebble box' core is divided into 14 14 14 basic cells, each of which contains a central pebble and eight octant pebbles except for the basic cells at the top plane. Each basic cell at the top plane has only four octant pebbles as shown in Fig. 4.151. Model B contains 5390 pebbles and the resultant packing fraction is about 60.97%. The number densities of the nuclides were adjusted to compensate the discrepancies between the packing fractions used and the value specified in the problem ($= 0.61$).

Figure 4.152 shows the packing fraction distribution of the two models shown in Fig. 4.151 along the basic cells on the X-axis. The power density profiles were obtained based on the packing fraction distributions in Fig. 4.152.

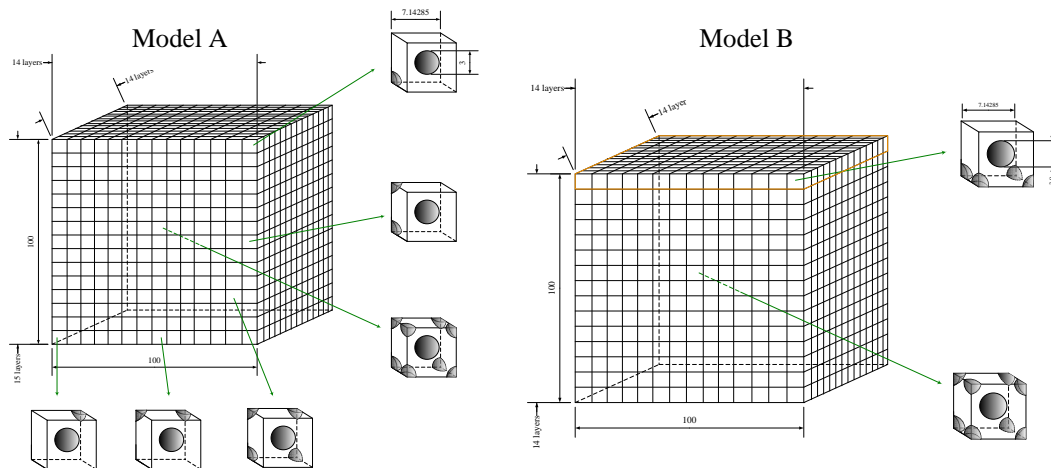


FIG. 4.151. Two geometry models for the benchmark problem.

For the double-heterogeneous cases (Cases 3, 6 and 7), the coated particles in the fuel zone are located in a Simple Cubic (SC) lattice structure with a pitch of 0.1621 cm. Broken particles are allowed at the boundary of the fuel zone as shown in Fig. 4.153.

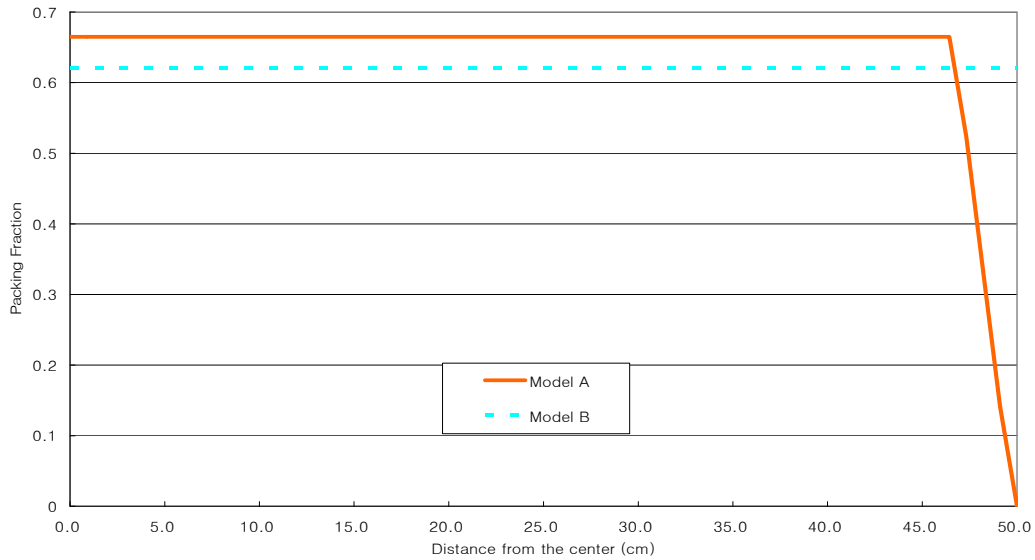


FIG. 4.152. Packing fraction distribution of model A and model B.

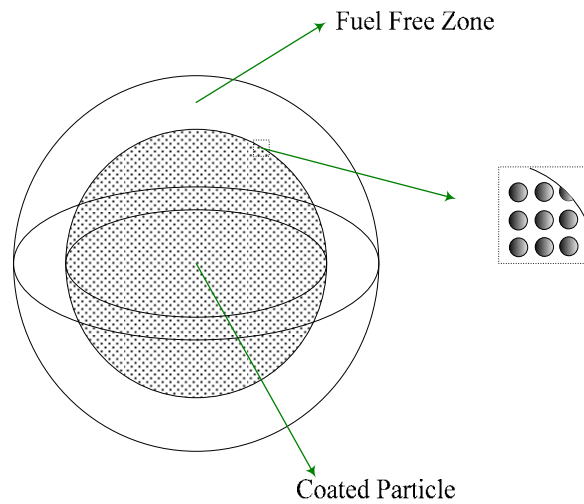


FIG. 4.153. A model for double-heterogeneous pebbles.

Diffusion analysis

A two-step procedure [4-34] was adopted for the diffusion analysis. In the first step, cross-sections are generated by solving a spectral geometry problem with the HELIOS code [4-37]. In the second step, the diffusion calculation is performed over the whole core by using the cross-sections generated in the first step. For Case 1, two group cross-sections were generated from a homogeneous single-cell calculation with the HELIOS code. For Case 2, the Equivalent Cylinder Model (ECM) [4-52] was used to transform a spherical pebble into an equivalent cylindrical fuel. The geometrical transformation using ECM enables two dimensional lattice physics codes such as HELIOS to model a spherical pebble. For Case 3, the Reactivity-equivalent Physical Transformation (RPT) [4-53] was used together with ECM to transform the double-heterogeneous spherical pebble fuel to an equivalent single-heterogeneous cylindrical fuel. Figure 4.154 shows the HELIOS models for Cases 2 and 3. The RPT radius was determined so that the k-effective from the HELIOS calculation should be the k-effective from the MCNP calculation.

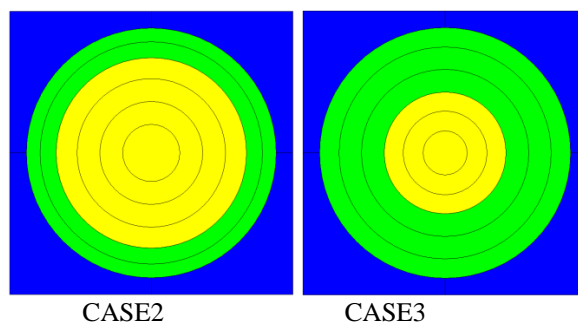


FIG. 4.154. Equivalent cylinder fuel modes for HELIOS code.

For the graphite reflected cases (Cases 4–7), infinite slab spectral geometries were used to generate cross-sections. Space-dependent two-group cross-sections were generated from the spectral geometry problem with the help of the Equivalence Theory (ET) [4-35]. Figure 4.155 shows the spectral geometries for the graphite reflected cases. The HELIOS models in Fig. 4.155 are consistent with Model A in Fig. 4.152. The packing fraction distribution of Model A was incorporated into the macroscopic cross-section distributions in the fuel region.

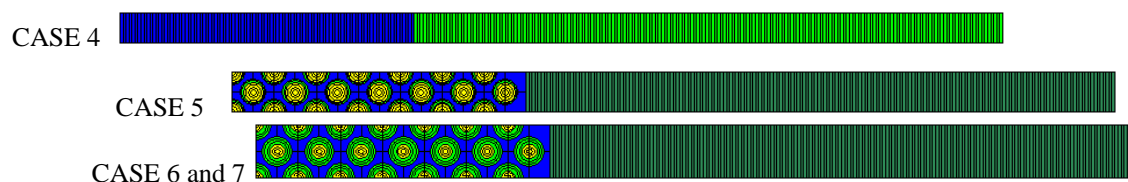


FIG. 4.155. Infinite slab spectral geometries for HELIOS code.

The first step using an infinite slab core of our two-step procedure relies on an assumption that the leakage in one direction is dominant and the transverse leakage is negligible, which is the case in a large power reactor. For example, it is evident that the radial leakage dominates the azimuthal or axial leakage in the PBMR-400 power reactor. However, this assumption is not valid in this small cubic core and it may cause a large error in our analysis. To resolve this problem, a transverse leakage correction technique was adopted, in which the transverse leakage was modelled in the HELIOS model by using an albedo boundary conditions at the surfaces faced in the Y-direction in the core region. The groupwise albedo values were updated iteratively using the groupwise fluxes and the groupwise currents at the interface between the core and the reflector until convergence.

An FDM solver in the CAPP code which has been developed for the analysis of VHTR cores was used to perform the whole-core diffusion calculation in the second step of our two-step procedure. 1.25 cm was used as the mesh size for $0 \text{ cm} < X, Y, Z < 100 \text{ cm}$ and 2.5 cm was used for other parts.

Results

Table 4.77 summarizes the effective multiplication factors for the cases. Relatively large errors in homogeneous and single-heterogeneous cases (Cases 1, 2, 4 and 5) are ascribed to the fact that the resonance integral table of heavy nuclides in the HELIOS cross-section library was generated for heterogeneous configurations. Table 4.77 also shows that the errors in the graphite reflected cases can be reduced by using the transverse leakage correction described in the previous chapter. Table 4.78 shows the RMS errors of the relative power density profile along the X-axis for the graphite reflected cases, in which MC results with Model A were taken as the reference solution. Figures 4.156–4.159 show the relative power density profile for the cases. From Figs 4.157 and 4.158, it can be established that the power density profile of Model A and that of Model B are quite different from each other although the effective multiplication factors of the two models in Table 4.77 are very similar.

TABLE 4.77. EFFECTIVE MULTIPLICATION FACTORS AND THEIR ERRORS (IN PCM)

Temp. [K]	Method		Case						
			1	2	3	4	5	6	7
300	MC	Model A	1.38333	1.41888	1.52234	0.98037	0.99154	1.02618	0.68306
		Model B		-58	+39		+29	-66	-
	Diff.	No Corr.	+852	+505	+29	+2578	+1259	+913	+1536
		TL Corr.				+1618	+780	+259	-31
800	MC	Model A	1.29901	1.3353	1.44939	0.92196	0.93388	0.97190	0.65089
		No Corr.	+864	+680	+7	+2296	+1081	+726	+1224
	Diff.	TL Corr.				+1485	+641	+72	-185
	1200	MC	Model A	1.25859	1.29848	1.40965	0.88480	0.89608	0.93421
No Corr.			+891	+374	+8	+2543	+1388	+1018	+1351
Diff.		TL Corr.				+1990	+1040	+446	+49
800 1200		MC	Model A	-	-	1.41670	-	-	0.96100
	No Corr.		-	-	+7	-	-	+531	+1040
	Diff.	TL Corr.				-	-	-66	-303

TABLE 4.78. RELATIVE POWER DENSITY ERRORS OF DIFFUSION CALCULATIONS (RMS, %)

Temp. [K]	Method	CASE			
		4	5	6	7
300	No Corr.	5.7	5.0	6.2	2.9
	TL Corr.	4.2	4.4	5.6	2.3
800	No Corr.	4.3	5.0	5.3	2.4
	TL Corr.	2.8	4.4	4.7	1.9
1200	No Corr.	3.8	4.5	4.7	2.4
	TL Corr.	2.6	3.9	4.0	1.8
800	No Corr.	-	-	5.5	2.5
1200	TL Corr.	-	-	4.9	2.0

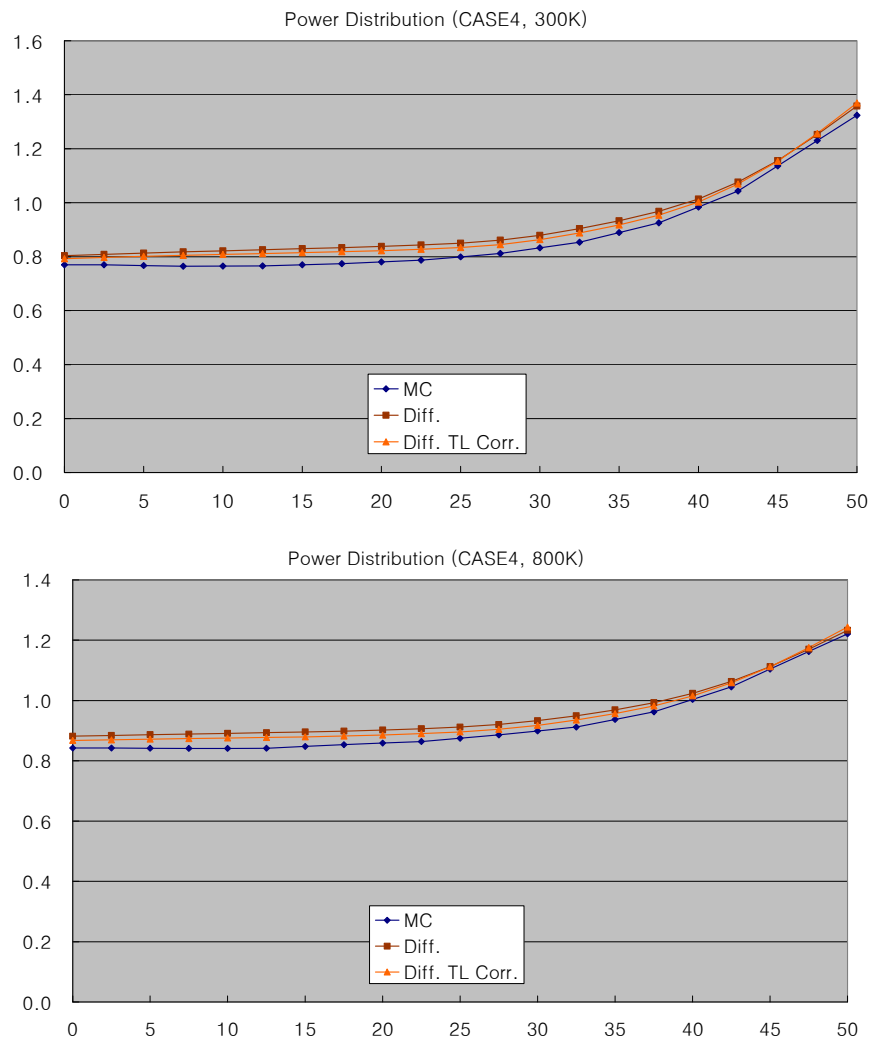


FIG. 4.156. Relative power distribution of case 4.

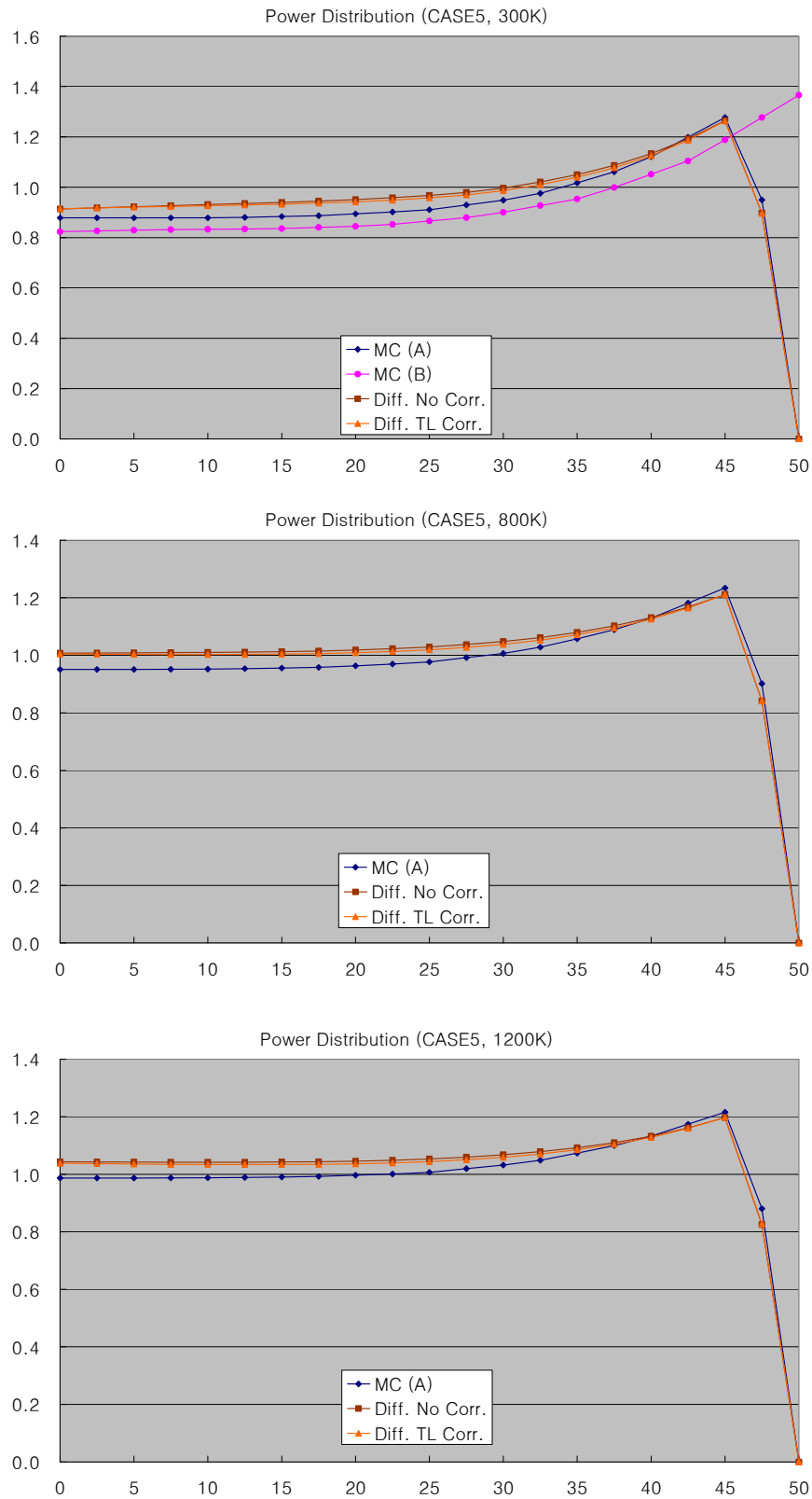


FIG. 4.157. Power distribution of case 5.

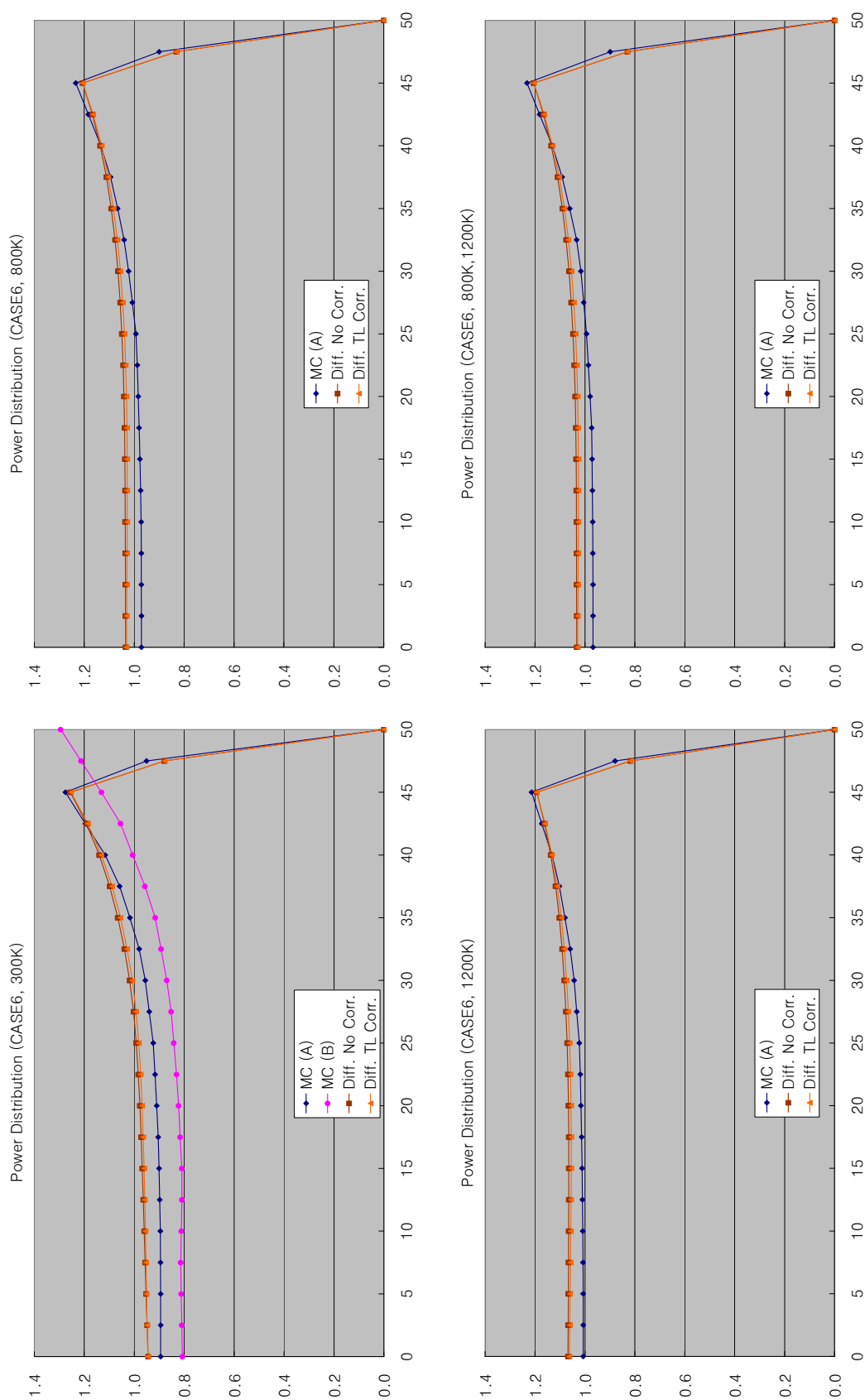


FIG. 4.158. Power distribution of case 6.

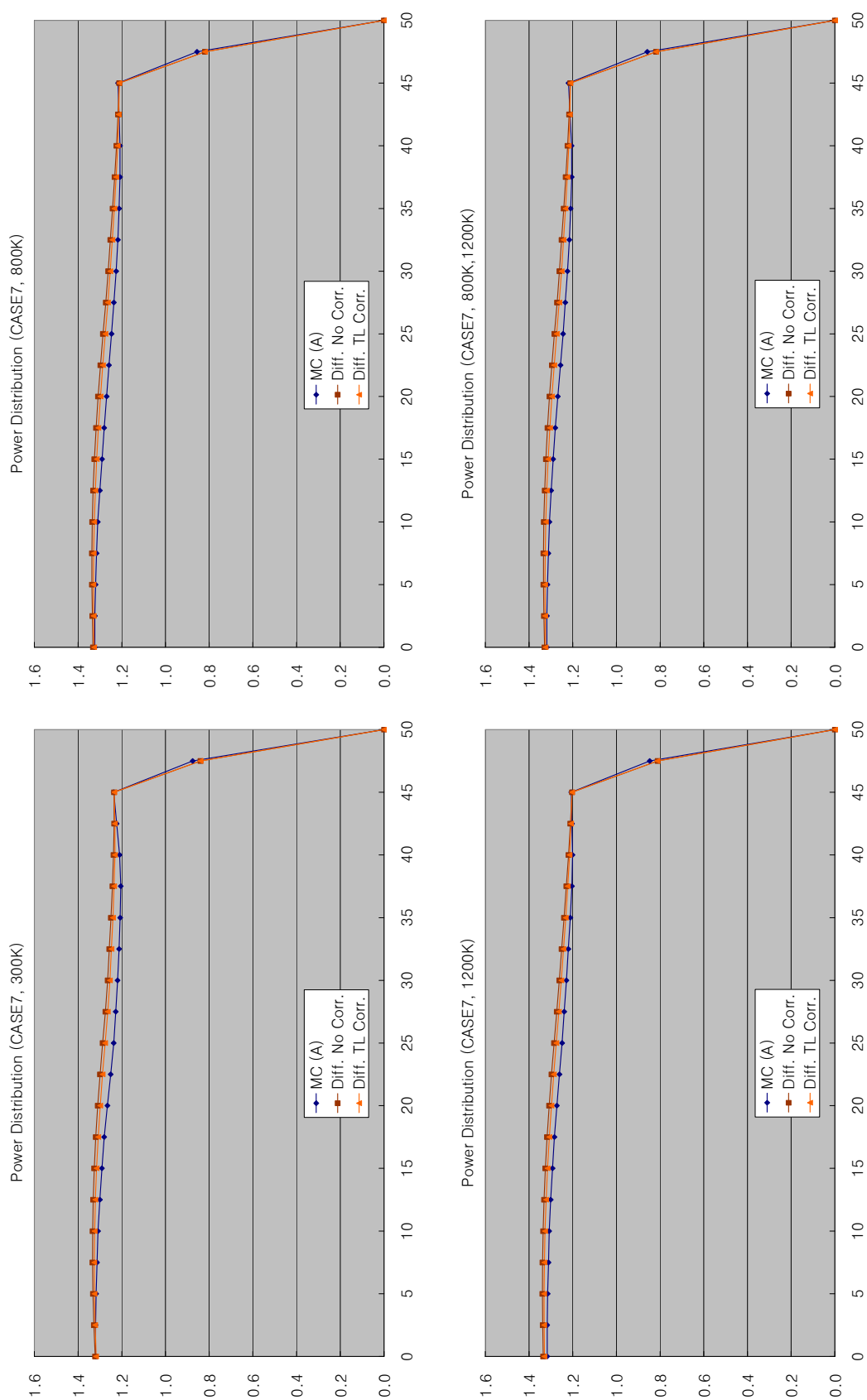


FIG. 4.159. Power distribution of case 7.

4.4. REFERENCES FOR CHAPTER 4

- [4-1] INTERNATIONAL ATOMIC ENERGY AGENCY, 'Status of Innovative Small and Medium Reactor Designs 2005', IAEA-TECDOC-1485, IAEA, Vienna (2006).
- [4-2] MATZNER, D., 'PBMR Project Status and the Way Ahead', HTR-2004 Conference, Beijing, China (2004).
- [4-3] MATZNER, D., PBMR Existing and Future R&D Test Facilities, HTR-2004 Conference, Beijing, China (2004).
- [4-4] REITSMA, F., 'The Pebble Bed Modular Reactor Layout and Neutronics Design of the Equilibrium Cycle,' PHYSOR 2004, Chicago, Illinois, April 25–29, 2004, on CD-ROM, American Nuclear Society, Lagrange Park, IL. (2004).
- [4-5] WALLACE, E., et. al., 'From Field to Factory-Taking Advantage of Shop Manufacturing for the Pebble Bed Modular Reactor', HTR-2004 Conference, Tsinghua University, Beijing, China (2004).
- [4-6] CASPERSSON, S., et. al., 'Pebble Bed Modular Reactor: The PBMR Advantage', ICAPP04 conference, Pittsburgh, United States of America (2004).
- [4-7] INTERNATIONAL ATOMIC ENERGY AGENCY, 'Current Status and Future Development of Modular High Temperature Gas Cooled Reactor Technology', IAEA-TECDOC-1198, IAEA, Vienna (2001).
- [4-8] WALLACE, E., Private communication with L Brey, PBMR (Pty) Ltd. (2005 and 2005).
- [4-9] ESKOM, 'PBMR Technical Description', Doc. Num. PB-000000-25, Pretoria, South Africa (1999).
- [4-10] PBMR (Pty) Ltd, 'PBMR Technology Fact Sheet', Delivered to the (U.S.) DOE, Washington, Revised (2004).
- [4-11] TSHELANE, P., 'PBMR Presentation', Presentation to IAEA, PBMR (Pty) Ltd, Vienna (November 2004).
- [4-12] MULDER, E., Private communication with L Brey, PBMR (Pty) Ltd., (2005).
- [4-13] WALLACE, E., Private communication with L Brey, PBMR (Pty) Ltd., (2004).
- [4-14] REITSMA, F., 'Data and boundary conditions to be used in VSOP and TINTE 400MW reactor models', PBMR Internal Document 010421-321 (2002).
- [4-15] MULDER, E., 'CRP-5 benchmark definition: PBMR-400 neutronics and thermal-hydraulics description', Document Number 022017 Rev A, PBMR Pty, Ltd, Pretoria, South Africa (2003).
- [4-16] REITSMA, F., 'CRP-5 benchmark definition: PBMR-400 neutronics and thermal-hydraulics description', Document Number 022017 Rev B, PBMR Pty, Ltd, Pretoria, South Africa (2006).
- [4-17] BINKELE, L., HARTLEIB, O., BIERGANS, W., 'Wärmeleitfähigkeit und spez. el. Widerstand neutronenbestrahlter Graphite in Abhängigkeit von der Temperatur', Internal report, KFA-IRW-IB-13/75 (1975).
- [4-18] VDI-Wärmeatlas: Berechnungsblätter für den Wärmeübergang, Verein Deutscher Ingenieure, Düsseldorf. 4. Auflage (1984).
- [4-19] ROBOLD, K., 'Wärmetransport im Inneren und in der Randzone von Kugelschüttungen', Kernforschungsanlage Jülich GmbH, Jül-1796 (1982).
- [4-20] GERWIN, H., SCHERER, W., 'Treatment of Upper Cavity in a Pebble-Bed High-temperature Gas-cooled Reactor by Diffusion Theory', Nuclear Science and Engineering, **97** (1987) 9–19.
- [4-21] Berechnung der Nachzerfallsleistung der Kernbrennstoffe von Hochtemperatur- reaktoren mit kugelförmigen Brennelementen, DIN 25485 (1990).

- [4-22] RUTTEN, H.J., HAAS, K.A., BROCKMANN, H., OHLIG, U., SCHERER, W., 'V.S.O.P. (99) for WINDOWS and UNIX computer code system for reactor physics and fuel cycle simulation', Jül –3820.
- [4-23] GERWIN, H., SCHERER, W., TEUCHERT, E., 'The TINTE Modular Code System for Computational Simulation of Transient Processes in the Primary Circuit of a Pebble bed High-temperature Gas-cooled Reactor', Nuclear Science and Engineering, **103** (1989) 302–312.
- [4-24] REITSMA, F., RUTTEN, H.J., SCHERER, W., 'An Overview of the FZJ-Tools for HTR Core Design and Reactor Dynamics, The Past, Present and Future,' M&C 2005, Palais des Papes, Avignon, France, September 12–15, 2005, on CD-ROM, American Nuclear Society, LaGrange Park, IL (2005).
- [4-25] INSTITUTE OF NUCLEAR and NEW ENERGY TECHNOLOGY, 'Calculation of PBMR-400 Neutronics and Thermal-hydraulics Description, Tsinghua University, Beijing, China (2004).
- [4-26] TEUCHERT, E., et al., 'V.S.O.P ('94) Computer Code System for Reactor Physics and Fuel Cycle Simulation', Jül-2897 (1994).
- [4-27] BALL, S.J., NYPAVER, D.J., 'GRSAC Users Manual,' ORNL/TM-13697, Oak Ridge, TN, United States of America (1999).
- [4-28] WICHNER, R.P., BALL, S.J., 'Potential Damage to Gas-cooled Graphite Reactors Due to Severe Accidents', ORNL/TM-13661, Oak Ridge, TN, United States of America (April 1999).
- [4-29] BALL, S.J., 'Sensitivity studies of modular high-temperature gas-cooled reactor postulated accidents,' Nucl. Eng. Des., **236** (2006) 454–462.
- [4-30] HSU, C.T., CHENG, P., WONG, K.W., 'Modified Zehner-Schlunder Models for Stagnant Thermal Conductivity of Porous Media', Int. J. Heat Mass Transfer, **37** (1994) 2751–2759.
- [4-31] CLEVELAND, J.C., GREENE, S.R., 'Application of THERMIX-KONVEK Code to Accident Analysis of Modular Pebble Bed High Temperature Reactors (HTRs)', ORNL/TM-9905, Oak Ridge, TN, United States of America (1986).
- [4-32] INTERNATIONAL ATOMIC ENERGY AGENCY, 'Heat Transport and Afterheat Removal for Gas Cooled Reactors under Accident Conditions', IAEA-TECDOC-1163, IAEA, Vienna (2001).
- [4-33] SHIM, H.J., et al., 'Monte Carlo Depletion Analysis of a PWR with the MCNAP,' M&C'99, Madrid, Spain, Sept. 27–30, CD-ROM (1999).
- [4-34] LEE, Hyun Chul, KIM, Kang-Seog, NOH, Jae Man, JOO, Hyung Kook, 'Two Step Procedure by using a 1-D Slab Spectral Geometry for a Pebble Bed Reactor Core Analysis,' PHYSOR-2006, Vancouver, BC, Canada, Sept. 10–14, CD-ROM (2006).
- [4-35] SMITH, K.S., 'Spatial Homogenization Methods for Light Water Reactor Analysis,' PhD Thesis, Massachusetts Institute of Technology, United States of America (1980).
- [4-36] KIM, Kang-Seog, et al., 'Development of Two-Step Procedure for the Prismatic VHTR Physics Analysis,' PHYSOR-2006, Vancouver, BC, Canada, Sept. 10–14, CD-ROM (2006).
- [4-37] STAMMLER, R., 'Helios Methods,' Scandpower (1994).
- [4-38] The ANSWERS Software Service, WIMS9 User Guide, ANSWERS/WIMS (99) 9, Serco Assurance Report (2004).
- [4-39] HUTTON, J.L., NEWTON, T.D., PERRY, R.J., POWNEY, D.J., 'Validation of WIMS9', PHYSOR 2004, American Nuclear Society, Chicago, Illinois, United States of America (2004).
- [4-40] BEHRENS, D.J., The effect of holes in a reacting material on the passage of neutrons. Proc. Phys. Soc., **62** (1949) 607.

- [4-41] PATANKAR, S.V., 'Numerical Heat Transfer and Fluid Flow', McGraw-Hill (1980).
- [4-42] SPALDING, D.B., 'PHOENICS Overview', TR 001, CHAM (2002).
- [4-43] Reactor Core Design of High-temperature Gas-cooled Reactors Part 3: Loss of Pressure through Friction in Pebble Bed Cores, KTA 3102.3, Nuclear Safety Standards Commission (KTA), Salzgitter (1981).
- [4-44] Reactor Core Design of High-temperature Gas-cooled Reactors Part 2: Heat Transfer in Spherical Fuel Elements, KTA 3102.2, Nuclear Safety Standards Commission (KTA), Salzgitter (1983).
- [4-45] COLBURN, A.P., 'A method of correlating forced convection heat transfer data and a comparison with fluid friction', Trans. AIChE, **19** (1933) 174–210.
- [4-46] MULDER, E., 'CRP-5 Problem Definition: Pebble Box for Code-to-Code Comparisons', PBMR 055767 Rev A, PBMR (Propriety) Limited, Centurion, South Africa (2005).
- [4-47] REITSMA, F., 'CRP-5 Problem Definition: Pebble Box for Code-to-Code Comparisons', PBMR 055767 Rev 1, PBMR (Pty) Ltd., Centurion, South Africa (2007).
- [4-48] BROCKMANN, H., RUTTEN, H.J., HAAS, K.A., SCHERER, W., 'Computer Code V&V Review of the Neutron Spectrum Calculation Methods in the Computer Code System V S O P – 99', FZJ internal report ISR-RC-5084/2004 (2004).
- [4-49] SEN, S., REITSMA, F., 'CRP-5 Pebble Box Benchmark Analysis', Internal report T000558, PBMR (Pty) Ltd., Centurion, South Africa.
- [4-50] KOKSAL, M., BARIK, M., COLAK, U., 'PBMR Pebble Box Benchmark Problem', Hacettepe University, Ankara, Turkey (2007).
- [4-51] BRIESMEISTER, J.F., et al., 1997, 'MCNP — A General Monte Carlo N-Particle Transport Code, Version 4B,' LA-12625-M (1997).
- [4-52] LEE, Hyun Chul, KIM, Kang-Seog, NOH, Jae Man, JOO, Hyung Kook, 'Equivalent Cylinder Models for the Homogenization of Pebble Bed Reactor Cores,' Trans. Am. Nucl. Soc. Vol. 93, Washington D.C. (2005).
- [4-53] KIM, Y., BAEK, M., 'Elimination of Double-Heterogeneity through a Reactivity-Equivalent Physical Transformation,' to be presented in GLOBAL 2005, Tsukuba, Japan (2005).

5. PEBBLE BED MICROMODEL

Technological advances in turbomachinery, magnetic bearings and heat exchanger design provide the potential for significant improvement in nuclear power generation economics through the use of the HTGR directly coupled to a gas turbine. PBMR (Pty) Ltd is currently in the detailed design and licensing process to build a demonstration pebble bed reactor coupled to a direct cycle helium turbine Power Conversion System (PCS).

The PBMM is a fully functional model depicting the initial design of the PCU of the PBMR, currently under development in South Africa. This unique type of power plant is based on the well-known Brayton power cycle (used in aircraft engines) but with the following distinguishing features:

It uses nitrogen as the working fluid;

The gas moves around in a closed circuit, which implies that no nitrogen is consumed in the power generation process (it merely acts as an energy carrier);

Use of three separate shafts, one for the HPC/High Pressure Turbine (HPT) pair, one for the LPC/Low Pressure Turbine (LPT) pair and one for the power turbine and generator. This allows the HPC/LPT and LPC/LPT pairs to run at high speeds, thereby reducing the size and therefore also the cost of the machines;

Use of a recuperator to recover heat that would otherwise have been rejected to atmosphere. The recovered heat is transferred elsewhere in the system, thereby reducing the heat required in the nuclear reactor and ultimately increasing the thermal efficiency of the plant.

Although the PBMR programme subsequently modified the PCS to a single-shaft configuration, the PBMM facility presents an excellent opportunity for code Verification and Validation (V&V) as it presents a complex thermal-fluid system with various thermal fluid components such as heat exchangers as well as dynamic components such as turbomachines and control problems [5-1].

5.1. LAYOUT OF THE PBMM

5.1.1. Description of the PBMM cycle

A schematic layout of the PBMM power conversion cycle is shown in Fig. 5.1. Starting at 10, nitrogen at a relatively low pressure and temperature is compressed by an LPC to an intermediate pressure (11) after which it is cooled in an intercooler to state 21. An HPC then compresses the nitrogen to state 31. From 40 to 41, nitrogen is preheated in the recuperator before entering the heat source, which heats the nitrogen to state 52. After the heat source, the hot high pressure nitrogen is expanded in an HPT to state 61 after which it is further expanded in an LPT to state 71. The HPT drives the HPC while the LPT drives the LPC. After the LPT, nitrogen is further expanded in the power turbine to pressure 81. From 90 to 91, the still-hot nitrogen is cooled in the recuperator after which it is further cooled in the precooler to state 101. This completes the cycle. The heat rejected from 90 to 91 is equal to the heat transferred to the nitrogen from 40 to 41.

Although the system layout of the PBMM closely resembles that of the PBMR plant, it is important to highlight the following differences:

- The PBMM uses nitrogen instead of helium as the working fluid. This does not subtract from the objective of the project, which is not to address specific issues related to the use of helium as the working fluid but to develop a system that will have the same overall characteristics as those of the prototype plant.
- The PBMM uses single-stage centrifugal compressors and turbines rather than axial flow machines. The performance characteristics of centrifugal machines resemble that of axial flow machines and therefore suffice for the purpose of this project.
- In the PBMM, the nuclear reactor is emulated by an electrical resistance heater which, like the pebble bed reactor, has a large thermal capacity.

- The generator is emulated by a load compressor connected to a power dissipation loop consisting of a flow control valve and a heat exchanger as shown in Fig. 5.1. Variations in load are affected by increasing or decreasing the pressure level in the load rejection loop.

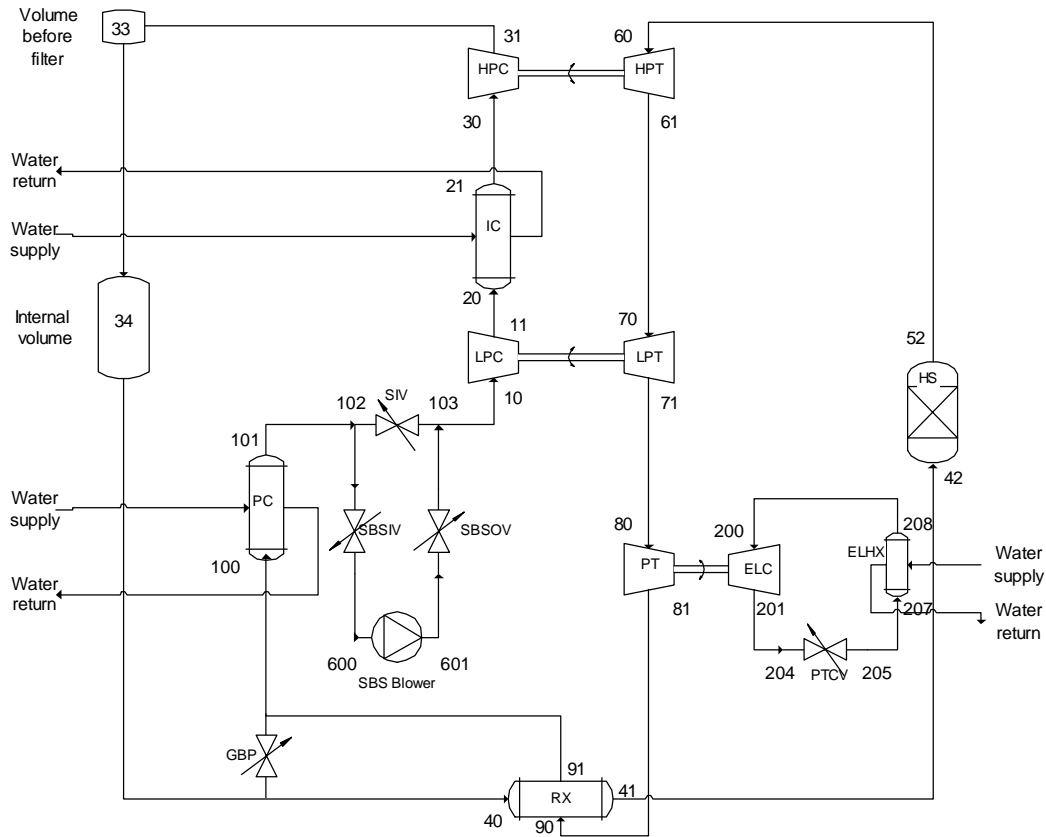


FIG. 5.1. Schematic layout of PBMM.

5.1.2. Objectives of the PBMM project

The objectives of the PBMM project are the following:

- To demonstrate that the three-shaft concept works and in particular that:

The system can be started up;

The system will run stably;

One will be able to vary the power output of the system in response to control commands.

- To demonstrate that the FLOWNEX code has the capability to accurately predict the dynamic behaviour of the system.

It was decided to make the PBMM information available to the IAEA member countries for further code-to-experiment validation.

5.2. COMPONENT DATA

5.2.1. Major components

TABLE 5.1. MAJOR COMPONENT DESCRIPTION

Number	Symbol	Description
10–11	LPC	Low pressure compressor
20–21	IC	Intercooler
30–31	HPC	High pressure compressor
40–41	RX_HP	Recuperator – high pressure side
42–52	HS	Heat source
60–61	HPT	High pressure turbine
70–71	LPT	Low pressure turbine
80–81	PT	Power turbine
90–91	RX_LP	Recuperator – low-pressure side
100–101	PC	precooler
200–201	ELC	External load compressor
207–208	ELHX	External load heat exchanger
600–601	SBS	Startup blower system

5.2.1.1. Pipe runs

No lengths are given for the fittings as these lengths are included in the total pipe length. The type of fitting is given to assist the reader to calculate an appropriate loss coefficient as well as the flow path length. Also note that a smooth reducer is used where two pipes with different diameters are joined.

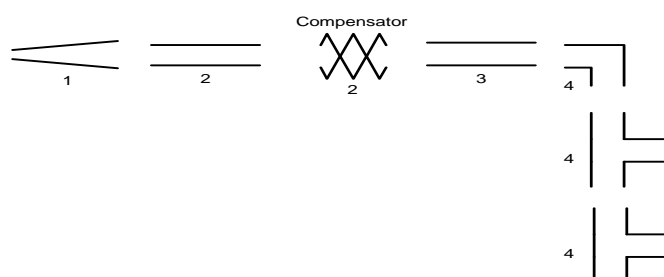


FIG. 5.2. Schematic representation of pipe run 11–20.

TABLE 5.2. TECHNICAL DETAILS FOR PIPE RUN 11–20

Pipe Run	No.	Component	Dimensions	Value
11–20	1	Diffuser	Length [m]	0.7
			Inlet diameter [m]	0.07
			Outlet diameter [m]	0.15405
	2	Pipe	Length [m]	0.4782
			Diameter [m]	0.15405
			Fittings	Compensator with L = 185 mm with no inner lining.
	3	Pipe	Length [m]	0.2624
			Diameter [m]	0.15405
			Fittings	None
	4	Pipe	Length [m]	1.32
			Diameter [m]	0.20272
			Fittings	Long radius 90° bend 2 × T-piece through flow

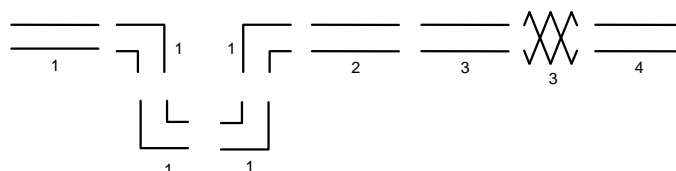


FIG. 5.3. Schematic representation of pipe run 21–30.

TABLE 5.3. TECHNICAL DETAILS FOR PIPE RUN 21–30

Pipe Run	No.	Component	Dimensions	Value
21–30	1	Pipe	Length [m]	8.321
			Diameter [m]	0.20272
			Fittings	4 × Long radius 90° bends
	2	Pipe	Length [m]	0.4324
			Diameter [m]	0.15405
			Fittings	None
	3	Pipe	Length [m]	0.592
			Diameter [m]	0.15405
			Fittings	Compensator with L = 185 mm with no inner lining.
	4	Pipe	Length [m]	1.4729
			Diameter [m]	0.10676
			Fittings	None

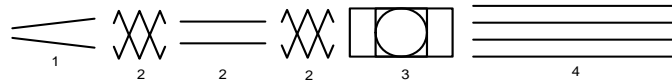


FIG. 5.4. Schematic representation of pipe run 31–40.

TABLE 5.4. TECHNICAL DETAILS FOR PIPE RUN 31–40

Pipe Run	No.	Component	Dimensions	Value
31–40	1	Diffuser	Length [m]	0.37
			inlet diameter [m]	0.069
			outlet diameter [m]	0.15405
	2	Pipe	Length [m]	0.65
			diameter [m]	0.15405
			fittings	2 × Compensator with L = 185 mm
				with no inner lining.
	3	Filter	Length [m]	0.5
			diameter [m]	0.179
			$\Delta P = k\rho Q^2$	k = 2
	4	Annulus	Outer diameter [m]	0.9
			inner diameter [m]	0.8
			fittings	None

Note: That the annulus is the area between the recuperator and the pressure boundary. Volume 33 is given in Section 5.2.1.

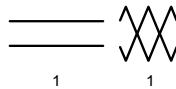


FIG. 5.5. Schematic representation of pipe run 41–42.

TABLE 5.5. TECHNICAL DETAILS FOR PIPE RUN 41–42

Pipe Run	No.	Component	Dimensions	Value
41–42	1	Pipe	Length [m]	0.588
			diameter [m]	0.20272
			fittings	Compensator with L = 185 mm
				with no inner lining.

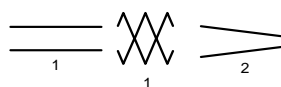


FIG. 5.6. Schematic representation of pipe run 52–60.

TABLE 5.6. TECHNICAL DETAILS FOR PIPE RUN 52–60

Pipe run	No.	Component	Dimensions	Value
52–60	1	Pipe	Length [m]	0.588
			diameter [m]	0.20272
			fittings	Compensator with L = 185 mm with no inner lining.
	2	Reducer	Length [m]	0.03
			inlet diameter [m]	0.20272
			outlet diameter [m]	0.0769

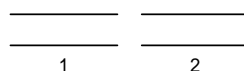


FIG. 5.7. Schematic representation of pipe run 61–70.

TABLE 5.7. TECHNICAL DETAILS FOR PIPE RUN 61–70

Pipe run	No.	Component	Dimensions	Value
61–70	1	Pipe	Length [m]	0.18
			diameter [m]	0.115
			fittings	None
	2	Pipe	Length [m]	0.01
			diameter [m]	0.0769
			fittings	None

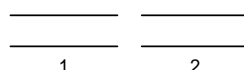


FIG. 5.8. Schematic representation of pipe run 71–80.

TABLE 5.8. TECHNICAL DETAILS FOR PIPE RUN 71–80

Pipe Run	No.	Component	Dimensions	Value
71–80	1	Pipe	Length [m]	0.18
			Diameter [m]	0.115
			Fittings	None
	2	Pipe	Length [m]	0.01
			Diameter [m]	0.081
			Fittings	None

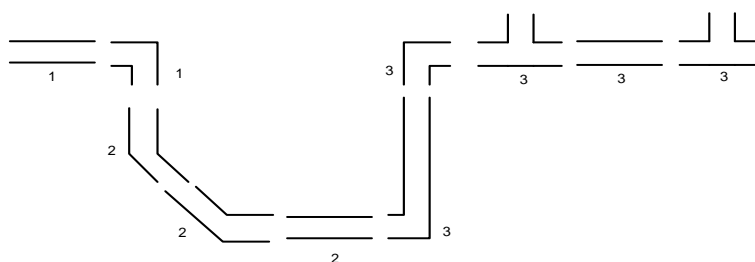


FIG. 5.9. Schematic representation of pipe run 81–90.

TABLE 5.9. TECHNICAL DETAILS FOR PIPE RUN 81–90

Pipe Run	No.	Component	Dimensions	Value
81–90	1	Pipe	Length [m]	1
			Diameter [m]	0.15405
			Fittings	Long radius 90° Bend
	2	Pipe	Length [m]	3.6312
			Diameter [m]	0.20272
			Fittings	2 × Long radius 45° Bends
	3	Pipe	Length [m]	9.013
			Diameter [m]	0.20272
			Fittings	2 × Long radius 90° Bends 2 × T-piece through flow



FIG. 5.10. Schematic representation of pipe run 91–100.

TABLE 5.10. TECHNICAL DETAILS FOR PIPE RUN 91–100

Pipe Run	No.	Component	Dimensions	Value
91–100	1	Pipe	Length [m]	9.013
			Diameter [m]	0.20272
			Fittings	2 × Long radius 90° Bends
				2 × T-piece through flow

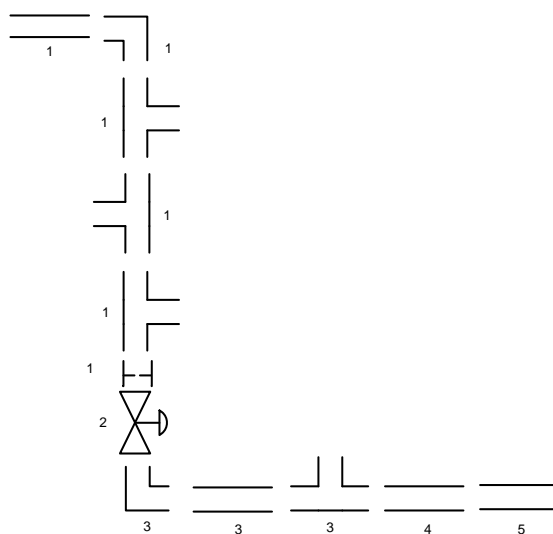


FIG. 5.11. Schematic representation of pipe run 101–10.

TABLE 5.11. TECHNICAL DETAILS FOR PIPE RUN 101–10

Pipe Run	No.	Component	Dimensions	Value
101–10	1	Pipe	Length [m]	8.218
			Diameter [m]	0.20272
			Fittings	Long radius 90° bend 3 × T-piece through flow Orifice with diameter ratio of 0.6114
	2	Valve (102 - 103)	Diameter [m]	0.20272
			Type	L-series
	3	Pipe	Length [m]	1.578
			Diameter [m]	0.20272
			Fittings	Long radius 90° bend T-piece through flow
	4	Pipe	Length [m]	0.875
			Diameter [m]	0.15405
			Fittings	None
	5	Pipe	Length [m]	0.0569
			Diameter [m]	0.1313
			Fittings	None

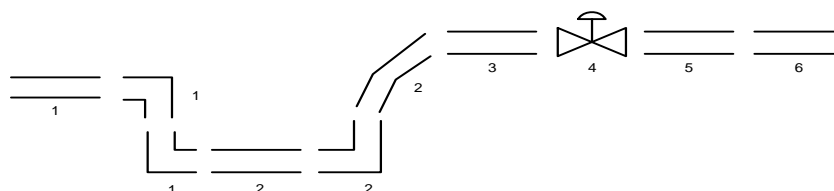


FIG. 5.12. Schematic layout of pipe run 201–207.

TABLE 5.12. TECHNICAL DETAILS FOR PIPE RUN 201–207

Pipe Run	No.	Component	Dimensions	Value
201–207	1	Pipe	Length [m]	4.6097
			Diameter [m]	0.15405
			Fittings	2 × long radius 90° bends
	2	Pipe	Length [m]	1.2445
			Diameter [m]	0.15405
			Fittings	Long radius 90° bend Long radius 45° bend
	3	Pipe	Length [m]	0.28
			Diameter [m]	0.07792
			Fittings	None
	4	Valve (204–205)	Diameter [m]	0.08
			Type	R-series
	5	Pipe	Length [m]	0.81
			Diameter [m]	0.15405
			Fittings	None
	6	Pipe	Length [m]	0.81
			Diameter [m]	0.15405
			Fittings	None

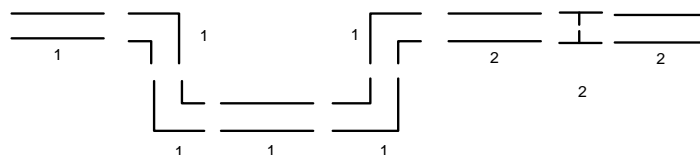


FIG. 5.13. Schematic representation of pipe run 208–200.

TABLE 5.13. TECHNICAL DETAILS FOR PIPE RUN 208–200

Pipe run	No.	Component	Dimensions	Value
208–200	1	Pipe	Length [m]	9.7869
			Diameter [m]	0.15405
			Fittings	4 × long radius 90° bends T-piece through flow
	2	Pipe	Length [m]	1
			Diameter [m]	0.15405
			Fittings	Orifice with diameter ratio of 0.52

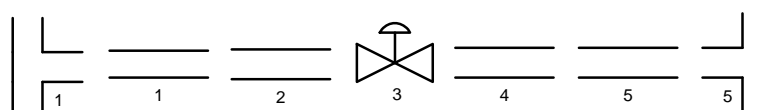


FIG. 5.14. Schematic representations of pipe run 34–100 (GBP).

TABLE 5.14. TECHNICAL DETAILS FOR PIPE RUN 34–100 GBP

Pipe Run	No.	Component	Dimensions	Value
34–100 GBP	1	Pipe	Length [m]	1.255
			Diameter [m]	0.10226
			Fittings	T-piece branch flow
	2	Pipe	Length [m]	0.232
			Diameter [m]	0.0779
			Fittings	None
	3	Valve	Diameter [m]	0.08
			Type	R-series
	4	Pipe	Length [m]	0.237
			Diameter [m]	0.07792
			Fittings	None
	5	Pipe	Length [m]	0.725
			Diameter [m]	0.10226
			Fittings	T-piece branch flow

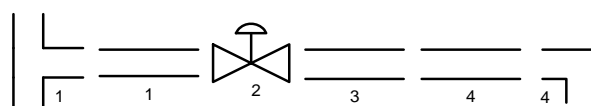


FIG. 5.15. Schematic representation of pipe run 102–600.

TABLE 5.15. TECHNICAL DETAILS FOR PIPE RUN 102–600

Pipe run	No.	Component	Dimensions	Value
102–600	1	Pipe	Length [m]	0.5
			Diameter [m]	0.15405
			Fittings	T-piece branch flow
	2	Valve	Diameter [m]	0.1524
			Type	L-series
	3	Pipe	Length [m]	1.38
			Diameter [m]	0.15405
			Fittings	None
	4	Pipe	Length [m]	0.717
			Diameter [m]	0.1282
			Fittings	Long radius 90° bend

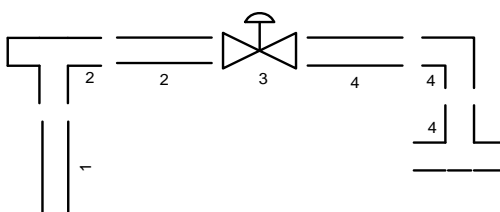


FIG. 5.16. Schematic representation of pipe run 601–103.

TABLE 5.16. TECHNICAL DETAILS FOR PIPE RUN 601–103

Pipe run	No.	Component	Dimensions	Value
601–103	1	Pipe	Length [m]	0.595
			Diameter [m]	0.1282
			Fittings	None
	2	Pipe	Length [m]	0.92
			Diameter [m]	0.15405
			Fittings	T-piece branch flow
	3	Valve	Diameter [m]	0.15424
			Type	L-series
	4	Pipe	Length [m]	1.473
			Diameter [m]	0.15405
			Fittings	Long radius 90° bend
			Fittings	T-piece branch flow

5.2.1.2. Volumes

TABLE 5.17. VOLUME VALUES

Number	Name	Description	Value
33	BV	Volume in front of filter (See Fig. 5.35)	0.7 m ³
34	IV	Internal volume (See Fig. 5.35)	7.1 m ³

5.2.2. Compressor and turbine data

5.2.2.1. Gas properties

The maps are based on the following gas properties as shown in Table 5.18.

TABLE 5.18. GAS PROPERTIES

	$\gamma = c_p/c_v$	c_p [kJ/kg.K]	R [kJ/kg.K]
Compressor	1.395	1.0132	0.2870
Turbine	1.340	1.1472	0.2908

5.2.2.2. Definitions of compressor and turbine efficiency

The compressor efficiency is the isentropic efficiency, which is defined as:

$$\eta_c = \frac{T_{01} \left[\left(p_{02} / p_{01} \right)^{\frac{\gamma-1}{\gamma}} - 1 \right]}{T_{02} - T_{01}} \quad (1)$$

The turbine efficiency on a turbine map is the so-called turbine mechanical efficiency, η_{T-m} , which is defined as the product of turbine isentropic efficiency times the shaft mechanical efficiency.

Consistent with the use of total-to-static pressure ratio, the turbine isentropic efficiency is defined as:

$$\eta_T = \frac{T_{01} - T_{02}}{T_{01} \left[1 - \left(p_2 / p_{01} \right)^{\frac{\gamma-1}{\gamma}} \right]} \quad (2)$$

The actual turbine work can be calculated as:

$$W_T = \eta_T \dot{m} c_p T_{01} \left[1 - \left(p_2 / p_{01} \right)^{\frac{\gamma-1}{\gamma}} \right] \quad (3)$$

The shaft mechanical efficiency is defined as:

$$\eta_m = \frac{W_C}{W_T} \quad (4)$$

Combining Eqs (3) and (4) we can write that:

$$\begin{aligned} W_C &= \eta_m \eta_T \dot{m} c_p T_{01} \left[1 - \left(p_2 / p_{01} \right)^{\frac{\gamma-1}{\gamma}} \right] \\ &= \eta_{T-m} \dot{m} c_p T_{01} \left[1 - \left(p_2 / p_{01} \right)^{\frac{\gamma-1}{\gamma}} \right] \end{aligned} \quad (5)$$

where

$$\eta_{T-m} = \eta_T \eta_m \quad (6)$$

5.2.2.3. Inertias

The inertias of the compressor and turbine wheels are as follows (Table 5.19):

TABLE 5.19. INERTIAS OF COMPRESSOR AND TURBINE WHEELS

Wheel	Inertia [lb-in-s ²]
HPC	0.0008840
HPT	0.0014310
LPC	0.0014700
LPT	0.0040739
ELC	0.0075818
PT	0.0151744

Note: The turbine inertia values include the shaft inertias.

5.2.2.4. Turbine outlet areas

The turbine pressure ratio in the turbine maps is defined as total inlet pressure divided by outlet static pressure. In order to calculate total outlet pressure, one needs to know the outlet areas of the turbines at which the static pressures were measured. These diameters are as follows:

HPT: 104.8 mm;

LPT: 130.2 mm;

PT: 158.8 mm.

5.2.2.5. Units of corrected mass flow and rotational speed

The following definition for compressor corrected mass flow and corrected speed:

Compressor corrected mass flow [lb/min]:

$$W^* = \frac{W \sqrt{T_{1C} / 545}}{P_{1C} / 28.4} \quad (7)$$

Compressor corrected speed [RPM]:

$$N_C = \frac{N}{\sqrt{T_{1C} / 545}} \quad (8)$$

where

W is the mass flow in [lb/min];

T_{1C} is the total inlet temperature [R];

P_{1C} is the total inlet pressure [inch Hg];

N is the rotational speed [RPM].

Turbine corrected mass flow [lb/min]:

$$W^* = \frac{W \sqrt{T_{1T} / 519}}{P_{1T} / 29.92}$$

$$\text{Compressor corrected speed [RPM]: } N_T = \frac{N}{\sqrt{T_{IT}/519}}$$

where

W is the mass flow in [lb/min];

T_{IT} is the total inlet temperature [R];

P_{IT} is the total inlet pressure [inch Hg];

N is the rotational speed [RPM].

5.2.2.6. Low pressure compressor (LPC)

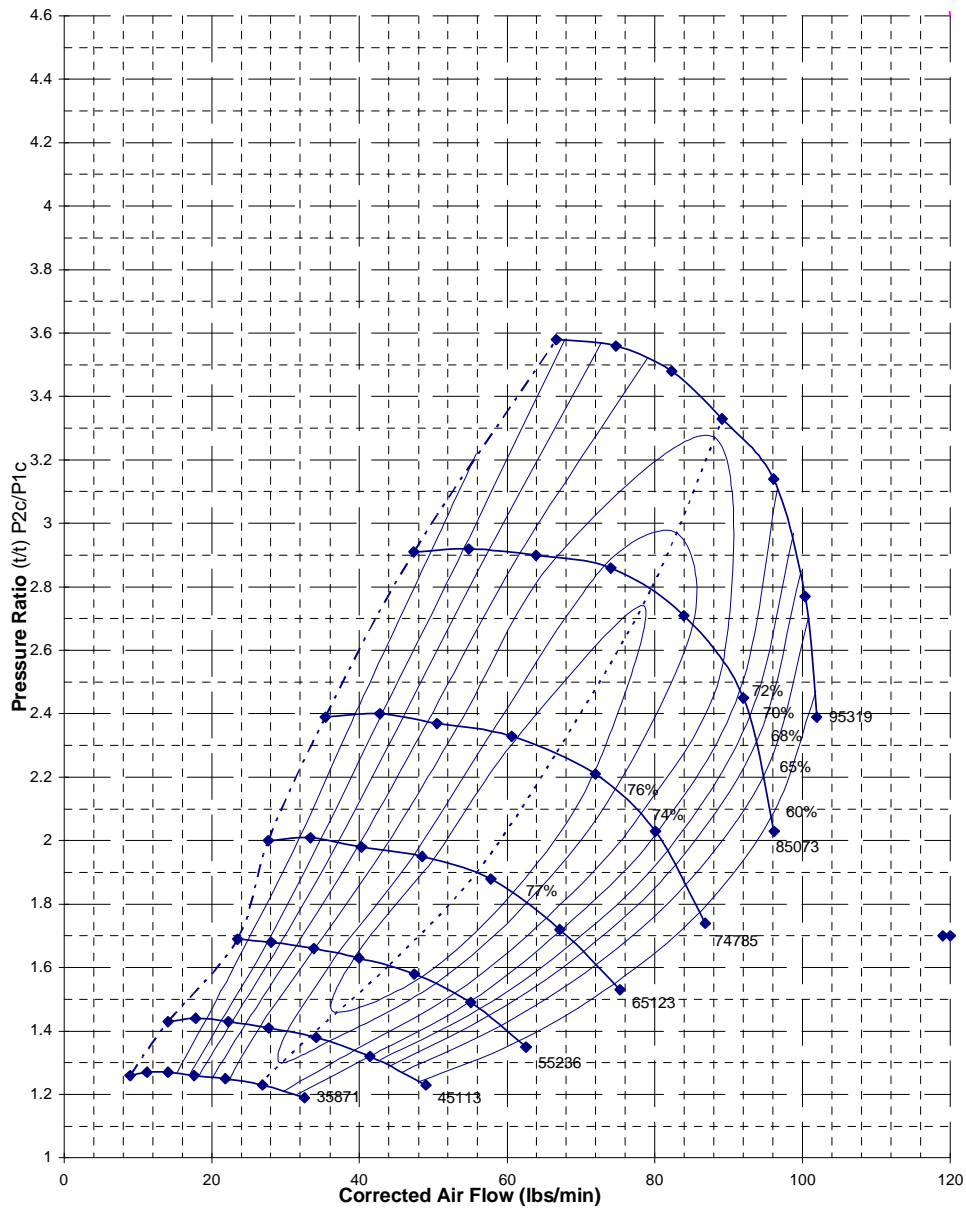


FIG. 5.17. Performance map of the LPC.

TABLE 5.20. PERFORMANCE MAP DATA FOR THE LPC

Compressor map data					
Label	X (lb/min)	Y (PRC)	Label	X (lb/min)	Y (PRC)
35871	Speed 1		68%	16.96	1.26
	8.94	1.26		21.24	1.43
	11.24	1.27		27.53	1.68
	14.12	1.27		34.91	2.01
	17.61	1.26		43.04	2.40
	21.86	1.25		54.13	2.92
	26.86	1.23		67.77	3.58
	32.57	1.19			
45113	Speed 2		70%	99.82	2.85
	14.10	1.43		94.12	2.33
	17.83	1.44		83.03	1.93
	22.27	1.43		70.31	1.65
	27.70	1.41		57.63	1.45
	34.14	1.38		44.13	1.29
	41.42	1.32			
	48.99	1.23			
55236	Speed 3		72%	18.28	1.26
	23.50	1.69		22.76	1.43
	28.04	1.68		29.38	1.68
	33.80	1.66		37.26	2.00
	39.97	1.63		45.91	2.39
	47.45	1.58		57.63	2.92
	55.09	1.49		72.78	3.57
	62.55	1.35		98.78	2.97
65123	Speed 4		74%	93.01	2.40
	27.68	2.00		81.75	1.97
	33.34	2.01		68.95	1.68
	40.27	1.98		56.32	1.47
	48.50	1.95		42.87	1.31
	57.80	1.88			
	67.15	1.72			
	75.31	1.53			
74785	Speed 5		76%	20.03	1.25
	35.41	2.39		24.53	1.42
	42.76	2.40		31.47	1.67
			78%	40.00	1.99
				49.35	2.38

Compressor map data					
Label	X (lb/min)	Y (PRC)	Label	X (lb/min)	Y (PRC)
	50.50	2.37		61.87	2.91
	60.63	2.33		78.93	3.52
	71.94	2.21			
	80.07	2.03		96.64	3.11
	86.84	1.74		91.47	2.47
	Speed 6			80.14	2.02
85073	47.39	2.91		67.39	1.72
	54.83	2.92		54.79	1.49
	63.94	2.90		41.36	1.32
	74.02	2.86		31.55	1.20
	83.94	2.71			
	92.02	2.45	74%	22.46	1.25
	96.16	2.03		26.72	1.42
	Speed 7			33.95	1.66
95319	66.66	3.58		43.21	1.97
	74.77	3.56		53.34	2.36
	82.26	3.48		66.90	2.90
	89.12	3.33		88.13	3.27
	96.09	3.14		89.21	2.56
	100.34	2.77		77.96	2.08
	101.94	2.39		65.50	1.76
Max ETAC	26.33	1.23		52.91	1.52
	33.14	1.38		39.39	1.34
	44.12	1.61		29.66	1.21
	55.89	1.90			
	66.76	2.28	76%	37.21	1.65
	79.65	2.80		47.26	1.95
	89.18	3.33		58.14	2.35
Surge Line	8.94	1.26		73.33	2.87
	14.10	1.43		83.04	2.97
	23.50	1.69		85.13	2.68
	27.68	2.00		74.59	2.16
	35.41	2.39		62.91	1.81
	47.39	2.91		50.32	1.55
	66.66	3.58		36.06	1.37
Efficiency Contour Data				29.25	1.30

Compressor map data					
	X	Y		X	Y
Label	(lb/min)	(PRC)	Label	(lb/min)	(PRC)
50%	10.81	1.33		30.21	1.40
				37.21	1.65
55%	14.55	1.45	77%	50.03	1.94
	19.28	1.57		61.52	2.33
	31.88	2.23		78.48	2.74
	27.87	2.01		71.71	2.21
60%	101.82	2.47		60.92	1.84
	96.11	2.09		48.35	1.57
	86.30	1.78		36.60	1.46
	74.57	1.55		39.56	1.64
	61.73	1.37		50.03	1.94
	48.08	1.24			
65%	15.33	1.27			
	19.28	1.44			
	25.00	1.69			
	31.90	2.01			
	39.46	2.40			
	49.66	2.91			
	55.82	3.22			
	100.79	2.70			
	95.25	2.23			
	84.54	1.87			
	72.09	1.61			
	59.33	1.42			
	45.76	1.27			

5.2.2.7. High pressure compressor (HPC)

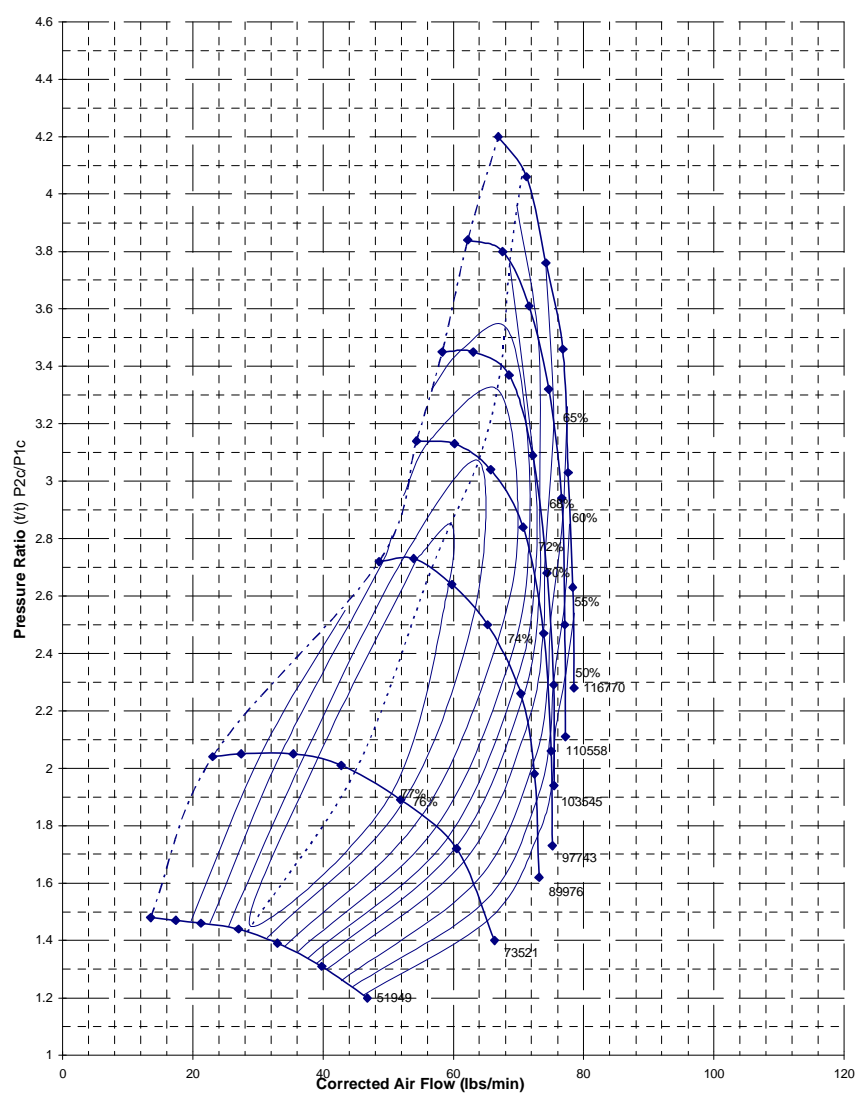


FIG. 5.18. Performance map of the HPC.

TABLE 5.21. PERFORMANCE MAP DATA FOR THE HPC

Compressor map data					
Label	X (lb/min)	Y (PRC)	Label	X (lb/min)	Y (PRC)
51949	Speed 1		60%	77.49	3.26
	13.55	1.48		76.80	2.87
	17.38	1.47		74.93	2.51
	21.27	1.46		74.46	2.29
	26.99	1.44		72.31	2.02
	33.00	1.39		63.71	1.61
	39.79	1.31		42.81	1.26
	46.79	1.20			
73521	Speed 2		65%	23.10	2.04
	23.07	2.04			
	27.43	2.05		74.17	3.77
	35.44	2.05		75.34	3.22
	42.78	2.01		74.08	2.75
	51.88	1.89		73.80	2.48
	60.49	1.72		71.47	2.16
	66.30	1.40		61.82	1.68
89976	Speed 3			40.64	1.30
	48.61	2.72		31.92	2.27
	53.93	2.73		63.17	3.93
	59.76	2.64			
	65.24	2.50	68%	69.75	3.96
	70.37	2.26		73.09	3.48
	72.46	1.98		73.22	2.92
	73.16	1.62		73.19	2.60
97743	Speed 4			70.60	2.24
	54.34	3.14		60.22	1.72
	60.17	3.13		39.01	1.32
	65.70	3.04		37.57	2.41
	70.70	2.84		60.04	3.62
	73.85	2.47			
	75.00	2.06	70%	68.63	3.76
	75.21	1.73		72.40	3.05
103545	Speed 5			72.56	2.68
	58.29	3.45		69.75	2.31
	63.04	3.45		58.86	1.75

Compressor map data					
Label	X (lb/min)	Y (PRC)	Label	X (lb/min)	Y (PRC)
	68.55	3.37		37.70	1.34
	72.19	3.09			
	74.37	2.68	72%	19.74	1.47
	75.39	2.29		30.70	2.06
	75.44	1.94		43.37	2.55
	Speed 6				
110558	62.20	3.84		56.66	3.32
	67.58	3.80		60.93	3.45
	71.62	3.61		67.89	3.54
	74.62	3.32		71.06	3.23
	76.63	2.94		71.60	2.77
	77.10	2.50		68.59	2.37
	77.23	2.11		57.16	1.79
	Speed 7			36.11	1.36
116770	66.89	4.20			
	71.22	4.06	74%	22.64	1.46
	74.21	3.76		33.74	2.06
	76.79	3.46		49.19	2.72
	77.63	3.03		50.56	2.81
	78.35	2.63			
	78.50	2.28		52.36	2.95
Max ETAC	28.40	1.43		56.32	3.14
	44.95	1.99		66.74	3.32
	56.77	2.70		69.92	2.88
	64.03	3.08		66.86	2.45
	67.31	3.40		55.02	1.83
	68.69	3.77		34.13	1.38
	70.66	4.09			
Surge line	13.55	1.48	76%	25.46	1.45
	23.07	2.04		37.27	2.05
	48.61	2.72		52.29	2.73
	54.34	3.14		63.86	3.07
	58.29	3.45		63.26	2.55
	62.20	3.84		52.23	1.88
	66.89	4.20		31.46	1.41
Efficiency Contour Data					

Compressor map data					
Label	X (lb/min)	Y (PRC)	Label	X (lb/min)	Y (PRC)
50%	78.55	2.54	78%	52.95	2.46
	77.25	2.33	77%	54.41	2.73
	75.62	2.12		59.69	2.85
	75.20	1.96		59.41	2.65
	73.20	1.78		50.44	1.91
	65.77	1.48		28.93	1.45
	46.21	1.21		39.31	2.04
55%	77.84	2.85		54.41	2.73
	77.07	2.58			
	75.37	2.30			
	74.88	2.12			
	72.84	1.89			
	64.96	1.54			
	44.62	1.24			

5.2.2.8. External load compressor (ELC)

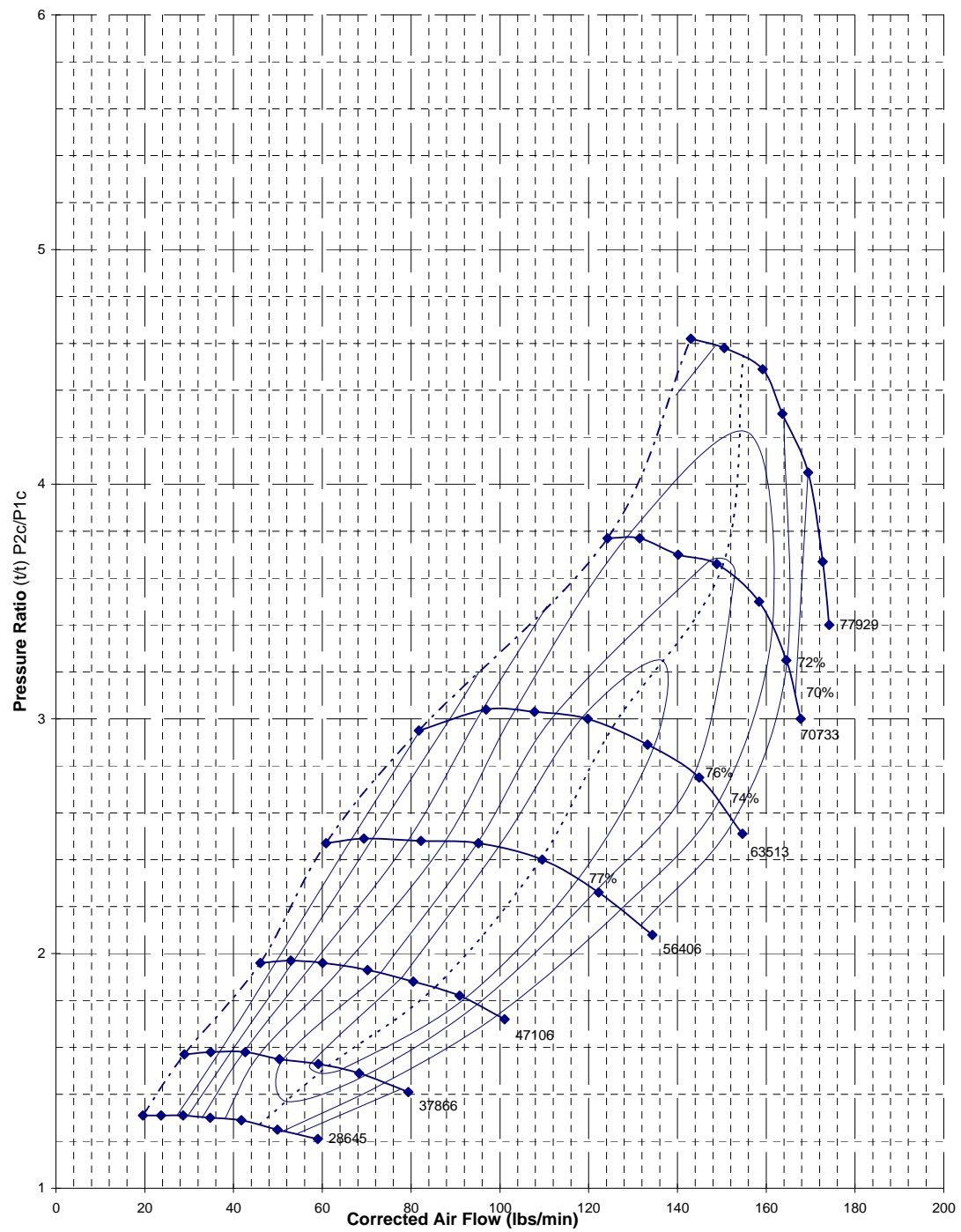


FIG. 5.19. Performance map of the ELC.

TABLE 5.22. PERFORMANCE MAP DATA FOR THE ELC

Compressor map data					
Label	X (lb/min)	Y (PRC)	Label	X (lb/min)	Y (PRC)
28645	Speed 1		70%	29.74	1.31
	19.59	1.31		39.41	1.58
	23.69	1.31		53.57	1.97
	28.65	1.31		71.29	2.49
	34.72	1.30		88.75	3.00
	41.76	1.29		95.30	3.20
	49.89	1.25		169.41	4.05
	58.98	1.21		166.59	3.11
37866	Speed 2		72%	56.45	1.22
	28.92	1.57		32.92	1.30
	34.89	1.58		42.30	1.58
	42.67	1.58		58.05	1.96
	50.35	1.55		79.26	2.48
	59.10	1.53		95.82	3.03
	68.31	1.49		110.58	3.48
	79.33	1.41			
47106	Speed 3			139.67	4.38
	46.01	1.96		148.52	4.59
	52.91	1.97			
	60.03	1.96		164.00	4.28
	70.15	1.93		164.66	3.24
	80.50	1.88		152.80	2.57
	90.93	1.82		131.65	2.12
	101.04	1.72			
56406	Speed 4		74%	77.33	1.42
	60.82	2.47		54.03	1.23
	69.38	2.49		38.17	1.30
	82.20	2.48		45.84	1.57
	95.16	2.47		64.40	1.94
	109.56	2.40		87.38	2.47
	122.22	2.26		103.49	3.04
	134.34	2.08		128.40	3.77
63513	Speed 5			155.99	4.22
	81.76	2.95		161.41	3.40
	96.88	3.04		149.68	2.66
	107.82	3.03		127.37	2.19
	119.78	3.00		99.57	1.74
	133.27	2.89		74.11	1.45
	144.90	2.75		50.75	1.24
	154.65	2.51			
70733	Speed 6		76%	73.27	1.92
	124.25	3.77		94.91	2.47
	131.46	3.77		112.48	3.02
	140.13	3.70		146.95	3.67
	148.87	3.66		150.90	3.68
	158.40	3.50		152.93	3.62
	164.53	3.25		143.91	2.77
	167.74	3.00		121.78	2.27
77929	Speed 7			95.34	1.79
	142.99	4.62		69.60	1.48
	150.57	4.58		51.77	1.37
	159.18	4.49			
	163.62	4.30			

Compressor map data					
Label	X (lb/min)	Y (PRC)	Label	X (lb/min)	Y (PRC)
	169.43	4.05		51.17	1.55
	172.72	3.67		73.27	1.92
	174.17	3.40			
Max ETAC	45.81	1.27	77%	78.02	1.90
	61.27	1.52		99.86	2.46
	85.59	1.86		118.71	3.01
	109.16	2.40		136.48	3.25
	125.57	2.97		134.66	2.88
	150.11	3.65		117.71	2.32
	154.88	4.55		92.20	1.81
Surge line	19.59	1.31		64.71	1.51
	28.92	1.57		59.50	1.49
	46.01	1.96		57.30	1.53
	60.82	2.47		78.02	1.90
	81.76	2.95			
	124.25	3.77			
	142.99	4.62			
Efficiency contour data					
60%	24.09	1.44			
65%	41.51	1.85			
68%	27.21	1.31			
	36.80	1.58			
	49.75	1.97			
	66.30	2.48			
	82.03	2.95			
	82.26	2.96			

5.2.2.9. Startup blower systems' (SBS) blower

TABLE 5.23. PERFORMANCE DATA FOR THE SBS BLOWER

SBS blower map data					
Corrected speed	X Corrected mass flow	Y Pressure ratio	Corrected speed	X Corrected mass flow	Y Pressure ratio
1.75	4.52	1.49	1.95	5.16	1.49
	4.74	1.35		5.3	1.35
	4.95	1.2		5.58	1.2
	5.09	1.1		5.79	1.1
2.14	5.79	1.49	2.34	6.43	1.49
	5.94	1.35		6.57	1.35
	6.15	1.2		6.78	1.2
	6.36	1.1		7	1.1
2.53	7.00	1.49	2.73	7.63	1.49
	7.21	1.35		7.85	1.35
	7.42	1.2		8.06	1.2
	7.63	1.1		8.2	1.1
1.75	4.52	69	1.95	5.16	71
	4.74	75		5.3	76
	4.95	78		5.58	82
	5.09	81		5.79	83
2.14	5.79	73	2.34	6.43	74
	5.94	76		6.57	78
	6.15	81		6.78	80
	6.36	79		7	83
2.53	7	74	2.73	7.63	75
	7.21	79		7.85	79
	7.42	82		8.06	82
	7.63	81		8.2	81

With:

Corrected Speed in [rev/s]/sqrt[K];

Corrected mass flow in [kg/s]*sqrt[K]/Pa;

Efficiency in %;

0.147 tia.

5.2.2.10. Low pressure turbine (LPT)

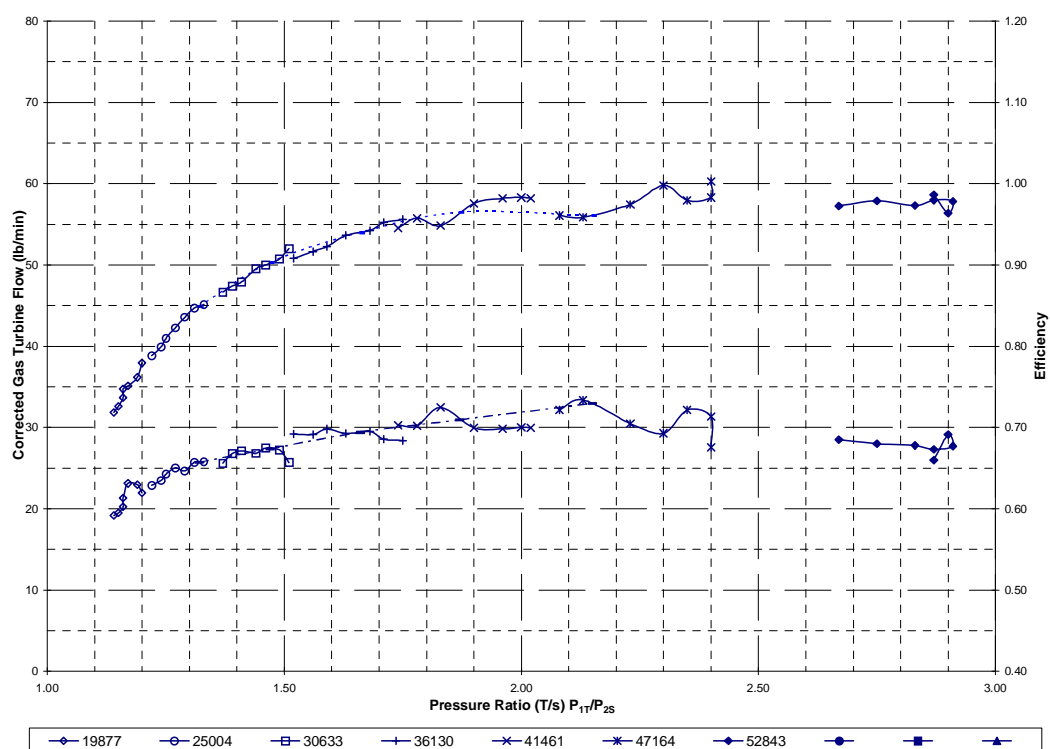


FIG. 5.20. Performance map of the LPT.

TABLE 5.24. PERFORMANCE MAP DATA FOR THE LPT

Turbine map data			
Label	PRT	WT (lbs/min)	ETATM
Speed 1			
19877	1.14	31.82	0.59
	1.15	32.62	0.59
	1.16	33.66	0.60
	1.16	34.72	0.61
	1.17	35.10	0.63
	1.19	36.16	0.63
	1.20	37.94	0.62
Speed 2			
25004	1.22	38.84	0.63
	1.24	39.91	0.63
	1.25	40.96	0.64
	1.27	42.28	0.65
	1.29	43.60	0.65
	1.31	44.71	0.66
	1.33	45.12	0.66
Speed 3			
30633	1.37	46.65	0.66
	1.39	47.41	0.67
	1.41	47.92	0.67
	1.44	49.53	0.67
	1.46	50.01	0.67
	1.49	50.77	0.67
	1.51	51.99	0.66
Speed 4			

Turbine map data			
Label	PRT	WT (lbs/min)	ETATM
36130	1.52	50.81	0.69
	1.56	51.67	0.69
	1.59	52.27	0.70
	1.63	53.64	0.69
	1.68	54.23	0.70
	1.71	55.24	0.69
	1.75	55.60	0.68
Speed 5			
41461	1.74	54.56	0.70
	1.78	55.76	0.70
	1.83	54.86	0.72
	1.90	57.58	0.70
	1.96	58.20	0.70
	2.00	58.30	0.70
	2.02	58.21	0.70
Speed 6			
47164	2.08	56.09	0.72
	2.13	55.87	0.73
	2.23	57.47	0.71
	2.30	59.79	0.69
	2.35	57.96	0.72
	2.40	58.30	0.71
	2.40	60.27	0.68
Speed 7			
52843	2.67	57.27	0.69
	2.75	57.90	0.68
	2.83	57.30	0.68
	2.87	57.98	0.67
	2.91	57.82	0.68
	2.90	56.39	0.69
	2.87	58.66	0.66

TABLE 5.25. PERFORMANCE MAP DATA FOR THE HPT

Turbine map data			
Label	PRT	WT (lbs/min)	ETATM
Speed 1			
28798	1.24	28.92	0.69
	1.27	30.32	0.69
	1.29	31.53	0.69
	1.33	32.92	0.68
	1.36	33.93	0.67
	1.39	34.85	0.66
	1.41	35.48	0.65
Speed 2			
40767	1.54	37.14	0.72
	1.59	38.07	0.72
	1.68	39.46	0.71
	1.73	40.48	0.71
	1.80	41.14	0.70
	1.87	41.78	0.69
	1.88	41.92	0.69
Speed 3			
49871	2.13	42.41	0.74
	2.23	42.84	0.70
	2.29	42.98	0.71
	2.33	43.09	0.70
	2.37	43.26	0.70
	2.36	43.07	0.71
	2.32	42.94	0.71
Speed 4			
54198	2.48	42.62	0.70
	2.58	43.09	0.69
	2.64	42.89	0.69
	2.68	42.99	0.69
	2.67	42.88	0.70
	2.63	42.98	0.69
	2.56	42.99	0.69
Speed 5			
57410	2.77	42.22	0.69
	2.87	42.32	0.68
	2.96	42.29	0.68
	2.95	42.32	0.68
	2.90	42.54	0.68
	2.85	42.54	0.68
	2.79	42.24	0.69
Speed 6			
61304	3.21	41.42	0.66
	3.37	41.51	0.64
	3.42	41.62	0.63
	3.42	41.59	0.64
	3.34	41.60	0.65
	3.21	41.52	0.66
	3.09	41.53	0.67
Speed 7			
64710	3.82	40.87	0.60
	3.95	40.82	0.58
	3.94	40.83	0.58
	3.94	40.88	0.58
	3.78	40.94	0.60
	3.61	41.00	0.61
	3.50	40.91	0.63

5.2.2.12. Power turbine (PT)

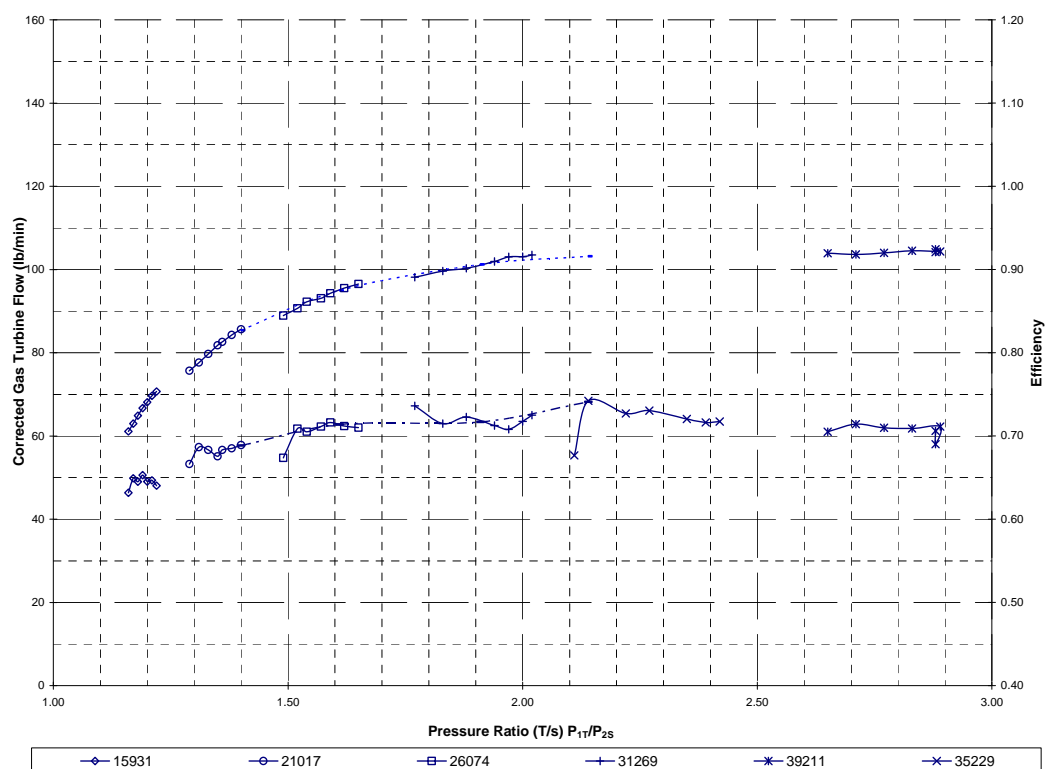


FIG. 5.22. Performance map of the PT.

TABLE 5.26. PERFORMANCE MAP DATA FOR THE PT

Turbine map data			
Label	PRT	WT (lbs/min)	ETATM
Speed 1			
15931	1.16	61.09	0.63
	1.17	62.96	0.65
	1.18	64.87	0.65
	1.19	66.71	0.65
	1.20	68.12	0.65
	1.21	69.64	0.65
	1.22	70.69	0.64
Speed 2			
21017	1.29	75.68	0.67
	1.31	77.65	0.69
	1.33	79.70	0.68
	1.35	81.79	0.68
	1.36	82.62	0.68
	1.38	84.28	0.69
	1.40	85.64	0.69

Turbine map data			
Label	PRT	WT (lbs/min)	ETATM
Speed 3			
26074	1.49	88.93	0.67
	1.52	90.66	0.71
	1.54	92.27	0.71
	1.57	93.10	0.71
	1.59	94.27	0.72
	1.62	95.53	0.71
	1.65	96.55	0.71
Speed 4			
31269	1.77	98.14	0.74
	1.83	99.66	0.71
	1.88	100.30	0.72
	1.94	101.94	0.71
	1.97	103.05	0.71
	2.00	103.10	0.72
	2.02	103.52	0.73
Speed 5			
35229	2.11	102.84	0.68
	2.14	103.12	0.74
	2.22	103.90	0.73
	2.27	104.79	0.73
	2.35	105.36	0.72
	2.39	105.75	0.72
	2.42	105.59	0.72
Speed 6			
39211	2.65	103.91	0.71
	2.71	103.65	0.71
	2.77	104.02	0.71
	2.83	104.51	0.71
	2.89	104.36	0.71
	2.88	104.89	0.69
	2.88	104.16	0.71

5.2.3. Heat exchangers

Note that the baffles in all of the shell-and-tube heat exchangers discussed below are equally spaced throughout the shell. The height of the baffles is as follows:

- RX = 465 mm;
- PC = 307 mm;
- IC = 268.5 mm;
- External load compressor = 268.5 mm.

5.2.3.1. Precooler (PC)

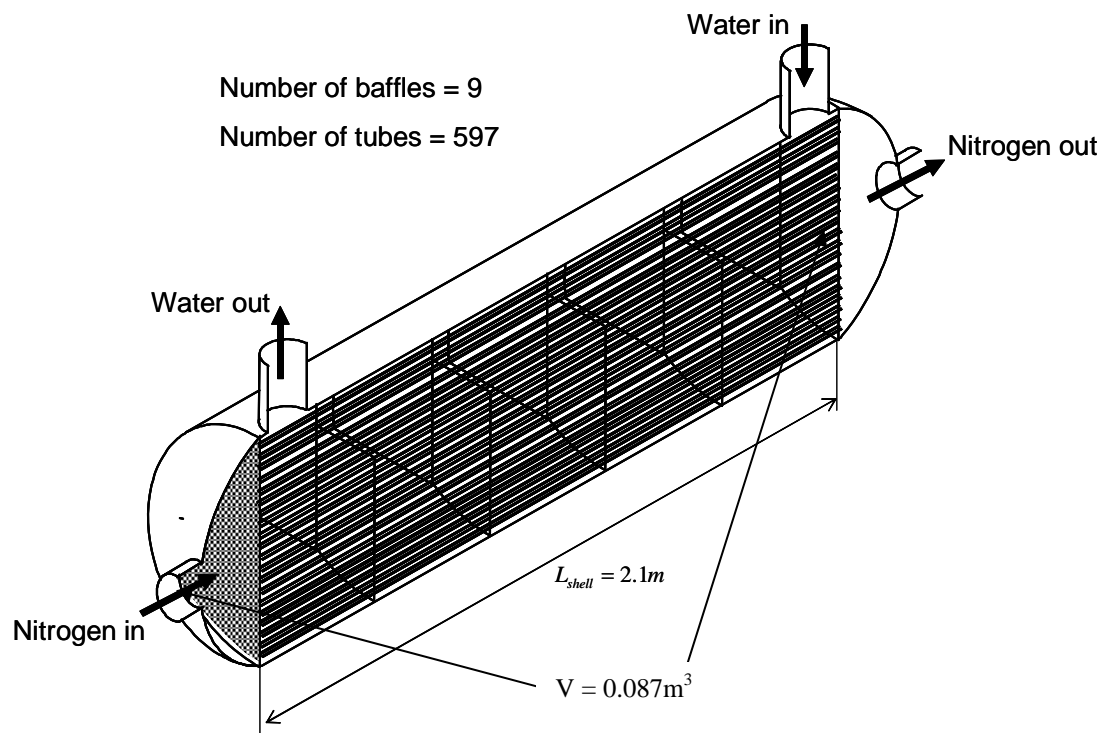


FIG. 5.23. PC general arrangement.

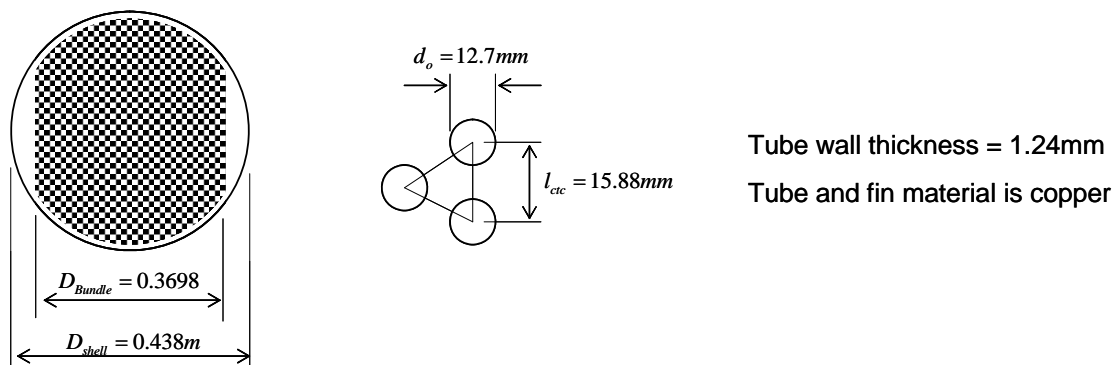


FIG. 5.24. PC detail.

5.2.3.2. Intercooler (IC)

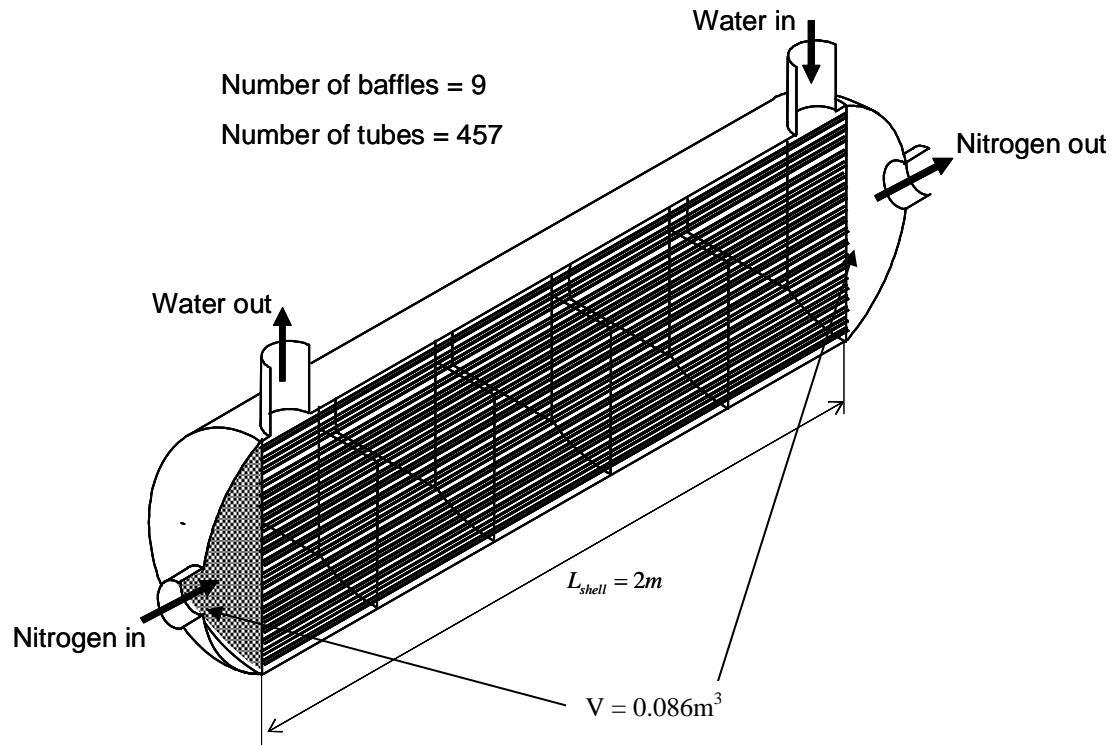


FIG. 5.25. IC general arrangement.

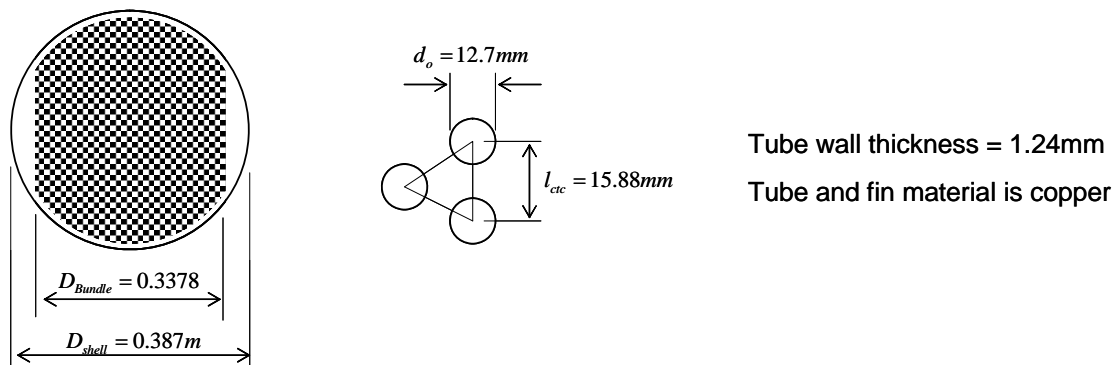


FIG. 5.26. IC detail.

5.2.3.3. External Load Heat Exchanger (ELHX)

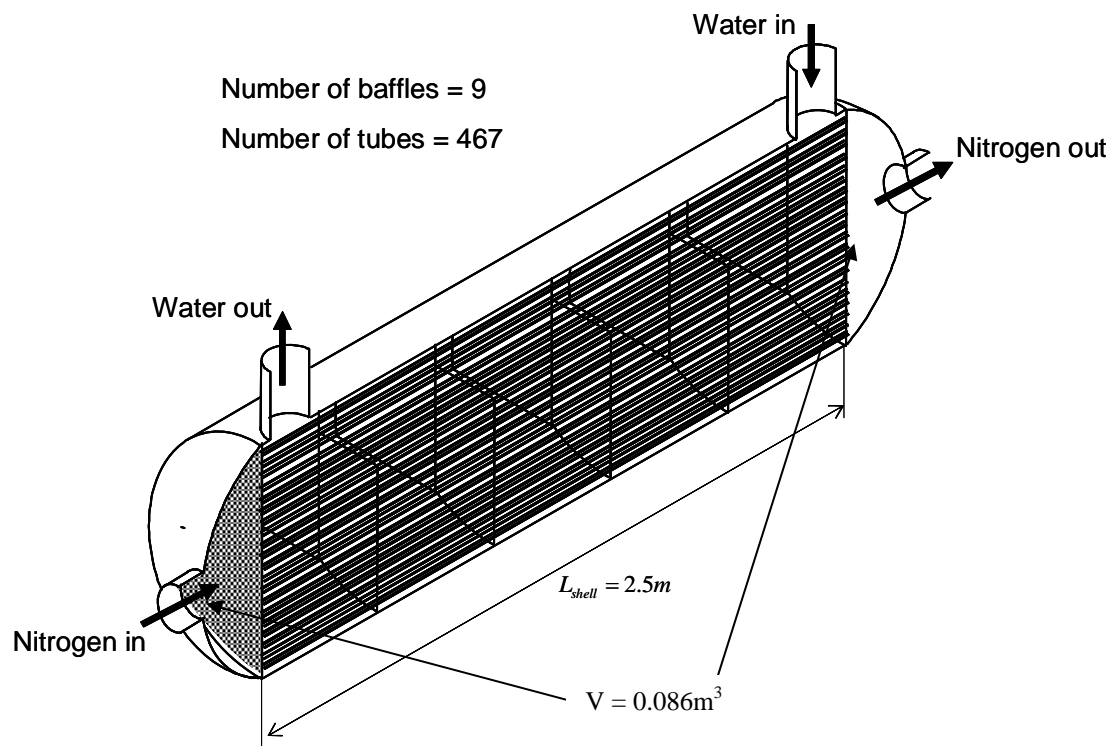


FIG. 5.27. ELHX general arrangement.

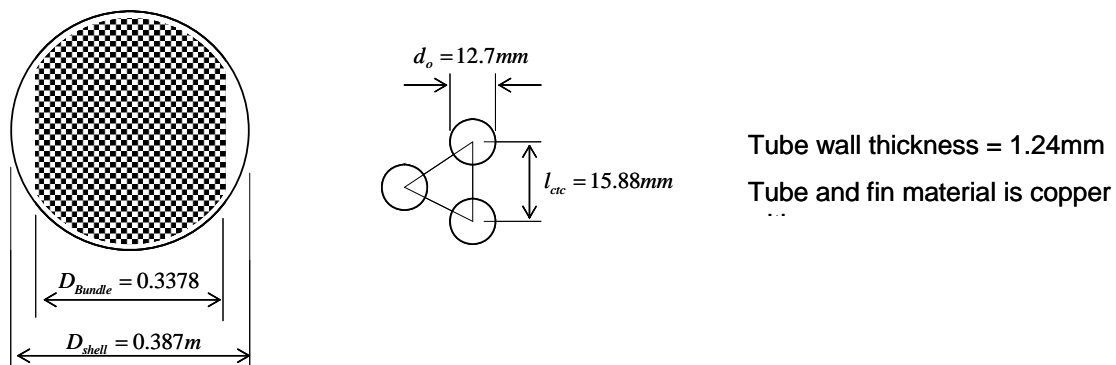


FIG. 5.28. ELHX detail.

5.2.3.4. Recuperator (RX)

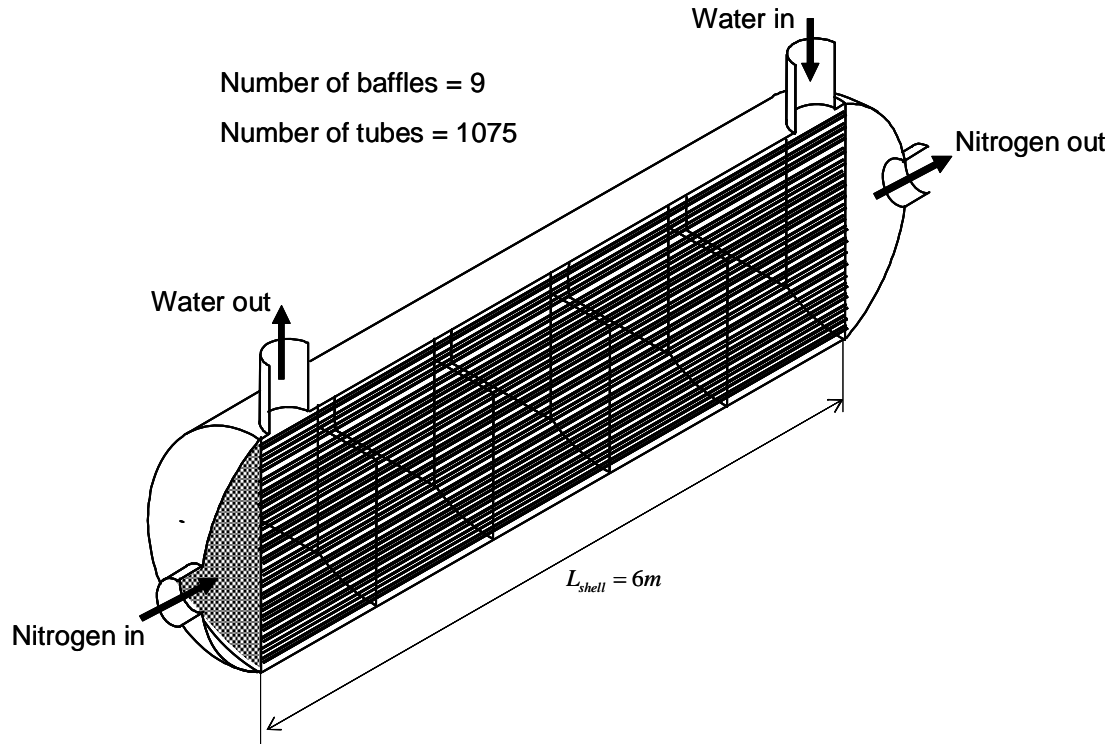


FIG. 5.29. RX general arrangement.

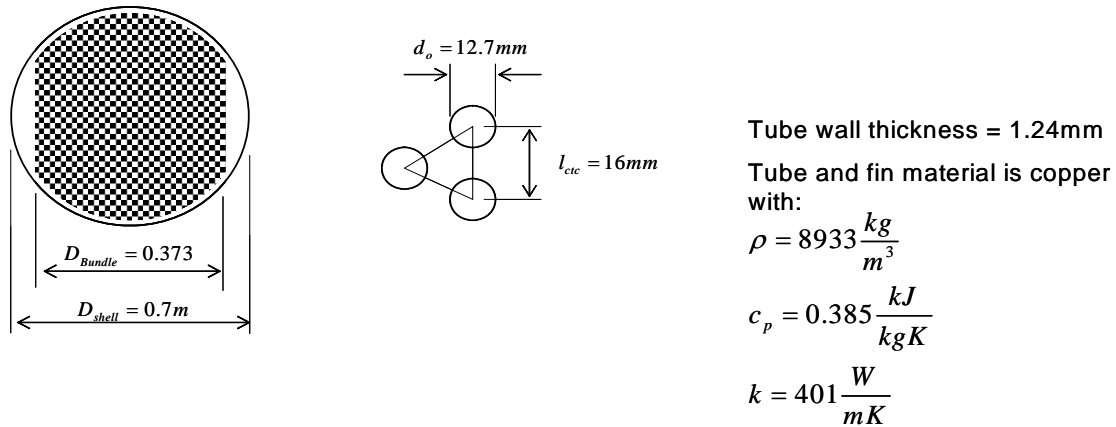


FIG. 5.30. RX detail.

Note that the figure of the recuperator is only a schematic representation and that the cone-shaped volumes are not applicable in this case.

5.2.4. Heat source

The heater (HS in Fig. 5.1) of the PBMM has a power rating of 420 kW and is contained inside the heater section of the pressure vessel. Its purpose is to raise the temperature of circulated nitrogen gas flowing from the recuperator inside the pressure vessel from about 400°C to a maximum of 700°C at 100% Maximum Continuous Rating (MCR) before it reaches the HPT in the compressor/turbine

section of the vessel. The heater is composed of three subassemblies or subsystems (Fig. 5.31) consisting of:

- Three heater cassettes (HCs) within a gas-tight cover or sheath;
- An aft duct subassembly (AftDuct);
- A forward duct subassembly (FwdDuct).

The Fwd Duct is connected to the exit flange of the recuperator with the aid of an NPS 10-inch compensatory pipe allowing for thermal linear expansion of the recuperator. The Aft Duct of the heater is coupled to the HPT on the compressor/turbine plate through an NPS 6-inch flanged pipe that is also compensated to allow for thermal heat expansion of the heater assembly. Subassemblies are appropriately insulated to restrict heat loss to the enclosing pressure boundary atmosphere to ensure that the metal surface temperature of the pressure boundary remains below the allowed design temperature upper limit of 120°C.

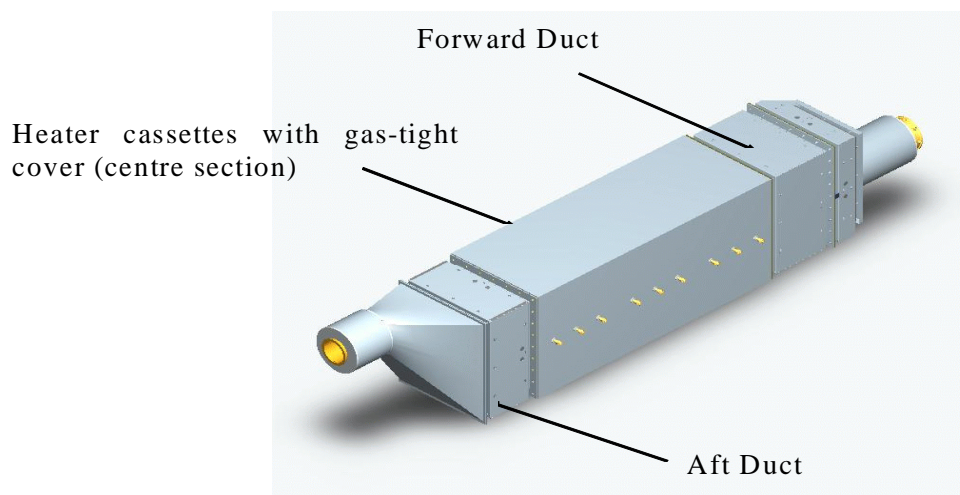


FIG. 5.31. 3-D view of the heater showing heater assembly (three heater cassettes are contained in the gas-tight centre cover).

5.2.4.1. Heater cassette heater subassembly

The three longitudinally coupled cassettes of the heater are rated at 140 kW each. Each cassette is floating star-connected to a 380 V three-phase electrical supply. Cassettes have effective inside dimensions of 500 × 600 mm and are 600 mm long, housing a total of 48 heating elements each. The heater elements are connected four in series and then four in parallel per phase. All series and parallel connections are made on the insides of the cassettes and these connections are linked to outside, side terminals, to facilitate connection to the external power supply (Fig. 5.31). Appropriately positioned alumina tubes are employed to electrically insulate parallel connections.

Cassettes are manufactured from SA312 TP304L stainless steel sheet and angle. A 600 × 560 × 600 mm long subframe, welded from 30 × 30 × 6 mm angles, forms the base of each cassette. Small rectangular stainless steel blocks, welded to the open-end sides of opposing subframe vertical angles, function as restrains to two opposing 640 × 572 mm side plates allowing for thermal expansion of these plates in three directions. These plates are provided with 48 tapped holes that are equally spaced in eight horizontal rows with six holes in a row, staggered in a zigzag fashion between rows. The side plates are provided with 45 mm long M10, stainless steel bolts (SA 312 TP 316) and with spring washers of the same, acting as central suspension anchor stubs to ceramic insulation tubes hung on the insides of the cassette subframes. Electrical insulation between protruding electrodes and side plates are provided by 6 × 24 mm 'T'-type (hole diameter 16.5 mm) alumina insulators on each cassette.

The insulation tubes form the bases to spirally wound heating elements giving rise to a seven-point star when viewed head-on. The subframe of each cassette is welded to two opposing $60 \times 60 \times 6$ mm thick stainless angles orientated in such a manner as to provide flanged open-ends to each cassette. The flange angles are provided with 28×14 mm diameter holes to allow for longitudinal stacking and bolting of cassettes.

The top and bottom sides of cassette subframes consist of latched profiled covers with inside dimensions of 588×556 mm produced from 1.5 mm thick steel sheets, which fit between cassette flange angles. 25 mm wide 90° bends limit further sideways displacement of these covers after assembly.

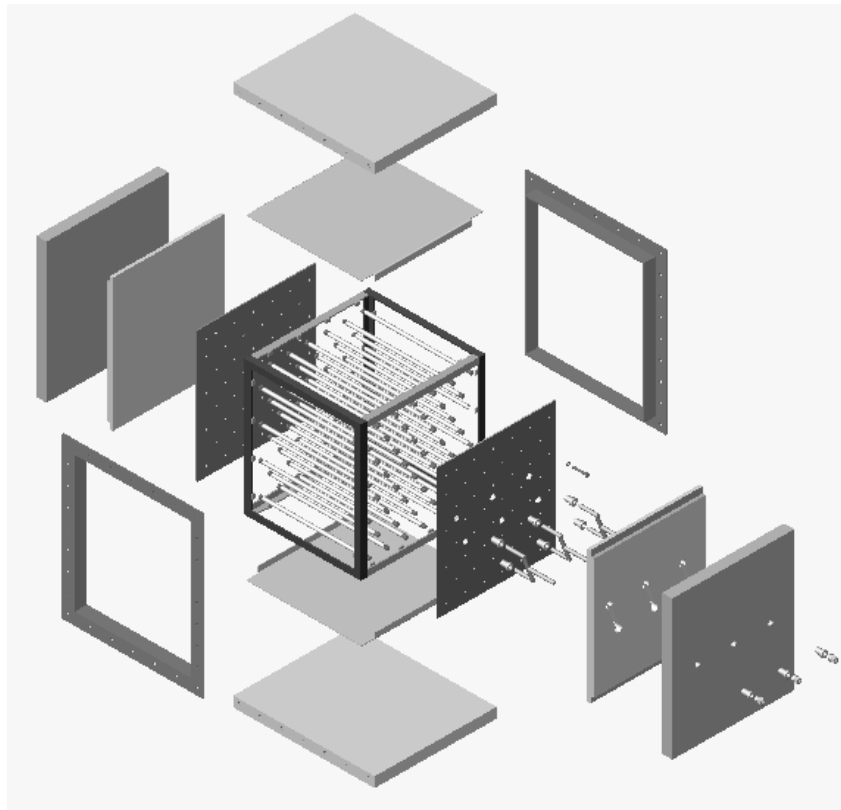


FIG. 5.32. Exploded view of the 3-D model of a heater cassette showing the subframe with heater element insulation tubes and other assembly parts. Spirally wound heater elements are not shown.

Longitudinally stacked cassettes are bolted to each other and are covered with an appropriately bent sheath produced from a 1.5 mm thick stainless steel sheet. One side of the sheet used to produce the sheath is provided with 9×24.2 mm holes to allow for cassette electrode protrusion. The sheath is welded length-wise and to the flanged angles of the aft and forward cassettes.

5.2.4.2. Heater elements and tubes

The heater element insulation tubes are 4 mm thick and about 495 mm long with an outside diameter of 17 mm.

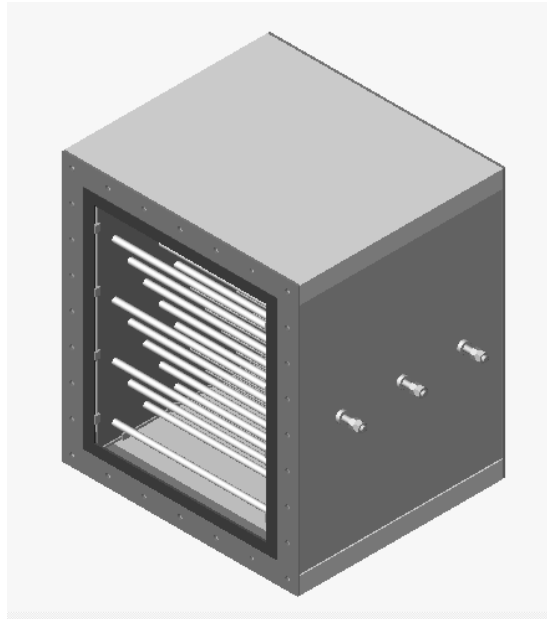


FIG. 5.33. Orientated PBMM heater cassette assembly illustrating, e.g. external electrical connectors and heater element insulation tubes. Spirally wound heater elements are not shown.

The spirally wound element wire has been insulated from subframe side plates through the use of alumina rings that fit over the insulation tubes and are held in place against the sub-frame side plates by the wound element wire.

5.2.4.3. Heater cassette thermal insulation

Heater cassette thermal insulation is provided by Type Kerform KVS 141 alumina-silica fibreboard with a continuous application rating of 1300°C. The mean specific heat capacity of the Type 141 board is 0.96 kJ/kg K for the temperature range 20°C to 400°C and 1.06 kJ/kg K for the temperature range between 400°C and 1200°C. Thermal conductivity in the temperature range 200°C to 800°C varies between 0.09 and 0.19 W/mK (0.15 W/mK at 600°C).

5.2.5. Aft and forward components

The aft and forward ducts are bolted to the heater cassette assembly via the flanged angles provided. Graphite gaskets produced to fit the flanged angles were originally used to seal the contact surfaces. The use of graphite as gasket material was later replaced by 0.25 mm stainless steel foil, as a precaution to eliminating carbon soot build-up on element insulator tubes which gave rise to electric short-circuiting of the Heater during preliminary test runs of the model.

Three staggered stainless steel sieves of sizes of 9, 16 and 64 mesh which are welded to stainless angle subframes, are bolted to the inside of the forward duct assembly. The sieve with the smallest sieve size (64 mesh) separates the other sieves in the sieve assembly from the first heater cassette. The aim of the sieves is to ensure uniform flow through the heater in order to prevent the formation of hot spots. The aft duct assembly similarly houses a sieve (64 mesh) in order to finally restrict the transmission of weld metal particles or other unwanted material to the HPT in the compressor/turbine section of the model.

The forward duct assembly is provided with an NPS 10" compensated pipe which couples to the recuperator with the aid of two stainless steel half-section clamps. The flange end of the pipe boasts eight equally spaced 20 mm sockets welded to the circumference of the pipe. Sockets at 12, 3 and 9 o'clock provide for 3/8 inch pressure measuring fittings. Four sockets equally spaced between the

above sockets (2, 5, 7, and 11 o'clock) provide for 1/4 inch temperature fittings (see tags on drawing model). Five holes were drilled through both the sockets and the pipe to accommodate, for example, the measuring thermocouples.

5.2.5.1. Aft and forward duct pipe insulation

Both the forward and aft duct pipe couplings are insulated with 75 mm thick refractory fibre blankets (Thermal Ceramics type Fiberfrax Durablanket) wrapped around each pipe. The blankets are enclosed by a 0.5 mm thick Grade 420 2B stainless steel sheet metal cladding and end-pieces. The alumina-silica-containing refractory blanket has a continuous operation rating of 1260°C, a mean thermal conductivity of 0.4 W/mK at 760°C and a packing density of 192 kg/m³ for the material employed. This would result in a hot face pipe temperature of about 650°C being reduced to 72°C for 75 mm thick material. A hot face temperature of 760°C would be reduced to 86°C based on a surface emissive factor of 0.9 at 27°C.

5.2.5.2. Aft and forward duct insulation

Insulation blankets of similar type and thickness as described in Section 5.4 were sandwiched between the outer and inner cowlings within both the forward and aft duct assemblies. The blanket material, however, was enclosed in a woven refractory matt stitched with stainless steel wire. This design was adopted to be able to place the blanket inside the contoured ducts of the aft assembly with relative ease and to further eliminate the possibility of blanket fibre escape through cowling joints, thereby contaminating nitrogen gas flow and negatively influencing the HPT operation.

5.2.6. Pressure boundary

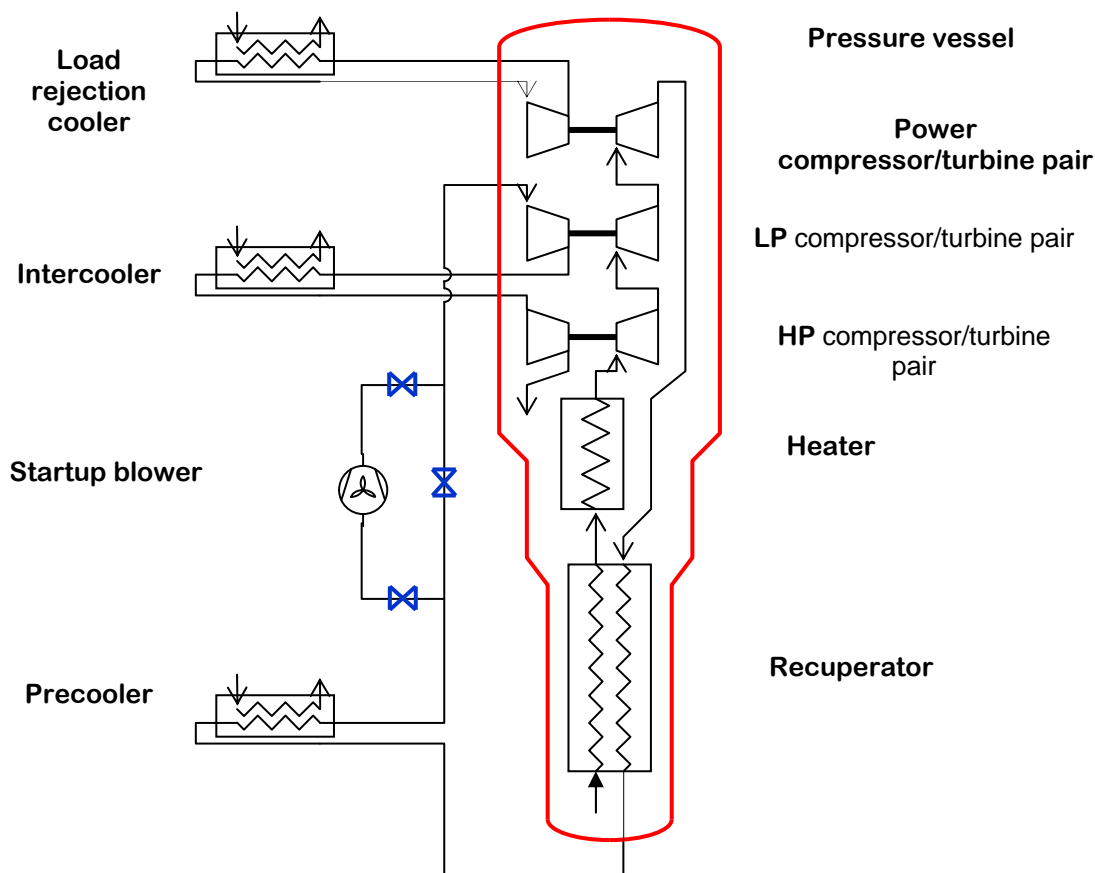


FIG. 5.34. Physical layout of the PBMM.

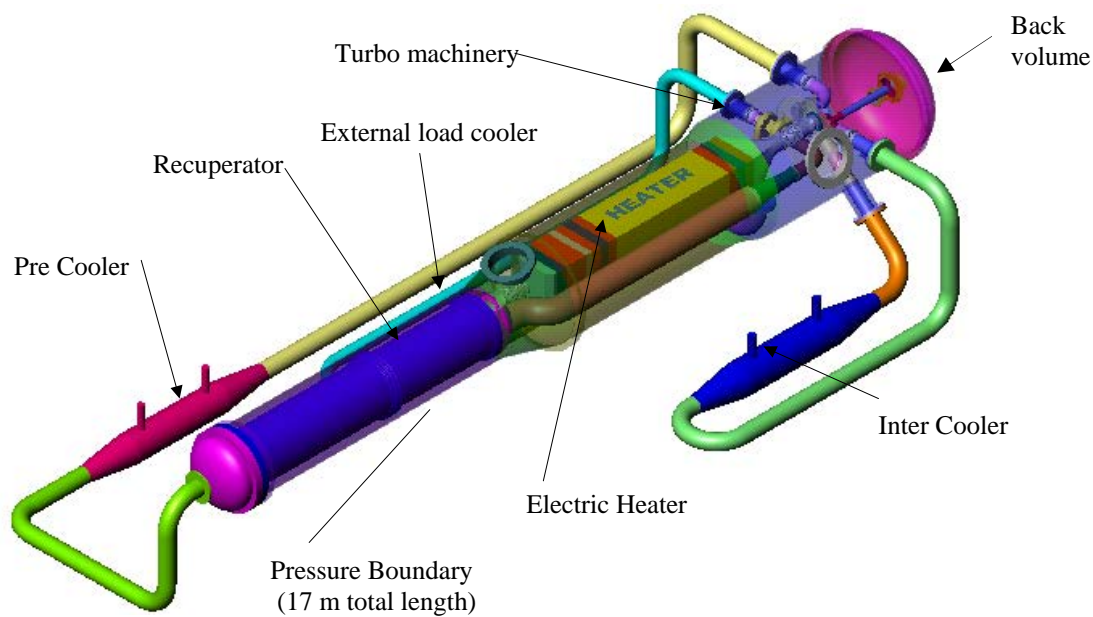


FIG. 5.35. Solid model of the PBMM.

5.2.7. Control valves

All the control valves in the PBMM are ANSI control vales. All the definitions and equations that were used are according to the ANSI/ISA-75.01 — 1985 (R1995) standard.

TABLE 5.27. R-SERIES CONTROL VALVE DATA

Size	Relative opening									
Inch	10%	20%	30%	40%	50%	60%	70%	80%	90%	100%
1	0.52	1.13	2.23	3.83	5.95	8.58	11.7	16.2	24.1	45
1.5	1.3	3.3	6.4	11.1	17.2	24.8	33.9	46.5	69.3	110
2	2	5	10	17.2	26.6	38.4	52.5	72.4	108	180
2.5	3.3	8	15.9	27.3	42.3	61	83.4	114	170	280
3	5	12	23	39	61	88	121	165	246	420
4	8	19	37	63	98	141	193	264	393	620
6	14	34	67	115	178	258	352	484	719	1260
8	23	55	109	187	290	418	571	784	1164	2030
Cv/d2	0.59	1.45	2.86	4.93	7.64	11	15.07	20.67	30.8	48.9
F1	0.94	0.93	0.92	0.88	0.85	0.81	0.78	0.72	0.61	0.42
xT	0.64	0.64	0.63	0.62	0.59	0.54	0.49	0.4	0.32	0.16
Z	0.44	0.43	0.41	0.38	0.35	0.31	0.28	0.25	0.2	0.16

TABLE 5.28. L-SERIES CONTROL VALVE DATA

Size	Relative opening									
Inch	10%	20%	30%	40%	50%	60%	70%	80%	90%	100%
3	12.5	31.3	51	75	103	137	174	208	238	245
4	17	40.4	73	108	152	198	225	321	413	450
6	38	82.6	139	212	306	430	596	820	1116	1500
8	77	168	283	432	622	874	1212	1668	2268	3050
Cv/d2	1.38	3.02	5.09	7.76	11.17	15.69	21.77	29.96	40.72	54.75
F1	0.87	0.85	0.83	0.81	0.77	0.73	0.67	0.6	0.49	0.36
xT	0.53	0.53	0.53	0.52	0.47	0.41	0.35	0.27	0.19	0.11
Z	0.38	0.34	0.31	0.28	0.25	0.23	0.2	0.17	0.14	0.11

5.3. BENCHMARK DEFINITIONS

The following comparisons are to be made for the PBMM:

- Comparisons between measured and experimental results to simulation results (code-to-plant);
- Comparisons between different simulation codes (code-to-code).

From a verification and validation point of view the comparisons with the experimental results are important. However, in the case of the PBMM, the uncertainty about the accuracy of the measurements may limit the usefulness of the comparison. For instance, accurate temperature measurements may not be possible at every point in the cycle because of short pipe lengths. It may sometimes also be very difficult if not impossible to include all phenomena in the simulation, for instance heat transfer between undefined geometries. On the other hand, the advantage of code-to-code comparisons is that the same phenomena can be included (or excluded) and valid comparisons made.

Successive benchmark definitions have been proposed throughout the CRP-5 at different RCM meetings. These can be distinguished by three series of calculations which differ by the proposed operating conditions of the PBMM (steady states at different system pressure and heater outlet temperature) and by the considered transients. These are summarized as follows:

Series 1:

Three steady state conditions: (100 kPa and 700°C), (100 kPa and 600°C) and (250 kPa and 700°C);

Four transients:

- (1) Load rejection;
- (2) Mass injection at high pressure point;
- (3) Mass injection at low-pressure point;
- (4) Startup.

Series 2:

Two steady state conditions: (95 kPa and 600°C) and (115 kPa and 600°C);

Three transients:

- (1) Load following;
- (2) Load rejection;
- (3) Opening of compressor bypass valves.

Series 3:

Two steady state conditions: (94 kPa and 644.6°C) and (113.5kPa and 647.6°C);

One transient corresponding to a:

- (1) Load following.

Only the last set (Series 3) was finally proposed for publication and comparisons, and it contains the exact conditions used in experiments specifically performed for this purpose. This is the definition found in Section 5.3.1. Unfortunately not all participants were able to repeat analysis based on this final set and some of the results presented in Section 5.4 are for earlier cases or based on presentations made at the RCM meetings. These are clearly identified as such. The focus of the comparisons in Section 7.4 is, however, on the last benchmark definition and its experimental results only.

5.3.1. Boundary conditions for steady state benchmarks

The process variables as shown in Tables 5.29 and 5.30 are the minimum necessary to define a unique operating condition for the PBMM. These are the actual process variables measured after steady state was reached. Two sets of variables, one for 95 kPa and one for 115 kPa (on the suction pressure of the LPC), are given. Two sets of variables are given as the heater outlet temperature is not exactly the same in the two cases.

TABLE 5.29. PROCESS VARIABLES FOR THE NOMINAL 95 KPA TEST RUN

Suction Pressure of the LPC	94 kPa (abs)
Heater outlet temperature (Dynamic or total)	647.7°C
Heater outlet temperature (Static)	644.6°C
Cooling water flow rate	
Precooler	2.05 kg/s
Intercooler	1.63 kg/s
External Load Cooler	1.20 kg/s
Cooling water temperature	14.2°C
Cooling water pressure	350 kPa
Nitrogen purity	100%
Valve opening on the external load cooler	Fully open
Compressor bypass valves	Closed

TABLE 5.30. PROCESS VARIABLES FOR THE NOMINAL 115 KPA TEST RUN

Suction pressure of the LPC	113.5 kPa (abs)
Heater outlet temperature (Dynamic or total)	649.7°C
Heater outlet temperature (Static)	647.6°C
Cooling water flow rate	
Precooler	2.05 kg/s
Intercooler	1.63 kg/s
External Load Cooler	1.19 kg/s
Cooling water temperature	14.8°C
Cooling water pressure	350 kPa
Nitrogen purity	100%
Valve opening on te external load cooler	Fully open
Compressor bypass valves	Closed

For each of the steady state cases experimental results available include the pressure and temperatures at several positions in the experiment (19 positions in total), the primary and secondary mass flows, and the speed of the high- and low-pressure turbines and the power turbine. The experimental values were provided in a spreadsheet to ensure that all participants reported the results in the same format.

5.3.2. Transient benchmark

In order to build confidence in analysis tools, it is necessary to test their ability to predict behaviour under new operating conditions. There are two possibilities for this:

- (a) The heat loss to the ambient can be reduced significantly and the ability of the software evaluated to predict the value of process variables under the new condition.
- (b) Perform transient tests and compare the results.

Various transient tests on the PBMM have been identified. These include load following, load rejection and startup. In this work the focus will be on nitrogen injection. Nitrogen is injected into the cycle just upstream of the Pre-Cooler in order to increase the inventory of nitrogen in the cycle. As the mass of nitrogen in the cycle increases, the power output of the power turbine also increases. Before injection commences, the plant is run at steady state with a 95 kPa LPC suction pressure and 650°C heater outlet temperature. Nitrogen is now injected into the cycle at a rate of 0.0227 kg/s for 63 s at the LPC inlet. The heater outlet temperature was maintained at 650°C.

The following experimental results are available for this transient (followed for 110 s):

- (a) The LPC suction [kPa(a)];
- (b) The LPT speed [rpm];
- (c) Annullus pressure [kPa(a)].

The experimental results were provided in a spreadsheet to ensure that all participants reported the results in the same format.

5.4. PBMM ANALYSIS AND RESULTS

5.4.1. Experimental and simulation results for the PBMM benchmarks, South Africa

5.4.1.1. Introduction

The design and analysis of fluid flow and heat transfer in complex closed-loop systems like nuclear reactors require the use of a variety of analysis techniques and simulation tools. These range from one dimensional pipe network codes to very advanced three dimensional CFD codes. Three dimensional CFD codes are useful for accurate geometrical and physical modelling of individual system components, but are not practical for analysing complete integrated systems due to the excessive computational resources required and the time it takes to solve. While one dimensional tools cannot resolve the detail flow field within components, they allow efficient analysis of complete systems. After careful validation and stringent qualification procedures, one dimensional codes are used to analyse the behaviour of nuclear power plants in both normal operation and various accident scenarios.

The systems CFD code Flownex has been developed by M-Tech Industrial in association with the Pebble Bed Modular Reactor company, and enables users to perform detailed analysis and design of complex thermal-fluid systems such as complete power plants and thermal-fluid networks. Similar to a conventional CFD code, the system is discretized into a number of spatial or conceptual control volumes to which a set of conservation equations are applied and then solved. Although the term 'CFD' is usually reserved for 3-D Navier Stokes solvers, Flownex does not solve the 3-D Navier Stokes equations, but a set of simplified 1-D momentum equations applied to 3-D spatial control volumes. This approach is valid for flow through a porous medium and is exactly the same approach used in classical CFD codes. Since Flownex solves porous flow in 3-D spatial volumes in the same way as classical CFD codes, and in addition to that also the balance of plant, the name 'systems CFD', or SCFD for short, is a fitting description.

The Flownex solver is based on an implicit Newton solver that solves the momentum equation in each element and the continuity and energy equation at each node in large arbitrarily structured networks for both steady state and dynamic situations. This gives Flownex a pseudo-CFD capability, which allows it to predict complex phenomena such as pressure and temperature waves in pipes and buoyancy effects in packed beds. The solver is optimized for steady state and transient flows and can deal with both fast and slow transients. Although components may be represented on a systems level as a single entity, they may in fact be complex subnetworks. The nuclear reactor and heat exchangers are not treated as lumped systems but as distributed systems, the nodalization of which can be user-defined. Flownex features two nuclear reactor simulation models that combine point kinetic neutronics with detailed two dimensional finite-difference thermal-fluid models. The model deals with feedback from isotope changes and therefore calculates reactivity changes due to changes in the xenon concentration. The code can also deal with one-, two- or three dimensional conductive heat transfer through solid structures. In order to ensure the accuracy of Flownex, a rigorous V&V process has been implemented to guarantee the integrity of engineering analyses and to satisfy statutory requirements regarding the licensing and operation of nuclear plants in South Africa and abroad. The analysis of the PBMM represents only one of these efforts. The results presented here were published as [5-2] and include other references that may be of interest to the reader.

When the experimental results of the PBMM were presented on a T-S diagram, it was seen that the collective entropy increase of the gas flowing through the turbines is less than expected. This can possibly be attributed to the following reasons:

- Significant heat loss from the turbines;
- Low-temperature gas leaking into the pipework connecting the turbines;
- Measurement error.

Considerable work was done to determine which of the three possible reasons was the most likely. Measurement error will always be present to some extent, but finally it was decided that the most probable reason was that significant heat loss is taking place from the turbines. It is possible to

calculate the magnitude of the heat loss from the turbines as well as the heat loss from the pressure vessel to the ambient from the experimental results.

These heat losses were not included in the original FLOWNEX simulation model. The FLOWNEX code (a systems CFD code), used by the PBMR Company, enables users to perform detailed analysis and design of complex thermal fluid systems such as complete power plants and thermal fluid networks. For the code-to-plant comparisons in this section, the FLOWNEX simulation code is used.

In this section, the heat transfer paths that were added to the original simulation code are described. The comparison between the experimental results and the simulation results (code-to-plant comparison) are then presented. Code-to-code comparison is provided in Section 7.4.

5.4.1.2. Heat transfer model used in FLOWNEX

Heat transfer takes place from one fluid stream (i) to another fluid stream (o) with heat conduction taking place through a solid wall.

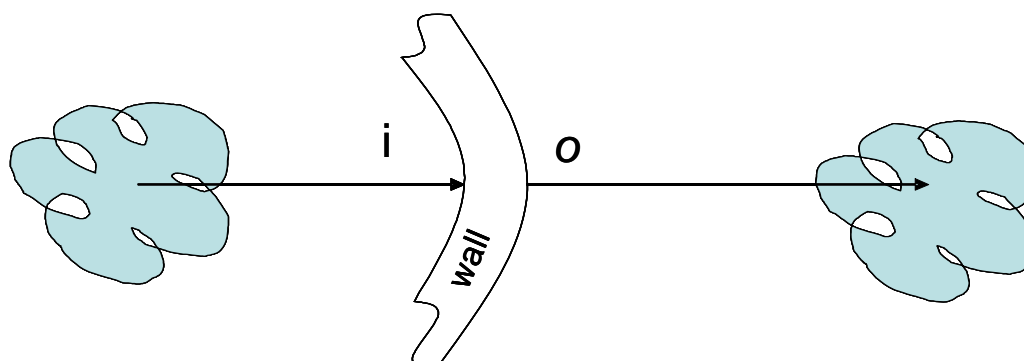


FIG. 5.36. Heat transfer diagram.

Heat transfer from the turbines.

In FLOWNEX, the heat loss through the turbine casings is simulated as a heat loss just upstream of the turbines. Heat is transferred from the gas entering the turbine (i) to the HP nitrogen in the internal volume of the pressure vessel point 34 (O) in Fig. 5.36. The parameters as shown in Table 5.31 are used for all three turbines.

TABLE 5.31. HEAT TRANSFER FROM THE TURBINES

	Inside (i)	Outside (o)
Area [m ²]	0.2	0.9
Convective heat transfer coefficient h [W/(m ² K)]	10000	30
Wall thickness [m]	0.05	
Conductivity of wall [W/(mK)]	22	

The outside area is large because it is assumed that the hot plate, which the turbines are attached to, acts as a fin releasing heat to the gas.

Heat transfer to the ambient:

- Heat is now transferred from the internal volume of the pressure vessel (point 34, i) through the pressure vessel to the ambient (o) via two parallel paths, namely;
- Through the exposed metal surfaces (manhole covers and flanges);

- Through the wall of the pressure vessel and the thermal isolation covering it.

Table 5.32 gives the transfer through the exposed metal surfaces.

TABLE 5.32. HEAT TRANSFER PARAMETERS THROUGH EXPOSED METAL SURFACES

	Inside (i)	Outside (o)
Area [m ²]	6	8
Heat transfer coefficient h [W/m ² K]	30	16
Metal wall thickness [m]	0.015	
Conductivity of wall [W/mK]	60	

The inside heat transfer coefficient is a convective heat transfer coefficient, while the outside heat transfer coefficient is an effective heat transfer coefficient that is calculated as the sum of the convective heat transfer coefficient to ambient and the linearized radiation heat loss coefficient to the ambient:

$$h_r = \varepsilon \sigma (T_{\text{surface}} + T_{\text{surroundings}})(T_{\text{surface}}^2 + T_{\text{surroundings}}^2)$$

The heat loss through the insulated part of the pressure vessel has two solid walls in series (the metal wall and the thermal insulation). The values are given in Table 5.33.

TABLE 5.33. HEAT LOSS PARAMETERS THROUGH THE INSULATED PORTION OF THE PV

	Inside (i)	Outside (o)
Area [m ²]	70	75
Convective heat transfer coefficient h [W/m ² K]	30	10
Metal wall thickness [m]	0.015	
Conductivity of wall [W/mK]	60	
Insulation thickness [m]	0.05	
Thermal conductivity of insulation [W/mK]	0.036	

As the insulation is covered with polished stainless steel sheeting, it is assumed that the emissivity is low and that no heat loss to the ambient due to radiation is taking place. For the transient runs, a Capacitance factor is included. The Capacitance factor is calculated as the product of the specific heat times the density of the metal.

5.4.1.3. Steady state results

Figure 5.37 shows the comparison between the experimental and simulated values on a T-s diagram. Due to the heat losses from the turbines, the entropy through the turbines does not increase a lot.

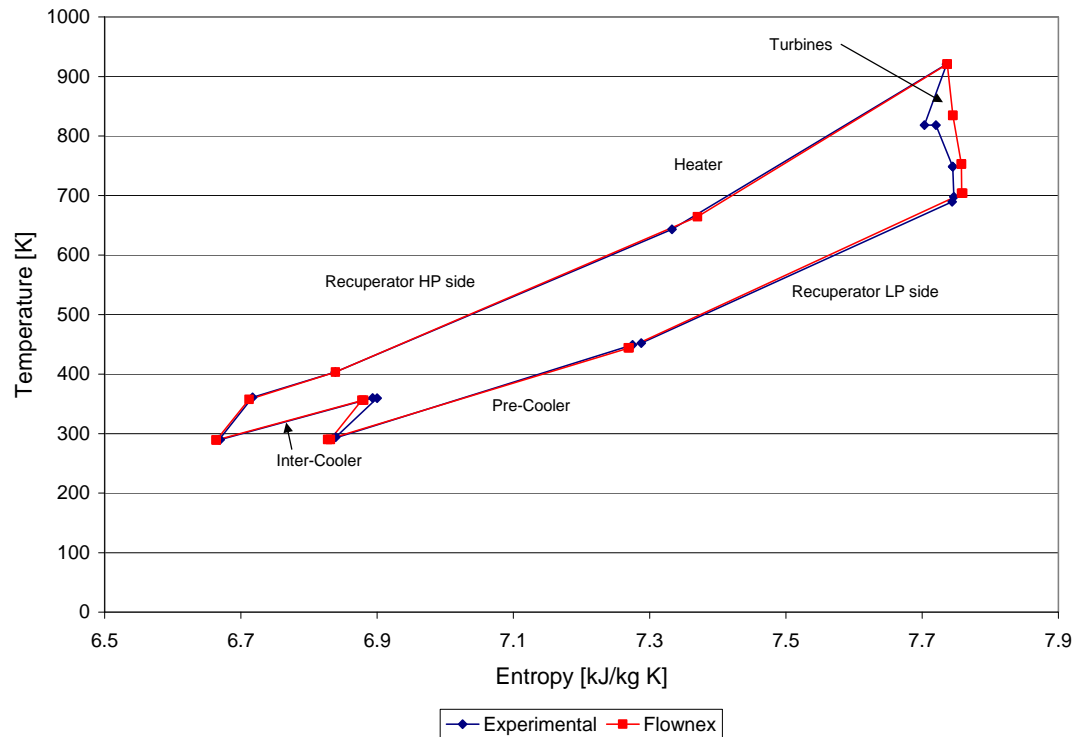


FIG. 5.37. *T-s Diagram of PBMM cycle.*

Table 5.34 shows the comparison between the measured temperatures (EXP) and the values obtained with FLOWNEX (FNX), with heat transfer included for the 95 kPa LPC suction pressure case. The absolute value of the percentage difference is also shown. In FLOWNEX, the temperature of the high pressure nitrogen entering the recuperator is fixed on the same value as the measured value and the heat gain of the high pressure nitrogen flowing on the outside of the heater is calculated. This was done because the heat balances showed that the electrical heater was losing heat to the gas on the outside but it was difficult to quantify this heat loss. The total (or dynamic temperature) is showed in the table. The measured values are static temperature and were converted into the total values.

The average of the differences is 1%. For the 115 kPa case, the percentages of the differences are similar with an average of 1.2%. The biggest differences are at the 'hot end' of the recuperator (RXLP inlet and RXHP outlet). This is because of the measured temperature drop from 697.8 K to 689.4 K between the power turbine outlet and the recuperator inlet. This was not modelled in FLOWNEX with a heat transfer path as the difference between the measured and simulated temperatures is not excessive (less than 5%). The effect is, however, that the hot end of the recuperator in FLOWNEX has a higher temperature than the actual plant.

TABLE 5.34. STEADY STATE (95 KPA) — TEMPERATURE COMPARISON

Position	Temperature [K]		Difference [%]
	EXP	FNX	
PC Inlet	449.2	444.2	1.1
PC Outlet	291.3	290.2	0.4
LPC Inlet	293.8	290.2	1.2
LPC Outlet	359.7	356.2	1.0
IC Inlet	359.7	356.2	1.0
IC Outlet	290.0	289.1	0.3
HPC Inlet	289.8	289.1	0.2
HPC Outlet	360.7	357.4	0.9
RXHP Inlet	403.4	403.5	0.0
RXHP Outlet	643.1	664.5	3.3
Heater outlet	920.9	920.9	0.0
HPT Inlet	920.9	920.9	0.0
HPT Outlet	818.2	834.5	2.0
LPT Outlet	748.2	753.1	0.7
PT Inlet	748.7	753.1	0.6
PT Outlet	697.8	703.7	0.9
RXLP Inlet	689.4	703.7	2.1
RXLP Outlet	452.0	444.2	1.7

Table 5.35 shows the comparison between the measured pressures (EXP) and the values obtained with FLOWNEX (FNX). The absolute value of the percentage difference is also shown.

TABLE 5.35. STEADY STATE (95 KPa) — PRESSURE COMPARISON

Position	Pressure [kPa]		Difference [%]
	EXP	FNX	
PC Inlet	94.0	94.0	0.0
PC Outlet	92.7	93.7	1.1
LPC Inlet	94.0	92.4	1.7
LPC Outlet	155.8	162.2	4.1
IC Inlet	159.4	160.9	0.9
IC Outlet	159.1	160.6	1.0
HPC Inlet	159.5	160.4	0.6
HPC Outlet	291.5	287.3	1.4
RXHP Inlet	286.6	286.4	0.1
RXHP Outlet	286.4	284.8	0.5
Heater outlet	286.9	284.4	0.9
HPT Inlet	286.9	284.4	0.9
HPT Outlet	202.0	189.3	6.3
LPT Inlet	195.4	189.3	3.2
LPT Outlet	123.2	122.9	0.3
PT Inlet	125.2	122.9	1.8
PT Outlet	96.0	95.4	0.6
RXLP Inlet	92.6	94.8	2.4
RXLP Outlet	94.1	94.3	0.2

The average of the differences is 1.5%. For the 115 kPa case, the percentages of the differences are similar with an average of 1.4%. Table 5.36 shows the correspondence between the measured and simulated turbine speeds and mass flow rates. For the 115 kPa case, the correspondence is similar.

TABLE 5.36. STEADY STATE (95 KPa) MASS FLOW RATE AND TURBINE SPEED COMPARISON

	EXP	FNX	Difference
Mass flow rate	[kg/s]		[%]
Brayton cycle	0.449	0.429	4.6
External load compressor	0.529	0.596	12.7
Turbine Speed	[rpm]		[%]
HPT speed	66298	64323	3.0
LPT speed	63707	62513	1.9
PT speed	32294	31757	1.7

The correspondence between the values is generally quite good. The biggest difference is in the mass flow rate in the external load loop.

5.4.1.4. Transient results

For this test, the plant was run under steady state with a 95 kPa LPC suction pressure and 650°C heater outlet temperature. Nitrogen was then injected at a rate of 0.0227 kg/s for 63 s at the LPC inlet. Figure 5.38 shows the measured and simulated suction pressure of the LPC during the injection transient.

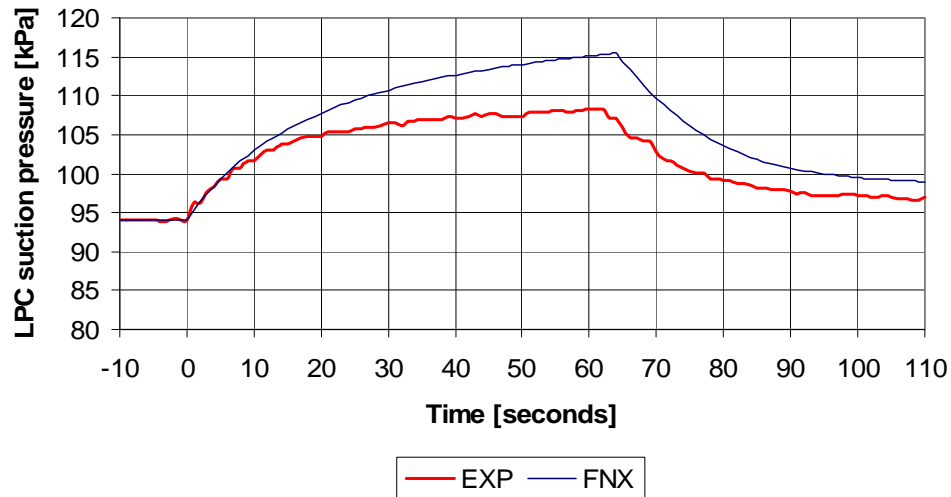


FIG. 5.38. Change in LPC suction pressure.

The simulated value changes by 21.4 kPa while the measured value changes by 13.2 kPa. This means that the calculated change is 163% of the measured change. Calculated as percentage of the measured value, the difference when injection is stopped is $(115.4-107.2)/107.2 = 7.7\%$

Figure 5.39 shows the measured and simulated speed of the LPC. In order to make comparison of the relative changes easier, the simulated values are adjusted to give the same initial speed as the measured value. It is clear from Table 5.36 that at the beginning of the transient, the simulated speed is lower than the measured speed.

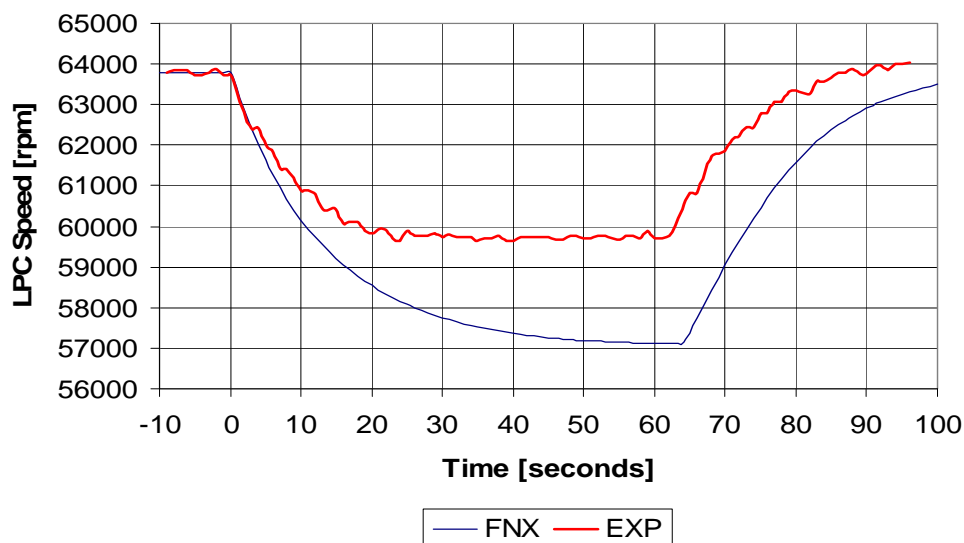


FIG. 5.39. Change in LP compressor speed.

The experimental value changes by 4090 rpm and the simulated value by 6674 rpm. This means that the calculated change is 163% of the measured change. The difference in the turbine speeds at the end of the injection is $(59707-57123)/59707 = 4.3\%$. Other compressors have similar differences. A summary is given in Table 5.37.

TABLE 5.37. DIFFERENCE IN TURBINE SPEEDS AT THE END OF INJECTION (AROUND 63 S)

	$\Delta\text{Simulated}/$ $\Delta\text{Measured} [\%]$	Difference [%]
HPT	173	2.8
LPT	163	4.3
Power turbine	213	7.9

Figure 5.40 provides the comparison between the measured and simulated pressure in the annulus before the recuperator high pressure inlet. The simulated values were adjusted to give the same initial value as the measured value.

The measured value changes by 209 kPa and the simulated value by 212 kPa. This means the simulated change is 102% of the measured change.

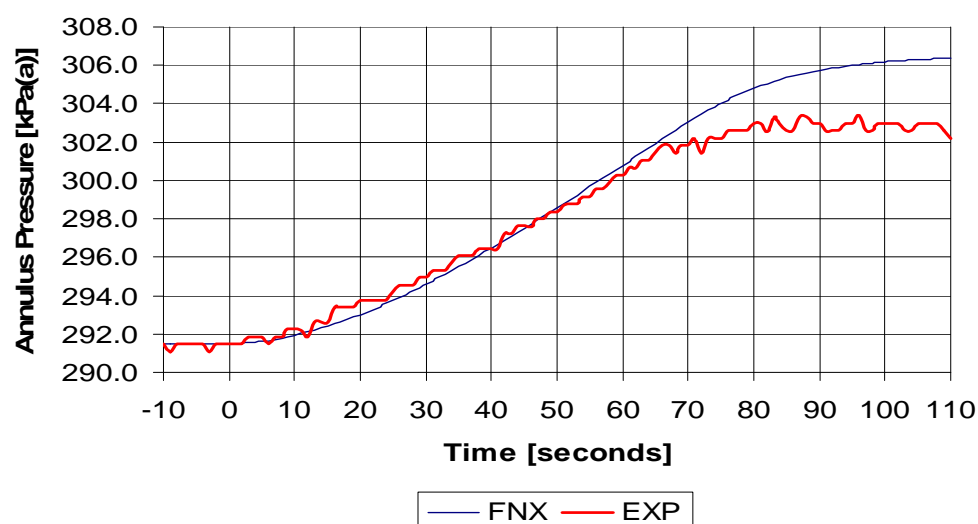


FIG. 5.40. Recuperator high pressure side.

5.4.2. PBMM results, United States of America

The summary provided here was submitted to the CRP as Ref. [5-3]. The case simulated is the steady state at a pressure level of 250 kPa and as such it does not correspond to the benchmark cases defined in this chapter. The data was taken from a preliminary experiment description presented at one of the RCM meetings. Unfortunately the contributors were unable to update the analysis after the benchmark cases and experimental conditions were finalized. The contribution is therefore included for completeness but can not be compared to the available experimental results or other submissions.

5.4.2.1. Introduction

The PBMM is an experimental apparatus for testing the PCU of the PBMR, which is being developed in South Africa as a new generation nuclear power plant. The PBMM benchmark is organized by the

IAEA as a verification exercise for HTGR gas turbine power plant simulations. The goals of this effort are:

- To determine accuracy and limitations of simulation models and assumptions;
- To gain a better understanding of the mechanisms and important processes in the dynamics of the PCU;
- To attempt to explain differences between various predictions by comparison with the PBMM measurements and other models and approaches.

5.4.2.2. PBMM description

The schematic layout of the PBMM power conversion cycle is shown in Fig. 5.1. It is a three-shaft turbomachinery arrangement, one shaft for the HPC/HPT pair, one shaft for the LPC/LPT pair, and one shaft for the power turbine and generator. The generator is emulated using a load rejection loop, in which a load compressor connects to a heat exchanger and a flow control valve. The heat is provided by an electrical resistance heater. The working fluid is nitrogen in the loops.

5.4.2.3. Simulation models

A PBMM model makes use of PCU component models and techniques previously developed at MIT and ORNL. The model has been developed using the ACSL language of acslXtreme [5-4]. The mass and energy balance is maintained while the momentum term for gas is neglected. For solving differential equations, the fourth-order Runge-Kutta integration algorithm was used and the time step was set as 0.1 s. The model includes the component submodels such as turbomachines, heat exchangers and valve. The pipe model is currently not included.

For the turbomachines, the pressure ratio and isentropic efficiency are obtained by interpolating their dynamic characteristics.

For turbines:

$$\text{Pr} = f(W_c, N_c)$$

$$\eta = f(\text{Pr}, N_c)$$

For compressors:

$$\text{Pr} = f(W_c, N_c)$$

$$\eta = f(W_c, N_c)$$

where

Pr is the pressure ratio;

η is the isentropic efficiency;

W_c is the corrected mass flow rate;

N_c is the corrected rotational speed.

As an example, Figs 5.41 and 5.42 show the LPT maps and Figs 5.43 and 5.44 show the LPC maps.

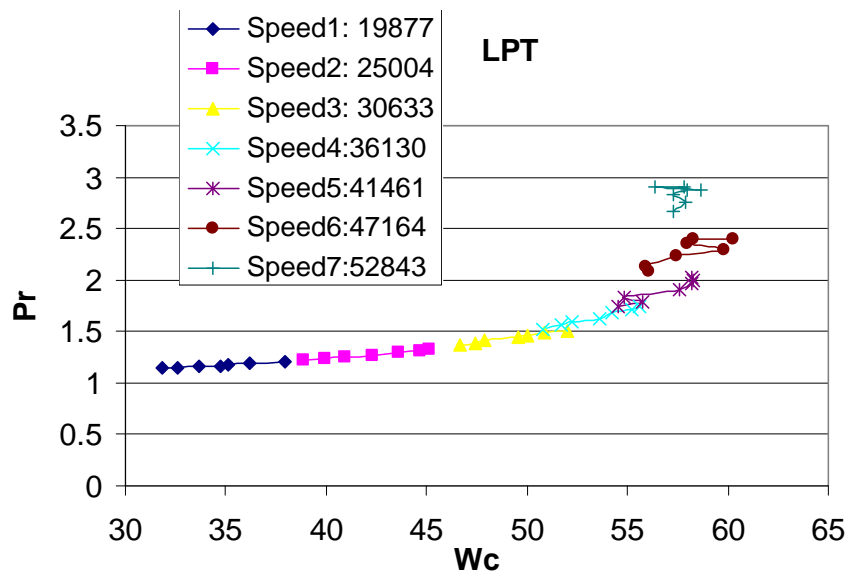


FIG. 5.41. Pressure ratio versus corrected mass flow rate for speed lines of the LPT.

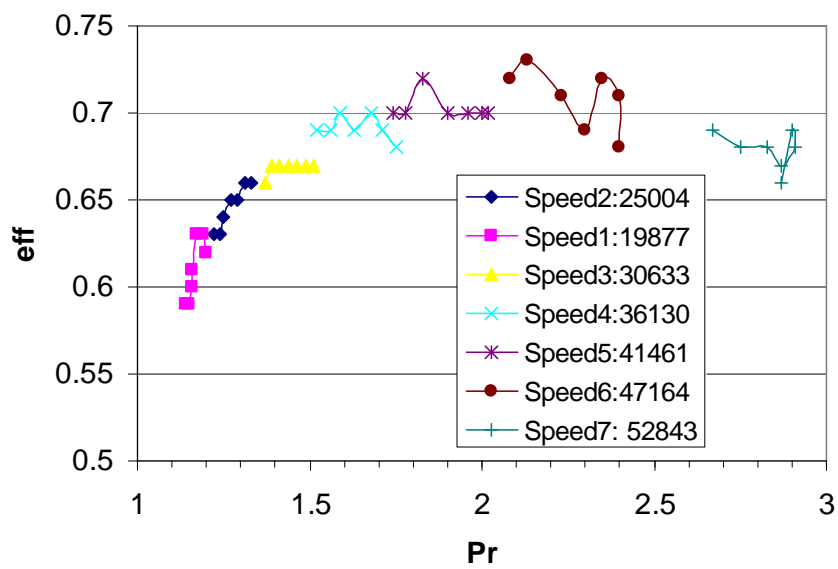


FIG. 5.42. Efficiency versus pressure ratio for speed lines of the LPT.

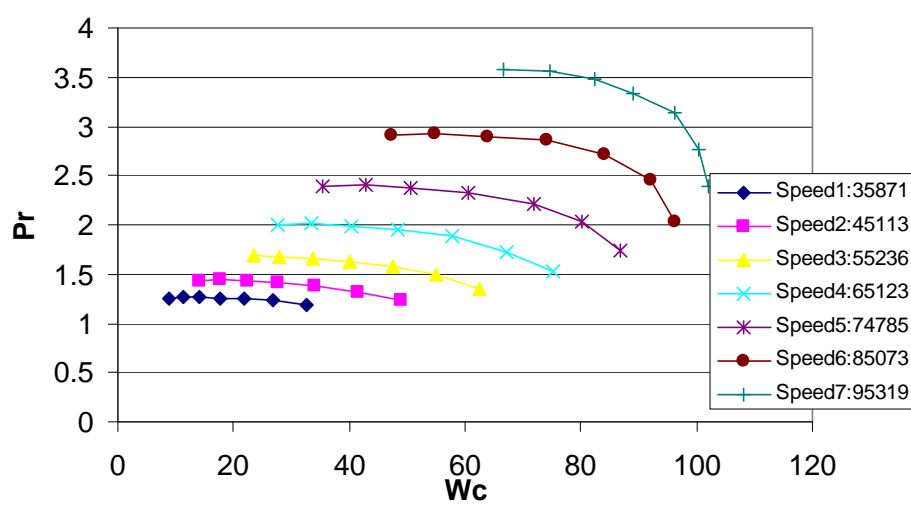


FIG. 5.43. Pressure ratio versus corrected mass flow rate for speed lines of the LPC.

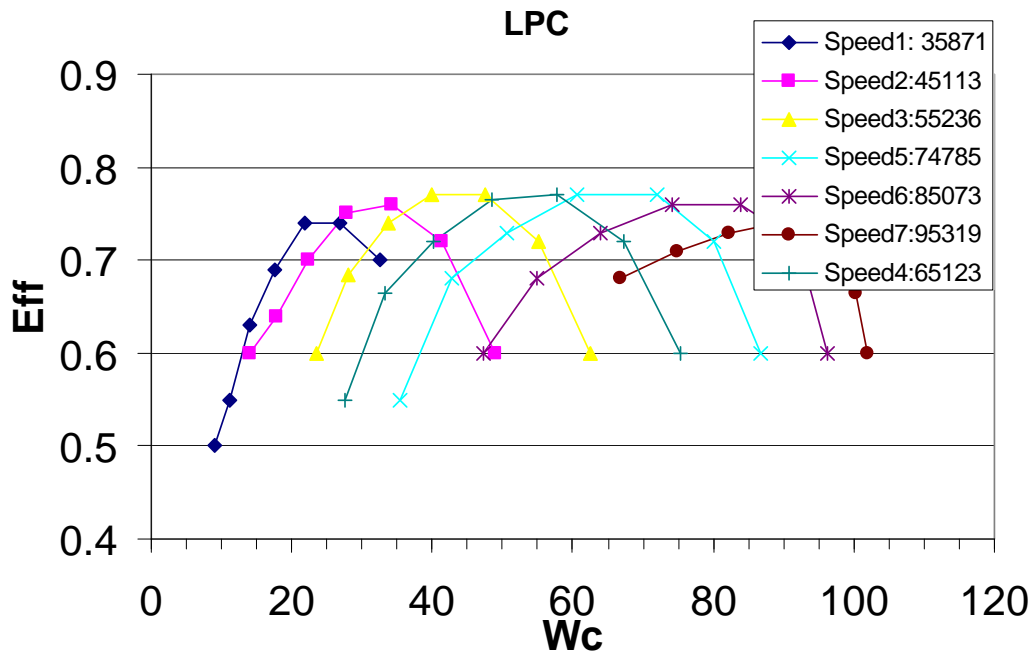


FIG. 5.44. Efficiency versus corrected mass flow rate for speed lines of the LPC.

The shaft speed is determined by the net torque exerted on it:

$$\frac{d\omega}{dt} = \frac{\tau}{I}$$

where ω is the rotational speed (radians/s) and τ (N·m) and I is inertia ($\text{kg}\cdot\text{m}^2$).

The recuperator, precooler, intercooler and external heat exchanger are treated as counter-flow heat exchangers consisting of three regions, namely, hot fluid side, metal wall and cold fluid side. The counter-flow heat exchanger is divided into several sections. The recuperator is discretized as ten sections while other heat exchangers are three sections. The energy equation can be derived for each

region of each section. The equations can be found in [5-5] for gas/gas and gas/water heat exchangers. The tube mass and other details of the heat exchangers are listed in Table 5.38.

TABLE 5.38. TUBE MASS OF THE HEAT EXCHANGERS

Heat exchanger	Tube length (m)	Tube inside diameter (mm)	Tube outside diameter (mm)	No. of tubes	Tube mass (kg)
PC	2.1	10.22	12.7	597	498
IC	2.0	10.22	12.7	457	363
EXHL	2.5	10.22	12.7	467	456
RX	6.0	10.22	12.7	1075	2563

The mass flow rate passing through an open valve is calculated based on the following equation [5-6]:

$$Q = \frac{1360C_v \sqrt{(\Delta P)P_2}}{\sqrt{GT_a}}$$

where

Q is the quantity, cu ft/hr at 14.7 psia and 60°F;

ΔP is the pressure drop at maximum flow, psi ($P_1 - P_2$);

P_1 is the inlet pressure at maximum flow, psi;

P_2 is the outlet pressure at maximum flow, psi;

G is the specific gravity (air = 1.0);

T_a is the flowing temperature absolute ($460 + ^\circ\text{F}$);

C_v is the valve flow coefficient.

When P_2 is less than $1/2 P_1$, use the value of P_1/P_2 in place of $\sqrt{(\Delta P)P_2}$.

By extrapolating the values in Table 5.11 of [5-1], C_v is 2.9 for 7% relative opening of the three-inch Gas Bypass (GBP) valve.

5.4.2.4. Simulation results

Steady state result

The steady state at the following conditions has been calculated:

- Supply pressure from the Nitrogen Inventory Control System (NICS) tanks (Point 100 in Fig. 5.1) is 250 kPa;
- The exit temperature (point 52) of the heat is 700°C;
- The shaft mechanical efficiency is assumed as a constant value of 99%.

The parameters of components at the steady state for 250 kPa pressure are listed in Table 5.39. The results give a recuperator effectiveness of 86% and the nitrogen mass flow rate is 1.26 kg/s. The interpolation of the HPT map gives a relatively lower power, which results in a lower rotational speed of the HPT.

TABLE 5.39. STEADY STATE RESULTS FOR
PRESSURE LEVEL OF 250 KPA AT THE LPC INLET

Component	Inlet T (°C)	Inlet P (kPa)	Power (kW)	Speed (rpm)
HPT	700.0	911.9	94.7	63065
LPT	634.8	642.6	122.3	70248
PT	549.3	386.5	84.5	44223
RX low pressure side	489.3	258.3	455.1	-
PC	153.0	253.6	165.9	-
LPC	26.5	251.2	121.1	70248
IC	117.0	522.4	118.7	-
HPC	26.3	520.9	93.8	63065
RX high pressure side	96.3	918.4	455.1	-

Load rejection

Load rejection occurs by opening the GBP valve between the high pressure and low-pressure sides. The load rejection has been simulated by opening the GBP valve by 7% based on the steady state at the pressure level of 250 kPa at the LPC inlet. It is assumed that there is a 'pressure equalization line' between the inlets of LPC and external load compressor. Since the interpolation of HPT map causes a strange pressure ratio trend, a scaled LPT map is used for the HPT during a load rejection scenario. The heater source (HS) outlet temperature is set as a constant value of 700°C.

The power and shaft speeds of the power turbine are shown in Figs 5.45 and 5.46. The mass flow rates are shown in Fig 5.47. Figures 5.48 and 5.49 show the compressor pressures and turbine temperatures. From the figures, a small oscillation occurs when using the scaled LPT map for the HPT. However, the oscillation does not occur when assuming constant pressure ratio and efficiency for the HPT. From Fig. 5.45, the power turbine power drops to a new steady state value which is lower than the full power operating level. It can be seen from Fig. 5.46 that the shaft speeds decrease to lower rotational speeds. By opening the GBP valve to 7%, the bypass mass flow rate is about 0.09 kg/s. From Fig. 5.48, the HPC outlet pressure decreases from 911.9 kPa to about 800 kPa after the transient. The power turbine outlet temperature increases from 489.3°C to about 519°C.

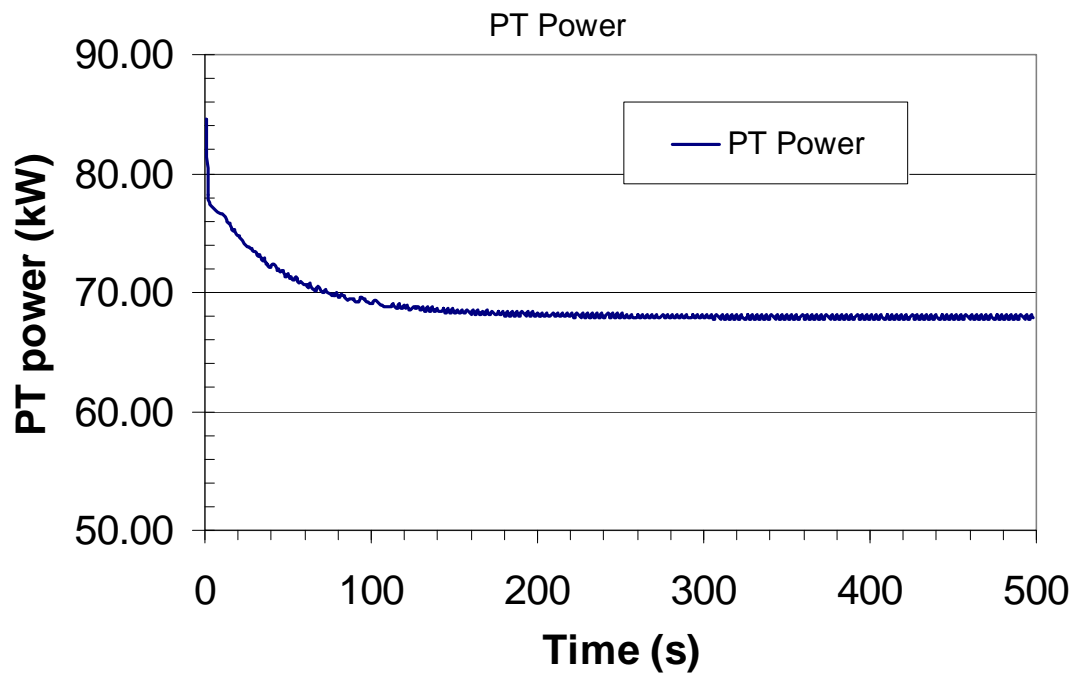


FIG. 5.45. PT power in a load rejection.

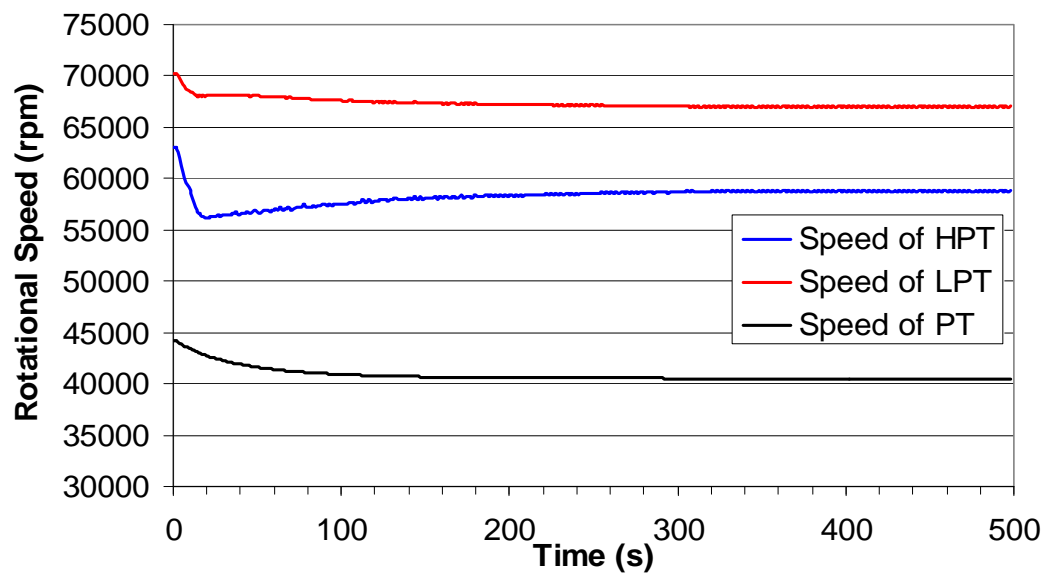


FIG. 5.46. Speed shifts in a load rejection.

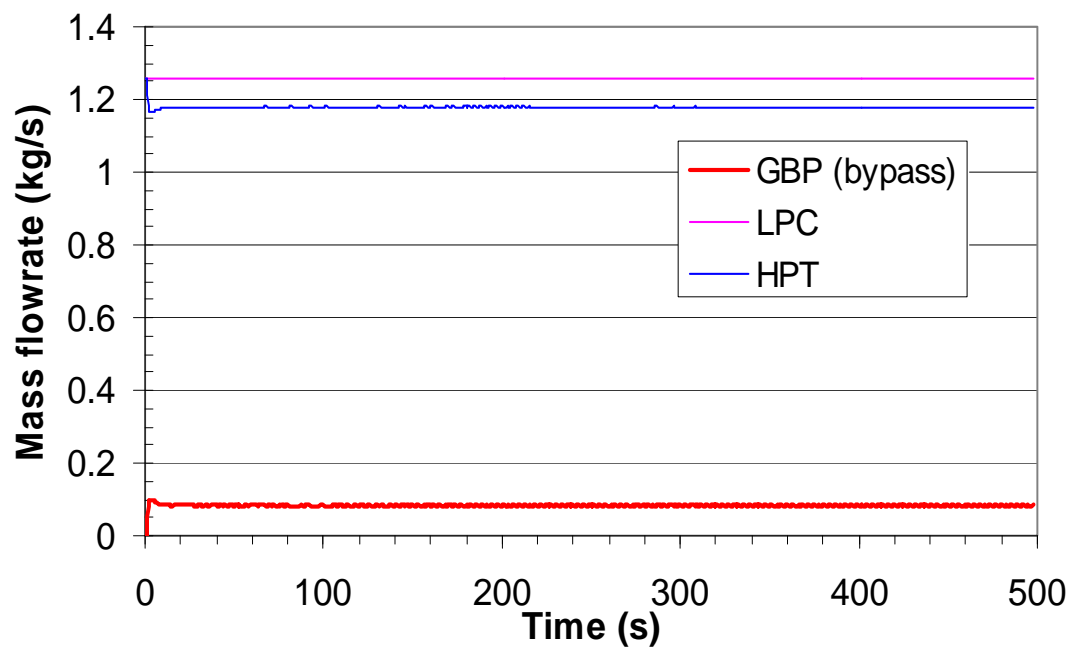


FIG. 5.47. Mass flow rate during a load transient.

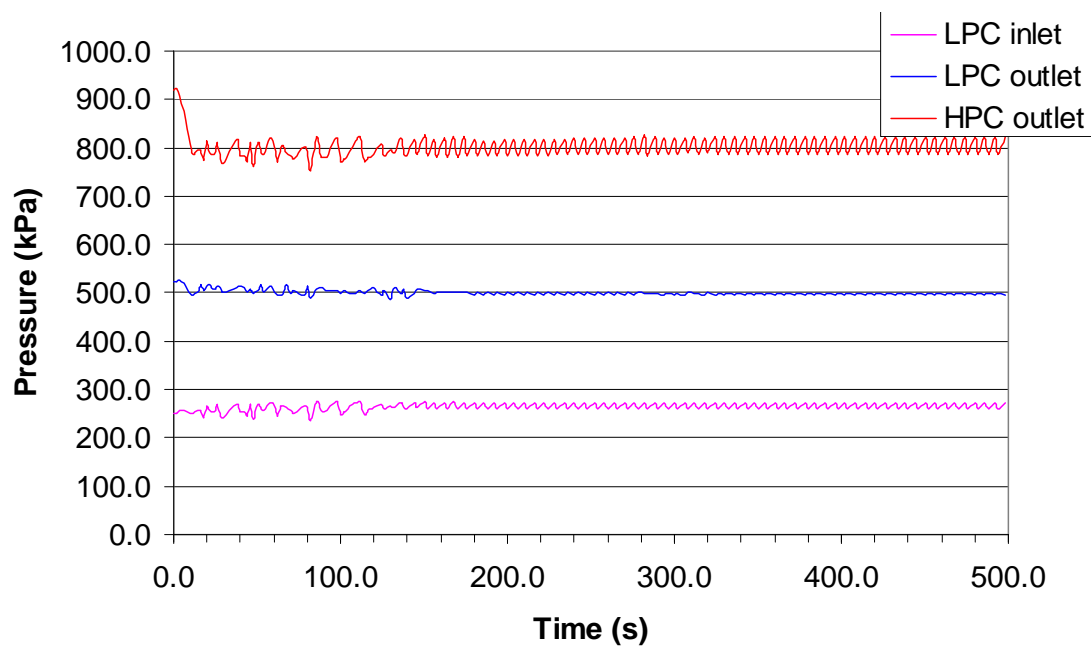


FIG. 5.48. Compressor pressures during a load ejection.

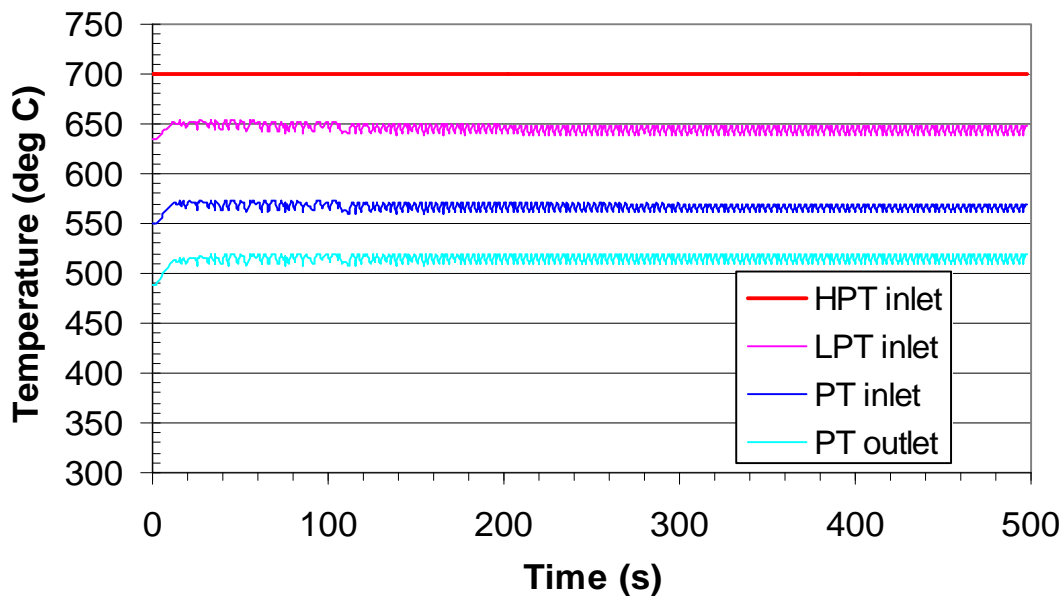


FIG. 5.49. Turbine temperatures during a load rejection.

5.4.2.5. Conclusions and future work

As a three-week effort, the steady state at pressure level of 250 kPa has been calculated and the load rejection has been simulated with a model developed using the ACSL language. When interpolating the HPT map, it gives lower output power at steady state and a strange pressure trend during transient. It would be helpful if more speed lines were provided between speed lines 28798 and 40767 rpm. Since the load-rejection loop determines the load variation, more data on this loop would be helpful.

Future work will include the 100 kPa steady state calculation, mass injection transient simulation, startup transient simulation, and comparison with the PBMM experimental data.

5.4.3. PBMM results, Japan

The summary provided here was submitted to the CRP as Ref. [5-7]. The case simulated is a steady state at pressure level of 95 kPa but at different temperature conditions. The heater outlet temperature was defined to be 540°C (compared to 645°C) while the mass flow rate of each water cooler (precooler, intercooler and external load heat exchanger) is 2 kg/s compared to the variation of between 1.2 and 2.05 kg/s in the steady state benchmark case. As such it does not correspond to the benchmark cases defined in this chapter, but is based on an earlier experiment performed at the PBMM and presented at one of the RCM meetings. Unfortunately the contributors were unable to update the analysis after the benchmark cases and experimental conditions were finalized, also partly due to the non-approval of the requested extension of the CRP. The contribution is therefore included for completeness and since some comparison to the preliminary experimental measurements has been made, it does add value to the code validation of the RELAP5/MOD3 code. The results can, however, not be compared to the available experimental results or other submissions made in Section 7.4.

5.4.3.1. Introduction

JAEA has carried out the initially defined (draft) benchmark calculations of the PBMM test results by using 'RELAP5/MOD3', a plant dynamics analysis code. This code was modified to calculate plant dynamics of a gas turbine system and an HTGR core. The test conditions and specification of the PBMM test facility are described in the draft version of two documents of the data pack [5-1, 5-8].

5.4.3.2. Calculation model

An electric heater, heat exchangers, turbomachineries, valves and pipes of the PBMM are modelled as shown in Fig. 5.50. The dimensions and shapes of pipes and heat exchangers are described in the data pack [5-1] and the document [5-8]. Pressure loss in the pipe element was calculated based on the shape and dimension of each pipe. Pressure ratio and efficiency of gas turbines and compressors described in the data pack were approximated with equations, as function of corrected flow rate and corrected rotation speed. Corrected flow rate and corrected rotation speed are given by the following equations as described in the data pack.

$$W^*_C = W_C(T_{IC}/545)^{1/2}/(P_{IC}/28.4) \quad (2.1)$$

$$N_C = N/(T_{IC}/545)^{1/2} \quad (2.2)$$

where

W^*_C is the compressor corrected mass flow [lb/min];

W_C is the mass flow [lb/min];

T_{IC} is the total inlet temperature [R];

P_{IC} is the total inlet pressure [inch Hg];

N_C is the compressor corrected speed [rpm];

N is the rotational speed [rpm].

$$W^*_T = W_T(T_{IT}/519)^{1/2}/(P_{IT}/29.92) \quad (2.3)$$

$$N_T = N/(T_{IT}/519)^{1/2} \quad (2.4)$$

where

W^*_T is the: turbine corrected mass flow [lb/min];

W_T is the mass flow [lb/min];

T_{IT} is the total inlet temperature [R];

P_{IT} is the total inlet pressure [inch Hg];

N_T is the turbine corrected speed [rpm];

N is the rotational speed [rpm].

The calculation method of the compressor power is shown in the data pack. That is calculated from the turbine power and shaft mechanical efficiency (η_m) by the following equations. Since η_m was not given in data pack, it was assumed to be constant a value of 0.99.

$$W_T = \eta_T m C_p T_{01} [1 - (P_2/P_{01})^{(\gamma-1)/\gamma}] \quad (2.5)$$

$$\eta_m = W_C/W_T \quad (2.6)$$

where

W_T is the turbine power;

η_T is the turbine isentropic efficiency;

m is the mass flow rate;

C_p is the specific heat;

T_{01} is the turbine inlet temperature;

P_2 is the turbine outlet pressure;
 P_{01} is the turbine inlet pressure;
 η_m is the shaft mechanical efficiency;
 W_C is the compressor power.

The transient behaviour of rotation speed of each turbomachinery is calculated by using the following equation:

$$(I_T + I_C)d\omega/dt = \tau_T - \tau_C - F\omega \quad (2.7)$$

where

I_T is the inertia momentum of turbine;
 I_C is the inertia momentum of compressor;
 ω is the rotation speed;
 τ_T is the turbine torque;
 τ_C is the compressor torque;
 F is the friction coefficient of turbine and compressor.

The outlet temperature and pressure in the turbines and compressors are calculated from inlet properties and characteristic map of each turbomachinery by using basic equations, which are the equation of state, energy equation, equation of work of turbomachinery, equation of shaft torque and rotation speed. The model of the turbomachinery is a one-stage model in each turbine and compressor.

The heat transfer coefficient for the shell- and tube-type heat exchangers with baffle plates, which is described in [5-9], is used in each heat exchanger.

5.4.3.3. Calculation methodology and code

The input data of the RELAP5/MOD3 code was arranged and material properties of helium gas and graphite were installed in order to calculate the reactor kinetics of HTGRs. Original subroutines for the calculation of characteristics of pumps in the RELAP5/MOD3 code were modified for the modelling of turbines and compressors. Modification was also conducted to input the heat transfer correlation for HTGRs and to use this correlation as a surface heat transfer coefficient. A subroutine to the input characteristics of the turbomachineries, which are the pressure ratio and efficiency of turbine and compressor as functions of corrected rotation speed and corrected mass flow rate, was added to the RELAP5/MOD3 code.

The main feature of the RELAP5/MOD3 code is the calculation of two-phase flow of a condensable gas. On the other hand, reactor coolant in HTGRs is single-phase, non-condensable helium gas and coolant water in the water cooler is also a single-phase liquid. The calculation of helium gas flow was validated by comparing it to the results of the HTTR safety demonstration tests. In this benchmark calculation the comparison is extended to include nitrogen as the working gas.

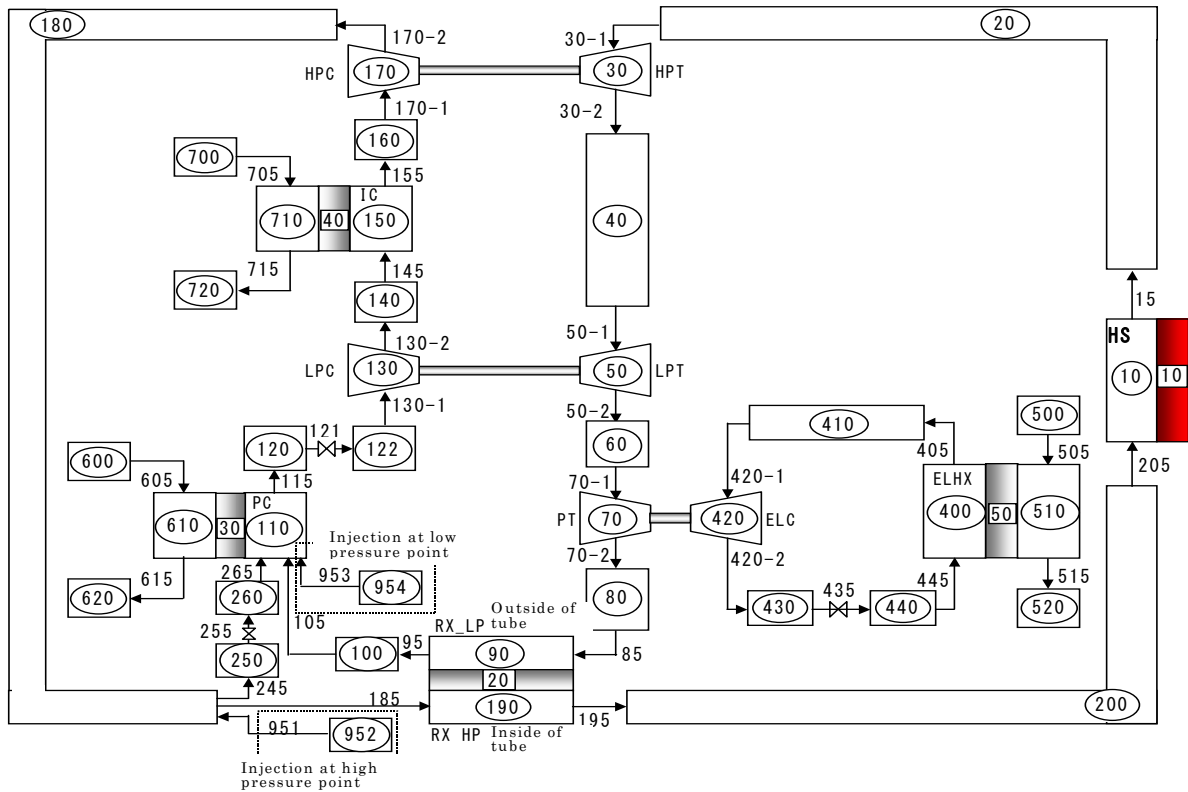


FIG. 5.50. Calculation model of the PBMM.

5.4.3.4. Calculation result

(a) Calculated benchmark problems

A steady state calculation and a transient calculation were carried out as follows:

A steady state condition;

A transient from steady state (mass injection at low-pressure point).

(b) Conditions and assumptions

Calculations of a steady state and a transient were carried out with conditions described in [5-8].

Steady state calculation conditions:

- Suction pressure of the LPC: 95 kPa;
- Heater outlet temperature: 540°C;
- Mass flow rate of each water cooler (precooler, intercooler and external load heat exchanger): 2 kg/s.

Transient calculation conditions:

- Initial condition of the transient: steady state calculation result;
- Position of mass injection: inlet of precooler (low pressure point);
- Mass injection rate: 0.02 kg/s;
- Duration of mass injection: mass injection is stopped when the inlet pressure of the LPT reaches 120 MPa;
- Condition after mass injection stopped: the same condition as steady state calculation.

Assumptions in a transient calculation are listed in Table 5.40. Some unknown values, such as the friction force of the turbomachineries, heat capacity of electric heater, and shaft mechanical efficiencies are assumed to be appropriate values.

TABLE 5.40. ASSUMPTIONS AND CONDITIONS FOR CALCULATION

Item	Assumption
Friction force of turbo-machinery	In proportion to a rotation speed of each turbo-machinery
A heat capacity of electric heater	Infinite
A shaft mechanical efficiency	0.99constant value)

(c) Preliminary calculation of steady state and transient

As a preliminary calculation, the compressor power was calculated by using Eq. (2.6) in which the compressor power is proportional to the turbine power. In this result, the rotation speed of each turbine/compressor shaft starts to increase with nitrogen injection. On the other hand, the rotation speed of the turbine/compressor shaft should decrease because a compressor load, which is a necessary power to drive a compressor, is increased by increase of the mass flow rate. Therefore, the following equation is introduced to the calculation model of the RELAP5/MOD3 code to calculate the compressor power.

$$W_C = (1/\eta_C)mC_pT_{C1}[1-(P_{C2}/P_{C1})^{(\gamma-1)/\gamma}] \quad (2.8)$$

where

W_C is the compressor power;

η_C is the compressor isentropic efficiency;

m is the mass flow rate;

C_p is the specific heat;

T_{C1} is the compressor inlet temperature;

P_{C2} is the compressor outlet pressure;

P_{C1} is the compressor inlet pressure.

(d) Result of steady state calculation

The calculated profiles of pressure and temperature of a steady state are shown in Figs 5.51 and 5.52. It was shown that steady state was well simulated by the RELAP5/MOD3 code. The maximum error of the calculated pressure is approximately 6%.

(e) Result of the transient calculation of mass injection at low pressure point

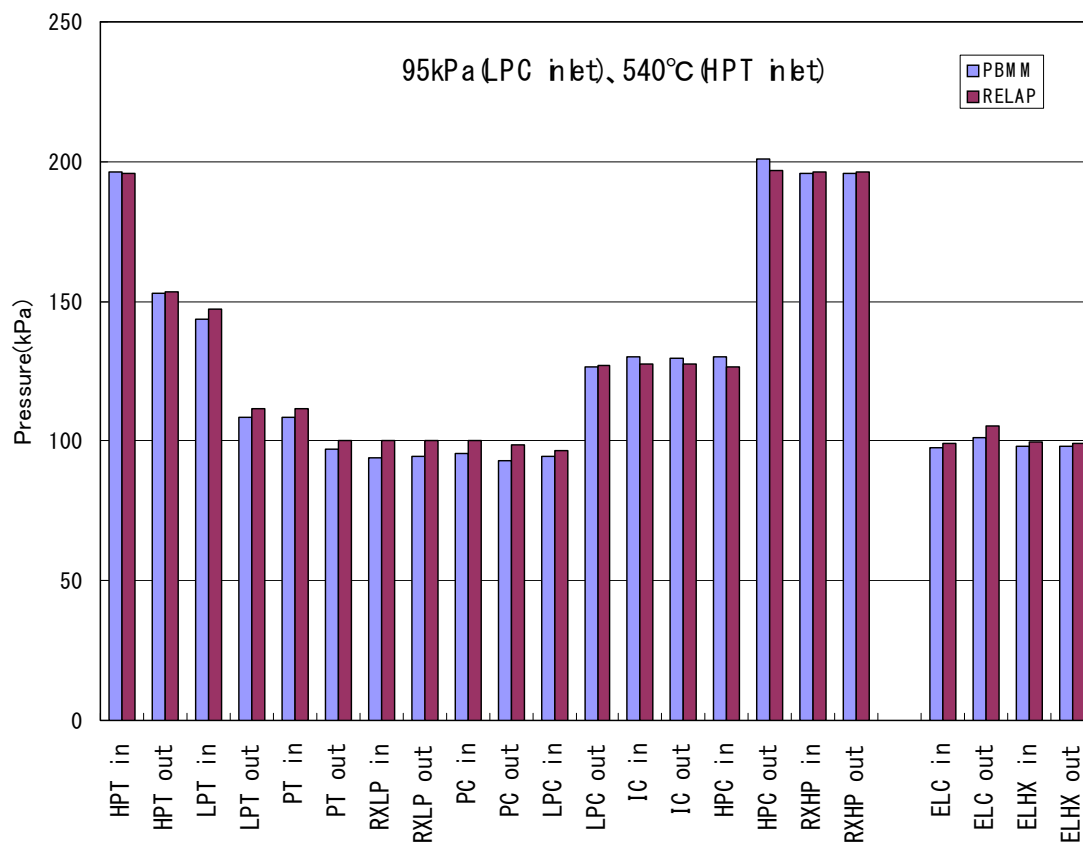


FIG. 5.51. Calculated pressure at each position in steady state.

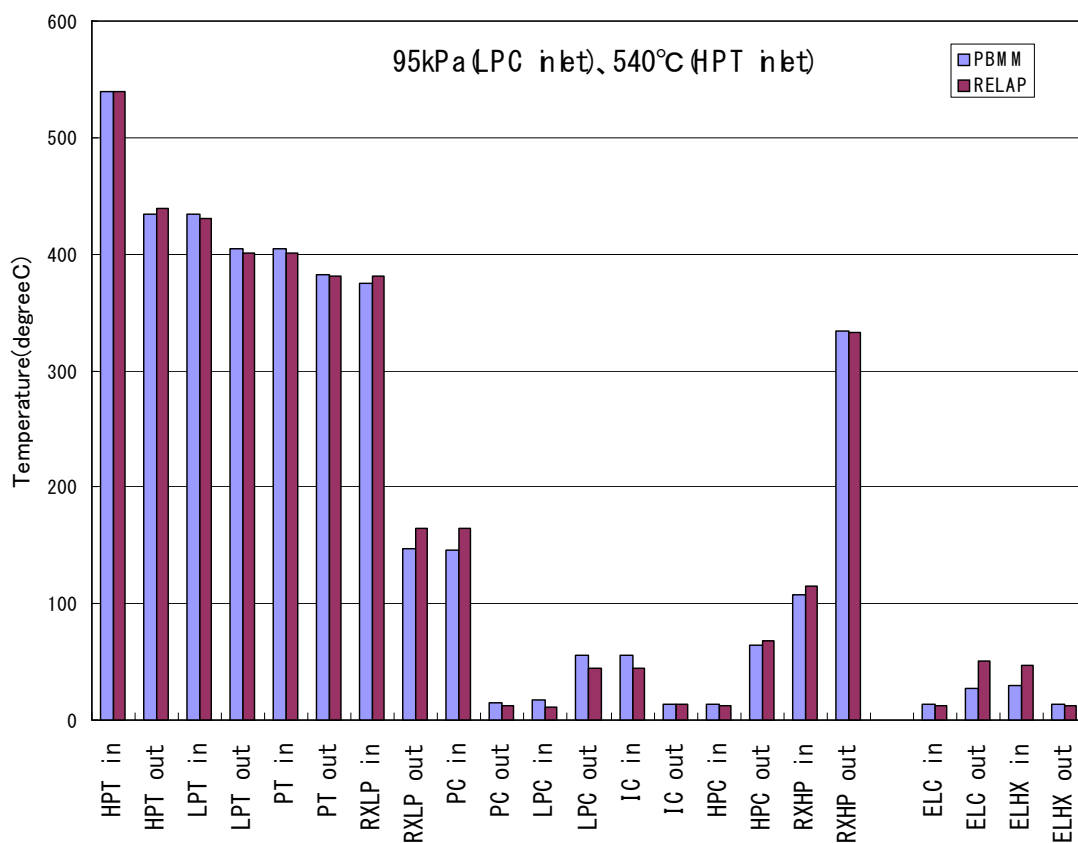


FIG. 5.52. Calculated temperature at each position in steady state.

The calculated time history of nitrogen pressure at the inlet of the LPC is shown in Fig. 5.53. At 134 s after the start of mass injection, the pressure reaches 120 kPa and mass injection is stopped. The calculated turbine power is shown in Fig. 5.54. As shown in this figure, power to the extra load compressor given by the power turbine becomes small after mass injection. Initial value and the maximum value of the calculated pressure and temperature at each position are listed in Tables 5.41 and 5.42. The calculated rotation speed of the HPT, LPT and power turbine is listed in Table 5.43.

TABLE 5.41. CALCULATED NITROGEN PRESSURE AT THE INLET OF EACH COMPONENT

Component	Initial pressure (kPa)	Maximum pressure (kPa)	Pressure after end of injection (kPa)
Low-pressure compressor	96.8	120	113
High pressure compressor	126	152	141
Electric heater	196	219	219
High pressure turbine	196	219	219
Low-pressure turbine	147	170	158
Power turbine	112	133	122

TABLE 5.42. CALCULATED NITROGEN TEMPERATURE AT THE INLET OF EACH COMPONENT

Component	Initial temperature (K)	Maximum temperature (K)	Temperature after end of injection (K)
Low-pressure compressor	284	284	284
High pressure compressor	286	286	286
Electric heater	606	672	548
High pressure turbine	812	870	735
Low-pressure turbine	704	788	620
Power turbine	674	757	594

TABLE 5.43. CALCULATED ROTATION SPEED OF EACH TURBINE

Component	Initial rotation speed (rpm)	Minimum rotation speed (rpm)
High pressure turbine	66,000	61,200
Low-pressure turbine	65,000	63,500
Power turbine	33,000	30,100

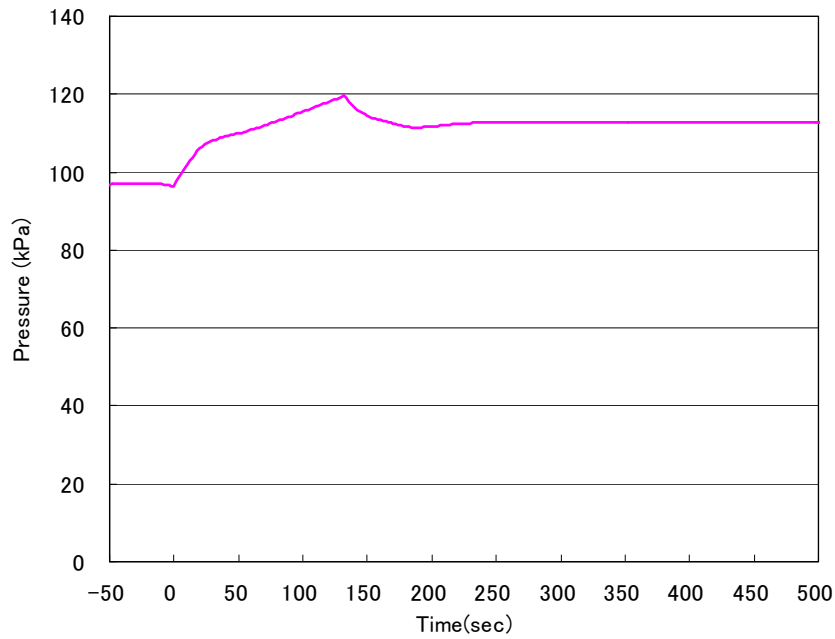


FIG. 5.53. Calculated inlet pressure of the LPC in mass injection.

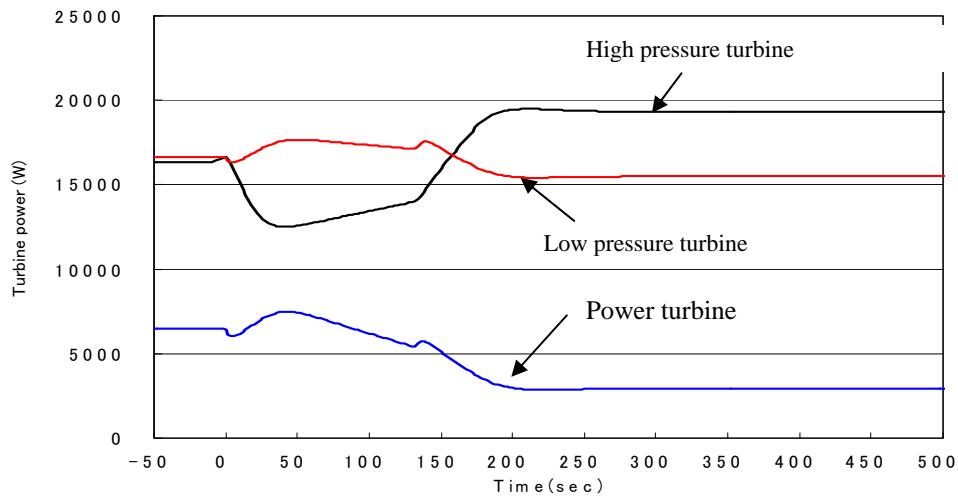


FIG. 5.54. Calculated turbine power in mass injection.

5.4.3.5. Discussion

(a) Calculation of compressor power

When the compressor power is calculated by Eq. (2.6) which is shown in the data pack, the dynamics of the turbine/compressor shaft derived by Eq. (2.7) depends on the turbine power only as expressed in Eq. (2.9).

$$(I_T + I_C)d\omega/dt = (1-\eta_m)\tau_T - F\omega \quad (2.9)$$

where

I_T is the inertia momentum of the turbine;

I_C is the inertia momentum of the compressor;

ω is the rotation speed;

η_m is the shaft mechanical efficiency;

τ_T is the turbine torque;

F is the friction coefficient of the turbine and compressor.

However, in the actual turbomachinery, thermohydraulic behaviour of the turbine and compressor is different. For example, the mass flow rate in the compressor is increased (that means increase of compressor load) but it is not increased in the turbine just after the start of nitrogen injection. Such different conditions between the turbine and compressor can be considered by using Eqs (2.5) and (2.8) which calculate the turbine and compressor power independently. Therefore, the tendency of dynamics of turbine/compressor shaft, that is a decrease of shaft rotation speed after start of nitrogen injection, is well calculated by introducing Eq. (2.8).

(b) Improvement of the transient calculation

It is considered that the power of each turbine would increase when the nitrogen gas is injected. On the other hand, the calculated power of the power turbine is decreased by the injection, as shown in Fig. 5.54. The dynamics of the turbine system are defined by the balance of turbine and compressor torque, as expressed in Eq. (2.7). Since there are three shafts of the turbine and compressor in the PBMM system, the torque balance in each shaft system and total balance of three shafts are important. The rotation speed of each shaft is sensitive not only to its torque balance, but also to that of the other shaft. Therefore, the accuracy of the total thermohydraulic model must be improved in order to make the simulation.

5.4.4. PBMM results, Republic of Korea

5.4.4.1. Introduction

Background and objectives

The PBMM is a model of the PCU to demonstrate the dynamic behaviour of a three-shaft PCS with nitrogen as a working fluid. This closed recuperative Brayton power conversion cycle is one of the viable options for the PCU of the VHTR.

It is important for the safety analysis code to be able to accurately predict the behaviour of the PCU. The CRP-5 PBMM benchmark problem consists of two parts, namely, the benchmark tests of the analysis code against the experimental data measured during the steady state test runs and during the mass injection transient respectively. In order to obtain data for a validation of the safety analysis code, the MARS-GCR code [5-10] is applied to the steady state and mass injection test runs of the PBMM benchmark problem.

Layout of the PBMM

The schematic layout of the PBMM is shown in Fig. 5.1. The PBMM uses a single-stage centrifugal compressor and turbine. It makes use of three shafts, which are the HPC/HPT pairs, LPC/LPT pairs and the power turbine and generator. A generator is emulated by a load compressor connected to a power dissipation loop consisting of a flow control valve and a heat exchanger. Variations in load are effected by increasing or decreasing the pressure level in the load rejection loop.

5.4.4.2. Analysis method

Description of the MARS-GCR Code

In an effort to develop a safety analysis code for GCR systems, the MARS code that was primarily developed for the thermohydraulic analysis of water-cooled reactors has been extended for application to the GCRs. In addition to the recent code implementations of MARS-GCR for the application to the GCRs, some more features are applied for the present study. The code was improved to model the coolant properties of nitrogen (N₂) as well as helium (He) and carbon dioxide (CO₂) as the working fluid. The gas heat transfer models, which are applicable to the TH conditions expected to occur during GCR transients, were evaluated and incorporated.

The gas property routines of the MARS-GCR version, which were extended for GCR applications, were verified and validated with various steady state and transient problems by using the NIST database [5-11]. It was also carried out to simulate the code-to-code benchmark problems. The PBMM consists of three shafts, which are the compressor and turbines pairs. The turbine model simply converts the enthalpy to work with a pressure drop. The turbine model is already well described and verified in the conventional Rankine cycle analysis. In this PBMM, the real efficiency behaviour, which is out of maximum state, should be considered. Among the components of the PBMM facility, the compressors are the most important machines to model the whole Brayton cycle. It relates the pressure increase of the cycle and required torque with efficiency at the operating pressure and mass flow condition.

The compressor model was also added by extending the existing 'PUMP' model [5-12]. The existing 'PUMP' model is to superimpose a quasi-static model for the pump performance on the RELAP5 volume junction flow path representation. The pump is a volume-oriented component and the head developed by the pump is apportioned equally between the suction and discharge junctions that connect the pump volume to the system. The pump model is interfaced with the two-fluid hydrodynamic model by assuming the head developed by the pump is similar to a body force.

Thus, the head term appears in the mixture momentum equation, but, like the gravity body force, it does not appear in the difference momentum equation used in RELAP5. The term that is added to the mixture momentum equation is $\frac{1}{2} \rho g H$, where H is the total head rise of the pump (m), ρ is the volume fluid density (kg/m³) and g is the acceleration due to gravity (m/s²). The factor 1/2 is needed because the term is applied at both the suction and discharge junctions.

In both the semi-implicit and nearly-implicit numerical schemes, the pump head is coupled implicitly to the velocities through its dependence on the volumetric flow rate, Q . The volumetric flow rate is defined as the volume mass flow rate divided by the volume density. It is assumed that the head depends on the volumetric flow rate and can be approximated by a two-term Taylor series expansion.

$$H^{n+1} = H^n + \left(\frac{dH}{dQ} \right)^n (Q^{n+1} - Q^n)$$

The basic parameters that characterize the pump performance are the rotational speed, ω or N , the volumetric flow, Q , the head rise, H , and the shaft torque, τ . The derivative of the head with respect to the volume flow rate is calculated by interpolation of the compressor performance curve data.

The modified 'PUMP' model requires the user's input for performance curves. The next section provides a detail description of this model that was suggested for use with the MARS-GCR code.

5.4.4.3. Modelling of the PBMM with MARS-GCR

Compressor

Compressors are modelled using the component models of the MARS-GCR code. The performance of the compressor model, which was extended from the existing 'PUMP' model, can be evaluated by computing the pressure ratio between the inlet and outlet pressures and the efficiency given in a function of circulator rotational speed and mass flow rates [5-13].

The compressor head (Δh) is obtained by the pressure ratio (PR), which is interpolated from the tabulated data. The head can be expressed as:

$$\Delta h = \frac{P_1(PR-1)}{\rho_m g} \quad (1)$$

$$PR = \frac{P_2}{P_1} \quad (2)$$

where

P_1 is the inlet pressure;

P_2 is the outlet pressure;

PR is the pressure ratio.

The compressor torque (τ) is obtained with using the interpolated efficiency (η) as:

$$\tau = \frac{\dot{m}P_1(PR-1)}{\omega\eta\rho_m} \quad (3)$$

where

τ is the compressor torque;

\dot{m} is the mass flow rate;

ω is the compressor rotational velocity;

η is the efficiency;

ρ_m is the mean density of the inlet and outlet densities of the compressor.

The compressor model is verified and validated against simple one- and two-circulator loops [5-13]. The model is used and activated by the performance curves of the experimental data.

In the PBMM test facility, a total of three compressors are used. The following charts and tables represent the compressor performance information for each compressor. Given N_c and M_c chart data is converted from British into SI units.

Turbine

The turbine model, which was used from the existing ‘TURBINE’ model, was modified to enable accepting the user’s input performance data. The old turbine model is considered due to the fact that the turbine is always working in the maximum efficiency state. A turbine model is used in the MARS code wherein a sequence of turbine stages is treated as a single-junction and volume. The stage group is then represented using modified energy, continuity and momentum equations.

An efficiency factor based upon the simple momentum and energy considerations is used to represent the non-ideal internal processes. A turbine can be modelled using a single-stage group, i.e. a single-volume and junction, or several stage groups, depending upon the resolution required. The single-stage turbine model is used in the current PBMM benchmark simulation. The turbine component is used by the performance curves in order to represent the efficiency change.

In the PBMM test facility, a total of three turbines are used. Given charts and tables represent the turbine performance information for each turbine. This real data should be interpreted as that the efficiency effect is already implemented.

Heater

The heater of the PBMM has a power rating of 420 kW and is contained inside the heater section in the pressure vessel. The heater is composed of three subassemblies or subsystems as shown in

Fig. 5.31. The heater consists of three heater cassettes within a gas-tight cover or sheath, an aft duct subassembly and a forward duct subassembly.

The heater of the PBMM was modelled using a pipe component which has five subvolumes. Among the five volumes, three in the middle of the pipe are connected to the heat structure model, which permitted calculation of the heat transfer across solid boundaries of hydrodynamic volumes. The heat transfer area is set as 1.269 m^2 and a uniform heat flux of 70 kW/m^2 is supplied.

Heat exchanger

All heat exchangers are modelled by a counter-current copper tube and shell-type heat exchanger. The shell-side correlation is used by the Churchill-Chu horizontal cylinder correlation. The tube-side correlation is computed by the Dittus-Boelter correlation. In this two-pipe heat exchanger model, the heat transfer area is conserved in order to maintain the time constant of thermal transient of working fluid, N_2 , but the thickness of the heat exchanger material is assumed to have 1.24 mm .

5.4.4.4. PBMM Benchmark problems

Steady state condition

The nodalization for the MARS-GCR code is shown in Fig. 5.55. A total of 210 volumes were used in the PBMM. The pressure boundaries of calculations were used in the inlet suction pressure of the LPC and the external load cooler. The operation conditions of steady state runs are listed in Table 5.44. The pressure boundaries at the inlet of the LPC are 95 and 115 kPa. The heater power was controlled to maintain the heater outlet temperature as a given set point. The inlet temperature and pressure of the cooling water in the secondary side are 14.2°C and 350 kPa respectively. The mass flow rates of the precoolers, intercooler and external load cooler are 2.05 kg/s , 1.63 kg/s and 1.2 kg/s , respectively.

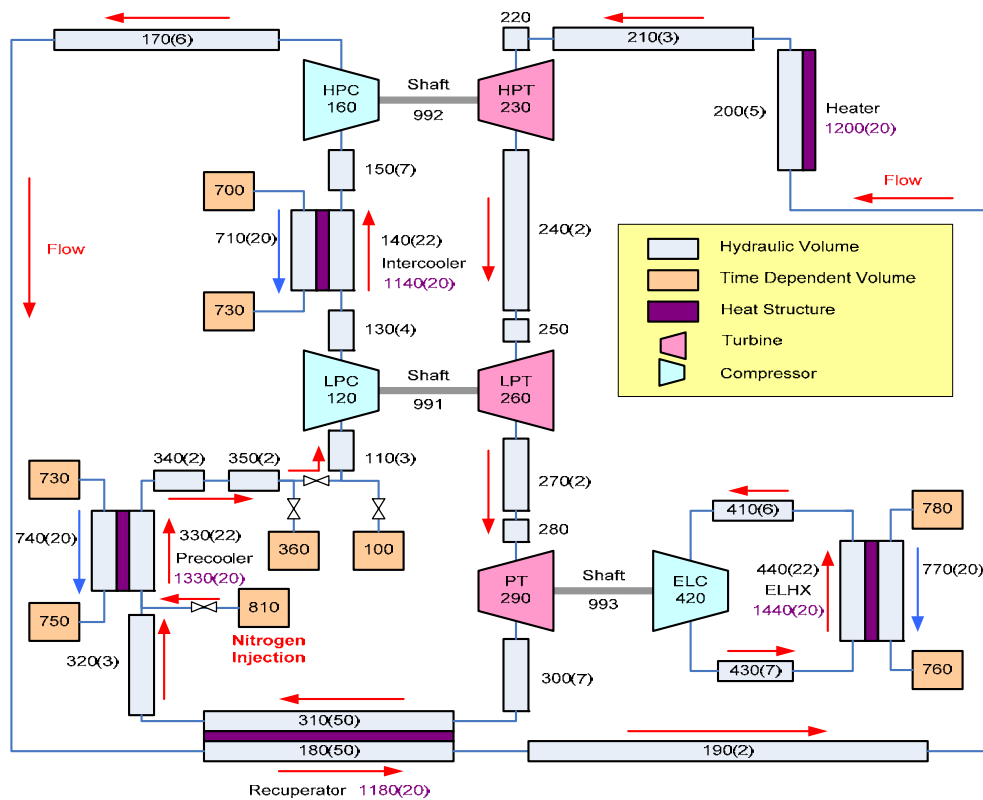


FIG. 5.55. The nodalization of MARS-GCR for the PBMM.

TABLE 5.44. OPERATING CONDITIONS FOR THE PBMM DURING THE TWO STEADY STATE RUNS

Nominal LPC Inlet Pressure	95 kPa	115 kPa
Suction pressure of the LPC [kPa]	94	113.5
Heater outlet temperature [°C]	647.7	649.7
CW flow rate PC [kg/s]	2.05	
CW flow rate IC [kg/s]	1.63	
CW flow rate ELHX [kg/s]	1.2	
CW temperature[°C]	14.2	
CW pressure [kPa]	350	
Nitrogen purity[%]	100	
Valve opening on the external load cooler	Fully open	
Compressor bypass valves	Closed	

At first, the valve between the node numbers 350 and 110 was closed and the time dependent volume (#360) was opened. The loop is maintained as the open state that the working N₂ gas is supplied from the volume 100 and drawn out into the volume 360. During this open-state run, the pressures of volumes 110 and 350 are checked to have the same value by adjusting the loop resistance. The heat flux value of the heater is adjusted so that the heat outlet temperature maintains the experimental data.

When the open loop reached the stable condition, the valve between the node numbers 350 and 110 was opened and the time dependent volume (#360) was closed simultaneously. In other words, after the steady state is reached, the pressure boundaries of the time dependent volume (#110 and #360) are removed and the whole loop closed. In this closed-state run, the temperature and pressure of the whole cycle components have been compared to the experimental data.

The transient simulation for the mass injection condition is performed using the output of the steady state run. The CPU time for the steady state run is 9700 s and the runtime is 500 s.

Steady state results

Tables 5.45 and 5.46 show the temperature and pressure comparisons between the measured (EXP) and calculated values in the case of 95 kPa. The percentage differences are also indicated in the tables. Table 5.45 shows that the calculated temperatures are very close to the measured values with a maximum difference of 9% at the RXLP outlet. The average percent difference of the temperature is 2.52%. A good agreement in the pressure comparison is also shown in Table 5.46. The maximum pressure difference of 5% occurs at the HPT outlet. Table 5.47 shows the comparison of the measured and calculated turbine speeds and mass flow rates. From these results, it can be concluded that the results of MARS-GCR are generally good enough for the safety analysis of the GCRs.

TABLE 5.45. STEADY STATE (95 KPA) — TEMPERATURE COMPARISON

Position	Temperature [K]		Difference [%]
	EXP	MARS-GCR	
PC inlet	449.2	412.2	+8.2
PC outlet	291.3	292.4	-0.4
LPC inlet	293.8	292.5	+0.5
LPC outlet	359.7	362.1	-0.7
IC inlet	359.7	362.2	-0.7
IC outlet	290.0	291.6	-0.6
HPC inlet	298.8	291.4	-0.5
HPC outlet	360.7	363.8	-0.9
RXHP inlet	403.4	370.0	+8.3
RXHP outlet	643.1	672.7	-4.6
Heater outlet	920.9	921.5	-0.1
HPT inlet	920.9	921.5	-0.1
HPT outlet	818.2	837.9	-2.4
LPT inlet	818.2	837.9	-2.4
LPT outlet	748.2	756.1	-1.1
PT inlet	748.7	756.3	-1.0
PT outlet	697.8	714.8	-2.4
RXLP inlet	689.4	717.3	-4.0
RXLP outlet	452.0	411.4	+9.0

TABLE 5.46. STEADY STATE (95 KPA) — PRESSURE COMPARISON

Position	Pressure [kPa(a)]		Difference [%]
	EXP	MARS-GCR	
PC inlet	94.0	92.4	1.7
PC outlet	92.7	91.7	1.1
LPC inlet	94.0	90.5	3.7
LPC outlet	155.8	163.4	-4.9
IC inlet	159.4	163.6	-2.6
IC outlet	159.1	163.3	-2.7
HPC inlet	159.5	162.3	-1.8
HPC outlet	291.5	294.8	-1.1
RXHP inlet	286.6	294.9	-2.9
RXHP outlet	286.4	294.8	-2.9
Heater outlet	286.9	294.6	-2.7
HPT inlet	286.9	294.6	-2.7
HPT outlet	202.0	191.9	+5.0
LPT inlet	195.4	191.7	+1.9
LPT outlet	123.2	119.6	+2.9
PT inlet	125.2	119.3	+4.7
PT outlet	96.0	94.4	+1.6
RXLP inlet	92.6	93.8	-1.3
RXLP outlet	94.1	93.1	+1.1

TABLE 5.47. STEADY STATE (95 KPA) MASS FLOW RATE AND TURBINE SPEED COMPARISON

	EXP	MARS-GCR	Difference
Mass Flow Rate	[kg/s]		[%]
Brayton cycle	0.449	0.4659	-3.76
External load compressor	0.529	0.5624	-6.3
Turbine Speed	[rpm]		[%]
HPT speed	66298	64958.14	+2.02
LPT speed	63707	64498.81	+1.24
PT speed	32294	29623.83	+8.26

No calculational results for the second steady state case at 115 kPa and heater outlet temperature of ~ 650°C were available at the time of this submittal.

Mass injection transient calculation

For this test, the experiment was run to steady state with a 95 kPa LPC suction pressure and 650°C heater outlet temperature. Nitrogen was injected at 0.0227 kg/s for 63 s at the LPC inlet. The mass injection point is located in node number 810, upstream of the precooler.

Figure 5.56 shows the measured and computed LPC suction pressure during the mass injection. The difference in pressure at around 63 s between the experimental and calculational value is 2.23% (Experiment = 107.16 kPa, MARS-GCR = 109.55 kPa). Differences in the original steady state values (about 4 kPa) and different behaviour during the period of injection (about 8 kPa at 20 s) need to be investigated in more detail. After stopping mass injection, the difference in results between the measured and simulated value due to the neglect of heat loss at the compressor is not good.

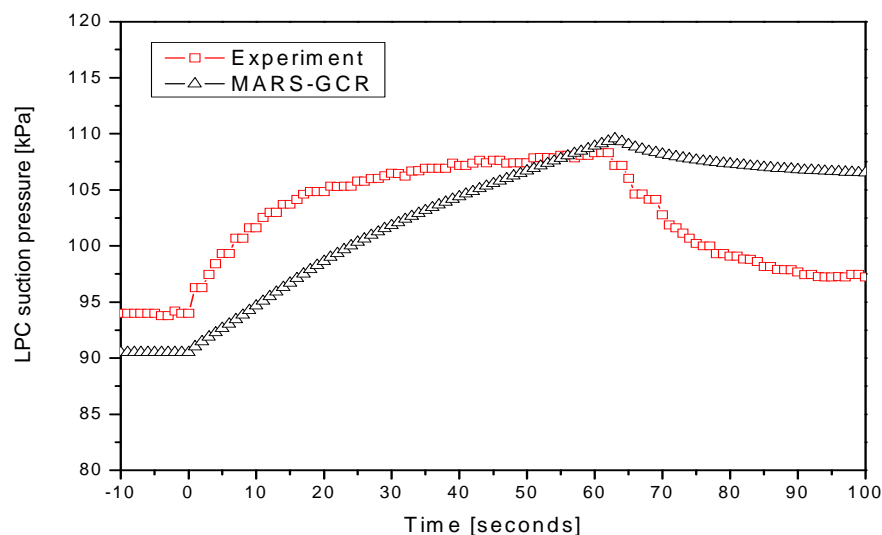


FIG. 5.56. Suction pressure during the injection transient.

Figure 5.57 shows the measured and computed speed of the LPC. The difference in the LPC speed at around 63 s between the experimental and calculational value is 2.63% (Experiment = 60017 rpm and MARS-GCR = 58437.9 rpm). The results of the other compressors have similar data. The differences in the measured value for the other turbines are shown in Table 5.48. After stopping mass injection, however, the LPC speed of MARS-GCR did not recover initial speed before starting the mass injection because the resistance effect of the LPC on the computation of the MARS-GCR code was not considered.

TABLE 5.48. DIFFERENCE IN TURBINE SPEEDS
AT THE END OF INJECTION (AROUND 63 S)

	% Difference
HPT	+1.12
LPT	+2.63
Power Turbine	+5.66

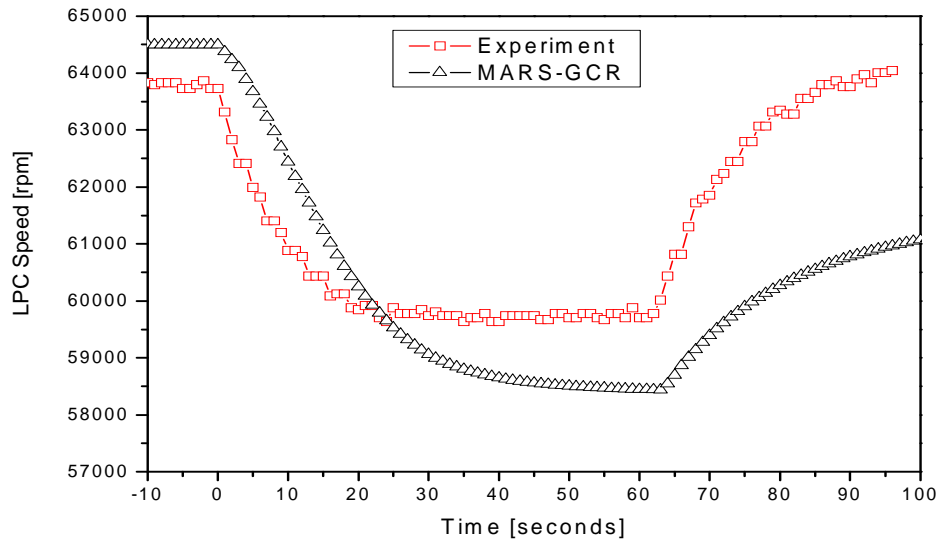


FIG. 5.57. Change in the LPC speed.

Figure 5.58 shows the comparison between the measured and computed pressure in the annulus before the recuperator high pressure inlet. The difference percentage between the measured and computed value at the stop injection is 4.87% (Experiment = 300.3 kPa and MARS-GCR = 314.94 kPa). After stopping the mass injection, however, the annulus pressure of MARS-GCR due to the neglect of the effects of the tube bundle at compressor is not good.

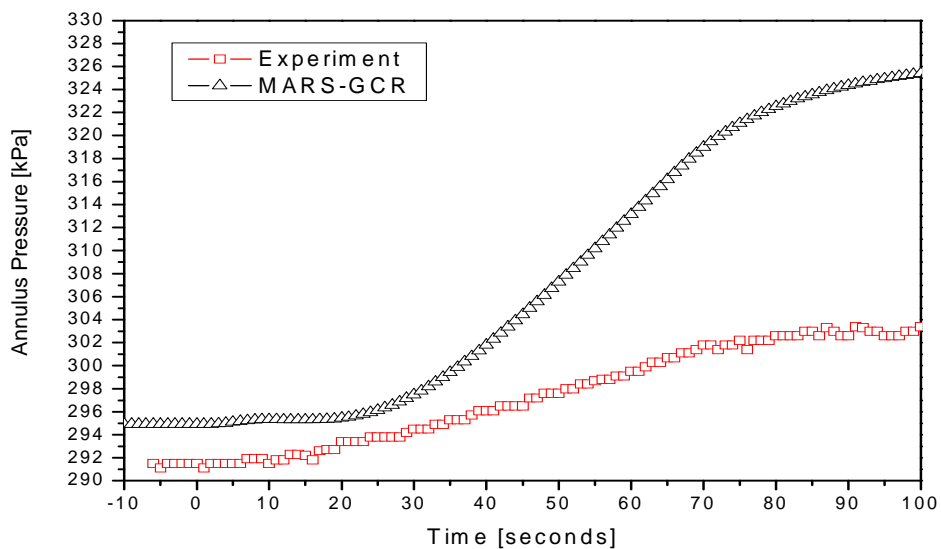


FIG. 5.58. Recuperator high pressure side for the injection transient.

5.4.4.5. Conclusions

The MARS-GCR code is applied to simulate the steady state test and mass injection transient runs of the three-shaft PCS of the PBMM. For the simulation of the working turbomachinery, a compressor model which is different from the conventional water pump model is developed and implemented in MARS-GCR.

For the steady state run, after the pressures of the end cycle volumes are set equal in the open cycle run, the PBMM loop is made to close by the trip valve operations. At the end of the steady state run, the heater outlet temperature and pressure of the LPC outlet are compared to the experimental data. From the results of the steady state run the average percent difference of temperature and pressure is 2.52% and 2.59% respectively. The results of the mass injection transient, due to neglect of the heat loss at the compressor, are not good.

From the results, the capabilities of the MARS-GCR code in simulating the PBMM benchmark problem were demonstrated. The MARS-GCR code showed accuracy in predicting the temperature and pressure distributions with a maximum error of about 10% for the steady state case analysed. In the transient cases, larger differences have been seen.

In future, further improvements and assessments for the reliable prediction of the compressor and turbine performance of the MARS-GCR code are required. The accurate prediction of the dynamic behaviour of the PBMM using the experiment results with the heat leakage of the system will be performed.

5.4.5. PBMM results, France

5.4.5.1. Introduction

The CATHARE thermohydraulic code has been used to model the PBMM loop, as outlined in the PBMR Micro Model Data Pack. Section 5.4.5.2 and 5.4.5.3 are dedicated to the description of the CATHARE code and to the PBMM modelling using CATHARE respectively.

Successive benchmark definitions have been proposed throughout the CRP-5. These can be distinguished by three series of calculations which differ by the proposed operating conditions of the PBMM (steady states at different system pressure and heater outlet temperature) and by the considered transients. These are summarized as follows:

Series 1 (see Section 5.4.5.4):

Three steady state conditions: (100 kPa and 700°C), (100 kPa and 600°C) and (250 kPa and 700°C);

Four transients:

- (1) Load rejection;
- (2) Mass injection at high pressure point;
- (3) Mass injection at low pressure point;
- (4) Startup.

These calculation definitions were taken from [5-1] and [5-14] and no comparisons have been made (neither with other codes nor with the experimental data).

Series 2 (see Section 5.4.5.5):

Two steady state conditions: (95 kPa and 600°C) and (115 kPa and 600°C);

Three transients:

- (1) Load following;
- (2) Load rejection;
- (3) Opening of compressor bypass valves.

The Series 2 test cases are as defined in [5-15]. Comparisons have been made between CATHARE and FLOWNEX and with the experiment for the steady state conditions. These results have been presented at the HEFAT2005 conference [5-16].

Series 3 (see Section 5.4.5.6):

Two steady state conditions: (94 kPa and 644.6°C) and (113.5 kPa and 647.6°C);

One transient corresponding to a

(1) Load following.

These calculations refer to the documents [5-17].

5.4.5.2. Description of the CATHARE Code

CATHARE is a reference safety code developed and validated in collaboration between CEA, EDF (Electricité de France), IRSN (L'Institut de Radioprotection et de Sécurité Nucléaire) and Framatome ANP for the French Pressurized Water Reactors (PWRs) and it has been adapted to also deal with GCR applications [5-18]. The code has a flexible modular structure for the thermohydraulic modelling in applications ranging from large and complex installations like nuclear power plants to simpler experimental facilities. The principal hydraulic elements are pipes (one dimensional), volumes, various boundary conditions and junctions. Other modules feature pumps and turbomachines, control valves, T-junctions, sinks and sources. All CATHARE modules are based on a six-equation two-fluid model (mass, energy and momentum equations for each phase), with additional optional equations for non-condensable gases. The discretization of interphase exchange, pressure and convection terms is fully implicit and the resulting nonlinear difference equations are solved using an iterative Newton solver. The code allows efficient use of several processors in parallel.

Although CATHARE was originally conceived for safety studies of PWR systems, it has obvious advantages to use the same code for future GCRs as well. The solver infrastructure is reliable and efficient and tools for pre- and post-processing can be used as is. Basic modelling features like various hydraulic elements, valves, walls, heat exchangers, etc. already exist and are well proven. The code has been extensively validated and qualified for PWR applications and there is an existing internal organization for maintenance and user support. In order to use the code for GCRs, efforts could thus be concentrated on minor modifications and the development of features unique to GCRs. Examples are the development of a comprehensive turbomachine module, special treatments for gas mixtures, and features for modelling of the core neutronics and heat transfer.

Rather than branching off a separate GCR version of CATHARE, new developments have been integrated as independent options in the standard version of the code, respecting the same stringent procedures for quality assurance. CATHARE has thus evolved into an efficient and reliable tool also for GCR applications, with results in good agreement with existing experimental data and other codes [5-19].

5.4.5.3. Modelling of the PBMM Loop

Available specifications

Apart from the official data pack, we have used information obtained in response to a number of questions posed by the benchmark participants. The additional information obtained concern the following areas in particular:

- Orientation of the recuperator (low-pressure circuit in tubes and high pressure circuit in the shell);
- No fins in any of the tube shell exchangers. Presence of leakage flows in the exchangers;
- The existence of a pressure equilibration line between the load rejection loop (upstream external load cooler) and the main circuit (downstream precoolers).

There are still a few open issues and some contradictory information, for which we have tried to make qualified assumptions of our own. These issues are addressed separately for each component as follows.

Heater

The modelling accounts for the thermal inertia of the ceramic rods. The heating wires around the rods are not modelled. The heat is instead supplied at the surface of the rod walls. The heat transfer coefficient used is for ideal flow across tube bundles. The fact that we heat the rods instead of an exterior wire is likely to overestimate the temperature of the solid and thus also overestimate the perceived thermal inertia of the heater.

There are four stainless steel sieves in the heater. They have mesh numbers 9, 16 and 64. In response to our question, the wire diameter was said to be 1.6 mm for all sieves. This wire diameter is probably correct for the number 9 sieve, but it is impossible for the number 16 and 64 sieves. The pressure drop across a number 9 sieve being relatively small, we have assumed that all four sieves have the same pressure drop.

We have had to assume that there is some kind of control system which controls the heater outlet temperature to a given set point (by varying the supplied electrical power) and that this regulation is also active during the transient of load rejection and load following (mass injection/extraction). Since the thermal inertia of the heater is relatively large, the performance of this control system may have an impact on the results. For the present calculations, we have assumed a control system consisting of a feed-forward signal (based on the measured inlet mass flow and inlet temperature) to estimate the heat required, in combination with a feedback loop minimizing the error between actual and desired heater outlet temperature. The feed-back loop is of PD type (proportional + derivative), with control parameters (gain and derivation time) optimized to obtain the fastest possible regulation without oscillations.

Heat exchangers

All heat exchangers are modelled as counter-flow heat exchangers, with heat transfer correlations appropriate for tube and shell heat exchangers. The tube-side correlations are of the Dittus-Boelter type, while the shell-side uses a Colburn correlation with geometrical correction factors computed for the specific exchanger geometries (Bell-Delaware method). Known internal leakage flows are also taken into account.

Turbomachines

Turbines, compressors, their common shafts and the SBS blower are all modelled using the turbomachine module of the CATHARE code. Statistical correlations are developed based on the performance maps of each turbomachine. Care was taken to account for the differences in gas properties between the performance data and the actual application. We also computed the total-to-total pressure ratio for the turbines (given as total-to-static in the data pack) and recomputed the provided isentropic efficiencies accordingly. The data pack gives the production of turbine efficiency and shaft mechanical efficiency. In order to obtain the turbine efficiency needed, we have assumed that the shaft mechanical efficiency is equal to unity. This appears reasonable since the shaft mechanical losses are likely to be small.

Available specifications

The PBMM data pack contains performance maps for all turbines and compressors. Table 5.49 gives the gas properties and flow conditions used for the measurements.

TABLE 5.49. GAS PROPERTIES AND MEASUREMENT CONDITIONS USED FOR THE PERFORMANCE MAPS

Gas Properties		Compressors	Turbines
Specific heat ratio	$\gamma = c_p / c_v$	1,395	1.340
Gas constant	R [J/(kg.K)]	287,0	290.8
Specific heat	c_p [J/(kg.K)]	1013,2	1147.2
Test Conditions			
Inlet total pressure	p_{01} [kPa]	96,2	101.3
Inlet total temperature	T_{01} [K]	302,8	288.3

The data pack does not contain any information at all about temperatures, pressures and flow rates in the system, not even for nominal working conditions. Although not strictly necessary for the modelling, it is convenient to use realistic approximate values as points of reference and for initialization of the simulations. As reference values for the turbomachines, we have used flow conditions reported at the HTR-2002 conference, based on pre-design steady state simulations with the FLOWNEX code. The information is summarized in Table 5.50.

TABLE 5.50. APPROXIMATE OPERATING CONDITIONS REPORTED AT THE HTR-2002 CONFERENCE (THESE CONDITIONS ARE FOR A SYSTEM PRESSURE OF 100 KPA AND A RESULTING MASS FLOW RATE OF ABOUT 0.54 KG/S.)

Component	p_{in} [kPa]	p_{out} [kPa]	T_{in} [°C]	T_{out} [°C]	Power [kW]	Speed [rpm]
LPC	100.0	200.8	22.9	109.6	51.0	72078
LPT	248.5	150.5	628.5	549.0		
HPC	198.4	381.9	22.9	102.3	46.7	70009
HPT	378.0	249.1	700.0	628.5		
External Load Compressor	105.0	150.7	21.1	65.9	32.1	39073
Power Turbine	149.7	105.0	549.0	498.2		

Generalized variables

The effect of a turbomachine is to change the total pressure of a flow, while adding energy (compressor), or removing energy from the fluid (turbine). These effects can be quantified by the ratio Π of total (or stagnation) pressures upstream (index 1) and downstream (index 2) of the turbomachine and the isentropic efficiency, η . These properties are defined differently for compressors and turbines.

For a compressor:

$$\Pi \equiv \frac{p_{02}}{p_{01}}, \quad \eta \equiv \frac{T_{01} \left(\Pi^{\frac{\gamma-1}{\gamma}} - 1 \right)}{T_{02} - T_{01}}$$

while for a turbine:

$$\Pi \equiv \frac{p_{01}}{p_{02}}, \quad \eta \equiv \frac{T_{01} - T_{02}}{T_{01} \left(1 - \left[\frac{1}{\Pi} \right]^{\frac{\gamma-1}{\gamma}} \right)}$$

These turbomachine characteristics are usually expressed as functions of two generalized flow variables representing the flow rate and the rotation velocity. If \dot{m} is the mass flow and ω the rotation velocity (in rad/s), these are:

$$\frac{\dot{m} \sqrt{T_{01}}}{p_{01}} \quad \text{Generalized flow rate;}$$

$$\frac{\omega}{\sqrt{T_{01}}} \quad \text{Generalized rotation velocity.}$$

These generalized variables are based on two non-dimensional groups respectively,

$$\frac{\dot{m} \sqrt{RT_{01}}}{D^2 p_{01} \sqrt{\gamma}} \quad \text{and} \quad \frac{\omega D}{\sqrt{\gamma RT_{01}}}$$

from which one has dropped parameters that usually remain constant for a given application (the geometric length scale D and the gas properties R and γ). These non-dimensional groups can be used to correct the fact that the characteristics were measured with gas properties other than those used in CATHARE for nitrogen. In order to simplify the equations used to derive correlations for the turbomachine modelling in CATHARE, we will at the same time correct the available data to the desired reference values of the inlet pressure and temperature for each turbomachine. If R and γ are the properties of nitrogen, the reference flow conditions are written with an index 'ref' and the measurement flow and gas properties are all written with primes, then the corrected flow rates and rotation velocities are:

$$\dot{m} = \dot{m}' \frac{p_{01,ref}}{p_{01}'} \sqrt{\frac{\gamma R' T_{01}'}{\gamma' R T_{01,ref}'}}$$

$$\omega = \omega' \sqrt{\frac{\gamma R T_{01,ref}'}{\gamma' R' T_{01}'}}$$

In the following, we will work with *reduced* generalized variables, i.e. variables normalized with respect to a reference point in the performance maps. Although the precise choice of the reference point is not important, it is usually taken as the nominal working point. For the PBMM modelling, the exact location of the working point is *a priori* unknown. For each turbo machine I component, we have chosen a reference point which coincides with a point in the dataset, close to the expected nominal conditions as suggested by published information from the pre-design calculations (HTR-2002 conference). The primary concern is to define consistent values of $\{\dot{m}_{ref}; \omega_{ref}; \Pi_{ref}; \eta_{ref}\}$, so that the reference point really belongs to the surface spanned by the points in the dataset. Since the datasets have already been corrected to the desired reference temperature and pressure, the reduced or normalized variables are:

$$\left(\frac{\dot{m}\sqrt{T_{01}}}{P_{01}}\right)^* = \left(\frac{\dot{m}\sqrt{T_{01}}}{P_{01}}\right) \bigg/ \left(\frac{\dot{m}\sqrt{T_{01}}}{P_{01}}\right)_{ref} = \frac{\dot{m}}{\dot{m}_{ref}}$$

$$\left(\frac{\omega}{\sqrt{T_{01}}}\right)^* = \left(\frac{\omega}{\sqrt{T_{01}}}\right) \bigg/ \left(\frac{\omega}{\sqrt{T_{01}}}\right)_{ref} = \frac{\omega}{\omega_{ref}}$$

Similarly, we introduce the reduced/normalized pressure ratio and isentropic efficiencies as follows:

$$\Pi^* = \Pi / \Pi_{ref},$$

$$\eta^* = \eta / \eta_{ref}.$$

Turbines: Calculating the ratio of total pressures and the turbine isentropic efficiency

In the PBMM data pack, the measured turbine pressure ratio is given as the total inlet pressure over the *static* outlet pressure:

$$\Pi_m = \frac{P_{01}}{P_2}$$

The measured ‘turbine mechanical efficiency’, called η_m , is the product of the turbine isentropic efficiency η_T , based on the total-to-static pressure ratio above and the mechanical shaft efficiency η_{shaft} :

$$\eta_m = \eta_T \eta_{shaft}$$

The measured efficiencies are around 70% and we can safely assume that the thermodynamic losses are much larger than the mechanical shaft losses. Since the mechanical shaft efficiency is also unknown, we will assume that $\eta_{shaft} \approx 1$, so that the measured efficiency is approximately equal to the isentropic efficiency: $\eta_m \approx \eta_T$. The measured efficiency can thus be written as:

$$\eta_m = \frac{T_{01} - T_{02}}{T_{01} \left[1 - \left(\frac{1}{\Pi_m} \right)^{\frac{\gamma-1}{\gamma}} \right]} \quad (1)$$

Prior to using the turbine data in the performance maps, we need to recalculate both the pressure ratio and the turbine efficiency in terms of the *total* outlet pressure, rather than the *static* pressure used in the data pack. This recalculation is possible (although complicated), since the documentation provides the diameter of the section where the outlet static pressure was measured. We must first calculate the Mach number at the outlet measurement point. If A_2 is the flow cross-section and V_2 is the local velocity,

$$M_2 \equiv \frac{V_2}{\sqrt{\gamma R T_2}} = \frac{\dot{m}}{\rho_2 A_2 \sqrt{\gamma R T_2}} = \frac{\dot{m}}{p_2 A_2} \sqrt{\frac{R T_2}{\gamma}} \quad (2)$$

The outlet static pressure appearing above can be calculated as:

$$p_2 = \frac{P_{01}}{\Pi_m}$$

The measured isentropic efficiency can be used to calculate the total outlet temperature as:

$$T_{02} = T_{01} - \eta_m T_{01} \left[1 - \left(\frac{1}{\Pi_m} \right)^{\frac{\gamma-1}{\gamma}} \right] \quad (3)$$

and the static temperature is given by:

$$T_2 = T_{02} \left(1 + \frac{\gamma-1}{2} M_2^2 \right)^{-1} \quad (4)$$

Since this expression itself contains the Mach number, we must iterate Eqs (2) and (4) to obtain a correct value for the Mach number. A starting value for M_2 can be computed using $T_2 \approx T_{02}$ calculated from Eq. (3). The iteration converges to three significant digits in two to three iterations.

Once a correct Mach number is known, the total-to-total pressure ratio can be computed as:

$$\Pi \equiv \frac{p_{01}}{p_{02}} = \left(\frac{p_{01}}{p_2} \right) \left(\frac{p_2}{p_{02}} \right) = \Pi_m \left(1 + \frac{\gamma-1}{2} M_2^2 \right)^{\frac{-\gamma}{\gamma-1}}$$

since

$$\frac{p_0}{p} = \left(1 + \frac{\gamma-1}{2} M_2^2 \right)^{\frac{\gamma}{\gamma-1}}$$

The isentropic efficiency based on the *total* quantities is defined as:

$$\eta \equiv \frac{T_{01} - T_{02}}{T_{01} \left(1 - \left[\frac{1}{\Pi} \right]^{\frac{\gamma-1}{\gamma}} \right)}$$

Combining this with Eq. (1) finally allows η to be computed as:

$$\eta = \eta_m \frac{\left(1 - \left[\frac{1}{\Pi_m} \right]^{\frac{\gamma-1}{\gamma}} \right)}{\left(1 - \left[\frac{1}{\Pi} \right]^{\frac{\gamma-1}{\gamma}} \right)}$$

Valves and orifices

All valves and orifices were modelled using existing CATHARE modules and based on the specifications provided in the data pack.

Mass sources and sinks

Mass injection and extraction were modelled using mass sources and sinks in the appropriate locations. The same sources and sinks were used also to establish the desired steady state conditions.

Pressure equilibration line

We have learned late in the project that the load rejection loop is pressurized via a pressure equilibration line connecting a point upstream of the electric load compressor with a point downstream of the precooler in the main circuit. We have no information about the length and dimensions of this line. For the moment, we have therefore emulated this line with a source/sink in the point upstream of the electrical load compressor, which maintains the same pressure as downstream of the precooler. As the mass exchanged across this line appears to be relatively small, we have not bothered to implement the corresponding source/sink in the main circuit.

Pipe runs

All pipe runs have been modelled using the geometrical information available in the data pack. Singular pressure drops for bends were taken from Idelchik. The flow in T-pieces is handled automatically by the code.

5.4.5.4. First series of calculations

PBMM steady state problem statement, 11 November 2004

These calculations refer to two documents [5-1], [5-14]. For this series of calculations, comparisons have not been performed, neither with other codes nor with experimental data.

Steady state results

Position of the PTCV control valve

The PTCV control valve located in the load rejection loop is used to choose the working point of electric load compressor. It appears to have little effect on the dissipated power. The position of the valve was not specified in the data pack. We have assumed that the valve is 50% open, as this assures the working point of the electric load compressor stays well inside the known performance map during all of the transients studied (see Fig. 5.59).

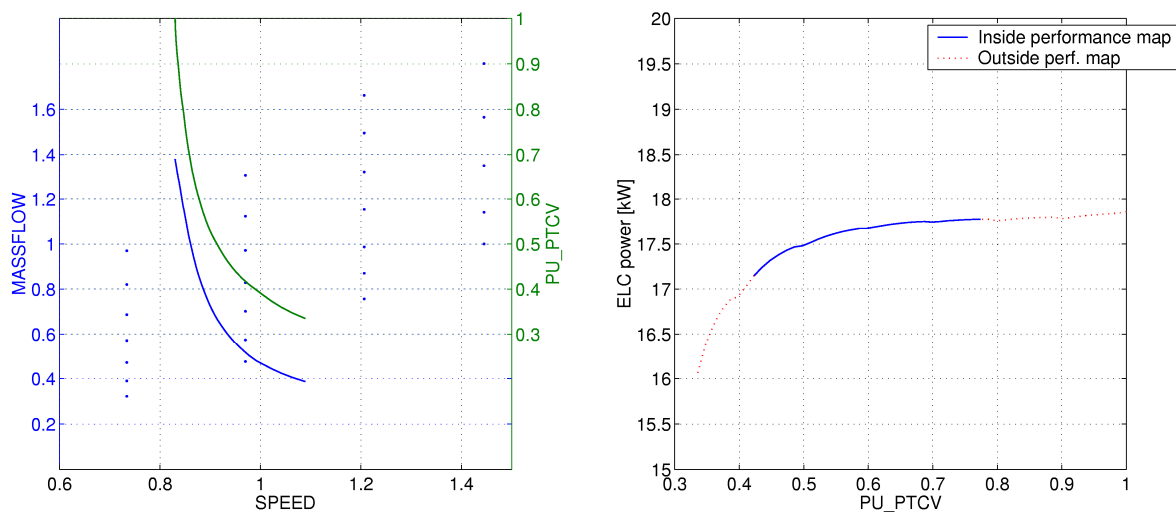


FIG. 5.59. Sensitivity to PTCV valve setting for the case of 100 kPa system pressure, 600°C heater outlet temperature. The left pane shows the relationship between the PTCV valve setting (green and right axis) and the working point of the electric load compressor (blue, left axis; normalized generalized variables). Blue dots show the data of the performance map. The right pane shows the PT power as a function of valve setting.

Work Points at 700°C Heater Outlet Temperature

The data pack defines two work points with a heater outlet temperature of 700°C. In the first, the system pressure provided by the NICS tanks (upstream of the precooler) is 100 kPa and in the second, the system pressure is 250 kPa. In the following, these two steady states are labelled ‘P100’ and ‘P250’ respectively. Table 5.51 summarizes the operating conditions for the major components at steady state.

TABLE 5.51. PREDICTED STEADY STATE INLET CONDITIONS (PRESSURE AND TEMPERATURE) FOR THE MAIN COMPONENTS FOR THE WORK POINTS ‘P100’ AND ‘P250’ DEFINED IN THE DATA PACK. FOR THE HEAT EXCHANGERS AND HEATER, THE EXCHANGED POWER IS ALSO GIVEN AND FOR TURBINES BOTH SHAFT POWER AND ROTATION SPEED ARE GIVEN.

Component	‘P100’				‘P250’			
	T _{in} [°C]	P _{in} [kPa]	Power [kW]	Speed [rpm]	T _{in} [°C]	P _{in} [kPa]	Power [kW]	Speed [rpm]
HPT	695,9	379,8	48,5	71483	695,9	944,4	120,8	71735
LPT	611,8	243,6	55,7	74499	611,7	606,2	138,7	74811
PT	511,5	136,7	32,9	42142	511,3	340,3	81,6	42094
RX_tube	474,5	101,4	208,3		474,5	253,0	495,1	
PC	135,2	100,0	65,8		146,0	250,0	180,3	
LPC	21,9	97,0			25,4	242,7		
IC	113,3	199,5	54,5		117,5	497,6	136,5	
HPC	22,6	197,5			26,0	492,8		
RX_shell	102,4	386,1	208,3		106,1	960,1	495,1	
HS	441,6	385,8	157,1		434,6	959,4	401,4	
ELC	20,7	99,2			22,6	248,3		
ELHX	82,4	108,1	32,9		84,0	270,0	81,6	

The efficiency of a heat exchanger can be defined as (P/S for primary/secondary):

$$\eta_{hx} \equiv \frac{T_{S,out} - T_{S,in}}{T_{P,in} - T_{S,in}}$$

This gives a recuperator (RX) efficiency of 91.1% for the low-pressure case and 89.2% for the high pressure case. We note that these values are higher than those reported by the PBMM team at the HTR-2002 conference (84% and 87% respectively).

The overall system efficiency (PT power over HS power) is found to be 20.9% and 20.3% for the two cases, respectively.

Steady state work points at 600°C heater outlet temperature

At the last minute, we have received a new specification of steady state operating conditions that differ considerably from those given in the original data pack. In particular, the system pressure and heater outlet temperatures have changed. In the heat exchangers, water pressure, water temperature and water flow rate have all changed. The only difference between the two new cases is the system pressure (95 kPa and 115 kPa respectively). The new operating conditions (as of November 11, 2004, in case it changes again) are defined in Table 5.52. The results of the predictions are summarized in Table 5.53.

TABLE 5.52. NEW STEADY STATE SPECIFICATIONS, AS OF NOVEMBER 11, 2004

Variable	Steady State #1	Steady State #2
Heater outlet temperature	600°C	600°C
Suction pressure of the LPC	95 kPa	115 kPa
Cooling water flow rate (all coolers)	2.6 kg/s	2.6 kg/s
Cooling water temperature	13°C	13°C
Cooling water pressure	350 kPa	350 kPa
Nitrogen purity	100%	100%
PTCV valve opening	Fully open	Fully open
Compressor bypass valves	Closed	Closed

The recuperator (RX) efficiencies are evaluated to 91.4% and 91.0% for the two cases respectively. The overall system efficiency (PT power over HS power) is found to be 18.3 and 18.2% respectively.

TABLE 5.53. PREDICTED STEADY STATE INLET CONDITIONS (PRESSURE AND TEMPERATURE) FOR THE MAIN COMPONENTS FOR THE NEW WORK POINTS ('STEADY STATE #1' AND #2'). FOR THE HEAT EXCHANGERS AND HEATER, THE EXCHANGED POWER IS ALSO GIVEN AND FOR TURBINES, BOTH THE SHAFT POWER AND ROTATION SPEED ARE GIVEN.

Component	'Steady State #1'				'Steady State #2'			
	T _{in} [°C]	P _{in} [kPa]	Power [kW]	Speed [rpm]	T _{in} [°C]	P _{in} [kPa]	Power [kW]	Speed [rpm]
HPT	596,4	306,7	35.3	66984	596.4	372.1	42.9	67077
LPT	523,9	200.6	37.2	66188	523.8	243.2	45.3	66361
PT	445,3	121.1	19.6	33458	445.0	146.7	23.8	33520
RX_tube	420,1	96.0	157.2		419.6	116.2	189.3	
PC	112,8	95.0	49.9		114.6	115.0	61.4	
LPC	14,7	92.8			15.2	112.3		
IC	87,2	172.4	36.8		88.0	209.0	44.8	
HPC	15,0	170.8			15.5	207.0		
RX_shell	83,9	311.7	157.2		84.5	378.1	189.3	
HS	391,1	311.5	106.9		389.5	377.8	130.7	
ELC	13,2	94.4			13.3	114.3		
ELHX	41,4	109.3	19.6		41.6	132.4	23.8	

Transient results

Load rejection specification

Initial conditions are the high pressure steady state at 250 kPa system pressure and 700°C heater outlet temperature. We assume that the heater outlet temperature is kept constant (700°C) during the transient, using the temperature control loop described earlier. We further assume that there is no change of inventory during the transient (NICS tanks closed).

Transient events:

$t = 0$ s: Open the GBP valve to 7% relative opening.

Load rejection results

The left pane of Fig. 5.60 shows the evolution of PT turbine power. The generated power falls from 81.6 kW to 52.5 kW in about 60 s. The right pane shows the evolution of turbine rotation speeds.

Mass flows in the system are illustrated in Fig. 5.61. The flow rate in the bypass line is nearly constant, due to sonic conditions in the GBP control valve. The right pane shows the injection/extraction flow rates in the source/sink pair used to emulate the pressure equilibration line between the load rejection loop and the main circuit.

Figure 5.62 shows the heat transfer on the primary and secondary sides of the heat exchangers. We see that the thermal inertia of the recuperator (~2700 kg of copper tubing) will have a very significant effect on the evolution of system temperatures. This is less of an issue for the water exchangers.

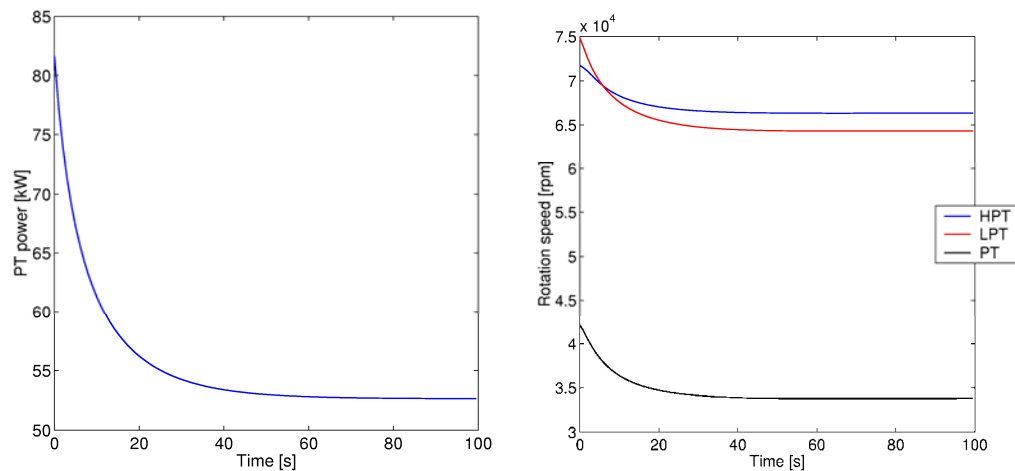


FIG. 5.60. PT turbine power (left) and turbomachine rotation speeds (right).

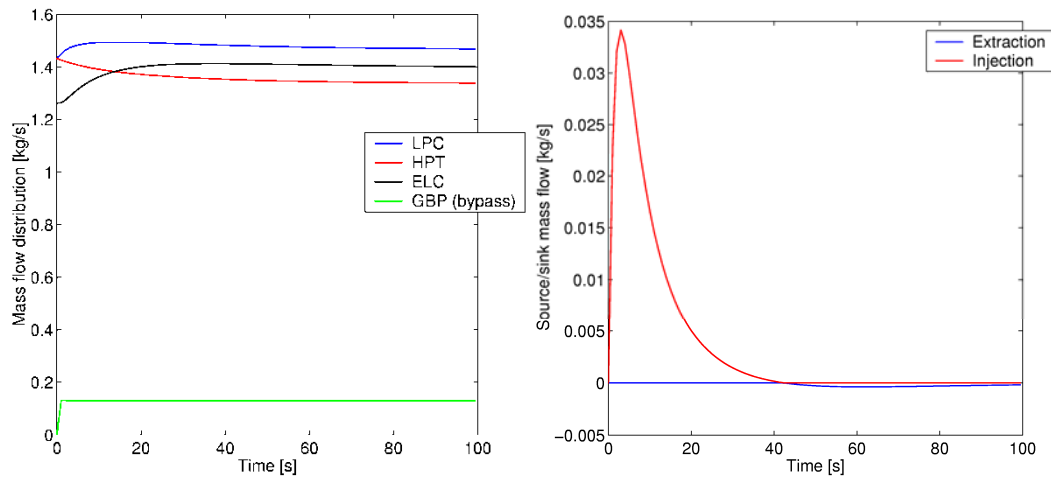


FIG. 5.61. Left pane: mass flows in different parts of the system. Right pane: mass injected/extracted in the load rejection loop (upstream of ELC) to simulate the pressure equilibration line.

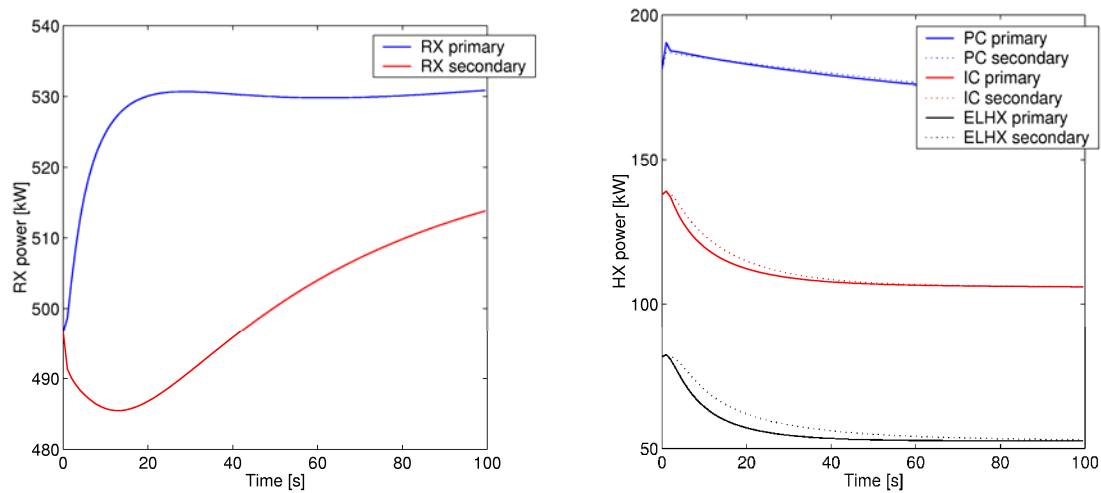


FIG. 5.62. Heat transfer on primary and secondary sides of the recuperator (left) and the water heat exchangers (right).

Mass Injection at high pressure point

Specification

Initial conditions used are the low-pressure steady state at 100 kPa system pressure. Note, however, that the data pack specifies the high pressure steady state as initial condition. We have assumed that this is an error because the transient would otherwise make no sense. Once the injection starts, the electrical heater would quickly reach its maximum power and the heater outlet temperature would start to decrease. The high pressure injection/extraction point is located in the large internal volume (Volume 34) downstream of the HPC.

Transient events:

- t = 0 s: Inject mass at a rate of 1 kg/s;
- t = 40 s: Stop injection;
- t = 60 s: Extract mass at a rate of -1 kg/s;
- t = 100 s: Stop extraction.

Results

Figure 5.63 shows the power turbine power and the turbine rotation velocities. Since injection/extraction is done in the large internal volume, the inventory can be modified very quickly without adverse effects on the system. There is a slight overshoot/undershoot on injection/extraction but the injection/extraction rate is also quite large relative to the system flow rate.

Figure 5.64 illustrates the performance of the control loop we have assumed exists for controlling the heater outlet temperature. Due to the thermal inertia of the electrical heater (mass of ceramic rods), the performance of the control loop may have an impact on the evolution of the transient, since it may be difficult to maintain the heater outlet temperature constant.

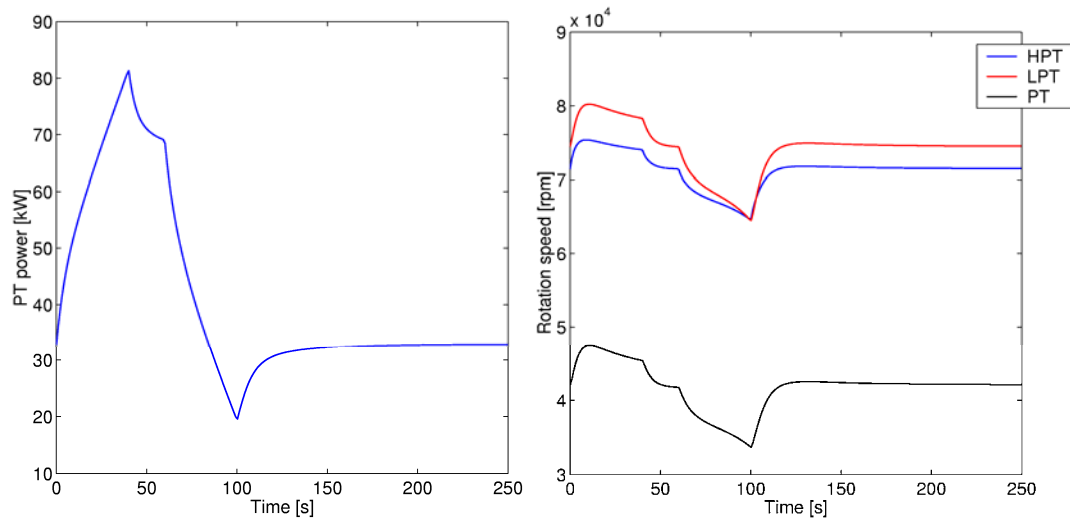


FIG. 5.63. PT Power (left) and turbine rotation speeds (right).

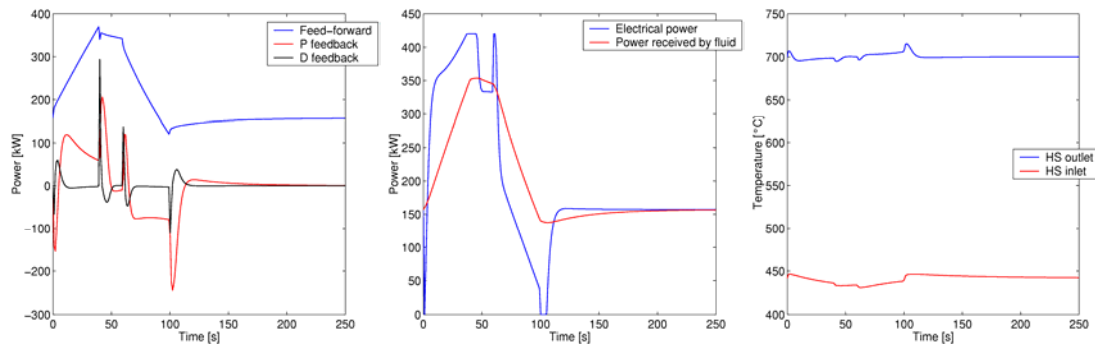


FIG. 5.64. Performance of the temperature regulation of heater outlet temperature. Left: Power contribution from the feed-forward and feed-back (P+D) loops. Middle: Comparison between electrical power and power actually transferred to the fluid. Right: Resulting heater inlet/outlet temperatures.

Mass injection at low-pressure point

Specification

Initial conditions used are the low-pressure steady state at 100 kPa system pressure. Note, however, that as for the previous transient, the data pack specifies the high pressure steady state as initial condition. The low-pressure injection/extraction point is located in point 100, immediately upstream of the precooler.

Transient events:

t = 0 s: Inject mass at a rate of 0.1 kg/s;

t = 399 s: Stop injection;

t = 499 s: Extract mass at a rate of -0.1 kg/s;

t = 900 s: Stop extraction.

Results

Although the injection/extraction rate in this case is ten times smaller than in the high pressure case discussed above, Fig. 5.65 shows that the power turbine power makes a large and rapid excursion in the *wrong direction* when injection or extraction is initiated. Had there been a large volume available on the low-pressure side as well, this effect might have been less pronounced, but the initial power excursion would still be in the wrong direction.

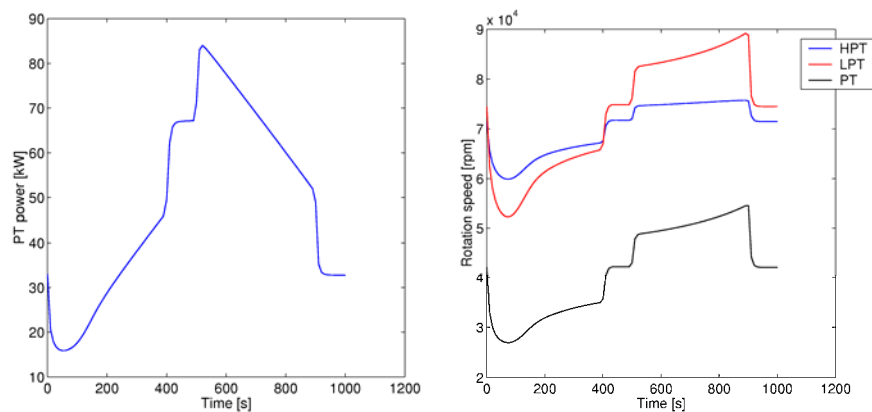


FIG. 5.65. PT Power (left) and turbine rotation speeds (right).

Startup

Startup specifications

The initial conditions assume a system pressure (NICS tanks) of 160 kPa and a heater outlet temperature of 200°C. Furthermore, it has been confirmed that the System Inline Valve (SIV) is initially closed, the SBSIV and SBSOV valves are fully open and the SBS blower is running at a constant speed of 2000 rpm.

Transient events (clarified after questions):

t = 0 s: Ramp the heater outlet temperature according to the equation: $T_{out} = 200 + 40 \cdot \text{time}$;

t = 12.5 s: 'Switch off the ramping and solve the flow in the heater element' (see comment below).

When the pressure difference across the SBS blower changes sign, open the SIV valve completely, shut down the SBS blower and close the SBSIV and SBSOV valves (see comment below).

Comments

The ramping of the heater outlet temperature is accomplished with an extra heat source in the heater outlet. The capacity of the heater is insufficient for a temperature increase this fast, due to the thermal inertia of the heater elements;

The data pack specifies that the SBS blower is shut down at $t = 15.04$ s. We found it more natural to trigger this event on the pressure difference across the blower. In the calculation, the event takes place at $t = 15.10$ s.

Startup results

Figure 5.66 shows the SBS blower and turbomachine power during the startup transient. We recall that the SBS blower is initially active, at a constant rotation speed. The shaft power of the SBS blower decreases with decreasing pressure difference across the blower. When the power and pressure difference becomes zero, the in-line SIV valve is opened, the blower is stopped and the blower is isolated with the SBSIV and SBSOV valves. According to the simulation, this takes place at $t = 15.10$ s, compared to 15.04 s prescribed by the benchmark specification.

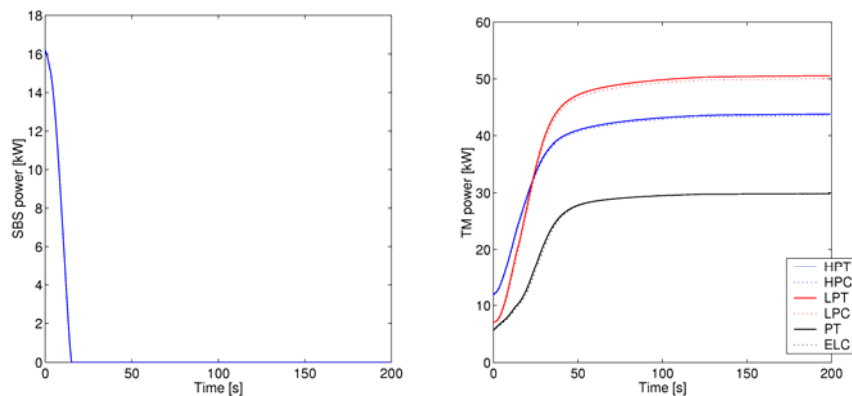


FIG. 5.66. SBS blower power (left) and turbomachine power (right) during startup.

Figure 5.67 shows the evolution of pressures and temperatures in the system during the startup transient. Note that the initial ramp of the heater outlet temperature was realized using an extra heat source placed just downstream of the heater outlet. The heater outlet temperature is therefore seen to rise very slowly, due to the large thermal inertia of the heater. The desired ramp is, however, visible in the HPT inlet temperature.

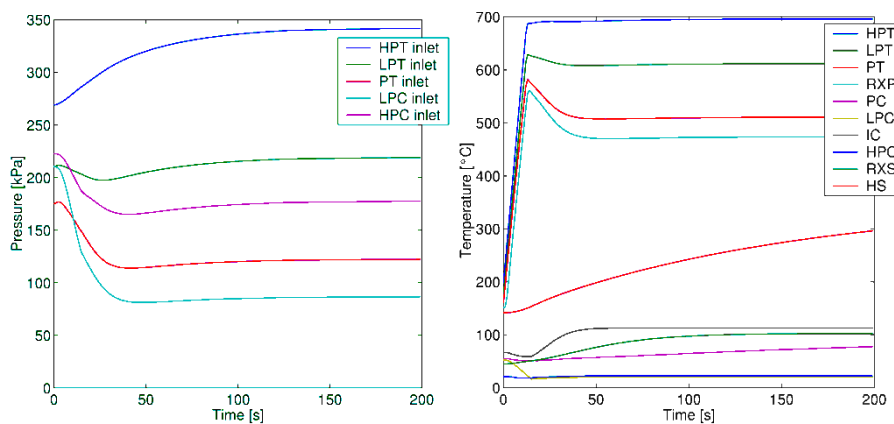


FIG. 5.67. Evolution of pressure and temperature in different parts of the system.

Turbomachine operating conditions

Figure 5.68 shows the trajectories of operating conditions traversed by each of the turbomachines during the transients of the benchmark. Blue dots mark the data given in the data pack performance maps. Only in the beginning of the startup transient does some of the turbomachines operate outside their documented operating range.

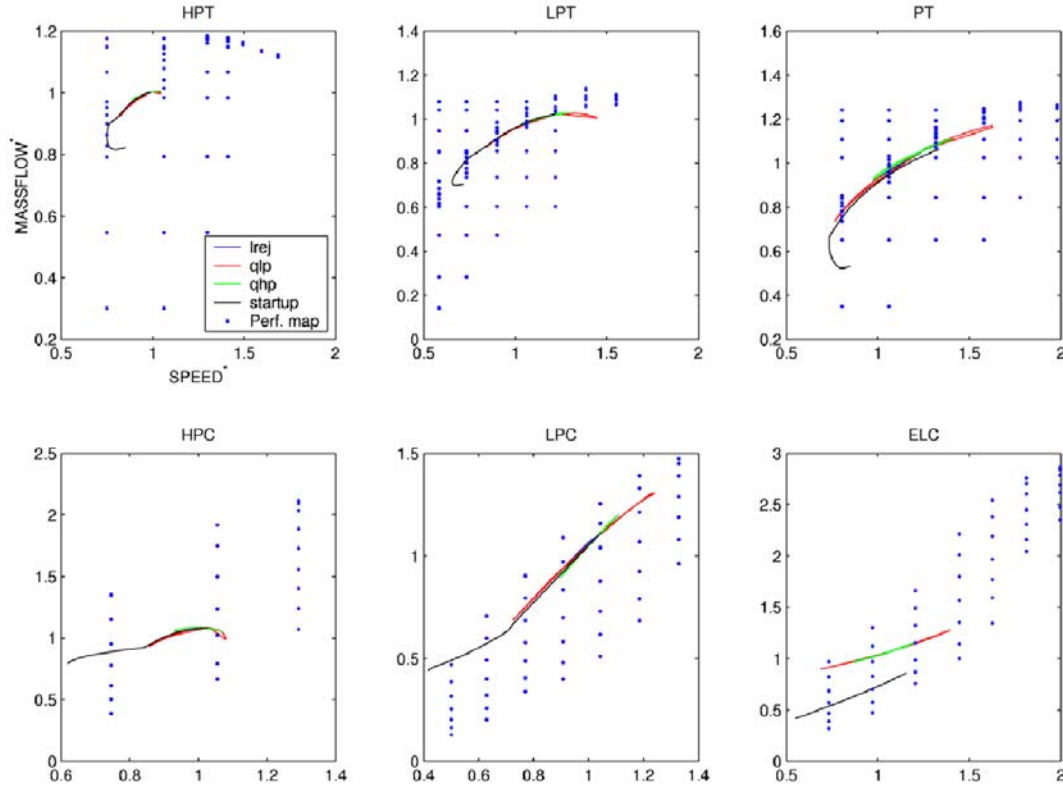


FIG. 5.68. For each turbomachine, the diagrams show the normalized generalized independent variables in the performance maps as blue dots. The lines represent the trajectories of operating conditions traversed during the transients.

Conclusions for the first series of calculations

We have not encountered any particular difficulties. The calculations run smoothly and the system as a whole appears to be robust under the present circumstances. Since we have no data for comparison, we cannot draw any conclusions at this point as to the agreement between the numerical predictions and the real installation. We can, however, identify a few issues in particular which may have an impact on the quality of the predictions.

- Heat exchangers

The recuperator is a critical component for the performance of the system, as it transfers even more heat than the heater itself. We have observed that our predicted recuperator efficiency is higher than that reported by the PBMM team at the HTR-2002 conference (pre-design calculations with FLOWNEX). In order to compare the results of different predictions, the most sensitive test is to compare an average heat exchange coefficient computed from the predicted exchanged power P and the temperature difference between the primary and secondary sides, ΔT_{P-S} . If the exchange surface is S , the average heat transfer coefficient is:

$$h_{average} = \frac{P}{S \cdot \Delta T_{P-S}}.$$

The shell-side exchange surface for the recuperator is about 257 m². Our steady state predictions give an average heat transfer coefficient of 24.6 W/(m² · °C) in the case ‘P100’ and 48.3 W/(m² °C) in the case ‘P250’.

- Turbomachine performance maps

The implementation of the performance maps introduce many sources of error: unit conversions, corrections for different gas properties, recalculation of pressure ratios and efficiencies in terms of total quantities (for the turbines) and last, but not least, the statistical fitting of correlations to the data.

5.4.5.5. Second series of calculations

These calculations refer to document [5-15]. Comparisons have been performed between CATHARE and FLOWNEX and with the experiment for the steady state conditions [5-16]. The following sections are based on this paper. Main results and comments are recalled here.

Steady state results

Table 5.54 provides the set of variables for the second series of calculations.

TABLE 5.54. SET OF VARIABLES

Heater outlet temperature	600°C
Suction pressure of LPC	95kPa (abs) and 115kPa (abs)
Cooling water flow rate through each cooler	2.5kg/s
Cooling water temperature	~13°C
Cooling water pressure	350 kPa
Nitrogen purity	100%
Valve opening on the electric load compressor	Fully open
Compressor bypass valves	Closed

Steady state #1–95 kPa LPC suction pressure

Table 5.55 shows the temperature and pressure obtained with CATHARE (CAT) and FLOWNEX (FNX) for the case of 95 kPa LPC suction pressure, as compared with the experimental data (EXP).

TABLE 5.55. STEADY STATE #1 (95 KPA) — PRESSURES AND TEMPERATURES IN THE CIRCUIT

Component	Pressure [kPa]			Temperature [°C]		
	EXP	CAT	FNX	EXP	CAT	FNX
LPC inlet	94.1	94.7	93.4	21.5	14.6	15.0
IC inlet	147.9	170.9	160.7	80.7	82.9	78.8
HPC inlet	148.4	169.3	160.2	17.4	14.9	14.6
HPC outlet	259.9	299.4	280.9	82.5	79.6	79.9
RX inlet (HP)	255.0	301.5	280.1	126.7	80.5	79.9
RX outlet (HP)	254.2	301.5	278.5	345.4	400.3	399.2
HS inlet	N/A	301.3	278.5	N/A	400.3	399.2
HS outlet	N/A	301.2	278.4	N/A	600.1	600.0
HPT inlet	252.0	296.5	278.1	586.0	596.3	600.0
LPT inlet	171.3	196.4	187.5	511.8	527.1	540.1
PT inlet	111.8	121.3	123.1	433.0	453.3	480.5
PT outlet	94.2	98.3	96.4	408.7	428.8	447.7
RX inlet (LP)	91.4	97.8	95.7	400.2	430.2	447.7
RX outlet (LP)	93.5	97.1	95.3	167.3	110.5	130.9
PC inlet	96.6	96.8	95.0	164.3	110.5	130.9
PC outlet	92.5	96.4	94.7	18.9	15.1	15.0
ELC inlet	95.5	96.3	94.7	16.6	13.2	13.4
ELC outlet	109.5	115.6	116.3	40.5	39.3	40.0
ELHX gas inlet	100.8	110.4	106.8	42.6	39.6	40.0
ELHX gas outlet	99.4	109.4	105.9	16.3	13.6	13.4

Steady state #2—115kPa LPC suction pressure

Table 5.56 shows the temperature and pressure obtained with CATHARE and FLOWNEX for the case of 115 kPa LPC suction pressure, as compared with the experimental data.

TABLE 5.56. STEADY STATE #2 (115 KPa) —
PRESSURES AND TEMPERATURES IN THE CIRCUIT

Component	Pressure [kPa]			Temperature [°C]		
	EXP	CAT	FNX	EXP	CAT	FNX
LPC inlet	114.1	114.7	113.1	24.7	15.1	15.2
IC inlet	179.2	207.1	194.7	84.2	83.7	79.1
HPC inlet	179.4	205.2	194.1	20.9	15.3	14.9
HPC outlet	310.7	363.1	340.0	85.8	80.2	80.2
RX inlet (HP)	306.6	365.6	339.0	129.5	81.1	80.2
RX outlet (HP)	305.8	365.6	337.3	349.8	398.6	394.5
HS inlet	N/A	365.3	337.2	N/A	398.6	394.5
HS outlet	N/A	365.2	337.1	N/A	600.1	600.0
HPT inlet	302.7	359.6	336.8	604.4	596.3	600.0
LPT inlet	205.9	238.1	227.1	510.4	527.0	540.1
PT inlet	132.7	146.9	148.9	436.9	453.0	480.4
PT outlet	114.8	118.9	116.6	408.7	428.4	447.5
RX inlet (LP)	112.0	118.3	115.8	402.0	429.8	447.5
RX outlet (LP)	113.9	117.5	115.3	176.1	112.3	135.9
PC inlet	116.7	117.2	115.0	172.3	112.3	135.9
PC outlet	112.6	116.7	114.6	22.8	15.6	15.2
ELC inlet	115.8	116.6	114.6	19.8	13.3	13.5
ELC outlet	132.2	140.0	140.5	43.5	39.5	39.8
ELHX gas inlet	122.4	133.7	129.1	45.4	39.8	39.8
ELHX gas outlet	121.2	132.4	128.1	19.8	13.7	13.5

Observed differences

The calculations with FLOWNEX and CATHARE compare reasonably, but there are important differences between measurements and calculations. The measurements in Tables 5.55 and 5.56 show that for both pressure levels, the gas leaving the HPC is reheated before entering the recuperator. The temperature increase is 42 and 44°C respectively.

We also note that the maximum pressure in the system downstream of the HPC is larger in the calculations than in the experiment. In the case of 95 kPa LPC suction pressure, the maximum pressure predicted by FLOWNEX is 8% higher than the measured value and for CATHARE; it is as much as 15% higher. In the high pressure case, the predicted values are higher by 7 and 14% respectively. Since the minimum circuit pressure is imposed (the LPC suction pressure), this suggests either that there are leakages in the experimental loop or that the turbomachine performance is overestimated in the simulations.

The differences between CATHARE and FLOWNEX, on the other hand, are probably due to the differences in how the turbomachines are modelled and possibly in how the performance data provided in the data pack is treated. Moreover, since the low-pressure point is imposed, an overestimation of the turbomachines performance will push the high pressure point up. This will automatically reinforce the tendency to generate too much power in the turbomachines (higher pressure on top means higher flow rate, more power in the heater, and more power to the compressors). Had we instead fixed the high pressure point, the impact of the turbomachine performance would be less visible. Another observation is that the efficiency of the recuperator is

overestimated in the CATHARE model, in comparison with both the experiments and FLOWNEX calculations.

In an attempt to quantify these differences in the simulations pending completion of further experimentation on the PBMM, it was postulated that heat is gained as nitrogen leaves the HPC and flows over the high temperature components, i.e. turbomachines, heater and recuperator. Subsequently, the recuperator high pressure side inlet temperature was fixed at 130°C for both CATHARE and FLOWNEX. The performance of the recuperator in the CATHARE model was also modified to be more in line with the experimental data. The results after these modifications are shown in Tables 5.57 and 5.58.

Steady state calculations with an imposed RX inlet temperature

Table 5.57 shows the CATHARE and FLOWNEX results for Steady State #1 (95 kPa) with the RX HP inlet temperature fixed at 130°C.

TABLE 5.57. STEADY STATE #1 (95 KPA) WITH IMPOSED RX (HP)
INLET TEMPERATURE — PRESSURES AND TEMPERATURES IN THE CIRCUIT

Component	Pressure [kPa]			Temperature [°C]		
	EXP	CAT	FNX	EXP	CAT	FNX
LPC inlet	94.1	94.7	93.4	21.5	15.9	15.8
IC inlet	147.9	169.6	159.8	80.7	83.5	79.1
HPC inlet	148.4	168.1	159.3	17.4	14.9	14.6
HPC outlet	259.9	296.7	278.9	82.5	79.4	79.7
RX inlet (HP)	255.0	298.7	278.0	126.7	130.0	130.0
RX outlet (HP)	254.2	298.7	276.4	345.4	385.9	408.0
HS inlet	N/A	298.5	276.4	N/A	385.9	408.0
HS outlet	N/A	298.4	276.3	N/A	600.1	600.0
HPT inlet	252.0	293.8	276.0	586.0	596.3	600.0
LPT inlet	171.3	194.9	186.3	511.8	527.4	540.3
PT inlet	111.8	121.0	122.7	433.0	454.3	481.2
PT outlet	94.2	98.3	96.4	408.7	430.3	448.9
RX inlet (LP)	91.4	97.9	95.8	400.2	431.7	448.9
RX outlet (LP)	93.5	97.1	95.3	167.3	175.8	172.8
PC inlet	96.6	96.8	95.0	164.3	175.8	172.8
PC outlet	92.5	96.4	94.7	18.9	16.4	15.8
ELC inlet	95.5	96.3	94.7	16.6	13.1	13.4
ELC outlet	109.5	115.2	115.9	40.5	38.8	39.5
ELHX gas inlet	100.8	110.1	106.6	42.6	39.2	39.5
ELHX gas outlet	99.4	109.1	105.7	16.3	13.6	13.4

Table 5.58 shows the CATHARE and FLOWNEX results for Steady State #2 (115 kPa) with the RX HP inlet temperature fixed at 130°C.

TABLE 5.58. STEADY STATE #2 (115 KPA) WITH IMPOSED RX (HP)
INLET TEMPERATURE — PRESSURES AND TEMPERATURES IN THE CIRCUIT

Component	Pressure [kPa]			Temperature [°C]		
	EXP	CAT	FNX	EXP	CAT	FNX
LPC inlet	114.1	114.7	113.1	24.7	16.6	16.0
IC inlet	179.2	205.3	197.4	84.2	84.4	81.8
HPC inlet	179.4	203.5	196.8	20.9	15.3	15.0
HPC outlet	310.7	359.2	341.9	85.8	79.9	79.2
RX inlet (HP)	306.6	361.7	340.9	129.5	130.0	130.0
RX outlet (HP)	305.8	361.7	339.0	349.8	383.3	400.6
HS inlet	N/A	361.4	339.0	N/A	383.3	400.6
HS outlet	N/A	361.3	338.8	N/A	600.1	600.0
HPT inlet	302.7	355.8	338.5	604.4	596.3	600.0
LPT inlet	205.9	236.0	229.7	510.4	527.3	541.0
PT inlet	132.7	146.4	149.0	436.9	454.2	479.6
PT outlet	114.8	118.9	116.7	408.7	430.1	446.8
RX inlet (LP)	112.0	118.4	115.9	402.0	431.5	446.8
RX outlet (LP)	113.9	117.6	115.4	176.1	178.2	178.3
PC inlet	116.7	117.2	115.0	172.3	178.2	178.3
PC outlet	112.6	116.7	114.6	22.8	17.1	16.0
ELC inlet	115.8	116.5	114.6	19.8	13.3	13.5
ELC outlet	132.2	139.4	140.7	43.5	39.0	40.1
ELHX gas inlet	122.4	133.3	129.2	45.4	39.3	40.1
ELHX gas outlet	121.2	132.1	128.2	19.8	13.7	13.5

For the cases where the RX HP inlet temperature is fixed for the simulations, FLOWNEX and CATHARE compare marginally better than in the previous case. In the CATHARE calculation, the modified RX performance (decreased) is compensated by a higher power in the heater. Differences in the maximum pressure level and in the turbomachine powers persist.

Transient results

Load-following transient

The FLOWNEX and CATHARE results for different plant parameters for the load-following transient are shown in the next few figures. Figure 5.69 shows the suction pressure for the LPC during the injection transient at the LPC suction point. It is clear that the two codes compare very well. Figure 5.70 shows the power and speed of the power turbine in the two simulations.

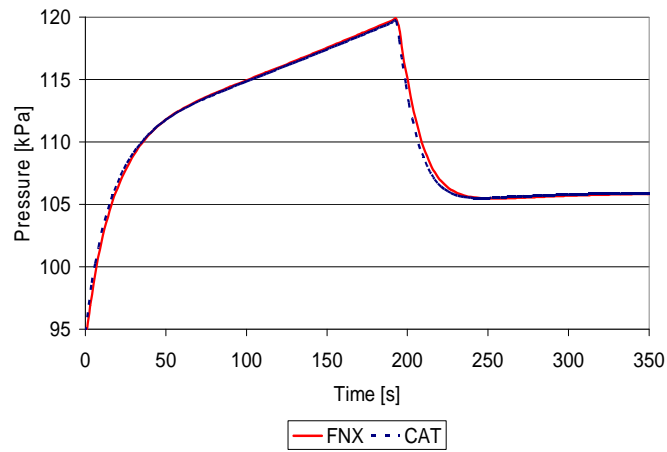


FIG. 5.69. TR1: LPC Suction pressure.

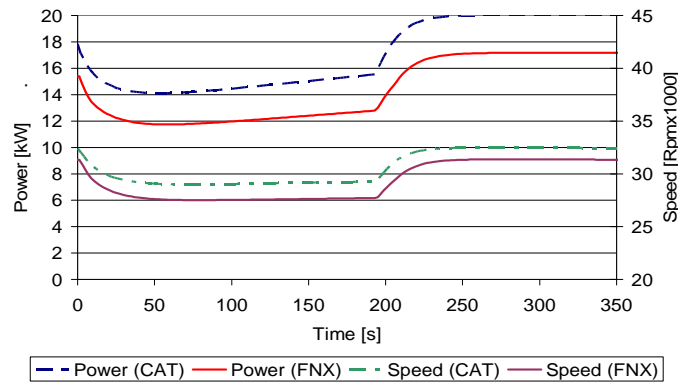


FIG. 5.70. TR1: Power turbine power and speed.

FIG. 5.71 shows the comparison between CATHARE and FLOWNEX for temperature and pressure at the recuperator high pressure inlet. The pressures and temperature are within 6% and 2% from each other respectively. Figure 5.72 shows the heat loads of the recuperator and intercooler. The results of the two codes compare very well.

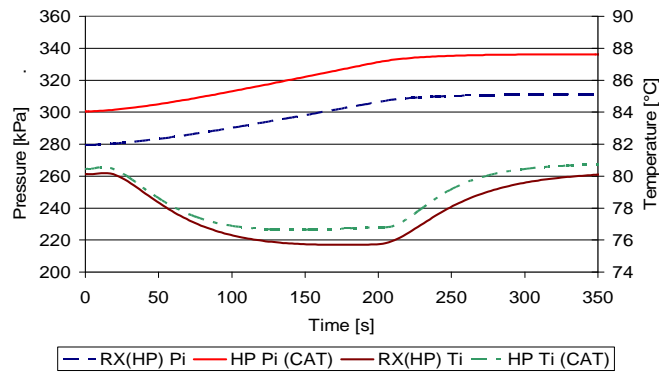


FIG. 5.71. TR1: Recuperator high pressure side.

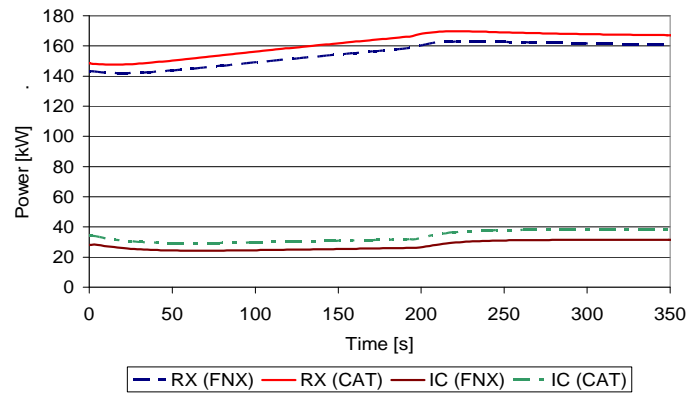


FIG. 5.72. TR1: RX and IC power.

Load rejection transient

In the definition of the benchmark, the transient is supposed to start at the end of transient 1, with 120 kPa at the LPC inlet. This is not consistent with the calculation results (LPC pressure = 104 kPa). This transient starts from a separately calculated steady state at 120 kPa at the LPC inlet. The bypass valve is opened at 20%. The flow observed in the bypass valve is sonic and equal to 0.2 kg/s. The TM quickly stops at 22 s. It is difficult to analyse where it originates. Its origin is probably the consequence of a very high bypass flow.

To conclude on this calculation:

- It is needed to have a clearer GBP valve;
- Beware sonic conditions elsewhere. In the experiment, the flow could be sonic in the T-junctions earlier, thus limiting the bypass flow at a much lower value. This could be difficult to handle with a numerical model.

Another problem lies in the fact that we quickly leave the TM performance map provided.

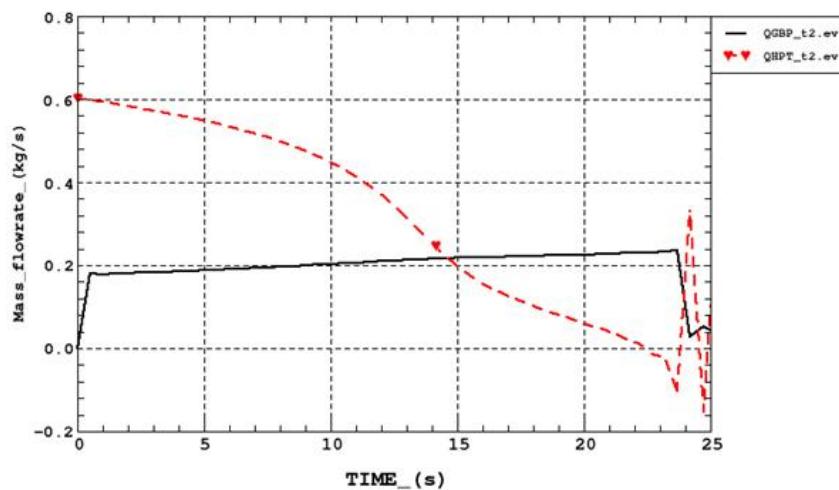


FIG. 5.73. Mass flow rates. HPT in red, bypass line in black.

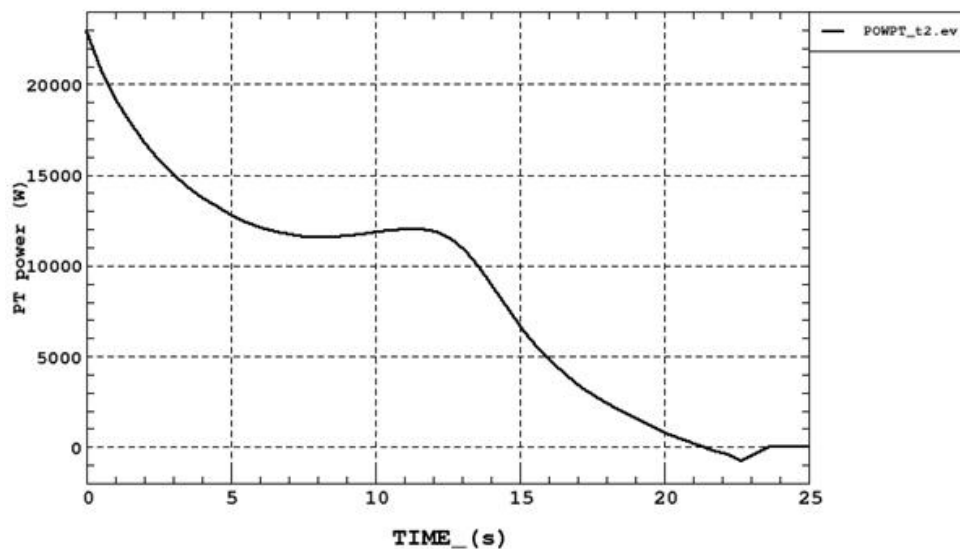


FIG. 5.74. PT power (W).

Opening of compressor bypass valve

No calculation has been performed. The following additional information was needed to perform the calculation:

- The length and dimensions of the compressor bypass lines;
- The size of the valves in question.

Conclusions for the second series of calculations

Similar conclusions as for the first series can be drawn. No particular difficulties have yet to be encountered. The calculations run smoothly and the system as a whole appears to be robust under the present circumstances.

Overall, the two codes agree quite well. However, there are some discrepancies that warrant further investigation. It is believed that the main reason for the discrepancies is the manner in which the turbine input data was treated by the two teams.

5.4.5.6. Third series of calculations

Those calculations refer to documents [5-17] and the results of those calculations are analysed in Section 7.4.

5.5. REFERENCES FOR CHAPTER 5

- [5-1] LABUSCHAGNE, J.T., 'PBMR Micro Model Data Pack, Document Number PBMM-0066, Rev. 2', Faculty of Engineering, Potchefstroom University, South Africa (2003).
- [5-2] VAN NIEKERK, W.M.K., GREYVENSTEIN, G.P., VAN RAVENSWAAY, J., LABUSCHAGNE, J.T., SWIFT, W.J., 'A comparison of the thermal fluid analysis code FLOWNEX with experimental data from the Pebble Bed Micro Model Proceedings' HTR2006: 3rd International Topical Meeting on High Temperature Reactor Technology, Johannesburg, South Africa (2006).
- [5-3] WANG, C., BALL, S., 'CRP-5 Benchmark: PBMM – PBMR Micro Model', Oak Ridge National Laboratory, Oak Ridge, TN United States of America (2005).
- [5-4] THE AEGIS TECHNOLOGIES GROUP, Inc., <http://www.aegisxcellon.com>.

- [5-5] BALL, S.J., 'Initial Simulation and Control System Studies of the MIUS Coal-fired Turbine Experiment', Oak Ridge National Laboratory, TN United States of America (1978).
- [5-6] CONSIDINE, D.M., 'Process Instrument and Controls Handbook', McGraw-Hill Book Co., New York (1957).
- [5-7] KATAMISHI, S., HAKAGAWA, S., 'JAEA Calculation of PBMM Benchmark Problem', Japan Atomic Energy Agency, Oarai, Japan (2006).
- [5-8] INTERNATIONAL ATOMIC ENERGY AGENCY, '5.1 MICRO-MODEL (PBMM)', 6TH Research Coordination Meeting of Evaluation of HTGR Performance, Vienna (September 2005).
- [5-9] JSME Data Book: Heat Transfer, 3rd edition, The Japan Society of Mechanical Engineers (1983).
- [5-10] LEE, W.J., et al., 'Development of MARS-GCR/V1 and its Application to Thermo-Fluid Safety Analysis of Gas cooled Reactors', ICAPP'05 Paper 5231, Seoul, Republic of Korea (2005).
- [5-11] NIST Standard Reference Database 12, NIST Thermodynamics and Transport Properties of Pure Fluids — NIST Pure Fluids, Version 5.0 (2000).
- [5-12] MARS Code Manual Volume I: Code Structure, System Models, and Solution Methods, KAERI/TR-2812/2004, Korea Atomic Energy Research Institute (2004).
- [5-13] BAE, S.W., et al., Development of Circulator Component in MARS-GCR for Gas Cooled Reactor System, Proc. KNS Autumn meeting (2005).
- [5-14] PEBBLE BED MICRO-MODEL, PBMM steady state problem statement (2004).
- [5-15] PEBBLE BED MICRO-MODEL, Problem statement: PBMM refined benchmarks 2005 (2005).
- [5-16] WIDLUND, O., VAN RAVENSWAAY, J., GEFFRAYE, G. VAN NIEKERK, W., 'Comparison of the Thermal-hydraulic Analysis Codes CATHARE and FLOWNEX with Experimental Data from PBMM', HEFAT2005 International Conference, Cairo, Egypt (2005).
- [5-17] Personal correspondences from VAN NIEKERK, W.,: 'PBMM benchmark 1 of 3 'Boundcodetocode' and 'PBMM benchmark 2 of 3' and 'Report on the code to plant comparison of the test runs performed on the PBMM 31 August, 2005 (2006).
- [5-18] BESTION, D., BARRE, F., FAYDIDE, B., 'Methodology, status and plans for development and assessment of CATHARE code', Proceedings of the International Conference of OECD/CSNI. Annapolis, United States of America (1999).
- [5-19] TAUVERON, N., SAEZ, M., MARCHAND, M., CHATAING, T., GEFFRAYE, G., CHEREL, J.M., 'Steady-state and transient simulations of gas cooled reactor with the computer code CATHARE', 10th International Topical Meeting on Nuclear Reactor Thermal Hydraulics (NURETH-10) Seoul, Republic of Korea (2003).

6. GAS TURBINE-MODULAR HELIUM REACTOR (GT-MHR)

6.1. GT-MHR GENERAL INFORMATION

Direct coupling of a gas turbine to a HTGR is unique in its use of the Brayton cycle to achieve a net electrical efficiency in the range of 47% combined with the attendant features of low initial capital costs due to plant simplification, public acceptance resulting from the safety attributes of the HTGR, and a reduction in radioactive wastes [6-1].

The gas turbine-modular helium reactor (GT-MHR) is one of the most significant HTGR gas turbine plant designs currently under investigation in the world. The GT-MHR is being developed on an international basis to optimize the HTGR capabilities and resources of many countries. The sponsoring organizations in the conceptual design of this plant include the Agency of Atomic Energy of Russia, the US Department of Energy (DOE), GA and ORNL from the United States of America, Framatome of France and Fuji Electric of Japan. In 1999, the DOE initiated support for the GT-MHR to dispose of weapons plutonium with a Russian contribution of matching funds [6-2].

Technological developments during the past two decades are providing key elements for obtaining this new source for electric production and different technologies using high temperature heat. These include:

The HTGR reactor size had been reduced by developing the passively safe module design. At the same time, the size of industrial gas turbines had increased. The technology was now available for a single turbo-machine to accommodate the heat energy from a single HTGR module;

Highly effective compact recuperators had been developed. The recuperator size and capital equipment costs are key economic considerations. Highly effective plate fin recuperators are much smaller than equivalent tube and shell heat exchangers, provide for substantially less complexity and capital cost, and are a key requirement for achieving high plant efficiency;

The technology for large magnetic bearings had been developed. The use of oil-lubricated bearings for the turbomachine with the reactor coolant directly driving the turbine is problematic with regard to potential coolant contamination by the oil. The availability of magnetic bearings eliminates this potential problem [6-3].

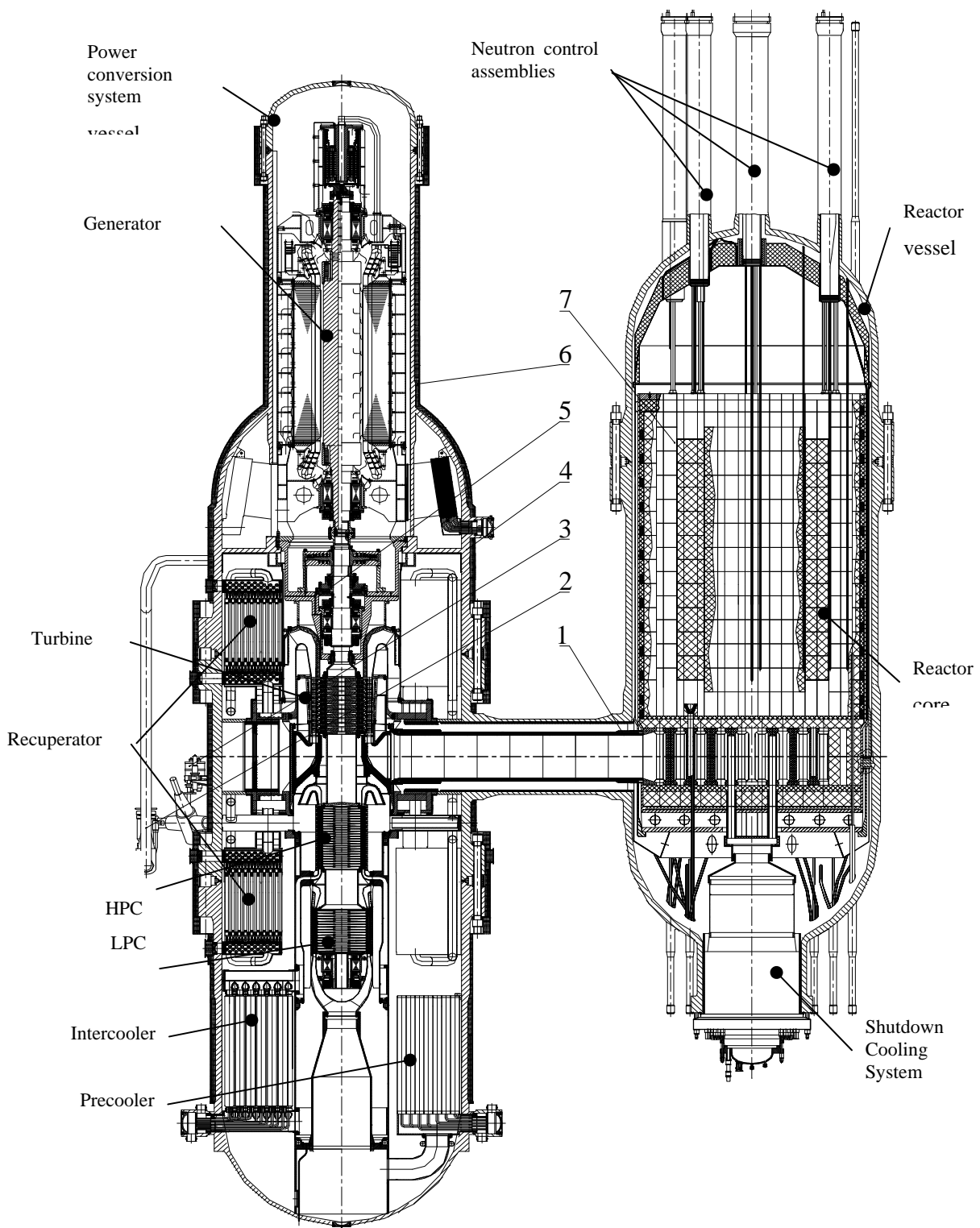
In addition, a major requirement was for the plant to be substantially simplified in order to provide a large reduction in the capital expenditure for new capacity additions.

6.1.1. Facility description

6.1.1.1. GT-MHR module description

The summary provided here was taken from Ref. [6-2].

The GT-MHR includes the nuclear heat source (i.e. the reactor system) and PCS consisting of equipment needed for electric power generation (turbocompressor, recuperator, generator, precooler, intercooler and connecting pipelines). The components of the reactor and PCS are located in separate vertical steel vessels interconnected by the horizontal cross-vessel as shown in Fig. 6.1.



1 — hot duct; 2 — assembly of locking and regulating fittings and bypass piping; 3 — safety unit; 4 — vessels unit; 5 — power conversion system; 6 — heat insulation of vessels unit; 7 — reactor.

FIG. 6.1. GT-MHR module arrangement.

Helium is the primary coolant and is circulated in the following manner:

The high pressure helium from the reactor upper collector plenum enters the reactor and is heated up as it passes through the core. The hot helium accumulates in the core lower collector plenum and flows

through the inner concentric hot duct in the cross-vessel to supply the PCS turbine. Helium enters the turbine at 850°C and 7.1 MPa. After expansion in the turbine, the helium at 510°C and 2.64 MPa is directed to the recuperator, where it flows through the hot side of twenty parallel heat exchange modules and heats the helium flowing back to the reactor along the cold side of the recuperator. The helium is cooled by heat exchange in the recuperator to the temperature of 125°C and then enters the precooler where it is cooled to 26°C.

Downstream of the precooler, the cold helium is compressed from 2.57 MPa to 7.24 MPa in two successive stages (low- and high pressure compressors). An intercooler between the compressors cools the helium to 27°C prior to entering the HPC unit. Downstream of the HPC, helium goes through the recuperator (along its cold side) where it is heated to 490°C and then collects in the PCS annular outlet chamber where it subsequently flows back to the reactor vessel through the annulus between the cross-vessel and hot duct. Within the reactor vessel, helium moves upward to the upper collector plenum through flow channels outside the core barrel.

6.1.1.2. General description of the GT-MHR reactor design

The GT-MHR reactor core (Fig. 6.2) represents an annular stack of hexahedral prismatic fuel assemblies with a distance of 36 cm across its flat sides (Fig. 6.3(a)), which form 102 columns of 800 cm height consisting of 10 Fuel Assemblies (FAs) stacked axially in each of these columns. Fuel assemblies can differ from each other by fuel composition because of different fuel burnup and the reloading scheme. Fuel assembly reloadings are organized in such a way that all fuel assemblies belonging to the same layer within the core height have the same fuel composition (i.e. burnup level).

There is an eccentrically located 13 cm diameter hole for control rods (Fig. 6.3(b)) in 12 fuel assemblies. In other 18 columns, there is a similar hole for the travelling RSS consisting of absorber elements on the basis of boron carbide. The fuel assembly columns are arranged with 0.25 cm gap to ensure performance of fuel assembly reloads during the reactor core life.

The active core is enclosed by graphite reflectors (Fig. 6.2). The core is surrounded by a Radial Reflector (RR) with the core internal surface contiguous with the Internal Reflector (IR). The Upper Axial Reflector (UAR) and Lower Axial Reflector (LAR) are located above and beneath the core respectively.

The reflectors are assembled from graphite blocks (GBs). As a rule, the graphite blocks have a hexahedron prismatic shape, similar to that of fuel assemblies. An exception to this is the graphite blocks of the radial reflector outer layer, which have a special shape to ensure the cylindrical form of the radial reflector outer surface. The graphite has a density of $\gamma = 1.74 \text{ g/cm}^3$. Impurities in graphite are accounted by means of equivalent (on neutrons absorbing) natural boron content (boron equivalent) of 1.1 ppm.

The radial reflector represents a stack of graphite blocks columns, which are arranged with 0.25 cm gap. The overall height of the columns equals 1060 cm with the height of a lower reflector graphite block being 50 cm. The outer diameter is 684 cm. For those graphite blocks that form the radial reflector columns contiguous with the core (36 columns), there is an eccentrically located hole of 13 cm diameter for the control rod.

The internal reflector represents a stack of columns of hexahedral prismatic graphite blocks which are arranged with a gap of 0.25 cm. The columns' height is 1060 cm. The internal reflector elements are located in the internal reflector columns contiguous with the core and within the core height limits to reduce non-uniformity of heat release in the core nearby the internal reflector.

The UAR is 130 cm high and consists of stacks of columns assembled from hexahedral prismatic graphite blocks. These are located above the core and are separated by a gap of 0.25 cm. In compliance with the core design, there is an eccentrically located hole of 13 cm diameter in 12 columns of the UAR to accommodate control rods. The other 18 columns include a similar hole for accommodating the RSS absorber elements.

The LAR is 130 cm high and consists of stacks of columns assembled from hexahedral prismatic graphite blocks. These are located under the core and are separated by a gap of 0.25 cm. In 12 of

the core columns and 24 of the side reflector ones, there is an eccentrically located hole of 13 cm diameter and 20 cm height to accommodate the control rods.

The main characteristics of the reactor active core are presented in Table 6.1.

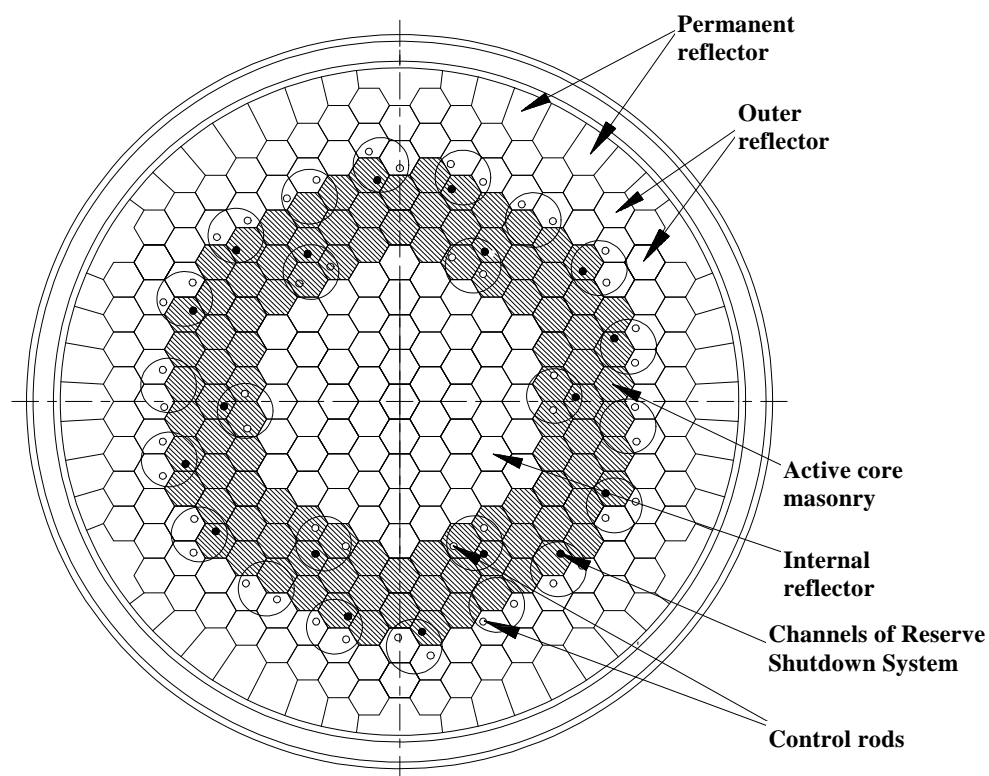


FIG. 6.2. Active core and its components arrangement.

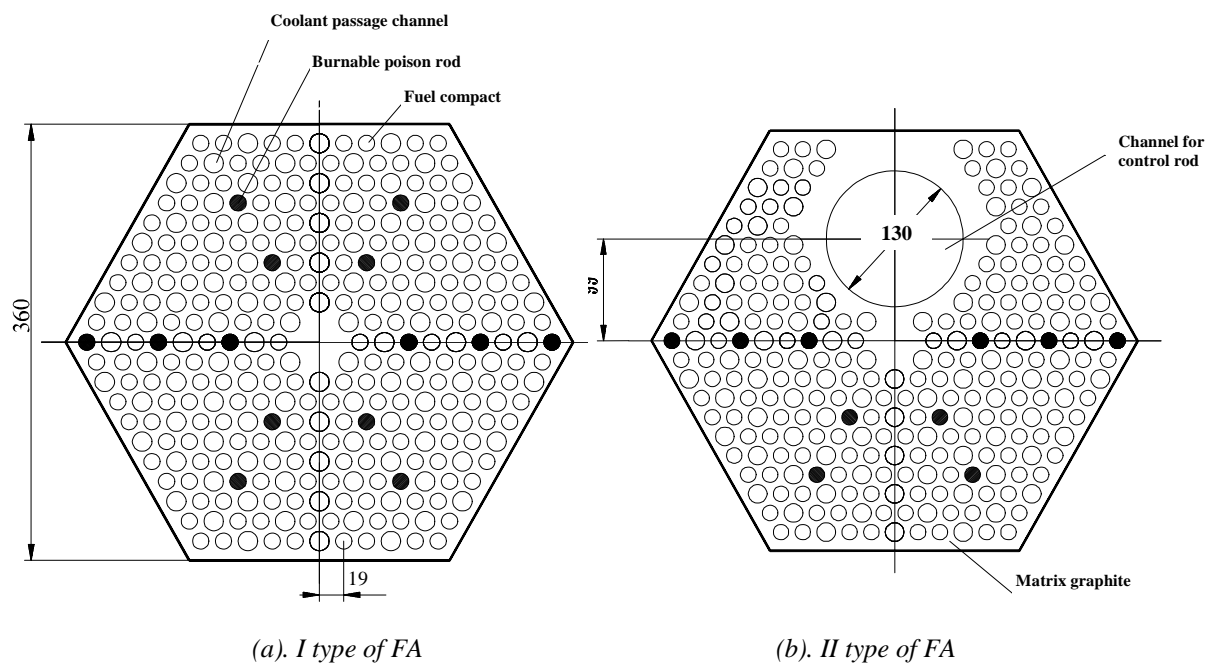


FIG. 6.3. Fuel blocks.

TABLE 6.1. REACTOR CORE MAIN CHARACTERISTICS

Parameter	Value
Full thermal reactor power, MW	600
Inlet helium temperature, °C	490
Outlet helium temperature, °C	850
Core geometric parameters:	
- equivalent core diameter, inside/outside, m	2.96/4.84
- core height, m	8.0
- inside reflector diameter, m	7.0
- axial reflector thickness, m	0.8
Average specific power, MW/m ³	6.5
Number of fuel blocks	1020
geometric parameters of prismatic fuel blocks:	
- height, m	0.8
- width, m	0.36
- number of fuel compacts per fuel block (average)	2862
- number of Er ₂ O ₃ compacts per fuel block (average)	192
Fuel compact parameters, erbium compact parameters:	
- diameter, mm	12.5
- height, mm	50.0
Plutonium load per compact, g	~ 0.24
Er (nat) load per compact, g	2.1
Coated particles parameters, µm/-/g/cm ³ :	
- kernel diameter /material/density	200/PuO _{1.8} /10.0
- 1st layer thickness/material/density	100/PyC/1.0
- 2nd layer thickness/material/density	35/PyC/1.8
- 3rd layer thickness/material/density	35/SiC/3.2
- 4th layer thickness/material/density	40/PyC/1.8
Diameter of coolant channel, mm	16.0
Number of reactivity control rods:	
- in-core	12
- in side reflector	36
Number of reserve shutdown system channels	18
Refuelling ratio	3
Core fuel load, kg :	
- initial	701
- in each reloading	234

The diagram in Fig. 6.4 shows the content of fuel composition at the beginning and at the end of partial fuel cycles in the equilibrium mode of reactor operation. The nomenclature 0 refers to ‘fresh poisoned’ fuel, 1/3 refers to fuel burnt by one-third, 2/3 refers to fuel burnt by two-thirds, and 3/3 refers to spent fuel (burnup value for discharged fuel is 720 MW·days/kgHM).

Variant		Number of layer through the core height										
		1	2	3	4	5	6	7	8	9	10	
1	1-st	2/3	0	2/3	0	1/3	1/3	0	2/3	0	2/3	
2	→ cycle	(3/3)	1/3	(3/3)	1/3	2/3	2/3	1/3	(3/3)	1/3	(3/3)	before → refueling
3	2-nd	2/3	0	1/3	0	1/3	1/3	0	1/3	0	2/3	
4	→ cycle	(3/3)	1/3	2/3	1/3	2/3	2/3	1/3	2/3	1/3	(3/3)	before → refueling
5	3-rd	2/3	0	2/3	1/3	1/3	1/3	1/3	2/3	0	2/3	
6	→ cycle	(3/3)	1/3	(3/3)	2/3	2/3	2/3	2/3	(3/3)	1/3	(3/3)	before → refueling

FIG. 6.4. Reloading scheme in the equilibrium fuel cycle.

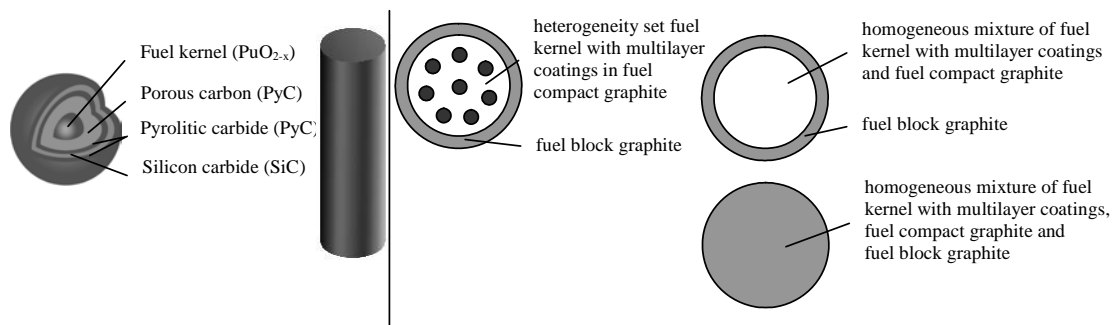
6.2. GT-MHR PLUTONIUM FUEL BENCHMARK PROBLEM DEFINITION

6.2.1. The GT-MHR benchmark — Investigation of elementary cells

6.2.1.1. Sketch of calculational models

The developed calculational models are schematically presented in Fig. 6.5.

The first stage: fuel compact cell with/without taking into account heterogeneity of fuel particle arrangement.



The second stage: burnable poison cell with/without taking into account heterogeneity of burnable poison particle arrangement.

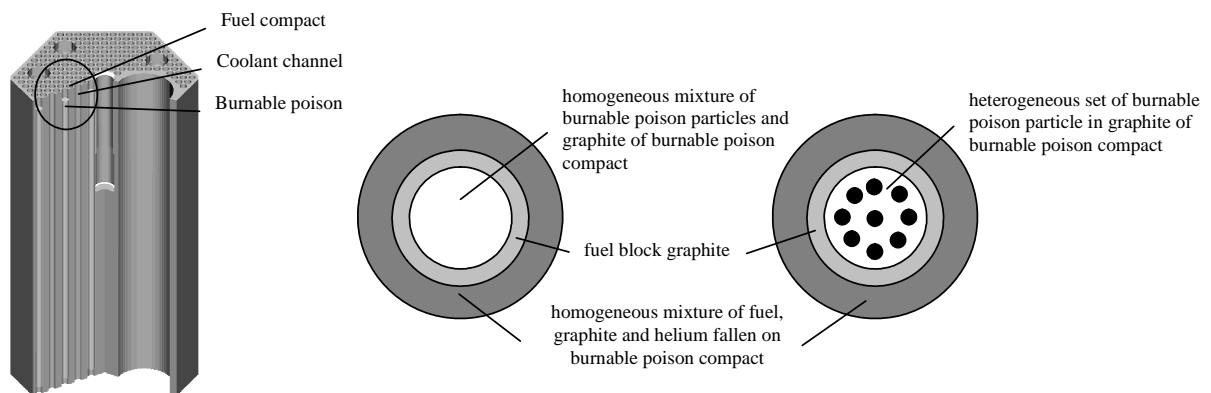


FIG. 6.5. Calculation models of stepwise benchmark — Investigation of the GT-MHR reactor.

6.2.1.2. Fuel compact cell

Description

The basic object is an infinite high equivalent cylindrical cell of the Fuel Compact Cell (FCC), namely, inner zone (fuel compact) and external zone (graphite of block). The fuel compact is an infinite high cylinder consisting from the graphite matrix of the fuel compact in which coated fuel microparticles (CP) are uniformly located (but the law of locations is not defined explicitly). Each microparticle consists of a fuel kernel ($\text{PuO}_{1.7}$) and a four-layer coating. There are 1039.975 microparticles per 1 cm^3 of the fuel compact (Table 6.2).

Temperatures of all materials are assumed to be the same. The calculational cases for all types of the fuel compact cell are designated as FCC-TI, FCC2-TI and FCC1-TI, where I is the temperature in K, for example, FCC-T300. It is proposed to calculate these cases at temperatures 300, 600, 900 and 1200 K. These variants are presented in Table 6.3.

TABLE 6.2. GEOMETRICAL AND MATERIAL PARAMETERS OF THE HETEROGENEOUS FCC

Zone	Name	Composition	Material	External Radius (cm)	Isotopes	Nuclear Density (barn·cm) ⁻¹	
Internal	Fuel compact	Spherical Zones of Microparticle					
		1040 (1039.975) spherical microparticles in 1 cm ³ of the graphite matrix of a fuel compact	1	kernel PuO _{1.7}	0.01	Pu-238	2.95284E-05
						Pu-239	2.07460E-02
						Pu-240	1.47535E-03
						Pu-241	2.62440E-04
						Pu-242	9.60531E-05
						O-16	3.84360E-02
			2	BPyC	0.02	C-12	5.01377E-02
			3	IPyC	0.0235	C-12	9.02479E-02
			4	SiC	0.027	C-12	4.80604E-02
						Si-29	4.80604E-02
			5	OPyC	0.031	C-12	9.02479E-02
Fuel Compact							
	graphite matrix of a fuel compact	graphite	0.625	C-12	8.52342E-02		
				B-10	2.07287E-08		
				B-11	8.34356E-08		
	graphite of fuel block	graphite	9.97571E-01	C-12	8.67383E-02		
				B-10	2.10945E-08		
				B-11	8.49079E-08		

TABLE 6.3. CALCULATIONAL CASES (EXAMPLE FOR FCC)

Name	Temperature of all Materials (K)
FCC-T300	300
FCC-T600	600
FCC-T900	900
FCC-T1200	1200

On the basis of the geometrical and material parameters of the fuel compact heterogeneous cell presented in Table 6.2, the following two supplementary simplified variants are derived. Both of them are infinite (in height) cylindrical cells:

- Two-zone fuel compact cell with homogenized internal zone (see Table 6.4). There are smeared densities over the volume of the fuel compact in the internal zone (up to boundary of 0.625 cm); the second (external) zone is similar to the external zone of the fuel compact heterogeneous cell (cylinder of 9.97571E-01 cm). Calculational cases for this cell are designated as FCC2-TI, where '2' is the index determining the two-zone fuel compact cell with the homogenized internal zone.
- One-zone cylindrical fully homogeneous fuel compact cell (see Table 6.5). There are smeared densities over the whole volume of the fuel compact (up to boundary of 9.97571E-01 cm). Calculational cases for this cell are designated as FCC1-TI, where '1' is the index-determining one-zone fuel compact cell.

The results are to be presented in Form 1 (see Table 6.6). R refers to the reaction rates for each of the isotopes and indicated reaction while '1PE11.4' refers to the required format (FORTRAN notation) and significant number of decimals.

TABLE 6.4. GEOMETRICAL AND MATERIAL PARAMETERS OF THE TWO-ZONE FUEL COMPACT CELL (FCC2)

Zone	Name	External radius (cm)	Isotopes	Nuclear density (barn·cm) ⁻¹
Internal	Homogeneous mixture of all isotopes of the fuel compact	0.625	Pu-238	1.28633E-07
			Pu-239	9.03745E-05
			Pu-240	6.42698E-06
			Pu-241	1.14325E-06
			Pu-242	4.18430E-07
			O-16	1.67436E-04
			C-12	8.30389E-02
			Si-29	1.40380E-03
			B-10	1.80279E-08
			B-11	7.25645E-08
External	Graphite of fuel block	9.97571E-01	C-12	8.67383E-02
			B-10	2.10945E-08
			B-11	8.49079E-08

TABLE 6.5. GEOMETRICAL AND MATERIAL PARAMETERS OF THE ONE-ZONE FUEL COMPACT CELL (FCC1)

Name	External radius (cm)	Isotopes	Nuclear density (barn·cm) ⁻¹
Homogeneous mixture of all isotopes of the fuel compact cell	9.97571E-01	Pu-238	5.04922E-08
		Pu-239	3.54747E-05
		Pu-240	2.52278E-06
		Pu-241	4.48760E-07
		Pu-242	1.64246E-07
		O-16	6.57237E-05
		C-12	8.52862E-02
		Si-29	5.51034E-04
		B-10	1.98908E-08
		B-11	8.00628E-08

TABLE 6.6. PRESENTATION OF THE RESULTS FOR INDIVIDUAL CODE —
EXAMPLE FOR FCC (FORM 1) *

Case	Code Name				
FCC-T300	$k_{inf} = 1PF11.4$				
	Isotope	R_{abs}	R_{fis}	Rv_{fis}	v
	Pu-238	1PE11.4	1PE11.4	1PE11.4	1PF11.4
	Pu-239	1PE11.4	1PE11.4	1PE11.4	1PF11.4
	Pu-240	1PE11.4	1PE11.4	1PE11.4	1PF11.4
	Pu-241	1PE11.4	1PE11.4	1PE11.4	1PF11.4
	Pu-242	1PE11.4	1PE11.4	1PE11.4	1PF11.4
	O-16	1PE11.4	1PE11.4	1PE11.4	1PF11.4
	C-12	1PE11.4	1PE11.4	1PE11.4	1PF11.4
	Si-29	1PE11.4	1PE11.4	1PE11.4	1PF11.4
	B-10	1PE11.4	1PE11.4	1PE11.4	1PF11.4
	B-11	1PE11.4	1PE11.4	1PE11.4	1PF11.4
	B-10 + B-11	1PE11.4	1PE11.4	1PE11.4	1PF11.4
	Sum	1PE11.4	1PE11.4	1PE11.4	

Calculations with burnup

Burnup calculations are conducted only for the infinite height fuel compact cell in the spectrum of the infinite lattice. Boron isotopes (^{10}B and ^{11}B) representing the equivalent impurities in graphite do not deplete.

A burnup calculation is performed with the same temperature for all materials (1200 K) and constant power density $W = 856.282 \text{ MW}/t_{\text{HM}}$, where t_{HM} is the amount of tons of heavy metals in the initial loading (equivalent value is also $13.1468 \text{ W}/\text{cm}^3$). Detailed information for the following five burnup points is requested: 0, 5, 250, 500 and 750 Effective Full Power Days (EFPD). Note that 1 EFPD is equivalent to the following burnup values: $856.282 \text{ MW} \cdot \text{d}/t_{\text{HM}}$ or $13.1468 \text{ W} \cdot \text{d}/\text{cm}^3$.

The proposed form of results presentation for an individual code (Form 2) is similar to Form 1 (see Table 6.7). It combines results for all burnup states. In comparison with Form 1, there are additional isotopes, which are: ^{241}Am , $^{242\text{m}}\text{Am}$, ^{243}Am , ^{242}Cm , ^{243}Cm , ^{244}Cm , ^{245}Cm , ^{246}Cm , ^{247}Cm , ^{248}Cm , ^{249}Bk , ^{249}Cf , ^{250}Cf , ^{251}Cf and ^{252}Cf . Important fission products (^{135}Xe and ^{149}Sm) are also treated explicitly, but all other isotopes (e.g. equivalent fission product + the rest of isotopes tracked in depletion chains of the individual code) are separated in a special cell named ‘All other isotopes’.

TABLE 6.7. PRESENTATION OF THE RESULTS FOR INDIVIDUAL CODE
IN DIFFERENT BURNUP STEPS (FORM 2) **

Case	Burnup (EFPD)	Code Name				
FCC- T1200	5.0	$k_{inf} = 1PF11.4$				
		Isotope	Nuclear Density * $10^{-24}/cm^3$	R_{abs}	R_{fis}	Rv_{fis}
		v				
		Pu-238	1PE11.4	1PE11.4	1PE11.4	1PE11.4
		Pu-239	1PE11.4	1PE11.4	1PE11.4	1PE11.4
		Pu-240	1PE11.4	1PE11.4	1PE11.4	1PE11.4
		Pu-241	1PE11.4	1PE11.4	1PE11.4	1PE11.4
		Pu-242	1PE11.4	1PE11.4	1PE11.4	1PE11.4
		Am-241	1PE11.4	1PE11.4	1PE11.4	1PE11.4
		Am-242	1PE11.4	1PE11.4	1PE11.4	1PE11.4
		Am-243	1PE11.4	1PE11.4	1PE11.4	1PE11.4
		Cm-242	1PE11.4	1PE11.4	1PE11.4	1PE11.4
		Cm-243	1PE11.4	1PE11.4	1PE11.4	1PE11.4
		Cm-244	1PE11.4	1PE11.4	1PE11.4	1PE11.4
		Cm-245	1PE11.4	1PE11.4	1PE11.4	1PE11.4
		Cm-246	1PE11.4	1PE11.4	1PE11.4	1PE11.4
		Cm-247	1PE11.4	1PE11.4	1PE11.4	1PE11.4
		Cm-248	1PE11.4	1PE11.4	1PE11.4	1PE11.4
		Bk-249	1PE11.4	1PE11.4	1PE11.4	1PE11.4
		Cf-249	1PE11.4	1PE11.4	1PE11.4	1PE11.4
		Cf-250	1PE11.4	1PE11.4	1PE11.4	1PE11.4
		Cf-251	1PE11.4	1PE11.4	1PE11.4	1PE11.4
		Cf-252	1PE11.4	1PE11.4	1PE11.4	1PE11.4
		Xe-135	1PE11.4	1PE11.4	1PE11.4	1PE11.4
		Sm-149	1PE11.4	1PE11.4	1PE11.4	1PE11.4
		O-16	1PE11.4	1PE11.4	1PE11.4	1PE11.4
		C-12	1PE11.4	1PE11.4	1PE11.4	1PE11.4
		Si-29	1PE11.4	1PE11.4	1PE11.4	1PE11.4
		B-10	1PE11.4	1PE11.4	1PE11.4	1PE11.4
		B-11	1PE11.4	1PE11.4	1PE11.4	1PE11.4
		B-10 + B-11	1PE11.4	1PE11.4	1PE11.4	1PE11.4
		All other isotopes	1PE11.4	1PE11.4	1PE11.4	1PE11.4
		Sum		1PE11.4	1PE11.4	1PE11.4

6.2.1.3. Burnable poison cell description

Two burnable poison cells were developed to the benchmark calculations:

- **Option 1:** The Burnable Poison Cell (BPC) is an infinite (in height) three-zone cylinder cell. The Internal zone (the first zone) is the homogeneous presentation of burnable poison compact including burnable poison (Er_2O_3) and the graphite of the compact, the intermediate zone (the second zone) is the graphite of the fuel block with $\gamma = 1.73 \text{ g/cm}^3$ and the external zone (the third zone) is the homogeneous mixture of fuel, graphite of block and helium. Nuclear densities for the third zone are calculated taking into account the amount of isotopes per one burnable poison compact in a fuel block. Detailed information for the burnable poison cell is presented in Table 6.8.
- **Option 2:** The Burnable Poison Cell (BPC_het) is an infinite (in height) three-zone cylinder cell with heterogeneous setting of Er_2O_3 particles. Internal zone (the first zone) is the heterogeneous presentation of burnable poison (Er_2O_3) particles in the graphite of compact, the intermediate zone (the second zone) is the graphite of the fuel block with $\gamma = 1.73 \text{ g/cm}^3$ and the external zone (the third zone) is the homogeneous mixture of fuel, The graphite of the block and helium. Nuclear densities for the third zone are calculated taking into account the amount of isotopes per one burnable poison compact in a fuel block. The burnable poison compact is presented as an infinite (in height) cylinder consisting of graphite matrix of burnable poison compact where Er_2O_3 spherical particles of 500 μm diameter without coatings are uniformly distributed (the law of locations is not defined explicitly). There are 692 (692.0322) Er_2O_3 microparticles per 1 cm^3 of the burnable poison compact. Detailed information for the burnable poison cell is presented in Table 6.9.

Calculational investigation

The calculations of burnable poison cell burnup are conducted in the spectrum of an infinite lattice (searching for k_{∞} , no leakage model was applied to avoid discrepancies caused by different treatment of leakage in different codes). The burning of both fuel isotopes and poison (erbium) isotopes is modelled. Depletion of boron isotopes representing the equivalent impurities in graphite is not modelled.

Burnup is performed with the same temperature (1200 K) for all materials and constant power density $W = 856.282 \text{ MW/t}_{\text{HM}}$, where t_{HM} is the amount of tons of heavy metals in initial loading (equivalent value is also 7.3973 W/cm^3). The information for the following five burnup points is requested: 0, 5, 250, 500 and 750 EFPD. Note that 1 EFPD is equivalent to the following burnup values: $856.282 \text{ MW}\cdot\text{d/t}_{\text{HM}}$ or $7.3973 \text{ W}\cdot\text{d/cm}^3$.

A form to present calculational results for both BPC and BPC_het at all burnup points is Form 3 (Table 6.10).

The dependence of k_{inf} on burnup is requested, as well as the ratio of absorptions in all considered erbium isotopes to the total absorption in the whole BPC (α^{Er}) in the given step of burnup. Normalization of R_a for each erbium isotope is that the sum of absorptions in considered erbium isotopes is equal to 1 at each burnup state.

TABLE 6.8. GEOMETRICAL AND MATERIAL PARAMETERS OF THE BPC

Zone	Name	External Radius (cm)	Isotopes	Nuclear Density (barn-cm) ⁻¹
1	Homogeneous mixture of burnable poison (Er ₂ O ₃) and graphite of the compact matrix	0.625	Er-166	4.14029E-04
			Er-167	2.82796E-04
			Er-168	3.30237E-04
			O-16	1.84834E-03
			C-12	8.13734E-02
			B-10	1.97898E-08
			B-11	7.96563E-08
2	Graphite of fuel block	9.97571E-01	C-12	8.67383E-02
			B-10	2.10945E-08
			B-11	8.49079E-08
3	Homogeneous mixture of fuel, graphite of block and helium	5.0515989	Pu-238	2.97259E-08
			Pu-239	2.08848E-05
			Pu-240	1.48522E-06
			Pu-241	2.64195E-07
			Pu-242	9.66955E-08
			O-16	3.86931E-05
			C-12	6.84220E-02
			Si-29	3.24406E-04
			He-4	1.10729E-04
			B-10	1.61419E-08
			B-11	6.49731E-08

TABLE 6.9. GEOMETRICAL AND MATERIAL PARAMETERS OF BPC_HET

Zone	Name	External Radius (cm)	Isotopes	Nuclear Density (barn-cm) ⁻¹
1	Heterogeneous location of burnable poison (Er ₂ O ₃) in graphite of the compact matrix	0.625	Er-166	9.14106E-03
			Er-167	6.24365E-03
			Er-168	7.29105E-03
			O-16	4.08081E-02
			C-12	8.52342E-02
			B-10	2.07287E-08
			B-11	8.34356E-08
2	Graphite of fuel block	9.97571E-01	C-12	8.67383E-02
			B-10	2.10945E-08
			B-11	8.49079E-08
3	Homogeneous mixture of fuel, graphite of block and helium	5.0515989	Pu-238	2.97259E-08
			Pu-239	2.08848E-05
			Pu-240	1.48522E-06
			Pu-241	2.64195E-07
			Pu-242	9.66955E-08
			O-16	3.86931E-05
			C-12	6.84220E-02
			Si-29	3.24406E-04
			He-4	1.10729E-04
			B-10	1.61419E-08
			B-11	6.49731E-08

TABLE 6.10. PRESENTATION OF THE RESULTS FOR INDIVIDUAL CODE
IN DIFFERENT BURNUP STEPS (FORM 3)

Case	Burnup (EFPD)	Code Name			
BPC-1200	0.0	$k_{inf} = 1PE11.4$			
		Isotope	Nuclear Density, (barn·cm) ⁻¹	R _{abs}	α^{Er}
		Er-166	1PE11.4	1PE11.4	1PE11.4
		Er-167	1PE11.4	1PE11.4	
		Er-168	1PE11.4	1PE11.4	
		Sum	1.0		
	5.0	$k_{inf} = 1PE11.4$			
		Isotope	Nuclear Density, (barn·cm) ⁻¹	R _{abs}	α^{Er}
		Er-166	1PE11.4	1PE11.4	1PE11.4
		Er-167	1PE11.4	1PE11.4	
		Er-168	1PE11.4	1PE11.4	
		Sum	1.0		
	250.0	$k_{inf} = 1PE11.4$			
		Isotope	Nuclear Density, (barn·cm) ⁻¹	R _{abs}	α^{Er}
		Er-166	1PE11.4	1PE11.4	1PE11.4
		Er-167	1PE11.4	1PE11.4	
		Er-168	1PE11.4	1PE11.4	
		Sum	1.0		
	500.0	$k_{inf} = 1PE11.4$			
		Isotope	Nuclear Density, (barn·cm) ⁻¹	R _{abs}	α^{Er}
		Er-166	1PE11.4	1PE11.4	1PE11.4
		Er-167	1PE11.4	1PE11.4	
		Er-168	1PE11.4	1PE11.4	
		Sum	1.0		
750.0	$k_{inf} = 1PE11.4$				
	Isotope	Nuclear Density, (barn·cm) ⁻¹	R _{abs}	α^{Er}	
	Er-166	1PE11.4	1PE11.4	1PE11.4	
	Er-167	1PE11.4	1PE11.4		
	Er-168	1PE11.4	1PE11.4		
	Sum	1.0			

6.2.2. The GT-MHR benchmark — Investigation of fuel assembly cell and 3-D reactor model

6.2.2.1. Detailed model of the GT-MHR

Basic preconditions

This section describes a full-scale neutronic model of the GT-MHR reactor. Typically this may be analysed by Monte Carlo methods as available in the MCU code [6-4–6-7] or by the MCNP code [6-8–6-10], or any other method or code capable of analysing the complex configuration.

In analysis of the GT-MHR reactor, fuel particle kernels are not homogenized with graphite matrix of fuel elements and the heterogeneous structure of the fuel particle arrangement is taken into account in direct calculations.

Neutronic model of fuel compact

The Fuel Compact (FC) neutronic model represents an effective matrix with dispersed spherical kernels of plutonium oxide fuel with different burnup levels. The kernel coatings are homogeneously mixed in the matrix. The sizes of the fuel compact neutronic model coincide with the dimensions indicated in Table 6.1. The initial nuclear composition of kernels with fresh fuel is given in Table 6.11. Nuclear densities of the fuel compact model effective matrix were calculated based on the actual design of the fuel compact and are given in Table 6.12.

TABLE 6.11. NUCLEAR DENSITIES OF THE FC KERNELS (FRESH FUEL)*

Isotope	Nuclear Density (barn·cm) ⁻¹
O-16	0.4046E-01
Pu-238	0.2935E-04
Pu-239	0.2062E-01
Pu-240	0.1467E-02
Pu-241	0.2609E-03
Pu-242	0.9548E-04

* Pu-238 –0.13% mass, Pu-239 –91.72% mass, Pu-240–6.55% mass, Pu-241–1.17 % mass and Pu-242 –0.43% mass.

TABLE 6.12. NUCLEAR DENSITIES OF THE FC MODEL EFFECTIVE MATRIX

Isotope	Nuclear density (barn·cm) ⁻¹
C-12	0.8339E-01
Si-28	0.1418E-02
B-10	0.1810E-07
B-11	0.7286E-07

* Physical density unit atoms/cm³ equals 10²⁴ atoms/barn·cm

The number of kernels in 1 cm³ of the fuel compact is 1046. The kernel diameter is 200 μm (0.02 cm). Nuclear compositions of kernels depend on fuel burnup. The following four types of kernels that differ by their fuel burnup level are considered:

- (a) Type (0) — fresh fuel with accumulation of equilibrium concentration of Xe-135;
- (b) Type (1/3) — fuel with 1/3 of full burnup level;
- (c) Type (2/3) — fuel with 2/3 of full burnup level;
- (d) Type (3/3) — discharged fuel.

The nuclear density values for kernels of these fuel types are derived from analysis of the GT-MHR reactor cell associated with the fuel assembly of Type 1 by considering the fuel and poison burnup process [6-11] (see Table 6.13).

Isotopes in Table 6.13 are sorted by the value of partial absorption of neutrons in them at the burnup level corresponding to discharged fuel. Partial absorption is the absorption of neutrons in a kernel by a given isotope listed in the table. The accumulated sum is defined as the sum of relative absorption of neutrons in a kernel over all isotopes given in foregoing lines. Absorption rates can be normalized in such a way that the total sums over all isotopes listed in two parts of the table equal 1 (for actinides and fission products each).

Solid lines indicate the boundaries in two parts of the table, at which the accumulated sum of absorptions in the given set of nuclides exceeds the given value. Thus, the solid line for actinides cuts

off the isotopes which have a net contribution to absorption of all actinides that is lower than $\sim 5 \cdot 10^{-4}$. (starting at actinide number 11: CM-245). The solid line for fission products cuts off all isotopes which have a net contribution to absorption of fission products that is lower than $\sim 2 \cdot 10^{-2}$ (starting at fission product number 41: I-127).

TABLE 6.13. ISOTOPIC CONTENT OF THE FUEL KERNEL FOR FOUR BURNUP STATES: BEGINNING (0), (1/3), (2/3) AND (3/3) — END OF THE FUEL LIFE

Isotope		Nuclear density (barn·cm) ⁻¹			
		(0) beginning ^{*)}	(1/3) 280 EFPD	(2/3) 560 EFPD	(3/3) 840 EFPD
Actinides					
1	PU-240	1.467E-03	2.429E-03	2.477E-03	1.542E-03
2	PU-241	2.609E-04	1.873E-03	2.736E-03	1.796E-03
3	PU-239	2.062E-02	1.238E-02	5.444E-03	7.394E-04
4	PU-242	9.548E-05	2.062E-04	5.814E-04	1.383E-03
5	AM-241		3.274E-05	7.821E-05	5.913E-05
6	AM-243		2.680E-05	9.314E-05	2.450E-04
7	PU-238	2.935E-05	2.827E-05	3.830E-05	7.123E-05
8	CM-244		4.760E-06	2.608E-05	9.443E-05
9	CM-242		4.093E-06	2.196E-05	5.726E-05
10	AM-242M		4.223E-07	1.489E-06	1.198E-06
11	CM-245		2.930E-07	1.773E-06	6.009E-06
12	CM-243		3.513E-08	3.222E-07	1.201E-06
13	U-234		1.602E-07	3.151E-07	5.580E-07
14	CM-246		1.812E-08	8.072E-08	6.652E-07
15	CM-247		1.639E-07	1.021E-07	6.376E-08
16	CM-248		4.587E-08	6.914E-08	8.275E-08
17	TH-230		1.667E-13	5.894E-13	1.287E-12
18	PA-231		1.426E-14	7.936E-14	1.995E-13
19	U-233		5.137E-14	1.661E-13	3.394E-13
20	U-232		4.627E-15	2.328E-14	1.406E-13
Fission products					
1	RH-103		2.73E-04	5.35E-04	6.84E-04
2	XE-135	5.72E-07	4.90E-07	3.53E-07	1.33E-07
3	ND-143		2.16E-04	4.28E-04	5.72E-04
4	XE-131		2.27E-04	4.05E-04	5.12E-04
5	CS-133		3.43E-04	6.57E-04	9.25E-04
6	SM-149	5.72E-07	7.05E-06	4.46E-06	1.50E-06
7	SM-152		4.12E-05	8.34E-05	1.17E-04
8	SM-151		2.15E-05	2.26E-05	1.23E-05
9	AG-109		8.70E-05	1.60E-04	2.21E-04
10	EU-155		2.34E-06	4.44E-06	6.91E-06
11	PM-147		7.55E-05	1.15E-04	1.28E-04

^{*)} Plutonium content is taken for the fresh fuel (Table 6.11) and concentrations of Xe-135 and Sm-149 are assumed to be the same and correspond to 5 EFPD state, when the equilibrium concentration of Xe-135 is reached.

Isotope	Nuclear density (barn·cm) ⁻¹			
	(0) beginning ^{*)}	(1/3) 280 EFPD	(2/3) 560 EFPD	(3/3) 840 EFPD
12 EU-154		3.69E-06	1.56E-05	2.04E-05
13 TC-99		3.22E-04	6.24E-04	8.92E-04
14 EU-153		2.91E-05	7.77E-05	1.32E-04
15 ND-145		1.60E-04	3.13E-04	4.53E-04
16 RH-105		2.26E-06	2.26E-06	2.15E-06
17 SM-150		6.18E-05	1.40E-04	2.21E-04
18 PD-105		2.92E-04	5.78E-04	8.48E-04
19 PM-148M		1.35E-06	1.58E-06	8.25E-07
20 PD-108		1.23E-04	2.56E-04	4.08E-04
21 RU-101		3.26E-04	6.45E-04	9.57E-04
22 MO-95		1.35E-04	3.75E-04	6.03E-04
23 CS-134		1.59E-05	5.92E-05	1.25E-04
24 PD-107		1.84E-04	3.76E-04	5.84E-04
25 PR-141		2.35E-04	5.11E-04	7.77E-04
26 GD-157		4.09E-07	2.88E-07	1.31E-07
27 LA-139		3.10E-04	6.24E-04	9.40E-04
28 SM-147		7.56E-06	2.44E-05	4.22E-05
29 CS-135		2.72E-04	4.86E-04	6.07E-04
30 KR-83		1.54E-05	2.86E-05	3.73E-05
31 CE-141		4.69E-05	4.64E-05	4.51E-05
32 CD-113		5.67E-07	3.37E-07	1.10E-07
33 I-129		7.14E-05	1.39E-04	1.97E-04
34 ZR-93		2.03E-04	3.97E-04	5.79E-04
35 MO-97		2.93E-04	5.80E-04	8.56E-04
36 PM-148		7.48E-07	1.16E-06	1.48E-06
37 ND-147		6.25E-06	6.38E-06	6.55E-06
38 EU-156		1.41E-06	2.67E-06	7.46E-06
39 GD-156		1.32E-05	4.64E-05	1.01E-04
40 CD-110		1.45E-05	5.75E-05	1.31E-04
41 I-127		1.35E-05	3.47E-05	5.35E-05
42 IN-115		1.52E-06	2.21E-06	2.30E-06
43 RU-102		3.40E-04	6.92E-04	1.06E-03
44 PD-104		3.21E-05	1.49E-04	3.75E-04
45 ND-144		6.37E-05	2.26E-04	4.98E-04
46 PR-143		1.69E-05	1.70E-05	1.71E-05
47 RU-104		3.36E-04	6.81E-04	1.04E-03
48 ND-148		9.19E-05	1.86E-04	2.84E-04
49 CD-111		1.63E-05	3.52E-05	5.73E-05
50 XE-133		9.99E-06	9.93E-06	9.77E-06
51 RU-103		7.65E-05	7.66E-05	7.56E-05
52 XE-132		3.13E-04	6.73E-04	1.07E-03
53 MO-98		3.17E-04	6.26E-04	9.23E-04
54 SM-148		1.50E-05	5.47E-05	1.10E-04

Isotope	Nuclear density (barn·cm) ⁻¹			
	(0) beginning ^{*)}	(1/3) 280 EFPD	(2/3) 560 EFPD	(3/3) 840 EFPD
55 MO-100		3.76E-04	7.46E-04	1.11E-03
56 PD-106		6.93E-05	2.30E-04	4.70E-04
57 ZR-96		2.64E-04	5.25E-04	7.77E-04
58 GD-155		7.15E-08	9.44E-08	4.82E-08
59 CE-142		2.75E-04	5.49E-04	8.20E-04
60 ND-146		1.41E-04	2.94E-04	4.66E-04
61 ND-150		5.38E-05	1.09E-04	1.68E-04
62 I-131		1.07E-05	1.01E-05	8.89E-06
63 RU-100		1.15E-05	4.68E-05	1.11E-04
64 ZR-91		9.34E-05	2.20E-04	3.41E-04
65 SM-154		1.47E-05	3.02E-05	4.69E-05
66 SM-153		4.90E-07	8.35E-07	1.39E-06
67 TB-159		1.23E-06	2.67E-06	4.48E-06
68 GD-158		6.88E-06	1.66E-05	2.94E-05
69 CE-140		2.75E-04	5.76E-04	8.85E-04
70 XE-134		4.22E-04	8.45E-04	1.27E-03
71 XE-136		5.26E-04	1.11E-03	1.77E-03
72 CE-144		1.50E-04	2.29E-04	2.73E-04
73 BA-138		3.38E-04	6.79E-04	1.03E-03
74 BR-181		9.34E-06	1.76E-05	2.41E-05
75 CS-137		3.59E-04	7.12E-04	1.06E-03
76 Y-89		6.86E-05	1.57E-04	2.40E-04
77 AG-0M		6.13E-07	1.90E-06	3.63E-06
78 NB-95		4.20E-05	4.53E-05	4.32E-05
79 SR-90		1.09E-04	2.12E-04	3.06E-04
80 SB-121		1.99E-06	3.79E-06	5.32E-06
81 GD-154		7.61E-08	1.14E-06	2.16E-06
82 RU-106		1.90E-04	3.15E-04	4.08E-04
83 BA-134		1.36E-06	1.05E-05	3.34E-05
84 SB-123		2.10E-06	4.23E-06	6.11E-06
85 ND-142		6.30E-07	3.31E-06	1.05E-05
86 TE-127M		1.17E-05	1.25E-05	1.06E-05
87 MO-96		2.03E-06	1.11E-05	3.08E-05
88 ZR-92		1.61E-04	3.17E-04	4.63E-04
89 BA-137		3.45E-06	1.31E-05	2.89E-05
90 CD-112		7.45E-06	1.60E-05	2.64E-05
91 ZR-95		8.12E-05	8.26E-05	7.82E-05
92 RB-85		2.44E-05	4.80E-05	7.00E-05
93 CD-114		7.28E-06	1.60E-05	2.58E-05
94 TE-126		1.31E-05	2.50E-05	3.45E-05
95 RB-87		5.41E-05	1.06E-04	1.54E-04
96 TE-130		1.12E-04	2.22E-04	3.29E-04
97 SB-125		8.89E-06	1.55E-05	1.95E-05

Isotope	Nuclear density (barn·cm) ⁻¹			
	(0) beginning ^{*)}	(1/3) 280 EFPD	(2/3) 560 EFPD	(3/3) 840 EFPD
98 EU-152		2.00E-08	4.48E-08	1.53E-08
99 TE-128		3.92E-05	7.55E-05	1.07E-04
100 ZR-94		2.33E-04	4.59E-04	6.75E-04
101 EU-151		3.46E-08	3.40E-08	7.39E-09
102 KR-84		2.63E-05	5.30E-05	8.10E-05
103 LA-140		2.58E-06	2.63E-06	2.76E-06
104 TE-125		8.71E-07	3.23E-06	6.59E-06
105 SN-117		2.48E-06	4.76E-06	6.70E-06
106 MO-99		4.78E-06	4.74E-06	4.67E-06
107 KR-82		6.03E-08	2.35E-07	5.20E-07
108 GD-152		1.09E-08	4.07E-08	5.36E-08
109 KR-185		6.56E-06	1.25E-05	1.75E-05
110 BA-140		1.95E-05	1.98E-05	2.02E-05
111 XE-128		1.91E-07	1.11E-06	2.95E-06
112 AG-111		6.90E-07	8.02E-07	1.02E-06
113 SN-124		4.97E-06	9.42E-06	1.30E-05
114 CS-136		4.62E-07	5.70E-07	8.12E-07
115 BA-136		5.59E-06	1.32E-05	2.28E-05
116 SN-119		2.03E-06	3.93E-06	5.62E-06
117 XE-130		2.11E-07	3.85E-07	4.98E-07
118 SE-80		5.93E-06	1.12E-05	1.52E-05
119 SN-126		1.31E-05	2.48E-05	3.42E-05
120 KR-86		4.13E-05	8.12E-05	1.19E-04
121 SE-77		3.65E-07	6.88E-07	9.35E-07
122 SR-89		2.32E-05	2.26E-05	2.05E-05
123 TE-122		4.51E-08	1.82E-07	4.15E-07
124 SN-118		1.93E-06	3.77E-06	5.44E-06
125 BA-135		3.21E-09	3.78E-08	1.95E-07
126 SE-78		1.47E-06	2.80E-06	3.91E-06
127 TE-123		1.73E-10	1.20E-09	3.37E-09
128 CD-116		2.63E-06	5.08E-06	7.23E-06
129 CD-115M		4.47E-08	5.01E-08	5.63E-08
130 TE-129M		2.12E-06	1.97E-06	1.67E-06
131 SN-122		2.86E-06	5.49E-06	7.73E-06
132 PR-142		6.24E-09	1.69E-08	5.53E-08
133 SN-120		1.84E-06	3.61E-06	5.26E-06
134 TE-124		2.10E-08	1.06E-07	2.65E-07
135 SE-82		1.18E-05	2.29E-05	3.28E-05
136 SR-88		7.11E-05	1.40E-04	2.03E-04
137 XE-129		2.15E-10	3.02E-09	1.78E-08
138 SB-126		1.20E-07	1.07E-07	7.95E-08
139 SB-124		1.55E-08	3.75E-08	6.47E-08
140 SR-86		2.55E-08	9.28E-08	2.07E-07

Isotope	Nuclear density (barn·cm) ⁻¹			
	(0) beginning ^{*)}	(1/3) 280 EFPD	(2/3) 560 EFPD	(3/3) 840 EFPD
141 ZR-90		9.94E-07	3.99E-06	8.92E-06
142 SN-125		1.85E-07	1.63E-07	1.19E-07
143 SN-123		2.72E-07	2.95E-07	2.33E-07
144 RB-86		4.49E-09	8.48E-09	1.47E-08
145 SR-87		1.01E-09	1.84E-09	2.37E-09
146 SN-116		7.86E-12	1.45E-11	1.89E-11

Note: CE = Control Element.

Neutronic model of burnable poison

The Burnable Poison (BP) neutronic model represents a graphite matrix with homogeneously dispersed natural erbium oxide, Er₂O₃, and ceramic coatings of poison particles. Dimensions of the burnable poison neutronic model coincide with the dimensions indicated in Table 6.1. The following four types of burnable poison on their burnup level are considered:

- (a) Type (0) — fresh burnable poison;
- (b) Type (1/3) — burnable poison at the fuel life point when the fuel has 1/3 of full burnup level;
- (c) Type (2/3) — burnable poison at the fuel life point when fuel has 2/3 of full burnup level;
- (d) Type (3/3) — burnable poison at the fuel life point for discharged fuel.

The nuclear density values for these burnable poison types are derived from analysis of the GT-MHR reactor cell associated with the fuel assembly of Type 1 by considering the fuel and poison burnup process [6-11] (see Table 6.14).

TABLE 6.14. ISOTOPIC CONTENT OF BP FOR TYPES 0, 1, 2 AND 3 VS FUEL BURNUP

Isotope	Atomic density (barn·cm) ⁻¹			
	(0) beginning	(1/3) 280 EFPD	(2/3) 560 EFPD	(3/3) 840 EFPD
C-12	0.8137E-01	0.8137E-01	0.8137E-01	0.8137E-01
O-16	0.1848E-02	0.1848E-02	0.1848E-02	0.1848E-02
B-10	0.1979E-07	0.1979E-07	0.1979E-07	0.1979E-07
B-11	0.7966E-07	0.7966E-07	0.7966E-07	0.7966E-07
ER-166	4.138E-04	4.043E-04	3.938E-04	3.807E-04
ER-167	2.798E-04	1.353E-04	4.256E-05	7.285E-06
ER-168	3.333E-04	4.840E-04	5.827E-04	6.254E-04

Neutronic model of helium coolant

The nuclear helium density at working temperature $T = 942$ K and under working pressure $P = 7.0$ MPa is $5.5 \cdot 10^{-4}$ (barn·cm)⁻¹.

Fuel assembly neutronic model

External dimensions of the fuel assembly models (see Fig. 6.3) are taken to be the same as those of the actual fuel assembly. The fuel assembly models are divided into two kinds, namely, FA1 and FA2, which differ in the presence or absence of holes for control rods. In FA2, a hole for control rods is filled with helium when the control rod is withdrawn. All the cavities in the hole are also filled with helium when the control rod is inserted. Each of these kinds of fuel assembly models is divided into

four types of fuel burnup. In one fuel assembly, one type (out of four) of fuel compact and burnable poison is used. The fuel assembly type corresponds to the burnup type of fuel compact and burnable poison used in it.

In the fuel assembly model, there are no gaps between the fuel compact or burnable poison surface and their surface of holes (diameter of the holes is adopted to be equal to the diameter of fuel compact or burnable poison) and no central hole intended for fuel assembly reloads. They are accounted by the homogenization of the fuel assembly graphite block material using a graphite effective density of 1.73 g/cm^3 (graphite density without homogenization is 1.74 g/cm^3). Impurities in the graphite are accounted for by means of equivalent (with respect to neutron absorption) natural boron content (boron equivalent) of 1.1 ppm. The graphite atomdensities is given in Table 6.15.

The holes for coolant passage have the actual diameters and are filled with helium. Other dimensions of the fuel assembly graphite block coincide with the ones indicated in Table 6.1.

TABLE 6.15. NUCLEAR DENSITIES OF FUEL ASSEMBLY GRAPHITE BLOCK

Isotope	Atomic density (barn-cm)-1
C-12	0.867E-01
B-10	0.211E-07
B-11	0.849E-07

Core neutronic model

The GT-MHR project provides for layer-by-layer reloading of fuel assemblies along the core height, without their repositioning in the radial direction. In the computational model of the core, the burnup level in each layer was taken as a constant value that does not depend on a radial coordinate.

The core model in its cross-section represents a ring formed by vertical columns of fuel assembly models. The columns are installed with 0.25 cm lateral gaps between them, which are filled with helium.

Each column of the core axially consists of ten fuel assemblies, with fuel assemblies being adjacent in an axial direction that differ in fuel particle burnup and, consequently, in the nuclear composition of fuel kernels. All fuel assemblies in all the columns belonging to the same axial layer have the same fuel burnup. Table 6.16 lists six variants of the core model being considered.

TABLE 6.16. THE ACTIVE CORE VARIANTS ON COMPOSITION OF FA LAYERS ALONG THE CORE MODEL AXIS

Option number	FA Kernels and poison burnup in axial layers of the core model									
Layer number from the top downwards	1	2	3	4	5	6	7	8	9	10
Variant 1	2/3	0	2/3	0	1/3	1/3	0	2/3	0	2/3
Variant 2	3/3	1/3	3/3	1/3	2/3	2/3	1/3	3/3	1/3	3/3
Variant 3	2/3	0	1/3	0	1/3	1/3	0	1/3	0	2/3
Variant 4	3/3	1/3	2/3	1/3	2/3	2/3	1/3	2/3	1/3	3/3
Variant 5	2/3	0	2/3	1/3	1/3	1/3	1/3	2/3	0	2/3
Variant 6	3/3	1/3	3/3	2/3	2/3	2/3	2/3	3/3	1/3	3/3

Neutronic model of the UAR

The model of the graphite UAR block represents a hexahedral prism having the “across-flats” size of 36 cm and height of 130 cm with 1.6 cm diameter holes for coolant. The number and arrangement of holes in the UAR block model cross-section coincide with those of the fuel assembly model. In reality, two UAR blocks are installed at a height of 130 cm.

The effective density of graphite in the UAR block model is taken to be 1.73 g/cm^3 (graphite density without homogenization is 1.74 g/cm^3). Impurities in graphite are taken into account by means of equivalent (by neutron absorption) natural boron content (boron equivalent) of 1.1 ppm.

The nuclear densities of the UAR graphite block coincide with those of the fuel assembly graphite block and are listed in Table 6.17.

The UAR block models, similarly to the fuel assembly models, are divided into two kinds (UARB1 and UARB2) that differ in the presence or absence of holes for control rods. The diameter of these holes and their arrangement in the UARB2 are the same as those in the FA2. The hole for control rods is filled with helium when the control rod is withdrawn, like all cavities in the hole when the control rod is inserted.

The UAR model is obtained by placing the UARB models above the core columns with the same lateral helium gap as between the core columns. The UARB2 are placed on the FA2 in such a way as to form a continuous channel for the movement of control rods in the reactor model.

TABLE 6.17. NUCLEAR DENSITIES OF THE UAR GRAPHITE BLOCK

Isotope	Atomic density (barn-cm) ⁻¹
C-12	0.867E-01
B-10	0.211E-07
B-11	0.849E-07

Neutronic model of the LAR

The model of graphite LAR block represents a hexahedral prism with 36 cm across-flats size and 130 cm height, with 1.6 cm diameter holes for coolant passage. The number and arrangement of holes over the LAR block model cross-section are the same as those for the FA model.

The effective density of graphite in the LAR block model is taken to be 1.73 g/cm^3 (graphite density without homogenization is 1.74 g/cm^3). Impurities in the graphite are accounted for by means of equivalent (of neutron absorption) natural boron content (boron equivalent) of 1.1 ppm. The atom densities are given in Table 6.18.

TABLE 6.18. NUCLEAR DENSITIES OF THE LAR GRAPHITE BLOCK

Isotope	Atomic density (barn-cm) ⁻¹
C-12	0.867E-01
B-10	0.211E-07
B-11	0.849E-07

The LAR block models, similarly to the fuel assembly, are divided into two kinds (LARB1 and LARB2), which differ in the presence or lack of holes for control rods. The diameter of the holes and their arrangement in LARB2 are the same as in FA2. A hole for control rods is filled with helium when the control rod is withdrawn. All the cavities in the hole are also filled with helium when the control rod is inserted.

The LARB2 and FA2 blocks are installed on each other in such a way as to form a continuous channel for control rods. The LAR model is formed by the LARB models' location under the active core columns with the same cross-helium gap as between the core columns.

Neutronic model of the internal reflector

The model of the graphite internal reflector represents a set of columns in the form of 1060 cm high hexahedral prisms having the “across flats” size of 36 cm, of which the number and arrangement over the internal reflector model cross-section are the same as in the actual reactor (Fig. 6.2).

The columns are installed with 0.25 cm lateral gaps between them which are filled with helium. The effective density of graphite in the internal reflector blocks model is taken to be 1.73 g/cm³ (graphite density without homogenization is 1.74 g/cm³). Impurities in the graphite are taken into account by means of equivalent (of neutron absorption) natural boron content (boron equivalent) of 1.1 ppm – see Table 6.19.

TABLE 6.19. NUCLEAR DENSITIES OF IR GRAPHITE BLOCKS

Isotope	Atomic density (barn·cm) ⁻¹
C-12	0.867E-01
B-10	0.211E-07
B-11	0.849E-07

Each of the internal reflector columns immediately adjacent to the core contains small poison rods made of a mixture of graphite with boron carbide. The internal reflector absorber element pins in the form of a solid cylinder with a 5 cm height and 1.25 cm diameter represent a mixture of natural boron carbide and graphite matrix with the mixture density of 1.70 g/cm³ and effective density of B₄C of 0.3 g/cm³.

The internal reflector absorber element pins are arranged symmetrically inside the vertical holes in the internal reflector graphite blocks, thus forming internal reflector absorber element rods of a 75 cm height (the internal reflector block height is 80 cm). The internal reflector absorber element pins are arranged along the internal reflector height within the active core height limits similar to the arrangement of the fuel compacts in the fuel assemblies of the active core. The nuclear densities of the internal reflector absorber elements are given in Table 6.20.

Two design options are considered, suggesting placement of 6 or 2 pins in the corners of the internal reflector block.

TABLE 6.20. NUCLEAR DENSITIES OF THE INTERNAL REFLECTOR ABSORBER ELEMENTS ^{*)}

Isotope	Nuclear density, (barn·cm) ⁻¹
C-12	0.735E-01
B-10	0.260E-02
B-11	0.105E-01

^{*)} It is assumed that boron density does not change during reactor operation.

Neutronic model of the internal reflector

The model of the radial graphite reflector (RR), with the exception of the peripheral part adjacent to the external cylindrical surface, represents a set of graphite columns in the form of 1060 cm high hexahedral prisms having the “across flats” size of 36 cm.

The columns are installed with a 0.25 cm lateral gap between them that is filled with helium. The effective density of graphite in the radial reflector model is taken to be 1.73 g/cm³. Impurities in the graphite are taken into account by means of equivalent (by neutron absorption) natural boron content

(boron equivalent) of 1.1 ppm. The nuclear densities of the radial reflector model graphite blocks coincide with those for the fuel assembly graphite blocks and are listed in Table 6.21.

The radial reflector with control rod (RRC) models are divided into two kinds (RRC1 and RRC2) that differ in the presence or absence of a 13 cm diameter hole (similar to the hole in FA2) for the control rods or the RSS absorber element system. The number of RRC2 and their arrangement in the radial reflector cross-section are shown in Fig. 6.2.

The hole for the control rods in the RRC2 is filled with helium when the control rod is withdrawn, just as all cavities in the hole when the control rod is inserted.

The peripheral part of the radial reflector with its external cylindrical surface models a 1060 cm high irreplaceable reflector and hexahedral graphite columns of the radial reflector installed with a 0.25 cm gap. The effective density of graphite in the model of the radial reflector periphery is taken to be 1.73 g/cm³. Impurities in the graphite are taken into account by means of equivalent (by neutron absorption) natural boron content (boron equivalent) of 1.1 ppm. The nuclear densities of graphite in the peripheral part of the radial reflector coincide with those of the fuel assembly graphite block and are listed in Table 6.21.

TABLE 6.21. NUCLEAR DENSITIES OF THE RR MODEL GRAPHITE

Isotope	Atomic density (barn·cm) ⁻¹
C-12	0.867E-01
B-10	0.211E-07
B-11	0.849E-07

Neutronic model of the control rod

In the control rod (CR) model, the absorber element of natural boron carbide is homogenized with regard for gaps between absorbing sections within the height of 930 cm. The nuclear densities of the control rod absorber element are given in Table 6.22. Figure 6.6 provides a schematic of the control rod.

TABLE 6.22. NUCLEAR DENSITIES OF THE CR ABSORBER ELEMENT

Isotope	Atomic density (barn·cm) ⁻¹
C-12	0.141E-01
B-10	0.111E-01
B-11	0.449E-01

In the radial direction, the control rod represents coaxially arranged graphite sleeves and a poison sleeve located in the following succession:

- A graphite tube with 6.2 cm outer diameter and 0.8 cm wall thickness;
- A graphite tube with 7.8 cm outer diameter and 0.4 cm wall thickness;
- An absorber element sleeve with 10.2 cm outer diameter and 1.2 cm thickness;
- A graphite tube with 11 cm outer diameter and 0.4 cm wall thickness.

The total height of the rod model is 930 cm.

The graphite density of all the graphite tubes is 1.74 g/cm³. Impurities in the graphite are taken into account by means of equivalent (by neutron absorption) natural boron content (boron equivalent) of 1.1 ppm. The nuclear densities of the control rod graphite tubes are given in Table 6.23.

TABLE 6.23. NUCLEAR DENSITIES OF THE CR GRAPHITE TUBES

Isotope	Nuclear density (barn·cm) ⁻¹
C-12	0.872E-01
B-10	0.212E-07
B-11	0.854E-07

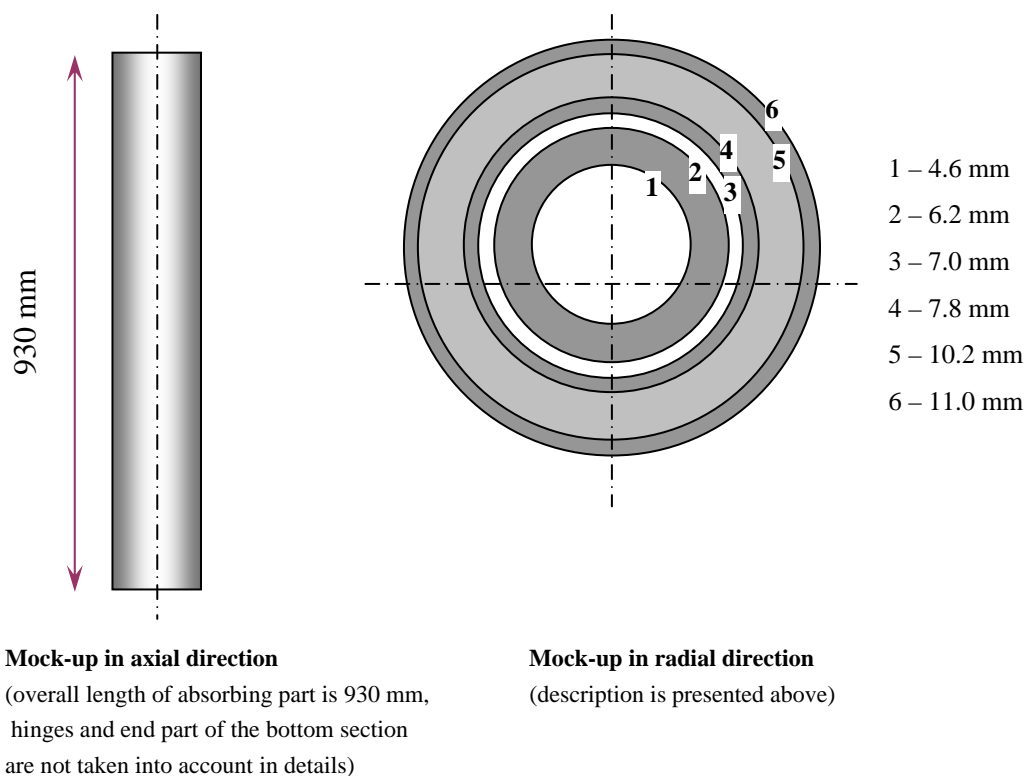


FIG. 6.6. A simple scheme of the control rod.

6.2.2.2. Proposed benchmark problems

The following benchmark problems of a GT-MHR core with plutonium fuel have been proposed:

- Standard fuel assembly cell calculations
 - Dependence of K_{inf} for a FA1 cell on burnup at given irradiation conditions;
 - Content of the main isotopes vs burnup (for four states – 0, 280, 560 and 840 EFPD);
- Reactor calculations
 - Isothermal reactivity coefficients versus temperature at the beginning and at the end of fuel cycle (see Table 6.16), i.e. for 2 of the 6 states — 1st and 6th variant (temperature step — 100 K, from 300 to 1200 K);
 - Control rod worth in the active core at the beginning and at the end of the fuel cycle;
 - Control rod worth in the side reflector at the beginning and at the end of the fuel cycle.

Fuel assembly burnup and full core calculations are carried out at the following approximations:

- Burning time: up to 840 EFPD;
- Active core nominal temperature: 1200 K;

- Reflector nominal temperature: 900 K;
- Power normalization factor: 0.856282 MW/kg Pu.

In the cell calculations, the cell of a fuel assembly without control rod cavity (FA1) is considered as a 'unit cell', which is calculated with reflecting boundary conditions. Dependent on code capabilities, it could be described either in the actual geometry or by equivalent unit cell models, which should take into account the fuel compacts, burnable poison compacts, coolant channels and fuel assembly graphite.

Forms to present results

Calculational codes

A brief description of calculational codes, techniques and models is presented according to Form 4 (Table 6.24).

TABLE 6.24. CALCULATIONAL CODES, TECHNIQUES AND MODELS (FORM 4)

Calculational code
Calculation technique
Library
Calculation
Fuel particle arrangement
Burnable poison arrangement
Energy structure
Statistic

Calculations results

Fuel assembly cell calculations

The results of the fuel assembly calculations are presented in Form 5 (Table 6.25). They correspond to the list of Section 6.2.2.2 and combine absolute values of multiplication factor, isotopic contents of Er-167, Pu-239, Pu-240, Pu-241 and Pu-242 in parts of full content for erbium isotopes and fuel ones for four states on burnup. The initial isotopic content is taken in accordance with the first column of Tables 6.13 and 6.14 for fuel and burnable poison respectively.

It is necessary to note that:

Isotopic contents at the beginning of the fuel cycle were determined so that the percentage of plutonium isotopes was assumed to be the following:

Pu-238 — 0.13% mass;

Pu-239 — 91.72% mass;

Pu -240 — 6.55% mass;

Pu-241 — 1.17% mass;

Pu-242 — 0.43% mass.

Isotopic contents of Xe-135 and Sm-149 were also set.

In the calculations, only three erbium isotopes (Er-166, Er-167 and Er-168) are taken into account, with initial contents 33.4%, 22.9% and 27.1% in natural mixture respectively.

TABLE 6.25. INFINITE MULTIPLICATION COEFFICIENT AND ISOTOPIC CONTENT VS BURNUP (FORM 5)

Irradiation Time	Functional	Value
Beginning of cycle	k_{inf}	1PF11.4
	Er-167	1PF11.4
	Pu-239	1PF11.4
	Pu-240	1PF11.4
	Pu-241	1PF11.4
	Pu-242	1PF11.4

The reactor calculation

The results of the reactor calculations are presented in Forms 6 and 7 (Tables 6.26 and 6.27). They correspond to the list of p. 6.2.2.2 and present the following:

- Absolute values of isothermal reactivity temperature coefficient for middle temperatures of all considered temperature intervals from 300 up to 1200 K with 100 K step for two states on burnup;
- Core control rod worth in percentages for two states on burnup;
- Reflector control rod worth in percentages for two states on burnup.

TABLE 6.26. ISOTHERMAL REACTIVITY TEMPERATURE COEFFICIENT (FORM 6)

Calculational code		Value (1/K)
Beginning of cycle (the 1 st state)	ρ_{350}	1PE11.2

	ρ_{1150}	1PE11.2
End of cycle (the 6 th state)	ρ_{350}	1PE11.2

	ρ_{1150}	1PE11.2

The isothermal reactivity temperature coefficients are estimated as:

$$\rho = \frac{k(T_2) - k(T_1)}{k(T_2) \cdot k(T_1)} \cdot \frac{1}{T_2 - T_1}, 1/K$$

TABLE 6.27. CONTROL ROD WORTH (FORM 7)

Code		Value (%)
Control rods worth in the core		
Beginning of cycle (the 1 st state)		1PF11.1
End of cycle (the 6 th state)		1PF11.1
Control rods worth in the reflector		
Beginning of cycle (the 1 st state)		1PF11.1
End of cycle (the 6 th state)		1PF11.1

The control rods worth is estimated as:

$$\rho = \frac{k(\uparrow) - k(\downarrow)}{k(\uparrow) \cdot k(\downarrow)} \cdot 100, \%$$

↑ means control rods are withdrawn;

↓ means control rods are inserted.

6.3. GT-MHR PLUTONIUM FUEL BENCHMARK RESULTS

6.3.1. GT-MHR plutonium fuel benchmark results, Russian Federation

6.3.1.1. Calculation of elementary cells, Russian Federation

List of participants

Up to now, the experts of different Russian institutions took part in the investigations using the codes which are described in Table 6.28.

TABLE 6.28. CODES USED IN BENCHMARK INVESTIGATIONS

Institute	IBRAE	OKBM, RRC KI	OKBM, RRC KI
Code	MCNP4C [6-9] MONTEBURNS (MCNP4C/ORIGEN2.1)	WIMS-D4 [6-12]	UNK [6-13]
Method of analysis	Monte Carlo	FCP, S ₈	FCP
Library	ENDF/BVI.8 (partially ENDB/B-V)	Base: UKNDL, ENDF/B6, FOND2.2 Optional: WLUP (IAEA)	ENDF/BVI
Energy structure	Continuous	69 groups	89 groups, (up to 7000 for some isotopes)
Statistics	up to 19·10 ⁶ histories		

Results of fuel cells calculations

At present, the majority of calculational results have been obtained for all types of fuel compact cells and burnable poison cells, both in the fresh state and in dependence on burnup (with the given specific volumetric power in a cell).

Table 6.29 shows the average of different codes values of studied functionals for fuel compact cells in the fresh state for different temperatures. The comparison of multiplication factors, reactions rates and neutron per fission for main isotopes is given in Figs 6.7–6.10, 6.11–6.14 and 6.15–6.18 for FCC, FCC2 and FCC1 correspondingly.

The results obtained for FCC in dependence on burnup are presented in Table 6.30 and in Figs 6.19–6.25.

The results of burnup calculations for the BPC with and without taking into account the heterogeneity of burnable poison particles arrangement are presented in Tables 6.31, 6.32 and in Figs 6.26–6.28.

TABLE 6.29(A). AVERAGE VALUES OF NEUTRONIC FUNCTIONALS
FOR FRESH FCCS (300 K)

Temperature		300 K			
FCC		$k_{\text{inf}} = 1.5417$			
		R_{abs}	R_{fis}	R_{vfis}	v
	Pu-238	2.6020E-04	2.6804E-05	7.8850E-05	2.9424
	Pu-239	8.3603E-01	5.2627E-01	1.5165E+00	2.8817
	Pu-240	1.4227E-01	2.3878E-04	7.2349E-04	3.0296
	Pu-241	1.0512E-02	7.8187E-03	2.3065E-02	2.9500
	Pu-242	2.5658E-03	9.7659E-06	3.0129E-05	3.0847
	O-16	1.9100E-05			
	C-12	5.8576E-03			
	Si-29	1.5159E-03			
	B-10				
	B-11				
	B-10 + B-11	1.0495E-03			
FCC2		$k_{\text{inf}} = 1.4595$			
		R_{abs}	R_{fis}	R_{vfis}	v
	Pu-238	2.2696E-04	2.5784E-05	7.5801E-05	2.9407
	Pu-239	8.0235E-01	5.0032E-01	1.4379E+00	2.8740
	Pu-240	1.7832E-01	2.3814E-04	7.2042E-04	3.0261
	Pu-241	9.4588E-03	7.0516E-03	2.0794E-02	2.9487
	Pu-242	2.5033E-03	9.3066E-06	2.8653E-05	3.0782
	O-16	1.7573E-05			
	C-12	5.0751E-03			
	Si-29	1.2860E-03			
	B-10				
	B-11				
	B-10 + B-11	8.3414E-04			
FCC1		$k_{\text{inf}} = 1.4396$			
		R_{abs}	R_{fis}	R_{vfis}	v
	Pu-238	2.1925E-04	2.5404E-05	7.4641E-05	2.9390
	Pu-239	7.9377E-01	4.9361E-01	1.4185E+00	2.8738
	Pu-240	1.8730E-01	2.3410E-04	7.0678E-04	3.0195
	Pu-241	9.2224E-03	6.8729E-03	2.0266E-02	2.9487
	Pu-242	2.5089E-03	8.9921E-06	2.7638E-05	3.0732
	O-16	1.6184E-05			
	C-12	4.9096E-03			
	Si-29	1.2428E-03			
	B-10				
	B-11				
	B-10 + B-11	7.8904E-04			

TABLE 6.29(B). AVERAGE VALUES OF NEUTRONIC FUNCTIONALS
FOR FRESH FCCS (600 K)

Temperature		600 K			
		$k_{inf} = 1.5144$			
FCC		R_{abs}	R_{fis}	R_{vfis}	ν
	Pu-238	2.3651E-04	2.6090E-05	7.6785E-05	2.9437
	Pu-239	8.2833E-01	5.1724E-01	1.4903E+00	2.8812
	Pu-240	1.5067E-01	2.4030E-04	7.2777E-04	3.0283
	Pu-241	1.0101E-02	7.5020E-03	2.2131E-02	2.9500
	Pu-242	2.5929E-03	9.7603E-06	3.0112E-05	3.0847
	O-16	1.9091E-05			
	C-12	5.5928E-03			
	Si-29	1.4364E-03			
	B-10				
	B-11				
	B-10 + B-11	9.8038E-04			
		$k_{inf} = 1.4329$			
FCC2		R_{abs}	R_{fis}	R_{vfis}	ν
	Pu-238	2.0992E-04	2.5276E-05	7.4332E-05	2.9418
	Pu-239	7.9260E-01	4.9140E-01	1.4121E+00	2.8735
	Pu-240	1.8853E-01	2.4012E-04	7.2604E-04	3.0246
	Pu-241	9.1361E-03	6.8028E-03	2.0060E-02	2.9488
	Pu-242	2.5335E-03	9.3065E-06	2.8653E-05	3.0782
	O-16	1.7574E-05			
	C-12	4.8993E-03			
	Si-29	1.2347E-03			
	B-10				
	B-11				
	B-10 + B-11	7.8918E-04			
		$k_{inf} = 1.4142$			
FCC1		R_{abs}	R_{fis}	R_{vfis}	ν
	Pu-238	2.0396E-04	2.4950E-05	7.3327E-05	2.9399
	Pu-239	7.8401E-01	4.8504E-01	1.3937E+00	2.8733
	Pu-240	1.9762E-01	2.3610E-04	7.1244E-04	3.0179
	Pu-241	8.9300E-03	6.6474E-03	1.9602E-02	2.9488
	Pu-242	2.5391E-03	8.9917E-06	2.7637E-05	3.0732
	O-16	1.6194E-05			
	C-12	4.7551E-03			
	Si-29	1.1968E-03			
	B-10				
	B-11				
	B-10 + B-11	7.4993E-04			

TABLE 6.29(C). AVERAGE VALUES OF NEUTRONIC FUNCTIONALS
FOR FRESH FCCS (900 K)

Temperature		900 K			
		$k_{inf} = 1.4935$			
FCC		R_{fis}	$R_{v_{fis}}$	R_{fis}	v
	Pu-238	2.1682E-04	2.5497E-05	7.5069E-05	2.9449
	Pu-239	8.1906E-01	5.0839E-01	1.4645E+00	2.8807
	Pu-240	1.6073E-01	2.4218E-04	7.3308E-04	3.0266
	Pu-241	9.6491E-03	7.1523E-03	2.1100E-02	2.9500
	Pu-242	2.6191E-03	9.7571E-06	3.0101E-05	3.0847
	O-16	1.9067E-05			
	C-12	5.3797E-03			
	Si-29	1.3719E-03			
	B-10				
	B-11				
	B-10 + B-11	9.2467E-04			
		$k_{inf} = 1.4066$			
FCC2		R_{fis}	$R_{v_{fis}}$	R_{fis}	v
	Pu-238	1.9593E-04	2.4863E-05	7.3140E-05	2.9427
	Pu-239	7.8171E-01	4.8258E-01	1.3866E+00	2.8732
	Pu-240	2.0001E-01	2.4233E-04	7.3229E-04	3.0228
	Pu-241	8.7921E-03	6.5373E-03	1.9278E-02	2.9488
	Pu-242	2.5663E-03	9.3070E-06	2.8654E-05	3.0782
	O-16	1.7559E-05			
	C-12	4.7649E-03			
	Si-29	1.1941E-03			
	B-10				
	B-11				
	B-10 + B-11	7.5384E-04			
		$k_{inf} = 1.3885$			
FCC1		R_{fis}	$R_{v_{fis}}$	R_{fis}	v
	Pu-238	1.9135E-04	2.4575E-05	7.2243E-05	2.9406
	Pu-239	7.7296E-01	4.7639E-01	1.3687E+00	2.8730
	Pu-240	2.0905E-01	2.3832E-04	7.1874E-04	3.0163
	Pu-241	8.6150E-03	6.4044E-03	1.8885E-02	2.9488
	Pu-242	2.5693E-03	8.9932E-06	2.7642E-05	3.0732
	O-16	1.6183E-05			
	C-12	4.6387E-03			
	Si-29	1.1605E-03			
	B-10				
	B-11				
	B-10 + B-11	7.1923E-04			

TABLE 6.29(D). AVERAGE VALUES OF NEUTRONIC FUNCTIONALS
FOR FRESH FCCS (1200 K)

Temperature		1200 K			
		$k_{nf} = 1.4645$			
FCC		$R_{v_{fis}}$	R_{fis}	$R_{v_{fis}}$	ν
	Pu-238	2.0461E-04	2.5128E-05	7.4003E-05	2.9457
	Pu-239	8.0972E-01	5.0087E-01	1.4427E+00	2.8804
	Pu-240	1.7063E-01	2.4402E-04	7.3829E-04	3.0252
	Pu-241	9.2989E-03	6.8829E-03	2.0305E-02	2.9501
	Pu-242	2.6501E-03	9.7554E-06	3.0096E-05	3.0846
	O-16	1.9064E-05			
	C-12	5.2577E-03			
	Si-29	1.3345E-03			
	B-10				
	B-11				
	B-10 + B-11	8.9197E-04			
		$k_{inf} = 1.3854$			
FCC2		$R_{v_{fis}}$	R_{fis}	$R_{v_{fis}}$	ν
	Pu-238	1.8746E-04	2.4610E-05	7.2406E-05	2.9431
	Pu-239	7.7200E-01	4.7542E-01	1.3659E+00	2.8729
	Pu-240	2.0988E-01	2.4425E-04	7.3776E-04	3.0214
	Pu-241	8.5422E-03	6.3454E-03	1.8712E-02	2.9489
	Pu-242	2.6000E-03	9.3087E-06	2.8659E-05	3.0781
	O-16	1.7557E-05			
	C-12	4.6889E-03			
	Si-29	1.1704E-03			
	B-10				
	B-11				
	B-10 + B-11	7.3309E-04			
		$k_{inf} = 1.3679$			
FCC1		$R_{v_{fis}}$	R_{fis}	$R_{v_{fis}}$	ν
	Pu-238	1.8377E-04	2.4351E-05	7.1595E-05	2.9411
	Pu-239	7.6326E-01	4.6939E-01	1.3485E+00	2.8728
	Pu-240	2.1893E-01	2.4025E-04	7.2423E-04	3.0149
	Pu-241	8.3906E-03	6.2322E-03	1.8377E-02	2.9488
	Pu-242	2.6035E-03	8.9961E-06	2.7650E-05	3.0731
	O-16	1.6175E-05			
	C-12	4.5720E-03			
	Si-29	1.1394E-03			
	10B-10				
	11B-11				
	B-10 + B-11	7.0138E-04			

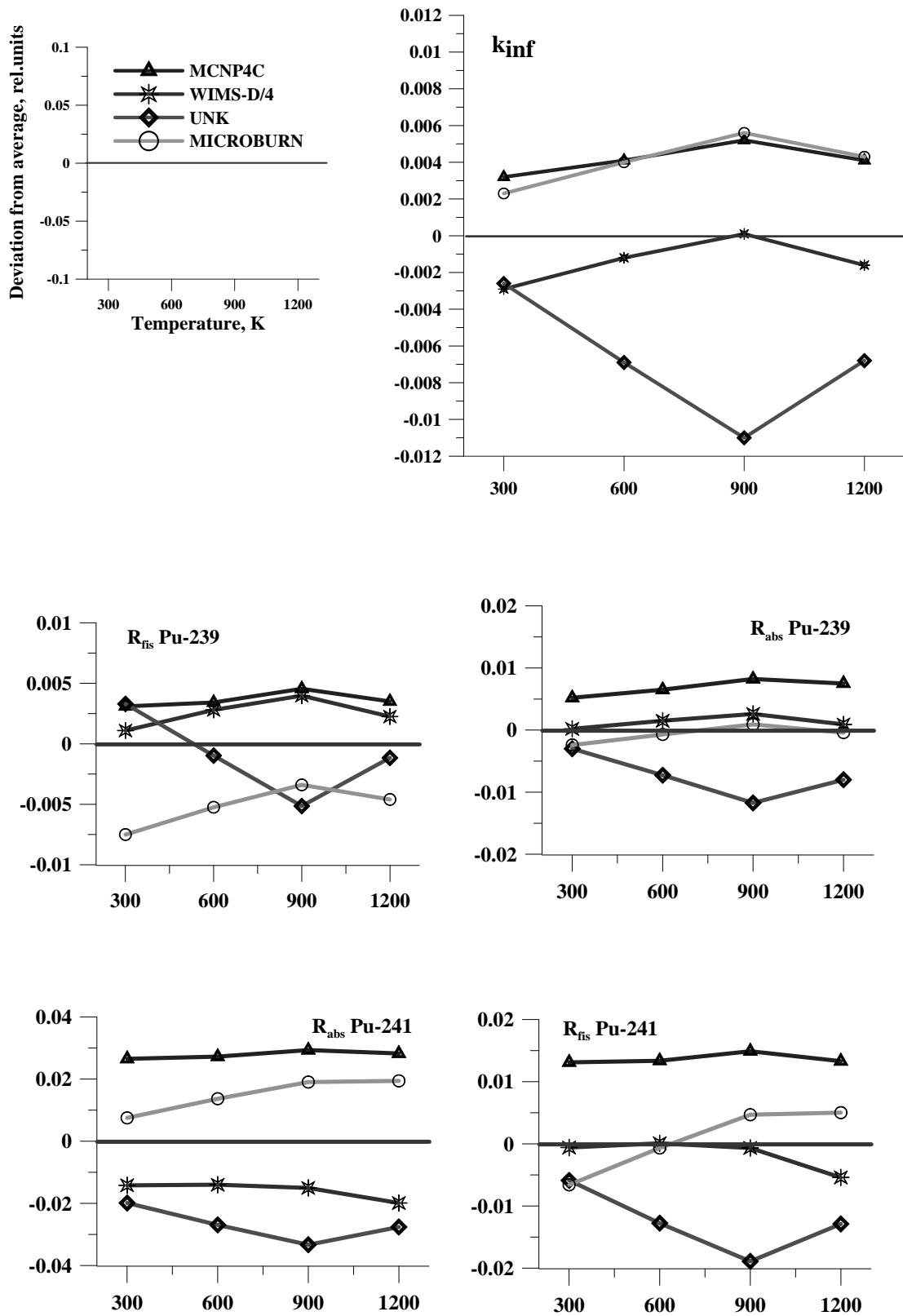


FIG. 6.7. Fresh FCC. Comparison of k_{inf} , R_{abs} and R_{fis} for odd plutonium isotopes.

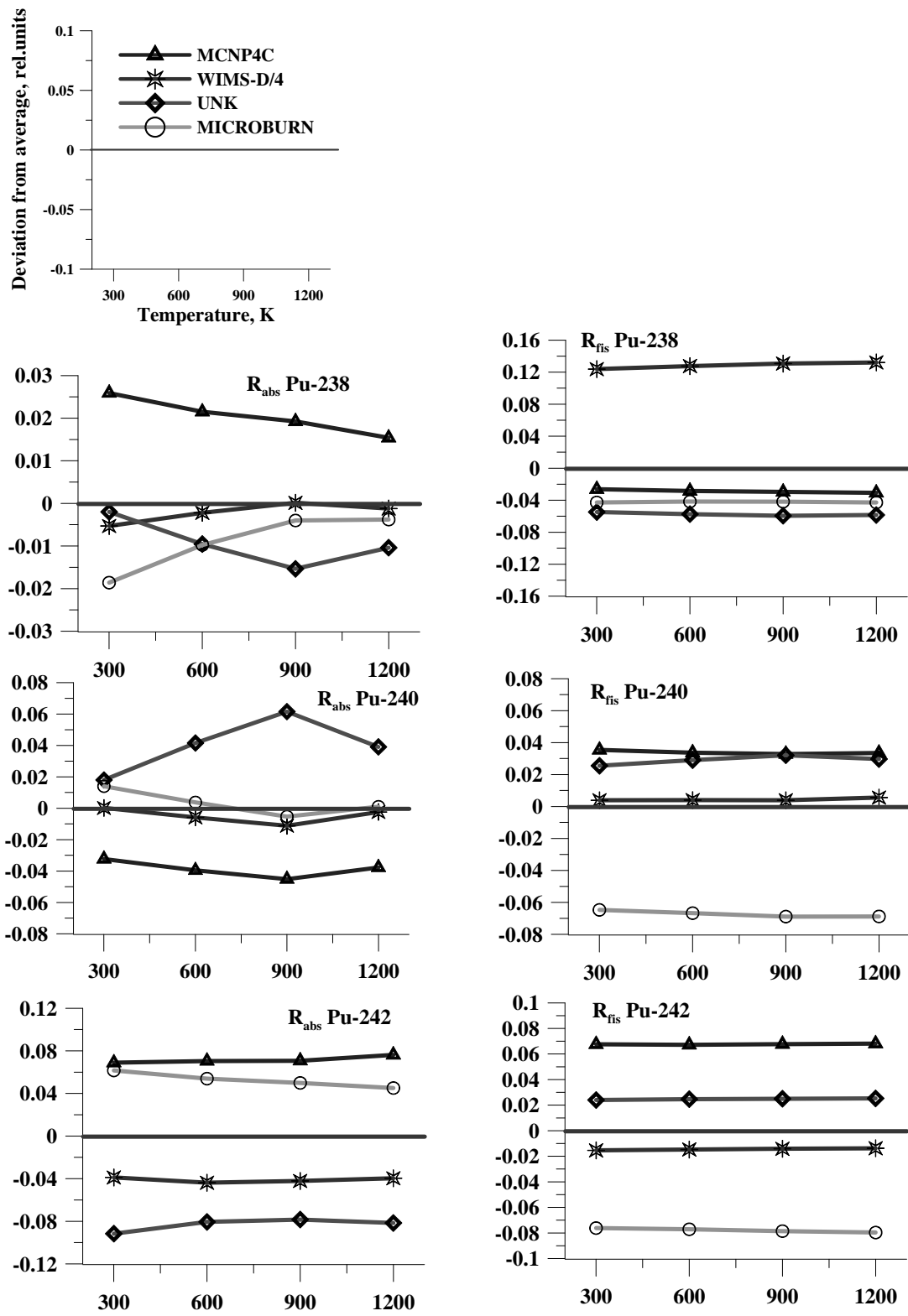


FIG. 6.8. Fresh FCC. Comparison of R_{abs} and R_{fis} for even plutonium isotopes.

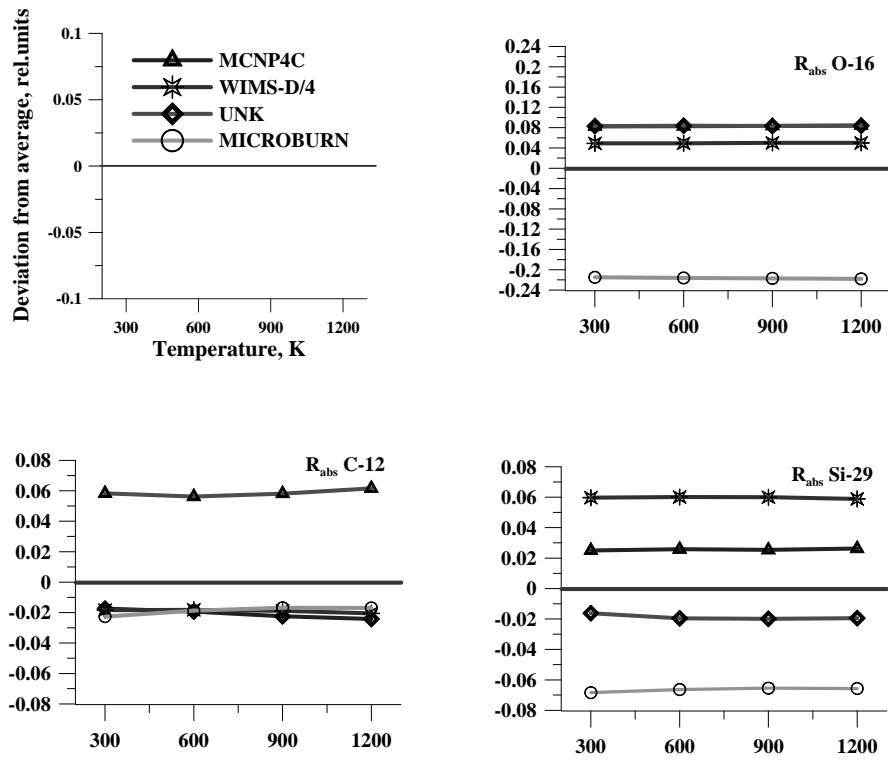


FIG. 6.9. Fresh FCC. Comparison of R_{abs} and R_{fis} for O-16, C-12 and Si-29.

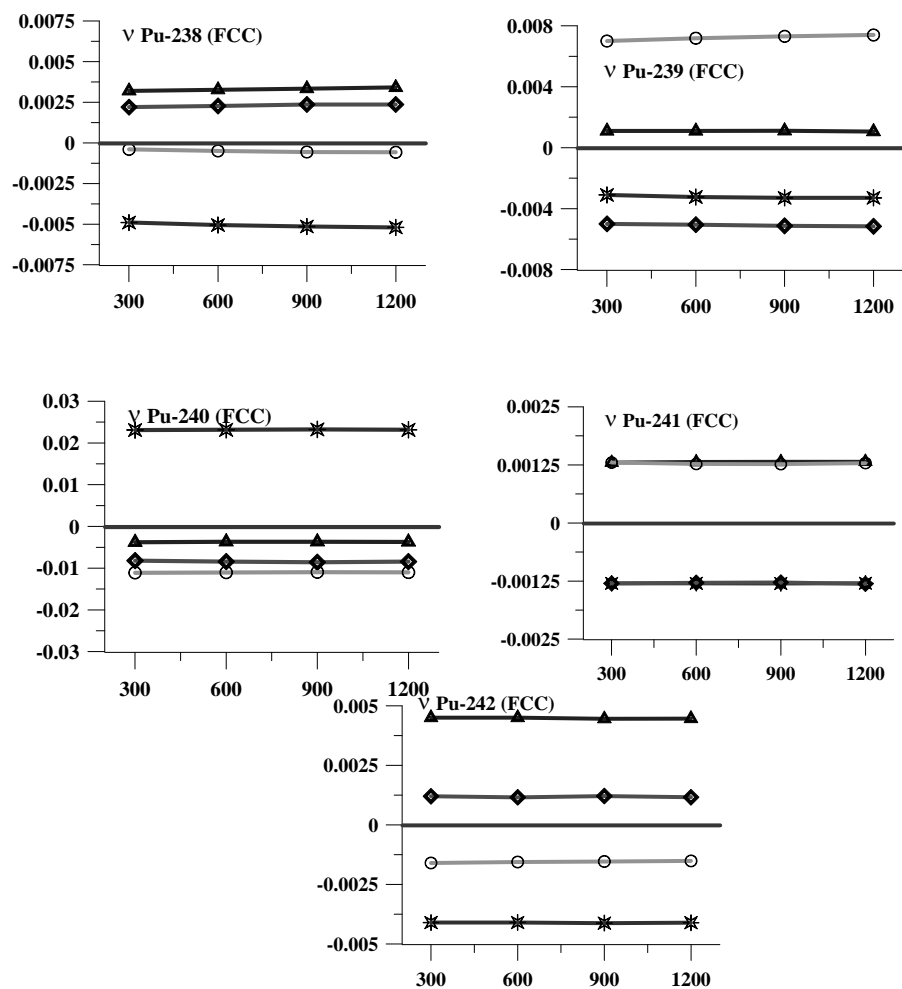


FIG. 6.10. Fresh FCC. Comparison of neutron per fission.

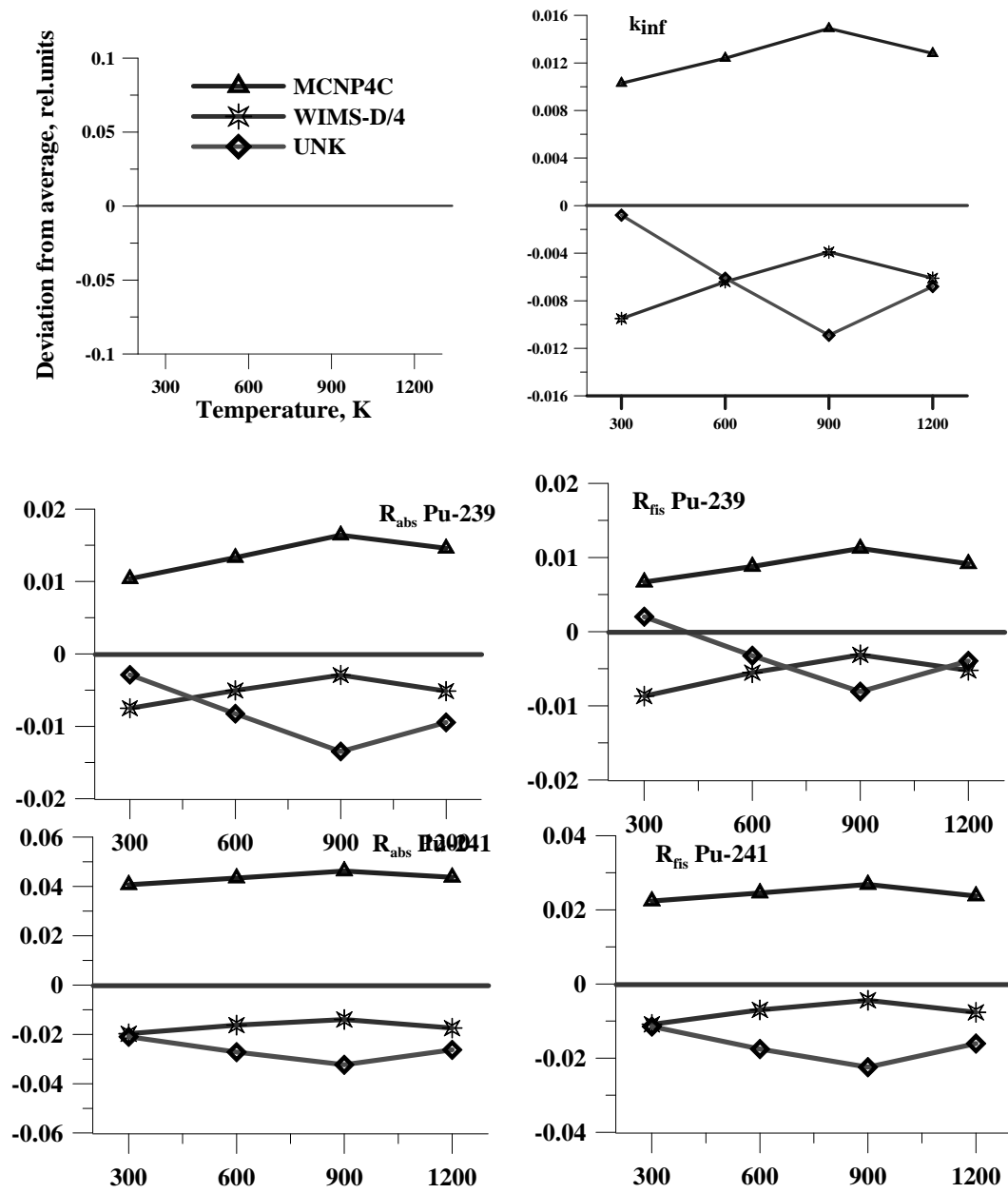


FIG. 6.11. Fresh FCC2. Comparison of k_{inf} , R_{abs} and R_{fis} for odd plutonium isotopes.

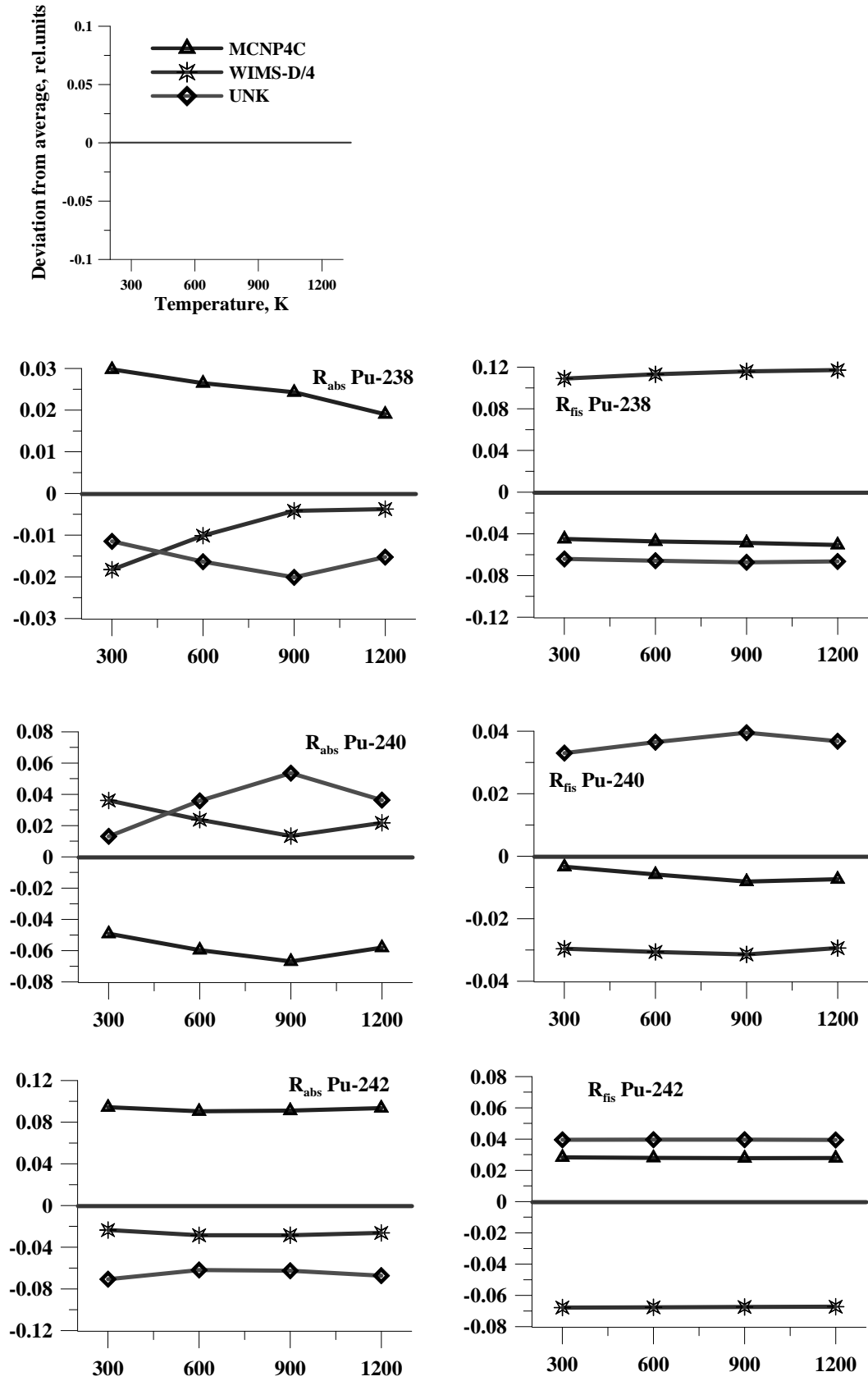


FIG. 6.12. Fresh FCC2. Comparison of R_{abs} and R_{fis} for even plutonium isotopes.

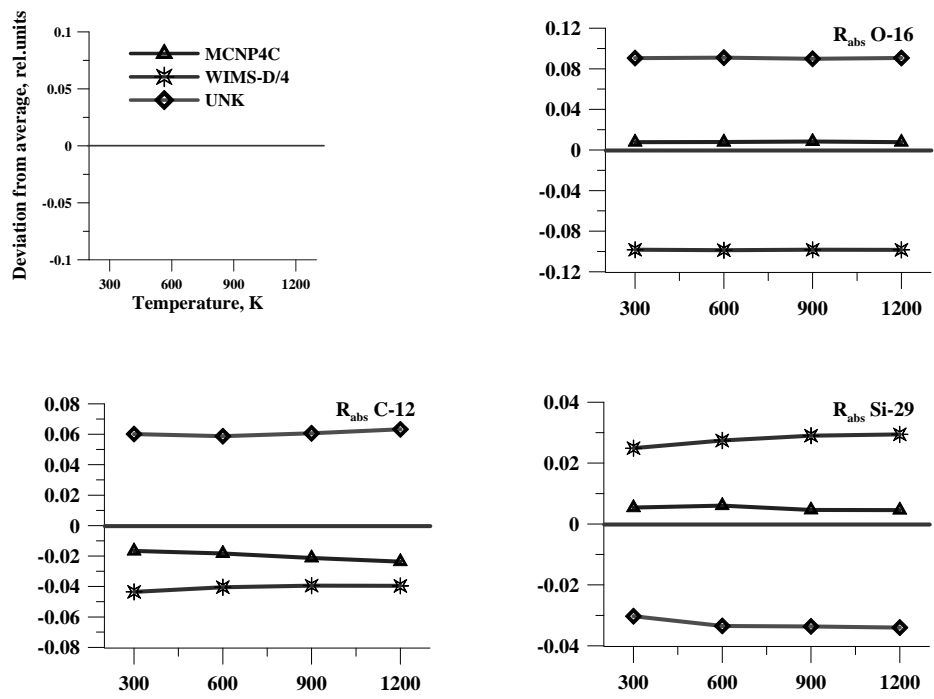


FIG. 6.13. Fresh FCC2. Comparison of R_{abs} and R_{fis} for O-16, C-12 and Si-29.

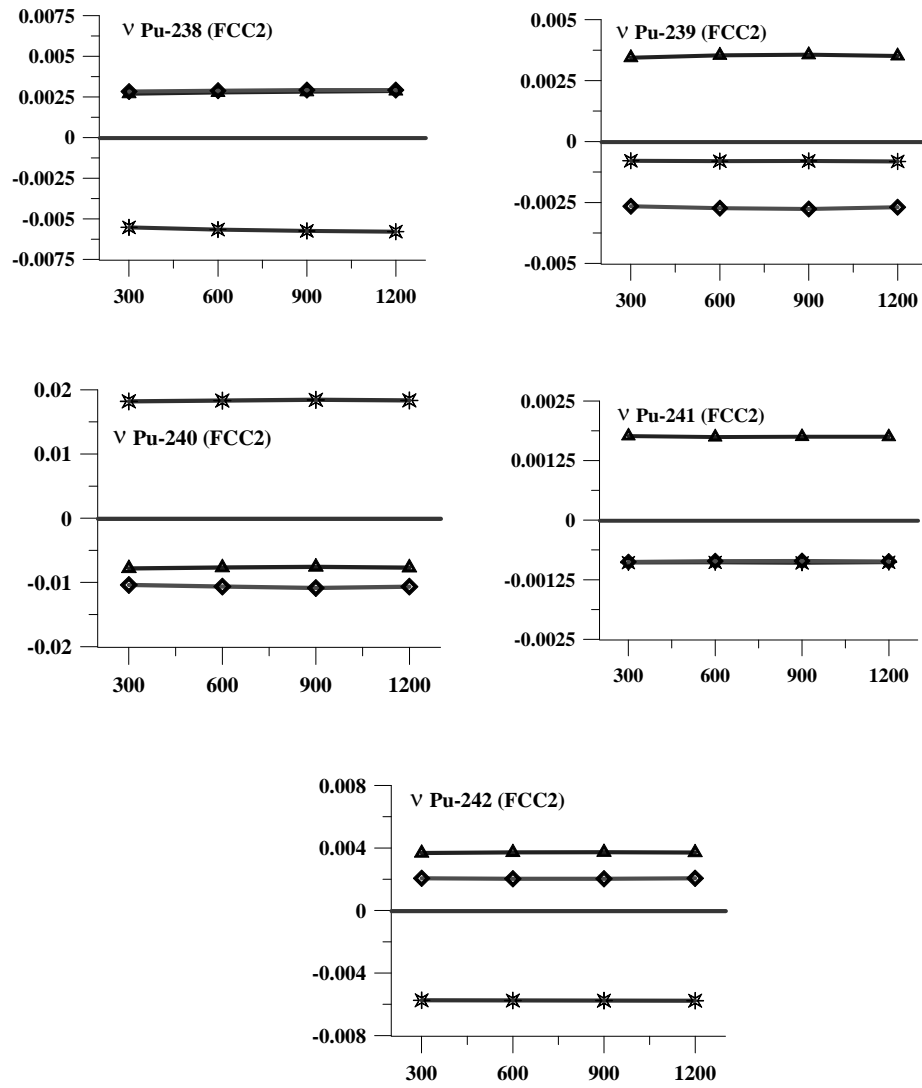


FIG. 6.14. Fresh FCC2. Comparison of neutron per fission.

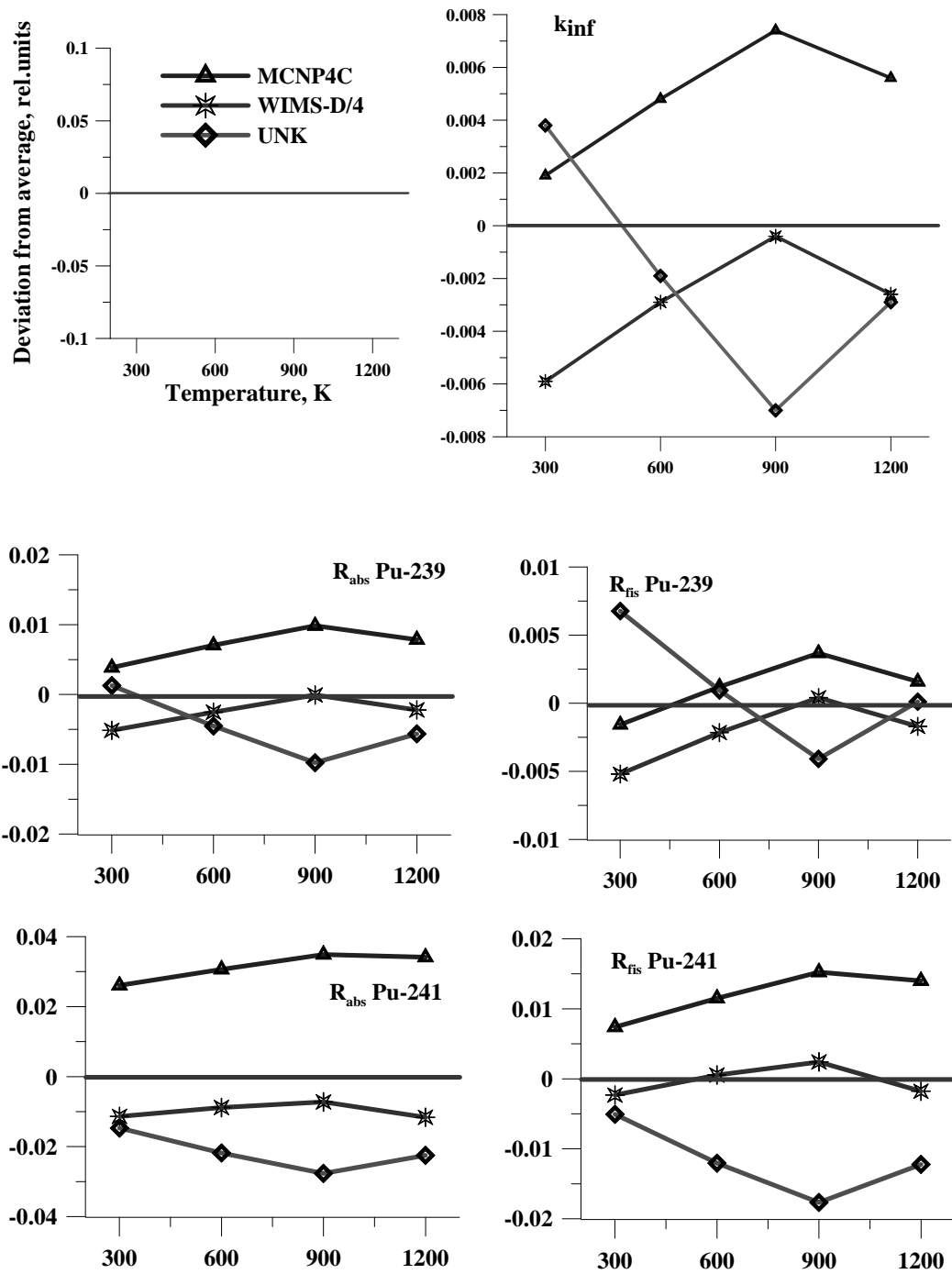


FIG. 6.15. Fresh FCC1. Comparison of k_{inf} , R_{abs} and R_{fis} for odd plutonium isotopes.

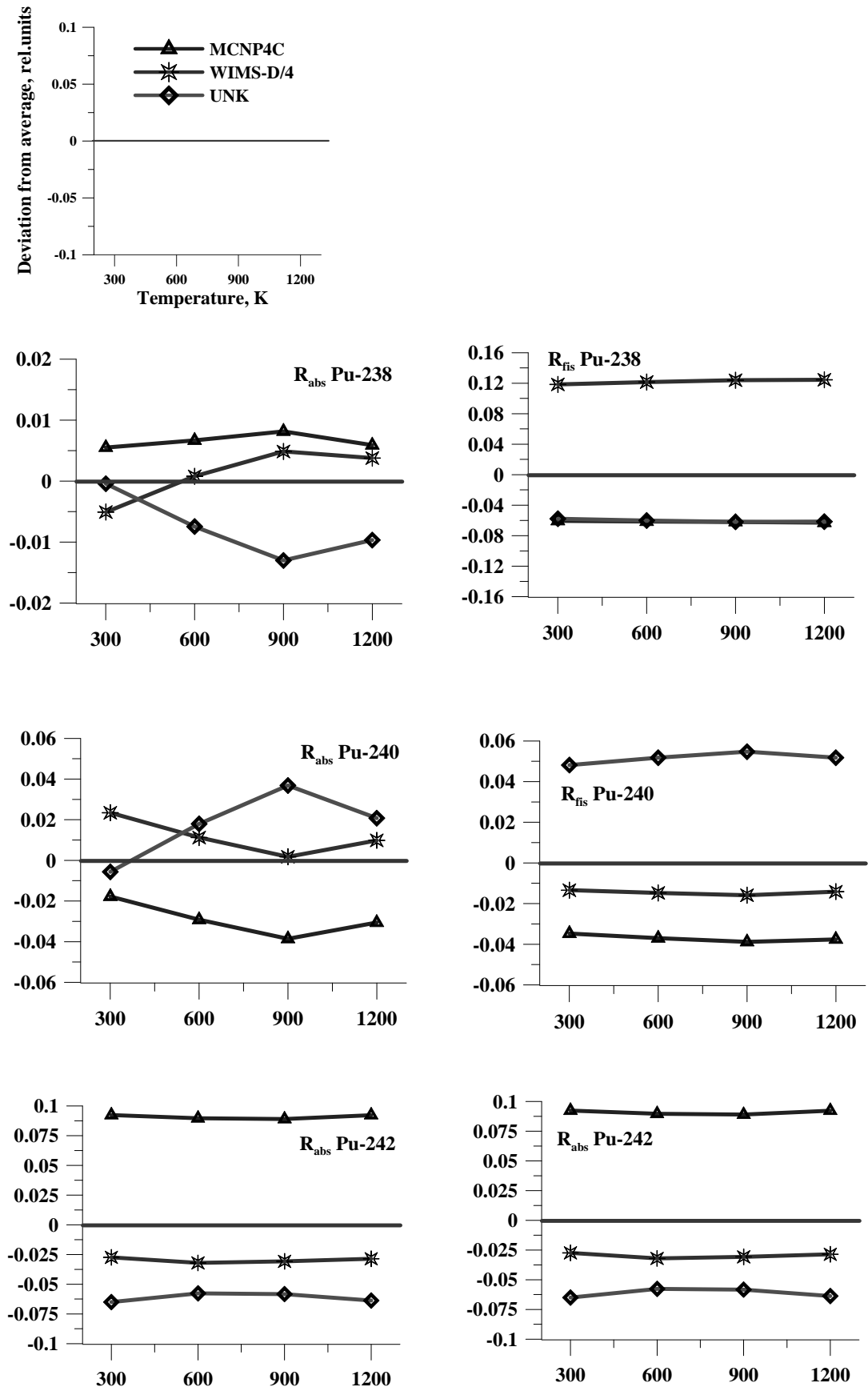


FIG. 6.16. Fresh FCCI. Comparison of R_{abs} and R_{fis} for even plutonium isotopes.

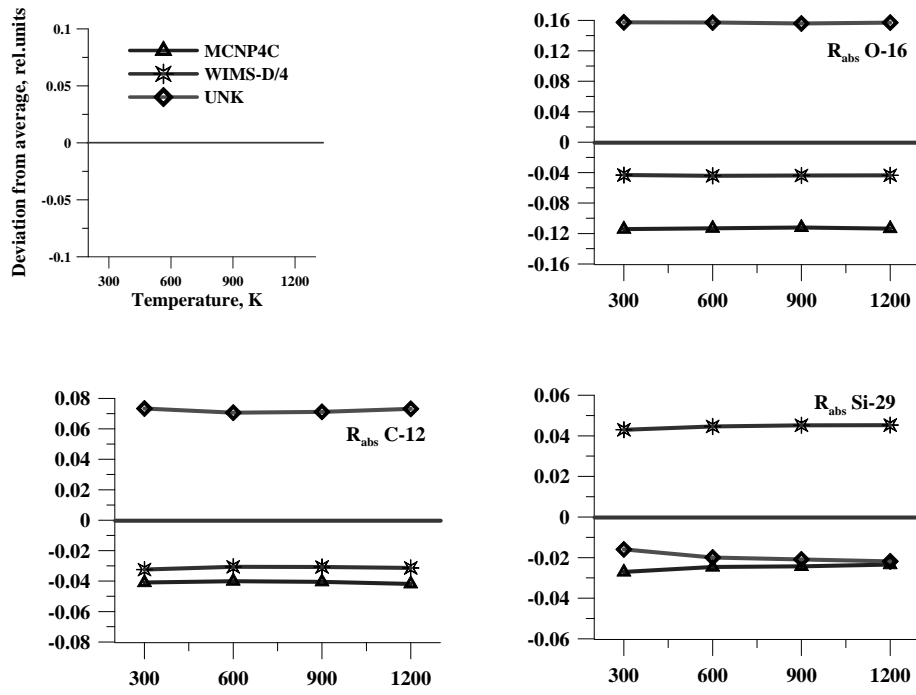


FIG. 6.17. Fresh FCCI. Comparison of R_{abs} and R_{fis} for O-16, C-12 and Si-29.

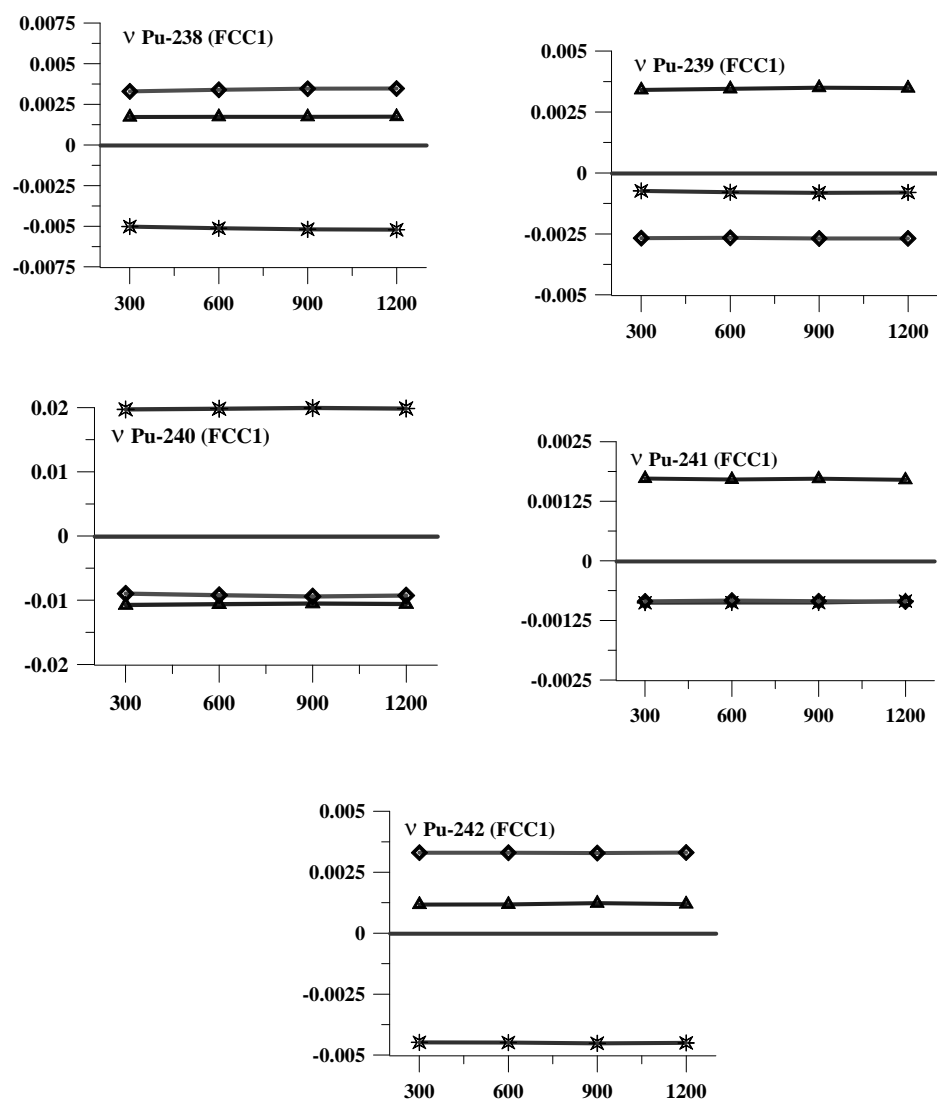


FIG. 6.18. Fresh FCC1. Comparison of neutron per fission.

TABLE 6.30(A). AVERAGED VALUES OF NEUTRONIC FUNCTIONALS
FOR FCC AS A FUNCTION OF BURNUP (0 AND 5 DAYS)

0 days					
$k_{inf}=1.4645$					
Isotope	Isotopic content*10 ⁻²⁴ /cm ³	R _{abs}	R _{fis}	R _{vfis}	ν
Pu-238	5.0556E-08	2.0461E-04	2.5128E-05	7.4003E-05	2.9457
Pu-239	3.5519E-05	8.0972E-01	5.0087E-01	1.4427E+00	2.8804
Pu-240	2.5259E-06	1.7063E-01	2.4402E-04	7.3829E-04	3.0252
Pu-241	4.4933E-07	9.2989E-03	6.8829E-03	2.0305E-02	2.9501
Pu-242	1.6446E-07	2.6501E-03	9.7554E-06	3.0096E-05	3.0846
Am-241					
Am-243					
Cm-242					
Cm-243					
Cm-244					
Cm-245					
Xe-135					
Sm-149					
O-16	6.5807E-05	1.9064E-05			
C-12	5.8940E-02	5.2577E-03			
Si-29	5.5112E-04	1.3345E-03			
B-10 + B-11	6.7776E-08	8.9197E-04			
5 days					
$k_{inf}=1.4395$					
Isotope	Isotopic Content*10 ⁻²⁴ /cm ³	R _{abs}	R _{fis}	R _{vfis}	ν
Pu-238	5.0543E-08	2.0196E-04	2.6077E-05	7.6678E-05	2.9415
Pu-239	3.5280E-05	7.9648E-01	4.9302E-01	1.4163E+00	2.8727
Pu-240	2.5743E-06	1.7264E-01	2.4849E-04	7.5753E-04	3.0498
Pu-241	5.0402E-07	1.0233E-02	7.6300E-03	2.2495E-02	2.9482
Pu-242	1.6458E-07	2.6093E-03	9.6574E-06	2.9783E-05	3.0834
Am-241	3.0985E-10	8.6628E-06	6.6674E-08	2.1911E-07	3.2856
Am-243	8.6471E-10	2.1821E-05	6.3238E-08	2.2149E-07	3.5116
Cm-242	8.5006E-13	1.6215E-09	1.8253E-10	6.1784E-10	3.5428
Cm-243	1.0300E-16	4.8788E-12	4.3393E-12	1.4890E-11	3.4319
Cm-244	3.3571E-12	2.8084E-08	6.6892E-10	2.3088E-09	3.4303
Cm-245	2.0541E-15	5.6642E-11	4.9963E-11	1.8025E-10	3.6077
Xe-135	1.0078E-09	8.9293E-03			
Sm-149	1.4800E-09	4.9358E-04			
O-16	6.5864E-05	1.9978E-05			
C-12	7.2111E-02	4.7973E-03			
Si-29	5.5191E-04	1.3642E-03			
B-10 + B-11	6.3853E-08	8.7104E-04			

TABLE 6.30(B). AVERAGED VALUES OF NEUTRONIC FUNCTIONALS
FOR FCC AS A FUNCTION OF BURNUP (250 AND 500 DAYS)

250 days					
$k_{inf}=1.3006$					
Isotope	Isotopic Content* $10^{-24}/\text{cm}^3$	R_{abs}	R_{fis}	R_{vfis}	ν
Pu-238	4.8482E-08	2.1699E-04	2.5859E-05	7.5994E-05	2.9398
Pu-239	2.2646E-05	6.3704E-01	3.9282E-01	1.1282E+00	2.8720
Pu-240	3.8682E-06	2.1499E-01	3.6490E-04	1.1140E-03	3.0541
Pu-241	3.2192E-06	7.6634E-02	5.6917E-02	1.6779E-01	2.9480
Pu-242	3.0331E-07	4.7352E-03	1.7562E-05	5.4165E-05	3.0834
Am-241	4.9730E-08	1.5225E-03	1.1467E-05	3.7625E-05	3.2792
Am-243	5.0557E-08	1.2426E-03	3.6201E-06	1.2689E-05	3.5117
Cm-242	5.8002E-09	1.1122E-05	1.1310E-06	3.8468E-06	3.5338
Cm-243	3.6107E-11	1.5617E-06	1.3886E-06	4.7650E-06	3.4318
Cm-244	9.9720E-09	8.1220E-05	1.9825E-06	6.8681E-06	3.4289
Cm-245	3.2308E-10	9.3040E-06	8.1999E-06	2.9582E-05	3.6076
Xe-135	8.9354E-10	1.0446E-02			
Sm-149	1.7002E-08	7.1767E-03			
O-16	6.5864E-05	1.9981E-05			
C-12	7.2111E-02	5.1546E-03			
Si-29	5.5191E-04	1.4748E-03			
B-10 + B-11	6.3853E-08	9.6140E-04			
500 days					
$k_{inf}=1.2252$					
Isotope	Isotopic content * $10^{-24}/\text{cm}^3$	R_{abs}	R_{fis}	R_{vfis}	ν
Pu-238	5.2909E-08	3.4958E-04	3.5041E-05	1.0285E-04	2.9362
Pu-239	1.1632E-05	4.8661E-01	2.9950E-01	8.5997E-01	2.8713
Pu-240	3.8026E-06	2.2010E-01	3.6074E-04	1.1010E-03	3.0529
Pu-241	5.0194E-06	1.6494E-01	1.2175E-01	3.5888E-01	2.9478
Pu-242	7.7034E-07	1.1865E-02	4.4330E-05	1.3672E-04	3.0832
Am-241	1.2733E-07	4.8823E-03	3.4873E-05	1.1394E-04	3.2649
Am-243	1.6221E-07	4.0025E-03	1.1542E-05	4.0437E-05	3.5104
Cm-242	3.0913E-08	6.2293E-05	6.4684E-06	2.1960E-05	3.5124
Cm-243	3.7078E-10	1.7260E-05	1.5367E-05	5.2734E-05	3.4317
Cm-244	5.3161E-08	4.3436E-04	1.0612E-05	3.6730E-05	3.4251
Cm-245	2.9223E-09	1.0597E-04	9.3312E-05	3.3660E-04	3.6072
Xe-135	7.0352E-10	1.3679E-02			
Sm-149	1.2347E-08	8.3941E-03			
O-16	6.5864E-05	2.0012E-05			
C-12	7.2111E-02	6.1935E-03			
Si-29	5.5191E-04	1.8001E-03			
B-10 + B-11	6.3853E-08	1.2291E-03			

TABLE 6.30(C). AVERAGED VALUES OF NEUTRONIC FUNCTIONALS
FOR FCC IN DEPENDENCE ON BURNUP (750 DAYS)

750 days					
$k_{inf} = 1.1601$					
Isotope	Isotopic content*10 ⁻²⁴ /cm ³	R _{abs}	R _{fis}	R _{vfis}	v
Pu-238	9.0914E-08	1.0630E-03	7.4730E-05	2.1867E-04	2.9270
Pu-239	3.4116E-06	2.9568E-01	1.8222E-01	5.2310E-01	2.8706
Pu-240	2.5972E-06	1.9627E-01	2.5544E-04	7.7787E-04	3.0451
Pu-241	4.5577E-06	2.9059E-01	2.1298E-01	6.2776E-01	2.9475
Pu-242	1.6511E-06	2.5441E-02	9.4633E-05	2.9183E-04	3.0829
Am-241	1.4489E-07	9.2232E-03	6.0340E-05	1.9561E-04	3.2390
Am-243	4.0453E-07	1.0620E-02	2.9297E-05	1.0244E-04	3.5058
Cm-242	7.7225E-08	1.7622E-04	1.9733E-05	6.6713E-05	3.4658
Cm-243	1.3446E-09	7.8485E-05	7.0125E-05	2.4063E-04	3.4315
Cm-244	1.7910E-07	1.5094E-03	3.7212E-05	1.2842E-04	3.4163
Cm-245	1.1410E-08	7.1653E-04	6.2992E-04	2.2719E-03	3.6066
Xe-135	3.9838E-10	1.8835E-02			
Sm-149	6.2075E-09	9.9031E-03			
O-16	6.5864E-05	2.0103E-05			
C-12	7.2111E-02	9.7471E-03			
Si-29	5.5191E-04	2.9209E-03			
B-10 + B-11	6.3853E-08	2.1536E-03			

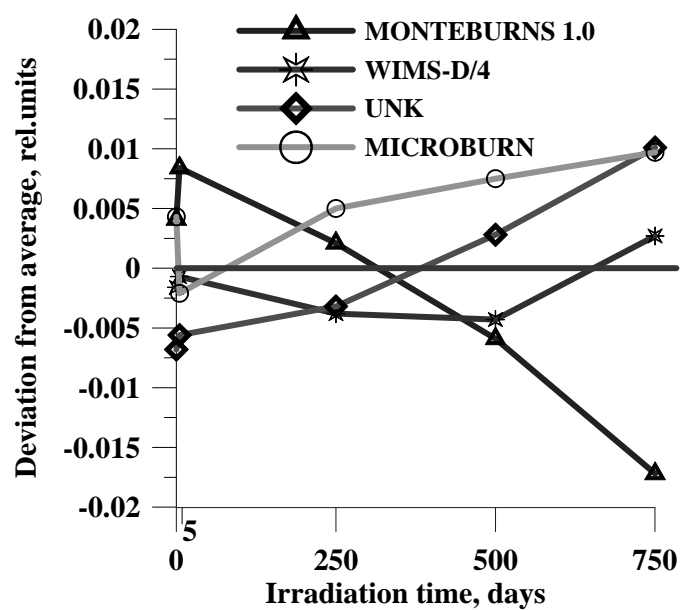


FIG. 6.19. Deviation of k_{inf} value from average in FCC as a function of burnup.

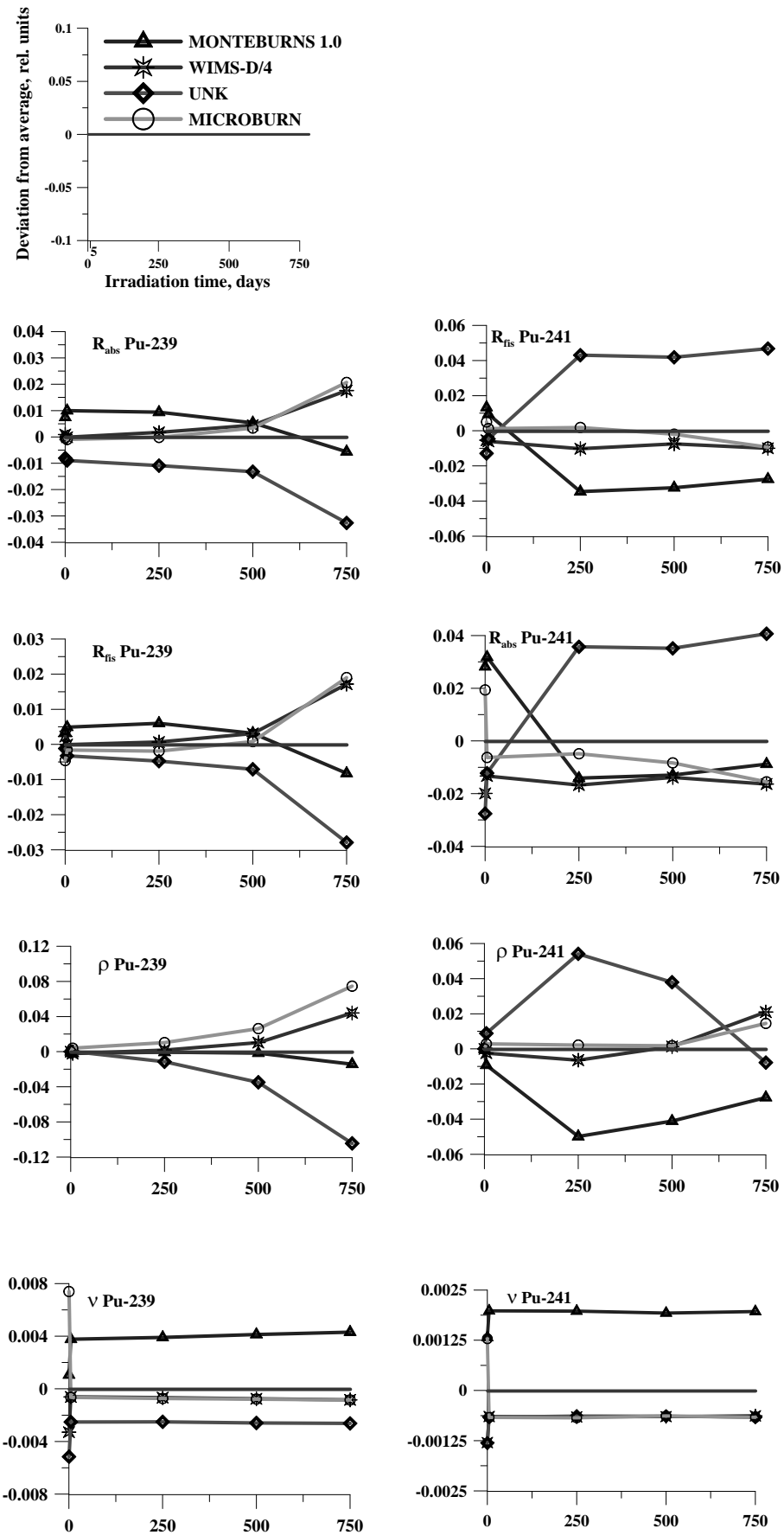


FIG. 6.20. FCC, R_{abs} , R_{fis} . Concentrations and neutron per fission for odd plutonium isotopes as a function of burnup.

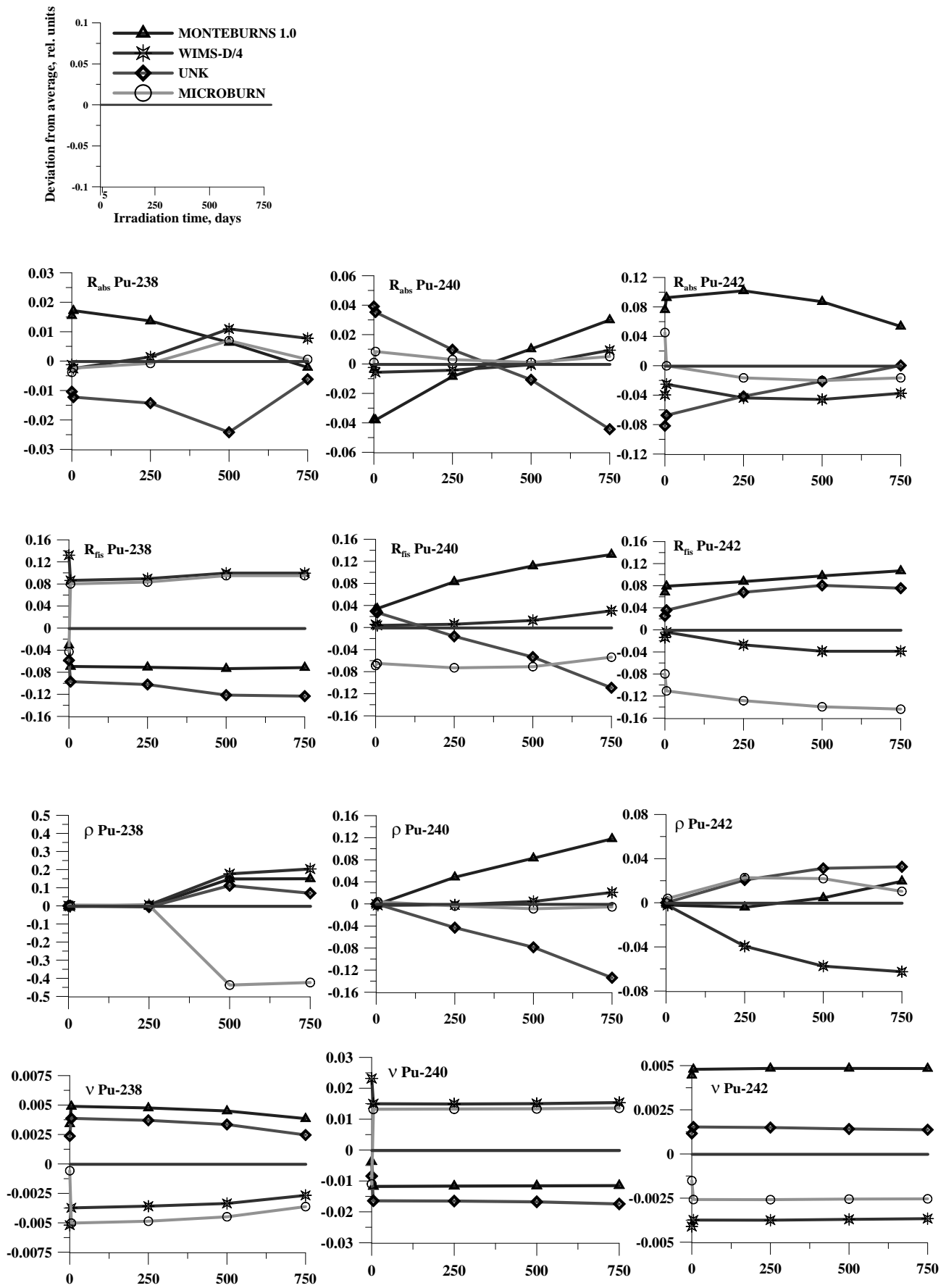


FIG. 6.21. FCC. R_{abs} , R_{fis} . Concentrations and neutron per fission for even plutonium isotopes as a function of burnup.

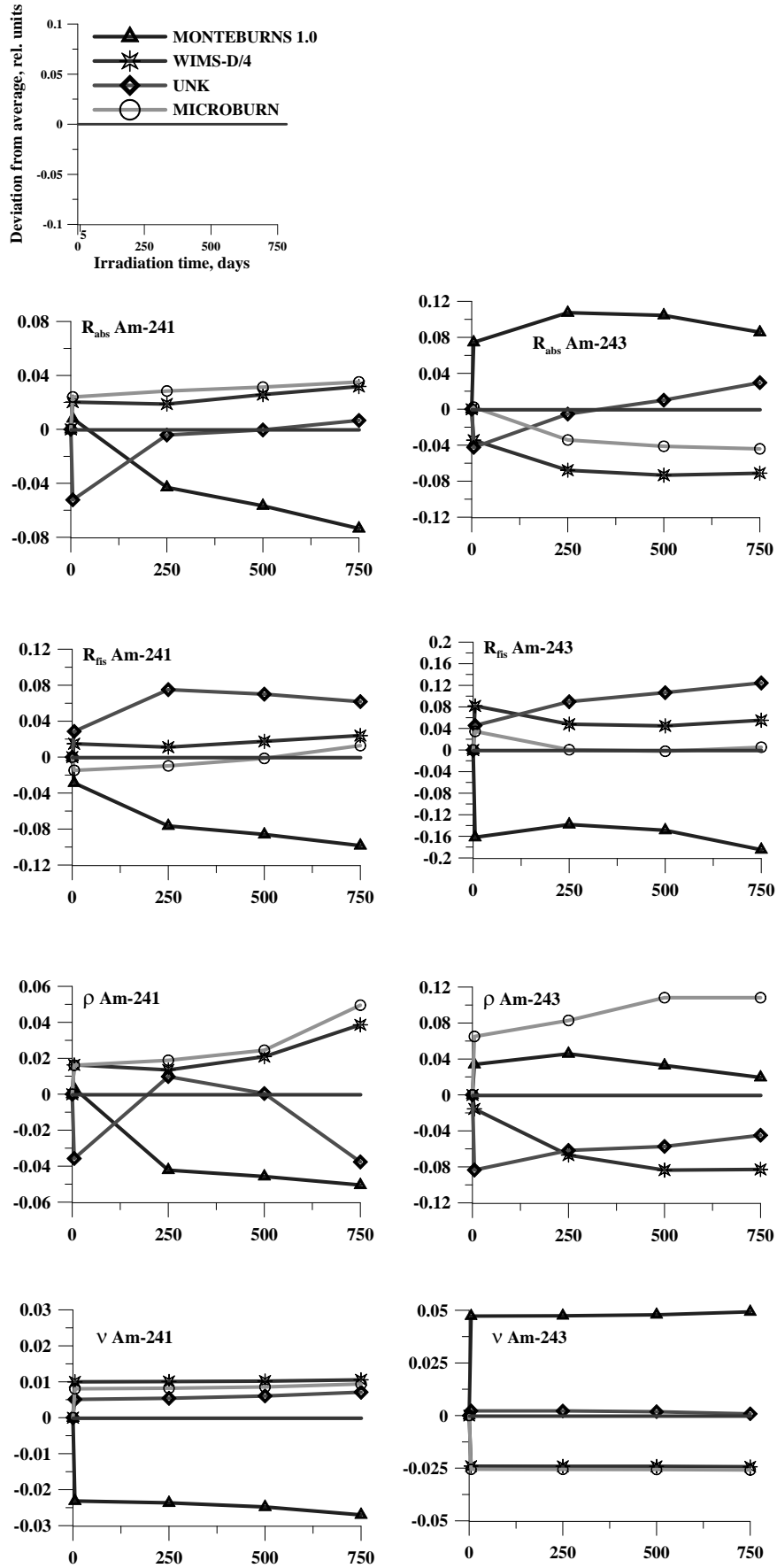


FIG. 6.22. FCC, R_{abs} , R_{fis} . Concentrations and neutron per fission for americium isotopes as a function of burnup.

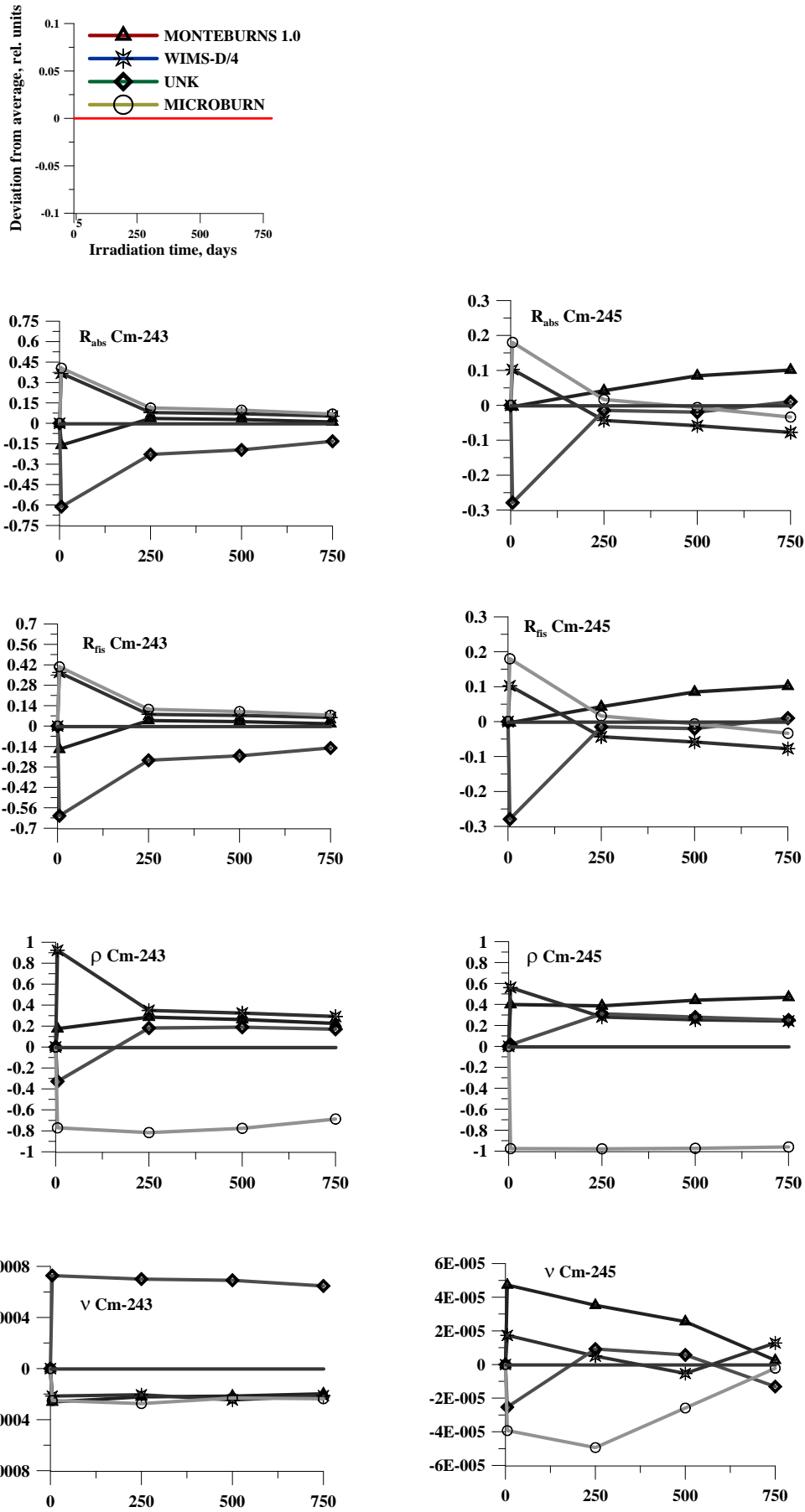


FIG 6.23. FCC. Comparison of R_{abs} , R_{fis} , Concentrations and neutron per fission for odd curium isotopes as a function of burnup.

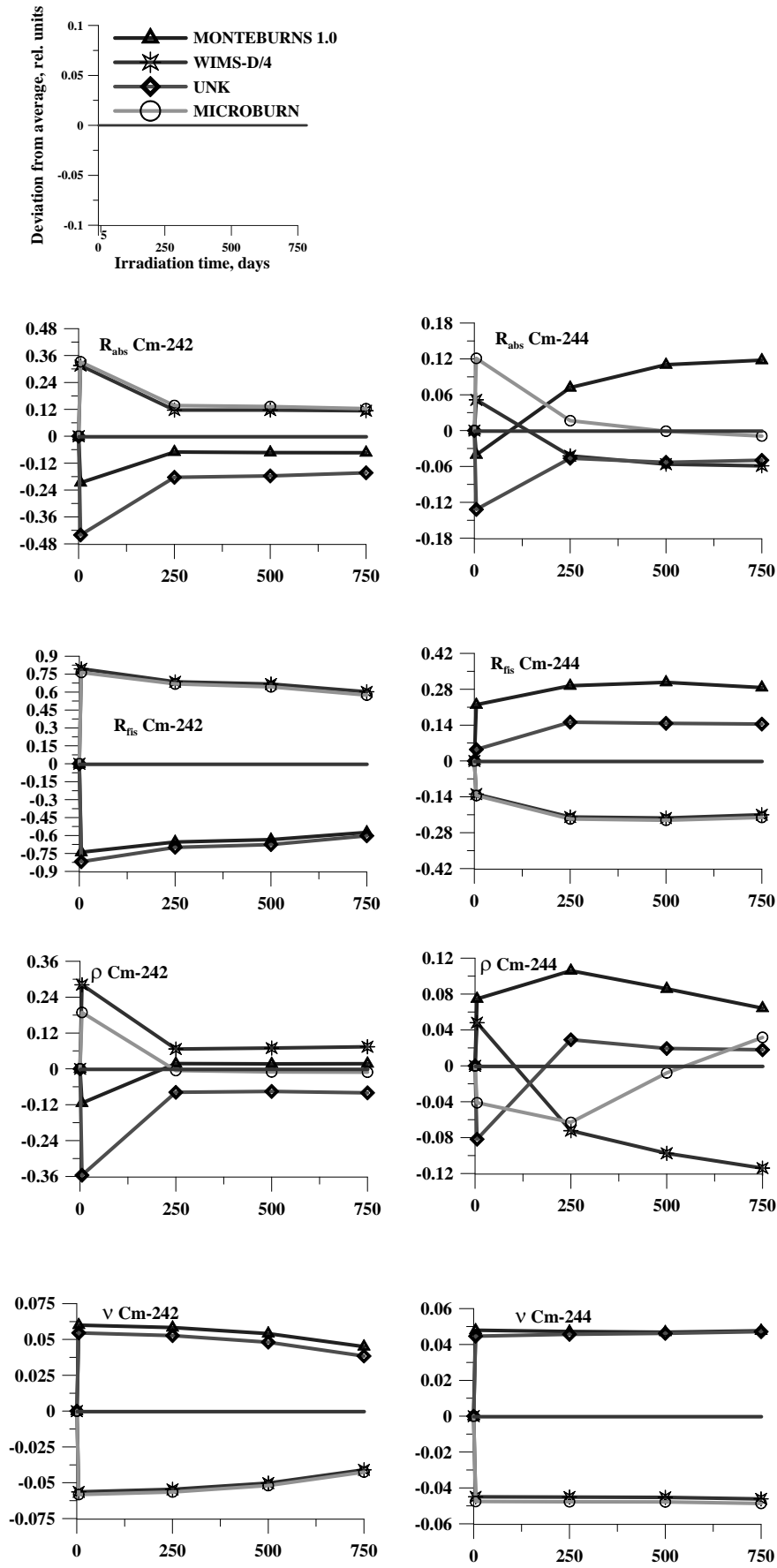


FIG. 6.24. FCC. Comparison of R_{abs} , R_{fis} , Concentrations and neutron per fission for even curium isotopes as a function of burnup.

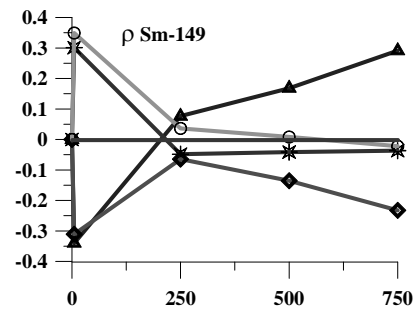
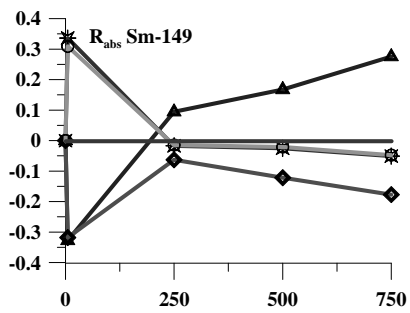
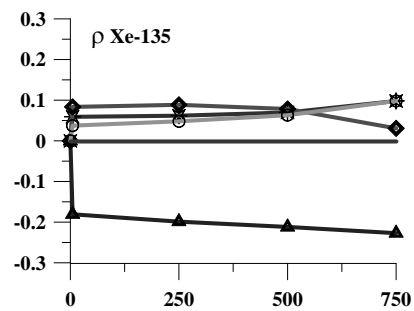
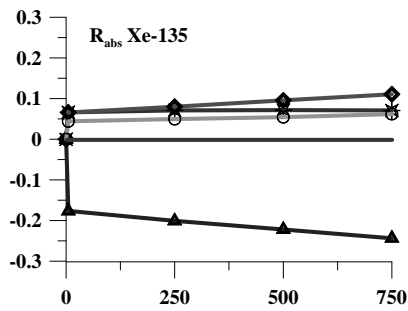
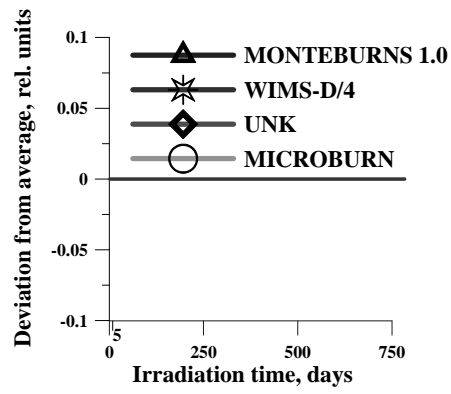


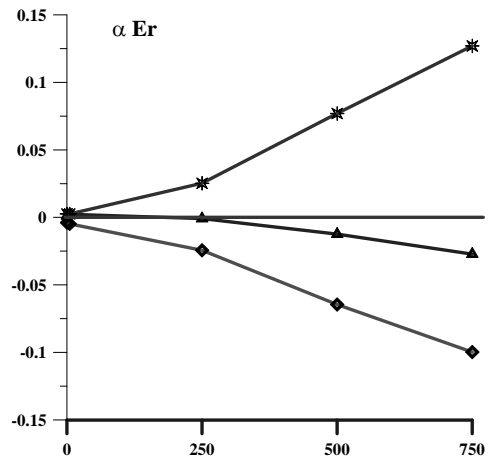
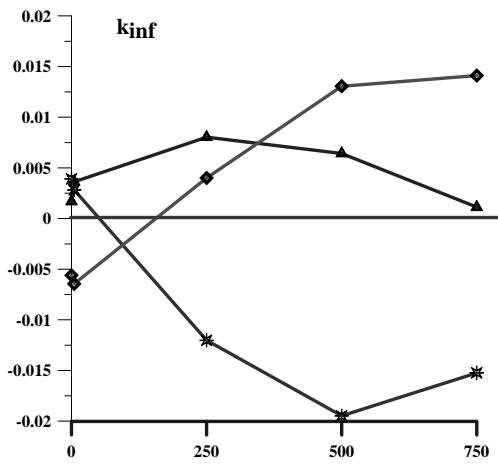
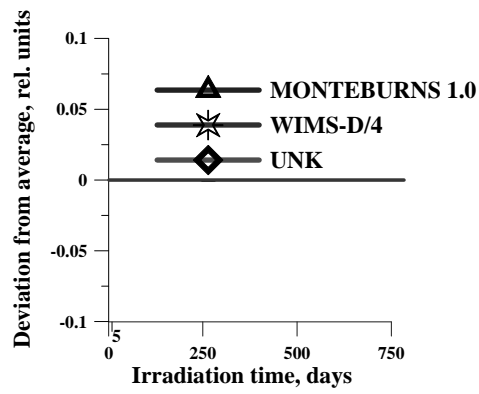
FIG. 6.25. FCC. Comparison of R_{abs} . Concentrations for xenon-135 and amarium-149 as a function of burnup.

TABLE 6.31. AVERAGED VALUES OF NEUTRONIC FUNCTIONALS FOR HOMOGENEOUS BPC IN DEPENDENCE ON BURNUP

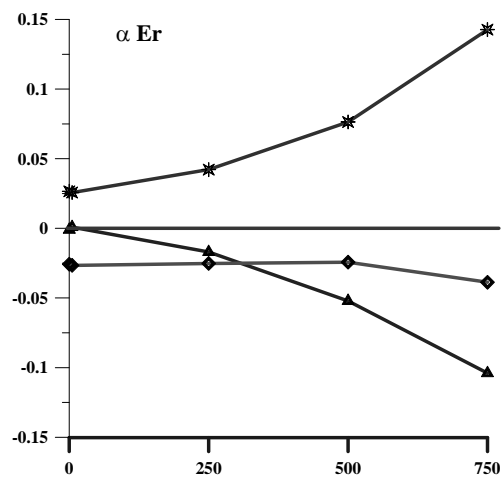
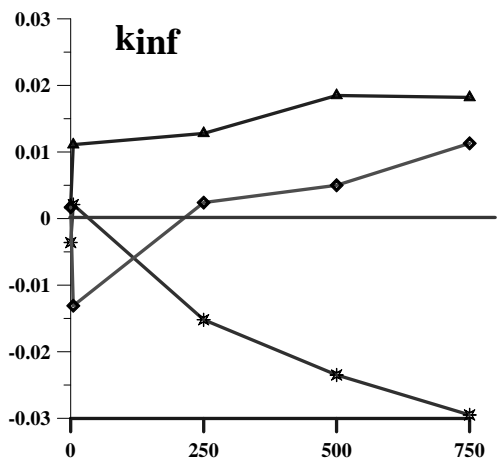
Variant	Irradiation time (eff.days)				
BPC-hom-1200	0.0	k _{inf} = 1.1244			
		Isotope	Isotopic content*10 ⁻²⁴ /cm ³	R _{abs}	α ^{Er}
		Er-166	4.1403E-04	5.0276E-02	1.9067E-01
		Er-167	2.8280E-04	9.1803E-01	
		Er-168	3.3024E-04	3.1697E-02	
		Sum	1.0000E+00		
	5.0	k _{inf} = 1.1118			
		Isotope	Isotopic content *10 ⁻²⁴ /cm ³	R _{abs}	α ^{Er}
		Er-166	4.1377E-04	5.0619E-02	1.8928E-01
		Er-167	2.7997E-04	9.1720E-01	
		Er-168	3.3307E-04	3.2177E-02	
		Sum	1.0000E+00		
	250.0	k _{inf} = 1.0674			
		Isotope	Isotopic content*10 ⁻²⁴ /cm ³	R _{abs}	α ^{Er}
		Er-166	4.0456E-04	6.1449E-02	1.5712E-01
		Er-167	1.5985E-04	8.8731E-01	
		Er-168	4.5660E-04	5.1242E-02	
		Sum	1.0000E+00		
	500.0	k _{inf} =1.1001			
		Isotope	Isotopic content*10 ⁻²⁴ /cm ³	R _{abs}	α ^{Er}
Er-166		3.9492E-04	8.6869E-02	1.1821E-01	
Er-167		6.8568E-05	8.3113E-01		
Er-168		5.4998E-404	8.1999E-02		
Sum		1.0000E+00			
750.0	k _{inf} =1.1314				
	Isotope	Isotopic content*10 ⁻²⁴ /cm ³	R _{abs}	α ^{Er}	
	Er-166	3.8464E-04	1.6706E-01	7.6006E-02	
	Er-167	1.8307E-05	6.7874E-01		
	Er-168	6.0174E-04	1.5419E-01		
	Sum	1.0000E+00			

TABLE 6.32. AVERAGED VALUES OF NEUTRONIC FUNCTIONALS FOR HETEROGENEOUS BPC IN DEPENDENCE ON BURNUP

Variant	Irradiation time (eff.days)				
BPC-hom-1200	0.0	k _{inf} = 1.1559			
		Isotope	Isotopic content*10 ⁻²⁴ /cm ³	R _{abs}	α ^{Er}
		Er-166	9.1411E-03	5.4193E-02	1.7153E-01
		Er-167	6.2437E-03	9.1236E-01	
		Er-168	7.2911E-03	3.3453E-02	
		Sum	1.0000E+00		
	5.0	k _{inf} = 1.1347			
		Isotope	Isotopic content*10 ⁻²⁴ /cm ³	R _{abs}	α ^{Er}
		Er-166	9.1367E-03	5.4543E-02	1.7056E-01
		Er-167	6.1941E-03	9.1158E-01	
		Er-168	7.3410E-03	3.3872E-02	
		Sum	1.0000E+00		
	250.0	k _{inf} = 1.0782			
		Isotope	Isotopic content*10 ⁻²⁴ /cm ³	R _{abs}	α ^{Er}
		Er-166	8.9492E-03	6.4527E-02	1.5139E-01
		Er-167	3.9082E-03	8.8240E-01	
		Er-168	9.6926E-03	5.3070E-02	
		Sum	1.0000E+00		
	500.0	k _{inf} = 1.0865			
		Isotope	Isotopic content*10 ⁻²⁴ /cm ³	R _{abs}	α ^{Er}
Er-166		8.7430E-03	8.2151E-02	1.2854E-01	
Er-167		1.9346E-03	8.3875E-01		
Er-168		1.1702E-02	7.9098E-02		
Sum		1.0000E+00			
750.0	k _{inf} = 1.1122				
	Isotope	Isotopic content*10 ⁻²⁴ /cm ³	R _{abs}	α ^{Er}	
	Er-166	8.5187E-03	1.3714E-01	9.3152E-02	
	Er-167	5.9158E-04	7.2962E-01		
	Er-168	1.3060E-02	1.3324E-01		
	Sum	1.0000E+00			



Homogeneous BPC



Heterogeneous BPC

FIG. 6.26. Deviation of k_{inf} and fraction of absorption in erbium from averaged values.

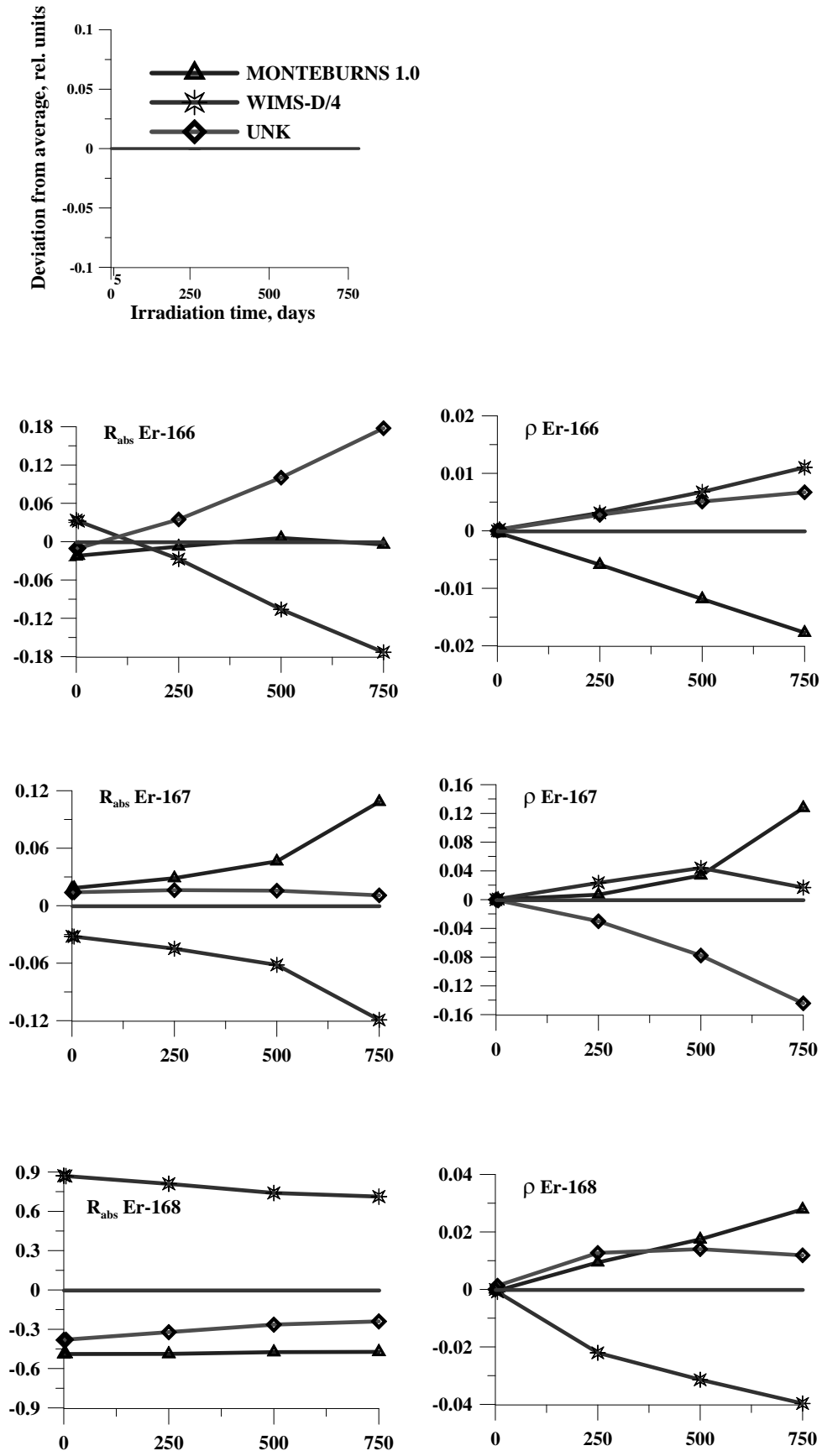


FIG. 6.27. Homogenous BPC — deviation of R_{abs} and erbium isotopic content from averaged values.

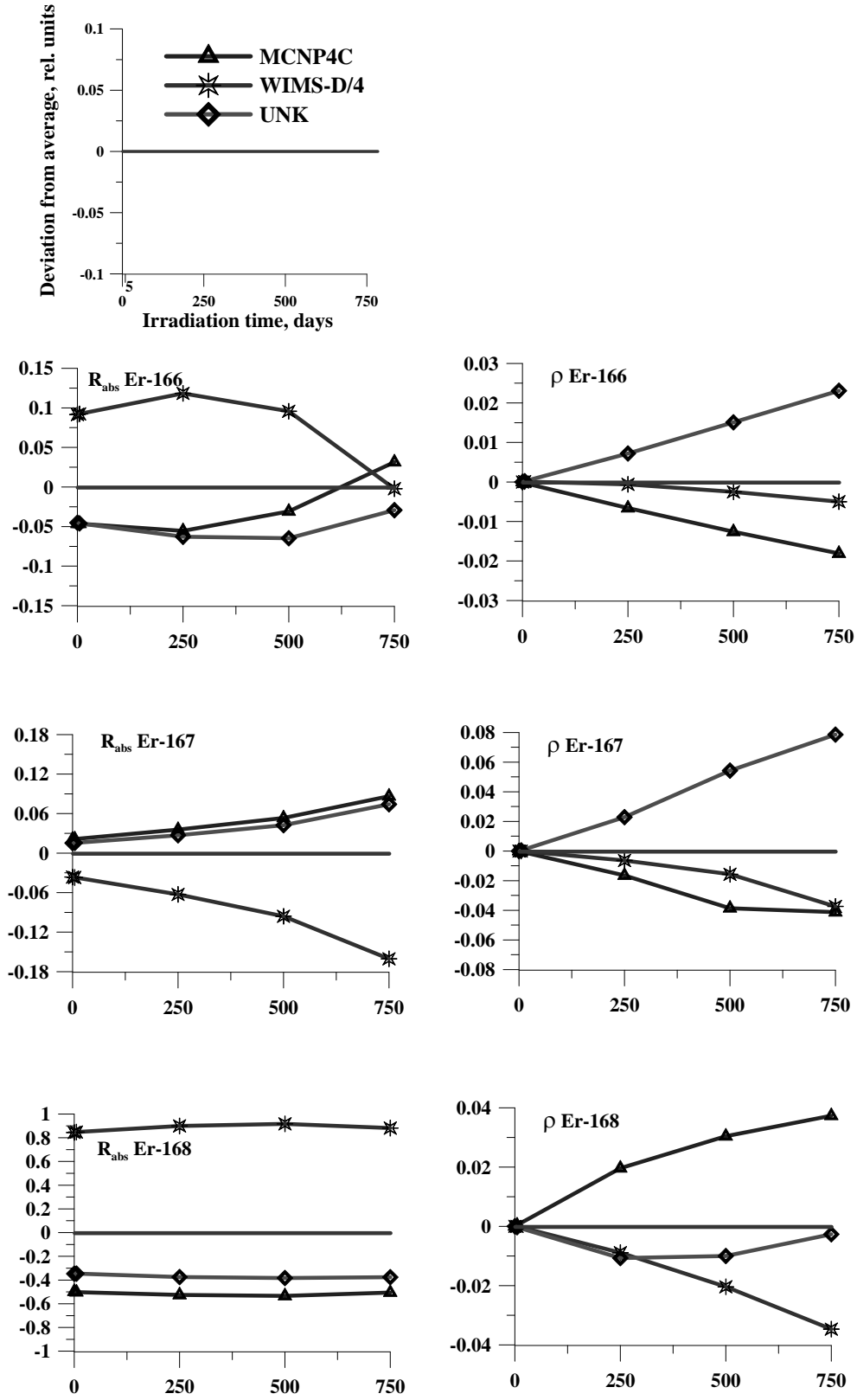


FIG. 6.28. Heterogeneous BPC — Deviation of R_{abs} and erbium isotopic content from averaged values.

6.3.1.2. Calculation of fuel assembly cell and reactor — Russian Federation

Calculational approaches

A short description of calculational codes, technique and model is presented in Table 6.33.

TABLE 6.33. CALCULATIONAL CODES, TECHNIQUE AND MODELS

Calculational code	MCU [6-5]	MCNP4 [6-9]	WIMS-D4 [6-12]	UNK [6-13]	JAR [6-14]
Calculation technique	Monte - Carlo	Monte-Carlo	FCP, S ₈	FCP	Finite-difference or nodal diffusion
Library	DLC/MCUDAT-1.0 DLC/MCUDAT-2.0	JENDL 3.3 ENDF/B6.7 ENDF/B6.8	UKNDL, ENDF/B6, FOND2.2, WLUP and others	ENDF/B6	macro cross-sections for physical zones
Calculation	cell, reactor	cell, reactor	cell	cell	reactor
Fuel particle arrangement	detailed setting	detailed setting	detailed setting homogeneously within compact	detailed setting	
Burnable poison arrangement	homogeneously within compact	homogeneously within compact	homogeneously within compact	homogeneously within compact	
Energy structure	continuous	continuous	69 groups	89 groups (up to 7000 for some isotopes)	Arbitrary number of groups
Statistic	up to 5·10 ⁶	up to 16·10 ⁶			

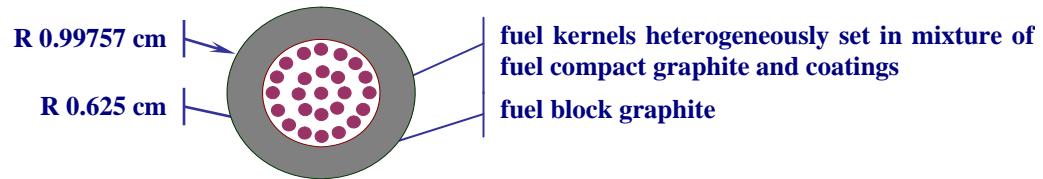
The proposed calculational models of the FA1 equivalent cell for the WIMS-D4 code are presented in Fig. 6.29. The calculation of the fuel assembly unit cell includes the following three stages:

- Stage 1 — ‘calculation of the fuel compact unit cell’ — forming of the WIMS input data including resonance cross-sections of plutonium and actinides;
- Stage 2 — ‘calculation of the burnable poison compact unit cell’ — forming of the WIMS input data including resonance cross-sections of erbium isotopes. At this stage the fuel composition is excluded from spectrum forming;
- Stage 3 — ‘calculation of the fuel assembly unit cell’ — the calculation of different models (Fig. 6.29) with the usage of resonance cross-section arrays of plutonium, actinides and erbium resulted at stage 1 and stage 2.

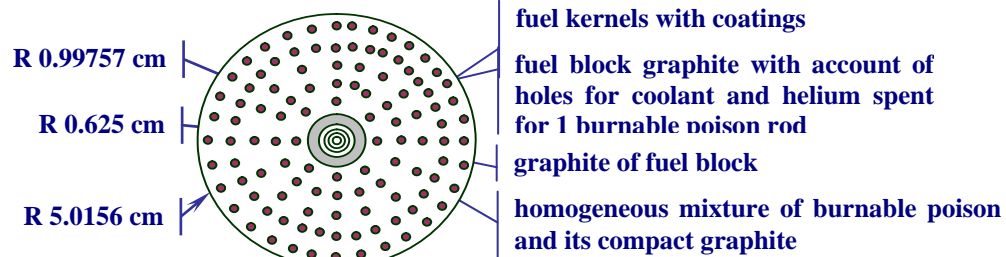
The results obtained by the MCU code are used as a reference in comparisons of neutronic functionals. The calculations by MCU/BURNUP were performed for the FA1 cell with a detailed description of the actual fuel assembly geometry.

When the codes based on the Monte Carlo method (MCU and MCNP) are used, a detailed model with heterogeneous fuel particle setting presented in the specification is used. The model as a whole represents a lattice of hexahedral prisms inscribed in the container that is the sector of a cylinder (Fig. 6.30).

Stage 1. Burnup calculation of the fuel compact unit cell

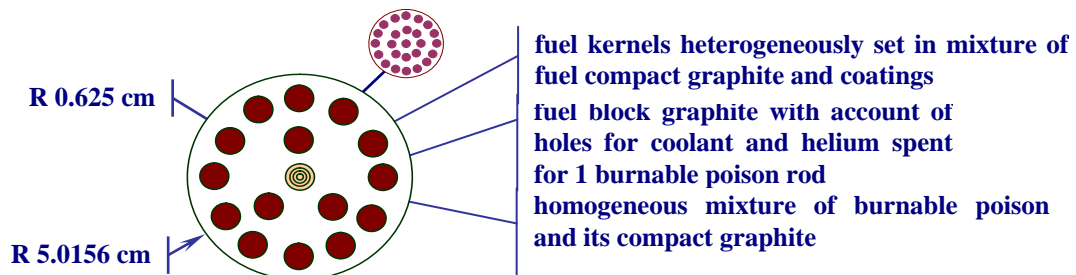


Stage 2. Burnup calculation of the burnable poison compact unit cell

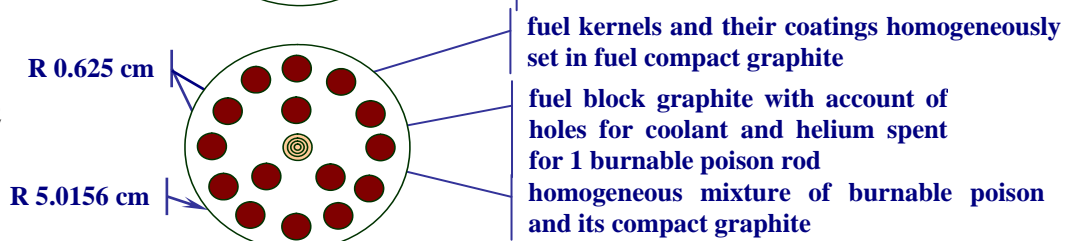


Stage 3. Burnup calculation of the fuel assembly unit cell

Model 1



Model 2



Model 3

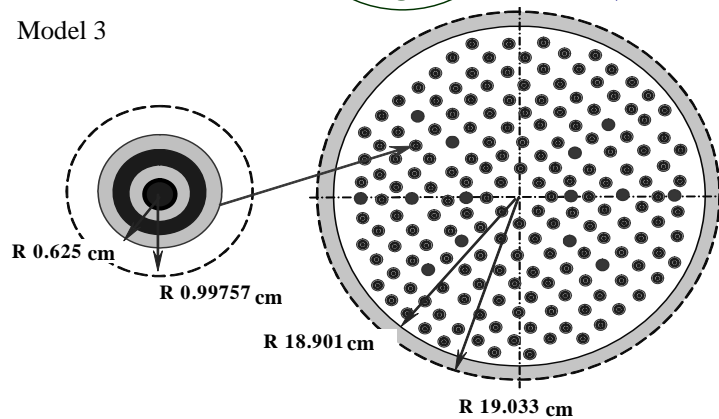


FIG. 6.29. Stage-by-stage approach to FA1 cell calculation by WIMS-D4.

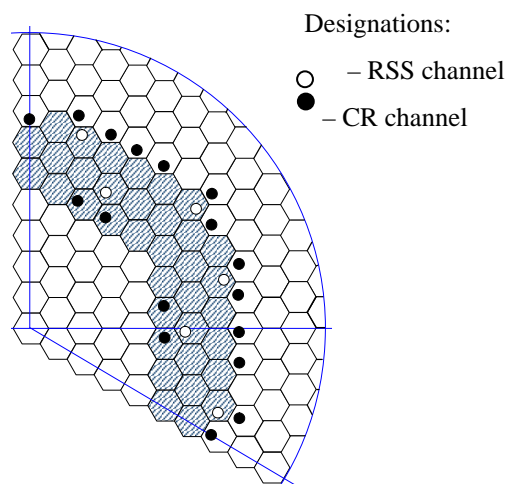


FIG. 6.30. Cross-section of the GT-MHR reactor computer model.

Three dimensional reactor calculations, implementing a calculational algorithm with full scattering cross-section matrix, were performed in the multigroup finite-difference diffusion approximation with the JAR-HTGR code.

Equivalent cells with maximal equivalence to the detailed model presented in the specification were used during preparation of neutron constants for different physical zones by WIMS-D4. The 69-group sets of cross-sections were further condensed to 13 groups and used for the GT-MHR full-scale reactor calculation.

A calculational mesh based on triangles was compiled for the 120° symmetry sector. Studies were performed both for 24 points per fuel assembly or reflector block. Sixteen points for blocks were considered along the height.

An example of the fuel assembly subdivision in the plane section is presented in Fig. 6.31.

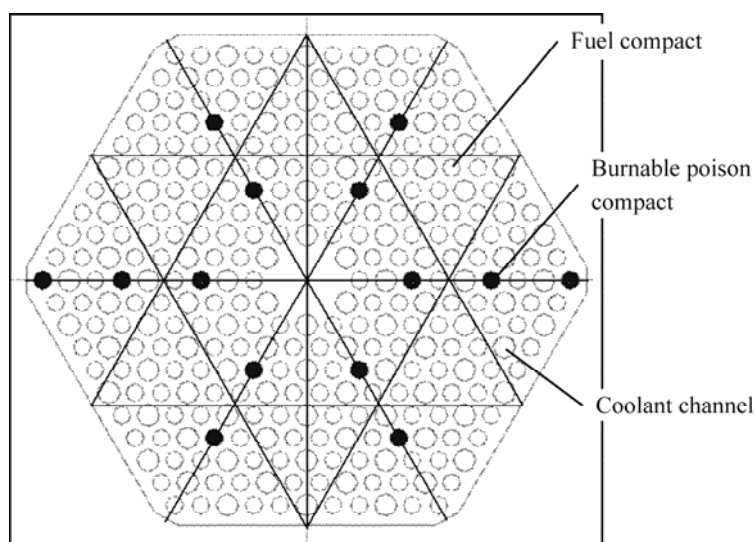


FIG. 6.31. Cross-section of the FA1 computer model.

Results of the FA cell calculations

TABLE 6.34. FA1 CELL MULTIPLICATION FACTOR AND ISOTOPE COMPOSITION VS BURNUP AND RELATIVE DEVIATION FROM MCU RESULTS, RELATED UNITS

Fuel life point	Functionals	MCU		MCNP		UNK	
		Detailed model	Detailed model	$\frac{MCNP - MCU}{MCU}$	Detailed model	$\frac{UNK - MCU}{MCU}$	
		Value	Value		Value		
Beginning of cycle	k _{inf}	1.1390	1.1376	-0.0012	1.1300	-0.0079	
	ρ _{Er-167}	0.2290	0.2290	0.0000	0.2290	0.0000	
	ρ _{Pu-239}	0.9175	0.9175	0.0000	0.9175	0.0000	
	ρ _{Pu-240}	0.0653	0.0653	0.0000	0.0653	0.0000	
	ρ _{Pu-241}	0.0116	0.0116	0.0000	0.0116	0.0000	
	ρ _{Pu-242}	0.0042	0.0042	0.0000	0.0042	0.0000	
(1/3) 280 eff. days	k _{inf}	1.0930	1.0892	-0.0035	1.0940	0.0009	
	ρ _{Er-167}	0.1110	0.1059	-0.0459	0.1040	-0.0631	
	ρ _{Pu-239}	0.5510	0.5449	-0.0111	0.5240	-0.0490	
	ρ _{Pu-240}	0.1080	0.1130	0.0463	0.1060	-0.0185	
	ρ _{Pu-241}	0.0830	0.0825	-0.0060	0.0920	0.1084	
	ρ _{Pu-242}	0.0090	0.0088	-0.0222	0.0090	0.0000	
(2/3) 560 eff. days	k _{inf}	1.1080	1.1077	-0.0003	1.1230	0.0135	
	ρ _{Er-167}	0.0350	0.0321	-0.0829	0.0280	-0.2000	
	ρ _{Pu-239}	0.2420	0.2322	-0.0405	0.2020	-0.1653	
	ρ _{Pu-240}	0.1100	0.1172	0.0655	0.1020	-0.0727	
	ρ _{Pu-241}	0.1220	0.1208	-0.0098	0.1300	0.0656	
	ρ _{Pu-242}	0.0260	0.0247	-0.0500	0.0280	0.0769	
(3/3) 840 eff. days	k _{inf}	1.0350	1.0073	-0.0268	1.0070	-0.0271	
	ρ _{Er-167}	0.0060	0.0061	0.0167	0.0030	-0.5000	
	ρ _{Pu-239}	0.0330	0.0268	-0.1879	0.0120	-0.6364	
	ρ _{Pu-240}	0.0790	0.0714	-0.0962	0.0450	-0.4304	
	ρ _{Pu-241}	0.0800	0.0755	-0.0563	0.0610	-0.2375	
	ρ _{Pu-242}	0.0620	0.0599	-0.0339	0.0690	0.1129	
Fuel life point	Functionals	WIMS-D4					
		Model 1	$\frac{WIMS - MCU}{MCU}$	Model 2	$\frac{WIMS - MCU}{MCU}$	Model 3	$\frac{WIMS - MCU}{MCU}$
		Value		Value		Value	
Beginning of cycle (table 6-4)	k _{inf}	1.1360	-0.0026	1.1302	-0.0077	1.1350	-0.0035
	ρ _{Er-167}	0.2290	0.0000	0.2290	0.0000	0.2290	0.0000
	ρ _{Pu-239}	0.9175	0.0000	0.9175	0.0000	0.9175	0.0000
	ρ _{Pu-240}	0.0653	0.0000	0.0653	0.0000	0.0653	0.0000
	ρ _{Pu-241}	0.0116	0.0000	0.0116	0.0000	0.0116	0.0000
	ρ _{Pu-242}	0.0042	0.0000	0.0042	0.0000	0.0042	0.0000

(1/3) 280 eff. days	k_{inf}	1.0843	-0.0080	1.0723	-0.0189	1.0860	-0.0064
	$\rho_{\text{Er-167}}$	0.1090	-0.0180	0.1204	0.0847	0.0950	-0.1441
	$\rho_{\text{Pu-239}}$	0.5468	-0.0076	0.5540	0.0054	0.5470	-0.0073
	$\rho_{\text{Pu-240}}$	0.1059	-0.0194	0.0845	-0.2176	0.1110	0.0278
	$\rho_{\text{Pu-241}}$	0.0876	0.0554	0.1041	0.2542	0.0830	0.0000
	$\rho_{\text{Pu-242}}$	0.0085	-0.0556	0.0092	0.0222	0.0080	-0.1111
(2/3) 560 eff. days	k_{inf}	1.1024	-0.0051	1.0999	-0.0073	1.1030	-0.0045
	$\rho_{\text{Er-167}}$	0.0330	-0.0571	0.0435	0.2429	0.0260	-0.2571
	$\rho_{\text{Pu-239}}$	0.2374	-0.0190	0.2549	0.0533	0.2370	-0.0207
	$\rho_{\text{Pu-240}}$	0.1055	-0.0409	0.0730	-0.3364	0.1150	0.0455
	$\rho_{\text{Pu-241}}$	0.1283	0.0516	0.1470	0.2049	0.1210	-0.0082
	$\rho_{\text{Pu-242}}$	0.0235	-0.0962	0.0252	-0.0308	0.0220	-0.1538
(3/3) 840 eff. days	k_{inf}	1.0331	-0.0018	1.0879	0.0511	1.0210	-0.0135
	$\rho_{\text{Er-167}}$	0.0051	-0.1500	0.0077	0.2833	0.0050	-0.1667
	$\rho_{\text{Pu-239}}$	0.0331	0.0030	0.0479	0.4515	0.0310	-0.0606
	$\rho_{\text{Pu-240}}$	0.0626	-0.2076	0.0431	-0.4544	0.0720	-0.0886
	$\rho_{\text{Pu-241}}$	0.0848	0.0600	0.0974	0.2175	0.0810	0.0125
	$\rho_{\text{Pu-242}}$	0.0549	-0.1145	0.0550	-0.1129	0.0530	-0.1452

Russian contributors

V. Boyarinov¹, V. Bryzgalov¹, E. Glushkov¹, E. Gomin¹, M. Gurevich¹, V. Davidenko¹, N. Kuzavkov², E. Marova², E. Mitenkova³, N. Novikov³, Yu. Sukharev², P. Fomichenko¹, V. Tsibulsky¹, M. Yudkevich¹

- (1) RRC Kurchatov Institute, Kurchatov sq., Moscow, Russian Federation, pf@dhtp.kiae.ru;
- (2) OKBM, Burnakovsky proezd/15, Nizhny Novgorod, Russian Federation, marova@okbm.nnov.ru;
- (3) IBRAE, Moscow, Russian Federation, mit@ibrae.ac.ru.

Results of the core calculations

TABLE 6.35. RESULTS OF THE GT-MHR REACTOR CALCULATIONS AND RELATIVE DEVIATION FROM MCU RESULTS

Temperature reactivity coefficient ($\Delta k/k/K$)					
		MCU	WIMS-JAR	$\frac{JAR - MCU}{MCU}$	
Beginning of the cycle	ρ_{350}	-6.8304E-06	-4.4824E-06	-0.34	
	ρ_{450}	-4.2352E-06	-3.1713E-06	-0.25	
	ρ_{550}	-7.2832E-06	-4.6596E-06	-0.36	
	ρ_{650}	-1.4842E-05	-9.9137E-06	-0.33	
	ρ_{750}	-2.5703E-05	-1.8556E-05	-0.28	
	ρ_{850}	-3.8582E-05	-3.1834E-05	-0.17	
	ρ_{950}	-5.2084E-05	-4.5109E-05	-0.13	
	ρ_{1050}	-6.4648E-05	-5.9059E-05	-0.09	
	ρ_{1150}	-7.4467E-05	-7.2836E-05	-0.02	
End of the cycle	ρ_{350}	1.3898E-05	1.8870E-05	0.36	
	ρ_{450}	4.0089E-05	5.2050E-05	0.30	
	ρ_{550}	4.2707E-05	5.0179E-05	0.17	
	ρ_{660}	2.9156E-05	3.0492E-05	0.05	
	ρ_{750}	6.2113E-06	8.3858E-06	0.35	
	ρ_{850}	-2.0102E-05	-1.3271E-05	-0.34	
	ρ_{950}	-4.4208E-05	-3.5106E-05	-0.21	
	ρ_{1050}	-6.0552E-05	-5.6551E-05	-0.07	
	ρ_{1150}	-6.3279E-05	-7.7293E-05	0.22	
Efficiency of the Control Rod System in the Core (%)					
	MCU	MCNP	$\frac{MCNP - MCU}{MCU}$	WIMS-JAR	$\frac{JAR - MCU}{MCU}$
2 B ₄ C Rods in a Reflector Block					
Beginning of the cycle	4.4			3.9	- 0.11
End of the cycle	4.7			4.6	- 0.02
6 B ₄ C Rods in a Reflector Block					
Beginning of the cycle	2.8	2.6	- 0.07	2.7	- 0.04
End of the cycle	3.4	3.1	- 0.09	3.3	- 0.03
Efficiency of the Control Rod System in the Reflector , %					
	MCU	MCNP	$\frac{MCNP - MCU}{MCU}$	WIMS-JAR	$\frac{JAR - MCU}{MCU}$
2 B ₄ C Rods in a Reflector Block					
Beginning of the cycle	11.2			9.6	- 0.14
End of the cycle	13.1			10.6	- 0.19
6 B ₄ C rods in a reflector block					
Beginning of the cycle	15.6	15.4	- 0.01	13.8	- 0.12
End of the cycle	17.8	17.9	- 0.01	15.3	- 0.14

*) Calculations with the MCU Monte Carlo code were performed in the following assumptions:
Temperatures for all components were assumed 1200 K;
For actinides and fission products, only isotopes above solid lines in Table 6.13 were taken into account.
GT-MHR benchmark results, France

6.3.2. GT-MTHR benchmark results, France

6.3.2.1. Introduction

This section presents the different phases of the French contribution to the GT-MTHR PHYS benchmark in the framework of the CRP-5. It gathers a synthesis of the results obtained at CEA and partially presented during the course of the different CRP-5 meetings.

A preliminary study had been carried out on the basis of the initial benchmark data pack provided by the Russian Federation in 2001. Only the first step of the problem had been envisaged and it concerned fuel element calculations. The APOLLO2 results were presented at the fourth RCM [6-15]) and compared with the Russian results presented previously at the third RCM of this CRP [6-16]. Large discrepancies had been observed and could not be explained easily. Therefore a simpler benchmark (simple geometry and smaller number of isotopes) was needed, in order to facilitate the interpretation of the results. In 2003, a series of new simplified benchmark cases for the GT-MTHR with weapon-grade plutonium was launched. These are simple cell models, whereby the fuel (plutonium) and the poison (erbium) are separately treated. The results for the various cases are presented.

In reactor physics, the definition of a calculation scheme for design studies of the reactor concepts implies qualification and validation phases that always follow the same strategy at the CEA. Through a multiconcept approach, a systematic validation against the Monte Carlo code constitutes a preliminary stage before complementary qualification phases on critical experimental and actual reactor configurations. These Monte Carlo validations are performed on a different scale than the reactor model (fuel rod, fuel assembly, two dimensional core and full scale-validation). This approach has been adopted all along this benchmark as well.

It is important to note that all the computations performed with deterministic and Monte Carlo methods were carried out on the base of coherent cross-section libraries generated by the same version of the NJOY and CALENDF codes [6-17], using the same options and same nuclear data input. This consistence allows comparing results of both types of codes using cross-sections of the same origin. Point-wise cross-sections are used in the TRIPOLI4 Monte Carlo code whereas multigroup cross-sections are used in the APOLLO2 transport calculations (at 172 groups). Three types of cross-section library have been used in the present simulations, namely, JEF2.2 and JEF3.0 (elementary cell calculations) and JEF3.1. Comparisons between libraries have been done and it turned out that some discrepancies have been observed.

6.3.2.2. Elementary cell benchmark

Summary of performed calculations

In the elementary cells benchmark exercise, the complex structure of the hexagonal fuel assembly has been simplified to facilitate the comparison of the results obtained from various code systems. The benchmark consists of five cases. There are three different unit cell configurations only with plutonium fuel (FCC), whereby the degree of heterogeneity of the models varies as follows: one homogeneous medium, a homogeneous compact plus its surrounding graphite, and finally, the actual compact with the fuel particles and the surrounding graphite. The fourth and fifth benchmark cases consist of a burnable poison (Burnable Poison Cell - BPC) compact with erbium as a burnable poison. In the fourth benchmark case, erbium is homogeneously smeared in the compact, and in the fifth case, erbium particles are modelled.

The APOLLO2 deterministic code system [6-18] and the TRIPOLI4 Monte Carlo code [6-19] have been used. The results are provided for the fresh fuel and also for a burnup up to 750 MWd/kg at temperatures from 300 K to 1200 K (see Table 6.36). The following parameters are investigated:

- k_{inf} values;
- Neutron balance components;
- Mass of nuclides.

Some sensitivity calculations of the self-shielding models (APOLLO2) on neutron balance components are performed. The impact of the nuclear data libraries JEF2.2 and JEFF3.0 on the reactivity and reaction rates is investigated using TRIPOLI4. Several comparisons with results recently released from the Russian Federation are presented.

TABLE 6.36. SUMMARY OF PERFORMED CALCULATIONS AT CEA

Code/Library	Temperature	Beginning of Life (BOL)					Burnup				
		FCC	FCC1	FCC2	BPC	BPCH	FCC	FCC1	FCC2	BPC	BPCH
APOLLO2 CEA93_V6 (JEF 2.2)	300 K	✓	✓	✓	✓						
	600 K	✓	✓	✓							
	900 K	✓	✓	✓							
	1200 K	✓	✓	✓	✓		✓			✓	
TRIPOLI4 JEF2.2	300 K		✓	✓	✓						
	1200 K		✓	✓	✓						
TRIPOLI4 JEFF3.0	300 K		✓	✓	✓						
	1200 K										

Fuel compact cell FCC1

The benchmark case 1 FCC (FCC1) has the simplest geometrical form of all benchmark cases. In this case, all relevant nuclides of the fuel assembly (fuel, coating and moderator, but no burnable poison) are homogeneously smeared in a cylinder. The outer radius of the cylinder is 0.997571 cm and the height is infinite. The nuclide densities are given in the benchmark data pack provided by the Russian Federation.

The calculations are performed with the APOLLO2 (version 2.5) deterministic code system in conjunction with the nuclear data library CEA93 (version 6) using a 172 energy group structure. A zero buckling (no neutron leakage) was applied, in order to facilitate the comparison between the various code systems and also to allow us to directly compare the results from the Monte Carlo codes with deterministic code systems. Calculations are performed at four different temperatures, namely, 300, 600, 900 and 1200 K. Apart from the k_{inf} values, the participants should calculate neutron balance components as fission rate, production rate and absorption rate.

These reaction rates are normalized to the sum of the total absorption rate. No burnup calculations are performed for this case. The following options are used for the cell calculations:

- Isotropic reflected boundary;
- The model 'all resonance' was applied to calculate shelf-shielded cross-sections for all plutonium isotopes.

The cell calculations are also performed with the TRIPOLI4 Monte Carlo code using continuous energy cross-section (JEF2.2 and JEFF3.0). The calculations were performed at 300 and 1200 K with JEF2.2 and at 300 K with JEFF3.0. White boundary conditions are used.

Results on FCC1

The APOLLO2 results for case FCC1 at a temperature 300 and 1200 K are shown in Table 6.37. It can be seen that the most important nuclides are ^{239}Pu , ^{240}Pu , graphite and ^{242}Pu and their relative absorption is about 79%, 19%, 0.5% and 0.24% respectively. The absorption of ^{241}Pu , silicon and boron is around 1%. About 98.5% of the total production rate arises from ^{239}Pu . The contribution of ^{241}Pu is rather small (less than 1.4%). At a temperature of 1200 K, the reactivity of the cell is about 7000 pcm lower than at ambient temperature. This is mainly due to the fact that the capture in ^{240}Pu is higher at 1200 K than at 300 K. Moreover, the ratio of the production rate to absorption rate of ^{239}Pu is shifted from 1.784 to 1.766. The data for all temperatures is given in Section 6.3.2.3.

TABLE 6.37. APOLLO2 RESULTS FOR CASE FCC1 AT 300 AND 1200 K

Temperature	300 K			1200 K		
k_{inf}	1.4330			1.3641		
Nuclide	Abs.	Fission	Prod.	Abs.	Fission	Prod.
Pu-238	0.0002	0.0000	0.0001	0.0002	0.0000	0.0001
Pu-239	0.7905	0.4925	1.4120	0.7615	0.4693	1.3450
Pu-240	0.1906	0.0003	0.0008	0.2210	0.0003	0.0008
Pu-241	0.0091	0.0068	0.0201	0.0083	0.0062	0.0182
Pu-242	0.0024			0.0025		
O-16	0.0000			0.0000		
GRAPH	0.0051			0.0048		
SINAT	0.0012			0.0011		
BNAT	0.0008			0.0007		
TOTAL	1.0000	0.4997	1.4330	1.0000	0.4758	1.3641

Table 6.38 gathers the results obtained from APOLLO2 and TRIPOLI4 for case FCC1 at a temperature of 300 K. Note that the total production rate (in bold numbers) is equal to the k_{inf} values. At the lower part of the table, the differences between APOLLO2 and TRIPOLI4 with JEF2.2 and the difference between TRIPOLI4 with JEFF3.0 and TRIPOLI4 with JEF2.2 are shown. The differences are expressed in pcm (10^{-5}).

The APOLLO2 results agree very well with the TRIPOLI4 results using cross-sections based on the same library (JEF2.2). This confirms that the applied self-shielding models and the flux neutron density calculation are quite accurate. The absorption, fission and production rates of the nuclide ^{239}Pu are slightly lower with APOLLO2 than the ones obtained with TRIPOLI4. The latter difference is about 233 pcm and is the main reason for the slightly lower k_{inf} value of APOLLO2. It is worth noting that the lower absorption rate of ^{239}Pu (-105 pcm) is nearly counter-balanced by a higher absorption rate in ^{240}Pu (+84 pcm).

The comparison of the TRIPOLI4 results using the library JEF2.2 and JEFF3.0 shows that:

- The k_{inf} value is about 350 pcm higher with JEFF3.0 because of a higher production rate of ^{239}Pu ;
- No significant difference occurs for the other nuclides. The difference is within the statistical uncertainty (see Table 6.38).

TABLE 6.38. REACTION RATES OF APOLLO2 AND TRIPOLI4 AT 300 K FOR CASE FCC1

Code	APOLLO2			TRIPOLI4			TRIPOLI4		
Library	CEA_93.V6 (JEF 2.2)			JEF2.2			JEFF3.0		
Nuclide	Abs.	Fission	Prod.	Abs.	Fission	Prod.	Abs.	Fission	Prod.
Pu-238	0.0002	0.0000	0.0001	0.0002	0.0000	0.0001	0.0002	0.0000	0.0001
Pu-239	0.7905	0.4925	1.4120	0.7916	0.4933	1.4144	0.7920	0.4951	1.4183
Pu-240	0.1906	0.0003	0.0008	0.1898	0.0003	0.0008	0.1896	0.0002	0.0007
Pu-241	0.0091	0.0068	0.0201	0.0092	0.0069	0.0202	0.0091	0.0067	0.0197
Pu-242	0.0024	0.0000	0.0000	0.0024	0.0000	0.0000	0.0025	0.0000	0.0000
O-16	0.0000			0.0000			0.0000		
GRAPH	0.0051			0.0048			0.0048		
SINAT	0.0012			0.0012			0.0009		
BNAT	0.0008			0.0008			0.0008		
<i>TOTAL</i>	<i>1.0000</i>	<i>0.4997</i>	<i>1.4330</i>	<i>1.0000</i>	<i>0.5005</i>	<i>1.4354</i>	<i>1.0000</i>	<i>0.5022</i>	<i>1.4389</i>
Difference in pcm, relative to TRIPOLI4 (JEF2.2)									
Nuclide	Abs.	Fission	Prod.	Abs.	Fission	Prod.	Abs.	Fission	Prod.
Pu-238	0	0	0				1	0	1
Pu-239	-105	-77	-233				42	186	395
Pu-240	84	0	0				-15	-3	-8
Pu-241	-7	-4	-12				-2	-15	-46
Pu-242	-3	0	0				3	0	0
O-16	0						0		
GRAPH	32						4		
SINAT	-1						-31		
BNAT	0						0		
<i>TOTAL</i>	<i>0</i>	<i>-81</i>	<i>-236</i>				<i>0</i>	<i>168</i>	<i>352</i>

For completeness, the statistical 1σ uncertainty of the reaction rates for the TRIPOLI4 calculations are presented in Table 6.39. In general, the reaction rates were determined with an uncertainty of 0.05 % or 50 pcm. For ^{16}O and graphite, the uncertainties are three times larger, however, ^{16}O can be negligible and the contribution of graphite to the total absorption rate is rather small (~between 0.3 and 0.5%). The uncertainty of k_{inf} is about 40 pcm.

TABLE 6.39. STATISTICAL 1σ UNCERTAINTY (%) OF K_{INF} AND REACTION RATES OBTAINED FROM TRIPOLI4

$k_{\text{inf}} = 0.04$			
Nuclide	Absorption	Fission	Production
Pu-238	0.06	0.04	0.03
Pu-239	0.04	0.04	0.04
Pu-240	0.06	0.03	0.03
Pu-241	0.04	0.04	0.04
Pu-242	0.10	0.03	0.03
O-16	0.14		
C_GRAPHITE	0.18		
B-10	0.05		
B-11	0.05		
SI	0.05		

Fuel compact cell FCC2

In this case, the cell consists of two concentric cylinders. The inner one consists of the fuel, coating and graphite matrix (representing the compact). The particles are homogeneously smeared with graphite and coating. The outer one contains the graphite of the graphite block. The outer radius of the inner zone and outer zone are 0.625 cm and 0.997571 cm respectively. The nuclide densities for each zone or region are given in the benchmark data.

Results on FCC2

The codes that were used and the nuclear data are the same as those already described in the previous chapter. Table 6.40 gathers the results obtained from APOLLO2 and TRIPOLI4 for Case FCC2 at temperatures of 300 and 1200 K.

TABLE 6.40. REACTION RATES OF APOLLO2 AT 300 AND 1200 K FOR FCC2

Temperature	300 K			1200 K		
k_{inf}	1.4473			1.3768		
Nuclide	Abs.	Fission	Prod.	Abs.	Fission	Prod.
Pu-238	0.0002	0.0000	0.0001	0.0002	0.0000	0.0001
Pu-239	0.7972	0.4974	1.4260	0.7680	0.4736	1.3575
Pu-240	0.1837	0.0003	0.0008	0.2143	0.0003	0.0008
Pu-241	0.0093	0.0070	0.0204	0.0084	0.0063	0.0184
Pu-242	0.0024			0.0025		
O-16	0.0000			0.0000		
GRAPH	0.0052			0.0048		
SINAT	0.0012			0.0011		
BNAT	0.0008			0.0007		
TOTAL	1.0000	0.5046	1.4473	1.0000	0.4802	1.3768

A similar analysis for the FCC2 case has been done and the results are gathered in Tables 6.41 and 6.42.

TABLE 6.41. COMPARISON OF APOLLO2 AND TRIPOLI4 RESULTS FOR FCC2 AT A TEMPERATURE OF 300 K

Code	APOLLO2			TRIPOLI4			TRIPOLI4		
Library	CEA_93.V6 (JEF 2.2)			JEF2.2			JEFF3.0		
Nuclide	Abs.	Fission	Prod.	Abs.	Fission	Prod.	Abs.	Fission	Prod.
Pu-238	0.0002	0.0000	0.0001	0.0002	0.0000	0.0001	0.0002	0.0000	0.0001
Pu-239	0.7972	0.4974	1.4260	0.7982	0.4981	1.4282	0.7987	0.5001	1.4325
Pu-240	0.1837	0.0003	0.0008	0.1829	0.0003	0.0008	0.1826	0.0002	0.0007
Pu-241	0.0093	0.0070	0.0204	0.0093	0.0070	0.0204	0.0093	0.0068	0.0201
Pu-242	0.0024	0.0000	0.0000	0.0024	0.0000	0.0000	0.0025	0.0000	0.0000
O-16	0.0000	0.0000	0.0000	0.0000			0.0000		
GRAPH	0.0052	0.0000	0.0000	0.0049			0.0049		
SINAT	0.0012	0.0000	0.0000	0.0012			0.0009		
BNAT	0.0008	0.0000	0.0000	0.0008			0.0008		
TOTAL	1.0000	0.5046	1.4473	1.0000	0.5054	1.4497	1.0000	0.5072	1.4534
Difference in pcm, relative to TRIPOLI4 (JEF2.2)									
Nuclide	Abs.	Fission	Prod.	Abs.	Fission	Prod.	Abs.	Fission	Prod.
Pu-238	0	0	0				1	0	1
Pu-239	-102	-77	-221				52	193	425
Pu-240	82	0	0				-23	-3	-8
Pu-241	-6	-4	-12				-2	-15	-46
Pu-242	-3	0	0				3	0	0
O-16	0						0		
GRAPH	30						2		
SINAT	-1						-32		
BNAT	0						0		
TOTAL	0	-81	-233				0	175	372

TABLE 6.42. UNCERTAINTIES TRIPOLI4 FCC2 IN %

Region	Nuclide	Absorption	Fission	Production
Fuel	Pu-238	0.03	0.01	0.01
	Pu-239	0.02	0.02	0.02
	Pu-240	0.03	0.01	0.01
	Pu-241	0.02	0.02	0.02
	Pu-242	0.04	0.01	0.02
	O-16	0.06		
	C_GRAPHITE	0.07		
	B-10	0.02		
	B-11	0.02		
	SI	0.03		
Graphite Block	C_GRAPHITE	0.02		
	B-10	0.02		
	B-11	0.01		

Fuel compact Cell FCC

This case is an extension of the FCC2 case. The cell once again consists of two cylindrical regions, however, the particle structure or double-heterogeneity of the fuel is modelled in this case. The dimensions and nuclide density are given in the benchmark data pack. Apart from the dimensions and nuclide densities, the APOLLO2 code requires the following additional data:

- Ratio of the particle mass to the mass of the compact (Particle + Graphite Matrix);
- Smeared density of the compact.

The cell calculations are performed under the same conditions as described in the previous section. The codes, nuclear data, models and hypothesis are the same as those already mentioned. Moreover, burnup calculations are performed with a uniform temperature of 1200 K and a constant power density of 856.282. MW/t. The letter t stands for the amount of heavy metals for the fresh fuel in tons. The power density is also equivalent to 7.3973 W/cm^3 . k_{inf} values, reaction rates and atomic densities at five burnup points (0, 5, 250, 500 and 750 EFPD) should be provided by the participants.

Burnup and Beginning of Life (BOL) calculations are only performed with the APOLLO2 code. The length of the interval between the recalculation of self-shielded cross-sections is not specified in the benchmark description. Indeed, in order to take into account the microscopic impact of the depletion, spectrum calculations must be performed at several time steps. Self-shielded cross-sections are generated at each time step. The burnup steps and the recalculation steps used for the deterministic calculations with the APOLLO2 code are shown in Table 6.43. It is worth noting that the CPU time for the self-shielding calculation and a single-cell calculation is rather small, therefore a very fine burnup grid is used. At the beginning, a cell calculation is performed each day (up to 10 days) and then every fifth day.

TABLE 6.43. TIME STEPS FOR CELL CALCULATIONS
OF SELF-SHIELDED CROSS-SECTIONS

1	2	3	4	5	6	7	8	9	10	15	20	25	30	35	40	45	50		
65	70	75	80	85	90	95	100	105	110	115	120	125	130	135	140	145	150		
155	160	165	170	175	180	185	190	195	200	205	210	215	220	225	230	235	240	245	250
255	260	265	270	275	280	285	290	295	300	305	310	315	320	325	330	335	340	345	350
355	360	365	370	375	380	385	390	395	400	405	410	415	420	425	430	435	440	445	450
455	460	465	470	475	480	485	490	495	500	505	510	515	520	525	530	535	540	545	550
555	560	565	570	575	580	585	590	595	600	605	610	615	620	625	630	635	640	645	650
655	660	665	670	675	680	685	690	695	700	705	710	715	720	725	730	735	740	745	750
755	760	765	770	775	780	785	790	795	800	805	810	815	820	825	830	835	840	845	850

Results on FCC

The reaction rates at temperatures of 300 and 1200 K are given in Table 6.44. Table 6.45 shows the concentration and reaction rates for various burnup steps up to 750 MWd/t.

TABLE 6.44. APOLLO2 FCC 300 AND 1200 K

Temperature		300 K			1200 K		
k_{inf}		1.5373			1.4610		
Nuclide	Abs.	Fission	Prod.		Abs.	Fission	Prod.
Pu-238	0.0003	0.0000	0.0001		0.0002	0.0000	0.0001
Pu-239	0.8363	0.5277	1.5135		0.8096	0.5023	1.4400
Pu-240	0.1421	0.0003	0.0009		0.1710	0.0003	0.0009
Pu-241	0.0103	0.0078	0.0228		0.0091	0.0068	0.0200
Pu-242	0.0024				0.0025		
O-16	0.0000				0.0000		
GRAPH	0.0060				0.0055		
SINAT	0.0015				0.0013		
BNAT	0.0011				0.0009		
TOTAL	1.0000	0.5358	1.5373		1.0000	0.5095	1.4610

TABLE 6.45. APOLLO2 RESULTS OF BURNUP CALCULATIONS FOR FCC CASE AT A TEMPERATURE OF 1200 K

Irradiation (EFPD)		0		5		250		500		750										
k_{inf}	$I.4610$	$I.4388$		$I.2970$		$I.2228$		$I.1615$												
Isotope	Conc	SIGA	SIGF	NUSIGF	Conc	SIGA	SIGF	NUSIGF	Conc	SIGA	SIGF	NUSIGF								
Pu-238	5.06E-08	2.90E-04	3.73E-05	1.10E-04	5.05E-08	2.82E-04	3.66E-05	1.08E-04	4.87E-08	2.74E-04	3.29E-05	9.72E-05	6.23E-08	4.25E-04	4.31E-05	1.27E-04	1.09E-07	1.24E-03	8.96E-05	2.63E-04
Pu-239	3.56E-05	1.18E+00	7.34E-01	2.10E+00	3.53E-05	1.15E+00	7.10E-01	2.04E+00	2.26E-05	8.25E-01	5.11E-01	1.46E+00	1.16E-05	5.95E-01	3.68E-01	1.05E+00	3.45E-06	3.47E-01	2.15E-01	6.16E-01
Pu-240	2.52E-06	2.50E-01	4.30E-04	1.27E-03	2.56E-06	2.48E-01	4.30E-04	1.27E-03	3.84E-06	2.77E-01	5.73E-04	1.70E-03	3.76E-06	2.66E-01	5.37E-04	1.59E-03	2.57E-06	2.26E-01	3.67E-04	1.09E-03
Pu-241	4.49E-07	1.33E-02	9.98E-03	2.93E-02	5.05E-07	1.46E-02	1.09E-02	3.21E-02	3.24E-06	9.87E-02	7.38E-02	2.17E-01	5.05E-06	2.00E-01	1.49E-01	4.37E-01	4.62E-06	3.35E-01	2.47E-01	7.24E-01
Pu-242	1.65E-07	3.66E-03	1.74E-05	5.27E-05	1.64E-07	3.60E-03	1.71E-05	5.19E-05	2.98E-07	5.85E-03	2.81E-05	8.54E-05	7.52E-07	1.36E-02	6.76E-05	2.05E-04	1.61E-06	2.72E-02	1.40E-04	4.27E-04
Am-241					3.13E-10	1.30E-05	1.19E-07	4.05E-07	5.03E-08	2.07E-03	1.85E-05	6.32E-05	1.28E-07	6.21E-03	5.37E-05	1.83E-04	1.45E-07	1.11E-02	9.01E-05	3.04E-04
Am-242					1.74E-13	1.89E-08	1.57E-08	5.05E-08	8.70E-10	1.03E-04	8.50E-05	2.73E-04	3.42E-09	5.55E-04	4.57E-04	1.47E-03	4.25E-09	1.36E-03	1.11E-03	3.57E-03
Am-243					8.54E-10	3.23E-05	8.66E-08	2.91E-07	4.70E-08	1.59E-03	4.32E-06	1.45E-05	1.47E-07	4.75E-03	1.30E-05	4.36E-05	3.58E-07	1.16E-02	3.11E-05	1.05E-04
Cm-242					1.12E-12	3.01E-09	2.96E-10	9.77E-10	6.34E-09	1.57E-05	1.57E-06	5.18E-06	3.32E-08	8.16E-05	8.65E-06	2.85E-05	8.18E-08	2.17E-04	2.71E-05	8.82E-05
Cm-243					2.14E-16	9.57E-12	8.23E-12	2.79E-11	5.21E-11	2.14E-06	1.84E-06	6.24E-06	5.19E-10	2.16E-05	1.85E-05	6.29E-05	1.84E-09	8.88E-05	7.59E-05	2.57E-04
Cm-244					3.86E-12	4.48E-08	1.34E-09	4.50E-09	9.99E-09	1.08E-04	3.21E-06	1.08E-05	5.12E-08	5.45E-04	1.61E-05	5.40E-05	1.65E-07	1.77E-03	5.28E-05	1.77E-04
Cm-245					3.46E-15	9.24E-11	8.00E-11	3.06E-10	4.47E-10	1.19E-05	1.03E-05	3.95E-05	4.00E-09	1.28E-04	1.11E-04	4.26E-04	1.54E-08	8.18E-04	7.12E-04	2.72E-03
Cm-246					7.41E-19	1.60E-15	1.31E-16	4.86E-16	5.51E-12	1.08E-08	8.83E-10	3.28E-09	1.16E-10	2.17E-07	1.78E-08	6.61E-08	9.51E-10	1.75E-06	1.43E-07	5.33E-07
Cm-247					7.05E-23	1.78E-18	1.07E-18	3.84E-18	2.65E-14	5.87E-10	3.54E-10	1.27E-09	1.05E-12	2.33E-08	1.41E-08	5.05E-08	1.13E-11	2.94E-07	1.77E-07	6.34E-07
Cm-248					2.81E-26	1.43E-22	7.60E-24	2.77E-23	5.44E-16	2.54E-12	1.35E-13	4.91E-13	4.49E-14	2.01E-10	1.07E-11	3.89E-11	7.91E-13	3.48E-09	1.84E-10	6.71E-10
Bk-249					4.61E-30	2.90E-25	1.92E-27	6.55E-27	4.10E-18	2.79E-13	1.80E-15	6.13E-15	5.59E-16	5.17E-11	3.19E-13	1.08E-12	9.90E-15	1.77E-09	1.03E-11	3.49E-11
Cf-249					6.22E-33	4.49E-28	3.26E-28	1.32E-27	2.48E-19	1.67E-14	1.21E-14	4.93E-14	5.91E-17	4.39E-12	3.20E-12	1.30E-11	1.27E-15	1.33E-10	9.76E-11	3.96E-10
Cf-250					8.56E-33	2.09E-27	1.86E-30	7.24E-30	3.58E-19	7.92E-14	7.04E-17	2.75E-16	1.05E-16	2.41E-11	1.96E-14	7.66E-14	3.77E-15	1.09E-09	6.80E-13	2.67E-12
Cf-251					5.55E-35	1.01E-29	7.37E-30	3.05E-29	1.01E-19	1.77E-14	1.28E-14	5.31E-14	5.03E-17	1.03E-11	7.34E-12	3.04E-11	2.19E-15	7.01E-10	4.92E-10	2.04E-09
Cf-252					6.55E-38	2.38E-34	1.68E-34	6.86E-34	6.93E-21	2.35E-17	1.65E-17	6.76E-17	8.62E-18	2.97E-14	2.07E-14	8.46E-14	8.56E-16	3.39E-12	2.32E-12	9.48E-12
Xe-135PF					1.03E-09	1.29E-02			9.17E-10	1.37E-02			7.32E-10	1.71E-02			4.27E-10	2.29E-02		
Sm-149PF					1.03E-09	5.06E-04			1.67E-08	9.37E-03			1.22E-08	1.03E-02			6.03E-09	1.12E-02		
O-16	6.58E-05	3.76E-05			6.58E-05	3.70E-05			6.58E-05	3.46E-05			6.58E-05	3.47E-05			6.58E-05	3.63E-05		
GRAPH	8.53E-02	7.98E-03			8.53E-02	7.81E-03			8.53E-02	7.52E-03			8.53E-02	8.39E-03			8.53E-02	1.21E-02		
SINAT	5.52E-04	1.88E-03			5.52E-04	1.83E-03			5.52E-04	1.80E-03			5.52E-04	2.10E-03			5.52E-04	3.32E-03		
BNAT	9.99E-08	1.32E-03			9.99E-08	1.28E-03			9.99E-08	1.28E-03			9.99E-08	1.53E-03			9.99E-08	2.51E-03		

Homogeneous burnable poison Cell BPC

The BPC consists of a cylindrical cell with three different zones. The cell is infinite in height. The inner zone (first zone) presents the burnable poison compact and contains Er_2O_3 as burnable poison and graphite of the compact (graphite matrix). The burnable poison is homogeneously mixed with the graphite matrix. The intermediate zone (second zone) contains the graphite of the fuel block (the density is 1.73 g/cm^3) and in the external zone (third zone), the fuel of the graphite block is homogeneously mixed with the graphite of the block and helium. Nuclear densities for the third zone are calculated from the mass balances of an entire block. Detailed information for the burnable poison cell is given in the benchmark data pack.

As for the fuel cell calculations, identical codes and methods have been used hereafter. The results obtained from APOLLO2 and TRIPOLI4 calculations are gathered in Tables 6.46 to 6.48. The neutron balance components at 300 and 1200 K are shown in Table 6.45. The reduction of the reactivity is about 7230 pcm. The most significant change occurs for the production of ^{239}Pu (from 1.1663 to 1.0961). It is worth noting that this change is partially due to a lower fission in ^{239}Pu , however, mainly due to an enhanced total absorption rate. The contribution of the absorption rates of the erbium nuclides and ^{240}Pu to the total absorption rate is larger to higher temperatures. On the other hand, the contribution of the fission rates of ^{239}Pu to ^{241}Pu to the total fission rate is reduced.

TABLE 6.46. APOLLO2 BPC 300 AND 1200 K

Temperature	300 K			1200 K		
k_{inf}	1.1834			1.1111		
Nuclide	Abs.	Fission	Prod.	Abs.	Fission	Prod.
Er-166	0.0098			0.0103		
Er-167	0.1731			0.1810		
Er-168	0.0028			0.0031		
GRAPH	0.0056			0.0050		
BNAT	0.0010			0.0008		
Pu-239	0.6495	0.4068	1.1663	0.6206	0.3825	1.0961
Pu-240	0.1478	0.0002	0.0006	0.1700	0.0002	0.0006
Pu-241	0.0075	0.0056	0.0165	0.0065	0.0049	0.0143
Pu-242	0.0017			0.0017		
TOTAL	1.0000	0.4126	1.1834	1.0000	0.3876	1.1111

Table 6.47 shows the neutron balance components obtained from APOLLO2 and TRIPOLI4 using JEF2.2 and JEFF3.0. At the lower part of the table, the differences between APOLLO2 and TRIPOLI4 (JEF2.2) are shown. Moreover, the differences between the results obtained from TRIPOLI4 with JEF2.2 and JEFF3.0 are illustrated. The APOLLO2 and TRIPOLI4 (JEF2.2) results agree well, e.g. the k_{inf} value calculated with TRIPOLI4 is about 200 pcm higher than the one obtained from APOLLO. Moreover, the contributions of the erbium absorption rate to the total absorption rate are slightly higher using TRIPOLI4 (JEF2.2).

The comparison of the JEF2.2 and JEFF3.0 libraries shows that:

- With the JEFF3.0 library, the k_{inf} value is 887 pcm higher than the one obtained from the JEF2.2 library, which is mainly due to a larger fission in ^{239}Pu ;
- Higher absorption in ^{239}Pu ;
- Lower absorption rates of ^{166}Er and ^{167}Er using JEFF3.0;

- No significant differences occur for the other nuclides.

Table 6.48 shows a more detailed analysis of the erbium absorption rate at different burnup steps. The results are obtained from APOLLO2 calculations. The relative absorption rate of each erbium nuclide to the total absorption rate of all erbium nuclides is presented and also the contribution of the erbium nuclides to the total absorption rate of the entire cell (α^{Er}).

TABLE 6.47. COMPARISON OF APOLLO2 AND TRIPOLI4 RESULTS AT 300 K

Code	APOLLO2			TRIPOLI4			TRIPOLI4		
Library	CEA_93.V6 (JEF 2.2)			JEF2.2			JEFF3.0		
Nuclide	Abs.	Fission	Prod.	Abs.	Fission	Prod.	Abs.	Fission	Prod.
Er-166	0.0098			0.0121			0.0099		
Er-167	0.1731			0.1758			0.1741		
Er-168	0.0028			0.0000			0.0000		
O-16	0.0000			0.0000			0.0001		
GRAPH	0.0056			0.0053			0.0053		
BNAT	0.0010			0.0010			0.0009		
Pu-238	0.0002			0.0002			0.0002	0.0000	0.0001
Pu-239	0.6495	0.4068	1.1663	0.6482	0.4061	1.1643	0.6519	0.4096	1.1735
Pu-240	0.1478	0.0002	0.0006	0.1472	0.0002	0.0006	0.1476	0.0002	0.0005
Pu-241	0.0075	0.0056	0.0165	0.0075	0.0056	0.0165	0.0075	0.0055	0.0162
P-242	0.0017	0.0000	0.0000	0.0017	0.0000	0.0000	0.0017	0.0000	0.0000
SINAT	0.0009			0.0009			0.0007		
He-4	0.0000			0.0000			0.0000		
<i>TOTAL</i>	<i>1.0000</i>	<i>0.4126</i>	<i>1.1834</i>	<i>1.0000</i>	<i>0.4119</i>	<i>1.1814</i>	<i>1.0000</i>	<i>0.4154</i>	<i>1.1903</i>
Difference in pcm, relative to TRIPOLI4 (JEF2.2)									
Nuclide	Abs.	Fission	Prod.	Abs.	Fission	Prod.	Abs.	Fission	Prod.
Er-166	-228						-224		
Er-167	-272						-171		
Er-168	285						1		
O-16	0						8		
GRAPH	31						-3		
BNAT	0						-1		
Pu-238	0	0	0				1	2	6
Pu-239	129	73	206				373	356	920
Pu-240	60	0	0				38	-2	-5
Pu-241	-2	-1	-3				2	-9	-28
Pu-242	-2	0	0				2	0	0
SINAT	0	0	0				-26		
He4-	0	0	0				0		
<i>TOTAL</i>	<i>0</i>	<i>72</i>	<i>203</i>				<i>0</i>	<i>345</i>	<i>887</i>

TABLE 6.48. CONCENTRATION AND ABSORPTION RATES OF ERBIUM NUCLIDES AT DIFFERENT BURNUP STEPS (THE RESULTS ARE OBTAINED FROM APOLLO2 CALCULATIONS AT A TEMPERATURE OF 1200 K.)

Burnup		APOLLO2 Results		
		$k_{inf} = 1.1111$		
0	Isotope	Conc	Abs.	α^{Er}
	Er-166	4.140E-04	0.0530	0.0103
	Er-167	2.828E-04	0.9310	0.1810
	Er-168	3.302E-04	0.0159	0.0031
	Sum		1.0000	0.1944
		$k_{inf} = 1.0984$		
5	Isotope	Conc	Abs.	α^{Er}
	Er-166	4.139E-04	0.0534	0.0103
	Er-167	2.800E-04	0.9305	0.1796
	Er-168	3.331E-04	0.0162	0.0162
	Sum		1.0000	0.2060
		$k_{inf} = 1.0656$		
250	Isotope	Conc	Abs.	α^{Er}
	Er-166	4.053E-04	0.0676	0.0106
	Er-167	1.573E-04	0.9058	0.1417
	Er-168	4.614E-04	0.0266	0.0042
	Sum		1.0000	0.1564
		$k_{inf} = 1.1050$		
500	Isotope	Conc	Abs.	α^{Er}
	Er-166	3.963E-04	0.1004	0.0113
	Er-167	6.680E-05	0.8551	0.0964
	Er-168	5.571E-04	0.0445	0.0050
	Sum		1.0000	0.1128
		$k_{inf} = 1.1412$		
750	Isotope	Conc	Abs.	α^{Er}
	Er-166	3.865E-04	0.1959	0.0137
	Er-167	1.906E-05	0.7189	0.0502
	Er-168	6.103E-04	0.0852	0.0059
	Sum		1.0000	0.0698

Preliminary Intercomparison with previous Russian results

Table 6.49 shows the difference between the APOLLO2 results and the averaged values reported by the Russian team. The difference is expressed in pcm and is determined as $\Delta k/\sqrt{k_1 k_2}$. The difference for the nuclides ^{238}Pu , ^{16}O , silicon and boron was smaller than 10 pcm and therefore the results were suppressed. The complete data is given in Section 6.3.2.3.

The APOLLO2 results agree very well with the values reported for the FCC case (particle structure is modelled). The k_{inf} values of APOLLO2 are slightly lower than the ones of the Russian team, e.g

251 pcm at 300 K and 87 pcm at 900 K. This is due to the fact that the Russian production rates are larger than the APOLLO2 results, although the fission rates are smaller. This surprising behaviour indicates the values for the number of neutrons per fission is significantly larger in the computational tools used by the Russian team. The difference in the total absorption rates is negligible.

For the FCC2 case, the differences between the code systems are significantly larger than for case FCC, particularly at a temperature of 300 K. The production rate given by the Russian team is again up to 817 pcm higher than the one obtained from APOLLO2. It can be seen that the total absorption rate is almost the same for the code systems, however, this is due to a compensation of the absorption of ^{239}Pu and ^{240}Pu , e.g. at 300 K, the absorption rate of ^{239}Pu is 519 pcm higher than the one calculated with APOLLO2 whereas the absorption rate of ^{240}Pu is 538 pcm lower. The same differences occur for the FCC1 case, but they are about a factor of 2 lower.

As mentioned earlier, the difference between the code systems can possibly be explained by the number of neutrons per fission that was used. Therefore the neutrons per fission were deduced for the plutonium nuclides from the fission rates and production rates and are shown in Table 6.50. The values of ^{239}Pu and ^{241}Pu are highlighted in bold because they are the important nuclides in a thermal neutron spectrum. The values (in italics) of the nuclides ^{238}Pu , ^{240}Pu and ^{242}Pu are given for completeness. These values do not play an important role in terms of neutron balance components. The comparison shows that the difference between the code systems is not only due to the cross-sections, but also due to the applied number of neutrons per fission (ν):

- The averaged ν -values ^{239}Pu and ^{241}Pu used in the Russian code systems are about 700 pcm and 1600 pcm higher than the ones for APOLLO2.
- The production rate of ^{239}Pu contributes mainly to the total production rate and therefore the values of the sums are similar to the values of ^{239}Pu .

TABLE 6.49. COMPARISON OF RUSSIAN RESULTS AND APOLLO2
FOR FCC, FCC1 AND FCC2 CASES IN PCM

		300 K			600 K			900 K			1200 K		
		$k_{inf} = 251$			$k_{inf} = 194$			$k_{inf} = 87$			$k_{inf} = 238$		
FCC	Nuclide	Abs.	Fission	Prod.	Abs.	Fission	Prod.	Abs.	Fission	Prod.	Abs.	Fission	Prod.
	Pu-238	1	0	0	1	0	0	1	0	0	1	0	0
	Pu-239	-22	-270	192	-87	-359	114	-143	-445	25	16	-286	185
	Pu-240	13	-9	-8	66	-9	-9	124	-10	-9	-34	-10	-9
	Pu-241	19	7	16	18	6	14	17	6	14	20	10	18
	Pu-242	14			15			15			15		
	O-16	-1			-1			-1			-1		
	GRAPH	-19			-20			-20			-20		
	SINAT	4			5			5			5		
	BNAT	-1			-1			-1			-1		
	TOTAL	10	-273	199	-5	-362	114	-3	-452	33	0	-285	197
		$k_{inf} = 838$			$k_{inf} = 602$			$k_{inf} = 406$			$k_{inf} = 636$		
FCC2	Nuclide	Abs.	Fission	Prod.	Abs.	Fission	Prod.	Abs.	Fission	Prod.	Abs.	Fission	Prod.
	Pu-238	1	0	0	1	0	0	1	0	0	1	0	0
	Pu-239	519	584	817	361	354	592	223	160	403	405	370	611
	Pu-240	-538	-6	-5	-387	-7	-5	-239	-7	-5	-441	-7	-5
	Pu-241	21	19	27	17	13	21	14	9	17	16	13	20
	Pu-242	8			10			10			10		
	O-16	0			0			0			0		
	GRAPH	-12			-15			-16			-16		
	SINAT	9			8			8			8		
	BNAT	0			0			0			-1		
	TOTAL	10	595	844	-5	361	609	0	162	413	-19	377	622
		$k_{inf} = 458$			$k_{inf} = 255$			$k_{inf} = 49$			$k_{inf} = 277$		
FCC1	Nuclide	Abs.	Fission	Prod.	Abs.	Fission	Prod.	Abs.	Fission	Prod.	Abs.	Fission	Prod.
	Pu-238	1	0	0	1	0	0	1	0	0	1	0	0
	Pu-239	324	217	450	159	12	246	-1	-191	42	178	20	257
	Pu-240	-333	-7	-6	-162	-7	-6	-10	-7	-6	-204	-8	-6
	Pu-241	12	6	14	9	3	10	8	0	7	11	5	12
	Pu-242	9			10			11			10		
	O-16	0			0			0			0		
	GRAPH	-19			-20			-20			-20		
	SINAT	6			7			7			7		
	BNAT	-2			-2			-2			-2		
	TOTAL	-1	215	458	0	7	248	-7	-200	42	-20	16	262

TABLE 6.50. COMPARISON OF NUMBER OF NEUTRONS PER FISSION
FOR THE VARIOUS CASES AT 300 K

	Averaged Russian values (1)		APOLLO2 (2)	Difference (1) -(2)
	Nuclide	Neutron per fission	Neutron per fission	pcm
FCC	<i>Pu-238</i>	<i>2.9417</i>	<i>2.9482</i>	<i>-652</i>
	Pu-239	2.8816	2.8681	1351
	<i>Pu-240</i>	<i>3.0299</i>	<i>2.9636</i>	<i>6635</i>
	Pu-241	2.9500	2.9336	1636
	<i>Pu-242</i>	<i>3.0851</i>	<i>3.0345</i>	<i>5067</i>
	Sum	2.8827	2.8691	1360
FCC2	Nuclide	Neutron per fission	Neutron per fission	
	<i>Pu-238</i>	<i>2.9398</i>	<i>2.9413</i>	<i>-143</i>
	Pu-239	2.8740	2.8671	682
	<i>Pu-240</i>	<i>3.0252</i>	<i>2.9369</i>	<i>8829</i>
	Pu-241	2.9488	2.9335	1538
	<i>Pu-242</i>	<i>3.0788</i>	<i>3.0140</i>	<i>6482</i>
FCC1	Sum	2.8753	2.8681	716
	Nuclide	Neutron per fission	Neutron per fission	
	<i>Pu-238</i>	<i>2.9382</i>	<i>2.9409</i>	<i>-274</i>
	Pu-239	2.8737	2.8669	679
	<i>Pu-240</i>	<i>3.0191</i>	<i>2.9348</i>	<i>8437</i>
	Pu-241	2.9487	2.9335	1516
	<i>Pu-242</i>	<i>3.0736</i>	<i>3.0127</i>	<i>6091</i>
	Sum	2.8749	2.8679	699

Fuel element transport calculations

Methodology

The deterministic calculations performed on the fuel block rely on the NEPHTIS calculation scheme developed at CEA for the prismatic block-type VHTR and based on the APOLLO2 and CRONOS2 codes [6-19–6-22]. It is worth noting that NEPHTIS, previously validated and qualified on a uranium-fuel-based reactor, is used in this instance to perform calculations of the GT-MHR loaded with weapons-grade Plutonium (WPu).

Main hypothesis of the 2-D transport model

Three types of two dimensional geometries have been developed and tested. Only the standard fuel element (Fig. 6.32 on the left) forms the subject of a comparison according to the proposed benchmark.

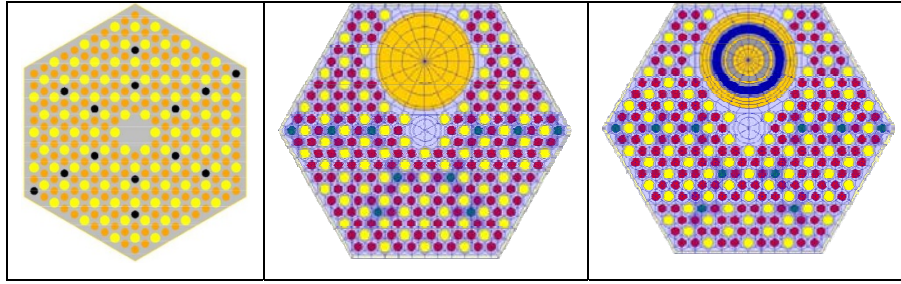


FIG. 6.32. Example of geometry used in the 2-D transport calculations.

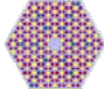

All those calculations are performed assuming 172-energy groups. The temperatures and concentrations at different burnups are those imposed by the benchmark problem. A rather complete chain of nuclei has been considered with 28 heavy nuclei and 110 fission products. Xenon and samarium are present at the beginning of cycle ($t = 0$).

The presence of the coated particles is taken into account through the double-heterogeneity model of APOLLO2. The spherical geometry of the fuel particles are fully described with their coatings and this geometry is itself embedded in the global geometry of the fuel element with its cylindrical fuel compacts and helium channels. The flux spectrum is therefore computed in the same unique run.

The self-shielding of the different plutonium isotopes is taken into account from the ^{238}Pu up to ^{242}Pu . The self-shielding calculations are performed successively for each isotope on a part of the whole element geometry and considering of course the double-heterogeneity. An elementary cell, part of the global geometry, has been chosen and represents one fuel compact surrounded by its first six neighbours (three helium channels and three other fuel compacts). A similar process has been followed as far as the three erbium isotopes are concerned in the burnable poison compacts.

An intermediate step of comparison with reference cases provided by the Monte Carlo method has been carried out at the level of the fuel element geometry. Some results are presented in Table 6.51.

TABLE 6.51. COMPARISON BETWEEN TRANSPORT DETERMINISTIC AND MONTE CARLO CALCULATIONS AT THE FUEL ELEMENT SCALE (FRESH FUEL (1200 K))

Element type		k_{eff} Deterministic (APOLLO2)	k_{eff} Monte Carlo (TRIPOLI4)	$\Delta k/k$ (pcm)
Standard		1.14327	1.14170 ± 0.00033	130
Control		1.20472	1.20355 ± 0.00032	98

It turns out that the observed results are in quite good accordance between the APOLLO2 and TRIPOLI4 k -effectives. Additional computations performed in the presence of the control rod in the control fuel element, allow concluding that the control rod worth calculated in infinite medium with APOLLO2 is estimated with a discrepancy of less than 1% compared to the TRIPOLI4 simulations.

Results of a burnup simulation of a fuel element

It should be stressed that the examined two dimensional configurations in this instance do not assume an axial homogenization of a three dimensional fuel block. That means that the graphite upper and lower parts of the fuel blocks are not taken into account. Therefore, the two dimensional transport calculations presented here correspond to a radial or horizontal cross-section of a standard fuel block.

The final results for the fuel depletion simulation in the standard fuel block are summarized in

Table 6.52. The first column of this table provides the isotope concentrations averaged on a two dimensional cross-section of the fuel element and therefore averaged on the global geometry. Since this global geometry takes into account a helium gap at the periphery of the fuel block, a second series

TABLE 6.52. BURNUP CALCULATIONS OF A STANDARD FUEL ELEMENT
AT 1200 K (JEF 3.1)

	0 day	Correction on the Fuel Element Volume
k_{inf}	1.14327	1.14327
Er-167	4.28301E-06	4.33073E-06
Pu-239	1.99541E-05	2.01764E-05
Pu-240	1.41963E-06	1.43545E-06
Pu-241	2.52475E-07	2.55288E-07
Pu-242	9.23968E-08	9.34263E-08
280 days		
k_{inf}	1.09966	1.09966
Er-167	1.99716E-06	2.01941E-06
Pu-239	1.19681E-05	1.21014E-05
Pu-240	2.38455E-06	2.41112E-06
Pu-241	1.79981E-06	1.81986E-06
Pu-242	1.87763E-07	1.89855E-07
560 days		
k_{inf}	1.11319	1.11319
Er-167	6.05495E-07	6.12241E-07
Pu-239	5.20055E-06	5.25849E-06
Pu-240	2.46922E-06	2.49673E-06
Pu-241	2.66502E-06	2.69471E-06
Pu-242	5.27013E-07	5.32885E-07
840 days		
k_{inf}	1.02617	1.02617
Er-167	1.02307E-07	1.03447E-07
Pu-239	6.82110E-07	6.8971E-07
Pu-240	1.53880E-06	1.55595E-06
Pu-241	1.78807E-06	1.80799E-06
Pu-242	1.27912E-06	1.29337E-06

of concentration values are given in the second columns to be compared with the values from other participants.

Monte Carlo simulations

Preliminary issue

As the VHTR fuel is in a form of dispersed particles in a graphite matrix, an assumption must be made with respect to the geometrical description of the fuel in the three dimensional core calculations. Indeed, the description of such a stochastic geometry would suppose to repeat some simulations several times based on different geometry with randomly distributed particles in the fuel compact. Only an average value coming from these repeated simulations and associated with a standard deviation could be considered as a definitive result.

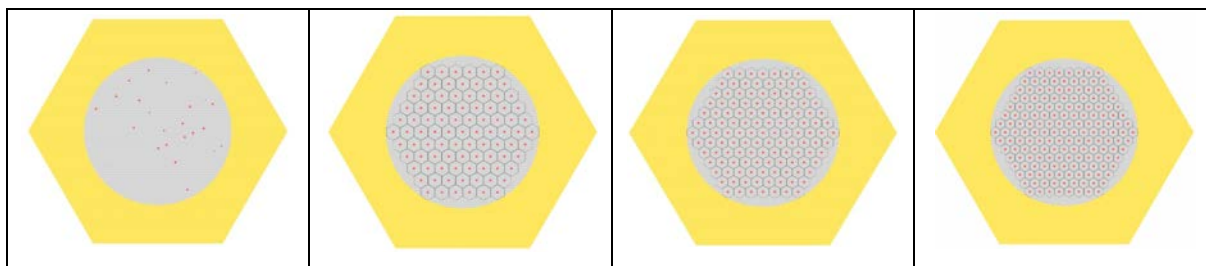


FIG. 6.33. Illustration of random and regular particles distribution in the fuel compact.

To avoid this long way to proceed, simulation of a regular arrangement of the particles into the fuel compact has been assumed in the three dimensional core calculations. Nevertheless, a preliminary verification phase has been done in order to verify that different regular arrangements and random distributions of the fuel particles (Fig. 6.33) lead to similar results in the present case of WPu and its related packing fraction (1046 particles per cm^3). These verifications have been carried out at the compact geometry level (cylindrical fuel compact in infinite medium) and the results are gathered in Table 6.53. From these results, it turns out that for the present envisaged quality of plutonium and packing fraction, the choice of regular or random description geometry seems to not influence the reactivity. The reactivity discrepancies between the different considered regular arrangements and the random one lead to values twice lower than the standard deviation. Therefore, because of the gain on the computation time, a regular arrangement has been selected in the following three dimensional core calculations. Taking into account the packing fraction of the benchmark, the hexagonal-7 lattice has been selected because it offers the possibility to get nearly the same radial and axial distances between the particles. According to this description, the final mass balance achieved in the core corresponds to 700,536 g of WPu with the exact number of 6048 particles per compact.

TABLE 6.53. IMPACT ON THE REACTIVITY OF THE PARTICLES MODEL USED IN ONE COMPACT (FRESH FUEL (1200 K, JEF3.1))

Particles description	k_{eff}	Std deviation (σ)	3σ	$\Delta k/k$ (pcm)
Random	1.34522	59		reference
Hexagonal 6	1.34429	29	88	69
Hexagonal 7	1.34487	30	89	26
Hexagonal 8	1.34489	28	84	24

3-D core calculations

Hypothesis (geometry)

Assuming a regular lattice of fuel particles with their coatings diluted in graphite, a full three dimensional core model has been constructed (Fig. 6.34). Each helium channel and gap between the fuel blocks are described from the bottom reflector to the top reflector. It should be stressed that if the specific orientation of the controlled fuel elements is taken into account, no orientation is considered for the standard fuel element which presents a special burnable poisons disposition (see Fig. 6.32) and which would strictly be required.

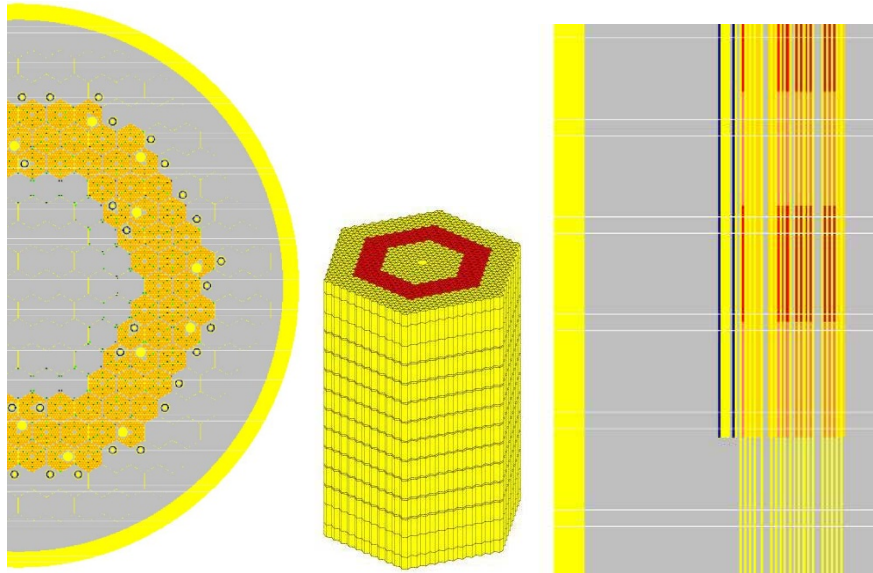


FIG. 6.34. Some illustrations of the 3-D core geometry.

Six burnable poisons are also included in each graphite block of the first row of the inner reflector. Finally, large holes cross through the upper reflector and through the active core zone. They are filled either with helium or with annular B₄C control rods.

Results

All the TRIPOLI4 calculations are based on the JEF3.1 cross-section library. Different types of calculations have been performed depending on the following:

- The temperature (300 and 1200 K considered here);
- The core configurations (six variants was imposed by the benchmark all corresponding to Beginning and End of Cycle of a batch-wise reloaded core managed by third);
- The presence or not of the different clusters of control rods.

The impact of the temperature on the core reactivity is given in the Table 6.54. It is worth noting that one of the analysed core configurations (variant v6) leads to a small positive integral temperature coefficient.

TABLE 6.54. CORE REACTIVITY AS A FUNCTION OF THE CORE CONFIGURATION AND THE TEMPERATURE

Core Configurations	k_{eff} (300 K) (TRIPOLI4)	k_{eff} (1200 K) (TRIPOLI4)	$\Delta k/k$ (pcm)	Temp. Effect (pcm/K)
v1	1.07407 ± 0.00031	1.04121 ± 0.00032	-3060	-3.40
v2	1.01031 ± 0.00043	1.00223 ± 0.00051	-800	-0.89
v3	1.07979 ± 0.00029	1.04249 ± 0.00033	-3454	-3.84
v4	1.03195 ± 0.00039	1.01695 ± 0.00050	-1454	-1.62
v5	1.05650 ± 0.00034	1.02924 ± 0.00039	-2580	-2.87
v6	0.99702 ± 0.00049	0.99819 ± 0.00096	+117	0.13

The global control worth has been estimated at 300 K whereas the reactivity worth of the startup control rods (core zone) of the operating control rods (reflector) and of all the rods have been computed separately at 1200 K. All the results are gathered in Table 6.55 and can be observed on the different charts presented in Figs 6.35–6.37.

TABLE 6.55. CONTROL ROD WORTH AS A FUNCTION OF THE CORE CONFIGURATION AND TEMPERATURE

Core Configurations		k_{eff} (300 K) (TRIPOLI4)	$\Delta k/k$ (pcm)	k_{eff} (1200 K) (TRIPOLI4)	$\Delta k/k$ (pcm)
v1	CR out	1.07407 ± 0.00031		1.04121 ± 0.00032	
	CR in	0.87488 ± 0.00026	20512	0.83317 ± 0.00026	22290
	Startup CR			1.01214 ± 0.00032	2831
	Operating CR			0.89238 ± 0.00025	15424
v2	CR out	1.05650 ± 0.00034		1.00223 ± 0.00051	
	CR in	0.81736 ± 0.00027	21194	0.78923 ± 0.00025	23892
	Startup CR			0.96998 ± 0.00033	3271
	Operating CR			0.84817 ± 0.00027	16690
v3	CR out	1.07979 ± 0.00029		1.04249 ± 0.00033	
	CR in	0.88092 ± 0.00026	20355	0.83669 ± 0.00026	21991
	Startup CR			1.01382 ± 0.00031	2789
	Operating CR			0.89551 ± 0.00025	15197
v4	CR out	1.07407 ± 0.00031		1.01695 ± 0.00050	
	CR in	0.83498 ± 0.00026	21179	0.80494 ± 0.00026	23379
	Startup CR			0.98657 ± 0.00035	3033
	Operating CR			0.86346 ± 0.00026	16362
v5	CR out	1.05650 ± 0.00034		1.02924 ± 0.00039	
	CR in	0.85893 ± 0.00027	20703	0.82077 ± 0.00027	22634
	Startup CR			0.99984 ± 0.00033	2899
	Operating CR			0.87999 ± 0.00026	15667
v6	CR out	1.07979 ± 0.00029		0.99819 ± 0.00096	
	CR in	0.80243 ± 0.00027	21712	0.78227 ± 0.00025	24374
	Startup CR			0.96614 ± 0.00038	3263
	Operating CR			0.84181 ± 0.00026	17040

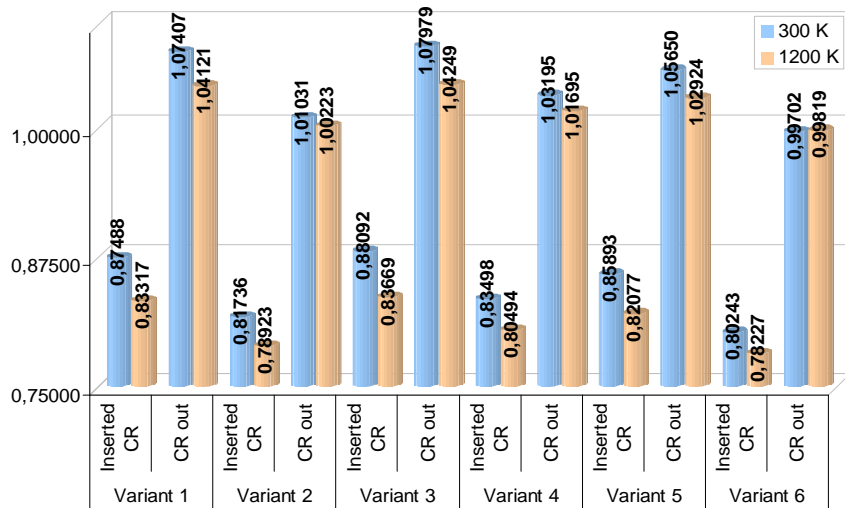


FIG. 6.35. Core reactivity as a function of the core configuration and temperature.

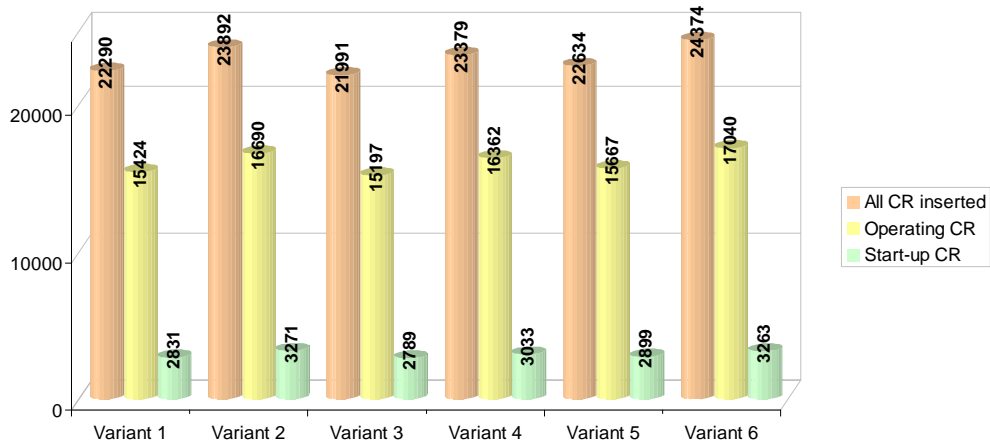


FIG. 6.36. Worth of different clusters of control rods as a function of the core configuration.

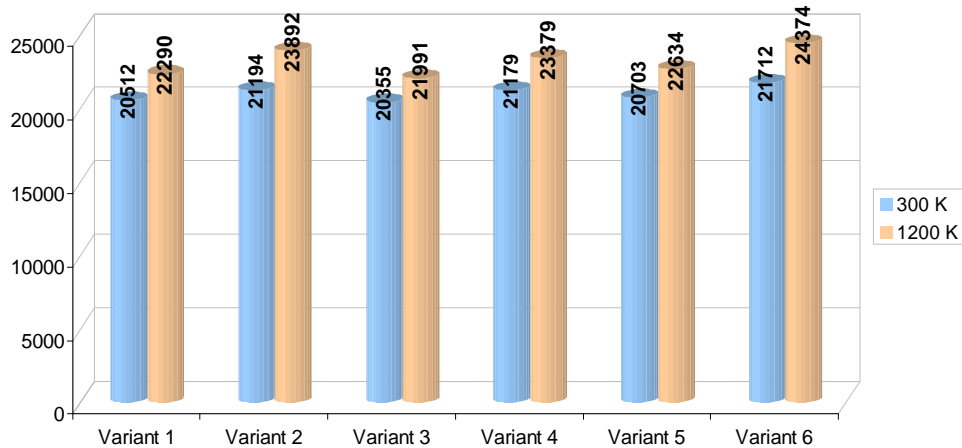


FIG. 6.37. Control rod worth at 300 and 1200 K.

Conclusion

Different types of calculations carried out with APOLLO2 and TRIPOLI4 have been performed in order to answer to the different steps proposed in the GTMHR PHYS benchmark of the CRP-5. For the first step, the investigated elementary fuel cells with plutonium and plutonium/erbium, lead to the results of the deterministic and Monte Carlo codes which agree quite well. Moreover, a significant impact of the nuclear data libraries (JEF2.2 and JEFF3) on the system reactivity has been observed. Higher k_{inf} values were obtained with JEFF3 due to larger fission rates in ^{239}Pu .

A second step, based on two dimensional transport calculations, was devoted to simulate the standard fuel burnup until 840 FPD of irradiation. A preliminary comparison at the beginning of cycle, which means with fresh fuel, has been performed between APOLLO2 and TRIPOLI4 and lead to very good agreement. Burnup calculation results have then been provided to the host country (Russian Federation) for final comparisons.

As a third step, a three dimensional core model has been implemented with the TRIPOLI4 code. Assuming a regular arrangement of the particles inside the fuel compact, several core configurations proposed by the benchmark have been computed and allow having an estimation of the control rod and the integral temperature effect between 300 and 1200 K.

Finally, a deterministic approach has also been implemented in the framework of this CRP-5. The results have been partially presented at the last CRP-5 meeting. For that, the NEPHTIS VHTR calculation scheme relying on the APOLLO2 and CRONOS2 codes has been used. Intensively validated and qualified for the uranium fuel (e.g. [6-23]), the frame of this GTMHR-PHYS benchmark constituted a first application for NEPHTIS with WPu and erbium as burnable poison. The observed discrepancies with the TRIPOLI4 code appeared larger than in the case of the uranium applications. These discrepancies have not been considered as acceptable to be provided as final results to the host country within the given time of the CRP-5. Nevertheless, this experience showed that the direct use of the NEPHTIS calculation scheme to model the specific *GT-MHR plutonium burner* case without questioning the modelling options defined for the uranium cases does not constitute a satisfying approach. This concerns especially the number of groups in diffusion calculations, the burnable poison model, the presence of burnable poison in the reflector, etc. Preliminary reasons for explaining the discrepancies with the reference TRIPOLI4 simulations have been identified. They constitute a basis for the next investigations that should be addressed in the near future.

6.3.2.3. Detailed tables of results

TABLE 6.56. DETAILED NEUTRON BALANCE COMPONENTS
CALCULATED WITH APOLLO2 FOR FCC, FCC1 AND FCC2

Case	Temp.		300°K			600°K			900°K			1200°K		
	K _{inf} =1.5373		0.000	K _{inf} =1.5115		0.000	K _{inf} =1.4860		0.000	K _{inf} =1.4610		0.0000		
	Nuclide	Abs.	Fission	Prod.	Abs.	Fission	Prod.	Abs.	Fission	Prod.	Abs.	Fission	Prod.	
FCC	Pu-238	0.0003	0.0000	0.0001	0.0002	0.0000	0.0001	0.0002	0.0000	0.0001	0.0002	0.0000	0.0001	
	Pu-239	0.8363	0.5277	1.5135	0.8292	0.5191	1.4886	0.8205	0.5107	1.4641	0.8096	0.5023	1.4400	
	Pu-240	0.1421	0.0003	0.0009	0.1500	0.0003	0.0009	0.1595	0.0003	0.0009	0.1710	0.0003	0.0009	
	Pu-241	0.0103	0.0078	0.0228	0.0099	0.0075	0.0219	0.0095	0.0071	0.0209	0.0091	0.0068	0.0200	
	Pu-242	0.0024			0.0024			0.0025			0.0025			
	O-16	0.0000			0.0000			0.0000			0.0000			
	GRAPH	0.0060			0.0058			0.0056			0.0055			
	SINAT	0.0015			0.0014			0.0013			0.0013			
	BNAT	0.0011			0.0010			0.0009			0.0009			
TOTAL	1.0000	0.5358	1.5373	1.0000	0.5269	1.5115	1.0000	0.5181	1.4860	1.0000	0.5095	1.4610		
K _{inf} = 1.4473		K _{inf} = 1.4243		0.000	K _{inf} = 1.4009		0.000	K _{inf} = 1.3768		0.0000				
	Nuclide	Abs.	Fission	Prod.	Abs.	Fission	Prod.	Abs.	Fission	Prod.	Abs.	Fission	Prod.	
FCC2	Pu-238	0.0002	0.0000	0.0001	0.0002	0.0000	0.0001	0.0002	0.0000	0.0001	0.0002	0.0000	0.0001	
	Pu-239	0.7972	0.4974	1.4260	0.7890	0.4896	1.4036	0.7795	0.4818	1.3809	0.7680	0.4736	1.3575	
	Pu-240	0.1837	0.0003	0.0008	0.1924	0.0003	0.0008	0.2024	0.0003	0.0008	0.2143	0.0003	0.0008	
	Pu-241	0.0093	0.0070	0.0204	0.0090	0.0067	0.0198	0.0087	0.0065	0.0190	0.0084	0.0063	0.0184	
	Pu-242	0.0024			0.0024			0.0025			0.0025			
	O-16	0.0000			0.0000			0.0000			0.0000			
	GRAPH	0.0052			0.0050			0.0049			0.0048			
	SINAT	0.0012			0.0012			0.0011			0.0011			
	BNAT	0.0008			0.0008			0.0008			0.0007			
TOTAL	1.0000	0.5046	1.4473	1.0000	0.4967	1.4243	1.0000	0.4886	1.4009	1.0000	0.4802	1.3768		
K _{inf} = 1.4330		K _{inf} = 1.4106		K _{inf} = 1.3878		0.000	K _{inf} = 1.3641							
	Nuclide	Abs.	Fission	Prod.	Abs.	Fission	Prod.	Abs.	Fission	Prod.	Abs.	Fission	Prod.	
FCC1	Pu-238	0.0002	0.0000	0.0001	0.0002	0.0000	0.0001	0.0002	0.0000	0.0001	0.0002	0.0000	0.0001	
	Pu-239	0.7905	0.4925	1.4120	0.7824	0.4850	1.3902	0.7730	0.4773	1.3681	0.7615	0.4693	1.3450	
	Pu-240	0.1906	0.0003	0.0008	0.1992	0.0003	0.0008	0.2092	0.0003	0.0008	0.2210	0.0003	0.0008	
	Pu-241	0.0091	0.0068	0.0201	0.0088	0.0066	0.0195	0.0085	0.0064	0.0188	0.0083	0.0062	0.0182	
	Pu-242	0.0024			0.0024			0.0025			0.0025			
	O-16	0.0000			0.0000			0.0000			0.0000			
	GRAPH	0.0051			0.0050			0.0048			0.0048			
	SINAT	0.0012			0.0011			0.0011			0.0011			
	BNAT	0.0008			0.0008			0.0007			0.0007			
TOTAL	1.0000	0.4997	1.4330	1.0000	0.4919	1.4106	1.0000	0.4840	1.3878	1.0000	0.4758	1.3641		

6.3.3. GT-MHR benchmark problem results, Republic of Korea

6.3.3.1. Introduction

An international GCR programme has been initiated by IAEA, of which the key objectives are the validation of analytical computer codes and the evaluation of benchmark models for the projected and actual VHTRs [6-24]. We applied the HELIOS/MASTER code system with the two-step procedure [6-25] for the analysis of this benchmark problem. This procedure includes the transport lattice calculation to generate a few group constants by the HELIOS code [6-26] and the three dimensional core calculation to perform the reactor physics analysis by the MASTER code [6-27].

Since the neutronic characteristics of the VHTR core are quite different from the PWR ones in many aspects, the conventional two-step procedure should be modified in order to facilitate an easy treatment of such characteristics. A particulate fuel with multicoating layers, called TRISO, is employed to achieve a high fuel performance and fission gas confinement, which is randomly dispersed in a graphite matrix. This causes a so-called double-heterogeneity problem in the lattice calculation which requires special treatment. The double-heterogeneity effect due to the self-shielding of the fuel particles was treated by using the recently developed RPT method [6-28]. This method transforms the double-heterogeneous fuel problem into a single-heterogeneous one, which renders the conventional lattice codes including HELIOS capable of analysing the VHTR fuel elements. This transformation is performed by reducing the fuel zone area where the TRISO particles are homogenized so that both the double- and single-heterogeneous problems may provide an identical self-shielding effect.

The spectrum shift due to the use of a graphite moderator and a higher operating temperature makes resonance absorption and upscattering more important in the VHTR cores. The two-step procedure is premised on an assumption that the cross-sections are so independent of the environment that they can be calculated by a simple spectral geometry. The spectrum shift in the VHTR core may not make this premise reliable any more if a two-energy group structure was used, which is widely adopted in the diffusion nodal core analysis for the Light Water Reactor (LWR) cores. In order to appropriately handle the effects of the spectrum shift, KAERI established a multi-energy group structure with appropriate group boundaries, within which all the cross-sections become relatively environment-free regardless of a state parameter change.

The long neutron diffusion length in a graphite-moderated core and the long and thin design of the VHTR core result in a strong neutron interaction between the fuel and reflector regions. The sharp flux gradient caused by the control rods located in the reflector region may also increase the neutron leakage through the fuel-reflector interface. The conventional two-step procedure based on the lattice calculation for an isolated fuel block with the reflective boundary condition may fail in modelling the strong neutron interaction across the fuel-reflector interface. This concern was easily resolved by applying the equivalence theory to a one dimensional mini-core geometry consisting of the fuel and reflector regions instead of a single fuel block geometry. The strong fuel-reflector interaction effect can be captured by the equivalent cross-sections of the fuel and the reflector derived from the mini-core geometry. Burnable poisons in the inner reflector and an asymmetrically located large control rod can also be treated by the equivalence theory applied for the multiblock models.

The GT-MHR benchmark calculations were performed to verify and validate the HELIOS/MASTER code system with the two-step analysis procedure. The MCNP Monte Carlo code served as a reference code in these calculations. The benchmark problems for fuel pins, burnable poison pins, blocks and six variant cores were analysed by HELIOS/MASTER and MCNP. See [6-29] for the general Monte Carlo N-Particle transport code.

The summary provided here was submitted to the CRP as Ref. [6-30].

6.3.3.2. Methodology

HELIOS/MASTER code system with two-step procedure

The HELIOS/MASTER code system originally developed for the PWR physics analysis is shown in Fig. 6.38. The two-step procedure developed originally for the LWR core analysis by using this code system has been modified for the VHTR physics analysis. In this two-step procedure, the transport lattice calculations are performed by the HELIOS code to generate a few group constants through the equivalent theory homogenization and group constants are tabularized as a function of the temperatures and burnups by using the HOPE and PROLOG codes and then the three dimensional core calculation for the reactor physics analysis is performed by the MASTER code. Our overall physics analysis procedure for the VHTR is as follows:

- (a) Perform the HELIOS lattice calculation for a one dimensional mini-core;
- (b) Edit cross-sections and discontinuity factors for fuel blocks and graphite reflectors from the mini-core calculation;
- (c) Perform the three dimensional core calculations using the MASTER code with the cross-sections and discontinuity factors obtained in the procedure mentioned in (b).

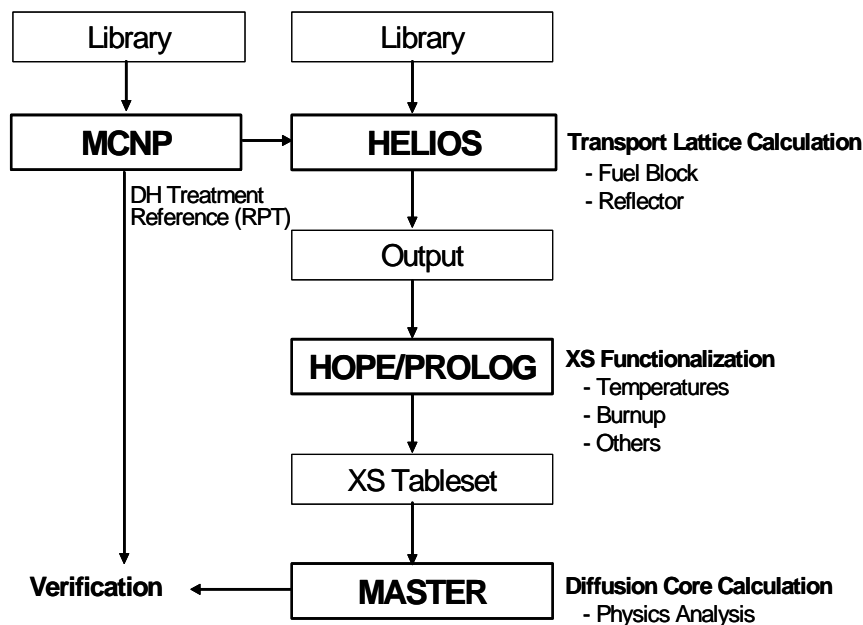


FIG. 6.38. Flow chart of the HELIOS/MASTER code system.

Double-heterogeneity treatment by the RPT method [6-28]

Most of the conventional transport lattice codes, including HELIOS, cannot appropriately treat the double-heterogeneity effects caused by the particulate form of VHTR fuels. The RPT method was recently developed to accurately capture the double-heterogeneity effects. This method makes the conventional lattice codes which cannot explicitly model the fuel particles applicable to the analysis of VHTR fuel elements by transforming the double-heterogeneous fuel problem into a single-heterogeneous one. In the RPT procedure, the self-shielding effect of randomly distributed fuel particles in the double-heterogeneous problem is preserved in the single-heterogeneous problem by separating the fuel region into two zones, one of which all the particles are homogenized into.

Incorporating the RPT method into HELIOS, its applicability to the VHTR core analysis has been tested against various sample calculations which include the calculations for pin cells, blocks and simple mini-cores consisting of fuel blocks and graphite reflectors. The results of the HELIOS calculations with a 190-group library have been proven to be very consistent with those of the MCNP calculations.

Multigroup energy group structure

In order to appropriately handle the effects of the spectrum shift, a study was performed to find an optimum neutron energy group structure to be used in the MASTER three dimensional core calculation. By exploring some hundreds of the HELIOS calculations for the mini-cores with different control rod or burnable poison rod configurations at various operating temperatures and burnups, we optimized the number of energy groups and their boundaries within which all the cross-sections become so relatively environment-free that they may be calculated by a simple spectral geometry. The resultant number of energy groups and their boundaries, shown in Table 6.57, are verified by the MASTER calculations for various core configurations.

Homogenization using mini-core geometry

To capture the strong fuel–reflector interaction effect, the equivalence theory was applied to a one dimensional mini-core geometry consisting of the fuel and reflector regions instead of an isolated fuel block geometry. The cross-sections and the discontinuity factors of the fuel and reflector to be used in the MASTER core analysis are obtained from the HELIOS calculations for the mini-cores in the way that the region-wise reaction rates and the neutron currents across the material discontinuities are preserved. Surface-dependent discontinuity factors for the fuel and reflector blocks with control rod insertions are estimated from the multiblock models.

TABLE 6.57. ENERGY GROUP BOUNDARIES FOR THE GT-MHR

Group	Upper (eV)	Lower (eV)	Group	Upper (eV)	Lower (eV)
1	2.000000E+07	1.012999E+02	6	3.576701E-01	2.276891E-01
2	1.012999E+02	1.307904E+00	7	2.276891E-01	1.457206E-01
3	1.307904E+00	8.336811E-01	8	1.457206E-01	4.275520E-02
4	8.336811E-01	4.500015E-01	9	4.275520E-02	1.239596E-02
5	4.500015E-01	3.576701E-01	10	1.239596E-02	0.0

6.3.3.3. Computational models

Fuel compact cell

Figures 6.39 and 6.40 show the MCNP and HELIOS models for the three different fuel compact cells respectively. In FCC, TRISO particles were explicitly treated in the MCNP model but were homogenized by the RPT method in the HELIOS model. Since the neutronic characteristics are not so sensitive to the types of particle configurations, a simple cubic centred array was employed for the TRISO particle distribution. The RPT radius of a homogeneous mixture of TRISO and graphite matrix has been determined to be 0.19924 cm by conserving the reactivity of the MCNP calculation at 1200 K.

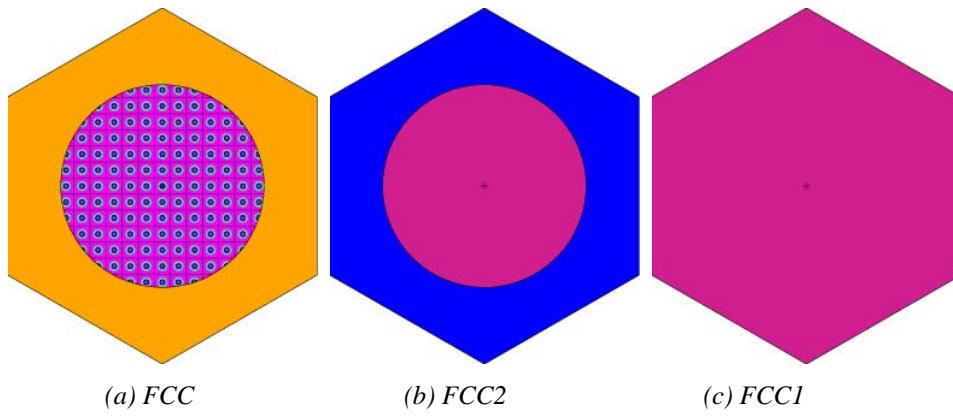


FIG. 6.39. The MCNP computational models for the fuel compact cell.

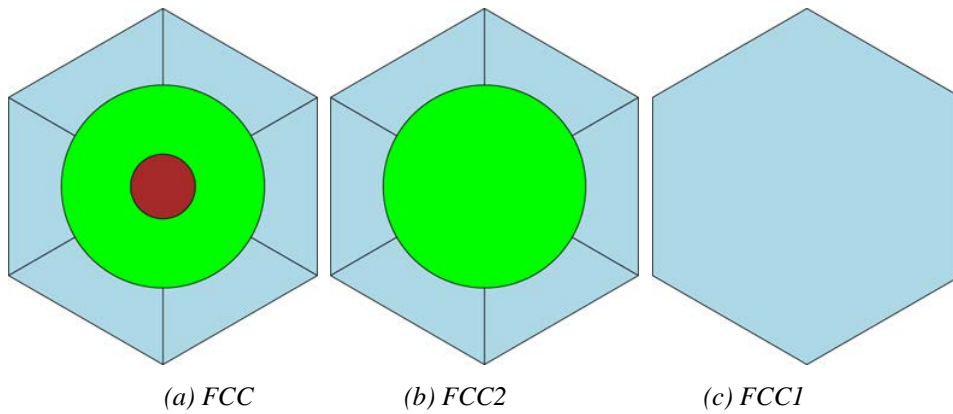


FIG. 6.40. The HELIOS computational models for the fuel compact cell.

Burnable poison cell

Figures 6.41 and 6.42 respectively show the MCNP and HELIOS models for the two different BPCs enclosed by the homogenized fuel. As in the FCC fuel cell, TRISO particles in the BPC were homogenized by the RPT method in the HELIOS model. A simple cubic centred array was again assumed for the Er_2O_3 particulate distribution. The RPT radius within which Er_2O_3 particles are homogenized has been estimated to be 0.48598 cm at 1200 K.

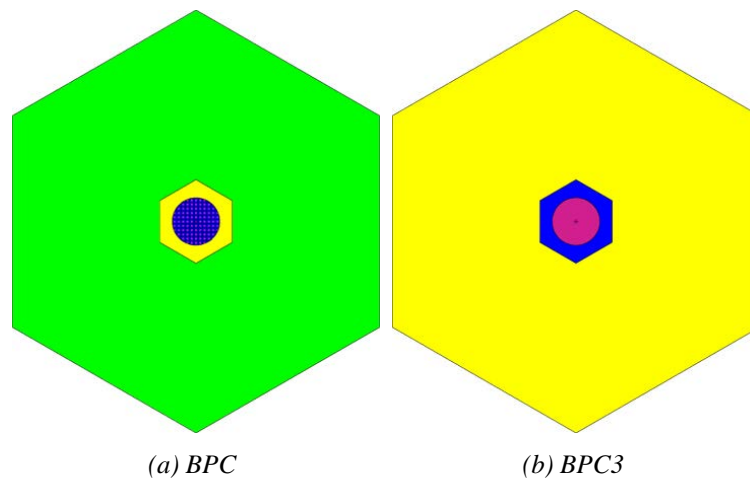


FIG. 6.41. The MCNP computational models for the burnable poison cell.

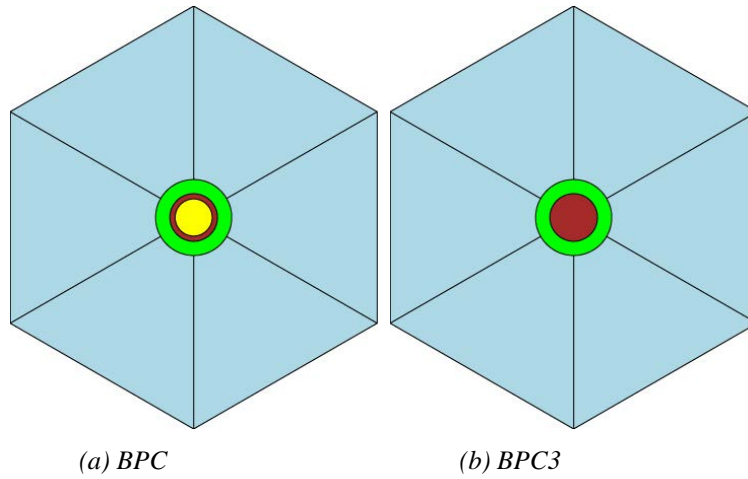


FIG. 6.42. The HELIOS computational models for the burnable poison cell.

Block

The GT-MHR fuel blocks include three different types of FB1, FB2 and FB3. FB1 is composed of the fuel compacts, burnable poison compacts and coolant passage channels in a hexahedral prismatic graphite block with a 36 cm “across flats” size. FB2 includes an eccentrically located 13 cm diameter hole for a control rod, which is filled with helium when the control rod is withdrawn. FB3 includes a control rod inserted in the hole in the FB2 model. Figure 6.43 shows the MCNP models for the three fuel blocks where the TRISO particulates were explicitly treated with a cubic centred array. Figure 6.44 shows the HELIOS models for the blocks where the TRISO particulates were homogenized by the RPT method. We used the RPT radii for the fuel compact and the burnable poison determined in the HELIOS models of FCC and BPC in the previous sections.

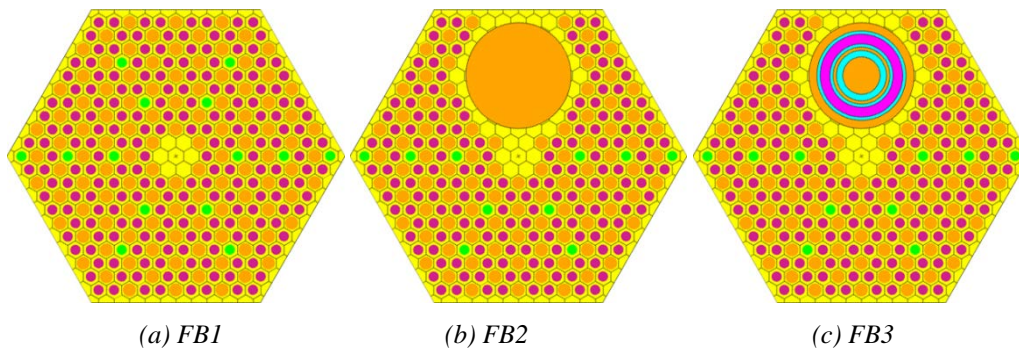


FIG. 6.43. The MCNP computational models for the fuel block.

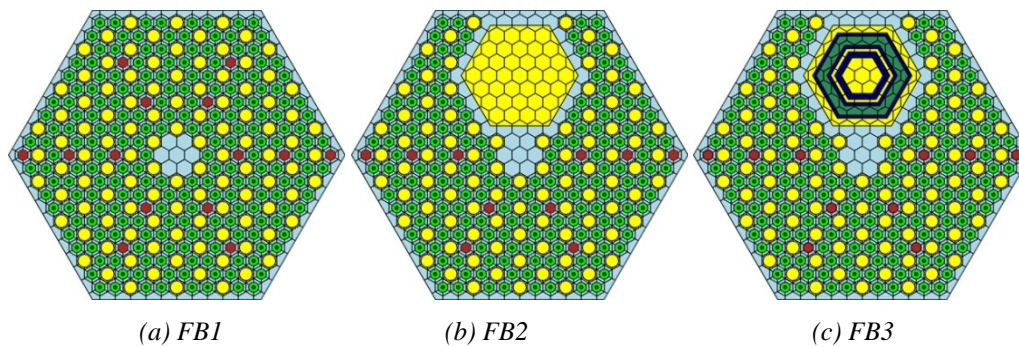


FIG. 6.44. The HELIOS computational models for the fuel block.

GT-MHR core

Figure 6.45 shows the MCNP models for the GT-MHR core and the constituent fuel blocks with and without control rod insertions. A mini-core model is employed instead of a single-block model to generate few group constants for each block, which are to be used in the diffusion core calculations by the MASTER code. Figure 6.46 shows the HELIOS mini-core models without control rod insertion, where the homogenized cross-sections are edited for each block. A single block is treated as a basic calculational mesh in the MASTER calculation. Figure 6.47 shows the HELIOS multiblock models to edit surface-dependent discontinuity factors to be used in the MASTER calculations for the inner reflector block with burnable poisons and the outer reflector and the fuel block with a control rod insertion.

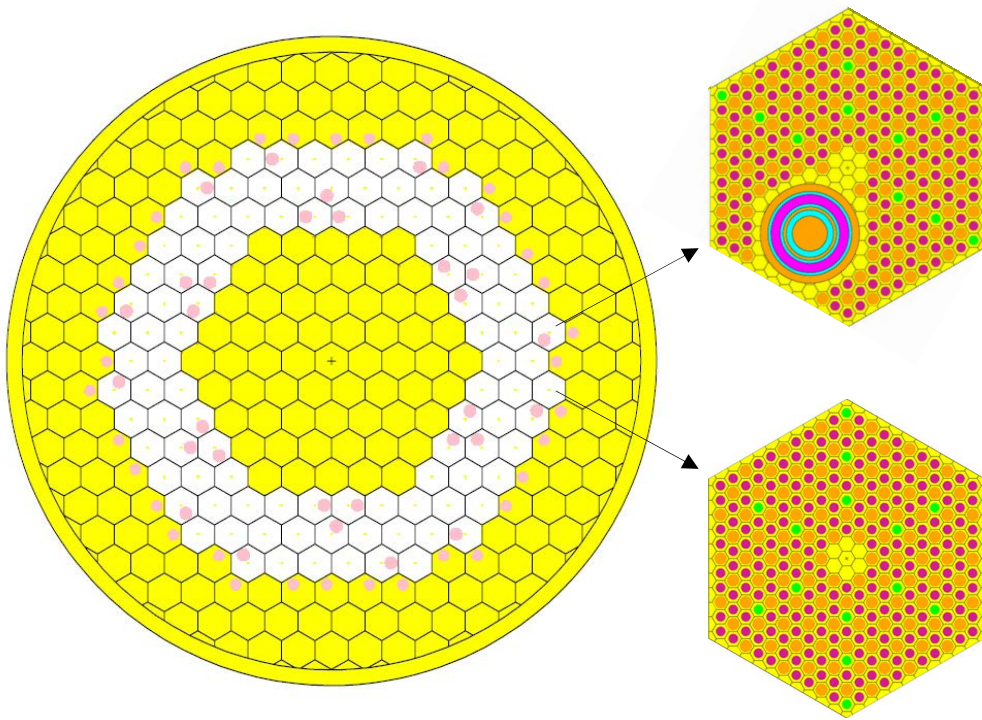
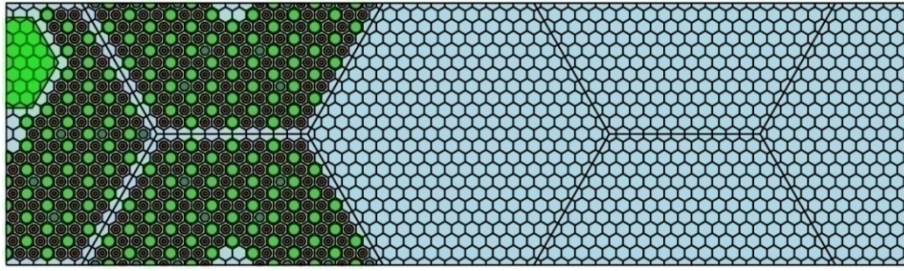
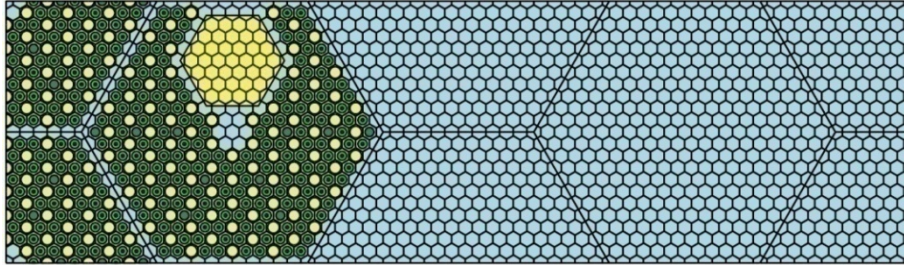


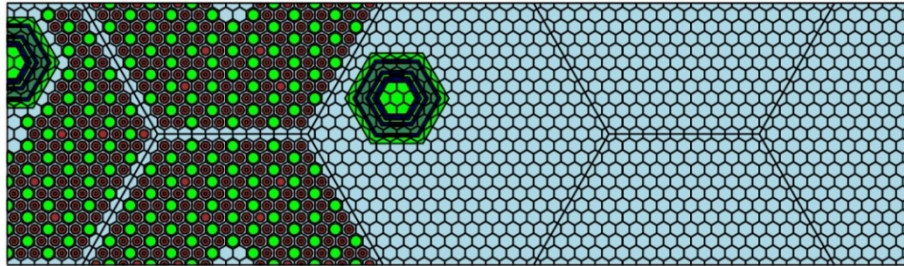
FIG. 6.45. The MCNP models for the GT-MHR core and fuel block.



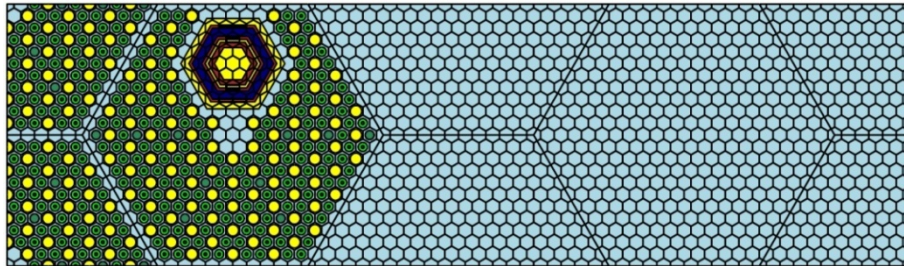
(a) Minicore-1



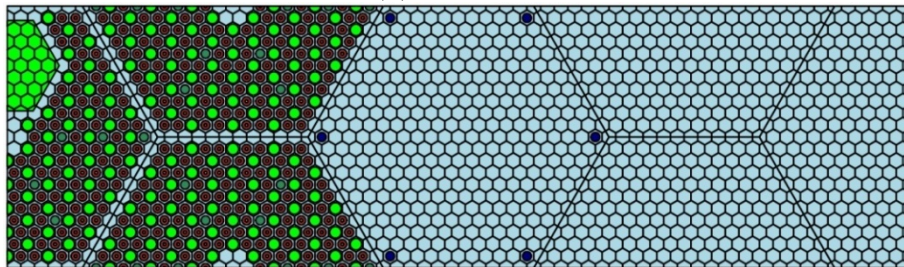
(b) Minicore-2



(c) Minicore-3



(d) Minicore-4



(e) Minicore-5

FIG. 6.46. The HELIOS mini-core models for the GT-MHR core.

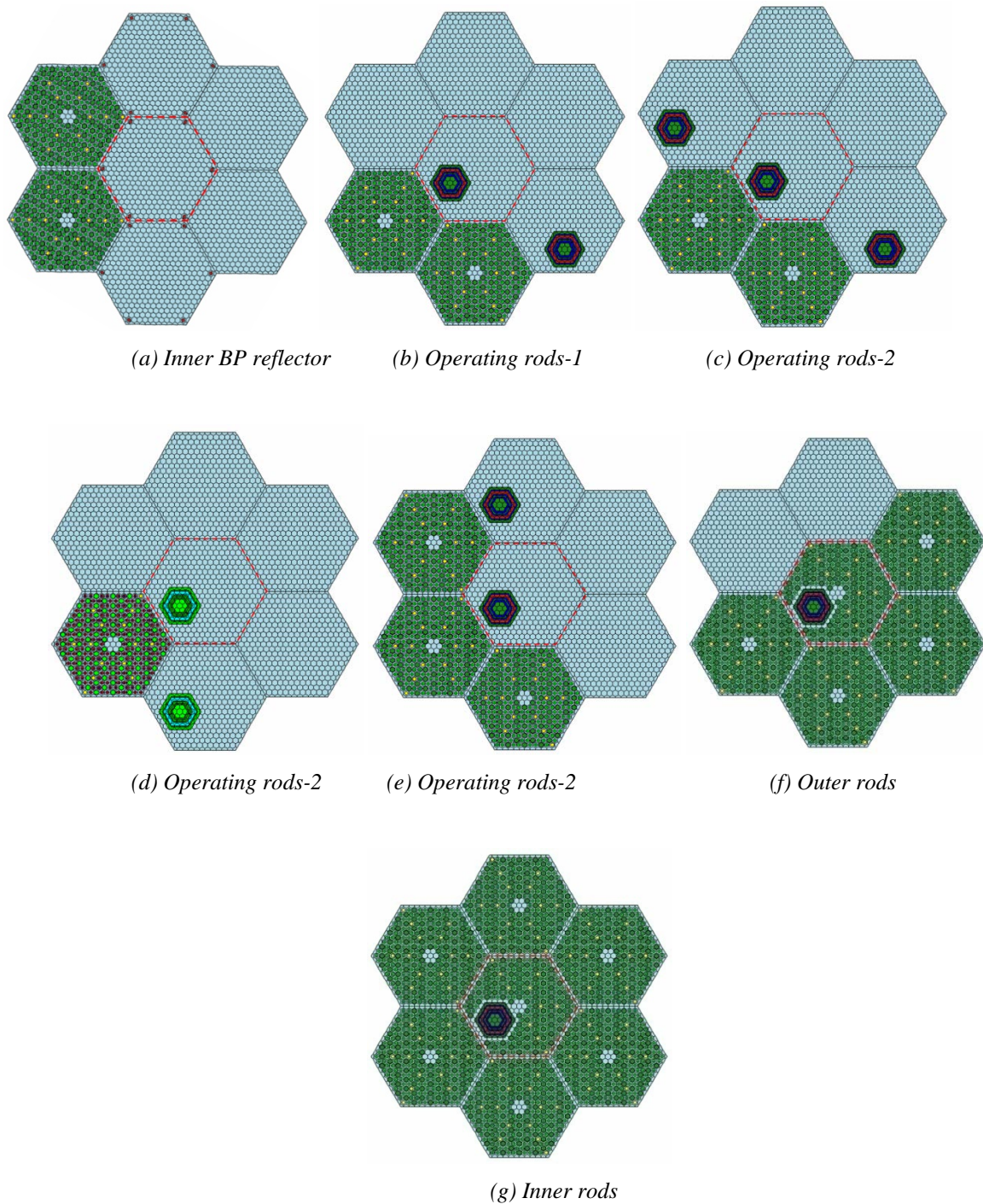


FIG. 6.47. The HELIOS multiblock models for discontinuity factors.

6.3.3.4. Computational results

Pin calculation

The HELIOS deterministic code and the MCNP Monte Carlo code were used for the pin calculations. All calculations were performed at four different constant temperatures, namely, 300, 600, 900 and 1200 K. ENDF/B-VI R0 and R8 libraries were used in the HELIOS and MCNP calculations respectively. Table 6.58 shows the comparison of the multiplication factors of HELIOS with those of MCNP. The multiplication factors agree well within the maximum error of 693 pcm for the pin model. Table 6.59 shows the multiplication factors of HELIOS as a function of burnup for FCC, BPC3 and

BPC at 1200 K. Tables 6.60 and 6.61 show the multiplication factors and nuclide-wise reaction rates for the FCCs at 300, 600, 900 and 1200 K calculated by HELIOS and MCNP respectively. The results of the HELIOS burnup calculation for FCC at 1200 K are shown in Table 6.62. Table 6.63 shows the multiplication factors and reaction rates calculated for the burnable poison cells by HELIOS. The results of the HELIOS burnup calculations for BPC3 and BPC at 1200 K are shown in Tables 6.64 and 6.65 respectively.

TABLE 6.58. COMPARISON OF THE MULTIPLICATION FACTORS FOR THE PIN MODELS

Type	Code	Temperature (K)			
		300	600	900	1200
FCC	MCNP ¹⁾	1.53699	1.51180	1.48589	1.46163
	HELIOS	88	-198	-314	0
FCC2	MCNP	1.45121	1.42910	1.40604	1.38184
	HELIOS	397	3	-187	244
FCC1	MCNP	1.43677	1.41354	1.39126	1.36808
	HELIOS	397	72	-137	274
BPC	MCNP	1.21931	1.19805	1.17425	1.14932
	HELIOS	211	-429	-693	0
BPC3	MCNP	1.18628	1.16375	1.13973	1.11449
	HELIOS	387	-206	-483	279

1) MCNP standard deviation < 0.00043.

TABLE 6.59. MULTIPLICATION FACTORS AS A FUNCTION OF BURNUP FOR PIN MODELS AT 1200 K

Type	Code	Burnup (EFPD)				
		0	5	250	500	750
FCC	HELIOS	1.46163	1.43938	1.30269	1.23068	1.17121
BPC3	HELIOS	1.11797	1.10499	1.07027	1.10740	1.14085
BPC	HELIOS	1.14932	1.13537	1.07930	1.09875	1.13086

58
 TABLE 6.60. MULTIPLICATION FACTORS AND NUCLIDE-WISE REACTION RATES
 FOR THE FUEL COMPACT CELLS FROM THE HELIOS CALCULATIONS

Case	Temperature	300 K				600 K				900 K				1200 K			
		$k_{inf} = 1.53906$				$k_{inf} = 1.50729$				$k_{inf} = 1.47899$				$k_{inf} = 1.46163$			
	Isotope	Rabs	Rfis	Rvfis	Rabs	Rfis	Rvfis	Rabs	Rfis	Rvfis	Rabs	Rfis	Rvfis	Rabs	Rfis	Rvfis	Rvfis
FCC	Pu-238	2.6015E-04	2.5437E-05	7.5049E-05	2.3528E-04	2.4702E-05	7.2921E-05	2.1495E-04	2.4102E-05	7.1185E-05	2.0358E-04	2.3767E-05	7.0214E-05				
	Pu-239	8.3549E-01	5.2852E-01	1.5154E+00	8.2510E-01	5.1793E-01	1.4847E+00	8.1487E-01	5.0853E-01	1.4574E+00	8.0829E-01	5.0277E-01	1.4408E+00				
	Pu-240	1.4477E-01	2.4110E-04	7.2674E-04	1.5601E-01	2.4334E-04	7.3302E-04	1.6700E-01	2.4551E-04	7.3910E-04	1.7402E-01	2.4690E-04	7.4300E-04				
	Pu-241	1.0277E-02	7.7462E-03	2.2822E-02	9.8167E-03	7.3923E-03	2.1779E-02	9.3535E-03	7.0318E-03	2.0718E-02	9.0580E-03	6.8010E-03	2.0038E-02				
	Pu-242	2.6535E-03	9.7501E-06	3.0265E-05	2.6787E-03	9.7500E-06	3.0265E-05	2.7248E-03	9.7499E-06	3.0265E-05	2.7766E-03	9.7499E-06	3.0265E-05				
	O-16	2.8804E-05			2.8794E-05			2.8786E-05			2.8782E-05						
	C nat.	4.0037E-03			3.7497E-03			3.5410E-03			3.4185E-03						
	Si nat.	1.4651E-03			1.3968E-03			1.3407E-03			1.3072E-03						
	B-10	1.0532E-03			9.8534E-04			9.2971E-04			8.9706E-04						
	B-11	6.6401E-09			6.2482E-09			5.9270E-09			5.7386E-09						
	B-10+B-11	1.0532E-03			9.8535E-04			9.2971E-04			8.9706E-04						
	Sum	1.0000E+00	5.3654E-01	1.5391E+00	1.0000E+00	5.2560E-01	1.5073E+00	1.0000E+00	5.1585E-01	1.4790E+00	1.0000E+00	5.0985E-01	1.4616E+00				
FCC2		$k_{inf} = 1.45961$				$k_{inf} = 1.42917$				$k_{inf} = 1.40235$				$k_{inf} = 1.38651$			
	Isotope	Rabs	Rfis	Rvfis	Rabs	Rfis	Rvfis	Rabs	Rfis	Rvfis	Rabs	Rfis	Rvfis	Rabs	Rfis	Rvfis	Rvfis
	Pu-238	2.2616E-04	2.4177E-05	7.1306E-05	2.0884E-04	2.3665E-05	6.9826E-05	1.9481E-04	2.3252E-05	6.8630E-05	1.8703E-04	2.3023E-05	6.7966E-05				
	Pu-239	8.0120E-01	5.0178E-01	1.4382E+00	7.8900E-01	4.9152E-01	1.4086E+00	7.7765E-01	4.8250E-01	1.3825E+00	7.7092E-01	4.7717E-01	1.3671E+00				
	Pu-240	1.8123E-01	2.3805E-04	7.1461E-04	1.9403E-01	2.4056E-04	7.2167E-04	2.0588E-01	2.4289E-04	7.2819E-04	2.1290E-01	2.4427E-04	7.3205E-04				
	Pu-241	9.2846E-03	6.9838E-03	2.0576E-02	8.9306E-03	6.7121E-03	1.9776E-02	8.5922E-03	6.4505E-03	1.9005E-02	8.3911E-03	6.2944E-03	1.8545E-02				
	Pu-242	2.6570E-03	9.1890E-06	2.8489E-05	2.6821E-03	9.1889E-06	2.8489E-05	2.7280E-03	9.1888E-06	2.8489E-05	2.7795E-03	9.1889E-06	2.8489E-05				
	O-16	2.6870E-05			2.6863E-05			2.6858E-05			2.6854E-05						
	C nat.	3.2046E-03			3.0478E-03			2.9206E-03			2.8415E-03						
	Si nat.	1.3305E-03			1.2832E-03			1.2448E-03			1.2209E-03						
	B-10	8.3739E-04			7.9574E-04			7.6198E-04			7.4100E-04						
	B-11	5.3943E-09			5.1538E-09			4.9589E-09			4.8378E-09						
	B-10+B-11	8.3740E-04			7.9575E-04			7.6198E-04			7.4100E-04						
	Sum	1.0000E+00	5.0903E-01	1.4596E+00	1.0000E+00	4.9850E-01	1.4292E+00	1.0000E+00	4.8922E-01	1.4024E+00	1.0000E+00	4.8374E-01	1.3865E+00				

Case	Temperature	300 K			600 K			900 K			1200 K		
		k _{inf} = 1.44502			k _{inf} = 1.41499			k _{inf} = 1.38862			k _{inf} = 1.37322		
	Isotope	Rabs	Rfis	Rvfis	Rabs	Rfis	Rvfis	Rabs	Rfis	Rvfis	Rabs	Rfis	Rvfis
FCC1	Pu-238	2.2113E-04	2.3992E-05	7.0758E-05	2.0491E-04	2.3514E-05	6.9373E-05	1.9179E-04	2.3128E-05	6.8255E-05	1.8453E-04	2.2914E-05	6.7636E-05
	Pu-239	7.9449E-01	4.9684E-01	1.4240E+00	7.8215E-01	4.8670E-01	1.3947E+00	7.7077E-01	4.7781E-01	1.3691E+00	7.6414E-01	4.7262E-01	1.3541E+00
	Pu-240	1.8826E-01	2.3800E-04	7.1398E-04	2.0116E-01	2.4054E-04	7.2109E-04	2.1301E-01	2.4286E-04	7.2760E-04	2.1990E-01	2.4421E-04	7.3139E-04
	Pu-241	9.1262E-03	6.8626E-03	2.0219E-02	8.7899E-03	6.6047E-03	1.9459E-02	8.4713E-03	6.3588E-03	1.8735E-02	8.2851E-03	6.2143E-03	1.8309E-02
	Pu-242	2.6572E-03	9.1110E-06	2.8241E-05	2.6822E-03	9.1109E-06	2.8241E-05	2.7282E-03	9.1108E-06	2.8241E-05	2.7796E-03	9.1108E-06	2.8241E-05
	O-16	2.6600E-05			2.6594E-05			2.6589E-05			2.6586E-05		
	C nat.	3.0961E-03			2.9523E-03			2.8360E-03			2.7628E-03		
	Si nat.	1.3098E-03			1.2657E-03			1.2300E-03			1.2075E-03		
	B-10	8.0823E-04			7.7005E-04			7.3921E-04			7.1982E-04		
	B-11	5.2260E-09			5.0055E-09			4.8275E-09			4.7156E-09		
	B-10+B-11	8.0823E-04			7.7005E-04			7.3921E-04			7.1982E-04		
	Sum	1.0000E+00	5.0397E-01	1.4450E+00	1.0000E+00	4.9358E-01	1.4150E+00	1.0000E+00	4.8445E-01	1.3886E+00	1.0000E+00	4.7911E-01	1.3732E+00

TABLE 6.61. MULTIPLICATION FACTORS AND REACTION RATES
FOR THE FUEL COMPACT CELLS FROM THE MCNP CALCULATIONS

Case	Temperature	300 K			600 K			900 K			1200 K		
		$k_{inf} = 1.53699 \pm 0.00032$			$k_{inf} = 1.51180 \pm 0.00035$			$k_{inf} = 1.48589 \pm 0.00033$			$k_{inf} = 1.46163 \pm 0.00033$		
	Isotope	Rabs	Rfis	Rvfis	Rabs	Rfis	Rvfis	Rabs	Rfis	Rvfis	Rabs	Rfis	Rvfis
FCC	Pu-238	2.5964E-04	2.5416E-05	7.4819E-05	2.3611E-04	2.4711E-05	7.2746E-05	2.1646E-04	2.4125E-05	7.1022E-05	2.0416E-04	2.3752E-05	6.9920E-05
	Pu-239	8.3455E-01	5.2787E-01	1.5460E+00	8.2794E-01	5.1956E-01	1.5217E+00	8.1846E-01	5.1049E-01	1.4952E+00	8.0803E-01	5.0250E-01	1.4716E+00
	Pu-240	1.4404E-01	2.3914E-04	6.8228E-04	1.5166E-01	2.4076E-04	6.8693E-04	1.6111E-01	2.4271E-04	6.9253E-04	1.7189E-01	2.4428E-04	6.9694E-04
	Pu-241	1.0162E-02	7.5797E-03	2.2582E-02	9.7815E-03	7.2822E-03	2.1697E-02	9.3544E-03	6.9494E-03	2.0705E-02	9.0092E-03	6.6817E-03	1.9906E-02
	Pu-242	2.6725E-03	9.6154E-06	2.7519E-05	2.7217E-03	9.6115E-06	2.7509E-05	2.7800E-03	9.6183E-06	2.7529E-05	2.8350E-03	9.5863E-06	2.7435E-05
	O-16	2.2692E-05			2.2714E-05			2.2771E-05			2.1594E-05		
	C nat.	5.8532E-03			5.5599E-03			5.3683E-03			5.2246E-03		
	Si nat.	1.4974E-03			1.4173E-03			1.3535E-03			1.3170E-03		
	B-10	1.1019E-03			1.0291E-03			9.7011E-04			9.3687E-04		
	B-11	6.8216E-09			6.4038E-09			6.0643E-09			5.8648E-09		
	B-10+B-11	1.1019E-03			1.0291E-03			9.7011E-04			9.3688E-04		
	Sum	1.0002E+00	5.3572E-01	1.5694E+00	1.0004E+00	5.2711E-01	1.5442E+00	9.9964E-01	5.1771E-01	1.5167E+00	9.9946E-01	5.0945E-01	1.4923E+00
		$k_{inf} = 1.45121 \pm 0.00035$			$k_{inf} = 1.42910 \pm 0.00039$			$k_{inf} = 1.40604 \pm 0.00036$			$k_{inf} = 1.38184 \pm 0.00040$		
	Isotope	Rabs	Rfis	Rvfis	Rabs	Rfis	Rvfis	Rabs	Rfis	Rvfis	Rabs	Rfis	Rvfis
FCC2	Pu-238	2.2420E-04	2.3973E-05	7.0480E-05	2.0836E-04	2.3507E-05	6.9111E-05	1.9520E-04	2.3118E-05	6.7968E-05	1.8689E-04	2.2873E-05	6.7242E-05
	Pu-239	7.9704E-01	4.9886E-01	1.4592E+00	7.8901E-01	4.9112E-01	1.4366E+00	7.8070E-01	4.8396E-01	1.4157E+00	7.6950E-01	4.7599E-01	1.3922E+00
	Pu-240	1.8369E-01	2.3283E-04	6.6337E-04	1.9210E-01	2.3467E-04	6.6863E-04	2.0165E-01	2.3656E-04	6.7402E-04	2.1321E-01	2.3835E-04	6.7906E-04
	Pu-241	9.1641E-03	6.8136E-03	2.0277E-02	8.8855E-03	6.5957E-03	1.9629E-02	8.6035E-03	6.3761E-03	1.8975E-02	8.3513E-03	6.1824E-03	1.8398E-02
	Pu-242	2.6854E-03	8.8441E-06	2.5276E-05	2.7346E-03	8.8471E-06	2.5284E-05	2.7845E-03	8.8482E-06	2.5288E-05	2.8377E-03	8.8232E-06	2.5214E-05
	O-16	1.9113E-05			1.9095E-05			1.9120E-05			1.8191E-05		
	C nat.	4.7689E-03			4.5908E-03			4.4865E-03			4.3799E-03		
	Si nat.	1.2314E-03			1.1822E-03			1.1452E-03			1.1232E-03		
	B-10	8.3208E-04			7.8928E-04			7.5667E-04			7.3704E-04		
	B-11	5.2398E-09			4.9960E-09			4.8073E-09			4.6900E-09		
	B-10+B-11	8.3208E-04			7.8929E-04			7.5668E-04			7.3704E-04		
	Sum	9.9965E-01	5.0593E-01	1.4802E+00	9.9952E-01	4.9798E-01	1.4570E+00	1.0003E+00	4.9061E-01	1.4354E+00	1.0004E+00	4.8244E-01	1.4114E+00

Case	Temperature	300 K			600 K			900 K			1200 K		
		$k_{inf} = 1.43677 \pm 0.00041$			$k_{inf} = 1.41354 \pm 0.00033$			$k_{inf} = 1.39126 \pm 0.00040$			$k_{inf} = 1.36808 \pm 0.00038$		
	Isotope	Rabs	Rfis	Rvfis	Rabs	Rfis	Rvfis	Rabs	Rfis	Rvfis	Rabs	Rfis	Rvfis
FCCI	Pu-238	2.1909E-04	2.3787E-05	6.9922E-05	2.0455E-04	2.3353E-05	6.8577E-05	1.9211E-04	2.2991E-05	6.7537E-05	1.8431E-04	2.2760E-05	6.6936E-05
	Pu-239	7.9099E-01	4.9429E-01	1.4456E+00	7.8253E-01	4.8651E-01	1.4214E+00	7.7322E-01	4.7887E-01	1.3996E+00	7.6177E-01	4.7085E-01	1.3777E+00
	Pu-240	1.9073E-01	2.3250E-04	6.6233E-04	1.9925E-01	2.3413E-04	6.6629E-04	2.0891E-01	2.3599E-04	6.7184E-04	2.2019E-01	2.3796E-04	6.7822E-04
	Pu-241	9.0139E-03	6.6986E-03	1.9932E-02	8.7502E-03	6.4928E-03	1.9300E-02	8.4759E-03	6.2797E-03	1.8673E-02	8.2430E-03	6.1014E-03	1.8164E-02
	Pu-242	2.6863E-03	8.7530E-06	2.5011E-05	2.7297E-03	8.7479E-06	2.4970E-05	2.7835E-03	8.7434E-06	2.4967E-05	2.8386E-03	8.7276E-06	2.4950E-05
	O-16	1.8664E-05			1.8647E-05			1.8633E-05			1.7835E-05		
	C nat.	4.6442E-03			4.5060E-03			4.3938E-03			4.3049E-03		
	Si nat.	1.2083E-03			1.1630E-03			1.1273E-03			1.1081E-03		
	B-10	8.0237E-04			7.6349E-04			7.3303E-04			7.1525E-04		
	B-11	5.0690E-09			4.8462E-09			4.6701E-09			4.5614E-09		
	B-10+B-11	8.0237E-04			7.6349E-04			7.3303E-04			7.1525E-04		
	Sum	1.0003E+00	5.0125E-01	1.4663E+00	9.9992E-01	4.9327E-01	1.4415E+00	9.9986E-01	4.8542E-01	1.4190E+00	9.9937E-01	4.7722E-01	1.3967E+00

5_∞ TABLE 6.62. THE HELIOS RESULTS OF BURNUP CALCULATION FOR FCC AT 1200 K

Case	Burnup		0 EFPD		5 EFPD		250 EFPD		500 EFPD		750 EFPD									
	PND	Rabs	Rfis	Rvifs	PND	Rabs	Rfis	Rvifs	PND	Rabs	Rfis	Rvifs								
k _{inf} = 1.46163																				
Pu-238	5.049E-08	2.036E-04	2.377E-05	7.021E-05	5.042E-08	2.008E-04	2.366E-05	6.990E-05	4.839E-08	2.147E-04	2.342E-05	6.914E-05	4.839E-08	3.398E-04	3.138E-05	9.253E-05	1.030E-07	9.891E-04	6.573E-05	1.931E-04
Pu-239	3.548E-05	8.083E-01	5.028E-01	1.441E+00	3.521E-05	7.9506E-01	4.942E-01	1.416E+00	2.285E-05	6.398E-01	3.967E-01	1.136E+00	1.202E-05	4.944E-01	3.061E-01	8.765E-01	3.801E-06	3.125E-01	1.934E-01	5.536E-01
Pu-240	2.523E-06	1.740E-01	2.469E-04	7.430E-04	2.565E-06	1.755E-01	2.507E-04	7.546E-04	3.765E-06	2.160E-01	3.591E-04	1.082E-03	3.686E-06	2.197E-01	3.519E-04	1.060E-03	2.575E-06	1.962E-01	2.530E-04	7.602E-04
Pu-241	4.488E-07	9.058E-03	6.801E-03	2.004E-02	5.035E-07	1.006E-02	7.551E-03	2.225E-02	3.207E-06	7.476E-02	5.591E-02	1.647E-01	5.047E-06	1.602E-01	1.191E-01	3.508E-01	4.747E-06	2.806E-01	2.070E-01	6.099E-01
Pu-242	1.643E-07	2.777E-03	9.750E-06	3.027E-05	1.641E-07	2.775E-03	9.741E-06	3.024E-05	2.863E-07	4.812E-03	1.693E-05	5.256E-05	7.093E-07	1.165E-02	4.169E-05	1.294E-04	1.515E-06	2.413E-02	8.818E-05	2.738E-04
Am-241					3.133E-10	8.739E-06	7.191E-08	2.378E-07	5.048E-08	1.542E-03	1.235E-05	4.076E-05	1.310E-07	4.963E-03	3.762E-05	1.238E-04	1.557E-07	9.470E-03	6.569E-05	2.147E-04
Am-242m					1.973E-13	1.499E-08	1.266E-08	4.134E-08	1.007E-09	9.045E-05	7.617E-05	2.486E-04	4.116E-09	5.232E-04	4.387E-04	1.432E-03	5.552E-09	1.387E-03	1.157E-03	3.777E-03
Am-243					9.189E-10	2.415E-05	7.496E-08	2.651E-07	4.969E-08	1.295E-03	4.039E-06	1.428E-05	1.525E-07	4.028E-03	1.243E-05	4.393E-05	3.684E-07	1.028E-02	3.051E-05	1.077E-04
Cm-242					1.003E-12	1.691E-09	5.997E-11	2.256E-10	5.693E-09	9.826E-06	3.573E-07	1.339E-06	3.026E-08	5.471E-05	2.161E-06	8.012E-06	7.587E-08	1.541E-04	7.626E-06	2.768E-05
Cm-243					1.739E-16	5.914E-12	5.280E-12	1.838E-11	4.351E-11	1.521E-06	1.359E-06	4.729E-06	4.343E-10	1.646E-05	1.473E-05	5.129E-05	1.534E-09	7.250E-05	6.525E-05	2.271E-04
Cm-244					4.020E-12	3.087E-08	8.970E-10	3.246E-09	1.034E-08	8.201E-05	2.350E-06	8.496E-06	5.245E-08	4.315E-04	1.219E-05	4.404E-05	1.684E-07	1.453E-03	4.073E-05	1.469E-04
Cm-245					3.229E-15	6.299E-11	5.557E-11	1.935E-10	4.270E-10	9.165E-06	8.078E-06	2.813E-05	3.791E-09	1.020E-04	8.986E-05	3.128E-04	1.460E-08	6.566E-04	5.773E-04	2.010E-03
Cm-246					5.814E-19	8.705E-16	6.922E-17	2.567E-16	4.756E-12	7.132E-09	5.649E-10	2.095E-09	1.002E-10	1.519E-07	1.191E-08	4.416E-08	8.197E-10	1.283E-06	9.872E-08	3.654E-07
Cm-247									2.223E-14	3.793E-10	2.289E-10	8.205E-10	8.866E-13	1.608E-08	9.696E-09	3.475E-08	9.646E-12	2.120E-07	1.277E-07	4.576E-07
Cm-248									4.444E-16	1.596E-12	8.277E-14	3.018E-13	3.690E-14	1.353E-10	6.947E-12	2.531E-11	6.519E-13	2.467E-09	1.248E-10	4.541E-10
Bk-249									3.273E-18	1.702E-13	1.087E-15	3.705E-15	4.524E-16	3.344E-11	2.049E-13	6.946E-13	8.226E-15	1.199E-09	6.980E-12	2.352E-11
Cf-249									2.074E-19	1.097E-14	8.800E-15	3.421E-14	4.781E-17	2.935E-12	2.349E-12	9.132E-12	1.052E-15	9.430E-11	7.512E-11	2.920E-10
Cf-250									2.900E-19	4.913E-14	4.221E-17	1.736E-16	8.373E-17	1.559E-11	1.216E-14	5.001E-14	3.062E-15	7.370E-10	4.416E-13	1.817E-12
Cf-251									8.633E-20	1.176E-14	8.517E-15	3.526E-14	3.920E-17	6.471E-12	4.636E-12	1.919E-11	1.750E-15	4.634E-10	3.253E-10	1.347E-09
Cf-252									1.469E-20	3.899E-17	2.733E-17	1.116E-16	6.472E-18	1.809E-14	1.262E-14	5.155E-14	6.463E-16	2.158E-12	1.477E-12	6.029E-12
Xe-135					1.066E-09	9.156E-03			9.576E-10	1.078E-02			7.718E-10	1.423E-02			4.664E-10	2.002E-02		
Sm-149					9.725E-10	3.189E-04			1.682E-08	6.968E-03			1.244E-08	8.113E-03			6.425E-09	9.377E-03		

Case	Burnup			0 EFPD			5 EFPD			250 EFPD			500 EFPD			750 EFPD		
				$k_{inf} = 1.46163$			$k_{inf} = 1.43938$			$k_{inf} = 1.30269$			$k_{inf} = 1.23068$			$k_{inf} = 1.17121$		
	Isotope	PND	Rabs	Rfis	Rvfis	PND	Rabs	Rfis	Rvfis	PND	Rabs	Rfis	Rvfis	PND	Rabs	Rfis	Rvfis	
FCC-TI200	O-16	6.572E-05	2.878E-05			6.572E-05	2.878E-05			6.572E-05	2.886E-05			6.572E-05	2.920E-05			
	C nat.	8.529E-02	3.419E-03			8.529E-02	3.386E-03			8.529E-02	3.716E-03			8.529E-02	7.838E-03			
	Si nat.	5.510E-04	1.307E-03			5.510E-04	1.297E-03			5.510E-04	1.401E-03			5.510E-04	2.656E-03			
	B-10	1.990E-08	8.971E-04			1.960E-08	8.752E-04			8.763E-09	4.296E-04			3.098E-09	1.915E-04			
	B-11	8.008E-08	5.739E-09			8.008E-08	5.688E-09			8.008E-08	6.199E-09			8.008E-08	1.251E-08			
	B-10+B-11	9.998E-08	8.971E-04			9.968E-08	8.752E-04			8.884E-08	4.296E-04			8.318E-08	1.915E-04			
Sum	8.594E-02	1.000E+00	5.099E-01	1.462E+00	8.594E-02	9.986E-01	5.021E-01	1.439E+00	8.593E-02	9.619E-01	4.530E-01	1.302E+00	8.592E-02	9.254E-01	4.2558E-01	1.229E+00	8.778E-01	
																	4.008E-01	
																	1.165E+00	

TABLE 6.63. MULTIPLICATION FACTORS AND REACTION RATES
FOR THE BURNABLE POISON CELLS FROM THE HELIOS CALCULATIONS

Case	Temperature											
	300 K				600 K				900 K			
	k _{inf} = 1.22245				k _{inf} = 1.19193				k _{inf} = 1.16477			
	Isotope	PND	Rabs	αEr	PND	Rabs	αEr	PND	PND	Rabs	αEr	αEr
BPC	Er-166	9.1411E-03	4.9391E-02	8.3447E-03	9.1411E-03	5.0107E-02	8.5778E-03	9.1411E-03	9.1411E-03	5.0162E-02	8.7102E-03	5.0356E-02
	Er-167	6.2437E-03	9.3020E-01	1.5716E-01	6.2437E-03	9.2984E-01	1.5918E-01	6.2437E-03	6.2437E-03	9.3014E-01	1.6151E-01	9.3018E-01
	Er-168	7.2911E-03	2.0412E-02	3.4486E-03	7.2911E-03	2.0051E-02	3.4325E-03	7.2911E-03	7.2911E-03	1.9694E-02	3.4197E-03	1.9462E-02
	Sum		1.0000E+00	1.6895E-01		1.0000E+00	1.7119E-01			1.0000E+00	1.7364E-01	1.0000E+00
BPC3	Isotope	PND	Rabs	αEr	PND	Rabs	αEr	PND	PND	Rabs	αEr	αEr
	Er-166	4.1403E-04	4.7539E-02	8.8863E-03	4.1403E-04	4.7996E-02	9.0988E-03	4.1403E-04	4.1403E-04	4.7868E-02	9.2122E-03	4.7921E-02
	Er-167	2.8280E-04	9.3385E-01	1.7456E-01	2.8280E-04	9.3374E-01	1.7701E-01	2.8280E-04	2.8280E-04	9.3420E-01	1.7979E-01	9.3437E-01
	Er-168	3.3024E-04	1.8607E-02	3.4782E-03	3.3024E-04	1.8265E-02	3.4626E-03	3.3024E-04	3.3024E-04	1.7928E-02	3.4502E-03	1.7713E-02
	Sum		1.0000E+00	1.8693E-01		1.0000E+00	1.8957E-01			1.0000E+00	1.9245E-01	1.0000E+00

TABLE 6.64. THE HELIOS RESULTS OF BURNUP CALCULATION FOR BPC3 AT 1200 K

Case	Burnup				
BPC3-T1200	0 EFPD	$k_{inf} = 1.11797$			
		Isotope	PND	Rabs	αEr
		Er-166	4.1403E-04	4.7921E-02	9.3143E-03
		Er-167	2.8280E-04	9.3437E-01	1.8161E-01
		Er-168	3.3024E-04	1.7713E-02	3.4429E-03
		Sum		1.0000E+00	1.9437E-01
	5 EFPD	$k_{inf} = 1.10499$			
		Isotope	PND	Rabs	αEr
		Er-166	4.1388E-04	4.8252E-02	9.3052E-03
		Er-167	2.8004E-04	9.3375E-01	1.8007E-01
		Er-168	3.3308E-04	1.8003E-02	3.4718E-03
		Sum		1.0000E+00	1.9285E-01
	250 EFPD	$k_{inf} = 1.07027$			
		Isotope	PND	Rabs	αEr
		Er-166	4.0625E-04	6.1209E-02	9.5854E-03
		Er-167	1.5721E-04	9.0775E-01	1.4216E-01
		Er-168	4.6016E-04	3.1041E-02	4.8611E-03
		Sum		1.0000E+00	1.5660E-01
	500 EFPD	$k_{inf} = 1.10740$			
		Isotope	PND	Rabs	αEr
		Er-166	3.9813E-04	9.1402E-02	1.0293E-02
		Er-167	6.6617E-05	8.5507E-01	9.6292E-02
		Er-168	5.5438E-04	5.3528E-02	6.0280E-03
		Sum		1.0000E+00	1.1261E-01
	750 EFPD	$k_{inf} = 1.14085$			
		Isotope	PND	Rabs	αEr
		Er-166	3.8930E-04	1.8113E-01	1.2469E-02
		Er-167	1.8413E-05	7.1540E-01	4.9246E-02
		Er-168	6.0622E-04	1.0347E-01	7.1227E-03
		Sum		1.0000E+00	6.8837E-02

TABLE 6.65. THE HELIOS RESULTS OF BURNUP CALCULATION OF BPC AT 1200 K

Case	Burnup				
BPC-T1200	0 EFPD	$k_{inf} = 1.14932$			
		Isotope	PND	Rabs	αEr
		Er-166	9.1411E-03	5.0356E-02	8.8288E-03
		Er-167	6.2437E-03	9.3018E-01	1.6309E-01
		Er-168	7.2911E-03	1.9462E-02	3.4122E-03
	5 EFPD	Sum		1.0000E+00	1.7533E-01
		$k_{inf} = 1.13537$			
		Isotope	PND	Rabs	αEr
		Er-166	9.1380E-03	5.0672E-02	8.8196E-03
		Er-167	6.1907E-03	9.2958E-01	1.6180E-01
		Er-168	7.3459E-03	1.9747E-02	3.4370E-03
		Sum		1.0000E+00	1.7405E-01
	250 EFPD	$k_{inf} = 1.07930$			
		Isotope	PND	Rabs	αEr
		Er-166	8.9811E-03	6.0852E-02	9.0862E-03
		Er-167	3.7397E-03	9.0781E-01	1.3555E-01
		Er-168	9.8822E-03	3.1334E-02	4.6786E-03
		Sum		1.0000E+00	1.4932E-01
	500 EFPD	$k_{inf} = 1.09875$			
		Isotope	PND	Rabs	αEr
		Er-166	8.8110E-03	8.2995E-02	9.7756E-03
		Er-167	1.7331E-03	8.6759E-01	1.0219E-01
		Er-168	1.1964E-02	4.9413E-02	5.8201E-03
		Sum		1.0000E+00	1.1779E-01
	750 EFPD	$k_{inf} = 1.13086$			
		Isotope	PND	Rabs	αEr
		Er-166	8.6233E-03	1.5598E-01	1.1959E-02
		Er-167	4.9908E-04	7.5304E-01	5.7735E-02
		Er-168	1.3273E-02	9.0980E-02	6.9754E-03
		Sum		1.0000E+00	7.6669E-02

Block calculation

Similarly to the cell calculations, all the block calculations were performed at four different constant temperatures of 300, 600, 900 and 1200 K by HELIOS and MCNP. The RPT radii for the fuel and burnable poison obtained for FCC and BPC were used in the HELIOS calculation. In order to test the HELIOS applicability to the Er_2O_3 burnable poison, the block calculations were performed in two

configurations, i.e. with and without burnable poison rods. Tables 6.66 and 6.67 show the multiplication factors of HELIOS and MCNP for the fuel blocks with and without burnable poison rods respectively. Table 6.68 shows the multiplication factors and assembly averaged isotopic inventories of HELIOS as a function of burnup for FB1.

TABLE 6.66. COMPARISON OF THE MULTIPLICATION FACTORS FOR THE BLOCKS WITH BURNABLE POISON RODS

Type	Code	Temperature (K)			
		300	600	900	1200
FB1	MCNP ¹⁾	1.20979	1.19042	1.16527	1.13857
	HELIOS	293	-229	-368	255
FB2	MCNP	1.27666	1.25547	1.23225	1.20623
	HELIOS	228	-115	-343	140
FB3	MCNP	0.58370	0.57598	0.56706	0.55485
	HELIOS	-1.746	-2.803	-3.459	-1.665
Rod Worth	MCNP	92.991	93.966	95.196	97.326
	HELIOS	94.966	96.653	98.312	99.131
	% Diff.	2.12	2.86	3.27	1.85

1) MCNP standard deviation < 0.00061.

TABLE 6.67. COMPARISON OF THE MULTIPLICATION FACTORS FOR THE BLOCKS WITHOUT BURNABLE POISON RODS

Type	Code	Temperature (K)			
		300	600	900	1200
FB1	MCNP ¹⁾	1.54880	1.52910	1.50962	1.49028
	HELIOS	228	5	-93	158
FB2	MCNP	1.56575	1.54513	1.52603	1.50655
	HELIOS	194	-6	-107	156
FB3	MCNP	0.72386	0.71658	0.70869	0.69906
	HELIOS	-1,474	-2,047	-2,282	-1,309
Rod worth	MCNP	74,281	74,832	75,576	76,672
	HELIOS	75,948	76,874	77,751	78,137
	% Diff.	2.24	2.73	2.88	1.91

1) MCNP standard deviation < 0.00063.

TABLE 6.68. MULTIPLICATION FACTORS AND ISOTOPIC CONTENT VS BURNUP FOR FB1 BY HELIOS

Irradiation Time	Functional	PND	Content
Beginning of cycle		$k_{inf} = 1.14188$	
	Er-167	4.28301E-06	0.2725
	Pu-239	1.99542E-05	0.9176
	Pu-240	1.41968E-06	0.0653
	Pu-241	2.52367E-07	0.0116
	Pu-242	9.24067E-08	0.0042
(1/3) 280 days		$k_{inf} = 1.10182$	
	Er-167	1.99858E-06	0.1276
	Pu-239	1.20160E-05	0.7334
	Pu-240	2.32523E-06	0.1419
	Pu-241	1.83799E-06	0.1122
	Pu-242	1.78366E-07	0.0109
(2/3) 560 days		$k_{inf} = 1.12752$	
	Er-167	6.06447E-07	0.0389
	Pu-239	5.33399E-06	0.4871
	Pu-240	2.37952E-06	0.2173
	Pu-241	2.71367E-06	0.2478
	Pu-242	4.85978E-07	0.0444
(3/3) 840 days		$k_{inf} = 1.06952$	
	Er-167	1.05463E-07	0.0068
	Pu-239	8.07350E-07	0.1483
	Pu-240	1.53169E-06	0.2813
	Pu-241	1.89364E-06	0.3477
	Pu-242	1.14708E-06	0.2106

6.3.3.5. Core calculation

The HELIOS/MASTER code system and the MCNP calculations were performed for the GT-MHR core variants at two different constant temperatures of 300 and 1200 K. As shown in Tables 6.69 and 6.70, the multiplication factors agree very well between the HELIOS/MASTER code system and the MCNP calculations within the maximum error of 400 pcm. For the six GT-MHR variant cores, the control rod worths were estimated by both the HELIOS/MASTER code system and the MCNP code at 300 and 1200 K. The computational results are shown in Tables 6.69 and 6.70, where various control rod worths of the HELIOS/MASTER calculations agree well with those of the MCNP calculations within the maximum error of 7.4%.

As shown in Table 6.71, Isothermal Temperature Coefficients (ITC) of the HELIOS/MASTER code system were obtained for middle temperatures of all considered temperature intervals from 300 up to 1200 K with 100 K step for the six variants cores. Isothermal reactivity temperature coefficients are estimated as:

$$\rho = \frac{k(T_2) - k(T_1)}{k(T_2) \cdot k(T_1)} \cdot \frac{1}{T_2 - T_1}$$

Figure 6.48 shows the radial power distributions of MCNP and MASTER for the variant-1 core at 1200 K when all the control rods are withdrawn. This figure shows a very good performance of the HELIOS/MASTER code system in the radial block power distributions with the maximum relative error of about 3.9%. Figure 6.49 shows the power distributions for the variant-1 core at 1200 K when the reflector control rods are inserted. A good performance is again shown in this figure with the maximum relative error of about 3.5%. Figure 6.50 shows the axial power distributions of MCNP and MASTER for the variant-1 core at 1200 K when all the control rods are withdrawn. This figure shows a very good performance of the HELIOS/MASTER code system in the axial block power distributions.

TABLE 6.69. COMPARISON OF CONTROL RODS WORTH (300 K)

Type	CR	K_{eff}			Rod Worth (pcm)		
		MCNP ¹⁾	MASTER	$\Delta\rho(\text{pcm})$	MCNP	MASTER	% Diff.
Variant-1	ARO ²⁾	1.06909	1.06965	49			
	ARI ³⁾	0.80300	0.81277	1496	30996	29548	4.67
	CRI ⁴⁾	0.87152	0.88028	1142	21205	20111	5.16
	ORI ⁵⁾	0.92959	0.93349	450	14037	13636	2.85
	SRI ⁶⁾	1.03861	1.04065	189	2745	2605	5.10
Variant-2	ARO	1.00753	1.01095	336			
	ARI	0.74675	0.75782	1955	34661	33041	4.67
	CRI	0.81552	0.82499	1408	23369	22296	4.59
	ORI	0.87183	0.87755	748	15449	15037	2.67
	SRI	0.97593	0.98086	515	3214	3034	5.58
Variant-3	ARO	1.07423	1.07453	26			
	ARI	0.80940	0.81897	1444	30458	29041	4.65
	CRI	0.87734	0.88601	1116	20891	19801	5.22
	ORI	0.93503	0.93890	440	13859	13444	2.99
	SRI	1.04359	1.04606	226	2733	2533	7.31
Variant-4	ARO	1.02769	1.02962	182			
	ARI	0.76309	0.77332	1734	33741	32188	4.60
	CRI	0.83259	0.84118	1227	22802	21757	4.58
	ORI	0.88965	0.89430	584	15098	14696	2.66
	SRI	0.99584	0.99967	385	3112	2910	6.51
Variant-5	ARO	1.05136	1.05260	112			
	ARI	0.78732	0.79692	1529	31898	30481	4.44
	CRI	0.85518	0.86426	1228	21820	20703	5.12
	ORI	0.91357	0.91730	445	14346	14013	2.32
	SRI	1.02054	1.02331	265	2872	2719	5.33
Variant-6	ARO	0.99446	0.99840	397			
	ARI	0.73223	0.74316	2009	36012	34399	4.48
	CRI	0.80179	0.81126	1455	24164	23105	4.38
	ORI	0.85835	0.86434	808	15946	15534	2.58
	SRI	0.96213	0.96733	559	3379	3217	4.80

1) MCNP standard deviation < 0.00030;

2) All rods out;

3) Operating and startup rods in;

4) Operating rods in;

5) Startup rods in.

TABLE 6.70. COMPARISON OF CONTROL RODS WORTH (1200 K)

Type	CR	K_{eff}			Rod worth (pcm)		
		MCNP ¹⁾	MASTER	$\Delta\rho$ (pcm)	MCNP	MASTER	% Diff.
Variant-1	ARO	1.03842	1.03654	-175			
	ARI	0.76620	0.77828	2025	34214	32014	6.43
	CRI	0.83063	0.84186	1606	24090	22310	7.39
	ORI	0.88740	0.89343	761	16389	15453	5.71
	SRI	1.01182	1.01081	-99	2532	2456	2.99
Variant-2	ARO	0.99949	1.00062	113			
	ARI	0.72176	0.73692	2850	38499	35762	7.11
	CRI	0.78809	0.80141	2109	26838	24842	7.44
	ORI	0.84410	0.85364	1324	18418	17208	6.57
	SRI	0.97182	0.97364	192	2849	2769	2.80
Variant-3	ARO	1.03884	1.03671	-198			
	ARI	0.77038	0.78183	1901	33545	31446	6.26
	CRI	0.83399	0.84458	1503	23644	21944	7.19
	ORI	0.89051	0.89550	626	16034	15210	5.14
	SRI	1.01289	1.01160	-126	2466	2394	2.93
Variant-4	ARO	1.01383	1.01411	28			
	ARI	0.73488	0.74938	2634	37441	34835	6.96
	CRI	0.80209	0.81406	1832	26038	24233	6.93
	ORI	0.85763	0.86641	1182	17965	16810	6.43
	SRI	0.98620	0.98766	150	2763	2641	4.42
Variant-5	ARO	1.02751	1.02568	-174			
	ARI	0.75392	0.76631	2144	35317	32999	6.56
	CRI	0.81898	0.82992	1609	24780	22997	7.20
	ORI	0.87495	0.88166	870	16970	15926	6.15
	SRI	1.00076	0.99969	-107	2601	2534	2.58
Variant-6	ARO	0.99700	0.99882	182			
	ARI	0.71364	0.72923	2996	39826	37012	7.07
	CRI	0.78227	0.79523	2083	27532	25632	6.90
	ORI	0.83851	0.84858	1415	18958	17726	6.50
	SRI	0.96844	0.97069	240	2958	2901	1.94

1) MCNP standard deviation < 0.00030;

2) All rods out;

3) Operating and startup rods in;

4) Operating rods in;

5) Startup rods in.

TABLE 6.71(A). ISOTHERMAL TEMPERATURE COEFFICIENTS OF
HELIOS/MASTER (STATES 1–3)

Core	Temperature (K)	ITC(1/K)
Beginning of cycle-1 (the 1 st state)	ρ_{350}	-8.0303E-06
	ρ_{450}	-7.3075E-06
	ρ_{550}	-4.7973E-05
	ρ_{650}	-6.0386E-05
	ρ_{750}	-1.6728E-05
	ρ_{850}	-2.8522E-05
	ρ_{950}	-3.6383E-05
	ρ_{1050}	-4.3179E-05
	ρ_{1150}	-5.0119E-05
End of cycle-1 (the 2 nd state)	ρ_{350}	2.6377E-05
	ρ_{450}	2.7060E-05
	ρ_{550}	-9.1650E-06
	ρ_{650}	-3.0768E-05
	ρ_{750}	1.2941E-05
	ρ_{850}	-9.7809E-06
	ρ_{950}	-2.5645E-05
	ρ_{1050}	-4.0047E-05
	ρ_{1150}	-5.3110E-05
Beginning of cycle-2 (the 3 rd state)	ρ_{350}	-1.4686E-05
	ρ_{450}	-1.3617E-05
	ρ_{550}	-5.6129E-05
	ρ_{650}	-6.6994E-05
	ρ_{750}	-2.2326E-05
	ρ_{850}	-3.2365E-05
	ρ_{950}	-3.9133E-05
	ρ_{1050}	-4.4279E-05
	ρ_{1150}	-5.0002E-05

TABLE 6.71(B). ISOTHERMAL TEMPERATURE COEFFICIENTS OF
HELIOS/MASTER (STAGES 4–6)

Core	Temperature (K)	ITC(1/K)
End of cycle-2 (the 4th state)	ρ_{350}	1.8613E-05
	ρ_{450}	1.9413E-05
	ρ_{550}	-1.8219E-05
	ρ_{650}	-3.8046E-05
	ρ_{750}	5.9993E-06
	ρ_{850}	-1.4310E-05
	ρ_{950}	-2.8375E-05
	ρ_{1050}	-4.0954E-05
	ρ_{1150}	-5.2595E-05
Beginning of cycle-3 (the 5th state)	ρ_{350}	9.5661E-07
	ρ_{450}	1.7954E-06
	ρ_{550}	-3.8392E-05
	ρ_{650}	-5.3311E-05
	ρ_{750}	-8.9186E-06
	ρ_{850}	-2.3753E-05
	ρ_{950}	-3.3958E-05
	ρ_{1050}	-4.2638E-05
	ρ_{1150}	-5.1146E-05
End of cycle-4 (the 6th state)	ρ_{350}	4.4475E-05
	ρ_{450}	4.4259E-05
	ρ_{550}	1.2078E-05
	ρ_{650}	-1.4177E-05
	ρ_{750}	2.7118E-05
	ρ_{850}	-4.2166E-07
	ρ_{950}	-1.8884E-05
	ρ_{1050}	-3.7141E-05
	ρ_{1150}	-5.3103E-05

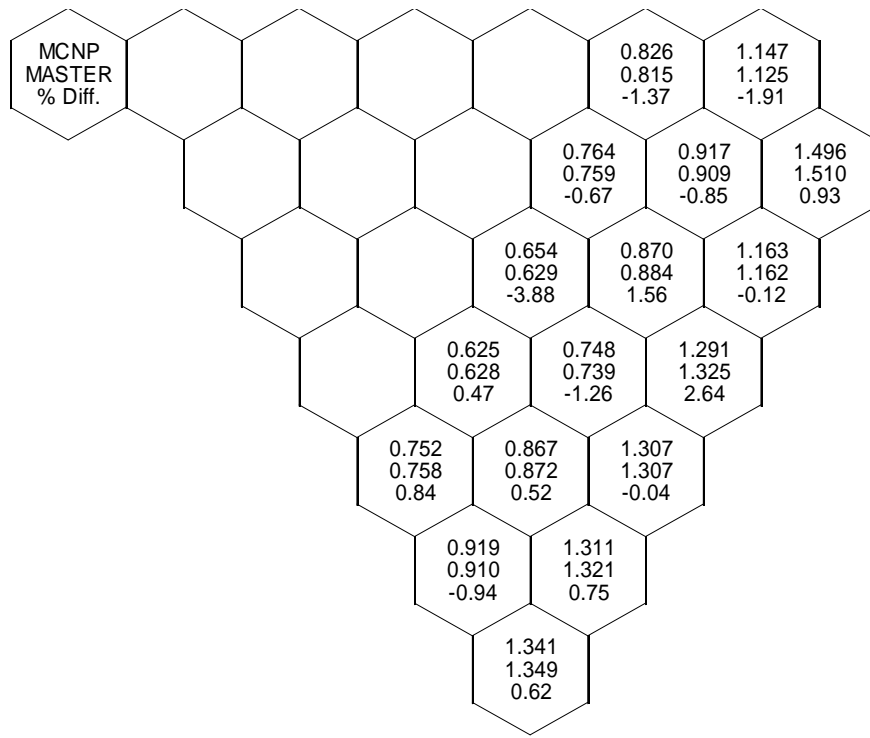


FIG. 6.48. Comparison of the radial block power distribution for the variant-1 core (All rods out, 1200 K).

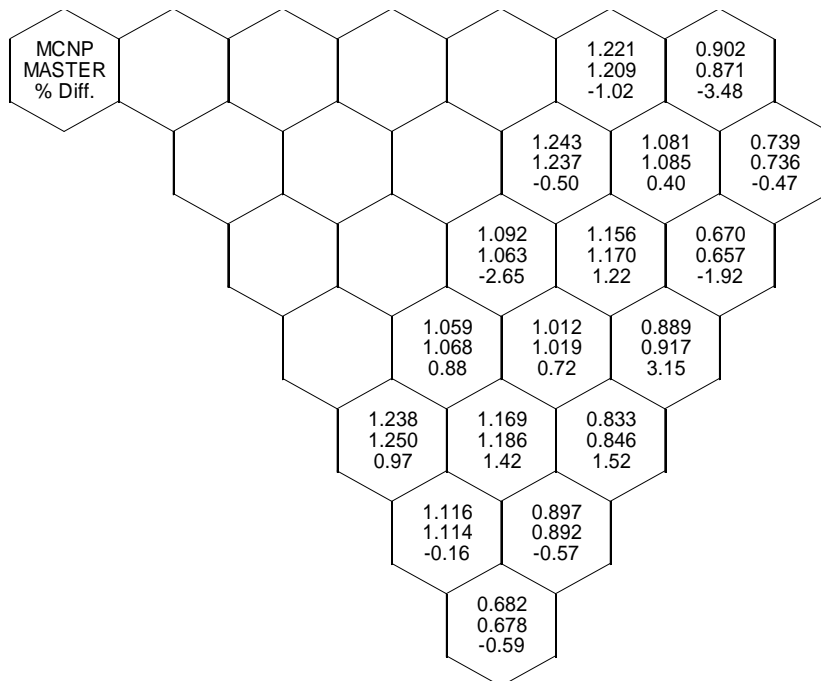


FIG. 6.49. Comparison of the radial block power distribution for the variant-1 core (Operating rods in, 1200 K).

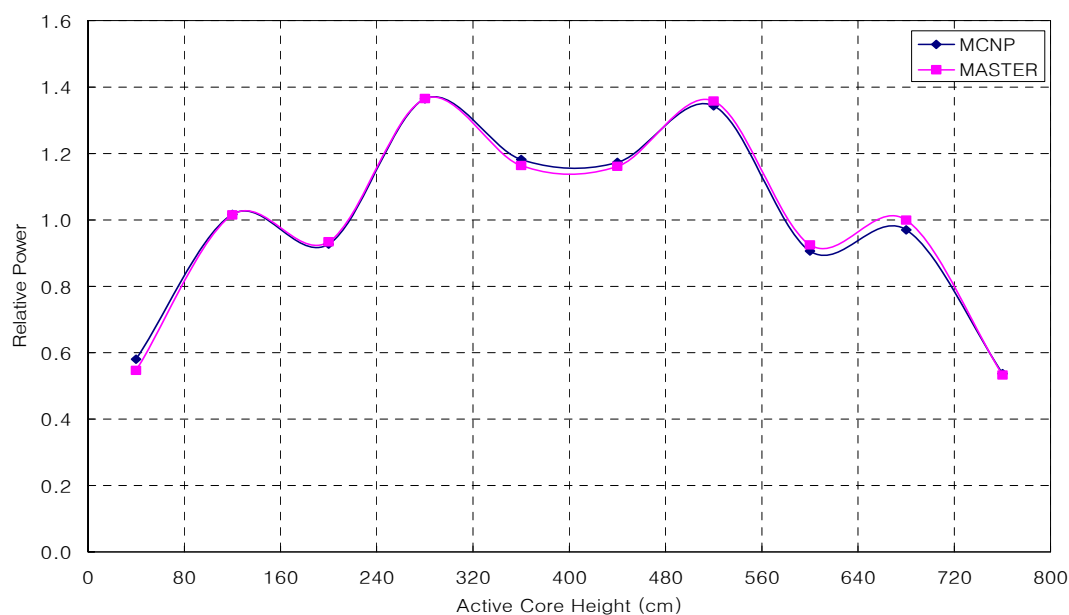


FIG. 6.50. Comparison of the axial block power distribution for the variant-1 core (All rods out, 1200 K).

6.3.3.6. Conclusions

KAERI has performed the IAEA GT-MHR benchmark calculations by using the HELIOS/MASTER code package with the two-step procedure. The MCNP Monte Carlo code served as a reference code in these benchmark calculations. In this procedure, the spectrum shift and the strong spectral interaction in the VHTR cores could be handled by optimizing the group structure used in the MASTER calculation and by applying the equivalent theory to a mini-core model instead of a single-block one to generate a few group cross-sections for fuel blocks and reflectors. The double-heterogeneity effect due to the random distribution of the particulate fuel could be removed by using the (RPT) method.

The computational results of the benchmark calculations show that the HELIOS/MASTER code system with the two-step procedure is working reasonably well. Although this benchmark problem includes only plutonium fuels, this code system was proven to be applicable to the problems consisting of uranium fuels through other benchmark tests. Therefore, KAERI will use this code system as a standard reactor physics analysis tool for the prismatic VHTR through the further V&V process.

6.4. REFERENCES FOR CHAPTER 6

- [6-1] INTERNATIONAL ATOMIC ENERGY AGENCY, Design and Development of Gas Cooled Reactors with Closed Cycle Gas Turbines, IAEA-TECDOC-899, IAEA, Vienna (1996).
- [6-2] INTERNATIONAL ATOMIC ENERGY AGENCY, Current Status and Future Development of Modular High Temperature Gas Cooled Reactor Technology, IAEA-TECDOC-1198, IAEA, Vienna (2001).
- [6-3] LA BAR, M.P., SIMON, W.A., "International co-operation in developing the GT-MHR," High Temperature Gas Cooled Reactor Technology Development. IAEA-TECDOC-988, Vienna (1997) 59–71.

- [6-5] ABAGIAN, L.P., ALEKSEEV, N.I., BRYZGALOV, V.I., et al., 'MCU-RFFI/A Code with DLC/MCUDAT-1.0 Nuclear Data Library, Applicant and Developer', RRC Kurchatov Institute, Certificate number PC No 61 of 10.17.96, Russian Federal Agency for Supervision of Nuclear and Radiation Safety, Moscow (1996).
- [6-6] ABAGIAN, L.P., ALEKSEEV, N.I., BRYZGALOV, V.I., et al., 'MCU: Monte-Carlo Code for Nuclear Reactor Calculations. Verification', RRC Kurchatov Institute, Preprint IAE-5751/5 (1994) (in Russian).
- [6-7] GUREVICH, M.I., BRYZGALOV, V.I., 'The Neutrons Flux Density Calculation by Monte Carlo Code for the Double Heterogeneity Fuel', Proc. of the Int. Conf. on Reactor Physics and Reactor Computations, Tel-Aviv (1994) 190–196.
- [6-8] LOS ALAMOS NATIONAL LABORATORY, MCNP — A General Monte Carlo Code for Neutron and Photon Transport, LA-7396-M, LANL, Los Alamos (1981).
- [6-9] BRIESMEISTER, J.F., (Ed.), 'MCNP — A General Monte Carlo N-particle Transport Code Version 4A', LA-12625-M, LANL, Los Alamos (1993).
- [6-10] MITENKOVA, E.F., NOVIKOV, N.V., SUKHAREV, Yu.P., 'Study of neutron physical performance of HTGR pebble bed core by Monte-Carlo method', Atomnaya Energiya, b.77, iss.3 (September 1994) (in Russian).
- [6-11] YUDKEVICH, M.S., 'BURNUP code for calculation of isotopic kinetics during fuel life in a nuclear reactor', RRC Kurchatov Institute, Preprint IAE-6048/5 (1997) (in Russian).
- [6-12] ASKEW, J.R., et.al. 'A general description of the lattice code WIMS', JBWES (1966).
- [6-13] DAVIDENKO, V.D., TSIBULSKY, V.F., 'Detailed Calculation of Neutron Spectrum in Cells of a Nuclear Reactor', Int. Conf. on the Physics of Nuclear Science and Technology (Oct. 5–8), 1998, Long Island, New York (1998) 1755–1760.
- [6-14] YAROSLAVTSEVA, L.N., 'JAR Code System for Nuclear Reactor Neutronics Calculations'. VANT, FTYaR series, issue 8 (37) (1983) 41–43 (in Russian).
- [6-15] INTERNATIONAL ATOMIC ENERGY AGENCY, 'Report of the 4th Research Coordination Meeting on the CRP5', (RCM Vienna, October 2002) Working Material, IAEA, Vienna (2002).
- [6-16] INTERNATIONAL ATOMIC ENERGY AGENCY, 'Report of the 3rd Research Coordination Meeting on the CRP5' (RCM Vienna, 12–16 March 2001) Working Material, IAEA, Vienna (2001).
- [6-17] SUBLET, J.C., RIBON, P., 'A probability Table Based Cross-section Processing System: CALENDF - 200', Journal of Nuclear Science and Technology (2002).
- [6-18] SANCHEZ, R., HEBERT, A., STANKOVSKI, Z., COSTE, M., LOUBIERE, S., VAN DER GUCHT, C., ZMIJAREVIC, I., 'APOLLO2 Twelve Years Later', Mathematics and Computation, Reactor Physics and Environmental Analysis in Nuclear Applications, Madrid (1999).
- [6-19] BOTH, J.P., PENELIAU, Y., 'The Monte Carlo code TRIPOLI4 and its first benchmark interpretations', International Conference PHYSOR 96, Mito, Ibaraki, Japan, (1996).
- [6-20] CAVALIER, C., STEPNIK, B., DAMIAN, F., RAEPSAET, X., 'Presentation of the HTR Neutronics Tool NEPHTIS', International Conference ENC2005, Versailles (December 2005).
- [6-21] DAMIAN, F., RAEPSAET, X., SANTANDREA, S., MAZZOLO, A., POINOT, C., KLEIN, J.C., BRAULT, L., GARAT, C., 'GT-MHR Core modelling: From reference modelling definition in Monte-Carlo code to calculation scheme validation', International Conference PHYSOR 2004, Chicago (2004).

- [6-22] DAMIAN, F., GROIZARD, M., POINOT, C., COURAU, T., THAREAU, S., 'VHTR Neutronic Calculation Scheme: Validation Elements using MCNP and TRIPOLI4 Monte-Carlo codes', MC2005, Avignon (September 2005).
- [6-23] DAMIAN, F., RAEPSAET, X., GROIZARD, M., POINOT, C., 'NEPHTIS: core depletion validation relying on 2D transport core calculations with the APOLLO2 code', PHYSOR 2006, Vancouver (September 2006).
- [6-24] INTERNATIONAL ATOMIC ENERGY AGENCY, 'Evaluation of High Temperature Gas Cooled Reactor Performance: Benchmark Analysis Related to Initial Testing of the HTTR and HTR-10', IAEA-TECDOC-1382, IAEA, Vienna (2004).
- [6-25] KIM, KANG-SEOG, et al., 'Development of Two-step Procedure for the VHTR Physics Analysis', PHYSOR-2006, Vancouver, Canada (2006).
- [6-26] STAMMLER, R.J., et al., 'HELIOS Methods', Studsvik Scandpower (1998).
- [6-27] CHO, B.O., et al., 'MASTER-2.0: Multi-purpose Analyzer for Static and Transient Effects of Reactors', KAERI/TR-1211/99 (1999).
- [6-28] KIM, Y.H., et al., 'Reactivity-Equivalent Physical Transformation for Elimination of Double Heterogeneity', Trans. Am. Nucl. Soc., 93 (2005) 959–960.
- [6-29] BREISMEISTER, J.F., 'MCNP — 'A General Monte Carlo N-Particle Transport Code, Version 4B', LA-12625-M, (1997).
- [6-30] KIM, KANG-SEOG., LEE, KYUNG HOON., SONG, JAE SEUNG., NOH, JAE MAN., 'IAEA GT-MHR Benchmark Calculations Using the HELIOS/MASTER Two-Step Procedure', Korea Atomic Energy Research Institute, Republic of Korea (2007).

7. COMPARISON OF RESULTS AND CONCLUSIONS

This CRP provides the unique opportunity for Member States to both share in the code-to-code evaluation of selected benchmark problems and also to compare their individual analyses to tests performed on the HTR-10 reactor and other test facilities. This chapter includes a comparison of the benchmark problem results obtained by each organization on benchmarks associated with the HTR-10 test reactor, the ASTRA critical facility, the PBMR-400, the PBMM and the GT-MHR. It also includes a synopsis by the CSIs as to the areas of uncertainty and diverse modelling options that may have contributed to differences in individual Member State results as well as recommendations for code and model improvements that can be applied to future reactor design and development activities.

7.1. HTR-10 BENCHMARK COMPARISON OF RESULTS

This section includes a summary of the Member State analyses and the experimental results for the HTR-10 steady state temperature distribution, loss of flow and CRD withdrawal benchmarks. Analyses by individual CSIs related to the HTR-10 benchmark problem calculations included a wide variety of codes, models and methods. These are described in Chapter 2 by each Member State.

7.1.1. Temperature distribution comparison of results

The purpose of this benchmark problem was to calculate and compare the HTR-10 steady state temperature distribution for FPIC. This benchmark has been widely participated in. It includes the following three problems:

- Calculation of temperature distribution within the pebble bed, including profiles of $R = 0$ cm, $R = 45$ cm, $R = 90$ cm, $Z = 0$ cm, $Z = 80$ cm and $Z = 170$ cm in the defined coordinate as shown in Chapter 2;
- Calculation of solid material temperature values at measured places. The exact coordinates of measured places can be found in Chapter 2;
- Calculation of the maximum temperature values of the main components, namely, the fuel elements (at centre and surface), side reflector and bottom reflector.

7.1.1.1. Temperature profiles within the pebble bed

Although there are six temperature profiles in the definition of the benchmark problem, the results comparison deals with two calculated profiles, namely; $R = 0$ cm and $Z = 80$ cm. Other calculated temperature profiles obtained by participants can be found in Chapter 2. Figure 7.1 provides the comparison of axial ($R = 0$ cm) temperature profiles. Japan's result departs severely from other profiles. The profile given by Turkey is high and that obtained by South Africa with the VSOP code is low. The Republic of Korea's profile departs from the majority in the fuel discharging tube. Figure 7.2 provides the comparison of radial ($Z = 80$ cm) temperature profiles. The profiles obtained by South Africa, Turkey and the United States of America with the VSOP code depart markedly from majority.

7.1.1.2. Solid material temperature values at measured places

Table 7.1 provides the comparison between the calculations and the experimental results of measured solid material temperatures for the HTR-10 full power initial core. Table 7.2 provides the deviations of calculation results obtained by all participants with the RMS difference of all results compared to the measured value. The temperature measurement uncertainties were not available and the coolant gas flow models were all simplified (no gas streaming between blocks, no neutron or gamma heating, etc.) and therefore it is not possible to set acceptance criteria for the C/E ratios. The engineering judgement of participants suggested that agreement within 10% (50–100K) should be achievable. At certain places in the side reflector and hot helium plenum, the deviation between calculated temperature values by the Republic of Korea and the United Kingdom and the measured values is larger than 100 K.

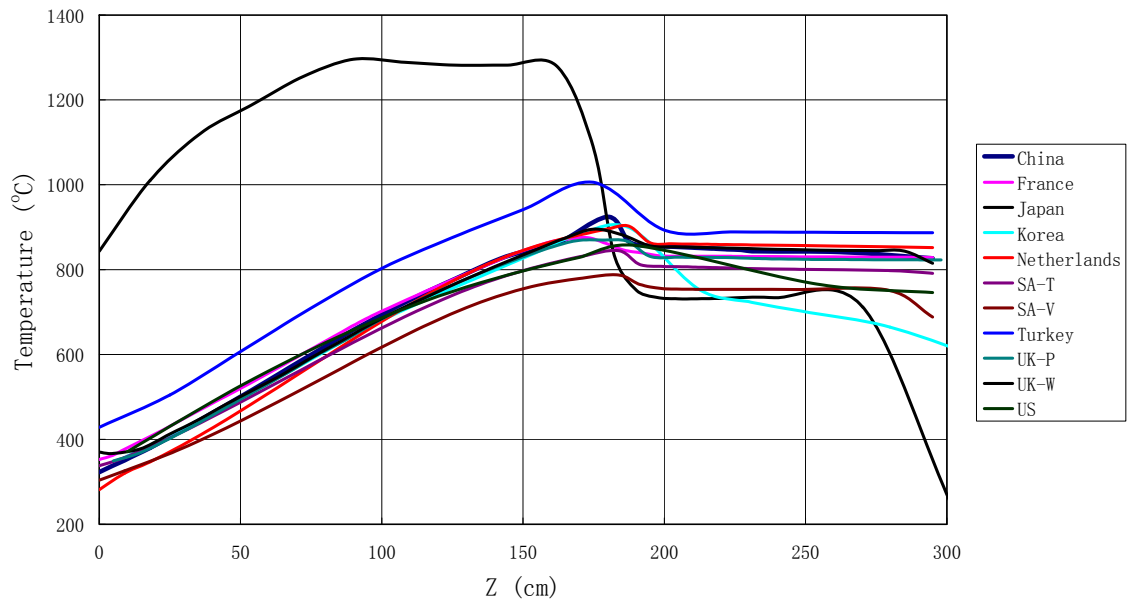


FIG. 7.1. Comparison of axial ($R = 0$ cm) temperature profiles.

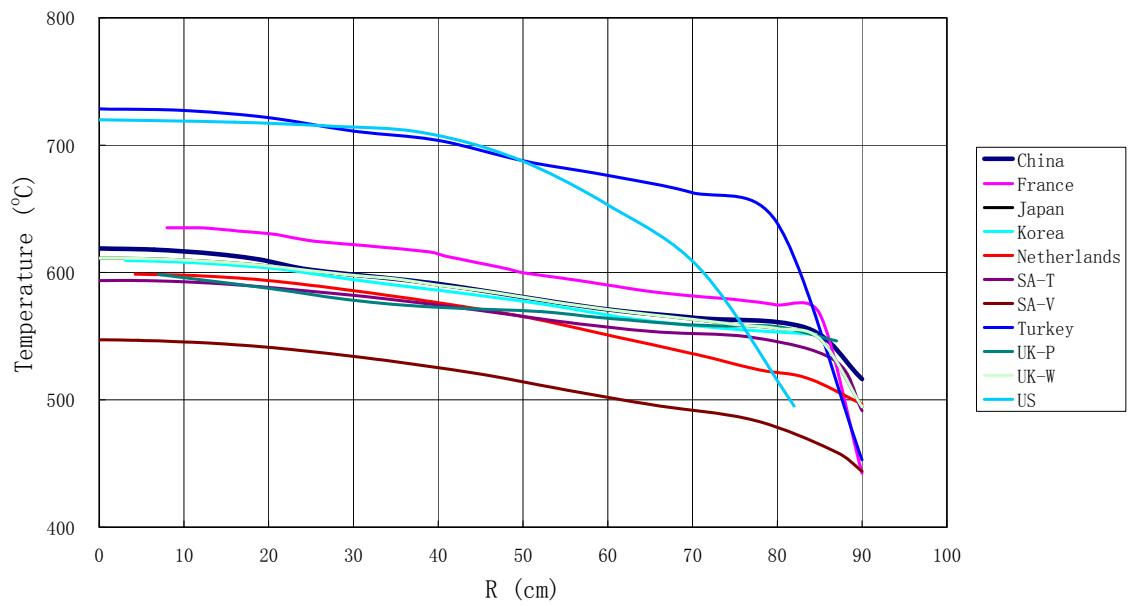


FIG. 7.2. Comparison of radial ($Z = 80$ cm) temperature profiles.

TABLE 7.1. COMPARISON OF SOLID MATERIAL TEMPERATURES FOR HTR-10 FPIC

No.	R(cm)	Z(cm)	Exp (°C)	Ch.	Fr.	Ja.	Kor.	NL	SA-T	SA-V	Tur.	UK-P1	UK-P2	UK-W	AVG	STD
Side reflector																
1	193	80	231.3	244	220	250	222	204	244	231	224	253	256	-	235	17
2	189	80	249.3	264	260	254	240	224	260	257	253	265	270	335	262	14
3	167	80	274.3	292	303	287	289	291	305	299	260	281	294	335	294	13
4	133	80	289.1	316	328	313	317	315	342	326	298	307	320	357	322	12
5	117	80	313.3	350	360	340	339	339	380	362	341	329	350	389	353	15
6	93	80	357.7	410	433	413	386	379	456	433	441	471	443	463	430	29
7	193	170	234.9	247	227	250	222	217	257	243	220	252	254	-	239	16
8	189	170	264.8	271	268	255	245	240	274	269	247	266	272	366	270	13
9	167	170	303.9	305	315	297	311	314	324	315	253	284	305	368	308	21
10	133	170	328.5	342	350	337	356	344	382	361	315	326	348	408	352	19
11	117	170	365.3	389	394	380	397	409	451	429	386	365	401	469	406	25
12	93	170	507.1	501	495	494	489	501	598	587	524	646	584	632	550	57
Top reflector																
13	60	-40	245.7	261	278	251	278	269	282	274	267	271	271	275	271	9
Hot helium plenum																
14	40	234	800.2	770	783	793	728	796	775	720	820	741	735	819	771	33
15	60	234	763.1	714	740	746	734	748	753	697	738	658	653	794	725	37
Bottom carbon bricks																
16	70	440	224.1	240	250	252	254	250	252	257	246	250	250	261	251	5
17	50	400	245.7	264	251	440	267	251	255	255	245	266	266	252	274	58
18	50	370	296.2	295	257	251	311	276	272	263	252	294	294	255	275	21
19	50	340	406.7	340	289	250	412	367	347	410	340	351	351	263	338	49
Fuel discharge tube																
20	26	340	334.2	317	305	289	352	340	309	399	323	321	329	254	322	30
21	26	300	806.1	707	760	434	488	754	715	640	820	379	389	462	595	169
22	26	260	881.7	793	796	791	585	793	783	726	829	728	725	832	762	70

Notes: Ch.: China; Fr.: France; Ja.: Japan; Kor.: Republic of Korea; NL: Netherlands; SA-T: South Africa with TINTE; SA-V: South Africa with VSOP; UK-P1: UK with PHOENICS, θ -plane 1; UK-P2: UK with PHOENICS, θ -plane 2; UK-W: UK with WIMSTER; AVG: Average of calculated values; STD: 1 sigma standard deviation.

For the measured points in the bottom carbon bricks, the deviations of most calculated values are lower than 100 K, except for certain values obtained by France, Japan and the United Kingdom with the WIMSTER code. For the measured points in the fuel discharging tube, many of the calculated values have large deviations. Generally, most calculations underestimate the temperature at measured places. The deviation of results obtained by the Republic of Korea and South Africa are larger than 150 K and those of results obtained by Japan and the United Kingdom are larger than 300 K.

TABLE 7.2. DIFFERENCES OF SOLID MATERIAL TEMPERATURES FOR HTR-10 FPIC

No.	R (cm)	Z (cm)	Exp (°C)	Ch.	Fr.	Ja.	Kor.	NL	SA-T	SA-V	Tur.	UK-P1	UK-P2	UK-W	RMS	STD
Side reflector																
1	193	80	231.3	13	-11	18	-9	-28	13	0	-8	22	24	-	17	17
2	189	80	249.3	14	11	5	-10	-25	11	8	4	16	21	86	29	27
3	167	80	274.3	17	29	13	15	16	31	25	-14	7	20	61	27	18
4	133	80	289.1	27	39	24	28	25	53	37	9	18	31	68	36	16
5	117	80	313.3	36	47	27	25	25	67	49	28	16	37	75	43	19
6	93	80	357.7	53	75	56	28	21	98	75	83	113	85	106	78	30
7	193	170	234.9	12	-8	15	-13	-18	22	8	-15	17	19	-	15	16
8	189	170	264.8	6	3	-10	-20	-25	10	5	-18	1	7	101	33	34
9	167	170	303.9	1	11	-7	7	10	20	11	-51	-20	2	64	27	28
10	133	170	328.5	13	22	8	27	16	53	32	-14	-3	19	80	34	26
11	117	170	365.3	24	29	14	32	44	86	64	21	-1	36	104	51	32
12	93	170	507.1	-6	-12	-13	-18	-6	91	80	17	139	77	125	72	60
Top reflector																
13	60	-40	245.7	15	32	5	32	24	37	28	21	25	26	29	26	9
Hot helim plenum																
14	40	234	800.2	-30	-17	-7	-72	-5	-25	-80	20	-59	-65	19	45	35
15	60	234	763.1	-49	-23	-17	-29	-15	-11	-67	-25	-105	-110	31	55	42
Bottom carbon bricks																
16	70	440	224.1	15	26	28	30	26	28	33	22	26	26	37	28	6
17	50	400	245.7	18	5	195	21	5	9	10	-1	20	20	7	60	56
18	50	370	296.2	-1	-39	-45	15	-20	-25	-34	-45	-2	-2	-42	30	21
19	50	340	406.7	-67	-118	-156	6	-40	-60	3	-67	-56	-56	-143	85	52
Fuel discharge tube																
20	26	340	334.2	-17	-29	-45	18	6	-25	65	-11	-13	-6	-80	37	37
21	26	300	806.1	-99	-46	-373	-318	-52	-91	-166	14	-428	-418	-344	264	167
22	26	260	881.7	-89	-86	-91	-297	-89	-99	-155	-53	-153	-157	-49	137	70

Note: Ch.: China; Fr.: France; Ja.: Japan; Kor.: Korea; NL: Netherlands; SA-T: South Africa with TINTE; SA-V: South Africa with VSOP; UK-P1: UK with PHOENICS, θ -plane 1; UK-P2: UK with PHOENICS, θ -plane 2; UK-W: UK with WIMSTER; RMS difference of all results; STD: 1 sigma standard deviation in the differences between calculated and measured.

7.1.1.3. Maximum temperature values of main components

Table 7.3 provides the comparison of calculated maximum temperature values of main components obtained by all participants. Regarding the fuel centre temperature, the result difference is within 150 K. Turkey gives a high value and South Africa, with VSOP, gives a low one. Regarding the side reflector temperature, the result difference is nearly 400 K. Turkey gives a high value and the Republic of Korea gives a low one. Regarding the bottom reflector temperature, the result difference is also more than 330 K. France gives a high value and Turkey gives a low one. The average of the submitted results and the standard deviation (1σ) are also included. The side reflector standard deviation is the largest while the fuel temperatures show lower values.

TABLE 7.3. COMPARISON OF CALCULATED MAXIMUM TEMPERATURE VALUES OF MAIN COMPONENTS

Comp.	Pos.	Ch.	Fr.	Ja.	Kor.	NL	SA-T	SA-V	Tur.	UK-P	UK-W	USA	AVG	STD
Fuel	Cent.	988	889		929	903	905	881	1026	958	983	951	941	48
	Surf.	925	865		897	973	845	812	1008	916	895	893	903	61
SideR	Surf.	512	520	576	447	514		561	836	647	652	504	577	116
BottomR	Surf.	789	808	783	730	808		724	581	784	833	766	761	75

Note: Ch.: China; Fr.: France; Ja.: Japan; Kor.: Korea; NL: Netherlands; SA-T: South Africa with TINTE; SA-V: South Africa with VSOP; UK-P: UK with PHOENICS, UK-W: UK with WIMSTER; USA: United States of America; AVG: Average of calculated values; STD: 1 sigma standard deviation.

7.1.2. Temperature distribution conclusions/recommendations

From Figs 7.1 and 7.2, the following points are readily observed:

- For the axial ($R = 0$ cm) temperature profiles, most calculation results have the same tendency, however, about 100 K difference exists among the results in the majority.
- For the radial ($Z = 80$ cm) temperature profiles, most calculation results have the same tendency, however, about 50 K difference exists among the results in the majority.

From Tables 7.1 and 7.2, the following conclusions can be obtained:

- Generally, most calculated temperature values of measured points in the side reflector, top reflector and hot helium plenum agree well with measured values, although the deviation of certain calculated values are higher than 100 K.
- Most calculated temperature values of measured points in the bottom carbon bricks basically agree with measured values.
- For the measured points in the fuel discharging tube, most calculations underestimate the temperatures at the measured places. The deviations of some results are quite large.

For the maximum fuel centre temperature, the difference of results obtained by all participants is relatively low. However, the difference of maximum reflector temperatures obtained by participants is quite large.

The following recommendations are suggested for further calculation and analysis:

- Carefully check the thermal properties of graphite, carbon bricks, pebble bed and steel, etc.
- Model the internal structure of the reactor core with greater detail, especially the bottom carbon bricks and the structure around the fuel discharging tube. There are complicated flow channels in this area.
- Reasonably set boundary conditions.
- The measurement uncertainties were not provided, making it difficult to give a final statement regarding the validation of codes.
- No coolant bypass flow measurements are available, so different assumptions were made by the participants.
- Omitted or incomplete data, such as the insulation and thermal shield material property data, needs to be supplied to ensure consistency in developing models of the HTR-10 benchmark problems by users of the various HTR analysis codes.

7.1.3. HTR-10 loss of flow comparison of results

The loss of flow without scram transient was run on the HTR-10 reactor facility. The primary helium blower was quickly stopped and then the primary system was isolated from the water cooling systems on the secondary side of the steam generator. All control units remain where they were before the

transient was started. The transient was run at partial load. It was proposed to calculate the reactor power transient response for this problem.

The transient was started (time point zero) by shutting down the primary helium blower, stopping the primary helium flow and isolating the primary system from the water cooling systems on the secondary side of the steam generator. For calculation purposes, these actions were assumed to be instantly complete. All control units remained where they were before the transient was initiated.

The experimental results of the loss of flow without scram test on the HTR-10 are provided in Chapter 2. Five Member States have participated in this benchmark. The calculated results obtained by all participants are shown in Figs 7.3 (short time) and 7.4 (long time). These results are compared with the experimental results.

The experimental results show a return to criticality at about 4300 s and a relative fission power of 0.25 while the second power peak appears about 1200 s later with a relative power of 0.098. In comparison, the Chinese results predicted the first recriticality quite accurately in time (only 100 s later), but the magnitude is much larger at 0.41 (thus C/E of 1.65). The analysis was stopped at 6000 s when the second oscillation just started, so the period between the two peaks was estimated to be about 1700 s (C/E of 1.4). The results from the Netherlands have peak values of 0.29 and 0.12 and compare favourably with the experiment (C/E of 1.16 and 1.24), but the first peak appeared at about 5350 s (1050 s late) with a period of 1450 s (C/E of 1.2) to the second peak. Similar values with good agreement in the magnitude of the peak was found for the South African contribution with peak values of 0.27 and 0.098 (C/E of 1.08 and 1.0), but the time of recriticality is even later at 5875 s (1575 s later than the experiment) and a oscillation period of 1625 s (C/E of 1.35). The result from Japan is the only one predicting a slightly lower relative fission power of 0.225 (C/E of 0.9) at about 5450 s (1150 s later than the experiment). No second peak was observed in the period calculated up to 7250 s. The results from Turkey shows a very early return to criticality at less than 1500 s, but the analysis was not completed to see the recriticality peak value.

7.1.4. Loss of flow conclusions/recommendations

From Figs 7.3 and 7.4, the following points can be concluded:

- In short time, all five results give a reasonable response, i.e. the reactor automatically shuts down due to the negative temperature feedback effect.
- In long time, except for Turkey, other results predict the recriticality phenomena. However, in the results there are evidently deviations regarding the recriticality time, recriticality peak power and interval between the first and second recriticality.

The following recommendations are suggested for further calculation and analysis:

- Utilize an appropriate model of xenon effect;
- Carefully calculate the distribution of decay heat power;
- Check the neutronics parameters, especially the temperature coefficients of reactivity.

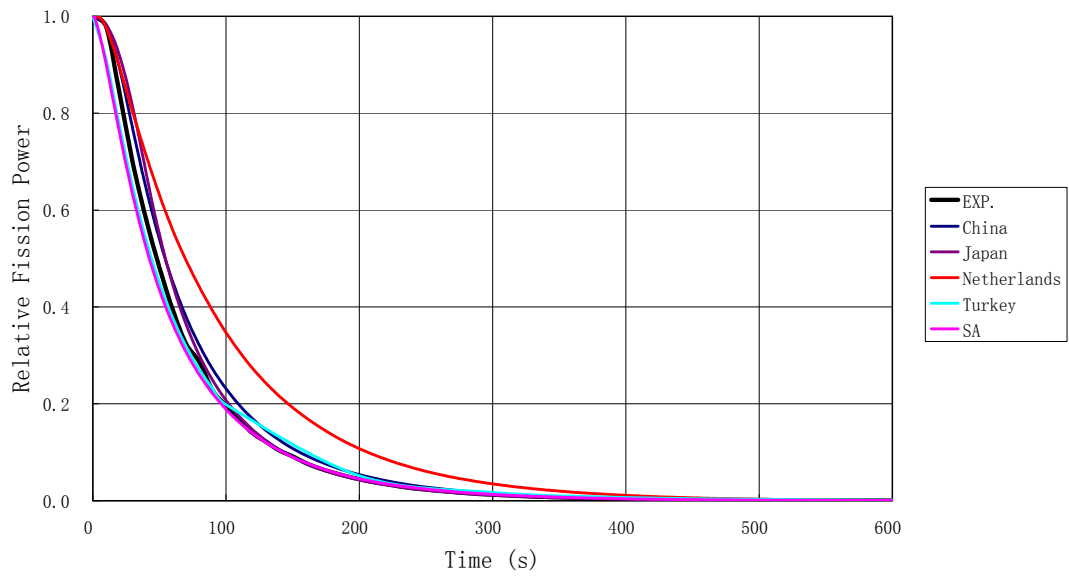


FIG. 7.3. HTR-10 power on first 600 s after loss of flow without scram transient.

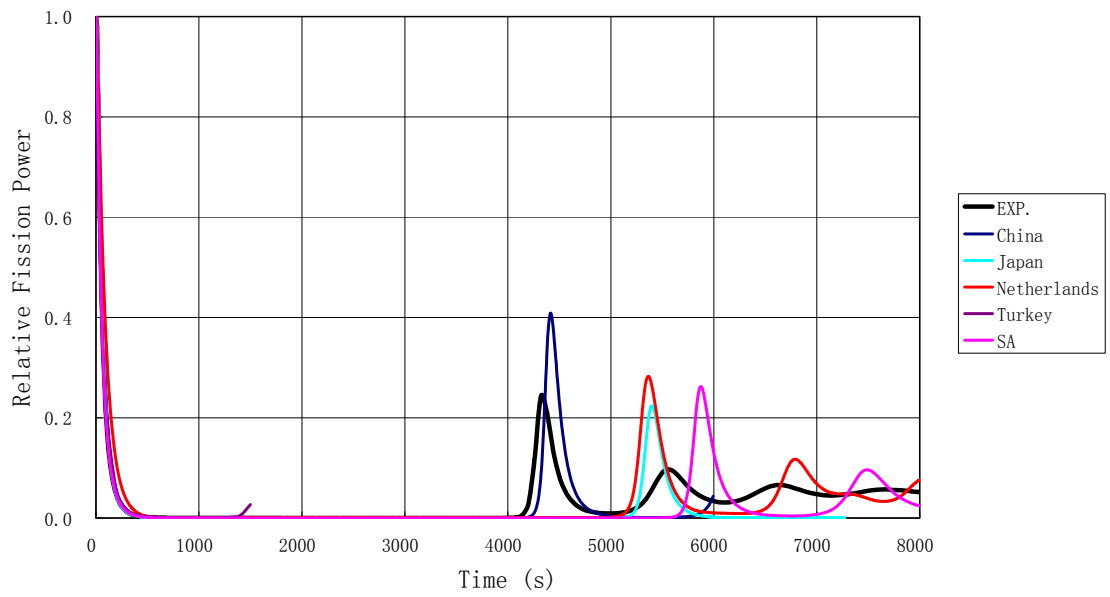


FIG. 7.4. HTR-10 power through 8000 s after loss of flow without scram transient.

The following observations were made during the exercise:

- Sensitivity studies showed the recriticality time and power level to be very sensitive to model variations.
- Differences in models either utilizing the provided reactivity temperature coefficients or internally calculated by the code (based on fission fractions) did show important differences.
- The spatial decay power distribution and the dissipation of the decay heat from the core and adjacent graphite structures are the controlling parameters for recriticality during an LOFC transient event.
- The analysis assumption that heat removal was stopped immediately could contribute to the late recriticality time calculated by many analyses:
 - Recriticality was typically predicted later than the experiment in many analyses.
 - This could indicate some additional heat loss in the system (it could be that some additional heat has been removed initially in the experiment before the circulator is stopped).
 - The results from NRG only improved (recriticality became earlier whereas previously it was much later) after some additional heat loss mechanisms (at the top) were added.
- The power operation history before the experiment was not defined in detail (duration and modes of operation). This data will be needed to:
 - Produce the correct power distribution in the core;
 - Predict the correct xenon behaviour;
 - Obtain the correct fission product isotopic concentrations for the decay power calculations.

7.1.5. HTR-10 CRD withdrawal without scram comparison of results

This transient on the HTR-10 reactor facility is the CRD withdrawal without scram benchmark. After reaching initial criticality, additional fuel and graphite balls (to the ratio of 57:43 which is the same as the already loaded pebble bed) have been loaded into the reactor core to such a level that the reactor can operate at full power. One control rod is then withdrawn at operational speed so that positive reactivity is introduced. The RPS responds, but the reactor is intentionally not tripped. The transient was run at partial load. It was proposed to calculate the reactor power transient response in this problem.

The experimental results of the CRD withdrawal without scram test on the HTR-10 are provided in Chapter 2. Only three Member States participated in this benchmark. The calculated results obtained by all participants are shown in Figs 7.5 (short time) and 7.6 (long time). These results are compared with the experimental results.

The initial relative fission peak due to the reactivity insertion is reached after about 31 s although the reactivity insertion due to control rod withdrawal took place over more than 120 s. The relative fission power peak predicted is about 2.4. The three sets of results shown predicted this time very well, with China only 3 s earlier (at 28 s) and Japan and South Africa predicting the peak at 33 s (2 s later than measured). The peak values were all underestimated by the analysis, with China at 2.3, Japan at 2.05, and South Africa at 1.8 relative fission power, resulting in C/E values of 0.96, 0.85 and 0.75 respectively.

The recriticality experimental peak relative power occurs after about 3400 s with a value of 0.28. In comparison, the analysis by China predicted a much higher peak value of 0.6 (with C/E of 2.1) and 800 s earlier at 2600 s. The other two sets of calculational results are both later than the experiment (Japan by 500 s and South Africa by 660 s) with peak value predictions of 0.2 and 0.3, respectively (C/E of 0.7 and 1.1). It is interesting to note that the relative behaviour of the calculated results for recriticality is the same as in the loss of flow experiment. The relative times to recriticality and the peak values shows exactly the same behaviour. In both cases the Chinese results show an earlier recriticality time and the highest peak value. This is followed in time by Japan with the lowest peak

value and then later recriticality predicted by South Africa but with the peak value predicted to be between the other two sets of results. For the second recriticality peak, the C/E values are similar for the different codes while the time between peaks are 1200 s for the experiment and 1250, 2400 and 1500 s for China, Japan and South Africa, respectively.

7.1.6. CRD withdrawal conclusions/recommendations

From Figs 7.5 and 7.6, the following points can be concluded:

- In short time, all of the three results gives a reasonable response, i.e. the reactor power first goes up and then down, and finally automatically shuts down due to negative temperature feedback effect. However, the power peaks are evidently underestimated;
- In long time, all results predict the recriticality phenomena. However, in the results, deviations are evident regarding the recriticality time, recriticality peak power and interval between the first and second recriticality.

The following recommendations are suggested for further calculation and analysis:

- Utilize an appropriate model of xenon effect;
- Carefully calculate the distribution of decay heat power;
- Check the neutronics parameters, especially the temperature coefficients of reactivity;
- Investigate the position of each control rod and its worth.

7.1.7. Final comments on the HTR-10 code to measured benchmark

The following are final comments and recommendations:

- It was an extremely valuable exercise in code validation;
- The cases represented a complex integrated problem with many unknowns and assumptions, as follows:
 - The bypass flows are not known and different assumptions had to be made.
 - The operational history was not defined in detail and was felt to be important by some participants.
 - The initial conditions of the core at the start of the transients were not fully known and did cause some assumptions to be made in the power distributions and decay heat.
 - Limited measurements are available.
- Excellent agreement was seen in the general phenomena, but the differences in the absolute values (size and time) were significant.
- The experimental uncertainties were not provided, making it difficult to give a final statement regarding the validation of the codes.
- The final inclusion of the safety experiments as an IRPhe reactor physics benchmark will be valuable since this process includes the clarification of all uncertainties as part of a rigorous documentation and analysis process that was not possible within the scope and time of the CRP.

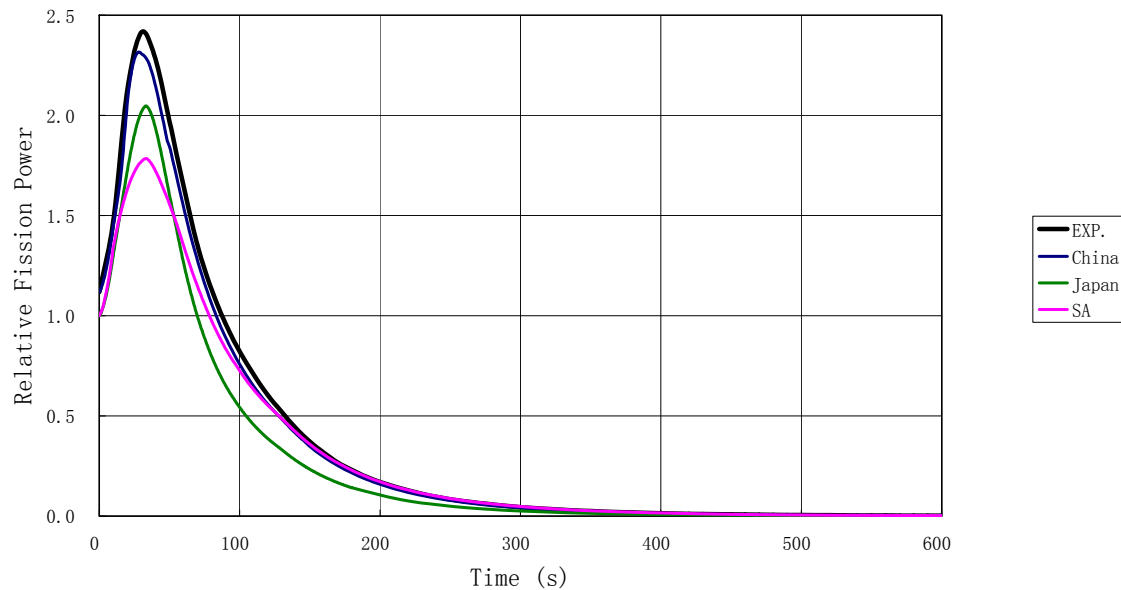


FIG. 7.5. HTR-10 power on first 600 s after CRD withdrawal without scram transient.

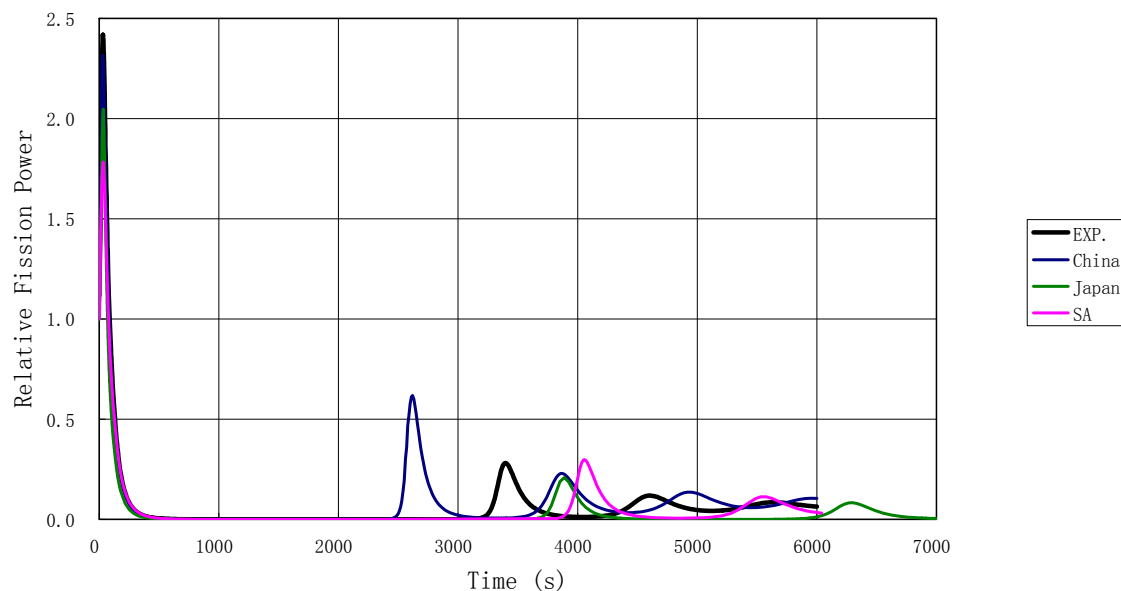


FIG. 7.6. HTR-10 power through 7000 s after CRD withdrawal without scram transient.

7.2. ASTRA CRITICAL FACILITY

This section includes a summary of the Member State analyses and the experimental results for the ASTRA critical facility benchmarks. Analyses by individual CSIs related to the ASTRA benchmark problem calculations included a wide variety of codes, models and methods. These are described in detail in Chapter 3 by each Member State.

7.2.1. Critical core height — Comparison of results

The purpose of this test was to predict the critical height of the ASTRA pebble bed experiment in the absence of control elements. The problem assumes that all control elements are to be withdrawn. The actual critical experiment, however, included the manual rod (MR1 with very low reactivity effect), that was inserted to a depth of 326.5 cm.

The Member States contributing results included China, France, Indonesia, South Africa, Turkey, and the United Kingdom. Table 7.4 lists the predictions of the height of the core needed to achieve criticality. The experimental value is shown as a reference although the core configuration does include the inserted MR1 control rod.

In the actual ASTRA critical experiment, the experiment and instrument channels in the reflector were unplugged and no top reflector or loading device was present. There is still some confusion about the status of the outer reflector blocks and if they were plugged or unplugged in the experiment, but this should have a minor effect on the criticality of the system. However, if all the side reflector elements (also those close to the core) are plugged or un-plugged, the effect is sizeable as is indicated by the results from Turkey. The % values in the right-most column of Table 7.4 represent the deviations from the mean and not the experimental value.

The results generated using the MCNP Monte Carlo transport code predicted the lowest heights for criticality (under 260 cm for both China and Turkey (for plugged)). The diffusion theory core simulators predicted criticality between 263 and 269 cm. The TRIPOLI French Monte Carlo transport code predicted a slightly higher value at 270 cm. The differences may also stem from the nuclear data libraries. Some of the codes use JEF2.2 and others rely on ENDF/B v6, but there seems to be no discernible pattern that can be attributed to the choice of libraries. The major differences are probably due to the distribution used for the absorber spheres, discrepancies in models, and uncertainties in the benchmark specification (for example, the packing fractions defined in the specification initially compared to the number of the different spheres types defined in other published sources).

7.2.2. Control rod worth — Comparison of results

In the first of the control rod worth experiments, the pebble bed core height was raised to 268.9 cm with control rods inserted to various depths. The worths of control rods CR2 and CR4 were measured using the rod-drop method at various distances from the core boundary (L_N). Participants were to estimate these values using their analytical tools.

South Africa and Turkey contributed results for this test. Table 7.5 summarizes the results.

The South African analysis of full and partial control rod worths yielded very close agreement with the experiment. A combination of one dimensional transport and three dimensional diffusion calculations were employed as part of the so-called MECS. The Turkish results agree in some cases, depending upon the modelling assumption. In the Turkish analysis, either all or none of the reflector channels (control, instrument and experiment) were plugged. In the actual experiment, some of the channels were plugged (the instrument channels) so one would expect the two sets of results to ‘bracket’ the experimental values. Except for the full inserted CR4 configuration, this appears to be the case.

In the second experiment, analysis methods were challenged to predict the worth of rod combinations by taking interference effects into account. Six different combinations were specified. Table 7.6 shows the results.

The South African results again agree well with the experimental results. The Turkish results overpredict the combined rod worth regardless of the reflector channel assumption, so only one of the sets is shown here. This is consistent with the previous result in which the rod worths are overpredicted. On the other hand, the interference coefficient, which is somewhat independent of the overall rod worth, is still predicted with some accuracy using their approach (see Table 3.40).

TABLE 7.4. PREDICTED CRITICAL HEIGHT OF ASTRA PEBBLE BED CORE

Experiment*	268.9	
Member State	Critical Height (cm)	% Deviation
China	253.6	-4.0
France	270.1	+2.1
Indonesia (WIMS)	259	-2.0
South Africa	269.0	+1.8
Turkey	270.5/255.06**	+2.3/-3.5
United Kingdom	263.4	-0.3
Mean	264.3	

* Control rod MR1 was inserted to a depth of 326.5 cm. Experiment and instrument channels in the reflector were unplugged.

** Results are shown for cases in which all the reflector channels were plugged.

TABLE 7.5. WORTH OF CR2 AND CR4 AS A FUNCTION OF POSITION

Control Rod Type	L _N (cm)	Exp. Rod Worth (%)	Estimated Rod Worth (%)	
			South Africa	Turkey*
CR2	12.5	-1.79	-1.77	-1.62/-1.83
CR2	37.5	-0.63	-0.50	-0.35/-0.85
CR2	62.5	-0.16	-0.18	-0.15/-0.28
CR2	87.5	-0.02	-0.01	-0.02/-0.14
CR4	17.7	-1.40	-1.41	-1.54/-1.60
CR4	53	-0.25	n/a	-0.41/-0.83

*Unplugged/plugged reflector holes.

TABLE 7.6. WORTH OF SPECIFIED ROD COMBINATIONS

Combination	Exp. Worth (%)	Estimated Worth (%)	
		South Africa	Turkey*
CR1+CR5	-3.72	-3.68	-4.19
CR2+CR5	-4.01	-3.98	-4.13
CR4+CR5	-3.10	-3.13	-3.57
CR1+CR2+CR5	-6.06	-6.07	-6.32
CR1+CR4+CR5	-5.15	-5.26	-5.76
CR2+CR4+CR5	-5.45	-5.58	-5.80

*Plugged reflector holes.

7.2.3. Differential rod worth vs insertion depth — Comparison of results

This test requires the participant to estimate the differential reactivity worth of the CR5 control rod as a function of insertion depth. The experiment results are compared to the two sets of calculated results. South Africa and Turkey provided results for comparison. These results are plotted in Fig. 7.7.

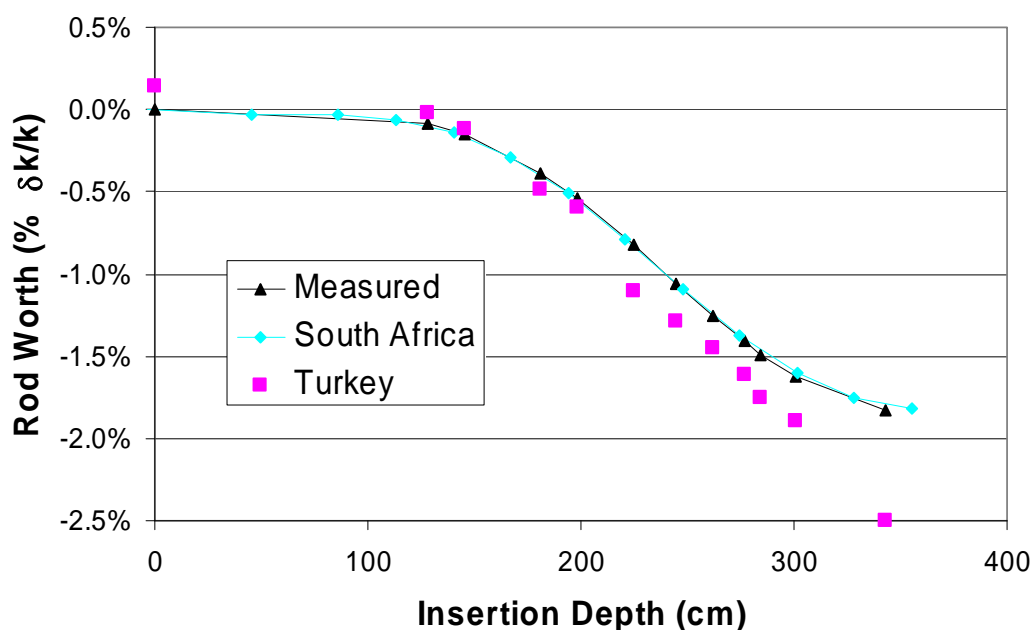


FIG. 7.7. Comparison of differential rod worth as a function of insertion depth — CR5.

In the case of the South African results, the total measured reactivity was used to determine the EBC to match the total measured control rod worth, thus explaining the good agreement. In other words, all that the results illustrate is that the total worth can be well predicted and the differential worth (or S-curve) can also be accurately calculated. The results from Turkey overpredicted the total worth (consistently with the previous results shown in Table 7.6) but do show the same general S-curve as the measured results (except for the last insertion point).

7.2.4. Effect of critical height on critical parameters — Comparison of results

The first part of this exercise is designed to compare the results for the reactivity of the pebble bed for various assumed heights. The control rods are assumed to be all out and the participants were to estimate the reactivity of the pebble bed at specified core heights. Only South Africa provided the results and thus no comparative analysis is provided here.

In the second part of the exercise, four control rods are inserted to various depths to obtain a critical core. Participants were to perform an eigenvalue calculation to reproduce a critical eigenvalue in each case. Table 7.7 lists the results provided by South Africa and Turkey.

The South African method predicted the core multiplication factor within 1% $\delta k/k$ in each case. The Turkish method had less success with the greater insertion of control elements and underpredicted the control rod worth in Cases 3 and 4. The MCNP4B code was used in the Turkish analysis and so one would assume that this transport code would have captured the strongly anisotropic scattering and absorption effects of the control rods at least as well as the hybrid transport diffusion MECS approach used by South Africa. It is reasonable to conclude that there are differences in the core models that may have led to the discrepancies. A detailed examination of the participant's models and assumptions would have to be undertaken to discover the source.

TABLE 7.7. COMPARISON OF CRITICALITY ESTIMATES
FOR VARIOUS CORE CONFIGURATIONS

Case	Configuration						Eigenvalue	
	Top reflector and support structure?	Height of pebble bed (cm)	CR1	CR2	CR5	MR1 (cm)	South Africa	Turkey
1	No	268.9	OUT	OUT	OUT	326.5±26	1.0037	1.0018
2	No	285.8	OUT	OUT	OUT	355±2	1.0095	1.0099
3	No	320.8	IN	OUT	OUT	325±1	1.0079	1.0104
4	Yes	320.8	OUT	IN	OUT	376±1	1.0085	1.0118

In addition to the studies compared above, the French participants noted a strong dependency of the flux distribution and eigenvalue upon the distribution of absorber spheres within the mixing and fuel zones of ASTRA. Various distributions were shown to change the computed eigenvalue by as much as 1.43% $\Delta k/k$. These results indicate a complex interplay of neutronic effects that could be the focus of further interesting study. The readers are referred to Section 3.2.5.6 for a discussion of the French analysis and results.

7.2.5. General comments

The detailed definition of the ASTRA facility as a benchmark case was only introduced late in the CRP activities. The inconsistency in the defined benchmark (packing density, pebble bed height and equivalent two dimensional diameter) lead to incomplete contributions and much time was spent by participants to try and resolve these discrepancies in the initial criticality configurations. For example, participants noted a strong dependency of the flux distribution and eigenvalue upon the distribution of absorber spheres within the mixing and fuel zones of ASTRA. Various distributions were shown to change the computed eigenvalue by as much as 1.43% $\Delta k/k$. The work performed also confirmed the negligible influence of the manner used to describe the fuel particles inside each pebble. These results indicate a complex interplay of neutronic effects that could be the focus of further interesting study.

The experimental or measurement uncertainties are an important part of a benchmark specification. This includes not only the uncertainties in material data and in the facility configuration, but also the measurement uncertainties. These did not form part of the current definition or evaluation. The CRP-5 effort ended before all issues could be fully resolved, but valuable experience was gained. In future, the inclusion of the ASTRA benchmark into the criticality handbook and/or IRPhe handbook will be of benefit for applying a similar effort within the IAEA to extract full V&V value.

7.3. PBMR-400 COLLATION OF RESULTS

This section includes a summary of the Member State analyses and the experimental results for the PBMR neutronics and thermohydraulic benchmarks. Analyses by individual CSIs related to the PBMR benchmark problem calculations included a wide variety of codes, models and methods. These are described in Chapter 4 by each Member State.

7.3.1. PBMR neutronics and thermohydraulic benchmarks — Comparison of results

Chapter 4 describes a series of neutronic and thermohydraulic exercises centred about the PBMR-400 reactor design in detail. Input data and output requirements were varied to maximize participation among members with different code capabilities. There are two series of benchmark exercises related to the PBMR. The first requires the construction and execution of simplified models of the reactor itself. The second omits many reactor features, focusing instead on a very simple geometry (a ‘pebble box’) that preserves just the important spectral features of the PBMR and allows a focused comparison of the differences between neutronic methods and codes.

The following subsections compare results for the PBMR-400 simplified reactor model.

7.3.1.1. F-1: Fresh fuel, cold conditions

Homogenized number densities were provided for a PBMR-400 core with uniformly distributed fresh pebbles of reduced enrichment corresponding to a startup core at 300 K. The results were provided by China, the Republic of Korea, South Africa and Turkey (Table 7.8).

TABLE 7.8. COMPUTED CORE MULTIPLICATION FACTORS FOR F-1 BENCHMARK

Participant	Eigenvalue
China	1.25823
Republic of Korea	1.20928 (Monte Carlo) 1.21342 (Diffusion)
South Africa	1.27178
Turkey	1.27808

The results reveal some unexpected differences. China and South Africa both employed the VSOP code system although different generations of the code. In the Chinese calculations, some impurities in the graphite material have been modelled making use of the material ‘Poison in C’ or material 150 in the VSOP94 GAM library. This was initially in the draft specification but removed (since it a VSOP specific definition) and thus not included by the others. This may explain at least part of the discrepancy. Other differences are that the South African VSOP model divides the core into 110 spectral zones. The Chinese VSOP model divides the core into five spectral zones. The higher resolution of the South African model may capture leakage effects more thoroughly than the Chinese model. One would expect better agreement between the South African diffusion model and a transport model such as the one used by the Turkish participants, and indeed this is the case.

The Korean result differs quite a bit from the others. A slightly different problem was defined that assumed for simplicity that the core and reflector regions are homogeneous. The work was reported to demonstrate the philosophy to be used. The one dimensional transport model employed by the Korean team is unique to this exercise and can in principle capture radial leakage effects. However, the homogeneous fuel assumed and the use of the slab geometry combined with the use of only four spectral zones in the core may account for some of the differences observed.

7.3.1.2. F-2: First core loading

Another fresh core was specified, but this time with a mixture of startup fuel pebbles (5.768% enriched) and graphite pebbles. The results were provided by China, South Africa, and Turkey. As explained above, the results from China include the absorption effects of the impurities (modelled with material 150) and other modelling differences (spectrum zones) compared to the South African VSOP results. The differences between the South African and Turkish results are of the same order of magnitude difference as before (for Case F1), but this time the MCNP (Turkey) results are the lower of the two sets. The Turkey result, at 900 K, seems incorrect (very small temperature effect).

TABLE 7.9. COMPUTED CORE MULTIPLICATION FACTORS FOR F-2 BENCHMARK

Participant	Eigenvalue		
	300K	600K	900K
China	1.14033	1.10059	1.06697
South Africa	1.16538	1.12424	1.08875
Turkey	1.15329	1.11724	1.10873

7.3.1.3. E-1: Equilibrium core profile with given number densities

In this case, sets of axially varying number densities that mimic an equilibrium core were provided. In part (i), a simple neutronic calculation was requested. In part (ii), variations that involved thermohydraulic calculations with and without feedback were specified. The eigenvalue, two-group flux and power profiles were generated by participants. Only South Africa provided results, so no comparison is provided here.

7.3.1.4. E-2: Equilibrium cycle calculation

The benchmark exercise involves the calculation of the equilibrium cycle. In this exercise, participants with depletion capability were requested to perform an equilibrium cycle calculation with thermohydraulic feedback and utilizing their own cross-section generation models. Material properties of the fresh fuel and thermohydraulic boundary conditions were specified, but each participant adjusted the pebble flow rate (and thus residence time) to obtain a critical core. Once equilibrium is reached, no significant changes can be observed in the properties of the core. For example, the k-eff, power profile, temperatures and isotopic concentration distribution no longer change.

South Africa and the United Kingdom provided results for comparison. The summarized result is shown in Table 7.10. Differences in the order of a few percent appear in these whole-core neutronic parameters and thus excellent agreement appears to have been achieved. In the United Kingdom analysis, WIMSD9, 2-D collision probabilities and the Behrens treatment of streaming are used to capture heterogeneity and other transport phenomena. Compare this with the RSA approach, which uses GAM-THERMOS, Gerwin and Scherer correction in void areas, and the Method of Equivalent Cross-sections for obtaining equivalent diffusion parameters. In other ways, however, the approaches are similar, such as in the use of a buckling term edited from the diffusion calculation to account for leakage in the spectrum calculations. The issue of resonance treatment was not discussed by the participants, although it may play a significant role in fuel performance and isotopics.

There are differences in the thermal fluid profiles that bear further examination. Although the core power, inlet temperature, and helium flow rates are fixed by the benchmark, the United Kingdom analysis predicts an average coolant temperature of 805°C, 317°C above the inlet temperature. The RSA (VSOP99-4/THERMIX) value of 794°C is 306°C above the inlet temperature, a difference of only 11°C, or about 4%. The average moderator and fuel temperatures only differ by 2°C and 12°C respectively, showing excellent agreement.

TABLE 7.10. CHARACTERISTICS OF THE PBMR-400 E-2 BENCHMARK

Parameter	South Africa	United Kingdom
Pebble Flow Rate (d^{-1})	2802	2824 (6.88 cm/day)
k_{eff}	0.99998	0.99995
Mean Discharge Burnup ($\text{MWD}/\text{kg}_{\text{hm}}$)	96.1	94.4
In-core downscattering	45.9	51.5
Leakage from fissile region (%)		
$> 1.86 \text{ eV}$	32.2	32.2
$< 1.86 \text{ eV}$	-17.7	-17.0
Total	14.5	15.2
Mean fast/thermal ratio		
Core	1.32	1.42
Reflector	0.135	0.153
Thermohydraulic Parameters		
Inlet Temperature ($^{\circ}\text{C}$)	488	488
Average Fuel Temperature ($^{\circ}\text{C}$)	876	888
Average Moderator Temperature ($^{\circ}\text{C}$)	858	860
Average Coolant Temperature ($^{\circ}\text{C}$)	794	805
Maximum Fuel Temperature ($^{\circ}\text{C}$)	1118	1205
Core Pressure Drop (Pa)	1.90	1.94

The peak-to-average (Kelvin) fuel temperature value reported by the United Kingdom is 1.27 compared to 1.21 for the RSA. The peak temperature reported by the United Kingdom is thus 87°C higher than that computed by VSOP99-4. Interestingly, the average moderator and fuel temperatures compare rather well. One possible reason is that the sub-grid models for computing fuel temperature are different, and another that the batch temperatures (for the different passes) are calculated differently. However, an important contributor is the difference in the calculated detailed power distribution. The detailed comparison between the calculated power densities is shown in Fig. 7.8. The axial power density profile is shown for the five radial regions (each 17 cm in radial width). The VSOP99-4/THERMIX results (RSA) show a significant lower peak of $10.6 \text{ MW}/\text{m}^3$ compared to the WIMS/WIMSTER (United Kingdom) calculated peak power density of $11.5 \text{ MW}/\text{m}^3$. The higher peaking will at least partially explain the higher maximum fuel temperatures.

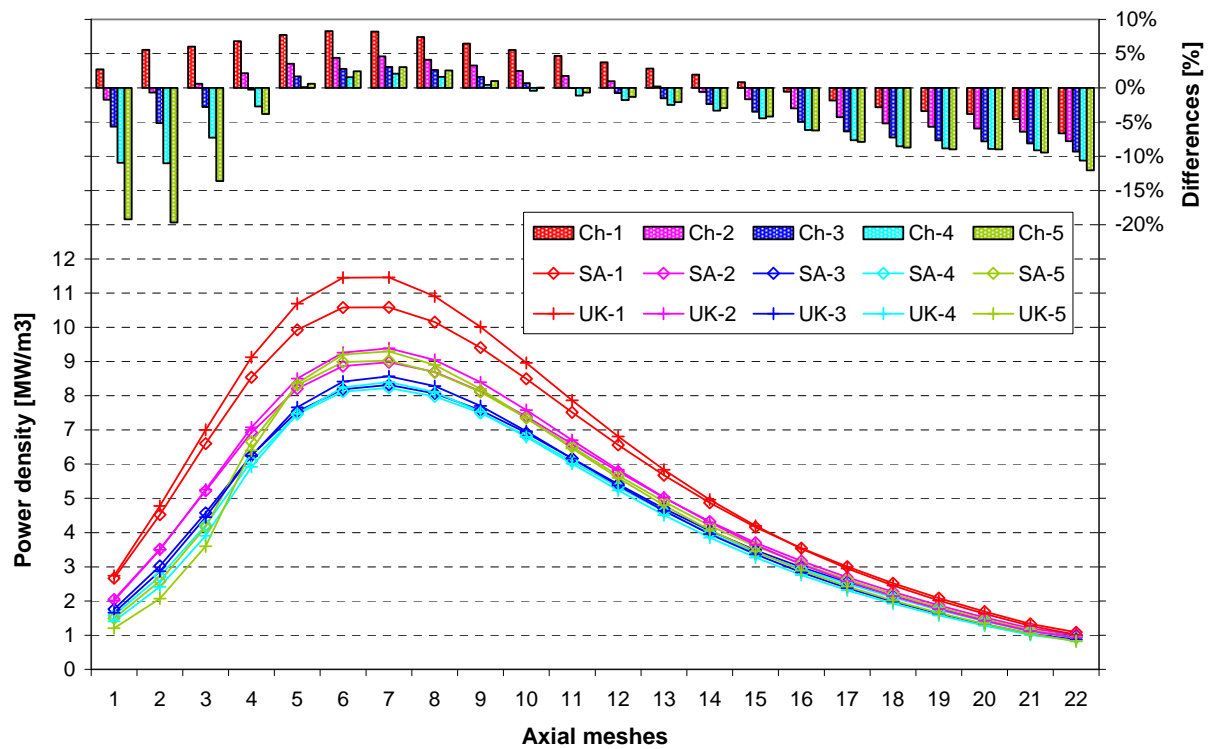


FIG. 7.8. Axial power density profiles and % differences (for the five radial positions).

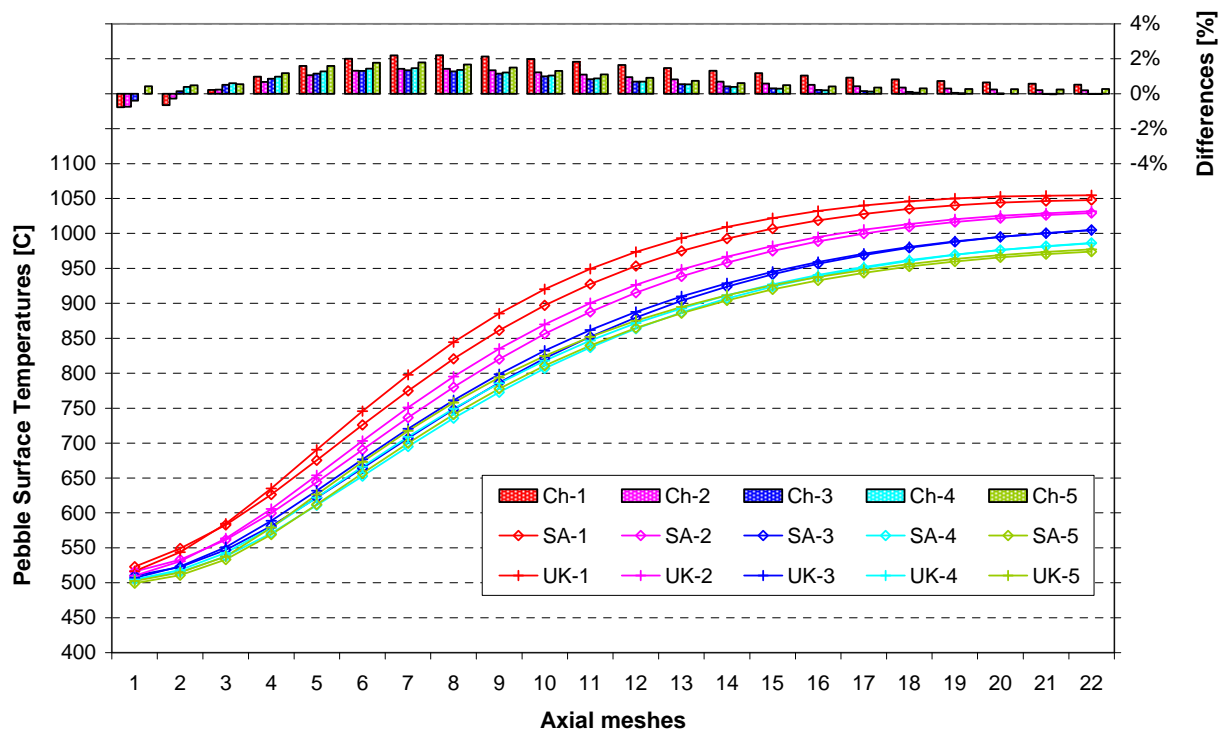


FIG. 7.9. Axial pebble surface temperatures [C] and % differences (for the five radial positions).

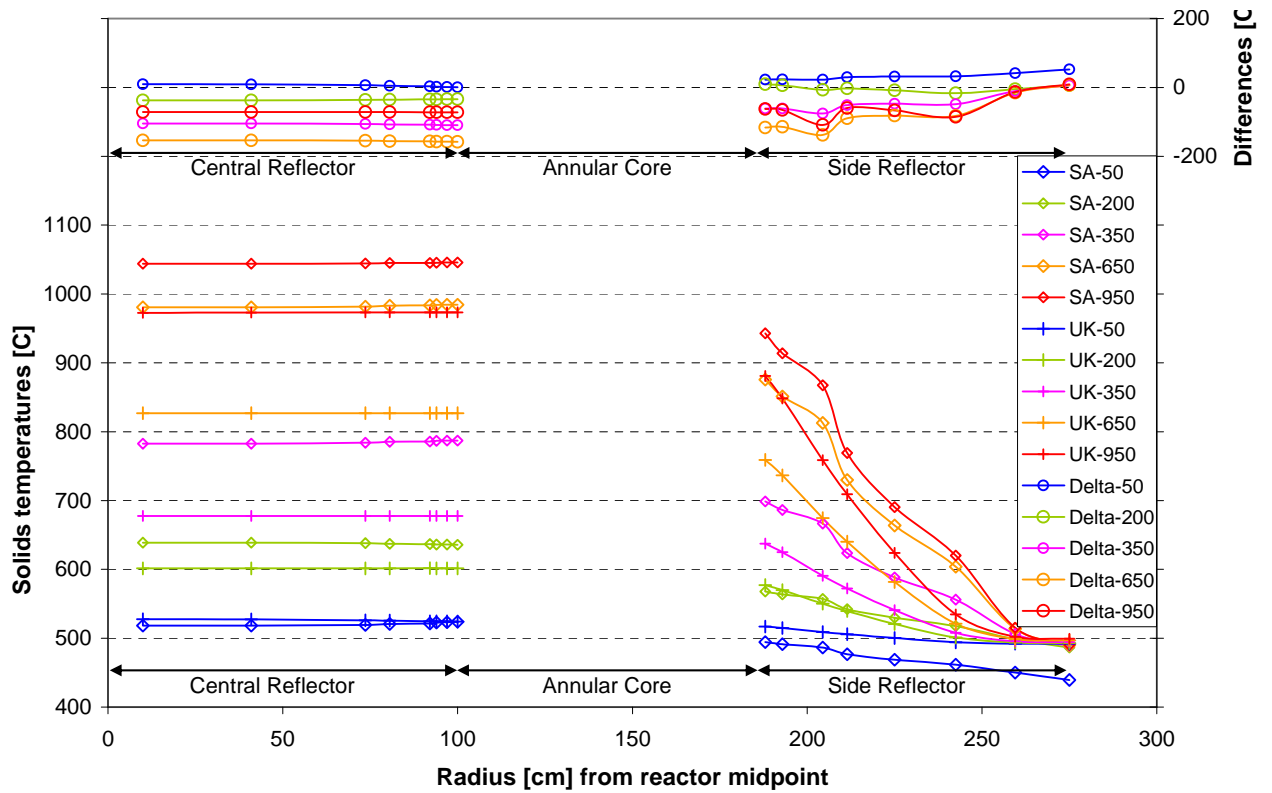


FIG. 7.10. Axial pebble surface temperatures [C] and % differences (for the five radial positions).

By studying the power density differences in more detail, one notes that the peak power density differences are only observed in the first channel next to the central reflector. For the outer channel (Ch-5) next to the side reflector, the power density in the upper core is significantly underpredicted by WIMS compared to VSOP99-4. At least in these upper core regions the proximity to the central reflector (Ch-1) and outer reflector with the control rods inserted (Ch-5) seems to play an important role. The different number of energy groups in the models (11 in WIMS and 4 in VSOP99-4) or the treatment of the environmental effects (leakages) in the spectrum calculations are two possible candidates that could explain these differences.

Figure 7.9 shows the average pebble surface temperatures profile (top to bottom) in the same five channels. The agreement is excellent with differences of less than 25°C (or 2.2% in Kelvin). Similarly, the coolant temperatures in the core also differ by a maximum of 2.6%. However, the picture changes when the reflector temperatures are compared.

The results in Fig. 7.10 are shown as radial cuts made for different axial heights along the active core height. The temperatures in the core are not shown. The central column temperature in WIMSTER is up to 200°C cooler in the lower core than calculated in THERMIX, while the temperatures close to the top reflector are nearly identical. A similar trend is seen for the outer reflector, with large temperature differences close to the core. The source of the differences is not yet known, but the most obvious candidate is the modelling of the heat transfer from the pebble bed to the graphite structures. It is known to play an important role (especially in the transient cases) and is not so straightforward to model. The temperature differences in the reflector will also influence the neutronics reflection and therefore the spectrum and leakage calculations.

Despite the large temperature differences in the reflector regions, most of the other data presented here compares well. The difference in the maximum fuel temperature needs to be investigated, as well as the neutron spectra ratios as reported in Table 7.10. The detailed flux comparisons were not made.

7.3.1.5. T-1: Steady state thermal balance and fluid dynamics

A power profile was provided as an input to a steady state thermohydraulic calculation. Participants were to generate maps for the solid structure and coolant temperatures and pressures in the PBMR-400 simplified model.

Some comparative results are shown in Table 7.11. The results were provided by South Africa, Turkey and the United Kingdom.

TABLE 7.11. LUMPED THERMOHYDRAULIC CHARACTERISTICS OF THE PBMR 400 T-1 STEADY STATE MODEL

Parameter	South Africa	Turkey	United Kingdom PHOENICS	United kingdom WIMSTER
Pebble bed pressure drop (MPa)	0.188	0.237	0.188	0.183
Average helium temperature (°C)	745	681	756	753
Average pebble surface temperature (°C)	772	741	779	776
Average moderator temperature (°C)	797		803	799
Average fuel temperature (°C)	809		n/a	823
Maximum fuel temperature (°C)	1167	>1027	n/a	1157

Interestingly, better agreement exists between the RSA and the United Kingdom thermal fluid results in the T-1 exercise than in the previous (E-2). Assuming that the thermohydraulic models are similar, this suggests that there is feedback from the neutronics calculation in E-2 that can cause a significant thermohydraulic response. The maximum fuel temperature of about 1170°C is squarely in between the two values predicted by South Africa and the United Kingdom in the previous exercise. This confirms that the differences in the calculated detailed power profile are the reason for the large maximum fuel temperature differences in Case E-2.

The average helium temperature is still noticeably higher in the United Kingdom analysis. Given the differences between the lumped-parameter VSOP99-4/THERMIX approach and the CFD approach used in WIMSTER, the actual definitions of average coolant temperature may differ and would be worth further investigation. It is also not clear if a consistent edit was performed since the codes could calculate the average of all volumes if the helium coolant in the reactor was compared to the average in the core volume only.

7.3.1.6. D-1: Depressurized loss of forced cooling

The D-1 exercise is a simulation of a DLOFC. The initial conditions are those generated in exercise E-1 and a decay heat correlation is provided. Only South Africa provided results that use the benchmark specification in its entirety. The USA simulation generated using GRSAC differed from the benchmark in some important respects and is provided in Table 7.12 only for discussion and consideration.

The predicted maximum fuel temperatures are within 5°C, but many other differences can be seen. The GRSAC simulation employed the temperature- and fluence-dependent Zehner-Schlünder/Robold

TABLE 7.12. IMPORTANT RESULTS OF THE DLOFC SIMULATION

Parameter	South Africa (TINTE)	United States * (GRSAC)
Time after Shutdown of Peak Fuel Temperature (hr)	38.4	54
Peak Fuel Temperature at time of Peak Fuel Temperature (°C)	1592	1587

correlation in which the conductivity of graphite is also a function of temperature. Other differences in the models and data contribute to the difference in the DLOFC result, the most dramatic of which is the time to peak (38 h vs 54 h). Other results would have to be generated to derive any further conclusions from these numbers.

7.3.2. ‘Pebble Box’ benchmark — Comparison of results

The complexity of the PBMR-400 core model and the variety of analysis methods employed poses a problem for a comparative benchmark study in that it is difficult to attribute differences in results to one or two factors. For this reason, the ‘pebble box’ benchmark was formulated as a simple way to compare various treatments of neutronics phenomena. The six cases described in Section 4.3.1 are designed to investigate the treatments and effects of leakage and heterogeneity.

7.3.2.1. Case 1: Infinite homogeneously mixed cube

In this case, the model consists of a homogeneous mixture of fuel and moderator with an unreflected cubicle shape. The participants generated spectral indices such as core multiplication factor and epithermal-to-thermal flux ratios. Bar charts of the results are shown in Fig. 7.11 for comparative purposes. The legends indicate the fuel and moderator temperatures for each case respectively.

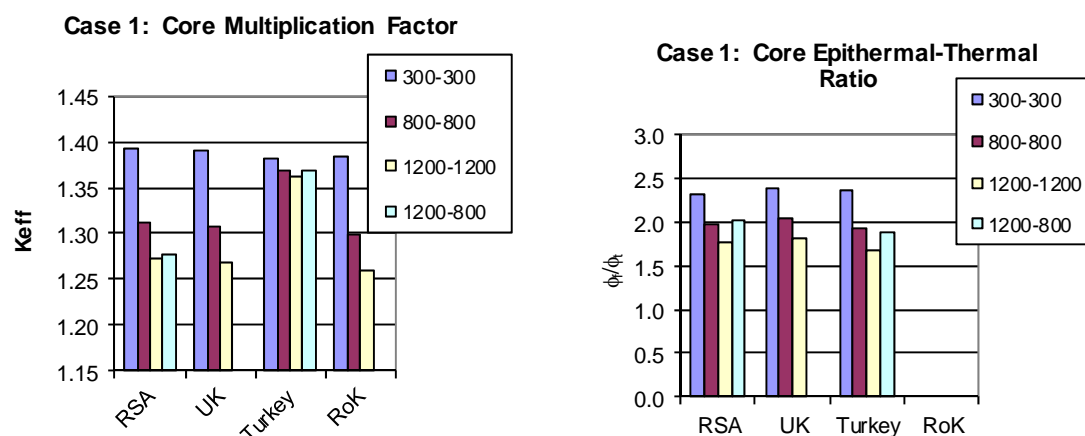


FIG. 7.11. Comparison of core eigenvalue and flux ratios for an infinite homogeneous cube.

The British, Korean and South African results all exhibit the same trends and the values differ by no more than a few percent in most cases. These differences can be attributed to libraries and neutron transport techniques. For example, South Africa used VSOP while others used MCNP and its continuous energy cross-sections derived from ENDF/B-VI data (Republic of Korea and Turkey). The United Kingdom used WIMS9 that includes the JEF 2.2 cross-section libraries, one and two dimensional collision probabilities modules for treating heterogeneity and the SNAP diffusion code for the flux profiles.

The Turkish eigenvalue results reveal a very weak dependence upon temperature not exhibited by the other participants’ results. This would indicate a modelling error or an incorrect reading of the cross-section libraries. The flux ratios agree better with the other results, but in this case the temperature difference is a little stronger than observed elsewhere.

7.3.2.2. Case 2: Infinite cube of pebbles (single heterogeneity)

In this case, pebble level heterogeneity is introduced. The pebbles themselves, however, are homogeneous mixtures of fuel and moderator. The core multiplication factor and epithermal-to-thermal flux ratios are shown in Fig.7.12.

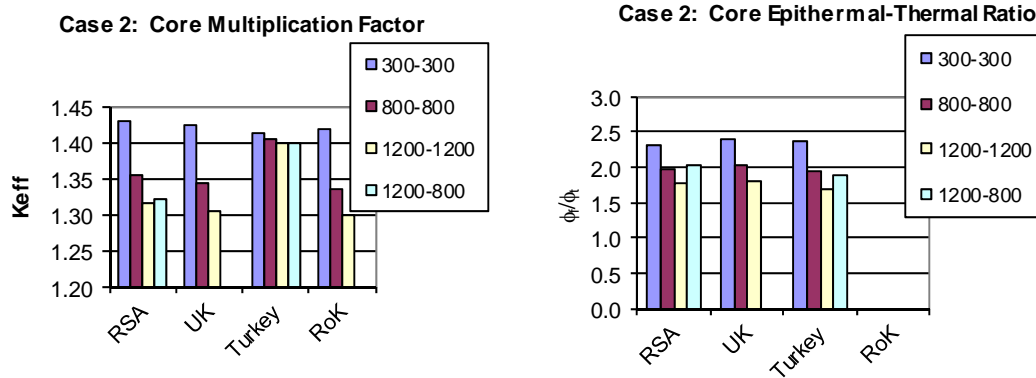


FIG. 7.12. Comparison of core eigenvalue and flux ratios for an infinite cube of homogeneous pebbles.

Once again the Turkish results reveal a low dependence upon temperature that cannot be explained by differences in codes or nuclear data. The Koreans solved the problems using both Monte Carlo and diffusion techniques, but only the Monte Carlo results are displayed in the plots. Their eigenvalues reveal a similar negative dependence of the eigenvalue and downscattering upon temperature. The three sets of results differ by no more than a few percent. Although it is not unexpected that the best agreement exists between the two diffusion codes, the MCNP result from ROK is also close.

7.3.2.3. Case 3: Infinite cube of pebbles containing fuel particles (double heterogeneity)

The core multiplication factor and epithermal-to-thermal flux ratios for the infinite system of pebbles containing fuel particles (double-heterogeneity) are shown in Fig. 7.13. These results largely confirm the trends and differences seen in the previous charts. The overall magnitude of the eigenvalues is higher due, at least in part, to self-shielding within the fuel lumps. The increase in eigenvalue (for example: 1.43–1.52 in the South African data) appears rather large to be attributed only to self-shielding in the particles. The flux ratios also drop in going from Case 2 to Case 3, indicating a relative decrease in the downscatter rate compared to the absorption rate. Presumably, self-shielding in the particles that contributes to the higher eigenvalue also contributes to a higher resonance escape probability.

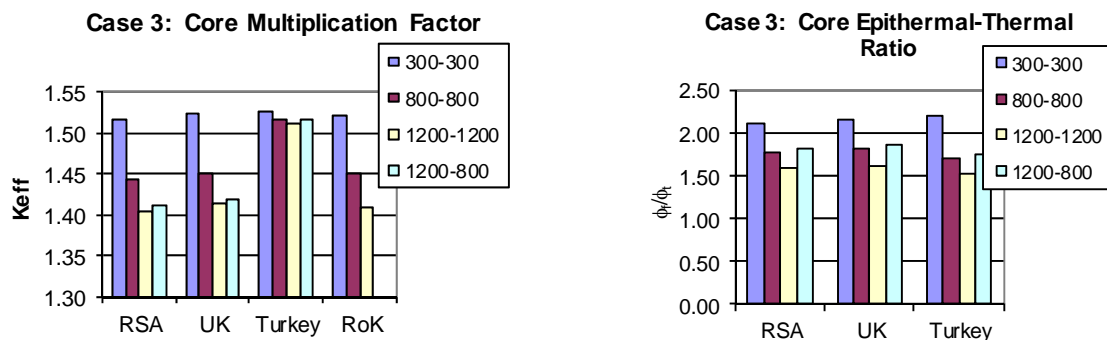


FIG. 7.13. Comparison of core eigenvalue and flux ratios for an infinite cube of heterogeneous pebbles.

7.3.2.4. Case 4: Reflected homogenous cube

The moderating and reflecting effects of a moderator are indicated in Cases 4, 5 and 6. These cases correspond to the homogeneous, single-heterogeneous and double-heterogeneous cases respectively. Furthermore, the bar charts of the leakage rate from the core (total % of fission neutrons born that leak into the reflector) are presented. The core multiplication factor and epithermal-to-thermal flux ratios are shown in Fig. 7.14, while the leakage from the core is shown in Fig. 7.15.

The Turkish results reveal a more plausible dependence upon temperature. Except for the 1200 K case, the core multiplication factors agree more favourably with those of the other participants. The flux ratios computed by Turkey are rather high compared to the RSA and the United Kingdom results, especially given the similarity in techniques.

The leakage rates differ by a few percent. Oddly, the higher (compared to the RSA value) United Kingdom leakage rate at 300 K does not correspond well with the slightly higher eigenvalue. At higher temperatures, the higher United Kingdom leakage rate is reflected in a lower eigenvalue as compared to the RSA result. The higher Turkish leakage result does not seem to correlate to the eigenvalue data, at least relative to the other participants.

7.3.2.5. Case 5: Reflected cube of pebbles (single heterogeneity)

The core multiplication factor and epithermal-to-thermal flux ratios for the reflected cube of pebbles (single heterogeneity) are shown in Fig. 7.16, while the leakage from the core is shown in Fig. 7.17.

These results are consistent with those of the previous cases. In particular, however, the flux ratios reported by Turkey are considerably different from the other participants, much more so than the differences in their eigenvalues. The Turkish model does predict the lowest core leakage which corresponds to the higher eigenvalues observed in Fig. 7.16.

7.3.2.6. Case 6: Reflected cube of pebbles containing fuel particles (double-heterogeneity)

The core multiplication factor and epithermal-to-thermal flux ratios for the reflected cube of pebbles (double heterogeneity) are shown in Fig. 7.18, while the leakage from the core is shown in Fig. 7.19.

The trends observed in the previous cases are continued here. Heterogeneity does not seem to be a significant cause of differences in the results of the participants. The basic modelling of scattering and resonances is more likely the cause. Particle heterogeneity does seem to accentuate the differences a bit, however. The spread in leakage rates shown in Fig. 7.19 is a bit higher than in Fig. 7.17.

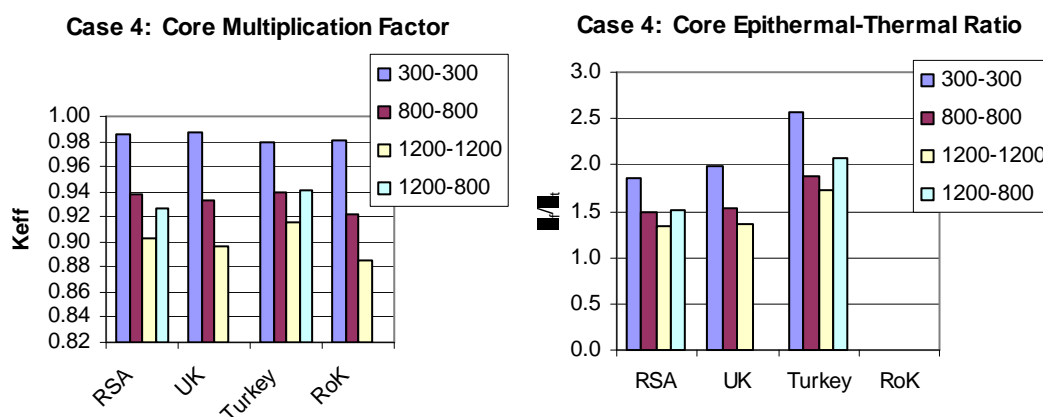


FIG. 7.14. Comparison of core eigenvalue and flux ratios for a reflected homogeneous cube.

Case 4: %Leakage from Core

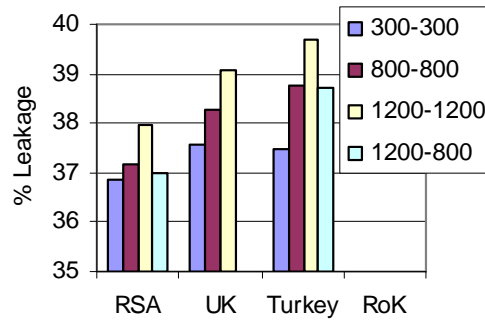
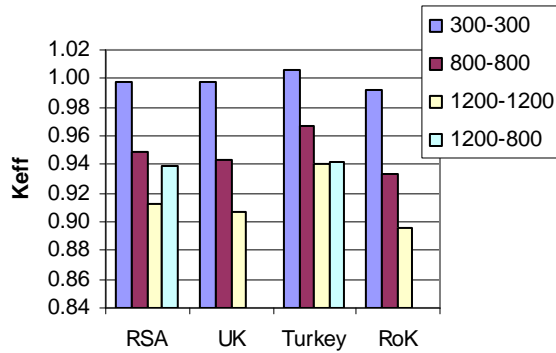


FIG. 7.15. Comparison of total leakage from a reflected homogeneous cube.

Case 5: Core Multiplication Factor



Case 5: Core Epithermal-Thermal Ratio

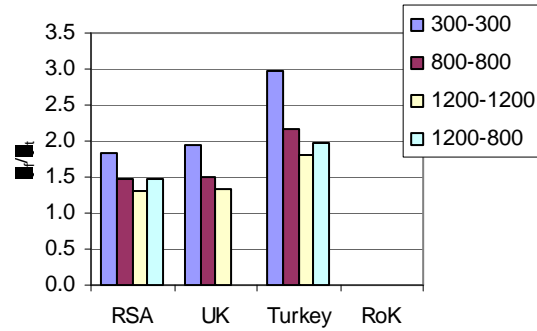


FIG. 7.16. Comparison of core eigenvalue and flux ratios for a reflected cube of homogeneous pebbles.

Case 5: %Leakage from Core

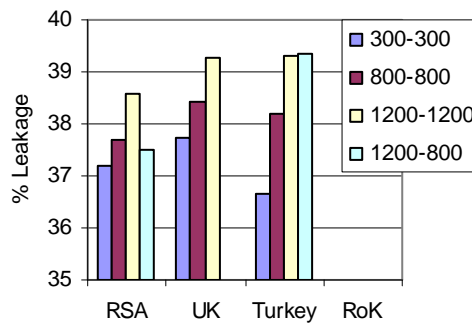


FIG. 7.17. Comparison of total leakage from a reflected cube of homogeneous pebbles.

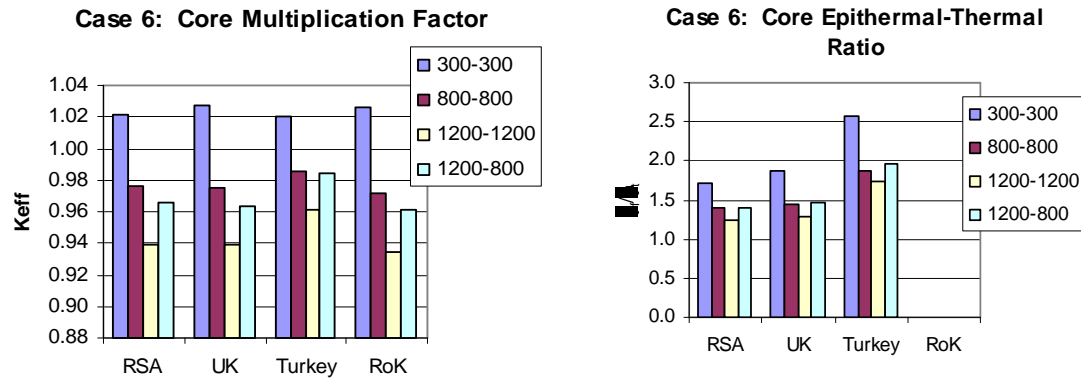


FIG. 7.18. Comparison of core eigenvalue and flux ratios for a reflected cube of heterogeneous pebbles.

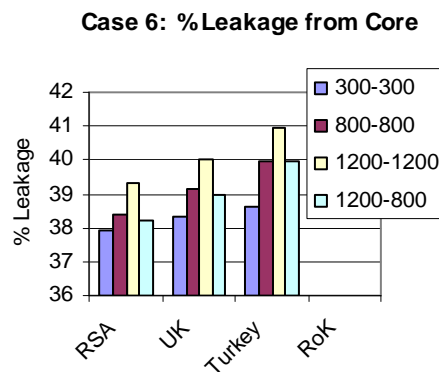


FIG. 7.19. Comparison of total leakage from a reflected cube of heterogeneous pebbles.

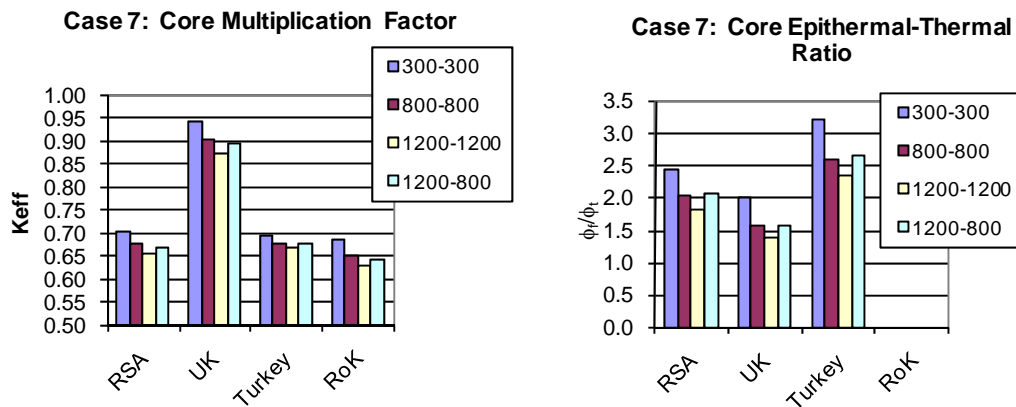


FIG. 7.20. Comparison of core eigenvalue and flux ratios for a reflected cube of heterogeneous pebbles.

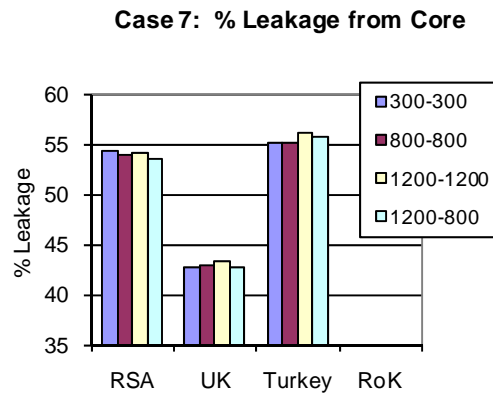


FIG. 7.21. Comparison of total leakage from a reflected cube of heterogeneous pebbles.

7.3.2.7. Case variations and additional comments

This case is the same as Case 6 except that boron is added to the graphite in the reflectors to mask the effect of the difference in carbon absorption that is known to exist between the VSOP and MCNP library (for example). The core multiplication factor and epithermal-to-thermal flux ratios for a reflected cube of heterogeneous pebbles are shown in Fig. 7.20 while the leakage from the core is shown in Fig. 7.21.

The added boron has a significant and similar effect on the Korean, South African and Turkish results. Oddly, the United Kingdom results do not exhibit the same decrease in the core eigenvalue or leakage from the core. According to the benchmark specification, boron is only added to the reflector graphite. The lower leakage into the graphite indicated by the United Kingdom result means a lower net loss of neutrons to absorption in the reflector. This is consistent with the higher eigenvalue predicted by the United Kingdom, but the reason for this phenomenon is obvious. The United Kingdom however, does use a diffusion code to generate the flux profiles and diffusion theory is understood to be less accurate deep within a reflector. The diffusion-based result provided by the Republic of Korea (not shown here, see Section 4.3.2.4) is consistent with this result. The diffusion-based eigenvalue generated by the Republic of Korea is 1536 pcm higher than their corresponding MCNP value.

For neutronically large systems like the PBMR-400, this possible deficiency in diffusion theory is not as significant as seen in a 1 m³ ‘pebble box’. The result is informative, however, and worth further investigation.

7.3.3. Comments and conclusions on the PBMR-400 and ‘Pebble Box’ benchmark test cases

It is important to add some general comments on the history of the two code-to-code comparison test cases discussed in this section. An initial benchmark definition was made based on the PBMR-400 that required the analysis of the first core loading (startup) followed by an equilibrium core. Although an interesting and challenging problem, the original definition was too general and very limited participation took place at that stage. In the first half of 2006, a significant update of the test cases definition was made, which included some simplifications that made wider participation possible.

The updated definition is well defined and also includes a template to report results. However, this new formalization happened too late since the further extension of the CRP-5 programme was not approved and only one RCM took place after the specification was finalized. This resulted in limited participation and only a few cases were calculated by more than two participants. Although only a code-to-code exercise, it still was a valuable exercise (especially for the South African/ United Kingdom detailed comparisons).

The PBMR ‘pebble box’ is a challenging and well-defined problem. It suffered the same fate as the PBMR-400 problems since it was introduced later and the evaluation of results did not mature enough during the CRP-5 duration. The results were therefore not discussed in detail at the last RCM and the current differences cannot be explained. To develop the real potential of this problem, more work is

required and the current status must be seen as only a good start towards this final potential. The applicability of the diffusion solutions applied to these very small problems should, for example, first be confirmed.

7.4. PBMM COLLATION OF RESULTS

This section includes a summary of the Member State analyses and the experimental results for the PBMM benchmarks. Analyses by individual CSIs related to the PBMM benchmark problem calculations included a wide variety of codes, models and methods. These are described in detail in Chapter 5 by each Member State.

Chapter 5 of this CRP made possible the comparison of the results from different simulation codes to the same problem (code-to-code comparisons) for the PBMM. It also made it possible to compare simulation results to experimental results (code-to-plant). The measured values from the experimental runs were used as inputs to the simulation codes. Initially, reliable experimental results were not available and it was necessary to estimate the boundary values for the steady state and transient benchmark problems. After some time, it became clear that it was not possible to run on the plant (and simulate) some of the benchmark problems with the boundary values envisaged initially. Therefore, the boundary values for the benchmark problems were changed and some benchmark problems were dropped.

It also became clear from the experimental results that significant heat transfer takes place from the turbines to the shell of the pressure vessel and also from the pressure vessel to the ambient. In order to improve the code-to-plant comparison, it was necessary to include this additional heat transfer paths in the simulation code (the additional heat transfer paths are described in Chapter 5). Unfortunately, it was not possible for all CSIs to change their simulation codes and/or redo their analyses for the benchmark problems with the final boundary values. Therefore, analyses by individual CSIs related to the PBMM benchmark problem calculations include a variety of models and boundary values.

The following comparisons can be made:

- Steady state code-to-plant comparison with the additional heat transfer paths included in the simulation code. South Africa was the only Member State to do this. The additional heat transfer paths and the results of the code-to-plant comparison are therefore described in Chapter 5.
- Steady state code-to-code comparison of the simulation codes without the additional heat transfer paths. The fact that the additional heat transfer paths are not included in the simulation code does not make the comparison less valuable at all. The additional heat transfer paths do not add significantly to the complexity of the system.
- Transient code-to-plant comparison without the additional heat transfer paths. Although the codes are without the additional heat transfer paths, the dynamics of the heat transfer are much slower than the dynamics of the system. The ability to simulate the deviation from steady state is demonstrated.
- Transient code-to-code comparison of the simulation codes without the additional heat transfer paths.

7.4.1. Comparison of results

A comparison between the results from the different Member States using the same boundary values is now provided.

7.4.1.1. Steady state benchmark: code-to-code

The simulated pressures throughout the cycle are compared in Table 7.13. This is for the 95 kPa case. The average value for all three codes for each position is given first, then the result for FLOWNEX, then the deviation of the FLOWNEX value from the average value, then the value for CATHARE, the deviation of the CATHARE value from the average, etc.

The FLOWNEX and CATHARE codes compare particularly well with the difference between average deviations of less than a percentage point. The MARS-GCR code is also very close, with an average deviation from the mean of less than five percentage points. For the 115 kPa case, the results are similar, with the difference between FLOWNEX and CATHARE being less than one percent. The Republic of Korea did not participate in the 115 kPa simulation.

The simulated temperatures throughout the cycle for the 95 kPa case are compared in Table 7.14. Once again, the average value for all three codes for the each position is given first, then the result for FLOWNEX, then the deviation of the FLOWNEX value from the average value, then the value for CATHARE, the deviation of the CATHARE value from the average, etc. The static temperatures are reported in this table (the total or dynamic temperatures are shown in Chapter 5).

The agreement between the codes is good. Due to the fact the temperatures are reported in Kelvin, the percentage deviation at high temperatures is reduced. Reporting the results in Celsius again amplifies the deviation at the cold end of the cycle. In FLOWNEX and CATHARE, the RXHP inlet temperature is fixed on the experimental value because of the heat transfer to the gas from the turbines. Due to the fact that there are positive and negative deviations, an average would not give a good indication of the agreement between the codes. The averages of the absolute value of the deviations are shown in Table 7.15. The agreement between the codes is good. The Republic of Korea did not perform the 115 kPa run.

TABLE 7.13. PRESSURE COMPARISON [KPA(A)] AND DEVIATION FROM AVERAGE VALUE FOR 95 KPA LPC SUCTION PRESSURE

	AVG	FNX	%	CTE	%	M-G	%
PC inlet	94.8	96.0	1.2	96.1	1.3	92.4	-2.6
PC outlet	94.3	95.5	1.3	95.7	1.5	91.7	-2.8
LPC inlet	92.7	94.0	1.4	93.7	1.0	90.5	-2.4
LPC outlet	171.9	178.0	3.6	174.2	1.4	163.4	-4.9
IC inlet	173.0	176.5	2.0	179.0	3.4	163.6	-5.5
IC outlet	172.7	176.2	2.0	178.7	3.5	163.3	-5.5
HPC inlet	171.9	176.0	2.4	177.3	3.2	162.3	-5.6
HPC outlet	314.1	322.1	2.6	325.4	3.6	294.8	-6.1
RXHP inlet	314.6	321.2	2.1	327.7	4.2	294.9	-6.3
RXHP outlet	313.9	319.4	1.7	327.6	4.4	294.8	-6.1
Heater outlet	313.6	318.9	1.7	327.3	4.4	294.6	-6.1
HPT inlet	311.0	316.2	1.7	322.2	3.6	294.6	-5.3
HPT outlet	206.7	210.8	2.0	217.3	5.1	191.9	-7.2
LPT inlet	202.9	206.7	1.9	210.4	3.7	191.7	-5.5
LPT outlet	128.1	131.9	3.0	132.7	3.6	119.6	-6.6
PT inlet	123.4	125.9	2.0	125.0	1.3	119.3	-3.3
PT outlet	96.6	97.6	1.0	97.9	1.3	94.4	-2.3
RXLP inlet	96.0	96.9	0.9	97.4	1.4	93.8	-2.3
RXLP outlet	95.3	96.4	1.1	96.5	1.2	93.1	-2.3
Average deviation			1.9		2.8		-4.7

Note: FNX: FLOWNEX, South Africa; CTE: CATHARE, France; M-G: MARS-GCR, Republic of Korea.

TABLE 7.14. TEMPERATURE COMPARISON [K] AND DEVIATION FROM AVERAGE VALUE FOR 95 KPa LPC SUCTION PRESSURE

	AVG	FNX	%	CTE(K)	%	M-G	%
PC inlet	439.3	452.7	3.1	453.2	3.2	412.2	-6.2
PC outlet	291.5	290.4	-0.4	291.8	0.1	292.4	0.3
LPC inlet	291.2	290.4	-0.3	290.7	-0.2	292.5	0.4
LPC outlet	364.4	366.1	0.5	365.1	0.2	362.1	-0.6
IC inlet	365.5	366.1	0.2	368.3	0.8	362.2	-0.9
IC outlet	290.5	289.6	-0.3	290.4	0.0	291.6	0.4
HPC inlet	289.7	289.6	0.0	288.1	-0.6	291.4	0.6
HPC outlet	361.5	360.9	-0.2	359.8	-0.5	363.8	0.6
RXHP inlet	392.3	403.5	2.9	403.5	2.9	370	-5.7
RXHP outlet	682.1	697.7	2.3	676	-0.9	672.7	-1.4
Heater outlet	920.1	920.9	0.1	918	-0.2	921.5	0.2
HPT inlet	918	918.6	0.1	913.8	-0.5	921.5	0.4
HPT outlet	846.4	855.8	1.1	845.6	-0.1	837.9	-1.0
LPT inlet	842.7	851.1	1.0	839.2	-0.4	837.9	-0.6
LPT outlet	769.4	786	2.2	766.1	-0.4	756.1	-1.7
PT inlet	762.2	775.7	1.8	754.7	-1.0	756.3	-0.8
PT outlet	727.7	744.2	2.3	724	-0.5	714.8	-1.8
RXLP inlet	729.1	744.2	2.1	725.7	-0.5	717.3	-1.6
RXLP outlet	439.1	452.7	3.1	453.2	3.2	411.4	-6.3

Note: FNX: FLOWNEX, South Africa; CTE: CATHARE, France; M-G: MARS-GCR, Republic of Korea.

TABLE 7.15. AVERAGE OF THE ABSOLUTE VALUE OF THE DEVIATIONS FROM THE MEAN TEMPERATURE

	Average deviation	
	95 kPa	115 kPa
FLOWNEX	1.2	0.5
CATHARE	0.8	0.5
MARS-GCR	1.7	

TABLE 7.16. COMPARISON BETWEEN OTHER VARIABLES
WITH THE DEVIATION FROM THE AVERAGE

	AVG	FNX	%	CTE	%	M-G	%
	kg/s	kg/s		kg/s		kg/s	
Primary mass flow	0.4836	0.4764	1.5	0.5084	-5.1	0.4659	3.7
Secondary mass flow	0.6563	0.6872	-4.7	0.7194	-9.6	0.5624	14.3
		rpm		rpm		rpm	
HPT speed	67253	65764	2.2	71037	-5.6	64958.14	3.4
LPT speed	67736	66942	1.2	71766	-6.0	64498.81	4.8
PT speed	34026	35616	-4.7	36838	-8.3	29623.83	12.9

Note: FNX: FLOWNEX, South Africa; CTE: CATHARE, France; M-G: MARS-GCR, Republic of Korea.

Table 7.16 shows the correspondence between the measured and simulated turbine speeds and mass flow rates. The correspondence is similar for the 115 kPa case.

The agreement between CATHARE and FLOWNEX is better than the agreement of MARS-GCR with the average. For the 115 kPa case, the average of the absolute values of the deviations of FLOWNEX and CATHARE differs by 6.2 percentage points.

7.4.1.2. Transient test: code-to-plant and code-to-code comparisons

The transient test is described in Chapter 5. Gas was injected just upstream of the LPC for 63 s. The time responses at three positions in the cycle are shown. The results of the two codes as well as the measured response are shown on a single graph.

LPC Suction pressure

The time response of the LPC suction pressure as well as the simulated values are shown in Fig. 7.22.

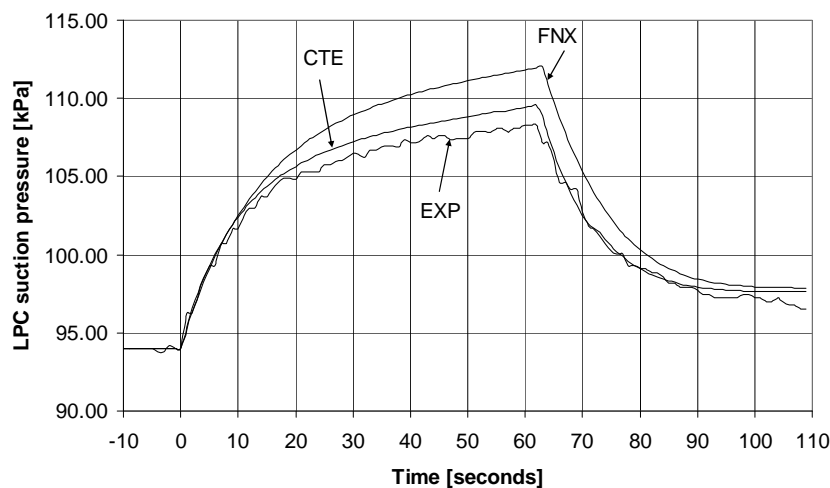


FIG. 7.22. Change in LPC suction pressure.

Both codes follow the measured time response reasonably well (CATHARE better than FLOWNEX). Both settle the measured value after 100 s very closely. The change is analysed in Table 7.17.

TABLE 7.17. CHANGE IN SUCTION PRESSURE

	Δ Pressue [kPa]	% of EXP
EXP	14.29	100.0
FNX	17.96	125.7
CTE	15.52	108.6

Figure 7.23 shows the measured and simulated speeds of the LPC. In order to make a comparison of the relative changes easier, the simulated values are adjusted to give the same initial speed as the measured value. It is clear from Table 7.16 that the simulated steady state values (at the beginning of the injection) are lower than the measured value and therefore a constant is added to all the values to make the initial values the same.

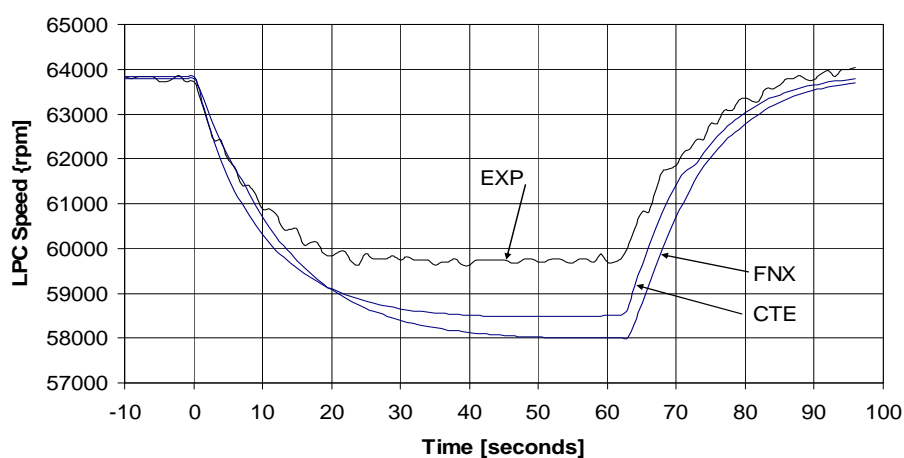


FIG. 7.23. Change in LPC speed.

The simulated values again agree reasonably well with the experimental value. The results of the other turbocompressors are shown in Table 7.18.

TABLE 7.18. DIFFERENCE IN TURBINE SPEEDS AT THE END OF INJECTION

	Δ Simulated / Δ Measured [%]	
	FNX	CTE
HP Turbine	134	107
LP Turbine	147	135
Power Turbine	193	142

The outlet pressure as function of time is shown in Fig. 7.24. The simulated values were adjusted to give the same initial value as the measured value.

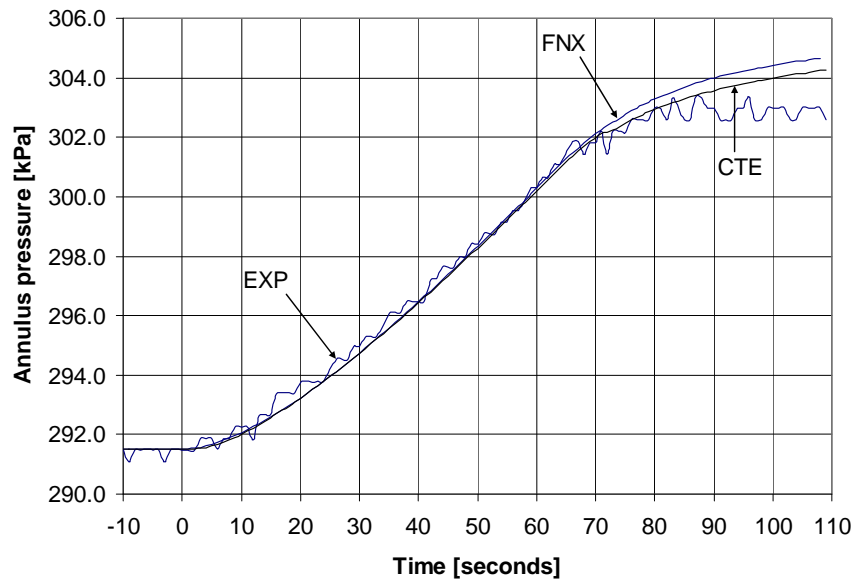


FIG. 7.24. Pressure inside the pressure vessel (outlet of the HPC).

The measured and simulated values are very close. They diverge somewhat only at the end (injection is stopped at 63 s).

7.4.2. Conclusions and recommendations

- The FLOWNEX, CATHARE, MARS-GCR and ACSL-XTREME codes have illustrated their ability to simulate a complex, integrated thermal fluid network. Given the many unknown factors in the PBMM, the agreement between the codes and the agreement between the codes and the plant are good.
- The accuracy of a simulation is determined by the ability to model all the important processes making up the system. To determine which processes are important and which are not, considerable skill and judgement are required. In the case of the PBMM, it became clear from the experimental results that all the important processes were not included in the initial simulation. It was not practical to model these processes from first principles. Therefore, the experimental results were used to quantify the heat transfer from the turbines. Additional heat transfer paths were then added to the original FLOWNEX simulation.
- If the integrity of a simulation is paramount, unknown factors must be eliminated.

The development of the simulation codes and benchmark tests was a complex and iterative process:

- The development of the simulation codes required interaction between the plant personnel and the people performing the simulation to clarify and confirm understanding of the descriptions of plant geometries, etc.
- It took time to define the ‘operation envelope’ of the plant. The United States of America was able to simulate the cycle, but could unfortunately not redo the simulation with the new boundary values.
- As mentioned in the previous paragraph, it became clear from experimental results that all processes were not included in the original simulation.

7.5. GT-MHR COLLATION OF RESULTS

This section presents a summary of the Member State analyses on the GT-MHR benchmarking including calculations of the simple cells, the fuel assembly cell and the three dimensional reactor model. The analysis of the individual CSIs results, and the description of codes and approaches related to the GT-MHR benchmark cases, are presented in Chapter 6 by each Member State (France, the Republic of Korea and the Russian Federation).

7.5.1. Analysis of simple cells benchmarking results

During the simple cells benchmarking, all results are compared with the average value accounting of results of all codes used for calculations.

Influence of fuel and burnable poison composition homogenization ratio

Calculations without burnup allow the influence of fuel composition homogenization on the multiplication coefficient and plutonium reaction rates depending on temperature to be recognized. In this case, the influence of the difference in library content (with respect to fission products) and difference of depletion chains for the main burnable isotopes is excluded.

In Fig. 7.25, the k-infinity results are compared. In general the results compare well, except for the single outlier. The maximal difference for the cell multiplication coefficient of 1.3% is reached in the case of fuel composition homogenization within the fuel compact with the external graphite layer (FCC2). Obviously, it is determined by self-shielding of isotopes and a separated graphite layer and it directly depends on taking into account the double-heterogeneity of fuel arrangement in HTGRs. On the other hand, the large difference may indicate a model error. This tendency is similar for the main isotope reaction rates. Figure 7.25 demonstrates the results for Pu-239, Pu-240 and C-12 as an example. The deviation increase for the C-12 absorption reaction rate is more significant for homogeneous cells. Inflection of curves for the cell with the external graphite layer (FCC2) indicates, probably, the influence of differences in approaches adopted in used codes for accounting of isotope self-shielding and scattering on graphite.

Accounting for the heterogeneous arrangement of burnable poison determines a deviation increasing as compared with homogeneous case:

- Multiplication coefficient (below 0.6%);
- Absorption on erbium isotopes (from 1.5 up to 3.5%);
- Absorption reaction rate (from 5 up to 11% for Er-166 and from 3.5 up to 5% for Er-167).

Essential divergence of absorption reaction rate for Er-168, which is determined by nuclear data in WIMS-D4, was obtained.

Influence of library data

Calculations with burnup are carried out for the heterogeneous FCC to analyse the plutonium and other minor actinide isotopic content and reaction rates behaviour vs irradiation time. As for BPCs, erbium (Er-166, Er-167 and Er-168) isotopic content, absorption rate and absorption ratio are additionally investigated.

With the increase of burnup, the deviation of the cell multiplication coefficient is changed but does not exceed 1.7% (Fig. 7.26). The k-infinity of MONTEBURNS follows a different trend with burnup while the other results are within a smaller band. The most essential difference is observed in the isotopic content and reaction rates for actinides. The main influence is most probably determined by the library data. It is also fair for results presented in Fig. 7.25.

Another evident reason is the different depletion chains used in different codes. For some minor actinides, this fact causes discrepancy in concentrations of one order in magnitude.

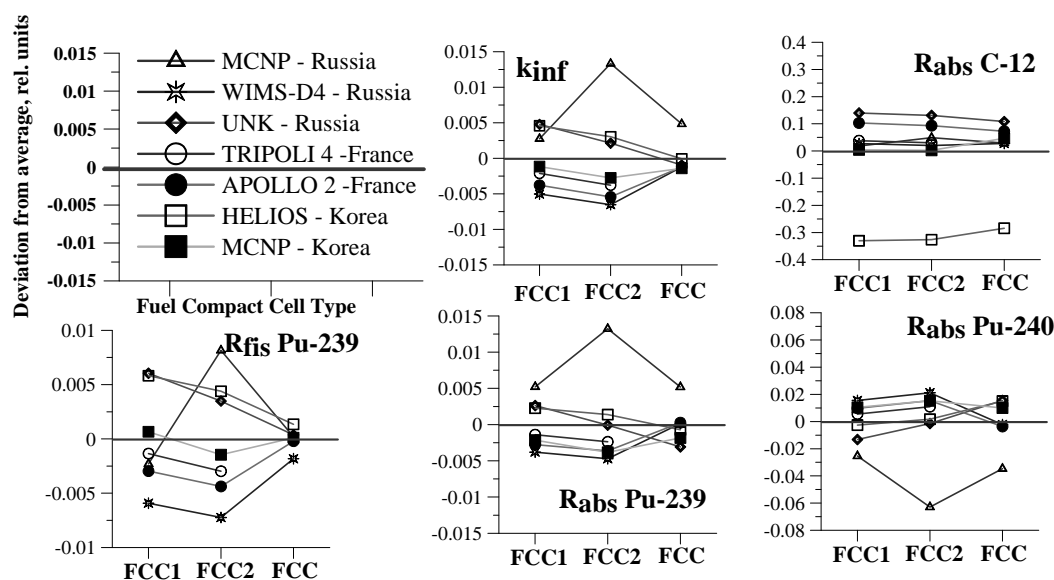


FIG. 7.25. Fuel compact cells.

Deviation from average in multiplication coefficient and reaction rates as a function of cell type.

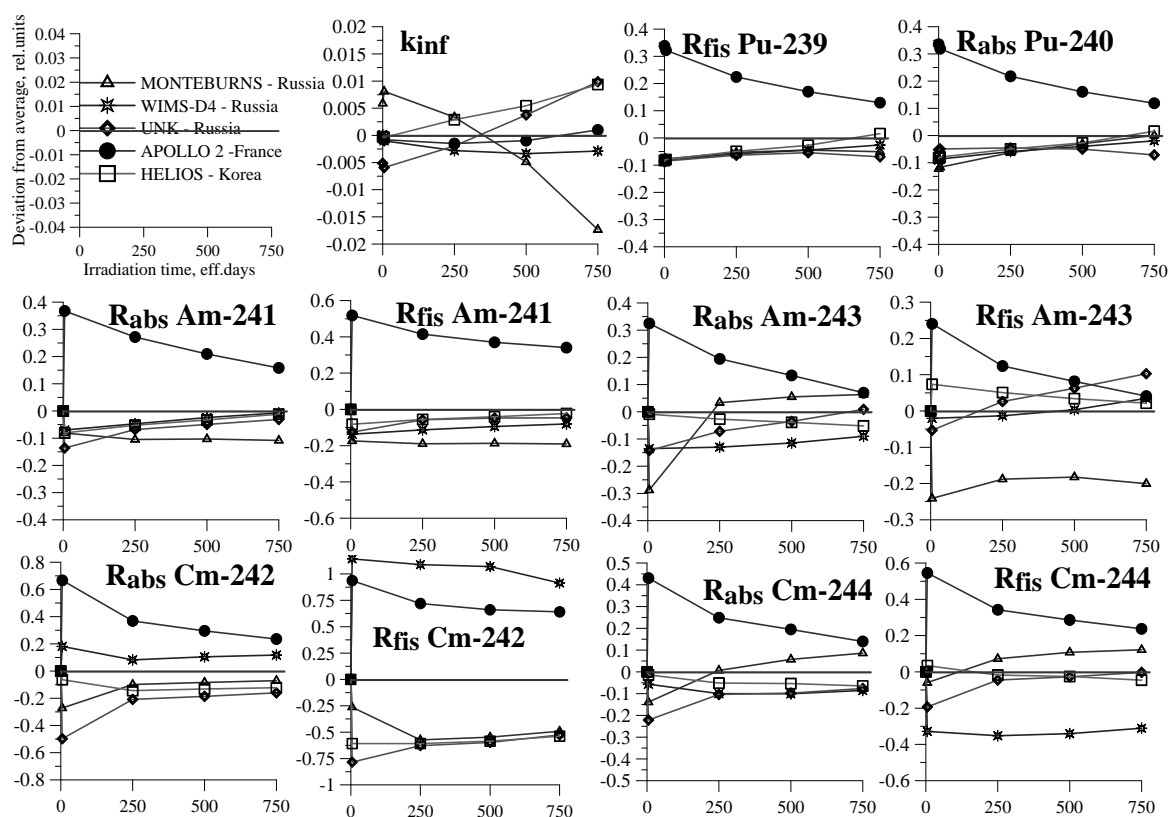


FIG. 7.26. Fuel compact cells deviation from average in multiplication coefficient and reaction rates as a function of irradiation time.

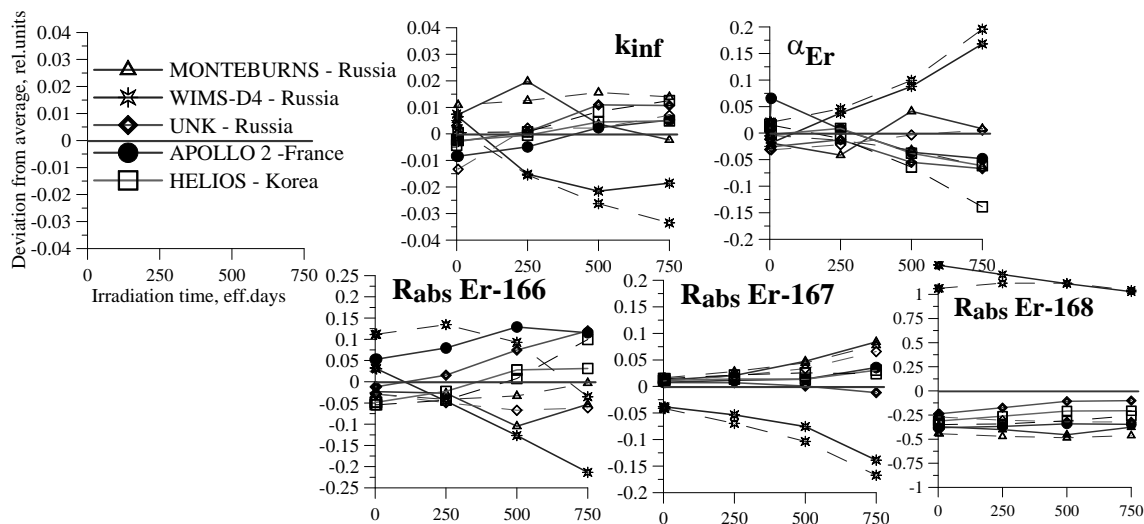


FIG. 7.27. Burnable poison compact cells. Deviation from average in multiplication coefficient, absorption on erbium isotopes and reaction rates as a function of irradiation time.

The calculational results for BPCs show that the main uncertainties are determined by erbium self-shielding, differences of nuclear data, and depletion chains. Accounting of the heterogeneity arrangement of burnable poison particles increases the deviations for considered functionals. Essential deviations in reaction rates are obtained for Er-168, but at the same time, one sees the difference of multiplication factors of about 3% (Fig. 7.27). Note that results for both the homogeneous and heterogeneous (dashed lines) burnable poison cells are also included in this comparison.

The relevance of conclusions about the essential influence of library data is confirmed by calculational results of the GT-MHR simple cell investigations performed in the past. They showed up to a 30% decrease of C-12 absorption reaction rate for UKNDL data used in WIMS-D4 in comparison with the results obtained by MCNP, UNK and MICROBURN using ENDF/B-based library data.

Comparative analysis of library data for graphite used in different codes allowed determination of the source of this discrepancy for graphite reaction rates. Figure 7.28 shows the dependences of graphite radiation capture cross-sections from different nuclear libraries which use is provided in WIMS-D4 (UKNDL and library upgraded in frames of IAEA project WLUP <http://iaeand.iaea.or.at/wimsd/>) with nuclear data from ENDF/B-6 and JENDL 3.2.

As shown in Fig. 7.28, C-12 radiation capture cross-sections from different libraries are the same in the thermal energy region and the main deviation lies in the intermediate and fast neutron energy region. The influence of this area determines the graphite reaction rate discrepancy. It was confirmed by the changing of ^{12}C absorption reaction rate after replacement of UKNDL data for graphite in WIMS-D4 library by those generated in frames of WLUP project. A decrease of deviation from 28 up to 8% was reached.

Thus, the necessity of revising C-12 data and of upgrading the WIMS-D4 nuclear library was confirmed. All results presented in this document for WIMS were obtained with the use of WLUP project data for graphite.

Note that MCNP4C calculations were conducted using ENDF/B5 data for ^{12}C . At the use of initial data for ^{12}C from JENDL3, the value R_{abs} of ^{12}C increased by 7%.

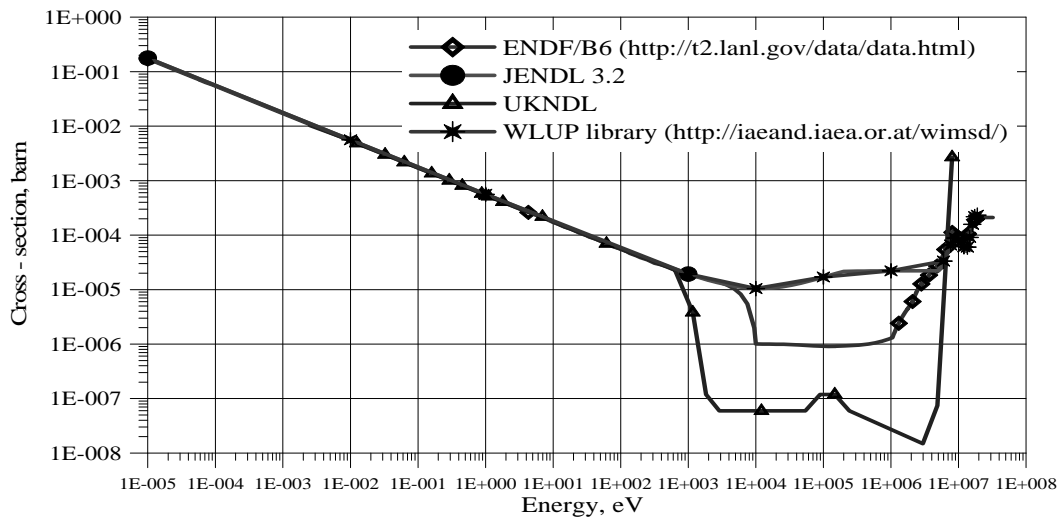


FIG. 7.28. C-12 capture vs energy.

Influence of cell meshing

Burnup of FCC and BPC is calculated by various computer codes in different approximations relative to the number of radial zones per fuel compact and burnable poison compact and number of burnup steps. Performed analyses by MONTEBURNS and WIMS-D4 showed that differences in concentrations of fuel and burnable poison isotopes and their reaction rates is about 1%. Enough correct results can be obtained with the breaking up of the burnable poison compact to five radial zones and burnup steps of no more than 10 days.

7.5.2. Analysis of FA1 and reactor benchmarking results

As for FA1 (Fig. 7.29) calculation results, it is possible to note the following:

- MCNP: The deviations between two Monte Carlo codes (MCNP and MCU) are, first of all, a result of differences in the library data as follows:
 - K_{inf} — no more than 0.4% up to 560 eff. days and 2.7% for 840 eff. days;
 - Isotopic content — no more than 10% for all isotopes up to 560 eff. days and about 19% for Pu-239 for 840 eff. days.
- WIMS-D4: Both the library data and model of fuel particle setting and energy structure are the reasons for results divergence. The heterogeneous description of fuel kernels (models 1 and 3) allows decreasing deviations in comparison with the homogeneous setting (model 2) as follows:
 - K_{inf} — from about 5% to no more than 0.8% for model 1 and 1.4% for model 3;
 - Plutonium isotopic content — from 45% to 2 and 20% for Pu-239 and Pu-240 respectively;
 - Erbium isotopic content — from 28% to about 15%.
- UNK: There is an essential deviation in neutronic functionals for 560 and 840 eff. days.
- APOLLO 2: Good agreement with the MCU results was obtained (k_{inf} — no more than 0.9%; isotopic content — within 10%).
- HELIOS: Essential deviation in neutronic functionals for 560 and 840 eff. days is observed (up to 3.3% for k_{inf} and up to 20% for Pu-239 and Pu-241 isotopic content).

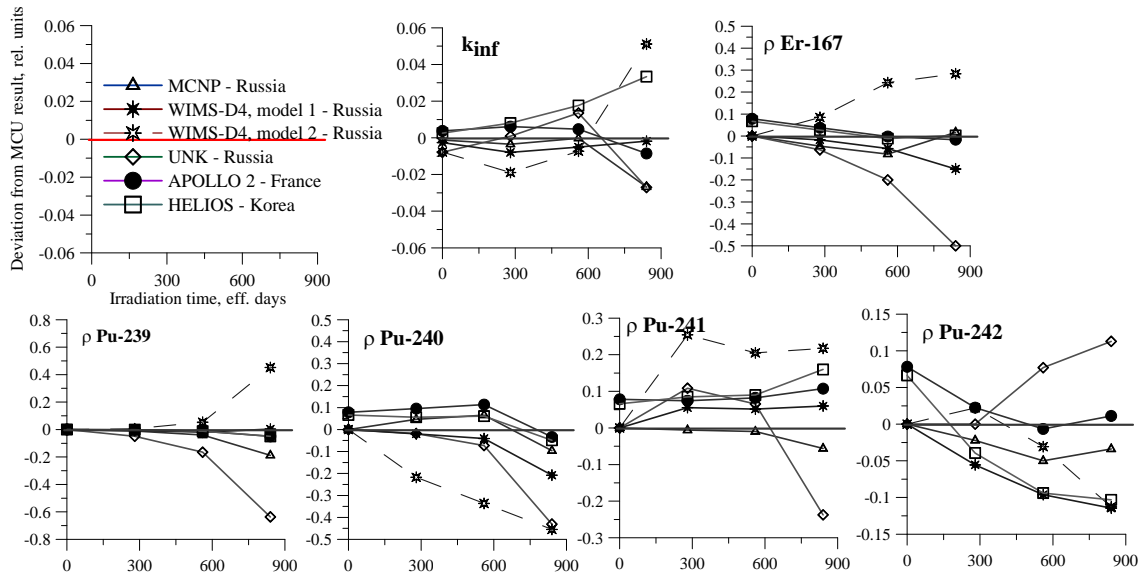


FIG. 7.29. Fuel assembly. Deviation from MCU result in multiplication coefficient, erbium and plutonium isotopic content.

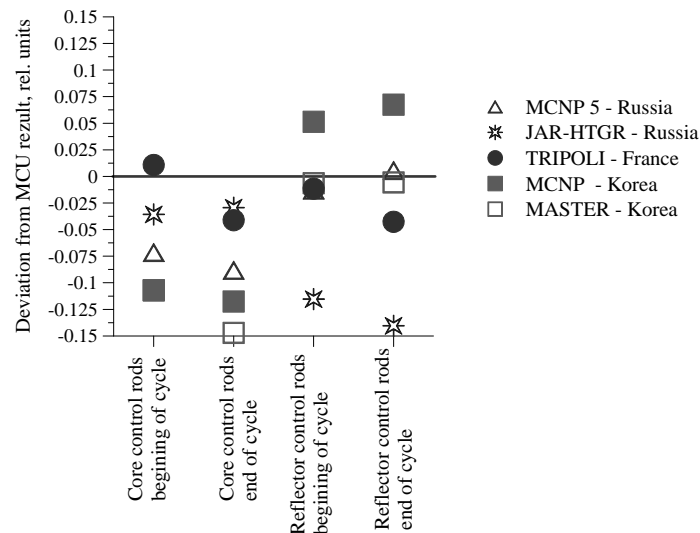


FIG. 7.30. Reactor. Deviation from MCU result in control rods worth.

There is no stable tendency in the behaviour of the temperature reactivity coefficient. A range of low temperatures (up to 700 K) is characterized by the deviation from MCU at times. These facts require additional analysis. The results divergence for 700–1200 K is about 30%.

The distinction for the control rod worth is about 10% for the Monte Carlo codes and about 15% for deterministic ones (see Fig. 7.30). These large differences could not be explained in the time of the CRP and need more detailed investigation.

Conclusions

The GT-MHR benchmarking showed the following:

- The adopted calculation techniques and models determine good agreement between investigated neutronic functionals.

- The heterogeneous setting of the fuel particle determines a decrease in calculation uncertainty.
- The main reasons for obtained deviation are the nuclear data library, depletion chains and energy structure stipulating for resonance interlocking; errors in the models used can also not totally be excluded.
- Therefore, it determines the necessity to investigate:
 - The power distribution under two- and three dimensional calculations;
 - The temperature reactivity coefficient behaviour;
 - The sensitivity of the basic neutronic characteristics to the initial standard files of evaluated nuclear data both to the graphite initial data and to plutonium and actinide data.

7.6. CONCLUSIONS AND RECOMMENDATIONS

The Coordinated Research Project (CRP5) on Evaluation of High Temperature Gas Cooled Reactor (HTGR) Performance was established to foster the sharing of research and associated technical information between participating Member States in the on-going development of the HTGR as a future source of nuclear energy. In the CRP5, computer codes and models are verified through code-to-code comparisons and actual test results from operating reactor facilities.

During the second phase the activities focused on the analysis of benchmark problems pertaining to the HTR-10 test reactor, the ASTRA critical test facility, the proposed Pebble Bed Modular Reactor and PBMR Micro Test module and the Gas Turbine-Modular Helium Reactor. In total, 12 institutes and organizations from 12 Member States participated in the second phase.

The following general lessons were learnt in the CRP:

- Standardized templates for results reporting were only introduced at a very late stage. These must be defined at a very early stage to facilitate easy comparisons and to ensure consistency of data, units, etc.
- Experimental or measurement uncertainties are important and must be specified at the beginning of a benchmark exercise. This includes specification of uncertainties of material data and measurement uncertainties.
- The IRPhe format from NEA/OECD can be used as an example of a standard template addressing all relevant data needs.
- It is necessary to prevent scope creep or to ensure adequate time to get to a final natural conclusion as this was seen to be a problem in the current CRP, which had already been extended several times as new problems and test cases were added.

APPENDIX

ADDITIONAL BENCHMARK ANALYSIS ASSOCIATED WITH IAEA-TECDOC-1382

A.1. INTRODUCTION

IAEA TECDOC 1382 addressed the initial benchmark analyses associated with the CRP on *Evaluation of HTGR Performance*. This document was published in November 2003 and included benchmark analyses related to the initial testing of the HTTR and HTR-10 test reactors.

This appendix provides additional benchmark analyses by selected Member States on the original problems addressed, but not published, in IAEA-TECDOC-1382. Refer to Chapter 2 of IAEA-TECDOC-1382 for details associated with the HTR-10 facility and the entire description of the benchmark problem

A.1.1. HTR-10 CONTROL ROD WORTH

A.1.1.1. Benchmark problem description

The HTR-10 control rod worth for full core (Benchmark problem B3)

This problem includes calculating the reactivity worth of the ten fully inserted control rods (B31) and of one fully inserted control rod (B32, the other rods are in withdrawn position) under helium atmosphere and a temperature of 20°C for the full core.

HTR-10 control rod worth for the initial core (Benchmark problem B4)

The calculation of the reactivity worth of the ten fully inserted control rods (B41) under helium atmosphere and a core temperature of 20°C for a loading height of 126 cm and the differential worth of one control rod (B42, with the other rods in the withdrawn position). The differential reactivity worth is proposed to be calculated when the lower end of the rod is at the following axial positions, namely, 394.2, 383.618, 334.918, 331.318, 282.618, 279.018 and 230.318 cm in a helium atmosphere and core temperature of 20°C for a loading height of 126 cm.

The core temperature is defined as the temperature of the balls and all the surrounding structures included in the core physics model as described above in the HTR-10 reactor model and core configuration. The full core volume of 5 m³ is defined as the total volume of the mixed and graphite balls in the conus region. The loading height is the height of the mixed balls starting from the upper surface of the conus region.

A.2. INDONESIA

BATAN of Indonesia has performed additional benchmark calculations on control element (CE) worth for the HTR-10 [A-1],[A-2]. The cell calculation was performed with the collision probability method. The core calculation was performed in the three dimensional geometry (θ -R-Z) with the diffusion method. All calculations were performed using the SRAC code system. The results of this calculation showed that at first criticality, the single control element worth and ten control elements' worth are 1.69% and 19.48% respectively. The worths under full core conditions are 1.30% and 16.22% respectively. Compared to the Monte Carlo calculation of the reference, these results are quite close, which is indicative of the use of a good solution method in the benchmark calculation.

Calculational method

There were two problems solved in the reactivity benchmark calculation of the HTR-10CR. These include problem B3 (control element reactivity full core) and problem B4 (control element reactivity at the initial criticality core). Each of the problems has been divided into two types of subproblems, namely, for all ten control elements inserted and for one control element inserted, as shown in the Table A.1.

To solve the problem, the cell and core calculations were performed using the SRAC95 code system [A-3],[A-4]. This code has been recompiled to run under PC-based Windows XP. The nuclear data used was the Japanese JENDL3.2 file.

TABLE A.1. HTR-10 BENCHMARK PROBLEM/CONTROL ELEMENT DESIGNATION AND LOCATION

HTR-10CR - B3 (full core)	B31 B32	All ten CEs inserted One CEs inserted
HTR-10CR - B4 (initial criticality core)	B41 B42	All ten CE inserted One CE inserted

The cell calculations were performed using the collision probability method to generate effective cross-sections for fuel and moderator balls, as well as structural materials. The multigroup cross-section sets were then condensed into a six-energy group.

The control rod worth was calculated as follows:

$$\rho = \rho_{ex} + \rho_{sm} \quad (1)$$

where

$$\rho_{ex} = (k_{eo} - 1) / k_{eo}, \quad (2)$$

is the core reactivity when all control elements were pulled out of the core, and k_{eo} is the core multiplication factor when all control elements were *fully out*.

The shutdown margin is defined as:

$$\rho_{sm} = (k_{ei} - 1) / k_{ei}, \quad (3)$$

which is the negative reactivity in the core when all ten control elements were fully inserted and k_{ei} is the multiplication factor when all control elements were fully inserted.

Results and conclusions

1. Cell Calculation

The zone arrangement in the reactor in the R-Z geometry is shown in Fig. A.1, while nuclide densities were taken directly from the references. In the cell calculation, natural boron concentration, N_B , inside the graphite matrix can directly be calculated from the graphite impurity as:

$$N_B = \text{impurity} \times \rho \times A / M, \quad (4)$$

where

ρ is the graphite density;

A is the Avogadro number (0.6022045×10^{24} /mol);

M , is the molecular weight of graphite (12.011 gr./mol).

As for the fuel matrix region, natural boron in uranium and graphite should be considered. The natural boron concentration, N_B , becomes,

$$N_B = f_{UM} \times N_{BU} + (1 - f_{UM}) \times N_{BG} \quad (5)$$

where

f_{UM} is the volume fraction occupied by all uranium kernels in the fuel region;

N_{BU} and N_{BG} are densities of boron inside uranium and graphite.

The group constant calculation for fuel mixture, moderator ball, reflector and control element was performed according to the following method.

Fuel mixture cell

The fuel mixture group constants were calculated using a spherical fuel cell model. The fuel mixture cell consists of the fuel and moderator ball homogenized in a cell to be placed inside the active core region. The materials for this model from the inner to the outer regions are fuel matrix, graphite shell and coolant. The radius of the fuel mixtures cell was determined from the following geometrical relationship.

The volume of a unit cell of the fuel mixture centred on one fuel ball is calculated as:

$$V_c = V_p (1+m)/f \quad (6)$$

where m is the moderator to the fuel ball ratio.

In the HTR-10, the values of m and f were given to be 43/57 and 0.61 respectively [A-5]. Therefore, the equivalent cell radius, R_2 , of the fuel mixture cell can be calculated using the relation $V_c = 4\pi/3 \times R_2^3$, which yields R_2 equal to 4.2663 cm.

Using the above geometric relationship and data given in Table A.2, atomic densities for the fuel balls in the HTR-10 core can be calculated and the results of this calculation are depicted in Table A.3.

Moderator and reflector cell

The moderator cell group constants were calculated using the same model as that of the fuel mixture. The moderator consists of graphite balls with the same radius as the fuel balls. The group constants of the moderator balls are needed for the evaluation of the cone region at the bottom of the core, which in the initial core of the HTTR is only filled with the graphite balls.

The volume of the unit cell associated with one moderator ball equals V_p/f , where V_p is the volume of a ball and f is the filling fraction.

The volume of the void space associated with one ball of any type = $V_p(1-f)/f$.

In the calculation of the group constant for moderator balls (dummy balls), the CFP volume fraction in the moderator ball was taken to be very small, such that almost all the fuel matrix volume is occupied by graphite. The filling fraction, f , of the moderator ball was assumed to be the same as that of the core region which is 0.61.

The cell volume of the moderator ball is therefore $V_c = V_p/f$ and the equivalent cell radius, R_2 , is 3.5373 cm.

As for the reflector and other structural material, the cross-sections were obtained by modelling in slab geometry. In this case, a two-slab region was used.

Control element cell

The group constants for the control element and other holed side regions were generated using appropriate modelling. In this paper, a multi-layered cylindrical region for the control element was used. As for the irradiation channel and the hole region left by the pulled-out control element, a two-region cylinder was used, in which the inner radius was equal to the radius of the hole and the outer radius equal to the outer region equivalent radius. The presence of the metal structure joining the control element parts was taken into account by homogeneous mixing into the control element.

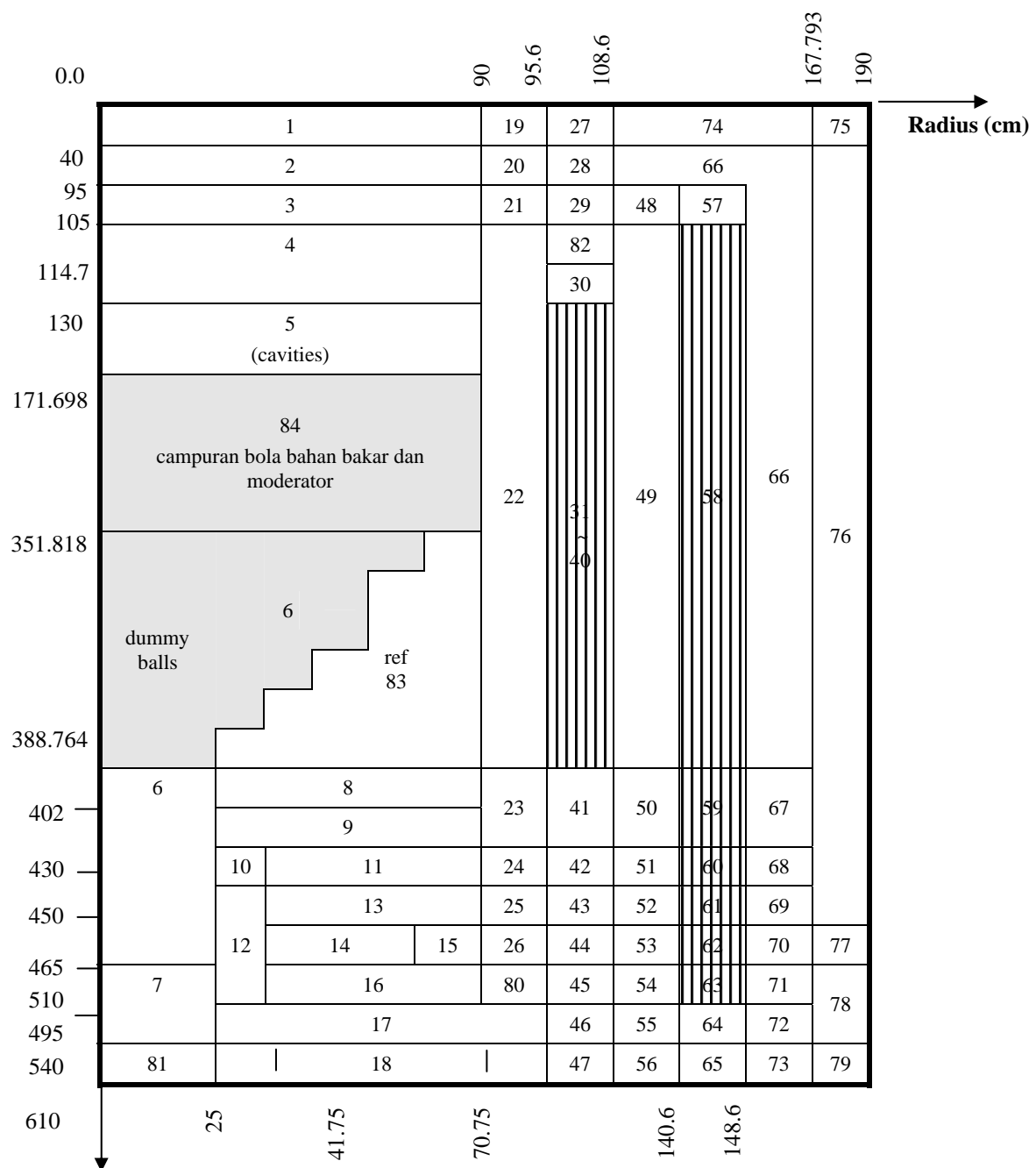


FIG. A.1. Zone division in R-Z geometry.

TABLE A.2. HOMOGENIZED ATOMIC DENSITY IN R-Z GEOMETRY ($\text{CM}^{-1} \text{BARN}^{-1}$)
FOR EACH ZONE SHOWN IN FIG. A.1

Zone No.	Carbon	Natural Boron	Remarks
0	0.851047E-01	0.456926E-06	Bottom reflector with hot helium
1	0.729410E-01	0.329811E-02	Boronated carbon bricks
2	0.851462E-01	0.457148E-06	Top graphite reflector
3	0.145350E-01	0.780384E-07	Cold helium chamber
4	0.802916E-01	0.431084E-06	Top reflector
5	-	-	Top core cavity
6,7	0.538275E-01	0.288999E-06	Dummy balls, simplified as low-density graphite
8	0.781408E-01	0.419537E-06	Bottom reflector structures
9	0.823751E-01	0.442271E-06	Bottom reflector structures
10	0.843647E-01	0.298504E-03	Bottom reflector structures
11	0.817101E-01	0.156416E-03	Bottom reflector structures
12	0.850790E-01	0.209092E-03	Bottom reflector structures
13	0.819167E-01	0.358529E-04	Bottom reflector structures
14	0.541118E-01	0.577456E-04	Bottom reflector structures
15	0.332110E-01	0.178309E-06	Bottom reflector structures
16	0.881811E-01	0.358866E-04	Bottom reflector structures
17, 55, 72, 74, 75, 76, 78, 79	0.765984E-01	0.346349E-02	Boronated carbon bricks
18, 56, 73	0.797184E-01	0.000000E+00	Carbon bricks
19	0.761157E-01	0.344166E-02	Boronated carbon bricks
20	0.878374E-01	0.471597E-06	Graphite reflector structure
21	0.579696E-01	0.311238E-06	Graphite reflector structure
22, 23, 25, 49, 50, 52, 54, 66, 67, 69, 71, 80	0.882418E-01	0.346349E-02	Graphite reflector structure
24, 51, 68	0.879541E-01	0.168369E-03	Graphite reflector structure
26	0.846754E-01	0.454621E-06	Graphite reflector structure
27	0.589319E-01	0.266468E-02	Boronated carbon bricks
28, 82	0.678899E-01	1.400000E-05	Graphite reflector structure
29	0.403794E-01	1.400000E-05	Graphite reflector structure
30, 41	0.678899E-01	0.364500E-06	Graphite reflector structure
31, 40	0.634459E-01	0.340640E-06	Graphite reflector, control rod boring region
42	0.676758E-01	0.125331E-03	Graphite reflector structure
43, 45	0.861476E-01	0.462525E-06	Graphite reflector structure
44	0.829066E-01	0.445124E-06	Graphite reflector structure
46	0.747805E-01	0.338129E-02	Boronated carbon bricks
47	0.778265E-01	0.000000E+00	Carbon bricks
48	0.582699E-01	0.312850E-06	Graphite reflector structure
53	0.855860E-01	0.459510E-06	Graphite reflector structure
57	0.728262E-01	0.391003E-06	Graphite reflector structure
58, 59, 61, 63	0.760368E-01	0.408240E-06	Graphite reflector, cold helium flow region
60	0.757889E-01	0.145082E-03	Graphite reflector, cold helium flow region
62	0.737484E-01	0.395954E-06	Graphite reflector, cold helium flow region
64	0.660039E-01	0.298444E-02	Boronated carbon bricks
65	0.686924E-01	0.000000E+00	Carbon bricks
70	0.861500E-01	0.462538E-06	Graphite reflector structure
77	0.749927E-01	0.339088E-02	Boronated carbon bricks
81	0.797184E-01	0.000000E+00	Dummy balls, artificially taken as carbon bricks

TABLE A.3. COMPARISON OF THIS CALCULATION RESULT TO THAT OF THE REFERENCES (BENCHMARK PROBLEM HTR-10CR-B3)

Benchmark problem	Parameter	This calculation	Reference diffusion	Difference	Reference Monte Carlo	Difference
B31	K_{eff} all CE out of core	1.10349	-	-	1.12192	-0.01843
	K_{eff} all CE inserted	0.93600	-	-	0.94611	-0.01011
	Worth of all CE	16.22%	15.24%	0.98%	16.56%	-0.34%
B32	K_{eff} one CE inserted	1.08792	-	-	1.10441	-0.01649
	Worth of one CE	1.30%	-	-	1.41%	-0.11%

Calculation of control element reactivity worth

The group constants for the HTR-10 were generated using 107 energy groups, consisting 61 fast and 46 thermal energies. The cross-sections were then condensed into six groups, three in condensed fast groups and three in condensed thermal groups.

The effective multiplication factor calculation was performed using the CITATION diffusion module [A-6] in the SRAC code system, in three dimensional geometry. The core reactivity can then be computed for different control element positions and fuel ball loading. The results of this calculation are shown in Tables A.3 and A.4 for the full core and initial core conditions respectively.

TABLE A.4. COMPARISON OF THIS CALCULATION RESULT TO THAT OF THE REFERENCES FOR INITIAL CRITICALITY CORE (BENCHMARK HTR-10CR-B4)

Benchmark problem	Parameter	This calculation	Reference diffusion	Difference	Reference Monte Carlo	Difference
	K_{eff} initial criticality	0.99905 (h = 130 cm)	-	-	0.99965 (h = 126 cm)	
B41	K_{eff} all CE in	0.83629	-	-	0.83756	-0.00127
	Worth of all CE	19.48%	18.27%	1.21%	19.36%	0.12%
B42	K_{eff} one CE in	0.98339	-	-	0.98205	0.00134
	Worth of one CE	1.69%	1.62%	0.07%	1.79%	-0.10c%

The result for the *benchmark* HTR-10 CR-B3 problem showed that the k-effective when all ten control elements are pulled out of the core was 1.10349 as shown in Table A.3. The Monte Carlo of the reference showed 1.12192, which means that the difference is -1.843%, while our calculation showed a slightly lower value. In the HTR-10 CR-B31 benchmark, our results of 16.22%, compared to the diffusion of the reference with 15.24% and Monte Carlo of the reference 16.56%, also showed a slight difference for all ten control elements inserted.

In the HTR-10 CR-B32 benchmark, the worth of one control element inserted according to our calculation is 1.30% while the Monte Carlo results of the reference showed 1.41% or a relative difference of -0.11%.

As for problem HTR-10 CR-B41 of initial criticality, our k-effective calculation result for all control elements inserted was 0.83629, while the referenced Monte Carlo gave 0.83756. The worth of all control elements was calculated to be 19.48%, while the referenced diffusion 18.27% and referenced Monte Carlo 19.36%. It was shown that our results tended to approach those of the referenced Monte Carlo. A similar case was obtained for one control element of the HTR-10 CR-B42, i.e. for the case of one control element inserted in the initial core. Our result showed that the worth of one control element was 1.69%, while the referenced diffusion gave 1.62% and referenced Monte Carlo gave 1.79%.

It can be seen that our results for benchmark problems HTR-10 CR-B3 and HTR-10 CR-B4 were close to those of either the diffusion method or Monte Carlo reference. In general, our results were closer to the reference Monte Carlo and most of our calculation results were located between the referenced diffusion and Monte Carlo.

Figure A.2 shows the relationship between the integral worth of control element and the insertion distance. Figure A.3 shows the corresponding differential worth. Both agreed with the theoretical description. Figures A.4 and A.5 show the thermal neutron flux when the core is fully loaded to 180 cm height.

Conclusion

The three dimensional calculation shows good results compared to those of the referenced Monte Carlo and diffusion method. The methods used in our models seemed to be appropriate for calculating the control element worth of HTGRs. Neutron streaming correction and validation is based on the HTR-10 benchmark problems.

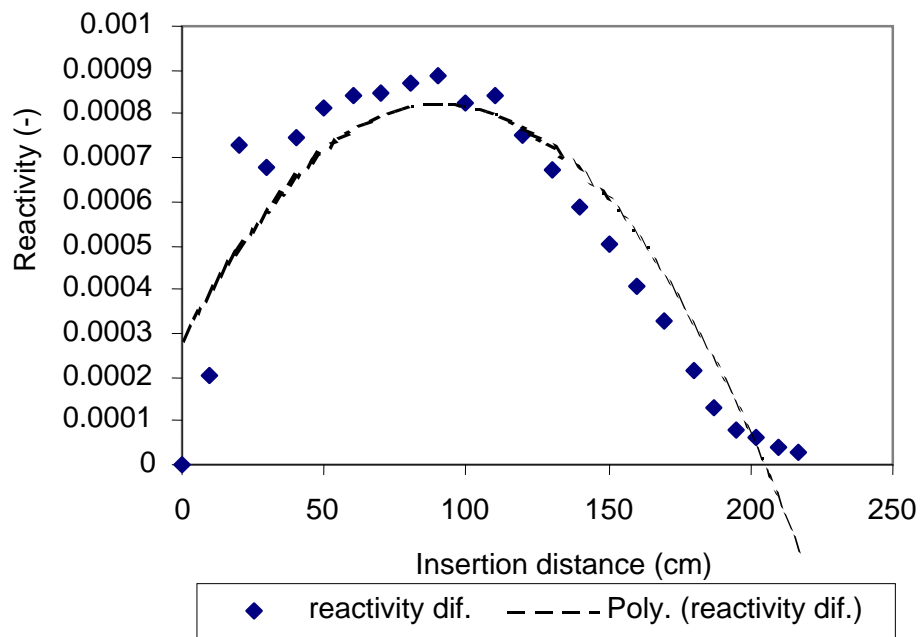


FIG. A.2. Relative differential reactivity of one control rod as a function of insertion depth into full core.

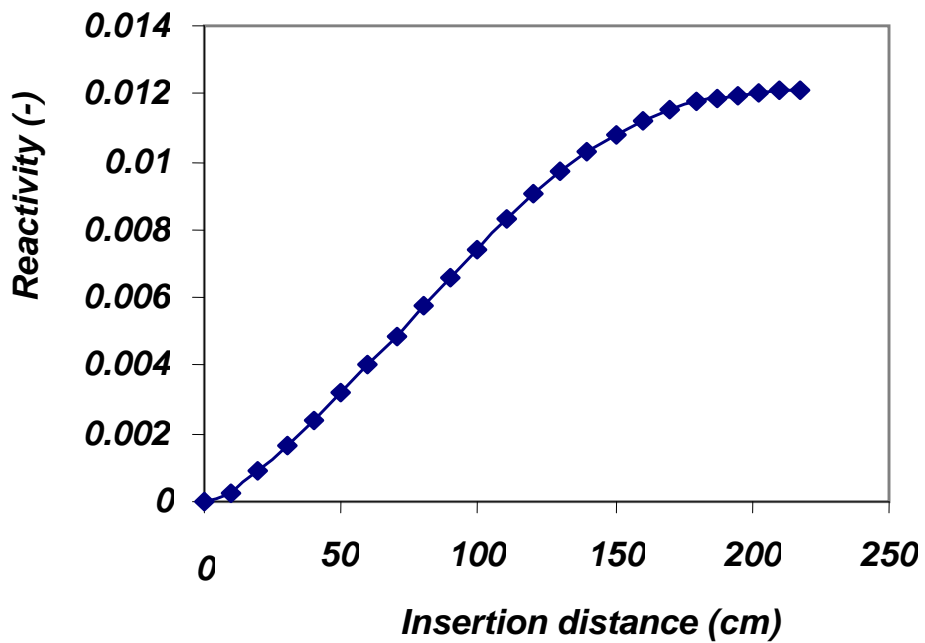


FIG. A.3. Relative reactivity worth of one control element as a function of insertion depth into full core.

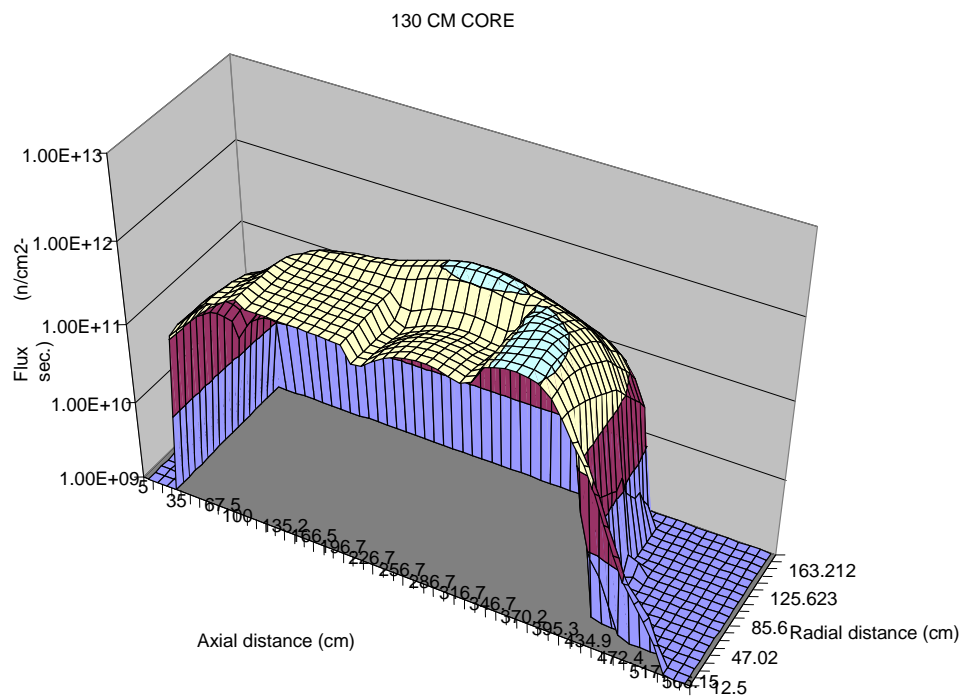


FIG. A.4. Thermal neutron flux distribution at first criticality (loading height 130 cm).

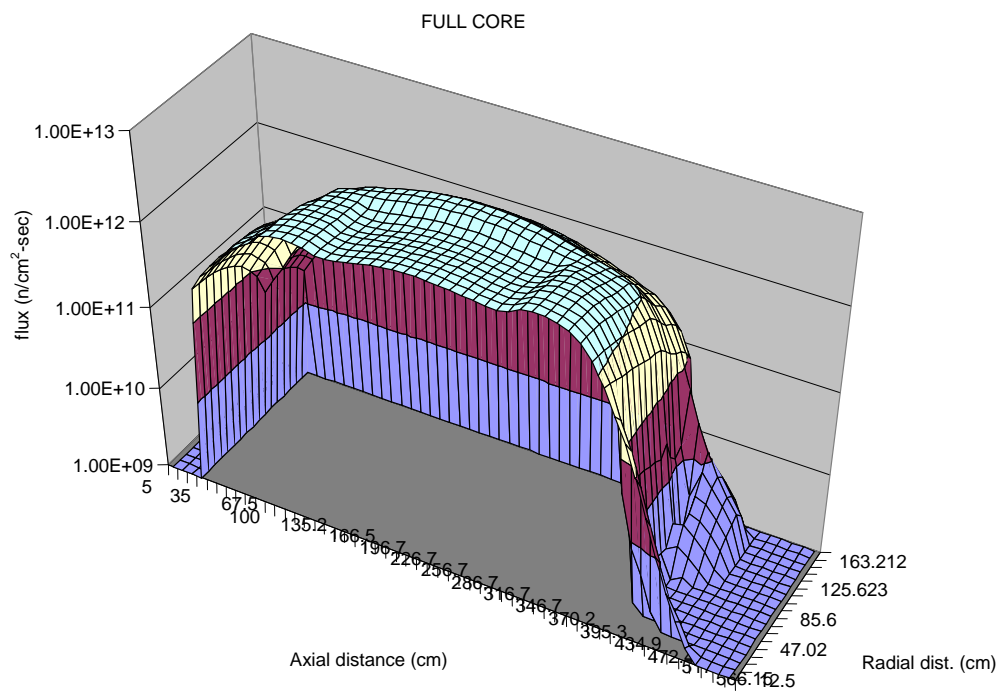


FIG. A.5. Thermal neutron flux distribution at full core (loading height 180 cm).

A.3. GERMANY

Introduction

In connection with the calculations for the HTR-10 benchmark problems [A-7], the problem of neutron streaming in the boring holes of this reactor and its treatment in the diffusion theory appeared once more. A possibility of treating this effect within the diffusion theory is the use of anisotropic diffusion coefficients. One possibility of getting accurate diffusion constants is to compare the corresponding streaming effects obtained by diffusion and Monte Carlo calculations and to adapt the anisotropic diffusion coefficients to the results of the Monte Carlo calculations.

Therefore, a comparison of diffusion and Monte Carlo calculations has been performed using a simplified HTR-10 core model, but with unchanged geometry. The anisotropic diffusion coefficients obtained by this comparison were then inserted into the detailed three dimensional diffusion calculations of the HTR-10 benchmark problems (the temperature coefficients, the control rod worths and the critical height of the initial core, in order to test their validation). These updated results are presented here [A8].

Determination of streaming correction factors

Calculational methods and simplified HTR-10 core model

The comparative streaming test calculations were performed on the one hand with the MCNP-4C3 Monte Carlo code [A-9] and on the other hand with the NITAWL-TOTMOS-CITATION code system (the NITAWL module of the AMPX-77 system [A-10] in order to calculate resonance cross-sections, the transport code TOTMOS [A-11] for the unit cell spectrum calculations and the cross-section generation, and the CITATION diffusion code [A-6] for the whole-core calculations in the two dimensional R,ϕ geometry and in the three dimensional R,ϕ,Z geometry).

For the diffusion and Monte Carlo calculations, a simplified core model of the HTR-10 was chosen, with identical geometry and identical void regions as in the detailed model. The core height was taken as 126 and 180 cm. The simplified core model, as shown in Fig. A.6, contains the following five different material zones:

- The core containing homogenized fuel with an U^{235} enrichment of 4 wt.%; no coated particles were considered and no spatial self-shielding was taken into account in the resonance region;
- A top and bottom reflector zone;
- The upper cavity represented by a cell containing diluted graphite;
- The radial reflector zone;
- The boring holes for the control rods and for the small absorber balls (KLAK) filled with graphite or vacuum respectively.

The 1-D cell calculations for these five different zones were performed by the TOTMOS integral spectrum code in the transport corrected P_0 -approximation using a 123 group cross-section library [A-12] generated from the JEF-2.2 nuclear data files [A-13]. A white boundary condition was assumed at the outer cell surface and the 123 group cross-sections were collapsed into 26 broad energy group constants and transferred as microscopic data to the CITATION diffusion code. The energy structure of the 26 groups is given in Table A.5. A homogeneous cell model was assumed, thus the coated particle structure was not taken into account and in the resonance region only the energetic self-shielding was considered and not the spatial self-shielding. No leakage iteration was considered because the use of sufficient fine group constants described the detailed energy dependence of the neutron flux adequately, as shown in [A-14].

Furthermore, in all test calculations, the following cases were considered:

- The control rod and KLAK holes were filled with graphite;
- The control rod holes were empty and all the KLAK holes were filled with graphite;
- All control rod holes were filled with graphite and the KLAK holes were empty;

- The control rod and KLAH holes were empty.
- In the void spaces, e.g. the upper cavity and the empty channels for the control rods and KLAHs, the microscopic cross-sections were set to zero, except the homogeneous diffusion constants, which were assumed to be equivalent to the radius of the upper cavity of the control rod or KLAH channels respectively ($D_{\text{hom}} = R_{\text{hole}}$).

Test calculations with the simplified HTR-10 core model

For a first series of calculations in order to determine the anisotropic diffusion coefficients in the R- and ϕ -direction, a two dimensional model in R, ϕ geometry was chosen with the reflected boundary condition at the top and bottom. This geometry represents a section through the three dimensional model. The results are collected in Tables A.6 and A.7. As can be seen, there exists an excellent agreement between the Monte Carlo and diffusion calculations, when all the holes are filled with graphite, showing once more that 26 group constants in a diffusion calculation without leakage feedback are sufficient to accurately describe the energy dependence of the neutron flux. When modifying the homogeneous diffusion constants of the control rod and KLAH channels by anisotropic diffusion coefficients in the R- and ϕ -direction, the best results were yielded when choosing $D_{r,\phi}/R_{\text{hole}} = 5.0$. The variation of D_{ϕ}/R_{hole} between 0.1 and 10.0 showed that there was no dependence of the k-effective values on the ϕ -direction. Tables A.6 and A.7 include the streaming test calculations and the influence of streaming with the simplified two dimensional (R, ϕ) model of the HTR-10 diffusion calculations with 26 group constants.

Then, in a second series, the diffusion coefficient in the axial direction had to be determined as follows:

A three dimensional R, ϕ ,Z model of this simplified core was assumed and the whole-core diffusion calculations were performed taking the diffusion coefficients in the R- and ϕ -direction yielded by the two dimensional diffusion calculations. First, a core height of 180 cm was considered with the upper cavity having a height of 41.7 cm. The results are collected in Tables A.8 and A.9 together with the corresponding Monte Carlo results. Once more, the Monte Carlo and diffusion calculations agreed excellently ($\Delta k = 0.00037$) when all the holes were filled with graphite, showing that the treatment of the upper cavity with $D_{r,\phi}/R_{\text{cavity}} = 0.1$ and $D_z/R_{\text{cavity}} = 0.5$ was correct.

In the case where the KLAH holes were filled with graphite and the control rod holes were empty, the corresponding diffusion correction factor in the Z-direction, D_z/R_{hole} , was adapted to the MCNP result.

When varying D_z/R_{hole} from 0.5 up to 1.08, the difference in the corresponding multiplication factors of the diffusion and the Monte Carlo calculations decreases from $\Delta k = 0.0024$ down to $\Delta k = 0.00006$. When using an axial streaming correction factor of $D_z/R_{\text{hole}} = 1.08$, the results of the diffusion and Monte Carlo calculations agreed well and also when regarding the neutron streaming effect in the KLAH holes. Tables A.8 and A.9 provide streaming test calculations for the simplified three dimensional R, ϕ ,Z model of the HTR-10 with the diffusion calculations and influence of streaming with 26 group constants and $H_{\text{core}} = 180$ cm.

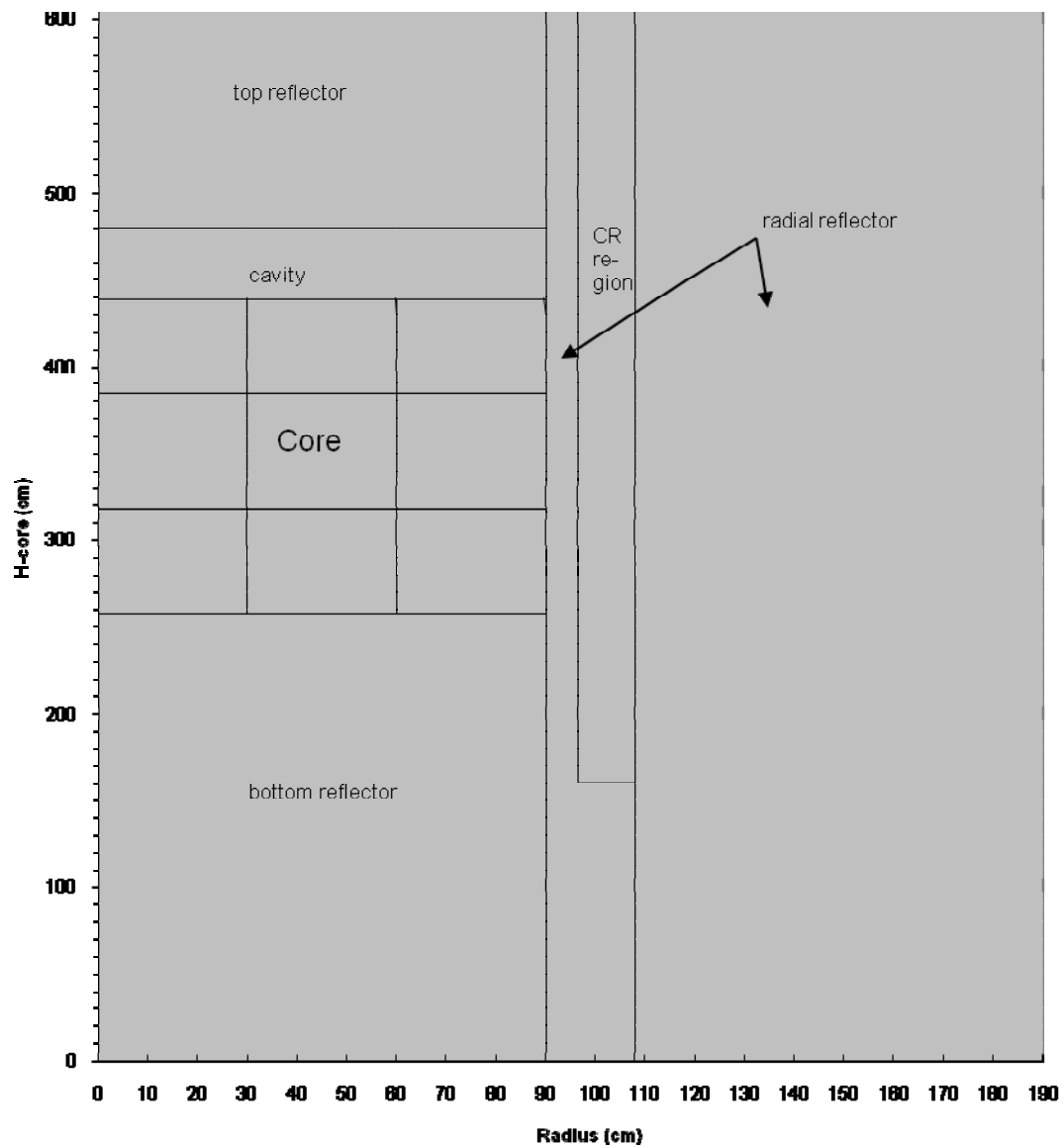


FIG. A.6. Simplified HTR-10 model with a core height of 180 cm.

TABLE A.5. GROUP STRUCTURE IN THE DIFFUSION CALCULATIONS

Group	Upper Energy Boundaries (eV)
1	1.492×10^7
2	7.408×10^6
3	3.679×10^6
4	6.721×10^5
5	1.111×10^5
6	1.931×10^4
7	3.355×10^3
8	1.585×10^3
9	7.485×10^2
10	2.754×10^2
11	1.301×10^2
12	6.144×10^1
13	29.0
14	13.7
15	8.32
16	5.04
17	2.38
18	1.29
19	0.65
20	0.35
21	0.20
22	0.12
23	0.08
24	0.05
25	0.02
26	0.01

TABLE A.6. EFFECTIVE MULTIPLICATION CONSTANTS
OBTAINED BY DIFFUSION AND MONTE CARLO CALCULATIONS

Case	K_{eff} Diffusion TOTMOS-CITATION	K_{eff} Monte Carlo MCNP4C3	Δk CITATION-MCNP
CR + KLAK holes filled	1.11396	1.11405±0.00030	-0.00009
KLAK holes filled CR holes empty $D_{r,\phi}/R_{\text{hole}} = 5.0$	1.10966	1.10945±0.00029	+0.00021
CR holes filled KLAK holes empty $D_{r,\phi}/R_{\text{hole}} = 5.0$	1.11145	1.11246±0.00030	-0.00101
CR + KLAK holes empty $D_{r,\phi}/R_{\text{hole}} = 5.0$	1.10790	1.10702±0.00032	+0.00088

TABLE A.7. INFLUENCE OF STREAMING

Case	Δk TOTMOS-CITATION	Δk MCNP	$\Delta(\Delta k)$
KLAK holes filled CR holes empty $D_{r,\phi}/R_{\text{hole}} = 5.0$	0.00430	0.00460	-0.00030
CR holes filled KLAK holes empty $D_{r,\phi}/R_{\text{hole}} = 5.0$	0.00251	0.00159	+0.00092
CR + KLAK holes empty $D_{r,\phi}/R_{\text{hole}} = 5.0$	0.00606	0.00703	-0.00097

TABLE A.8. EFFECTIVE MULTIPLICATION CONSTANTS
OBTAINED BY DIFFUSION AND MONTE CARLO CALCULATIONS

Case	K_{eff} Diffusion TOTMOS-CITATION	K_{eff} Monte Carlo MCNP4C3	Δk CITATION-MCNP
CR + KLAK holes filled	0.99094	0.99057±0.00030	+0.00037
CR holes empty	0.98490 ($D_z/R_{\text{hole}}=0.50$)	0.98247±0.00030	+0.00243
KLAK holes filled	0.98419 ($=0.66$)		+0.00172
$D_{r,\phi}/R_{\text{hole}}=5.0$	0.98273 ($=1.0$)		+0.00026
	0.98241 ($=1.08$)		-0.00006
	(adjusted to MCNP result)		
CR holes filled	0.98720 ($D_z/R_{\text{hole}}=0.50$)	0.98493±0.00029	+0.00227
KLAK holes	0.98674 ($=0.66$)		+0.00181
empty	0.98578 ($=1.0$)		+0.00085
$D_{r,\phi}/R_{\text{hole}}=5.0$	0.98556 ($=1.08$)		+0.00063
CR + KLAK holes empty	0.98151 ($D_z/R_{\text{hole}}=0.50$)	0.97825±0.00031	+0.00326
	0.98036 ($=0.66$)		+0.00211
$D_{r,\phi}/R_{\text{hole}}=5.0$	0.97803 ($=1.0$)		-0.00022
	0.97751 ($=1.08$)		-0.00074

TABLE A.9. INFLUENCE OF STREAMING

Case	Δk TOTMOS+CITATION	Δk MCNP	$\Delta(\Delta k)$
KLAK holes filled	0.00853	0.00810	+0.00043
CR holes empty	($D_z/R_{\text{hole}}=1.08$)		
CR holes filled	0.00538	0.00564	-0.00026
KLAK holes empty	($D_z/R_{\text{hole}}=1.08$)		
CR + KLAK holes empty	0.01343	0.01232	+0.00111
	($D_z/R_{\text{hole}}=1.08$)		

TABLE A.10. EFFECTIVE MULTIPLICATION CONSTANTS
OBTAINED BY DIFFUSION AND MONTE CARLO CALCULATIONS

Case	K_{eff} Diffusion TOTMOS-CITATION	K_{eff} Monte Carlo MCNP4C3	Δk CITATION-MCNP
CR + KLAK holes filled	0.90719	0.90521±0.00034	+0.00198
CR + KLAK holes empty	0.89693 ($D_z/R_{\text{hole}} = 0.50$) 0.89555 (= 0.66)	0.89211±0.00030	+0.00482 +0.00344
$D_{r,\phi}/R_{\text{hole}} = 5.0$	0.89290 (= 1.0) 0.89231 (= 1.08)		+0.00079 +0.00020

TABLE A.11. INFLUENCE OF STREAMING

Case	Δk TOTMOS-CITATION	Δk MCNP	$\Delta(\Delta k)$
CR + KLAK holes empty	0.01429 ($D_z/R_{\text{hole}} = 1.0$) 0.01488 (= 1.08)	0.01310	+0.00119 +0.00178

When taking a core height of 126 cm (the upper cavity then has a height of 95.8 cm), the agreement between diffusion and Monte Carlo calculations was not so satisfying, as can be noticed in Tables A.10 and A.11. When the control rod and KLAK channels were filled with graphite, the effective multiplication factor of the diffusion calculation exceeded the Monte Carlo result by about $\Delta k = 0.002$, whereas the agreement was excellent ($\Delta k = 0.0002$) when all channels were empty and $D_{r,\phi}/R_{\text{holes}} = 5.0$, $D_z/R_{\text{hole}} = 1.08$. According to this reason, the streaming effect was overestimated in the diffusion calculation by about 13.6% compared to the Monte Carlo result.

In order to check this finding, diffusion and Monte Carlo calculations had been performed for four different core heights, namely, 126, 144, 162, and 180 cm, with all channels filled. The results given in Table A.12, together with the height of the core and of the upper cavity, showed that with increasing the cavity height, the difference between diffusion and Monte Carlo results was increasing too. Therefore, the anisotropic diffusion coefficients used in the upper cavity according to the formula of Gerwin and Scherer [A-15] were once more checked and more accurately calculated. However, as one can see in Table A.13, the k-effective values were not very sensitive to the accuracy of the input diffusion coefficients. Thus, the discrepancy in the k-effective values of diffusion and Monte Carlo calculations ($\Delta k = 0.002$) at a core height of 126 cm could not clearly be explained and the streaming effect seemed to be overestimated in the diffusion calculations. The following tables provide streaming test calculations using the simplified three dimensional (R,φ,Z) model of the HTR-10 with diffusion calculations with 26 group constants and $H_{\text{core}} = 126$ cm.

Streaming test calculations with a simplified three dimensional (R,φ,Z) model of the HTR-10 and diffusion calculations with 26 group constants.

TABLE A.12. EFFECTIVE MULTIPLICATION FACTORS AT DIFFERENT CORE HEIGHTS

Core Height (cm)	Height of the Upper Cavity (cm)	K_{eff} TOTMOS CITATION	K_{eff} MCNP	Δk CITATION-MCNP
126	95.8	0.90719	0.90521±0.00034	+0.00198
144	77.8	0.94154	0.94048±0.00035	+0.00106
162	59.8	0.96881	0.96824±0.00027	+0.00057
180	41.7	0.99094	0.99057±0.00039	+0.00037

TABLE A.13. DEPENDENCY OF K_{EFF} ON THE ACCURACY OF THE ANISOTROPIC DIFFUSION COEFFICIENTS

H_{core} (cm)	H_{cavity} (cm)	$H_{\text{cav.}}/R_{\text{core}}$	$D_{r,\phi}/R_{\text{cav.}}$	$D_z/R_{\text{cav.}}$	k_{eff}	k_{eff}
						$D_{r,\phi}/R_{\text{cav.}}=.1$
						$D_z/R_{\text{cav.}}=.5$
126	95.8	1.064	0.110	0.5166	0.90698	0.90719
144	77.8	0.864	0.110	0.512	0.94137	0.94154
162	59.8	0.664	0.1047	0.507	0.96875	0.96881
180	41.7	0.463	0.097	0.504	0.99096	0.99094

Comparison of the HTR-10 benchmark problems between diffusion and Monte Carlo calculational results

Temperature coefficients

As in our former benchmark calculations [A-16], the effective multiplication factors showed a strong temperature dependence. This effect has once more been investigated, varying the axial diffusion coefficients in the boring holes of the HTR-10 reactor. The radial and azimuthal diffusion coefficients remained unchanged ($D_{r,\phi}/R_{\text{hole}} = 5.0$) because it has been demonstrated in the comparative test calculations before that the k-effective values of diffusion and Monte Carlo calculations agreed well with $D_{r,\phi}/R_{\text{hole}} = 5.0$ (see Table A.6). The results are collected in Tables A.14 and A.15. As it can be seen, the difference between multiplication constants at different core temperatures is considerably high compared to the INET results [A-17] obtained by two dimensional diffusion calculation with VSOP. (A comparison with Monte Carlo results is not possible because INET only performed Monte Carlo calculations for one temperature. However, it can be noticed in Table A.14 that at a temperature of 20°C, the k-effective value of the diffusion calculation approaches the result of the Monte Carlo calculation when increasing the axial streaming correction factor.) The results show that this strong temperature dependence is almost not influenced by the neutron streaming effect in the channels of the control rods and KLAKs.

The following includes temperature coefficients of the detailed three dimensional (R,φ,Z) model of the HTR-10 with VSOP diffusion calculations with four group constants and leakage iteration $H_{\text{core}} = 180$ cm.

TABLE A.14. EFFECTIVE MULTIPLICATION FACTORS
AT DIFFERENT CORE TEMPERATURES (ORIGINAL BENCHMARK PROBLEM B2)

Diff. Corr. Factor Dz/Rhole	K _{eff} values		
	T = 200°C	T = 1200°C	T = 2500°C
0.50	1.12800	1.11466	1.09729
0.66	1.12611	1.11267	1.09531
1.00	1.12222	1.10877	1.09128
1.08	1.12137	1.10790	1.09039
2-D VSOP (INET)	1.1197	1.1104	1.0960
MCNP (INET)	1.12192±0.00082	-	-
0.50	$\Delta k = -0.0133$	$\Delta k = -0.0174$	
0.66	$\Delta k = -0.0134$	$\Delta k = -0.0174$	
1.00	$\Delta k = -0.0134$	$\Delta k = -0.0175$	
1.08	$\Delta k = -0.0135$	$\Delta k = -0.0175$	
2-D VSOP (INET)	$\Delta k = -0.0093$	$\Delta k = -0.0144$	

Temperature coefficients of the detailed three dimensional (R,φ,Z) model of the HTR-10 using VSOP diffusion calculations with four group constants and leakage iteration $H_{core} = 180$ cm.

TABLE A.15. EFFECTIVE MULTIPLICATION FACTORS
AT DIFFERENT CORE TEMPERATURES (DEVIATED BENCHMARK PROBLEM B2)

Diff. Corr. Factor Dz/Rhole	K _{eff} values		
	T = 200°C	T = 1200°C	T = 2500°C
0.50	1.13814	1.12451	1.10677
0.66	1.13627	1.12261	1.10488
1.00	1.13251	1.11880	1.10094
1.08	1.13166	1.11790	1.10006
(Air Atmosphere)			
2-D VSOP (INET)	1.13578	1.12616	1.11112
MCNP (INET)	1.13813	-	-
(He Atmosphere)			
0.50	$\Delta k = -0.0136$	$\Delta k = -0.0177$	
0.66	$\Delta k = -0.0137$	$\Delta k = -0.0177$	
1.00	$\Delta k = -0.0137$	$\Delta k = -0.0179$	
1.08	$\Delta k = -0.0138$	$\Delta k = -0.0178$	
2-D VSOP (INET)	$\Delta k = -0.0096$	$\Delta k = -0.0150$	

When splitting up the temperature coefficient into fuel, moderator and reflector coefficients, the calculations showed that the moderator coefficient dominated the total value and thus was responsible for the strong temperature dependence. However, when considering the experimental results as mentioned by Sun [A-18] and comparing them with the corresponding temperature coefficient

calculations, shown in Fig. A.7, it becomes clear that there is a good agreement between the experiment and calculation in the temperature region of 160–230°C, whereas at lower average core temperatures, the discrepancy is considerable. This effect shows that it is extremely difficult to simulate a temperature distribution in the whole-core calculations corresponding to experimental conditions.

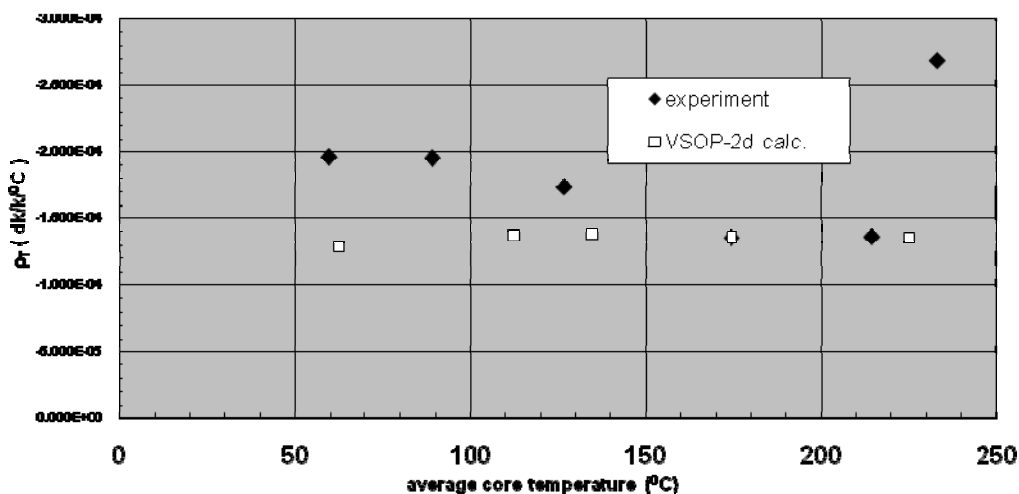


FIG. A.7. HTR-10 temperature coefficients.

Control rod worths

In addition, when varying the axial streaming correction factors in the empty channels of the whole-core calculations performed in order to determine the reactivity worth of one and of ten control rods, the tendency was the same as in the case of the temperature coefficient calculations as the control rod worths themselves remained almost unchanged. All results for the control rods at full core and at a core height of 126 cm are summarized in Tables A.16 and A.17 together with the Monte Carlo results of INET. In both cases, the reactivity worth of ten and of one control rod(s) are slightly decreased when increasing the axial diffusion coefficient. The reactivity worth of one control rod was overestimated by about 11% compared to the Monte Carlo result when using a streaming correction factor of $D_z/R_{\text{hole}} = 0.50$ in the diffusion calculation. By the increase of this diffusion coefficient up to 1.08, the overestimation was reduced to 9%. On the other hand, when considering the standard deviation given for the Monte Carlo calculations of INET [A-17], the reactivity worth of one single control rod lays in between the statistical uncertainty (2σ) i.e. $\Delta\rho/\rho = 18.7\%$ in the case of the full core and $\Delta\rho/\rho = 20.7\%$ in the case of the 126 cm core height.

When comparing the multiplication constants themselves, it is once more remarkable that there is a quite good agreement between diffusion and Monte Carlo results at a core height of 180 cm and $D_z/R_{\text{hole}} = 1.0$ or 1.08, whereas at a loading height of 126 cm, the difference between corresponding multiplication factors increases with increasing the axial streaming correction factor. This effect cannot be explained and has to be examined in future.

The following includes the control rod worth of the detailed three dimensional (R,φ,Z) model of the HTR-10 using VSOP diffusion calculations with four group constants and leakage iteration $H_{\text{core}} = 180$ cm.

TABLE A.16. REACTIVITY WORTH OF THE CONTROL RODS AT FULL CORE
(ORIGINAL BENCHMARK PROBLEM B3)

Case	K_{eff}	Δk	$\Delta\rho\%$
	VSOP-CITATION	MCNP- CITATION	
Unrodded Core	1.12797	-0.006	
$D_z/R_{\text{hole}}=0.50$	1.12606	-0.004	
$= 0.66$	1.12222	-0.0003	
$= 1.00$	1.12135	+0.0006	
$= 1.08$			
10 Rods Inserted	0.94917	-0.003	16.70
$D_z/R_{\text{hole}}=0.50$	0.94882	-0.0027	16.59
$= 0.66$	0.94809	-0.002	16.37
$= 1.00$	0.94793	-0.002	16.31
$= 1.08$			
1 Rod Inserted	1.10832	-0.004	1.572
$D_z/R_{\text{hole}}=0.50$	1.10658	-0.002	1.563
$= 0.66$	1.10307	+0.0013	1.547
$= 1.00$	1.10228	+0.0021	1.543
$= 1.08$			
MCNP (INET)	1.12192 \pm 0.00082		
Unrodded	0.94611		16.56
10 Rods Inserted	1.10441		1.413
1 Rod Inserted			

The following includes the control rod worths of the detailed three dimensional (R, ϕ ,Z) model of the HTR-10 using VSOP diffusion calculations with four group constants and leakage iteration $H_{\text{core}} = 126$ cm.

TABLE A.17. REACTIVITY WORTH OF THE CONTROL RODS AT 126 CM CORE HEIGHT (ORIGINAL BENCHMARK PROBLEM B4)

Case	K_{eff} VSOP-CITATION	Δk MCNP- CITATION	$\Delta\rho\%$
Unrodded Core			
Dz/Rhole = 0.50	0.99665	+0.0030	
= 0.66	0.99437	+0.0053	
= 1.00	0.98970	+0.0100	
= 1.08	0.98970	+0.0110	
10 Rods Inserted	0.82685	+0.0107	20.60
Dz/Rhole=0.50	0.82638	+0.0112	20.44
= 0.66	0.82543	+0.0121	20.11
= 1.00	0.82522	+0.0123	20.05
= 1.08			
1 Rod Inserted	0.97717	+0.0050	2.000
Dz/Rhole=0.50	0.97506	+0.0070	1.992
= 0.66	0.97090	+0.0112	1.956
= 1.00	0.96988	+0.0122	1.976
= 1.08			
MCNP (INET)	0.99965±0.00091		19.36
Unrodded	0.83756		1.793
10 Rods Inserted	0.98205		
1 Rod Inserted			

Critical core height

When determining the critical core height of the HTR-10 initial core by the three dimensional diffusion calculation, the result is very sensitive to the consideration of the increased neutron streaming in the control rod and KLAK channels. In our former three dimensional diffusion calculations in R,φ,Z geometry, we had the best results when assuming an axial streaming correction factor of $D_z/R_{\text{holes}} = 0.50$ or 0.66 as can be noticed in Tables A.18 and A.19 and Figs A.8 and A.9. The k-effective values of the diffusion calculations are presented there as a function of the the core loading height and of four different axial diffusion coefficients. In the case of the deviated benchmark problem which corresponds to the critical experiment, the deviation from the experimental H_{crit} amounts to $\Delta H = 0.5$ cm with $D_z/R_{\text{holes}} = 0.50$, but increases up to 2.8 cm when inltcreasing the axial diffusion coefficient to the value of 1.08.

In both benchmark problems the H_{crit} -value is determined by the multiplication factors at 120 cm and 126 cm core height. As shown above in the case of the control rod worth, the agreement between diffusion and Monte Carlo calculation gets worse with increased axial neutron streaming at these low core loading heights with large upper cavities. At a heigher core loading or at full core, the diffusion and Monte Carlo calculations agree better when increasing the axial neutron streaming in the empty channels of the HTR-10 core model. Thus, we have two contradicting effects which cannot be clearly explained and need further investigation.

TABLE A.18. MULTIPLICATION FACTORS AS A FUNCTION OF THE CORE LOADING HEIGHT AND OF THE AXIAL DIFFUSION COEFFICIENT (ORIGINAL BENCHMARK PROBLEM B1)

H_{core} (cm)	K_{eff} -values at $T = 200^{\circ}\text{C}$				K_{eff} at $T = 270^{\circ}\text{C}$
	VSOP-CITATION				MCNP (INET)
	3-D geometry				
	D_z/R_{holes} = 0.50	D_z/R_{holes} = 0.66	D_z/R_{holes} = 1.00	D_z/R_{holes} = 1.08	
180.12	1.12803	1.12607	1.12223	1.12138	1.12192±0.00082
150.10	1.06607	1.06396	1.05977	1.05880	1.06201±0.00081
130.09	1.01009	1.00782	1.00334	1.00232	
126.00	0.99653	0.99424	0.98970	0.98883	0.99965±0.00091
120.08	0.97632	0.97411	0.96948	0.96845	0.98148±0.00088
H_{crit} (cm)	127.0	127.7	129.1	129.3	126.1
Deviation in cm from $H_{\text{crit}}(\text{MCNP})$	+0.9	+1.6	+3.0	+3.2	

TABLE A.19. MULTIPLICATION FACTORS AS A FUNCTION OF THE CORE LOADING HEIGHT AND OF THE AXIAL DIFFUSION COEFFICIENT (DEVIATED BENCHMARK PROBLEM B1)

H_{core} (cm)	K_{eff} values at $T = 20^{\circ}\text{C}$				k_{eff} at $T = 27^{\circ}\text{C}$
	VSOP-CITATION				MCNP (INET)
	3-D geometry				
	D_z/R_{holes} = 0.50	D_z/R_{holes} = 0.66	D_z/R_{holes} = 1.00	D_z/R_{holes} = 1.08	
180.12	1.13811	1.13626	1.13249	1.13165	1.13813 (He atm.)
150.10	1.07678	1.07471	1.07057	1.06968	
130.09	1.02126	1.01903	1.01464	1.01367	
126.00	1.00807	1.00581	1.00144	1.00045	1.01002 ±0.00087 (Air atm.)
120.08	0.98769	0.98541	0.98098	0.98001	0.99079±0.00080 (Air atm.)
H_{crit} (cm)	123.6	124.3	125.6	125.9	122.9
Deviation in cm from $H_{\text{crit}}(\text{exp.})$ = 123.1	0.5	1.2	2.5	2.8	-0.2

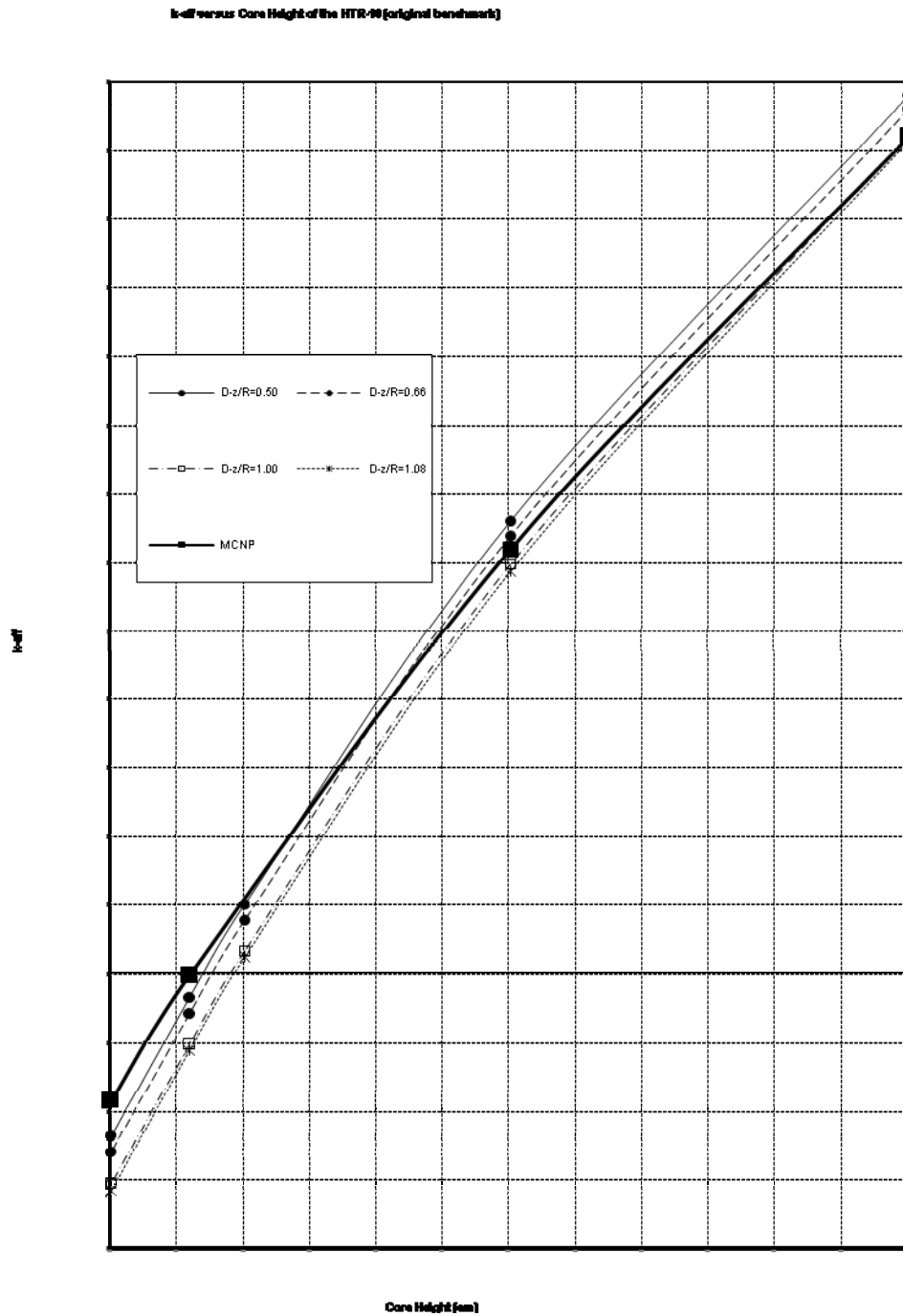


FIG. A.8. Influence of different streaming correction factors on k_{eff} of the HTR-10 (original benchmark).

k-eff versus Core Height of the HTR-10 (deviated benchmark)

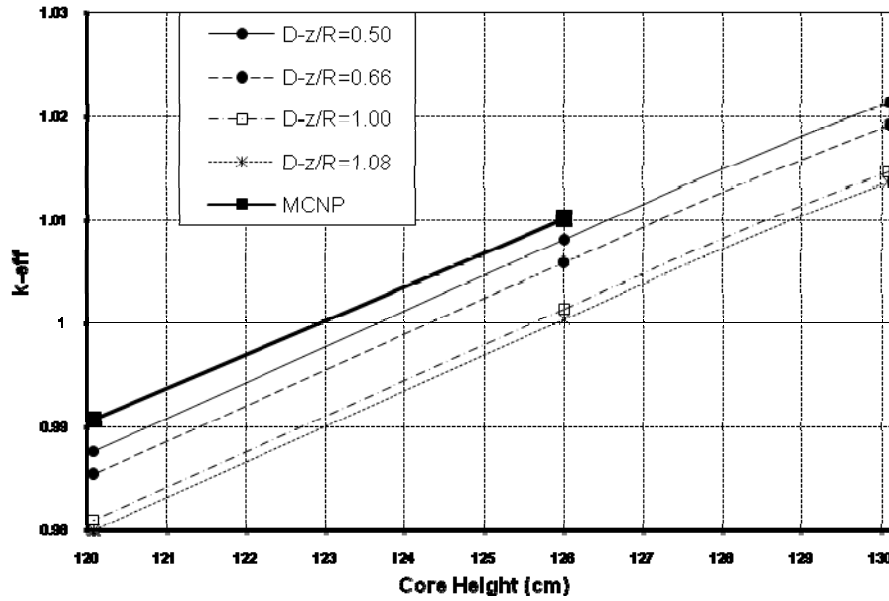


FIG. A.9. Influence of different streaming correction factors on k_{eff} of the HTR-10 (deviated benchmark).

Conclusion

In order to adequately calculate the increased neutron streaming in the boring holes of the HTR-10 core, corresponding streaming effects obtained by diffusion and by Monte Carlo calculations were compared using a simplified HTR-10 core model, but with identical geometry and identical void regions as in the detailed core model. The comparison showed that the streaming effects in the diffusion and Monte Carlo calculations agreed well when assuming the anisotropic diffusion coefficients to be $D_{r,\phi}/R_{hole} = 5.0$ and $D_z/R_{hole} = 1.08$ in the control rod and KLAK boring holes of this simplified core model.

Thus, in the recalculation of the detailed HTR-10 benchmark problems (first criticality, temperature coefficients and control rod worths), these modified anisotropic diffusion coefficients were used. The present investigations demonstrated that the temperature coefficients and the control rod worths remained almost unchanged. Only when comparing the multiplication factors themselves can it be noticed that at full core, the agreement between diffusion and Monte Carlo results is satisfactory, but at 126 cm loading height of the pebbles in the core, there is a remarkable discrepancy between diffusion and Monte Carlo calculational results when increasing the axial neutron streaming. Therefore, when calculating the critical core height, the agreement between three dimensional diffusion and Monte Carlo calculation is not as good as in the former calculations with an axial streaming correction factor of $D_z/R_{hole} = 0.50$ and a deviation of about 0.6%. This deviation increases up to 2.5% when increasing the axial streaming correction factor.

A.4. NETHERLANDS

Introduction

Calculations have been performed by NRG-Petten within the framework of the HTR-10 initial core benchmark [A-19]. The HTR-10 is the Chinese prototype pebble bed gas cooled reactor. For a description and the main data of the reactor, reference is made to the Benchmark Description [A-19].

Codes and methodology

The HTR-10 has been modelled in the PANTHERMIX code [A-20], a combination of the 3-D diffusion reactor code PANTHER 5.1 [A-21] coupled to the 2-D thermohydraulics code THERMIX./DIREKT [A-22]. The nuclear data necessary for the PANTHER code has been generated by means of the WIMS8 [A-23] code system.

Cell calculations

Library

The calculations with WIMS8 has been performed with an adapted version of the standard 172-groups 1997 WIMS library based on JEF-2.2. Adaptations has been made for plutonium, americium and curium isotopes to extend the range of temperatures and of the potential scattering to improve the resonance treatment.

Calculational method

The method followed to overcome the impossibility of modelling the pebbles on coated fuel particle (CFP) scale is to model a cylindrical cell with an equivalent radius. This method has been proved adequate in the PROTEUS benchmark.

The spherical pebble is transformed into an infinitely long cylinder but with the same mean chord length. The mean chord length of a concave body is given by the simple relation: four times the ratio of volume over surface.

So the fuelled part of the pebble (radius 2.5 cm) is translated into a cylinder of 1.667 cm radius and contains the fuel kernels, coatings and matrix graphite. This cylinder is surrounded by an annulus of radius 2.191 cm to accommodate the unfuelled shell of 0.5 cm based on conservation of volume ratio. Finally, the radius of the outer cylinder which contains the admixed moderator pebbles and the void between the pebbles amounts to 3.716 cm in our model. These dimensions and densities are fed into the WIMS module WPROCOL to produce collision probabilities for use in the resonance treatment for U235, U238 and Pu239 in WRES after an approximate resonance treatment in WHEAD for all other resonant isotopes not treated explicitly in WPROCOL/WRES. This treatment is based on equivalence theory with calculated potential scatter cross-section applied on slabs with thickness according to mean chord lengths of the fuel kernel, coatings and matrix graphite belonging to the kernel. In this approximation, a Dancoff factor has been used which is derived analytically to account for the double-heterogeneity of kernels and pebbles [A-24]. After smearing and condensation of the pebble and kernel materials to one material and in 16 neutron energy groups, a pseudo-reactor calculation has been started in the axial direction (infinite radius) as well as in the radial direction (infinite length) in the real reactor dimensions. This has been done for the case without control rods (unrodded) and with control rods inserted (rodded).

Three kinds of control rod banks have been used:

- (a) the normal control rods to govern the power level;
- (b) the KLAK system for cold shut-down of the reactor;
- (c) a 'gas' control rod bank. This is a control rod bank which comprises all core channels in the PANTHER model. This bank in the unrodded state returns the nuclear data of the fuel in the unrodded axial meshes of the core; in the rodded state it returns the nuclear data of the helium void on top of the pebble bed in the rodded axial intervals. By moving this 'gas' rod in and out, one can simulate the level of the pebble bed height in the core. The gas space above the pebble bed has 'artificial' and anisotropic diffusion coefficients obtained according to the Gerwin-Scherrer method [A-15].

KLAK system and control rod calculations have been performed for the radial pseudo-reactor calculations by means of the WIMS CACTUS-module (Fig. A.10.). After these pseudo-reactor calculations, the materials comprising the reactor were smeared and condensed into two neutron groups, one thermal and one fast neutron group, for the PANTHER full-core calculations. The division between the thermal and the fast energy group was at 2.1 eV.

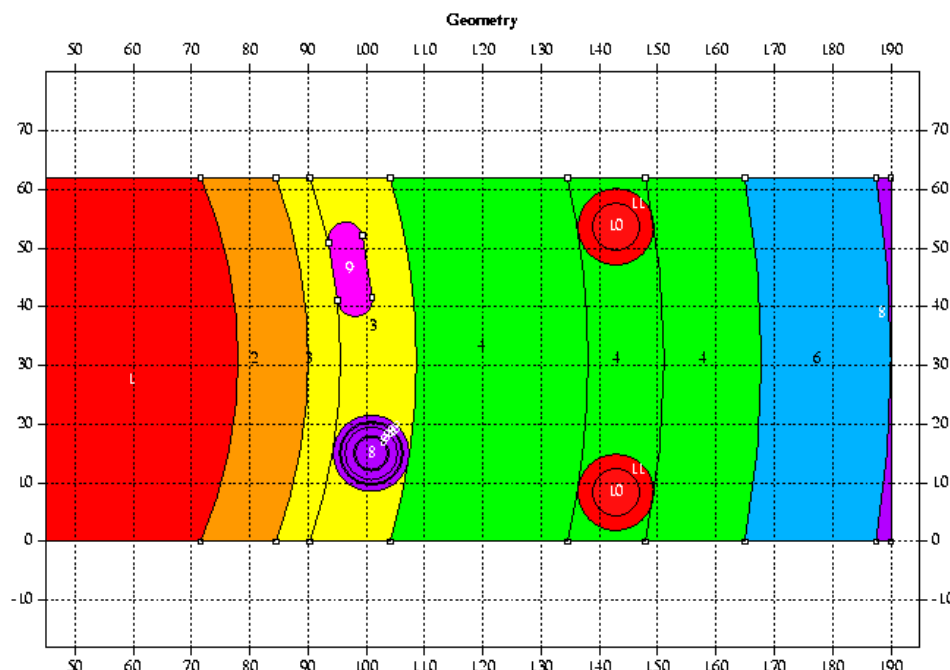


FIG. A.10. CACTUS model of control rod holes, KLAK holes and coolant channels.
The red and orange areas on the right are part of the core.

These pseudo-reactor calculations were done for different depletion levels and at different temperatures. In this way a database has been constructed, which is temperature, burnup, control rod and xenon-dependent, in which PANTHER can perform a multidimensional interpolation in the nuclear data, according to the local condition in the reactor.

Core calculations

PANTHER

The HTR-10 has been approximated in the diffusion code PANTHER in the 3-D X-Y-Z mode with radial 861 square meshes (channels) of 11.48 cm by 11.48 cm and 52 axial intervals of different height but over the core height, all are 11.10 cm high. The full model comprises 193 core channels, 668 reflector channels, 20 core layers (plus 8 layers to model the bottom cone), 14 bottom reflector layers and 10 top reflector layers. The size of the square mesh has been chosen such that concentric ‘rings’ can be composed from these meshes in a manner that those rings fit snugly with the main radial dimensions of the reactor structures (Figs A.11–A.13).

Each mesh in the PANTHER model contains a distinct material with a corresponding set of nuclear data. In each mesh the nuclear data will be generated according to the local burnup, temperature, etc. from the nuclear database to perform a new time step. An algorithm has been added to PANTHER to simulate the flow of the pebbles through the reactor after each time step by means of transfer of basic parameters (local burnup) to the neighbouring meshes and to keep track of the classes of the local burnup distribution.

The aforementioned rings coincide with the radial meshing of the thermohydraulic code THERMIX, part of the PAN(THER THER)MIX code package. They are used to transfer the power distribution from PANTHER to THERMIX and receive back the temperature field from THERMIX.

CORE CHANNELS

UNITS = WATTS

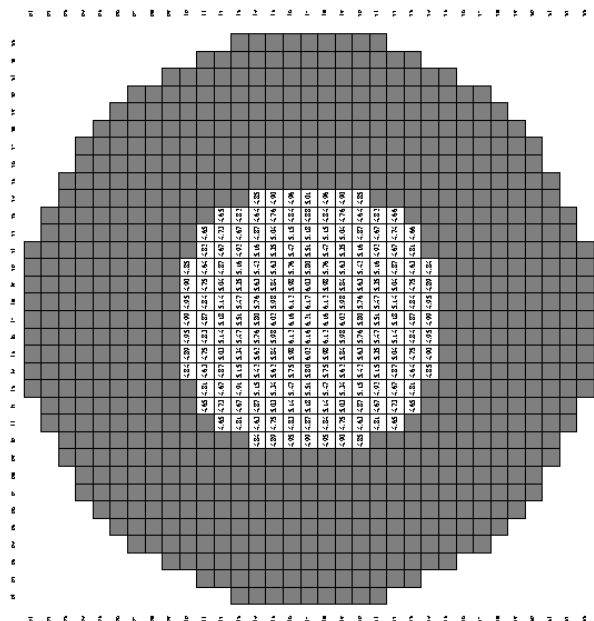


FIG. A.11. Layout of the core and reflector channels in PANTHER.

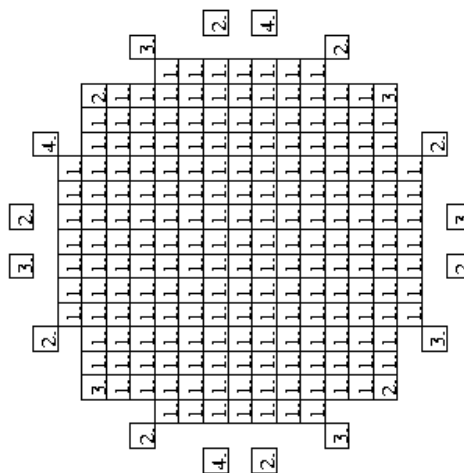


FIG. A.12. Layout of the rod types. The 'gas' rod bank, which insertion determines the core height, is indicated by a 1, the normal control rods in the reflector are numbered with a 2, the KLAKE system by a 3 and the instrumentation channels are designated by a 4.

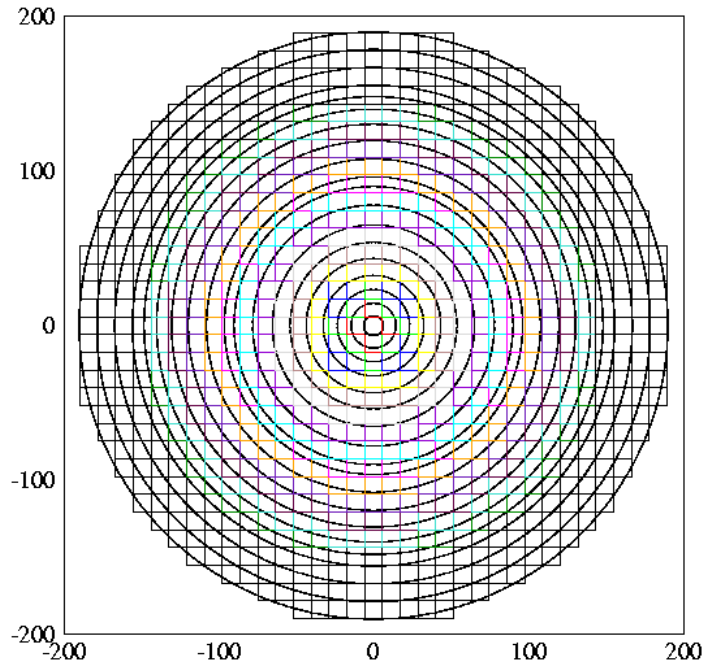


FIG. A.13. Reactor channels and assigned rings to correspond with the 2-D R-Z THERMIX model.

THERMIX

THERMIX or, better, the THERMIX/DIREKT code, is a 2-D R-Z thermohydraulics code to calculate the temperature distribution for the solid and gaseous materials in the reactor from a given power distribution (by PANTHER). For the mapping of the 3-D power profile on the 2-D grid of THERMIX, the power in the squares which form a 'ring' in PANTHER are radially averaged and transferred to the mesh in THERMIX. For the temperature profile from THERMIX, the values for an R-Z set are unfolded to a PANTHER ring. There are 19 radial rings comprising the PANTHER model and 22 radial meshes in the THERMIX model of which the extra meshes form the boundary conditions. The THERMIX part of the code solves the (time dependent) equations for the conductive and radiative heat transfer, whereas DIREKT solves the (time dependent) equations for the heat transfer from solid material to the gaseous coolant and the continuity equation of the gas flow. Contrary to the thermohydraulic options in PANTHER, THERMIX allows for cross-channel flows necessary to simulate natural convection in a situation without mass flow.

The complex heat transfer and heat conductivity in the pebble bed is chosen as modelled in THERMIX according to the Zehner-Schlünder method [A-25].

Thermal data like heat conductivity and heat capacity of the different materials are calculated as a function of temperature and pressure according to built-in equations. For the graphite, the properties of un-irradiated A3 grade have been used.

HTR-10 BENCHMARK results

HTR-10 critical core level

Under benchmark conditions, with an isothermal reactor temperature of 20°C, the control rods at 114.7 cm and atmospheric helium in the coolant spaces, a critical search on the core level ('gas'rod insertion) has been performed by PANTHER. The critical core level was found to be:

$$H_{\text{crit}} = 125.3 \text{ cm},$$

above the bottom cone filled with moderator balls.

HTR-10 isothermal temperature coefficient

With the reactor at isothermal temperatures of 20, 120, 200 and 250°C and a core height of 180 cm (full core), PANTHER calculated the corresponding multiplication factor.

According to the definition of $\rho(T) = (k_{T1} - k_{T2}) / ((k_{T1} * k_{T2}) * (T_1 - T_2))$ we found the following values, listed together with the values as obtained by VSOP at INET in Table A.20:

TABLE A.20. TEMPERATURE COEFFICIENTS OF REACTIVITY COMPARISON

Temp (°C)	k _{eff} INET	k _{eff} NRG	ρ(T) NRG	ρ(T) INET
20	1.119747	1.11759		
120	1.110435	1.10846	-7.37E-05	-7.49E-05
200		1.10115	-7.49E-05	
250	1.095961	1.09629	-8.05E-05	-9.15E-05
		average	-7.64E-05	-8.32E-05

HTR-10 scram reactivity

With the core level at 180.0 cm (full core) and a uniform reactor temperature of 20°C, the insertion of the control rods from 119.2 cm to 394.2 cm gave rise to a reactivity effect of:

$$\rho_{\text{scram}} = 0.1186.$$

And with the core level at 125.3 cm (critical level) and a uniform reactor at of 20°C,

the insertion of the control rods from 119.2 cm to 394.2 cm gave rise to a reactivity effect of:

$$\rho_{\text{scram}} = 0.1367.$$

This is rather low compared with the measured data of 0.18 (INET) and can probably be explained by strong steaming in the holes to accommodate the control rods and the KLAK system. Recalculations will be done later with modified anisotropic diffusion coefficients according to the Behrens method.

HTR-10 control rod worth

TABLE A.21. CONTROL ROD WORTHS

rod fract.	rod (cm)	k _{eff}
0.00	0.0	1.00233
0.05	30.5	1.00234
0.10	61.0	1.00219
0.15	91.5	1.00156
0.20	122.0	1.00005
0.25	152.5	0.99342
0.30	183.0	0.98584
0.35	213.5	0.97838
0.40	244.0	0.96887
0.45	274.5	0.94921
0.50	305.0	0.91803
0.55	335.5	0.89298
0.60	366.0	0.88344
0.65	396.5	0.88153

With the reactor at 20°C and the core level at 125.3 cm, a series of calculations has been done for different insertion fractions of all control rods (Table A.21). Fraction 0 is at the top of the reactor and fraction 1 at the bottom of the reactor: 610 cm (Fig. A.14).

Calculation of the worth for a single control rod is not sensible because in our model, as can be seen from Fig. A.13, the control rods are on three distinct positions with only the average midpoint radius equal to the stated radius.

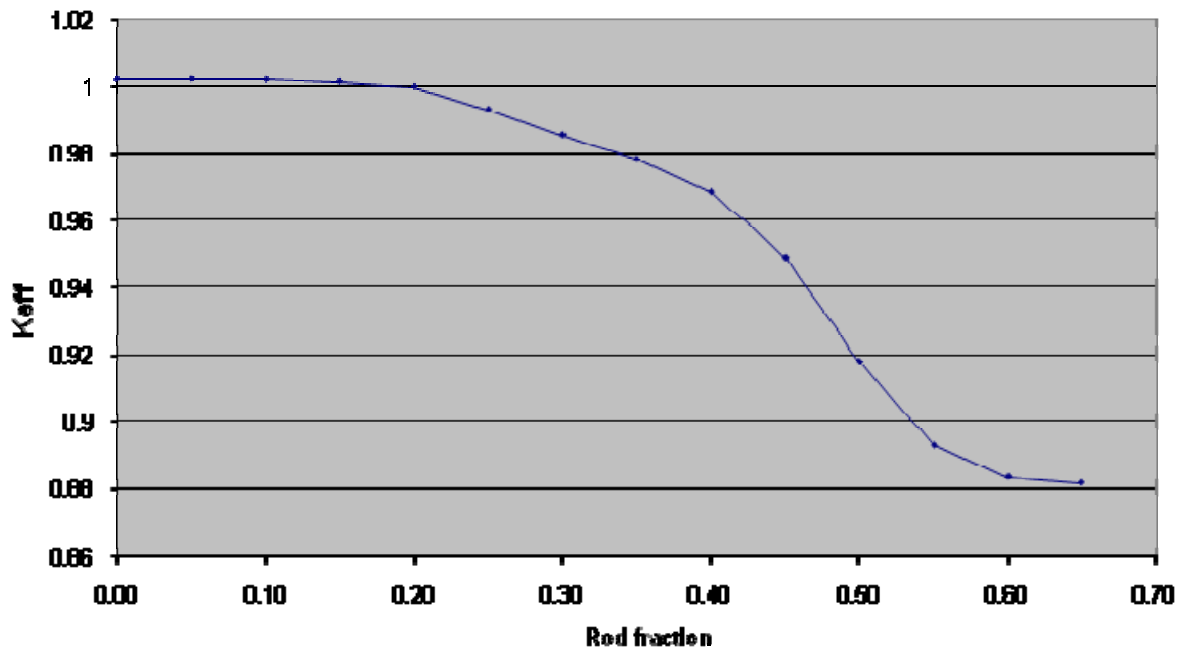


FIG. A.14. Reactivity of the reactor as function of the control rod bank insertion for the critical core (core level at: 125.3 cm).

Full power calculations

A thermohydraulics model has been built to be able to calculate the full power (10 MW) conditions as flux distributions, power distribution, solid structure temperatures and coolant temperature and mass flow over the reactor. Results for the hot critical initial core (core level at 155 cm) can be seen in Figs A.15–A.18.

Some key values are:

Maximum pebble temperature	867 °C;
Maximum coolant temperature	804 °C;
Maximum power density	3.41 MW/m ³ ;
Pressure difference inlet/outlet	0.017 bar.

Planned activities

A re-evaluation of the control rod model with anisotropic diffusion coefficients as well as transient calculations is foreseen. After installation of the flow pattern for the pebbles, burnup calculations can be done and an equilibrium core can be investigated.

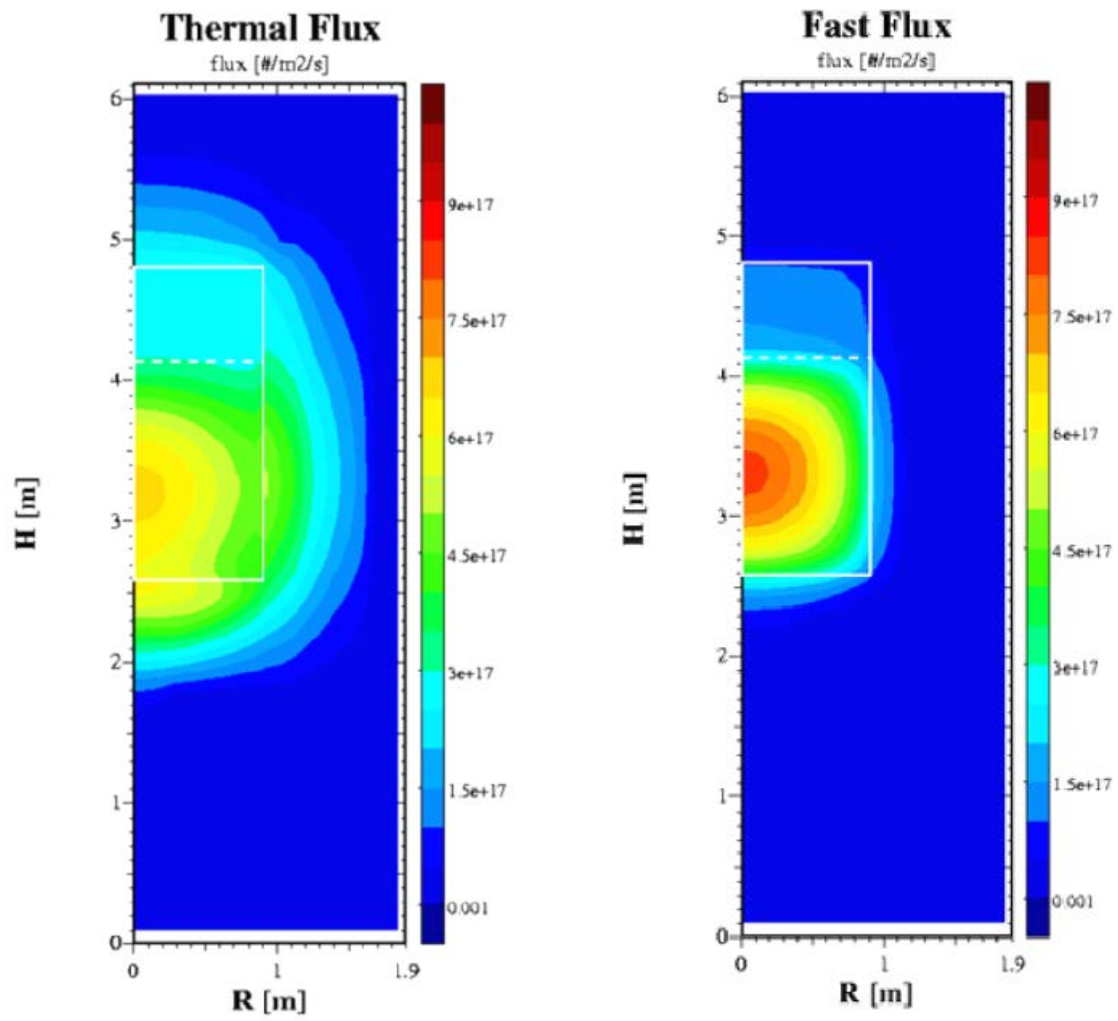


FIG. A.15. Thermal and fast flux (fluence rate) over the reactor. White lines indicate the core boundaries whereas the dashed line gives the core level.

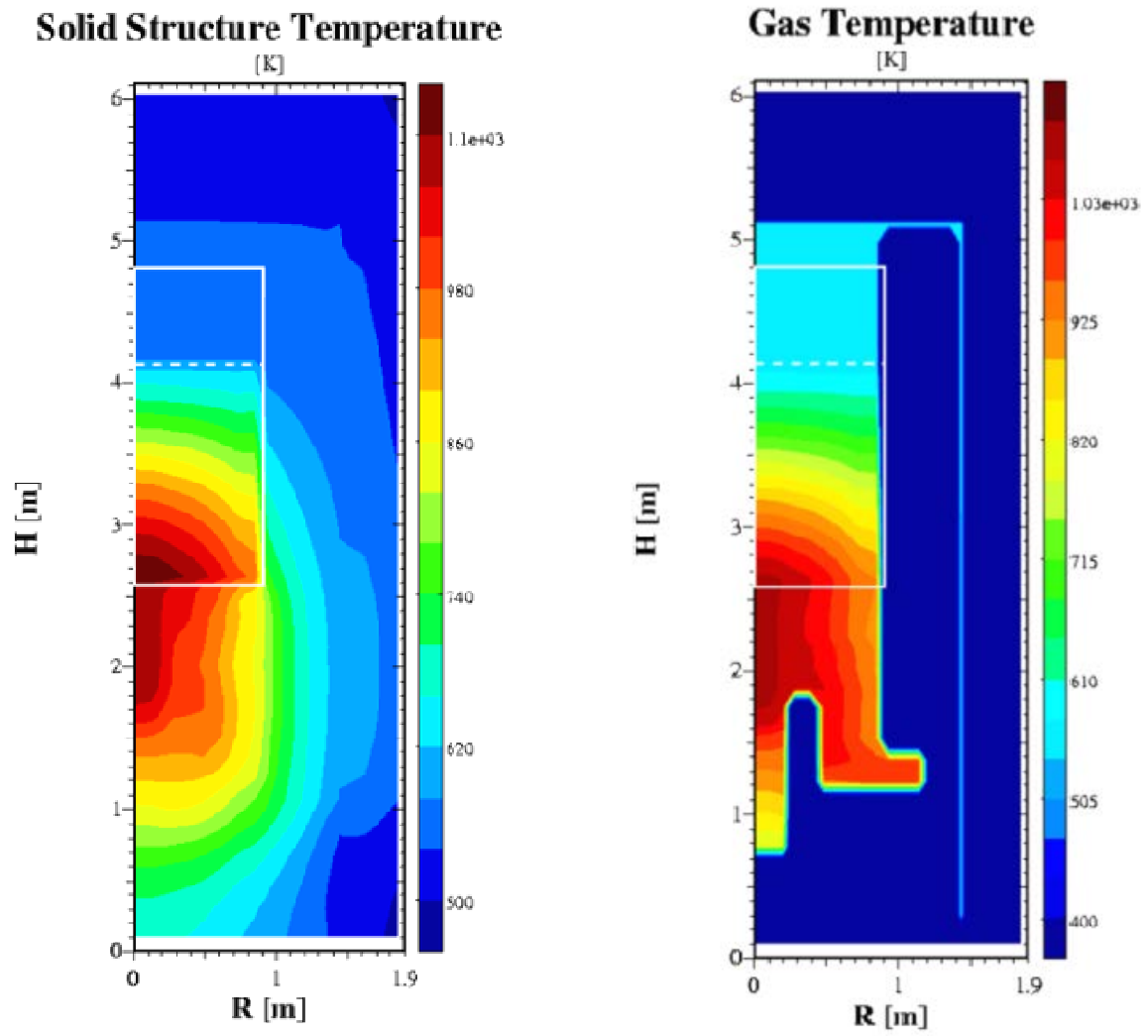


FIG. A.16. Temperature distribution for the coolant and reactor structure in kelvin.

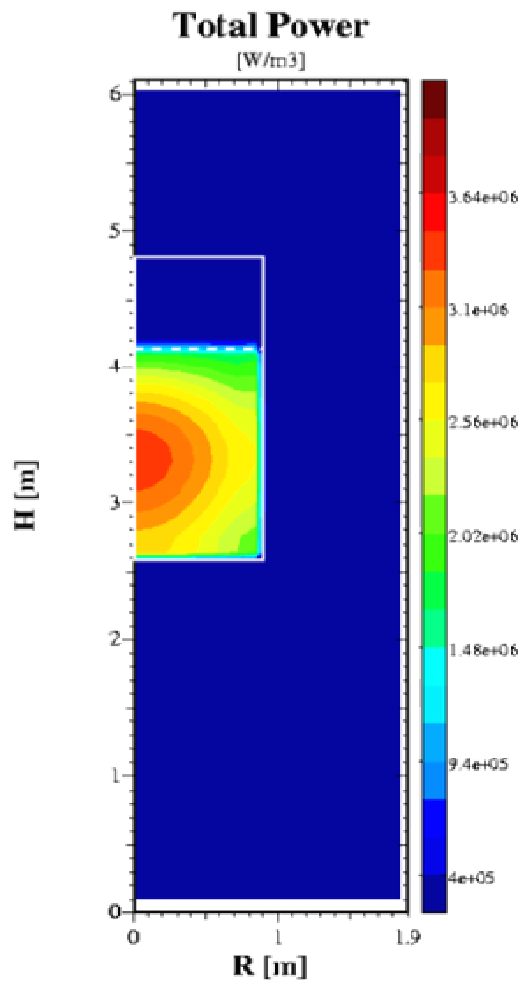


FIG. A.17. Power density distribution at full power.

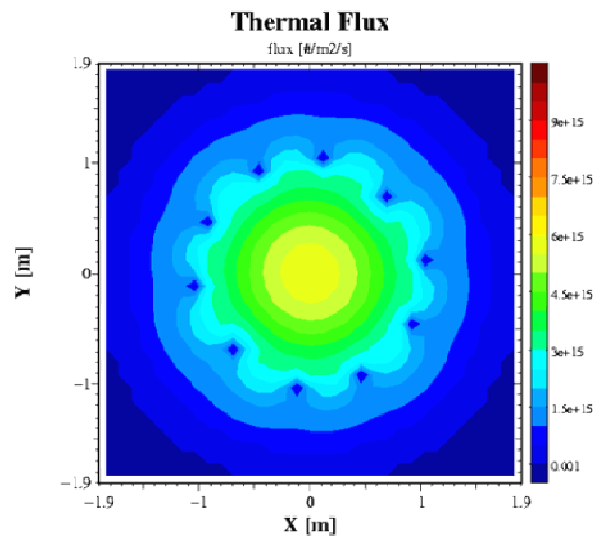


FIG. A.18. Radial plot of the thermal flux over the reactor with inserted control rods (arbitrary units).

A.5. REFERENCES FOR APPENDIX

- [A-1] AZIZ, F., et al., “Post-criticality Analysis of China’s High Temperature Reactor HTR-10,” Proceedings of National Workshop on Computation in Nuclear Science and Technology, Jakarta (July 4-5, 2001) (in Indonesian).
- [A-2] AZIZ, F., “Progress Report for the 5th Coordinated Research Programme on Evaluation of HTGR Performance,” National Nuclear Energy Agency of Indonesia, Serpong, Indonesia (2004).
- [A-3] TSUCHIHASHI, K., et al., Revised SRAC Code System, JAERI 1302 (1986).
- [A-4] OKUMURA, K., “SRAC95: The comprehensive neutronics calculation code system,” JAERI (unpublished).
- [A-5] JING, X., SUN, Y., “Benchmark Problem of HTR-10 Initial Core,” Draft Version, INET, Beijing (1998).
- [A-6] FOWLER, T.B., et al., :Nuclear Reactor Core Analysis Code: CITATION,” ORNL-TM-2496, Rev.2, Oak Ridge, United States of America (July 1971).
- [A-7] SUN, Y., JING, X., Benchmark Problems of the HTR-10 Initial Core Prepared for the IAEA Coordinated Research Programme CRP-5, 2nd RCM of the IAEA CRP-5, Beijing, China, 18.-22 (October 1999).
- [A-8] OHLIG, U., BROCKMANN, H., “Neutron Streaming Correction and its Validation on the Basis of the HTR-10 Benchmark Problems,” FZJ Research Centre Jülich, ISR, Jülich, Germany (November 2004).
- [A-9] BRIESTMEYER, J.F. (Ed.), MCNP-A general Monte Carlo N-particle Transport Code (Version 4C), LA-13709-M (March 2000).
- [A-10] GREENE, N.M., et al., “AMPX-77: A Modular Code System for Generating Coupled Multigroup Neutron-Gamma,” Cross-Section Libraries from ENDF/B-IV and/or ENDF/B-V, Oak Ridge National Laboratory, ORNL/CSD/TM-282 (Oct. 1992).
- [A-11] BROCKMANN, H., “TOTMOS: An Integral Transport Code for Spectrum Calculations,” FZ-Jülich, ISR, Jülich, Germany (1995).
- [A-12] PHLIPPEN, P., Private Communication (1994).
- [A-13] ROWLANDS, J., TUBBS, N., “JEF-2.2 Nuclear Data Libraries, The Joint Evaluated File: A New Data Resource for Reactor Calculations,” Proc. Int. Conf. on Nuclear Data for Basic and Applied Science, Santa Fe N.M., United States of America (1985).
- [A-14] BROCKMANN, H., OHLIG, U., “Test Calculations with Leakage Feedback For Annular Core Assemblies,” FZ-Jülich, FZJ-ISR-IB-2/2000, Jülich, Germany (2000).
- [A-15] GERWIN, H., SCHERER, W., “Treatment of the Upper Cavity in a Pebble-Bed High-temperature Gas-cooled Reactor by Diffusion Theory,” Nuc. Sci. Eng. 97, 9–19 (1987).
- [A-16] OHLIG, U., “Calculational Results for the Benchmark Problems of the HTR-10 Initial Core,” 4th RCM of the IAEA CRP-5, Vienna, Austria, 6–10 (October 2002).
- [A-17] SUN, Y., JING, X., “Benchmark Problems of the HTR-10 Initial Core,” 3rd RCM of the IAEA CRP-5, Oarai, Japan (16–19 March 2001).
- [A-18] SUN, Y., Private Communication (July 2003).
- [A-19] JING, X., SUN, Y., Benchmark Problem of the HTR-10 Initial Core (Draft Version), Institute of Nuclear Energy Technology, Tsinghua University, Beijing, December 1998.
- [A-20] OPPE, J., DE HAAS, J.B.M., KUIJPER, J.C., PANTHERMIX: A PANTHER-THERMIX interaction. Technical Report ECN –I-96-022, Netherlands Energy Research Foundation (ECN) Petten, Netherlands, May 1996.

- [A-21] HUTT, P.K., Overview Functional Specification of PANTHER: A Comprehensive Thermal Reactor Code for Use in Design, Assessment and Operation. Technical Report PANTHER/FSPEC/OVERVIEW 2.0, Nuclear Electric Plc., United Kingdom, December 1992.
- [A-22] STRUTH, S., THERMIX-DIREKT: Ein Rechenprogramm zur instationären, zweidimensionalen Simulation Thermohydraulischer Transienten. Forschungszentrum Juelich GmbH, September 1995.
- [A-23] AEA Technology: The ANSWERS Software Package WIMS. (A WIMS Modular Scheme for Neutronics Calculations). User Guide ANSWERS/WIMS. Atomic Energy Agency Technology (AEA), Winfrith, United Kingdom, 1997.
- [A-24] BENDE, E.E., HOGENBIRK, A.H., KLOOSTERMAN, J.L., VAN DAM, H., Analytical Calculation of the Average Dancoff-factor for a Fuel Kernel in a Pebble-Bed High Temperature Reactor. Nuclear Science and Engineering, 133: 147–162, October 1999.
- [A-25] ZEHNER, P., SCHLÜDER, E.U., Einfluss der Wärmestrahlung und des Druckes auf der Wärmetransport in nicht durchströmten Schüttungen. Chemie-Ing.-Technik, 44:1303, 1972.

CONTRIBUTORS TO DRAFTING AND REVIEW

Aziz, F.	National Nuclear Energy Agency (BATAN), Indonesia
Badulescu, A.	International Atomic Energy Agency, Austria
Ball, S.	Oak Ridge National Laboratory, United States of America
Brey, H.	United States of America
Brey, V.	United States of America
Brockmann, H.	FZJ, Germany
Caron-Charles, M.	Organization for Economic Co-operation and Development/Nuclear Energy Agency, France
Chang, J.	Korea Atomic Energy Research Institute, Republic of Korea
Colak, U.	Hacettepe University, Turkey
De Haas, J.B.M.	Nuclear Research and Consultancy, Netherlands
Dong, Y.	Institute of Nuclear and New Energy Technology, China
Du Toit, J.	Potchefstroom University, South Africa.
Emslie, F.	Pebble Bed Modular Reactor (Pty) Ltd., Centurion, South Africa
Gao, Z.	Institute of Nuclear and New Energy Technology, China
Geffraye, G.	CEA-Grenoble, France
Gougar, H.	Idaho National Engineering and Environmental Lab., United States of America
Jing, X.	Institute of Nuclear and New Energy Technology, China
Kadiroglu, O.	Nuclear Engineering Dept. Hacettepe University, Turkey
Kunitomi, K.	Japan Atomic Energy Research Institute, Oarai, Japan
Kuzavkov, N.	OKBM/Kurchatov Institute, Nizhny Novgorod, Russian Federation
Lee, Y.	Korea Atomic Energy Research Institute, Republic of Korea
Makihara, Y.	International Atomic Energy Agency, Austria
Methnani, M.	International Atomic Energy Agency, Austria
Marova, E.	OKBM/Kurchatov Institute, Nizhny Novgorod, Russian Federation
Mulder, E.	Pebble Bed Modular Reactor (Pty) Ltd, Centurion, South Africa
Murgatroyd, J.	AMEC NNC Limited, Cheshire, United Kingdom
Nakagawa, S.	Japan Atomic Energy Research Institute, Oarai, Japan
Noh, J.	Korea Atomic Energy Research Institute, Republic of Korea
Ohlig, U.	Research Centre Juelich (ISR), Germany
Pautz, A	Germany
Raepsaet, X.	CEA, France
Reitsma, F.	Pebble Bed Modular Reactor (Pty) Ltd, Centurion, South Africa
Sen, S.	Pebble Bed Modular Reactor (Pty) Ltd., Centurion, South Africa
Stainsby, R.	AMEC NNC Limited, United Kingdom
Sukharev, Y.	OKBM/Kurchatov Institute, Nizhny Novgorod, Russian Federation

Sun, Y.	Institute of Nuclear and New Energy Technology, China
Tachibana, Y.	High Temperature Engineering Test Reactor, Japan Atomic Energy Research Institute, Japan
Turkcan, E.	Delft University of Technology (IRI), Netherlands
Van Heerden, G.	Pebble Bed Modular Reactor (Pty) Ltd., Centurion, South Africa
Van Niekerk, W.	North-West University, Noordbrug, South Africa
Van Ravenswaay, J.	M-Tech Industrial (Pty) Ltd., Potchefstroom, South Africa
Wallace, E.	Pebble Bed Modular Reactor (Pty) Ltd, Centurion, South Africa
Yamashita, K.	High Temperature Engineering Test Reactor, Japan Atomic Energy Research Institute, Japan
Zafirakis-Gomez, M.	International Atomic Energy Agency, Vienna, Austria

RESEARCH COORDINATION MEETINGS

24–28 August 1998	International Atomic Energy Agency, Vienna, Austria
18–22 October 1999	Institute of Nuclear Energy Technology, Beijing, China
12–16 March 2001	Japan Atomic Energy Research Institute, Oarai, Japan
30 September–4 October 2002	International Atomic Energy Agency, Vienna, Austria
6–10 December 2004	International Atomic Energy Agency, Vienna, Austria
5–9 September 2005	International Atomic Energy Agency, Vienna, Austria
25–29 September 2006	International Atomic Energy Agency, Vienna, Austria

RELATED IAEA PUBLICATIONS

1996	INTERNATIONAL ATOMIC ENERGY AGENCY, Design and Development of Gas Cooled Reactors with Closed Cycle Gas Turbines, IAEA-TECDOC-899, IAEA, Vienna (1996).
1996	INTERNATIONAL ATOMIC ENERGY AGENCY, Graphite Moderator Lifecycle Behaviour, IAEA-TECDOC-901, IAEA, Vienna (1996).
1997	INTERNATIONAL ATOMIC ENERGY AGENCY, Non-electric Applications of Nuclear Energy, IAEA-TECDOC-923, IAEA, Vienna (1997).
1997	INTERNATIONAL ATOMIC ENERGY AGENCY, Fuel Performance and Fission Product Behaviour in Gas Cooled Reactors, IAEA-TECDOC-978, IAEA, Vienna (1997).
1997	INTERNATIONAL ATOMIC ENERGY AGENCY, High Temperature Gas Cooled Reactor Development, IAEA-TECDOC-988, IAEA, Vienna (1997).
1999	INTERNATIONAL ATOMIC ENERGY AGENCY, Hydrogen as an Energy Carrier and Its Production by Nuclear Power, IAEA-TECDOC-1085, IAEA, Vienna (1999).
2000	INTERNATIONAL ATOMIC ENERGY AGENCY, Irradiation Damage in Graphite Due to Fast Neutrons in Fission and Fusion Systems, IAEA-TECDOC-1154, IAEA, Vienna (2000).
2001	INTERNATIONAL ATOMIC ENERGY AGENCY, Heat Transport and Afterheat Removal for Gas Cooled Reactors under Accident Conditions, TECDOC-1163, IAEA, Vienna (2001).
2001	INTERNATIONAL ATOMIC ENERGY AGENCY, Current Status and Future Development of Modular High Temperature Gas Cooled Reactor Technology, IAEA-TECDOC-1198, IAEA, Vienna (2001).
2001	INTERNATIONAL ATOMIC ENERGY AGENCY, Safety Related Design and Economic Aspects of HTGRs, IAEA-TECDOC-1210, IAEA, Vienna (2001).
2001	INTERNATIONAL ATOMIC ENERGY AGENCY, Gas Turbine Power Conversion Systems for Modular HTGRs, IAEA-TECDOC-1238, IAEA, Vienna (2001).
2001	INTERNATIONAL ATOMIC ENERGY AGENCY, Design and Evaluation of Heat Utilization Systems for the High Temperature Engineering Test Reactor, IAEA-TECDOC-1236, IAEA, Vienna (2001).
2001	INTERNATIONAL ATOMIC ENERGY AGENCY, Critical Experiments and Reactor Physics Calculations for Low Enriched High Temperature Gas Cooled Reactors, IAEA-TECDOC-1249, IAEA, Vienna (2001).

2003 INTERNATIONAL ATOMIC ENERGY AGENCY, Evaluation of High Temperature Gas Cooled Performance: Benchmark Analysis Related to Initial Testing of the HTTR and HTR-10, IAEA-TECDOC-1382, IAEA, Vienna (2003).



IAEA

International Atomic Energy Agency

No. 22

Where to order IAEA publications

In the following countries IAEA publications may be purchased from the sources listed below, or from major local booksellers. Payment may be made in local currency or with UNESCO coupons.

AUSTRALIA

DA Information Services, 648 Whitehorse Road, MITCHAM 3132
Telephone: +61 3 9210 7777 • Fax: +61 3 9210 7788
Email: service@dadirect.com.au • Web site: <http://www.dadirect.com.au>

BELGIUM

Jean de Lannoy, avenue du Roi 202, B-1190 Brussels
Telephone: +32 2 538 43 08 • Fax: +32 2 538 08 41
Email: jean.de.lannoy@infoboard.be • Web site: <http://www.jean-de-lannoy.be>

CANADA

Bernan Associates, 4501 Forbes Blvd, Suite 200, Lanham, MD 20706-4346, USA
Telephone: 1-800-865-3457 • Fax: 1-800-865-3450
Email: customercare@bernan.com • Web site: <http://www.bernan.com>

Renouf Publishing Company Ltd., 1-5369 Canotek Rd., Ottawa, Ontario, K1J 9J3
Telephone: +613 745 2665 • Fax: +613 745 7660
Email: order.dept@renoufbooks.com • Web site: <http://www.renoufbooks.com>

CHINA

IAEA Publications in Chinese: China Nuclear Energy Industry Corporation, Translation Section, P.O. Box 2103, Beijing

CZECH REPUBLIC

Suweco CZ, S.R.O., Klecakova 347, 180 21 Praha 9
Telephone: +420 26603 5364 • Fax: +420 28482 1646
Email: nakup@suweco.cz • Web site: <http://www.suweco.cz>

FINLAND

Akateeminen Kirjakauppa, PO BOX 128 (Keskuskatu 1), FIN-00101 Helsinki
Telephone: +358 9 121 41 • Fax: +358 9 121 4450
Email: akatilauk@akateeminen.com • Web site: <http://www.akateeminen.com>

FRANCE

Form-Edit, 5, rue Janssen, P.O. Box 25, F-75921 Paris Cedex 19
Telephone: +33 1 42 01 49 49 • Fax: +33 1 42 01 90 90
Email: formedit@formedit.fr • Web site: <http://www.formedit.fr>

Lavoisier SAS, 145 rue de Provigny, 94236 Cachan Cedex
Telephone: + 33 1 47 40 67 02 • Fax +33 1 47 40 67 02
Email: romuald.verrier@lavoisier.fr • Web site: <http://www.lavoisier.fr>

GERMANY

UNO-Verlag, Vertriebs- und Verlags GmbH, Am Hofgarten 10, D-53113 Bonn
Telephone: + 49 228 94 90 20 • Fax: +49 228 94 90 20 or +49 228 94 90 222
Email: bestellung@uno-verlag.de • Web site: <http://www.uno-verlag.de>

HUNGARY

Librotrade Ltd., Book Import, P.O. Box 126, H-1656 Budapest
Telephone: +36 1 257 7777 • Fax: +36 1 257 7472 • Email: books@librotrade.hu

INDIA

Allied Publishers Group, 1st Floor, Dubash House, 15, J. N. Heredia Marg, Ballard Estate, Mumbai 400 001,
Telephone: +91 22 22617926/27 • Fax: +91 22 22617928
Email: alliedpl@vsnl.com • Web site: <http://www.alliedpublishers.com>

Bookwell, 2/72, Nirankari Colony, Delhi 110009
Telephone: +91 11 23268786, +91 11 23257264 • Fax: +91 11 23281315
Email: bookwell@vsnl.net

ITALY

Libreria Scientifica Dott. Lucio di Biasio "AEIOU", Via Coronelli 6, I-20146 Milan
Telephone: +39 02 48 95 45 52 or 48 95 45 62 • Fax: +39 02 48 95 45 48
Email: info@libreriaaeiou.eu • Website: www.libreriaaeiou.eu

JAPAN

Maruzen Company Ltd, 1-9-18, Kaigan, Minato-ku, Tokyo, 105-0022
Telephone: +81 3 6367 6079 • Fax: +81 3 6367 6207
Email: journal@maruzen.co.jp • Web site: <http://www.maruzen.co.jp>

REPUBLIC OF KOREA

KINS Inc., Information Business Dept. Samho Bldg. 2nd Floor, 275-1 Yang Jae-dong SeoCho-G, Seoul 137-130
Telephone: +02 589 1740 • Fax: +02 589 1746 • Web site: <http://www.kins.re.kr>

NETHERLANDS

De Lindeboom Internationale Publicaties B.V., M.A. de Ruyterstraat 20A, NL-7482 BZ Haaksbergen
Telephone: +31 (0) 53 5740004 • Fax: +31 (0) 53 5729296
Email: books@delindeboom.com • Web site: <http://www.delindeboom.com>

Martinus Nijhoff International, Koraalrood 50, P.O. Box 1853, 2700 CZ Zoetermeer
Telephone: +31 793 684 400 • Fax: +31 793 615 698
Email: info@nijhoff.nl • Web site: <http://www.nijhoff.nl>

Swets and Zeitlinger b.v., P.O. Box 830, 2160 SZ Lisse
Telephone: +31 252 435 111 • Fax: +31 252 415 888
Email: info@swets.nl • Web site: <http://www.swets.nl>

NEW ZEALAND

DA Information Services, 648 Whitehorse Road, MITCHAM 3132, Australia
Telephone: +61 3 9210 7777 • Fax: +61 3 9210 7788
Email: service@dadirect.com.au • Web site: <http://www.dadirect.com.au>

SLOVENIA

Cankarjeva Založba d.d., Kopitarjeva 2, SI-1512 Ljubljana
Telephone: +386 1 432 31 44 • Fax: +386 1 230 14 35
Email: import.books@cankarjeva-z.si • Web site: <http://www.cankarjeva-z.si/uvvoz>

SPAIN

Díaz de Santos, S.A., c/ Juan Bravo, 3A, E-28006 Madrid
Telephone: +34 91 781 94 80 • Fax: +34 91 575 55 63
Email: compras@diazdesantos.es, carmela@diazdesantos.es, barcelona@diazdesantos.es, julio@diazdesantos.es
Web site: <http://www.diazdesantos.es>

UNITED KINGDOM

The Stationery Office Ltd, International Sales Agency, PO Box 29, Norwich, NR3 1 GN
Telephone (orders): +44 870 600 5552 • (enquiries): +44 207 873 8372 • Fax: +44 207 873 8203
Email (orders): book.orders@tso.co.uk • (enquiries): book.enquiries@tso.co.uk • Web site: <http://www.tso.co.uk>

On-line orders

DELTA Int. Book Wholesalers Ltd., 39 Alexandra Road, Addlestone, Surrey, KT15 2PQ
Email: info@profbooks.com • Web site: <http://www.profbooks.com>

Books on the Environment

Earthprint Ltd., P.O. Box 119, Stevenage SG1 4TP
Telephone: +44 1438748111 • Fax: +44 1438748844
Email: orders@earthprint.com • Web site: <http://www.earthprint.com>

UNITED NATIONS

Dept. I004, Room DC2-0853, First Avenue at 46th Street, New York, N.Y. 10017, USA
(UN) Telephone: +800 253-9646 or +212 963-8302 • Fax: +212 963-3489
Email: publications@un.org • Web site: <http://www.un.org>

UNITED STATES OF AMERICA

Bernan Associates, 4501 Forbes Blvd., Suite 200, Lanham, MD 20706-4346
Telephone: 1-800-865-3457 • Fax: 1-800-865-3450
Email: customercare@bernan.com • Web site: <http://www.bernan.com>

Renouf Publishing Company Ltd., 812 Proctor Ave., Ogdensburg, NY, 13669
Telephone: +888 551 7470 (toll-free) • Fax: +888 568 8546 (toll-free)
Email: order.dept@renoufbooks.com • Web site: <http://www.renoufbooks.com>

Orders and requests for information may also be addressed directly to:

Marketing and Sales Unit, International Atomic Energy Agency

Vienna International Centre, PO Box 100, 1400 Vienna, Austria
Telephone: +43 1 2600 22529 (or 22530) • Fax: +43 1 2600 29302
Email: sales.publications@iaea.org • Web site: <http://www.iaea.org/books>

INTERNATIONAL ATOMIC ENERGY AGENCY
VIENNA
ISBN 978-92-0-137610-7
ISSN 1011-4289